RTD-TDR-63-4197, Vol. I
Part I

Proceedings of Symposium on Aeroelastic & Dynamic Modeling Technology

23-24-25 SEPTEMBER 1963
DAYTON, OHIO

RESEARCH & TECHNOLOGY DIVISION

RTD

AIA

AEROSPACE INDUSTRIES ASSOCIATION

MARCH 1964

NOTICES

When Government drawings, specifications, or other data are used for any purpose other than in connection with a definitely related Government procurement operation, the United States Government thereby incurs no responsibility nor any obligation whatsoever; and the fact that the Government may have formulated furnished, or in any way supplied the said drawings, specifications, or other data, is not to be regarded by implication or otherwise as in any manner licensing the holder or any other person or corporation, or conveying any rights or permission to manufacture, use, or sell any patented invention that may in any way be related thereto.

Qualified requesters may obtain copies of this report from the Defense Documentation Center (DDC), (formerly ASTIA), Cameron Station, Bldg. 5, 5010 Duke Street, Alexandria, Virginia, 22314.

This report has been released to the Office of Technical Services, U.S. Department of Commerce, Washington 25, D. C., in stock quantities for sale to the general public.

Copies of this report should not be returned to the Research and Technology Division, Wright-Patterson Air Force Base, Ohio, unless return is required by security considerations, contractual obligations, or notice on a specific document.

500 - March 1964 - 162-34-657

B

FOREWORD

The Symposium on Aeroelastic and Dynamic Modeling Technology, sponsored by the Air Force Flight Dynamics Laboratory of the Research and Technology Division, Air Force Systems Command, in association with the Dynamics and Aeroelasticity Research Panel of the Aerospace Industries Association, was held in Dayton, Ohio, on 23-24-25 September 1963. The purposes of the Symposium were to: (a) review the state-of-the-art, (b) present the latest developments and applications for solution of current problems, (c) determine the maximum extent to which modeling techniques can be employed for efficient design and substantiation of full scale vehicle safety and reliability and (d) provide a basis for future applied research for aeroelastic and dynamic modeling technology. The symposium subject matter covers the theory, design and testing of both static and dynamic elastic models used in the development of aircraft, missiles, aerospace vehicles and equipment.

The proceedings are arranged in two parts: Part I contains the unclassified papers grouped by subject as presented, and Part II contains the classified papers and is Confidential. The authors' names and company affiliation are given at the beginning of each paper.

An effort has been made to minimize errors and omissions, however, if any serious discrepancies are noted, they should be brought to the attention of Mr. M. H. Shirk, FDDS, AF Flight Dynamics Laboratory, WPAFB, Ohio. Necessary errata sheets will be prepared and distributed.

The success of the Symposium in attaining its purposes and the subsequent compilation of this report for wide distribution as a reference document were made possible by the fine contribution of the Symposium speakers, session chairmen and authors of the technical papers. The AFFDL and the AIA gratefully acknowledge these contributions and express their appreciation.

ABSTRACT

The unclassified proceedings of the Air Force Flight Dynamics Laboratory and Aerospace Industries Association Symposium on Aeroelastic and Dynamic Modeling Technology are presented in this report.

Modern day aerospacecraft requirements are calling more and more for systems which are greatly influenced by aero and thermoelastic effects. In line with this trend, model testing technology has been required to keep pace by advancing the state-of-the-art in the simulation of elastic, thermal, aerodynamic and dynamic effects. The objective of this symposium was to bring together the members of the scientific community who are intimately concerned with this area of endeavor, thereby promoting a mutual understanding of current developments and problem areas. The papers presented at the symposium were divided into appropriate technical area sub-groups and individual sessions were devoted to each. These sub-groups were: Theory and Design, Model Testing Techniques, Dynamic Loads and Aeroelastic Applications, and Structural Design Applications with two classified sessions on Aerospace Vehicle Applications and Aircraft Applications.

PUBLICATION REVIEW

The publication of this report does not constitute approval by the Air Force of the findings or conclusions contained herein. It is published only for the exchange and stimulation of ideas.

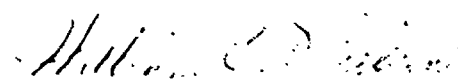

WILLIAM C. NIELSEN
Colonel, USAF
Symposium Chairman

TABLE OF CONTENTS

PART II PAGE

CLASSIFIED PROCEEDINGS
CONFIDENTIAL

SYMPOSIUM COMMITTEE ORGANIZATION

Symposia Director: Dr. John E. Keto, Chief Scientist

Symposium Chairman: Colonel William C. Nielsen, Director, AF Flight Dynamics Laboratory

Symposium Deputy Chairman: Howard A. Magrath, Chief, Vehicle Dynamics Division, AF Flight Dynamics Laboratory

Technical Committee:

Mr. E. F. Baird, Chairman, Grumman Aircraft Engineering Corp.
Mr. W. J. Mykytow, Co-Chairman, AFFDL
Mr. H. M. Davis, AFFDL
Mr. L. I. Mirowitz, McDonnell Aircraft Corp.
Mr. R. F. Hoener, AFFDL
Mr. L. A. Tolve, Lockheed Aircraft Company
Mr. M. H. Shirk, AFFDL
Mr. H. A. Wood, AFFDL
Mr. W. G. Williams, AFFDL

Arrangements Committee:

Mr. A. J. Cannon, Executive Manager, RTD
Mr. J. P. Reese, Executive Manager, AIA
Mrs. F. R. Dempsey, Secretary
Mr. J. M. Kelly, Registration and Security Manager
Mr. I. L. Schwartz, Protocol
Mr. R. C. Kahelin, Financial Manager
Mr. R. Maltby, Publicity Manager
Mr. C. High, Press Relations Manager
Mr. C. E. Sondergelt, Printing Manager
Miss M. McMurtrie, Technical Publications Manager
Mr. T. F. Cherwin, Visual Communications Manager
S/Sgt. C. R. Knifley, Chief Projectionist
Mr. R. E. Hendrickson, Transportation Manager
Capt. William F. Bocich, Senior Escort Officer

OPENING REMARKS

by

Colonel William C. Nielsen

Director, AF Flight Dynamics Laboratory

Gentlemen:

I am Colonel Nielsen, Chairman of this "Symposium on Aeroelastic and Dynamic Modeling Technology" and Director of the new Air Force Flight Dynamics Laboratory. This Laboratory is part of the Research and Technology Division of Air Force Systems Command.

It is my distinct pleasure to open this meeting of distinguished scientists and engineers who have convened to discuss an important and timely subject. Moreover, it is most fitting that sponsorship of this meeting exemplifies the very high degree of cooperation between the Government and the Aerospace Industry that is so necessary to promote progress in research, applications and aerospace vehicle development.

This symposium will be conducted in two parts. The first unclassified portion, consisting of four sessions here at this hotel, is sponsored jointly by the Dynamics and Aeroelasticity Research Panel of the Aerospace Industries Association and the Air Force Flight Dynamics Laboratory. Two Confidential sessions will convene at Wright-Patterson Air Force Base on Wednesday. These Classified sessions are sponsored by the Flight Dynamics Laboratory because of administrative reasons but the AIA also contributed significantly to this portion of the program.

Meetings on theoretical contributions to the state-of-the-art are held rather frequently. The remarkable contributions of theory and analyses are thus comparatively well disseminated. While the usefulness of the model is well recognized and while, in many cases, the payoffs from the model approach have been greater than analytical efforts and full scale tests, nevertheless, the state-of-the-art in dynamic model simulation has not received in technical meetings an attention which is justly proportional to its importance and contribution. Thus, the sponsoring groups considered it most desirable, particularly from the standpoint of greater future impact, to hold this meeting on modeling technology and to discuss where models could return maximum information on aerospace feasibility, safety, reliability and efficiency in the area of stability and control, structural dynamics and aerothermoelasticity.

As you know, the supersonic transport development is being directed by the Federal Aviation Agency with contributions from the Air Force, the National Aeronautics and Space Administration and many Aerospace Industry members. Experimental model efforts will contribute significantly to the development of this advanced aircraft.

One of our distinguished guests will be Mr. Gordon Bain, Deputy Administrator for Supersonic Transport Development of the FAA. He will be our banquet speaker tomorrow night and will present an exceedingly interesting discussion on the Supersonic Transport. I urge all of you to attend.

Now, I am most pleased to place you in the hospitable hands of our official welcomer, Mr. Peter Murray, Assistant for Research and Technology, Office of the Deputy Commander/Research and Engineering.

WELCOME ADDRESS

by

Peter R. Murray

Assistant for Research and Technology

Thank you, Colonel Nielsen. Gentlemen, it is indeed a pleasure for me to welcome you to this Symposium on Aeroelastic and Dynamic Modeling Technology on behalf of its co-sponsors, the Aerospace Industries Association of America and the Research and Technology Division of the Air Force Systems Command.

We of the RTD, as our Division is referred to, believe strongly in the worth of the Symposia which we hold from time to time. Our job for today and for tomorrow is to formulate and then accomplish programs of research and investigation that will advance the state-of-the-art in all of the aerospace disciplines. You have all, I am sure, heard it said before that we must do this in the most knowledgeable way we can so that we will obtain the best return on our committed dollars; but of equal importance today is that we must also obtain significant progress in a scientific and engineering sense on the investment of time and talent that these programs entail. Selectivity, then, becomes our hardest task and to do a good job here we need the assistance of the managers and experts of Industry, the Research Institutes, the Universities and our sister government agencies whom you represent.

I believe that the subject which you have chosen to explore in this Symposium on aeroelastic and dynamic modeling technology is of extreme importance not only to progress in flight vehicle design and development but also to the entire spectrum of research and development activity. Certainly, aeronautical engineering has always made extensive use of engineering modeling ever since the time of the Wright brothers when model tests in wind tunnels taught them not only how to design but also how to fly powered aircraft. An important forward step in modeling technology took place when the complex problems of structural dynamics yielded to the techniques of dynamic models of wings, tails, control surfaces and even entire aircraft and afforded an engineering check on the flutter safety of aircraft. The record of the prevention of catastrophic flutter failures in all classes of aircraft to date is indeed an excellent one, a tribute to the skills and dedication of all of you. But even more complex problems are pressing on us today.

It has never been a simple matter even to scale models for aeroelastic effects; and the present necessity to provide thermal duplication is a major area of investigation in itself. It has been

concluded that correct scaling between a model and prototype for all the aerothermoelastic parameters requires a scale ratio of unity. This is a discouraging result, but progress by scale modeling is being made nevertheless by the judicious selection of test parameters and test procedures combined with analytical approaches. This enables extrapolation to the full scale with some degree of confidence. But depending upon how we approach the many problems involved here, there will be a tremendous impact on the utilization of our present test facilities, the design of our future test facilities and the relative role that flight testing will play. A more important and significant area for discussion and consultation would be difficult to imagine.

The great advantages of testing of scaled models, whether for the acquisition of scientific data or for development of design criteria, are being realized on many problems in aeronautical engineering. This is itself a significant sign of progress and it is most appropriate that this Symposium has gathered together experts in structural loadings, stability and control, sonic fatigue, space vehicle entry, photomechanics, orbital mooring and others. It is by such an interdisciplinary approach that we can best learn one from another, pool our knowledge and thus effectively exploit modeling technology.

This Symposium, then, presents to you many challenging problems, the solution of which will have a great impact on the entire R&D household. I am, therefore, together with the sponsors, deeply gratified at your enthusiastic response to our invitation to participate in this Symposium. In extending a heartfelt welcome, I also wish for you a successful and rewarding meeting.

KEYNOTE ADDRESS

by

Robert J. Lutz

Aerospace Industries Association

I am honored to represent the Aerospace Industries as your keynote address speaker. When I contemplate a keynote address, I recall the image of a distinguished political figure delivering the keynote address to a nominating convention. Such speeches are made with great fervor and extol in clarion tones the virtues of one party and the deficiencies of the opposition. Such speeches are highly emotional and no doubt serve to provide a spirited sense of direction for all of the speakers that follow. As I understand it, this is the purpose of a keynote address.

Our symposium is not a political convention, nor am I a politician. Ours is a technical meeting--a serious technical meeting held to review the state-of-the arts as they affect structural dynamics and, in particular, modeling techniques. Furthermore, we are concerned with the application of dynamic modeling to the solution of complex problems involved in design and the development of large high-performance aerospace vehicles. In the context of a technical symposium, it's very difficult to deliver a speech having an emotionally charged message.

But, exciting or not, there are challenges that each of us as members of the technical community should consider. These are the challenges that confront the growth and expansion of our technology. Those of us who work in the technical fields and who have been trained as engineers or scientists regard technical progress as being a good thing. The history of our civilization shows this. Technical developments have made life fuller and better in most respects and, certainly, more comfortable. We accept these to be facts.

But here are some forces that are attempting to slow or stop technological growth. In nearly every popular journal or periodical, you will find the well-expressed concern that technical progress is now threatening humanity. You will find this expression ranging from the fear of total destruction of civilization due to radiological hazards connected with nuclear programs on one hand, to the fear that man will be displaced by the machine; that the computer age will arrive; that man will become obsolete and be relegated to a parasitic role.

But over and above these natural fears of the future, there is an increasing concern with the economic costs of our technical progress. How shall it be paid for? Is the technical advancement

truly worthwhile? Does it produce a better, or a more simple, or a more useful product? These are the questions that are asked not only by the man on the street but by his representatives in government which, as you are well aware, funds a major portion of our research and development program. These questions are likewise asked by men in business, managers who are responsible for the activities of the corporations that conduct major business of our nation.

So we must face up to the fact that we do have a problem which may have serious impact upon our technical progress. A part of our problem can be charged to indifference. Perhaps this is a strong word, but let me explain. As technical people, we are apt to lose touch with the lay world. We are like the monks of medieval times. We tend to associate so consistently with people who speak our own technical language and who share our own purposes and beliefs that we fail to consider the need to be understood by the uninitiated lay world. In fact, there are instances where the isolation can be so effective that technical people working within one specific field are unable to communicate with associates in other fields. I am sure that each of us from time to time has experienced the frustration of attempting to read an over-sophisticated paper in which the author succumbs to the temptation to use highly specialized terminology to express simple ideas.

The failure of our technical community to woo and win the understanding of the layman frequently extends into industry as failure to win the understanding of management. There are many programs proposed to management by which it is understandably perplexed not only by the cost, but by the rather inconclusive promises of gain or purpose. As a result, we often find that the technical research worker rarely believes he has sufficient resources in terms of men or facilities to accomplish his task; while the manager on the other hand is at a loss to understand his Research Department's insatiable appetite for continuing and growing of support.

So as incongruous as it may appear, we the flag bearers of our technological advancement, and that includes the whole of us in this assembly, have the job of selling the idea of technical growth and its benefits. We must accept the responsibility for attempting to win the wholehearted support and understanding of the taxpayer and of the various agencies who have a responsibility in administering our programs whether within the government or within industry. This understanding can only be gained by our efforts to present our objectives in clear and simple terms--to honestly estimate costs and to attempt to assess the probability of success.

This communication of understanding most certainly extends to the subject we are going to discuss in this symposium. The appreciation of the importance played by structural dynamics in modern

design is still relatively restricted. The subject did not appear in the curriculums of our engineering schools until the period following the end of World War II, so that there are many in the industry who have only a passing and superficial feel for the importance that dynamics plays in the design of our modern vehicles. Add to this the concept of dynamic modeling and you can appreciate that management may be mystified at some of the proposals that are from time to time advanced for its consideration.

In light of these thoughts, I hope that some of the papers delivered today and throughout the rest of this symposium will attempt to emphasize the practical importance of dynamic considerations and the use of modeling techniques in the development of high performance aerospace vehicles. But more than that, I hope that this symposium and others to follow can serve as vehicles to further understanding not only between ourselves, but with our non-technical supporters--the taxpayers.

SESSION I

THEORY AND DESIGN

Chairman: Dr. Raymond L. Bisplinghoff
Office of Advanced Research and
Technology, NASA

OPENING REMARKS OF SESSION I

by

Dr. Raymond L. Bisplinghoff

It is a distinct honor to chair this first session on Theory and Design. We can observe, since more than 300 of our colleagues are present, that we are dealing with a very popular subject. As youngsters we all played with toys and many of us built models. As adult scientists and engineers we spend much of our time building models. In fact, our success often depends upon our ability to devise mathematical and physical models. The former can be used to exploit the laws of mathematics and the latter the laws of physics. Bohr's classical hydrogen atom is an example of a physical model devised by a scientist to study the microscopic world. Many examples can be cited of models employed by engineers to study the macroscopic world.

Development of the field of aeronautical engineering has been profoundly influenced by models. We are told of an ornithopter model constructed by Leonardo da Vinci. Samuel Pierpont Langley demonstrated heavier than air flight for the first time by means of a very successful steam driven model airplane. He was unfortunately unable to translate model technology into that of a successful man-carrying machine. Flying and wind tunnel models of various kinds were employed usefully to various degrees by Alexander Graham Bell, Otto Lilienthal, and the Wrights.

The wind tunnel model, at first, and later the dynamic model became important development tools for the aeronautical engineer. Today, the space program offers a vast potential for increased employment of a wide variety of models. The high costs of full scale prototypes demand that we learn as much as possible about these prototypes prior to their construction. The NASA is taking the first steps in the dynamic modeling of large boosters. Our ability to construct a gaseous core nuclear rocket will depend upon simulation by means of hydrodynamic models of the flow pattern of the fissionable material in the gaseous phase. Modeling techniques may be employed to advantage in both reentry and space vehicles.

Regardless of which model is employed, there exists the problem of how model behavior is extrapolated to full-scale. Nature rarely permits full simulation, and in most cases we must be content with limited purpose models. The simplicity of the reduced frequency scaling parameter of potential flow flutter will rarely be equaled in the more complex problems which lie ahead.

In this morning session we will be privileged to hear of new applications of dynamic modeling and of the similitude requirements which relate to them.

ABSTRACT

DYNAMIC MODELING, ITS PAST AND FUTURE

by

Dale E. Cooley and Robert F. Cook

In the field of aeroelastic instabilities, experimental results obtained from dynamic models have been a vital source of information needed to verify the accuracy of prediction methods, establish design criteria and to determine the structural adequacy of flight vehicles. Recently, the use of modeling for vibration and sonic fatigue prediction has been investigated and results indicate that modeling may be a valuable technique. This paper covers, first, the historical background of dynamic modeling and the evolution to the current state-of-the-art of modeling methods and uses. A review and discussion of recent research efforts dealing with various modeling problems, including flutter models for inflatable structures, high angles-of-attack, high temperature environments, vibration and sonic fatigue prediction are presented. Also included are remarks concerning future requirements and problem areas where research is needed to assure the availability of adequate modeling technology for the potential dynamic problems of advanced flight vehicles.

LIST OF ILLUSTRATIONS

DYNAMIC MODELING - ITS PAST AND FUTURE

Dale E. Cooley and Robert F. Cook
AF Flight Dynamics Laboratory

INTRODUCTION

One of the oldest hobbies of mankind is the making and use of models. According to the Encyclopaedia Britannica (Ref. 1) the early Egyptians believed that the human spirit after death could travel on land, but required assistance to cross water. Therefore, a small model boat called a "Spirit Ship" was buried with their dead to help their soul across the troubled river Nile. Others believed models could frighten away evil spirits. We might say that even today we use dynamic models to assist us across the troubled waters of aircraft design and to frighten away the evils of dynamic problems.

Leonardo de Vinci (1452 - 1519) was an early pioneer of the science of flight. He made an intense study of the flight of birds for application of similarity methods for manned flights. According to his notes, (Ref. 2), he used a form of dynamic model to investigate principles or check-out theories. For example, Figure 1 shows an interesting sketch from his notes of a bird suspended from a bracket by means of a pulley which he used to restrain the bird to study its flying characteristics. This may have been one of the earliest flutter model studies. Dynamic modeling technology had its very early beginning in the three following areas:

Steady state aerodynamic models - Model aircraft were built back as far as Leonardo de Vinci, but models of manned aircraft began with Orville and Wilbur Wright in about 1899, (Ref. 3). The Wright brothers built a five foot wing span model to investigate the wing twisting principle for turning control. In about 1901, the Wright brothers built a wind tunnel and tested model wings to determine their flight characteristics. Since that time models have been used extensively to test the aerodynamic characteristics of all aircraft components such as wheels, nacelles, pods, wing as well as the complete aircraft configuration.

Structural models - The first scientific investigation of the resistance of solids to structural failure appears to have been about 1638 by the Italian genius, Galileo, who considered a beam built into a wall at one end and loaded by its own or applied weight, (Ref. 4). Since there was no known relation between load and displacement at the time, Galileo's inquiry did not give satisfactory results. This relation between stress and strain was experimentally discovered in England in 1660 by Robert Hooke and provided the foundation for the mathematical theory of elasticity including elastic vibrations. Some of the earliest correct, published accounts of experimental studies on the vibration of strings is credited to the Franciscan friar, Marin Mersenne about 1636, (Ref. 5). Mersenne measured the frequency of vibration of a long string and from this inferred the frequency of a short string of the same density and tension. This was apparently the first direct determination of the frequency of a musical note. Around 1755, Daniel Bernoulli worked on the various vibration modes of strings

and Lagrange developed theoretical methods for the solution of the vibrating string problem in 1759. Euler and Daniel Bernoulli conducted studies on the vibration of rods and bars around 1750. While the analytical solution of plates came much later, E.F.F. Chladni published in 1787 a description of his experimental work on plates using sand sprinkled on the vibrating plates to show nodal lines, (Ref. 5). The method of using sand to determine node lines on vibratory models is still widely used. Around 1900, the analytical work and observation of E. Mathieu and also, Lord Rayleigh contributed to the extension of vibration analytical methods from flat plates to curved plates and shells, (Ref. 4). These early investigations formed a basis for the structural dynamics investigations required for the intricate, lightweight structure used in aircraft.

Acoustic models - Acoustic modeling originated shortly after 1900 by Sabine and Watson (Ref. 6) in the field of Architectural Acoustics. Two dimensional models of auditoriums were excited by noise sources and the wave propagation recorded by Schlieren photography. Water models were also used in architectural work. These models consisted of a shallow tray having rectangular rods to form the shape to be studied, filled with water. An exciter, usually a small plunger mounted on a variable speed crank, was used to disturb the water surface, thus producing waves much like that from a stone thrown in a pond. The wave propagation and reflections around complex objects could then be studied, (Figure 2).

REQUIREMENT FOR VEHICLE DYNAMIC MODELS

Any aircraft must of necessity be of light construction, and, therefore, is flexible and subject to deformations. As a result, dynamic problems in aeroelasticity, vibration, and related dynamic areas occurred early in aircraft history.

Adequate prediction and control of structural dynamic problems is an important consideration in the development of flight vehicles because of the need for higher reliability and more efficient use of materiel to achieve the performance desired. Some of these dynamic problems which have been experienced in the development of flight vehicles are:

1. Lifting Surface Flutter

2. Control Surface Buzz

3. Panel and Shell Flutter

4. Missile body bending - thrust vector instabilities

5. Sonic Fatigue

6. Excessive Noise and Vibration

7. Landing Impact Loads

8. Excessive response in resonant vibration modes due to buffet, gusts, exhaust noise, or other random aerodynamic forces.

These dynamic problems are very complex phenomena involving many parameters such as inertia forces, damping forces, aerodynamic loading, noise pressures, elastic forces, gravitational forces and control system inputs. Because of this

complexity, the theoretical treatment is often lacking or inadequate to represent and predict these phenomena. Experimental investigations have thus become fundamental in the study and treatment of these dynamic phenomena. Models are often used in tests because testing of full scale specimens are often impractical because of equipment limitations, expense of testing large specimens, lack of test facilities, etc. Therefore, much work has been done in developing the now generally accepted techniques for scaled dynamic modeling. Today the use of dynamic models has become a vital part of most investigations of dynamic phenomena to assure adequate design and flight safety for flight vehicles. Some of the important uses of dynamic models are:

1. Provide guidance for the development or verification of useful theories by pointing out important parameters, and trends.

2. Evaluate immediate practical problems and fixes where theory is not yet dependable.

3. Allow "proof-tests" of final vehicle designs to assure absence of dynamic problems. This depends upon validity of the model which is not always known. In some cases, such as missiles, a model is the only vehicle available for test.

When models are used to investigate dynamic problems rather than the actual flight vehicle in the true environment, some assumptions or approximations may need to be made. Great care must be taken in order to achieve results on a reduced scale dynamic model which will have application to the full-scale actual vehicle. A general similarity analysis between the dynamic model test conditions and full-scale or prototype conditions will provide a set of many parameters and variables which lead to various conflicting model requirements which would at first appear to be hopeless. It is far from easy to obtain model results which are truly representative of the full scale phenomena. Clearly many compromises must be made. But the primary and secondary parameters which must be similar or proportional between model and full scale vehicle can be established by careful attention to the physical phenomena to be investigated, the environmental conditions and the vehicle characteristics. These principles of similarity for dynamic models have been evolved over many years of research and development work and some are discussed in detail in References 7, 8 and 9. In general, the broad requirements for dynamic models are as follows:

1. Geometric similarity (for establishing model scale and also shape where aerodynamics are important).

2. Similarity of distribution of stiffness and of restraints. In general, model and prototype should have similarity in recurrent frequencies and mode shapes for those vibration modes which can influence the phenomena.

3. Similarity of the ratio of stiffness to dynamic pressure for flutter tests. $\frac{E}{\frac{1}{2}\rho V^2}$

4. Similarity of mass-altitude parameter, μ. (which governs material density to air density).

5. Similarity of Mach number if compressibility effects are important to aerodynamic loads.

6. Similarity of Reynolds number where flow separation or boundary layer or other viscous flow effects are significant.

7. Where thermal effects are important many additional requirements must be met such as similarity of temperature distribution, thermal strains, and often structural details such as joints must be accurately simulated.

8. Similarity of the spatial distribution, level and appropriate frequency spectrum in the noise field for sonic fatigue tests.

APPLICATIONS OF DYNAMIC MODELS

Aeroelastic phenomena such as flutter are among the most spectacular and dangerous dynamic phenomena facing the aircraft designer. Dynamic problems in aeroelasticity, which involve the aircraft structural deformations and aerodynamic forces date back to the early days of World War I when control surface flutter became wide spread. The flutter oscillations were caused by the interaction of the motion of the surface with the induced, destabilizing aerodynamic forces. During World War I, several cases occurred where flutter caused the ailerons, and in severe cases portions of the wings, to break and tear off, (Ref. 10). Model tests were used to study these early flutter problems and to establish design requirements which define the mass needed ahead of the control surface hinge line to decouple the modes of vibration and thus prevent flutter. In this early stage of flutter investigation experimental results were generally relied upon because the very early theoretical work was usually inadequate to represent the aerodynamic oscillation forces.

The early biplanes, with their wing bracing, had a relatively stiff structure and serious wing flutter problems were generally avoided. However, as the speed increased, for even those early days, the flutter problem began to appear in the late 1920's and early 1930's.

An example of the model work of this period is that by Perring of Britain (Ref. 11 and 12) involving wind tunnel model tests of the wing of a single seater biplane. The model was a semispan bi-wing mounted in a five foot wind tunnel as shown in Figure 3. The experiments included an extensive investigation of aileron parameters such as viscous damping, inertia; wing mass parameters such as struts, and quantity of fuel in the tank. Some simple fuselage inertia parameters were simulated although elastic effects of the fuselage were not simulated. This type of test provided useful parameter trends which gave insight into the flutter mechanism and verified analytical results.

In Germany some unconventional biplane designs experienced flutter difficulties around 1930 such as the He60 (Ref. 10). The aircraft is shown in Figure 4. The lower wing was braced against floats, but there was no bracing between the upper and lower wings. Also, steel was used in the spar rather than wood. Since the ratio of elasticity to strength was lower for steel than the wood, the wing had lower frequencies for the same strength design. Therefore, the upper wing was relatively flexible and in addition the aileron system was not balanced. In an attempt to reach the design diving speed of about 227 miles/hour the airplane experienced dangerous wing flutter at about 215 miles/

hour and crashed as a result of a torn upper wing.

Two dynamically similar models were designed and built of 1:5.6 scale to determine the cause of the accident and to evaluate structural changes in the wing to prevent flutter. Whereas, most early flutter model tests were to study trends of parameter variations, great care was taken during this model investigation to obtain the reduced frequency, parameter $\frac{b\omega}{V}$, similar to the full-scale airplane for nearly complete dynamic similarity. The reduced frequency is a ratio of the product of the wing semichord, b, and wing torsional frequency, ω, to the forward velocity. Such similarity between model and prototype is required for flutter models today.

During the 1930-1940 time period the work of several scientists such as Glauert (Ref. 13), Duncan and Collar (Ref. 14) in England, and Kussner (Ref. 15 and 16) in Germany and by T. Theodorsen (Ref. 17) in the United States, and others, provided the improved unsteady aerodynamic theoretical methods for treating and understanding the dynamic flutter phenomena. A series of tables of unsteady aerodynamic coefficients computed from the complex theories, along with suggested procedures for flutter analyses, was published by Wright Field in Air Force Technical Report 4798 "Application of Three Dimensional Flutter Theory to Aircraft Structures" (Ref. 18). This report became the handbook for conducting flutter analyses for several years.

With these analytical tools it was possible to obtain a better understanding of the flutter phenomena and to predict potential flutter problems in the design of aircraft. With these theories, corrective steps could be undertaken in most cases, to prevent or correct problems. However, unconventional aircraft such as the Vultee XP-54 which appeared about 1942 provided some unorthodox flutter problems. This fighter airplane had a pusher propulsion system on the aft fuselage. Twin booms extended aft from the wing to support the horizontal and vertical tails. Because of its unusual design a plastic replica flutter model of the airplane was specified by the Air Force and built and tested by Vultee. This flutter model is shown in Figure 5. An elevator flutter problem was detected during the wind tunnel tests and corrections prevented this problem on the airplane. This model cost about $25,000.

The XB-35 flying wing with its 30° wing sweep also provided an unconventional problem in flutter predictions for which the aerodynamic theory was not adequate. A complete airplane flutter model shown in Figure 6 was constructed by modeling each part and tested in the 20 foot wind tunnel at Wright Field about 1945. These tests showed the airplane should be free from flutter and extensive flight flutter tests were not needed.

Other complexities in design, such as the flexibilities of the pylon mounted engines began to appear on aircraft. The XB-47 had a highly swept wing and pylon mounted engines. Flutter model tests were therefore required by the Air Force. The model tested by The Boeing Company was essentially free flying on a rod in the wind tunnel providing good representation of the actual flight characteristics, (Figure 7). The flexibilities of these complex designs such as the B-47, B-52 and larger modern jet transport aircraft provided many dynamic problems which have been resolved and safety verified by flutter model tests in the wind tunnel. A B-52 flutter model being tested in the wind tunnel is shown in Figure 8.

Around 1950 flight at sonic speeds became possible with improved aerodynamic and propulsion techniques. Compressibility effects on the unsteady aerodynamic forces in the transonic speed range generally have a detrimental effect on flutter stability and theoretical flutter prediction methods were not available for this speed range. Also, the thin wings for high speed aircraft had lower stiffness levels. Therefore, flutter model tests were used extensively to establish stiffness requirements for preventing flutter at transonic and low supersonic speeds.

About 1950 when transonic wind tunnels suitable for flutter testing were very scarce some flutter model tests were conducted by the ASD on rocket sleds (Figure 9), and on the wing of an F-80 aircraft up to about M = 1, (Figure 10). Free flight rocket models have also been used for high speed flutter model tests. Figure 11 shows a B-58 free flight flutter model on a rocket launcher. Around 1957, Cornell Aeronautical Laboratory (Ref. 19) completed a research program in their transonic wind tunnel sponsored by the Air Force to carefully and systematically define flutter boundaries in the Mach number range up to about 1.2, for straight, swept and delta planforms. The models used a lightweight plastic foam core covered with aluminum foil. This provided a lightweight model as required for dynamic similarity in the transonic wind tunnel. The transonic speed range in most cases continues to be critical from a stiffness standpoint for prevention of flutter and thus, much transonic wind tunnel modeling work is generally required for most new high speed vehicles.

The use of flutter models has provided design stiffness requirements and verified adequacy of design for most of the modern high speed aircraft. A very fine safety record has been established, in a large part due to the use of flutter models to verify adequacy of the design from a flutter safety standpoint. Big flutter problems which have been resolved by model tests include all-movable stabilizers, T-tails, and wings with suspended engines and stores. Aircraft which have used flutter models to verify safety and resolve problems early in the design include the F-100, F-101, F-104, F-105, B-52, B-58 and the X-15. Flutter model tests are also an important part of the B-70 flutter program including low speed, transonic and supersonic tests. Figure 12 shows the B-70 flutter model. Replica type model construction by scaling the important structural members was used to assure adequate simulation of the advanced structural designs and complex vibration modes.

The supersonic and hypersonic speed regimes are growing increasingly important for advanced vehicles. Extensive flutter model investigations have been conducted to extend flutter trends into the supersonic and hypersonic speed regimes. An example of this type of investigation is the work sponsored by the ASD with Massachusetts Institute of Technology to cover the Mach number range from 1.5 to 5.0. This was completed in 1959 (Ref. 20). Another with Cornell Aeronautical Laboratory covered the range 5 to 8 and was completed about 1961 (Ref. 21 and 22) and extended to M = 10 this year. At M = 10 the stagnation temperature was around 1400°F (to prevent liquidation in the air), so that the model must be very temperature resistant. The hypersonic models were constructed with a ceramic foam core with a fiberglass covering. The NASA has done some exploratory flutter model work at about M = 15 in a new facility at Langley which uses helium as a test medium. With helium, stagnation temperatures can be kept lower, avoiding many thermal problems with the models. These data indicate the supersonic and hypersonic speed regimes will generally require less stiffness to prevent flutter than the transonic speed regime. But for the very lightweight

structural designs of advanced vehicles and the high temperature caused by aerodynamic heating at these speeds, these high speed regimes will have to be carefully investigated for advanced systems.

An Air Force sponsored program to determine the effects of angle of attack on flutter at supersonic and hypersonic speeds with North American Aviation, Columbus Division has been recently completed. The first phase covered the Mach number range from 1.0 to 5.0 and is reported in Ref. 23. The second phase from M = 5 to 8 was recently completed and will be reported soon. Some of the results are shown in Figure 13 and indicate that over the Mach number range tested up to 8, high angles of attack can have a very detrimental effect on flutter velocity index. The models were semi-rigid with a flexible root support mechanism shown in Figure 14. This mechanism provided automatic control to maintain the model at the correct angle of attack and at zero roll angle as the dynamic pressure and lift increased as flutter was approached. This control consisted of electric motors which adjusted the tension in the pitch and roll springs to maintain the pre-set angle. This adjustment of spring force was necessary during the test because at high angles of attack the lift forces generated would tend to deflect the model greatly since the restraint spring must be quite flexible to obtain flutter in the wind tunnel.

An advanced method of testing to obtain flutter data from wind tunnel models that can be interpreted as free-flight data through the use of mechanical admittance measurements has been recently investigated by The Boeing Company under sponsorship of the Air Force, (Ref. 24 and 25). Figure 15 is a schematic drawing of an admittance model restrained with excitation equipment which is mounted on a sting in the wind tunnel in such a manner that the model is more stable with the restraints than without the restraints. The free flight flutter characteristics of the model can be determined without danger of loss of the model by providing forced excitation to the model and observing response, together with mathematical removal of the restraint effects. Under an Air Force contract with Aerojet General, the indicial method of flutter predictions has been evaluated. This method includes obtaining aerodynamic influence coefficient on a segmented delta wing model and applying these aerodynamic data in a flutter analysis to predict flutter speeds. Figure 16 presents a drawing of the model showing the three segments and location of balances used to determine the aerodynamic load on each segment. These data have been shown to give very good correlation with experimental flutter results at supersonic speeds. The method is to be checked in the transonic speed range in the near future. The Massachusetts Institute of Technology is investigating the flutter characteristics of an inflatable wing model up to M = 6 under Research and Technology Division sponsorship. This investigation will be covered in detail by another paper at this Symposium.

Acoustic and vibration investigations on Air Force aircraft began around 1940. The investigations were required because of crew discomfort and reduction of efficiency on long missions. Noise investigations by models included work by Yudin (Ref. 26) in 1944 on sound eminating from rotating rods. Hubbard (Ref. 28) utilized model propellers to determine the free space fluctuating pressures near the tips of propellers. Lighthill (Ref. 29) performed experiments using model jets to determine the characteristics of noise generated by turbulence. Lighthill's work provided the basis for the following studies.

The first concerted effort in applying the acoustic modeling technology to advanced flight vehicles was about 1957. This effort was directed toward deter-

mining the use of model jets for turbojet noise prediction for the B-58 airplane, (Ref. 33).

Lighthill's studies show that the acoustic power generated by air jets is proportional to approximately the eighth power of the jet velocity. The jet velocity is then considered as the modeling parameter which must remain fixed.

Starting in 1960, modeling of propulsion systems was investigated quite thoroughly by Morgan in WADD TR 61-178 (Ref. 30) and by Gray in ASD TR 61-547 (Ref. 31).

These studies have shown that the sound pressure level at given ratios of distance to jet diameter, for equal jet velocity, will be the same for both model and full scale systems. The frequency spectrum is shifted upward inversely proportional to the scale factor. The spatial characteristics remain unchanged for the scaled frequency and the power spectrum level of the noise is reduced directly in proportion to the scale factor. The results of some of the experimental work are shown in Figures 17 and 18. The correlation of sound pressure level (or power spectral density between model and full scale jets) is quite good. The jet sizes in these studies were varied by a factor of 8.

Modeling of simple structures was investigated by Gray (Ref. 31) in order to determine the feasibility of using structural models for sonic fatigue prediction. His investigation indicated that the same material should be used for the model as for full scale. The investigation showed that the natural frequency of the panel would shift upward as does the spectrum of the jet. Since the sound pressure level is to be the same for the scale model as for the full scale model, the stress at similar locations should be equal in the scale model to that of the full scale model. Figure 19 shows the correlation of stress of a scale model and a full size specimen. With the stress level being the same in both the model and full scale specimen it was evident that the time to failure in the scale model should be proportional to the scale factor. Figure 20 presents the study results of two specimen designs. It is to be noted that the trend was as expected even though the failure time was slightly different than being directly proportional to the scale factor.

An investigation of a method for predicting the vibratory response of flight vehicle structures has also led to the use of models, (Ref. 32). In this investigation a portion of a one quarter scale SNARK (SM-62) missile was built to study the modeling approach. Of course, the previous studies on modeling jets and structure were used in designing the quarter scale vehicle. Similar points on the model were excited by a loud speaker and the transfer functions measured. A typical result is shown in Figure 21.

The above studies of flutter, aeroelasticity, sonic fatigue, jet noise and vibration response using models have given a clear indication that modeling may be a feasible, as well as an economical, approach to the solution of dynamic problems in future aerospace vehicles.

FUTURE

The demands of high reliability, greater payloads, higher speeds and altitudes, and greater range on future aerospace vehicles will require a highly efficient vehicle design. Efficient vehicle designs can only be achieved by knowing and

properly applying by analysis and experiment the environmental forces which the vehicle will encounter in its lifetime. Conservatism in the way of safety factors, component over-design, etc., must be minimized in order to obtain the most efficient vehicle design for the defined mission.

At present most aerospace vehicle designs do not consider the combined effects of all environmental forces, because a lot of these forces cannot be handled analytically. Therefore, additional "weight" is added to assure the desired reliability.

The technical area of dynamics will likely be an increasingly important consideration in the design of future aerospace vehicles. One such vehicle under study is the Aerospace Plane, an advanced concept for manned, winged, earth-to-space vehicle with an air breathing propulsion system. These future vehicles must have an extremely lightweight, efficient structural design to be feasible. Yet these designs must have sufficient strength and stiffness to prevent dynamic instabilities of lifting surfaces and skin panels, and also maintain a reasonable fatigue life and internal acoustic environment. This will be a difficult undertaking in view of the extremely wide speed range, intense thermal and acoustic environment, high angles of attack and unusual configuration being proposed. Reduced scale modeling will be a requirement for the very large vehicles under consideration for extended aerospace missions. Some future problems which will likely require extensive effort, including advances in dynamic modeling technology, to resolve and verify vehicle safety and reliability are listed as follows:

1. High temperature effects. The extreme thermal environment of reentry for orbital and superorbital vehicles will require improved approaches in modeling technology, especially in the area of aerothermoelastic models.

2. Exhaust noise from rockets, multiple nozzle turbojets, ducted fans, etc. Prediction techniques for these propulsion systems are accurate for only the simpler configurations. High acoustic power is generated by large rockets; and the volume of air, both in silos and in the open, containing these rockets will have high noise levels during launch and early flight. Jets impinging on the ground will provide high noise levels on the under surface of vehicles. A modeling approach would seem to be an excellent way to study and optimize the vehicle configuration from acoustic effects. Much more effort is required to obtain adequate prediction techniques for propulsion systems.

3. High angles of attack. The reentry of advanced vehicles at high angles can aggravate flutter and buffeting problems. Advances in modeling technology to investigate flutter of elastic models in the wind tunnel at high angles and extreme temperatures are needed.

4. Fuel slosh in large fuel tanks and coupling with elastic vehicle modes. This effect can cause dynamic load and instability problems in advanced aerospace vehicles; methods to simulate these fuel slosh effects with reduced scaled models will be important.

5. Noise from separated boundary layer, shock waves, base pressures and wakes. The pressure fields associated with these phenomena is sufficient to cause structural fatigue failures. There is almost a complete lack of prediction techniques for these phenomena. Both full scale and model experiments are required to determine the modeling technology.

6. Dynamic stability and control of missiles, including effects of structural flexibilities. Wind tunnel modeling techniques, including simulated servo systems are needed to assure freedom from such aeroelastic problems.

7. Stability augmentators and gust alleviators on Supersonic Transport and other advanced vehicles are intended to provide improved structural response and damping characteristics. To investigate the characteristics of these systems and to assume safety from flutter by coupling of the control inputs with the elastic modes, improved modeling technology to simulate these characteristics are needed. While it is considered highly undesirable by flutter engineers to depend on a "black box" to prevent catastrophic flutter, it may be possible in some cases in the future to use very reliable servo systems to provide inputs to the control surfaces in such a manner as to avoid wing flutter in critical speed ranges with less weight penalty than would be possible with the addition of structure.

8. Developing techniques for testing complete vehicle models in supersonic and hypersonic tunnels. With the very flexible fuselage configurations of advanced vehicles, it becomes increasingly important to test complete vehicle models rather than wall-mounted component models. Improved technology will be needed for wind tunnel models of the large, flexible complete models of advanced aerospace vehicles which will not have significant mounting effects and simulate free flight conditions.

9. Shell-like lifting bodies. Such configurations are under consideration for superorbital reentry missions. Dynamic problems in these vehicles will require model studies. Vibration and flutter modeling technology for shells will require accurate simulation of a large number of structural vibration modes, including not only bending and torsion, but breathing modes as well.

10. Panel flutter. A considerable amount of panel flutter research by NASA and the Air Force is improving panel flutter testing technology, but improvements will be required in obtaining valid data on models because of difficulties in accurate simulation of the many important parameters and nonlinearities. Some of these important parameters are panel edge conditions, pressure differential from inside to outside the panel, in-plane stresses, buckling, curvature, temperature, angle of attack, and size of the cavity behind the panel.

11. Inflatables, expandables, Rogallo wing dynamics. This is a fairly new field and will likely be of growing importance as advanced vehicles of this type are developed. Methods to provide valid dynamic model results must be developed.

12. Ground vibration tests of small scale replica of prototype too large or not capable of ground vibration tests. The large size and delicate nature of some advanced vehicles may prevent the conventional ground vibration test. Replica models may be used to represent the prototype to obtain these vibration data. Improvements in obtaining highly accurate modeling methods, including the effects of joints between vehicle stages and other complex modeling problems will be required if valid results are to be obtained.

13. Hypersonic control surface "buzz" instabilities may be a problem and require models. This phenomena apparently involves the interaction of shock waves and boundary layer to give an oscillatory instability of controls similar to the buzz problem experienced by many aircraft in the transonic speed range. A few cases have been recently noted on models at hypersonic speeds. Further investigation to evaluate the significance of this phenomena to advanced vehicles are needed.

14. Aerodynamic interference effects of vehicles components. This could include such problems as the effect of highly swept wings on horizontal tail flutter or buffet in variable sweep wing configurations. Methods to theoretically analyze this highly complex unsteady aerodynamic phenomena are not reliable and model technology will play an important part in investigating this problem.

15. Dynamic models are needed to determine unsteady aerodynamic loads for oscillating surfaces at high speeds and for new, blunt, highly swept configurations for which theoretical prediction methods are unproven or not available.

16. Dynamic load problems of advanced vehicles include alightment with crushable, collapsible or energy absorbing devices; space rendezvous impacts; and dynamic loads on spinning space station modules connected by long elastic cables. Advances in modeling technology will be required to provide the experimental data needed for these phenomena on the new design concepts of spacecraft and in view of the new space environments such as artificial gravity which will be experienced by these vehicles.

17. Vibration and fatigue characteristics of structures. Sonic fatigue facilities which can provide the required acoustic field, apply static loads, high temperatures, etc., will be required. Advances in modeling technology will be required in order to use many facilities due to size limitation.

18. Improved instrumentation and facilities for conducting tests on dynamic models will be necessary if adequate measurements and simulations of the high speed intense thermal and acceleration environments are to keep pace with advanced vehicle performance and missions.

19. Control of internal and external noise environment of advanced vehicles. The use of models will most surely be of benefit in providing optimum configurations to minimize noise environments.

CONCLUSION

In conclusion, dynamic problems will likely continue to be prominent in the design of advanced aerospace vehicles. In view of the increasingly complex nature of these problems, advanced dynamic modeling techniques will be extremely important in resolving these problems for future aerospace vehicles.

REFERENCES

1. Encyclopaedia Britannica, 14th Edition, Vol. 15, 1940.

2. "The Mechanical Investigations of Leonardo de Vinci" by Ivan B. Hart Linden (Chapman & Hall Ltd.)

3. "How We Invented the Airplane", Orville Wright. Kay 1953.

4. "The Mathematical Theory of Elasticity" by A.E.H. Love, Fourth Edition, New York Dover Publications, 1944.

5. "The Theory of Sound" by Lord Rayleigh with a historical introduction by Robert Bruce Lindsay, Second American Edition, New York Dover Publications, 1945.

6. "A Textbook of Sound", A. B. Wood - G. Bell and Sons, LTD. 1957.

7. "Aeroelasticity", Bisplinghoff, R. L.; Ashley, Holt; and Halfman, Robert L., Addison-Wesley Publishing Co., Inc.

8. "High Temperature Effects in Aircraft Structure, Models and Analogs" by R. R. Heldenfels. Pages 323-353 Pergamon Press.

9. "The 1957 Minta Martin Aeronautical Lecture" by I. E. Garrick on Some Concepts and Problem Areas in Aircraft Flutter.

10. NASA TM No. 782, "Status of Wing Flutter", by H. G. Kussner January 1936.

11. British ARC R&M No. 1197, "Wing Flutter Experiments Upon a Model of a Single Seater Biplane", by W. G. A. Perring, Nov 1928.

12. British ARC R&M No. 1464, "Wind Tunnel Tests of Recommendations for the Prevention of Wing Flutter", by B. Lockspeiser; C. Callen, 11 Feb 1932.

13. British ARC R&M 1242, "The Force and Movement on an Oscillating Aerofoil," by H. Glauert, 1929.

14. British R&M 1500, "Resistance Derivatives of Flutter Theory", by W. J. Duncan and A. R. Collar, 1932.

15. Schwingonger von Flugzengflugeln Luftfahrtforschung", by H. G. Kussner, Vol. 4, 1929, P.41.

16. "Augenblicklicher Enturcklurgstand der Frage des Flugelflatterns Luftfortrolforschung", Vol. 12, by H. G. Kussner, 1935, P 193.

17. NACA Report 496, "General Theory of Aerodynamic Instability and the Mechanism of Flutter", by T. Theodorsen, 1935.

18. AFTR 4798, "Application of Three Dimensional Flutter Theory to Aircraft Structures", by B. Smilg and L. Wasserman, 1942.

19. WADC TR 56-214, "Transonic Flutter Model Tests"
Part I "45 Degree Swept Wings" 1957

Part II "Straight Wings" 1958
Part III "60 Degree Delta Wings" 1958
(Unclassified Titles - Confidential Report)

20. WADC TR 59-407, "Flutter Model Tests at Mach Numbers 1.5 - 5.0", by John R. Martuccelli, September 1959. (Unclassified Title - Confidential Report).

21. WADD Technical Report 60-328, "Flutter Model Tests at Hypersonic Speeds M = 5 to 7", by R. White, Jr., S. King, J. Balcerak, 1960. (Unclassified Title - Confidential Report).

22. WADD Technical Report 60-328, Supplement 1, "Flutter Model Tests at Hypersonic Speeds. M5-8" by R. White, Jr. and J. Balcerak, 1961 (Unclassified Title - Confidential Report).

23. ASD-TDR-62-498, "Flutter Model Tests of Advanced Wing Configurations at Initial Angles of Attack", by D. A. Brown 1963. (Unclassified Title - Confidential Report).

24. WADD TR 61-31, "Admittance Techniques in High Speed Flutter Model Testing"

Part I "Experimental Results" by G. Asher and R. Watanabe
(Unclassified Report - Unclassified Title)
Part II "Correlation of Experiment and Theory" by G. Asher 1961
(Unclassified Title - Confidential Report)

25. ASD-TDR-62-1008, "Supersonic Wind Tunnel Flutter Model Tests Including Free-Flight Data from Admittance Measurements", by G. Asher and F. Hyland 1963. (Unclassified Title - Confidential Report).

26. NACA TM 1136 "On the Vortex Sound from Rotating Rods". E. Y. Yudin 1947.

27. Principles of Sound Control in Airplanes OSRD No. 1543. Beranek. L. L. and Others. Craft Laboratories, Harvard University.

28. NACA TN 1870, "Free Space Oscillating Pressures Near the Tips of Rotating Propellers. Hubbard, H. H. and Regier, A. A.

29. On Sound Generated Aerodynamically II Turbulence as a Source of Sound, 21 July 1953, Dept. of Mathematics, University of Manchester.

30. WADD TR 61-178, "The Use of Acoustic Scale Models for Investigating Near Field Noise of Jet and Rocket Engines". W. V. Morgan, L. C. Sutherland, K. J. Young. April 1961. WPAFB, Ohio.

31. ASD TR 61-547, "Study in the Use of Structural Models for Sonic Fatigue", C. L. Gray, November 1961, WPAFB, Ohio.

32. ASD TDR 62-801, "Investigation of a Method for the Prediction of Vibratory Response and Stress in Typical Flight Venicle Structure". R. W. White, K. L. Eldred, W. H. Roberts. August 1962, WPAFB, Ohio.

33. CONVAIR REPORT, "Methods for Predicting the Acoustic Environment for the B-58 Weapon System." E. H. Stepp February 1957.

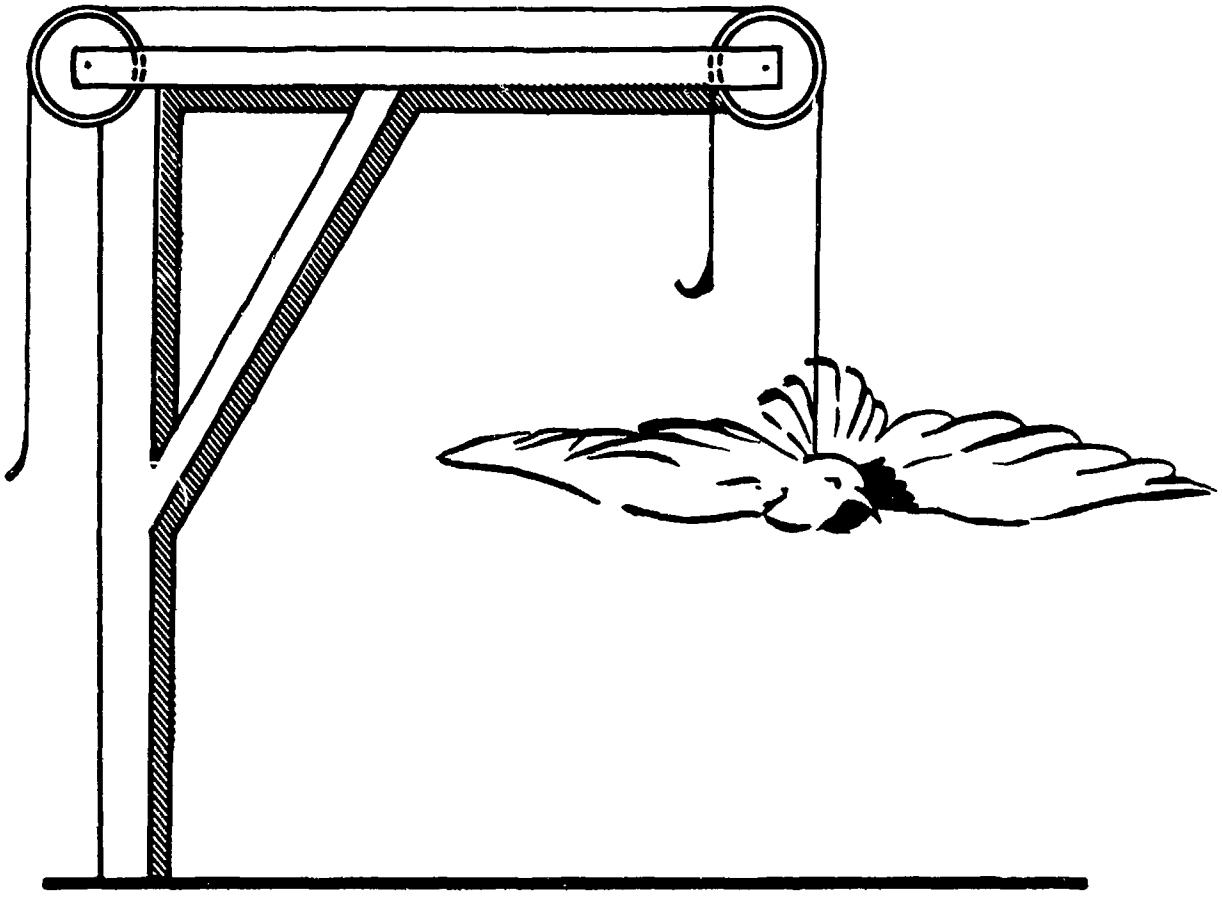

Figure 1. Leonardo da Vinci's Study of the Flight of Birds

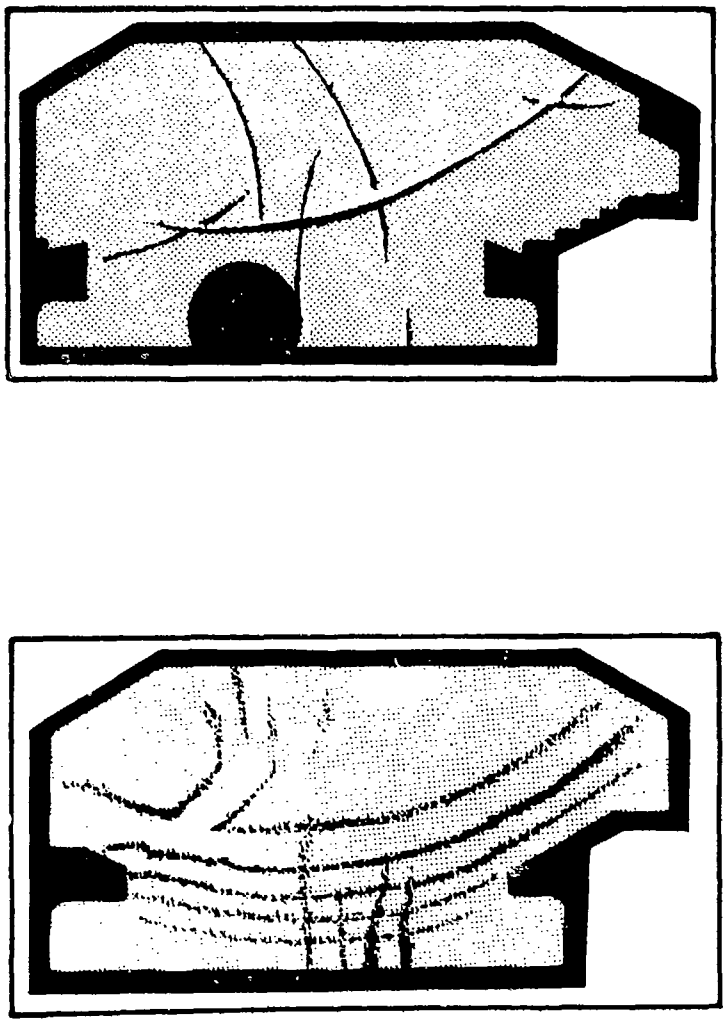

Figure 2. Model Auditorium - Study of Reflecting Characteristics by Spark and Ripple Techniques

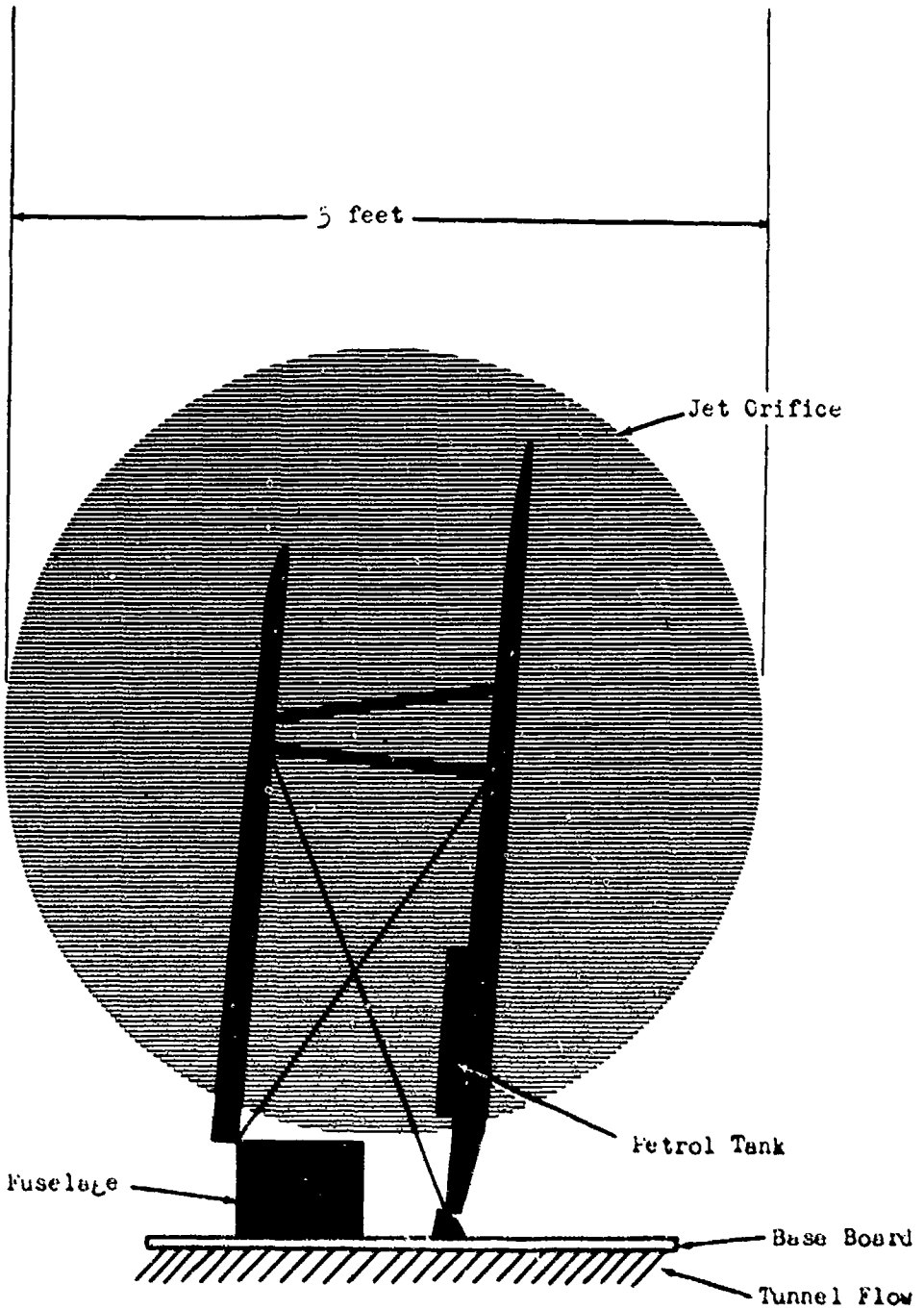

Figure 3. Flutter Model Tests of an English Single Place Biplane (About 1931)

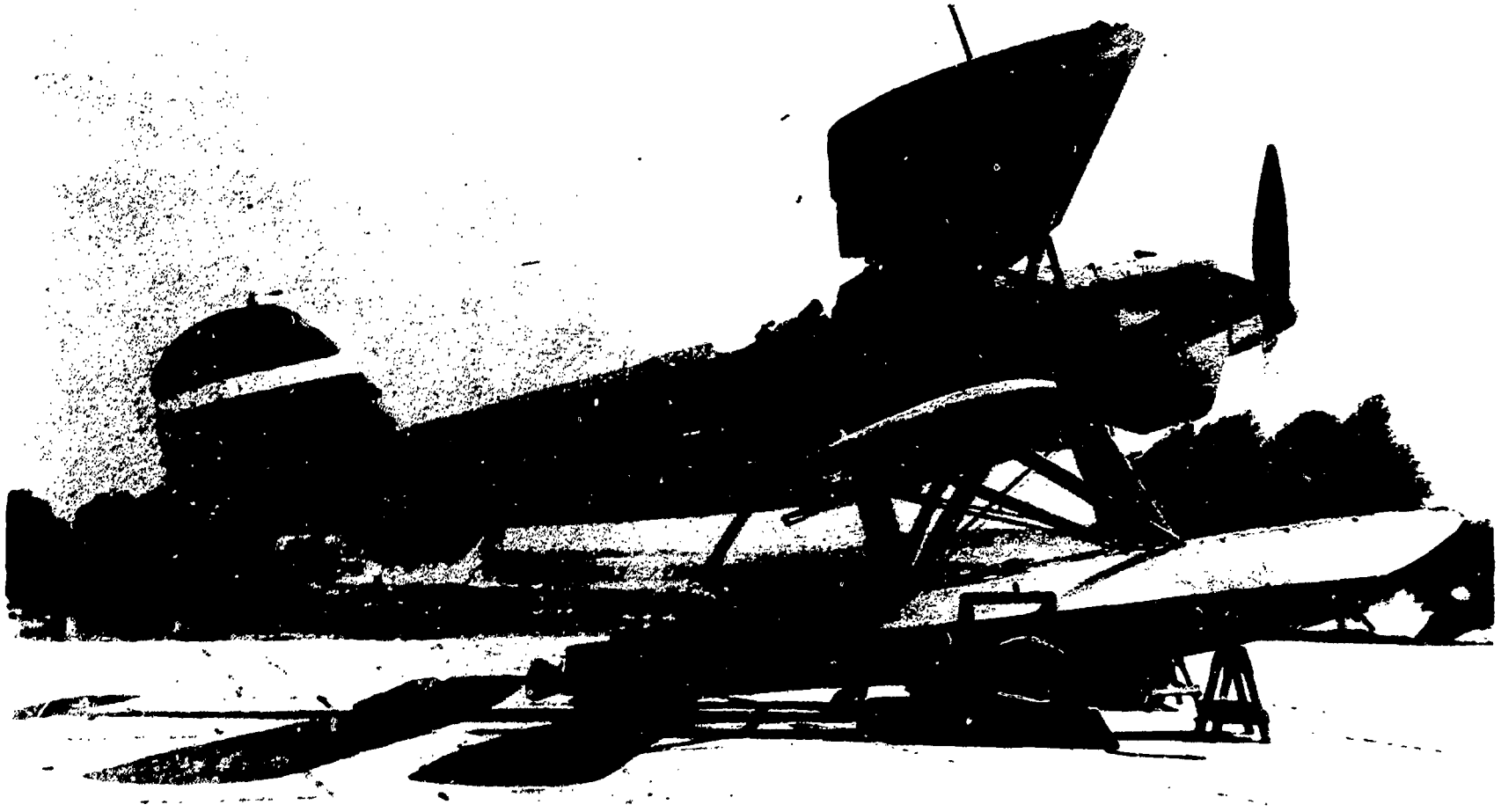

Figure 4. Heinkel He 60

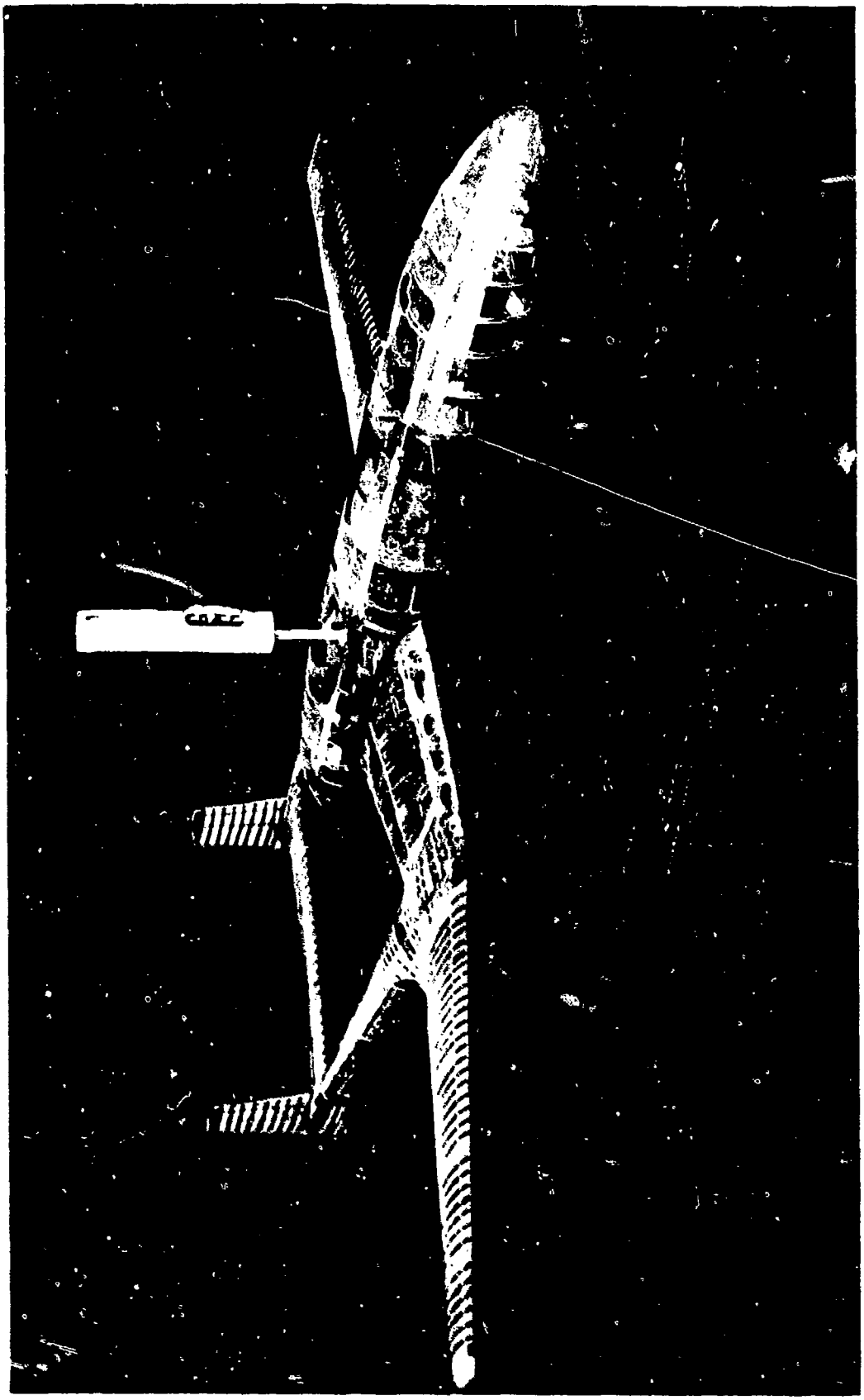

Figure 5. XF-54 Flutter Model

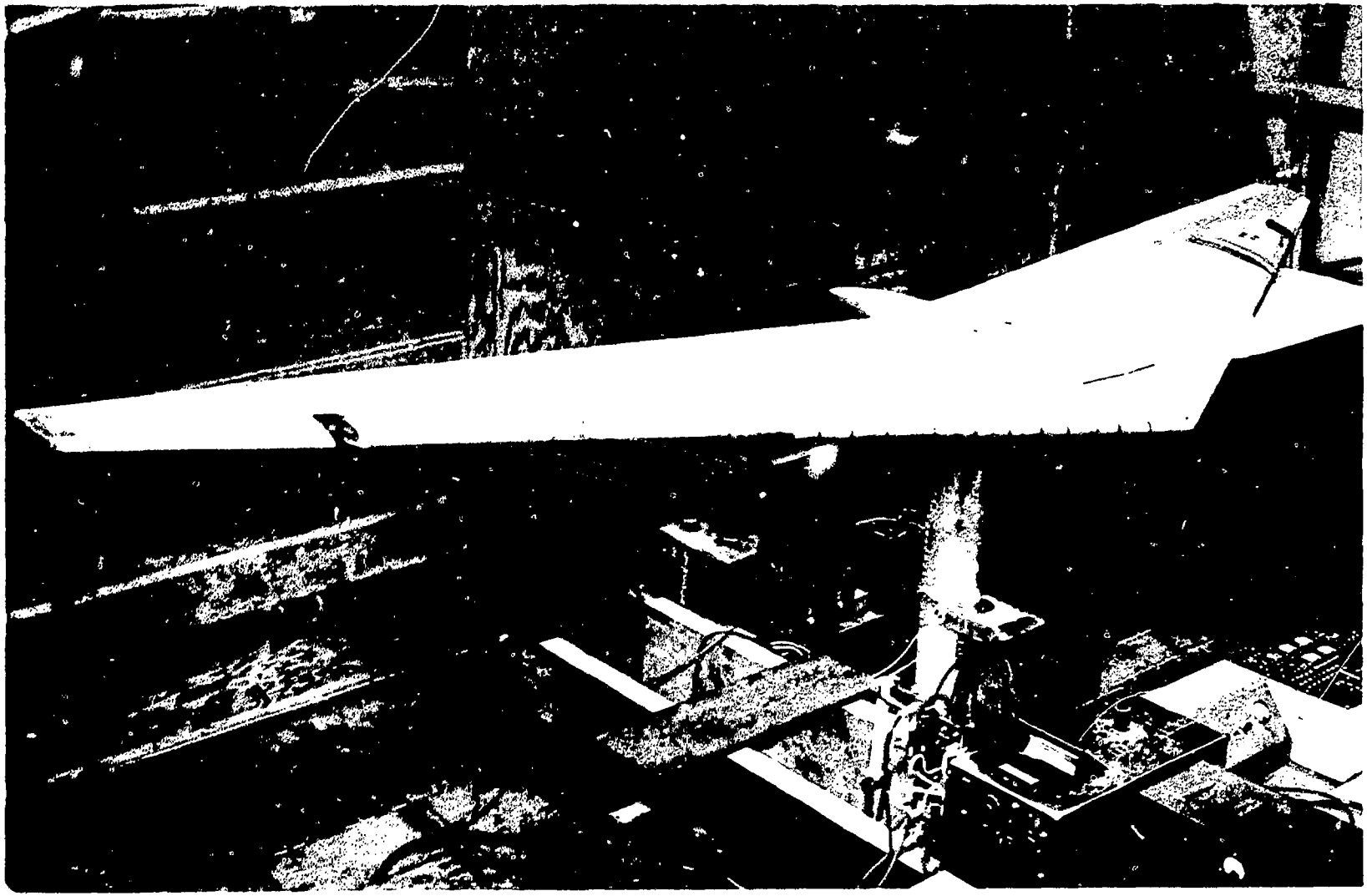

Figure 6. XB-35 Flutter Model

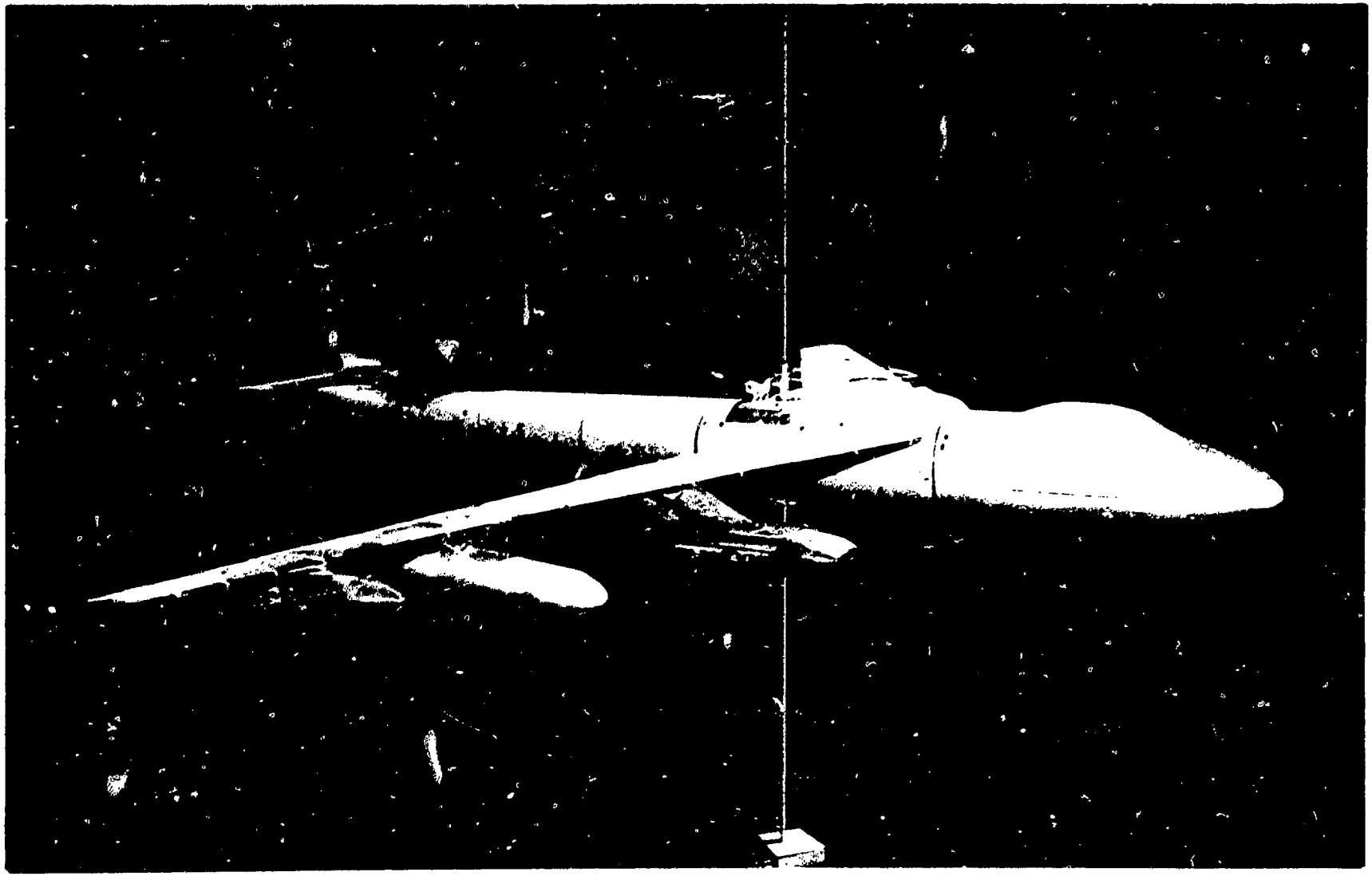

Figure 7. B-47 Flutter Model on Wind Tunnel Rod Support

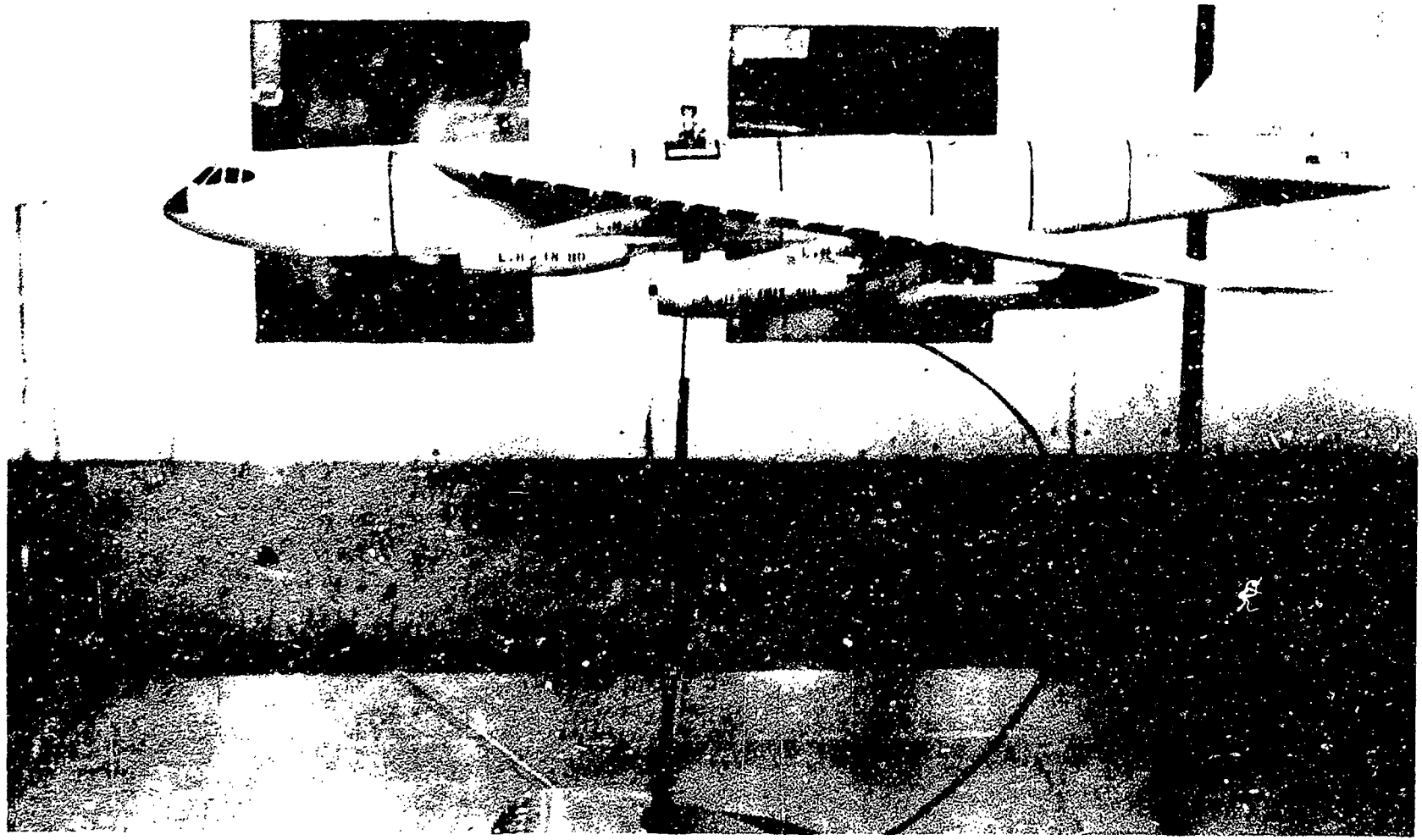

Figure 8. B-52 Flutter Model

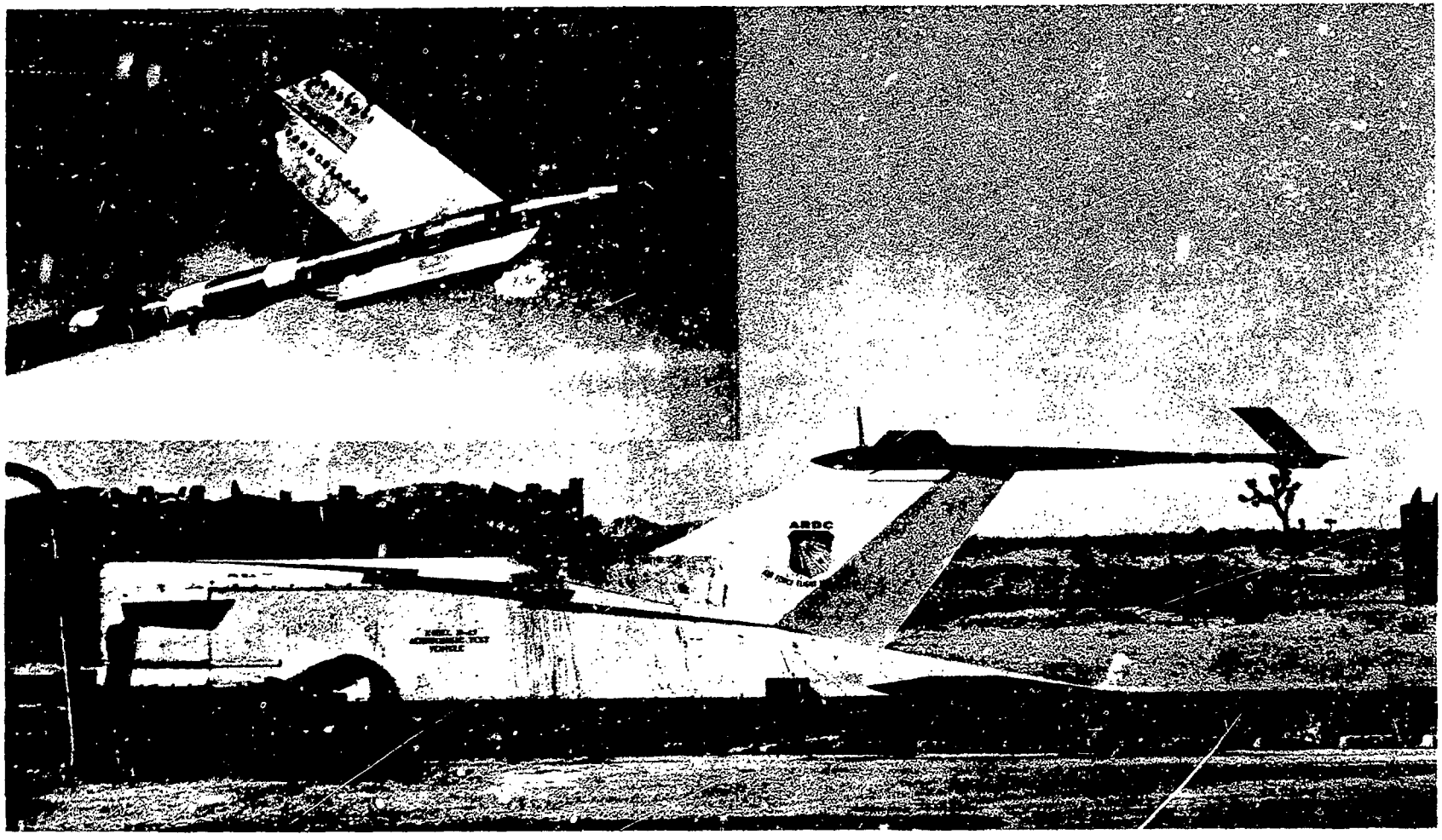

Figure 9. Rocket Sled Flutter Model Tests (Inset - Model After Flutter Test)

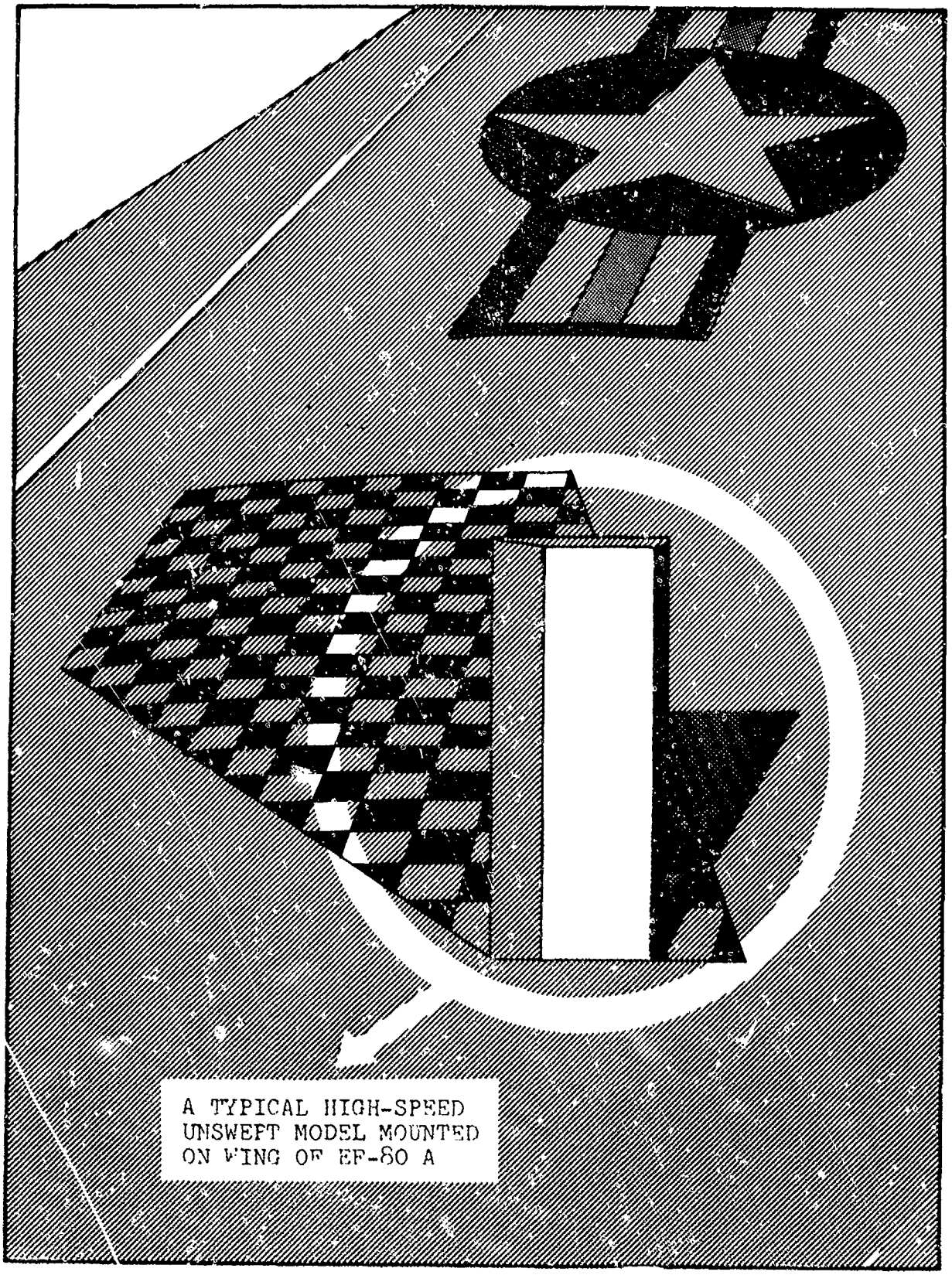

Figure 10. Transonic Flutter Model Test Using a Flying Aircraft

Figure 11. B-58 Flutter Model on Rocket Launcher

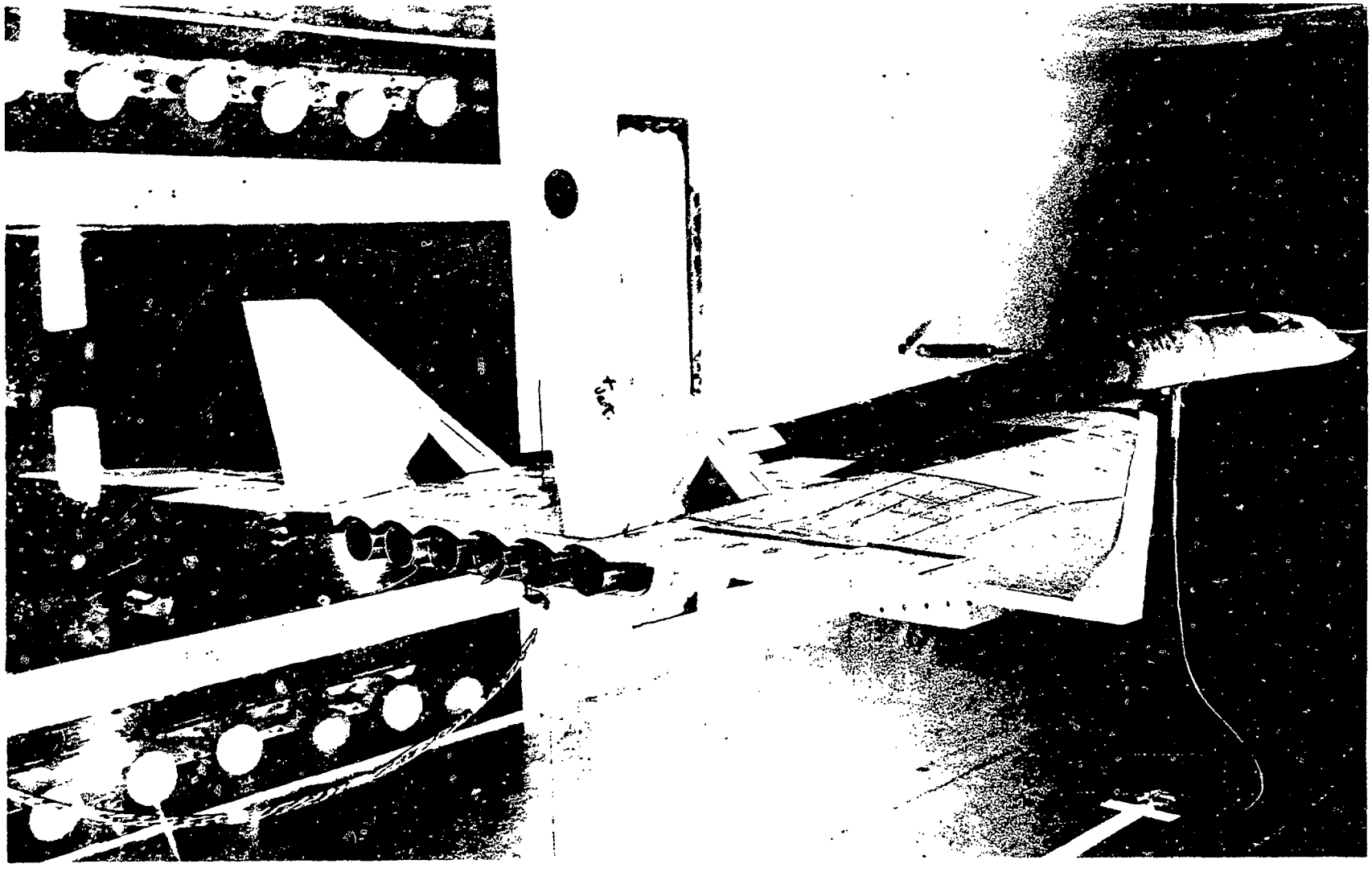

Figure 12. B-70 Wind Tunnel Flutter Model

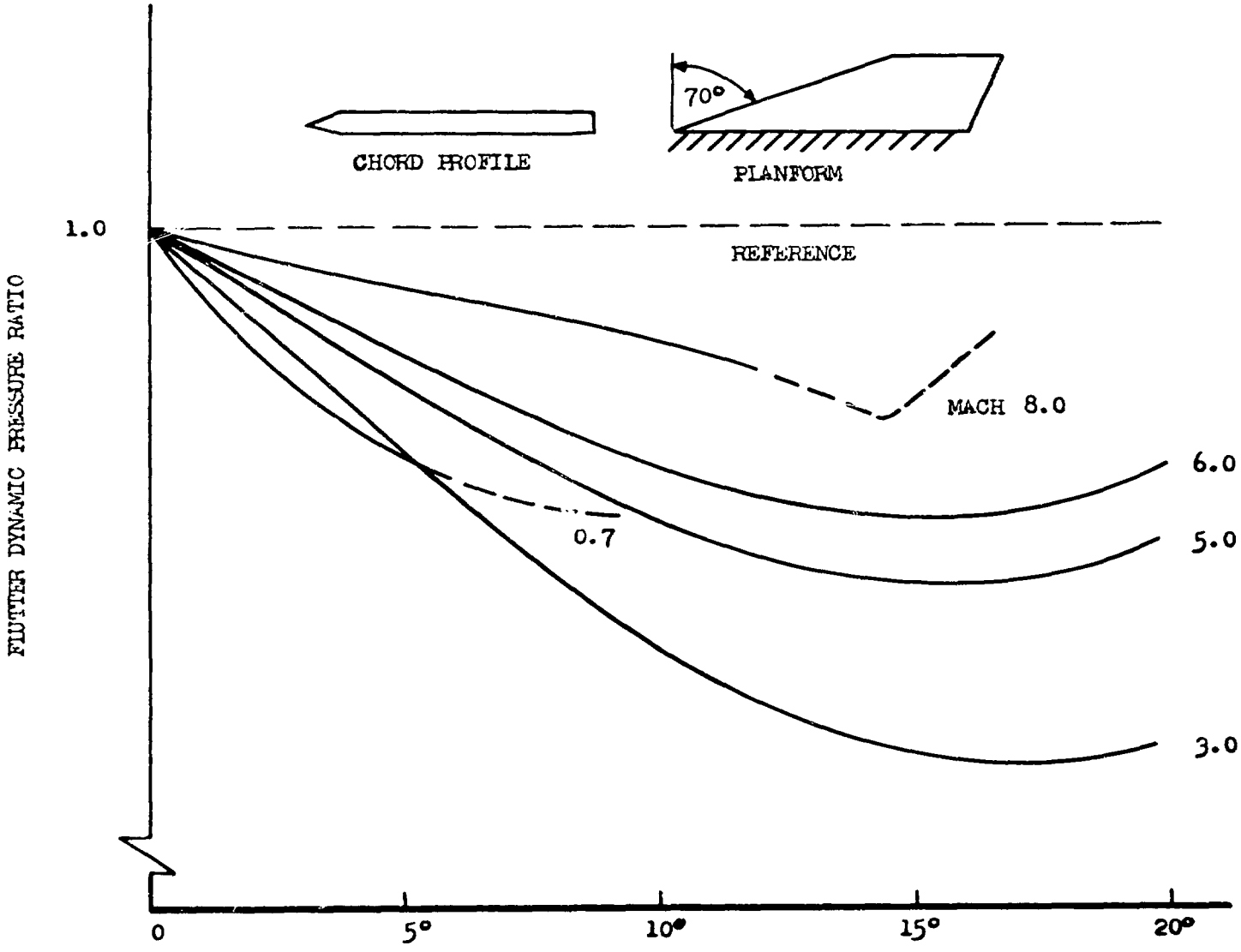

Figure 13. Effects of Angle of Attack on Flutter

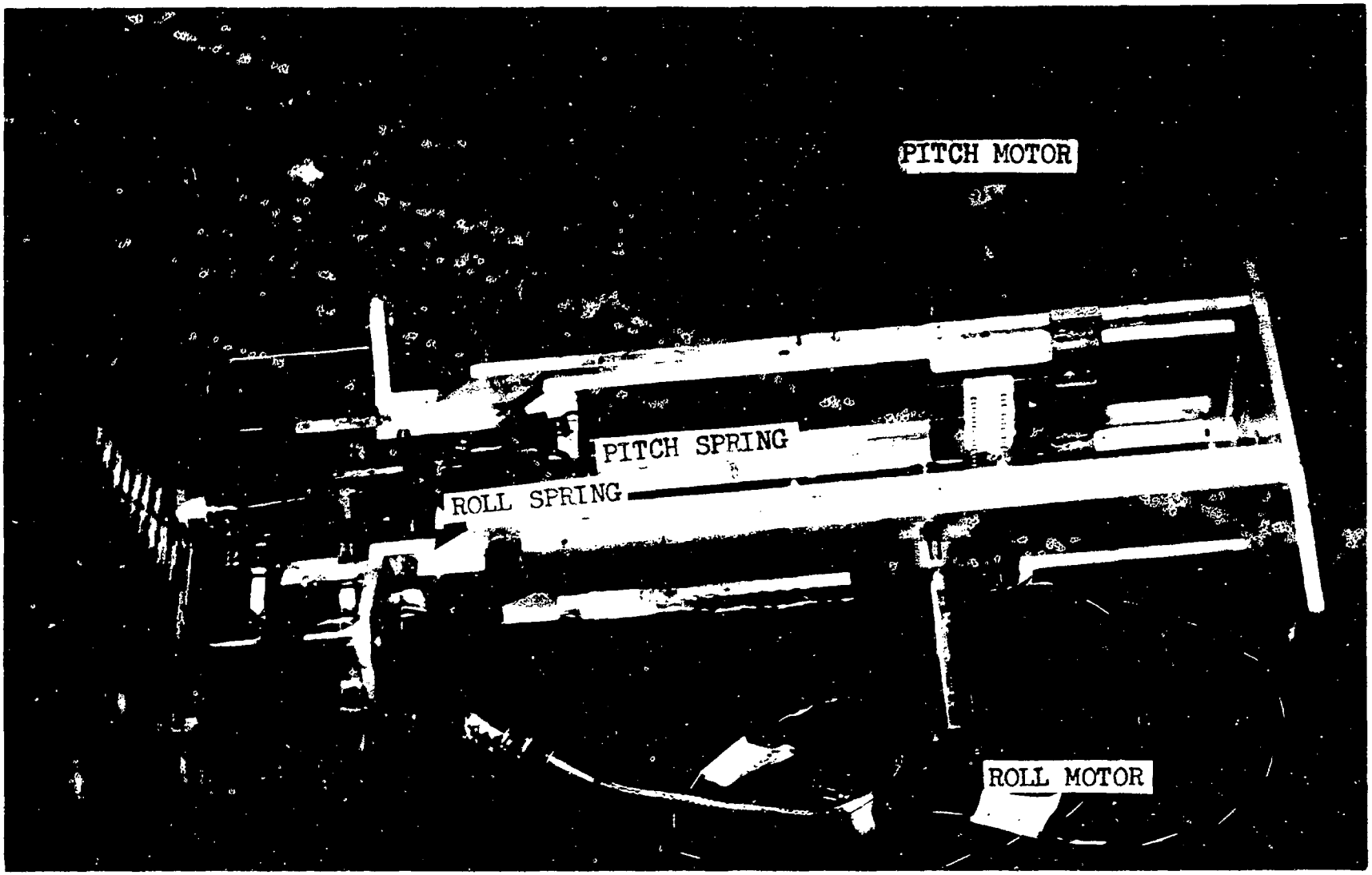

Figure 14. Flutter Model and Suspension Mechanism for High Angles of Attack Wind Tunnel Test

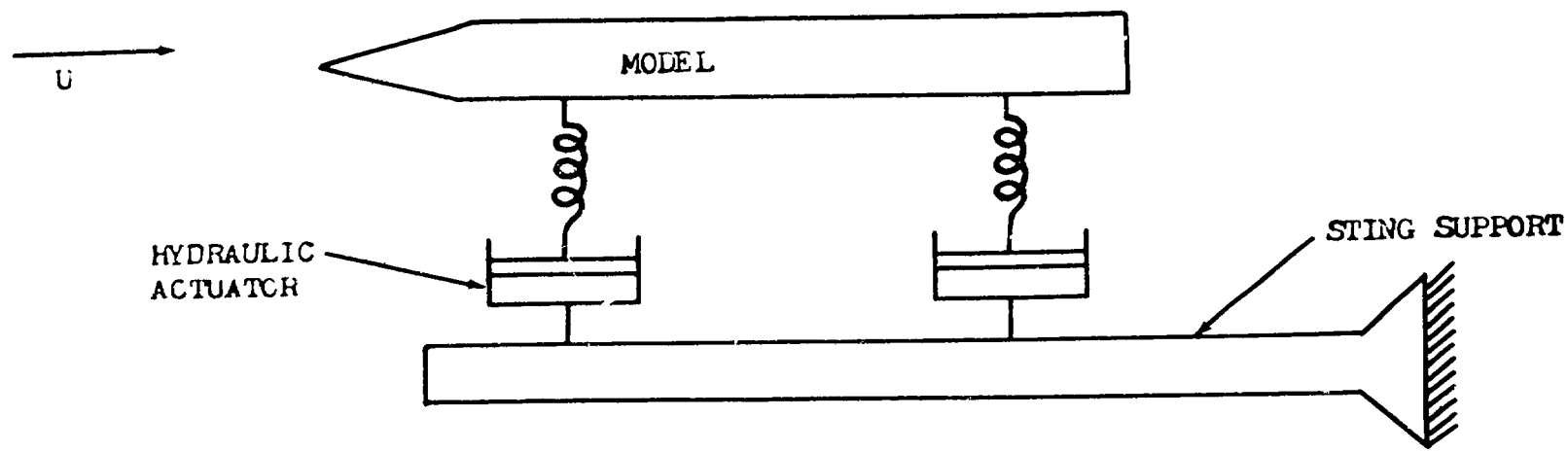

Figure 15. Schematic Admittance Test Arrangement

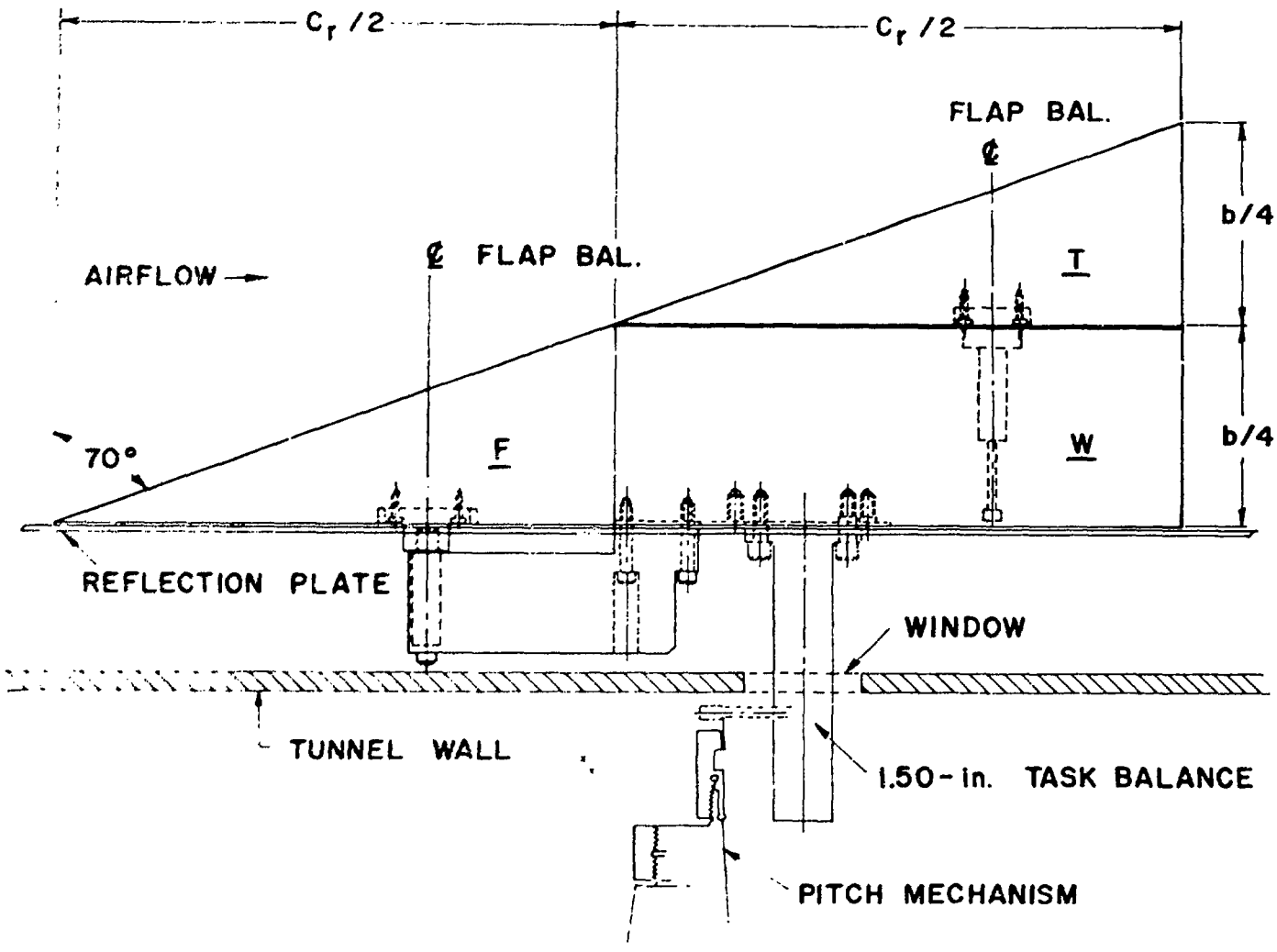

Figure 16. Model to Obtain Aerodynamic Data for Indicial Flutter Analysis

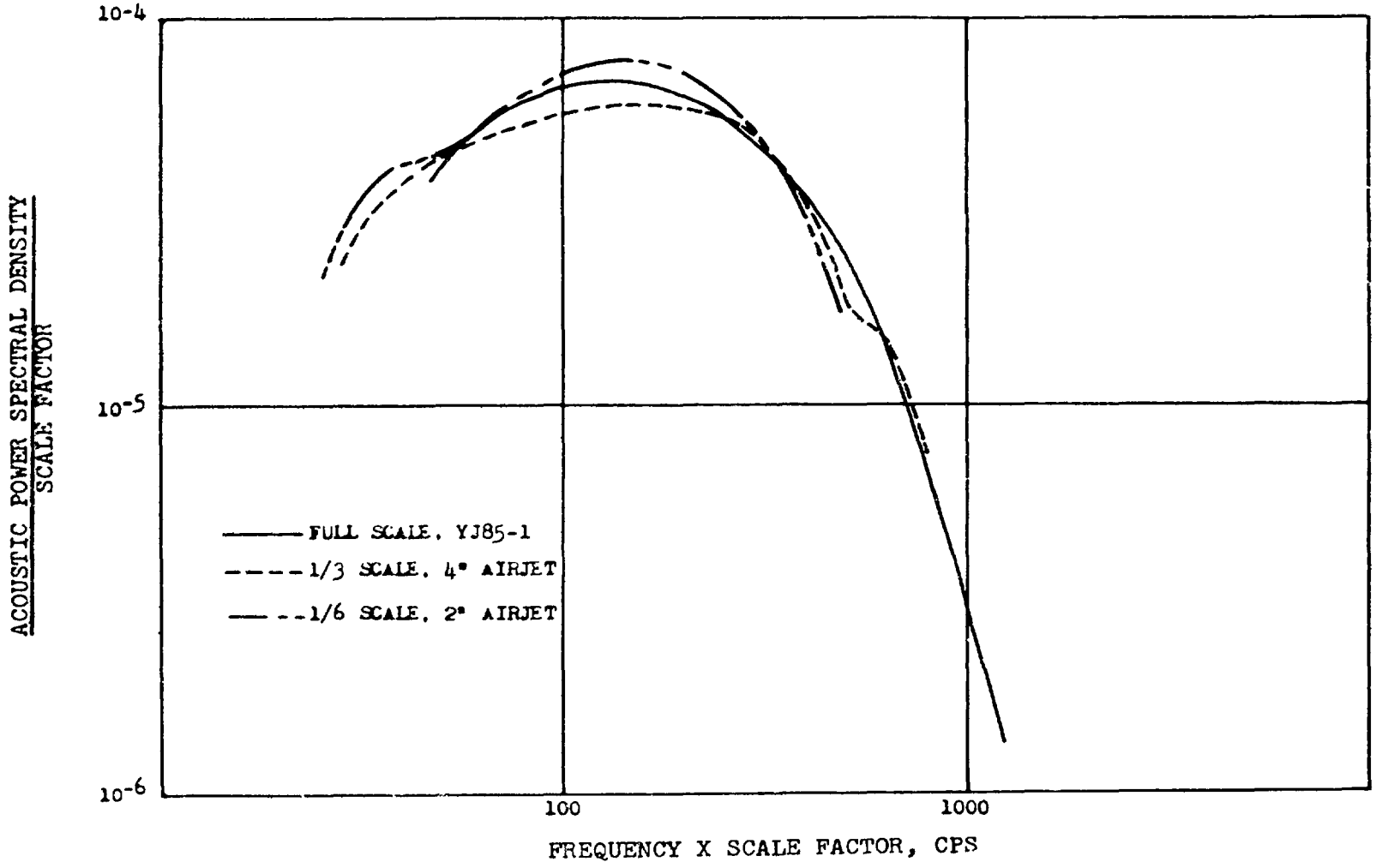

Figure 17. Normalized Acoustic Power Spectra

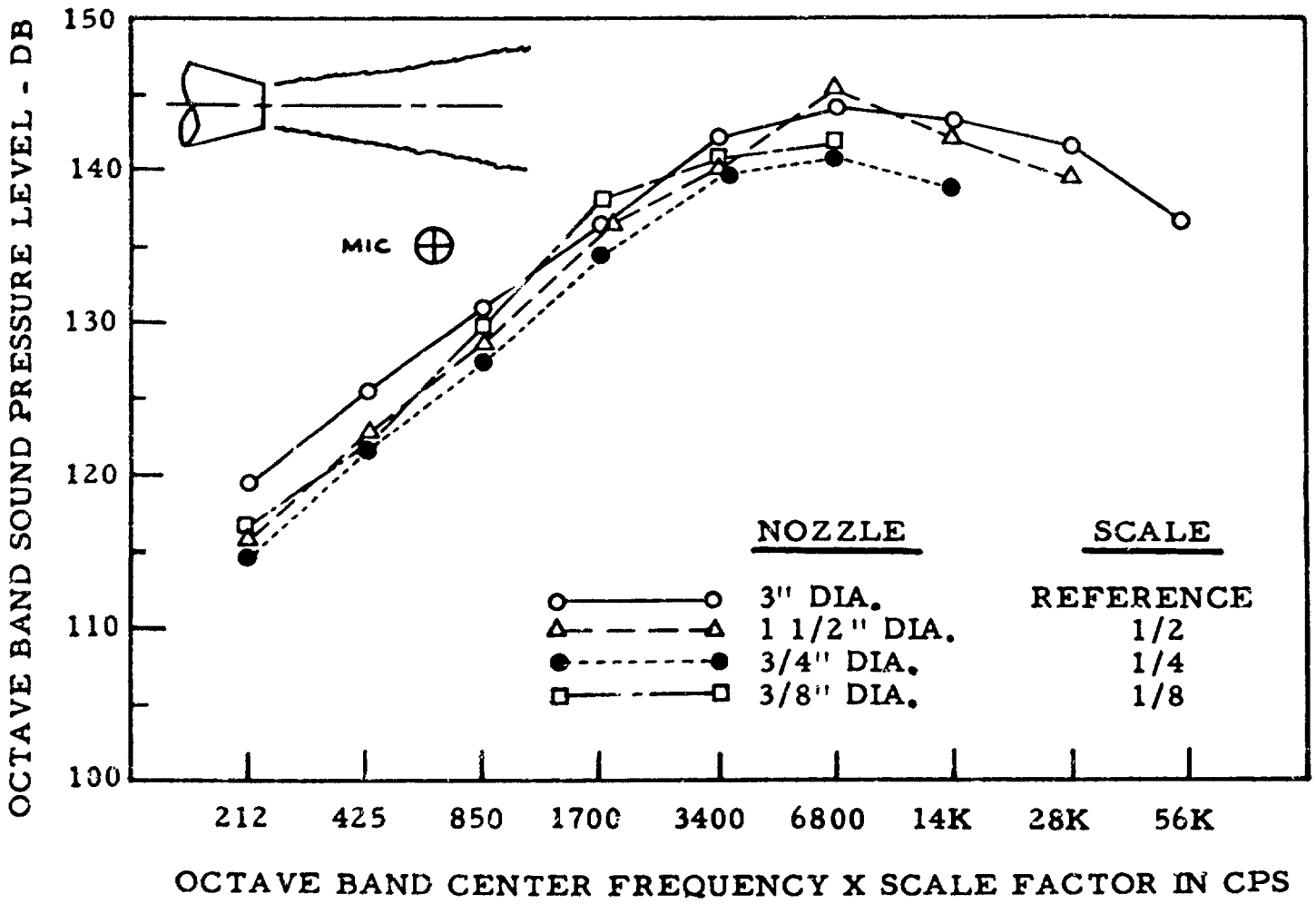

Figure 18. Similarity of Noise Produced by Four Nozzles Varying in Diameter by a Factor of 8, all Operating at the Same Plenum Condition - Results are Averages for a Number of Test Points at Scaled Locations

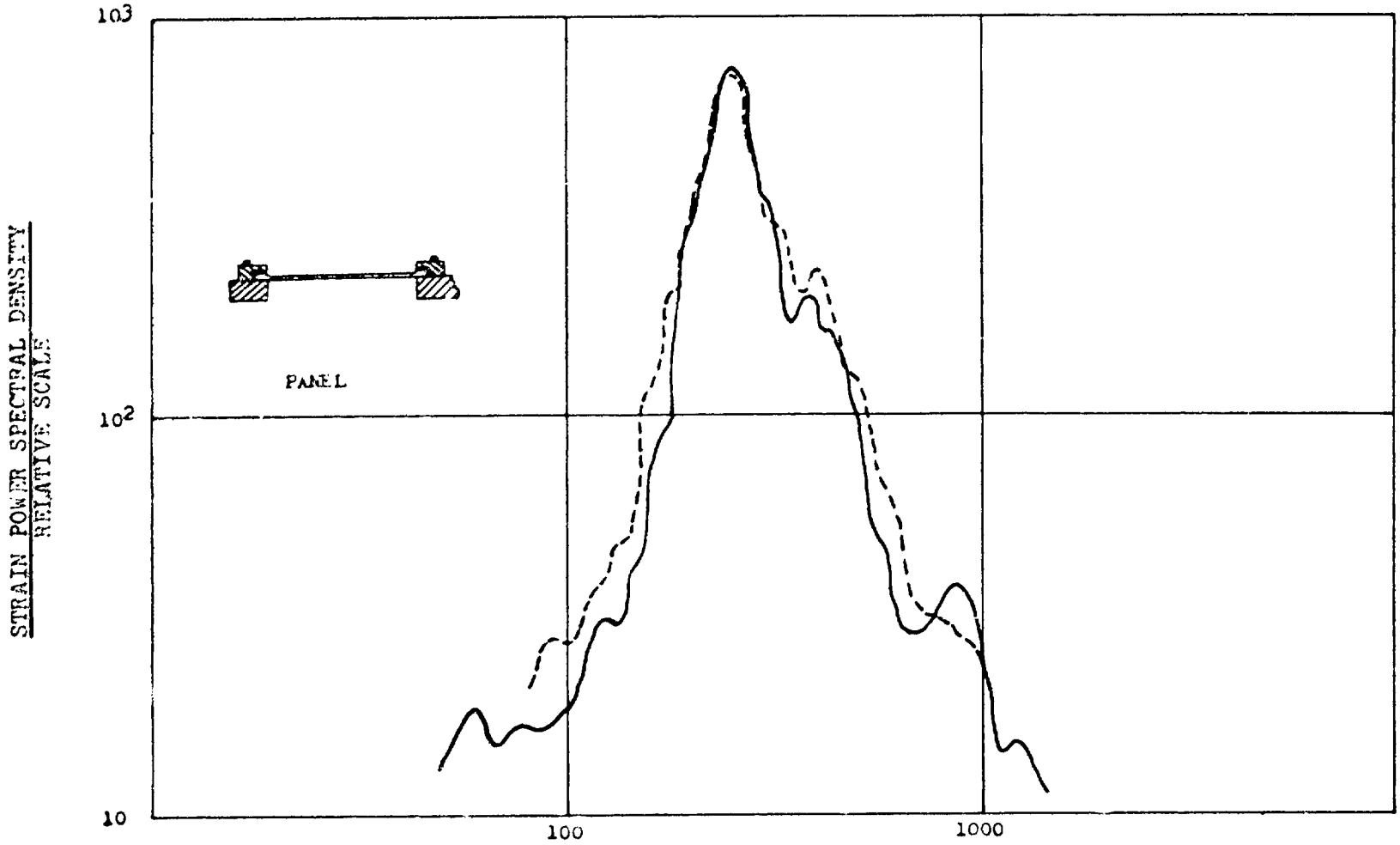

Figure 19. Normalized Strain Power Spectra

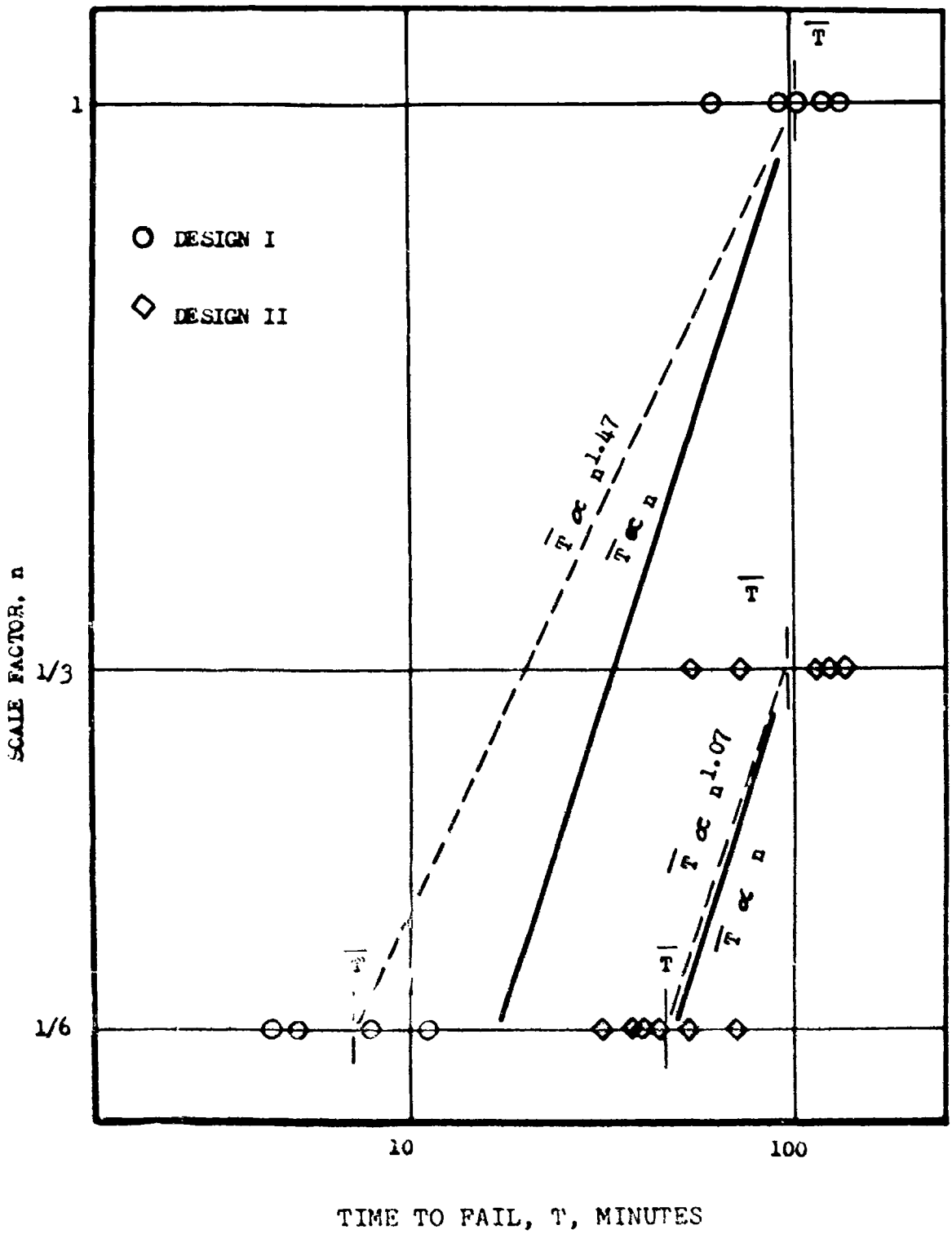

Figure 20. Failure Time and Scatter as a Function of Scale Factor for Sonic Fatigue Test Specimens

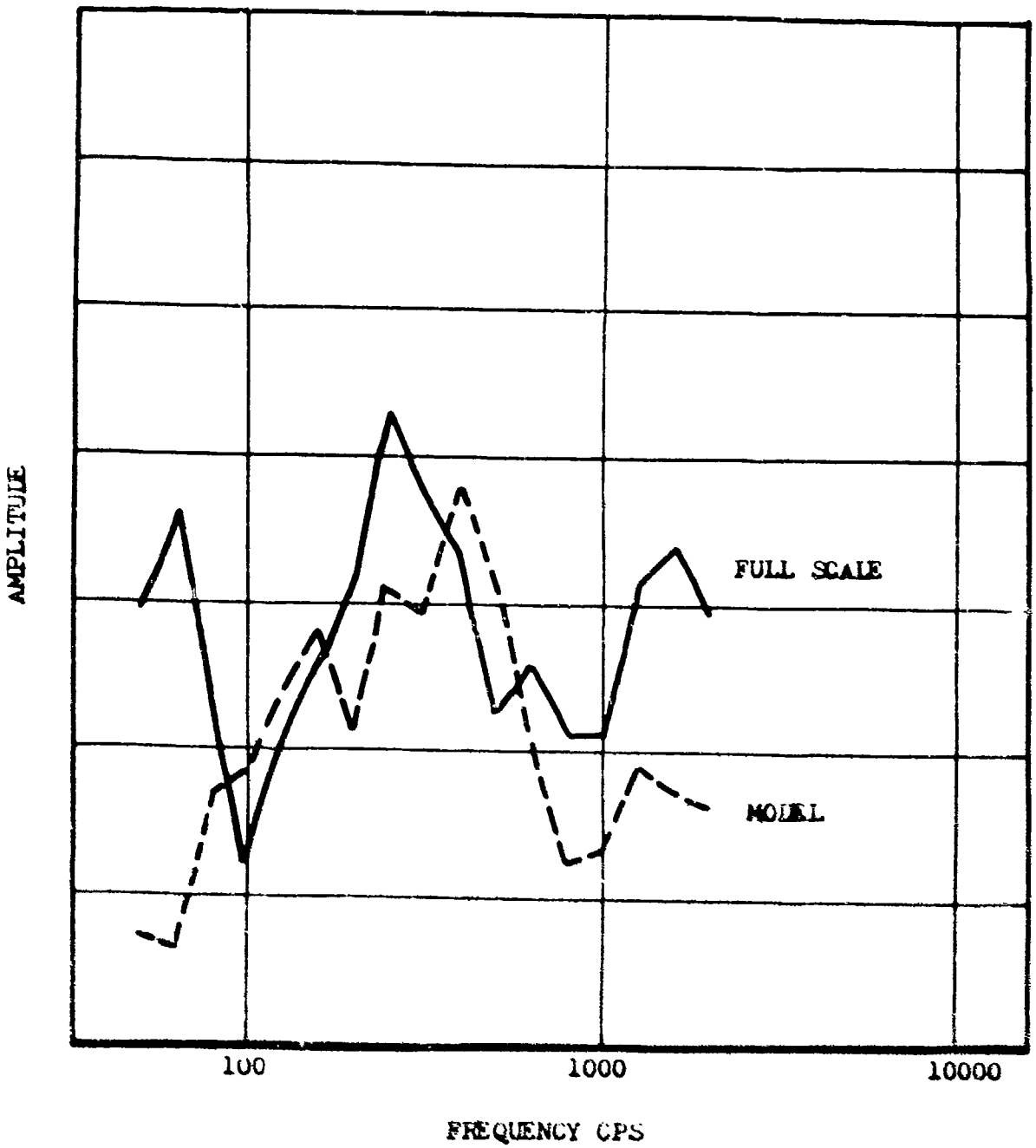

Figure 41. Comparison of Full Scale and Model Longitudinal Response Transfer Functions

ANALYSIS OF SIMILITUDE REQUIREMENTS AND SCALING LAWS FOR TRANSONIC BUFFETING

By H. C. Peterson and A. A. Ezra

The Martin Company

Denver, Colorado

ABSTRACT

When a launch vehicle accelerates through Mach 1, a shock wave forms, remains attached to the nose for a brief time and then separates as the Mach number increases. During the period of shock wave attachment, intense local unsteady aerodynamic pressures of an oscillatory nature are generated.

These unsteady pressures which give rise to the violent shaking referred to as transonic buffeting contain a wide spectrum of frequencies. Thus the transonic buffeting forces must be specified, for analytical purposes, as a non-dimensional plot of power spectral density versus frequency. Due to the limitations of the present theoretical knowledge, these power spectral density curves must be derived from wind-tunnel tests.

In order to conduct valid scale model tests, to determine the transonic buffeting excitation, a careful analysis of similitude requirements is necessary; and it is mandatory to determine the importance of those similitude requirements that cannot be provided due to the limitations of existing wind tunnels.

This paper derives the similitude requirements and the corresponding scaling laws for small scale experimental work and describes the different experimental approaches that can be used to circumvent the practical difficulties of fulfilling all the similitude requirements.

I. INTRODUCTION

The violent shaking which occurs when the velocity of a flight vehicle approaches Mach 1 was observed with alarm by the pilots of fighter aircraft during World War II. This buffeting often resulted from shock-induced flow separation on the wings of the aircraft. The turbulent wake created by the flow separation produced random fluctuating airloads which could cause buffeting of the wing itself or buffeting of the tail section. As flight at high subsonic Mach numbers became a commonplace event, the problem of transonic buffeting increased in importance. The problem was sometimes "solved" by limiting Mach number and incidence to values below a buffet boundary which existed for each configuration. This buffet boundary could be modified by boundary layer control to reduce the tendency for shock-induced separation. When supersonic flight became a necessity, the buffet problem was "solved" by rapidly accelerating through Mach 1 in order to avoid the violent dynamic excitation produced by sustained transonic flight.

As could be expected, transonic buffeting has continued to be an important problem in the era of launch vehicles, ICBM's, manned space probes, and manned orbiting military systems during the exit and re-entry phases of flight. In a sense the problem has become more severe because, while the supersonic aircraft evolved toward compact configurations with low-aspect-ratio wings, the rocket-powered launch system has evolved toward a long, slender, shell-structure which may have a bulbous payload*, or a configuration with control surfaces for use in launch or re-entry. Since on this type of configuration random fluctuating airloads may result from flow separation and unsteady shock waves near the nose, the overall bending response of the vehicle may result in severe dynamic stresses. Since on typical trajectories, Mach 1 occurs at a relatively low altitude (say 25,000 feet) these dynamic stresses are added to the substantial stresses resulting from steady-state airloads. In addition to the overall bending response loads, there is also the problem of response of panels, sections of stiffened shells, and equipment installations to local high-intensity aerodynamic noise.

II. IDEALIZATION OF BUFFET RESPONSE PROBLEM

Solution of the actual in-flight loads problem associated with transonic buffeting would involve computation of the response of a dynamic model of the structure to an unsteady pressure field which has a complicated spatial distribution and which has nonstationary random fluctuations with time. This solution would require time histories of the unsteady pressures. The local

---

* It should be noted that, however desirable a bulbous payload may be from the standpoint of the space vehicle (or space experiment) designer, it is incompatible with good aerodynamic design and places a very severe added burden on the structural designer.

unsteady flow which produces transonic buffeting is characterized by flow separation and oscillating shock waves that may be attached to the vehicle. The time-dependence of the unsteady pressures is extremely complicated; and the spectrum of the unsteady pressures contains a wide range of frequencies. The spatial distribution of the unsteady pressure field is highly dependent on the configuration (particularly nose shape) and for a given configuration is markedly affected by changes in Mach number and angle of attack. Time histories of the pressures acting on the vehicle could only be obtained by exact simulation of the flight parameters - that is, the time dependence of Mach number, angle of attack, dynamic pressure, and Reynolds number - in either a wind tunnel or free-flight test of a geometric model (perhaps full-scale) of the configuration.

The lack of facilities to provide such simulation, and to a lesser extent the lack of adequate analytical techniques to solve the non-stationary structural response problem, has led to the adoption of an idealization of the actual problem. In lieu of data on the nonstationary excitation, data on the excitation at constant wind tunnel test conditions is used. Instead of computing the response of the structure to nonstationary excitation, the response is calculated by assuming that the excitation is a stationary, ergodic, Gaussian process. If the excitation is a random stationary ergodic Gaussian process, then the Gaussian statistics of the excitation are specified by the mean value and the cross power spectral density* (CPSD) of the fluctuations about the mean. If the dynamic behavior of the structure is adequately described by linear differential equations, the Gaussian statistics of the response are determined by the mean response and the CPSD of the fluctuations of the response about the mean.

Even in this idealization of the buffet problem to a stationary excitation-response calculation, the complications in the excitation producing transonic buffeting make the simple determination of a coefficient of pressure inadequate. The stationary transonic buffeting excitation is most conveniently specified by the mean value of the pressures and the resulting forces and the cross power spectral density* (CPSD) of the fluctuations about the mean with the implied assumption that the excitation is a stationary ergodic Gaussian process. At the present time it is not possible to predict by analytical means alone the mean value and CPSD. They have to be derived from scale model tests in a wind tunnel.

Experimental methods are beset by their own difficulties. One of these is the inability of existing wind tunnels to provide complete similitude for the independent variables. Some of the discrepancies between the experimental results of different investigators may be ascribed to this cause. To overcome this difficulty, systematic investigations have to be conducted to determine the effect of lack of similitude for each one of the important independent variables.

---

* In what follows cross power spectral density will sometimes be abbreviated as CPSD; and power spectral density will sometimes be abbreviated as PSD.

III. SCALING LAWS AND SIMILITUDE REQUIREMENTS FOR VALID SCALE MODEL WORK

The use of small scale models can be a very powerful research tool for exploring unknown or poorly understood physical phenomena. To use it effectively, the investigator must be prepared to derive valid scaling laws for the dependent variables without being able to meet similitude requirements for all of the independent variables and possibly without even being sure they have all been identified. This is a situation that is encountered more often in practice than is discussed in theory, but is really not quite as hopeless as it sounds. It is the lack of knowledge of the governing physical laws that makes scale model work necessary for prediction purposes.

A. General Principles

The validity of scale model work is based on two main principles. One is that a physical phenomenon is independent of the units of measurement. The second is that the physical laws governing the phenomenon are the same for both model and full scale. From these basic principles it is possible to derive the similitude requirements for the independent variables and the scaling laws for the dependent variables.

A certain amount of knowledge of the physical phenomena is necessary, however. First of all, the investigator must be able to distinguish clearly between the dependent and independent variables. Independent variables are, by definition, those that can be varied in magnitude independently of each other by the experimenter without affecting each other. For example, the load on the beam, the span of the beam, the modulus of elasticity and area moment of inertia of a beam are independent variables. The deflection and bending moment are dependent variables, since the magnitude of each is fixed by a prescribed set of values for the independent variables. While the bending moment may be derived theoretically from the deflection, this does not permit the deflection to be classed as an independent variable along with load and span. This is because the value of any one of the other, truly independent variables (like load and span) cannot be changed arbitrarily without altering the values of deflection. It must also be possible for the investigator to make at least an intelligent guess as to the identity of most of the important independent variables. In case of doubt as to the importance of an independent variable, it should be included rather than left out. If it is really unimportant, or does not belong, scale model work will reveal this without any harm being done. If it is omitted and is really important, this too will eventually be discovered with enough experimental work, but not without a good deal of extra effort.

Starting with a clear knowledge of the difference between the dependent and independent variables and an identification of the independent variables, the scaling laws and similitude requirements may be determined.

B. Derivation of Similitude Requirements and Scaling Laws

A physical phenomenon, y, may depend on several variables, x_1, x_2, ..., x_n, in some unknown manner. If the independent variables x_1, x_2, ..., x_n are known, this already indicates that a considerable amount of knowledge has been amassed on the subject, even if it is not known exactly how y depends on the variables, x. In spite of this limitation, it is possible now to predict the outcome, y, for a given set of values of the variables, x, it depends on. This is achieved by model testing.

The relationship between the dependent variable, y, and the independent variables, x, can be expressed in general as

$$G(y, x_1, x_2, x_3, \ldots, x_n) = 0 \tag{1}$$

where G is some function of $y, x_1, \ldots, x_n$. If the exact nature of the function G were known, then this would be the mathematical expression of the physical law governing the dependence of the phenomenon of y on the variables $x_1, \ldots, x_n$.

This physical law should be independent of the units used in measurement, and should apply just as well to the model as it does to the prototype. Model testing depends on this principle. Using the subscripts m to apply to the model and p to apply to the prototype, we have the relationship

$$G(y_m, x_{1m}, x_{2m}, \cdots, x_{nm}) = G(y_p, x_{1p}, x_{2p}, \cdots, x_{np}) = 0. \tag{2}$$

Using Buckingham's Pi Theorem, from the theory of dimensional analysis, the n + 1 variables $(y, x_1, \ldots, x_n)$ can be combined into (n + 1)-4 dimensionless groups if four basic dimensions* are used. We have then

$$G\left[\pi_{1m}, \pi_{2m}, \ldots, \pi_{(N-3)m}\right] = G\left[\pi_{1p}, \pi_{2p}, \ldots, \pi_{(N-3)p}\right], \tag{3}$$

where π_{1m}, π_{1p} contain the dependent variable y, and the remaining dimensionless groups contain the independent variables x_i. Now if the model is so constructed that

$$\pi_{2m} = \pi_{2p}, \ldots, \tag{4}$$

$$\pi_{(N-3)m} = \pi_{(N-3)p}$$

---

* In what follows we will consider temperature to be the fourth basic dimension.

then it must follow from Equation (3) that

$$\pi_{1m} = \pi_{1p} . \tag{5}$$

The value of y_m contained in π_{1m} can be measured from the model test. The value of π_{1m} (which is equal to π_{1p}) can then be calculated from the result of the experiment. From this value of π_{1p}, the desired value of y_p that it contains can now be calculated.

Therefore, it can be seen that knowing x_{1p}, x_{2p}, . . . , x_{np}, the value of y_{1p} can be found by testing a model, even though the nature of the function G is unknown, provided the model is built to satisfy the relationships of Equation (4). These relationships determine the required scale factors to be used.

C. Scale Factors and Similitude Requirements

It must be stressed that Equation (5) will in general yield the scaling law for the dependent variable if and only if the similitude requirements ($\pi_{km} = \pi_{kp}$, k = 2, 3, . . . , N-3, Equations -4) are satisfied.

A number of these requirements are satisfied by the choice of the arbitrary scale factors. The number of scale factors that may be chosen arbitrarily is equal to the number of basic dimensions in the problem. For example, if all the variables in the physical law are expressible in terms of four basic dimensions, i.e., mass, length, time and temperature, four scale factors may be chosen arbitrarily, corresponding directly or indirectly to each of them, to suit test requirements. The remaining scale factors will then be expressed in terms of one or more of these four.

As stated above, the present wind tunnel facilities cannot provide test conditions which satisfy all of the scaling laws. This means that the wind tunnel tests to determine the transonic buffeting excitation are tests of distorted scale models. Tests of this type are discussed in detail in the next section.

D. Derivation of Scaling Laws When Complete Similitude is Lacking (Distorted Scale Models)

1. General Principles

In practice it is not possible to satisfy all the similitude requirements for transonic buffeting wind tunnel tests. Systematic methods have been developed for dealing with this problem. These methods will be discussed in some detail.

The basic principle underlying the successful use of scale models when similitude is lacking is this. For every similitude requirement that cannot be satisfied in a model test, there must be provided a relationship, theoretical or empirical, between the dependent variable and that independent variable for which similitude could not be provided. This relationship can then be used in a manner analogous to a correction factor for the scaling law. Put more precisely, for every similitude requirement that cannot be met for an independent variable, an adequate knowledge must be available of the partial derivatives of the dependent variable with respect to that independent variable, for the range of values of interest to the investigator. For example, if it were impossible to make $\pi_{km} = \pi_{kp}$ and if the value of π_{km} that can be provided in the model test is not too far removed from the required value of π_{kp}, then a knowledge of $\frac{\partial \pi_1}{\partial \pi_k}$ in the neighborhood of π_{km} will suffice for a linear correction to the scaling law. If the value of π_{km} that can be provided is appreciably different from the required value of π_{kp}, then $\frac{\partial \pi_1}{\partial \pi_k}$ must be a sufficiently well defined function of π_k to permit an accurate correction to be made to the value of π_1. This may be explained as follows. The required value of π_1 at the proper value of π_{kp} may be obtained from the observed value of π_1 at the model value of π_{km} by means of a Taylor series if the partial derivatives are known up to a sufficiently high order at the model value of $\pi_k = \pi_{km}$. This is shown below.

$$(\pi_1)_{\pi_k = \pi_{kp}} = (\pi_1)_{\pi_k = \pi_{km}} + \left(\frac{\partial \pi_1}{\partial \pi_k}\right)_{\pi_k = \pi_{km}} (\pi_{kp} - \pi_{km}) \tag{6}$$

$$+ \frac{1}{2!} \left(\frac{\partial^2 \pi_1}{\partial \pi_k^2}\right)_{\pi_k = \pi_{km}} (\pi_{kp} - \pi_{km})^2 + \ldots$$

The case for the lack of similitude of two or more important independent variables will be discussed later.

2. Lack of One Similitude Requirement

Consider the case where only a single similitude requirement π_k cannot be satisfied for practical reasons, i.e., $\pi_{km} \neq \pi_{kp}$. According to general principles, this difficulty can be overcome by providing a relationship, either theoretical or experimental, between the dependent variable and the independent variable for which similitude cannot be provided.

The simplest situation occurs when the effect of the unscaled independent variable is small, ie., π_1 is weakly dependent on π_k. In this case, the scaling law for the dependent variable, i.e., $\pi_{1p} = \pi_{1m}$, will be approximately true, and the observed value of the dependent variable may be scaled up to full size accordingly. If it is not possible to demonstrate theoretically that π_k is an unimportant variable, then this must be done experimentally, over as wide a range of values of π_{km} as possible, keeping all other values of the independent variables constant. To do this, it may even be necessary to use a number of scale models of different sizes, if there is no other way to vary the value of π_{km}.

When the unscaled independent variable is important, and no theoretical relationship exists to show its effect on the dependent variable, then a similar experimental program must be conducted to determine π_{1m} as a function of π_{km}. Ideally, the range of experimental values of π_{km} should straddle the desired value of π_{kp}, or should be brought as near π_{kp} as possible. If this too is impossible, then the functional relationship between π_{1m} and π_{km} should be defined by a sufficiently large number of values of π_{km} to permit a valid extrapolation to the desired value of $\pi_{km} = \pi_{kp}$ on the basis of Equation (6).

3. Lack of More Than One Similitude Requirement

Let the general form of the unknown physical law be represented in dimensionless form by the following:

$$\pi_1 = F(\pi_2, \pi_3, \ldots, \pi_k, \ldots, \pi_r). \tag{7}$$

If the corresponding values of $\pi_3, \ldots, \pi_r$ could be kept the same for model and full scale at a set of constant values then an experimental plot of π_1 vs. π_2 would be identical for all sizes of scale model. For example, a range of model sizes, one twentieth, one tenth, one fifth, etc., would yield identical plots of π_1 vs. π_2. This would not be true if the similitude requirements for $\pi_k, \ldots, \pi_r$ were not met, i.e., if the corresponding values of $\pi_k, \ldots, \pi_r$ are different for different size scale models. If the resulting plots of π_1 vs. π_2 from different sizes of models are not very different from each other, in spite of lack of similitude for $\pi_k, \ldots, \pi_r$ this would indicate that the combined effect of all the unsatisfied similitude requirements represented by $\pi_k, \ldots, \pi_r$ is not significant and $\pi_{1m} = \pi_{1p}$ will give an approximately true scaling law. This is the first possibility that should be checked when a large number of similitude requirements cannot be met.

At the other extreme, let us suppose that the similitude requirements $\pi_k, \ldots, \pi_r$ are all important and none of them can be satisfied. A straightforward, though cumbersome approach, would be to keep all but one of the dimensionless independent variables constant at a time, and find experimentally how π_1 depends on it. Then in a manner similar to that based on the use of Equation (6), the scaling law may be corrected for lack of similitude of one variable at a time.

There is a much more economical solution, which is particularly useful when all but one of the dimensionless independent variables cannot be held constant to determine its effect on π_1. To do this successfully, the experiments must be designed in such a manner that even though $\pi_k, \ldots, \pi_r$ are allowed to vary simultaneously, each of these π terms varies over as wide a range of values as possible. For these experiments, $\pi_2, \ldots, \pi_{k-1}$ are kept constant at desired values corresponding to those of the prototype. A surface of best fit, analogous to a curve of best fit for two variables can then be computed to represent π_1 mathematically as a function of the variables $\pi_k, \ldots, \pi_r$ from the experimental results.

The importance of a careful design of the experiments can now be seen since a wide spread of values for each of $\pi_k, \ldots, \pi_r$ will insure an accurate formulation of the surface of best fit. This mathematical expression for $\pi_1 = f(\pi_k, \ldots, \pi_r)$ can then be used to provide the necessary correction for lack of similitude in the variables $\pi_k, \ldots, \pi_r$ for the scaling law.

Thus, it is possible to conduct valid scale model tests even when similitude cannot be provided for one or more independent variables and the physical law governing the phenomenon is unknown. The most difficult situation occurs when similitude cannot be provided for a number of important independent variables. In this case, proper design of an experimental program combined with the technique of deriving a surface of best fit in n-space may be used to overcome this difficulty. These techniques may be applied to practical problems of interest which have hitherto been considered "unscalable". Such efforts would be very rewarding, not only in advancing the ability to work with distorted scale models, but as a powerful research tool for exploring the unknown.

IV. SIMILITUDE REQUIREMENTS FOR WIND TUNNEL TESTS OF SCALE MODELS TO MEASURE TRANSONIC BUFFETING EXCITATION

A. Choice of Dependent and Independent Variables

In the similitude analysis of any physical problem, it is necessary to decide in advance the dependent variables that need to be measured and to distinguish clearly between the dependent and the independent variables in the problem. Consideration of the problem of determining the aerodynamic loads due to transonic buffeting leads to the following conclusions. The dependent variables to be measured are 1) the dynamic response of the model, 2) the local differential pressures, 3) sums of these differential pressures, (these sums are to be considered as approximations to the random lateral load at a station on the model), and 4) the frequency of oscillations of the unsteady pressure field. From recorded time histories of these local differential pressures and their sums, the local lateral loads, the cross-power-spectral-densities can be computed for use in the calculations of the response of the prototype*. The dependent variables to be measured by the wind tunnel tests are outlined in Table 1.

In writing down the dependent variables in Table 1, it has been assumed that the loads $w(\xi, t)$ are not dependent on the motion of the model in the wind tunnel (or the prototype structure in flight).

Table 1 Dependent Variables to be Measured

		Dimensions
$p(\vec{r}_i, t) \equiv p_i(t)$	= Local differential pressure at location of i^{th} transducer	$M L^{-1} T^{-2}$
$w(\xi_i, t) \equiv w_i(t)$	= Random lateral load per unit length at station $\xi = \xi_i$	$M T^{-2}$
$y(\xi_i, t) \equiv y_i(t)$	= Random lateral response at station $\xi = \xi_i$	L
ω	= Frequency of oscillation of unsteady pressures	T^{-1}

* Note that the random excitation can be completely described by the cross-power-spectral-density obtained from single time histories of the pressures only if the unsteady pressure field is a random stationary ergodic Gaussian process. We are in essence assuming that this is true. Later the validity of this assumption must be checked.

Thus, the similitude analysis and the scaling laws developed in this section apply only to buffeting excitation which is independent of body motion. If the excitation depends on the body motion, then the equations of motion for the vehicle take a form different from the case discussed in Appendix A. Namely, the normal mode coordinates, $q_n(t)$, are solutions of equations of the form

$$M_n \left[\ddot{q}_n + 2 \xi_n \omega_n \dot{q}_n + \omega_n^2 q_n \right] = Q_n \left[y(x, t) \right] \tag{8}$$

where $y(x, t) = \sum_n q_n(t) \phi_n(x)$.

The response analysis is then concerned with determining aerodynamic instabilities and stable limit cycle oscillations. Wind tunnel tests to investigate the buffet phenomenon of this type require an aeroelastic ("flutter") model, or an articulated model which simulates the nodes of the modes of vibration.

However, in the case of negligible coupling between the motion of the vehicle and the aerodynamic forces, a dynamically scaled model of the prototype is not required. In this case the measured pressures and the measured response are independent of one another. This means that there are two basic techniques for measuring the excitation producing transonic buffeting. We can measure the space and time correlation of the unsteady pressure field acting on a model system with transducers and use these measurements and the properties of the structure to predict the dynamic response of the full-scale vehicle; or we can measure the space and time correlation of the dynamic response of a calibrated model system(one of known dynamic properties) and use this measured response along with the known dynamic properties, to compute the CPSD of the unsteady pressure field that is exciting the model system. This computed CPSD of the pressure field can then be used in the response calculations for the full-scale vehicle.

There are several types of wind tunnel tests which can be (and have been) run. Three types of wind tunnel tests to determine design criteria for the buffeting excitation are discussed in Reference 4. These include 1) a pressure model test, 2) a test of a dynamically calibrated wind tunnel model system, and 3) a test of a dynamically scaled wind tunnel model. A fourth type of test should now be added. This is a test utilizing the inertia-compensated-balance system which will be discussed in a paper to be presented in the fifth session of this Symposium. The similitude analysis and the scaling laws developed here apply to all of these tests.

The choice of the independent variables is governed by knowledge of the fundamental physics of the problem plus physical insight and intuition. The independent variables chosen to be significant are given in Table 2. These variables can be divided into three groups: 1) the variables describing the geometry of the body, 2) the variables describing the dynamic elastic behavior of the vehicle structure, and 3) the variables describing fluid flow at high subsonic and low supersonic velocities. The variables in group 3 (namely, V, μ, ρ, γ, β, R) are inter-dependent since for example μ depends on β.

If the effects of variations of one of these variables are to be studied, then this inter-dependence must be kept in mind. For example, the effects of β cannot be determined unless the density is varied to keep Reynolds number a constant.

It may be argued that the vortexes shed or the thickness of the boundary layer affect the unsteady aerodynamic loads and that these loads should, therefore, be considered to be functions of these variables. However, the vorticity and boundary layer thickness are themselves determined by the independent variables listed above. These independent variables, therefore, ultimately determine the unsteady aerodynamic loads.

Table 2 Independent Variables

			Dimensions
D	=	Reference Diameter	L
λ	=	Any typical dimension	L
τ	=	Any characteristic time associated with the flow	T
e	=	Any typical dimension representing roughness	L
ν_i	=	Natural frequency of structure in the i^{th} mode	T^{-1}
m	=	Structural mass per unit length	ML^{-1}
ξ_i	=	Damping coefficient of i^{th} mode of bending vibration	$ML^{-1}T^{-1}$
EI	=	Bending Stiffness of structure	ML^3T^{-2}
V	=	Velocity of air flow relative to missile	LT^{-1}
μ	=	Absolute viscosity of the air	$ML^{-1}T^{-1}$
ρ	=	Mass density of air	ML^{-3}
γ	=	Specific heat ratio of air	Dimensionless
β	=	Temperature of air	Θ
R	=	Gas constant of air	$L^2T^{-2}\Theta^{-1}$
α	=	Angle of attack	Dimensionless

NOTE: $a = \left[\gamma R \beta\right]^{1/2}$ is the velocity of sound in air. The subscript i refers to the i^{th} mode. When ∞ is used as a subscript, it refers to the model.

B. Dimensionless Parameters Containing the Independent and Dependent Variables

From the 15 independent variables given in Table 2 we can construct 11 [(15-4) = 11] dimensionless parameters containing the independent variables. These parameters are listed in Table 3.

Table 3 Dimensionless Parameters Containing the Independent Variables

$\pi_1 = \frac{\lambda}{D}$

$\pi_2 = \frac{D}{V\tau}$

$\pi_3 = \gamma$

$\pi_4 = V/\sqrt{\gamma \beta R} = \frac{V}{a}$, the Mach number

$\pi_5 = \rho VD/\mu$, the Reynolds number

$\pi_6 = e/D$

$\pi_7 = \nu_i \tau$

$\pi_8 = \rho D^2/m$

$\pi_9 = EI/q D^4$, where $q \equiv \frac{\rho V^2}{2}$ is the dynamic pressure

$\pi_{10} = \zeta_i = \frac{Ci}{2 \nu_i \mathcal{M}_i^{\dagger}}$, the equivalent viscous damping ratio for the i^{th} mode

$\pi_{11} = \alpha$, angle of attack

$\dagger \mathcal{M}_i$ = generalized mass of the i^{th} mode.

From the four (4) dependent variables for the pressure model test (Table 1) and the independent variables (Table 2) we can construct four (4) dimensionless parameters containing the dependent variables. These are listed in Table 4.

Table 4 Dimensionless Parameters Containing the Dependent Variable

$$\pi_{12} = \omega\tau \qquad \pi_{13} = \frac{p_i(t)}{q}$$

$$\pi_{14} = \frac{w_i(t)}{qD} \qquad \pi_{15} = \frac{y_i(t)}{D}$$

where $q = \frac{\rho V^2}{2}$ is the dynamic pressure.

C. Dimensionless Parameters for the Cross Correlation Functions and CPSD Functions

The cross correlation functions and CPSD functions for the unsteady pressure field and the dynamic response are defined in terms of the dependent variables $p_i(t) = p(\vec{r}_i, t)$ and $y_i(t) = y(\xi_i, t)$. We can therefore write these CPSD functions in dimensionless form in terms of the dimensionless parameters from Table 3 and Table 4.

Let us consider two functions of time $\eta_1(t)$ and $\eta_2(t)$. The cross-correlation functions, $\Psi_{\eta_1\eta_2}(t')$, and the cross power spectral density function, $F_{\eta_1\eta_2}(\omega)$, are Fourier transform pairs which may be written in the form.

$$F_{\eta_1\eta_2}(\omega) = \int_{-\infty}^{\infty} \Psi_{\eta_1\eta_2}(t')\, e^{-i\omega t'} dt'$$

and

$$\Psi_{\eta_1\eta_2}(t') = \frac{1}{2\pi} \int_{-\infty}^{\infty} F_{\eta_1\eta_2}(\omega) e^{i\omega t'} d\omega.$$

In the above $\Psi_{\eta_1\eta_2}(t')$ is defined in terms of $\eta_1(t)$ and $\eta_2(t)$ by

$$\Psi_{\eta_1\eta_2}(t') = \lim_{T\to\infty} \frac{1}{2T} \int_{-T}^{T} \eta_1(t)\, \eta_2(t+t')dt.$$

Thus, $\psi_{\eta_1 \eta_2}(t')$ has the same units as the product $\eta_1(t)\,\eta_2(t)$.

Applying the above relations and definitions to the CPSD of $p(\vec{r}_i, t)$, $w(\xi, t)$ and $y(\xi, t)$ we obtain the following dimensionless parameters:

Cross Correlation Functions:

$$\pi_{16} = \frac{\psi_{p_i F_j}(t')}{q^2} = \lim_{T\to\infty} \frac{1}{2T} \int_{-T}^{T} \left[\frac{p_i(t)}{q}\right]\left[\frac{p_j(t+t')}{q}\right] dt$$

$$\pi_{17} = \frac{\psi_{w_i w_j}(t')}{(qD)^2} = \lim_{T\to\infty} \frac{1}{2T} \int_{-T}^{T} \left[\frac{w_i(t)}{qD}\right]\left[\frac{w_j(t+t')}{qD}\right] dt$$

$$\pi_{18} = \frac{\psi_{y_i y_j}(t')}{D^2} = \lim_{T\to\infty} \frac{1}{2T} \int_{-T}^{T} \left[\frac{y_i(t)}{D}\right]\left[\frac{y_j(t+t')}{D}\right] dt$$

CPSD functions:

$$\pi_{19} = \frac{V}{q^2 D} F_{p_i p_j}(\omega) = \int_{-\infty}^{\infty} \frac{\pi_{16}\left[t' \,\middle|\, p_i, p_j\right] e^{-i\omega t'}\, d(t'/\tau)}{(D/V\tau)}$$

$$\pi_{20} = \frac{V}{q^2 D^3} F_{w_i w_j}(\omega) = \int_{-\infty}^{\infty} \frac{\pi_{17}\left[t' \,\middle|\, w_i, w_j\right] e^{-i\omega t'} d(t'/\tau)}{(D/V\tau)}$$

$$\pi_{21} = \frac{V}{D^3} F_{y_i y_j}(\omega) = \int_{-\infty}^{\infty} \frac{\pi_{18}\left[t' \,\middle|\, y_i, y_j\right] e^{-i\omega t'}\, d(t'/\tau)}{(D/V\tau)}$$

Letting $\left[\theta \equiv \frac{t}{T};\ \theta' \equiv \frac{t'}{T};\ \Theta \equiv \frac{T}{T}\right]$ and using the π_i given in Table 3 and Table 4, we can rewrite the above in dimensionless form:

$$\pi_{16}(\theta') = \lim_{\Theta \to \infty} \frac{1}{2\Theta} \int_{-\Theta}^{\Theta} \pi_{13}\left[p_i(\theta)\right] \pi_{13}\left[p_j(\theta+\theta')\right] d\theta$$

$$\pi_{17}(\theta') = \lim_{\Theta \to \infty} \frac{1}{2\Theta} \int_{-\Theta}^{\Theta} \pi_{14}\left[w_i(\theta)\right] \pi_{14}\left[w_j(\theta+\theta')\right] d\theta$$

$$\pi_{18}(\theta') = \lim_{\Theta \to \infty} \frac{1}{2\Theta} \int_{-\Theta}^{\Theta} \pi_{15}\left[y_i(\theta)\right] \pi_{15}\left[y_j(\theta+\theta')\right] d\theta$$

$$\pi_{19}(\pi_{12}) = \frac{1}{\pi_2} \int_{-\infty}^{\infty} \pi_{16}\left[\theta' \middle| p_i, p_j\right] e^{-i\pi_{12}\theta'} d\theta'$$

$$\pi_{20}(\pi_{12}) = \frac{1}{\pi_2} \int_{-\infty}^{\infty} \pi_{17}\left[\theta' \middle| w_i, w_j\right] e^{-i\pi_{12}\theta'} d\theta'$$

$$\pi_{21}(\pi_{12}) = \frac{1}{\pi_2} \int_{-\infty}^{\infty} \pi_{18}\left[\theta' \middle| y_i, y_j\right] e^{-i\pi_{12}\theta'} d\theta'$$

D. Scaling Laws

Since all the variables in the problem can be expressed in terms of the four basic dimensions of mass, length, time and temperature, four scale factors can be chosen arbitrarily. These are:

$n_1 = D_p/D_m$ (the length scale factor)

$n_2 = V_p/V_m$

$n_3 = \rho_p/\rho_m$

$n_4 = R_p/R_m$

The subscripts p and m refer to the prototype and model, respectively.

All other scale factors can be expressed in terms of these four by making the dimensionless paramters $\pi_1, \ldots, \pi_{21}$ the same for the model and the prototype. If $\pi_1, \ldots, \pi_{11}$ can be made the same for model and prototype, it follows that $\pi_{kp} = \pi_{km}$, k = 1, 2, . . . , 21; giving the scale factor for the dependent variables.

The following scaling laws are obtained by choosing $n_1, \ldots, n_4$ and setting $(\pi_i)_m = (\pi_i)_p$:

Independent Variables

$$(\pi_1)_m = (\pi_1)_p \longrightarrow \lambda_m = \frac{1}{n_1}\ \lambda_p$$

$$(\pi_2)_m = (\pi_2)_p \longrightarrow \tau_m = \frac{n_2}{n_1}\ \tau_p$$

$$(\pi_3)_m = (\pi_3)_p \longrightarrow \gamma_m = \gamma_p$$

$$(\pi_4)_m = (\pi_4)_p \longrightarrow \beta_m = \frac{n_4}{n_2}\ \beta_p$$

$$(\pi_5)_m = (\pi_5)_p \longrightarrow \mu_m = \frac{1}{n_1\ n_2\ n_3}\ \mu_p$$

$$(\pi_6)_m = (\pi_6)_p \longrightarrow \epsilon_m = \frac{1}{n_1}\ \epsilon_p$$

$$\left.\begin{array}{l}(\pi_7)_m = (\pi_7)_p \\ (\pi_2)_m = (\pi_2)_p\end{array}\right\} \longrightarrow (\nu_i)_m = \frac{n_1}{n_2}\ (\nu_i)_p$$

$$(\pi_8)_m = (\pi_8)_p \longrightarrow m_m = \frac{1}{n_3 n_1^2} m_p$$

$$(\pi_9)_m = (\pi_9)_p \longrightarrow (EI)_m = \frac{1}{n_1^4 n_2^2 n_3} (EI)_p$$

$$(\pi_{10})_m = (\pi_{10})_p \longrightarrow (\xi_i)_m = (\xi_i)_p ,$$

$$\text{or } (C_i)_m = \frac{1}{n_1^2 n_2 n_3} (C_i)_p$$

$$(\pi_{11})_m = (\pi_{11})_p \longrightarrow \alpha_m = \alpha_p$$

Dependent Variables

$$(\pi_{12})_m = (\pi_{12})_p \longrightarrow \omega_m = \frac{n_1}{n_2} \omega_p$$

$$(\pi_{13})_m = (\pi_{13})_p \longrightarrow \left[p_i(t)\right]_m = \frac{1}{n_2^2 n_3} \left[p_i(t)\right]_p$$

$$(\pi_{14})_m = (\pi_{14})_p \longrightarrow \left[w(\xi_j, t)\right]_m = \frac{1}{n_1 n_2^2 n_3} \left[w(\xi_j, t)\right]_p$$

$$(\pi_{15})_m = (\pi_{15})_p \longrightarrow \left[y_i(t)\right]_m = \frac{1}{n_1} \left[y_i(t)\right]_p$$

$$(\pi_{16})_m = (\pi_{16})_p \longrightarrow \left[\psi_{p_i p_j}(t')\right]_m = \frac{1}{n_2^4 n_3^2} \left[\psi_{p_i p_j}(t')\right]_p$$

$$(\pi_{17})_m = (\pi_{17})_p \longrightarrow \left[\psi_{w_i w_j}(t')\right]_m = \frac{1}{n_1^2 n_2^4 n_3^2} \left[\psi_{w_i w_j}(t')\right]_p$$

$$(\pi_{18})_m = (\pi_{18})_p \longrightarrow \left[\psi_{y_i y_j}(t')\right]_m = \frac{1}{n_1^2}\left[\psi_{y_i y_j}(t')\right]_p$$

$$(\pi_{19})_m = (\pi_{19})_p \longrightarrow \left[F_{p_i p_j}(\omega)\right]_m = \frac{1}{n_1 n_2^3 n_3^2}\left[F_{p_i p_j}(\omega)\right]_p$$

$$(\pi_{20})_m = (\pi_{20})_p \longrightarrow \left[F_{w_i w_j}(\omega)\right]_m = \frac{1}{n_1^3 n_2^3 n_3^2}\left[F_{w_i w_j}(\omega)\right]_p$$

$$(\pi_{21})_m = (\pi_{21})_p \longrightarrow \left[F_{y_i y_j}(\omega)\right]_m = \frac{n_2}{n_1^3}\left[F_{y_i y_j}(\omega)\right]_p$$

E. Discussion of Scaling Laws

The scaling laws for the frequency of the oscillating loads, temperature, surface roughness, fluid viscosity (Reynolds number), and model structure are of particular interest.

The scaling law for the frequency of oscillating loads is

$$\omega_m = \frac{n_1}{n_2}\ \omega_p .$$

This requires that the unsteady pressures of the model should be observed at frequencies that are $\frac{n_1}{n_2}$ times the value of those frequencies of concern on the full-scale prototype. Note that while a characteristic time associated with the flow, (say, $\tau = D/V$) is considered to be an independent variable, the characteristic frequencies of oscillation of the unsteady aerodynamic pressures are considered to be dependent variables. This implies that the scaling of the frequency coordinate of the nondimensional PSD's is a function of the similitude paramters involving the independent variables and is not simply a reduced frequency (Strouhal number) based on a characteristic length, such as body diameter or boundary-layer thickness. This viewpoint has the advantage that it forces one to investigate the effects of lack of similitude on the abscissa of the nondimensional PSD's as well as the effects on the ordinate of the nondimensional PSD's.

The scaling law for temperature is

$$\beta_m = \frac{n_4}{n_2^2} \beta_p .$$

For $n_4 = 1$, i.e., the same gas is used for model and prototype, then the scaling law for temperature becomes

$$\beta_m = \frac{1}{n_2^2} \beta_p .$$

It is generally not possible to satisfy this criterion exactly in wind tunnel tests. However, it is believed that this is not an important variable, and does not affect the results appreciably if the value provided is not too far from the required value. The sensitivity of the results to this variable can be checked by varying the total temperature of the wind tunnel. Here it should be noted that variations in temperature also effect the Reynolds number. This coupling effect must be considered in the planning of a test and in the interpretation of the data.

The surface roughness of the flight structure is difficult, if not impossible, to define precisely - let alone simulate. The effect of surface roughness can be investigated qualitatively in the model test by changing the model roughness. If the magnitude of the unsteady aerodynamic forces and pressures were found to increase with roughness, it would be necessary to choose a particular roughness that would give conservative results for the full-scale missile. The surface roughness parameter becomes especially important if the buffet phenomenon being investigated involves shock-boundary layer interaction and boundary layer separation. The separation of the boundary layer may be significantly affected by the surface roughness. If no flow separation exists on the "smooth" wind tunnel model, while it does exist on the full-scale prototype, the loads measured on the model would not accurately predict the loads on the prototype.

The scaling law for absolute viscosity cannot generally be satisfied, and hence the Reynolds number (π_5), cannot generally be made the same for model and prototype. A Reynolds number of about half the full-scale value can usually be provided in the wind tunnel for a prototype which is about 10 feet in diameter. As the size of the prototype increases, the fraction $\frac{(R_N)_m}{(R_N)_p}$ will necessarily decrease unless larger and larger tunnels are built. Since the latter alternative is a very costly and lengthy procedure, it is necessary to investigate the Reynolds number dependence on the buffet phenomenon more thoroughly by careful analysis of test results and systematic planning of future tests. For a given wind tunnel facility, the Reynolds number can be varied by varying the total pressure or temperature of the flow, by varying the model from a small size to the maximum possible size, or by using a working fluid other than air; for example, Freon.

In the case of tests of a dynamically scaled wind tunnel model system, additional practical difficulties in scaling the model structure make it impossible to scale up the measured response of the model to full size directly by the given scaling laws.

One difficulty is the requirement of equal damping for model and full-scale, expressed by the relationship $\xi_p = \xi_m$. The damping for the full scale structure is not known before it is built, and, even if it were, it is practically impossible to build a model with a specified damping ratio. Since the peak response of an elastic structure to a random excitation is sensitive to the amount of damping, this factor alone makes it desirable to eliminate the effects of the dynamic properties of the model by computing the CPSD of the excitation forces using Equation (15), p. 28.

Another difficulty is the similitude requirement for all the natural frequencies of the structure. A liquid-fuel missile contains slosh masses that cannot be adequately simulated in a scale model. This is because of the difficulty, if not the impossibility, of choosing a material for the model structure that simultaneously satisfies the ratio $\rho_m/\rho_p = 1/n_3$, the bending stiffness ratio $(EI)_m/(EI)_p = \frac{1}{n_1^4 n_2^2 n_3}$, and the mass ratio given by $m_m/m_p = \frac{1}{n_1^2 n_3}$, which includes the weight of the liquid propellant as well as the structure. For example, if a value of $n_3 = \frac{1}{5}$ is chosen to provide the same Reynolds number for model and full scale, it becomes necessary to choose a structural material for the model that is five times denser that the prototype material. If this requirement is neglected and the same material is chosen for model and full scale, then the satisfaction of the bending stiffness ratio will provide a model structure that is too light. This is compensated by simulating propellant masses by a model material that is much denser that five times the fuel, so that the overall mass ratio for both structure and propellant is satisfied. Therefore, it can be seen that the model response or internal loads on the structure cannot be scaled up directly from the results of a scale-model test.

It is possible, however, to use the measured response to compute the unsteady aerodynamic loads and to scale up those loads acting on the model.

V. REVIEW OF PREVIOUS WORK AND SUGGESTED AREAS FOR FUTURE RESEARCH

In the recent past, wind tunnel tests of all four types noted above have been conducted. The Ames Laboratory of NASA has conducted tests of a variety of nose shapes. These tests have investigated the effects of nose shape on the rms fluctuation level, the shape of the power spectral density (PSD) curves, and the amount of aerodynamic damping. The coupling between the model deflection and the excitation forces has also been investigated. Some of these tests have been directly associated with a development project, e.g., Atlas Able V, and Centaur.

In addition to the work at Ames Laboratory, considerable work has been done at the NASA Langley Research Center. These tests have investigated the buffet problem on the Mercury-Atlas and, more recently, on the manned lunar vehicle configurations.

Transonic buffet studies of Titan II with the Mark 4 and Mark 6 re-entry vehicles were conducted by the Martin Company at the Propulsion Wind Tunnel at the Arnold Engineering Development Center. (This work is outlined in some detail in Reference 4). The Martin Company is also responsible for the tests of Titan III with a Dyna-Soar payload, and also with a bulbous payload.

In the course of this work, attempts have been made to investigate the accuracy and limitations of the scaling laws given here. In the Ames tests, Reynolds number was varied both by varying total pressure and by varying the model scale factor. Some of this work is being presented at this Symposium in Session 5, by Mr. C. F. Coe. At Langley, tests of the same configuration were run with different gases (air and Freon) but the same Reynolds number. (Ref. 6) These test results indicate that for equal Reynolds number the scaling laws given above for π_{19} and π_{12} hold.

The investigations to date have indicated that there are two types of transonic buffeting: 1) Wake buffeting (e.g., buffeting by the wake of the escape rocket on the Mercury-Atlas), and 2) Buffeting by loads created by intermittent flow attachment and detachment. (This type of buffeting usually involves a shock-wave-boundary layer interaction at the point of onset of the flow separation.) The wake buffeting is characterized by unsteady pressure fluctuations which have a relatively flat PSD curve, similar to "white noise". The separated flow buffet is characterized by a large amount of energy at the low frequency and of the spectrum. Thus, this type of buffeting produces more severe dynamic response of the structure in the bending modes.

The question of coupling between the transonic aerodynamic forces and the motion of the vehicle has not been conclusively answered. The tests at Ames Research Center have indicated that coupling may exist for profiles which have a gradual boattail. Tests using an articulated balance and light-weight fiberglass models have indicated that the bulbous payloads may have negative aerodynamic damping at transonic Mach numbers. Further investigation of this aspect of the transonic buffet problem is required.

Another area requiring further investigation is the axial correlation and the circumferential correlation of the unsteady pressure field. The dependence of the CPSD of the pressure field should be determined as a function of Mach number, angle of attack, Reynolds number, surface roughness, and body shape. This dependence is of particular importance with regard to the resulting cross-correlation of the forces in the pitch and yaw planes. If these forces are correlated in such a way to produce bending moment response in pitch and yaw which have high correlation, then the mean-square bending stresses will be higher than either the mean-square bending stress resulting from the pitching moment or the mean square bending stresses resulting from the yawing moment. Another important application of this information is in the design of pressure model tests. The number of pressure transducers required to give an accurate approximation for the force acting on an area of a model is a function of the cross-correlation of the unsteady pressure field.

VI. SUMMARY AND CONCLUSIONS

Scaling laws which apply to scale model tests to determine transonic buffeting excitation have been derived by direct application of the Buckingham Pi Theorem. The difficulties arising from inability to provide exact similitude have been pointed out. The theory of distorted scale models have been reviewed.

It has been noted that several important areas require additional study:

1) The effects of time variation of the flow parameters (M, α, RN, q, β) on the level of the unsteady pressures.

2) The dependence of the scaling laws on Reynolds number and the properties of the test medium.

3) The dependence of the excitation on motion of the wind tunnel model. (The importance of this effect is expected to depend on the configuration geometry).

4) The variation in cross-correlation of the unsteady pressures (with axial distance and circumferential angle) with changes in geometry.

It is hoped that this review of the similitude requirements and other factors associated with the design of scale model tests to measure the transonic buffeting excitation will help engineers with the planning of future tests and with the interpretation of test results.

APPENDIX A

RESPONSE OF NONUNIFORM BEAM TO TRANSONIC BUFFETING FORCES

This appendix presents a brief review of the analytical tools which are available for calculation of the response of a non-uniform beam model of the missile structure to stationary random excitation. The analysis as discussed here applies to the gross loads problem. It should be noted, however, that the local loads problem can be handled simply by substituting an appropriate structural model which describes the dynamic response of the shell structure or panels. In this appendix the normal mode approach of beam vibration analysis is used; and it is assumed that the modes are not coupled because of damping. This review of the response analysis for the idealized transonic buffet problem indicates what information must be obtained from a wind tunnel test.

Powell* has shown that the cross power spectral density of the response of this non-uniform beam is given by an integral equation:

$$F\left[\omega \,|\, y(x_k, t),\ y(x_\ell, t)\right] = \sum_m \sum_n \frac{\varphi_n(x_k)\,\varphi_m(x_\ell)}{Z_n^*(\omega)\,Z_m(\omega)}$$

$$\int_0^L \int_0^{L'=L} \varphi_m(\xi)\,\varphi_n(\xi')\,F\left[\omega \,|\, w(\xi', t),\ w(\xi, t)\right] d\xi\, d\xi' \,; \qquad (9)^{**}$$

where $\varphi_n(x)$ is the $(n)^{th}$ normal mode of vibration of the beam;

$$Z_n(\omega) = m_n\left(\omega_n^2 + 2i\zeta_n\omega_n - \omega^2\right)$$

is the complex impedance for the $(n)^{th}$ mode; and

$$F\left[\omega \,|\, w(\xi', t),\ w(\xi, t)\right]$$

is the cross power spectral density of the disturbing force $w(\xi, t)$ (Fig. 1).

---

* S. H. Crandall: Random Vibration, Technical Press of Massachusetts Institute of Technology, and John Wiley and Sons, New York, 1958, p. 192.

** In Equation (9) and in following equations asterisk (*) denotes complex conjugate.

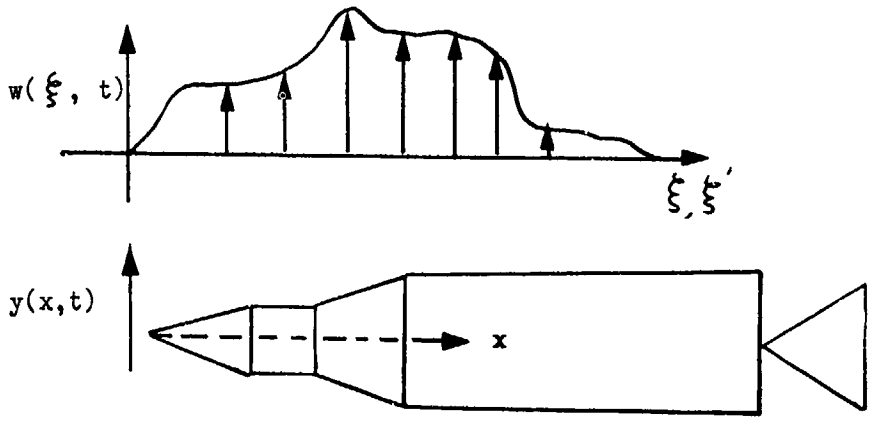

(a) Distributed Random Excitation Force

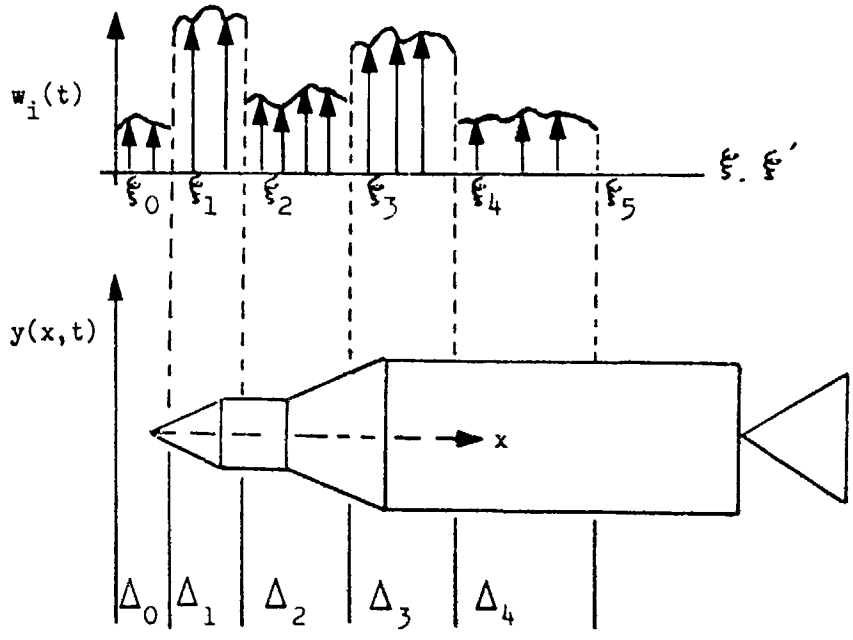

(b) Lumped Random Excitation Force

Fig. 1 Nonuniform Beam

If the length of the beam can be divided into discrete lengths[+]

$$\Delta_i \equiv \xi_{i+1} - \xi_i ,$$

over which the distributed excitation $w(\xi, t)$ has a unity spatial correlation but is random in time; then $w(\xi, t)$ can be written in the form

$$w(\xi, t) = W_i(\xi)\, Q_i(t) \tag{10}$$

for

$$\xi_i < \xi < \xi_{i+1}.$$

For excitation of the form of Eq(10) the (integral) Eq (9) can be transformed to a matrix equation as follows:

$$\left[F(\omega \mid y_k, y_\ell)\right] = \left[\varphi_{nk}\right]^T \left[\frac{1}{Z_n^*}\right] \left[\Gamma'_{nj}\right] \left[F_{ji}\left[\omega \mid Q_j(t), Q_i(t)\right]\right] \left[\Gamma_{mi}\right]^T \left[\frac{1}{Z_m}\right] \left[\varphi_{m\ell}\right], \tag{11}$$

where

$$y_k \equiv y(x_k, t), \quad \varphi_{nk} \equiv \varphi_n(x_k), \quad \Gamma'_{nj} \equiv \int_{\xi'_j}^{\xi'_{j+1}} W_j(\xi')\, \varphi_n(\xi')\, d\xi',$$

and

$$\Gamma_{mi} \equiv \int_{\xi_i}^{\xi_{i+1}} W_i(\xi)\, \varphi_m(\xi)\, d\xi ;$$

[+] See Figure 1.

[*] $[\,]$ Symbol denotes a diagonal matrix.

$F_{ji}(\omega | Q_j(t), Q_i(t))$ is the cross power spectral density of $Q_j(t)$ and $Q_i(t)$. The value of $\overline{y_k(t)y_\ell(t)}^{\dagger}$ is then determined by integrating Eq (11) over frequency.

By assuming that power spectral density of the response has a negligible value expect in the neighborhood of the natural frequencies of the system, Eq (11) can be greatly simplified. Reference 5 shows that Eq (11) can be reduced to

$$F\left(\omega_q \mid y_k, y_\ell\right) \doteq \beta_q^2\left(\omega_q\right)\phi_q\left(x_k\right)\phi_q\left(x_\ell\right) F_{qq}\left(\omega_q \mid P_q, P_q\right) \tag{12}$$

where

$$\beta_q^2(\omega_q) = \frac{1}{\left(2\xi_q \omega_q^2 m_q\right)^2}$$

and

$$F_{qq}(\omega_q \mid P_q, P_q) = \left[\gamma'_{qj}\right]\left[F_{ji}(\omega_q \mid Q_j, Q_i)\right]\left[\gamma_{qi}\right]^T ;$$

γ_{qi} and $F_{ji}(\omega_q \mid Q_j, Q_i)$ are defined in Eq (11). By multiplying each peak value (at $\omega = \omega_q$) by the half width of the resonance peak ($\Delta\omega_q = \pi\xi_q\omega_q$), an approximate value for the integral of Eq (12) is obtained which is $\overline{y_k(t)y_\ell(t)}$; namely,

$$\overline{y_k(t)y_\ell(t)} \doteq \sum_q \frac{\pi F_{qq}(\omega_q \mid P_q, P_q)\,\phi_q(x_k)\,\phi_q(x_\ell)}{4\xi_q m_q^2 \omega_q^3} . \tag{13}$$

† By definition $\psi_{y_k y_\ell}(\tau) = \overline{y_\ell(t+\tau)y_k(t)} = \lim_{T\to\infty} \frac{1}{2T}\int_{-\infty}^{\infty} y_\ell(t+\tau)y_k(t)\,dt.$

The determination of the transonic buffet loads imposed on a launch vehicle thus involves three steps:

1) Determination of the steady state and unsteady aerodynamic forces by conducting a wind tunnel test;

2) Determination of the normal mode model of the missile structure by analytical vibration analysis and by vibration tests; and

3) Determination of the transonic buffet response of the vehicle by use of the results of 1) and 2) and Equation (11) or (12).

Botman[†] shows that the matrix Equation (11) may be inverted so that the input spectra appear on the left hand side of the equation. The right hand side of the equation includes the output spectra of the mechanical system and transfer matrices $H(\omega)$ that depend on the dynamic properties of the mechanical system.

$$\left[F_{ji} \left\{ \omega \middle| Q_j(t), Q_i(t) \right\} \right] = \left\{ \left[H^{-1} \right]^{*}_{mxn} \right\}^{T} \cdot \left[F_{yy} \left\{ \omega \middle| y(x_k, t, y(x_\ell, t) \right\} \right]_{mxm} \left[H^{-1} \right]_{mxn} \quad (14)$$

From Equation (12) we can solve for the PSD of the generalized force P_q, i.e.,

$$F_{qq} \left[\omega_q \middle| P_q, P_q \right] \doteq \frac{F(\omega_q \mid y_k, y_\ell)}{\beta^2(\omega_q)\phi_q(x_k)\phi_q(x_\ell)} \quad (15)$$

Equation (15) shows that since in a lightly damped model the response is restricted to small frequency bands about the values of $\omega = \omega_q$, only the PSD of the generalized force P_q at $\omega = \omega_q$ can be obtained by the inversion procedure.

The details of the spatial distribution are lost. If several modes are excited, then the PSD several integrals (one for each mode) of the excitation are determined for the values of $\omega = \omega_q$. Additional values of the PSD of P_q can be obtained by 1) changing the mode shapes $\varphi_n(x)$ and 2) changing the natural frequencies ω_q.

[†] M. L. Botman: The Response of Linear Systems to Inhomogeneous Random Excitations; IAS Paper No. 61-32, presented at IAS 29th Annual Meeting, New York, NewYork, 23-25 January, 1961.

BIBLIOGRAPHY

1. Ezra, A. A., and Penning, F. A., "Development of Scaling Laws for Explosive Forming," Experimental Mechanics, August, 1962.

2. Langhaar, H. S., Dimensionless Analysis and Theory of Models, New York: John Wiley and Sons, Co., Inc., 1951.

3. Ezra, A. A., Scaling Laws and Similitude Requirements for Valid Scale Model Work, presented at the Shock and Vibration Colloquium, Winter Annual Meeting of ASME, Philadelphia, November, 1963.

4. Ezra, A. A., and Peterson, H. C., Determination of Design Criteria for Transonic Buffeting Forces Acting on Launch Vehicles, ARS Paper, 2407-62, ARS Launch Vehicles: Structures and Materials Conference, Phoenix, Arizona, April, 1962.

5. Peterson, H. C., Dynamic Response of Launch Vehicles to Transonic Buffeting Forces, AIAA Preprint No. 63-209, presented at the AIAA Summer Meeting, Los Angeles, California, June, 1963.

6. Raine, A. G., and Runyan, Harry, L., Structural Dynamics Aspects of the [illegible] Lunar Space Vehicle Launch Phase, SAE National Aeronautics Meeting, New York, New York, April, 1962.

7. Hedgepeth, J., and Widmayer, E., Jr., Dynamic and Aeroelastic Problems of Lifting Re-entry Bodies, Aerospace Engineering, January, 1963, pp. 148-153.

8. Crandall, S. H., Random Vibration, Technical Press of MIT and John Wiley and Sons, Inc., New York, 1958.

9. Botman, M. L., The Response of Linear Systems to Inhomogeneous Random Excitation, IAS Paper No. 61-32, IAS 29th Annual Meeting, New York, New York, January, 1961.

10. Jones, W. P., Research on Unsteady Flow, Sixth Minta Martin Lecture, Journal of Aerospace Sciences, March, 1962, pp. 249-263.

11. Martin, D. J., Silveira, M. A., Hanson, Perry, W., and Leadbetter, Summer, A., Recent Studies of Several Inputs to Missile Dynamic Problems, Proceedings of Symposium on Structural Dynamics of High Speed Flight, Los Angeles, California, 24-25 April 1961, (CONFIDENTIAL).

12. Goldberg, A. P., and Adams, R. H., Mercury Atlas Buffeting Loads at Transonic and Low Supersonic Speeds, Report No. TR-60-0000-AS431, Space Technology, Inc., November, 1960, (CONFIDENTIAL).

13. Coe, C. F., Steady and Fluctuating Pressures at Transonic Speeds on Two Space Vehicle Payload Shapes, NASA TMX-503, (CONFIDENTIAL).

14. Coe, C. F., The Effects of Some Variations in Launch Vehicle Nose Shape on Steady and Fluctuating Pressures at Transonic Speeds, NASA TMX-646, (CONFIDENTIAL).

15. Fung, Y. C., The Analysis of Wind Induced Oscillations of Large and Tall Cylindrical Structures, STL/TR-60-0000-09134, Space Technology Laboratories, Inc., June, 1960.

16. Thomson, W. T., and Barton, M. V., The Response of Mechanical Systems to Random Excitation, Journal of Applied Mechanics, June, 1957, pp. 248-251.

17. Woods, P. W., and Ericsson, L. E., Aeroelastic Considerations in a Slender, Blunt-Nose, Multistage Rocket, Aerospace Engineering, May, 1962, pp. 42-51.

DYNAMIC STRUCTURAL MODELING USING DISSIMILAR MATERIALS

by
Gale E. Nevill, Jr.
Southwest Research Institute

ABSTRACT

Use of structural models made of materials different from full-scale offers promise of allowing considerable latitude in choice of model test conditions, particularly in the intensity and duration of loading. An analytical and experimental evaluation of the feasibility and potential of this approach has therefore been made. Presented are an analysis of the general similitude requirements for the modeling of dynamic response of aerospace structures utilizing dissimilar materials and an investigation of the problems associated with meeting these requirements. Also, model tests involving the elastic-plastic response of impulsively loaded beams and plates made of relatively weak and dense lead-loaded plastic are described and their results are compared with independent full-scale results for aluminum. Agreement indicates probable usefulness of approach.

LIST OF ILLUSTRATIONS

SYMBOLS

a	Acceleration (LT^{-2})
d	Displacement (L)
e	Strain component (-)
$\dot{e}$	Strain-rate component (T^{-1})
E	Young's modulus (FL^{-2})
f	Function (-)
F	Force (F)
g	Gravitational acceleration (LT^{-2})
i	General identifying subscript (-)
I	Impulse ($FL^{-2}T$)
k	Strain-rate sensitivity (T)
l	Characteristic length (L)
m	Subscript referring to model (-)
o	Subscript referring to original or characteristic state (-)
p	Pressure (FL^{-2}), subscript referring to prototype (-)
P	Material plastic modulus (FL^{-2})
r	Subscript indicating ratio, model to prototype (-)
R	Radius (L)
S	Stress (FL^{-2})
t	Time (T)
Y	Yield stress (FL^{-2})

z	Displacement (L)
θ	Angle (-)
μ	Poisson's ratio (-)
ρ	Mass density ($FL^{-4}T^2$)
ϕ	Function (-)

DYNAMIC STRUCTURAL MODELING USING DISSIMILAR MATERIALS

Gale E. Nevill, Jr.
Southwest Research Institute

INTRODUCTION

The formal rules leading to the development of modeling or similitude criteria are relatively simple. Since these formal rules are well known and comprehensively treated in various references, they will not be presented here. This simplicity is somewhat deceptive, however, and it is easy to neglect the crucial need for sound judgment in the application of these rules to specific problems. It is considered appropriate therefore to emphasize two points of this theory. First, it is noted that exact modeling requires that all parameters significant to the model and prototype systems be included in the analysis and that the same parameters and natural laws apply to the model system and the prototype system. The second point is that the use of model techniques to solve real problems will invariably require compromises and approximations to exact modeling and that the choice of appropriate compromises and approximations remains primarily an art, dependent on the judgment and experience of the experimenter rather than on established mathematical procedures.

In this presentation, consideration will be restricted to modeling of the response of structures subjected to specified dynamic loads. The specific class of problems to be considered will involve large dynamic deflections of complex structures; an example of the area of concern would be the response of stiffened shells to blast loads. This presentation will not consider the important areas of coupled problems in which the loads are dependent on displacements and thus cannot be specified independently. Neither will problems be considered which would allow gross approximations of the structure in the nature of a lumped stiffness. In spite of this necessarily restricted scope, however, it is intended that the extension of the concepts presented here to the broad field of dynamic modeling be evident.

MODELING OF THE RESPONSE OF STRUCTURES TO DYNAMIC LOADS

As a first step, consider the elastic response of a structure made of a single material to some prescribed dynamic loading condition

The geometry of this structure will be described by a single characteristic length l and by various nondimensional length ratios l_i and angles θ_i. The elastic material behavior will be described by the properties E, μ and ρ. If the applied load at any point can be represented by a relation of the form $p_i = p_o f_i(t/t_o)$, then the significant load parameters will be p_o, f_i, and t_o. Here the response parameter of interest will be restricted to some displacement z. Application of the well-known Buckingham π Theorem then leads to a relation of the form

$$z/l = \phi(l_i, \theta_i, \mu, f_i, p_o/E, \rho l^2/E t_o^2) \qquad (1)$$

The nondimensional response parameter z/l will then be identical in model and prototype if all of the nondimensional parameters on the right-hand side of Eq. (1) are identical in model and prototype. Note that the requirement is that the nondimensional groups be the same in model and prototype—not that individual properties be the same.

The usual approach in modeling is to construct a geometrically similar model from the same material as the prototype and to accept the limitations in test conditions which result. Consider now the consequences of this choice of model material. First, identical l_i and θ_i in model and prototype requires a geometrically similar model. The requirement that $f_{im} = f_{ip}$ means that the shapes of the loading functions must be identical. Since the same material is used in model as in prototype, $\mu_m = \mu_p$ and $E_m = E_p$. The parameter p_o/E then leads to the requirement that the pressures involved in the model tests must be identical with the pressures associated with prototype tests. Finally, since $\rho_m = \rho_p$, the nondimensional parameter $\rho l^2/E t_o^2$ leads to the requirement that $t_{om}/t_{op} = l_m/l_p$. Thus, it is seen that in the conventional approach, in which the model is made from the prototype material, model tests must be conducted at pressures equal to those for the prototype tests and the model time scale will be reduced in proportion to the reduction in geometric scale.

As a next step, consider the possibilities of exact modeling if the restriction of construction of the model from the prototype material is removed. The requirement that $\mu_m = \mu_p$ remains; however, since in many problems Poisson's ratio is not a significant parameter, it is expected that deviations from this requirement may often prove to be quite satisfactory. It will be noted that thus far there have been no specific restrictions placed on the value of E_m. Therefore, a model material might be selected such that E_m is significantly smaller than E_p. Let us investigate the consequences of selecting a model material with $E_m = E_p/100$. First, it is seen that the model tests will now be conducted at pressures $p_m = p_p/100$, often a very significant experimental advantage. Second, if the model material selected has $\rho_m = 4\rho_p$ then, for a geometric

scale ratio $l_m = l_p/5$, the resulting model system time scale will be increased to four times that of the prototype, i.e., $t_{om} = 4\, t_{op}$. This choice of properties for the model material would thus result in an experimental situation in which the model would be tested at significantly lower pressures and longer times than the prototype system. With regard to the very important practical problem of how an actual structure, made of aluminum for example, might be modeled, a lead-loaded plastic material might be considered.

Let us next investigate the possibility of testing models at significantly lower pressures and shorter times than those associated with the prototype situation. Such model tests would be valuable in connection with the problem of predicting the response of structures to the loads resulting from large thermonuclear blasts. If a model material is selected which has properties $E_m = E_p/10$ and $\rho_m = \rho_p/10$, then the model tests could be conducted at pressures lower by a factor of 10 than those associated with the prototype, and the model characteristic times will be shorter than the prototype times by the same factor as the geometric scale reduction. In this case, perhaps an appropriate set of material properties could be obtained using foamed plastics or foamed metals.

As a third example of the potential application of models made from different materials than the prototype, consider the need to include the effects of gravity or other external accelerations on a structural dynamics modeling problem. Such a problem might arise in the consideration of the response of re-entry vehicles to blast loads during re-entry. In this case, the characteristic acceleration, a, must be added to the list of significant problem parameters and one additional nondimensional group would be added to Eq. (1). Such an appropriate nondimensional group is $\rho a l/E$. From this new modeling parameter it is seen that if the same material is used in model as in prototype, geometric scaling $l_m = l_p/10$ would lead to $a_m = 10\, a_p$, i.e., the model accelerations must be ten times the full-scale accelerations for similar stresses, deformations, etc. If it is desired to test the model at the same acceleration as the prototype, then this might be accomplished for a 1/10 linear scale model through the use of a model material with $E_r = 1/10$ and $\rho_r = 1$. As another situation of potential interest, consider the need to make model tests at 1g of a prototype situation involving 50g. In this case, $a_r = 1/50$ and for a scale model with $l_r = 1/5$, E_r/ρ_r must equal 1/250. This might be accomplished using a very weak and very dense model material such that $E_r = 1/100$ and $\rho_r = 2.5$.

The preceding examples of the possible control of experimental conditions for model testing should give some feeling for the flexibility which the dissimilar materials approach provides to the experimenter. Next, it seems appropriate to consider certain generalizations and

sophistications of this approach. Thus far, effects of rate of strain have been neglected. Since many materials are quite insensitive to strain-rate effects*, this neglect can often be justified. However, it is important to note that the use of the same material in model and prototype precludes the exact scaling of rate effects and thus this conventional approach cannot be used when rate effects are important, which is the case for many of the plastic structural materials. This preclusion can be seen from the facts that the modeling described requires strains to be the same in model and prototype whereas times must be different by the same factor as the geometric scale; therefore strain rates in model and prototype would differ by the same factor as the geometric scale. For the elastic case, the situation might be appropriately expressed as $E = E_o\, f_1 (k_1 \dot{e})$ and $\mu = \mu_o\, f_2 (k_2 e)$ In this case, exact modeling would require that $(k_1/t_o)_m = (k_1/t_o)_p$, $(k_2/t_o)_m = (k_2/t_o)_p$, $f_{1m} = f_{1p}$ and $f_{2m} = f_{2p}$. For a specific example, if a simple linear relationship $E = E_o\, k_1 \dot{e}$ would hold, then if $t_{or} = 1/5$, the model material strain-rate sensitivity k_{1m} would have to be 1/5 that of the prototype material strain-rate sensitivity k_{1p}. From this it is also seen that there exists the possibility of exact modeling of strain-rate effects if model materials with appropriate sets of properties can be either selected or formulated.

Next, let us consider the extension of the proposed modeling techniques into the inelastic material behavioral range. In general terms, the material behavior might be described by a function relating stresses, strains, strain history, temperature, and time. The complexities of any attempt at such a general definition seem rather overwhelming at this stage, however, and it is believed that the only acceptable course of action is to assume greatly simplified models for the particular problem or class of problems contemplated. For the present class of problems, namely the dynamic response of engineering-type structures, we will restrict consideration to materials with constitutive relationships adequately expressed by an equation of the form

$$S/E = f(e, k_i) \qquad (2)$$

In this case, exact modeling would require $f_m = f_p$ and $(k/t_o)_m = (k/t_o)_p$, as well as appropriate equality of the other nondimensional parameters described previously, between model and prototype situations. To see what these requirements might mean in a practical problem, let us examine the requirements associated with modeling of simple uniaxial tensile stress situations. If the material tensile stress/strain curve

---

* For example, compression properties of aluminum 6061-T6 vary less than 5% at strain rates of 2.0×10^{-2} in/in/min and 1.0×10^{4} in/in/min.

obtained at a certain constant strain rate is as shown in Figure 1, one possible approximation of f would be in terms of the initial slope E_o, the yield stress Y_o, and the post-yield slope P_o of the curve as shown in Figure 1. Further, if testing at other strain rates indicates relations of the common form $E = E_o \log k_1\dot{e}$, $Y = Y_o \log k_2\dot{e}$ and $P = P_o \log k_3\dot{e}$, then the material behavior can be described in terms of the six parameters E_o, Y_o, P_o, k_1, k_2, k_3. In this case, a model material would be required to have properties such that the ratios Y_o/E_o, P_o/E_o, k_1/k_2 and k_1/k_3 would be the same as in the prototype material. Of course, one of the strength and one of the rate parameters, say E_o and k_1, would have to have values compatible with equality of the other previously described nondimensional parameters.

In the general case, where more complex stress and strain states exist, a very significant problem arises in defining and carrying out the experiments necessary to obtain an adequate description of the material properties. It is, of course, not feasible to make a complete determination of the material constitutive behavior and therefore it is believed necessary to examine carefully the anticipated model system behavior and to suggest appropriate tests accordingly. For example, if the model material deformation is expected to be primarily of a bending nature, then it would likely be appropriate to utilize simple bending tests to define the material properties. If, on the other hand, a combined stress situation is anticipated, then it may be necessary to define material properties using combined stress tests.

Perhaps the most difficult problem associated with modeling utilizing dissimilar materials is the selection or formulation of model materials with appropriate combinations of properties. This problem is aggravated when several materials must be considered simultaneously, for in that case not only must the properties of each material have the proper relation to one another but they must also have the appropriate relation to the properties of other materials. Nevertheless, the potential of this approach is believed high.

EXPERIMENTAL INVESTIGATION

In order to obtain some better feeling for the potential of the dissimilar model material concepts presented and of the problems to be encountered in their use, a limited number of simple experiments were conducted. The prototype situation chosen for modeling involved the response of simply supported rectangular beams and plates of aluminum 6061-T6 subjected to normal impulsive loading produced by sheet high explosives in contact with the surface. * The model test situation selected

---

* These prototype tests were made at Stanford Research Institute and reported in AFSWC TDR 62-94, Vol. 1.

involved impulsive loading, at considerably reduced pressures and longer times, as produced by a shock wave in air. In view of this contemplated modeling situation, a model material was sought having low strength and high density. The low strength would allow testing at significantly reduced pressure and impulse levels while the combination of low strength and high density would provide for relatively long model characteristic times and thus allow longer impulse times.

Since primarily bending deformation was contemplated, a simple bending test definition of the properties of the prototype aluminum 6061-T6 beams was chosen. A simple approximate characterization of the stress/strain behavior, consisting of two straight lines, as defined in Figure 2 and discussed previously, was then made. The bending behavior of the prototype material was considered characterized by the values $E_o = 1.03 \times 10^7$ psi, $Y_o = 6.50 \times 10^4$ psi and $P_o = 2.14 \times 10^6$ psi. A model material was then sought which would have a significantly lower strength but would have bending properties with the same nondimensional ratios $E_o/Y_o = 159$ and $E_o/P_o = 4.82$ as the aluminum.

An evaluation of the properties of a large number of available plastics was then made. The results of this study indicated that a wide range of properties and of combinations of properties could be obtained, but that in general the ratio E_o/Y_o was far lower than the desired value, usually in the order of 25 to 35. Next, a search was made to determine the properties of the common dense metals Generally speaking, the more common dense metals in their relatively pure forms had E_o/Y_o ratios much higher than the desired figure, the ratio for lead, for example, being approximately 2000. Also, these metals had mechanical properties in the same order as the aluminum properties and thus were significantly stronger than desired.

In view of the fact that the ratio E_o/Y_o was generally too small for the plastics and too large for the metals, an approach of attempting to combine metals and plastics was chosen with the hope of achieving the proper ratio at some appropriate combination of materials. Since practically no experimental results or other information could be found on the mechanical properties of metal/plastic combinations, an experimental material development program was initiated After some exploratory work utilizing various metal powders and plastics formulated with various plasticizing agents, curing agents, solvents, etc., a combination of commercially pure lead powder and epoxy plastic was chosen. After further development work, the final model material used was a 14 to 1 by weight combination of 100-200 mesh standard grade lead powder and plasticized Epon 828. *

---

* See AFSWC TDR 63-, "Similitude Studies of Re-Entry Vehicle Response to Impulsive Loading"(U), Vol. I unclassified, Vol II Secret, for a complete description of this and related work.

The properties of the model material were determined using the same bending test technique as was described for the aluminum 6061-T6. The mechanical properties resulting, together with the properties of the aluminum prototype material, are shown as follows.

	6061 T-6 Aluminum	Beam Model Material	Plate Model Material
ρ (lb sec^2 in^{-4})	2.53×10^{-4}	0.596×10^{-3}	0.596×10^{-3}
E_o (lb in^{-2})	1.03×10^{7}	1.79×10^{5}	1.19×10^{5}
Y_o (lb in^{-2})	6.5×10^{4}	6.6×10^{2}	6.1×10^{2}
P_o (lb in^{-2})	2.14×10^{6}	4.47×10^{4}	3.20×10^{4}
E_o/Y_o	159	253	195
E_o/P_o	4.82	4.83	3.70
P_o/Y_o	33	56	52

The Stanford Research Institute prototype tests were made on simply supported beams of depth 1/4", width 1", and span 18" and on simply supported circular plates with diameter 8" and depth 1/4". The Southwest Research Institute models were made to one-half geometric scale, resulting in beams of 1/8" depth, 1/2" width and 9" span and plates of 4" diameter and 1/8" depth, and were made of the lead/plastic material described previously. The impulsive loading was applied to the models through the interaction with the shock wave in air produced by a simple shock tube. Since the prototype loading was on one surface only, the models were appropriately shielded so that only normal surface loading was involved. In these model tests, a photographic record was made of the oscilloscope trace representing the impulsive load. This trace was obtained from Kistler 701 quartz pressure pickups feeding into Kistler 655 amplifiers-calibrators. A typical pressure-time picture is shown in Figure 3. After each test, the permanent deformation of the center of the plate or beam was measured, using a micrometer, from a reference point on the support fixture.

Before direct comparison of results could be made, it was necessary to make corrections for the dynamic properties of the model material, which were quite strain-rate sensitive, and for the impulse duration for the model plates where the response time was not sufficiently high as compared with the impulse duration to allow treatment of the loading as an idealized initial impulse. For the model materials, dynamic compression properties were measured using a modified Hopkinson pressure bar facility and an appropriate dynamic strength was obtained by interpolation between these results and quasi-static compression results.

For this interpolation, a constitutive relationship of the form $S = S_o \log k\dot{e}$ was used. The strain rates used were based on the maximum strains occurring and the periods of elastic oscillation of the beams and plates in appropriate modes. Since relatively small deviations from elastic behavior occurred, this seemed a reasonable approach.

The correction for impulse time duration for the plate results was based on the maximum deflection occurring in a simple oscillator due to a triangularly shaped impulse, as shown in Figure 4, of constant magnitude with various ratios of impulse duration to oscillator period.

Since in most of these tests the impulse duration was much shorter than the response time of the structure, it was deemed satisfactory to consider only total impulse and to neglect the shape of the pulse. Under this assumption, the exact pressure-time history of the loading would not be included but would be replaced by the initial impulse I. Under these circumstances, the response parameter d/l should be equal in model and prototype tests if the nondimensional impulse parameter $I/\sqrt{\rho E l^2}$ and the other previously mentioned parameters are maintained equal in the model and prototype situations.

The results of the beam and plate experiments, with appropriate corrections made for material properties and impulse durations as discussed previously, are shown in Figures 5 and 6. In these plots, the characteristic lengths l used are the plate radius and one-half the beam span.

The results presented for beams indicate that the threshold impulse for permanent deformation of the beams was quite accurately predicted, but that the results of the two situations diverged significantly at larger permanent deformations. This divergence is believed attributable to several factors. First, the model material property description used was meaningful only for strains relatively close to elastic behavior. Second, the average value of strain-rate sensitivity used might be off significantly for large strains. Also, the influence of strain rate was not the same for the various different material properties and thus the actual nondimensional shape of the stress/strain curve might be significantly altered under dynamic conditions.

Unfortunately, the experimental facility used in the model tests was not capable of producing impulses which were both sufficiently short in time and large in magnitude to allow larger deformations of the plates. In light of this situation, it is believed that no conclusions, other than that the results are not unreasonable, are considered justified from the plate tests. It should be mentioned also that the primary emphasis in the

modeling effort concerned bending properties and that since the plate deformations would involve multi-dimensional stress effects, the modeling of the plate response was not expected to be as satisfactory as that for the beams. Another factor, of course, is that the correction made for long impulse time duration may not be accurate.

CONCLUDING REMARKS

It is hoped that this presentation has clearly demonstrated the potential of dynamic structural modeling using dissimilar materials and has pointed out a number of the associated problems. While the experimental work accomplished thus far has been relatively crude and cannot be considered conclusive, the model test results presented here do show good qualitative agreement and reasonably good quantitative agreement with the prototype results. In view of the very significant alteration in material properties and in model test conditions, these results are considered quite encouraging. Although many questions remain incompletely answered, these results are believed to demonstrate the feasibility and promise of the use of dissimilar materials for modeling dynamic structural response.

ACKNOWLEDGMENT

The research described in this paper was conducted at Southwest Research Institute under Contract AF29(601)-4923 with the Air Force Special Weapons Center. The assistance and advice of Captain Donald L. Lamberson and Lieutenant Richard E. Brightman, contracting officers, are gratefully acknowledged.

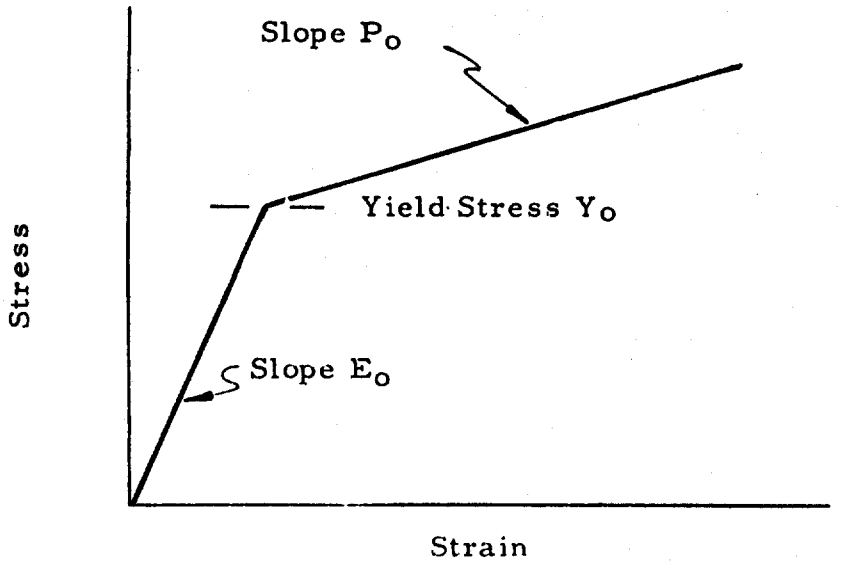

Figure 1 TENSILE TEST RESULT

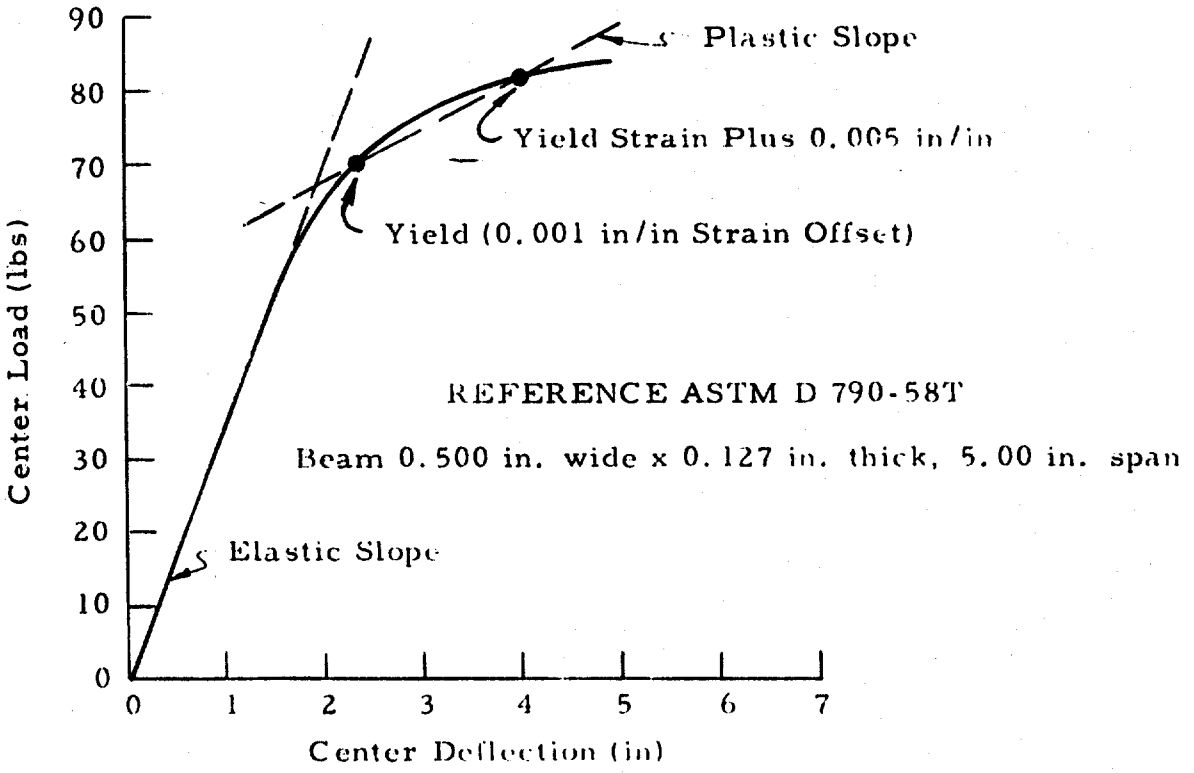

Figure 2 BENDING TEST PROPERTY DEFINITION

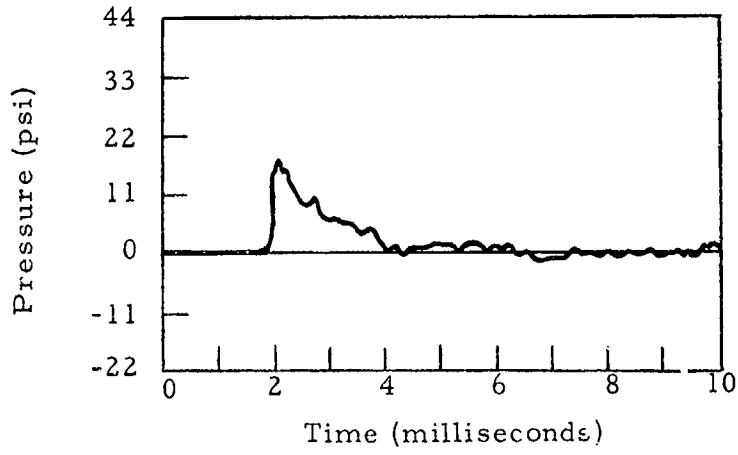

Figure 3 TYPICAL MODEL TEST IMPULSE

$I = F_o t_o/2$
$= \text{Constant}$

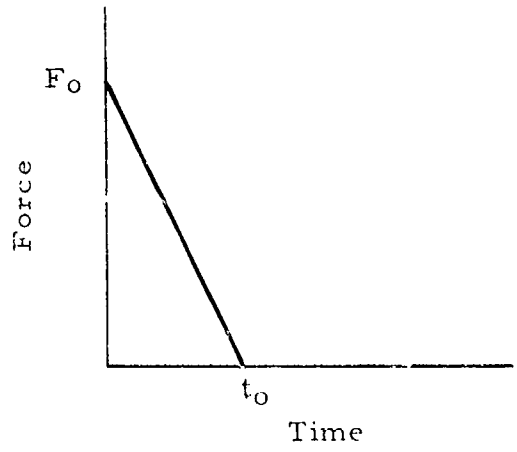

Figure 4 IMPULSIVE LOADING

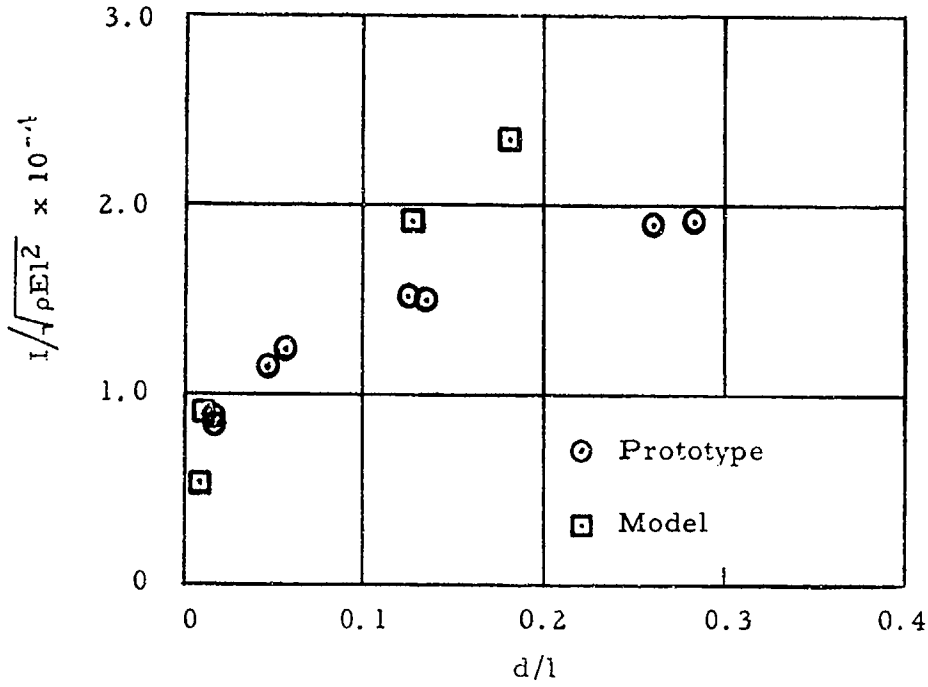

Figure 5 BEAM RESULTS

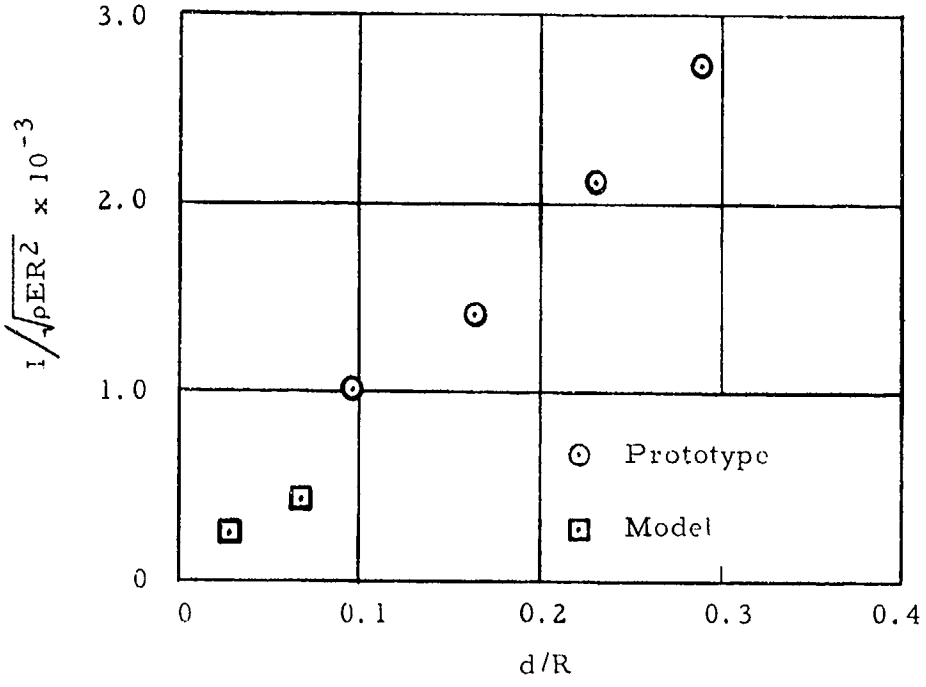

Figure 6 PLATE RESULTS

A STUDY OF THERMAL SCALE MODELING TECHNIQUES

J. M. F. Vickers

ABSTRACT

The techniques which may be evolved from the basic laws of thermal scale modeling for spacecraft are described. All but two of these techniques can be rejected at once, since they require conditions which are very difficult to fulfill in practice. A comparison is drawn between the two remaining techniques, the technique of preserving temperature from prototype to model and of preserving materials from prototype to model. It is found that, for steady state conditions, the technique of preserving temperature has inherent advantages over that of preserving materials, but that when transient conditions are to be modeled much of this advantage is lost.

LIST OF ILLUSTRATIONS

NOMENCLATURE

A	area of surface
$A_{i,v}$	area of A_i which is visible from dA_j
c_p	specific heat
C	thermal contact conductance
F_{ji}	thermal radiation configuration factor from surface i to surface j
k	thermal conductivity
L	length
q	net heat input to a certain portion of the spacecraft
q''	net heat flux
q'''	internal power generated per unit volume
r	magnitude of the vector $\vec{r}$ between elemental areas dA_i and dA_j
R	scale ratio, L_m/L_p
S	radiant flux from external source
t	temperature
T	absolute temperature
α	thermal diffusivity
α_s	absorptivity of surface to external radiation spectrum
α_{ij}	absorptivity of surface i to radiation from surface j
ϵ	total hemispherical emissivity
ρ	density
σ	Stefan-Boltzmann constant
τ	time
ϕ	angle formed by $\vec{r}$ and the normal to the respective elemental area
Φ_{ji}	intensity of radiation from surface j incident on surface i

Subscripts:

m and p refer to model and prototype respectively
t and 70 refer to temperatures of the material in degrees fahrenheit and to the reference temperature, 70° F respectively
Cu, Al and Ni refer to Copper, Aluminum and Nickel respectively

A STUDY OF THERMAL SCALE MODELING TECHNIQUES

J.M.F. Vickers

Jet Propulsion Laboratory, California Institute of Technology

The physical size of spacecraft is steadily increasing and is likely to increase futher as larger boosters become available. This leads to a demand for an increase in the size of thermal test facilities. The prime cost for such facilities, including some form of solar simulation, will be considerably greater than for those presently in use. The difficulty and cost of operation will also be much greater. The type of solar simulation in the test chamber is of extreme importance, since the surface coatings are very sensitive to the spectrum of the light striking the surface. At present, the simulation system which apparently gives the best approximation to the Johnson curve for the spectral energy distribution of sunlight in space is given by carbon arcs with rare earth cores in the rods (Ref. 1). Such systems, however, are limited to areas of good collimation of about three feet in diameter.

For these reasons it appears that thermal scale modeling will be an attractive technique when it can be developed into a working method. The use of reduced scale models will extend the useful life of test chambers already built, and will also enable the testing of still smaller scale models in conditions closely approximating actual sunlight if they can be reduced to less than three feet in diameter.

The basic laws of thermal scale modeling are well established, but experimental difficulties exist in their practical implementation. The purpose of this paper is to examine how the basic laws should be applied and what inherent advantages exist with any particular modeling basis. It will be shown that the steady state conditions (existing in interplanetary flight) have to be considered separately from the transient conditions (present during planetary encounter or midcourse maneuvers). There appears to exist a clear cut case for using a technique which preserves temperature from model to prototype in the steady state condition. The choice of the technique to be used in the transient case is not so clear, but certain recommendations are made.

DIMENSIONLESS GROUPS

The basic dimensionless groups for thermal scale modeling in a high vacuum, where the only heat transfer mechanisms are conduction and radiation, may be derived either from the differential equations or from consideration of the physical parameters involved. They have been stated by Clark (Ref. 2), Clark and Laband (Ref. 3) and Katz (Ref. 4), and may be conveniently written in the form used by the present author (Ref. 5) as follows:

$$\frac{\epsilon_m \sigma T_m^3 L_m}{k_m} = \frac{\epsilon_p \sigma T_p^3 L_p}{k_p} \tag{1}$$

$$\frac{C_m L_m}{k_m} = \frac{C_p L_p}{k_p} \tag{2}$$

$$\frac{(\rho c_p)_m L_m^2}{k_m \tau_m} = \frac{(\rho c_p)_p L_p^2}{k_p \tau_p} \tag{3}$$

$$\frac{q_m}{L_m k_m T_m} = \frac{q_p}{L_p k_p T_p} \tag{4}$$

$$\frac{q_m'' L_m}{k_m T_m} = \frac{q_p'' L_p}{k_p T_p} \tag{5}$$

$$\frac{q_m''' L_m^2}{k_m T_m} = \frac{q_p''' L_p^2}{k_p T_p} \tag{6}$$

$$\frac{\alpha_{sm} S_m L_m}{k_m T_m} = \frac{\alpha_{sp} S_p L_p}{k_p T_p} \tag{7}$$

$$\frac{\alpha_{ijm} L_m \phi_{jim}}{k_m T_m} = \frac{\alpha_{ijp} L_p \phi_{jip}}{k_p T_p} \tag{8}$$

Where $$\Phi_{ji} = \frac{F_{ji}\, \epsilon_j\, \sigma T_j^4\, A_j}{A_i} \tag{9}$$

and $$F_{ji} = \frac{1}{A_j} \int_{A_j} \int_{A_{i,v}} \frac{\cos \phi_j \cos \phi_i \, dA_i \, dA_j}{\pi r^2} \tag{10}$$

according to Jakob (Ref. 6).

Equation (1), which may be considered an analog of the Biot modulus, may be used to relate the temperatures, surface emissivities and thermal conductivities to the scaling ratio, L_m/L_p or R. Similarly, Eq. (2) relates the joint conductances to the thermal conductivities and R. Equation (3), which is the Fourier modulus, can be used to relate the time to the thermal diffusivities and R. Equations (4), (5), and (6) can relate the net heat input, the heat flux, and the heat generated per unit volume to temperatures, thermal conductivities and R. Finally, Eqs. (7) and (8) can be used to relate the heat flux absorbed at a surface from outside sources and that absorbed from other portions of the spacecraft to temperatures, thermal conductivities and R. From this set of equations the basic modeling laws must now be deduced.

At first sight it would appear that within the restrictions imposed by the groupings above, a complete freedom of choice should exist in deciding the modeling laws to be followed. Katz (Ref. 4) briefly mentions some of the problems associated with two techniques, but makes no attempt to recommend either, while Clark (Ref. 2) and Clark and Laband (Ref. 3) consider only one method of attack on the problem. It is felt that these papers present only a limited discussion of the problems associated with thermal scale modeling. In the present paper, a more complete discussion is presented, together with recommendations on various modeling techniques.

TECHNIQUES AVAILABLE

Many modeling techniques in other areas use distorted scaling systems in which the scale ratio in one direction differs from that used in the other two. This is opposed to a geometric scale modeling system where dimensions along all three axes are reduced by the same factor. However, in all problems involving thermal radiation, it is immediately apparent that geometric scaling is vital to success since if this rule is not followed, the thermal radiation configuration factor, F_{ji}, from surface i to surface j will vary from model to prototype. While these factors can be evaluated with reasonable accuracy for simple shapes, it is extremely difficult even to estimate their values for the complex shapes involved with spacecraft. When the conditions of multiple reflectances and the variation of emissivity with direction from the normal are considered, the problem becomes impossible unless the geometry is preserved. Under these circumstances it is felt that geometric scaling of all radiating surfaces is essential to success.

The two most attractive techniques at first glance are: (1) setting the temperatures of the model and prototype the same and, (2) using the same materials for both the model and the prototype. With both of these techniques the surface emissivity would be identical for model and prototype. This comparison has been summarized by the author (Ref. 5) and the results are shown in Table 1.

An initial comparison may be drawn between the two techniques. Examination of Eqs. (5a), (7a), and (8a) shows that technique 1 involves preserving the heat flux from model to prototype. This, together with the fact that the thermal gradient is greater in the model due to the temperature preservation and the reduced geometric scale, accounts for Eq. (1a). This in turn indicates that lower conductivity materials must be used for the model. If the exact scale size is fixed by the test chamber and the prototype sizes, the thermal conductivities of all portions of the model are determined from the ratio and the thermal conductivities of the prototype materials. It is more likely, however, that the exact scale will be decided from the ratio of the thermal conductivity of the material occurring most often in the prototype to that of the most convenient modeling material which will give approximately the desired scale. This will then determine the exact conductivity ratio to be used in choosing all the other modeling materials. Katzoff (Ref. 7) suggested one method in which it is possible to produce any required thermal conductivity by cutting grooves or slots in the material (though extreme care must be taken to avoid affecting the surface properties of the material). Another method is to choose a modeling material with a thermal conductivity below that called for in the model, and then plate the surface with copper or silver. A very thin coat, a few ten-thousandths of an inch thick, will considerably modify the effective thermal conductivity without seriously affecting the geometric shape, and also without introducing any major modification of the surface geometry. A final plate or coat of paint will provide the correct surface properties.

Both of these methods may lead to considerable technical problems. It appears, therefore, that the material used most commonly in the prototype should be modeled with an available material rather than a manufactured one. The combination of flux preservation and temperature preservation accounts for Eq. (2a), which indicates that the thermal contact conductance or joint conductance must be preserved from model to prototype. Examination of Eq. (5b) shows that in technique 2 the heat flux, and, as a consequence, the temperature gradients within the structure vary as $(1/R)^{4/3}$. This means that both the heat fluxes and the temperature gradients increase rapidly as the model size is reduced. Equation (1b) shows that the absolute temperatures within the model vary as $(1/R)^{1/3}$, and will increase also as the model size is reduced. Equation (2b) indicates that the joint conductances vary as $(1/R)$, and must therefore increase as the size of the model is reduced.

STEADY STATE

TECHNIQUE 1 (TEMPERATURE PRESERVATION)

This first technique has an immediate advantage, since the critical item in spacecraft temperature control is the actual temperature involved. The maximum or minimum temperature to which a component is exposed is

Table 1. Comparison of emissivities for model and prototype

Technique 1 Temperature and surface emissivities the same in model and prototype.	Technique 2 Materials and surface emissivities the same in model and prototype.
$\frac{k_m}{k_p} = \frac{L_m}{L_p} = R$ (1a)	$\frac{T_m}{T_p} = \left(\frac{L_p}{L_m}\right)^{1/3} = \left(\frac{1}{R}\right)^{1/3}$ (1b)
$\frac{C_m}{C_p} = 1$ (2a)	$\frac{C_m}{C_p} = \frac{L_p}{L_m} = \frac{1}{R}$ (2b)
$\frac{\tau_m}{\tau_p} = \frac{(\rho c_p)_m L_m}{(\rho c_p)_p L_p}$ (3a)	$\frac{\tau_m}{\tau_p} = \left(\frac{L_m}{L_p}\right)^2$ (3b)
$\frac{q_m}{q_p} = \left(\frac{L_m}{L_p}\right)^2$ (4a)	$\frac{q_m}{q_p} = \left(\frac{L_m}{L_p}\right)^{2/3}$ (4b)
$\frac{q''_m}{q''_p} = 1$ (5a)	$\frac{q''_m}{q''_p} = \left(\frac{L_p}{L_m}\right)^{4/3}$ (5b)
$\frac{q'''_m}{q'''_p} = \frac{L_p}{L_m}$ (6a)	$\frac{q'''_m}{q'''_p} = \left(\frac{L_p}{L_m}\right)^{7/3}$ (6b)
$\frac{\alpha_{sm} S_m}{\alpha_{sp} S_p} = 1$ (7a)	$\frac{\alpha_{sm} S_m}{\alpha_{sp} S_p} = \left(\frac{L_p}{L_m}\right)^{4/3}$ (7b)
$\frac{\alpha_{ijm} \phi_{jim}}{\alpha_{ijp} \phi_{jip}} = 1$ (8a)	$\frac{\alpha_{ijm} \phi_{jim}}{\alpha_{ijp} \phi_{jip}} = \left(\frac{L_p}{L_m}\right)^{4/3}$ (8b)

the most important criterion in deciding its performance and life so far as pure thermal behavior is concerned.

Certain inherent experimental difficulties exist with this technique, most of them associated with the variation of thermal properties with temperature. The values of the conductivity ratio between model and prototype for certain materials modeling other materials are shown in Fig. 1, over the temperature range 32° F to 572° F. In the range 32° F to 200° F, the normal range of temperatures for the major electronic components, fuels and batteries in spacecraft, the variation in the conductivity ratios for aluminum modeling copper is about 4%; for nickel modeling aluminum, about 7%; and for nickel modeling copper, about 2%. While these materials are not representative of those normally used in spacecraft, the actual values of their thermal conductivity and the variation of their thermal conductivity with temperature cover the range of values which exists for actual spacecraft materials. It should be noted, further, that the upper curve will give about 1/2 scale modeling at 70° F, the middle curve will give about 1/3 scale, and the lower curve about 1/6 scale.

The variation in Fig. 1 shows that neither the set of Eqs. (1a) through (8a) nor the set of Eqs. (1) through (8) will actually hold, since the assumption of constant thermal properties with temperature is inherent to their derivation. It will be shown later, however, that this variation is not serious and the effect on model temperatures is small in the range of temperatures normally encountered in spacecraft.

The effect of the variation of thermal properties will be ignored and Eqs. (7a) and (8a) will be considered. Taking Eq. (8a), if temperature is preserved from model to prototype, emissivity is preserved, and geometric scaling is used, then it is possible to write $F_{jim} = F_{jip}$ and $\Phi_{jim} = \Phi_{jip}$. This means that $\alpha_{ijm} = \alpha_{ijp}$, or both the long wave length absorptivity and the emissivity are preserved from model to prototype. Equation (7a) must be treated for two separate cases; first, where true solar simulation is available and second the case, obtained in practice with all chambers, where either the solar intensity or the solar spectrum or both of these are not available in the chamber. For the first case Eq. (7a) reduces to $\alpha_{sm} = \alpha_{sp}$, that is the complete surface properties are preserved from model to prototype. For the second case, Eq. (7a) indicates that $\alpha_{sm}/\alpha_{sp} = S_m/S_p$, that is that the short wavelength absorptivities must be scaled in relation to the change in light intensity and wavelength/energy distribution. At the same time the long wave length absorptivity and the emissivity must be preserved from model to prototype.

Since the spectral distribution of monochromatic emissive power for ideal radiators is a direct function of the temperature of the source, it is possible that the conditions imposed by the equation relating the short wave length absorptivities can be satisfied. The maximum in the curve for sunlight occurs at a wavelength of about 0.5μ, while that for a black body below 1000° F lies beyond 3.5μ. If one had available a solar simulation source for a test chamber behaving approximately like a black body above 10,000° F, then the peak will lie at about 1μ. Under these circumstances it seems that suitable surface coatings can be found to satisfy the model requirements, that is identical long wave length absorptivities and emissivities in model and prototype with scaled short wavelength absorptivities.

This point was not considered by Clark and Laband (Ref. 3), since they assumed the use of a source whose spectrum closely approximates that of the sun. They assume, in effect, that they have true solar simulation, and can therefore use emissivities and absorptivities throughout their model which are identical to those of their prototype. However, when other sources are considered, the spectral behavior of these lamps is sufficiently different from that of the sun that the scaling of the absorptivities can no longer be ignored unless the surfaces of the prototype approximate grey body behavior.

TECHNIQUE 2 (MATERIALS PRESERVATION)

As already pointed out with the modeling technique involved in using the same materials for model and prototype, the absolute temperatures in the model will be equal to the product of the absolute temperatures of the prototype for the corresponding point and the inverse of the scale ratio raised to the one third power according to Eq. (1b). This means that a reduced scale model will have temperatures that are higher than those of the prototype.

From Eq. (1b) it can be calculated that the model temperatures corresponding to 70° F in the prototype for scales of 1/2, 1/4, 1/6, 1/8 and 1/10 are respectively, 207° F, 382° F, 503° F, 600° F and 682° F. These values, together with the ratios of the thermal conductivity at the corresponding temperature to the thermal conductivity at 70° F are shown in Figure 2. When these results are considered, it is immediately obvious that the thermal conductivity is not constant for the material, and that for aluminum and nickel the error increases rapidly as the model decreases in physical size. At 1/10 scale, this error is approximately 20% and 12% respectively. This means that, as with technique 1, neither the special Eqs. (1b) through (8b) nor the general Eqs. (1) through (8) will apply. The corresponding temperatures and the errors in thermal conductivity ratio assuming that the thermal conductivity is constant are shown in Table 2. It will be noted that the percentage error for aluminum in the prototype is -0.2 at 32° F and 1.2 at 200° F, giving a range of percentage error of 1.4, while the range for a 1/10 scale model of aluminum for the corresponding temperatures is from 14.8 to 33.5, or a range of error of 18.7. On the other hand for a copper prototype and model, the range decreases from 5.8 in the prototype to 1.9 in the 1/10 scale model and for nickel from 5.3 in the prototype to 3.4 in the model. The percentage error is based on the thermal conductivity at 70° F for the prototype and for the model on the thermal conductivity at the model temperature equivalent to 70° F in the prototype. It will be demonstrated later that the effect of this variation of thermal conductivity is far more serious with this technique than it was with technique 1.

Even if the change of properties with temperature is neglected, which may be legitimate for the half scale model where the errors in assuming $k_m = k_p$ are small (Table 2), the use of Eqs. (7b) and (8b) present difficulties. When the values of Φ_{ji} from Eq. (9) are substituted in Eq. (8b) this reduces, as with technique 1, to $\alpha_{ijm}/\alpha_{ijp} = 1$. However, from Eq. (7b), with true solar simulation, the short wavelength absorptivity must be scaled according to

$$\frac{\alpha_{sm}}{\alpha_{sp}} = \left(\frac{L_p}{L_m}\right)^{4/3} \tag{11}$$

Table 2. Temperatures and errors in thermal conductivity ratio

Temperature, °F			% error in k_t* based on $(k_p)_{70}$**					
	Lower	Upper	Al	Cu	Ni	Al	Cu	Ni
Prototype	32°F	200°F	-0.2	4.0	1.6	1.2	-1.8	-3.7
Scale	Temperature in model equivalent to 32°F prototype	Temperature in model equivalent to 200°F prototype	Model temperature equivalent to 32°F			Model temperature equivalent to 200°F		
			Al	Cu	Ni	Al	Cu	Ni
1/2	160	372	0.7	-1.3	-2.6	5.6	-3.3	-6.5
1/4	321	588	3.8	-3.0	-5.7	14.1	-4.8	-9.8
1/6	434	739	7.2	-3.8	-7.4	22.6	-5.2	-11.0
1/8	524	860	11.0	-4.2	-8.8	28.2	-5.9	-12.3
1/10	600	962	14.8	-4.8	-10.0	33.5	-6.7	-13.4

*k_t = thermal conductivity of prototype or model material at temperature, °F

**$(k_p)_{70}$ = thermal conductivity of prototype material at 70°F

This means that the emissivity and the low temperature absorptivity must be preserved from model to prototype, while the high temperature absorptivity must be scaled. This is the same problem as that encountered with technique 1 without true solar simulation. If, on the other hand, true solar simulation is not available, then Eq. (7b) must be used, with the correct values of S_m/S_p. Again, the same situation arises. The high temperature absorptivity must be scaled (though differently than for the case of true solar simulation), while the low temperature absorptivity and the emissivity must be retained. Regardless of whether or not true solar simulation is available, an extensive search must be made for surfaces with the correct properties.

In summary, technique 1 involves a search for materials for the model which have the correct thermal conductivities, or the manufacture of materials with such conductivities, but with the temperatures of the model the same as those of the prototype. If true solar simulation is available, the complete surface treatment of the model will be identical to that of the prototype; if solar simulation which does not correspond to the solar spectrum either in intensity or in spectral energy distribution or both is the only type available, then the short wave length absorptivities of the model must be scaled from those of the prototype. In technique 2 the identical materials are used in model and prototype, but the temperatures of the model are scaled from those of the prototype. In the case of small-scale models, this leads to a considerable increase in temperature for the model. The short wave length absorptivities of the model must be scaled from those of the prototype regardless of whether or not true solar simulation is available. Under all circumstances, for both techniques, the emissivities and long wave length absorptivities of the model and prototype are identical.

OTHER TECHNIQUES

Considering the number of basic parameters and equations which are available it seems that there should be many modeling techniques that could be used. However, more detailed analysis reveals that this is not so.

If the surface treatment is assumed constant, that is the emissivities and absorptivities are retained (technique 3), then for true solar simulation this reduces to technique 1. Without true solar simulation the equations become Eqs. (1c) through (8c), Table 3. This is potentially a useful system, since if S_m/S_p is less than 1, which can always be arranged, then T_m is less than T_p. This would have many advantages over technique 2 where T_m was greater than T_p with many inherent experimental problems.

The following systems will not be listed as techniques since a single group eliminates them from practical use in each case.

System 1. If the absorptivities as well as the materials are fixed, it is possible to obtain the following relationship for the emissivities:

$$\frac{\epsilon_m}{\epsilon_p} = \frac{L_p}{L_m}^4 \tag{12}$$

Table 3. Technique 3

Surface treatment same for model and prototype

$$\frac{T_m}{T_p} = \left(\frac{S_m}{S_p}\right)^{1/4} \qquad (1c)^{\dagger}$$

$$\frac{C_m}{C_p} = \left(\frac{S_m}{S_p}\right)^{3/4} \qquad (2c)$$

$$\frac{\tau_m}{\tau_p} = \left(\frac{(\rho c_p)_m}{(\rho c_p)_p}\right)\left(\frac{L_m}{L_p}\right)\left(\frac{S_p}{S_m}\right)^{3/4} \qquad (3c)$$

$$\frac{q_m}{q_p} = \left(\frac{L_m}{L_p}\right)^2\left(\frac{S_m}{S_p}\right) \qquad (4c)$$

$$\frac{q''_m}{q''_p} = \frac{S_m}{S_p} \qquad (5c)$$

$$\frac{q'''_m}{q'''_p} = \left(\frac{L_p}{L_m}\right)\left(\frac{S_m}{S_p}\right) \qquad (6c)$$

$$\frac{k_m}{k_p} = \left(\frac{L_m}{L_p}\right)\left(\frac{S_m}{S_p}\right)^{3/4} \qquad (7c)$$

$$\frac{T_m}{T_p} = \left(\frac{S_m}{S_p}\right)^{1/4} \qquad (8c)^{\dagger}$$

†Note that Eqs. (1) and (8) yield Eqs. (1c) and (8c) which are identical.

This result cannot possibly be satisfied since, for example, the emissivity of a 1/10 scale model would have to be 10,000 times that of the prototype. In practice, the emissivity range of the present spacecraft is from 0.04 to 0.93, so that any factor increasing or decreasing this range will either lead to a demand for materials with emissivities above unity, which is impossible theoretically, or with emissivities below the lowest available, which might be possible to meet in principle but cannot be attained in practice.

System 2. If the variation of the surface emissivity of future spacecraft should happen to be reduced so that the highest emissivity used is less than 0.5, then it would be possible to set an upper limit for the emissivity ratio of 2. If this is then assumed, together with the preservation of materials and absorptivities, then true solar simulation cannot be used and the required values for the solar simulation are given by:

$$\frac{S_m}{S_p} = \frac{1}{1.26}\left(\frac{L_p}{L_m}\right)^{4/3} \tag{13}$$

For a 1/10 scale model this gives a simulated intensity of over 17 times that of the sun, which is excessively large, and a value for the vicinity of Venus of about 30 times that due to the sun in the vicinity of the Earth. In general, it appears that any attempt to modify the emissivity of the model is unlikely to succeed.

System 3. If the emissivity and q''' are preserved, then:

$$\frac{T_m}{T_p} = \left(\frac{L_m}{L_p}\right)^{1/4} \tag{14}$$

$$\frac{\alpha_{sm}}{\alpha_{sp}} = \frac{L_m}{L_p} \tag{15}$$

$$\frac{k_m}{k_p} = \left(\frac{L_m}{L_p}\right)^{7/4} \tag{16}$$

This system appears to have no advantages over techniques 1 and 2; the temperature is not preserved, the thermal conductivity is scaled more radically than for technique 1, and the short wavelength absorptivity is not preserved even if good solar simulation is available.

From the above discussion, it appears that only three techniques are feasible, 1, 2 and 3. Technique 3 neither preserves temperature from prototype to model (though with suitable choice of simulation intensity the small

scale model can run at temperatures lower than the prototype), nor does it preserve materials from prototype to model. Technique 3 is only an individual system when true solar simulation is not available - otherwise it is identical to technique 1. Techniques 1 and 2 will now be examined in greater detail.

COMPARISON OF TECHNIQUES 1 AND 2

There exists one basic requirement in thermal scale modeling which must be met as closely as possible. The model must predict the temperature of the prototype throughout. This means that the model must predict the heat flux through any particular part of the prototype.

In order to assess the two techniques, three simple mathematical models were analyzed, the prototype version of which is shown in Figure 3. This prototype was chosen as the simplest geometry which would approximate a spacecraft-type temperature control problem. It consists of a source of energy and two heat paths of different thermal conductivity leading from the heat source to separate radiating surfaces operating at different temperatures. The temperatures in the system were fixed by the heat flow distribution and the radiating characteristics of the surfaces. Technique 1 was then used to design two models at 1/10 scale, the assumed behavior of the thermal conductivity with temperature being different in the two cases. Technique 2 was used to design a third model at 1/10 scale. By using the results from the technique 2 model to forecast the prototype temperatures, the results from all three models could be compared.

The radiating surfaces at the ends of the prototype are not shown in Figure 3, but they are assumed to be 16 square feet and 20 square feet in area, with emissivities of 1.0 and 0.943 respectively. All three dimensional effects caused by the radiating surfaces are ignored since they are merely considered a convenient rejecting device. The high input power of 1,000 watts was used deliberately to show the effects that might appear. This power was assumed to be delivered at a plane source of zero thickness situated at the boundary between the aluminum portion, or leg, of the model on the right and the cast iron leg of the model, on the left. All other external surfaces were considered adiabatic. The cross sectional areas of the legs were one foot^2.

While the materials chosen are not representative of those used in spacecraft, the thermal conductivity of aluminum is as high as, or higher than, any normal spacecraft material with the exception of the copper used in the cabling. The thermal conductivity of cast iron is comparable to that of the lowest thermal conductivity metal used on spacecraft. In addition, the thermal conductivity of aluminum increases with increase in temperature (positive slope), while the thermal conductivity of cast iron decreases (negative slope), so that both the conditions of thermal conductivity range and of thermal conductivity behavior are fulfilled here.

No particular significance should be attached to the radiating areas or their assumed emissivities. The 16 square foot area will dissipate 65% of the input power with an emissivity of unity at about 70° F. The 20 square feet was chosen simply as the nearest round number which will dissipate with an emissivity less than unity the remaining power, at the temperature fixed

by that of the right hand end of the model, and the remaining conditions specified for the model. The exact value of the emissivity was calculated for the temperature and dissipation involved for the chosen area.

No materials exist with exactly the right values of thermal conductivity for 1/10 scale modeling of either aluminum or cast iron by technique 1. Materials were assumed with the correct values of thermal conductivity, but varying with temperature more rapidly than do actual materials. In addition, for the first technique 1 model, it was assumed that the slopes of thermal conductivity were the reverse of those of the prototype, i.e., the material modeling the aluminum had a negative slope, while that for cast iron a positive slope. This means that the conditions assumed were worse than the worst attainable in practice. For the second model using technique 1 the slopes of thermal conductivity for the model were assumed to be the same as those of the corresponding prototype materials. For technique 2 the actual values of the thermal conductivity at the temperatures involved were used.

The results of the calculations are shown in Fig. 4 for the prototype, the technique 1 models, and for the technique 2 model. The actual technique 2 model would run at temperatures considerably above those of the prototype, however these are converted back into the corresponding figures which the model forecasts for the prototype, and it is these latter figures which were plotted in Fig. 4. The results for the second technique 1 model were indistinguishable from the prototype on this scale.

The errors involved in the two techniques can be calculated from Fig. 4 for the first model using technique 1 and the model using technique 2. The maximum errors in the absolute temperatures are 0.3% and 1.7%. While both of these are small, the difference between them is significant considering that each is inherent to its technique and will be compounded in the actual experimental work. Since all heat from a spacecraft must be dissipated finally by radiation, it is also significant to examine the error involved in T^4 if these stations were radiating instead of adiabatic. In this case the error for technique 1 is less than 1.5% while that for technique 2 is nearly 7%. For the second model using technique 1 the corresponding errors in temperature and radiant flux are 0.1% and 0.4%.

A final comparison may be drawn between the flux distributions in the left and right legs of the prototype and models. The actual ratio (right leg flux/left leg flux) is 1.857 for the prototype, 1.849 for the first technique 1 model, 1.860 for the second technique 1 model, and 2.049 for the technique 2 model. This means that the inherent errors in the flux distributions in these models are 0.43% and 0.16% for technique 1 and 10.34% for technique 2.

Considering the variety of materials already used in spacecraft, and the probability that materials with even wider ranges of behavior will be used in the future (in spacecraft where the temperature ranges are considerably larger), it was felt that the results obtained above might not be representative of certain future problems. For this reason, and in order to assess the effects of large differences in the variation of thermal conductivity with temperature, the following more extreme example was taken.

The prototype shown in Fig. 3 was assumed to be made of two materials different from those used in the earlier models, with the radiating surfaces on one square foot, the thermal conductivity of one varying with temperature

from 1.0 to 0.97 and the other from 0.5 to 0.47, in a temperature range of 180° F (i.e., the thermal conductivities fell in this range by 3% and 6% respectively). The models, 1/4 scale, were assumed to be made of materials whose thermal conductivities varied in the same temperature range from 0.25 to 0.22 and 0.125 to 0.095 respectively. None of the values for the thermal conductivity have counterparts in practice, though the variation of 3% in 180° F is representative of the behavior of many materials. These variations were assumed, for the first model, to have the same slope as the prototype materials and for the second model to have the reverse slope, all thermal conductivities being in $w/(ft)^2\,°F/ft$. These models differ from those described earlier. They were set up to amplify the effects of variable thermal conductivity far beyond that attained in practice in order to determine trends rather than to establish the behavior of actual materials. The results for the models are demonstrated in Fig. 5 with 10w input to the prototype. It should be borne in mind that the results shown here are deliberately forced, the temperature drops in the two legs of each model are considerably larger than for Fig. 4, and the variation in thermal conductivity assumed for the various materials over the temperature range is very much larger than that encountered with real materials except for the right leg of the prototype. These results should not be compared with those obtained for the preservation of materials earlier, since if materials with property values varying like that of the prototype postulated here were used, the errors would be very much greater than those shown in Fig. 4. It does appear however, that where the thermal conductivity may be expected to vary widely with temperature, such as that of nickel, a reverse sign slope is to be prefered over a slope of the same sign, since the maximum error and the mean error is considerably less under these circumstances.

TRANSIENT CONDITIONS (COMPARISON OF TECHNIQUES)

Most of the life of a spacecraft is spent in interplanetary coast during which steady state heat transfer conditions apply, or at the most the extremely slow transients over periods of many days due to changes in the local value of the solar constant. However, certain transients of extreme importance do occur. They include the initial stabilization to interplanetary conditions after launch, the perturbations due to both the energy release and the change of attitude during any midcourse maneuvers which may be carried out, and the transient conditions imposed by planetary encounter. For earth satellites or planetary orbiter vehicles the transient condition is predominant. For these reasons it is necessary to examine the laws of scale modeling for transient conditions.

If Eq. 3 is rewritten to give the time scale, it is found that the scale is dependent upon the square of the scaling ratio and the inverse of the diffusivity ratio of the model and prototype.

$$\frac{\tau_m}{\tau_p} = \frac{\alpha_p}{\alpha_m}\left(\frac{L_m}{L_p}\right)^2 \qquad (17)$$

For the case in which the variation of materials properties with temperature is ignored, the controlling dimensionless group may be derived for technique 1 from Eq. (3a) and for technique 2 from Eq. (3b).

The behaviors of the thermal diffusivity with temperature for copper, aluminum and nickel are shown in Fig. 6. The specific behavior of these three materials should be noted, since they are representative of spacecraft materials in general. First, the diffusivity of copper decreases by about 15% in the temperature range shown; second, the diffusivity of aluminum decreases by about 6% in the first 300° F of the range, and then increases again reaching a value at 750° F which is about 1.5% above that of the value at 0° F; third, the diffusivity of nickel decreases by about 42% in the temperature range shown. These three different behaviors will be shown to have a profound effect on the modeling of transient phenomena.

The diffusivity ratios of these materials are shown in Fig. 7 over the range from 32° F to 572° F. Examination of Figs. 6 and 7 in conjunction with Eq. (17) shows that the assumptions inherent to the derivation of Eqs. (3a) and (3b) are in error, so that only the effect of the results in Eq. (17) will be considered here.

Equation (17) shows that if the temperature varies from one portion of the model to another at any instant of time, and hence the thermal diffusivity ratio varies from point to point, then the time scale at that instant will vary from point to point in the model. In addition, during a transient, the time scale at any particular point is a function of the temperature, i.e., the time scale at any given point will vary with the temperature-time history.

The effect of temperature on the time scale is shown in Table 4. The results for technique 1 are shown in Table 4a, the model scale being fixed by Eq. (1a) from the thermal conductivity ratio for the model and prototype at 70° F. The percentage variation over the temperature range in the scaled time is shown in Table 4c. It should be noted that the time scale variation for aluminum modeling copper is extremely small, but that for aluminum modeling nickel or nickel modeling copper is of the order of 10%.

The results for technique 2 are shown in Table 4b, and the percentage variation over the temperature range is shown in Table 4c. Here it is necessary to determine both the scaled time and the percent variation for each of the three materials to be preserved for each scale. This is because the temperature range in the model is a function of the scale ratio, Eq. (1b), and this determines the diffusivity ratio. The actual time scale is then a function of the particular diffusivity ratio and the square of the scale ratio according to Eq. (17).

Table 4c may now be used to compare the two techniques. For modeling at approximately half scale, technique 1 has a definite advantage if the behavior of the materials in question resembles that of copper and aluminum. At about 1/3 scale the errors inherent with technique 1 have increased by nearly an order of magnitude, while for technique 2 they are about the same for copper and nickel and have been reduced by 60% for aluminum. This means that, if the prototype and model materials behave like copper or aluminum, there is a definite advantage at this scale in using technique 2. Finally, for about 1/6 scale, technique 1 appears to offer about the same

Table 4. Comparison of time scales for techniques 1 and 2

a. Technique 1

			Minutes in model equivalent to 1 hr in prototype	
Prototype	Model	Scale	at 32° F	at 200° F
Copper	Aluminum	0.5280	22.15	21.80
Aluminum	Nickel	0.3013	28.65	31.25
Copper	Nickel	0.1559	10.05	10.80

b. Technique 2

Prototype and model		Minutes in model equivalent to 1 hr in prototype					
		At temperature equivalent to 32° F in prototype			At temperature equivalent to 200° F in prototype		
	Scale	0.5280	0.3013	0.1559	0.5280	0.3013	0.1559
Copper		16.23	5.13	1.33	15.51	4.90	1.25
Aluminum		16.23	5.23	1.42	16.13	5.38	1.52
Nickel		15.12	4.32	1.04	12.6	3.71	0.85

c. Percent variation in model time scale from lowest model temperature to highest model temperature

Scale	Technique 1	Technique 2		
		Copper	Aluminum	Nickel
0.5280	1.6	4.4	9.1	16.7
0.3013	9.1	4.5	2.9	14.1
0.1559	7.1	6.0	7.1	18.3

accuracy as technique 2 using materials behaving like copper and aluminum, but has definite advantages over technique 2 using materials behaving like nickel.

One further comparison may be drawn between the two techniques. From Table 4a it can be seen that the time scale for technique 1 lies between 1/2 and 1/6, while from Table 4b the time scales for technique 2 lie between 1/4 and 1/60. This will lead to some degree of flexibility in modeling, since for the modeling of such slow transients as the time taken to reach stable conditions in interplanetary space the time scale 1/60 may reduce the test time to reasonable proportions; for such rapid transients as those involved in a midcourse maneuver it will be desirable to use a time scale at least as large as 1/2.

CONCLUSIONS

While many modeling laws can be postulated from the dimensionless groups controlling conductive and radiative heat transfer occurring together, the actual behavior of materials and surfaces appears to prevent the use of all but two sets of these laws. Technique 1, in which the model is so designed as to have the same temperatures as the prototype, and technique 2 in which the model is designed with the same materials as the prototype.

When these two techniques are compared for steady state problems, technique 1 appears to have many advantages, whether true solar simulation is available in the test chamber or not. First, the inherent errors of technique 1 are considerably less than those encountered in technique 2, and are actually of the same order as the standard experimental errors of heat transfer. Second, if good solar simulation is available, technique 1 also involves using identical surface treatments on the model and prototype, which is considerably simpler than the absorptivity scaling called for by technique 2. Third, contact resistance, which will probably have to be simulated for some years to come, is preserved in technique 1; it has to be decreased as the model size decreases with technique 2. Fourth, it is probably more convenient to use a model in which the temperature is the same as that of the prototype, as in technique 1, than to use a model in which the temperature of the prototype must be calculated from the experimental results of the model, as in technique 2.

The problems associated with the modeling of the steady state will increase as the temperature range within a given spacecraft increases. Obviously it will be more difficult to model the solar cell array together with the rest of the spacecraft than to model either of these alone, and the introduction of nuclear reactors in spacecraft will compound the problems of modeling. However, increased temperature ranges within spacecraft will still give rise to fewer problems using technique 1 than using technique 2.

Technique 1 will lead to some difficulties in finding materials with the correct thermal conductivities, since each material in the spacecraft prototype will call for a specific thermal conductivity in the corresponding material of the model. Two approaches may be used here; first, where radiant heat exchange is insignificant and therefore the radiation configuration factor need not be preserved, the cross sectional areas of the heat conducting members may be modified rather than scaled exactly; second, where

radiation is significant and the configuration factors must be preserved, the effective thermal conductivity of the path must be modified without affecting the geometric scaling. The various techniques that could be used to manufacture materials with the required thermal conductivity have been discussed.

The time scale variations within the model for transient phenomena will cause considerable difficulties, and a compromise between the relatively inaccurate temperature readings and relatively inaccurate time predictions must be sought for individual cases. Technique 1 has no overall advantage, though it appears that it will be more useful in the modeling of rapid transients. Technique 2 will be more useful in the prediction of extremely slow transients and the transition to equilibrium after launch. In general the relative behavior of the thermal diffusivities of the materials used will have to be carefully assessed for either technique. However, the transient case will be inherently more difficult to model than the steady state and since the transient times are modeled differently for different temperatures and time intervals, there will always exist errors in heat fluxes throughout the model which will then feed back causing increasing errors in the temperatures.

A contract from the Jet Propulsion Laboratory to study the feasibility of experimental thermal scale modeling has been undertaken by Arthur D. Little Incorporated of Cambridge, Massachusetts. The first phase of this contract showed that it was possible to model a fin, heated at one end and radiating to liquid nitrogen cooled walls. The fin was divided into two sections separated by a simulated contact resistance (Refs. 9 and 10). In the second phase, a more complicated prototype is being modeled in two and three dimensional heat flow at 1/2 scale and 1/5 scale (Ref. 11). These experiments seem to indicate that the use of technique 1 provides satisfactory results. A report on this contract will be made later.

In summary, it appears that there is no inherent theoretical reason why steady state conditions cannot be successfully modeled for spacecraft. Obviously there is much to be done in developing the experimental and fabrication techniques, but no major technical breakthrough is required. The inherent errors involved with the technique recommended here are of the order of normal experimental error. The modeling of transient conditions is less clear cut, more compromise is required and the inherent errors are larger due to feedback between errors in scaled time and errors in temperature. However, it appears that it will be possible to develop a reasonable technique, though the effort involved will be considerably greater than for the steady state.

REFERENCES

1. Uguccini, O. W. and Pollack, J. H., "A Carbon-Arc Solar Simulator," ASME paper number 62-WA-241, November 1962.

2. Clark, L. G., "Temperature Balance of Manned Space Stations," NASA TN D-1504, pp 21-31, August 1962.

3. Clark, L. G. and Laband, K. A., "Orbital Station Temperature Control," Astronautics, Vol. 7, No. 9, pp 40-43, September 1962.

4. Katz, A. J , "Thermal Testing," Space/Astronautics, Technical Reference Series, Part 2, pp 30-34, October 1962.

5. Vickers, J. M. F., Jet Propulsion Laboratory, Space Programs Summary No. 37-18, Vol. IV, pp 80-83, December 1962.

6. Jakob, M., Heat Transfer, Vol. II, pp 6-10, John Wiley and Sons, New York, 1957.

7. Katzoff, S., "Similitude in Thermal Models of Spacecraft," NASA TN D-1631, April 1963.

8. McAdams, W. H., Heat Transmission, Third Edition, pp 445-461, McGraw-Hill, New York, 1954.

9. Vickers, J. M. F., Jet Propulsion Laboratory, Space Programs Summary No. 37-18, Vol. IV, pp 83-85, December 1962.

10. Vickers, J. M. F., Jet Propulsion Laboratory, Space Programs Summary No. 37-19, Vol. IV, p 89, February 1963.

11. Vickers, J. M. F., Jet Propulsion Laboratory, Space Programs Summary No. 37-21, Vol. IV, pp 48-50, June 1963.

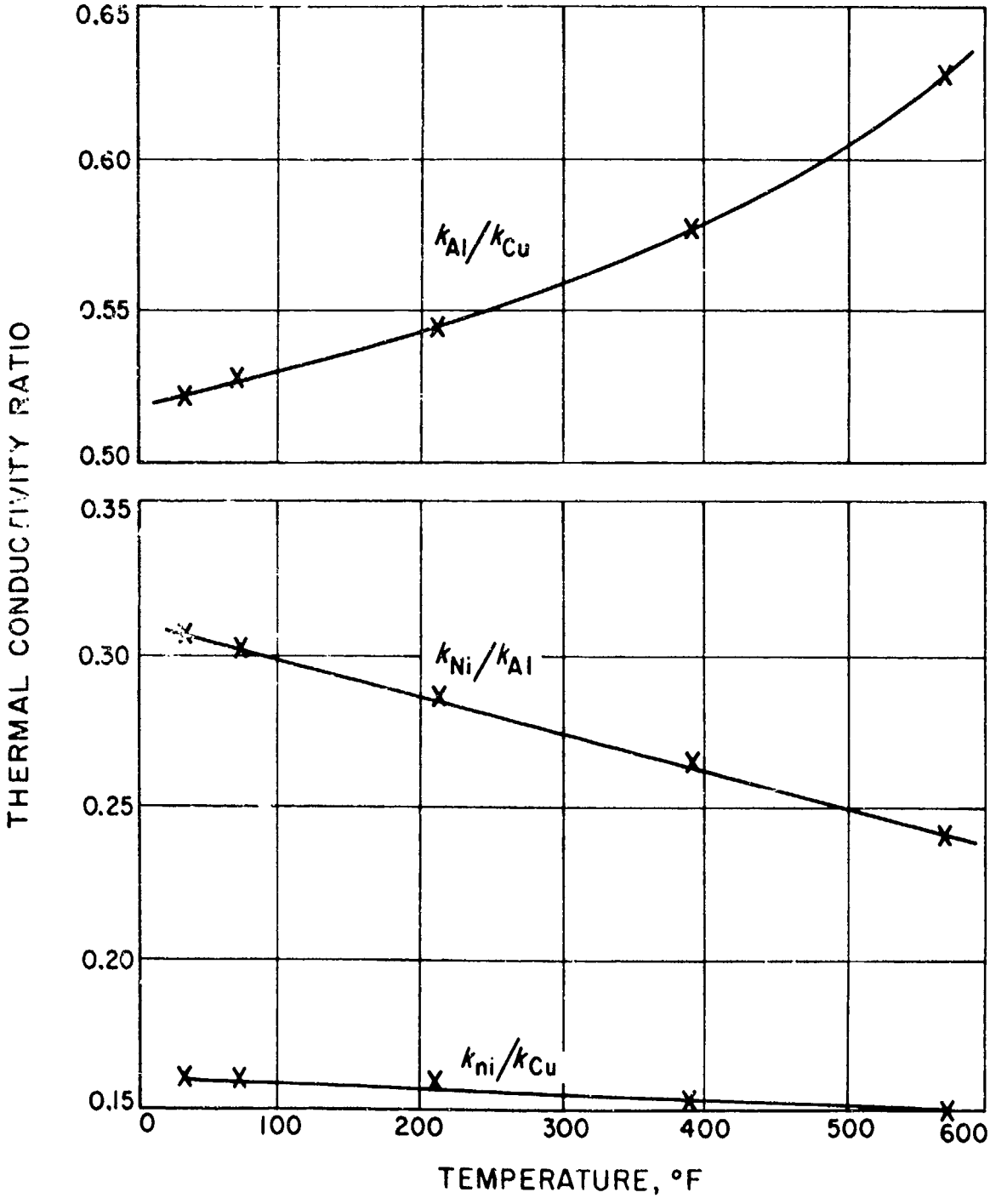

Figure 1. Effect of Temperature on Thermal Conductivity Ratio. Values Taken from McAdams (Ref. 8)

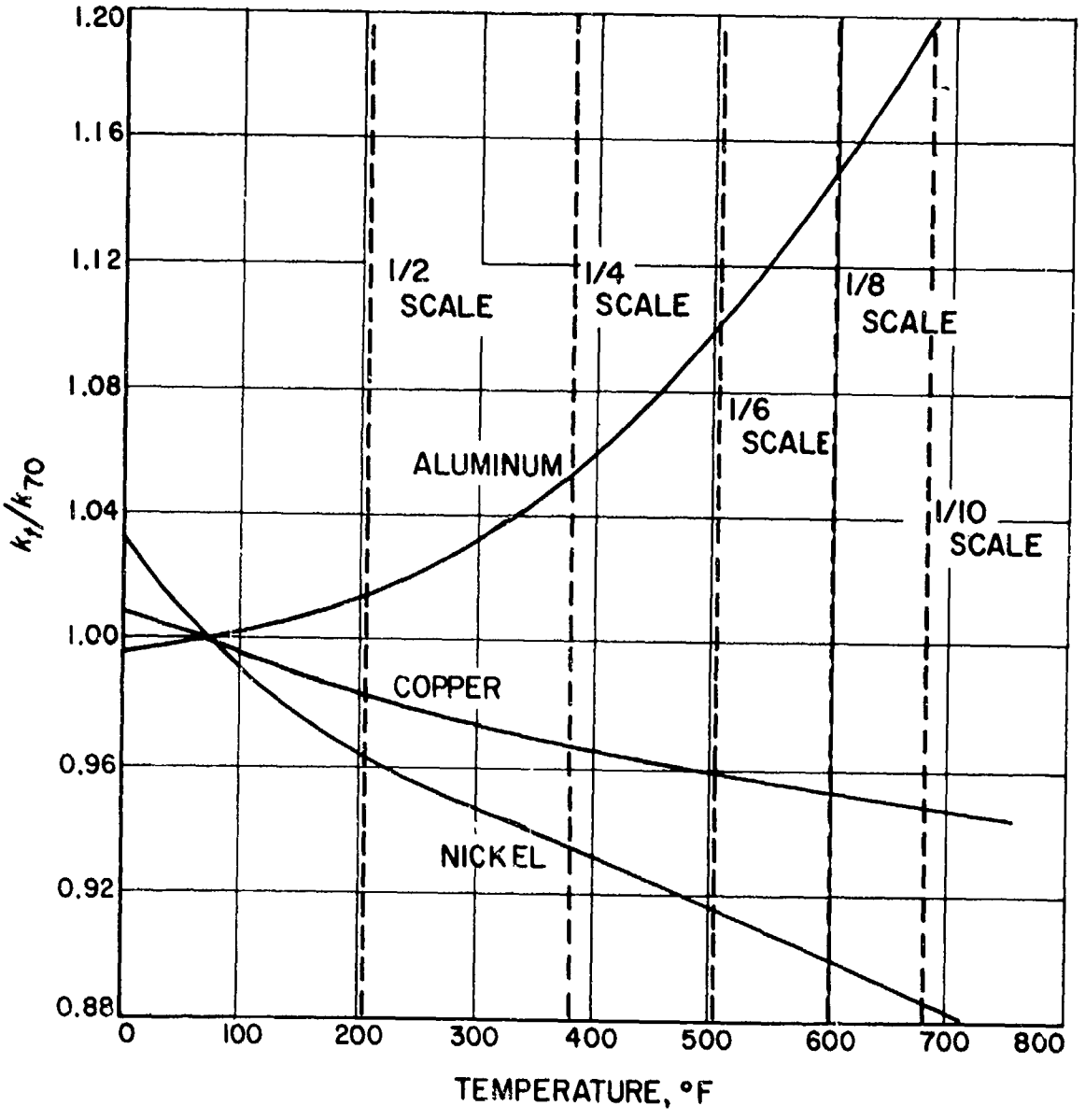

Figure 2. Thermal Conductivity Ratios for Aluminum, Copper, and Nickel

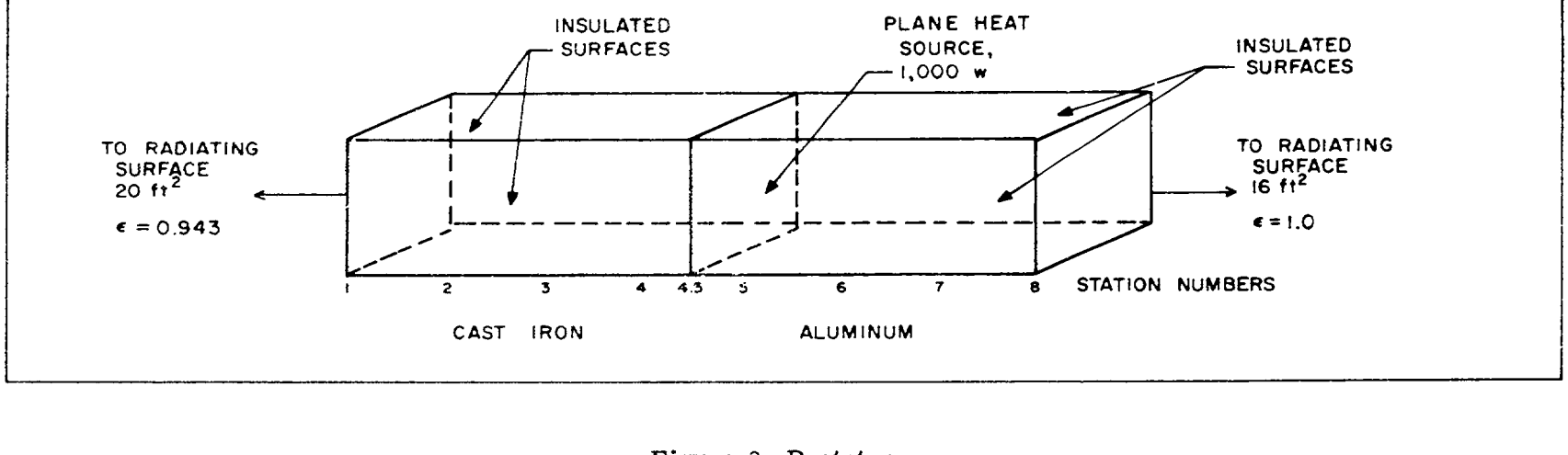

Figure 3. Prototype

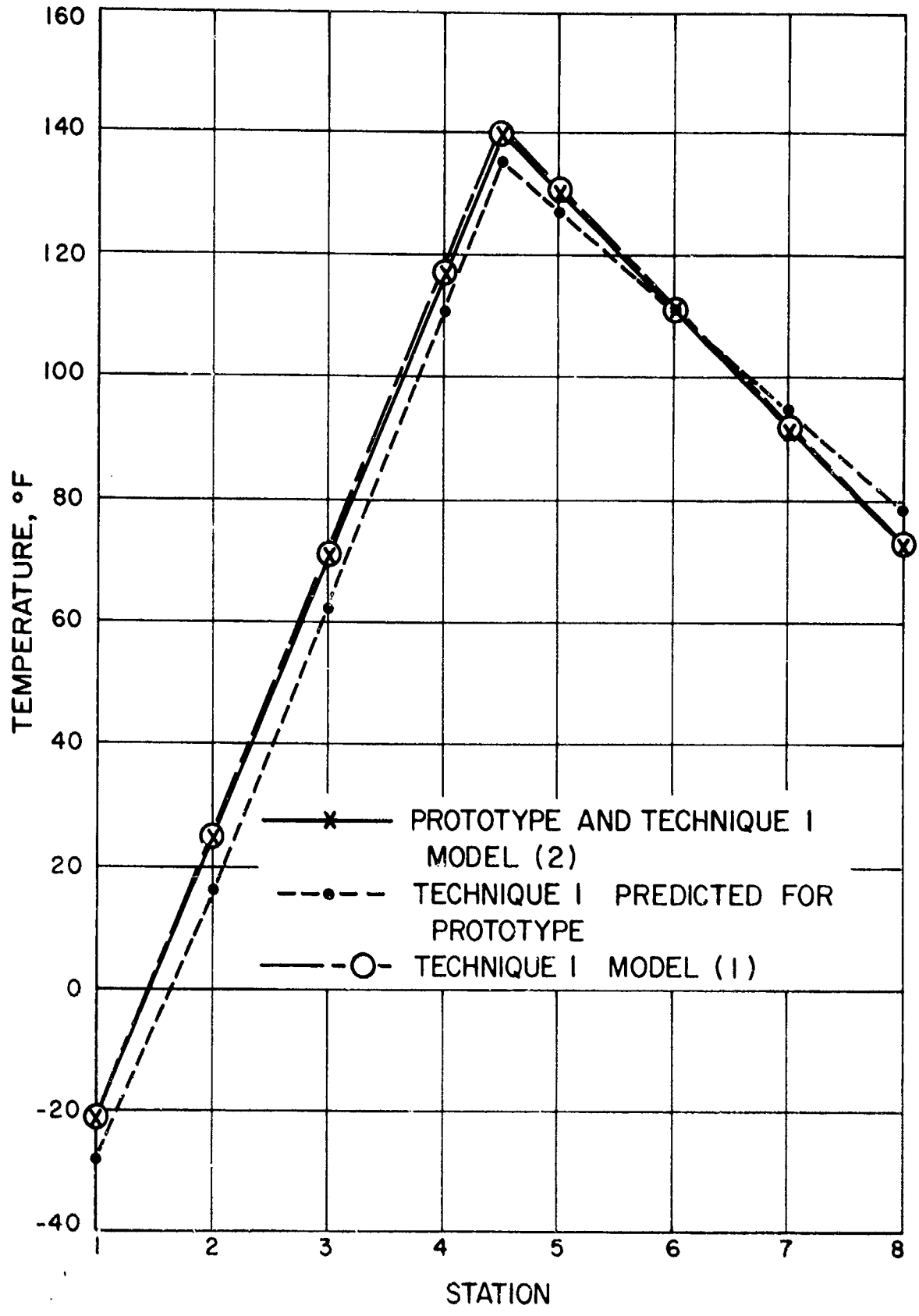

Figure 4. Comparison of Temperature and Material Preservation Techniques

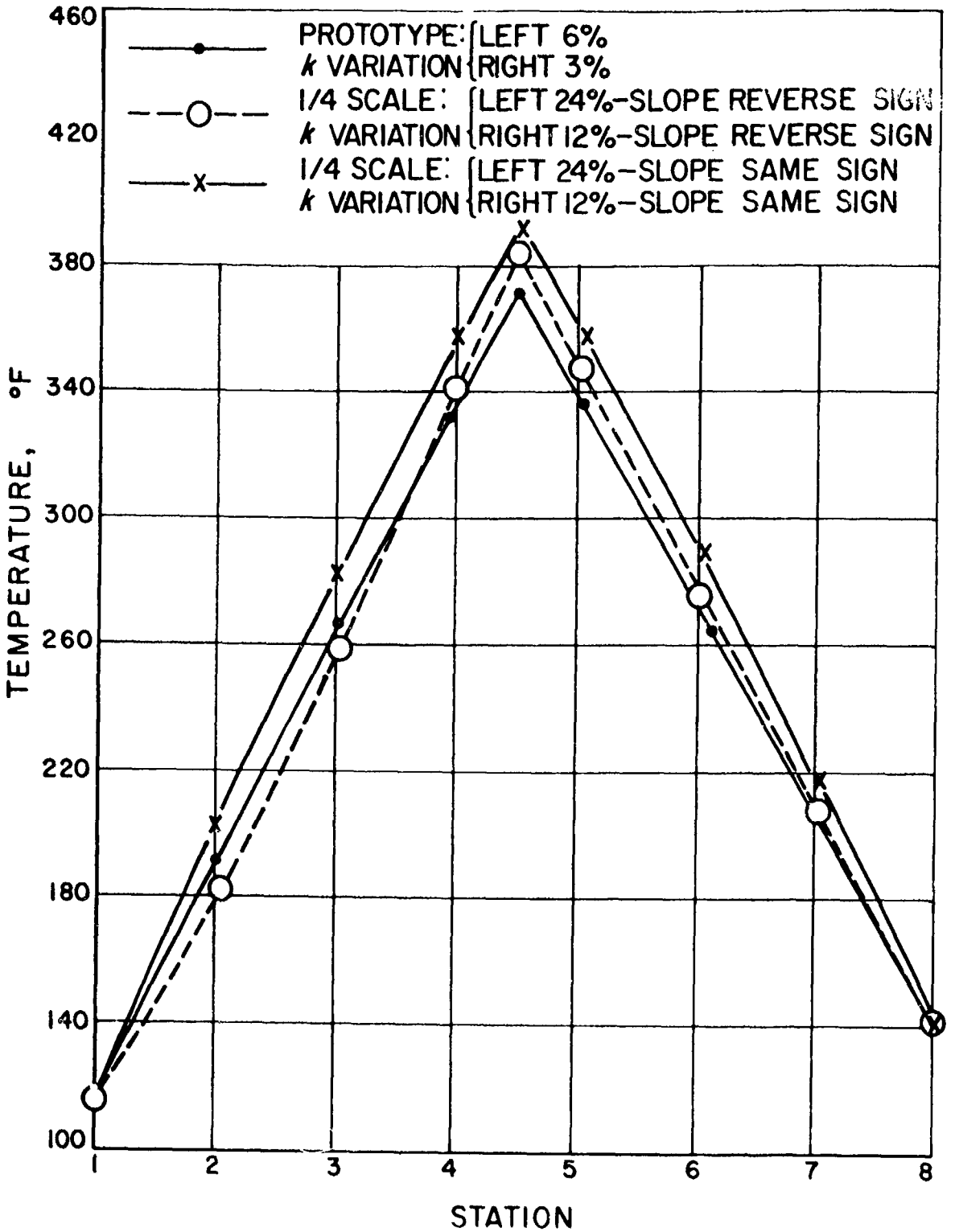

Figure 5. Temperature Distributions of Prototype and Models, Amplified Effects

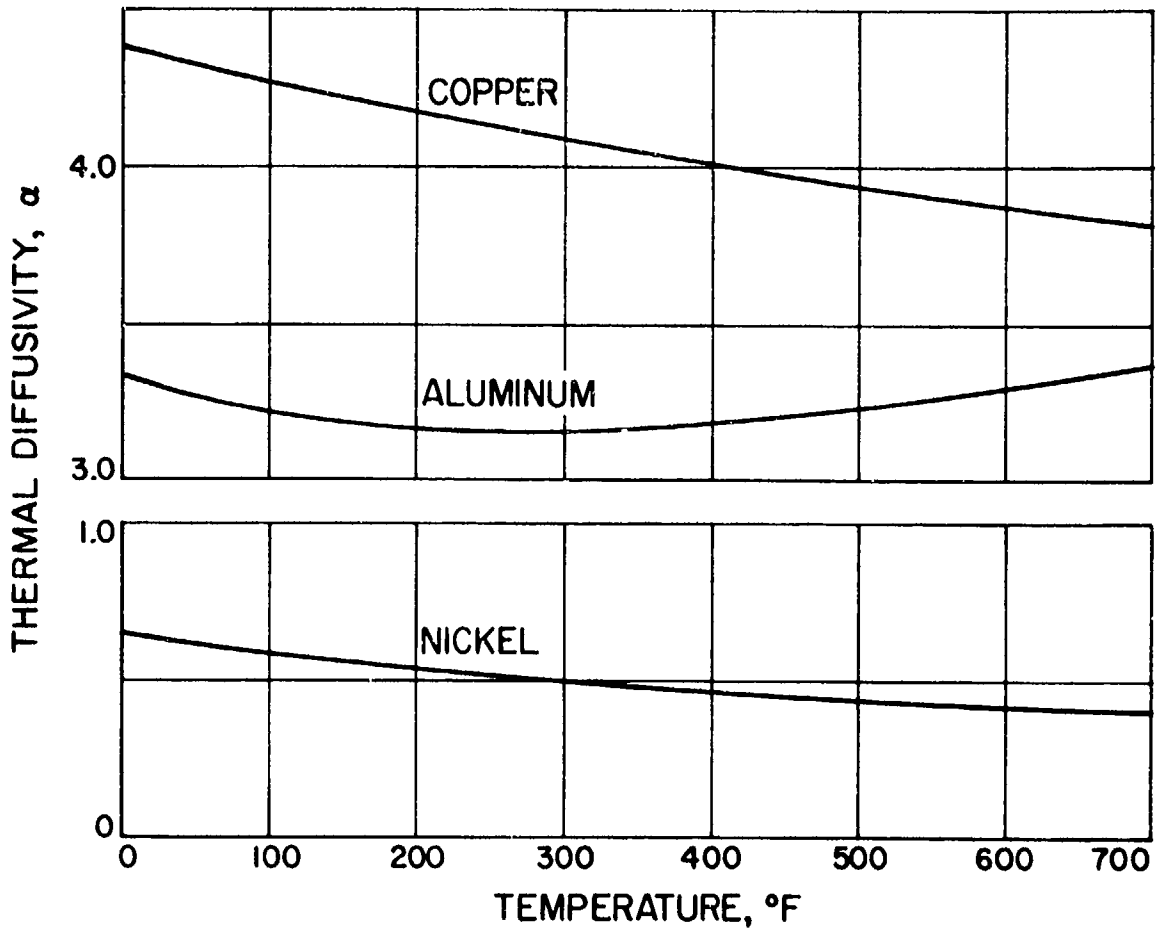

Figure 6. The Effect of Temperature on the Diffusivity of Aluminum, Copper, and Nickel

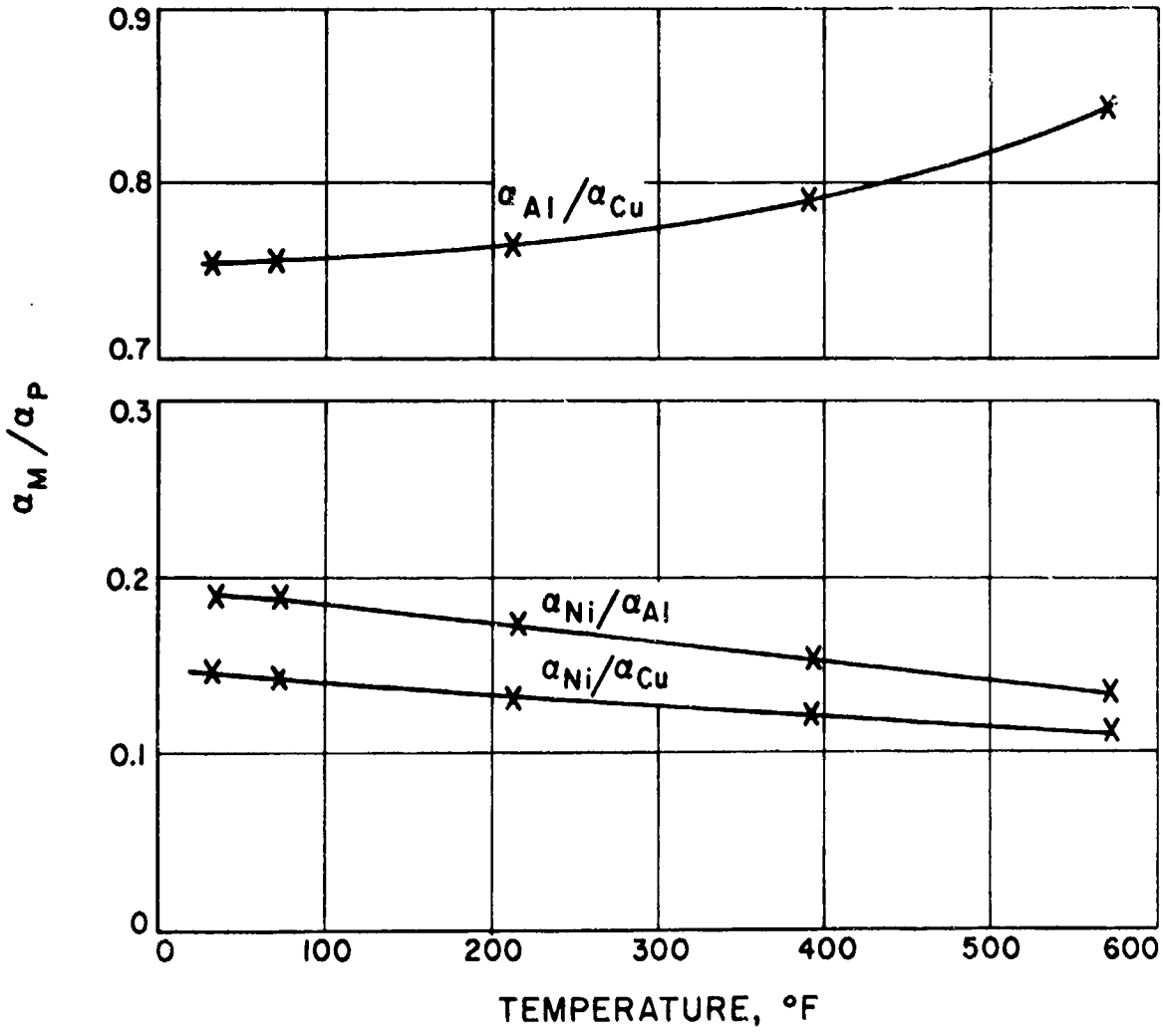

Figure 7. The Variation of Diffusivity Ratio with Temperature for Aluminum, Copper, and Nickel

SESSION II

MODEL TESTING TECHNIQUES

Chairman: Dr. Irving C. Statler
Cornell Aeronautical Laboratories

APPLICATION OF AEROELASTIC MODELING TECHNIQUES TO THE DETERMINATION OF STRUCTURAL LOADS AND STABILITY AND CONTROL DYNAMIC CHARACTERISTICS

by

J. A. Hill

X. A. Gikas

Astromechanics Research Division
Giannini Controls Corporation

ABSTRACT

This paper considers the application of aeroelastic modeling techniques to the determination of structural loads and stability and control characteristics. Specifically, the paper deals with considerations for development of static and dynamic flexible wind tunnel models to be used to measure structural loads and stability and control characteristics. The need for development in these facets of modeling is indicated by reviewing the present technological status of aerodynamic wind tunnel simulation and testing. It is emphasized that these modeling extensions provide another, but significant, "development tool" for the vehicle designer and a means, whereby, a significant cost savings can be realized during prototype flight test. The technical considerations required for these modeling extensions are divided into seven areas: similitude, model, mounting system, control system, sensors, data transmission, and data handling. The requirements and problems pertinent to each of these areas are defined. It is concluded that these extensions of aeroelastic modeling techniques are feasible and desirable from both technical and economic points of view.

INTRODUCTION

This paper presents a summary of aerodynamic modeling and scaling techniques available to the flight industry today. It briefly considers velocity/altitude ranges from subsonic through hypersonic and from sea level through orbital or super-orbital. Theoretical scaling considerations are discussed as well as model hardware availability. The technological status of testing mechanisms, data transmission and data reduction, and instrumentation is given. Wind tunnel testing is exclusively considered.

The paper skirts the specific problems associated with the "thermal" environment, i.e. neither scaling nor modeling technologies are summarized for thermal considerations. (See Reference 1).

Emphasis is placed on methods for determining structural loads and stability and control criteria. The central theme for the paper is, in fact, the development of suitable modeling methods for determination of these items.

A status report for the MODEL FLY program is given.

The authors are presenting all data made available through written documentation, limited personal discussions, and past experiences. It is appreciated that we represent but a small segment of this technological area, and we therefore hope that this paper will stimulate interest and entice others to contribute any additional technologies or methodologies not herein presented.

It is the opinion of the authors that additional work in aeroelastic modeling will yield results which are economically, technically, and seasonably gratifying to the aerospace industry.

The discussion follows a format which presents, first a broad outline of the status and follows with a detailed discussion of each main area. Particular emphasis in the discussion is placed on the present technological boundaries. The MODEL FLY project is placed in context of the total aeroelastic modeling technology presented.

TECHNOLOGICAL STATUS

The purpose of Table 1 is to place the subject of aeroelastic modeling applications to flight loads and stability and control into the context of the symposium and to define the scope of the paper at the onset. The table encompasses rigid model testing also, so that conventional loads and stability and control testing can be related to the symposium. Space limitations obviously restrict allowable detail.

The N's (no capability) in the right hand column point out the deficiency of our present very high speed test facilities. Some orbital velocity parameters (e.g., Mach Number) can be simulated but the need for a greater expansion of all parameters continues to exist.

Line 4 points out some important accomplishments related to dynamic modeling that are sometimes overlooked.

Servo driven stings (line 5) have been used where the mechanical complexity can be justified to reduce the test time required to map aerodynamic characteristics. Coupled with a flexible model (line 6) through an analogue computer which simulates the dynamics including the structural inertia terms, it could serve a more important role with little, if any, additional research required.

Lines 7, 8 and 9 will be discussed in detail by several authors at the symposium.

Lines 9 and 10 are the apparent next steps for intensive development on this list and are the subject of this paper.

Some trajectory simulation (line 11) has been reported by NASA using ballistic ranges but no results on extensively instrumented and/or dynamic models are available.

TECHNOLOGICAL STATUS OF AERODYNAMIC WIND TUNNEL SIMULATION FOR STRUCTURAL LOADS AND STABILITY AND CONTROL - 1963

TYPE DATA	SUBSONIC	TRANSONIC	SUPERSONIC	HYPERSONIC	ORBITAL & SUPER ORBITAL
1. Rigid Body Static Derivatives	Conventional	Conventional Control terms difficult	Conventional	Conventional with heating & considerations	N
2. Rigid Body Steady Airloads (Pressures)	Conventional	Conventional (possible tunnel unsteady effects)	Conventional	Low pressure instrumentation limits accuracy	N
3. Rigid Body Dynamic Derivatives	Combined derivatives can be measured using appropriate techniques. Cross dynamic derivative and pure dynamic derivative difficult.			Tests possible in continuous tunnels	N
4. Rigid Body Dynamic Stability and Response	Spin, free flight tunnel and special mounts	Special cable mounts	N	N	N
5. Static, Servo Driven Sting Mounts	Computer controlled sting(s) used to measure derivatives along a trajectory segment - particularly useful for separation study.			N	N
6. Static, Flexible Airload Models	Feasibility demonstrated by successful wind tunnel tests.			N	N
7. Flutter Stability	Conventional	Conventional	Conventional	Research	N
8. Limited or Simulated Unrestrained Flutter Stability	Conventional using cables, rods	Subsonic methods extension	Limited to wall mounts or rotations on sting	N	N
9. Gust and Dynamic Response (Wind Tunnel only)	Recent mount and gust generator research at NASA		N	N	N
10. Maneuvering Aeroelastic Response	Demonstrated with special mounts	Research	Research	N	N
11. Lifting Trajectory Simulation	See #5 - No dynamic study reported	Research	Research	N	N
12. System Simulation (complete lashup with wind tunnel aero)	N	N	N	N	N

TABLE 1

The last line was added as an ultimate, perhaps unrealizable and now impractical simulation involving simulated equipment tied into a wind tunnel model. Frequently, control system components are tied into some iron mock-up, thus obtaining extensive system characteristics data. It would be ideal to tie-in control systems to a wind tunnel model, but because of model scaling, it would require simulated hardware for many components. The high cost and limited possibilities for test on the actual flight vehicle for the huge systems of the future may mean that complete model simulation systems must be recognized as a seriously considered alternate test.

USEFULNESS OF AERODYNAMIC TESTING

The conventional aerodynamic testing techniques listed in Table 1 have and will continue to play an important role in the development of new vehicles. Their contributions to researching and developing new configurations are immeasurable and cannot be quantitized. We are presenting considerations for the application of aeroelastic modeling techniques to the determination of structural loads and stability and control characteristics. The need for such extension can be best indicated by reviewing the modeling techniques which are currently used and their range of utility.

The techniques for measuring static force derivatives and pressure data have proven to be the most reliable tool of the experimental aerodynamicist. For complex configurations, they have no equal. The combination of pressure data correlated with force test data for a specific configuration usually yields good load distributions.

Dynamic derivative testing methods, especially rigidly or inexorably forced techniques, have provided excellent data. The rigid oscillation techniques are very good for obtaining experimental data needed for systems with low stability typical of high performance vehicles. Reliable dynamic derivatives have been measured in subsonic through supersonic flows.

The present state of knowledge concerning spin has been largely derived from tests of complete models in the wind tunnel. Because spin is a low speed, high lift phenomenon dependent on non-linear aerodynamics, analysis has not proven very reliable. Full scale flight test experiments have yielded meager results because testing is limited by safety considerations.

Flutter model tests have been invaluable in design for flutter prevention. Because of unsteady aerodynamics and complex modal interactions, the analysis of flutter has frequently lacked reliability. Complete aeroelastic modeling for flutter in the transonic and supersonic regimes has been limited by the lack of mounting systems which allow rigid body degrees of freedoms.

Modeling for gust response has been rather limited until recently. Lack of a high-speed five degree of freedom mount, has made it difficult to study problems such as platform stability, riding comfort, and guidance

information. These characteristics are affected by pitching, plunging, yawing and rolling motions. Gust alleviation methods can be studied by pitching models, but complete airplane simulation would be a better means for designing alleviation systems.

POTENTIAL EXTENSIONS OF AEROELASTIC MODELING

The design of modern high speed vehicles has been significantly influenced by aeroelastic effects. As a result, considerable progress has been achieved in the art of constructing and testing flutter models. The effects of aeroelasticity on the other aspects of airplane design and performance e.g., structural loads, maneuverability, control system design, dynamic stability, have been engineered largely by theoretical analysis. As evidenced by previous discussion on aerodynamic testing methods, considerable progress has been made in rigid static and dynamic data measurement. Therefore, it appears that the progress made can be consolidated by application to the simulation of aeroelastic effects, both static and dynamic, on structural loads and stability and control characteristics.

The feasibility of constructing static, flexible structural loads models has been demonstrated before, most recently by a program at MIT. The trend for future vehicles is toward low aspect ratio, complex configurations. Prediction of elastic effects becomes increasingly difficult. More accuracy is needed for predicting tail loads, control effectiveness and stability as a function of q, M, α, etc. Static aeroelastic modeling presents a feasible, reasonable approach which is technologically possible at this time.

A maneuvering, flexible dynamic model is another extension of aeroelastic modeling techniques which merits considerable investigation. Such an extension would essentially permit us to "flight test" in the wind tunnel and thus provide a significant new "development tool" for the vehicle designer.

The major application of this modeling and testing technique would be to perform all or a part of an aircraft flight loads program in the wind tunnel. The airplane maneuvers could be flown, maneuvering limits established or verified, critical load conditions determined and possibly aircraft structural integrity could be demonstrated. This modeling and testing technique could also be used to demonstrate the airplane stability and control characteristics. Also, during the development phase, this technique would be amenable to simulating and testing possible stability augmentation schemes. In addition, the gust response flight test requirements could be satisfied if the atmospheric turbulence can be suitably represented. Thus, the maneuvering flexible model would provide a means whereby gust alleviation schemes could be developed.

The flight tests mentioned above are only a part of the total development program for an airplane. Other tests such as landing and take-off performance, drag measurements, local environmental studies, etc., are more efficiently performed using conventional modeling techniques. However, the

accomplishment of flying loads maneuvers, and obtaining stability and control, and gust response in the wind tunnel will save considerable development time and money.

For example, the structural flight loads program as defined in MIL-S-5711, is conducted in two phases. Phase One consists of maneuvering grids at airspeeds and three altitudes defined in MIL-S-5711. The maneuvers, e.g., pullouts, pushdowns, rolls, etc., are performed at various percentages, i.e. 50, 60, and 80%, of the design limit load factor in an effort to determine critical conditions. This phase of the program is flight time consuming because weight and c.g. must be maintained to close tolerances, thus requiring many flights to explore the entire flight envelope. Phase Two of the program consists only of the demonstration of the airplane structural integrity at 100% limit load factor for the critical conditions.

Phase One of the flight loads program generally constitutes about 75% of the flight time. Even if the critical conditions must be demonstrated on the full scale airplane, a considerable savings will be realized (cost per hour of flight test is approximately $10,000). In addition, if the critical load distributions can be accurately defined utilizing the loads model, the full scale loads airplane will not require extensive instrumentation if it is to be used only for the 100% demonstration maneuvers. Reduction of instrumentation requirements will introduce additional cost savings, e.g., transducers, calibration and checkout manhours.

It is certain that adequate flight testing for advanced vehicles, such as Dynasoar and Spaceplane, will be very costly, time consuming and possibly hazardous. Actually, for maneuvering reentry vehicles, flight testing per se can not be realistically performed. Since major aeroelastic effects and maximum load factor are suspected to occur supersonically or transonically, a maneuvering flexible model technique could be a valuable development tool. This modeling technique would permit a thorough investigation of these problem areas before the vehicle leaves the launch pad.

FACTORS IN DYNAMIC MODELING

The application of aeroelastic modeling techniques to the determination of structural loads and stability and control characteristics will represent a significant advance in the modeling and testing art. This modeling extension encompasses all technical aspects of airplane design and test. The technical considerations necessary for achieving the proposed modeling technology are divided in seven areas: similitude, model, mounting system, control system, sensors, data transmission, and data handling. Each of these areas will now be discussed.

SIMILITUDE. The development of any modeling technology begins with the derivation of the similitude requirements. Ideally, the laws of similitude define the absolute bounds of simulation attainable. However, the practical elements of the simulation, i.e. wind tunnel characteristics, mounting scheme, model construction, etc., determine the degree of simulation which can be truly realized.

The similitude parameters for a physical process can be derived in two ways; (1) studying the equations which describe the process or (2) through the standard algebraic procedure of dimensional analysis. The relative importance of these parameters can only be established by viewing them in respect to the objectives of the modeling technology under consideration.

We are presently considering the extension of aeroelastic modeling techniques for application to static and dynamic response i.e., loads, and stability and control characteristics. The dimensionless parameters which describe the dynamic aeroelastic system are listed in Appendix A. According to Buckingham's Theorem, the following functional expression completely describes the dynamic aeroelastic system,

$$f\left(M, R_e, \frac{m_o}{\rho l_o^3}, \frac{V}{g l_o^2}, \frac{Vt}{l_o}, \frac{P_A}{\rho V^2 l_o^2}, \frac{k_o}{\rho V^2 l_o}, \frac{\omega}{l_o}, \gamma, \frac{k(\eta,\xi)}{k_o}, \frac{m(\eta,\xi)}{m_o}, \frac{l(\eta,\xi)}{l_o}, \delta, \alpha, \theta\right) = 0 \quad \text{(A)}$$

The comparable expression for the static aeroelastic system can be expressed

$$f\left(M, R_e, \frac{m_o g}{\rho V^2 l_o^2}, \frac{P_A}{\rho V^2 l_o^2}, \frac{k_o}{\rho V^2 l_o}, \frac{\omega}{l_o}, \gamma, \frac{k(\eta,\xi)}{k_o}, \frac{m(\eta,\xi)}{m_o}, \frac{l(\eta,\xi)}{l_o}, \delta, \alpha, \theta\right) = 0 \quad \text{(B)}$$

The formal derivation of this expression is obtained by changing primary dimension system in the dimensional analysis procedures from MLT to FL system. The result is apparent; i.e., the time parameter Vt/l_o is dropped and the mass parameter combines with the Froude number (weight becomes important rather than mass in the equilibrium or static system).

The areas of non-simulation for these systems are well known (Expression(A)also describes the flutter model). They are non-scaling of Reynold's number and the effects of gravity.

Interdependency of the parameters M, R_e, and $k_o/\rho V^2 l_o$ does not permit simultaneous satisfaction of all three parameters for aeroelastic models. We generally chose to neglect Reynold's number, but match M and $k_o/\rho V^2 l_o$. Physically, it is well known that Reynold's number is a ratio of the fluid inertia force to the viscous force acting on a body in a streaming flow. For high Reynold's number at which prototypes generally operate, inertia forces predominate. Viscous forces are primarily drag forces; longitudinal forces have negligible effect on the pitch-plunge loads. Therefore, they are generally of little consequence in aeroelasticity.

The Reynold's number non-simulation affects both static and dynamic aeroelastic systems in the same manner. From Expression (A), the law of mass similitude derived utilizing the relative mass parameter $m_o/\rho l_o^3$, states that mass of the model should scale as the length scale cubed times the prototype mass. From the static aeroelastic systems expression, the law of mass similitude derived utilizing the parameter $m_o g/\rho V^2 l_o^2$ dictates that the mass be scaled proportional to the length scale squared. Therefore, when we simulate the mass using the dynamic scaling law, the model weight is

less than required for static considerations. Noting that the parameter $m_0 g/\rho V^2 l_0^2$ is the equilibrium lift coefficient, this non-scaling of weight causes the model to fly at an improper trim angle of attack.

Achieving Trim Angle Simulation. Non-simulation of prototype weight manifests itself in a reduced model equilibrium or trim angle of attack (when compressibility simulation has been achieved). The trim angle for an elastic prototype or model consists of two components, the rigid airplane (mass) trim angle and the aeroelastic increment due to deadweight deformation (twist and camber) of the lifting surfaces. Both of these angle components cannot be truly simulated due to non-scaling of gravity. This non-simulation would be of no consequence to the simulation of dynamic stability response and would yield conservative load distributions, if the aerodynamics are linear. However, in the transonic region the aerodynamics are generally non-linear; and it will therefore be important to correctly simulate prototype trim angle.

Similitude of equilibrium angle due to rigid mass non-simulation can be achieved by introduction of a massless vertical force independent of the model motion. This capability will be available with the dynamic mount - inertia cancelling device which will be discussed later under mounting requirements.

The aeroelastic increment to the trim angle can be simulated by building a twist and warp distribution into the model lifting surface equivalent to the deformation which would be developed if the weight increment required for true similitude were applied. Built-in warp or camber and twist affects the zero-lift (basic load) distribution of the surface, but the additional load distribution (load due angle of attack) is essentially unaltered. Total load and moment distributions are matched. This technique obviously violates the requirement of strict geometric similitude i.e. $(\pi_{12})_M = (\pi_{12})_P$ (Appendix A), but applied force and mass distribution are simulated. Therefore, dynamic similitude can be achieved.

Maneuver Potential in the Wind Tunnel. We are considering the use of aeroelastic maneuvering models in the wind tunnel. Theoretically, a model built to match the derived dynamic scaling laws will be kinematically similar to the prototype when forced similarly. Thus, by properly scaling control inputs or external forces, i.e. gusts, the model maneuver response can be directly related to the prototype response. There are practical modeling and testing considerations which will affect the maneuverability in the wind tunnel.

The primary limitations on the maneuverability are:

(1) Tunnel and model safety considerations
(2) Tunnel test section dimensions
(3) Geometric and physical system limitations

For obvious wind tunnel safety reasons, a maneuvering mounting system will be required to keep the model from flying downstream. As will be discussed later, the mounting system must be capable of driving itself to follow the model motions, thus, effectively leaving the model in free flight. Any mount restraint on the model would affect its maneuverability, hence, essentially none is tolerable. The mount should also keep the model from slamming into the walls, thus, preventing damage to the model and subsequent damage to the wind tunnel.

The tunnel dimensions limit the equivalent maneuvering altitude. The tunnel equivalent maneuvering altitude is a function of the model length scale. For practical utilization, the theoretical maximum equivalent altitude is reduced by safety consideration and also because wind tunnel interference effects would distort the model aerodynamics, i.e. shock reflections, pseudo-ground effects, etc. The apparent solution to the situation of limited tunnel altitude is to reduce model scale. However, decreasing the model size imposes other limitations on the maneuvering system. First, model frequency is increased as length scale is decreased. Although both model and mount mass are decreased, the frequency response capability of the mount must be increased to permit it to follow the smaller model motions. Reduced model scale also comprises or at least makes the construction of an accurate model more difficult, and reduces the amount of instrumentation that can be installed.

Flight test maneuvers are a function of the prototype maneuverability and design mission. A maneuvering model on any proposed mounting system can not perform all possible maneuvers. Because of physical limitations spins and LABS maneuvers will not be possible. However, the major portion of the flight loads demonstration program, e.g. symmetrical pull-ups, push downs, flaps down pullouts, roll and yaw maneuvers, and the control pulsing maneuvers for stability and control response could be performed in the wind tunnel.

During the full-scale maneuver program, the pilot does not generally concern himself with the altitude used to perform the maneuver. His primary objective is to pull the desired limit load factor. Therefore, it might not be feasible to attempt duplication of the exact flight test maneuver within the wind tunnel. To illustrate this point, let us assume we are flying a one-tenth scale F-106 model in a 16 x 16-foot wind tunnel section. Figure 1 depicts the scaled time history of the model response in a typical symmetric 7g pull-up (70g model scale), (flight condition 55-201, Reference 2). The time histories reveal that the pilot has not attempted to check the maneuver; the airplane has vertical velocity and continues to gain altitude. The maneuver as depicted could not be confined to the wind tunnel, i.e., equivalent altitude is approximately 100 feet.

As mentioned before, the pilot's objective was only to match the limit load factor without concern toward the consumed altitude or time history. Now consider the load factor time history superimposed upon the actual flight history (Figure 1). This maneuver takes advantage of the model jerk (time rate of acceleration) ability and the maximum negative load factor to decelerate the maneuver. As a result, the maneuver can be performed in

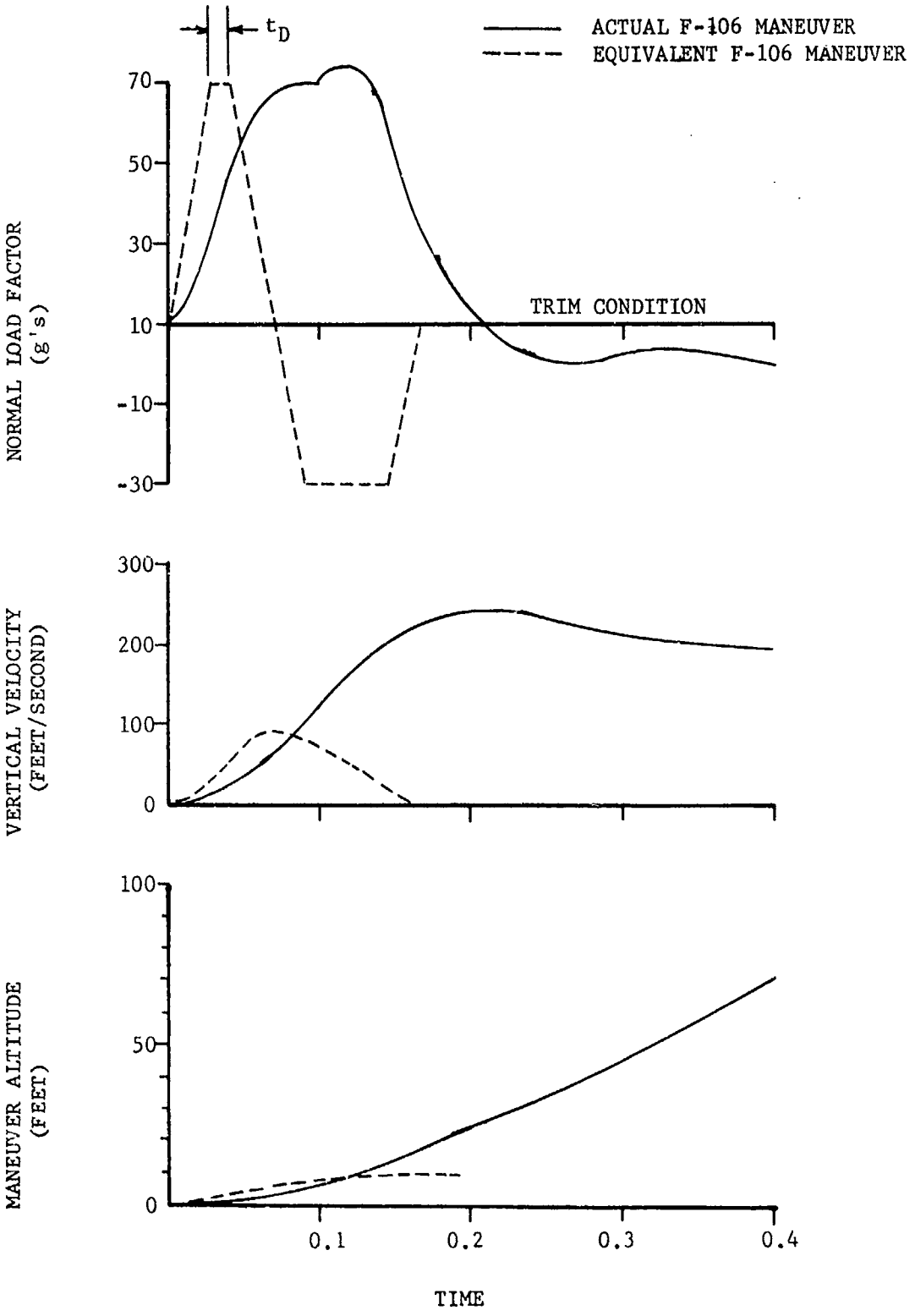

FIGURE 1. SCALED TIME HISTORY OF A TYPICAL F-106 SYMMETRIC PULL-OUT MANEUVER

approximately eight feet of equivalent altitude, and matches the desired limit load factor. The data time, t_D for the assumed maneuver, was arbitrarily set at t_D = .01 seconds. This value can be changed with a proportional change in equivalent altitude. Thus, it appears quite feasible to perform flight load maneuvers in the wind tunnel using scaled models.

MODELING. The design philosophy for the aeroelastic model is guided by similitude theory. The structure of the aeroelastic model must as a result

(1) provide external geometric contours to simulate prototype aerodynamics
(2) scale stiffness magnitude and distribution
(3) scale mass magnitude and distribution.

These are the design requirements for the flutter and aeroelastic dynamic stability models. An additional requirement for the static and maneuvering aeroelastic loads model would be to provide a structure which is capable of withstanding the scaled limit loads.

Direct scaling or a replica type structure will match all similitude requirements plus provide adequate strength. However, the aeroelastic loads model construction may be simplified provided the similitude design requirements are met. The departure from scaled replica-type construction for flutter models has long been the standard practice when aerodynamic heating (aerothermoelastic) simulation is not desired. This deviation from strict similitude can simplify model fabrication at a very slight loss of aerodynamic, mode shape, and low frequency response accuracy.

Direct scaling of the prototype structure has some reward; model stresses would be in one-to-one correspondence with respective prototype stresses. From these stresses, the external load distribution can be calculated. Deviation from replica-type structure, for fabrication ease, destroys the model-to-prototype stress correspondence but the loads distribution can still be obtained in the same manner.

It is hoped that the above discussion has not imbedded the thought that strain gauge instrumentation is the only means of extracting loads information from the dynamic loads model. Miniature pressure transducers appear to be quite feasible and offer a distinctive advantage over strain gauges. Using pressure data, direct integration yields the external (airloads) loads distributions. The transformation from stress to loads is a two step calculation. First, net loads distributions are obtained and then the inertia loads must be algebraically combined with the net loads to yield the airloads. The inertia loads are not known directly, but must be analytically derived.

There are problems which must be resolved if pressure transducers are to be used. The main problem is maintaining the mass distribution required by similitude. This requirement might impose a restriction on the number of transducers which can be utilized, and thus limit the accuracy of load resolution.

MOUNTING SYSTEM. Holding a model in a wind tunnel poses one of the most serious problems associated with wind tunnel testing. To list a few of the considerations that must be taken into account:

(1) Model aerodynamic interference
(2) Force measurement - data readout
(3) Wind tunnel blockage
(4) Strength
(5) Dynamic response
(6) Stability
(7) Safety provisions

The primary function of the mounting system is to hold or support the model in the wind tunnel. The mount also provides a position reference, supports instrumentation, and sometimes provides coolants. There are a variety of ways that it is desired to hold the model, for example: in static testing it is desired to hold the model rigidly at a fixed position and at a fixed angle in order to measure lift, drag, or other various rigid body static derivatives. Any motion of the model or perturbations of the airstream are a source of noise in the system and are eliminated if possible. In other types of mounts, it is desired to place as little restraint as possible on the model - ideally reacting only drag forces. An example of this mount would be a flutter model test wherein "rigid" body degrees of freedom are deemed important and purposefully the body is allowed nearly unrestrained motion.

It would be beneficial to point out the difference between flutter model and dynamic stability model mounting requirements. For dynamic stability modeling, it is of utmost importance that the mounting system has a frequency response capable of following all rigid body motions and possibly some of the lower structural frequencies. The latter requirement is of course dependent on the frequency separation between the structural and rigid body modes. The flutter mount must have a frequency response that provides good simulation of at least the first three or four free-free structural modes.

Static mounts are no doubt familiar to all, and except for certain subtleties, their designs and operation are generally straightforward. Dynamic mounts are much less common, however, and deserve some special mention.

There are two general classes of dynamic mounts, those which force the model through prescribed motions and those which appear (or attempt to appear) passive to the model. The first type of mount ordinarily is used in measuring dynamic stability derivatives and lately has found use in measuring flutter stability criteria (as developed by Boeing in their admittance technique) (Reference 3). Several mounts which are currently in use and appear at least semi-passive to the model are:

Princeton University Forward Flight Facility. This facility which is not a wind tunnel utilizes a 750 foot long track with a five

degree of freedom mounting system. The mount is designed and especially suited to studying dynamic behavior of V/STOL aircraft or helicopters during transition phases. Maximum forward velocity is 40 feet per second. (Reference 4).

Ling-Temco-Vought High Speed Wind Tunnel. This facility has a static servo-driven mount especially designed and used for docking and body separation studies. The mount senses aerodynamic forces which are fed to an Analog Computer. The computer adds the necessary rate derivatives, solves a six degree of freedom set of equations, and prescribes the motion for the hydraulically driven mount to follow.

National Aeronautics and Space Agency, Langley Field, Transonic Dynamics Tunnel. This facility utilizes a cable suspension system especially for flutter model testing. The mount has cables running both forward and aft which essentially restrain only fore-and-aft motion of the model.

Many low speed wind tunnels have provision for vertical rods especially suited for flying low speed flutter models. These rods allow nearly complete freedom in the vertical direction and by proper gimbal arrangements the angular degrees of freedom are realized. Some lateral and fore-and-aft restraint is offered.

Other dynamic mounting systems which are under development are:

At the Massachusetts Institute of Technology, a mounting system using magnetic force to hold and control a small model is under development. This mount will be used for static testing models and for stability derivative measurements. The stability derivatives will be measured by forced motions of the model. (Reference 5). Additional work on magnetic mounts has been performed by the University of Virginia (Reference 6).

At the Cornell Aeronautical Laboratories, a dynamic mount is being developed which will allow separation of dynamic derivatives.

At the Astromechanics Research Division of Giannini Controls Corporation, a dynamic mount is under development as a part of the MODEL FLY system. This mount is being designed under Air Force sponsorship for use in the 16-foot Transonic Wind Tunnel at AEDC. The mount will allow a model to be maneuvered in the wind tunnel in order to measure loads and stability and control characteristics.

MODEL SENSORS. In measuring model data, it is necessary to know both the input force and the model internal response. Ordinarily basic wind tunnel instrumentation (static pressure, temperature, density, etc.) in conjunction with model attitude variables provide sufficient data to determine the input forces to the model. However, if a distributed or localized description of these forces is required, then additional instrumentation is needed.

In a dynamic model, the distribution of transducers in lifting surfaces presents two problems - weight and size. Heating can also present a problem depending on the wind tunnel temperature. There are three primary dynamic sensors which can practicably be placed in lifting surfaces; strain gages, accelerometers, and pressure transducers. Table 2 presents the properties of each of these basic types. It is assumed that miniature solid state devices are used.

Item \ Sensor	Strain	Accelerometer	Pressure
Frequency Response (cps)	$0 \leq 1000$	$3 \leq 1000$	$0 \leq 1000$
Size	.003"x.125"x.250"	.100"x.500" dia.	.200"x.350" dia.
Weight	1 gram	1 to 3 grams	1 to 2 grams
Output Level	1 volt full scale	1.5m volt/g	1/2volt full scale
Power Requirements	0.1 watt	0	0.3 watt
Environmental Limit.	Temp.comp.req'd.	Cross talk Acoustic sens.	Acceleration sens. Acoustic sens.

TABLE 2

Other instrumentation important in controlling and data analysis of dynamic models but usually placed in the fuselage is:

Control surface position sensors
Pitch, roll, and yaw rate sensors
Translation velocity sensors

These sensors are usually available off-the-shelf, but should be kept small and light weight.

Another very important bit of external instrumentation is a visual record of the dynamic motions sustained by the model. Both high speed cameras and the Mark I Eyeball system are recommended.

MODEL CONTROLS. Model controls can be divided into two classes - those which are external to the model as with a mount which moves the model, or those located within the model and actually move the control surfaces. Controls external to the model are a function of the mounting system and as such are designed into the mount.

Controls which are to be placed within or directly adjacent to a dynamic model generally have a severe set of restrictions imposed upon them. The power source must be very light in weight, small in size, good resolution good repeatibility, high power, good frequency response, etc.. The power transfer system and position sensors have the same general restrictions imposed upon them. Figure 2 presents a comparison of typical weight vs. power curves for small power systems. These curves were derived from modified or off-the-shelf hardware. It should be noted that there is no off-the-shelf equipment which is readily usable in model control systems. There are, however, some components which when modified are satisfactory for use, e.g. small pneumatic actuators or hydraulic dampers.

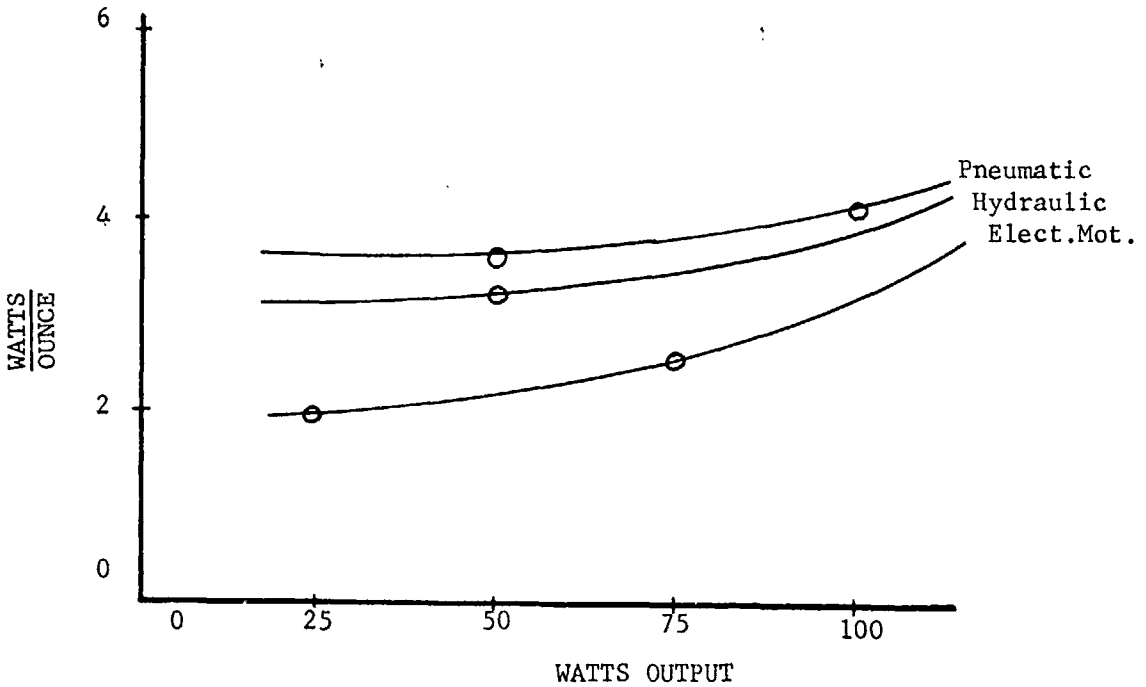

FIGURE 2. COMPARISON OF TYPICAL WEIGHT VS POWER CURVES

Design requirements for control equipment for model use are somewhat different from conventional small industrial equipment. Some of the significant differences are:

Very high reliability
Short life - say less than 50 hours of operation
Intermittent operation
High structural efficiency
Lower power conversion efficiency permissible
Withstand rugged environments.

DATA TRANSMISSION. The data transmission system for the maneuvering model must perform two functions: (1) transmit the data measurements in a form suitable for recording and future data processing, and (2) provide a communication link for purposes of control and safety of the model. The

familiar low speed flutter model data system performs these same functions. However, hardware and design considerations required for the maneuvering model system are more difficult and sophisticated because of the required number of measurements and their frequency characteristics. These factors are important considerations in selecting the mode of data transmission.

There are three modes of data transmission which can be considered for the maneuvering model. These are (1) parallel hardwire transmission (2) time sharing hardwire by means of commutation and (3) commutation with radio frequency (RF) telemetry. A data flow chart showing the flow of data and equipment utilized in these modes can be found in Figure 3. It will be noted that all of these modes of transmission are suitable for both functions previously mentioned.

A description of each transmission mode and its advantages and disadvantages follows:

Parallel Hardwire. The parallel hardwire mode is the most commonly used mode of data transmission. In this mode, signal wires lead from each transducer to the recorder and/or control center. The data signals from each transducer are transmitted and recorded simultaneously. Thus, the name "parallel hardwire" is derived.

The quantity of information to be transmitted is the prime limitation of this transmission mode. The maneuvering loads model will be extensively instrumented. Although it cannot be instrumented exactly as the full scale flight loads airplane (primarily because of matching scaled weight requirements), the model will require a large number of transducers to obtain loads distributions, local accelerations, control position, etc. The exact number of transducers required will be a function of the vehicle tested. However, an estimate of fifty (50) transducers would be reasonable and would suffice to carry the point of discussion. Each of these transducers would require two (2) signal wires plus shielding to minimize the effects of wind tunnel noise. The power wires to drive the transducers need not be considered because all transmission modes require them and their number can be minimized by common use. This bundle of wire (100 wires plus shielding) could prove to be physically unwieldy and impede the free flight response of the model. This factor, by far, overshadows the advantage of parallel hardwire over the other modes. That is, no additional weight is required for signal conditioning.

Time Sharing Hardwire by Means of Commutation. The name of this mode is derived from the fact that the data signals, which occur in parallel, are converted by means of the commutator into serial signals which are transmitted over the same wire (time sharing). The output from the commutator is a pulse-amplitude-modulated(PAM) signal. The reliability of PAM when transmitted over a long wire is greatly reduced by signal attenuation and the noise environment. To minimize or eliminate these signal errors, the PAM signal is generally amplified and passed through an analog-to-digital (A/D) converter. The signal emerging from the (A/D) converter is a

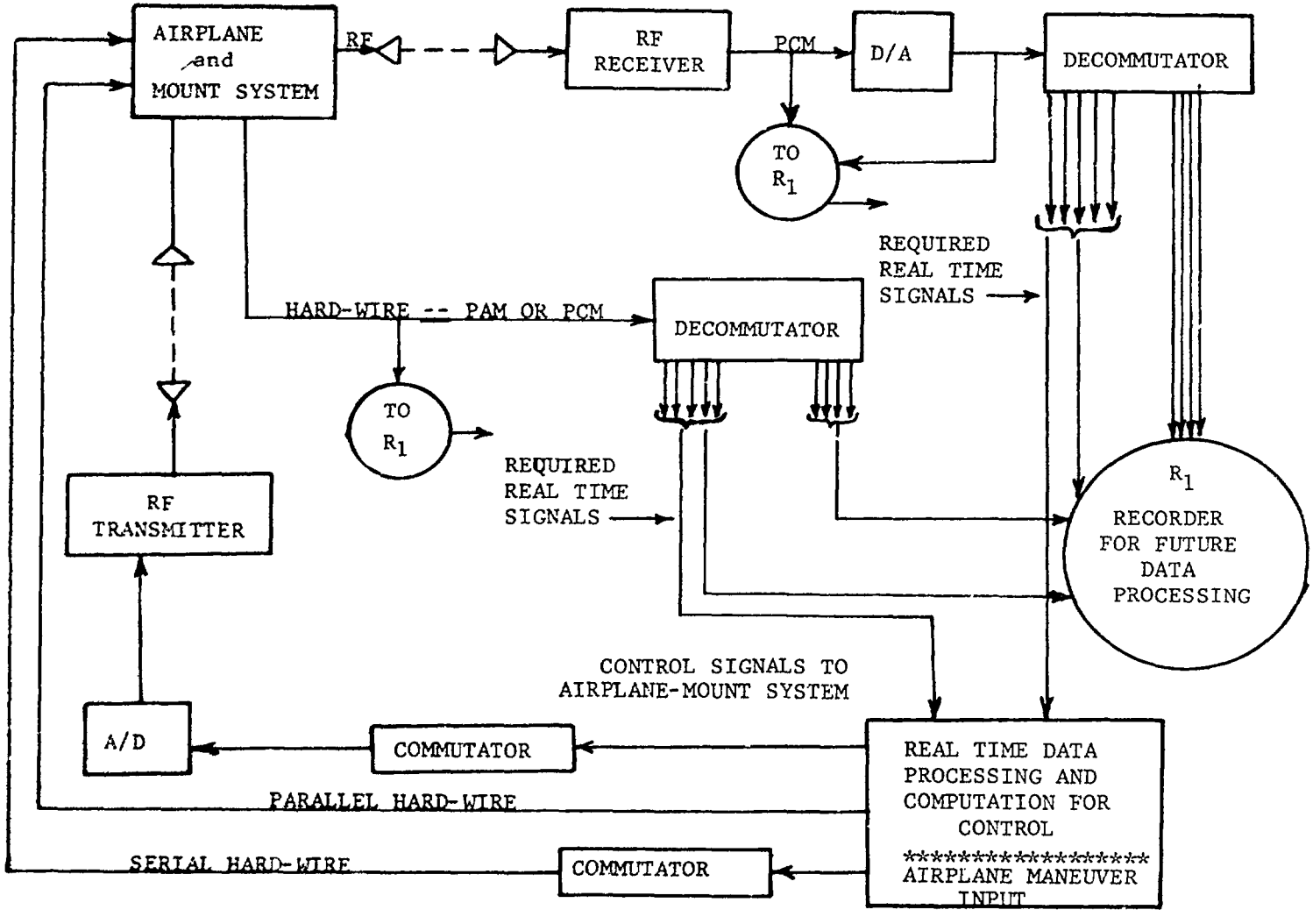

FIGURE 3. SCHEMATIC OF DATA TRANSMISSION MODES

pulse-code-modulated signal (PCM) whose reliability is unaffected by noise. The transmitted signal must pass through the inverse of the above described procedure to retrieve the data in parallel analog form for either real time control processing or data recording for further analysis (see Figure 3).

The advantage of this mode over parallel hardwire is obvious; the "big bundle" of wires has been replaced with just one wire. However, a weight compromise is needed to enable this achievement. The package of commutator, amplifier and analog-to-digital converter must be housed in the model. For a dynamically scaled model, this added weight could be intolerable. The commutator is the heaviest component. Its size is dependent on the number of data channels and frequency resolution desired. Therefore, the allowable size of commutator could limit the amount and quality of the systems data output.

Commutation with Radio Frequency (RF) Telemetry. This transmission mode is exactly the same as the second mode discussed above except that the PCM signal leaving the A/D converter is transmitted to the control center by means of a radio frequency transmitter rather than the single hardwire. Therefore, the advantage of this system, if batteries can be provided to power the transmitter, commutator, and transducers, is that all wires are eliminated. The disadvantages are that the weight of the radio transmitter (and batteries) must be added to the model and the cost of the transmission system would be increased.

The consideration of the second and third modes is made possible by recent advances in solid-state electronic components. Present off-the-shelf components, will permit us to assemble the system described above, with a capability of handling 50 data channels with frequency resolution up to 100 cps. This package would be approximately 4" x 3" x 6" in size and weigh approximately eleven (11) pounds. This weight might be untolerable. However, there are currently in development, micro-miniaturized components which would be considerably smaller in size and weigh approximately one pound. Therefore, these data transmission modes will be quite feasible.

DATA HANDLING SOFTWARE. An important factor for utilization of aeroelastic maneuvering models will be the development of the data handling software or processing system which can provide on site data reduction of model response and loads parameters while testing or shortly thereafter. A system with such capability would greatly enhance the application of this type of model to performance in the wind tunnel of all or a major portion of a prototype's flight loads and stability and control program.

With a data reduction system as envisioned, the model test engineer could have model response data and loads information shortly after his test, check the validity and magnitude of the loads frequencies, decay factors, etc., and use this information to either "refly" the maneuver or proceed with the next maneuver. This data processing capability would enhance the overall testing technique, especially when applied to the flight loads program. A typical test sequence for a Phase One survey

maneuver as flown in the wind tunnel would be as follows: fly maneuver at 50% limit load factor and review data; maneuver at 60% and 80% limit load factor; plot data and extrapolate data to limit load factor; decide whether model could withstand limit load; perform maximum load maneuver. This sequence of maneuvers, of course, differs from that followed in full-scale flight. For the full scale, the 100% load factor condition can not be performed prior to static load test demonstration and correlation with data from survey maneuvers. Thus, the data processing system provides a significant savings in program time duration as a result of maneuver sequencing. This time savings in addition to the time gained by model scale greatly reduces the time duration for the entire flight program.

Although the desired data handling system is quite important and sophisticated, there do not appear to be any real problems in achieving the system desired.

The dynamic analysis methods, i.e., inverse Laplace transformation, harmonic analysis, etc., for stability and control computations have been developed and coded for the computer by NASA and others and are readily available. The only possible problem envisioned in assembling the desired data system would be non-compatability of programs with equipment at the test facilities. This problem has been encountered previously, and standard conversion programs or minor input/output format changes will provide the "fix". The envisioned, almost on line, data system will probably not include the transfer function and power spectral density computations. These computations should be deferred until daily testing has ended; they require considerable computer time and core storage and would "tie-up" the facility. Also, it might be more economical to perform these computations on special transfer function computers or spectrum analyzers to obtain increased accuracy.

The primary loads programs necessary for the envisioned system are a pressure integration scheme and a strain gauge load calibration matrix with a matrix operation package. These programs have been coded and can be found in the computing library at all wind tunnel facilities.

MODEL FLY PROGRAM SUMMARY

OBJECTIVE. The objective of the MODEL FLY program is to develop a general testing technology whereby the flight loads, dynamic response characteristics and dynamic stability and control of full scale air vehicles can be obtained from tests of suitably scaled models in a wind tunnel.

BACKGROUND. It is evident that in order to accomplish the above objective and obtain the most accurate estimate of the dynamic characteristics of the vehicle, the model must be allowed to maneuver in the tunnel much as the full scale air vehicle would in free flight. Therefore, it was realized at the onset of this program, that existing schemes for testing models would not suffice. Some wind tunnel mounting schemes, such as holding the model in the tunnel by means of wires or rods, do have merit. For high speed flow, these mounts cause significant aerodynamic interference and impose restraints on the model which in effect do not permit "free flight".

Secondly, these other mounting systems were designed for other purposes, e.g. the estimation of stability derivatives. It, therefore, became clear that a mounting system was required that would provide the propulsive force to "propel" the model with respect to the air (restrain the model in the tunnel) and yet add no spurious forces to the model. Thus, the MODEL FLY mounting scheme was conceived.

LOW-SPEED DEMONSTRATION SYSTEM. The details of the operation and components which make up the system are given below. It should be emphasized that the low speed phase of this program was conceived only for the purpose of demonstrating the principles embodied in this mounting scheme; i.e. proof of model-mount stability and the ability of servo-wings to cancel the mount reactive forces on the model. The demonstration mount was designed specifically for this purpose and is shown in Figure 4. It was never intended to be a prototype for larger scale mounts and it should not be regarded as such.

Servo-Wings. As noted previously the dynamic mount was designed to add no spurious forces to the model other than providing the propulsive force required to "propel" the model in the tunnel. To accomplish this, the effect of the mount static and dynamic forces on the model must be eliminated. Simply balancing the mount with the model off so that the mount center of gravity is at the center of rotation will provide static balance. In this way, the model when flying at a trim condition need only provide a lift force sufficient to cancel its own weight. There still remains the problem of removing the mount force sensed on the model resulting from model acceleration. This force is mount inertia reaction. Hereafter, cancellation of this force with an equal magnitude acceleration-phased force will be called "inertia cancellation".

The inertia cancellation is accomplished by introduction of an inertia nulling device denoted as servo-wings and shown diagrammatically in Figure 5. Here, the servo-wing is free to pivot at a point forward of the servo wing center of pressure and center of gravity. Local acceleration is sensed at the center of gravity of this pendulous system. (The servo wing is trimmed to desired steady state lift during operation by means of a tab located at the trailing edge of the wing).

Consider further the behavior of the inertia nulling system illustrated in Figure 5 under any input of local acceleration. Acceleration causes the driving force $M_s\ddot{z}$ which rotates the servo wing to the angle θ_s. Accordingly, the lift force L_s is generated on the servo wing. It is shown here in its correction directional sense, a directional sense which makes it capable of cancelling a large inertia force in the structure to which it is attached. The angle θ_s is determined by the balance between the inertial moment, $M_s\ddot{z}\,\ell_{cg}$ and the aerodynamic centering moment $L_s\,\ell_{cp}$.

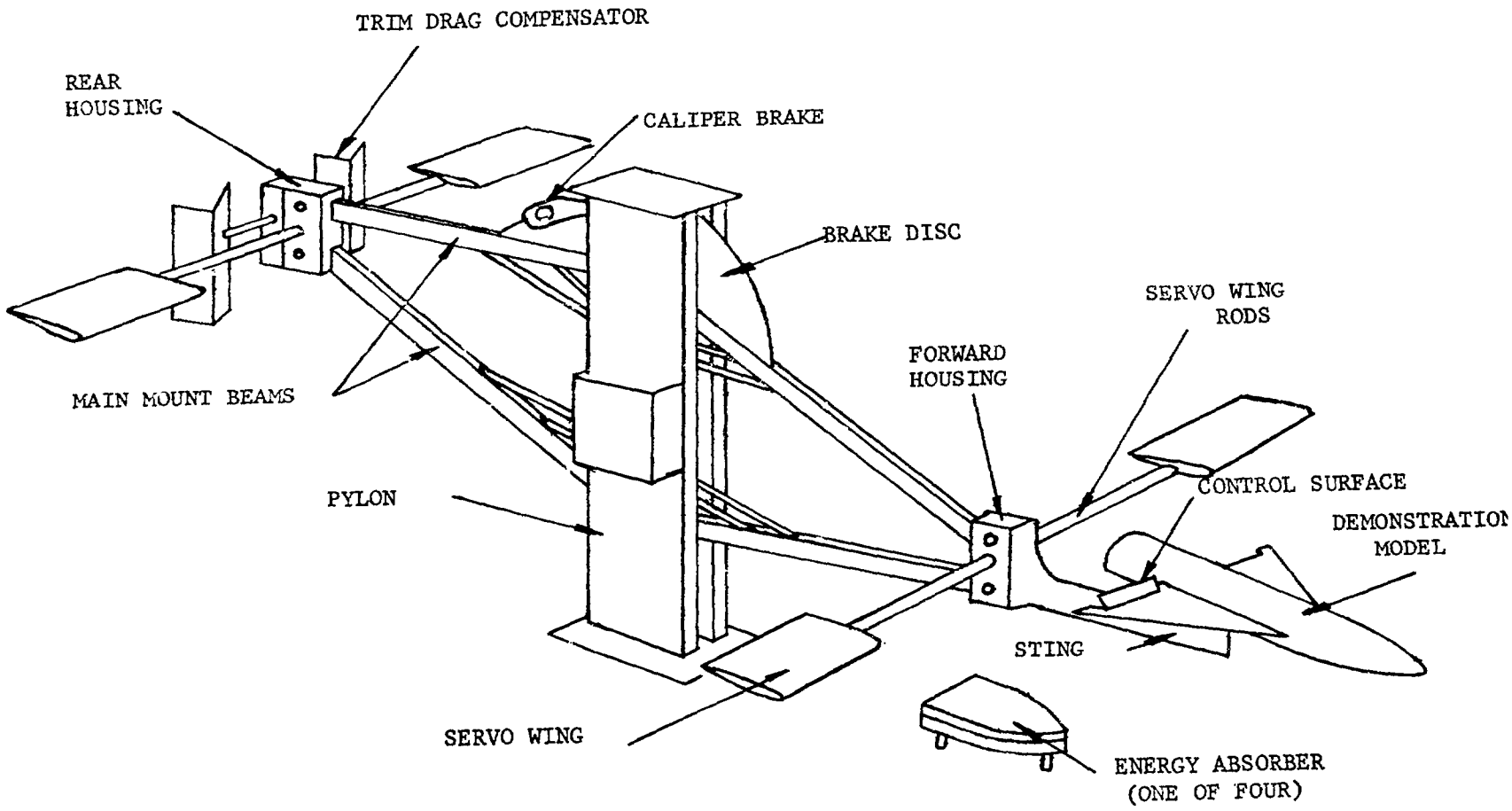

FIGURE 4. LOW-SPEED MODEL FLY DEMONSTRATION

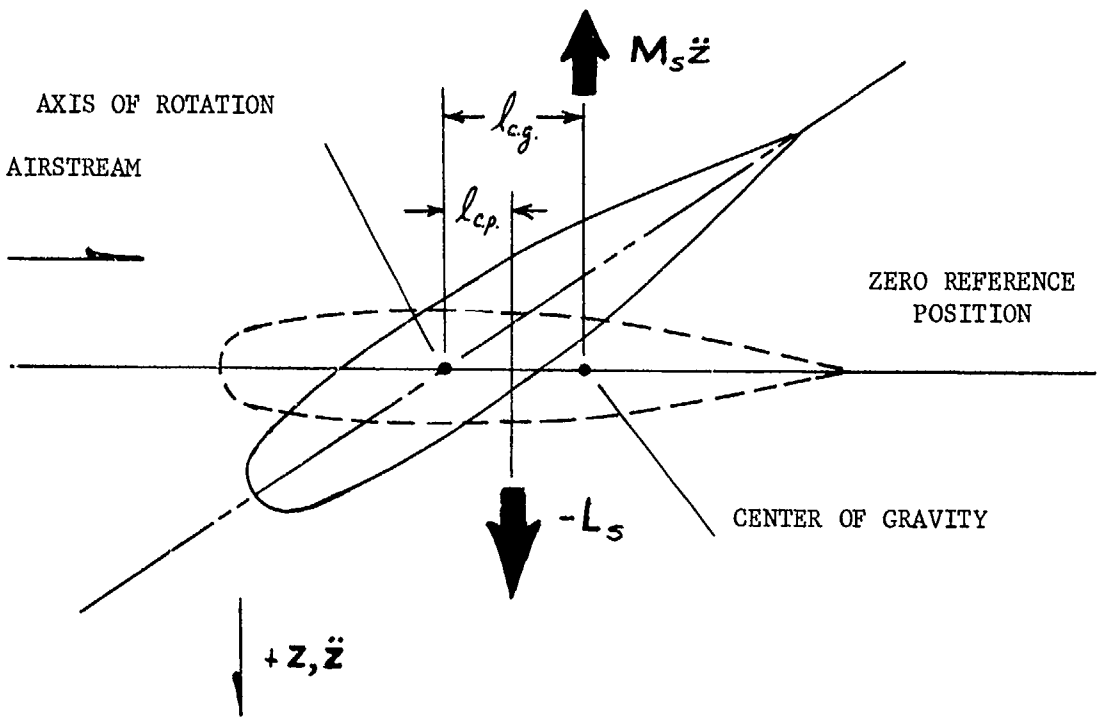

FIGURE 5. SERVO WING UNDER ACCELERATION

The servo wing assemblies are placed on the dynamic mount in such a way as to cancel entirely the inertial moment of the dynamic mount without introducing any spurious spring or damping forces. The servo wing location for the demonstration mount was selected to be the forward and rear box sections, since any hardware attached to these sections will remain horizontal due to the 4 bar (beam) parallel linkage system, thereby, sensing vertical acceleration exactly.

As in the design of any practical mechanical system, some criteria must be set up to ensure efficient operation. For the servo wing assembly these are:

1. Wing angle, θ_s, per "g" acceleration - This value must be low enough so that the wing operates over its most efficient and practical aerodynamic range. The parameters which affect this quantity are determined from a summation of the moments over the airfoil. Consider Figure 5 once again. Summation of the quasi-static moments at the pivot point gives (written about the trim angle)

$$-L_{\alpha_s}\,\ell_{c.p.}\,\theta_s = M_s\,\ell_{c.g.}\,\ddot{z} \qquad (1)$$

Solving for wing angle

$$\theta_s = \frac{-M_s \, l_{c.g.} \, \ddot{z}}{L_{\alpha_s} \, l_{c.p.}} \tag{2}$$

Therefore, changing any of these parameters will affect the wing angle per g. However, because of other equations (to follow) which must be satisfied, only two variables for each velocity remain which directly control this equation. They are $C_{L_{\alpha s}}$ and S_s, the lift curve slope and servo wing area respectively.

2. Low pitch inertia - This ensures that the wing will have good dynamic response (high natural frequency). To accomplish this in the present design, the wing was constructed of foam plastic with a fiberglas cover. This construction results in a wing of high strength and stiffness.

3. High structural rigidity - This ensures that servo wing flutter speed will be well above any operating velocity. This would be a compromise with the aforementioned criterion #2, since high rigidity would probably also cause an increase in overall weight and, therefore, inertia.

It is probably quite apparent that there exist means by which the amount of inertia to be cancelled can be approximately predicted. If it is assumed that all the weight of the mount acts as a point mass at the servo wing rotation points, then from a summation of the quasi-static forces for one wing

$$-L_{\alpha_s} \theta_s = \frac{I_M}{R^2} \ddot{z} \tag{3}$$

where I_M is the inertia of the mount and R is the distance from the mount rotation point to the servo-wing pivot point.

Combining Equations (2) and (3)

$$\frac{M_s \, l_{c.g.} \, R^2}{l_{c.p.}} = I_M \tag{4}$$

Inspection of this quasi-static equation written for steady-state acceleration shows that inertia cancelling is not a function of wind tunnel velocity; an important result since barring compressibility effects the same wing could operate over the entire speed range. (However, $l_{c.p.}$, the distance between the pivot point and the center of pressure, can change with Mach number and angle of attack or both). Equation (4) was derived for one wing only. To obtain the total inertia cancellation capability of the system, the left hand side of Equation (4) must be multiplied by the total number of servo wings utilized.

A complete dynamic analysis has been performed on servo wings. This

analysis included such input parameters as:

Mass of mount
Mass of model
Servo-wing inertia
Tunnel velocity
Dynamic pressure
Servo-wing aerodynamic terms
Servo-wing aerodynamic damping terms
Servo-wing geometry (M wings, W wings, thickness)

Plots and cross-plots were made for such variables as natural frequency versus C_{L_α}, C_{M_q}, $I_{c.p.}$ and $I_{c.g.}$; and damping ratio versus these same variables.

It has been found that Equation 4 presents a good first order approximation to this complete dynamic analysis so long as the natural frequency of the servo-wing is about one octave higher than the mount natural frequency.

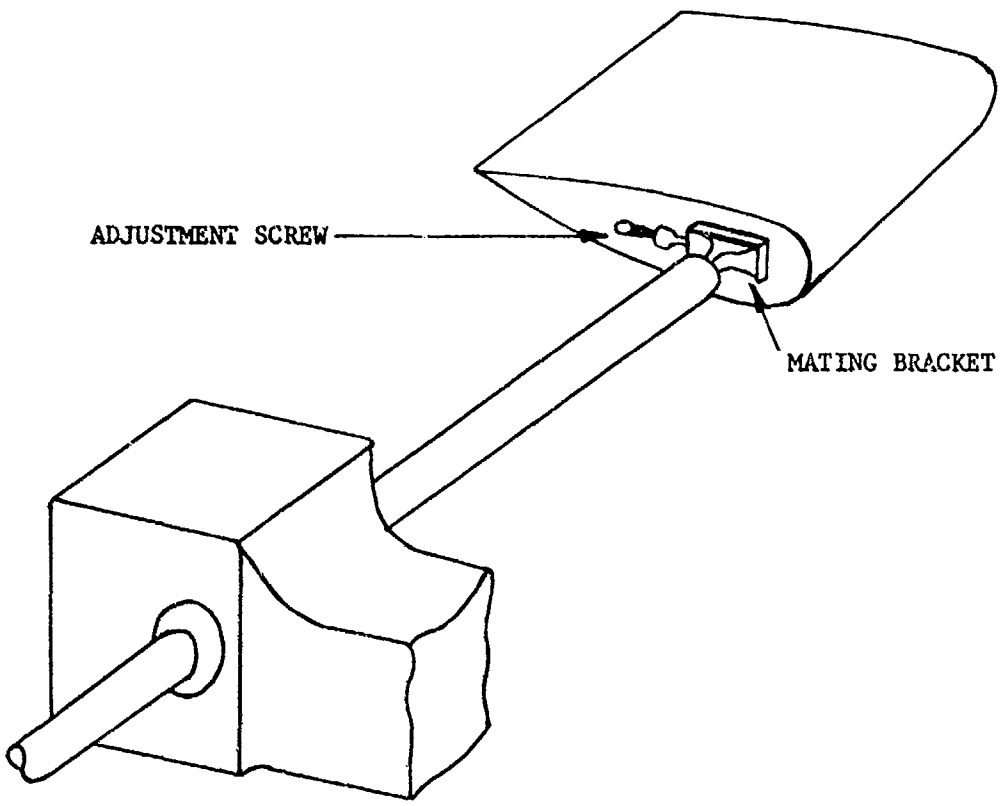

FIGURE 6. DETAIL DRAWING OF SERVO WING-ROD ATTACHMENT

Several sets of servo-wings were constructed. Originally a wing-tail configuration was tried; the addition of the tail added so much inertia that an impractical system resulted. Wings of delta planform were also tried but were discarded because of their inferior inertia and aerodynamic properties in the low speed range.

The fixture holding the servo-wing to the rod is illustrated in Figure 6.

Dynamic Mount. The demonstration dynamic mount shown in Figure 4 was designed to support the model in the wind tunnel test section, yet add to the flying model no spurious forces, that is, forces or moments not felt by the flying prototype. The basic components of the dynamic mount are two main beams, upper and lower, supporting a sting at the forward end and a drag compensator at the aft end. The motions of both sting and drag compensator are constrained to be translatory by the two beams since the beam linkage points, center and ends, are along two parallel lines, thus leaving the sting and drag compensator horizontal at all times. The model is attached to the sting by a pivot at the model c.g. The two beams are pivoted at their centers to the two vertical members denoted as the pylon.

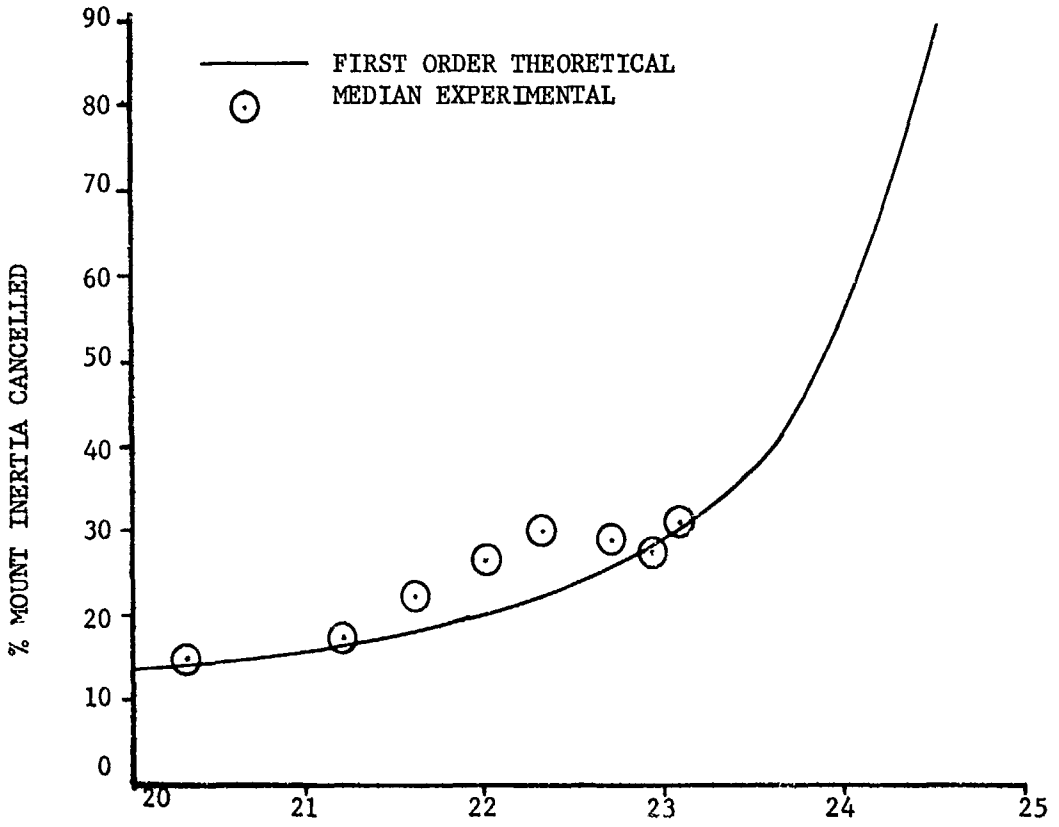

FIGURE 7. SERVO WING AXIS OF ROTATION % c

The purpose of the drag compensator, pictured in Figure 4, is to provide a drag moment on the linkage which nominally cancels the model destabilizing drag moment. By adjusting the angle between the two hinged plates, a drag force can be obtained which creates sufficient moment to balance the pitching moment due to the trim drag of the model.

In designing the dynamic mount it was always sought to keep the strength to weight ratio at a maximum. Aluminum structure and balsa wood fairings were used for this purpose.

Tests. Tests were conducted at the University of Michigan low speed wind tunnel during the spring of 1962. These tests were performed on a basic mount-spring configuration without servo-wings, on the mount-spring configuration with servo-wings, and on the complete system with model attached (no springs). The tests on the basic mount-spring configuration with and without servo-wings were conducted to measure the inertia cancelling capabilities of the servo-wings. The tests with the model were to demonstrate overall mount-model stability.

Results. The tests satisfactorily demonstrated that significant inertia cancelling is possible. With certain configurations some stability problems were encountered with the servo-wings and mount coupling to form a limited amplitude instability. This instability is predictable and preventable. The model was flown on the mount and encountered no stability problems. Noticeable changes in model response were observed as increasing amounts of inertia were cancelled. Figure 7 illustrates measured and first order predicted inertia cancelling capabilities for a typical configuration.

CURRENT PROGRAM. The current MODEL FLY program retains the objectives that have been basic with the project since inception. A dynamic mount is now being developed that will be capable of passively following a maneuvering aeroelastic model in transonic flow. The 16-foot PWT transonic wind tunnel at AEDC is the facility that has been selected for this installation.

Mount Requirements. The mount will be capable of acceleration rates of up to 70 g's, velocities of 160 feet per second, frequency response of at least 30 cycles per second, and angular rates of up to 300 degrees per second. The mount will be able to support dynamic loads at sting end of up to 2500 pounds. It is planned for the first development phase to develop the mount for only the pitch plane, i.e. vertical translation and pitch. Later phases extend the mount to the yaw and roll planes and into the 16 foot supersonic wind tunnel at AEDC.

Model Requirements. A model of a recent high performance aircraft (probably the F-106) will be developed with a capability for maneuvering at scaled maximum normal load factor, flying with its own control surfaces through stability and control maneuvers, and measuring distributed load values, and response criteria. This model in the case of the F-106 would probably be a 0.10 scale, weigh approximately 30 pounds, maneuver at normal load factors of 70 g's, and measure approximately 50 parameters while dynamically maneuvering.

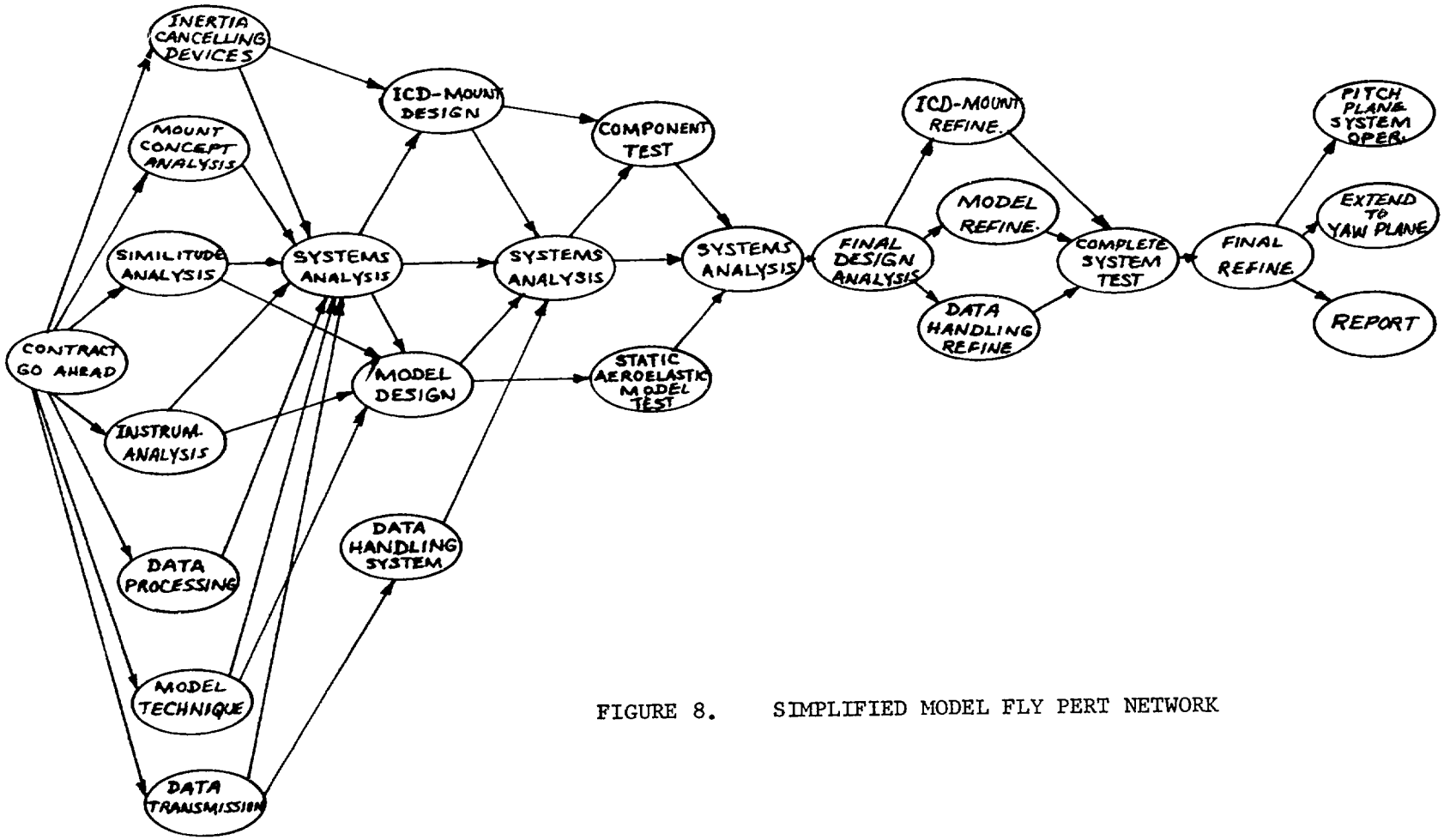

FIGURE 8. SIMPLIFIED MODEL FLY PERT NETWORK

Inertia Cancelling Device. Pure seismic servo-wings in high speed - especially transonic flow are not suitable for the inertia cancelling requirements. This is due to the center of pressure shift with Mach number and with angle of attack change. A series of M and W wings were tested at AEDC in an attempt to find a configuration which exhibited a C.P. shift within the desired tolerance over a reasonable Mach number range - none were found. Consequently, it has been decided to use one of two potentially satisfactory means for accomplishing inertia cancellation. These methods are large hydraulic actuators which by cables would move the sting as prescribed, or servo augmented wings which would not depend on external conditions for control. There is also a possibility of using both servo augmented wings and large actuators in combination, the large actuators for high amplitude, low frequency following and the servo wings for the higher frequency perturbations.

Schedule. Current PERT schedules indicate that testing in the AEDC wind tunnel will commence in about 18 months with the complete pitch plane system checked out and ready for use in about 30 months. A very simple PERT chart for this program is shown in Figure 8. This PERT chart depicts the interactions of some of the major considerations of the program.

CONCLUSIONS

In summary, it can be said that the considerations for the application of aeroelastic modeling techniques to the determination of structural loads and stability and control characteristics have been presented. It can be concluded that:

1. The required aeroelastic modeling extension is feasible and does not represent a severe extrapolation of the present state of modeling technology.

2. The modeling extensions proposed will provide a significant new "development tool" for the vehicle designer.

3. The proposed modeling and testing technique would yield a significant cost and time savings during prototype development.

4. The major technological status improvement required is the development of a mounting system with adequate frequency response to passively follow a maneuvering model.

REFERENCES

(1) Practical Aspects of Aerothermoelastic Modelling, M. Schlessinger, B. Omilian, J. Deutschman, and J. S. Isenberg, ASD-TDR-62-705, December 1962.

(2) Results of Flight Airloads Measurement on the F-106A Airplane - Final 100% Phase, A. H. Ryan and T. J. Condon, Convair Report ZU-8-066, Volume III.

(3) Admittance Techniques in High Speed Flutter Model Testing, G. W. Asher and R. K. Watanabe, WADD TR 61-31, January 1961.

(4) The Evaluation of Stability and Control Characteristics of Aircraft at Low Speeds Using Dynamically Similar Models in Semi-Free Flight. H. C. Curtiss, Jr., W. F. Putnam, and E. Martinez, Presented at the American Helicopter Society, May 3 to 5, 1962.

(5) The Design and Initial Operation of a Magnetic Model Suspension and Force Measurement System, E. L. Tilton III, et al., ARL-63-16, January 1963.

(6) An Electromagnetic Suspension System for the Measurement of Aerodynamic Characteristics, H. Parker, J. May, and G. Nurre, Virginia University Research Labs, Report AST 4443-106-62U, March 1962.

(7) The Aeroelastic Design of Lifting Surfaces, William R. Laidlaw, Presented at the MIT Summer Session on Aeroelasticity, June 23 to July 3, 1958.

APPENDIX A

DIMENSIONLESS Π PARAMETERS

This appendix lists the dimensionless Π parameters that completely described the prototype system. Their derivation can be found in Reference (7). The prototype can be described as a structurally elastic, winged vehicle, flying through a viscous, compressible fluid, air, at a particular altitude and velocity relative to inertial or fixed space. The Π parameters which completely describe the environment, motions, geometry and forces acting on the prototype are:

$\Pi_1 = M = V/a$	Mach Number
$\Pi_2 = R_e = \rho V l_o / \mu$	Reynolds Number
$\Pi_3 = V^2/g l_o$	Froude Number
$\Pi_4 = P_A/\rho V^2 l_o^2$	Force Coefficient
$\Pi_5 = m_o/\rho l_o^3$	Relative Mass Parameter
$\Pi_6 = k_o/\rho V^2 l_o$	Relative Stiffness Parameter
$\Pi_7 = w/l_o$	Non-dimensional Deflection
$\Pi_8 = Vt/l_o$	Non-dimensional Time
$\Pi_9 = \gamma$	Ratio of Specific Heats
$\Pi_{10} = \frac{k(\eta,\xi)}{k_o}$	Dimensionless Stiffness Distribution
$\Pi_{11} = \frac{m(\eta,\xi)}{m_o}$	Dimensionless Mass Distribution
$\Pi_{12} = \frac{l(\eta,\xi)}{l_o}$	Length Distribution, i.e., Thickness Distribution
$\Pi_{13} = \delta$	Control Deflection
$\Pi_{14} = \theta$	Pitch Angle
$\Pi_{15} = \alpha$	Angle of Attack
$\Pi_{16} = \psi$	Yaw Angle
$\Pi_{17} = \phi$	Roll Angle
$\Pi_{18} = \beta$	Sideslip Angle

DYNAMIC TESTING TECHNIQUES FOR A WIND TUNNEL MODEL

G. L. Kugler

General Dynamics/Astronautics

ABSTRACT

This paper presents testing methods and techniques which were used to define the structural dynamic characteristics of wind tunnel models. These models and techniques were developed for a wind tunnel test program on ground wind induced oscillatory loads on Atlas Space Launch Vehicles. Models of nine different space launch vehicles, utilizing the Atlas Space Booster, were tested. The 1/15 scale aluminum model was so constructed as to facilitate the simulation of various propellant loads with the resultant varying dynamic parameters. The structural dynamic characteristics of interest were the damping factor of the first bending mode, the first elastic mode shape, the first mode frequency, and load deflection information. Discussion will include the model excitation method, vibration measurements, model instrumentation, and certain model construction details.

DYNAMIC TESTING TECHNIQUES FOR A WIND TUNNEL MODEL

G. L. Kugler

General Dynamics/Astronautics

Ground wind induced oscillations of specific missile and payload configurations were studied recently by General Dynamics/Astronautics in the 12-foot pressure wind tunnel at NASAs Ames Research Center. (1, 2, 3) In order to extrapolate prototype behavior from model studies, it was necessary to determine; for each configuration and in several orientations, the frequency, shape, and damping factor of the first elastic mode, together with the oscillatory load-deflection relationship. Ground wind induced oscillations, normal to the wind, are caused by vortex shedding around a cylindrical body. The problem is further complicated by various protuberances extending from a cylindrical-shaped vehicle. (4, 5)

Program management was under the direction of the Air Force Space Systems Division with technical direction provided by the Aerospace Corporation. Tests were conducted to determine the critical orientation of the vehicle protuberances with respect to wind direction and speed, the effect of surface roughness, and the effects of tanking conditions. The various umbilical towers were also simulated. Vehicles simulated included the Atlas booster as a first stage, Centaur and Agena second stage configurations with Ranger and other payloads. The wind tunnel test resume will be presented in a General Dynamics/Astronautics' report by E. F. Gaffney. A general discussion on the results of ground wind induced oscillations is being published. (6)

Knowledge of certain structural dynamic characteristics was required in order to predict full-scale vehicle response from the model study. It was necessary to determine these characteristics with the model mounted in the wind tunnel, due to the contributing influence of the wind tunnel response on the model. In order to test a model which would retain relatively constant dynamic characteristics, certain model design criteria were suggested by the Ames Research Center personnel. This paper describes the model fabrication, and techniques and equipment used to determine the dynamic characteristics.

TEST PARAMETERS

The wind tunnel test program covered models of nine separate booster/payload configurations including several payloads with and without environmental shrouds. Three tanking conditions were simulated for each configuration tested. A design, to meet the above requirements, resulted in a model with 1) basic assemblies which could be used with several configurations, 2) ease of assembly for rapid configuration changes, 3) structural rigidity between sections to insure relatively

consistent damping coefficient.

Prior to each wind tunnel test, it was necessary to determine the first elastic mode frequency, shape, damping factor, and oscillatory load deflection relationship for each model configuration in the drag and lateral directions. In addition the damping factor was determined each time the model was moved on the mounting pedestal. The first elastic mode frequency was in the range of 15 to 70 cps and the damping factor in the range of 0.001 to 0.008 for the various models. Maximum design bending moment on the model pedestal was in the range of 65,000 and 95,000 in. lb. for the different models.

MODEL FABRICATION

The model, as shown in Figure No. 1, was built in sections such that the basic assembly could be used in several of the different models. The lower section, or Atlas portion, was used with all of the models. Two interchangeable midsections were fabricated simulating the Agena or the Centaur. The forward section consisted of the appropriate different payloads for the Agena and Centaur. All protuberances extending from the basic cylindrical structure of the prototype such as fairings, pods, ducting, and cable ways were included on the model. These protuberances were removed and/or replaced when changing from one model configuration to another such as from Agena B to Agena D.

The 1/15 scale basic model was machined from aluminum forgings and heat treated. The protuberances were attached with small machine screws. All screw head holes were filled with dental cement. The entire model was then polished to approximately a 20-microinch finish. The sections of the model were bolted together at internal flanged interfaces, assembling from the aft end forward. Access for bolting the payload section to the midsection was gained by removing a threaded nose cap.

Additional weight, to simulate various propellant load conditions, and thereby changing the fundamental frequency, was added to the inside of the model by several means. Weight was added to the Agena and Centaur midsection by attaching one of several solid steel cylinders. The cylinder was screwed into the forward end of the lower section and clamped to the forward end of the midsection. Weight was added to the Atlas body by bolting a steel slug to the aftside of the forward flange of the lower section. Additional weight was added to the payloads by filling with "Cerrobend", or bolting steel-jacketed lead slugs to the nose cap.

The model was mounted on a compliant, instrumented pedestal which was bolted to the wind tunnel floor. A "Marmon" clamp attached the model to the pedestal and afforded an infinite number of model orientations with respect to wind direction. Five interchangeable pedestals, each with a different spring rate resulting in a fundamental frequency change of approximately 1 to 3 cps, were used as a method of varying the first modal frequencies of a given configuration.

The umbilical towers associated with various payloads were also modeled. Two umbilical towers were used with the Agena, AMR and PMR launch

complexes, and a third for the Centaur complex. The towers were orientated according to model position in the wind tunnel.

DYNAMIC TESTING EQUIPMENT

In order to obtain the maximum number of wind tunnel tests in a given time pertiod, certain criteria and limitations were imposed on the type and usage of the dynamic test equipment. As it was necessary to determine the above mentioned structural dynamic parameters for each configuration or orientation change, it was highly desirable to have test equipment that could easily be placed in the tunnel, setup and operated. To this end, plus the required performance capability, the test equipment was selected.

The test equipment required to obtain the structural dynamic information consisted of a very simple setup. The equipment included a small (20-pound peak force output) permanent magnet electro-dynamic vibration exciter as shown in Figure No. 2. The exciter was driven and controlled by an audio amplifier and signal generator. The vibration exciter was mounted in a trunnion such that the drive link and exciter could be rotated up and away from the model for complete mechanical decoupling. The exciter and trunnion assembly was supported on a tripod which could be adjusted for height alignment with the different models. Weight of the vibration exciter system was approximately 80 lbs. The vibration exciter system was essentially seismic in the frequency range of interest. The remainder of the test equipment consisted of two strain gage type accelerometers operating through a carrier amplifier system to a direct writing oscillographic recorder, voltmeter, and an oscilloscope.

Instrumentation on the model consisted of strain gages mounted on the pedestal calibrated to measure bending moment in the direction of wind (drag) and normal to the wind (lateral). The strain gage bridges were attached to the inside of the pedestal in such a manner as to provide temperature compensation and to respond to strain caused from bending only. During the first series of tests, strain gage type accelerometers were used to measure drag and lateral vibratory acceleration. The accelerometers were located in the payload section of the model. The strain gage bridges located in the pedestals were excited and the signals amplified by a carrier amplifier system. The amplified signals were then paralleled into a direction writing oscillographic recorder, tape recorder, oscilloscope and a voltmeter. Calibration of the strain gaged pedestals was accomplished by applying a steady state load at a given moment arm through a dummy aft section. The strain gage type accelerometers were dynamically tested in the laboratory for amplitude linearity and frequency response. In the wind tunnel the accelerometers were calibrated by the flip-flop static method. The calibrations were repeated each time a signal cable was disconnected.

DYNAMIC TESTING TECHNIQUES

The first modal frequency was determined by manually striking the model while recording a response signal on an electrically-timed record. This frequency would then be tuned in on the vibration exciter oscillator.

The mode shape for each model configuration was determined by exciting the model at the first modal frequency and measuring the response at several predetermined longitudinal locations. The vibration exciter, mounted on the tripod, was attached with a steel band around a cylindrical portion of the model. The model was vibrated at approximately one-third the maximum design bending moment as measured at the pedestal. Response measurements were then taken at each of the several predetermined locations by moving the accelerometer from one location to the next while maintaining a constant oscillatory peak bending moment. The bending mode response data was normalized and plotted as the measurements were taken, thus greatly reducing the chance of error.

The oscillatory deflection bending moment relationship was determined using the same vibration excitation setup as described for the mode shape determination. Payload deflection was measured by the use of a visual sight gage which takes advantage of the persistence of the human eye. Deflection was held constant at a nominal distance, such as 1/8 or 1/4 inch peak-to-peak, while the oscillatory strain (read as bending moment) was recorded.

The damping factor was determined each time the model configuration or orientation was changed. The model was excited with the same equipment as previously described with the exception that the mechanical linkage attaching the exciter to the model could be completely decoupled during model vibration. The coupling mechanism consisted of a truncated cone, attached to the vibration exciter stinger, which was mated into a similar cone attached to the steel band around the model. The act of decoupling the exciter was accomplished manually. The damping factor was obtained by exciting the model at the first modal frequency, at an amplitude of maximum design bending moment, and completely disconnecting the vibration exciter while recording the bending moment and subsequent decay. The value of the damping factor was then calculated for quick-look information by dividing the constant 0.11 by the number of cycles for the amplitude to decay 50%.

CONCLUDING REMARKS

The use of the portable seismic vibration exciter and other associated test equipment to obtain the desired dynamic information was accomplished in approximately 25% of the time required using a previous method. To date over 200 runs have been conducted with a time savings of one to three hours per run. Accuracy of the damping factor by mechanically decoupling the vibration exciter from the model, was improved by 20 to 100% over the previous method of electrically disconnecting the vibration exciter.

REFERENCES

1. "Guide for Planning Investigations in the Ames 12-foot Pressure Wind Tunnel," NACA Ames Aeronautical Laboratory 55, January 1957.

2. "Work Specifications, Wind Tunnel Test Program, Ground Wind Induced Oscillations for Atlas/Agena and Atlas/Centaur," Aerospace Corp., 1975. 1-18 June 1961.

3. Conly, J. F., "Test Plan for Atlas 'D" Space Booster Wind Tunnel Vortex Shedding Models," General Dynamics/Astronautics AE61-1141, November 1961.

4. Buell, Donald A., and Kenyon, George C., "The Wind-Induced Loads on a Dynamically Scaled Model of a Large Missile in Launching Position." NASA TM X-109, 1959.

5. Runyan, H. L.; Morgan, H. G.; Mixson, J. S., "Role of Dynamic Models in Launch Vehicle Development." ASME Experimental Techniques in Shock and Vibration.

6. Buell, D. A.; McCullough, G. B.; Steinmetz, W. S., "A Wind Tunnel Investigation of Ground Wind Loads on an Axisymmetric Launch Vehicle." NASA TM X-851, 1963.

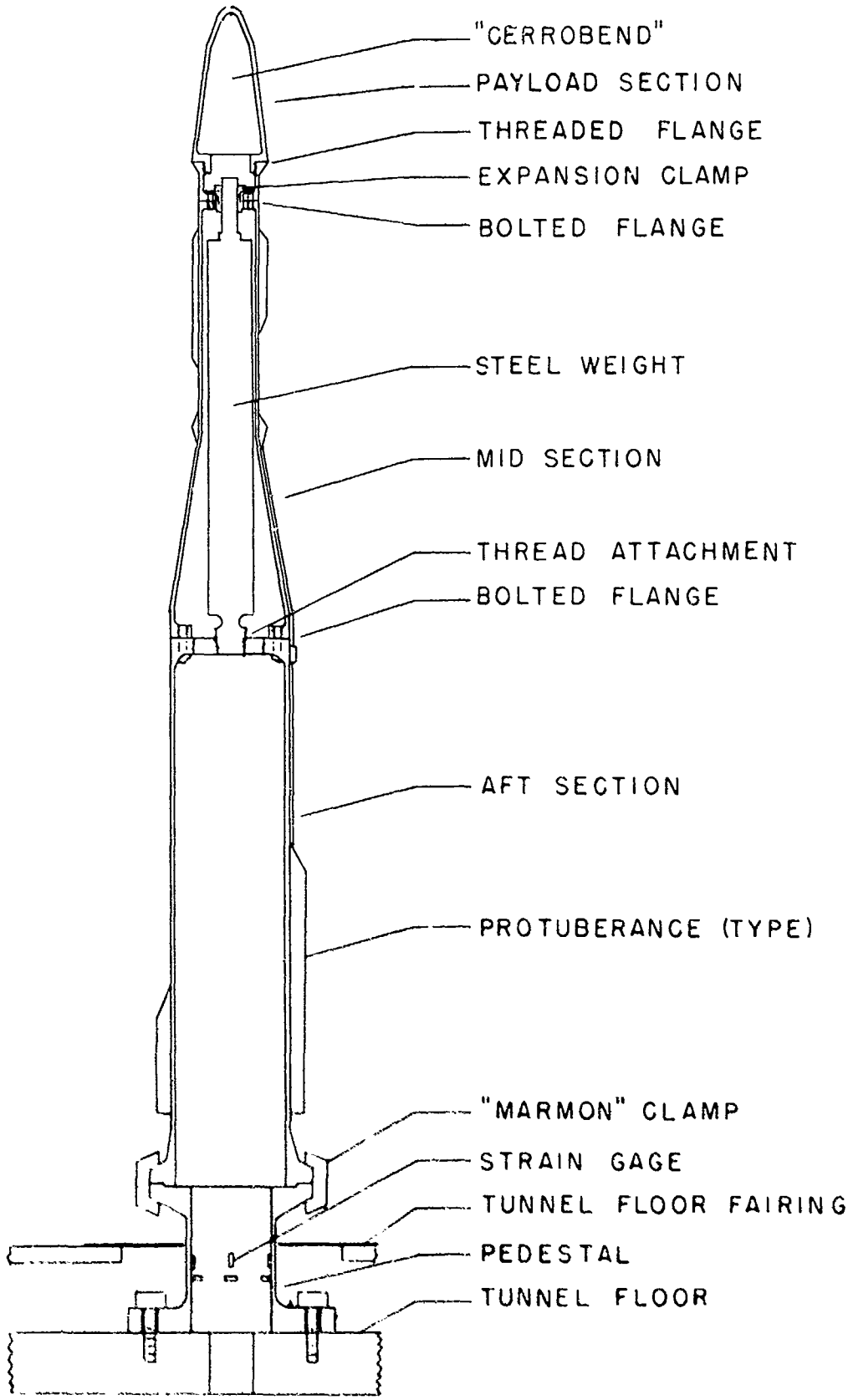

FIGURE 1. A TYPICAL MODEL CONFIGURATION (CUT-AWAY VIEW)

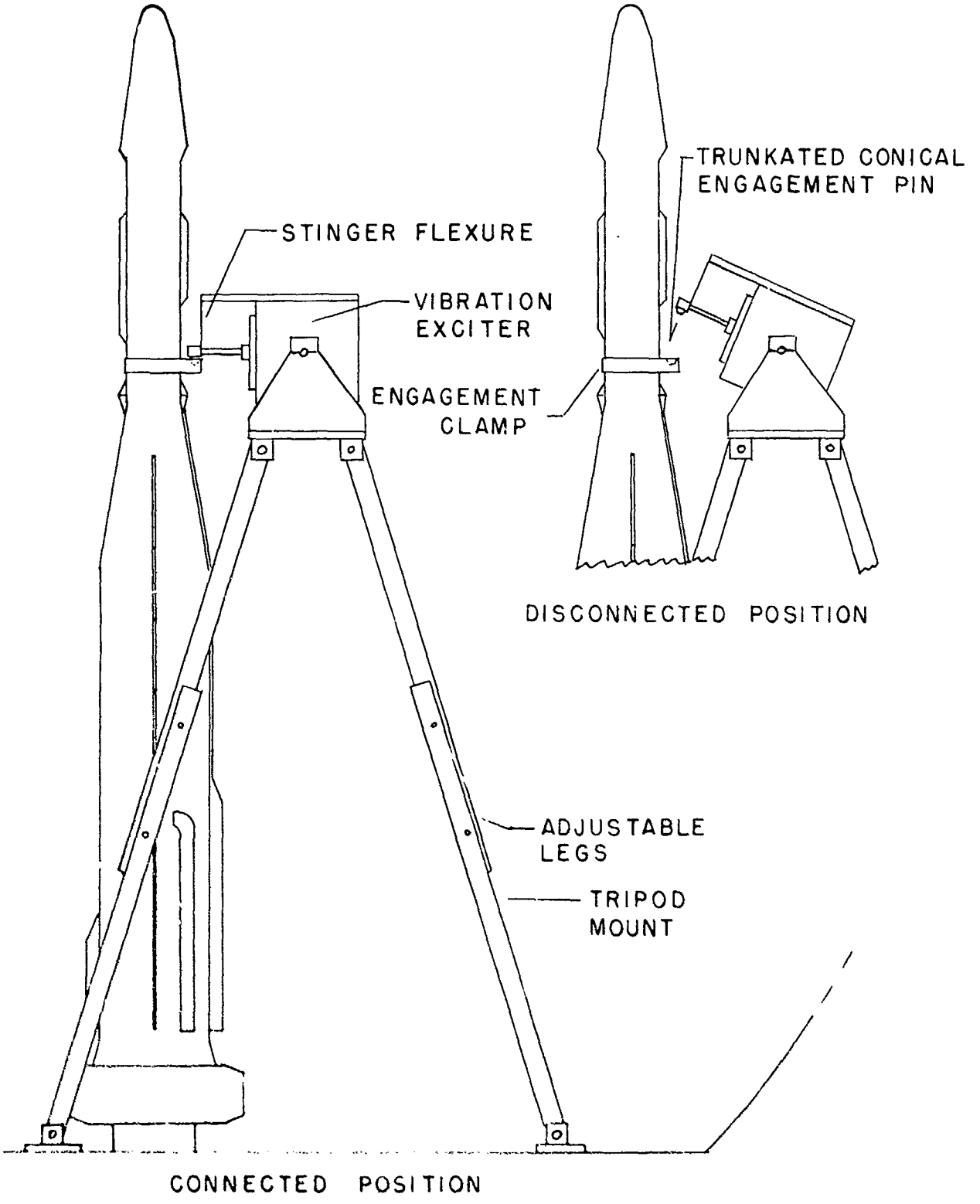

FIGURE 2. VIBRATION EXCITATION SYSTEM

A NEW "FREE-FLIGHT" MOUNT SYSTEM FOR HIGH-SPEED WIND-TUNNEL FLUTTER MODELS

By Wilmer H. Reed III and Frank T. Abbott, Jr.

NASA Langley Research Center

ABSTRACT

Wind-tunnel investigations of aeroelastic models often require that rigid body as well as elastic modes of the test article be simulated. In effect, the mount system must allow the model to be "flown" in the test section and have negligible aerodynamic interference at transonic Mach numbers. Such a system has been developed for flutter and gust response investigations on complete models in the NASA Langley transonic dynamics tunnel. The system consists of a pair of cables which pass through pulleys in the model and run upstream and downstream of the test section in mutually perpendicular planes. Stability and natural frequencies of the cable-supported model are controlled by the preload tension in a spring in one of the cables. The paper describes some evaluation tests and presents a stability analysis which shows the influence of various parameters that govern dynamic characteristics of the system.

LIST OF ILLUSTRATIONS

A NEW "FREE-FLIGHT" MOUNT SYSTEM FOR HIGH-SPEED WIND-TUNNEL FLUTTER MODELS*

By Wilmer H. Reed III and Frank T. Abbott, Jr.

NASA Langley Research Center

INTRODUCTION

Wind-tunnel investigations in such areas as flutter, gust response, dynamic stability and the like often require that the dynamic behavior of the test article in free flight be simulated. For example, flutter instabilities on an aircraft may involve interaction between elastic and rigid-body modes. If, in wind-tunnel studies of the problem, these modes are significantly altered by constraining forces associated with the model support device, corresponding alterations in the flutter characteristics of the model as compared with those of the free-flying aircraft might be expected. On the other hand, if the model is mounted in some arbitrary manner that might permit simulation of free-flight rigid-body modes, we have no guarantee that the resulting system will be satisfactory. In fact, without careful consideration of the dynamics of the overall system, violent instabilities may occur, making the dynamic behavior of the model on its mount strikingly different from what it would be in free flight.

The present paper concerns a new free-flight mount system that has been developed for flutter and gust response studies in the NASA Langley transonic dynamics tunnel. Practical experience with the present and some earlier mount systems is described, and a stability analysis presented to show the influence of various controllable parameters on the dynamic characteristics of the system.

SYMBOLS

a	horizontal distance between center of gravity and outer cable-tangency-point on rear pulleys (positive when c.g. ahead of rear pulleys)
b	span of wing
c	mean aerodynamic chord

*Patent applied for.

a_{ij}, b_{ij}, c_{ij} coefficients in longitudinal equations of motion

$\bar{a}_{ij}, \bar{b}_{ij}, \bar{c}_{ij}$ coefficients in lateral equations of motion

d horizontal distance between model plane of symmetry and outer cable-tangency-point on rear pulleys

e horizontal distance between model center of gravity and outer cable-tangency-point on front pulleys

g acceleration due to gravity

h vertical distance between model center of gravity and outer cable-tangency-point on front pulleys

I_{xz} product of inertia

k spring constant

k_{ij} cable stiffness influence coefficient giving increment in cable restraining forces or moments in mode i due to unit deflection in mode j

l_i length of cable i from wall attachment point outer cable-tangency-point on pulley i

L,M,N roll, pitch, and yaw moments about x-, y-, and z-axes, respectively

m mass of model including pulleys

N_{SF} static stick-fixed-neutral point

q dynamic pressure, $\frac{1}{2}\rho U^2$

r_x, r_y, r_z radius of gyration about x-, y-, and z-axes, respectively

s Laplace operator

S wing area

T cable tension

U wind-tunnel test-section velocity

W weight of model including pulleys

x,y,z displacement coordinates of model center of gravity

X,Y,Z external forces on model

C_D coefficient of drag, $\frac{\text{Drag}}{qS}$

C_{D_o} C_D at $\alpha = 0$

C_L coefficient of lift, $\frac{\text{Lift}}{qS}$

C_{L_o} C_L at $\alpha = 0$

C_l rolling-moment coefficient, $\frac{\text{Rolling moment}}{qSb}$

C_m pitching-moment coefficient, $\frac{\text{Pitching moment}}{qSc}$

C_{m_o} C_m at $\alpha = \delta = 0$

C_n yawing-moment coefficient, $\frac{\text{Yawing moment}}{qSb}$

C_y side-force coefficient, $\frac{\text{Side force}}{qSc}$

α angle of attack, $\theta_o + \theta + \frac{\dot{z}}{U}$

β angle of sideslip, $\frac{\dot{y}}{U} - \psi$

β_1, β_2 angle in vertical plane between x axis and cables 1 and 2, respectively

β_3, β_4 angle in horizontal plane between x axis and cables 3 and 4, respectively (for trimmed flight $\beta_3 = \beta_4 = \beta_R$)

β_R angle in horizontal plane between x axis and rear cables for trimmed flight

δ_o elevator deflection angle for trimmed flight

ζ_i effective viscous damping ratio of mount in mode i for no wind condition

ξ damping ratio of model in flight

η real part of root of characteristic equation

θ pitch angle pertubation from trim condition

θ_o pitch angle of trimmed flight

$\bar{\theta} = \theta_o + \theta$

ρ mass density of wind-tunnel test medium

$\sigma = \frac{\rho US}{2m}$

φ angle of roll

ψ angle of yaw

ω circular frequency

$\omega_{ij} = \sqrt{\frac{k_{ij}}{m}}$

ω_n undamped natural frequency

Stability derivatives are indicated by subscript notation; for example:

$$C_{l_r} = \frac{\partial C_l}{\partial\left(\frac{\dot{\psi}b}{2U}\right)} \qquad C_{n_p} = \frac{\partial C_n}{\partial\left(\frac{\dot{\varphi}b}{2U}\right)} \qquad C_{m_q} = \frac{\partial C_m}{\partial\left(\frac{\dot{\theta}c}{2U}\right)}$$

$$C_{y_\beta} = \frac{\partial C_y}{\partial \beta} \qquad C_{L_\alpha} = \frac{\partial C_L}{\partial \alpha} \qquad \text{etc.}$$

Subscripts:

1,2,3,4 cable numbers (see fig. 12)

F front

R rear

GENERAL REMARKS

Mount System Requirements

Let us consider some general requirements which represent desirable and perhaps essential features in a free-flight mount system (see fig. 1). First, the system should provide a soft support such that the natural frequencies associated with the mount are well below the frequencies of the free-flight rigid body and elastic modes of interest. A soft support implies that the model should be given freedom to respond with large amplitude motions. A second requirement is that moving masses associated with the mount are negligible relative to the total mass of the test article. Also, aerodynamic interference associated with mount structure exposed to the airstream should be low, especially if the system is to be operated at high subsonic or transonic Mach numbers. Another very important requirement is that the system have both static and dynamic stability under all operating conditions. In cases where it is necessary to simulate the steady-state air loads

corresponding to level flight (Froude number simulation), the mount should be capable of applying a steady vertical force to the model which is essentially independent of model motions. Finally, a simple, passive system is preferred over one requiring black boxes or other complex gadgetry in order to meet the above requirements.

Some Typical Systems

Various techniques for mounting dynamic wind-tunnel models have been proposed (see, for example ref. 1). Some typical systems with which the authors are familiar will be discussed with the aid of schematic diagrams shown in figure 2. (Motion pictures illustrating the performance of models utilizing these systems are presented in the oral version of the paper.) The tow-line mount system, described in reference 2, has low aerodynamic interference and provides considerable freedom of motion for the model in all but the longitudinal direction. The major drawback of the system is that a complex, fast-response, autopilot is generally required in order to achieve satisfactory lateral stability and keep the model flying within the confines of the tunnel test section. With the endless wire mount system the model is attached to a vertical wire which passes through pulleys outside of the tunnel to form a continuous loop. While this system has a number of desirable qualities previously mentioned, it was found that models mounted in this way tended to become unstable in yaw. The vertical rod mount system was developed by Boeing Airplane Company and has been used successfully in low-speed wind-tunnel tests for many years (see refs. 3 and 4). At transonic Mach numbers, however, shock waves generated by the rod support become a problem as well as deflections of the rod under high drag loads. The mount system which appears to satisfy the greatest number of the previously mentioned requirements is the two-cable mount, which is the subject of the present paper.

TWO-CABLE MOUNT SYSTEM

Description

The basic two-cable mount system is shown schematically in figure 3. The model is held by two cable loops, one extending to the tunnel walls in the upstream direction and the other in the downstream direction. One loop lies in a vertical plane (either upstream or downstream as best suits the model) and the other loop is in a horizontal plane. Each cable loop passes through pulleys located within the fuselage contour. The cables are kept under tension by stretching a soft spring in the rear cables. The model has freedom to translate horizontally and vertically as well as to rotate in pitch, roll, and yaw. With springs in both cables the model can also be given freedom to translate fore and aft.

Since the model has considerable freedom of motion, it is necessary to provide remote trim controls to keep it centered in the tunnel throughout the test range. Usually only pitch and roll trim control are required. Experience has shown that models can be easily flown by a single operator or

"pilot," using a miniature airplane-type control stick which actuates pitch and roll control surfaces on the model.

Three key parameters that influence the dynamic characteristics of the system shown in figure 3 are:

e distance from front pulleys to center of gravity

a distance from rear pulleys to center of gravity

T_R tension in rear cables

The ability to vary these parameters for a given model provides one with a "handle" by which the stability and flying characteristics of the model can be regulated. The lengths and angles of the cable loops can also be adjusted to satisfy particular requirements. For example, by using unequal angles in the cable loop that lies in a vertical plane, a resultant vertical force may be applied to the model. Since the cables are long (long relative to model deflections) and have tension applied through a soft spring, this resultant vertical force is approximately independent of model motion, and thus provides a reasonable simulation of gravitational forces. By varying tension in the cables steady-state loads on the model can be properly simulated - a feature that may be required when elastic deformations due to steady loads on the aircraft are of importance.

Wind-Tunnel Model

A specific application of the two-cable mount system will now be discussed. Wind-tunnel and theoretical studies of the dynamic characteristics of the mount have been conducted for a model of a modern jet transport. (Similar experience with the present mount system has also been obtained on a supersonic fighter configuration.)

The model, pictured in figures 4 and 5, has a span of approximately 8.5 feet and weighs 70 pounds. It is restrained by a 3/32-inch-diameter forward cable and a 1/16-inch-diameter rear cable through which the tension is applied. Forward and aft pulley locations in the model are $e/c = 1.6$ and $a/c = 0$. When the model is centered in the tunnel, the length of the cables from the model to the wall attachment points is approximately 20 feet; the forward cables are in a vertical plane and the rearward cables in a horizontal plane. The cut-away view in figure 4 gives a schematic indication of the pulley installation. Figure 5 shows the model in a preflight attitude. The large static deflection of the model, which amounts to about 5 feet for the condition shown, is indicative of the softness of the restraining forces involved. Electrical leads for the trim control actuators and accelerometers in the model enter the underside of the fuselage near the center of gravity and are supported at the downstream end by a sting, as can be seen in figures 4 and 5.

Stability Analysis

Equations of motion for the two-cable mount system are derived in the appendix for the general case of six degrees of freedom. Cable-restraining forces are represented in the analysis by a set of stiffness influence coefficients k_{ij} which give the cable force or moment in mode i due to a unit deflection in mode j. Equations for these coefficients in terms of the system parameters are given in table 2. It can be shown that with the assumption of small pertubations from trimmed flight, which make the equations of motion linear, the lateral equations and longitudinal equations for the cable-restrained model are uncoupled and can thus be treated separately as in conventional linearized stability analyses for free-flight conditions (see, for example, ref. 5). Energy dissipation in the pulleys is accounted for by means of an effective viscous damping in each mode.

In the present analysis, a soft spring was assumed to be only in the rear cable, thus the fore-and-aft degree of freedom is suppressed. With this assumption, the dynamic behavior of the system is determined from the roots of a fourth-order characteristic equation for the longitudinal modes and a sixth-order characteristic equation for the lateral modes (see eqs. (12) and (15) in appendix). Tunnel conditions assumed in the analysis are 225 pounds per square foot dynamic pressure and 0.89 Mach number. The aerodynamic derivatives (see table 1) were estimated by the aircraft manufacturer. Damping introduced by the pulleys was assumed to be 5 percent of critical damping for all modes. ($\zeta_n = 0.05$.)

RESULTS AND DISCUSSION

Root-Locus Plots

Before presenting results of the study, it might be appropriate to mention certain features of the root-locus method which will be used to interpret the dynamic characteristics of the system. This method involves plotting roots of the characteristic equation in the complex plane. As shown in figure 6 the imaginary axis indicates the circular frequency of a natural mode and the real axis gives a measure of the damping. The radial distance from the origin to a complex root is the undamped natural frequency ω_n and the angle between the radial vector and the $\pm$im axis is equal $\sin^{-1}\zeta_n$, where ζ_n is the damping ratio relative to critical damping. The system is stable when the real part of every root has a negative sign and is neutrally stable when a root lies on the imaginary axis. A more complete description of the method may be found in reference 5.

Figure 7 shows a typical root-locus plot for the longitudinal modes as tension in the rear cable is varied from 0 to 2.0 times the model weight. (Since the complex roots appear in conjugate pairs, only the upper half of the complex plane is presented.) Shown for comparison is the corresponding short-period mode for free-flight conditions. Note that two oscillatory modes are present for the cable-restrained model. One mode closely corresponds to the free-flight short-period mode and the other is a lightly damped low-frequency

mode which involves primarily vertical translation of the model. This latter mode is associated with the mount restraints and has no counterpart in free flight. The corresponding root-locus plot for the lateral modes is presented in figure 8. Again, both the free-flight and the mount modes are shown. When the model is in free flight, the characteristic equation is of fourth order having one pair of complex conjugate roots and two real roots. The complex roots characterize the Dutch-roll oscillation mode; the real roots are associated with a heavily damped roll mode and an almost neutrally damped spiral mode. When cable restraints are added, the free-flight roots are altered slightly and a new pair of complex conjugate roots comes into the picture. This root involves primarily lateral translation of the model and, as can be seen in figure 8, is unstable except when the tension applied to the rear cable exceeds approximately the weight of the model. These trends are in good qualitative agreement with the experimental results. Motion pictures are available showing the development of lateral instability as cable tension is reduced below $T_R/W = 1.0$.

The root-locus plots given in figures 7 and 8 for various cable tensions are representative of the plots obtained when other parameters are varied in that the free-flight modes are altered slightly and new low-frequency modes are introduced because of the mount restraints. The question of primary interest, then, is whether these mount modes have stable or unstable damping characteristics. Therefore, in the following discussion attention will be focused on the damping ratio associated with the longitudinal and lateral mount modes.

Stability of Mount Modes

Effect of front pulley location.- Figure 9 illustrates the effect of varying the location of the front pulleys when the rear pulleys are at the center of gravity. (See table 1 for values assumed for other parameters in the calculations.) Here it can be seen that the longitudinal mode has satisfactory damping for all conditions; however, the lateral mode for most front pulley locations is unstable when $T_R/W < 1.0$. (Negative values of ζ indicate unstable oscillations.) Note that for zero rear cable tension there is a close correspondence between the present system and the tow-line mount. Thus the requirement for an autopilot to stabilize a tow-line model, such as reference 2, is also evidenced here by the predicted lateral instability shown when $T_R/W = 0$.

Effect of rear pulley location.- Figure 10 indicates the influence of rear pulley location on stability of the mount modes. The front pulleys were assumed to be 1.5c ahead of the center of gravity for these calculations. The parameter being varied, a/c, is taken to be positive when the rear pulleys are aft of the center of gravity. Again, as in the previous case, it is seen that increasing tension in the rear cable has a significant stabilizing influence. Also with tension applied, moving the rear cables aft increases the stability. On the basis of figures 9 and 10 it appears that pulleys equally spaced ahead and behind the c.g. a distance of, say, one mean aerodynamic chord would provide adequate stability over a somewhat larger range of cable-tension values than was possible on the model which had the rear pulleys at the c.g. Equal fore and aft spacing of the pulleys relative

to the c.g. also tends to reduce the coupling between pitch and vertical translation - a feature that may be desired in order to avoid large variations between the no-wind and flight-attitude angle of the model.

Effect of static margin.- In the previously discussed results it was found both analytically and experimentally that the longitudinal mount mode was stable for all conditions considered. Let us now examine analytically how longitudinal stability is influenced by changes in the static margin of the model. The static margin, defined as the distance between the stick-fixed neutral point and the c.g. of the model in mean aerodynamic chords, was varied by moving the c.g. and at the same time the pulley locations such that $e/c = 1.5$ and $a/c = 0$. Variations in the moment of inertia due to c.g. changes were neglected. The results are given in figure 11. Note that as the c.g. is moved aft the stability of the mount mode falls off rather abruptly for all values of cable tension considered. (The nominal c.g. location used in other cases was 0.25c giving a static margin of 0.263c.) Thus it might be concluded that configurations having a small margin of static stability in free flight are likely to develop instabilities when restrained by cables in a wind tunnel.

CONCLUDING REMARKS

It has been shown that by means of a rather simple two-cable mount system the free-flight rigid-body modes of complete aircraft can be closely simulated in a wind tunnel. A stability analysis and wind-tunnel evaluation of the system indicate that by proper selection of such parameters as cable tension and pulley spacing, stable dynamic behavior of the mount can be achieved over a broad range of test conditions. In addition to flutter and gust response applications, the system offers potential as a research tool for measuring stability derivatives and maneuver loads on complete aeroelastic models.

APPENDIX

STABILITY ANALYSIS OF CABLE MOUNT SYSTEM

Consider the cable configuration shown schematically in figure 12. The x, y, and z axes form a right-hand set of space-fixed orthogonal coordinates with the origin at the center of gravity of the model in steady trimmed flight. The model is assumed to be rigid so that its motion is completely described by six degrees of freedom - namely, x, y, and z translations of the center of gravity and φ, θ, ψ rotations about the x, y, and z axes, respectively. The equations of motion are linearized by the assumption of small pertubations from trimmed flight. Inertia and vibratory characteristics of the restraining cables are neglected.

The dynamical equations of motion for the system can be written as follows:

Longitudinal translation:

$$X_C + X_A = m\ddot{x} \tag{1a}$$

Lateral translation:

$$Y_C + Y_A = m\ddot{y} \tag{1b}$$

Vertical translation:

$$Z_C + Z_A + mg = m\ddot{z} \tag{1c}$$

Roll:

$$L_C + L_A = r_x^2 m\ddot{\varphi} - I_{xz}\ddot{\psi} \tag{1d}$$

Pitch:

$$M_C + M_A = r_y^2 m\ddot{\theta} \tag{1e}$$

Yaw:

$$N_C + N_A = r_z^2 m\ddot{\psi} - I_{xz}\ddot{\varphi} \tag{1f}$$

Where the C and A subscripts denote cable and aerodynamic terms, respectively.

Cable Restraints

As shown in figure 12 the particular cable configuration chosen for analysis has the forward cables in a vertical plane and the rearward cables in a horizontal plane. Tension is applied to the cables by stretching a soft spring in the rear cable. It has been assumed that in trimmed flight

the rear cables are symmetrical with respect to the plane of symmetry of the model; however, in order to permit the possibility of applying a steady-state vertical force to the model, the cable angle of the upper front cable β_1 is not necessarily the same as that of the lower front cable β_2.

The total forces and moment about the center of gravity are obtained by summing the contribution of each of the four cables:

$$X_C = X_{C1} + X_{C2} + X_{C3} + X_{C4} \tag{2a}$$

$$Y_C = Y_{C1} + Y_{C2} + Y_{C3} + Y_{C4} \tag{2b}$$

$$Z_C = Z_{C1} + Z_{C2} + Z_{C3} + Z_{C4} \tag{2c}$$

$$L_C = (h + e\bar{\theta})Y_{C1} - (h - e\bar{\theta})Y_{C2} - (a\bar{\theta} - d\varphi)Y_{C3} - (a\bar{\theta} + d\varphi)Y_{C4}$$
$$+ (h\varphi + e\psi)Z_{C1} - (h\varphi - e\psi)Z_{C2} - (d + a\psi)Z_{C3} + (d - a\psi)Z_{C4} \tag{2d}$$

$$M_C = -(h + e\bar{\theta})X_{C1} + (h - e\bar{\theta})X_{C2} + (a\bar{\theta} - d\varphi)X_{C3} + (a\bar{\theta} + d\varphi)X_{C4}$$
$$+ (h\bar{\theta} - e)Z_{C1} - (h\bar{\theta} + e)Z_{C2} + (a - d\psi)Z_{C3} + (a + d\psi)Z_{C4} \tag{2e}$$

$$N_C = -(e\psi + h\varphi)X_{C1} - (e\psi - h\varphi)X_{C2} + (d + a\psi)X_{C3} - (d - a\psi)X_{C4}$$
$$+ (e - h\bar{\theta})Y_{C1} + (e + h\bar{\theta})Y_{C2} + (d\psi - a)Y_{C3} - (d\psi + a)Y_{C4} \tag{2f}$$

where $\bar{\theta} = \theta_0 + \theta$. The x, y, and z components of tension in each cable are assumed to act at the outermost point of tangency between the cable and its pulley, and the model center of gravity is assumed to be on the line formed by the intersection of the planes of symmetry of the front and rear pulleys. From the geometry of the situation, these force components can be expressed:

$$\left.\begin{aligned}
&X_{C1} = \bar{T}_F \cos\bar{\beta}_1, \quad Y_{C1} = -\bar{T}_F \frac{y_1}{\ell_1}, \quad Z_{C1} = -\bar{T}_F \sin\bar{\beta}_1 \\
&X_{C2} = \bar{T}_F \cos\bar{\beta}_2, \quad Y_{C2} = -\bar{T}_F \frac{y_2}{\ell_2}, \quad Z_{C2} = \bar{T}_F \sin\bar{\beta}_2 \\
&X_{C3} = \bar{T}_R \cos\bar{\beta}_3, \quad Y_{C3} = -\bar{T}_R \sin\bar{\beta}_3, \quad Z_{C3} = -\bar{T}_R \frac{z_3}{\ell_3} \\
&X_{C4} = -\bar{T}_R \cos\bar{\beta}_4, \quad Y_{C4} = \bar{T}_R \sin\bar{\beta}_4, \quad Z_{C4} = -\bar{T}_R \frac{z_4}{\ell_4}
\end{aligned}\right\} \tag{3}$$

The terms on the right-hand side of equations (3) consist of a steady-state part plus increments proportional to motions of the model. By way of illustration consider the vertical component of force on pulley number 1 (see eqs. (3) and fig. 12).

$$Z_{C1} = -\bar{T}_F \sin \bar{\beta}_1$$
$$= -\left(T_F + \Delta T_F\right)\sin\left(\beta_1 + \Delta\beta_1\right)$$

which can be written

$$Z_{C1} = Z_{C1_o} + \Delta Z_{C1}$$
$$= -T_F \sin \beta_1 - \Delta T_F \sin \beta_1 - \Delta\beta_1 T_F \cos \beta_1 \tag{4}$$

The increments ΔT_F and $\Delta\beta_1$ can, in turn, be expressed in terms of pertubations of the model center of gravity as follows:

$$\Delta T_F = k_F\left(\Delta l_1 + \Delta l_2\right)$$
$$= k_F\left[\left(z_1 \sin \beta_1 - x_1 \cos \beta_1\right) - \left(z_2 \cos \beta_2 + x_2 \cos \beta_2\right)\right] \tag{5}$$

and

$$\Delta\beta_1 = \frac{x_1}{l_1} \sin \beta_1 + \frac{z_1}{l_1} \cos \beta_1 \tag{6}$$

where x_n and z_n denote components of displacement of the outermost points of cable tangency on pulley n

$$\left.\begin{aligned} x_1 &= x - h\bar{\theta}, & z_1 &= z - e\bar{\theta} \\ x_2 &= x + h\bar{\theta}, & z_2 &= z + e\bar{\theta} \end{aligned}\right\} \tag{7}$$

Thus, with equations (5), (6), and (7) substituted into equation (4) the vertical-force component on pulley 1 can be written in the form

$$Z_{C1} = Z_{C1_o} - k_{zx_1}x - k_{zz_1}z - k_{z\theta_1}\theta \tag{8}$$

where the coefficients k_{ij_1} are stiffness-influence coefficients associated with the upper front cable which goes to pulley 1. In a similar manner the three components of cable force are derived for each of the four pulleys. When these relations are substituted into equations (2) and all terms involving products of the pertubations x, y, z, φ, θ, and ψ discarded, the following set of linear relations are obtained for cable restraints on the overall system:

$$X_C = X_{C_o} - k_{xx}x - k_{xz}z - k_{x\theta}\theta \tag{9a}$$

$$Y_C = -k_{yy}y - k_{y\varphi}\varphi - k_{y\psi}\psi \tag{9b}$$

$$Z_C = Z_{C_o} - k_{zx}x - k_{zz}z - k_{z\theta}\theta \tag{9c}$$

$$L_C = -k_{\varphi y}y - k_{\varphi\varphi}\varphi - k_{\varphi\psi}\psi \tag{9d}$$

$$M_C = M_{C_o} - k_{\theta x}x - k_{\theta z}z - k_{\theta\theta}\theta \tag{9e}$$

$$N_C = -k_{\psi y}y - k_{\psi\varphi}\varphi - k_{\psi\psi}\psi \tag{9f}$$

Equations for the steady-state terms and the influence coefficients appearing in equations (9) are given in table 2.

It is important to note in equations (9) that the cable restraints produce no coupling between the longitudinal modes (x, z, and θ) and the lateral modes (y, φ, and ψ). Thus, if the lateral and longitudinal modes of an aircraft configuration can be isolated and studied separately for free-flight conditions, as is most generally done in linearized stability analyses, the same simplifications can also be enjoyed for the cable-supported model. The assumption of separable longitudinal and lateral modes will be made throughout the remainder of the present analysis.

Aerodynamic Forces and Moments

For small pertubations from the space-fixed axes considered herein and with the assumption $\dot{x}/U, \dot{y}/U, \dot{z}/U \ll 1.0$, the aerodynamic forces and moments about the center of gravity of the model can be expressed as follows:

Longitudinal modes:

$$X_A = -qS\left[\left(C_{D_o} + C_{D_\alpha}\theta_o\right) + 2\left(C_{D_o} + C_{D_\alpha}\theta_o\right)\frac{\dot{x}}{U} + \left(C_{D_\alpha} - C_{L_o} - C_{L_\alpha}\theta_o - C_{L_\delta}\delta_o\right)\frac{\dot{z}}{U} + C_{D_\alpha}\theta\right] \tag{10a}$$

$$Z_A = -qS\left[\left(C_{L_o} + C_{L_\alpha}\theta_o + C_{L_\delta}\delta_o\right) + 2\left(C_{L_o} + C_{L_\alpha}\theta_o + C_{L_\delta}\delta_o\right)\frac{\dot{x}}{U} + \left(C_{L_\alpha} + C_{D_o} + C_{D_\alpha}\theta_o\right)\frac{\dot{z}}{U} + C_{L_\alpha}\theta\right] \tag{10b}$$

$$M_A = -qSc\left[\left(C_{m_o} + C_{m_\alpha}\theta_o + C_{m_\delta}\delta_o\right) + 2\left(C_{m_o} + C_{m_\alpha}\theta_o + C_{m_\delta}\delta_o\right)\frac{\dot{x}}{U} + C_{m_{\dot{\alpha}}}\frac{\dot{z}}{U} + \frac{c}{2U}C_{m_{\dot{\alpha}}}\frac{\ddot{z}}{U} + C_{m_\alpha}\theta + \frac{c}{2U}\left(C_{m_{\dot{\alpha}}} + C_{m_q}\right)\dot{\theta}\right] \tag{10c}$$

Lateral modes:

$$Y_A = qS\left[\left(C_{y_\beta} - C_{D_o} - C_{D_\alpha}\theta_o\right)\frac{\dot{y}}{U} + \left(C_{L_o} + C_{L_\alpha}\theta_o + C_{L_\delta}\delta_o\right)\varphi + C_{y_p}\frac{b}{2U}\dot{\varphi} - C_{y_\beta}\psi + C_{y_r}\frac{b}{2U}\dot{\psi}\right] \tag{11a}$$

$$L_A = qSb\left(C_{l_\beta}\frac{\dot{y}}{U} + C_{l_p}\frac{b}{2U}\dot{\Phi} - C_{l_\beta}\psi + C_{l_r}\frac{b}{2U}\dot{\psi}\right) \tag{11b}$$

$$N_A = qSb\left(C_{n_\beta}\frac{\dot{y}}{U} + C_{n_p}\frac{b}{2U}\dot{\Phi} - C_{n_\beta}\psi + C_{n_r}\frac{b}{2U}\dot{\psi}\right) \tag{11c}$$

With the cable terms defined by equations (9) and the aerodynamic terms by equations (10) and (11), the equations of motion for the cable mount system become a set of linear second-order differential equations with constant coefficients. In writing out the final form of these equations, it was found convenient to divide each equation through by an appropriate inertia. In addition, energy dissipation in the pulleys has been represented by an effective viscous damping ratio ζ_i for each mode.

Linearized Equations of Motion

The equations of motion expressed in Laplace transform notation are:

Longitudinal modes:

$$\left(s^2 + a_{11}s + a_{10}\right)x(s) + \left(b_{11}s + b_{10}\right)z(s) + c_{10}\theta(s) = \frac{X_o}{m} \tag{12a}$$

$$\left(a_{21}s + a_{20}\right)x(s) + \left(s^2 + b_{21}s + b_{20}\right)z(s) + c_{20}\theta(s) = \frac{Z_o}{m} \tag{12b}$$

$$\left(a_{31}s + a_{30}\right)x(s) + \left(b_{32}s^2 + b_{31}s + b_{30}\right)z(s) + \left(s^2 + c_{31}s + c_{30}\right)\theta(s) = \frac{M_o}{mr_y^2} \tag{12c}$$

where

$$a_{11} = 2\zeta_x\omega_{xx} + 2\sigma\left(C_{D_o} + C_{D_\alpha}\theta_o\right) \qquad b_{11} = \sigma\left(C_{D_\alpha} - C_{L_o} - C_{L_\alpha}\theta_o - C_{L_\delta}\delta_o\right) \qquad c_{10} = \omega_{x\theta}^2 + U\sigma C_{D_\alpha}$$

$$a_{10} = \omega_{xx}^2 \qquad b_{10} = \omega_{xz}^2 \qquad c_{20} = \omega_{z\theta}^2 + U\sigma C_{L_\alpha}$$

$$a_{21} = 2\sigma\left(C_{L_o} + C_{L_\alpha}\theta_o + C_{L_\delta}\delta_o\right) \qquad b_{21} = 2\zeta_z\omega_{zz} + \sigma\left(C_{D_o} + C_{D_\alpha}\theta_o + C_{L_\alpha}\right) \qquad c_{31} = \frac{2\zeta_\theta\omega_{\theta\theta}}{r_y} - \frac{c^2\sigma}{2r_y^2}\left(C_{m_{\dot\alpha}} + C_{m_q}\right)$$

$$a_{20} = \omega_{zx}^2 \qquad b_{20} = \omega_{zz}^2 \qquad c_{30} = \frac{\omega_{\theta\theta}^2}{r_y^2} - \frac{U\sigma c}{r_y^2} C_{m_\alpha}$$

$$a_{31} = -\frac{2c\sigma}{r_y^2}\left(C_{m_o} + C_{m_\alpha}\theta_o + C_{m_\delta}\delta_o\right) \qquad b_{31} = -\frac{c\sigma}{r_y^2} C_{m_\alpha}$$

$$a_{30} = \frac{\omega_{\theta x}^2}{r_y^2} \qquad b_{30} = \frac{\omega_{\theta z}^2}{r_y^2}$$

$$b_{32} = -\frac{c^2\sigma}{2r_y^2 U} C_{m_{\dot\alpha}}$$

and

$$X_o = -qS\left(C_{D_o} + C_{D_\alpha}\theta_o\right) + XC_o \qquad \sigma = \frac{\rho US}{2m}$$

$$Z_o = -qS\left(C_{L_o} + C_{L_\alpha}\theta_o + C_{L_\delta}\delta_o\right) \qquad \omega_{ij}^2 = \frac{k_{ij}}{m}$$

$$M_o = +qSc\left(C_{m_o} + C_{m_\alpha}\theta_o + C_{m_\delta}\delta_o\right) + MC_o \qquad \zeta_i = \text{Effective viscous damping ratio of mount for mode } i$$

The terms on the right-hand side of equations (12) are the static aerodynamic and cable restraint forces and moments acting on the model. They are defined

$$X_o = X_{C_o} + X_{A_o} = \frac{T_F}{m}(\cos \beta_1 + \cos \beta_2) - 2\frac{T_R}{m}\cos \beta_3 - \omega_{x\theta}^2 \theta_o - U\sigma\left(C_{D_o} + C_{D_\alpha}\theta_o\right) \tag{13a}$$

$$Z_o = Z_{C_o} + Z_{A_o} = \frac{T_F}{m}(\sin \beta_2 - \sin \beta_1) - \omega_{z\theta}^2 \theta_o + g - U\sigma\left(C_{L_o} + C_{L_\alpha}\theta_o + C_{L_\delta}\delta_o\right) \tag{13b}$$

$$M_o = M_{C_o} + M_{A_o} = \frac{eT_F}{r_y^2 m}\left(\sin \beta_1 - \sin \beta_2 - \frac{h}{e}\cos \beta_1 + \frac{h}{e}\cos \beta_2\right) - \frac{\omega_{\theta\theta}^2 \theta_o}{r_y^2} + \frac{U\sigma c}{r_y^2}\left(C_{m_o} + C_{m_\alpha}\theta_o + C_{m_\delta}\delta_o\right) \tag{13c}$$

These equations set equal to zero define the conditions on T_F, θ_o, and δ_o which must be simultaneously satisfied in steady trimmed flight with specified tension in the rear cables. (T_F and θ_o are required to evaluate the cable influence coefficients in table 2.) In most instances it is not necessary to know precise values for T_F, θ_o, and δ_o and they may therefore be calculated independently in the following approximate manner:

In equation (13a) neglect θ_o and solve for T_F

$$T_F = 2T_R\left(\frac{\cos \beta_3}{\cos \beta_1 + \cos \beta_2}\right) + \frac{mU\sigma C_{D_o}}{\cos \beta_1 + \cos \beta_2} \tag{14a}$$

In equation (13b) neglect δ_o and $\omega_{z\theta}^2$ and, with T_F as given by equation (14a), solve for θ_o

$$\theta_o = \frac{1}{U\sigma C_{L_\alpha}}\left[\frac{T_F}{m}(\sin \beta_2 - \sin \beta_1) + g\right] - \frac{C_{L_o}}{C_{L_\alpha}} \tag{14b}$$

From equation (13c) solve for the remaining unknown δ_o

$$\delta_o = -\frac{eT_F}{mcU\sigma C_{m_\delta}}\left(\sin \beta_1 - \sin \beta_2 - \frac{h}{e}\cos \beta_1 + \frac{h}{e}\cos \beta_2\right) - \frac{C_{m_o} + C_{m_\alpha}\theta_o}{C_{m_\delta}} \tag{14c}$$

(Note from the latter two equations that when $\beta_1 = \beta_2$ the cable restraints do not affect θ_o or δ_o.)

Lateral equations:

$$\left(s^2 + \bar{a}_{11}s + \bar{a}_{10}\right)y(s) + \left(\bar{b}_{11}s + \bar{b}_{10}\right)\varphi(s) + \left(\bar{c}_{11}s + \bar{c}_{10}\right)\psi(s) = 0 \qquad (15a)$$

$$\left(\bar{a}_{21}s + \bar{a}_{20}\right)y(s) + \left(s^2 + \bar{b}_{21}s + \bar{b}_{20}\right)\varphi(s) + \left(\bar{c}_{22}s^2 + \bar{c}_{21}s + \bar{c}_{20}\right)\psi(s) = 0 \qquad (15b)$$

$$\left(\bar{a}_{31}s + \bar{a}_{30}\right)y(s) + \left(\bar{b}_{32}s^2 + \bar{b}_{31}s + \bar{b}_{30}\right)\varphi(s) + \left(s^2 + \bar{c}_{31}s + \bar{c}_{30}\right)\psi(s) = 0 \qquad (15c)$$

where

$$\bar{a}_{11} = 2\zeta_y\omega_{yy} - \sigma\left(C_{y_\beta} - C_{D_o} - C_{D_\alpha}\theta_o\right) \qquad \bar{b}_{11} = -\frac{b}{2}\sigma C_{y_p} \qquad \bar{c}_{11} = -\frac{b}{2}\sigma C_{y_r}$$

$$\bar{a}_{10} = \omega_{yy}^2 \qquad \bar{b}_{10} = \omega_{y\varphi}^2 - U\sigma\left(C_{L_o} + C_{L_\alpha}\theta_o + C_{L_\delta}\delta_o\right) \qquad \bar{c}_{10} = \omega_{y\psi}^2 + U\sigma C_{y_\beta}$$

$$\bar{a}_{21} = -\frac{b}{r_x^2}\sigma C_{l_\beta} \qquad \bar{b}_{21} = 2\zeta_\varphi\frac{\omega_{\varphi\varphi}}{r_x} - \frac{b^2}{2r_x^2}\sigma C_{l_p} \qquad \bar{c}_{22} = -\frac{I_{xz}}{mr_x^2}$$

$$\bar{a}_{20} = \frac{\omega_{\varphi y}^2}{r_x^2} \qquad \bar{b}_{20} = \frac{\omega_{\varphi\varphi}^2}{r_x^2} \qquad \bar{c}_{21} = -\frac{b^2}{2r_x^2}\sigma C_{l_r}$$

$$\bar{a}_{31} = -\frac{b}{r_z^2}\sigma C_{n_\beta} \qquad \bar{b}_{32} = -\frac{I_{xz}}{mr_z^2} \qquad \bar{c}_{20} = \frac{\omega_{\varphi\psi}^2}{r_x^2} + \frac{Ub\sigma}{r_x^2}C_{l_\beta}$$

$$\bar{a}_{30} = \frac{\omega_{\psi y}^2}{r_z^2} \qquad \bar{b}_{31} = -\frac{b^2}{2r_z^2}\sigma C_{n_p} \qquad \bar{c}_{31} = \frac{2\zeta_\psi\omega_{\psi\psi}}{r_z} - \frac{b^2}{2r_z^2}\sigma C_{n_r}$$

$$\bar{b}_{30} = \frac{\omega_{\psi\varphi}^2}{r_z^2} \qquad \bar{c}_{30} = \frac{\omega_{\psi\psi}^2}{r_z^2} + \frac{bU}{r_z^2}\sigma C_{n_\beta}$$

Lateral and longitudinal stability of the system is determined from roots of the characteristic equations obtained by setting the determinant of the coefficients in equations (12) and (15) equal to zero. These roots appear as complex conjugate pairs ($s = \eta \pm i\omega$) for the oscillatory modes and as pure real numbers ($s = \eta$) for the aperiodic modes. In either case the system is stable when $\eta < 0$, neutrally stable when $\eta = 0$, and unstable when $\eta > 0$.

REFERENCES

1. Bisplinghoff, R. L., Ashley, H., and Halfman, R. L.: Aeroelasticity. Addison-Wesley Pub. Co., Inc., 1955, pp. 791-800.

2. Schneider, W. C.: Development of a New Flutter Testing Technique Using a Towed Dynamic Airplane Model Equipped With an Automatic Stabilizing System. NACA RM L54L23, 1954.

3. Kinnaman, E. B.: "Flutter Analysis of Complex Airplanes by Experimental Methods." Jour. Aero. Sci., vol. 19, no. 9, Sept. 1952.

4. Abbott, F. T., Jr., Kelly, H. N., and Hampton, K. D.: Investigation of Propeller-Power-Plant Autoprecession Boundaries for a Dynamic-Aeroelastic Model of a Four-Engine Turboprop Transport Airplane. NASA TN D-1806, 1963.

5. Etkin, B.: Dynamics of Flight, Stability and Control. John Wiley & Son, Inc., 1959.

TABLE 1.- CONDITIONS ASSUMED FOR STABILITY ANALYSIS

Physical properties of model:	
Weight, W, lb	70.0
Wing span, b, ft	8.46
Wing area, S, sq ft	8.94
Mean aerodynamic chord, c, ft	1.168
Moments of inertia:	
$I_x = mr_x^2$, slug-ft^2	5.25
$I_y = mr_y^2$, slug-ft^2	2.59
$I_z = mr_z^2$, slug-ft^2	7.30
I_{xz}, slug-ft^2	0
Center-of-gravity location (nominal)	0.25c
Stick fixed neutral point, N	0.513c
Aerodynamic derivatives:	
C_{L_o}	0.035
C_{D_o}	0.02
C_{D_α}	0.034
C_{L_α}	4.64
C_{m_α} (nominal)	-1.22
$C_{m_{\dot{\alpha}}}$	-3.85
C_{m_q}	-15.65
θ_o	0
C_{y_β}	-0.725
C_{y_p}	0.105
C_{y_r}	0.0051
C_{l_β}	-0.0617
C_{l_p}	-0.401
C_{l_r}	0.078
C_{n_β}	0.117
C_{n_p}	-0.019
C_{n_r}	-0.1[illegible]
Test conditions:	
Test medium	Freon-12
Dynamic pressure, q, lb/sq ft	225.0

TABLE 1.- CONDITIONS ASSUMED FOR STABILITY ANALYSIS - Concluded

Mach number	0.89
Velocity, U, ft/sec	470
$\sigma = \frac{\rho US}{2m}$, sec^{-1}	1.98
Mount system parameters:	
Cable length, $l_1 = l_2 = l_3 = l_4 =$, ft	20.0
Cable angles, $\beta_1 = \beta_2 = \beta_3 = \beta_4 =$, deg	20.0
Front pulley separation distance, 2h, ft	0.70
Rear pulley separation distance, 2d, ft	0.60
Pulley damping ratio, ζ_n (all modes)	0.05
Front cable tension, T_F, lb	$T_R + 21.4$
Rear cable tension, T_R, lb	$0 \leqq T_R \leqq 140$
Distance between center of gravity and front pulleys, e	$0 \leqq \frac{e}{c} \leqq 2.0$
Distance between center of gravity and rear pulleys, a	$-0.5c \leqq \frac{a}{c} \leqq 1.0$
Spring constant in rear cable, k_R, lb/in.	5.0
Spring constant in front cable, k_F, lb/in.	∞

TABLE 2.- CABLE INFLUENCE COEFFICIENTS

[See eqs. (9)]

Longitudinal force:

$$X_{C_o} = T_F(\cos \beta_1 + \cos \beta_2) - 2T_R \cos \beta_R - k_{x\theta}\theta_o$$

$$k_{xx} = \frac{T_F}{l_1} \sin^2\beta_1 + \frac{T_F}{l_2} \sin^2\beta_2 + \frac{2T_R}{l_R} \sin^2\beta_R + k_F(\cos \beta_1 + \cos \beta_2)^2 + 4k_R \cos^2\beta_R$$

$$k_{xz} = \frac{T_F}{l_1} \cos \beta_1 \sin \beta_1 - \frac{T_F}{l_2} \cos \beta_2 \sin \beta_2$$

$$- k_F(\cos \beta_1 + \cos \beta_2)(\sin \beta_1 - \sin \beta_2)$$

$$k_{x\theta} = - \frac{T_F}{l_1} \sin \beta_1(h \sin \beta_1 + e \cos \beta_1) + \frac{T_F}{l_2} \sin \beta_2(h \sin \beta_2 + e \cos \beta_2)$$

$$- k_F(\cos \beta_1 + \cos \beta_2)\left[e(\sin \beta_2 - \sin \beta_1) + h(\cos \beta_1 - \cos \beta_2)\right]$$

Lateral force:

$$k_{yy} = \frac{T_F}{l_1} + \frac{T_F}{l_2} + \frac{2T_R}{l_R} \cos^2\beta_R$$

$$k_{y\varphi} = T_F\left(\frac{h}{l_1} - \frac{h}{l_2}\right)$$

$$k_{y\psi} = T_F\left(\frac{e}{l_1} + \frac{e}{l_2}\right) - \frac{2T_R \cos \beta_R}{l_R}(d \sin \beta_R + a \cos \beta_R)$$

Vertical force:

$$Z_{C_o} = T_F(\sin \beta_2 - \sin \beta_1) - k_{z\theta}\theta_o$$

$$k_{zx} = k_{xz}$$

$$k_{zz} = \frac{T_F}{l_1} \cos^2\beta_1 + \frac{T_F}{l_2} \cos^2\beta_2 + \frac{2T_R}{l_R} + k_F(\sin \beta_2 - \sin \beta_1)^2$$

TABLE 2.- CABLE INFLUENCE COEFFICIENTS - Continued

$$\kappa_{z\theta} = -T_F h\left(\frac{\sin\beta_1 \cos\beta_1}{l_1} + \frac{\sin\beta_2 \cos\beta_2}{l_2}\right) - T_F e\left(\frac{\cos^2\beta_1}{l_1} + \frac{\cos^2\beta_2}{l_2}\right) + 2T_R \frac{a}{l_R}$$

$$- k_F(\sin\beta_2 - \sin\beta_1)\left[e(\sin\beta_2 - \sin\beta_1) - h(\cos\beta_2 - \cos\beta_1)\right]$$

Roll:

$$\kappa_{\varphi y} = k_{y\varphi}$$

$$k_{\varphi\varphi} = hT_F\left(\frac{h}{l_1} + \frac{h}{l_2} + \sin\beta_1 + \sin\beta_2\right) + 2dT_R\left(\frac{d}{l_R} + \sin\beta_R\right)$$

$$k_{\varphi y} = hT_F\left(\frac{e}{l_1} - \frac{e}{l_2}\right) + T_F e(\sin\beta_1 - \sin\beta_2)$$

Pitch:

$$M_{C_o} = eT_F(\sin\beta_1 - \sin\beta_2) - hT_F(\cos\beta_1 - \cos\beta_2) - k_{\theta\theta}\theta_o$$

$$k_{\theta x} = k_{x\theta}$$

$$k_{\theta z} = k_{z\theta}$$

$$k_{\theta\theta} = T_F\left[l_1\left(\frac{e}{l_1}\cos\beta_1 + \frac{h}{l_1}\sin\beta_1\right)^2 + \frac{1}{l_2}(e\cos\beta_2 + h\sin\beta_2)^2 + h(\sin\beta_1\right.$$

$$\left. + \sin\beta_2) + e(\cos\beta_1 + \cos\beta_2)\right] + 2T_R\, a\cos\beta_R + k_F\left[e(\sin\beta_2 - \sin\beta_1)\right.$$

$$\left. + h(\cos\beta_1 - \cos\beta_2)\right]^2 + \frac{2a^2 T_R}{l_R}$$

TABLE 2.- CABLE INFLUENCE COEFFICIENTS - Concluded

Yaw:

$$k_{\psi y} = k_{y\psi}$$

$$k_{\psi\varphi} = hT_F\left(\frac{e}{l_1} - \frac{e}{l_2} \therefore \cos \beta_1 - \cos \beta_2\right)$$

$$k_{\psi\psi} = eT_F\left(\frac{e}{l_1} + \frac{e}{l_2} + \cos \beta_1 + \cos \beta_2\right) + 2T_R\left[a \cos \beta_R + d \sin \beta_R + \frac{1}{l_R}(a \cos \beta_R + d \sin \beta_R)^2\right]$$

- SOFT SUPPORT
- NEGLIGIBLE MASS
- LOW AERODYNAMIC INTERFERENCE
- STABLE
- SIMPLE

Figure 1.- Mount requirements.

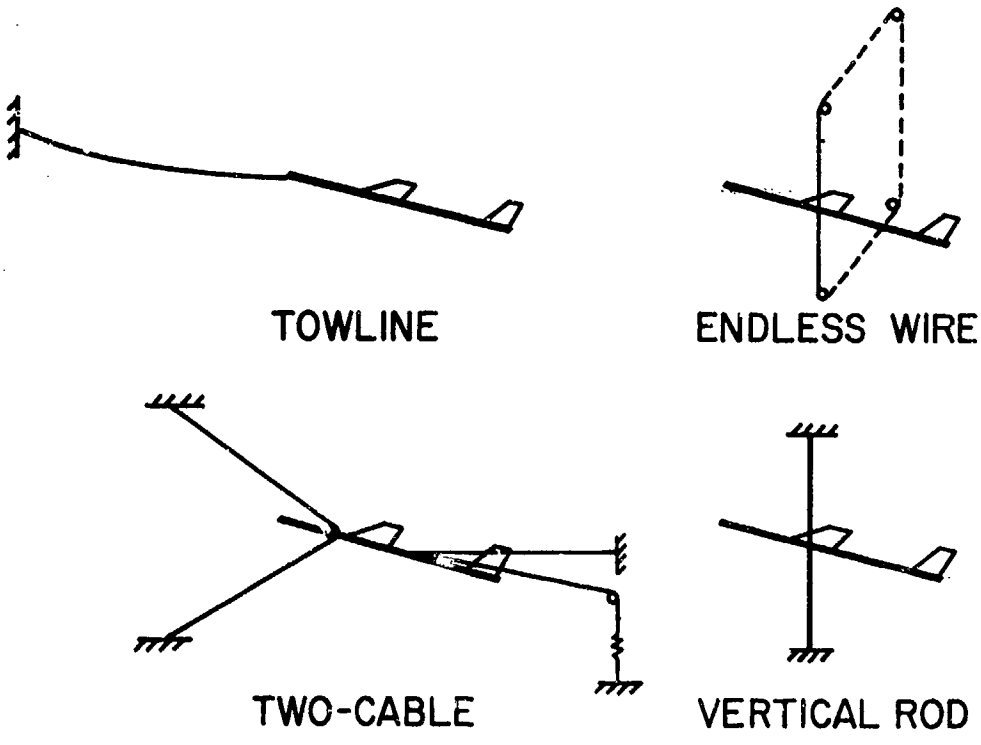

Figure 2.- Free-flight mount systems.

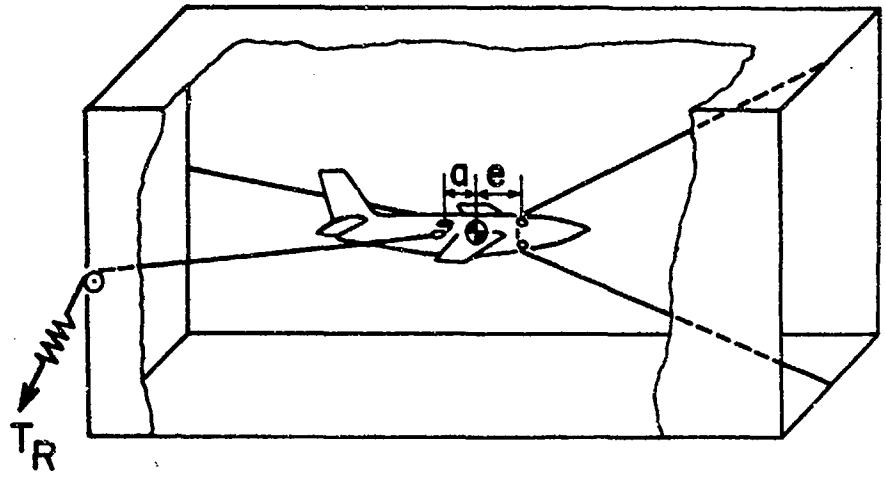

Figure 3.- Two-cable mount.

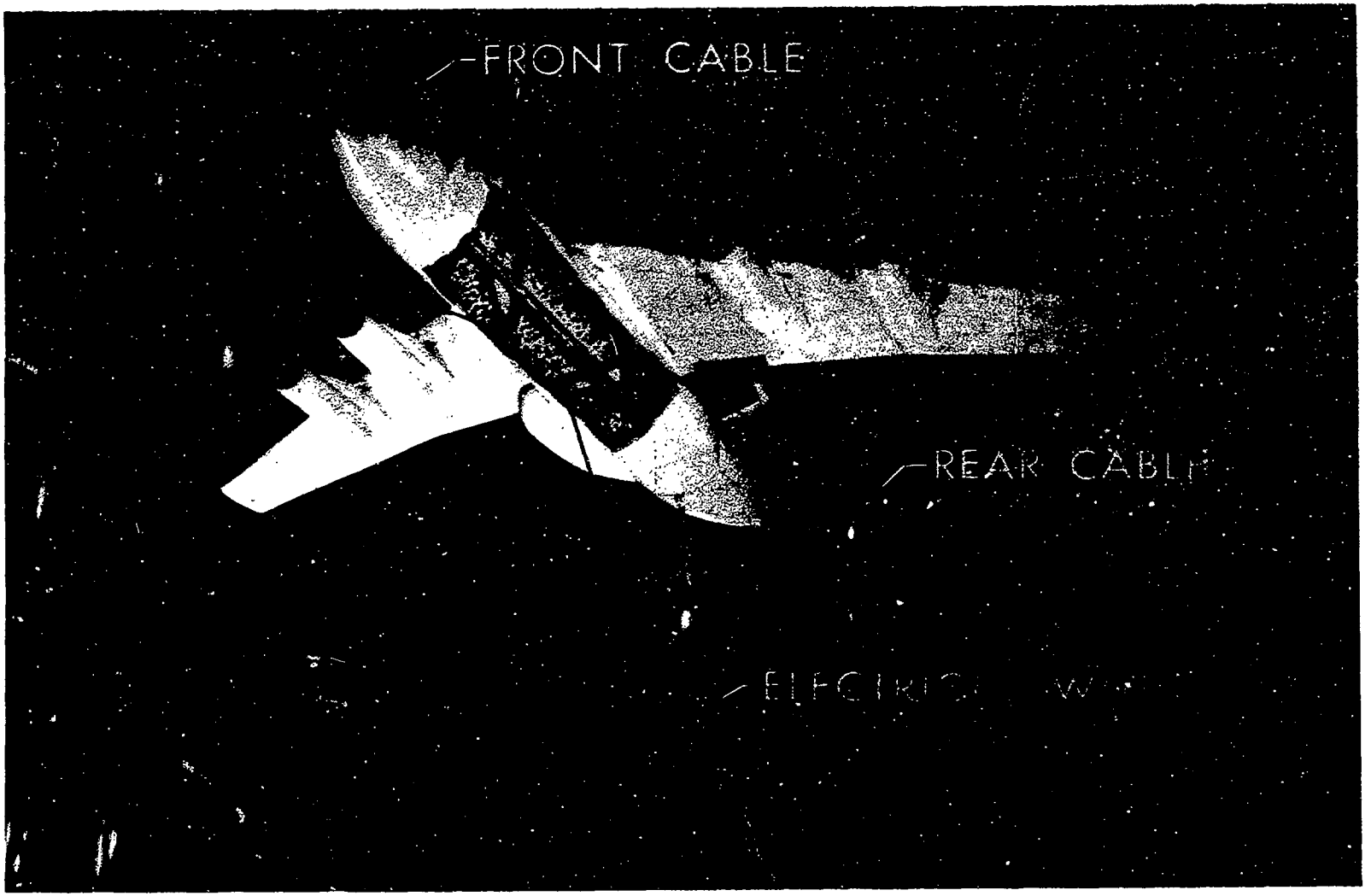

Figure 4.- Model on two-cable mount.

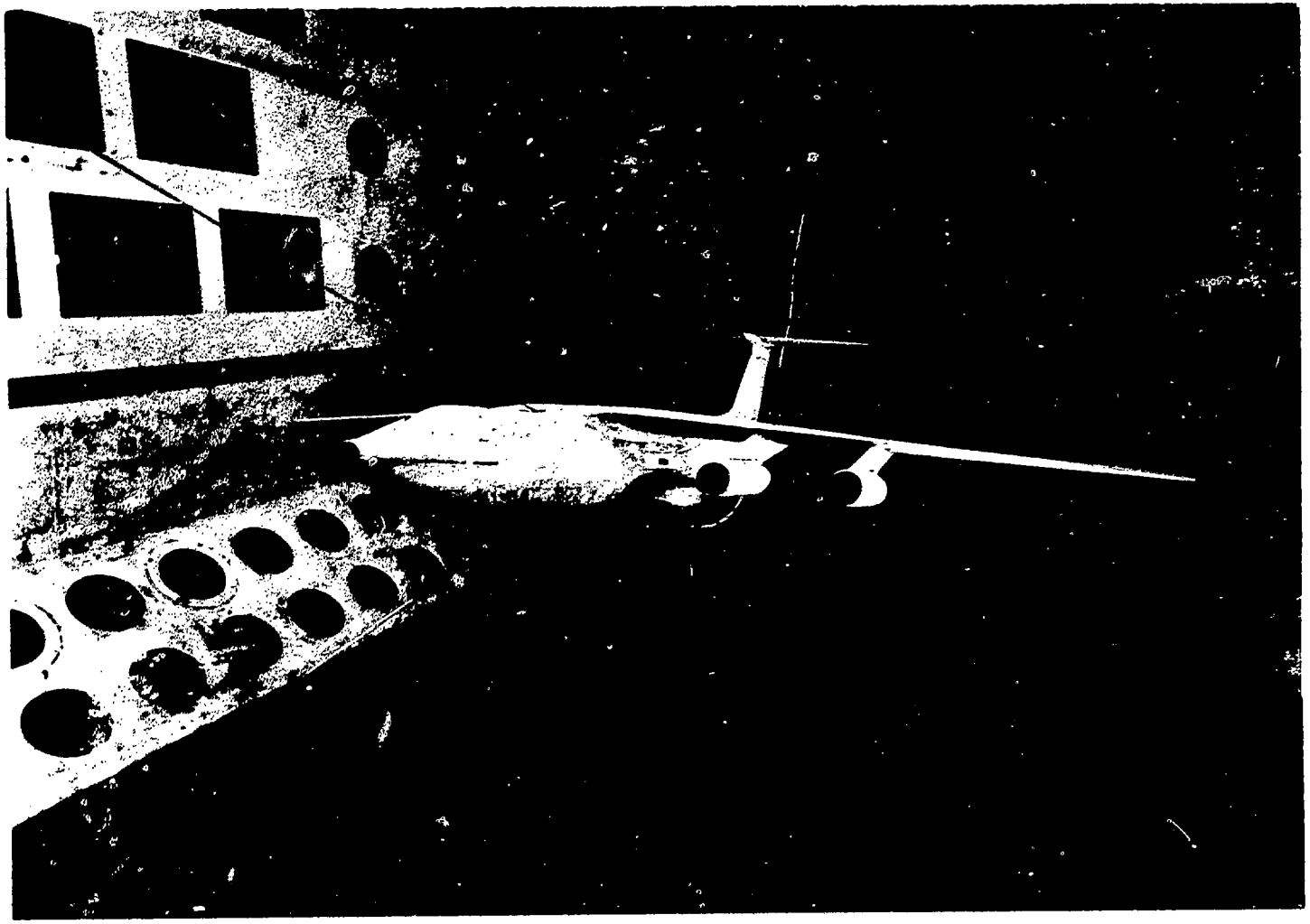

Figure 5.- Cable mounted model in preflight attitude.

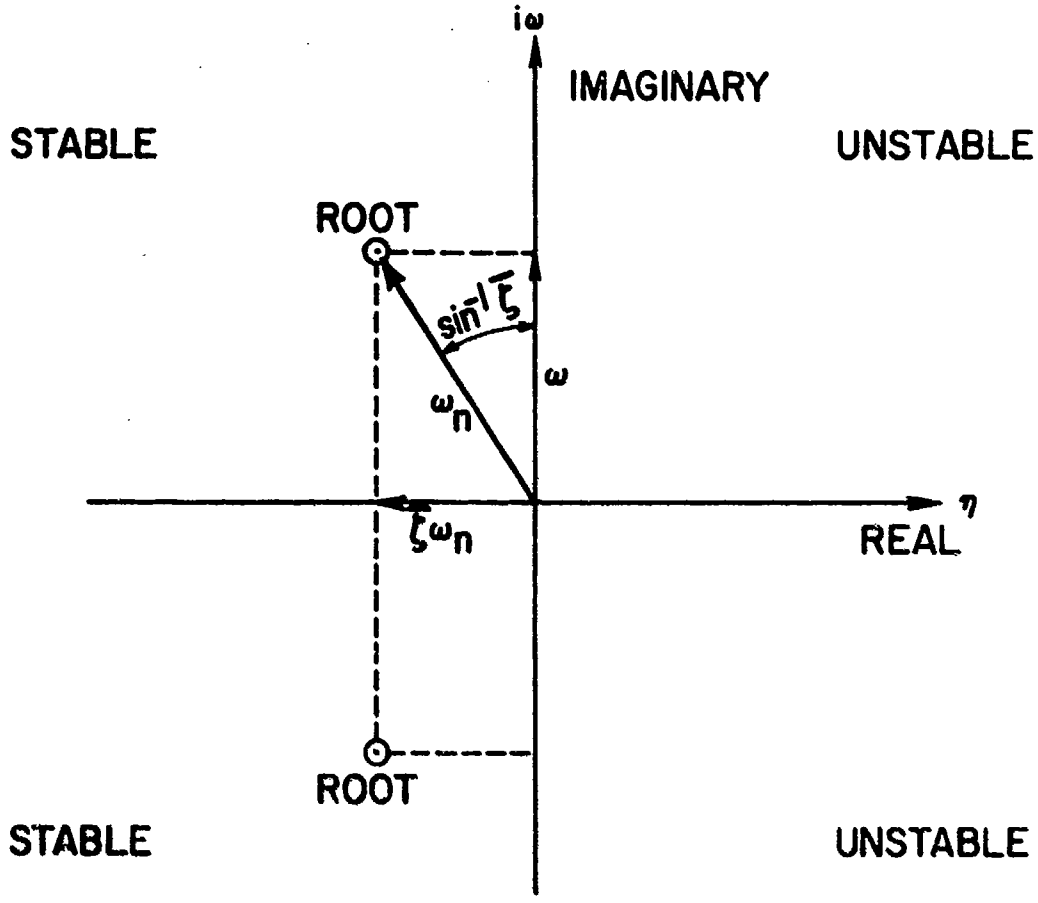

Figure 6.- Frequency and damping from root-locus plot.

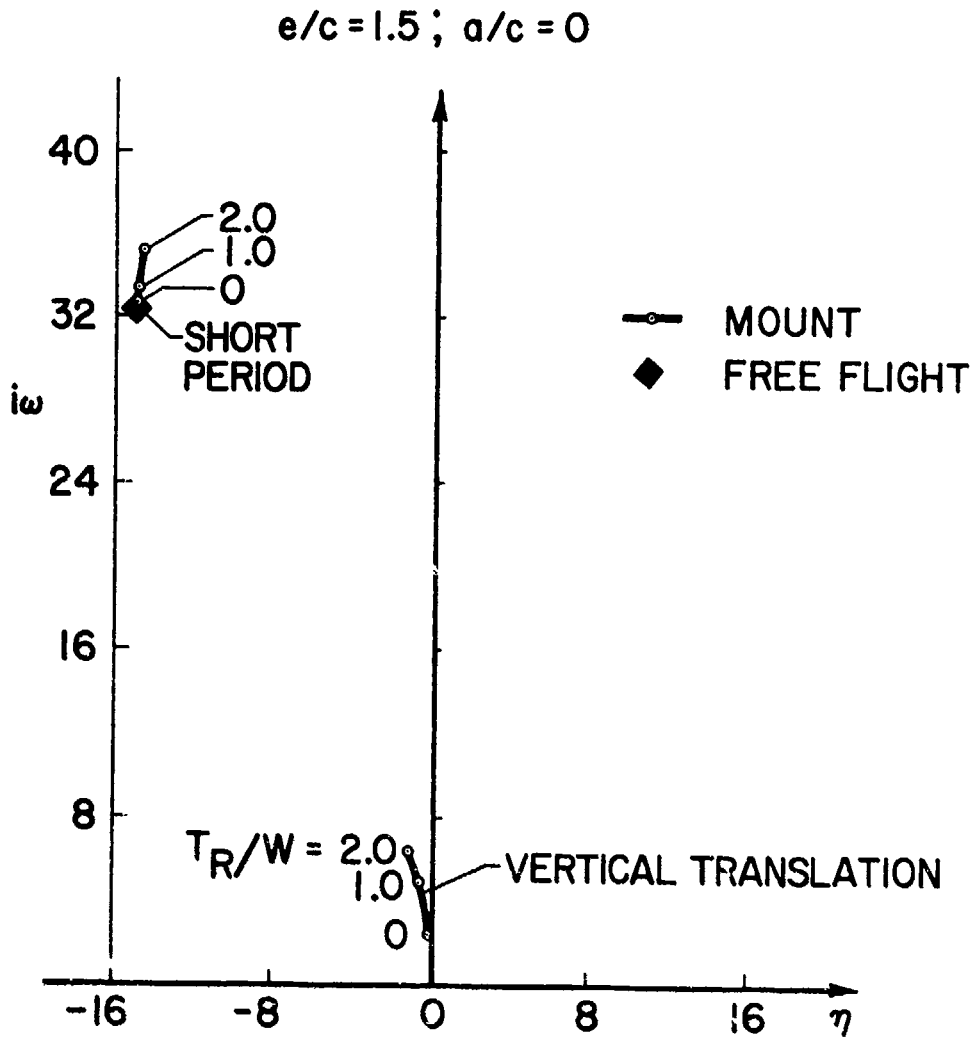

Figure 7.- Root locus of longitudinal modes.

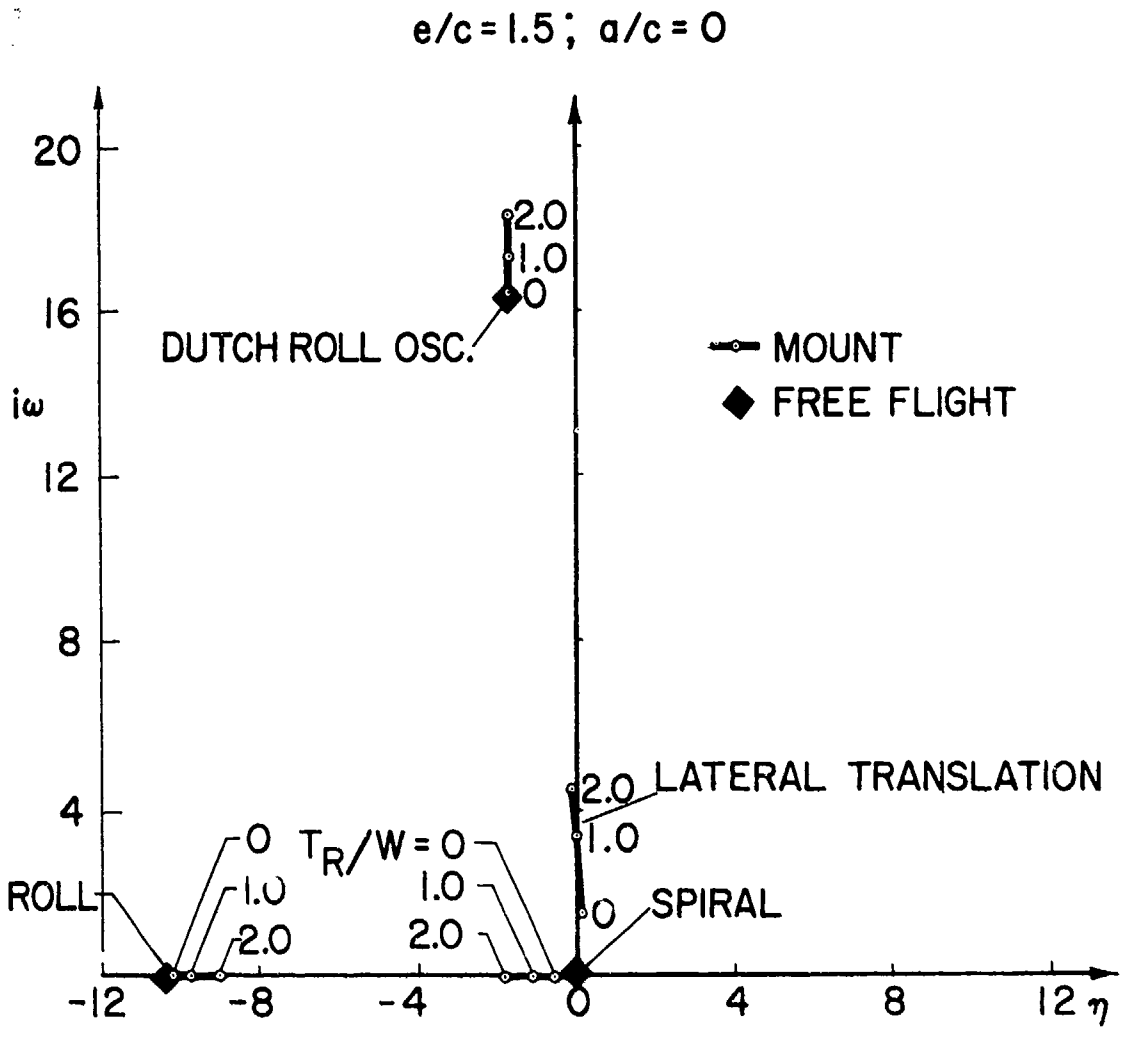

Figure 8.- Root locus of lateral modes.

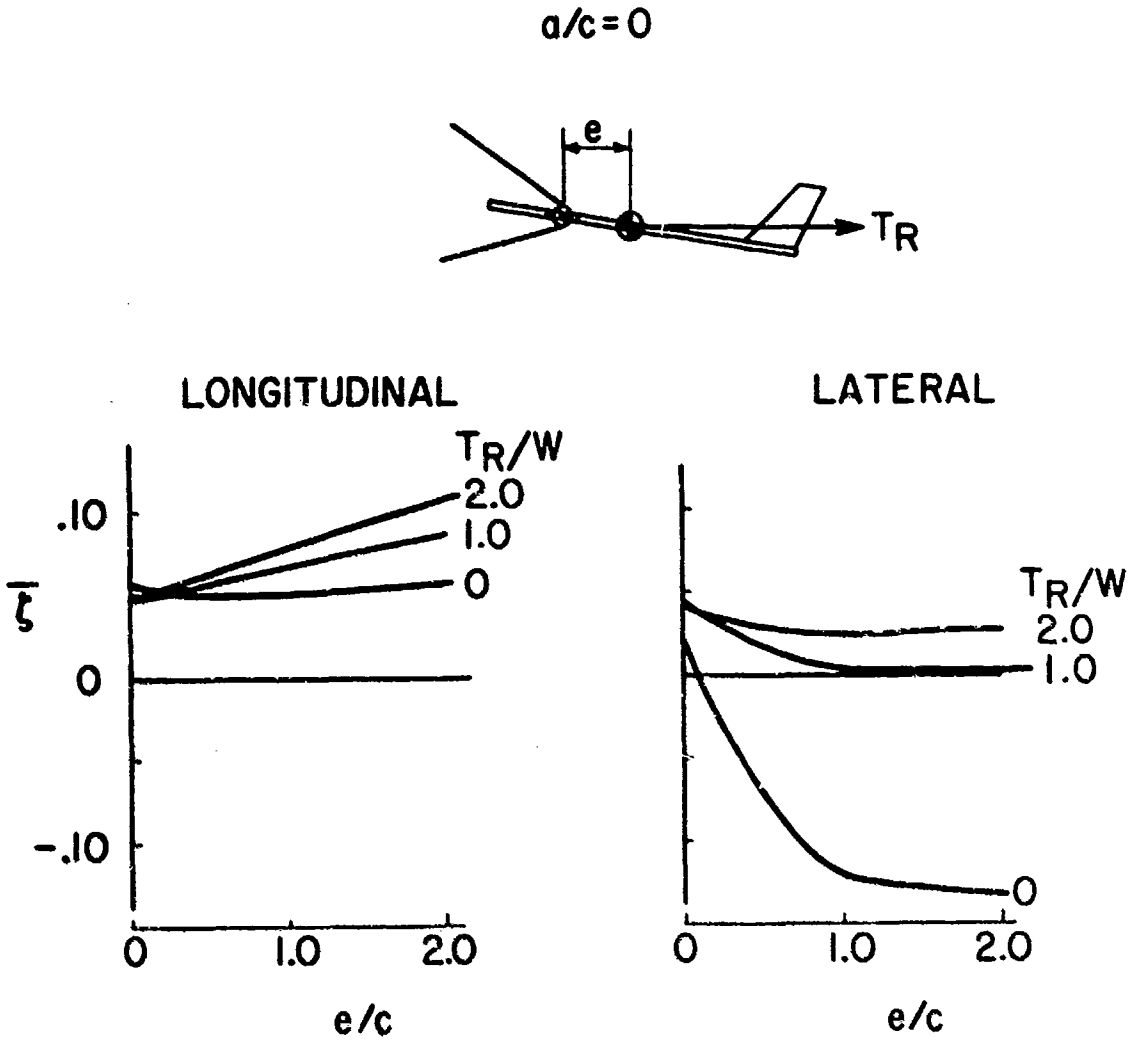

Figure 9.- Effect of front pulley location.

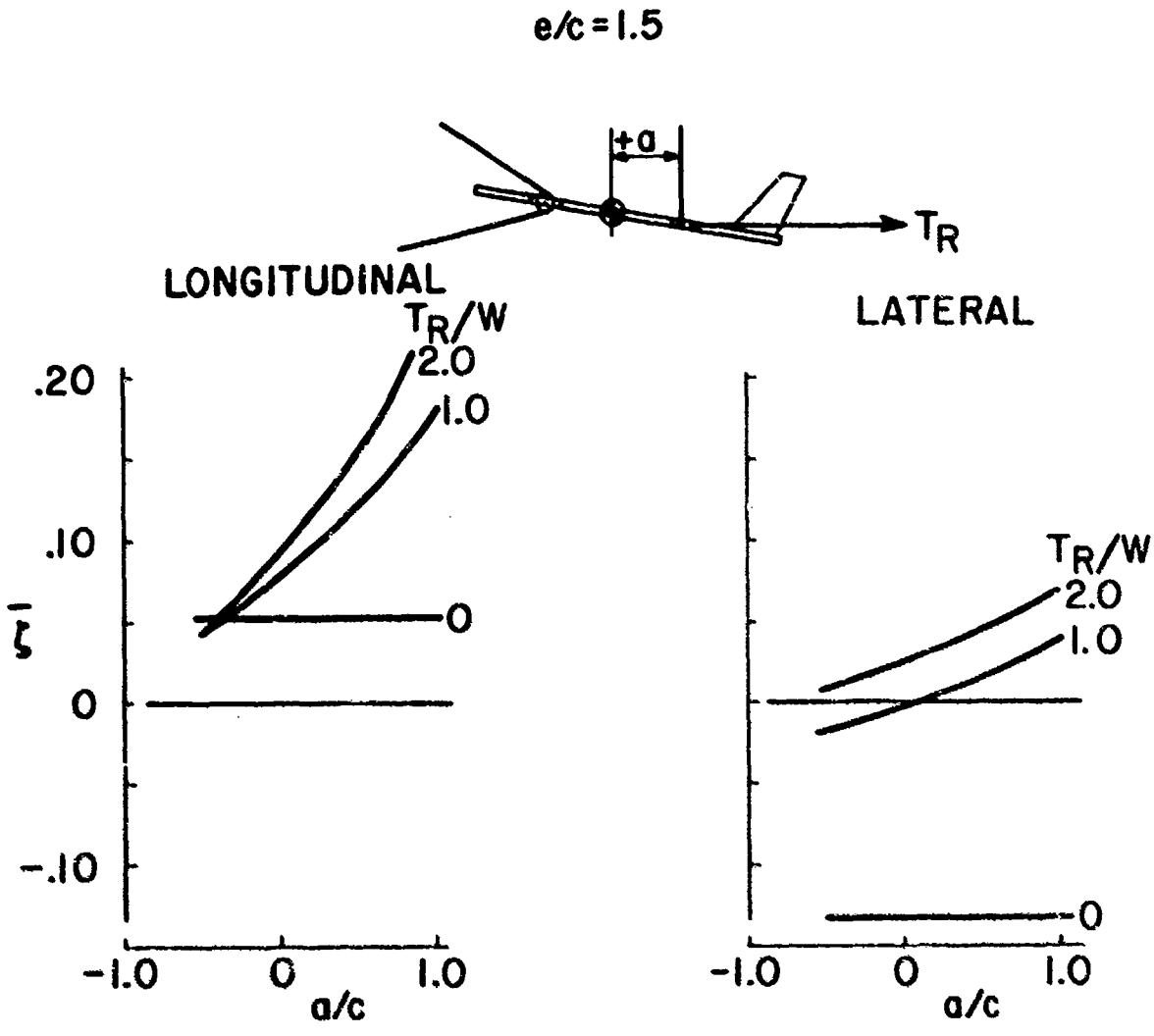

Figure 10.- Effect of rear pulley location.

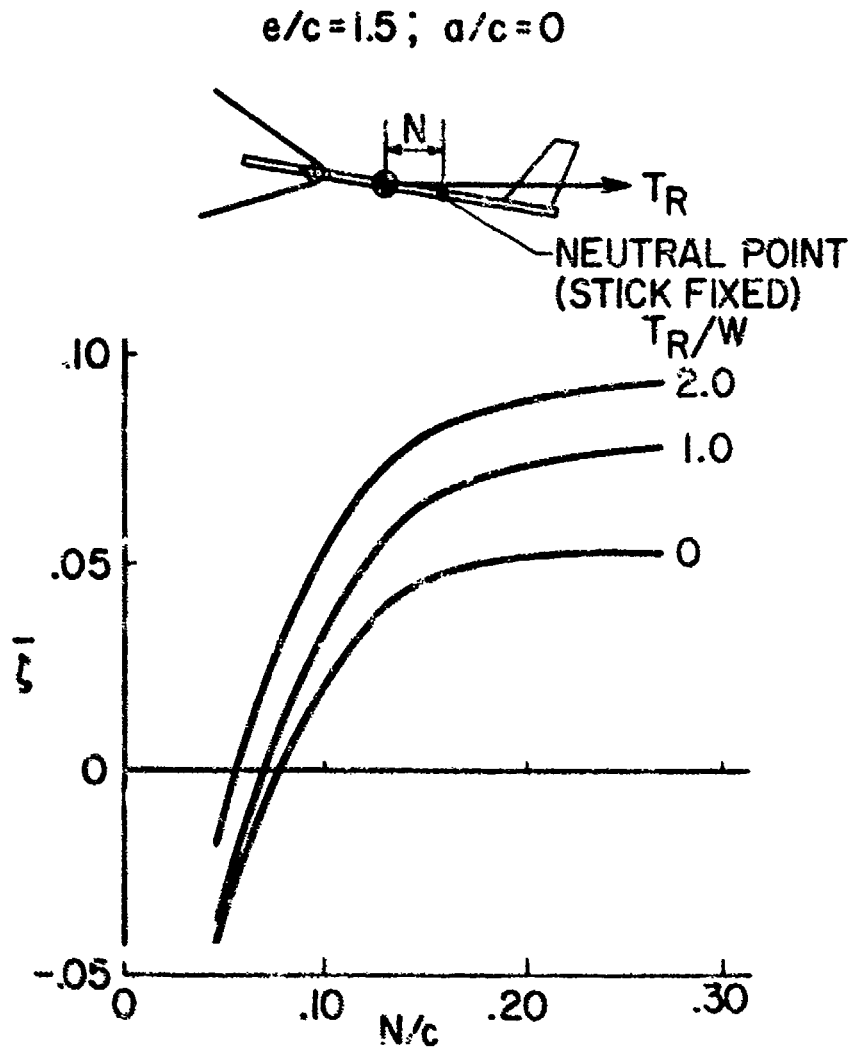

Figure 11.- Effect of static margin on longitudinal mode.

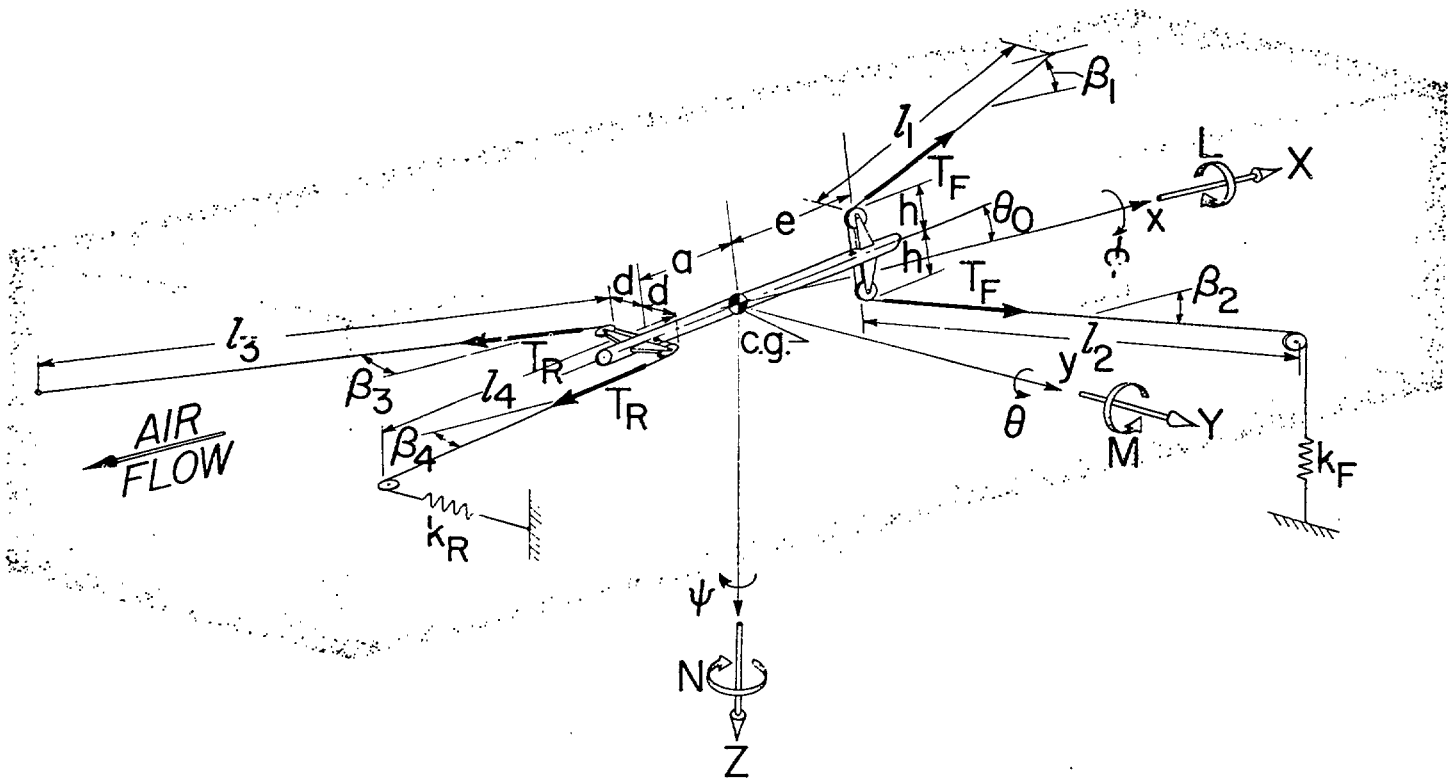

Figure 12.- Cable-mount configuration analyzed.

CONSTRUCTION AND TESTING TECHNIQUES OF INFLATABLE FLUTTER MODELS

J. R. Martucelli

F. H. Durgin

R. B. McCallum

MASSACHUSETTS INSTITUTE OF TECHNOLOGY

ABSTRACT

A method is presented of constructing inflatable AIRMAT* type models which are suitable for use as wind tunnel flutter models. The techniques used in static and dynamic model test are also presented along with the results of some tests on a series of sharply swept back, inflatable delta wings. The vibration mode shapes of a delta wing as determined by use of mirrors, mounted on the model, are presented. The importance of shear and bending type deformations are presented by comparing the results of static and dynamic tests with theoretical calculations. A limited amount of experimental results on the properties of the model surface material are also included.

* Trademark of Goodyear Aircraft Company

LIST OF ILLUSTRATIONS

CONSTRUCTION AND TESTING TECHNIQUES OF INFLATABLE FLUTTER MODELS

J. R. Martuccelli *
F. H. Durgin **
R. B. McCallum ***

MASSACHUSETTS INSTITUTE OF TECHNOLOGY

INTRODUCTION

Among the many configurations proposed for reentry vehicles, the concept of an inflatable structure (Refs. 1, 2, 3) offers some important advantages which bear directly on the problems encountered during reentry. The configurations representative of the types likely to be used for recoverable inflatable vehicles are shown in Fig. 1. The basic features of these configurations are a hemispherical nose, a swept-back leading edge (usually a large diameter tube), and a sail, AIRMAT,+ or several tubes connecting the right and left leading edges (see Fig. 2).

Two trajectories, which are typical for the types of reentry vehicle shown in Fig. 1, are presented in Fig. 3 in terms of dynamic pressure vs. Mach number. The additional parameters T (temperature), h (altitude), a (acceleration), and t (time from entry) are also given since they also affect the final design of an actual vehicle. The trajectories were obtained from Ref. 1 and some additional calculations based on the 1959 USAF model atmosphere. The angle of attack α ‡ and the lift-drag ration, L/D = 0.577, are assumed constant during entry. The entry height is 400,000 ft., the flight path angle is -1 degree, and the leading-edge radius is taken as one foot.

---

* Executive Officer, Aeroelastic and Structures Research Laboratory
** Research Engineer, Aerophysics Laboratory
*** Research Engineer, Aeroelastic and Structures Research Laboratory
+ Trademark of Goodyear Aircraft Company
‡ The angle of attack, or alternatively the lift coefficient, is not specified in Ref. 1, but it is believed that the lift coefficient is about 0.5.

From the foregoing and other published feasibility studies of inflatable reentry vehicles (Refs. 2, 4), one can draw the following general observations which are applicable to most situations:

(1) With the light wing loadings required (W/S of the order of unity) the maximum dynamic pressures will occur at relatively high Mach numbers, say $2 < M < 10$, at altitudes in the neighborhood of 200-250,000 ft.

(2) The variation in dynamic pressure is less than 20 per cent.

(3) While the descent at the higher altitudes will be at very shallow angles, the lifting surfaces will be oriented at relatively large angles of attack (between 20 and 60 degrees), because of the low dynamic pressure which will be encountered at these higher altitudes. The minimum C_L will be dependent on the maximum tolerable leading-edge temperature.

(4) Maximum allowable heating conditions dictate blunt leading edges for such surfaces.

(5) The lower wing loadings give lower values of the radiation equilibrium stagnation-point temperature because lower speeds are encountered at any given altitude.

(6) The very compact packaging of the vehicle for launching into orbit and assembly in space removes the necessity of having to place a large lifting surface vehicle on top of a large rocket vehicle, and thereby puts the task of placing such a vehicle in orbit within the capabilities of present day boosters. A packaged volume to inflated volume ratio of 0.03 to 0.05. is possible for an AIRMAT wing, while for a complete reentry vehicle, ratios of 0.15 are possible (Ref. 2).

The high degree of flexibility exhibited by these inflatable structures indicates that the prevention of instabilities such as flutter may be a significant problem. For the past year, the Aeroelastic and Structures Research Laboratory, Massachusetts Institute of Technology, under the sponsorship of the A. F. Flight Dynamics Laboratory, U. S. Air Force, Dayton, Ohio has been involved in a program of research on analytical studies and experimental verification of the vibration and flutter characteristics of inflatable structures, to establish design criteria which will insure that lifting surfaces for future inflatable vehicles will be free from dynamic instabilities. This paper is a report of the initial work performed on the construction and structural testing techniques of inflatable models which are suitable for use in wind-tunnel tests. Although other types of structures are being investigated under the research program, this paper will be concerned only with the AIRMAT type structure where the spacing of the surfaces is achieved by chords held in tension by

internal pressure. The results of some tests on a series of sharply swept-back, inflatable delta wings are presented, including the vibration mode shapes of one model as determined by use of mirrors mounted on the model. The relative importance of shear and bending-type deformations are determined by comparing experimental results with some simplified theoretical calculations. Some experimental results on the properties of the model surface material are also included. The results of the wind-tunnel tests will be presented in a subsequent, classified paper.

MODEL CONSTRUCTION

The AIRMAT type of lifting surface construction, where the spacing of the surfaces is achieved by chords held in tension by internal pressure, was conceived and is presently under development by Goodyear Aircraft Company, Akron, Ohio. Special looms have been developed which weave the two surfaces and the drop chords in one integral operation, and the elastomer used to make the surface material air tight is applied after the weaving operation. Variable depth mats can also be formed on these looms.*

Since the total number of models required for the program was small, methods with high productivity capabilities with their correspondingly long setup times and scheduling difficulties were not desirable. Even more important, it is almost certain on the basis of past experience that some future efforts will have to be made toward simulating the full-size vehicles with scaled-down models. The full-size vehicles will be constructed of a stainless steel mesh sealed with an elastomer capable of withstanding the temperatures of 1500°F which will be experienced during reentry. To achieve dynamic similarity, the materials used in the scaled-down model will necessarily have to be different than those used for the full-scale vehicle. In such cases, it is considered likely that simple rubber or impermeable cloth material will suffice. On the basis of these considerations, it was decided to explore alternate methods of model construction which would require very little equipment and permit a large degree of flexibility insofar as model properties were concerned. The following method of model construction was finally adopted.

---

* Development work on these looms was sponsored by the Manufacturing Technology Laboratory, Wright Patterson Air Force Base, Dayton, Ohio under Contract No. AF 33(600)-43036.

A styrofoam mandril, shaped to the dimensions of the desired model, is attached to a wooden root fitting. A nylon or dacron cloth, which has been pre-impregnated with latex rubber and cut to the correct size, is wrapped around the styrofoam core and root fitting. All seams are sealed with neoprene cement. Next, the drop chords are put in by sewing back and forth through the top and bottom surfaces with a needle and thread. To insure that the drop chords are reasonably perpendicular to the model surface, it has been found necessary to pre-drill the styrofoam core using an array of heated needles, since the sewing needle has a tendency to wander when piercing the styrofoam. For the present model, a drop chord spacing of one-quarter inch has been found to be satisfactory. Also, it is not necessary to sew the leading and trailing-edge regions since they are rounded and will automatically assume the desired cylindrical shape upon inflation. After all the drop chords are sewn, a coat of latex is applied to seal the holes made by the drop chords. The next step is to remove the styrofoam core by dissolving it with a common solvent such as Toluene.

It is evident that the foregoing is a relatively quick and inexpensive way of producing inflatable models. One of its greatest advantages is that the size or shape of the model depends on the styrofoam core, and can be very easily changed. The material properties can be changed by (1) selecting a different cloth, (2) selecting a different latex, (3) varying the number of layers of cloth imbedded in the latex, (4) varying the number of coats of latex, and (5) varying the orientation of the cloth threads.

A large number of delta-wing models, as well as square and rectangular models and even a model with a large initial curvature, have been constructed using this procedure by ASRL personnel and by students working on thesis or laboratory projects. Photographs of some of the models are shown in Fig. 4, which also includes a picture of a model constructed and donated by the Goodyear Aircraft Company.

A system for maintaining any desired pressure differential between model internal pressure and any reference pressure (atmospheric pressure during static and vibration testing, tunnel static pressure during wind-tunnel tests), is connected to the model through the wooden root fitting (see Fig. 5).

Strain gages (Baldwin, PA-3 post-yield type) for use in static and dynamic measurements are fastened to the model surface using neoprene cement and covered with a protective coating of latex. Because of the large deflections encountered in these models, care must be taken to allow enough slack in the strain-gage leads (such as zig-zagging the leads, (Fig. 5)) to prevent lead-wire breakage during model tests.

MODEL VIBRATION

The excitation system used for vibration tests is shown in Fig. 6. It consists of a basic audio system with a low frequency speaker. The speaker cone is covered by a tapered aluminum cover with a 1-1/4 inch orifice to concentrate the air column at the model surface. The vibration frequencies and damping coefficients were obtained from vibration decay records. Node lines were determined by sprinkling carborundum dust (no. 40 grit) on the model surface while the model was vibrating in a natural mode. This system is extremely well-suited for vibrating light models and the only problem has been one of over-excitation, especially for the higher modes. If the excitation force is too large, local responses are superimposed on the natural mode response. This effect can be minimized by positioning the speaker for each mode at the point of maximum vibration amplitude, so as to excite the mode with a minimum force.

Vibration data for two, single-ply, nylon models with 65° sweep is shown in Fig. 7, and the results for two-ply dacron models with 65° and 75° sweep are given in Fig. 8. The model properties are given in Table 1. The node lines for the first three modes are very similar to those for a uniform aluminum swept back plate (Ref. 5). The effect of the warp direction shows up mainly in the difference in mode shape for the fourth mode of Models A and B. The difference in frequencies between the two models is due to the different model weights. Changing over to double layers of dacron causes a large change in the frequencies although the mode shapes remain similar, at least for the first three modes. The most noticeable effect is in the closeness of the second and third frequency for Model C.

Table 1. PROPERTIES OF INFLATABLE MODELS

Model	Chord	Angle	Depth	Weight	Remarks
A	23.5 in.	65°	1-5/16 in.	0.348 lbs.	Single-Ply Nylon*
B	24	65	1-3/8	0.280	Single-Ply Nylon
C	24	65	1-3/8	0.324	Double-Ply Dacron**
D	24	75	1-3/8	0.219	Double-Ply Dacron
E	24	65	1-3/8	0.240	Single-Ply Nylon
F	24	--	2	1.38	Single-Ply Nylon, rectangular planform of 12 x 24 inches
Good-year	24	--	2	0.323	Loom-Woven Nylon, Neoprene coating, rectangular planform of 12 x 24 inches

* The nylon cloth had 100 thread counts per inch in both the warp and fill directions.

** The dacron cloth had 100 thread counts per inch in the fill direction and 75 in the warp direction.

The experimental frequencies are compared with calculations based on the assumption of only pure shear type deformations (Appendix A) in Table 2, which shows that the assumption is not a valid one. For Models A and B, the experimental frequencies are much lower than those predicted by theory, indicating that the stiffness properties of the surface material have an appreciable effect and must be accounted for. For Model C, the results are completely reversed, with theory predicting much lower frequencies. This is probably due to two causes. First, bending effects should be much lower in Model C with its double layer of dacron material. Second, Model C actually has four layers of cloth material along the leading and trailing edge, due to overlap at the seams, and the transverse shear rigidity of these edges adds a large amount of stiffness to the model.

Table 2. COMPARISON OF EXPERIMENTAL AND THEORETICAL FREQUENCIES FOR DELTA-WING MODELS

Mode	Experiment			Theory		
	Model A	B	C	Model A	B	C
1	14.3 cps	16.7	26.4	18.2	20.4	19.0
2	30.7	33.7	52.5	36.6	40.9	38.0
3	47.9	52.6	59.2	50.5	56.4	52.4

The effect of model pressure on the vibration frequencies of Models B and C is given in Tables 3 and 4. It should be observed that the frequencies do not vary as the square root of the model pressure, as would be expected if the deformations were mainly of the shear type.

Table 3. EFFECT OF MODEL PRESSURE ON VIBRATION FREQUENCIES OF MODEL B

Pressure	Mode			
	1	2	3	4
1 psig.	14.2	27.5	41.8	59.4
2	16.7	33.7	52.6	76.5
4	19.8	40.8	64.9	97.0

Table 4. EFFECT OF MODEL PRESSURE ON VIBRATION FREQUENCIES OF MODEL C

Pressure	Mode			
	1	2	3	4
2 psig.	26.4	52.5	59.2	85.1
4	30.0	62.9	77.5	113
6	33.0	70.0	89.0	133
8	34.6	75.0	96.6	146
10	36.3	80.0	117	161

Because of the lightness of the models, it is evident that there will be a small but noticeable apparent-mass effect on the vibration frequencies measured in air as compared with those that would be measured in a vacuum. This effect can be estimated for the fundamental mode by assuming the mass of air, m_a, contained in the cone formed by rotating the delta model about its root chord, is uniformly distributed over the planform and added to the total mass of the model. If m is the total mass of the model, f_v is the fundamental frequency in vacuum, and f_p is the fundamental frequency at any ambient pressure, the following relation holds:

$$\frac{f_p}{f_v} = \sqrt{\frac{m}{m + m_a}} \tag{1}$$

For small $\frac{m_a}{m}$, which applies here,

$$\frac{f_p}{f_v} \cong 1 - \frac{1}{2}\,\frac{m_a}{m} \tag{2}$$

To check the apparent-mass effects, one model (Model E) was vibrated in a vacuum chamber at several values of reduced ambient pressures, and at model pressures of 2 and 4 psig. The experimental values are given in Fig. 9, where a straight line is passed through the points, since f_p/f_v is essentially linear in m_a/m as noted in Eq. (2). For Model E the predicted reduction in frequency of the fundamental mode due to the apparent-mass is approximately 12 percent, which is of the same order of magnitude as the experimentally observed values of about 9 percent. For the higher frequencies, one anticipates an even smaller influence, and this is confirmed by the experimental results.

A comparison between two models, one built and donated by Goodyear Aircraft Co., and the other constructed using the techniques described previously (Model F), was made in Reference 6 and some of the results are reproduced in Fig. 10. The model data corresponding to the results of Fig. 10 are given in Table 1. The M.I.T. model is much heavier than the Goodyear model because of extra coatings of latex. The effect of the number of coatings was investigated in Reference 5 and only the results for the heaviest configuration are given here.*

---

* Adding extra coats of latex decreases the frequencies, but also adds some additional stiffness as evidenced by the fact that the change in frequencies was not inversely proportional to the square root of the total mass (Ref. 6).

From Fig. 10, it is seen that the first two modes are similar for both models. However, it was not possible to excite mode shapes on the Goodyear model corresponding to those obtained for the third and fourth modes of the M.I.T. model. The fifth mode of the M.I.T. model appears to correspond to the fourth mode of the Goodyear model. The mode shapes of the Goodyear model were particularly clear which is undoubtedly due to its more uniform construction, as it is machine woven rather than hand sewn. It would be noted that the M.I.T. model had a uniform drop chord spacing of 1/4 inch, while the Goodyear model had drop chords spaced every 1/4 inch in the chordwise direction, and every 1/2 inch followed by 1/8 inch, alternately, in the spanwise direction.

The results of calculations carried out for the case of pure shear (Appendix A) are compared with the experimental data in Table 5. Here, the assumption of pure shear type deformations appears to yield reasonably good predictions for both models.

Table 5. COMPARISON OF EXPERIMENTAL AND THEORETICAL FREQUENCIES FOR THE M.I.T. AND GOODYEAR RECTANGULAR MODELS

Mode	M.I.T.		Goodyear	
	Theory	Experiment	Theory	Experiment
1	11.8 cps	11.7	24.5	22.3
2	17.6	14.6	36.4	38.1
3	31.5	27.9	65.2	58 4

STATIC TESTS

Model A was tested for static deflection under a uniform load by placing sheets of lead on the model surface and measuring the deflection at three points along the leading and trailing edges. The lead sheet was cut into small pieces (2 x 2 in.) which were joined by tape so that the lead contributes negligible stiffness. The results of the tests are given in Fig. 11. In Table 6, the experimental values are compared with theoretical predications based on the assumption of shear deformation only.

Table 6. COMPARISON OF THEORETICAL AND EXPERIMENTAL DEFLECTIONS OF MODEL A UNDER A STATIC UNIFORM LOAD (MODEL PRESSURE IS 2 PSIG.)

Total Load		Station		
		1	2	3
2.33 lbs.	Theory	0.164 in.	0.290	0.242
	Exp.	0.22	0.60	0.36
4.66	Theory	0.328	0.580	0.484
	Exp.	0.56	1.32	0.78
6.99	Theory	0.492	0.870	0.726
	Exp.	0.94	2.14	1.34

From the results, several important observations can be made: (1) the experimental system does not exhibit linear behavior with change in pressure (2) the range of linearity with respect to load depends on the model pressure, and (3) the theoretical deflections, wherein bending deformations are excluded are considerably less than the observed deflections, indicating the presence of bending deformations which are of the same order of magnitude as the shea deformations.

Figure 12 shows the effect of angle of attack on the steady deflection of Model B while flying at a Mach number of 5 in Tunnel A of the Von Karman Gas Dynamics Facility, ARO, Tullahoma, Tennessee. Although the dynamic pressure under which the photographs were taken were about two orders of magnitude larger than those which would be experienced during an actual flight (Fig. 3), it is interesting to note the extremely large deflections which these models are capable of sustaining without collapse. Vibration tests made after these photographs were taken showed the vibration characteristics of the model to be unchanged.

VIBRATION MODE SHAPES

An accurate knowledge of the vibration mode shapes of the inflatable models would be extremely useful for checking the results of theoretical vibration calculations and also for calculating the generalized mass and aerodynamic forces needed in the flutter calculations. In this way, the mode shape data can be used in the final steps of one problem area (vibration analysis) and the initial steps of another problem area (flutter analysis), making it possible to attack both problems independently of one another.

As an initial effort, an attempt was made to measure the first six vibration mode shapes of Model B using an optical technique which has proved successful in other mode shape measurements (7, 8, 9). For the tests, optically flat mirrors (3/16 x 3/16 x 0.020 inches) were glued to one side of the wing at each of 37 stations using bee's wax as an adhesive

(see Fig. 13). The wing was mounted vertically, with the root parallel to the floor, and with the mirrors facing a 4 x 8 foot board located about 10 feet away and covered with grid lines spaced at 0.40 inch intervals. Light, from a point light source placed under the 4 x 8 foot board, was passed through 37 lenses (1/4" and 1" diameter) mounted just in front of the wing in a rigid board. The light was made parallel by the lenses and then reflected from the mirrors back through the lenses, forming an image of the point source (called a dot from here on) on the 4 x 8 foot board, for each mirror on the wing. A schematic of the optical system for one mirror is shown in Fig. 14.

When the wing is vibrated at one of its natural frequencies, the dots trace out lines on the 4 x 8 foot screen which are a direct measure of the relative magnitude and direction of the change in slope of the wing, during each cycle of vibration, at each mirror station. The change in slope in the horizontal (x or streamwise) and vertical (y or spanwise) directions can be determined by measuring appropriate components of the resulting traces. Integration of the slopes along any given direction yields the model deflection amplitude at the various stations.

To facilitate data reduction and insure that the data was all recorded at the same vibration amplitude, a photograph was taken of all the lines on the board while the model was vibrating in a natural mode. No particular effort was devoted to placing the dots in a particular initial spot on the board. The dots were identified prior to taking the photograph and an identification number was written beside each dot on the board. This procedure required a double exposure. The first exposure was made with room lights on to record the grid lines and identifying numbers. The second was made in complete darkness to record the dot traces. Figure 15 is typical of the photographs obtained.

Mode shape data was taken for the first six modes of Model B at model pressures of 1, 2, 3 and 4 psig. Only the data for the first three modes at a model pressure of 2 psig has been reduced to date. The mode shapes are given in Figs. 16-18. As previously mentioned, the data was reduced by measuring the streamwise and spanwise components of the line for each mirror. The data was plotted in both directions and along diagonals as well, and the curves were used to find values of the slope at the root and at intermediate stations where there were no mirrors. It should be pointed out that the algebraic sign of the slopes is not obtained directly from the photographs, but must be determined by making recourse to previous vibration data where the mode lines have been determined; this presents a difficult problem for the higher modes. The vibration amplitude was then found by numerical integration of the curves obtained in the previous step. To find the vibration amplitude at any point, there are two main paths along which one may proceed. Taking point 22 in Fig. 13, for example, it is possible to find its amplitude by, (1) integrating along the spanwise direction starting from point 20R, or (2) integrating along another spanwise section, say the rearmost section,

from point 1R to point 3 and from there integrating in a streamwise direction to point 22. In practice it has been found necessary to carry out such a process for each point, compare the results, and then reinterpret the original data to make the overall agreement better. From the type of agreement obtained for the inflatable models by this procedure, it is evident that the results shown in Figs. 16-18 are not nearly as accurate as previous results obtained by applying the same techniques on solid wings (7, 8). The main source of error lies in determining the spanwise slope at the model root. For solid models, this slope is zero, while for inflatable models it is not. In fact, there are very marked fluctuations in the spanwise slope near the root and the mirrors should have been placed much closer to the root than the one-inch spanwise spacing shown in Fig. 13.

Another problem encountered during the tests was that the mirrors were found to bend as the model pressure was increased. This was caused by local stretching of the model surface between drop chords and could be alleviated by using slightly stronger (and heavier) mirrors. The bending of the mirrors manifested itself by turning the dot on the board into a line. In an extreme case, the dot, which is normally about 5/32 inches in diameter, was expanded into a 3/16 x 3/4 inch line. When this occurred, it was necessary to remount the mirrors. The effect was found to be minimized by installing the mirrors at the maximum model pressure, the bending being less noticeable with decrease in pressure. With regards to the effect of the mirrors on the vibration results, the frequencies and node lines were determined at a model pressure of 2 psig, using the technique previously described, both with and without the mirrors, and there was no measureable difference between the results for the two cases.

Finally, the mode shapes for the first three modes were used to compute the following generalized masses:

$M_{11} = 1197$ $\quad$ $M_{12} = 34.4$

$M_{22} = 582.4$ $\quad$ $M_{13} = 39.0$

$M_{33} = 141.3$ $\quad$ $M_{23} = 18.3$

Since the cross terms are not zero, it is evident that the modes are not normal to each other and are therefore not the true vibration modes. An estimate of the error can be determined by comparing M_{ij} with the square root of $M_{ii} \times M_{jj}$. In the worst case (M_{13} compared with $\sqrt{M_{11} M_{33}}$), this amounts to a little less than ten percent. It should be noted that the generalized masses computed about having been corrected for the effect of a non-uniform mass distribution caused by material lap-over at the seams along the leading and trailing edges. In some cases, this correction, which was only approximate in the sense that the exact amount of lap-over was not known, was of the same order of magnitude as the cross terms and could account for an appreciable part of the error.

MATERIAL PROPERTIES

From the comparison between experimental vibration results and theoretical calculations based on the assumption of pure shear type deformations, it is evident that the bending deformations, which are dependent upon the properties of the model surface material, are important and must be accounted for. Accordingly, a limited amount of work was performed to determine the material properties of the nylon cloth used in the construction of the models. The test specimens were two, 4" diameter, 17" long, rubberized nylon cylinders. Each cylinder was sealed at both ends with an aluminum disk and inflated to a pressure which made the skin stress in the cylinder equal to that value encountered in the model. The values of the extensional moduli in the warp and fill direction, $E_w t$ and $E_f t$, respectively, and the shear stiffness, Gt, were obtained from the test results. The two cylinders differed from each other only in that one had the cloth warp in the axial direction, whereas the other had the warp in the circumferential direction.

Since the material properties are known to be a function of the stress condition, it is necessary to run the tests at the stress conditions present in the model in the inflated condition. To find the required pressure for the cylinders, consider the typical model where the stress in the material is essentially equal in all directions, and is given by

$$\sigma t = \frac{p_i h}{2} \qquad (3)$$

where

σt is the stress times material thichness.

p_i is the model pressure, psi.

h is the depth of the model, in.

The hoop stress in the cylinder, $\sigma_h t$, is given by

$$\sigma_h t = p_{i_c} \frac{D}{2} \qquad (4)$$

where

p_{i_c} is the cylinder pressure, psi.

D is the cylinder diameter, in.

Requiring that the model and hoop stress be equal, gives

$$p_{i_c} = \frac{h}{D} p_i \tag{5}$$

as the required cylinder pressure. The axial stress in the cylinder is one-half the hoop stress, and an additional load must therefore be added to the cylinder in the axial direction to increase the axial stress level to that of the hoop stress. The additional load required is

$$\text{LOAD} = \pi p_{i_c} \frac{D^2}{4} \tag{6}$$

The tests were run with the longitudinal axis of the cylinder in a vertical direction so that the extra load could be applied by simply hanging the required weight from the bottom edge of the cylinder. This configuration requires that Eq. (6) be modified to account for the effect of the weight of the cylinder and cylinder end plates. In the tests, therefore, the extra load given by Eq. (6) was reduced by one-half the total weight of the cylinder test units.

A test consisted of setting up equilibrium conditions in the cylinder corresponding to some value of model pressure and recording the distance between two reference points near each end of the cylinder. The axial load was then varied through a range which bracketed the original load by removing or adding weights, and the distance between the reference points was recorded for each loading condition. After each reading, the cylinder was loaded as in the original loading condition, and allowed to return to its original zero. All readings were taken as quickly as possible to minimize the effects due to creep.

The results of these tests are presented in Table 7, where the values given are averages from a number of trials. It is estimated that the error in $E_f t$ is about $\pm$ 8% for the $p_{i_c} = 0.688$ psi case and about $\pm$ 4% for the $p_{i_c} = 1.03$ psi case. For the $E_w t$, the error is about $\pm$ 3% for the $p_{i_c} = 0.688$ psi case, and about 8% for $p_{i_c} = 1.03$ psi case.

Table 7. AVERAGE EXPERIMENTAL VALUES OF THE EXTENSIONAL, Et, MODULUS FOR SINGLE PLY, LATEX IMPREGNATED, NYLON CLOTH

Cylinder Internal Pressure (psig)	Corresponding Model Pressure (psig)	$E_w t$ (lb/in)	$E_f t$ (lb/in)
0.688	2.0	148	109
1.03	3.0	163	119

The material is more stiff in the warp direction than in the fill direction, probably due to the fact that, at low stresses, extensions are dominated by thread straightening, and the warp threads, which are straighter than the fill threads, are less susceptible to this type of extension. This would also explain the increase of stiffness with internal pressure.

The two inflatable cylinders were also tested at the same stress levels in torsion to measure the shear stiffness, Gt, of the material. Rotation of the bottom of the cylinder due to an applied torque were measured with a double ended pointer attached to the bottom disk of the cylinder. Angles were read from a protractor mounted on a shelf below the rotating cylinder. Torque was applied to either side of a pulley mounted below the pointer. As was done with the axial tests, readings after load application were read as quickly as possible, and after every reading, the torque was removed and the cylinder was allowed to return to zero deflection. The shear stiffness was determined from

$$Gt = \frac{4T}{\pi \theta D^3} \tag{7}$$

where

T is the applied torque, in.-lb.

θ is the twist per unit length, rad/in.

D is the diameter of the cylinder, in.

The results, as given in Table 8 (again only average values are given), reveal that the shear stiffness is essentially the same in both the warp and fill directions and that the shear stiffness increases with pressure.

Table 8. AVERAGE EXPERIMENTAL VALUES OF TORSIONAL STIFFNESS, Gt, FOR SINGLE PLY LATEX IMPREGNATED NYLON CLOTH

Type of Test	Cylinder Internal Pressure (psig)	Corresponding Model Pressure (psig)	$G_w t$ (lb/in/rad)	$G_f t$ (lb/in rad)
Static	0.688 1.03	2.0 3.0	4.35 5.79	4.64 5.51
Dynamic	0.688 1.03	2.0 3.0	5.53 6.28	4.41 none available

As a check on the results of the static torsion tests, the cylinders were tested dynamically, using each in turn as a torsional pendulum. This method hopefully minimizes the effect of creep, which is difficult to control in the static method. The cylinder being tested had one of its ends clamped to a horizontal strut from which the model was hung vertically. A rod, 14" long, was fixed horizontally to the lower free end of the cylinder. To each end of this rod, equal masses were attached (the distance of each known mass from the center of the rod could be varied). A hook from which weights could be hung was attached to the bottom of the cylinder using a thin wire. This allowed the cylinder to twist independently of the weights, since the added stiffness of the wire can be considered to be negligible compared to the cylinder's stiffness. After the required weights were added to the bottom of the cylinder (to equalize the biaxial stresses) the cylinder was inflated to the required pressure, and the adjustable rotating weights were set at their maximum distance from the center of the rod (condition no. 1). Then, using a stop watch, the natural torsional frequency of the cylinder-weight combination was found. Since there was considerable damping in the system, the cylinder required continuous exciting torque and was twisted slightly by hand during each cycle. The weights were next moved in towards the center (condition no. 2), and a new natural frequency was determined. The shear stiffness from the dynamic tests can be shown to be given by

$$Gt = \frac{16\pi l}{12 D^3} \cdot \frac{f_1^2 f_2^2}{f_1^2 - f_2^2} \Delta I_\alpha \qquad (8)$$

where

l is the length of cylinder, in.

f_1, f_2 are the measured frequencies corresponding to test conditions 1 and 2, respectively, cps.

D is the diameter of cylinder, in.

ΔI_α is the change in moment of inertia between conditions 1 and 2, slugs-in^2.

The results of the dynamic tests are included in Table 8.

A comparison of the static and dynamic tests (Table 8) for $G_w t$ suggests that the effect of creep in the static tests is important and leads to lower measured values of torsional stiffness. It is not known why the dynamic value for $G_f t$ should be lower than the corresponding static value.

Some attempts have also been made to measure Poisson's ratio by measuring the change in circumference of the cylinders with a strip of graph paper and comparing this change with the variation in length of the cylinder under different loading conditions. Because of the size of the specimen, friction between the measuring tape and cylinder, and nonuniform tension in the measuring tape during measurements, no meaningful results could be obtained.

CONCLUDING REMARKS

As previously stated, this paper is presented in the sense of a progress report on the preliminary phases of a program on flutter of inflatable vehicles. Within the scope of the work reported on here, it is not possible to draw many definite conclusions. However, it is possible to briefly summarize the results as follows:

1. The model construction technique presented here is simple and yields relatively inexpensive models. It is particularly applicable when only a few models are desired and when different surface materials are to be used in the individual models.
2. The experimental procedures used in testing the inflatable models are very similar to those used in other model programs. With the exception of the "mirror" made shape tests, no new or special techniques appear to be required.

3. With a little more effort, the mirror tests can be made to yield mode shapes which will be sufficiently accurate for use in flutter calculations. The results will also be applicable for checking theoretical vibration calculations.

4. The apparent mass effects due to vibration in still air on the measured vibration characteristics are significant and should be accounted for.

5. Any theoretical calculations used to predict the static or dynamic behavior of inflatable delta wing models of the type presented here should include the effect of both shear and bending type deformations. The effect of any heavy or stiff seams along the leading and trailing edges should also be accounted for.

6. The problem of accurately determining the stiffness properties of the model surface material must be resolved before the effects of bending type deformations can be included in the vibration calculations. From the preliminary results, dynamic testing methods applied to cylindrical test specimens appear to offer an alternate, and possibly more promising approach to the static methods now in common use.

ACKNOWLEDGEMENTS

The work reported on here was supported by the A. F. Flight Dynamics Laboratory, Wright-Patterson Air Force Base, Dayton, Ohio under Contract No. AF 33(657)-8468.

The authors are also indebted to Mr. G. Zartarian and Prof. J. Dugundji for their help and continuing efforts in the theoretical portions of the work.

APPENDIX A
THEORETICAL CONSIDERATIONS

For an inflatable model, the internal strain energy may be written as

$$U = \frac{1}{2}\iint_S \left[\bar{A}_{11}\alpha_x^2 + \bar{A}_{22}\beta_y^2 + 2\bar{A}_{12}\alpha_x\beta_y + \bar{A}_{33}(\alpha_y+\beta_x)^2 \right] dx\,dy$$
$$+ \frac{1}{2}\iint_S p_d h \left[(w_x+\alpha)^2 + (w_y+\beta)^2 \right] dx\,dy \qquad \text{(A.1)}$$

Here $\bar{A}_{11}$, ... are dependent on the structural properties of the covers, and are constants for uniform depth h. w is the lateral deflection from the plane x-y of the plate, p_d is the differential pressure across the model surface, and α and β are the angles of rotation of the drop chords in x and y directions, respectively. The coordinate directions are shown in Fig. 16 . The subscripts indicate partial differentiation with respect to the indicated direction.

It is constructive to consider the two limiting cases of (a) pure shear and, (b) pure bending deformations. For pure shear, $\alpha = \beta = 0$. In the second case, p_d is large so that no shear deformations are present and $w_x = -\alpha$, $w_y = -\beta$. To assess the relative importance of these two types of deformations, consider the case of pure shear, for which

$$U = \frac{1}{2} p_d h \iint (w_x^2 + w_y^2)\,dx\,dy \qquad \text{(A.2)}$$

for constant depth h. A Rayleigh-Ritz approach is utilized, which requires the assumed model function w_n to satisfy the geometric boundary conditions. Thus, one may set for a cantilevered wing

$$w_s = \sum_n w_n q_{sn} \qquad \text{(A.3)}$$

where

w_s is the deformation due to shear only

q_{sn} is the generalized coordinate of the n^{th} mode

The kinetic energy is

$$T = \frac{1}{2} \iint_S m \dot{w}_s^2 \, dx dy \tag{A.4}$$

where

m is mass per unit area.

The work function is

$$Q = \int\int_S F \left(\sum_n W_n q_{sn} \right) dx dy \tag{A.5}$$

where

F is the external force per unit area

Application of Lagrange's equation results in

$$\iint_S m w_i \sum_n \ddot{q}_{sn} w_n \, dx dy + p_d h \iint \left[w_{ix} \sum_n q_{sn} w_{nx} + w_{iy} \sum_n q_{sn} w_{ny} \right] dx dy = \iint_S F w_i \, dx dy$$

The simultaneous equations given by Eq. (A.6) may be solved by any of the well-known methods, once a set of assumed modal functions have been selected.

The vibration and static deflection calculations referred to in the paper have been carried out for the case of pure shear using the following set of nine assumed modal functions:

$$w_1 = y \qquad w_4 = x^2y \qquad w_7 = x^2y^2$$

$$w_2 = xy \qquad w_5 = xy^2 \qquad w_8 = xy^3$$

$$w_3 = y^2 \qquad w_6 = y^3 \qquad w_9 = y^4$$

Unless otherwise noted; all calculations are, based on a uniform mass distribution with the extra mass (due to seams) at the leading and trailing edges simply included as part of the total mass. Further calculations incorporating the effect of bending have necessarily been postponed until the required values of the material properties have been determined.

REFERENCES

1. Rogallo, F.M., Lawry, J.G., Croom, D.R., and Taylor, R.T., Preliminary Investigation of a Paraglider. NASA TN D-443, August 1960.

2. Sandgren, F.B., and Harris, J.T., Application of Inflated, Expandable Structures to Orbital Flight and Re-Entry. ARS Preprint 1093-60, presented at the ARS meeting on Structural Design of Space Vehicles, Santa Barbara, California, April 6-8, 1960.

3. Leonard, R. W., Brooks, G.W., and McComb, H.G., Jr., Structural Considerations of Inflatable Re-Entry Vehicles. NASA TN D-457, September 1960.

4. Olstad, W.B., A Study of the Feasibility of Inflatable Re-Entry Gliders. NASA TN D-538, October 1960.

5. Gristofson, P.N., Stokey, W.F., and Zorowski, C.F., "An Experimental Study of Natural Vibrations of Cantilevered Rectangular Plates." Journal of the Aeronautical Sciences, May 1953, pp. 331-337.

6. Matlin, R.W., Experimental Natural Frequencies, Damping Coefficients and Mode Patterns of an Inflatable Rectangular Wing. B.S. Thesis, Department of Aeronautics and Astronautics, M.I.T., June 1963.

7. Durgin, Frank H., A Final Report on Phase I of a Program of Experimental and Theoretical Research on the Use of Quasi-Steady Airloads in Aeroelastic Analysis. M.I.T. Naval Supersonic Laboratory, TR 360, August 1959.

8. Durgin, Frank H., Polutchko, Robert J., A Final Report on Part 1 Phase II of a Program of Experimental and Theoretical Research on the Use of Quasi-Steady Airloads in Aeroelastic Analysis. M.I.T. Naval Supersonic Laboratory TR 423, February 1960.

9. Durgin, Frank H., Bartlett, Charles, J., A Measurement of the Static Aeroelastic Deformation and Loading of a Wing in Supersonic Flow. M.I.T. Aerophysics Laboratory TR 19, March 1963.

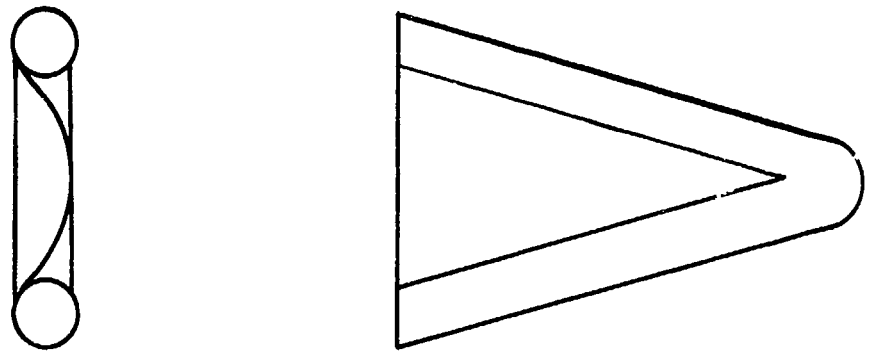

Cylinder - Sail - Hemisphere Construction

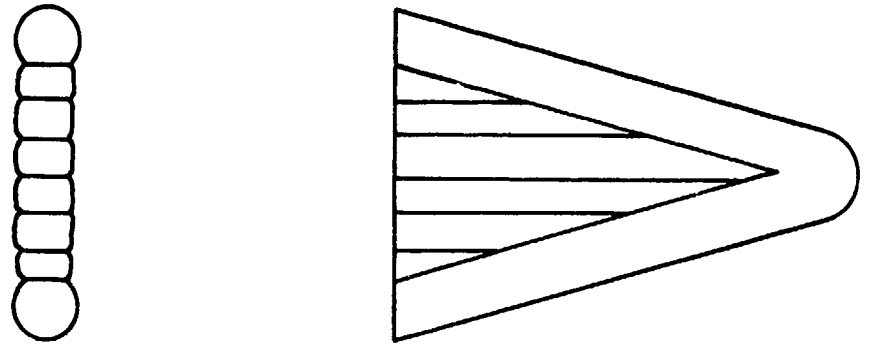

Tubular - Cylinder - Hemisphere Construction

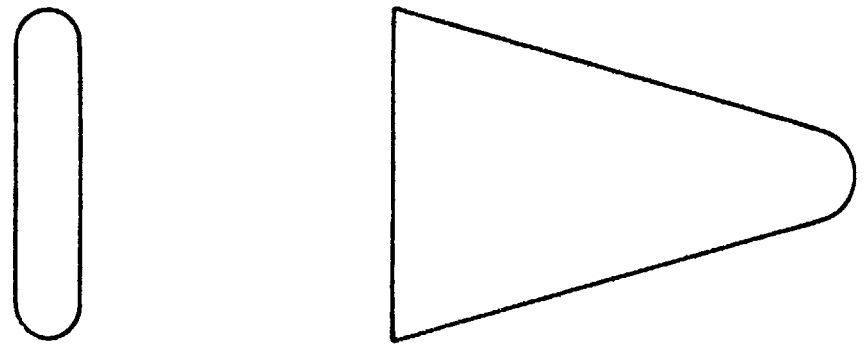

AIRMAT - Hemisphere Construction

FIGURE I. SKETCHES OF TYPICAL BLUNTED DELTA INFLATABLE VEHICLES, SHOWING TYPES OF CONSTRUCTION

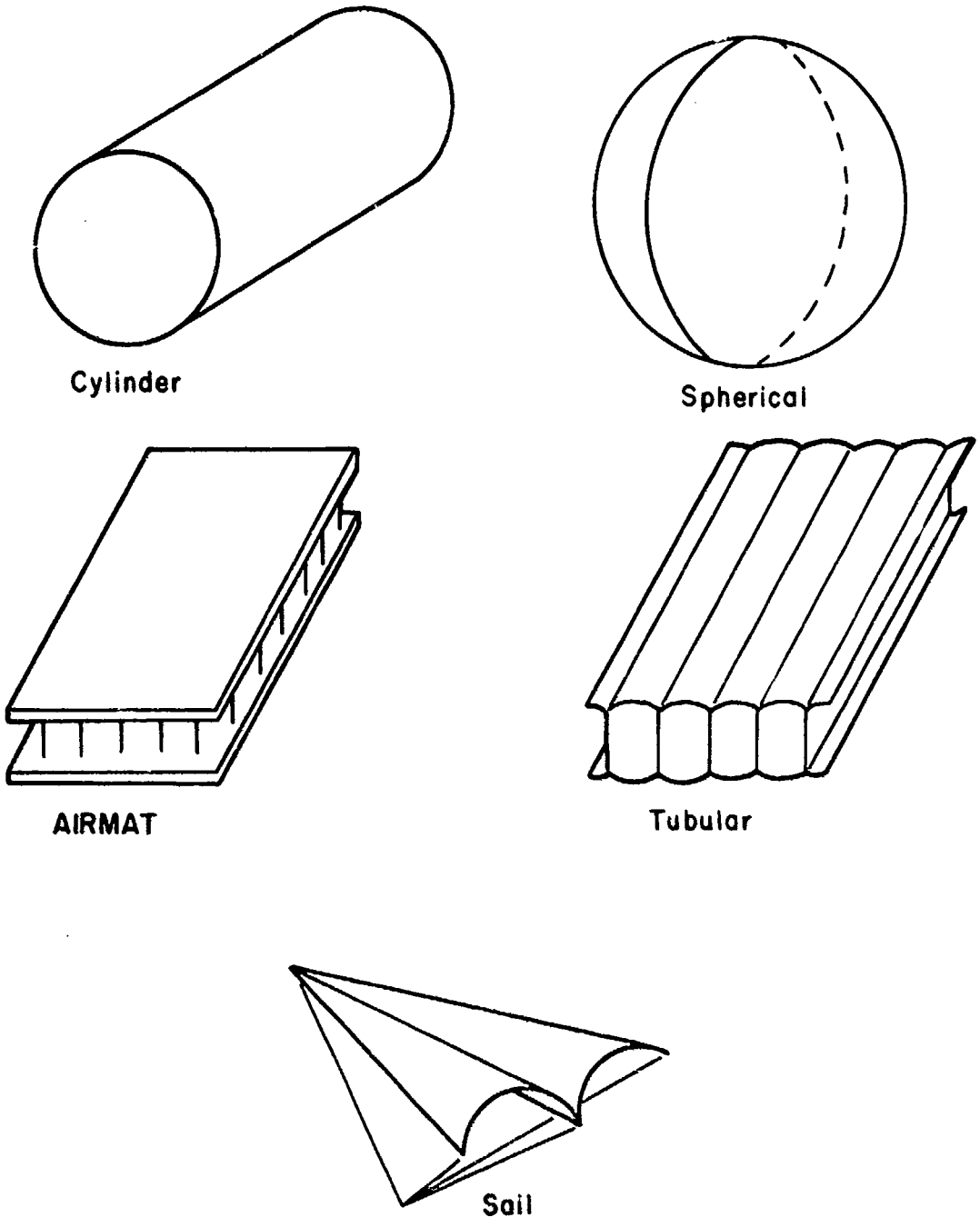

FIGURE 2. BASIC STRUCTURAL COMPONENTS OF INFLATABLE REENTRY VEHICLES

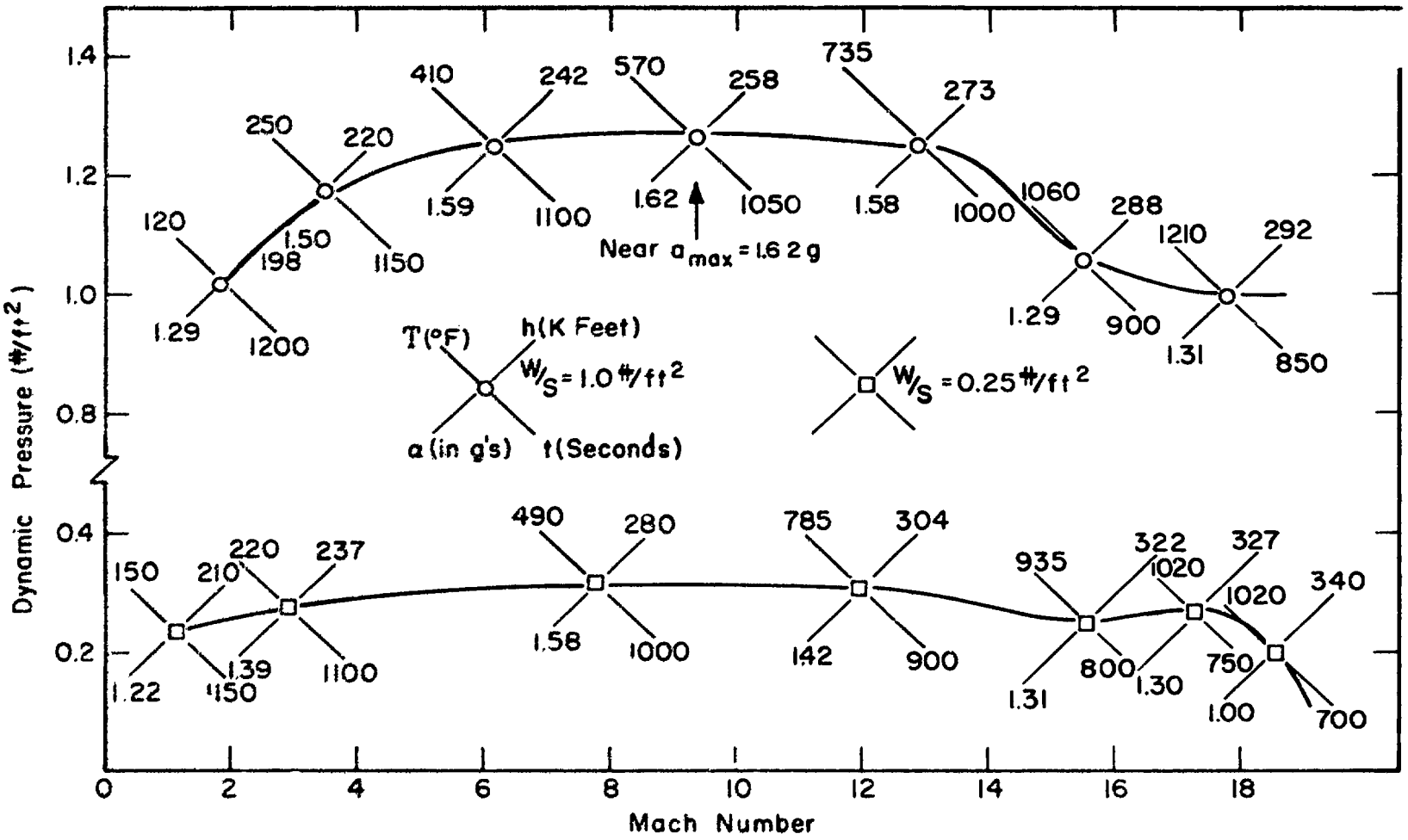

FIGURE 3. TYPICAL REENTRY TRAJECTORY FOR AN INFLATABLE VEHICLE
$\gamma_i = -1°$ (ENTRY ANGLE), $L/D = 0.577$, $h_0 = 400$ Kft

MIT Delta Model

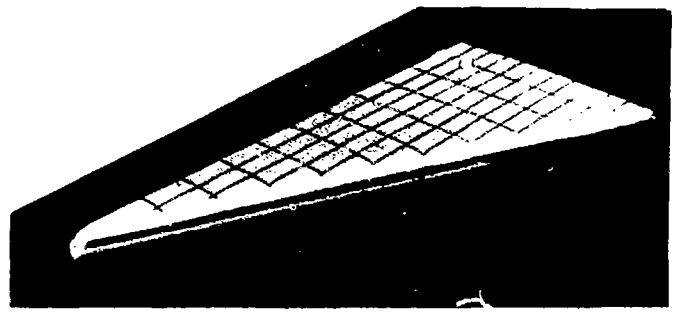

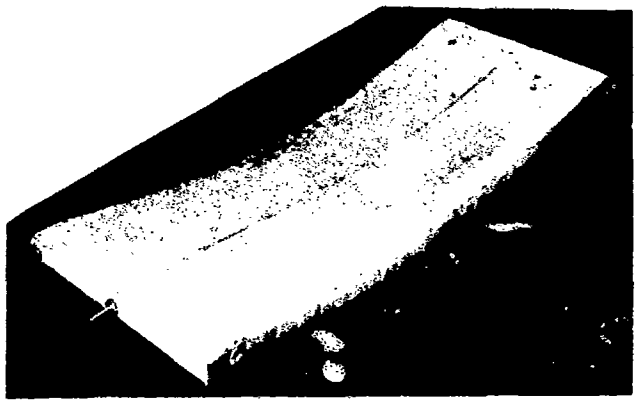

Rectangular Model with Built in Curvature

MIT Rectangular Model

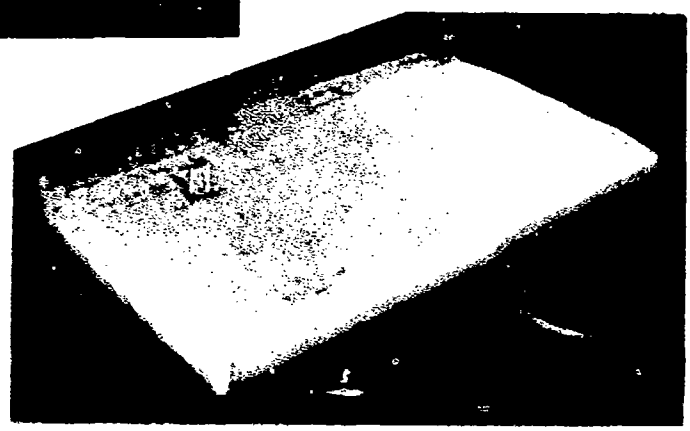

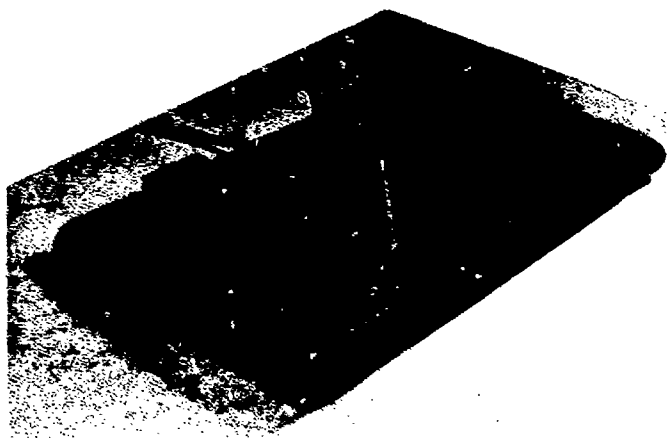

Goodyear Rectangular Model

FIGURE 4. SAMPLES OF INFLATABLE MODELS

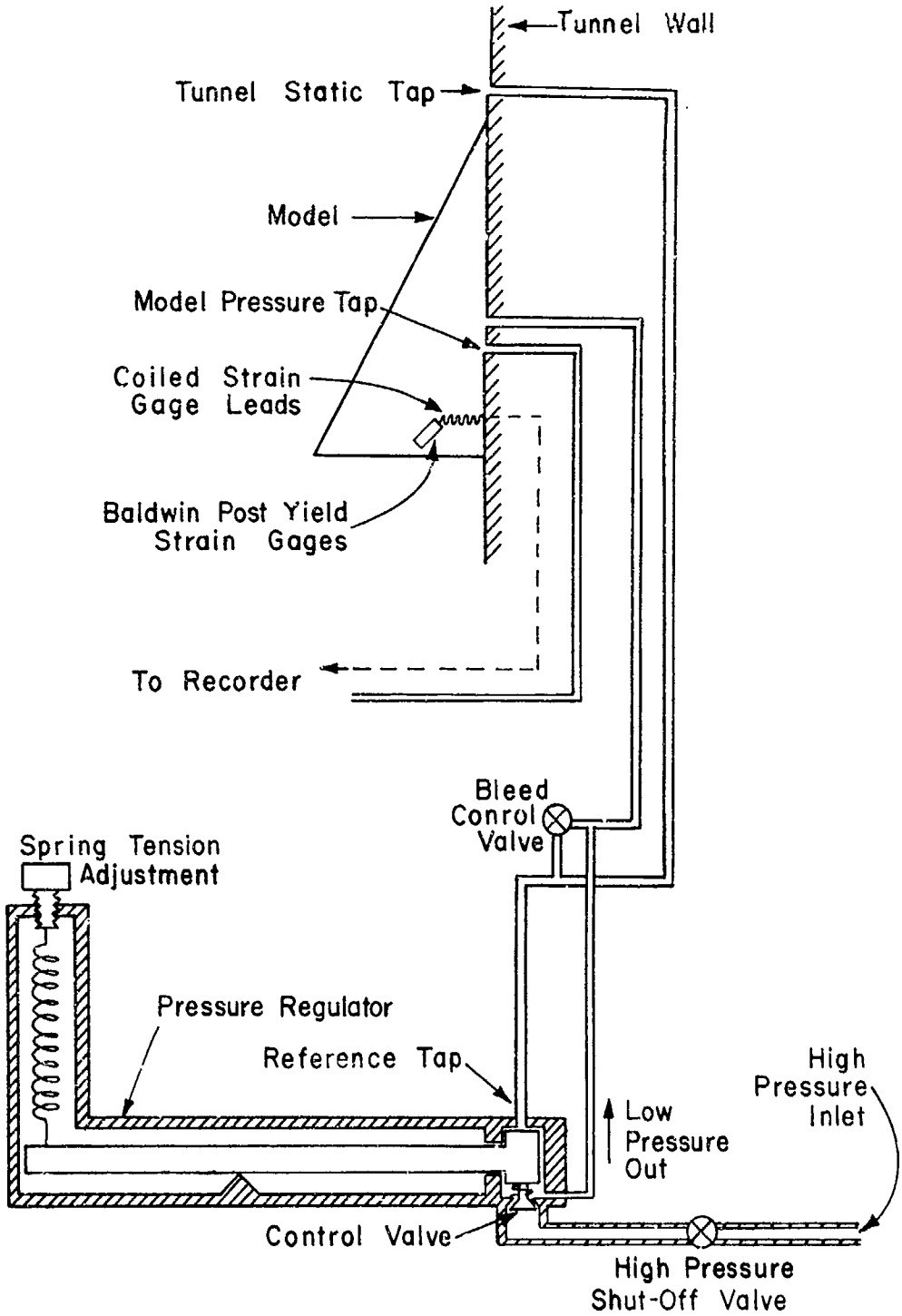

FIGURE 5. SCHEMATIC OF MODEL PRESSURE REGULATING SYSTEM & STRAIN GAGES.

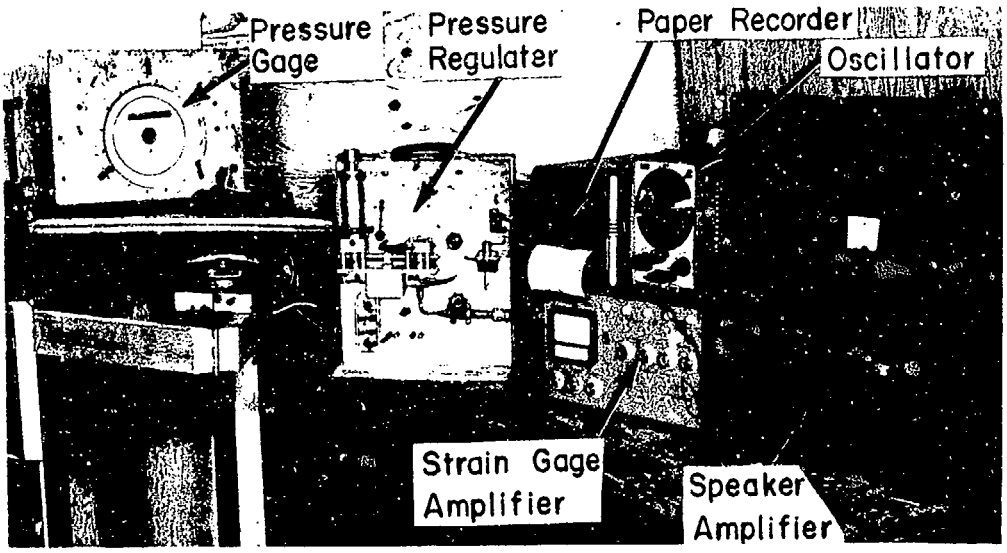

Complete System

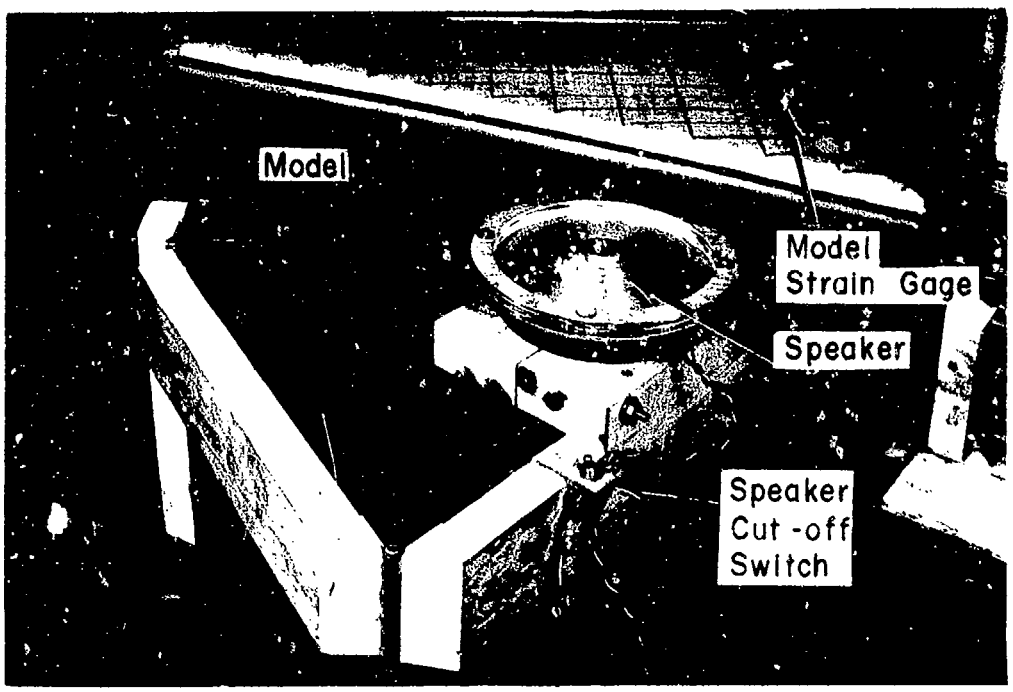

Close Up of Speaker & Model

FIGURE 6. EXCITATION SYSTEM USED FOR VIBRATION TESTS

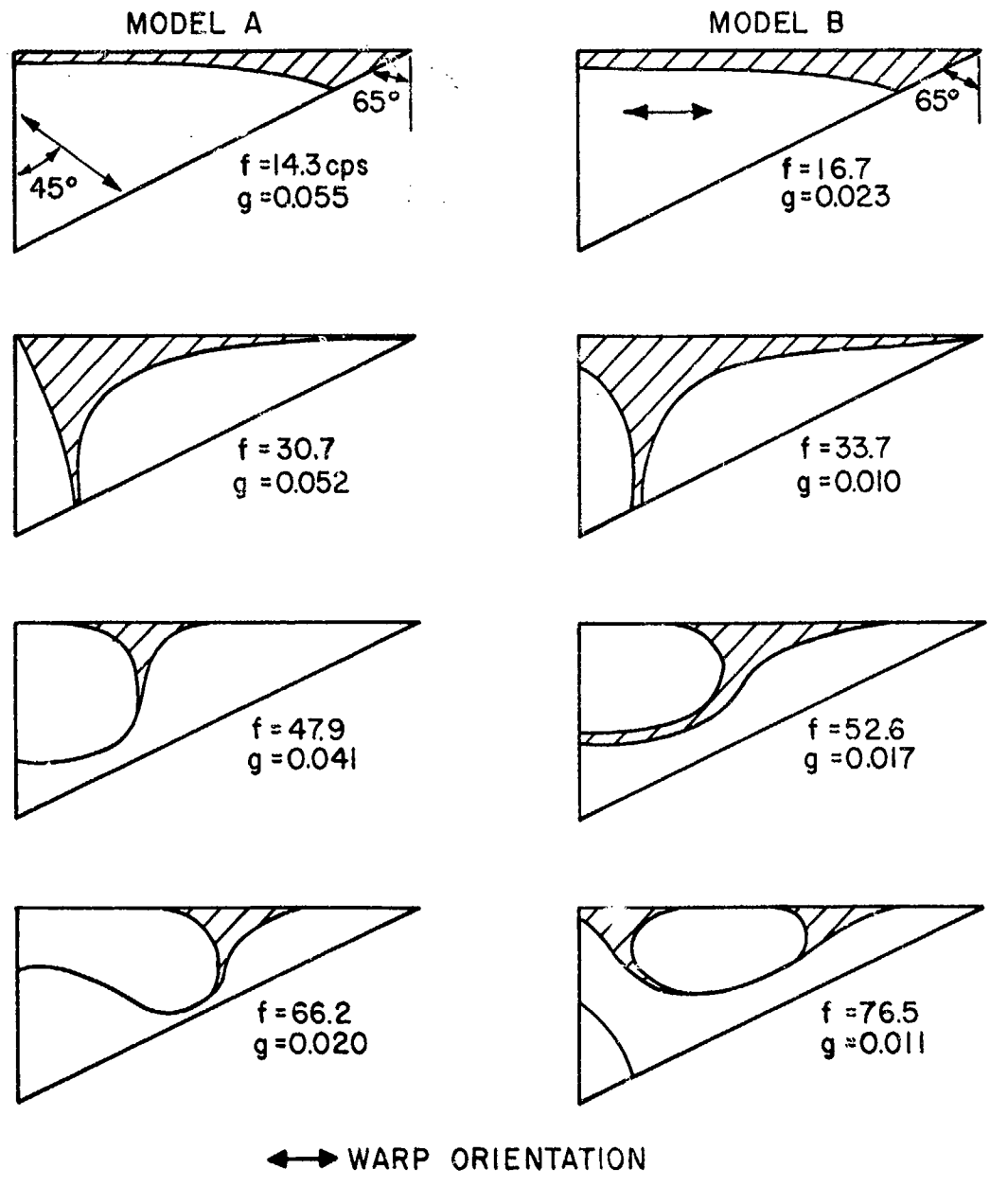

FIGURE 7. VIBRATION RESULTS FOR TWO, SINGLE-PLY, NYLON MODELS AT A MODEL PRESSURE DIFFERENTIAL OF 2 psig

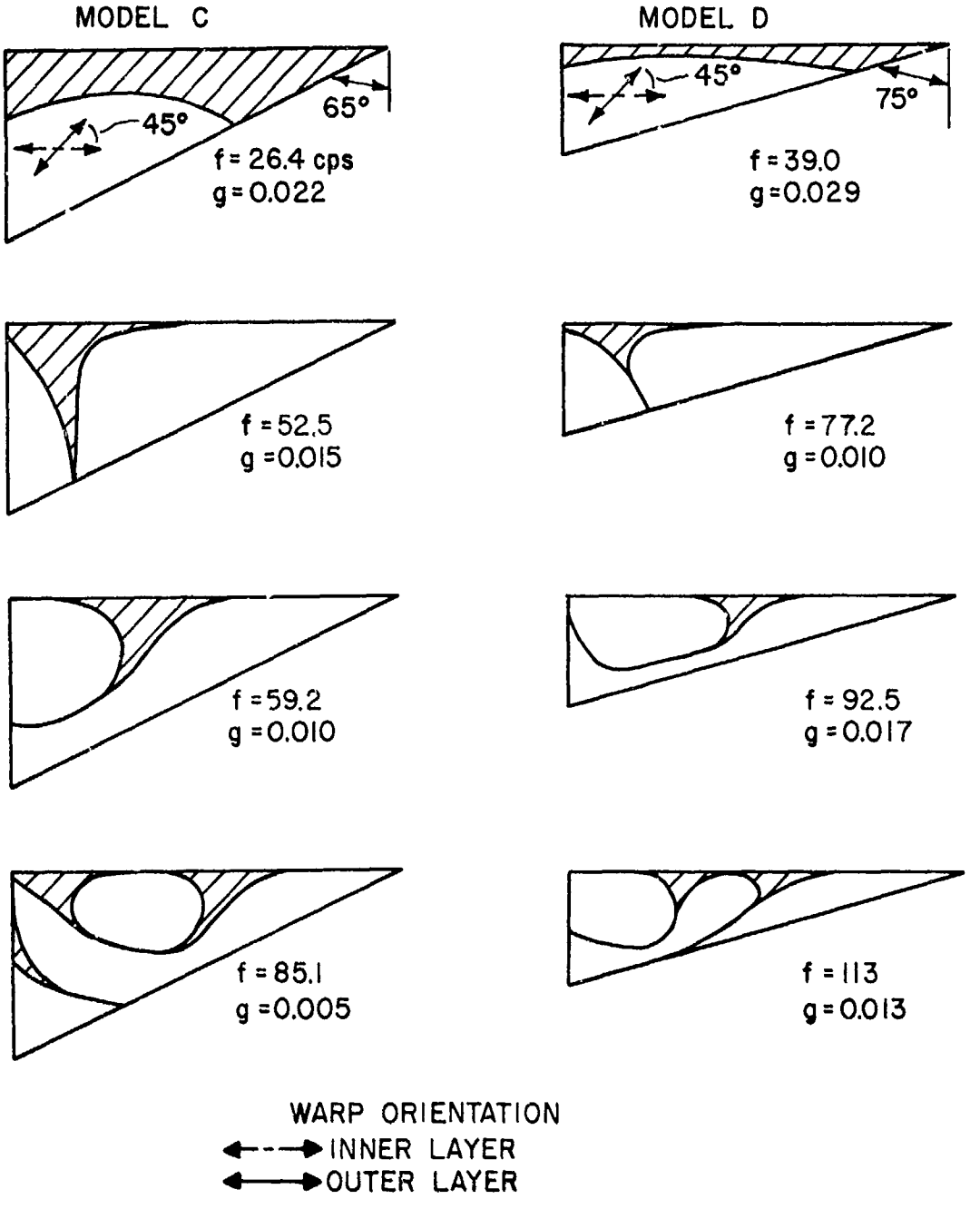

FIGURE 8. VIBRATION RESULTS FOR TWO, DOUBLE-PLY, DACRON MODELS AT A MODEL PRESSURE DIFFERENTIAL OF 2 psig

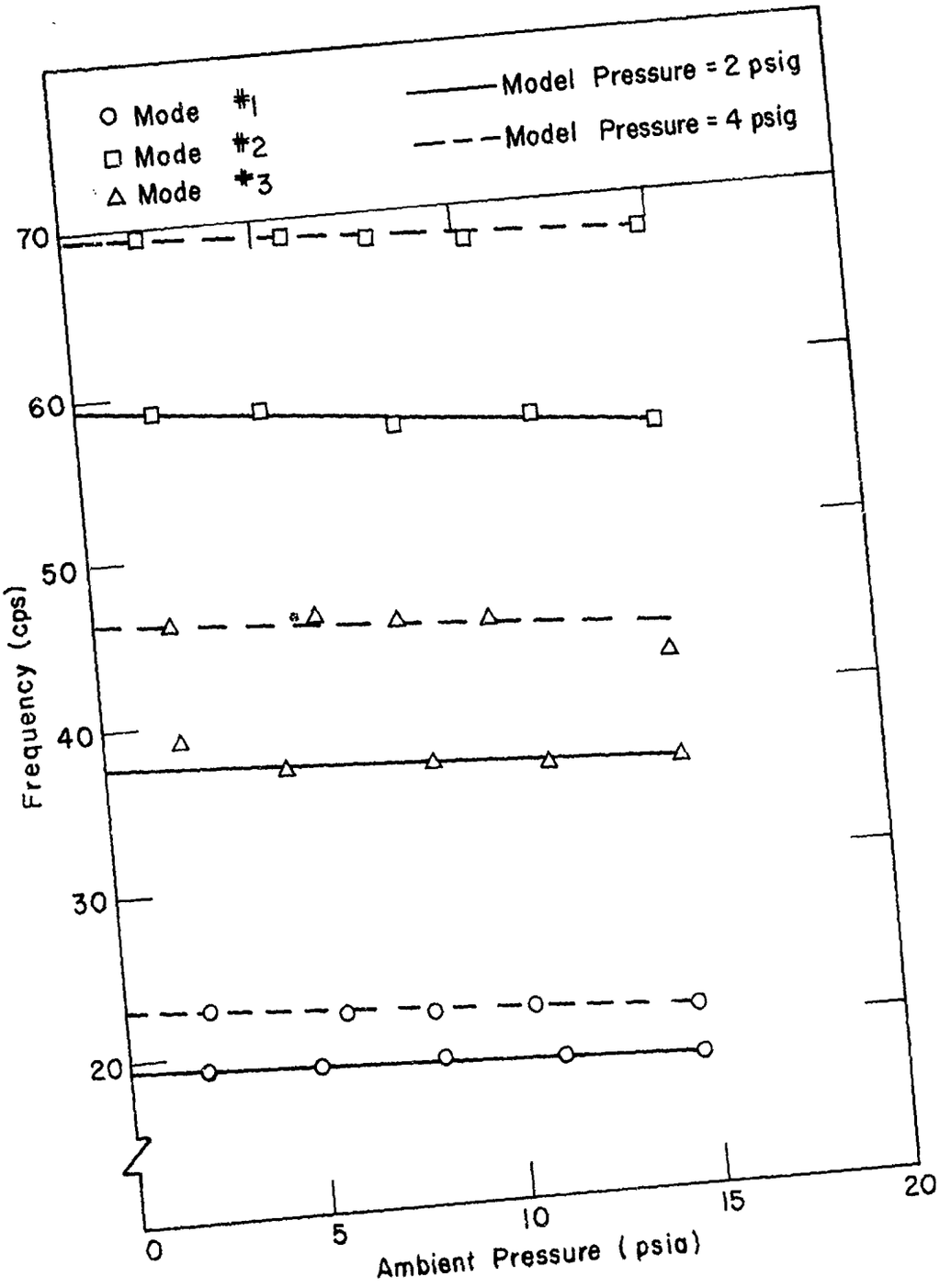

FIGURE 9. EFFECT OF AMBIENT PRESSURE ON FREQUENCIES OF FIRST THREE MODES OF MODEL E

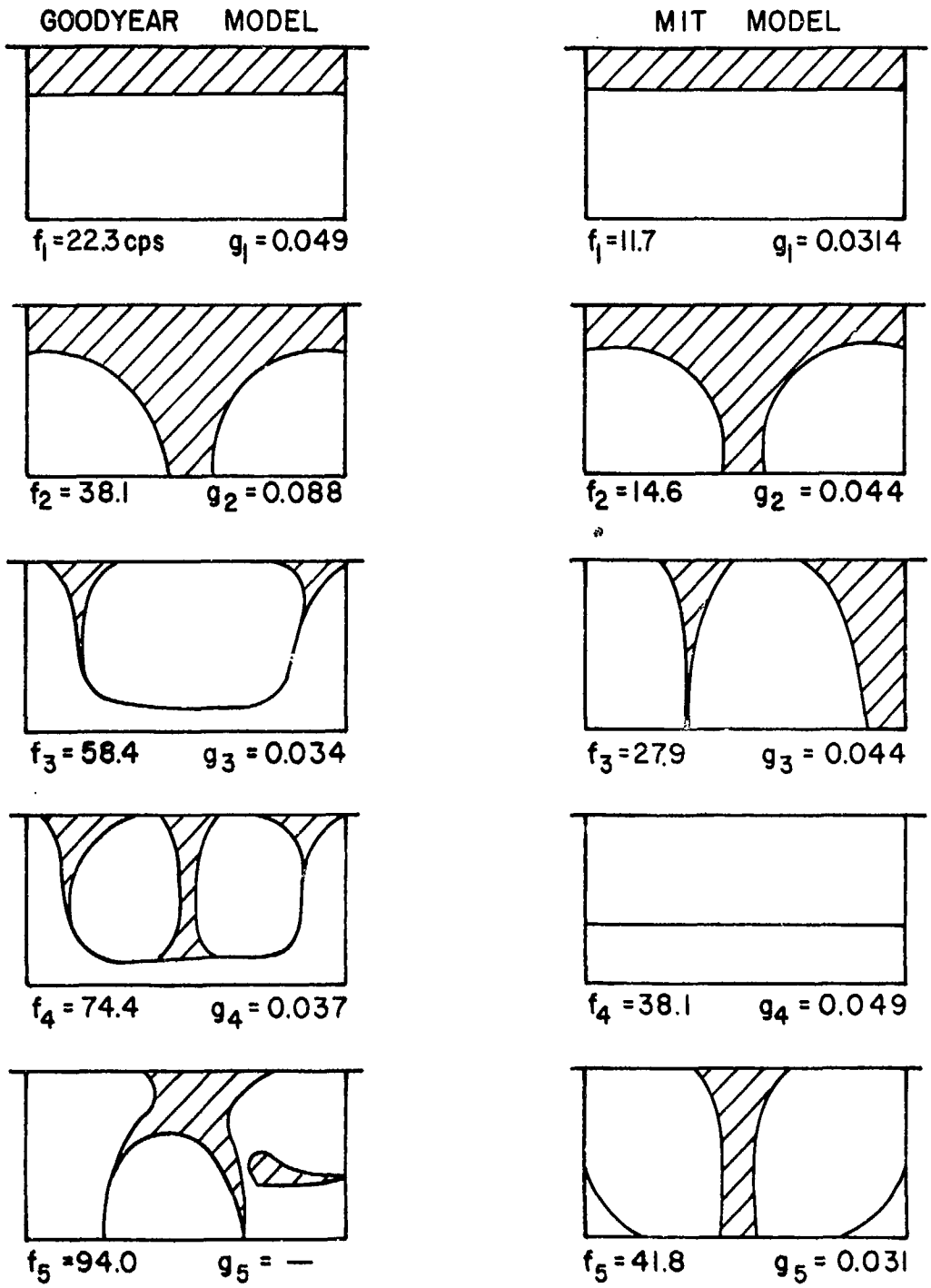

FIGURE 10. COMPARISON OF VIBRATION RESULTS FOR GOODYEAR AND MIT RECTANGULAR MODELS

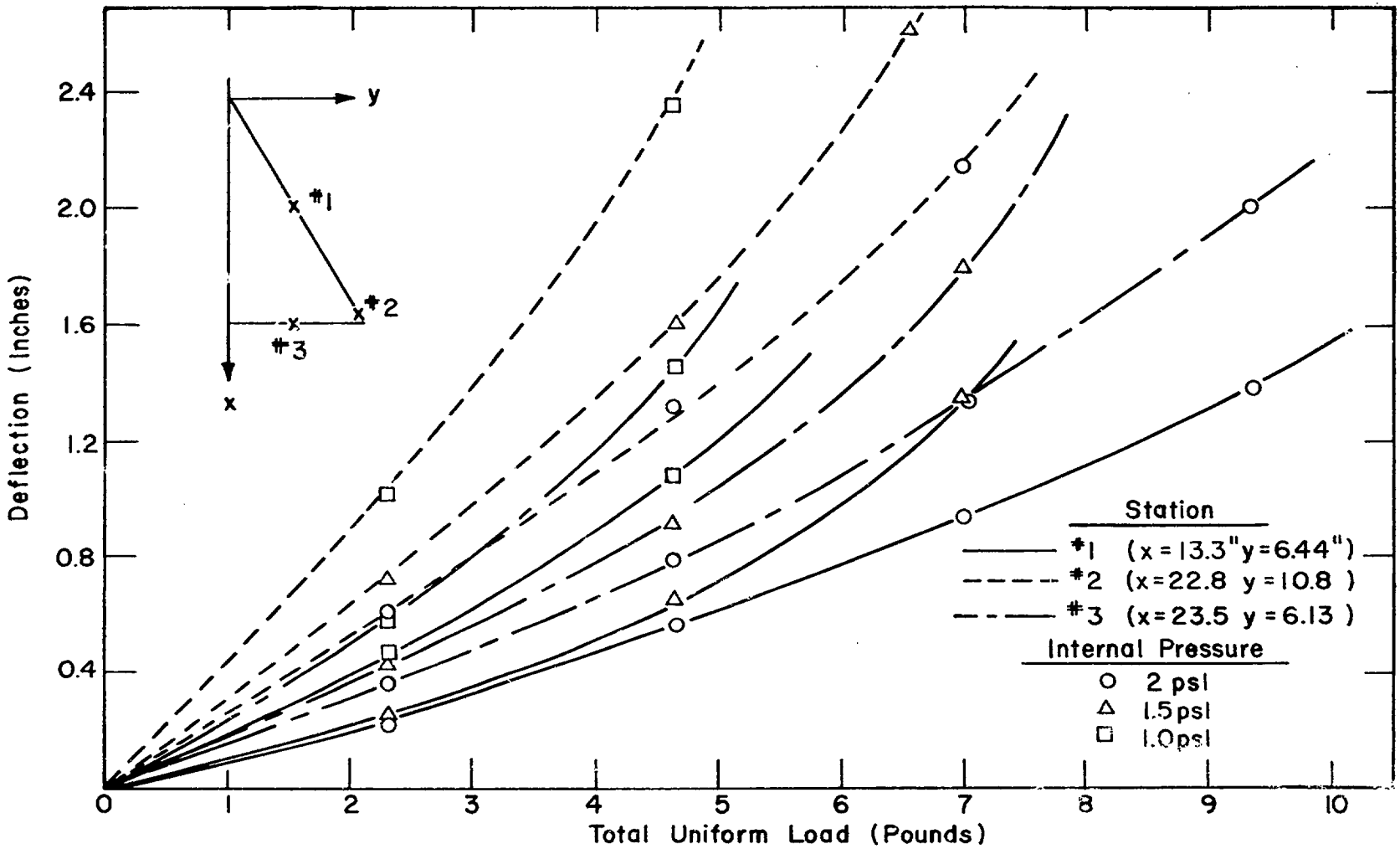

FIGURE 11. WING DEFLECTION VS UNIFORM LOAD FOR MODEL A.

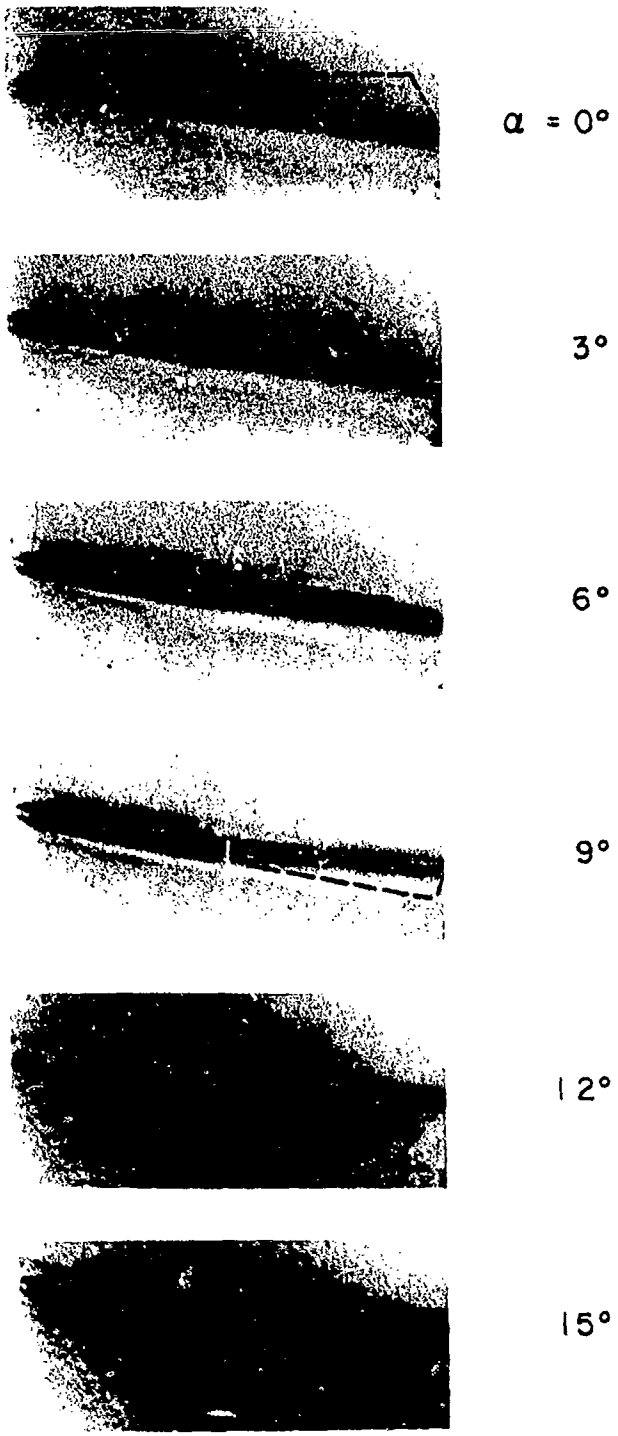

FIGURE 12. PHOTOGRAPHS SHOWING DEFLECTION OF MODEL B AT SEVERAL ANGLES OF ATTACK. MACH NUMBER = 5. PORTIONS OF ROOT AND TRAILING EDGES ARE INDICATED BY DOTTED LINE.

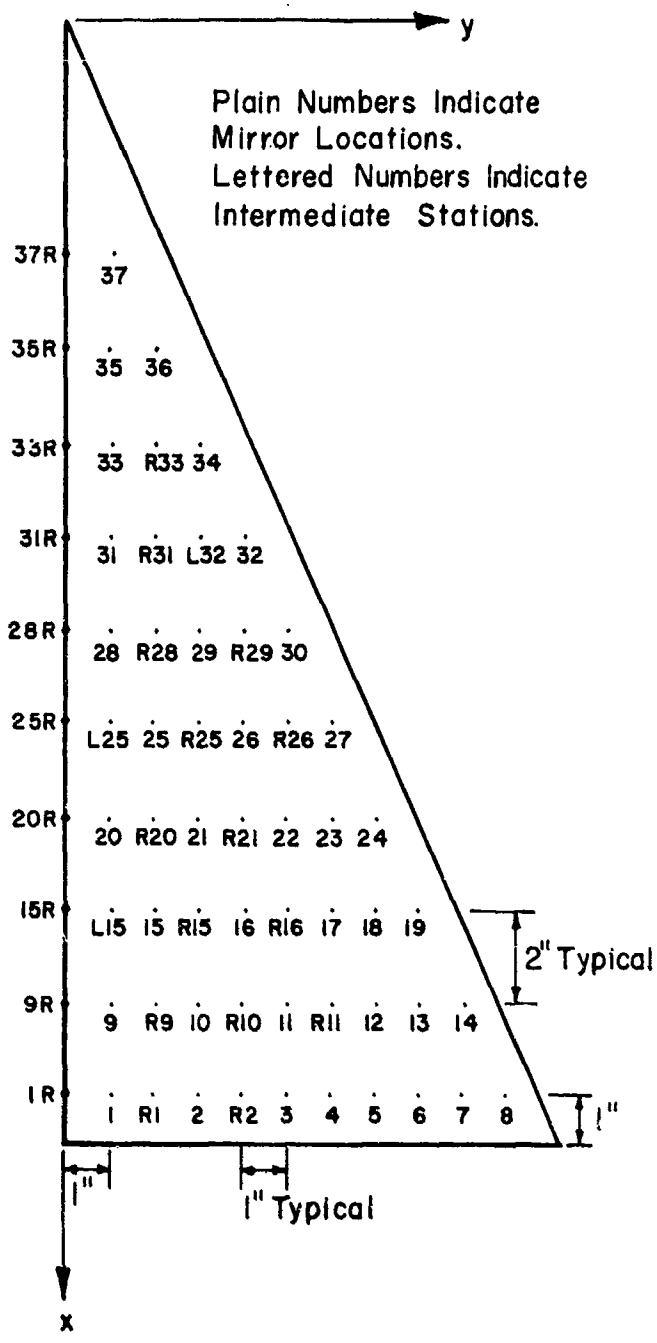

FIGURE 13. MIRROR STATIONS USED FOR DETERMINING VIBRATION MODE SHAPES OF MODEL B

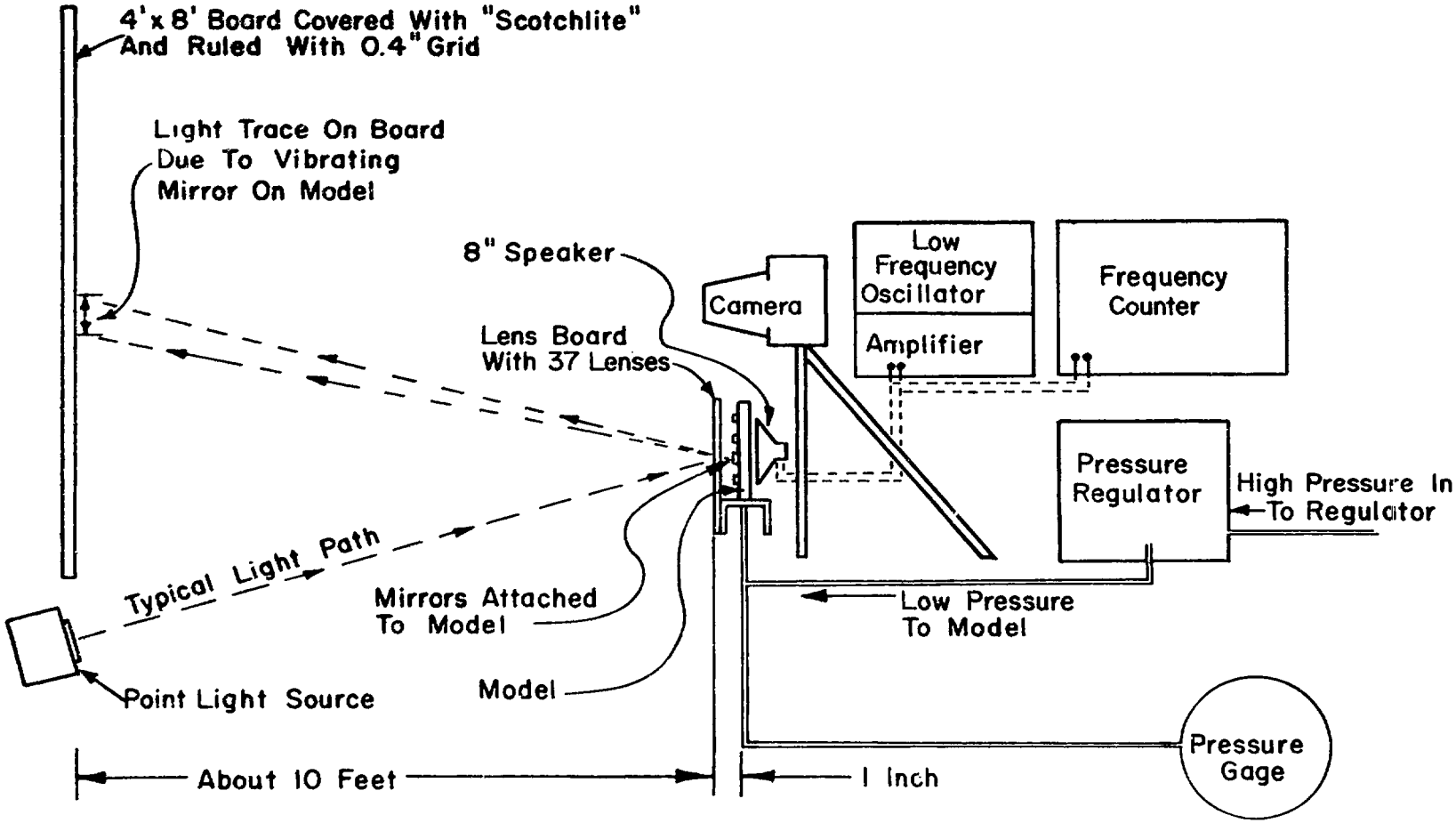

FIGURE 14. SCHEMATIC OF TEST SETUP FOR "MIRROR" TESTS

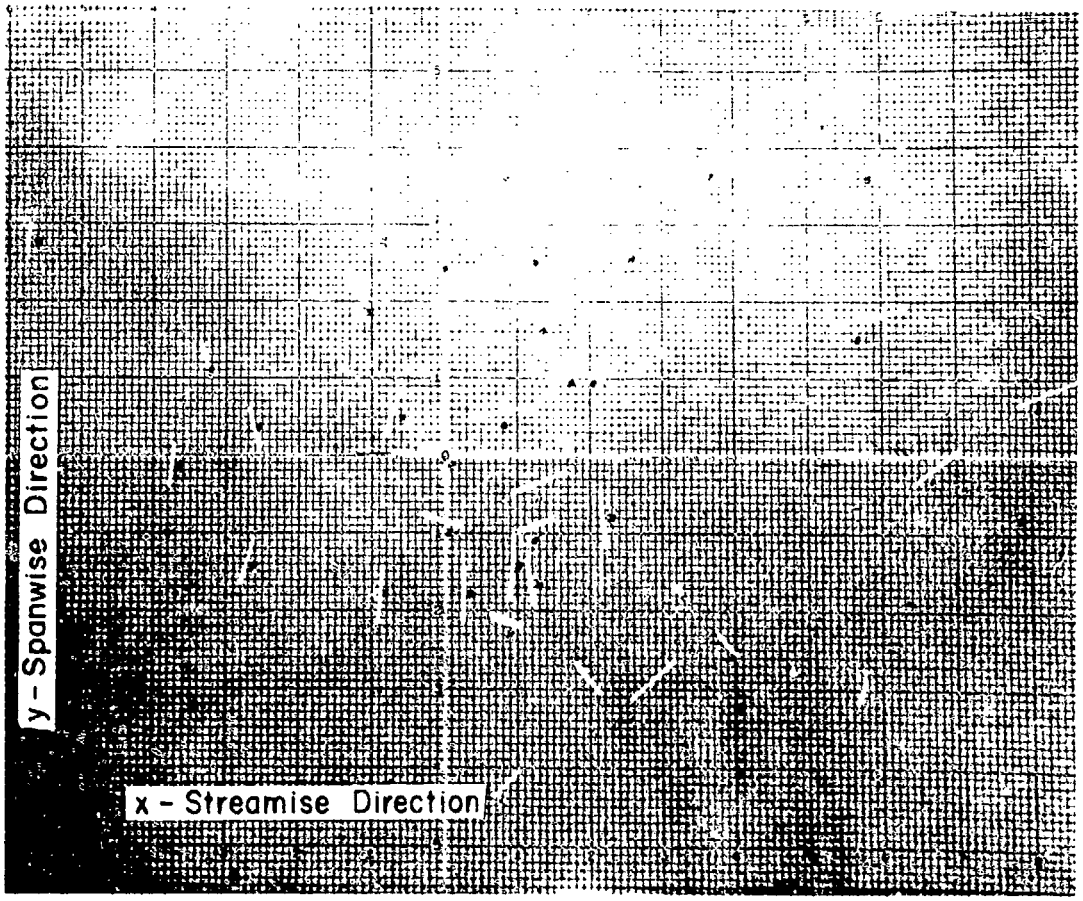

FIGURE 15. TYPICAL PHOTOGRAPH OF MODE SHAPE DATA. FOR DATA REDUCTION, A 15 X 24 IN. PRINT IS USED.

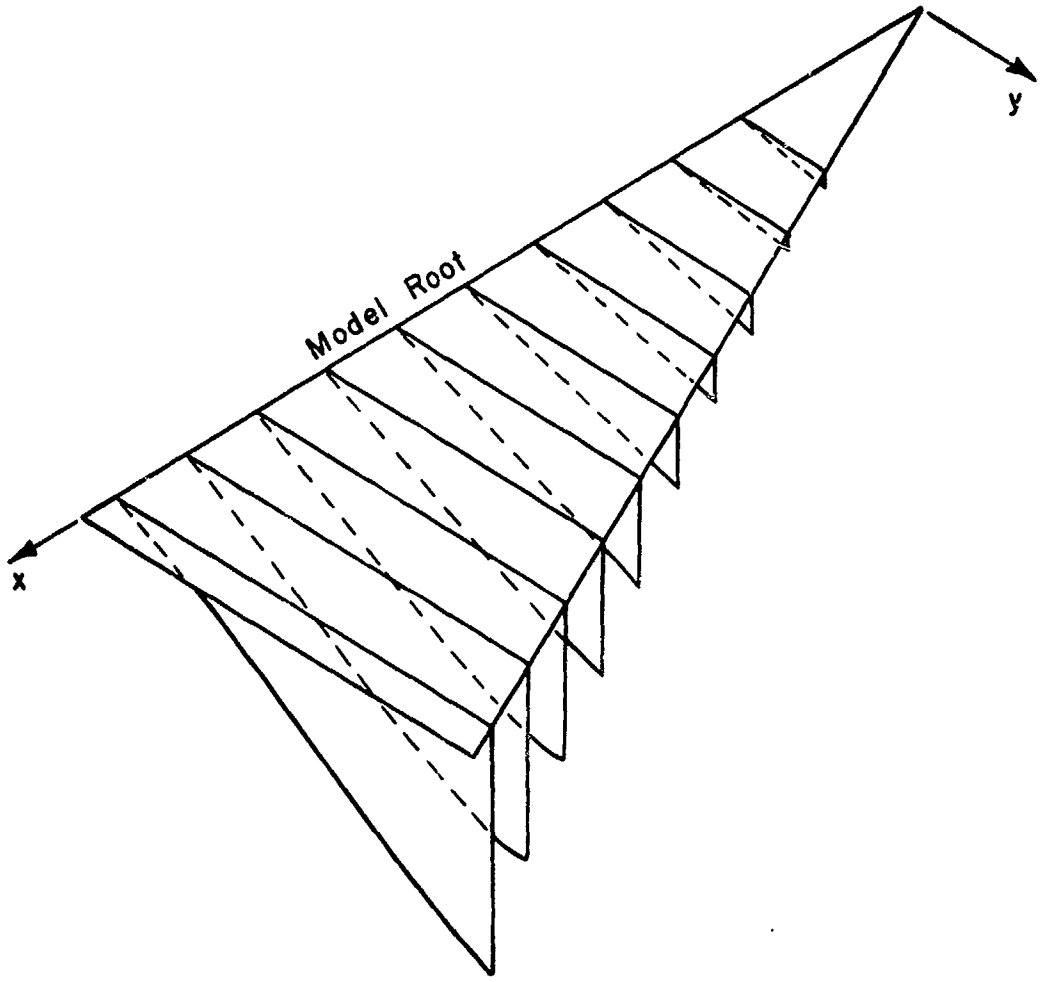

FIGURE 16. EXPERIMENTAL "MIRROR" MODE SHAPE FOR FIRST VIBRATION MODE OF MODEL B (MODEL PRESSURE = 2 psig)

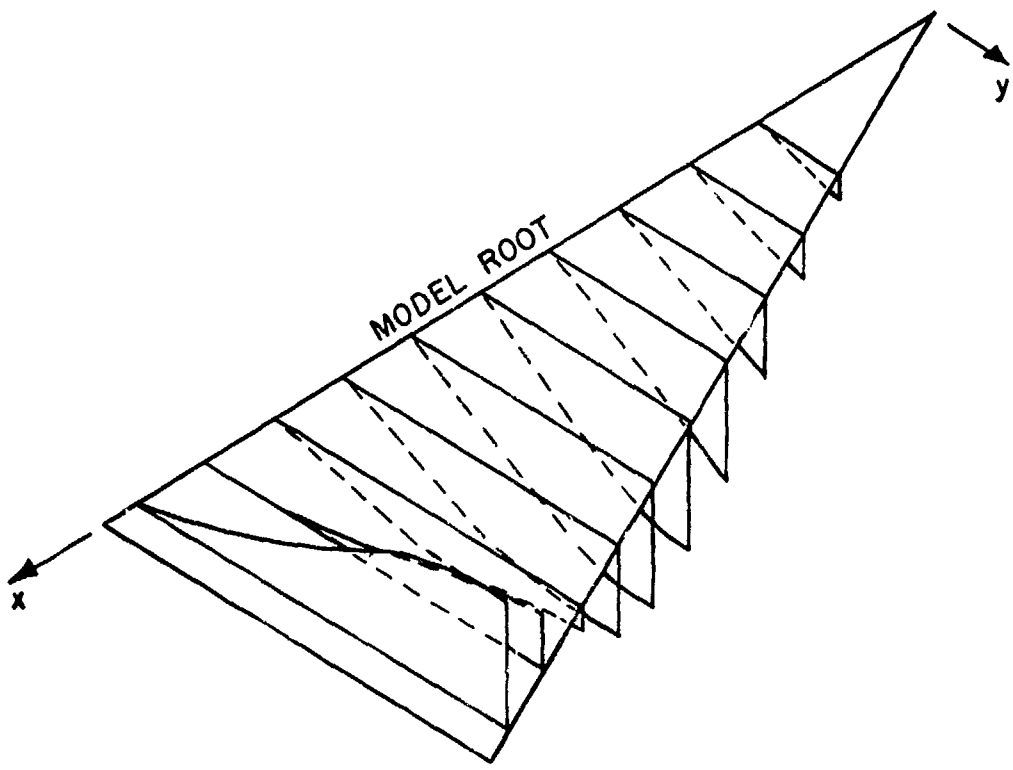

FIGURE 17. EXPERIMENTAL "MIRROR" MODE SHAPE FOR SECOND VIBRATION MODE OF MODEL B (MODEL PRESSURE = 2 p g)

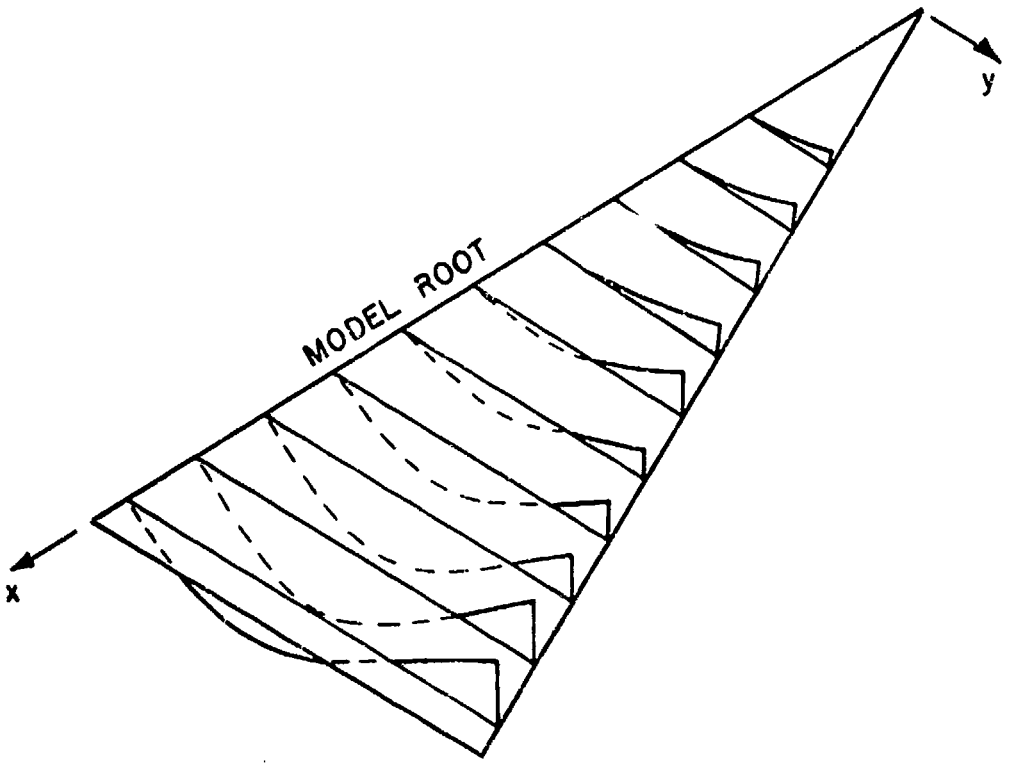

FIGURE 18. EXPERIMENTAL "MIRROR" MODE SHAPE FOR THIRD VIBRATION MODE OF MODEL B
(MODE PRESSURE = 2 psig)

SUPPORT SYSTEMS AND EXCITATION TECHNIQUES FOR DYNAMIC MODELS OF SPACE VEHICLE STRUCTURES

Robert W. Herr and Huey D. Carden

NASA Langley Research Center

ABSTRACT

This paper discusses several techniques for supporting and exciting dynamic models of space vehicle structures to study their dynamic properties such as natural frequencies, mode shapes, damping, and response. Particular attention is given to a unique support harness for vertical support of missile-like structures with minimum lateral restraint. Included in the discussion of vibration exciters is an air shaker which is particularly useful for excitation of the natural modes of light structures and those having thin skins such as encountered on dynamic models of space vehicles.

INTRODUCTION

The accurate experimental determination of the free-free lateral vibration modes of launch vehicles is complicated by the fact that during vibration testing, the vehicle must be restrained against gravity. A massless restraint added to the vehicle anywhere other than at a nodal point will increase the natural frequencies. This increase in the natural frequencies is dependent on both the location and the magnitude of the restraint.

Obviously, the ideal location for the restraint is at the nodal points. From a practical standpoint, this is often not feasible; particularly when the vehicle is liquid fueled and must be orientated vertically. In this case, the only part of the structure capable of supporting the mass of the vehicle is usually at the base where the engine thrust is transmitted to the structure.

One of the primary worries of the dynamics engineer is just how much his suspension system is affecting the natural frequencies. In many cases he worries needlessly and in others, he worries too little. One of the objectives of this paper is to give the dynamics engineer some guidelines as to the importance of restraints imposed by various support techniques.

Also of concern to the dynamicist during the testing and experimental investigations is whether the means of applying the desired force to the structure alters or significantly influences the mass and stiffness properties of the structure. That is, does the exciting and measuring apparatus change and distort the quantities he seeks to measure.

In the cases where large, massive, or relatively rigid structures such as full-scale boosters or space vehicles are being tested, the added mass is quite often only a few percent of the local structure mass and its effects can be neglected. Of the many types of large vibration machines utilized for such tests the most commonly used are the electrodynamic and hydraulic. Since the effects of these exciters on larger structures are generally small or can be minimized through the use of flexible couplings and by placement of the attachment point near nodal locations, only brief and limited comments on these machines will be included.

On the other hand, as the size of the structure decreases the problem and headache of distortion and influence on the structure of the exciter becomes, in many instances, so large that the data in these cases are questionable or cannot be obtained. This emphasizes the necessity for using equipment of a scale appropriate to the structure to be tested. This is particularly true for tests on flexible panels, light, thin-walled conical or cylindrical structures, or small dynamic models of space vehicles. Somewhat more detailed discussions of excitation equipment useful in these areas will be indicated with particular attention given to the description, use, and principle of operation of an air-jet shaker.

SUSPENSION SYSTEMS

General

In general, the most convenient type of spring for the restraint of a launch vehicle during lateral vibration testing is the gravity spring. In this type of suspension, the test vehicle is supported by a cable or cables attached to a rigid overhead framework. The direction of vibration excitation is normal to the plane of the cables.

For a replica model of a vehicle and its cable suspension, dynamic similarity is obtained if the ratio of the pendulum to structural frequencies remains constant. Thus,

$$\left(\frac{\omega_p}{\omega}\right)^2 \propto \frac{g/L}{\omega^2} = \frac{g}{\omega^2 L} = C$$

where ω_p is the pendulum frequency; ω, a structural frequency; g, the acceleration; and L, a characteristic length. Since the characteristic frequency of a model which possesses replica proportions is inversely proportional to its size, it follows that $gL = C$. Hence, for a 1/5-scale vehicle and cable suspension, dynamic similarity is achieved only by testing in a 5g gravity field.

Since the objective of scale model vibration tests is not usually to duplicate the results of full-scale shake tests, but rather to determine, as accurately as possible, the free-free vibration frequencies, the logical approach is to conduct the tests in a 1g gravity field utilizing a suspension system which has a minimum effect on the natural frequencies.

In order to give some insight into the magnitude of the effects of various suspension systems on the free-free frequencies, the resonant frequencies of uniform beams restrained as indicated in figure 1 were determined experimentally and/or calculated and compared with the free-free frequencies. The effects of the parameter $g/\omega_{ff}^2 L$ were also determined by utilizing uniform beams of varying length or stiffness. ω_{ff} is the first free-free frequency in radians per second and L the length of the beam.

The physical significance of the value of $g/\omega_{ff}^2 L$ is not readily apparent. For replica models, $g/\omega_{ff}^2 L$ is proportional to the size of the vehicle. For a given size vehicle, the parameter is proportional to its mass and inversely proportional to its stiffness. With cognizance of the fact that the stiffness and mass distributions of launch vehicles are seldom uniform, the approximate values of $g/\omega_{ff}^2 L$ for some launch vehicles are: Vanguard, 0.0008; Redstone, 0.0011; Saturn SA-1, 0.0011; Titan, 0.0017; and Saturn 5, 0.0020. A proposed version of Nova would have a relatively large value for $g/\omega_{ff}^2 L$ of 0.0045. The uniform beams utilized in the experiments covered the range of $g/\omega_{ff}^2 L$ up to approximately 0.010 which represents an extremely flexible beam.

Perhaps a better feel for the significance of $g/\omega_{ff}^2 L$ is afforded by the fact that for a horizontally supported beam, the static deflection relative to its length is proportional to $g/\omega_{ff}^2 L$. For a horizontal cantilever, the static deflection at the tip divided by the length of the beam is equal to $62.8\left(g/\omega_{ff}^2 L\right)$. Thus, the static deflection curves for horizontal cantilevers would appear as depicted below.

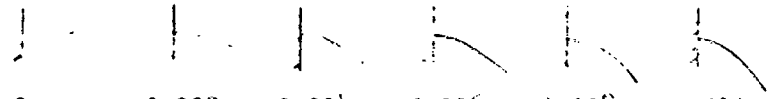

$$\frac{g}{\omega_{ff}^2 L}$$

Two-Cable Horizontal Suspension

If the structure of the vehicle is rugged enough to withstand the bending moments, the suspension system depicted in figure 1(a) is probably the most desirable due to its simplicity. If the support cables are located at nodal points, their effect on the free-free frequencies are negligible.

It is not always feasible to support a vehicle at the nodal points. The increase in the resonant frequency then depends on the location of the support points, the length of the cables, and the value of the parameter $g/\omega_{ff}^2 L$.

In figure 2, the increase in the first natural free-free frequency, indicated by the ratio ω/ω_{ff}, is plotted as a function of the ratio of the distance to the support points from the ends of the beam to the beam length, S/L, for cable lengths of 1/8, 1/4, and 1/2 the length of the beam and for beams having values of $g/\omega_{ff}^2 L$ of 0.00202, 0.00402, and 0.00605. The free-free reference frequency ω_{ff} used in this figure, as well as in all other experimental figures pertaining to uniform beams, is the experimental frequency for a value of S/L of 0.224.

For the range of parameters investigated, the data of figure 2 show that the increase in frequency due to the suspension is approximately proportional to $g/\omega_{ff}^2 L$ and inversely proportional to the cable length l/L.

For the most flexible beam $\left(\frac{g}{\omega_{ff}^2 L} = 0.00605\right)$ supported on short cables $(l/L = 1/8)$, the location of the cable attachment points can be as much as 8 percent of the length of the beam from the nodal points without exceeding an error of 1 percent in the measurement of the free-free first natural frequency. For a more practical value of $\frac{g}{\omega_{ff}^2 L} = 0.002$, the short cables may be located anywhere within 14 percent of the length of the beam from the nodal points without exceeding a 1-percent error.

It is therefore apparent that for cable lengths greater than 1/8 the beam length and for practical values of $\frac{g}{\omega_{ff}^2 L} < 0.002$, there is no need to go to great pains to support the beam precisely at the nodal points. Although not shown here, the cable attachment location has even less effect on the higher free-free modes.

Multicable Horizontal Suspension

In cases where it is not feasible to support a vehicle horizontally at two points due to excessive static bending moments or localized stresses, it may be practical to support it on many cables distributed along the length of the beam as indicated in figure 1(b). If an infinite number of cables are assumed, an elastic lateral foundation results, the modulus of which is K. The frequency equation is

$$\omega^2 = \frac{K}{m} + \omega_{ff}^2$$

where

m = total mass of beam

$K = mg/l$

l = length of cables

Substituting the value of K into the frequency equation and rearranging

$$\frac{\omega}{\omega_{ff}} = \sqrt{\left(\frac{g}{\omega_{ff}^2 L}\right)\left(\frac{L}{l}\right) + 1}$$

In figure 3 the increase in frequency ω/ω_{ff} due to the cable restraint is plotted as a function of $g/\omega_{ff}^2 L$ for cable lengths of $l/L = 1/16$, $1/8$, $1/4$, and $1/2$.

As with the two-cable suspension, the data show that the effect on the first free-free frequency is approximately proportional to $g/\omega_{ff}^2 L$ and inversely proportional to the cable length.

For cable lengths greater than 1/8 of the beam length and for the common range of $\frac{g}{\omega_{ff}^2 L} < 0.002$, the error is less than 1 percent. For corresponding cable lengths and values of $\frac{g}{\omega_{ff}^2 L}$, the error is approximately one-quarter of the error obtained when the beam is supported by a cable at each end.

In order that the tension in the many cables be properly distributed, it is usually advisable to use elastic shock cords in place of relatively inelastic cables. One experimental data point for which elastic shock cords were utilized is shown in figure 3 and it agrees very well with the theoretical result.

One-Cable Vertical Suspension

Other than its simplicity, the one-cable vertical suspension depicted in figure 1(c) has little to offer. As is the case with liquid-fueled launch vehicles, it is frequently necessary to orientate a test vehicle vertically

during vibration tests. It is a rare vehicle, however, that can withstand the rigors of being hung by its nose.

Despite their lack of general usefulness, the effects of the one-cable suspension on the free-free vibration frequencies are interesting; especially when compared to the results utilizing the two-cable vertical suspension illustrated in figure 1(e).

In figure 4(a) the increase in the first free-free frequency ω/ω_{ff} is plotted as a function of cable length L/l for four beams for which the values of $g/\omega_{ff}^2 L$ are 0.00291, 0.00631, 0.0114, and 0.0255.

It should be noted that increasing cable lengths are denoted by decreasing values of L/l so that $L/l = 0$ represents an infinitely long cable or zero lateral restraint.

The most interesting feature of this plot is that when the curves are extrapolated to a value of $L/l = 0$, there is still a substantial increase in the natural frequency over the free-free frequency. This increase in frequency can be attributed to the tension in the beam.

In figure 4(b), the curves of figure 4(a) have been cross-plotted to show the increase in the natural frequency as a function of $g/\omega_{ff}^2 L$ for relative cable lengths l/L of 1/8, 1/4, 1/2, 1, and ∞.

It can be seen that for cable lengths greater than one-quarter the length of the beam, the tension in the beam has a greater effect on the natural frequency than does the cable restraint.

Vertical Orientation With Restraint at Base

An often used type of restraint for shake tests of liquid-fueled launch vehicles is illustrated in figure 1(d). In this system, all of the pitch and lateral restraint is concentrated at the base of the vehicle. Any of several types of restraining springs may be used, such as a series of coil springs spaced around the periphery at the base, pneumatic bags, or a combination of vertical cables to provide lateral restraint and torsion springs to provide pitch restraint.

No matter what type of restraint is used, a minimum spring constant of mgL_{cg}, must be provided in the pitch direction to restrain a vehicle from toppling. L_{cg} as used here is the distance from the base of the vehicle up to its center of gravity.

If a variation in $g/\omega_{ff}^2 L$ is assumed to represent a change in the gravitational field g, acting on a given vehicle, it is seen that the minimum pitch spring restraint required at the base mgL_{cg} is proportional to

$g/\omega_{ff}^2 L$. It is thus apparent that as the gravitational attraction on a given vehicle is increased, the minimum spring restraint must also be increased resulting in a larger effect on the natural frequencies. Similarly, for replica models tested in a constant gravitational field, the greater the size of the vehicle, the greater will be the effect of the minimum spring restraint on the natural frequencies.

The effect that this minimum pitch restraint has on the first free-free frequency has been computed and is presented in figure 5. In this analysis the lateral restraint was assumed to be zero. Although it is realized that these restraints are impractical from an experimental standpoint, the results indicate the absolute minimum increase in the natural frequencies that can be obtained with this type of restraint.

Figure 5 shows that for a uniform beam having a value of $g/\omega_{ff}^2 L$ corresponding to that of Titan (0.002), the minimum pitch restraint mgL_{cg} $\left(\text{denoted by } \omega_p/\omega_{ff} = 0\right)$ increases the first natural frequency by 4 percent; a relatively large increase when compared to the results obtained utilizing horizontal suspensions with reasonable cable lengths.

When the pitch restraint at the base is increased to provide a finite rigid-body pitch frequency (ω_p), the effect on the first flexural frequency can become quite pronounced. Although a ratio of rigid-body frequency to first free-free frequency of 1/5 may intuitively seem like a soft suspension, it is noted that for a value of $\frac{g}{\omega_{ff}^2 L} = 0.002$ the increase in frequency amounts to 12 percent.

Two-Cable Vertical Suspension

A method of supporting a launch vehicle in a vertical position with a minimum of rigid-body restraint but yet safe from the standpoint of toppling has been conceived by the senior author and is depicted in figure 6. The weight of the vehicle is carried by two support cables attached to the bottom of the vehicle. Stability is provided by two restraint cables tied between the support cables and the periphery of the vehicle at some point e_1 above the vehicle's center of gravity. This support system has essentially two degrees of freedom in the plane normal to the cables; translation as a pendulum and pitching.

In terms of the dimensions of figure 6, the total pitching moment acting on the vehicle (including the moments due to gravity) can be shown to be

$$\frac{M}{W} = \frac{\theta e\left(\frac{a-d}{f} + \frac{c-d}{e}\right)}{2\sqrt{\left(\frac{b-d}{2e_1}\right)^2 - \theta^2}} - \theta e\left(1 + \frac{e_1}{f}\right)$$

Taking the derivative of the moment expression with respect to θ gives the effective spring constant of the system in pitch.

$$\frac{K}{W} = \frac{dM}{Wd\theta} = \frac{e\left(\frac{a-d}{f} + \frac{c-d}{e}\right)\left(\frac{b-d}{2e_1}\right)^2}{2\left[\left(\frac{b-d}{2e_1}\right)^2 - \theta^2\right]^{3/2}} - e\left(1 + \frac{e_1}{f}\right)$$

Solving the spring constant equation for a when K and θ are set equal to zero results in an expression defining the cable separation necessary to maintain the vehicle in a vertical altitude with zero pitch frequency.

$$a = f\left(\frac{b-d}{e_1} - \frac{c-d}{e}\right) + b = a_0$$

when $a < a_0$, the vehicle will topple a few degrees to a stable position and when $a > a_0$ it will possess a frequency in pitch >0.

Experimental verification of the critical cable separation distance is shown in figure 7. For a given location of the restraining cables e the support cables were progressively separated until the vehicle would just stand erect. Correlation of the experimental results with theory shows excellent agreement.

In figure 8(a), the pitch moments imposed by the harness relative to the unstable gravity moments $\frac{M_{harness}}{mgL_{cg}\theta}$ have been plotted as a function of the angle of tilt for three values of the relative cable separation a/a_0 for each of two restraining cable locations. The center curves in each case is for $a/a_0 = 1$ which results in a zero pitch frequency when $\theta = 0$. When $a/a_0 < 1$ the vehicle will tilt over until the restraining moment imposed by the harness exceeds the moment due to gravity.

The effective spring constant of the harness in pitch relative to the gravity spring $\frac{K_{harness}}{mgL_{cg}}$ has been plotted in figure 8(b) as a function of the angle of tilt. As may be observed, the effective spring is decidedly nonlinear.

In practice, this harness is extremely simple to use. It is not necessary, as it is with many types of suspension systems, to alter the stiffness of the restraint whenever the fuel load is varied over a wide range. The only adjustment that need be made is the support cable separation as the center of gravity changes.

For large liquid-fueled vehicles it may be necessary to distribute the concentrated loads imposed on the structure at the cable attachment points by means of a lightweight truss. Radial loads applied to the structure due to the tension in the restraining cables may be alleviated by replacing the restraining cables with two parallel cables as illustrated in the sketch.

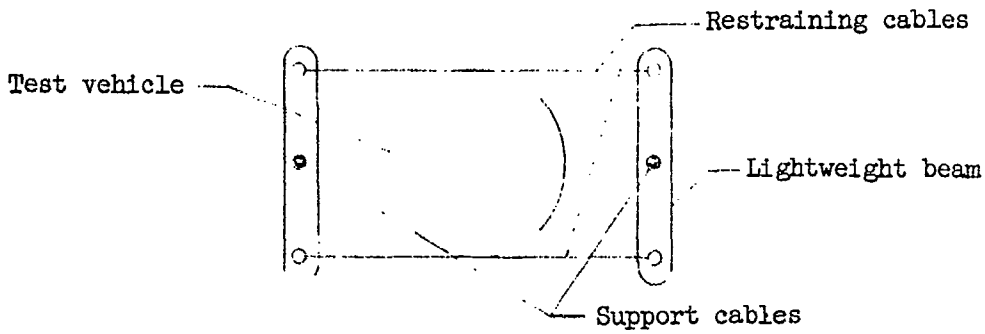

The fact that the rigid-body pitch frequency can be readily adjusted to zero does not imply that the harness has no effect on the free-free frequencies. There is a small amount of lateral restraint at the cable attachment points. In order to establish the effects of these restraints, vibration tests were made of three uniform beams suspended in the harness depicted in figure 9. The effect of the harness on the free-free frequencies will vary with the lengths of the support and restraining cables used but the trends and the magnitude of the effects caused by a particular harness are of interest.

The effects of the location of the restraining cables are indicated in figure 9(a) in which the first natural frequency, relative to the minimum faired frequency, is plotted as a function of restraining cable location l/L. As expected, the location of the restraining cables does have an effect on the natural frequency, but the magnitude of the effect is exceedingly small. For the beam with a value of $\frac{g}{\omega_{ff}^2 L} = 0.002$, the maximum change in frequency attributable to a variation of the restraining cable location is 0.3 percent; a negligible effect.

In figure 9(b), the data to figure 9(a) have been plotted relative to the first free-free frequency. Rather than increasing the natural frequency, as a massless restraint must, the figure shows that natural frequencies of a uniform beam suspended in this harness are appreciably less than the free-free frequencies. Just as tension in a beam increases its flexural frequencies (fig. 4), compression decreases the natural frequencies. Although this effect is small for present-day launch vehicles $\left(\text{perhaps 2 percent at } \frac{g}{\omega_{ff}^2 L} = 0.002\right)$, the important point is that the effects due to the harness restraint are far less, even when the restraining cables are located at the tip of the vehicle.

As mentioned previously, most launch vehicles are not uniform beams. They are, in general, stiffer and more massive at their base resulting in relatively large vibration amplitudes at the tip. Intuitively, it would seem that, compared to a uniform beam, the frequencies of such a vehicle would be affected less by compression due to gravity and relatively more due to a restraint near the tip. In view of such a possibility, the natural frequencies of two nonuniform beams mounted in a harness were obtained and are compared to their free-free frequencies in figure 10. The upper and lower half of each beam was uniform, with the upper half having one-half the mass and one-eighth the stiffness of the lower half. Values of $g/\omega_{ff}^2 L$ for the two beams were 0.002 and 0.006. Although it is not possible to separate experimentally the effects due to restraint and compression, when the results are compared to the uniform beam results of figure 9(b), it can be said that the compression effects are less and/or the restraint effects are greater for the stepped beam. The compression effects still outweigh the restraint effects since the natural frequencies in the harness are lower than the free-free frequencies.

The variation in the natural frequencies associated with a change in location of the restraining cables can be seen to be somewhat greater for the stepped beam than for the uniform beam.

It is not to be implied from these results that the compression effects will in all cases outweigh the restraining effects of the harness.

Although there is no good reason to use a support cable separation greater than the optimum a_0, the results shown in figure 11 indicate that the cable separation is not critical even for an extremely flexible uniform beam. In this figure, the natural frequency is plotted as a function of the cable separation relative to the optimum cable separation a_0. ω_{ref} is the natural frequency obtained with the restraining cables at the nodal point and the support cables separated the optimum distance. The results indicate that when the restraining cables are located at the tip, the effect of increasing the cable separation by 50 percent is about the same order of magnitude as is obtained by moving the restraining cables from the nodal point to the tip.

In figure 12 the effects of the harness type of suspension on the first two free-free frequencies are compared with results obtained when the beams were suspended on one cable attached at the tip as in figure 1(c). The interesting aspect of this figure is the near symmetry of the data about the abscissa. Assuming that tension and compression of uniform beams have equal but opposite effects on the natural frequencies for the range of parameters investigated, the near symmetry of the data indicates a comparatively small effect of the restraint of either suspension system. It is apparent that both suspension systems affect the first free-free frequencies to a much greater extent than the second free-free frequencies. It may also be observed that for the harness suspension, moving the restraining cables from the second mode nodal point to the tip of the beam has an extremely small effect.

With respect to the relatively large increase in frequencies predicted when all of the pitch restraint was applied at the base of the vehicle (fig. 5), it should be noted that these results would have been alleviated

somewhat had compression effects been included in the analysis. It is believed, however, that in this case the compression effects are relatively small compared to the effects attributable to the restraint.

VIBRATION EXCITERS

Electrodynamic Vibration Machines

As the name implies, the electrodynamic vibration machine derives its name from the method of force generation. The force is produced electrodynamically from the interaction between a current flow in a driver coil and the intense magnetic field which cuts the coil.

In utilizing these exciters for exploratory vibration studies, the electrodynamic shaker has the advantages of relatively wide frequency ranges, and availability of random and sinusoidal vibrations or a combination of both. In multiple shaker applications, in-phase and out-of-phase control between the various machines can be accomplished. Although these shakers are versatile and widely used, they have the disadvantage in that it is difficult to provide adequate power and displacement at the low frequencies commonly encountered in large-scale vehicle studies. In their use on smaller scale structures, care must be exercised to minimize the effects of the attachment between the test vehicle and the shaker coil in order to avoid significant influences on the structural responses.

Hydraulic Vibration Machines

The hydraulic vibration machine transforms power in the form of a high-pressure flow of fluid from a pump to a reciprocating motion of the table of the vibration machine. High-pressure fluid delivered to one side of the piston in the actuator and then to the other side, forces the actuator to execute a reciprocating motion.

Some of the disadvantages found in the electrodynamic shaker have been overcome in the hydraulic shaker. For example, the hydraulic shaker is capable of generating large forces and large displacements or strokes at frequencies as low as desired. Relative to the forces attainable, the hydraulic machine is small and lightweight which can be advantageous in certain applications. However, this fact also requires a rigid connection to firm ground or a large massive base to anchor the machine in place which can be inconvenient and difficult in many cases. Among some of the other disadvantages are: secondary resonances, seepage, leakage, nonlinearities, necessity of clean hydraulic fluid, and poor high-frequency performance.

Electromagnetic Vibration Machines

In many applications where the limiting conditions of the other types of vibration testing machines cannot be circumvented, electromagnetic exciters have been successfully utilized. The electromagnetic vibration machine generates a vibratory force which is transmitted to the table, giving it motion;

the force is derived from magnetic attraction or repulsion due to intensity or direction changes of a magnetic flux linking several flux-carrying members.

The simplest form of an electromagnetic vibration exciter, called an unbalanced-force type, consists of an electromagnetic core with a single winding and an armature. Both the core and armature are laminated from magnetic-core material. This simple device, which is generally user-built, has several desirable and useful features. It has been useful in driving structures for resonant mode testing where the structure supplies the position force and where the distortion of the generated force is of little consequence. In these cases, the armature can be bolted or cemented to the test structure at any appropriate location. In the tests for which no addition of mass to the structure can be tolerated, the device can be used without the armature. In these instances, if the structure is magnetic, it acts as the armature and supplies the magnetic circuit. For materials that are conducting but nonmagnetic, eddy currents are generated which produce electrodynamic forces. This shaker is particularly adaptable to the synchronized use of several units for resonant testing of light dynamic wind-tunnel models and the like. Its usable frequency range can easily extend from a few cycles per second to several hundred cycles per second. Among the undesirable features of this exciter are the presence of a large constant attractive force in addition to the vibratory force, and the nonlinearity of the resulting force of the device.

Air-Jet Vibration Exciters

Although our Vibration and Dynamics Laboratory at Langley has a wide variety of electrodynamic and hydraulic shaking equipment, one of the most popular vibration exciters, where low force outputs are sufficient, is the air-jet shaker. As the name implies, an air-jet shaker derives its driving force from the kinetic energy of a stream of high-velocity air, periodically impinging upon the test specimen. Proper modulation of the airflow results in a sinusoidal force output.

The chief assets of the air-jet shaker are that no mass is added to the test specimen and it is extremely simple to use since no mechanical connections to the test specimen are required. Its major liability in the past has been the rapid decrease of force output with increasing frequency. This loss of available force at high frequencies has been due to the internal valving used to modulate the airflow. Most of the potential energy was being wasted in accelerating and decelerating the air column during each cycle.

This problem can be overcome simply by external interruption of the air jet as depicted in figure 13. The stream of high-velocity air which impinges upon the test specimen, exits from the nozzle at a constant velocity and pressure. The airstream is then deflected periodically by a motor-driven notched disk. A nearly sinusoidal force may be obtained by use of a diamond-shaped nozzle, the length of which is equal to the length of the notch in the interrupter disk.

All of the air-jet shakers built in our shop have a single nozzle which results in an unbalanced force. This unbalance is of little consequence for most vibration tests but for some highly damped and flexible test specimens or nonlinear systems it is desirable to have a balanced force input. In such

cases, the air jet may be counterbalanced by directing a steady stream of air onto the opposite side of the test specimen. If the second nozzle has an area equal to one-half the area of the shaker nozzle and is fed from the same pressure line, the net force on the specimen will be closely balanced.

The magnitude of the oscillating force can be controlled by a pressure or flow regulating valve in the air supply line. The maximum peak-to-peak force output when the jet is directed at a large flat plate is approximately 1.3 AP, where A is the area of the nozzle and P the line pressure. The area of the nozzles on present Langley shakers is 0.025 sq in. (0.1-in. x 0.5-in. diamond) which results in a maximum peak-to-peak force of $3\frac{1}{4}$ pounds when connected to a 100-psi air-supply line. Although this may seem to be a rather small force as vibration exciters go, it has been found to be more than ample to excite the natural modes of panels, thin-wall cylinders, and numerous wind-tunnel models. Since the added mass effects of the air jet are negligible, the driving force may be applied at the point of maximum vibratory amplitude thus transmitting a maximum amount of energy to the test vehicle. The force of a given shaker can be doubled by directing the air jet into a lightweight pelton bucket attached to the test specimen in order to effect a 180° change in the airstream direction.

Larger force outputs may, of course, be obtained by the use of larger nozzles and higher pressure lines but the jet noise soon becomes intolerable and may well distort the output of piezoelectric-type pickups.

As previously indicated, one of the major shortcomings of the electrodynamic and electromagnetic exciters often encountered is the limited stroke or travel which they impose. The air-jet exciter, in this respect, however, permits very large, unrestrained amplitudes of oscillations. This asset of the air-jet shaker can be illustrated with the aid of figure 14. Shown in the figure is the force coefficient as a function of the plate distance for various size plates, where the force coefficient is the ratio of the force exerted on the plate to the product of nozzle area times the line pressure. The significant point to be made here is that for sufficiently large air-jet impingement areas, there is no appreciable drop in the excitation force even at very large distances. The nozzle used in these experiments was a 0.1-inch x 0.5-inch diamond.

The complexity of the motor-speed control depends upon the use for which the shaker is intended. In applications where accurate control of the frequency is not required, variation of the voltage to an electric motor may be satisfactory. The best all-around speed control that we have tried consists of a small (1/75 hp) synchronous motor driving the interrupter disk through a commercially available variable-speed friction drive. Since the torque required to drive the interrupter disk is very small, there is essentially no slippage in the variable-speed friction drive. The frequency range of our present units covers the range from 0 to 900 cps. A counter, geared to the speed control crank, indicates the frequency directly in cycles per second.

In summing up, it can be said that this type of air-jet shaker exhibits the following assets which make it a valuable tool in dynamic model testing: it is extremely convenient to use since no attachment to the test specimen is required; it is essentially massless; its available force can be calibrated statically and is constant with frequency; the force transmitted to the

structure is independent of frequency and motion of the structure, simplifying control and giving repeatability even with nonlinear structures; and its cost is relatively low.

The chief liabilities of the air-jet shaker are the noise associated with large force outputs and the difficulties encountered in multiple shaker applications.

CONCLUDING REMARKS

In general, the results indicate that when typical launch vehicles are suspended in a horizontal attitude by cables or shock cords, the free-free flexural frequencies are affected very little by the cable restraint when reasonable length cables are utilized. For vertically orientated vehicles where all of the restraint is concentrated at the base, the effect of this restraint on the first natural frequency may become appreciable even when the rigid-body frequencies are very low. Vibration results of vertically orientated beams restrained by a two-cable harness indicate that the effects of the harness restraint on the natural frequencies are small in comparison to the effects of compression in the beam due to gravity.

An air-jet vibration exciter is also described which is easy to use and has a constant force output regardless of frequency. This shaker is particularly useful for vibration testing of small panels, thin-wall cylinders, and lightweight dynamic models where the addition of any mass may have a critical effect on the measured frequencies.

LIST OF ILLUSTRATIONS

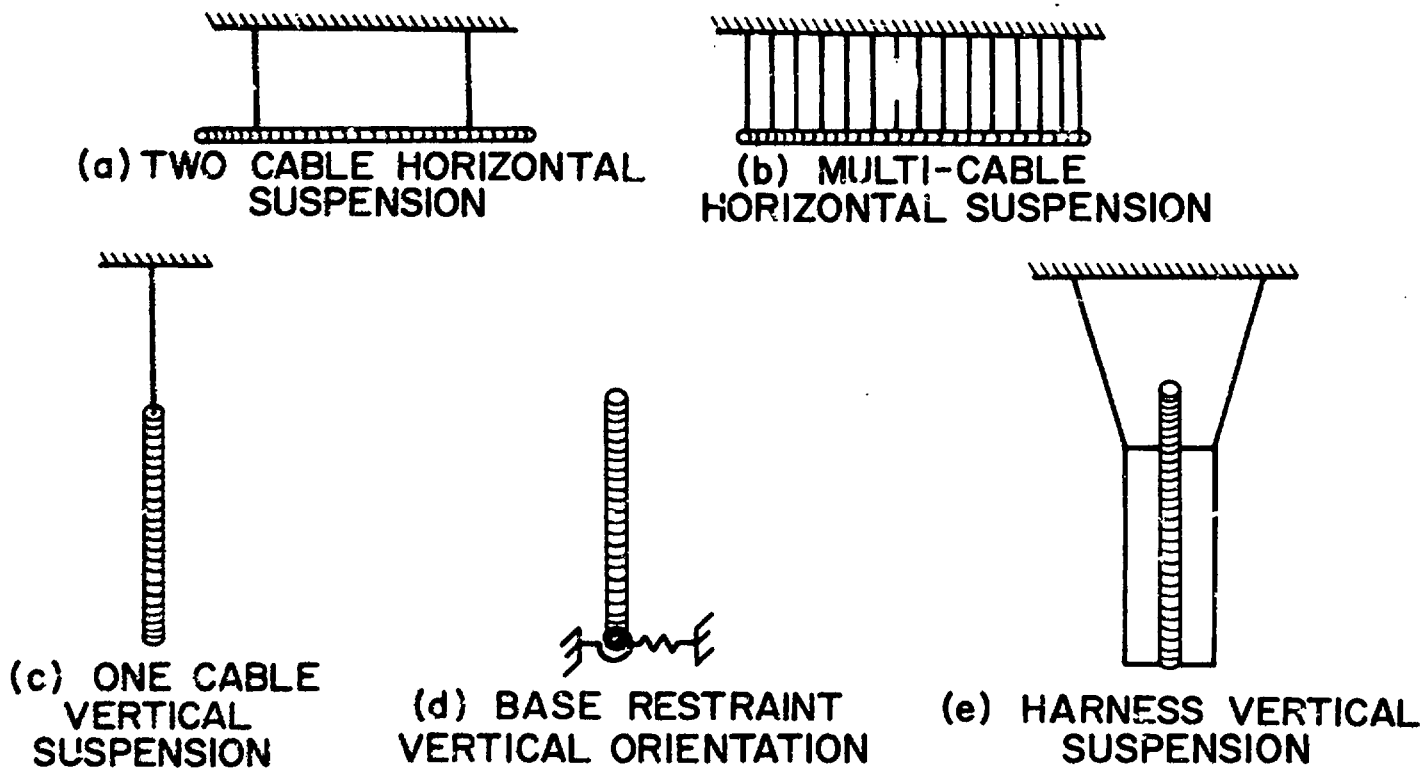

Figure 1.- Types of suspension systems investigated.

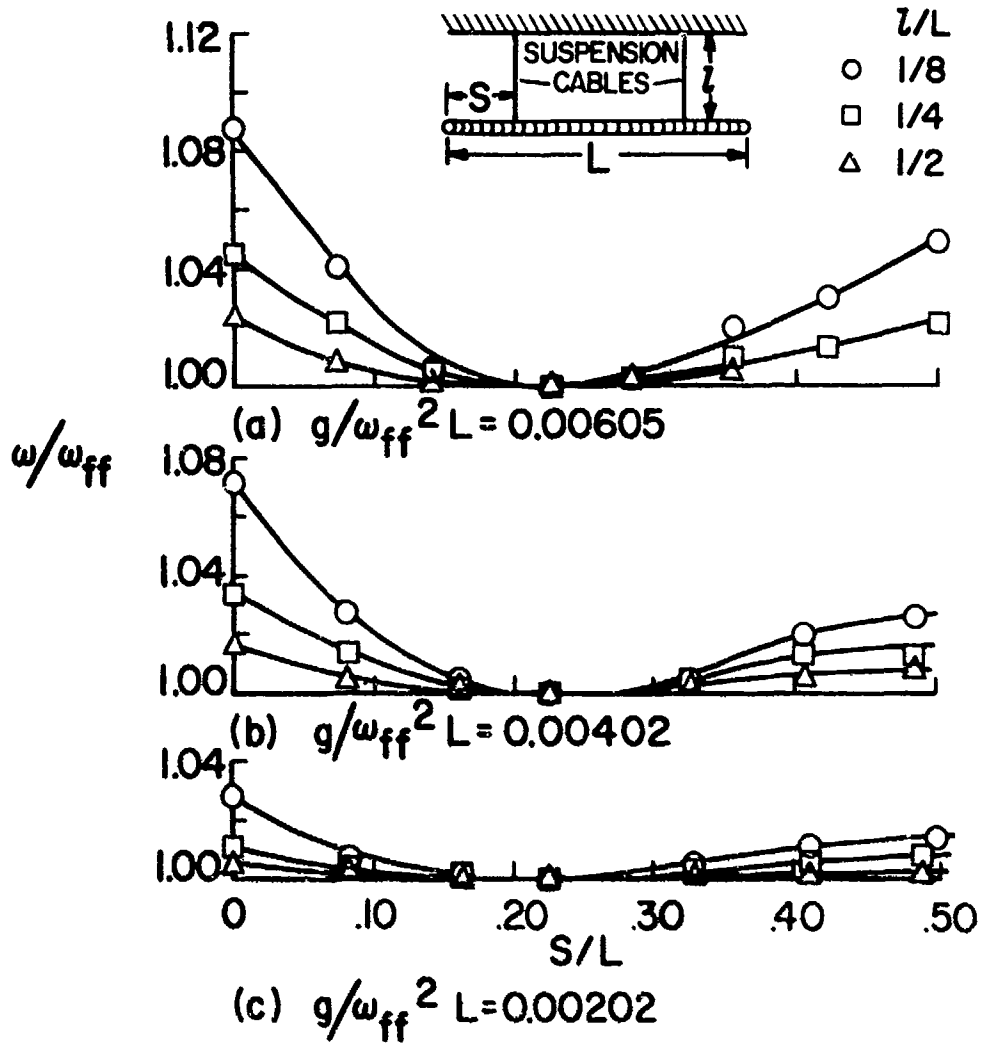

Figure 2.- Effects of the two-cable horizontal suspension on the first free-free frequency.

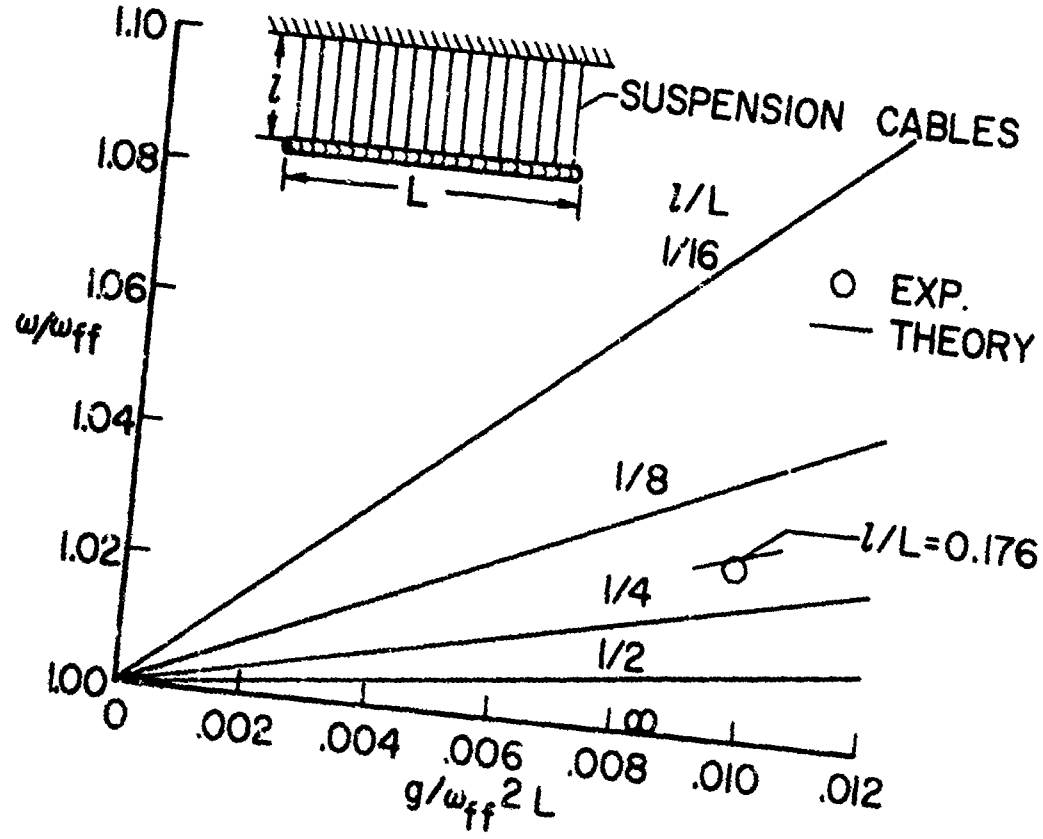

Figure 3.- Effects of the multicable horizontal suspension on the first free-free frequency.

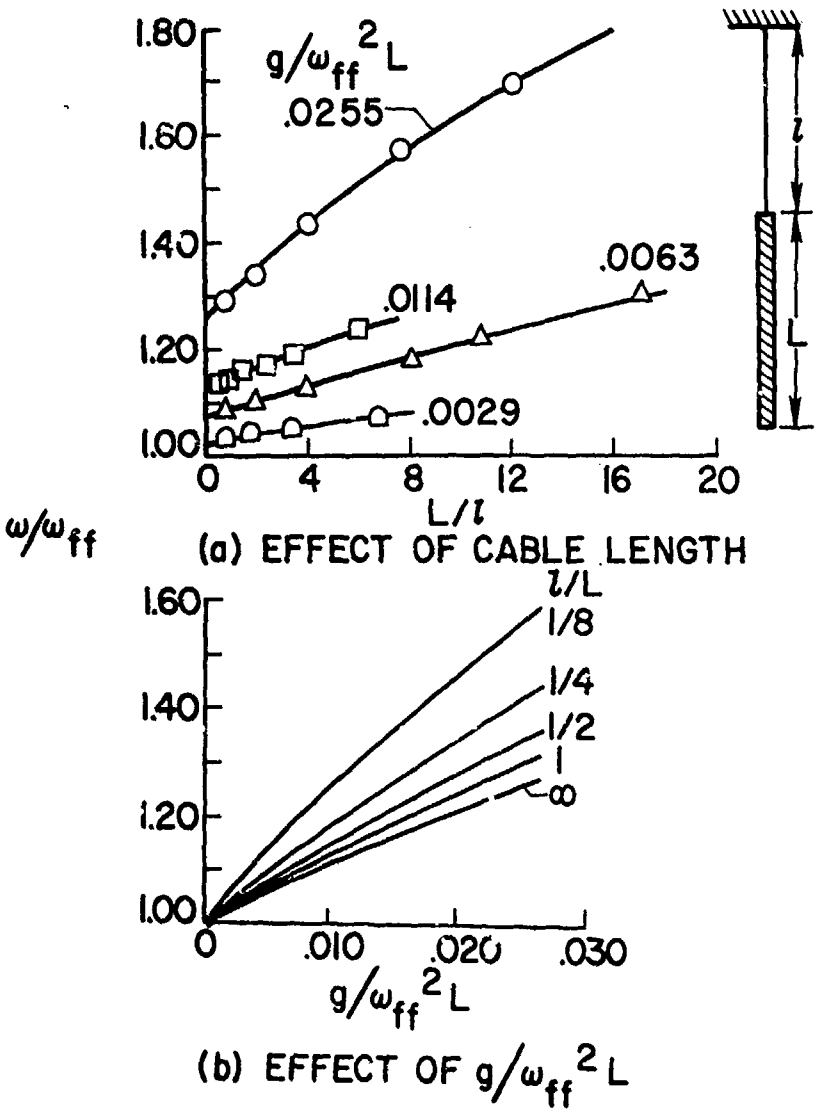

Figure 4.- Effects of the one-cable vertical suspension on the first free-free frequency.

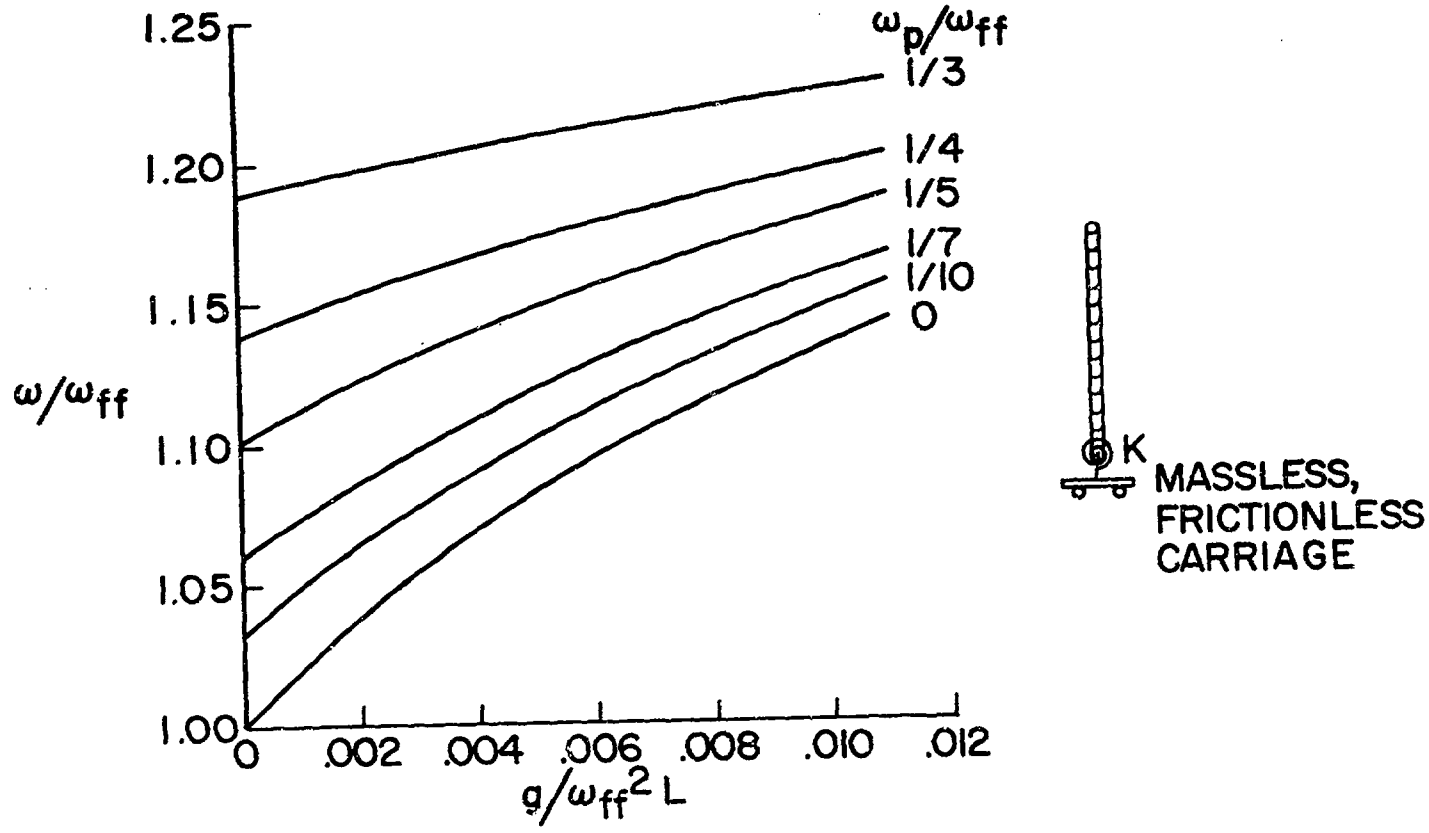

Figure 5.- Effect on the first free-free frequency of a suspension system having all restraint at the base of the vehicle.

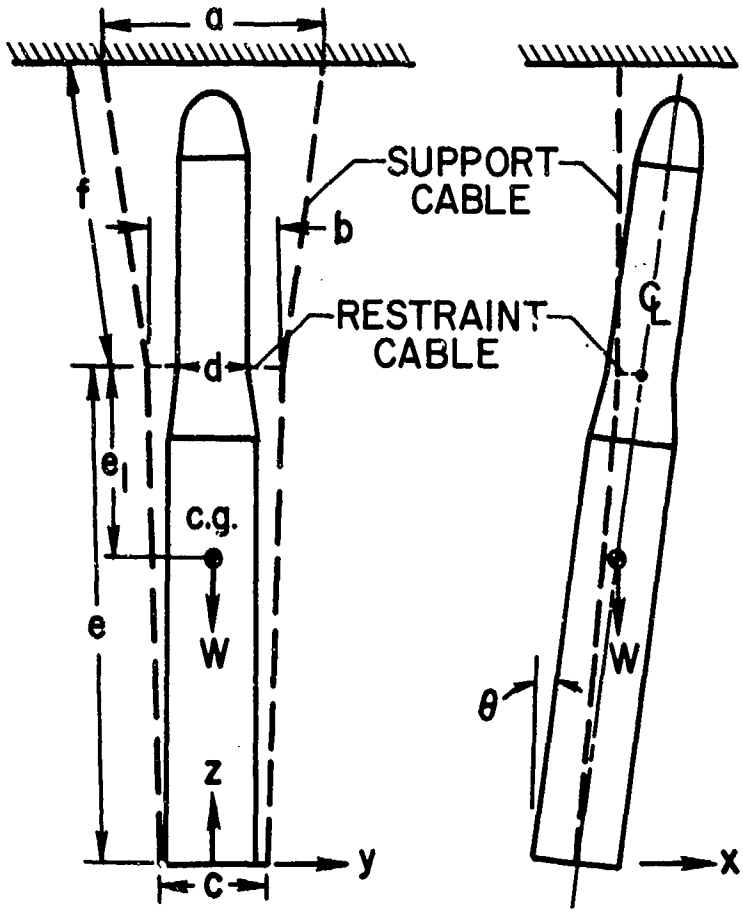

Figure 6.- Two-cable vertical suspension system.

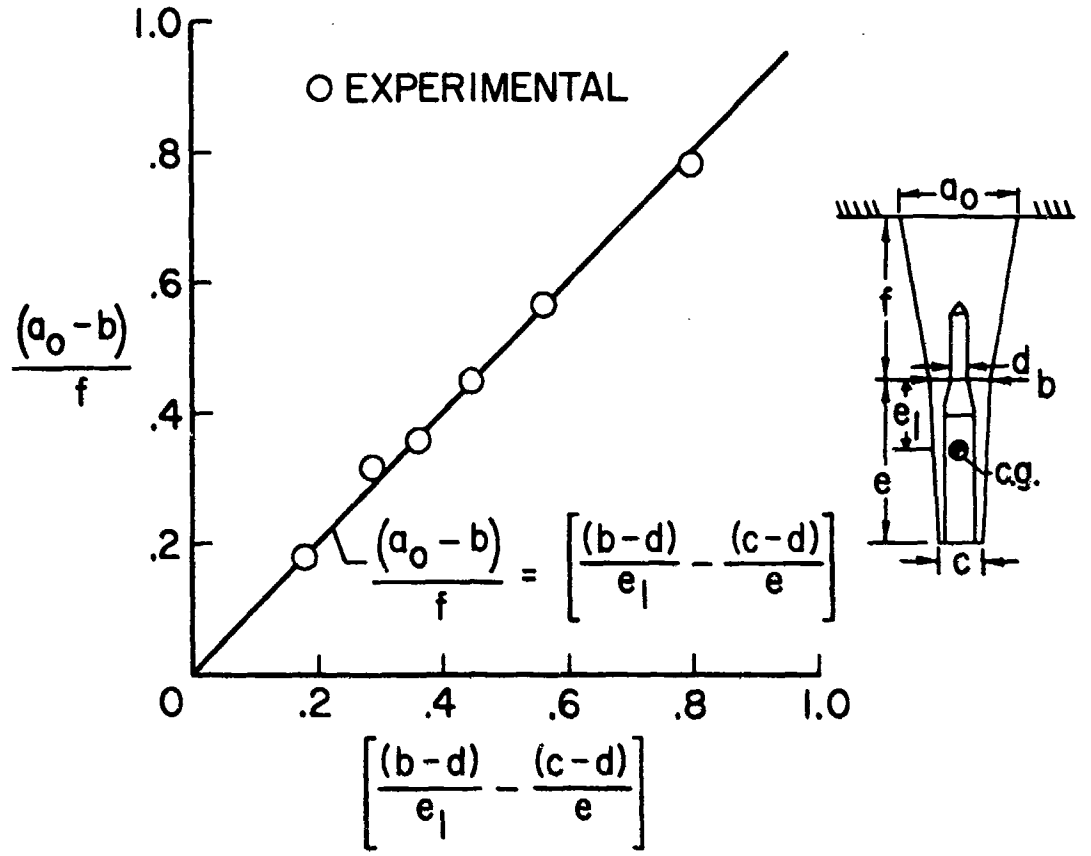

Figure 7.- Comparison of experimental and calculated values of minimum support-cable separation a_o required to maintain vertical attitude.

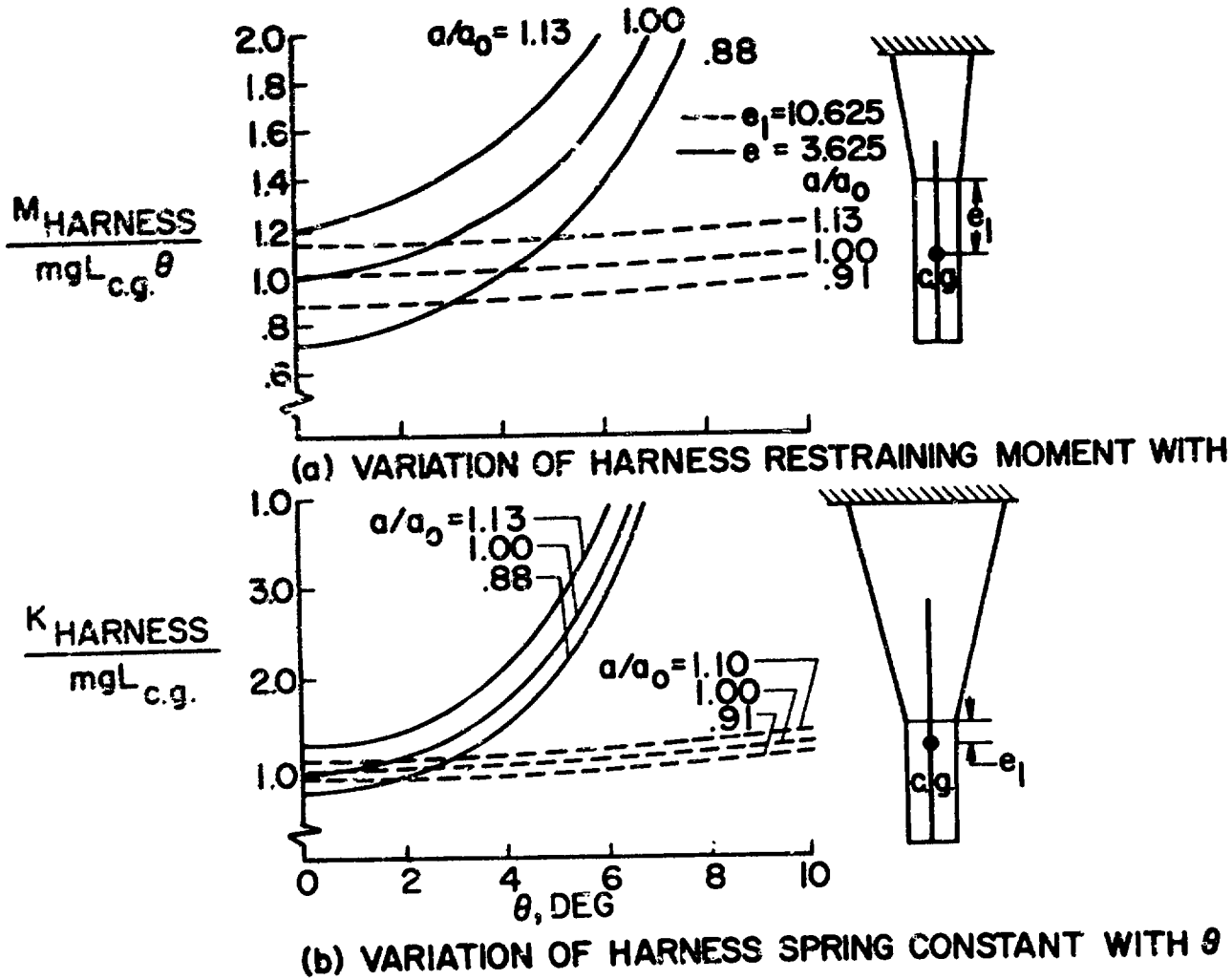

Figure 8.- Restraining moment and spring constant for two locations of restraining cables e_1. (e+f) = 42.25 in.; (e - e_1) = 9.375; b = c = 4 in.; d = 0.

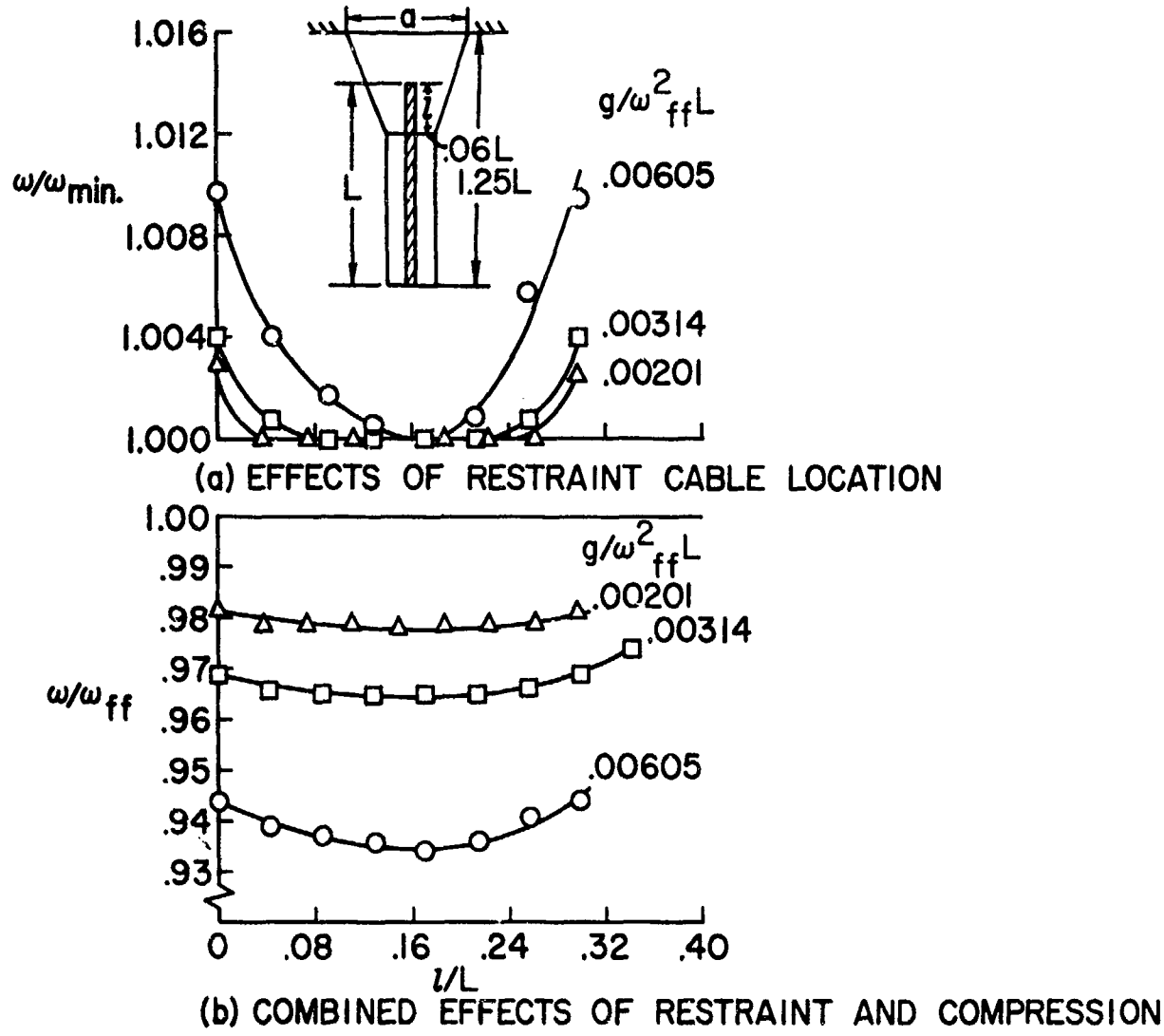

Figure 9.- Frequencies of uniform beams suspended in harness.

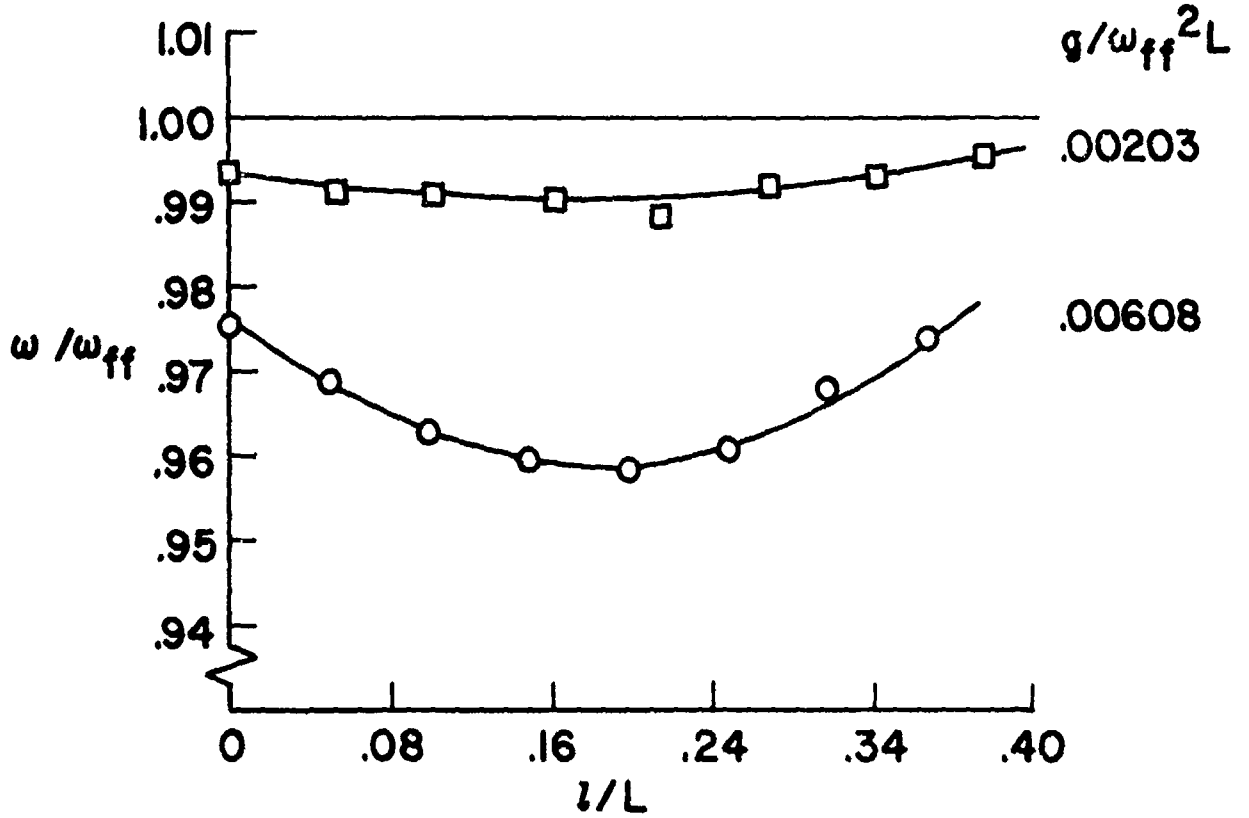

Figure 10.- Frequencies of nonuniform beams suspended in harness.

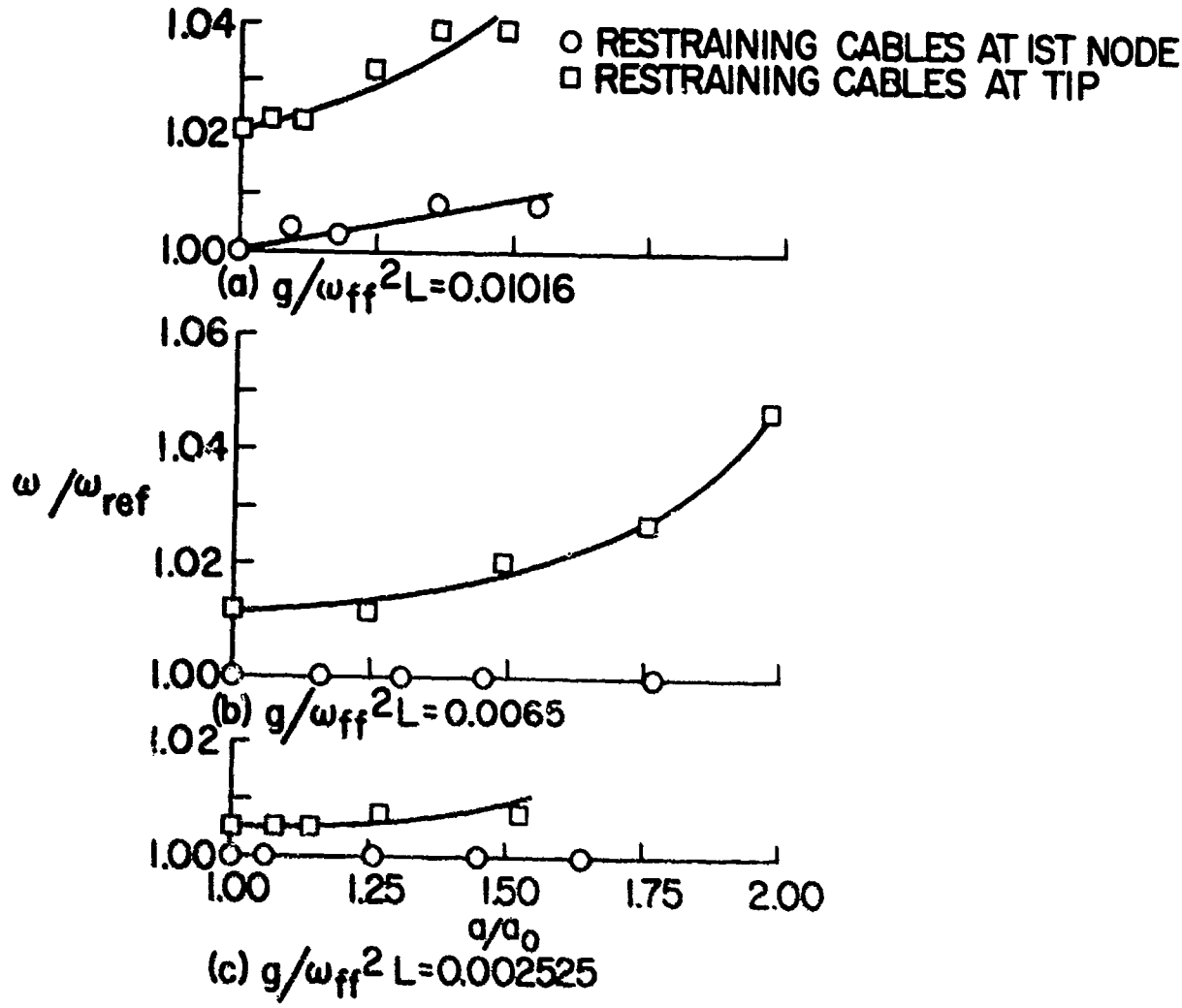

Figure 11.- Effects of using support-cable separation greater than optimum.

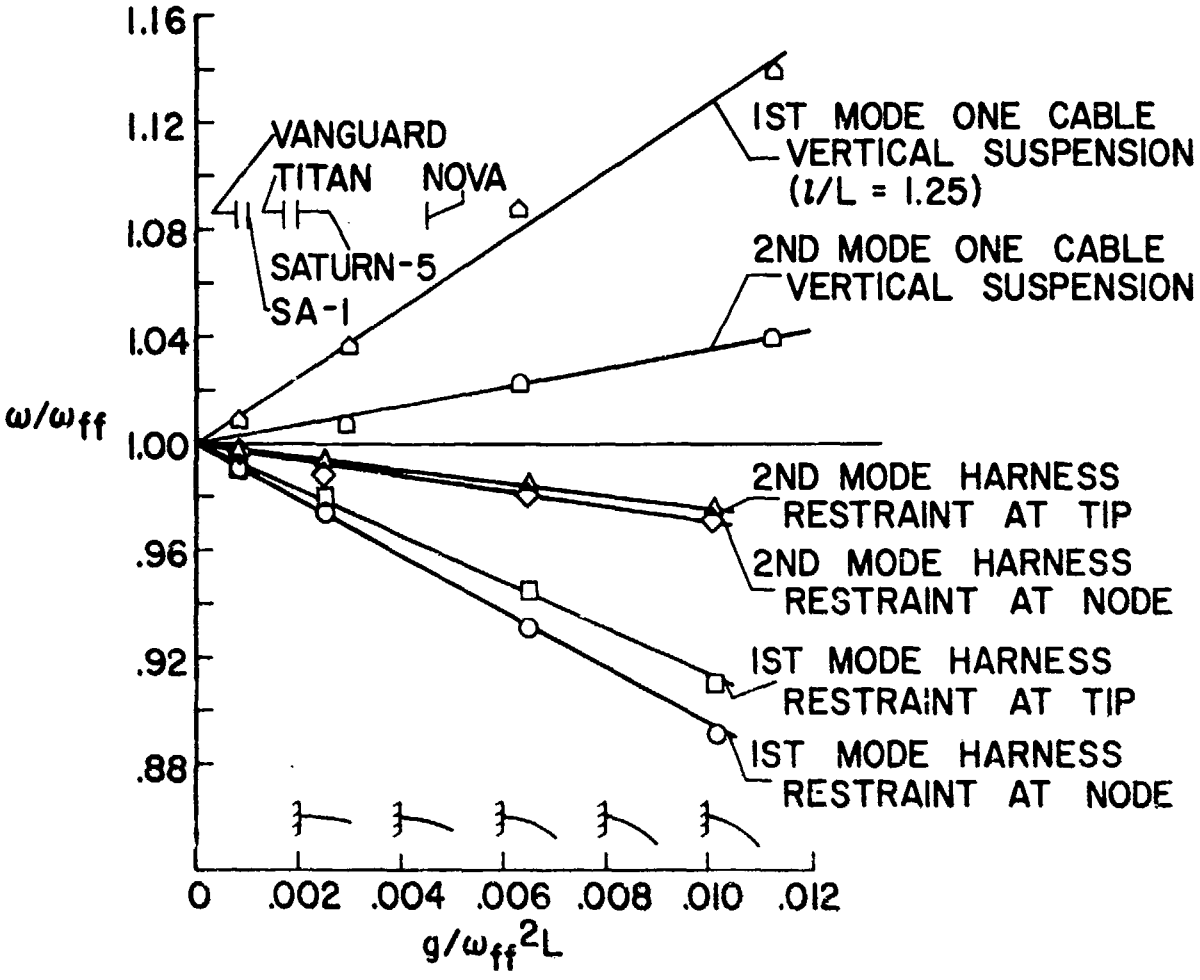

Figure 12.- Comparison of results obtained with one-cable vertical suspension and harness suspension.

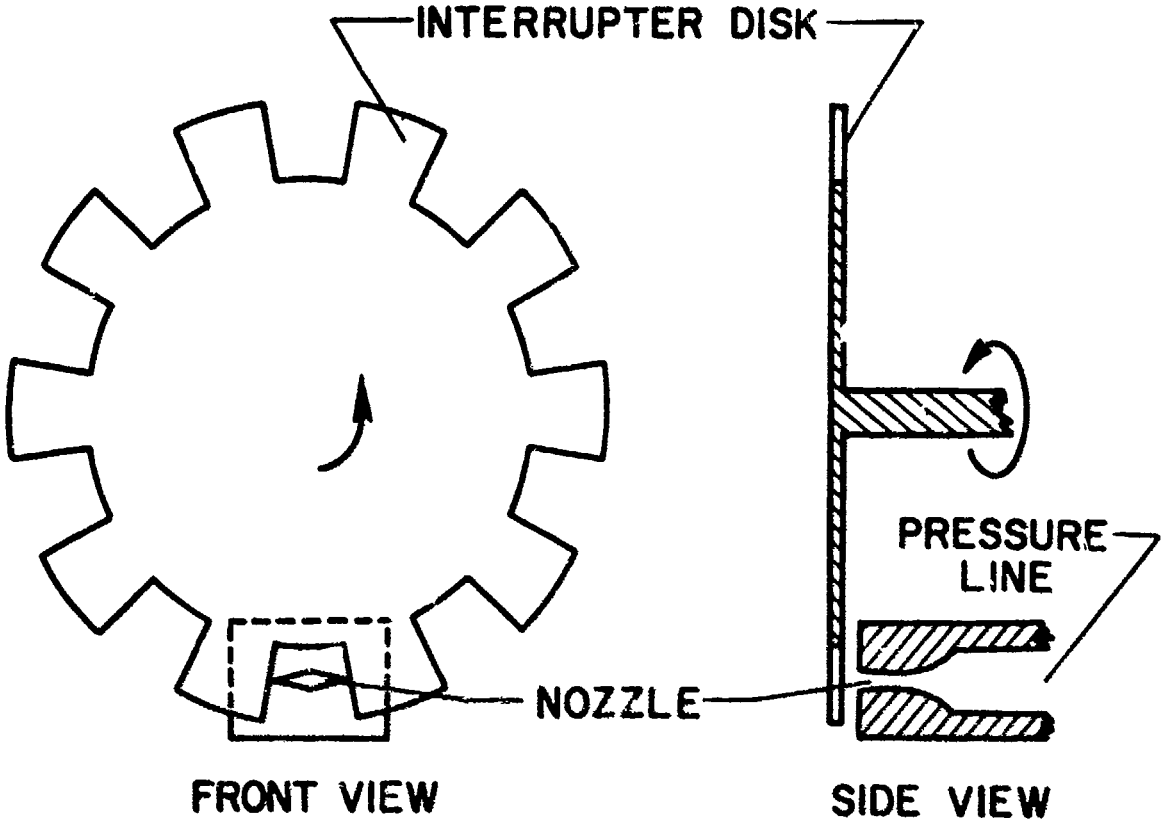

Figure 13.- Sketch of interrupter disk and nozzle.

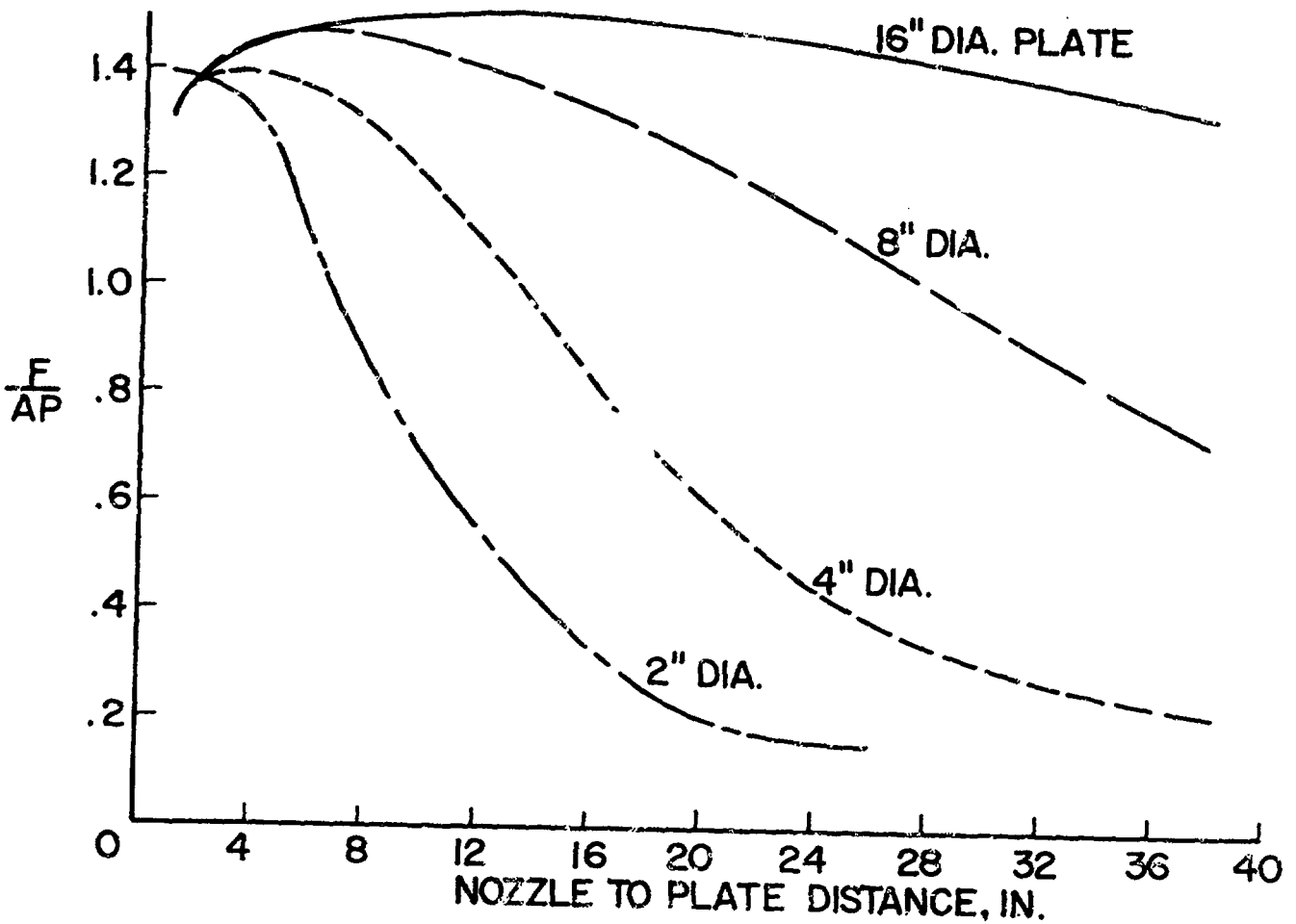

Figure 14.- Force coefficient as function of plate distance for various size plates.

DIAGNOSIS OF FLUTTER MODEL RESPONSE USING TIME CORRELATION TECHNIQUES

R.J. Werdes and M.A. Ferman

McDonnell Aircraft Corporation

ABSTRACT

The analysis of flutter model time history records and the determination of flutter onset is often a matter of judgment. A unique method for analyzing flutter model time histories is presented. The method, which yields repeatable results, utilizes as the diagnostic parameter the continuous analog evaluation of the aerodynamic work imparted to the model in a flutter mode per unit time, i.e., the aerodynamic power. The Aerodynamic Power Function (APF) is readily evaluated for the case of wing bending-torsion flutter in terms of the average running cross-correlation of wing bending and torsion responses sensed by strain gages. Typical experimental results are presented for swept wings tested in transonic blow-down tunnels. Applications to systems involving more degrees of freedom are presented.

LIST OF ILLUSTRATIONS

DIAGNOSIS OF FLUTTER MODEL RESPONSE USING TIME CORRELATION TECHNIQUES

R.J. Werdes and M.A. Ferman

McDonnell Aircraft Corporation

INTRODUCTION

The determination of the precise moment of flutter onset for a system under test is often a matter of judgment. This is particularly true when one considers the complex response behavior of a flutter system under some of the combined effects of turbulence, beating of modes, mild flutter onset, regions of low damping, and limited amplitude flutter. This paper describes a technique which circumvents the analysis difficulties presented by the presence of these masking phenomena. The technique employs the concept that the flutter significant aerodynamic energy input to a system per unit time (the Aerodynamic Power Function, APF) can be determined from the system response time history.

LIST OF SYMBOLS

M	Wing section mass
S_α	Wing section mass unbalance, positive for center of gravity aft of elastic axis
I_α	Wing section mass moment of inertia about the elastic axis
ω_h	Wing plunging frequency
ω_α	Wing pitch frequency
ω	Frequency of oscillation
C_h	Wing plunging damping coefficient
C_α	Wing pitch damping coefficient
q	Free stream dynamic pressure
q_F	Flutter dynamic pressure
q_i	Generalized coordinate, subscript denoting degree of freedom
C_{L_α}	Wing lift-curve slope
S	Wing section area
V	Free stream velocity
h	Wing plunging (or bending) coordinate

α	Wing pitch (or torsion) coordinate
d	Distance from the wing aerodynamic center to the elastic axis
k_h	Wing plunging spring constant, equals $M\omega_h^2$
k_α	Wing pitch spring constant, equals $I_\alpha \omega_\alpha^2$
E	Total energy of a flutter system
T	Kinetic energy
U	Generalized potential energy; includes some aerodynamic stiffness effects
P	$qCL_\alpha S$
$P_{jk}/2$	Skew-symmetric aerodynamic stiffness associated with q_j and q_k
t	Real time
D_p	Dissipative power
Dp_M	Mechanical part of D_p
Dp_A	Aerodynamic part of D_p
APF	Aerodynamic Power Function
e	Base of the Natural Logarithms
e_i	Electrical voltage, subscript defined in the text
a	Damping constant, equals $-\omega(c/c_c)$, where (c/c_c) is critical damping ratio
K	Amplitude ratio of α to h
A , B	Integration constants defined by initial conditions
ψ	Phase lag of α with respect to h
$R(\tau)_{\delta\beta}$	Cross-correlation function; bar denotes Correlator measured function
{ }	Column matrix
[ ]	Row matrix
[ ]	Square matrix
$\bar{\tau}$	Integration period; Correlator time constant
c_o	Calibration constant of Correlator

AERODYNAMIC POWER FUNCTION

It is well known that flutter is a self-excited oscillation which occurs when energy is extracted from the airstream by an oscillating airfoil. To explain the use of time correlation of response time history signals in measuring the Aerodynamic Power Function as an indicator of this energy, it is necessary to show the mathematical expressions involved in the APF for a typical flutter system. For simplicity, use will be made of the most elementary flutter mechanism as a basis of discussion. Consider the equations of motion for the airfoil shown in Figure 1. If

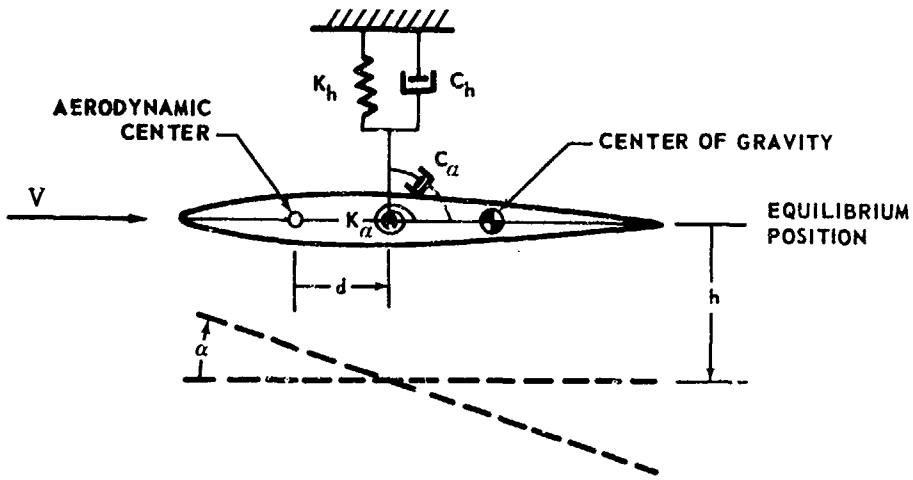

FIGURE 1. TWO DEGREE OF FREEDOM FLUTTER SYSTEM

quasi-steady aerodynamic forces are assumed, and the airfoil is considered to have only plunging and pitch freedoms, the equations of motion are

$$M\ddot{h} + S_\alpha\ddot{\alpha} + C_h\dot{h} + k_h h = -qC_{L_\alpha}S(\alpha + \dot{h}/V) \tag{1a}$$

$$S_\alpha\ddot{h} + I_\alpha\ddot{\alpha} + C_\alpha\dot{\alpha} + k_\alpha\alpha = qC_{L_\alpha}Sd(\alpha + \dot{h}/V) \tag{1b}$$

The significance of the total energy (E) associated with a flutter system has been discussed by several authors, including Frazer and Duncan (Ref. 1), Duncan (Ref. 2), Fung (Ref. 3), Crisp (Ref. 4), Griedanus (Ref. 5), and Bisplinghoff (Ref. 6). Crisp (Ref. 4) examined the time rate of change of E to develop an ultimate stability criterion. It is the intent of this paper to utilize some of these concepts to explain the use of time correlation in assessing flutter stability.

The total energy (E) of the system is

$$E = T + U \tag{2}$$

where T is the kinetic energy of the system, and U is the generalized potential energy and includes some aerodynamic stiffness effects.

$$T = \tfrac{1}{2}\begin{bmatrix}\dot{h} & \dot{\alpha}\end{bmatrix}\begin{bmatrix}M & S_\alpha \\ S_\alpha & I_\alpha\end{bmatrix}\begin{Bmatrix}\dot{h} \\ \dot{\alpha}\end{Bmatrix} \tag{3}$$

$$U = \tfrac{1}{2}\begin{bmatrix}h & \alpha\end{bmatrix}\begin{bmatrix}k_h & P/2 \\ P/2 & k_\alpha - Pd\end{bmatrix}\begin{Bmatrix}h \\ \alpha\end{Bmatrix} \tag{4}$$

$$\text{where } P = qC_{L_\alpha}S$$

The time rate of change of E determines the stability characteristics of the system. When $dE/dt < 0$, the system is stable; when $dE/dt = 0$, the system is neutrally stable (or has reached a limit cycle if the system is nonlinear) and when $dE/dt > 0$, the system is unstable. The time derivative of E can be shown to have the following form for the system described by Equation 1:

$$\dot{E} = -\begin{bmatrix}\dot{h} & \dot{\alpha}\end{bmatrix}\begin{bmatrix}C_h + P/V & -Pd/2V \\ -Pd/2V & C_\alpha\end{bmatrix}\begin{Bmatrix}\dot{h} \\ \dot{\alpha}\end{Bmatrix} - \begin{bmatrix}\dot{h} & \dot{\alpha}\end{bmatrix}\begin{bmatrix}0 & P/2 \\ -P/2 & 0\end{bmatrix}\begin{Bmatrix}h \\ \alpha\end{Bmatrix} \tag{5}$$

The above equation is developed when Equation 1, expressed in matrix form, and the time derivative of the expression for (T + U), as defined by Equations 3 and 4, are appropriately combined. It is to be noted that the forms of Equations 4 and 5 depend on representing an unsymmetric matrix as the sum of a symmetric and a skew-symmetric matrix, a technique employed by Duncan (Reference 2) and Crisp (Reference 4). The energy dissipated per cycle is

$$\int_0^{2\pi/\omega} \dot{E}\, dt \tag{6}$$

and the dissipative power is

$$D_p = \frac{\omega}{2\pi}\int_0^{2\pi/\omega} \dot{E}\, dt \tag{7}$$

$$D_p = -\frac{\omega}{2\pi}\int_0^{2\pi/\omega} \begin{bmatrix}\dot{h} & \dot{\alpha}\end{bmatrix}\begin{bmatrix}C_h + P/V & -Pd/2V \\ -Pd/2V & C_\alpha\end{bmatrix}\begin{Bmatrix}\dot{h} \\ \dot{\alpha}\end{Bmatrix} dt$$

$$-\frac{\omega}{2\pi}\int_0^{2\pi/\omega} \begin{bmatrix}\dot{h} & \dot{\alpha}\end{bmatrix}\begin{bmatrix}0 & P/2 \\ -P/2 & 0\end{bmatrix}\begin{Bmatrix}h \\ \alpha\end{Bmatrix} dt \tag{8}$$

The dissipative power is seen to be composed of a mechanical part and an aerodynamic part,

$$D_p = D_{p_M} + D_{p_A} \tag{9}$$

where

$$D_{p_M} = -\frac{\omega}{2\pi}\int_0^{2\pi/\omega} (C_h\dot{h}^2 + C_\alpha\dot{\alpha}^2)\, dt \tag{10}$$

and

$$D_{p_A} = -\frac{\omega}{2\pi}\int_0^{2\pi/\omega} \begin{bmatrix}\dot{h} & \dot{\alpha}\end{bmatrix}\begin{bmatrix}P/V & -Pd/2V \\ -Pd/2V & 0\end{bmatrix}\begin{Bmatrix}\dot{h} \\ \dot{\alpha}\end{Bmatrix} dt$$

$$-\frac{\omega}{2\pi}\int_0^{2\pi/\omega} \begin{bmatrix}\dot{h} & \dot{\alpha}\end{bmatrix}\begin{bmatrix}0 & P/2 \\ -P/2 & 0\end{bmatrix}\begin{Bmatrix}h \\ \alpha\end{Bmatrix} dt \tag{11}$$

The mechanical part is obviously stabilizing and will not be considered further. The first term of the aerodynamic part is due to aerodynamic damping effects and is, in general, of less importance in influencing flutter stability (excluding single degree of freedom instability) than the second term which contains the so-called skew-symmetric part of the aerodynamic stiffness. Attention will be focused on this latter term as the primary indicator of flutter stability involving at least two degrees of freedom. This term, the Aerodynamic Power Function, is defined

$$APF = -\frac{\omega}{2\pi}\int_0^{2\pi/\omega} \begin{bmatrix}\dot{h} & \dot{\alpha}\end{bmatrix}\begin{bmatrix}0 & P/2\\ -P/2 & 0\end{bmatrix}\begin{Bmatrix}h\\ \alpha\end{Bmatrix} dt \tag{12}$$

$$= -\frac{\omega}{2\pi}\,(P/2)\int_0^{2\pi/\omega}(\dot{h}\alpha - h\dot{\alpha})\,dt. \tag{13}$$

(It is pointed out that the omission of the terms due to aerodynamic damping in the definition of the APF does not exclude the effects of aerodynamic damping on the flutter stability, since the correct aerodynamic forces and moments are applied to a test specimen in the wind tunnel and do have influence on the APF as defined above through the values of h, α, $\dot{h}$, and $\dot{\alpha}$).

Let us now consider the APF as a continuous time function,

$$APF(t) = -\frac{1}{\bar{\tau}}\,P/2\int_{t-\bar{\tau}/2}^{t+\bar{\tau}/2}(\dot{h}\alpha - h\dot{\alpha})\,dt \tag{14}$$

where the time reference has been shifted by $(t - \bar{\tau}/2)$ and where $\bar{\tau} = 2\pi n/\omega$ is the averaging time, with n an integer. To illustrate the behavior of the APF(t), let the motion of the flutter system be represented by

$$h = e^{at}\,[A\cos\omega t + B\sin\omega t] \tag{15a}$$

$$\alpha = Ke^{at}\,[A\cos(\omega t - \psi) + B\sin(\omega t - \psi)]. \tag{15b}$$

Substituting the above expressions into the definition of APF(t) (Equation 14) gives

$$APF(t) = K\left(\frac{\omega}{\bar{\tau}}\right)(P/2)(A^2 + B^2)\,\frac{\sin\psi}{2a}\,e^{2at}\,(e^{a\bar{\tau}} - e^{-a\bar{\tau}}) \tag{16}$$

If n is not an integer, some error is introduced in the APF(t). However, for $\bar{\tau}$ sufficiently large, the error is negligible since that part of the integral due to inclusion of a fraction of a cycle is averaged over the number of full cycles included in the integral. For example, for $10 < n < 11$, the maximum error in the APF(t) is approximately ±5%; for $100 < n < 101$, the maximum error is approximately ±½%, etc..

Consider, now, the transient behavior of the APF(t) for various values of free-stream dynamic pressure. As shown in Figure 2, for q less than q_F, $a < 0$ and $|\sin\psi|$ is approximately zero; the APF(t) has a damped response to any transient disturbance, or a very small continuous response to a continuous disturbance. For q equal to q_F, $a = 0$ and $|\sin\psi|$ is again small;

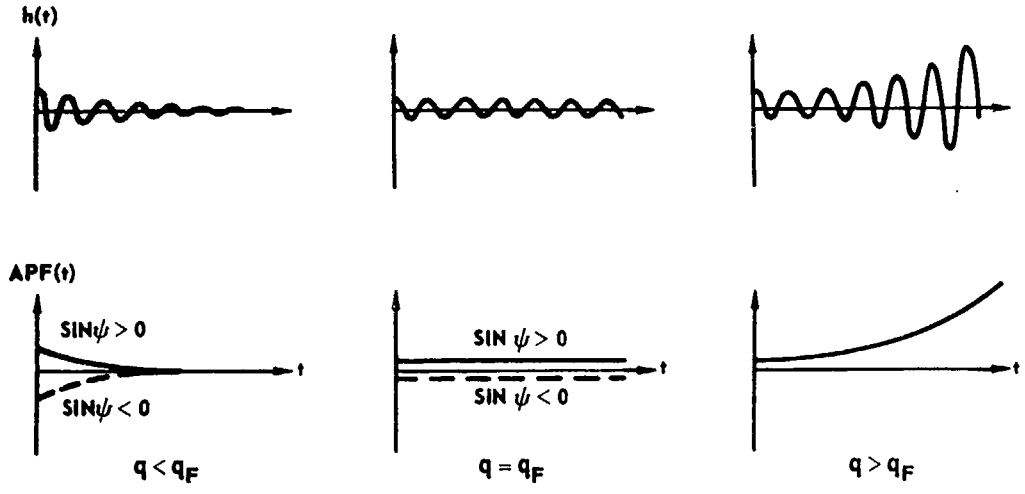

FIGURE 2. IDEAL TRANSIENT BEHAVIOR OF THE APF(t)

the APF(t) has a small constant amplitude response to any transient disturbance, or a linearly increasing response to a continuous distrubance. For q greater than q_F, a > 0 and sin $\psi > 0$; the APF(t) has an exponentially divergent response to any transient disturbance, or a slightly more divergent response to a continuous disturbance. The transient behavior of the APF(t) is seen to be a good indicator of flutter occurrence.

MEASUREMENT OF THE AERODYNAMIC POWER FUNCTION

Measurement of the APF has been achieved through use of the McDonnell Analog Signal Correlator Computer, hereafter referred to as the Correlator. This device is a portable analog weighing only a few pounds, and has an output voltage which is the cross-correlation function of any two input voltages. For the present application of the Correlator, its output signal, e_o, is related to the input signals as follows:

$$e_o = c_o\, e^{-t/\bar{\tau}} \int_0^t e^{t/\bar{\tau}}\, e_1(t)\, e_2(t)\, dt \tag{17}$$

where c_o is a calibration constant, and $e_1(t)$ and $e_2(t)$ are the voltage signals to be correlated. The Correlator output is basically a D.C. signal which indicates the real-time (running) cross-correlation function of the input signals. The definition of the running cross-correlation function is analogous to the definition of "Running Spectrum" as applied to finite length experimental records by Kharkevich (Reference 7). This cross-correlation function has been utilized because of its similarity to the APF, Equation 14. The cross-correlation function is usually defined as

$$R_{\delta\beta}(\tau) = \frac{1}{\bar{\tau}} \int_0^{\bar{\tau}} \delta(t + \tau)\, \beta(t)\, dt \tag{18}$$

for finite length records. If $\tau = 0$, and the running cross-correlation function is utilized, then a correlation function defined as

$$R_{\delta\beta} = \frac{1}{\bar{\tau}} \int_{t-\bar{\tau}/2}^{t+\bar{\tau}/2} \delta(t)\, \beta(t)\, dt \tag{19}$$

is the function employed in the following derivations. If the following running cross-correlation functions are obtained and combined as shown in Equation 22, we obtain essentially the APF.

$$R_{\dot{h}a} = \frac{1}{\bar{\tau}} \int_{t-\bar{\tau}/2}^{t+\bar{\tau}/2} \dot{h}(t)\, a(t)\, dt \tag{20}$$

$$R_{h\dot{a}} = \frac{1}{\bar{\tau}} \int_{t-\bar{\tau}/2}^{t+\bar{\tau}/2} h(t)\, \dot{a}(t)\, dt \tag{21}$$

and

$$R_{\dot{h}a} - R_{h\dot{a}} = \frac{1}{\bar{\tau}} \int_{t-\bar{\tau}/2}^{t+\tau/2} (\dot{h}(t)\, a(t) - h(t)\, \dot{a}(t))\, dt \tag{22}$$

Consider the measurement of the correlation functions, Equations 20 and 21, in a flutter test set-up which might be represented by Figure 1. If bending and torsion strain gage bridges are used as transducers, the bridge output signals are related to the coordinates, h and a (Equations 15a and 15b), as follows:

$$\begin{aligned} B(t) &= \text{bending bridge signal} \\ &= k_B\, h(t) \\ &= k_B e^{at} [A \cos \omega t + B \sin \omega t] \end{aligned} \tag{23}$$

and

$$\begin{aligned} T(t) &= \text{torsion bridge signal} \\ &= k_T\, a(t) \\ &= k_T K e^{at} [A \cos (\omega t - \psi) + B \sin (\omega t - \psi)] \end{aligned} \tag{24}$$

The ideal cross-correlation function for this case is

$$R_{\dot{B}T} - R_{B\dot{T}} = k_B k_T K \left(\frac{\omega}{\bar{\tau}}\right) (A^2 + B^2)\, \frac{\sin \psi}{2a}\, e^{2at} (e^{a\bar{\tau}} - e^{-a\bar{\tau}}) \tag{25}$$

which is proportional to the APF(t), Equation 16. In actual practice the Correlator will obtain the following function:

$$e_o = c_o k_B k_T K \frac{\omega}{\left(\frac{1}{\bar{\tau}} + 2a\right)} (A^2 + B^2) \sin \psi\, (e^{2at} - e^{-t/\tau}) = \bar{R}_{\dot{B}T} - R_{B\dot{T}} \tag{26}$$

This expression indicates tha: the Correlator signal approaches the ideal cross-correlation function asymptotically. In Figure 3 Correlator measurements of the ideal transient behavior of the APF(t) are shown for three values of dynamic pressure, $q < q_F$, $q = q_F$, and $q > q_F$. Comparing Figure 3 with Figure 2, it is seen that the Correlator measurement of the ideal transient behavior of the APF(t) is similar to the corresponding theoretical behavior.

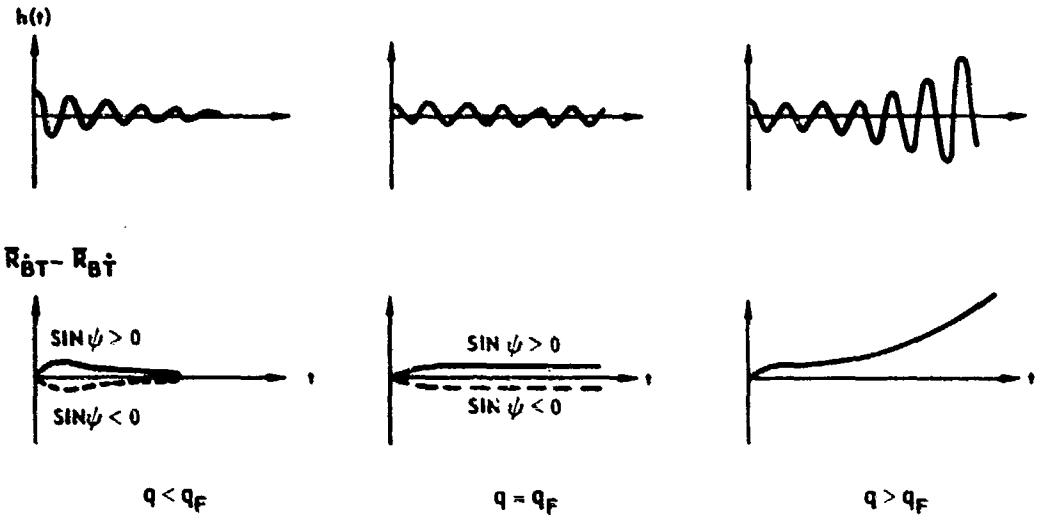

FIGURE 3. CORRELATOR MEASUREMENT OF THE IDEAL TRANSIENT BEHAVIOR OF THE APF(t)

An experimental set-up which shows the means of obtaining the desired Correlator output signal is shown in Figure 4. The use of $+90^{\circ}$ phase shifting devices are indicated. The phase

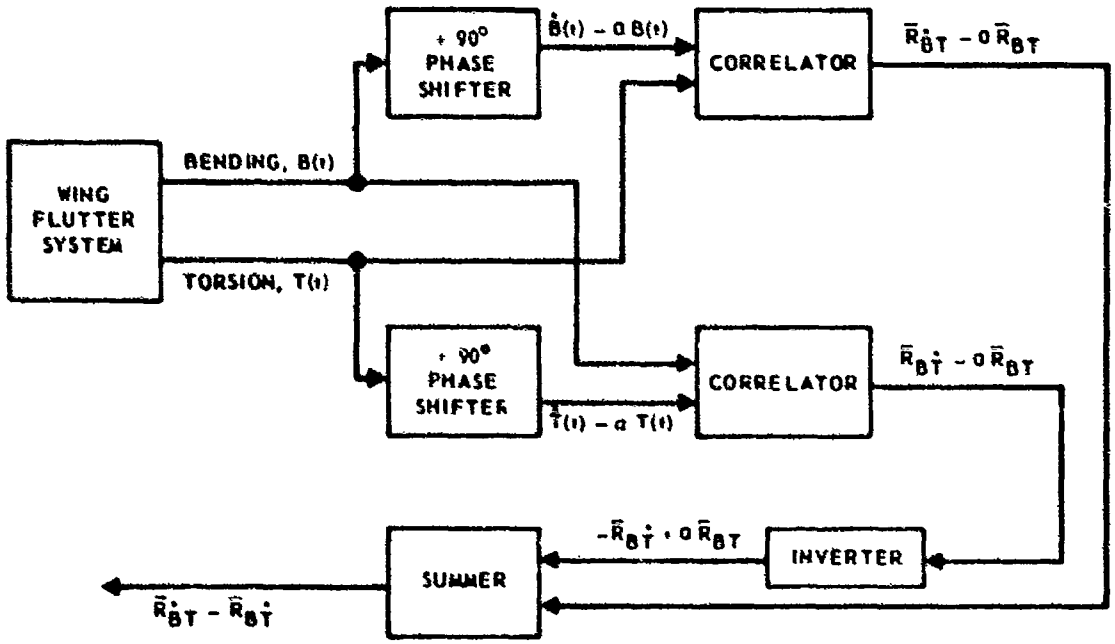

FIGURE 4. SCHEMATIC FOR MEASURING THE APF (t)

shifted signals, when correlated with the original signals, give

$$\bar{R}_{\dot{B}T} - a\,\bar{R}_{BT} \quad \text{and} \quad \bar{R}_{B\dot{T}} - a\,\bar{R}_{BT}.$$

Combining these signals as shown in Figure 4 results in

$$[\bar{R}_{\dot{B}T} - a\,\bar{R}_{BT}] - [\bar{R}_{B\dot{T}} - a\,\bar{R}_{BT}] = \bar{R}_{\dot{B}T} - \bar{R}_{B\dot{T}}.$$

When applying the technique described above to testing in a blowdown tunnel, the effects of aerodynamic turbulence, limited amplitude flutter, and continuously varying tunnel conditions must be considered. Shown in Figure 5 is a typical time history of wing bending and torsion responses and APF(t) measurement. When turbulence is present, the flutter system is acted upon by a random fluctuating pressure field. The resulting generalized random forces associated with the various normal modes have intrinsic time correlation. The time response of the system's coordinates to turbulence will likewise exhibit correlation. However, the effects of turbulence excitation in the subcritical velocity region are minimized by the nature of the APF(t) since the APF(t) is proportional to the sine of the phase angle between modes, the angle being near zero or π subcritically. When in the region of limited amplitude flutter, the APF(t) is likewise limited. The effect of varying tunnel conditions has been found to produce a continuously varying APF(t) which is qualitatively valid in assessing flutter characteristics. The shape of the APF(t) shown in Figure 5 is only typical. The APF(t) is strongly influenced by the phase angle between the critical degrees of freedom, and its shape may be somewhat different for different flutter systems.

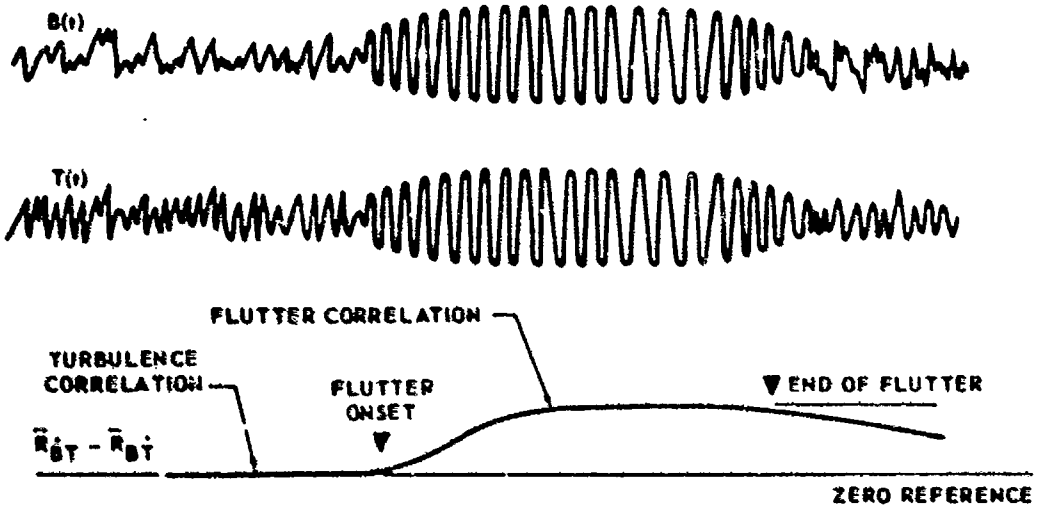

FIGURE 5. TYPICAL MEASURED BEHAVIOR OF THE APF (t) IN BLOWDOWN WIND TUNNEL TESTING

In the application of this technique, post-test analysis has been employed to date. However, it is applicable to on-line monitoring during actual testing. Correlation measurement of the expression $\bar{R}_{\dot{B}T} - \bar{R}_{B\dot{T}}$ is shown in Figures 9 and 10 for typical blowdown tunnel tests. This expression (Equation 26), when adjusted by the relatively small variation of P/2, here assumed to be constant, becomes the APF(t). The results shown indicate the merit of the APF(t) in assessing flutter model response.

BENDING-TORSION CO-POWER FUNCTION

Another application of real-time correlation of flutter model response signals for flutter onset detection relies on measurement of the bending-torsion Co-Power Function. This technique is shown to provide a reasonably clear picture of model stability characteristics as a function of dynamic pressure, and has been employed both on-line and post test. In order to obtain the bending-torsion Co-Power Function, the following running cross-correlation function is defined:

$$R_{BT} = \frac{1}{\bar{\tau}} \int_{t-\bar{\tau}/2}^{t+\bar{\tau}/2} B(t)\, T(t)\, dt. \tag{27}$$

This cross-correlation term is seen to be a time varying measure of the bending-torsion Co-Power Function. When using the forms for B(t) and T(t) indicated in Equations 23 and 24, the evaluation of the expression in Equation 27 yields

$$R_{BT} = k_B k_T K (A^2 + B^2) \left(\frac{\cos \psi}{4a\bar{\tau}} \right) e^{2at} (e^{a\bar{\tau}} - e^{-a\bar{\tau}}) \tag{28}$$

for the application herein. Likewise, the Correlator measurement of the Co-Power Function can be shown to be

$$\bar{R}_{BT} \simeq c_o k_B k_T K (A^2 + B^2) \left(\frac{\cos \psi}{\frac{1}{\bar{\tau}} + 2a} \right) (e^{2at} - e^{-t/\bar{\tau}}) \tag{29}$$

and is seen to approach the ideal Co-Power Function asymptotically. A typical set-up for measurement of the Co-Power Function is shown schematically in Figure 6. The theoretical and measured transient behavior of the Co-Power Function are shown schematically in Figure 7 for the ideal case where transient response is excited at three values of dynamic pressure: $q < q_F$, $q = q_F$, $q > q_F$. The results presented in Figure 7 clearly show that the Co-Power Function indicates the flutter stability characteristics in this ideal case.

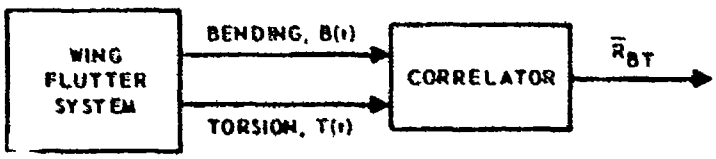

FIGURE 6. SCHEMATIC FOR MEASURING THE BENDING - TORSION CO-POWER FUNCTION

The behavior of the measured Co-Power Function as applied to blowdown testing will now be examined. In this case, the effects of turbulence, limited amplitude flutter, and varying tunnel conditions must be considered. Figure 8 presents typical bending and torsion time histories together with the Correlator measurement of the Co-Power Function. In the subcritical and post-critical regions, the effect of turbulence creates random response of the model, these response functions (bending and torsion in the case presented) are intrinsically correlative. This

correlation has been noted as Turbulence Correlation and has been found to increase approximately proportional to the dynamic pressure in the subcritical region. The Co-Power Function reaches a maximum then decreases as the limited amplitude flutter region is traversed, the correlation in the critical region being noted as Flutter Correlation. The time varying tunnel conditions affect the Co-Power Function in the same manner as discussed previously for the APF(t).

Typical experimental results from blowdown tunnel tests are presented in Figures 9 through 11. The results of the Co-Power measurements shown indicate that the Co-Power Function presents a definite indication of flutter onset.

It should be noted that the bending-torsion Co-Power Function is proportional to cos ψ whereas the APF(t) is proportional to sin ψ. This fact implies that the bending-torsion Co-Power is less sensitive than the APF(t) to flutter response involving a large phase angle, ψ, and that the bending-torsion Co-Power Function will measure more power associated with turbulence in the subcritical regions than would the APF(t). Hence in certain cases, it is anticipated that the bending-torsion Co-Power may not indicate flutter as dramatically as the APF(t). The bending-torsion Co-Power Function, when adjusted by the functions, P/2 and ω, has the form of the derivative of APF(t) with respect to ψ.

MANY DEGREES OF FREEDOM

When systems having more than two degrees of freedom are considered, the APF(t) associated with each constituent binary can be represented in a manner similar to Equation 14:

$$APF(t)_{jk} = -\frac{1}{\bar{\tau}} P_{jk}/2 \int_{t-\bar{\tau}/2}^{t+\bar{\tau}/2} (\dot{q}_j q_k - q_j \dot{q}_k)\, dt \tag{30}$$

where j, k = 1, 2, ..., n, and $P_{jk}/2$ are skew-symmetric aerodynamic stiffness coupling terms associated with the generalized coordinates q_j and q_k, again assuming quasi-steady aerodynamic forces. The total APF(t) for the many-degree of freedom system can be written as

$$APF(t) = -\frac{1}{\bar{\tau}} \sum_{j=1}^{n} \sum_{j=k}^{n} P_{jk}/2 \int_{t-\bar{\tau}/2}^{t+\bar{\tau}/2} (\dot{q}_j q_k - q_j \dot{q}_k)\, dt. \tag{31}$$

This expression is similar to the energy expression given by Crisp (Ref. 4) to define in a very general way "all kinematically admissible flutter configurations," except for the omission in the expression above of terms associated with the symmetric aerodynamic damping forces.

Consider, now, an actual flutter test where the flutter system has n degrees of freedom, or more probably, the system has been idealized to have n degrees of freedom corresponding to the first n normal modes. In the latter case, the required values of the coordinates and their first time derivatives can be obtained from the output of n strain gage bridges used as transducers, the bridges being located judiciously such that at least one bridge has an adequate output for

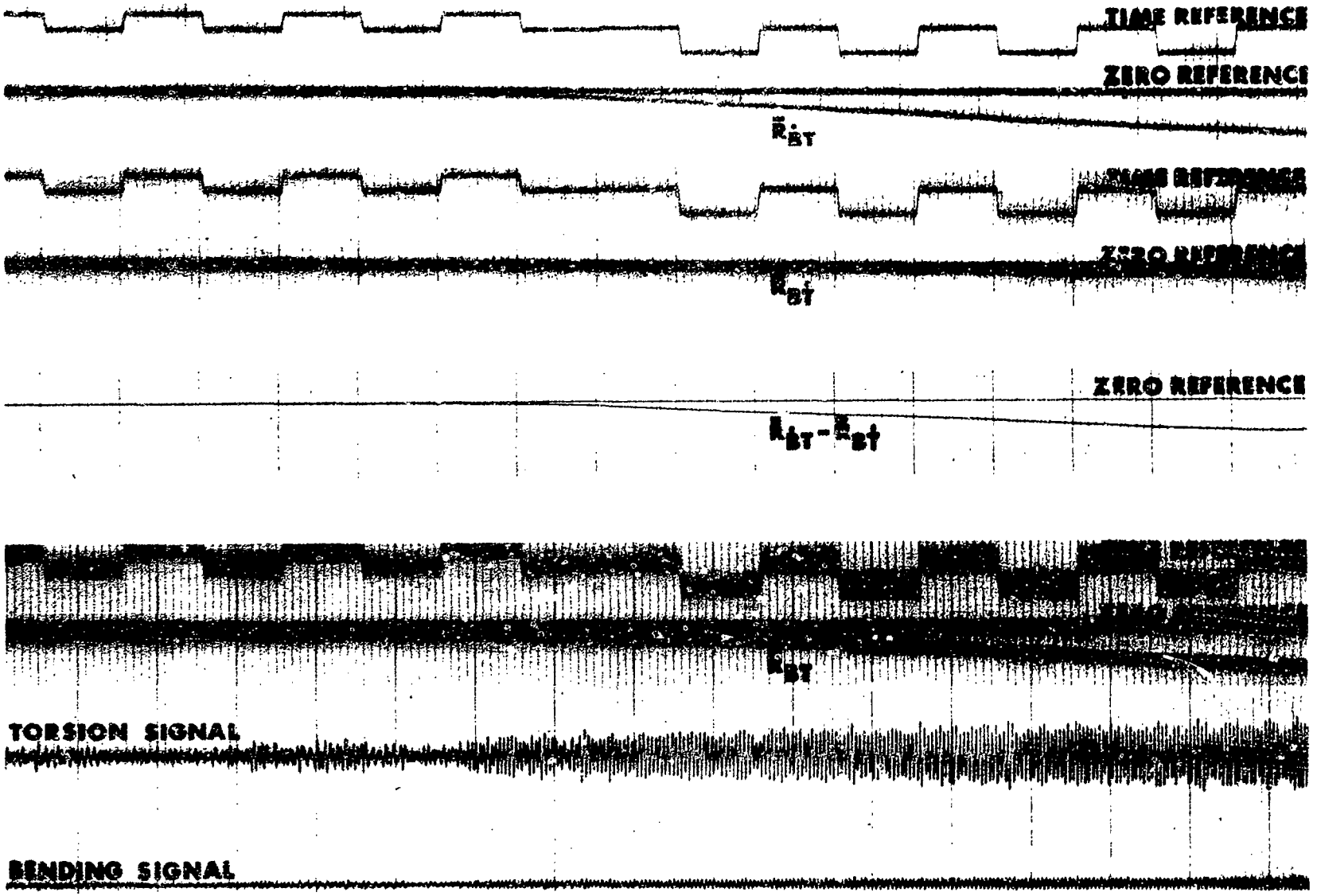

FIGURE 9. TYPICAL CORRELATION MEASUREMENTS TUNNEL TEST A - RUN 1

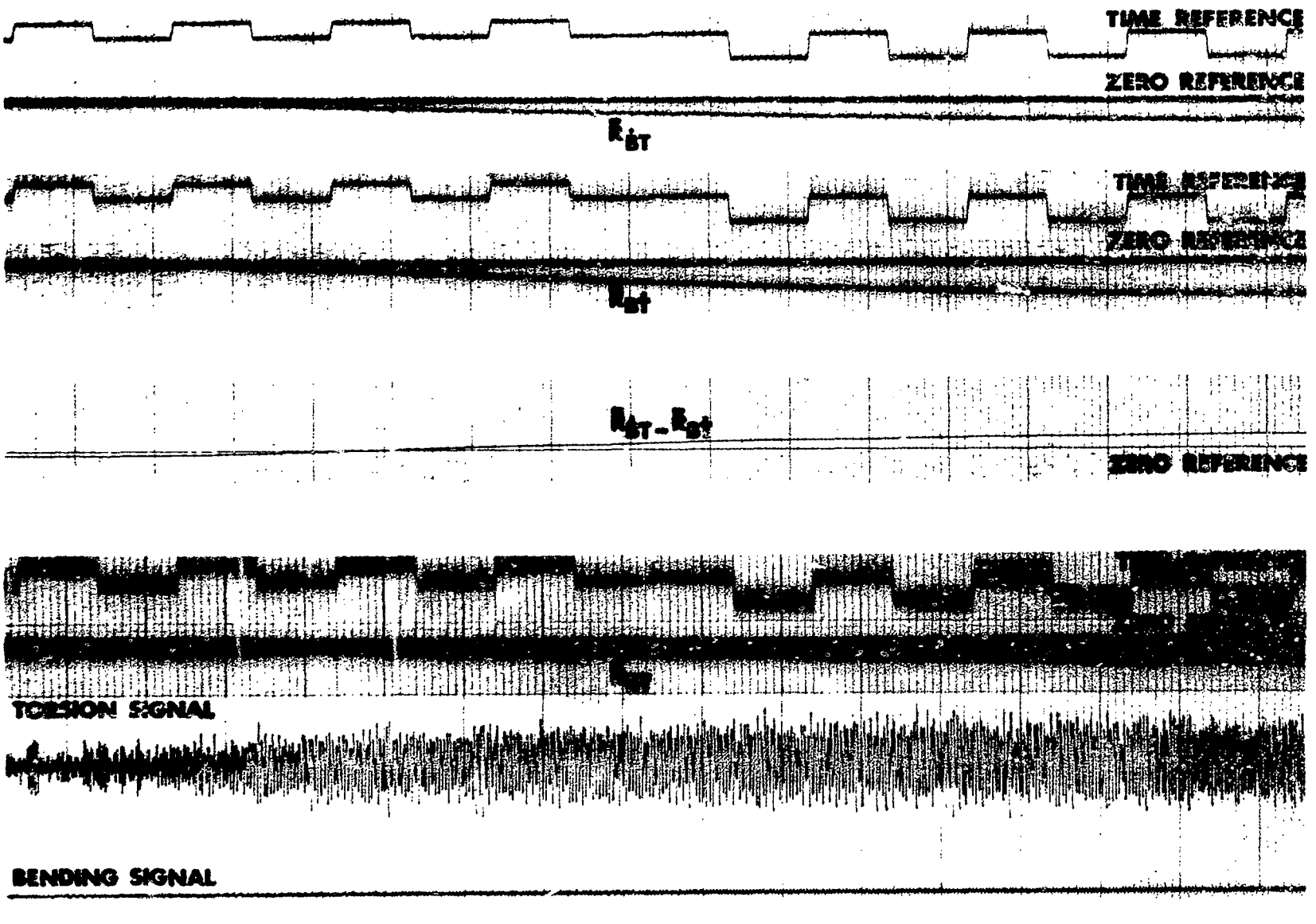

FIGURE 10. TYPICAL CORRELATION MEASUREMENTS TUNNEL TEST A - RUN 2

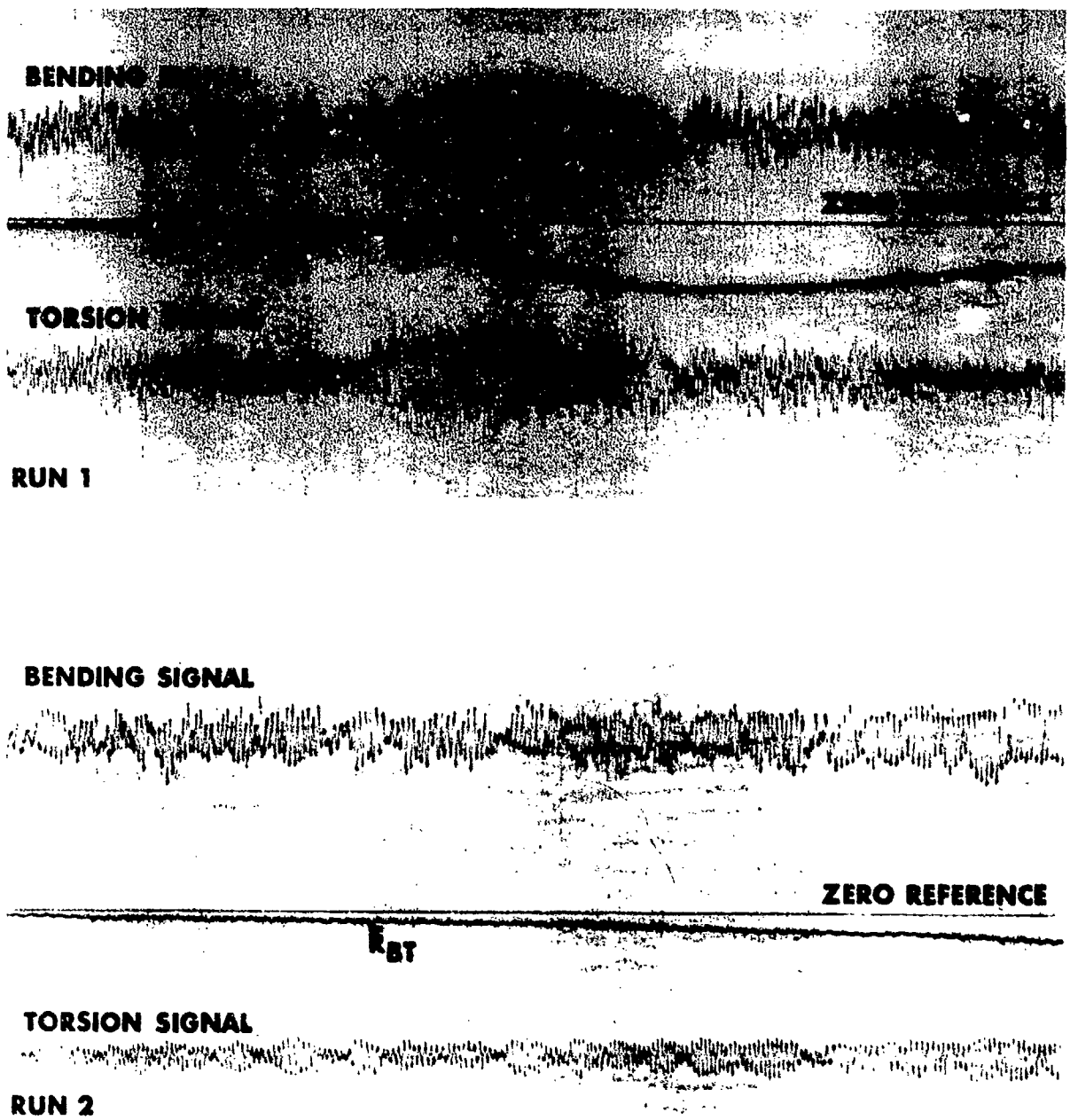

FIGURE 11. TYPICAL CORRELATION MEASUREMENTS
TUNNEL TEST B - RUNS 1 AND 2

each degree of freedom considered. The output from the n bridges can then be related to the coordinates as

$$\{e\} = [C]\{q\} \tag{32}$$

where e is a column matrix of voltage outputs and C is a matrix of calibration constants established through a vibration test. For example, if n = 3,

$$\begin{Bmatrix} e_1 \\ e_2 \\ e_3 \end{Bmatrix} = \begin{bmatrix} C_{11} & C_{12} & C_{13} \\ C_{21} & C_{22} & C_{23} \\ C_{31} & C_{32} & C_{33} \end{bmatrix} \begin{Bmatrix} q_1 \\ q_2 \\ q_3 \end{Bmatrix} \tag{33}$$

If only the first normal mode is excited, Equation 33 becomes

$$\begin{Bmatrix} e_1 \\ e_2 \\ e_3 \end{Bmatrix} = \begin{bmatrix} C_{11} & C_{12} & C_{13} \\ C_{21} & C_{22} & C_{23} \\ C_{31} & C_{32} & C_{33} \end{bmatrix} \begin{Bmatrix} q_1 \\ 0 \\ 0 \end{Bmatrix} \tag{34}$$

from which $C_{11} = e_1/q_1$, $C_{21} = e_2/q_1$, and $C_{31} = e_3/q_1$. The other columns of calibration constants can be obtained similarly, exciting the second, and then the third normal mode. The coordinates can then be written as

$$\{q\} = [D]\{e\} \tag{35}$$

where

$$[D] = [C]^{-1}. \tag{35a}$$

The total Aerodynamic Power Function can be shown to be

$$APF(t) = -\frac{1}{\bar{\tau}} \sum_{j=1}^{n} \sum_{k=j}^{n} \frac{P_{jk}}{2} \begin{vmatrix} D_{jj} & D_{jk} \\ D_{kj} & D_{kk} \end{vmatrix} \int_{t-\bar{\tau}/2}^{t+\bar{\tau}/2} (\dot{e}_j e_k - e_j \dot{e}_k)\, dt \tag{36}$$

where

$$\begin{vmatrix} D_{jj} & D_{jk} \\ D_{kj} & D_{kk} \end{vmatrix} \tag{36a}$$

is a determinant formed from the elements of the matrix D. Specifically, if n = 3,

$$\begin{aligned} APF(t) = &-\frac{1}{\bar{\tau}} \frac{P_{12}}{2} (D_{11}D_{22} - D_{12}D_{21}) \int_{t-\bar{\tau}/2}^{t+\bar{\tau}/2} (\dot{e}_1 e_2 - e_1 \dot{e}_2)\, dt \\ &-\frac{1}{\bar{\tau}} \frac{P_{13}}{2} (D_{11}D_{33} - D_{13}D_{31}) \int_{t-\bar{\tau}/2}^{t+\bar{\tau}/2} (\dot{e}_1 e_3 - e_1 \dot{e}_3)\, dt \\ &-\frac{1}{\bar{\tau}} \frac{P_{23}}{2} (D_{22}D_{33} - D_{23}D_{32}) \int_{t-\bar{\tau}/2}^{t+\bar{\tau}/2} (\dot{e}_2 e_3 - e_2 \dot{e}_3)\, dt \end{aligned} \tag{37}$$

The relative participation in the flutter mode of each binary subsystem can thus be established from measurements of the parts of Equation 36 weighted by theoretical relative values for the aerodynamic skew-symmetric stiffness terms, $P_{jk/2}$. By combining all measured contributions to form the total APF(t), a single function is provided which is useful for monitoring flutter onset in any mode involving the original n normal modes.

CONCLUSIONS

The analog techniques which have been presented for the analysis of flutter model time history records are unique, present repeatable results, and are believed to be a significant step forward in the state of the art.

REFERENCES

1. Frazer, R.A. and Duncan, W.J., "The Flutter of Aeroplane Wings," British A.R.C. Reports and Memoranda 1155, August 1928.
2. Duncan, W.J., "Flutter of Systems of Many Degrees of Freedom," Aeronautical Quarterly, Volume 1, Part 1, May 1949, pages 59–76.
3. Fung, Y.C., An Introduction to the Theory of Aeroelasticity, John Wiley and Sons, Copyright 1955, pages 166–172.
4. Crisp, J.D.C., "The Equation of Energy Balance for Fluttering Systems with Some Applications in the Supersonic Regime," Journal of the Aerospace Sciences, Volume 26, No. 11, November 1959, pages 703–716.
5. Griedanus, J.H., "Low Speed Flutter," Journal of Aeronautical Sciences, Readers Forum, Volume 16, No. 2, February 1949, pages 127–128.
6. Bisplinghoff, R.L. and Ashley, H., Principles of Aeroelasticity, John Wiley and Sons, Copyright 1962, pages 274–277.
7. Kharkevich, A.A., Spectra and Analysis, Consultants Bureau, New York, 1960, Chapter 1, Section 5, pages 18–19.

SESSION III

DYNAMIC LOADS AND AEROELASTIC APPLICATIONS

Chairman: Mr. Martin Goland
Southwest Research Institute

COMPUTER VS MODEL

Lee S. Wasserman
Dynamic Devices, Incorporated
Dayton, Ohio

and

Walter J. Mykytow
AF Flight Dynamics Laboratory
Research and Technology Division
Wright-Patterson Air Force Base, Ohio

ABSTRACT

Problems of airplane and space vehicles which must be analyzed thoroughly from from the standpoint of dynamics are summarized. Tools available for the solution of such problems include the digital and analog electronic computers and mechanical analogs such as dynamically similar models. Since computer techniques are largely based on simplified mathematical representations of the pertinent phenomena an attempt is made in this paper to evaluate such simplifications for some of the modern theoretical procedures.

Practical difficulties in the fabrication of dynamically similar models, limitations in the availability of test environments and basic effects of scale on dynamic phenomena require the use of certain assumptions in the design, fabrication and testing of dynamically similar models. The assumptions required in advanced dynamically similar model techniques are listed for the information of dynamics engineers and are compared with those listed above for analytical procedures.

Recommended procedures involving the use of both models and analytical techniques are outlined for the solution of specific problems in dynamics for airplane and space vehicles.

LIST OF ILLUSTRATIONS

TABLES

COMPUTER VS MODEL

In this paper the analytical and experimental tools available to the aerospace dynamicist are discussed from the standpoint of how these tools were developed and how they may be used to enable the dynamicist to do a better job in the future. This responsibility is the prevention of excessive dynamic loads in aerospace vehicles caused by:

1. Instabilities such as flutter or other unfavorable couplings between structural vibration and sources of vibratory energy.

2a. Transient inputs due to gusts and landing impacts.

2b. Steady state and/or random inputs due to power plants and flow separation.

The history of aerospace dynamics (See Tables 1 through 5 and References) show that even as late as the mid-forties, the effect of the dynamicist on the design of aircraft was basically limited to isolation of the power plant, fixing minor vibration problems and mass balancing of the control surfaces. The airplane was designed on the basis of wind tunnel tests of rigid models plus static strength requirements. The Wright Field flutter group was vibrating aircraft before 1939 to determine the natural structural frequencies and attempting to use these data to draw conclusions regarding the safety of the design from the standpoint of flutter. However, the methods used to make these decisions during this period were almost completely empirical.

The use of theoretical developments by Wright Field in the early forties resulted from an attempt to make better use of aircraft vibration frequency data. It turned out that these data and the resulting analyses were of little value from the standpoint of designing improved aircraft during that period since the flight speeds were just too slow at the time to make lifting-surface flutter a real problem for the configurations then in use.

Despite this situation, the early theoretical developments of Theodorsen, Garrick, Biot, and many others turned out to be of great value for solving dynamics problems in future aircraft. These developments formed the basis of AAF TR 4798 which put the flutter theory into suitable form for practical flutter analysis by engineers. The advent of high speed aircraft with configurations such as heavy engine and stores located outboard on the wing, T-tails and all movable tails resulted in flutter limitations of static strength designs so that modifications were required to change the configuration, rigidity and/or mass distribution.

To assure safety and assess these modifications from the standpoint of effectiveness, weight and cost the following possibilities existed: the use of dynamically similar models, theoretical analysis or a combination of model tests and theory. Neither model nor theory was completely adequate in itself. Limitations in the theory included aerodynamic and structural assumptions and limitations in the model consisted of errors in dynamic similarity, wind tunnel wall effects and the fact that the flow over the model was in many cases not at the true flight Mach No. In view of these limitations, it was found to be desirable to obtain a physical understanding of the mechanisms involved in

flutter cases measured in the wind tunnel. The use of the theory for explaining test data permitted us to comprehend the problem in a quantitative sense so that the limitations of both the theory and model data could be evaluated. This type of correlation inspires practical engineers with a high degree of confidence in test results.

The early theoretical work preceded early developments of flutter models of actual aircraft because computed margins of safety were high and techniques for building suitable models were not available. Some of the first models represented unconventional designs such as the XP-54, B-35 and B-36 and did not pay off because they were replica type models which have limitations as discussed later. The first major payoff came from the B-47 flutter model which was designed primarily to represent only those modes of vibration expected to be significant from the standpoint of flutter. This simplification in dynamic modeling technology turned out to be extremely important since flutter models based on this concept have been used in the development of nearly every modern aircraft. It is of interest to note that the B-47 flutter model program was recommended by the Wright Field flutter group in lieu of a theoretical program requested by the contractor. There was not enough confidence in the theory for high performance configurations which were unconventional.

During this same period, improvements in flutter prediction procedures were attempted with digital and analog computer techniques. A multi-degree of freedom analysis was carried out on an IBM punch card machine for the B-36 aircraft. Biot and Wiancko developed an electronic analog for flutter analysis of three degree of freedom systems. Neither of these developments paid off at the time although some of the techniques were used in later developments along similar lines.

The limited payoff of complicated theoretical and experimental approaches indicates the importance of simplicity combined with depth of understanding in such developments (Reference 103). This statement does not mean that computer techniques are of no value. Essential theoretical calculations which are carried out more efficiently with computer equipment are justified and in fact have proven extremely valuable for dynamic analysis. However, the fact that computer equipment can handle more complicated theories is no reason for the use of such theories. We should have no respect for theory or tests per se; improvements in the aerospace vehicle resulting from the theory or tests is all that matters.

The advent of transonic, supersonic and hypersonic vehicles led to significant experimental and theoretical advances. Of particular significance was the use of the NASA 26 inch blowdown tunnel and the requirement of the Wright Field flutter group for model tests at full scale Mach numbers. The high density ratios available in this facility made it possible to extend the B-47 model concept to transonic speeds. In addition, the theoretical work of Possio, Garrick and Rubinow, Lighthill, Pines and others extended the unsteady aerodynamic theory from subsonic to hypersonic speeds. The theory was not good enough to be acceptable in itself but in combination with model test data, flutter problems in these speed ranges could be solved with sufficient accuracy for engineering purposes.

The importance of the flutter model to the aerospace industry makes it worthwhile to discuss technological developments used to design and fabricate such models. It is sometimes stated that such models are complicated, expensive and take a long time to build. However, similar statements are applicable to the design and fabrication of any number of devices which must conform to definite specifications and for which detailed design procedures have not been developed. In the case of dynamically similar models of aircraft the following factors must be considered:

1. The dynamic phenomena to be studied with the model.

2. Available fabrication techniques.

3. Possible model designs consistent with 1. and 2. above.

4. Engineering procedures for determination of the optimum model design.

5. Test procedures for measuring the dynamic characteristics of the model.

Since there have been no standard procedures for the design of dynamically similar models, a number of design approaches have been used, namely:

1. Exact geometric scaling — the replica model

2. Approximate geometric scaling

3. Scaling of external geometry only

4. Significant mode or modal approach

5. Combined modal and equivalent structural approach.

In our opinion, the first three approaches are impractical for small scale models of structures which are relatively complicated such as are used in aircraft. On the other hand the modal approach has been completely successful for the low speed flutter model and a corresponding success has been achieved with the combined modal and equivalent structural approach for the high speed flutter model.

The failure of the relatively popular geometric scaling approach is due mainly to limitations in manufacturing technology which are economically feasible for the fabrication of dynamically similar models. One must not only fabricate all the multitude of parts and fasten them together but all tolerances must also be scaled. Non-compliance with this very severe requirement on tolerances after spending a lot of money trying to make the model, can easily result in a dynamical behavior of the model that is nothing like the full scale. This failure which can be very serious results from the fact that the model has actually been approximately geometrically scaled instead of exactly scaled. It represents a complete failure of a mathematically exact decision because of a lack of consideration of practical fabrication problems.

After taking a beating by trying exact or approximate geometric scaling, the dynamics engineer sometimes throws in the sponge and tries to get by with a model that has the correct external contours and some stiffness and mass distribution that he thinks might flutter in the wind tunnel. The plan here is to obtain a flutter point and conduct calculations for the model to obtain a general fudge factor for the theory. While it is believed that this approach is superior to the exact scaling principle, fudge factors for the theory are functions of the model parameters and can lead to significant errors.

As previously mentioned, the modal approach was first used in this country by Boeing for the B-47. This approach may be said to be a physical representation of the equations of motion in terms of the zero airspeed modes expected to be significant from the standpoint of flutter. This limited objective made it possible to represent the elasticity of the model with a single spar which was convenient to design, machine and test. For the same reason the aerodynamic contours could be made of balsa wood which were attached to the spar in spanwise sections so as not to affect its stiffness; and the correct weight distribution could be obtained by concentrated weights installed in these sections.

The modal approach illustrates some sound principles which are perhaps the key to success in any dynamic model program namely:

1. Limiting the scope of the model program to only those dynamic problems which must be solved to properly design the full scale vehicle.

2. Simplifying the model design to include only the significant parameters.

3. Designing the parts of the model so that elementary engineering procedures are adequate for analysis and inexpensive shop practices are adequate for fabrication.

4. Designing the model so that mass, stiffness and vibration characteristics can be measured quickly and accurately with inexpensive equipment such as mirrors for stiffness tests, bifilar pendulums for inertia measurements and miniature electronic shakers for excitation.

Proof of dynamic similarity by means of these simple tests and correlation with full scale data gives a high degree of confidence in such models not only to dynamics engineers but also to supervisory engineers responsible for the success of complicated aircraft projects. It is of interest to repeat here that a mathematically approximate but practical approach resulted in a huge success in dynamical modeling while the exact or replica approach proved to be impractical.

The desire to obtain answers to dynamic problems at transonic, supersonic and hypersonic Mach Numbers lead to the combined modal and equivalent structural approach. The number of modes to be modeled is still limited to those required to provide the answers to specific design problems. Because of the higher true airspeeds, higher stiffnesses must be provided in such models; however, the weight is the same as that of the low speed model for

a given air density and scale. The efficiency of the model structure must therefore approach that of the full scale structure so that the model spar resembles the full scale spar especially if the full scale vehicle utilizes a main box. For most cases a simple box spar is designed that has the scaled local GJ and EI of the full scale surface and, if applicable, the chord of the spar on the model has the correct scaled value. Leading and trailing edge chordwise rigidities are generally represented by a small number of ribs attached to this spar. The space in between the ribs and final aerodynamic contours are obtained by balsa wood glued to the spars and ribs. Chordwise slots in the wood are generally not necessary because of the relatively high stiffness levels of the model spar.

It can be seen from the above that this combined modal and equivalent structural approach is a natural outgrowth of the modal approach used for the low speed flutter model. However, as mentioned above, spars and other elastic elements for such models designed on the basis of elementary structural formulae have a tendency to resemble the full scale components in regard to scaled dimensions. In fact the most successful models have been those where there is a marked similarity. This means that if two-dimensional structural analysis indicates a spar which is structurally equivalent and geometrically similar to the full scale spar, there will be an advantage in using this spar over one which the theory indicates is also structurally equivalent but not geometrically similar. This result at first appears contradictory to previous statements regarding approximate geometric scaling but in this case the design is based on elementary structural analysis rather than on geometry. The improved result comes from the fact that elementary structural theory is two dimensional so that similarity between model and full scale structures tends to incorporate the proper three dimensional effects.

One might think that many years in the business of dynamic models might result in a number of trade secrets but actually this is not the case. Success depends strictly on numerical evaluation of proposed designs plus tests in the laboratory to verify the results of the analysis. Experience with various programs when coupled with analysis and test should continually reduce the number of mistakes although unfortunately the same mistake pops up more than once. Problem areas which are encountered frequently are:

1. Meeting the weight and stiffness specifications

2. Designing attachments with sufficient rigidity within weight limits; for example, the attachment between spars and balsa sections.

3. Designing concentrated springs to represent actuator stiffnesses, engine pylons, supports of heavy items such as external stores, and joints between major items such as wing and tail surfaces to fuselage and vertical to horizontal tails on T-tails.

4. Reduction of friction and play in hinges to small enough values to have a negligible effect on the dynamic characteristics.

5. Obtaining good shear transfer where shear deflections control the stiffness.

6. Prevention of buckling of thin sheets when such sheets are required for the model.

Experience and testing combined with a knowledge of shop practices plus an extensive application of two-dimensional structural theory is necessary to overcome these problems. It is not a job for the hobbyist, the pure theoretician, or the expert in manufacturing technology, but an across the board combination of these skills plus experience is required.

The importance of manufacturing technology in the design of dynamically similar models has been mentioned above. The method used to design the model is based on the application of sound but elementary engineering principles correlated with simple tests to obtain the required mass and stiffness distributions and aerodynamic contours with the simplest manufacturing technology. The full range of simple technologies is applicable from the blacksmith shop to the modern standard machine tool. Chemical etching has been quite valuable for obtaining sheets which are non-standard in thickness. Epoxy resins in combination with mechanical fasteners is another technique that has proven extremely useful. Welding is used where possible to obtain good shear transfer. Key materials in such models are magnesium, aluminum and balsa wood.

Other major items that affect model design are the wind tunnel "q" and Mach No. to be used for the program. There is an advantage in testing at low "q" for low speed models since the loads on the model are reduced and spar weight requirements are easier to meet. From the standpoint of obtaining scaled static deflections, it is desirable that "q" be proportional to scale although in practice lower values of "q" seem to be desirable especially on light weight structures. For true Mach No. models, the blowdown tunnel with a relatively high density ratio has been very useful as indicated previously. A recent NASA facility that has also proven to be very useful in the transonic range is the 16 ft. Freon tunnel. This tunnel permits the use of low speed flutter model techniques to obtain data at the correct Mach No. because the speed of sound in Freon is only about 40% of that in air. Freon models are somewhat more difficult to design than either low speed or high speed air models because the stiffness levels are between those required for such models. Strength will be inadequate if an external skin is used, while weight will be a problem with an internal spar. However, the advantages of testing in Freon far outweigh these disadvantages.

Testing of the model in the wind tunnel requires the use of a dynamic mount if body freedoms are important to the problem being studied. The flying rod mount seems adequate for low speed tests and the NASA cable mount is suitable for high speed tests. It is not important that the mount have zero effect on the motions being studied but merely that the effects be kept to a small value. In other words, the impedance caused by mount constraints should be small compared to the impedance of the body itself in dynamic motions being studied. It goes without saying that the model must be statically and dynamically stable on its mount. A further requirement is that if a part of the model is lost due to flutter, the mount should prevent the loss of the complete model. This criterion has led to the development of the six degree

of freedom spring type mount which has recently proved successful in a number of flutter model tests. The travel on such a mount is naturally restricted but it has been possible, although sometimes somewhat difficult, to fly models on such a mount through the transonic range. It is desirable that improvements be made in the mount area, but it is believed that simple approaches to overcome existing limitations should be evaluated by accepted methods of dynamic analysis and then correlated by testing.

It is not clear at this time what part dynamically similar models will play in the future of aerospace technology. In the space area the theoretical effort in dynamics is considerably greater than the test effort using dynamically similar models. Since the theory without substantiation is seldom relied upon by practical engineers and mistakes are probable in lengthy computational procedures, one may expect from past experience that an increasing amount of dynamic analysis will be based on model tests correlated with theory.

Some trends are indicated by recent models of aircraft and space vehicles fabricated by Dynamic Devices, Incorporated.

1. Tilt Wing VTOL Flutter Model - Figure 1

2. Tilt Duct VTOL Flutter Model - Figure 2

3. Gemini Landing Model - Figure 3

4. Ground Wind Model - Figure 4

The designs of the VTOL Aircraft are so unconventional that it is not practical to risk the safety of these aircraft by relying solely on theoretical calculations. The reasons for the Gemini Landing Model were the nonlinear effects of the shock struts and skids. The ground wind model involves the effect of vortex forming flows on bending vibration for which there is no adequate theory. Other areas where models will possibly be used are as follows:

1. Autopilot Stability - Dynamic Model with Autopilot

2. Structural Vibration - Natural Modes and Response to Environmental Excitation

3. Buffeting - Wind Tunnel Dynamic Model

4. Dynamic Loads - Gusts -- Landing - Rendezvous

5. Fuel Sloshing - Tanks with Baffles and/or Odd Shaped Tanks

6. Aerothermoelasticity - Wind Tunnel Tests at High Temperatures

We may wonder why the theory currently has the upper hand in space technology. One of the key reasons is that the electronic computer permits more complicated calculations but perhaps the most important reason is that

the computed results do not have to be as reliable as those required for aircraft flutter since space vehicles do not normally encounter a go or no-go destructive phenomenon like flutter. The only problem that seems similar to flutter is autopilot stability which at present is determined by theoretical analysis, and in this case it is possible that improved systems could be developed by a combination of model tests and theory.

There is a recent trend toward complicated numerical methods of analysis using high speed digital computers which give improved analytical solutions for complicated problems in dynamics. Since each solution applies to only one vehicle configuration and it is not exact, model technology together with less complicated but more generally applicable theory may give more reliable answers at lower costs.

The large dependence on theory is hard to take for practical engineers who have spent their lives believing in the importance of good tests. This situation could be alleviated somewhat if computers were programmed to tell engineers not only what happens but why it happens in suitable language so that the engineer feels that he understands the mechanism involved. The development of such programs will cut down the number of mistakes that are made. Possible examples are: (1) strain energy distributions for major structural elements such as the main leading edge and trailing edge boxes in the various modes of vibration and (2) vector diagrams representing the energy balance in the important degrees of freedom involved in instabilities such as flutter.

It is believed that the simplest and least expensive tools should be used to solve the dynamic problems of the future. These tools either theory or model cannot be perfect and, in fact, any approach to the solution of dynamics problems which requires perfect tools must be incorrect. It is believed that the quest for perfect approaches has: (1) delayed model developments in sonic fatigue and aerothermoelasticity (2) resulted in a large amount of improper use of computer capabilities and (3) produced complicated and expensive models with a very limited payoff. The entire flutter model technology may be said to have paid off because a practical but imperfect approach was adopted.

It is our opinion that future problems will be adequately handled by our imperfect but practical tools both model and theory. We should use these tools to tell us why as well as what since it is only by knowing why that we can achieve performance, safety and reliability of aerospace systems at minimum cost.

Table 1

Dynamics and Aerothermoelasticity Problems and Analytical and Experimental Developments

1935 - 1940 Approximately

Actual Vehicle Problem or (Possible Vehicle Problem)	Analytical Development	Modeling Development
	General Flutter Theory (1)	
Control surface flutter		Empirical mass balance data from semi-rigid flutter models.
Trim tab flutter		
	Design charts for analysis of typical two dimensional sections. (2)	
	Parametric variations for lifting and control surface flutter. Systematic survey for two dimensional sections. (3)	Simple, high aspect ratio, flutter models for correlations with theory. (3)

Table 2

Dynamics and Aerothermoelasticity Problems and Analytical and Experimental Developments

1940 - 1945 Approximately

Actual Vehicle Problem or (Possible Vehicle Problem)	Analytical Development	Modeling Development
	Numeric tabulation of two dimensional aerodynamic coefficients including aerodynamically balanced control surfaces. Three dimensional method available for aircraft applications. (4)	
	Natural mode, natural frequency and flutter predictions of wings with concentrated weights. (5)(6)	
(Fighter with twin booms.)		Replica flutter model. Plastic.
	Electric network model and flutter predictor for three degrees of freedom. (7)(8)	
Spring tab flutter	Tabulation of tab aerodynamic coefficients; tab flutter analysis procedures. (9)	

Table 3

Dynamics and Aerothermoelasticity Problems and Analytical and Experimental Developments

1945 - 1950 Approximately

Actual Vehicle Problem or (Possible Vehicle Problem)	Analytical Development	Modeling Development
(Heavy Bombardment Flying Wing with Trailing edge Engines)		Replica flutter model. Magnesium.
(Heavy Bombardment Aircraft with Pusher Engines on Trailing Edge)		Replica flutter model. Plastic.
(Design of Swept Wing, Transonic Heavy Bombardment Aircraft with Engines on Flexible Pylons)		Beginning of "equivalent beam" or spar flutter model development in US and practical "free flying" support for wind tunnel tests (10).
Transonic Control Surface Buzz		Empirical prevention criteria from tests. (11)
	Low Aspect ratio wing aerodynamics. (12)	
	Supersonic theories for zero thickness oscillating wings. (13)(14)	
Dynamic Landing Load problems (16)(19)	Methods for prediction of loads; measurements and correlations with theory. (15)(16)(17)(18)(19)	
Aileron reversal of swept wings	Lift distribution for straight and swept wings. Static aeroelasticity trends and investigations. (20)(21)(22)(23)(24)	

Table 3 (Cont'd)

Dynamics and Aerothermoelasticity Problems and Analytical and Experimental Developments

1945 - 1950 Approximately

Actual Vehicle Problem or (Possible Vehicle Problem)	Analytical Development	Modeling Development
	Use of IBM machines for flutter analyses. (25)	
Aeroservoelastic problems. Fuselage bending, rudder rotation, autopilot coupling.		
	Subsonic swept wing flutter prediction methods. Strip aerodynamics. (26)(27)	Elementary flutter model tests to determine effects of sweep.

Table 4

Dynamics and Aerothermoelasticity Problems and Analytical Experimental Developments

1950 - 1955 Approximately

Actual Vehicle Problem or (Possible Vehicle Problem)	Analytical Development	Modeling Development
	Solution of Dynamic and aeroelastic problems by electronic analogue computers. (28)(29)(30)(31)	
(Effect of tip tanks on wing flutter)		Beam type spar for wind tunnel flutter model. (32)
(Anti-symmetric flutter of wings with engines)		Trends from flutter model tests. (33)
Control Surface Buzz		
T-tail flutter		
	Aeroelastic-aeroservoelastic prediction methods. (34)(35)	
All-movable tail flutter		Flutter model investigations to determine important parameters and define criteria. (36)(37)(38)
	Prediction of thickness effects on airfoils oscillating at high Mach numbers. (39)(40)	
Flutter of wings with external stores.		
	Three-dimensional, subsonic aerodynamics for oscillating airfoils. (41)(42); later (43)(44)	

Table 4 (Cont'd)

Actual Vehicle Problem or (Possible Vehicle Problem)	Analytical Development	Modeling Development
	Theory for low aspect ratio wings at transonic speeds. (45)	
		T-tail flutter trends from model tests. (46)(47)
	Prediction of noise fields and structural fatigue from random loadings. (48)(49)	
	Initial efforts on panel flutter theories. (50) See earlier references (51). For later references see (52)(53).	Initial panel flutter experiments and correlations with theory. See earlier references in (51).

Table 5

Dynamics and Aerothermoelasticity Problems and Analytical and Experimental Developments

Approximately 1955 - Present

Actual Vehicle Problems or (Possible Vehicle Problems)	Analytical Development	Modeling Development
	Aeroelasticity textbooks (54)(55)	
(Flutter prevention of low thickness ratio wings at transonic speeds and low altitude)		Beginning of development of low weight flutter models with foam or balsa filler and metal foil covering. Equivalent structure simulating structural aspect ratio and actual construction. (49)
	Effects of heating and aerothermoelastic analysis methods. (57)(58)(59)	
	Aeroelastic effects on stability and control. (See earlier efforts also.) (60)	
	Finite span aerodynamics for airfoils oscillating in a low supersonic Mach number stream. (61)(62)	
	Prediction of dynamic loads for random processes. (63)(64)(65)	
Sonic fatigue (66)		
	Piston theory developments (67)	
Panel flutter	Panel flutter prediction methods See references (51)(52)(53)	Correlations with theory and trends. See references (51)(52)(53)

Table 5 (Cont'd)

Actual Vehicle Problems or (Possible Vehicle Problems)	Analytical Development	Modeling Development
		Transonic flutter model tests and trends. (68) Supersonic flutter model tests and trends. (69)
Aeroservoelastic problems (70)(71)	Prediction of aeroservoelastic problems. (70)(71) Stiffness and deflection analyses. Deflection and force methods. (72)(73)(74)(75)(76)(77)(78)(79) Supersonic and hypersonic flutter trends from piston theory. (80)(81)(82) Unsteady transonic flow with shock waves. (83)	
Fatigue of aircraft structures (84)		
Propeller whirl flutter	Prediction of whirl flutter (85)(86)	
Dynamic problems of aerospace vehicles: Aeroservoelasticity (87) Ground Winds Boosted Flight Transonic Buffet Fuel Slosh	Prediction and prevention of problems: Aeroservoelasticity (88) Ground Winds (89)(90) Boosted Flight (91) Staging Re-entry Landing and Recovery Fuel Slosh (93)	

Table 5 (Cont'd)

Actual Vehicle Problems or (Possible Vehicle Problems)	Analytical Development	Modeling Development
		Correlation of piston theory with supersonic flutter model tests. (94)
	Theoretical hypervelocity unsteady aerodynamics (95)(96)	
	Prediction of aerodynamic interference and interaction effects. (97)	
	Analysis of non-linear structures. (98)(99)(100)(101)	
		Use of structural models for sonic fatigue. (102)

REFERENCES

1. Theodorsen, T., "General Theory of Aerodynamic Instability and the Mechanism of Flutter", NACA Report 496, 1935.

2. Kassner, R., and Fingado, H., "The Two-Dimensional Problem of Wing Vibration", Journal of the Royal Aeronautical Society, Vol XLI, 1937, pp. 921-944, Translation from Luftfahrtforschung, Vol 13, No 11, November 1936, pp. 374-387.

3. Theodorsen, T. and Garrick, I. E., Mechanism of Flutter — A Theoretical and Experimental Investigation of the Flutter Problem", NACA Report 685, 1940.

4. Smilg, B. and Wasserman, L. S., "Application of Three-Dimensional Flutter Theory to Aircraft Structures", Air Force Technical Report 4798, 1942.

5. Biot, M. A., "Flutter Analysis of a Wing Carrying Large Concentrated Weights", CALCIT Flutter Report 1A for USAF, California Institute of Technology, 1941.

6. Rasof, B., "Vibration Analysis of a Wing Mounting Flexibility Suspended Engines", CALCIT Flutter Report 10 for USAF, California Institute of Technology, 1943.

7. Biot, M. A. and Wianko, T. H., "Electric Network Model for Flexure Torsion Flutter", CALCIT Flutter Report 3 for USAF, California Institute of Technology, 1941.

8. Biot, M. A. and Wianko, T. H., "Theory of Electrical Flutter Predictor for Three Degrees of Freedom", CALCIT Flutter Report 8 for USAF, California Institute of Technology, 1943.

9. Wasserman, L. S., Mykytow, W. J. and Spielberg, I. N., "Tab Flutter Theory and Applications", USAF Technical Report 5153, 1944.

10. Kinnaman, E. B., "Flutter Analysis of Complex Airplanes by Experimental Methods", Journal of the Aeronautical Sciences, Vol 19, No 9, Sept. 1952.

11. Smilg, B., "The Prevention of Aileron Oscillations at Transonic Airspeeds", USAF Technical Report 5530, 1946.

12. Jones, R. T., "Properties of Low-Aspect Pointed Wings at Speeds Below and Above the Speed of Sound", NACA Report 835, 1946.

13. Garrick, I. E. and Rubinow, S. I., "Flutter and Oscillating Air Force Calculations for an Airfoil in Two-Dimensional Supersonic Flow", NACA Report 846, 1946.

14. Garrick, I. E. and Rubinow, S. I., "Theoretical Study of Air Forces on an Oscillating or Steady Thin Wing in a Supersonic Main Stream", NACA Report 872, 1947.

15. [illegible], H. A. and Hasslinghoff, K. L., "Dynamic Load on Airplane Structures During Landing", NACA ARR No. 4H10, 1944.

16. Lunney, S. J., "Dynamic Landing Loads on B-29 Airplane Landing Gear", Army Air Forces Air Technical Service Command Report No. TSEAC5-45128-2-10, February 1946.

17. Wasserman, L. S., "The Prediction of Dynamic Landing Loads", Proceedings of the Seventh International Congress of Applied Mechanics, London, 1948.

18. Wasserman, L. S. and Kramer, E. H., "A Method for Predicting Dynamic Landing Loads", USAF Air Material Command Memorandum Report No. MCREXA5-4595-8-2, February 1948. Also see WADC Technical Report 54-28, "A Method for Predicting Dynamic Landing Loads" by Eisenman, R. L. and Kramer, E. H.

19. Goland, M., Luke, Y. L., and Kahn, E. A., "Prediction of Dynamic Landing Loads", USAF Air Material Command Technical Report 5815, January 1949.

20. Multhopp, H., "Methods for Calculating the Lift Distribution of Wings, Subsonic Lifting Surface Theory", British A.R.C. Reports and Memoranda 2884, 1950.

21. Weissinger, J., "The Lift Distribution of Sweptback Wings", NACA Technical Memorandum 1120, 1947.

22. Groth, E., "Determination of the Rolling Effectiveness and Aileron Reversal Speed of an Elastic Wing", USAF Air Material Command Memorandum Report MCREXA5-4595-8-10, October 1949.

23. Groth, E., "Evaluation of Methods for Calculating the Rolling Effectiveness and Aileron Reversal Speed of a Straight Wing", USAF Air Material Command Memorandum Report MCREXA5-4595-8-6, December 1948.

24. Diederich, F. W. and Budiansky, B., "Divergence of Swept Wings", NACA Technical Note 1680, 1948.

25. Lenobert, E. L., "An Application of IBM Machines to the Solution of the Flutter Determinant", Journal of Aeronautical Sciences, Vol 14, No 3, pp. 171-174, March 1947.

26. Spielberg, I., Pettis, H., and Toney, H., "Methods for Calculating the Flutter and Vibration Characteristics of Swept Wings", USAF Air Material Command Report MCREXA5-4595-8-4, August 1948.

27. Barmby, J. G., Cunningham, H. J., and Garrick, I. E., "Study of Effects of Sweep on the Flutter of Cantilever Wings", NACA Report 1014, 1951.

28. Baird, E. F. and Kelley, H. J., "Formulation of the Flutter Problem for Solution on an Electronic Analog Computer", Journal of the Aeronautical Sciences, Vol 17, pp. 189-190, 1950.

29. MacNeal, R. H., McCann, G. D., Wilts, C. H., "The Solution of Aeroelastic Problems by Means of Electronic Analogies", Journal of the Aeronautical Sciences, Vol 18, pp. 777-789, 1951.

30. Winson, J., "The Solution of Aeroelastic Problems by Electronic Analogue Computation", Journal of the Aeronautical Sciences, Vol 17, pp. 385-395, 1950.

31. Kelley, M. J. and Fogel, G. D., "Application of the Reeves Electronic Analogue Computer to the Analysis of the Subsonic Flutter and Gust Problems", Grumman Aircraft Engineering Corporation Research Department Report RE-35, March 1950.

32. Gayman, W. H., "An Investigation of the Effect of a Varying Tip Weight Distribution on the Flutter Characteristics of a Straight Wing", Journal of the Aeronautical Sciences, May 1952.

33. Andreopolus, T. C., Chee, C. F., and Targoff, W. P., "The Effect of Engine Locations on the Antisymmetric Flutter Mode", USAF Wright Air Development Center Technical Report 6353, August 1951.

34. Dugundji, J., "A Nyquist Approach to Flutter", Journal of the Aeronautical Sciences, Readers Forum, Vol 19, No 6, pp. 422-423, June 1952.

35. McRuer, D. T., Benun, D., and Click, C. E., "The Influence of Servomechanisms on the Flutter of Servo-Controlled Aircraft", Air Force Technical Report 6287, October 1953.

36. Hoffman, N. R. and Spielberg, I. N., "Subsonic Flutter Tests of an Unswept All-Movable Horizontal Tail", USAF Wright Air Development Center Technical Report 54-53, March 1954.

37. Hoffman, N. R., "Subsonic Flutter Model Tests of an All-Movable Stabilizer with 35 Degrees Sweepback", USAF Wright Air Development Center Technical Note 55-623, November 1955.

38. Cooley, D. E. and Murphy, J. A., "Subsonic Flutter Model Tests of a Low Aspect Ratio Unswept All-Movable Tail", USAF Wright Air Development Center Technical Report 58-31, February 1958.

39. Lighthill, M. J., "Oscillating Airfoils at High Mach Number", Journal of Aeronautical Sciences, Vol 20, No 6, June 1953.

40. Van Dyke, M. D., "Supersonic Flow Past Oscillating Airfoils Including Non-linear Thickness Effects", NASA Report 1183, 1953.

41. Watkins, C. E., Runyan, H. L., and Woolston, D. S., "On the Kernel Function of the Integral Equation Relating the Lift and Downwash Distributions of Oscillating Finite Wings in Subsonic Flow", NACA Report 1234, 1955.

42. Runyan, H. L. and Woolston, D. S., "Method for Calculating the Aerodynamic Loading on an Oscillating Finite Wing in Subsonic and Sonic Flow", NACA

Technical Note 3694, 1956.

43. Hsu, P. T., "Some Recent Developments in the Flutter Analysis of Low-Aspect Ratio Wings", Proceedings of National Specialists Meeting on Dynamics and Aeroelasticity, Fort Worth, Texas, November 1958.

44. Cunningham, H. J. and Woolston, D. S., "Developments in the Flutter Analysis of General Plan Form Wings Using Unsteady Air Forces from the Kernel Function Procedure", Proceedings of National Specialists Meeting on Dynamics and Aeroelasticity, Fort Worth, Texas, November 1958.

45. Landahl, M. T., "The Flow Around Oscillating Low-Aspect Ratio Wings and Wing-Body Combinations at Transonic Speeds", Proceedings of the Ninth International Congress of Applied Mechanics, Brussels, August 1956.

46. Pengelley, C. D., Wilson, L. E., Epperson, T. B., and Ransleben, G. E., "Flutter Characteristics of a T-tail", USAF Wright Air Development Center Technical Report 52-162, November 1954.

47. Goldman, R. L., "Flutter of T-tails with Dihedral", Report on Tests at David Taylor Model Basin, Martin Report ER 8205, 1957.

48. Lighthill, M. J., "On Sound Generated Aerodynamically". I, General Theory, Proceedings of the Royal Society, London, 1952. II Turbulence as a Source of Sound, 1954.

49. Miles, J. W., "On Structural Fatigue under Random Loading", Journal of the Aeronautical Sciences, 1954.

50. Jordan, P. F., "Note on the Flutter of Sheet Panels", Glenn L. Martin Company Memorandum, October 1953.

51. Fung, Y. C. B., "A Summary of the Theories and Experiments on Panel Flutter", AFOSR Technical Note 60-224 (Based on an article written for the "AGARD Manual on Aero-elasticity", NATO under the editorship of W. P. Jones) May 1960.

52. Guy, L. D. and Dixon, S. C., "A Critical Review of Experiment and Theory for Flutter of Aerodynamically Heated Panels", Presented at the AFOSR and GE Symposium on Dynamics of Manned Lifting Planetary Entry, Philadelphia, October 1962.

53. Fung, Y. C., "Some Recent Contributions to Panel Flutter Research", American Institute of Aeronautics and Astronautics, Volume 1, No 4, April 1963.

54. Fung, Y. C., An Introduction to the Theory of Aeroelasticity , John Wiley and Sons, Inc., 1955.

55. Bisplinghoff, R. L., Ashley, H., and Halfman, R. L., Aeroelasticity , Addison-Wesley Publishing Company, 1955.

56. Head, A. L., "A Philosophy of Design for Flutter", Proceedings of the

National Specialists Meeting on Dynamics and Aeroelasticity, Institute of the Aeronautical Sciences, Fort Worth, Texas, November 1958.

57. Dryden, H. L. and Duberg, J. E., "Aeroelastic Effects of Aerodynamic Heating", paper presented at the Fifth General Assembly of AGARD, Ottawa, June 1955.

58. Bisplinghoff, R. L., "Some Structural and Aeroelastic Considerations of High Speed Flight", the Nineteenth Wright Brothers Lecture, Journal of the Aeronautical Sciences, Vol 23, April 1956.

59. Bisplinghoff, R. L. and Dugundji, "Influence of Aerodynamic Heating on Aeroelastic Phenomena", Chapter 14 of Agardograph No 23, High Temperature Effects in Aircraft Structures, N. J. Hoff, Editor, Pergamon Press, London, 1958.

60. J. B. Rea Company, Inc., "Aeroelasticity in Stability and Control", USAF Wright Air Development Center Technical Report 55-173, March 1957.

61. Pines, S., Dugundji, J., and Neuringer, J., "Aerodynamic Flutter Derivatives for a Flexible Wing with Supersonic and Subsonic Edges", Journal of the Aeronautical Sciences, Vol 22, No 10, October 1955.

62. Zartarian, G. and Hsu, P. T., "Theoretical Studies on the Prediction of Unsteady Supersonic Airloads on Elastic Wings," Part 1, "Investigations on the Use of Oscillatory Supersonic Aerodynamic Influence Coefficients", WADC Technical Report 56-97, December 1955. Part 2 by G. Zartarian "Rules for Application of Oscillatory Supersonic Aerodynamic Influence Coefficients", WADC Technical Report 56-97, February 1956.

63. Fung, Y. C., "The Analysis of Dynamic Stresses in Aircraft Structures During Landing as Nonstationary Random Processes", Journal of Applied Mechanics, Vol 22, No 4, December 1955.

64. Liepmann, H. W., "Extension of the Statistical Approach to Buffeting and Gust Response of Wings of Finite Span", Journal of the Aeronautical Sciences, Vol 22, No 3, March 1955.

65. Bisplinghoff, R. L., Pian, T. H. H., and Foss, K. A., "Response of Elastic Aircraft to Continuous Turbulence", AGARD Report No 117, April-May 1947.

66. Bingman, R. N., "Resonant Fatigue Failures Associated With Noise", SAE preprint 164B, SAE National Aeronautic Meeting, New York, April 1960.

67. Ashley, H. and Zartarian, G., "Piston Theory - A New Aerodynamic Tool for the Aeroelastician", Journal of the Aeronautical Sciences, Vol 23, No 12, December 1956.

68. Targoff, W. P. and White, R. P., "Flutter Model Testing at Transonic Speeds", Journal of the Aeronautical Sciences, Aeronautical Engineering Review, June 1957.

69. McCarthy, J. F. Jr. and Halfman, R. L., "The Design and Testing of Supersonic Flutter Models", Journal of the Aeronautical Sciences, June 1956.

70. Edelen, D. G. B., "The Problem of Structural Feedback for a Rocket Structure". Glenn L. Martin Report. 1957.

71. Bisplinghoff, R. L. and Ashley, H., Principles of Aeroelasticity , John Wiley and Sons, Inc., 1962. See figure 1-6.

72. Klein, B., "A Simple Method of Matrix Structural Analysis", Journal of the Aero/Space Sciences, Part I, Vol 24, January 1957; Part II, Vol 24, November 1957; Part III, Vol 25, June 1958; Part IV, Vol 26, June 1959; Part V, Vol 27, November 1960.

73. Denke, P. H., "A Matrix Method of Structural Analysis", Proceedings of the Second U.S. Congress of Applied Mechanics, June 1954.

74. Turner, M. J., Clough, R. W., Martin, H. C., and Topp, L. J., "Stiffness and Deflection Analysis of Complex Structures", Journal of the Aeronautical Sciences, Vol 23, Number 9, p. 805, September 1956.

75. Levy, S., "Computation of Influence Coefficients for Aircraft Structures with Discontinuities and Sweepback", Vol 14, No 10, p. 547, October 1947.

76. Rand, T.,"An Approximate Method for the Calculations of Stresses in Sweptback Wings", Journal of the Aeronautical Sciences, Vol 18, No 1, p. 61, January 1961.

77. Wehle, L. B., Lansing, W., "A Method for Reducing the Analysis of Complex Redundant Structures to a Routine Procedure", Journal of the Aeronautical Sciences, Vol 19, No 10, p. 677, October 1952.

78. Argyris, J. H. and Kelsey, S., Energy Theorems and Structural Analysis , Butterworths, 1960.

79. Gallager, R. M. and Rattinger, I., "The Experimental and Theoretical Determination of the Elastic Characteristics of Modern Airframes", Report to the AGARD Structures and Materials Panel, Athens, Greece, September 1960.

80. Ashley, H. and Zartarian, G., "Supersonic Flutter Trends as Revealed by Piston Theory Calculations", USAF Wright Air Development Center Technical Report 58-74, January 1958.

81. Morgan, H. G., Runyan, H. L. and Huckel, V., "Theoretical Considerations of Flutter at High Mach Numbers", Journal of the Aeronautical Sciences, Vol 25, No 6, June 1958.

82. Chalwa, J. P., "Aeroelastic Instability at High Mach Number", Journal of the Aeronautical Sciences, Vol 25, No 4, April 1958.

83. Eckhaus, W., "Two-Dimensional Transonic Unsteady Flow with Shock Waves", USAF Office of Scientific Research Technical Note 59-491, 1959.

84. Many authors, "Proceedings of WADC Symposium on Fatigue of Aircraft Structures", WADC TR 59-507, August 1959.

85. Taylor, E. S. and Browne, K. A., "Vibration Isolation of Aircraft Power Plants", Journal of the Aeronautical Sciences, Vol 6, No 2, December 1938.

86. Reed III, W. H. and Bland, S. R., "An Analytical Treatment of Aircraft Propeller Precession Instability", NASA Technical Note D-659.

87. Waymeyer, W. K. and Sporing, R. W., "An Industry Survey on Aeroelastic Control System Instabilities in Aerospace Vehicles", Presented to IAS 30th Annual Meeting, New York, January 1962.

88. Lukens, D. R., Schmitt, A. F. and Broucek, G. T., "Approximate Transfer Functions for Flexible - Booster - and - Autopilot Analysis", USAF Wright Air Development Division Technical Report TR 61-93, April 1961.

89. Bohne, C. R., Clingan, B. E., deCeault, C. W., and Deutschle, P. C., "The Dynamic Response of Advanced Vehicles", USAF Wright Air Development Division Report 60-518, September 1960.

90. Bohne, C. R., "Ground Wind - Induced Loads on Launch Vehicles", USAF Aeronautical Systems Division Technical Documentary Report ASD-TDR-62-371. August 1962. (Unclassified title, Confidential Report.)

91. Clingan, B. E., Gates, R. E. and Andrews, J. S., "Dynamic Loads During Boosted Flight", USAF Aeronautical Systems Division Technical Documentary Report -63-302, May 1963.

92. Ezra, A. A. and Peterson, H. C., "Determination for Transonic Buffeting Forces Acting on Launch Vehicles", American Rocket Society Paper 2407-62, April 1962.

93. Bauer, H. F., "Dynamics of Liquid Propellant Vehicles", NASA MTP - AERO 61-34, April 1961.

94. Ashley, H., Rykytow, W. J. and Martuccelli, J. R., "Prediction of Lifting Surface Flutter at Supersonic Speeds", Second International Congress, International Council of the Aeronautical Sciences, Zurich, September 1960.

95. Ashley, H. and Zartarian, G., "Theoretical Hypervelocity Unsteady Aerodynamics", Proceedings of Symposium on Aerothermoelasticity, USAF Aeronautical Systems Division Technical Report 61-645, October - November, 1961.

96. Rodden, W. and Revell, J., "The Status of Unsteady Aerodynamic Influence Coefficients", Fairchild Fund Paper No FF-13, presented at 30th Annual Meeting of Institute of the Aerospace Sciences, New York, January 1962.

97. Ashley, H., "Some Recent Developments in Interference Theory for Aeronautical Applications", MIT Fluid Dynamics Research Laboratory Report No 63-3, July 1963.

98. Denke, Paul H., "Digital Analysis of Non-Linear Structures by the Force Method", Presented to Structures and Materials Panel, AGARD, NATO, July 1962.

99. Lansing, W., Jones, I. W., Ratner, P., "Non-Linear Analysis of Heated, Cambered Wings by the Matrix Force Method", Journal of the American Institute of Aeronautics and Astronautics, Volume 1, Number 7, p. 1619, July 1963.

100. Turner, M. J., Martin, H. C., and Weikel, R. C., "Further Development and Applications of the Stiffness Method", Paper presented to AGARD Structures and Materials Panel, NATO, Paris, France, July 1962.

101. Weikel, R., Jones, R., Seiler, J., Martin, H., Greene, B., "Non-Linear and Thermal Effects on Elastic Vibrations", ASD Technical Documentary Report 62-156, June 1962.

102. Gray, C. L., "Study in the Use of Structural Models for Sonic Fatigue", Aeronautical Systems Division Technical Report 61-537, April 1962.

103. Biot, M. A., "Science and the Engineer", Applied Mechanics Reviews, Volume 16, Number 2, February 1963.

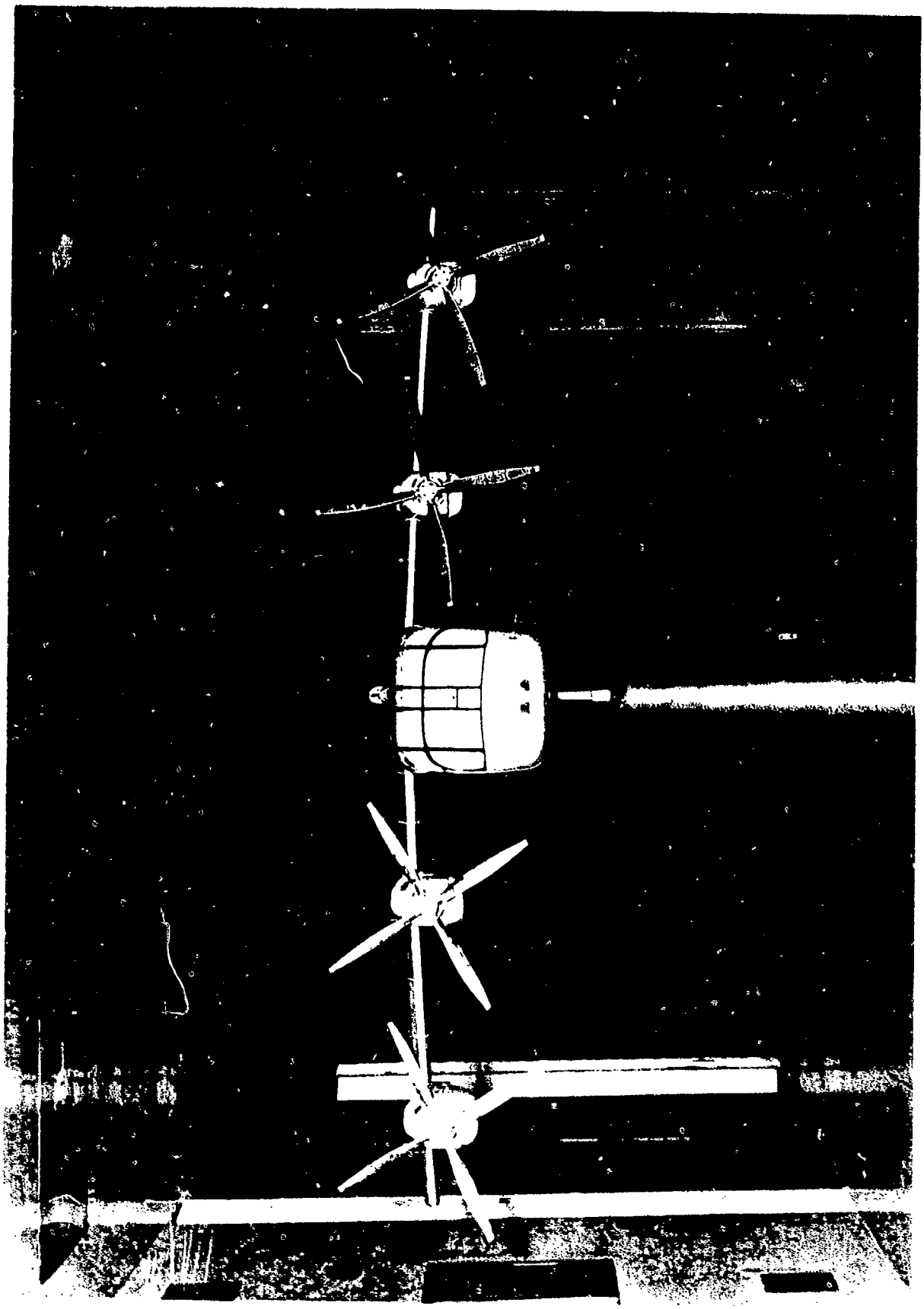

Figure 1 Tilt Wing VTOL Flutter Model

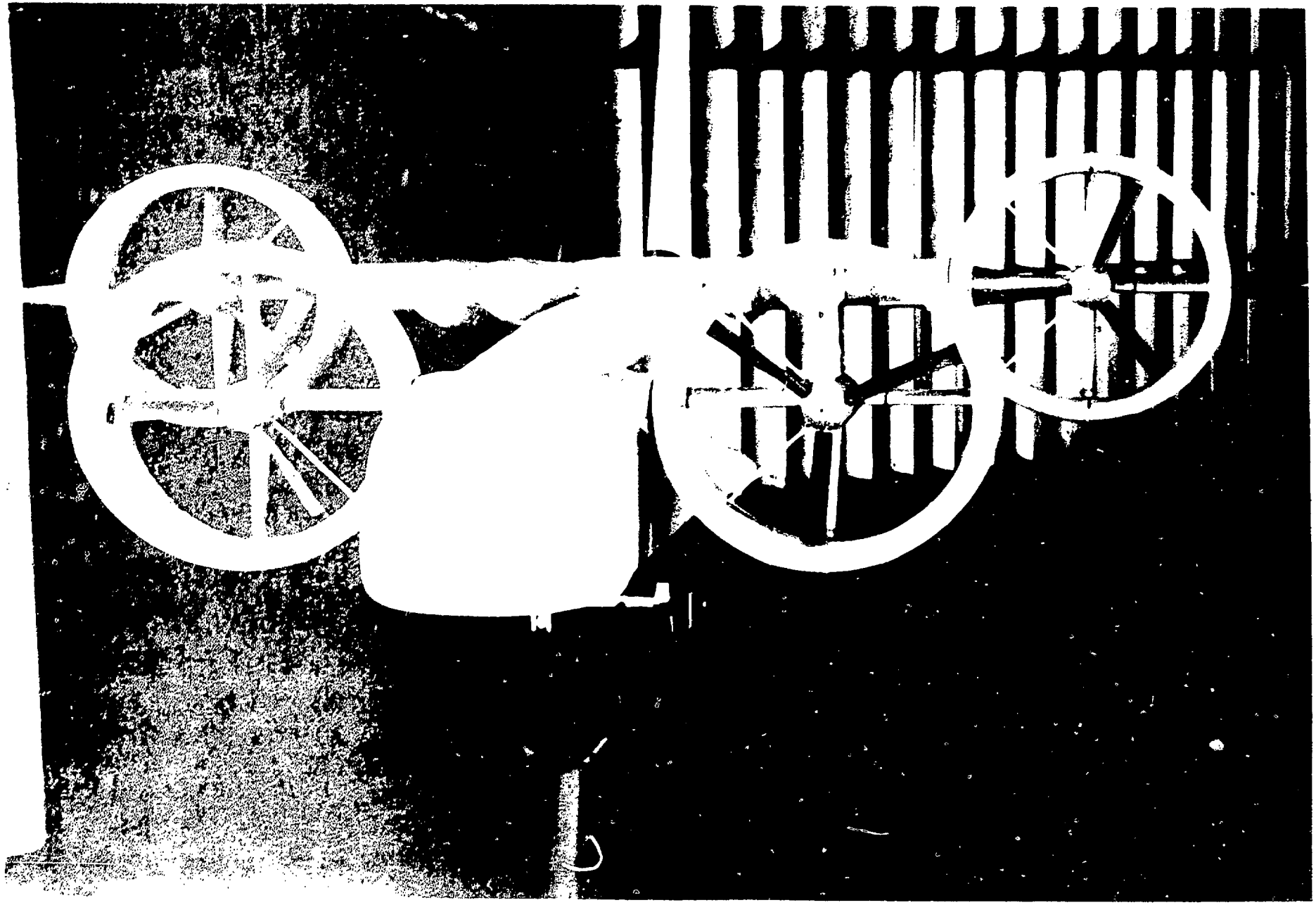

Fig. 2 [illegible] VTOL Flutter Model

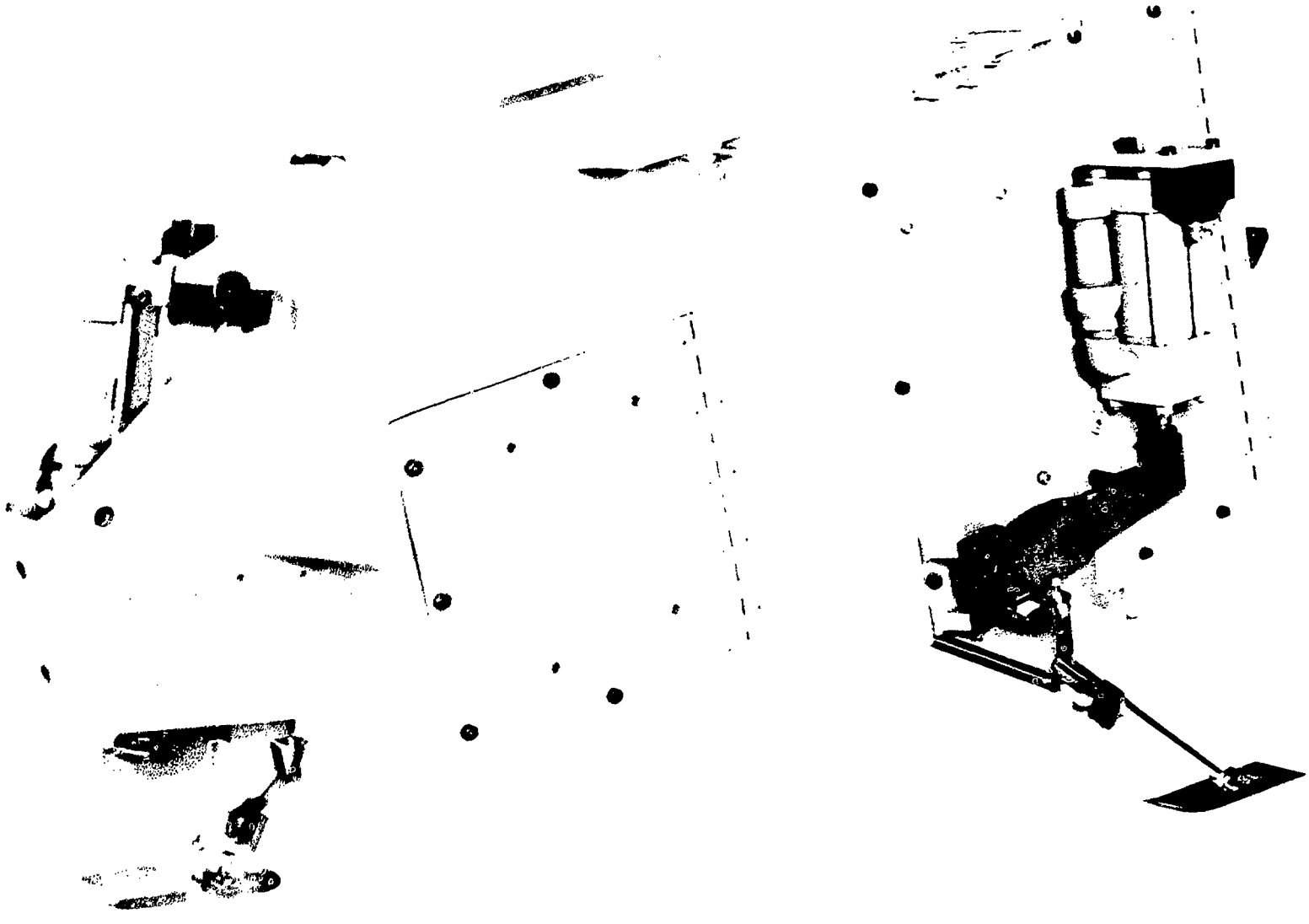

Figure 3 Gemini Landing Model

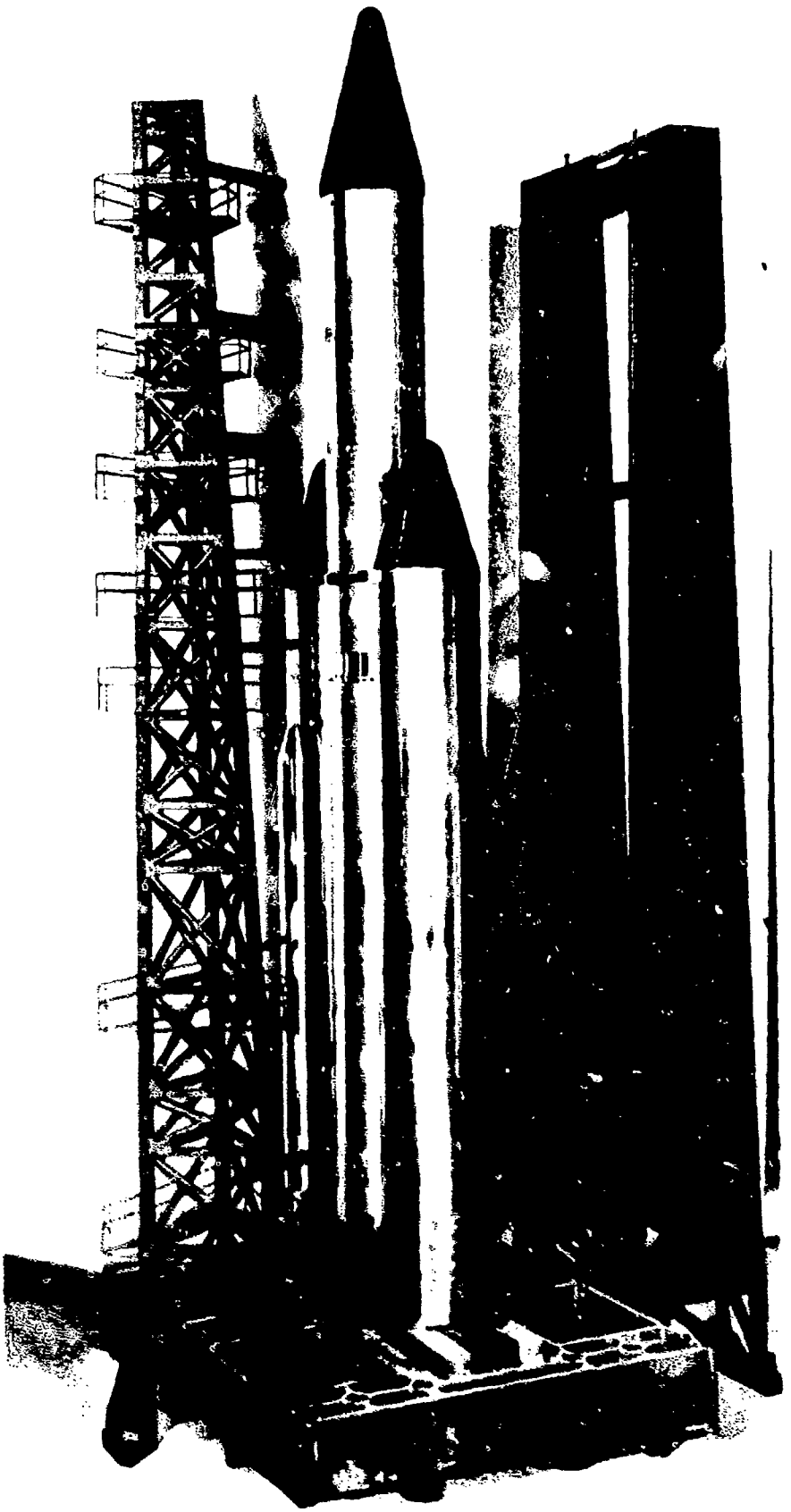

Figure 4 Ground Wind Model

ON THE USE OF DYNAMIC MODELS FOR STUDYING LAUNCH VEHICLE BUFFET AND GROUND-WIND LOADS

By Perry W. Hanson and George W. Jones, Jr.

NASA Langley Research Center

Langley Station, Hampton, Va.

ABSTRACT

The complex nature of the random aerodynamic input forces associated with transonic buffet and ground winds leads to difficulty in analytical treatment of the response of launch vehicles to these important loading conditions. The application of aeroelastically scaled models in the wind tunnel as a mechanical analog of the mathamatically complex problem requiring solution is described. Scaling relationships involved in this approach are developed and some checks on their validity are presented. Model design and support techniques are discussed and some typical results given. Some problems arising from the increased size of launch vehicles are discussed.

LIST OF ILLUSTRATIONS

FIGURE PAGE

SYMBOLS

$\hat{C}_L(k)$ correlation function

C_A aerodynamic damping coefficient

C_c control-system damping

C_{cr} critical value of damping

C_s structural damping coefficient

D reference diameter

f natural frequency

k reduced frequency, $L\omega/V$

L total length

l reference length, usually diameter

l effective moment arm

M Mach number

M'_n generalized mass of nth mode

q dynamic pressure, $\frac{1}{2}\rho V^2$, $\frac{1}{2}\rho U_e^2$

R_N Reynolds number

R reference radius

U_e equivalent ground-wind velocity

u random velocity fluctuations of ground wind in drag direction

v random velocity fluctuations of ground wind in lift direction

V free-stream velocity

Z_o any particular longitudinal station

σ^2 mean-square bending moment

σ root-mean-square bending moment

σ_T total root-mean-square bending moment, $\sqrt{\sigma_1^2 + \sigma_2^2 + \sigma_3^2}$

ϵ surface roughness height

ω circular frequency

ρ fluid density

PSD power spectral density

Subscripts:

F full scale

M model

n nth natural free-free bending mode, n = 1, 2, 3, . . .

ON THE USE OF DYNAMIC MODELS FOR STUDYING LAUNCH VEHICLE BUFFET AND GROUND-WIND LOADS

By Perry W. Hanson and George W. Jones, Jr.

NASA Langley Research Center

INTRODUCTION

Aeroelastic models of proposed aircraft or components have, of course, long been used to prove the stability of the design and to establish flutter and buffet boundaries. In view of the contributions that aeroelastic and dynamic model testing have made in the field of aircraft design, it is only natural that consideration be given to using such models for evaluation of launch vehicle designs. The relative importance of the various loading conditions on launch vehicles may be different with respect to those on aircraft structures but the reliable prediction of the loads is as important as ever.

This paper is concerned with the prediction of gross loads due to the response of lightly damped systems to the effects of separated flow. Two such load conditions are loads induced by ground winds and loads due to transonic buffeting.

As shown in figure 1, ground winds can be responsible for a variety of loading conditions. A drag load is produced in the direction of airflow that may be fluctuating due to atmospheric turbulence, gusts, etc. Vortex shedding can induce fluctuating loads in the direction of and perpendicular to the wind direction that may very well dictate strength requirements over a large portion of the vehicle.

Soon after lift-off the vehicle may be subjected to transonic buffeting loads, that, if not properly accounted for, could cause failure. Different types of buffet flow produce fluctuating pressures which can have quite different characteristics. An illustration of the differences in the power spectral density of the fluctuating pressures for two buffet flow conditions is given in figure 2. Although the total energy in each of the two pressure power spectra is about the same, it is seen that the distribution of energy is quite different. Most of the energy for the shock-boundary-layer interaction type of flow is in the low-frequency band; however, the wake buffet spectrum is nearly "white" and extends into the high-frequency range. The shock-boundary-layer interaction type distribution would be of concern for the booster elastic bending modes, whereas the wake buffet would contain energy of concern for higher frequency modes such as panel response.

The complex nature of these random aerodynamic input forces associated with transonic buffet and ground winds leads to difficulty in analytical treatment of the response of launch vehicles to these important loading conditions. Consequently, an extensive wind-tunnel launch vehicle buffet and

ground-winds loads study program has been undertaken at the Ames and Langley Research Centers.

Most of the buffet data reported to date have been concerned with the fluctuating pressure input part of the problem. (See refs. 1 and 2, for example.) In reference 3 fluctuating pressure data are presented for different size models of a large manned launch vehicle tested in air and in Freon-12. Although pressure data play a significant role in understanding the overall buffet characteristics of a particular configuration, application of these input data in the prediction of gross structural response is usually quite difficult. However, a relatively simple loads prediction technique can be applied which makes use of an aeroelastically scaled model in a wind tunnel as a mechanical analog of the mathematically complex problem requiring solution. That is, a suitable model in a suitable wind tunnel first generates the correct aerodynamic input forces and then performs the very difficult time and space integrations producing the desired response which can be measured readily. The application of this concept to the two problem areas, gross bending response due to transonic buffeting and ground-wind loads, will now be discussed. Model design considerations, including the support system and scale factors, and the data analysis methods applied to the two problems are somewhat dissimilar. For instance, the ground-winds model must be essentially cantilevered perpendicular to the flow direction, whereas the buffet model must be supported in as nearly a free-flight condition as practical. Also the relative importance of scale factors is different for the two models. The major aerodynamic scale parameter for the buffet model is Mach number but Reynolds number is the primary aerodynamic scale parameter for ground-winds models. Because of these differences, the two areas of concern may be more conveniently discussed separately. First, consider the dynamically scaled aeroelastic model approach applied to the problem of predicting vehicle gross bending loads due to transonic buffet.

PREDICTION OF TRANSONIC BUFFET LOADS

Design Considerations

A suitable model is, of course, a prime requirement. In addition to properly scaling the mass and stiffness distributions of the launch vehicle, the model must be supported in such a manner that it is essentially free to respond in its "free-free" bending modes. Model designs at Langley satisfying these requirements to varying degrees have progressed from relatively simple models and mounting systems to rather complex ones. Shown in figure 3 is a simple aeroelastic model the stiffness of which is determined by the thickness of the fiber-glass shell. Lead ballast was fixed to reinforcing rings along the model length to obtain the proper mass.

A more sophisticated model, a 2-percent aeroelastic model of the Saturn SA-1, is shown in figure 4. Here again the stiffness distribution is determined by the thickness and radius along the model of the fiber-glass shell. The skeleton reinforces the very thin scalloped section in the radial or "hoop" plane and serves as instrument and ballast mounts while contributing negligible bending stiffness. The sting incorporates an air-cooled electromagnetic shaker and a model restraining device. The model is supported on the

sting by leaf springs attached to the model at the first free-free mode points.

Results of recent investigations (ref. 4, for example) have indicated that vibration modes higher than the fundamental flexural mode may need to be simulated. The power spectrum of bending-moment response for a configuration tested is shown in figure 5, which indicates that the first two elastic modes are of equal importance in defining total response of this particular configuration. Note the low level of response in the low-frequency range associated with the support system. It has been found that supporting the model at the first free-free node points on springs that are soft relative to the model flexural stiffness provides a system that introduces negligible restraint even in the higher modes. Shown in figure 6 are some calculated free-free mode shapes and frequencies of a model recently tested compared with the mode shapes actually measured on the model mounted on the support system. The agreement is considered to be very good, and indicates that the free-free modes were not unduly influenced by the mounting system. In addition to supporting the model so that it experiences a minimum of restraint in its free-free vibration modes, other factors need to be considered. The rigid body effective pitch stiffness may be simulated but the sting-support system bending frequency must not be near the flexible mode frequencies. Another requirement for the model support system is that a means be provided for measuring the structural and aerodynamic damping of the model since these parameters enter into the scaling relationships necessary for extrapolating tunnel test data to full-scale conditions.

An example of such a support system that has been used recently is shown schematically in figure 7. The model was supported on a sting by means of a system of cables, pulleys, leaf springs, and torque rod springs. The leaf springs, attached to the model at the forward and rear node points of the first free-free mode, restrained the model in the drag and yaw directions. They contributed approximately 25 percent of the pitch stiffness required to simulate the full-scale pitch frequency. The model weight was supported by cables (also attached to the model at the first free-free node points) reeved over pulleys on the sting and routed out the rear of the model to a system of torque springs outside the test section. These torque springs provided the remaining 75 percent of the required pitch stiffness. Figure 8 is a photograph of the sting and shows the water-cooled electromagnetic shaker field coils which were built onto the sting. The moving coils of the shaker were attached directly to the inside of the model at the rear. The shaker was used to excite the model in its elastic vibration modes in order to determine the aerodynamic damping in each mode. Also shown are the pulleys used to guide the weight-supporting cables down the sting and the pneumatically operated "snubbers" which were used to restrain the model motion with respect to the sting whenever the need arose. Another requirement to be considered, of course, is the suitability of the tunnel in which the model is to be flown. The larger the model it can accommodate, the lesser will be the fabrication problem. The tremendous size and low stiffness levels of launch vehicles already dictate drastically reduced scale models with the accompanying difficulty in realizing the low scaled stiffness levels required and yet making them strong enough to withstand the loads imposed in wind-tunnel testing. Needless to say, the tunnel must have the capability of operating through the transonic speed range at reasonable levels of dynamic pressure, and the turbulence level must be sufficiently low so that the buffet response is not obscured by the response to turbulence.

Buffet Loads Scaling Relationships

Wind-tunnel buffet loads studies rely on the validity of certain scaling parameters for extrapolating the model results to full-scale conditions. The usefulness of these parameters has been reasonably well verified for the airplane wing buffet problem. Some experiments designed to provide further insight regarding the validity of their application to the launch vehicle buffet case have been conducted in reference 3. Some typical results are shown in figure 9. In this figure, the power spectra of fluctuating pressures acting on rigid models of a launch vehicle configuration are presented. The spectra in the upper part of the figure are, essentially, raw data measured on two models which differed in size by a factor of five and which were tested in air and Freon-12. Consider the upper portion of figure 7(a) which shows data for a 1.6-percent and an 8-percent model tested in Freon-12. The two models produced two spectra which form separate functions of frequency out to the limit of the instrumentation of about 600 cps. The spectra of the lower portion of the figure have been scaled to full-scale conditions by scaling relationships which involve ratios of the dynamic pressure, velocity, and body diameter. The scaling relationships used are, for the ordinate

$$(PSD)_F = (PSD)_M \left(\frac{q_F}{q_M}\right)^2 \left(\frac{D_F}{D_M}\right) \left(\frac{V_M}{V_F}\right)$$

and for the abscissa

$$f_F = f_M \left(\frac{D_M}{D_F}\right) \left(\frac{V_F}{V_M}\right)$$

It can be seen that the spectra of the lower part of the figure could reasonably well be represented by a single function indicating that, in this case, the scaling relationships seem to be applicable at least over a range of five to one. Figures 7(b) through 7(e) generally indicate the same conclusion. Figure 7(b) presents data from a transducer located at a position different from that of figure 7(a), and the data in figure 7(c) are for a different Mach number and much lower pressures. Figure 7(d) compares data from a model tested in Freon-12 and in air. Finally, figure 7(e) compares the data from a 1.6-percent model tested in Freon-12 and an 8-percent model tested in air. Results of this type encourage the belief that model buffet data can be extrapolated to full-scale conditions. Further results concerning buffet pressure scaling are contained in reference 5.

In order to predict the magnitude of full-scale buffet loads from tests on dynamically scaled aeroelastic models, it is necessary, of course, to determine the proper scaling relationships for such a system. A dynamic analysis of launch vehicle buffeting has been considered in some detail in reference 4. In the analysis, based on simple beam theory and the techniques of generalized harmonic analysis (which is treated in some length in ref. 6 and was first applied to the analysis of buffeting in ref. 7), the vehicle was assumed to be flying at constant altitude with a constant velocity. The only aerodynamic forces present in addition to the random component were damping forces proportional to the velocity of the bending vibrations of the system. No loss of generality results from neglecting the aerodynamic inertia and spring forces since such forces usually are small when compared with their

structural counterparts for a slender launch vehicle (see, for instance, refs. 8 and 9). Structurally, the vehicle was considered to be a linear multidegree-of-freedom system.

The final result obtained from this analysis for the total root-mean-square bending moment at some longitudinal station Z_o is

$$\sigma_T^2(Z_o) = \sum_{n=1}^{\infty} l_n^2 \left[\frac{\pi \omega_n}{4\left(\frac{C}{C_{cr}}\right)_n} \right] \frac{q^2}{V} R^2 L^3 \hat{C}_{L,n}(k_n) \qquad (1)$$

(Although eq. (1) has been developed for mean-square bending moment, it should be pointed out that expressions similar to eq. (1) could be obtained for any quantity which is proportional to displacement.) The total mean-square bending moment is a superposition of single-degree-of-freedom results (coupling terms were neglected in the derivation), each mode being independently treated as a separate system. The right-hand side of equation (1) may be conveniently separated into three parts. The first part, the term l_n^2, is the square of an effective moment arm. The second term, enclosed in brackets, is an admittance type term. In particular, it is $\pi/2$ times the maximum value of the mechanical admittance in the nth mode multipled by the width of the admittance curve at the one-half power point. The damping ratio which appears in the second term of the right-hand side of equation (1) is

$$\left(\frac{C}{C_{cr}}\right)_n = \frac{C_s}{C_{cr}} + \frac{C_c}{C_{cr}} + \frac{C_A}{C_{cr}}$$

where

$\frac{C_s}{C_{cr}}$ structural damping ratio

$\frac{C_c}{C_{cr}}$ control-system damping ratio

$\frac{C_A}{C_{cr}}$ aerodynamic damping ratio

The remaining terms are associated with the random aerodynamic loading. The function $\hat{C}_{L,n}(k_n)$ is the correlation function of the random section lift coefficients for the nth mode. Although not mathematically exact, a convenient way of thinking of this function is that it is the power spectrum of an effective random aerodynamic coefficient in the nth mode. The quantities R, L, q, and V are, respectively, reference radius, vehicle length, free-stream dynamic pressure, and free-stream velocity.

The use of equation (1) for scaling buffet loads is readily apparent. Since $\hat{C}_{L,n}(k_n)$ would be the same for both a dynamically scaled aeroelastic

model and the full-scale vehicle, the total full-scale bending moment is related to the corresponding model value by the following expression:

$$\sigma^2(Z_o)_{T,F} = \sum_{n=1}^{\infty} \left(\frac{L_F}{L_M}\right)^7 \left(\frac{\omega_F}{\omega_M}\right)_n \left(\frac{q_F}{q_M}\right)^2 \left(\frac{V_M}{V_F}\right) \left[\frac{\left(\frac{C_A}{C_{cr}}\right)_M + \left(\frac{C_s}{C_{cr}}\right)_M}{\left(\frac{C_A}{C_{cr}}\right)_F + \left(\frac{C_s}{C_{cr}}\right)_F + \left(\frac{C_c}{C_{cr}}\right)_F}\right] \sigma^2(Z_o)_{n,M} \qquad (2)$$

where, from dimensional considerations, the model-to-full-scale damping relationship is given by

$$\left(\frac{C_A}{C_{cr}}\right)_F = \left[\left(\frac{\rho_F}{\rho_M}\right)\left(\frac{V_F}{V_M}\right)\left(\frac{L_F}{L_M}\right)^2\left(\frac{W_M}{W_F}\right)\left(\frac{f_M}{f_F}\right)\right]\left(\frac{C_A}{C_{cr}}\right)_M \qquad (3)$$

Although the full-scale bending moment at a particular location along the vehicle can be determined directly from equation (2), the missile or launch vehicle designer needs to know the distribution of bending moments along the structure. Therefore, in making dynamic bending-moment measurements on a model using a single strain-gage bridge, a strain-gage-location sensitivity factor must be determined since a bridge located say at the point of maximum bending moment in the first mode may not be very sensitive to moments produced by response in the second mode. This factor can be determined by calculating the bending-moment distribution due to inertia loading for motion in each mode, respectively.

Application of Buffet Bending-Moment Scaling Relationships

As an example of the technique, consider its application to an 8-percent dynamically scaled aeroelastic buffet model of the Saturn-Apollo launch configuration (built by the Los Angeles Division of North American Aviation for the NASA) that was tested recently in the transonic dynamics tunnel at the Langley Research Center. The Mach 1 point on the trajectory was chosen as the design point. The full-scale trajectory conditions and the tunnel performance capability and size dictate the model-to-full-scale design scaling ratios. The model design concept is shown in figure 10 which is a photograph of a portion of the model.

The backbone of the model was an 8-inch-inside-diameter central aluminum tube the thickness of which provided the properly scaled stiffness distribution (except for minor deviations because of model structural considerations) and the necessary strength to resist the loads imposed during testing. Lead weights attached to the aluminum tube provided the proper weight distribution. The aluminum tube and lead weights were covered by styrofoam segments which provided the correct external contour. The model was mounted in the tunnel on the support system described previously and shown in figures 3 and 4. The completed model, shown in figure 11, mounted in the Langley Research Center transonic dynamics tunnel was approximately $14\frac{1}{2}$ feet long and weighed about 786 pounds.

The primary instrumentation on the model consisted of several electric resistance-type strain-gage bridges bonded to the aluminum tube and calibrated to indicate bending moments. The gage outputs were recorded on tape during the tests. An accelerometer at the point of application of the shaker force to the model was used in conjunction with the shaker force output to determine the structural and aerodynamic damping.

In order to scale up the model test results to full-scale values using equation (2), it is first necessary to determine the relative contribution of each natural mode to the total bending moment measured on the model at a particular location. This can be accomplished by integrating the power spectra in the neighborhood of the resonant frequency of the desired mode. A typical bending-moment power spectrum for this model is shown in figure 12. Note that for this case, the first three free-free bending modes contribute to the total power.

The damping in a given vibration mode can be determined from the single-degree-of-freedom relationship for a distributed mass system: at resonance, damping is equal to the applied force multiplied by the normalized deflection at the point of application of the force and divided by the velocity of the point of normalization that is in phase with the applied force. (See, for example, ref. 8.) An electronic transfer function analyzer was used to measure these quantities. The model aerodynamic damping ratios $\left(\frac{C_A}{C_{cr}}\right)_M$ were determined by measuring the total damping with wind on and subtracting from that value the structural damping determined with the wind off. Full-scale aerodynamic damping was obtained from the model aerodynamic damping by the relation given in equation (3). An example of full-scale aerodynamic damping data is presented in figure 13 as the variation of the ratio of aerodynamic damping to critical damping with flight time for the first three free-free bending modes of the Saturn-Apollo launch vehicle. In this figure and in subsequent data figures concerning the Saturn-Apollo vehicl . values of damping and bending moments have been omitted in order to avoid a confidential classification. The values of damping shown in figure 13 are small, however. The maximum values are less than the estimated sum of the full-scale structural and control-system damping. The solid portion of the curves represents the range of the wind-tunnel studies for the model ($M = 0.90$ to $M = 1.2$). The dashed portions of the curves are estimated values. The peaks at $M = 1.2$ are caused primarily by the parameter ρV which diminishes rapidly after about 60 seconds of flight.

The full-scale bending moments for a particular mode at the point of measurement were then used in conjunction with the calculated bending-moment distribution due to the inertia loading to obtain the buffet bending-moment distribution in that mode. Figure 14 is an example of the distributed root-mean-square bending moment in the first three free-free modes. The data are for zero degrees angle of attack at the $M = 0.9$ point on the trajectory.

The mean-square buffet bending moments at each station for the various modes were then added to obtain the total bending-moment distribution. The final result is shown in figure 15 where the total root-mean-square buffet bending-moment distribution is presented for zero and 6° angle of attack.

Based on tests on the model with a "Jupiter" nose-cone payload with and without fins, it is felt that some of the measured model response may have been due to tunnel turbulence, and due to buffet load input from the relatively thick fins. Further investigations concerning these factors are in progress. Although no full-scale flight data are yet available for comparison with the predicted bending moments, definite plans have been made to attempt to obtain relevant full-scale data during the forthcoming SA-5 launch.

PREDICTION OF GROUND-WIND LOADS

Considerations in the Use of Models for Ground-Winds Loads Prediction

As shown in figure 16, a launch vehicle erected on its pad or on a transporter prior to launch is subjected to a variety of loading conditions imposed by variable surface winds during those periods in which the protective gantry is removed. A steady wind imposes both a steady load due to aerodynamic drag and oscillatory loads due to flow separation or vortex shedding around the vehicle. These oscillatory loads are greatest in the plane perpendicular to the surface wind direction. Additional unsteady loads are caused by gusts and turbulence in the ground-wind flow. These ground-wind loads create problems in structural strength, guidance alinement, and ground handling; in fact, they are frequently the design loads for the lower stages of launch vehicles. The basic problem is to insure that the vehicle free-standing on the launch pad or transporter can satisfactorily withstand the ground wind specified for completion of the mission. For some missions this wind may be the 99.9-percent probable maximum wind during the month of highest winds at the launch site (see ref. 10).

Although considerable effort has been expended in study of the problem (see refs. 11 through 13), no satisfactory theoretical method exists for predicting the loads due to vortex shedding from ground winds on launch vehicles. Preliminary estimates of the oscillatory loads from vortex shedding may be made using a method described by Ezra (ref. 14) provided wind-induced response data are available for a vehicle of similar size and geometry. An alternate method based on unsteady pressure distributions was developed by Bohne (ref. 15). Such methods are useful for preliminary design purposes.

The best present means of obtaining quantitative data on ground-wind loads on launch vehicles, once the design is finalized, is from wind-tunnel studies of dynamically and elastically scaled models. Photographs of a number of typical ground-winds models tested in the Langley transonic dynamics wind tunnel are presented in figures 17(a) through 17(e). Notice the presence of the umbilical or service tower in most of these figures. If such a structure remains near the vehicle, it should be geometrically simulated because of its significant effect on the flow of ground winds over the vehicle.

There are uncertainties in the use of aeroelastic model wind-tunnel techniques for predicting ground-wind loads. The wind tunnel presents a steady wind of constant velocity profile without gusts and with a scale of turbulence different from atmospheric turbulence. Thus an adjustment must be

made for the difference between the actual velocity profile of atmospheric surface winds and the constant velocity profile of the wind tunnel. Also theoretical means such as Bohne's analysis in reference 16 must be used to determine the dynamic loads due to atmospheric turbulence and gusts. The aeroelastic models in the wind tunnel give the steady-state response of the vehicle due to ground winds and most importantly give the oscillatory response due to vortex shedding. In such tests, scatter in the dynamic response data is often present even though the test conditions are closely controlled. It has been found that vortex shedding has a stong three-dimensional end effect such that minor changes in shape or surface condition near the nose of the vehicle often have large effects on the response (see refs. 19 through 26). Therefore the model must reflect the geometry of the full-scale vehicle in great detail in the upper stages and nose regions of the model.

Scaling of Models

The dynamic response of the models to the random load inputs is in the model fundamental mode. This is illustrated in figure 18 by the power spectral density of the bending-moment response of a typical launch vehicle model to wind-tunnel simulated ground winds. Examination of response spectra of several models and of the full-scale Scout vehicle indicates this result is typical in that there is a single peak in the response at the fundamental frequency and virtually no response at higher frequencies. Such response is typical of the response of a lightly damped mechanical system to a random input (see ref. 27).

Just as for the case of the buffet-type model, scaling laws based on the response of mechanical systems to random inputs (refs. 14 and 27) are used to determine the nondimensional parameters to be duplicated by the model if the response of the model to tunnel-simulated ground winds is to simulate accurately the response of the full-scale vehicle to ground winds. It is required that the following parameters be the same for model and full-scale vehicle:

1. External shape

2. Reynolds number $\rho V l/\mu$

3. Reduced frequency $f_n l/V$ where f_n is natural frequency of nth mode $(n = 1, 2)$

4. Mass ratio $M_n'/\rho l^3$ where ρ is mass density of test medium and M_n' is generalized mass of nth mode $(n = 1, 2)$

5. Damping ratio C_s/C_{cr} where C_s is structural damping and C_{cr} is critical damping

6. Surface roughness ratio ϵ/l where ϵ is surface roughness height per representative length

From the dimensionless parameter design requirements just specified and from a knowledge of the wind-tunnel capabilities, the fundamental scale factors

(model-to-full-scale ratios) for scaling model length, mass, and time are readily obtained. The scale factors for any other physical parameter is obtained by substituting in the dimensional expression for the desired parameter the value of the model scale factors for length, mass, and time.

As mentioned in the introduction, the primary flow parameter to be simulated for ground-wind models is Reynolds number. The primary flow variable for buffet models, Mach number, is of importance in ground-wind model work only because the tunnel Mach number must not exceed 0.4 if compressibility effects not present in atmospheric ground winds are to be avoided. This Mach number limitation and the design requirement that full-scale Reynolds number shall be simulated combine to limit the range of ground winds which can be simulated in the wind tunnel. Figure 19 shows for several launch vehicles the ground-wind velocity simulation which can be obtained under these restrictions in the Langley transonic dynamics wind tunnel which is a large, variable-density wind tunnel with an approximately 16-foot-square test section. For large vehicles such as Saturn V and Nova the ground-winds simulation range is far lower than design ground-wind values.

A tentative solution to this problem is to change the design restriction that full-scale Reynolds number shall be simulated to a design restriction that the Reynolds number on both model and full-scale vehicle shall be supercritical ($R_N > 500,000$) for the ground-wind velocities of interest. The assumption is that the flow simulation is adequate if the model Reynolds numbers are supercritical although less than full-scale Reynolds number. This technique has been used for Titan III and Saturn V models to enable higher ground-wind velocities to be simulated. Full-scale data to test the validity of the results are not yet available.

Model Construction and Mounting

The model construction usually follows one of two techniques frequently used in dynamic model design. One technique uses a metal outer shell of varying thickness. This shell forms the basic exterior shape of the vehicle and simulates the stiffness distribution along the longitudinal axis. Additional weights required to simulate the vehicle weight distribution along the longitudinal axis are attached to the interior of the stiffness carrying shell in such a manner that they do not contribute significantly to the bending stiffness. The other technique involves a center beam or spar of varying cross section along the longitudinal axis which provides the correct scaled bending stiffness along the longitudinal axis. This central spar is surrounded by a low stiffness material which gives the correct external shape and has imbedded weights to provide the correct scaled mass distribution.

Structural damping in the model (C_s) has in the past been difficult to control as accurately as other design parameters. If the model damping differed from that of the full-scale vehicle, scaling corrections are made in the data in accordance with the scaling relationships in reference 14 which show that the model response varies inversely with the square root of the structural damping. There has recently been developed by Mr. Wilmer H. Reed III of the Langley Research Center a viscous damper suitable for installation on ground-winds models such as we are discussing. Figure 20 shows the construction of the damper. A cylinder filled with viscous oil has

a number of lead discs resting on concave trays in the cylinder. As the model oscillates perpendicular to its longitudinal axis, the combined action of the fluid and lead weights provides a means for energy dissipation. The damper is mounted as shown in the upper stage of the vehicle. By varying the viscosity of the oil or the weight of lead discs, various values of structural damping can be obtained. On its initial test on a model whose structural damping was approximately 0.007 without the damper installed, controlled variations in damping from 0.01 to 0.03 were obtained with the use of the damper. The damper promises to be very useful in the initial and future tests.

The models are mounted at the station corresponding to the full-scale vehicle tie-down station on a base mount fixture designed to simulate the scaled tie-down stiffness of the full-scale vehicle. Since at the time of model testing, an accurate value of full-scale tie-down stiffness is often not known, a variable stiffness base mounting fixture has been developed which is shown in figure 21. The fixture has a center cylinder with heavy flanges on either end. The center cylinder supports the model weight and has a value of stiffness somewhat lower than the scaled tie-down stiffness should be. Eight pretensioned steel rods with or without cylindrical sleeves can be fastened between the upper and lower flanges to increase the stiffness of the fixture. By varying the diameter of the peripheral rods, different values of tie-down stiffness may be obtained. The model is attached by bolts to the upper flange. The lower flange bolts to a massive 8-foot-diameter turntable which may be rotated from the control room to any desired wind azimuth angle. Desirable features of this variable stiffness base mounting fixture are that it has repeatable values of stiffness which can be changed without dismounting the model, and its design and fabrication are simple.

Instrumentation

The primary instrumentation for measuring model response consists of two strain-gage bridges mounted near the model base station in planes 90° apart around the circumference and two accelerometers mounted on the model near the nose in the same two reference planes. These sensors are used to obtain time histories of the bending-moment and deflection responses of the model to simulated ground winds. Conventional readout instrumentation such as recording oscillographs, oscilloscopes, and thermocouples (for mean square of response) are used.

One interesting component of readout instrumentation which has been developed for the ground-wind tests is the use of time exposure photographs of an oscilloscope set up to display the response from one bending-moment strain gage on one axis and the response from the strain gage in the other reference plane on the other axis. Figure 22 shows this arrangement schematically. A no-wind position spot shows no-load position. As the model responds both statically and dynamically, the outputs from these strain gages trace an elliptical pattern on the oscilloscope since the lift response is greater than the drag response. The borders of the ellipse thus formed represent the curve of maximum dynamic bending-moment response during a data sample and the distance the center of the ellipse has shifted from the no-wind spot gives the magnitude and direction of the static bending-moment response. The maximum length vector which can be drawn from the wind-off zero spot to the outside of the dynamic-response envelope is the maximum resultant bending moment. An

excellent feature of this type of presentation is that it has the correct relationship between the maximum oscillatory response in the lift and drag directions.

Tests and Results

The usual procedure in ground-wind tests is to set the tunnel at a constant velocity which simulates a sizable ground wind and then rotate the model and umbilical tower through 180° or 360° of wind azimuth angle, stopping at various azimuth angles to record 1- or 2-minute data samples of the model response. The time scale factor is such that 1- or 2-minute model data samples represent many minutes of full-scale data. Due to the presence of the umbilical tower or asymmetries in the model, there are usually one or more wind azimuth angles for which the response is larger than at other angles. This variation of the response with wind azimuth angle is strikingly shown in figure 23 by the oscillograph time histories taken at a constant velocity but varying wind azimuth angle. The model and umbilical tower are represented schematically in top view in the center of the figure. The five wind azimuth angles are shown by the broad arrows and the oscillograph response for each wind angle is opposite the point of the arrow. It is readily seen that the wind flow through the umbilical tower affects the model response with the maximum response at 135°. Note that the steady-state vector has a lift as well as a drag component which is believed to be caused by the partial blockage of one side of the umbilical tower by a series of conduit cable shields.

Once the wind azimuth angles of greatest response are determined, the variation of model response with simulated ground-wind velocity is determined for each of these angles over a range of simulated ground winds up to the $M = 0.4$ compressibility limit.

Typical plots of the constant velocity, variable wind azimuth response and constant azimuth, variable ground-wind responses are shown in figure 24. The base bending-moment response is plotted against turntable angle in the upper figure for a simulated velocity of 40 knots and the base bending response of the maximum response wind azimuth angle of 135° is shown in the bottom figure as a function of tunnel dynamic pressure which varies as the square of simulated ground-wind velocity.

Application of Model Data to Full-Scale Vehicle

By use of the scale factors derived for the model, the model ground-wind response measured in the wind tunnel can be scaled to the full-scale vehicle. These data give the loads on the model imposed by a uniform stream velocity, namely (a) steady drag and lift loads and (b) unsteady loads associated with vortex shedding due to flow separation. Modifications must be made to the wind-tunnel measured loads to account for differences between the uniform velocity in the wind tunnel and the parabolic velocity gradient near the ground in the atmosphere. In addition, the response from unsteady loads due to gusts and turbulence found in atmospheric winds but not present in the tunnel flow must be calculated.

The modification of tunnel test data for velocity profile shape is accomplished by finding an equivalent uniform velocity U_e which distributed along the vehicle gives the same steady-state bending moment at the base as the design ground-wind profile.

Two approaches may be used to estimate the unsteady loads on the vehicle caused by gusts and turbulence in the atmosphere. The first approach assumes the wind input to be in the form of a discrete gust tuned to the vehicle natural frequency. The other approach assumes the wind input from gusts and turbulence can best be represented by the statistical properties of a stationary random process (see, for example, ref. 16). The second approach more realistically represents the effects of structural damping and is the one favored herein. Components of velocity (from gusts and turbulence) in the direction of and perpendicular to the wind direction are considered. In this approach the components of the velocity fluctuations due to gusts and turbulence are assumed to be random functions of time perfectly correlated along the vehicle length. Aerodynamic loads are defined by a two-dimensional strip analysis. An equivalent uniform velocity profile is used. The equations of motion are linearized. The dynamic model response is assumed to occur in the fundamental mode. A specific power spectrum for atmospheric turbulence developed by Von Karman (ref. 17) and applied by Houbolt (ref. 18) is used. A scale of turbulence is assumed and the intensity of turbulence is specified such that the 3σ level of the turbulence velocity components corresponds to $0.4U_e$, the amount by which the peak design wind exceeds the mean equivalent wind U_e. The envelope of the 3σ bending-moment response due to turbulence and gusts calculated from the preceding assumptions is an ellipse similar to that for maximum dynamic response due to vortex shedding except the major axis is in the plane of the wind.

The equivalent velocity profile U_e, and the 3σ turbulence-response envelope, both calculated as described, are combined with the steady-state response and response due to vortex shedding, both measured in the wind tunnel. The method of combining these loads to get a final answer for the full-scale vehicle response to ground winds is shown in figure 25. In this figure the input winds are the equivalent velocity U_e plus the u and v components of atmospheric turbulence and gusts. The 3σ turbulence response envelope has its center at the end of the steady drag vector. The vortex shedding response envelope is moved with its center on the boundary of the turbulence-response envelope to establish a locus of points from which the maximum resultant base bending moment may be determined.

At present there are little or no full-scale data available to verify the assumptions in this analysis and the data from ground-wind model in wind-tunnel tests. However, preparations are currently being made for erecting surplus Jupiter and Thor vehicles at Wallops Island for obtaining full-scale ground-winds data. Ground-wind full-scale measurements on full-scale Saturn vehicles are also being planned.

REFERENCES

1. Coe, Charles F.: "Steady and Fluctuating Pressures at Transonic Speeds on Two Space-Vehicle Payload Shapes." NASA TM X-503, 1961.

2. Coe, Charles F.: "The Effects of Some Variations in Launch-Vehicle Nose Shape on Steady and Fluctuating Pressures at Transonic Speeds." NASA TM X-646, 1962.

3. Jones, George W., Jr., and Foughner, Jerome T., Jr.: Investigation of Buffet Pressures on Models of Large Manned Launch Vehicle Configurations. NASA TN D-1633, 1963.

4. Doggett, Robert V., Jr., and Hanson, Perry W.: An Aeroelastic Model Approach for the Prediction of Buffet Bending Loads on Launch Vehicles. NASA TN D-2022, 1963.

5. Coe, Charles F.: "The Effect of Model Scale on Rigid-Body Unsteady Pressures Associated With Buffeting." Presented at the Symposium on Aeroelastic and Dynamic Modeling Technology, Dayton, Ohio, September 23-25, 1963.

6. Rice, S. O.: "Mathematical Analysis of Random Noise." Pts. I and II, Bell System Tech. Jour., Vol. XXIII, No. 3, July 1944, pp. 282-332; Pts. III and IV, Vol. XXIV, No. 1, Jan. 1945, pp. 46-156.

7. Liepmann, H. W.: "On the Application of Statistical Concepts to the Buffeting Problem." Jour. Aero. Sci., Vol. 19, No. 12, Dec. 1952, pp. 793-801.

8. Hanson, Perry W., and Doggett, R. V., Jr.: Wind-Tunnel Measurements of Aerodynamic Damping Derivatives of a Launch Vehicle Vibrating in Free-Free Bending Modes at Mach Numbers From 0.70 to 2.87 and Comparisons With Theory. NASA TN D-1391, 1962.

9. Hanson, Perry W., and Doggett, Robert V., Jr.: Aerodynamic Damping of a 0.02-Scale Saturn SA-1 Model Vibrating in the First Free-Free Bending Mode. NASA TN D-1956, 1963.

10. Daniels, Glenn E.: Natural Environment (Climatic) Criteria Guidelines for Use in MSFC Launch Vehicle Development. 1963 Revision MSFC MPT-AERO-63-9, Jan. 28, 1963. (Supersedes MPT-AERO-61-93.)

11. Fung, Y. C.: "Fluctuating Lift and Drag Acting on a Cylinder in a Flow at Supercritical Reynolds Numbers." Jour. Aerospace Sciences, Vol. 27, No. 11, Nov. 1960, pp. 801-804.

12. Humphreys, J. S.: "On a Circular Cylinder in a Steady Wind." Jour. of Fluid Mechanics, Vol. 5, Pt. 4, Dec. 1960, p. 603.

13. Roshko, Anatol: "Experiments on the Flow Past a Circular Cylinder at Very High Reynolds Number." Jour. of Fluid Mechanics, Vol. 10, pt. 3, May 1961, pp. 345-356.

14. Ezra, A. A., and Birnbaum, S.: "Design Criteria for Space Vehicles to Resist Wind-Induced Oscillations." Am. Rocket Soc. Paper 1081-60. Presented at the Structural Design of Space Vehicles Conf., Santa Barbara, Calif., Apr. 6-8, 1960.

15. Bohne, Quentin R.: Ground Wind-Induced Loads on Launch Vehicles. Tech. Doc. Rept. ASD-TDR-62-371, Aug. 1962.

16. Bohne, Quentin R.: "Power Spectral Considerations on the Launch Pad." USAF Geophysics Res. Dir. A.F. Surveys in Geophysics., No. 140, Proc. of National Symposium on Winds for Aerospace Vehicle Design, Vol. 1, AFCRL-62-273(1), Mar. 1962.

17. Von Karman: "Progress in Statistical Theory of Turbulence." (Paper 101, Anniversary Series, Vol. IV.)

18. Houbolt, John C., Steiner, Roy, and Pratt, Kermit G.: "Flight Data and Consideration of the Dynamic Response of Airplanes to Atmospheric Turbulence." Presentation to the Structures and Materials Panel, Advisory Group for Aeronautical Research and Development, Paris, France, July 3-13, 1963. (To be published as a NASA TR.)

19. Buell, Donald A., and Kenyon, George C.: "The Wind-Induced Loads on a Dynamically Scaled Model of a Large Missile in Launching Position." NASA TM X-109, Dec. 1959.

20. Young, J. P.: "Wind-Induced Oscillation Tests of 1/6-Scale Pershing Model." The Martin Company Engineering Rep. No. 11461, Aug. 1960.

21. Rich, Roy L.: "Preliminary Ground Wind Induced Oscillation Test, Dyna Soar, Step I." Boeing Aircraft Company Document No. D-2-8147, Aug. 1961.

22. Killough, T. L.: "Wind-Induced Loads on a Dynamic 1/5-Scale Unfueled SM-78 Jupiter in the Launch Position (U)." U.S. Army Ordnance Missile Command, Rep. No. RG-TM-62-65, July 10, 1962.

23. Cincotta, J. J., and Lambert, W. H.: "Preliminary Report 7.5 Percent 624A Ground Wind and Wind-Induced Oscillation Wind Tunnel Tests (U)." Martin Company, Mar. 1963, Contract No. AF-04(695)-150.

24. Farmer, Moses G.: "Response to Simulated Ground Winds of a Dynamically and Elastically Scaled Model of the Unfueled Jupiter Missile in the Launch Position." Prospective NASA TM.

25. Jones, George W., Jr., and Farmer, Moses G.: "Response to Ground Winds and Booster Static Pressure Distribution on a 0.075-Size Model of Saturn Block I (SA-1) Vehicle in Launch Configuration." Prospective NASA TM.

26. Buell, Donald A., McCullough, George B., and Steinmetz, William J.: "A Research Investigation in the Ames 12-Foot Pressure Wind Tunnel of Wind-Induced Loads on Axisymmetric Missiles in Launch Position." Prospective NASA TM.

27. Thompson, W. T., and Barton, M. V.: "The Response of Mechanical Systems to Random Excitations." Jour. Appl. Mech., Vol. 24, No. 2, pp. 248-251, June 1957.

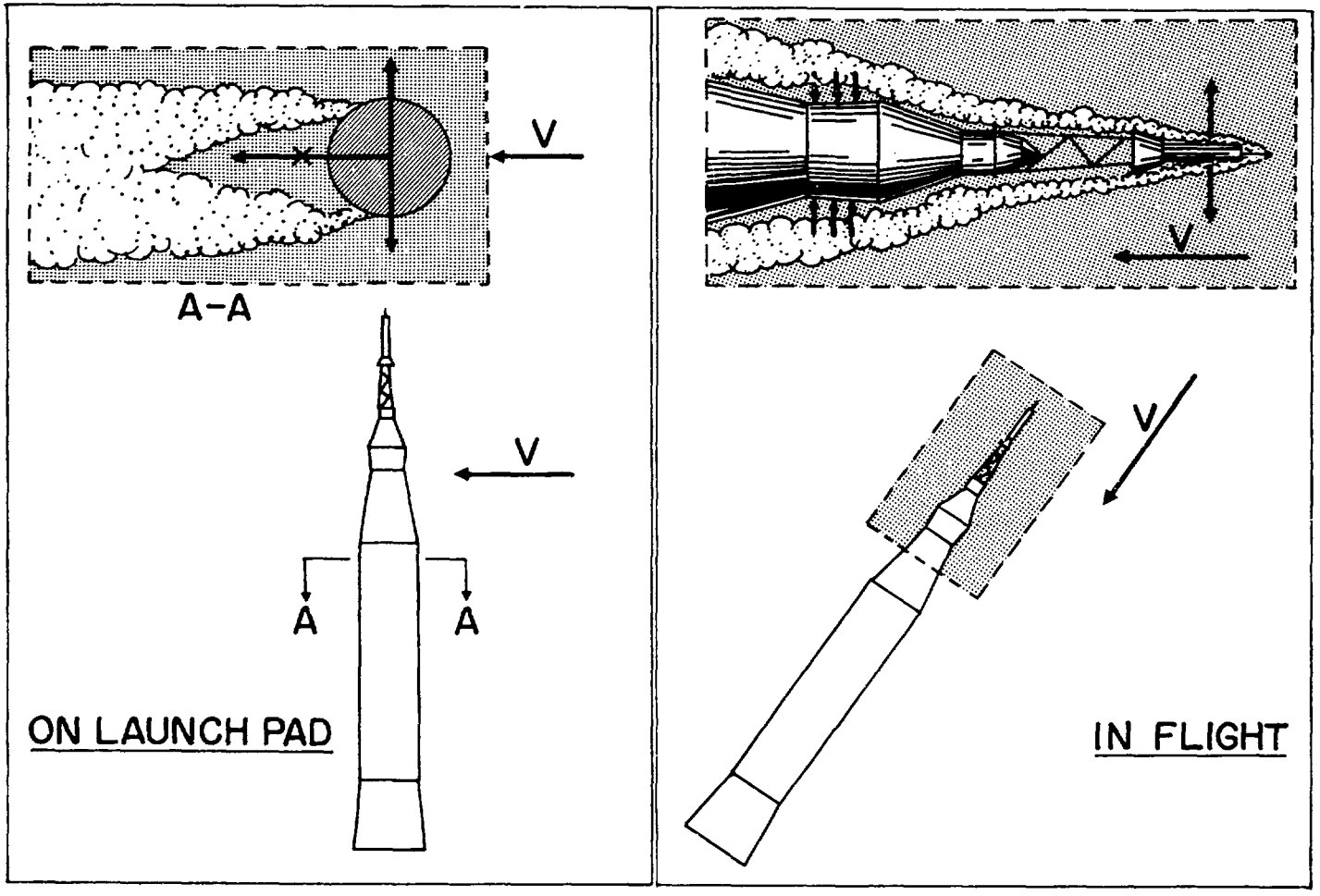

Figure 1.- Schematic illustration of loads caused by separated flow over a vehicle on launch pad and in flight.

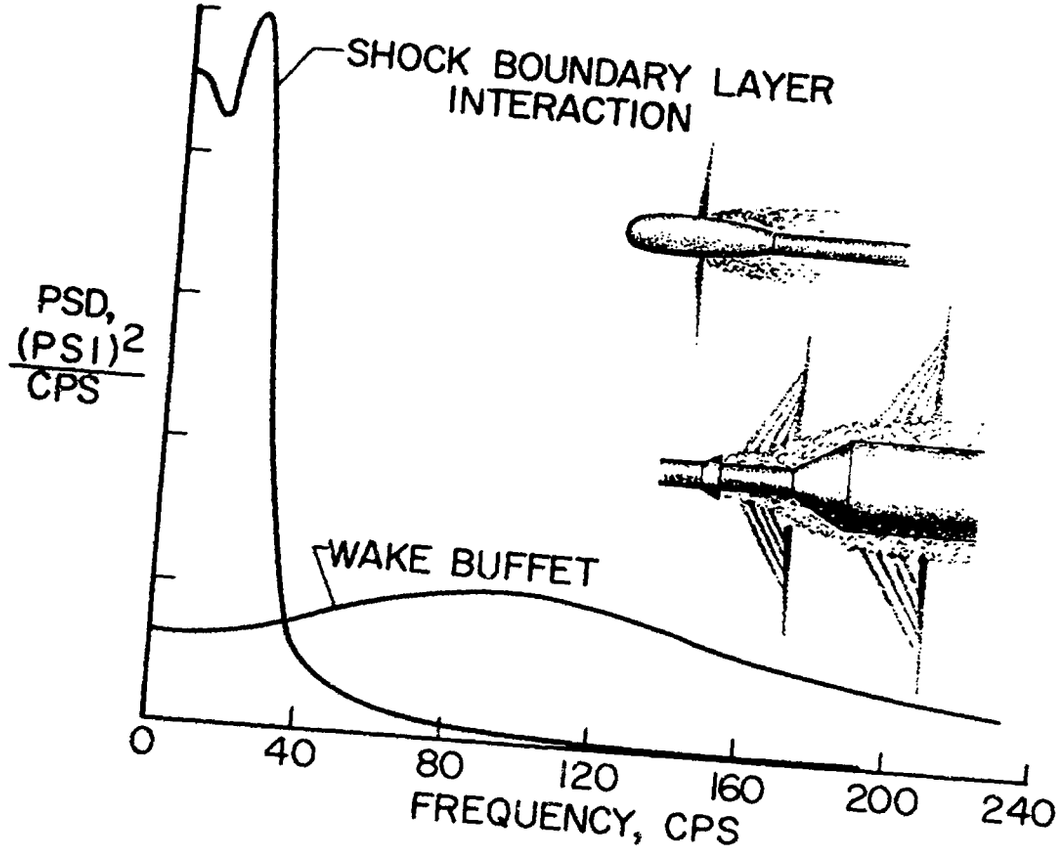

Figure 2.- Pressure power spectra of two transonic buffet flows.

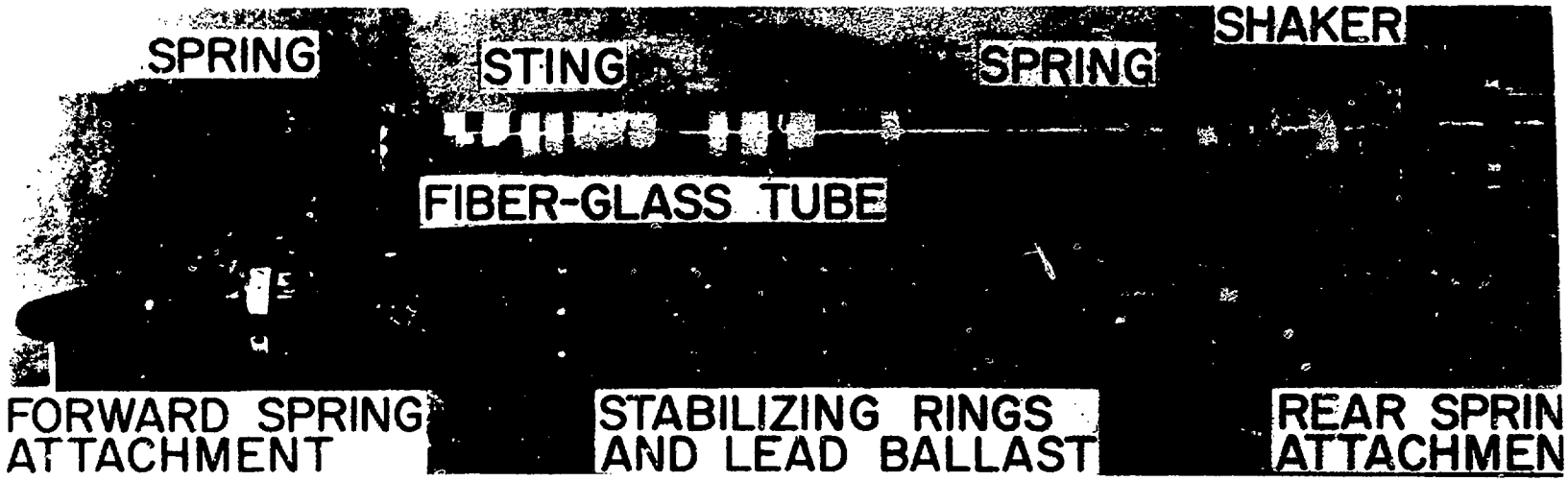

Figure 3.- Simple aeroelastic model and sting.

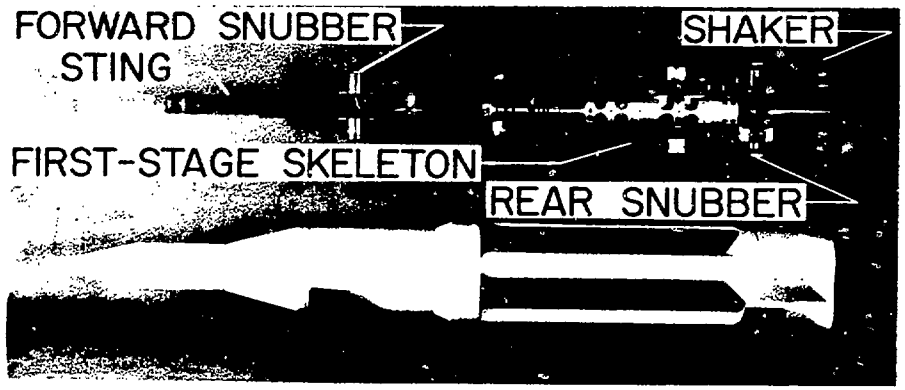

(a) Assembled model shell with first-stage skeleton and electromagnetic shaker on sting.

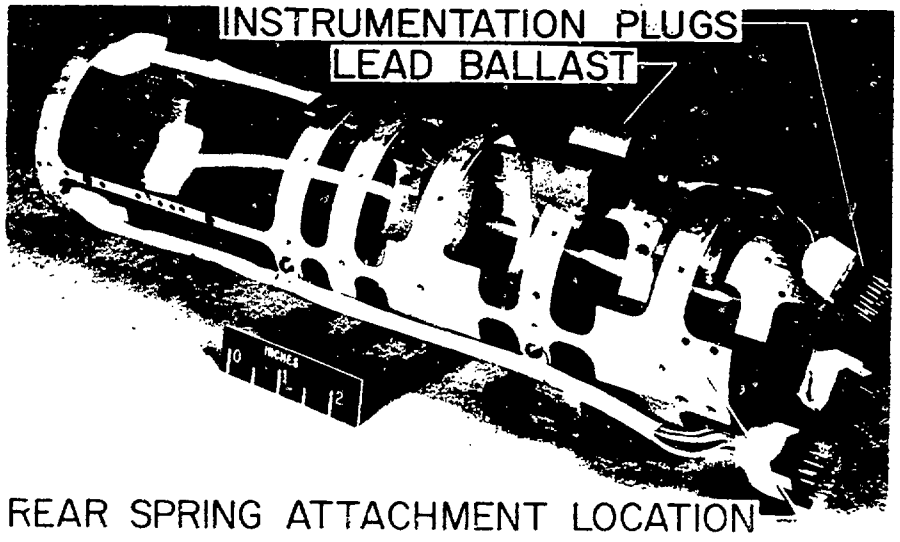

(b) Details of first-stage skeleton.

Figure 4.- Two-percent Saturn aeroelastic model.

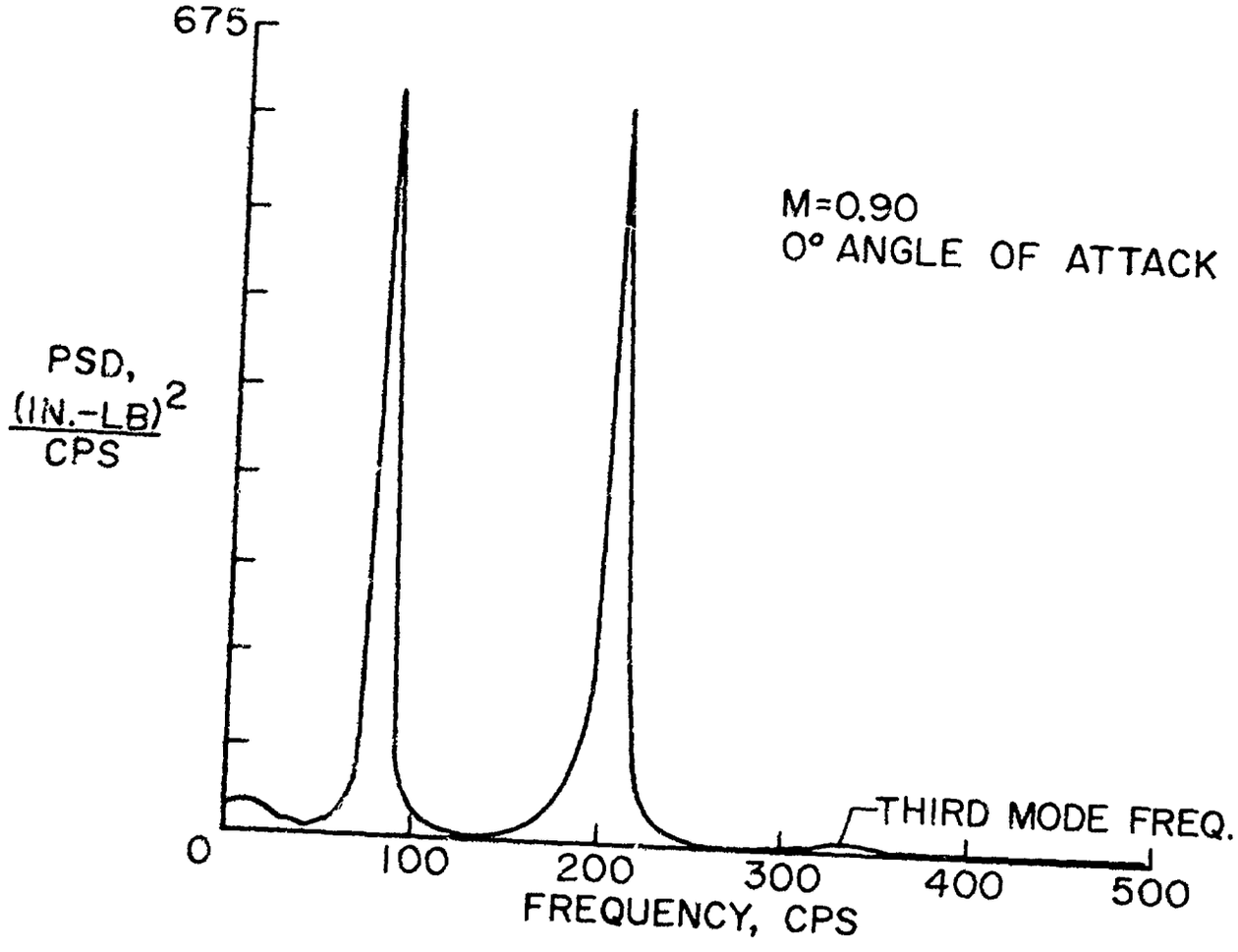

Figure 5.- Spectrum of bending-moment response of a "bulbous nose" configuration.

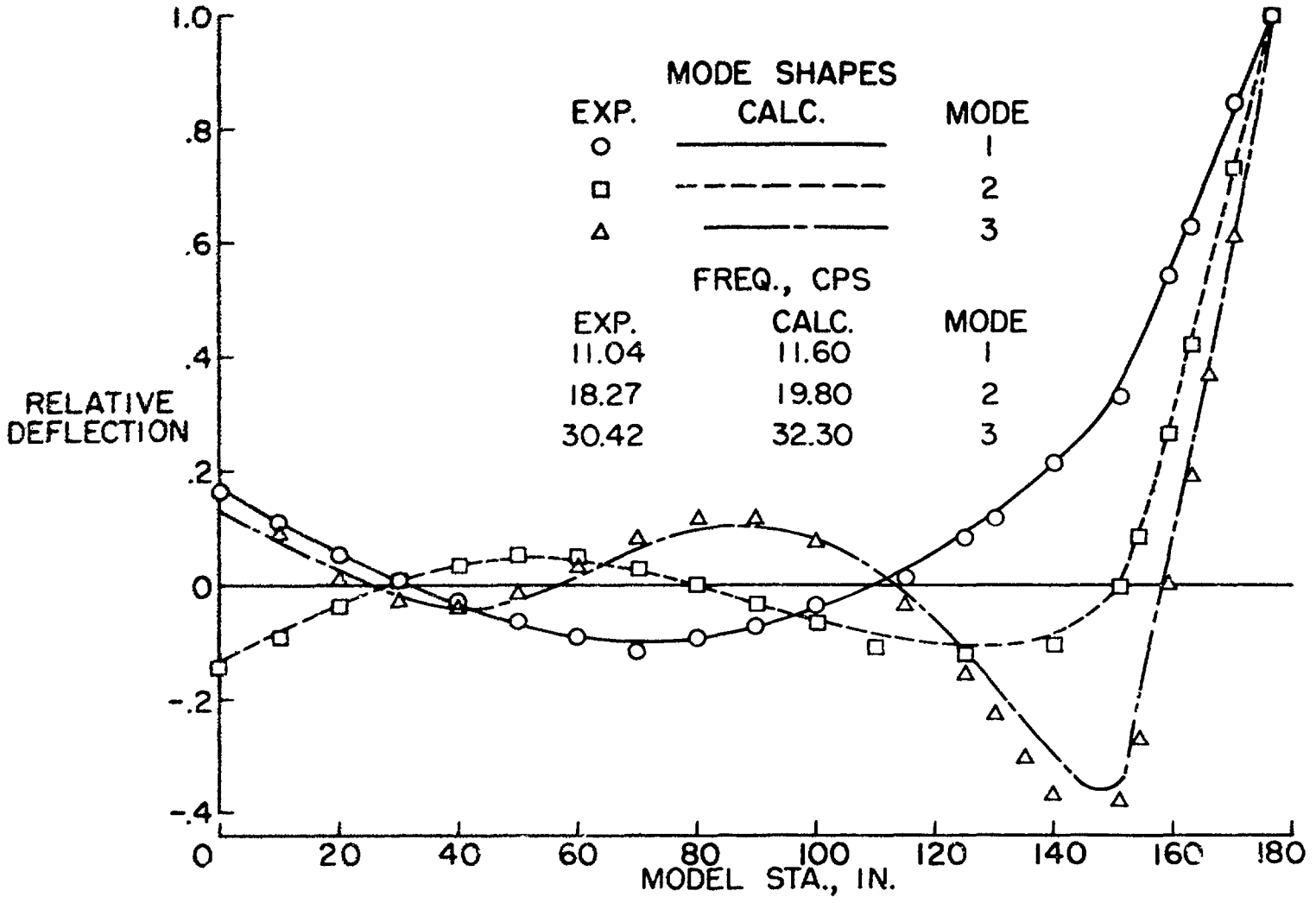

Figure 6.- Calculated free-free mode shapes and frequencies compared with measured mode shapes and frequencies of mounted model.

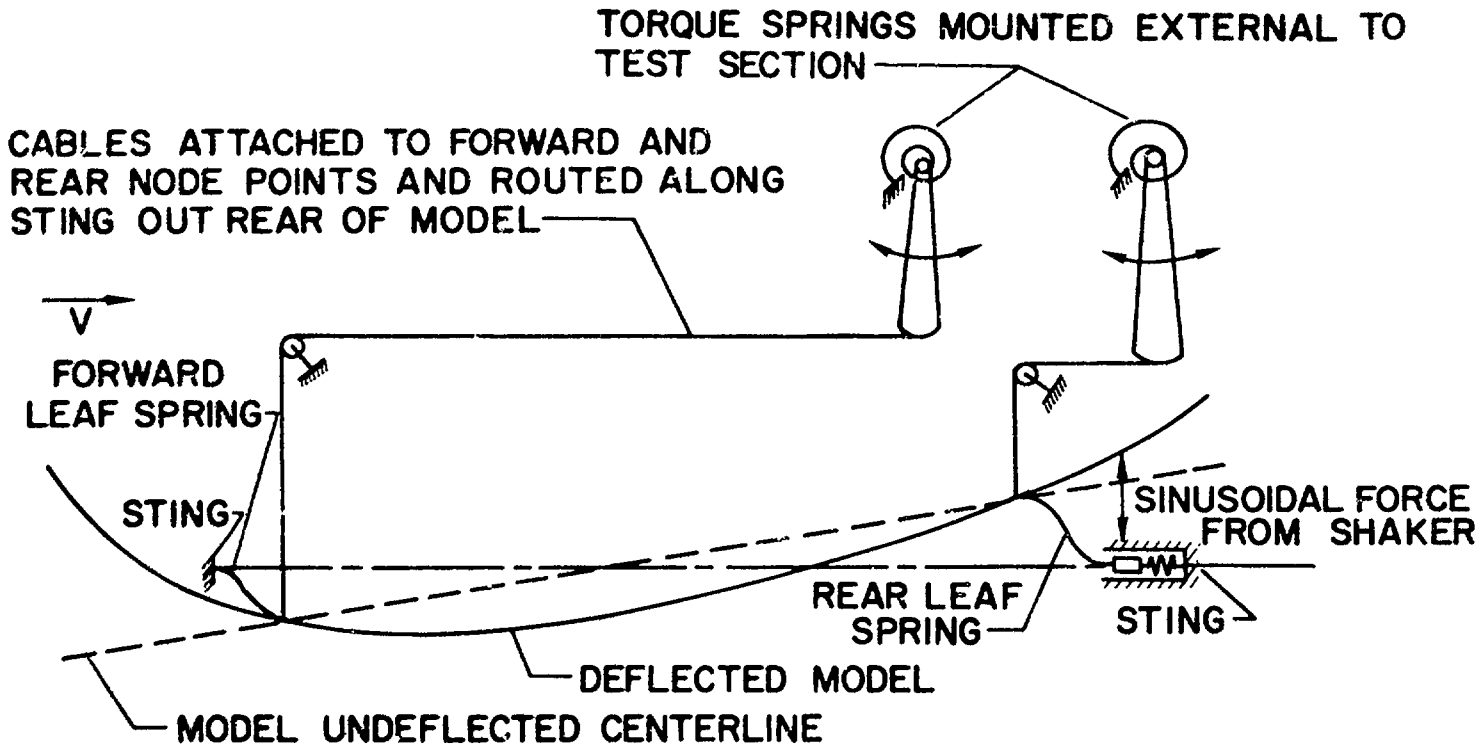

Figure 7.- Schematic diagram of aeroelastic buffet model support system.

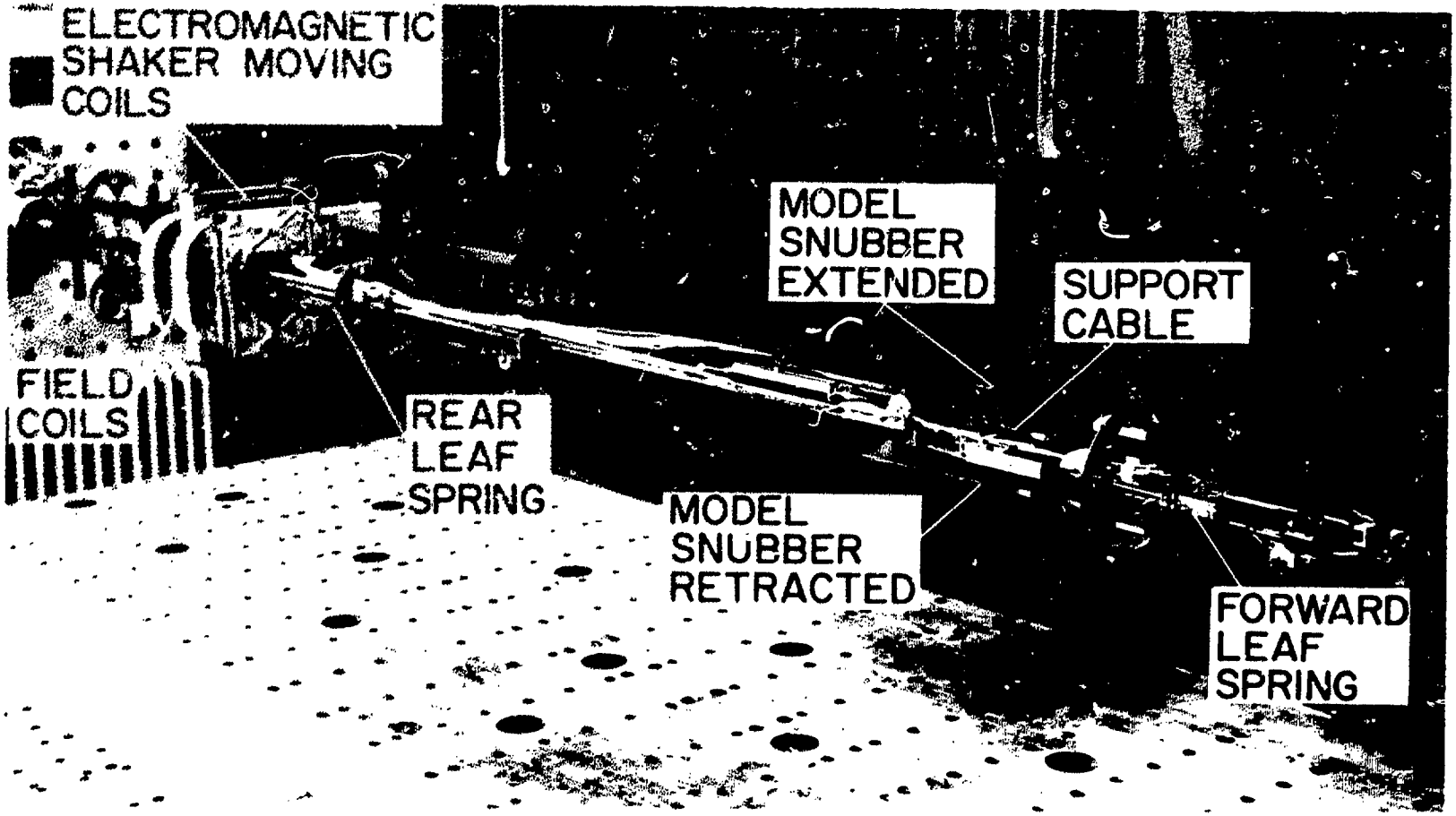

Figure 8.- Photograph of sting used for testing 8-percent Saturn-Apollo buffet model.

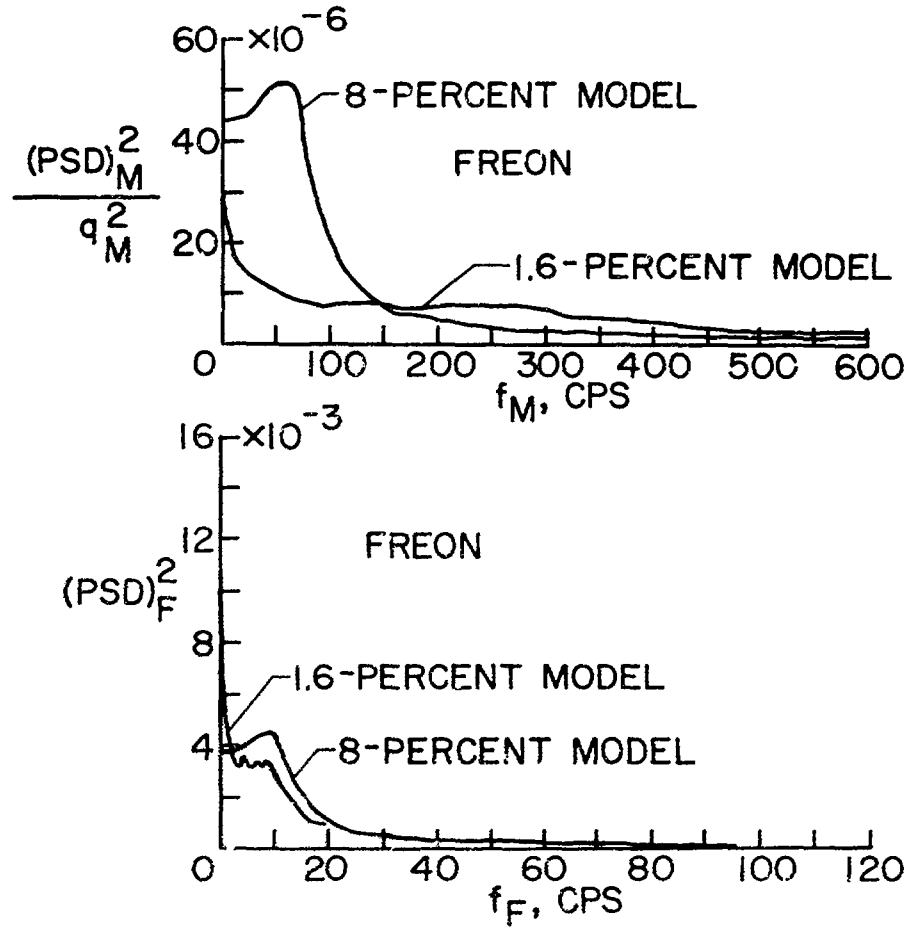

(a) Comparison of data at station "a" for 1.6- and 8-percent models tested in Freon, M = 0.8.

Figure 9.- Evaluation of buffet scaling relationships as applied to rigid fluctuating pressure models.

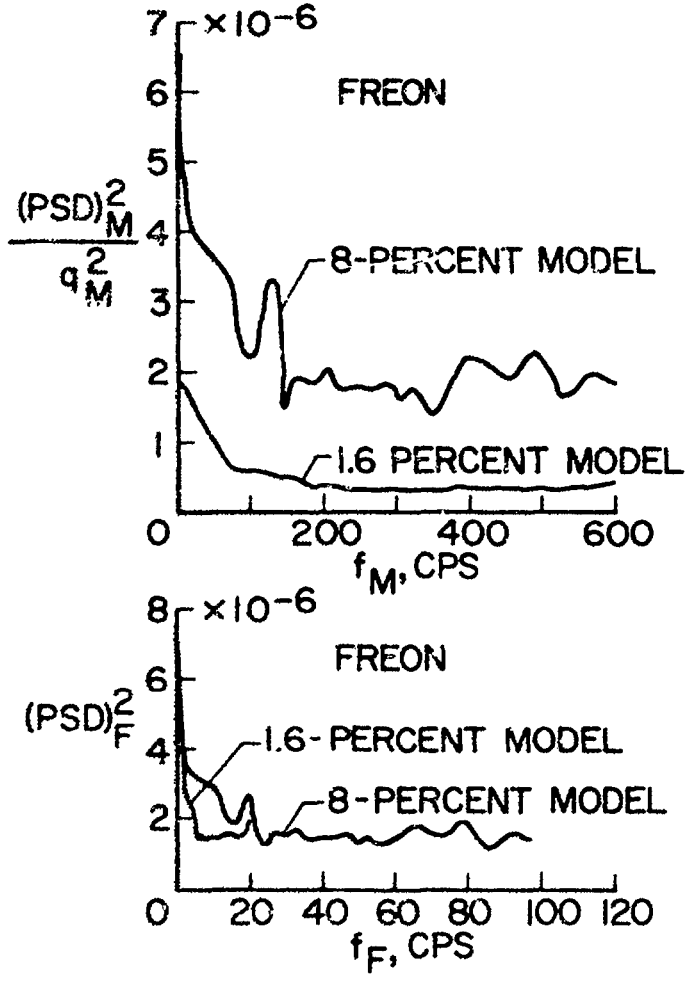

(b) Comparison of data at station "b" for 1.6- and 8-percent models tested in Freon, M = 0.81.

Figure 9.- Continued.

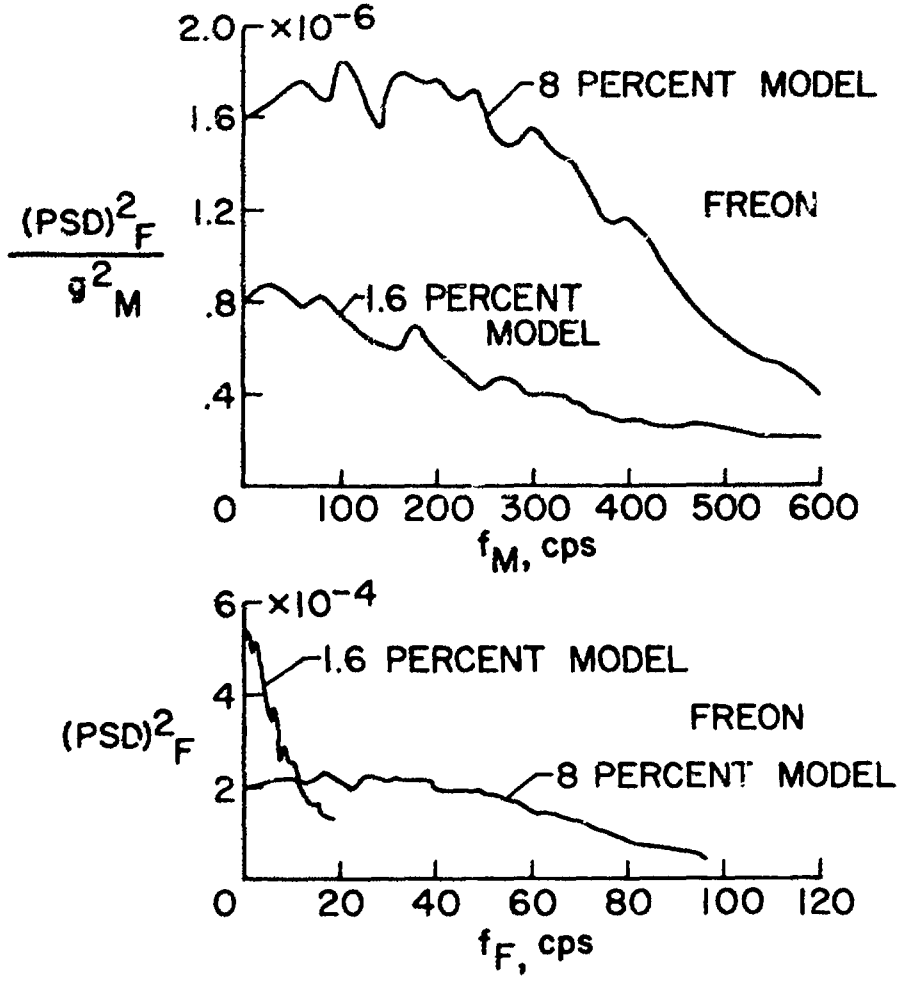

(c) Comparison of data at station "a" for 1.6- and 8-percent models tested in Freon, M = 1.01.

Figure 9.- Continued.

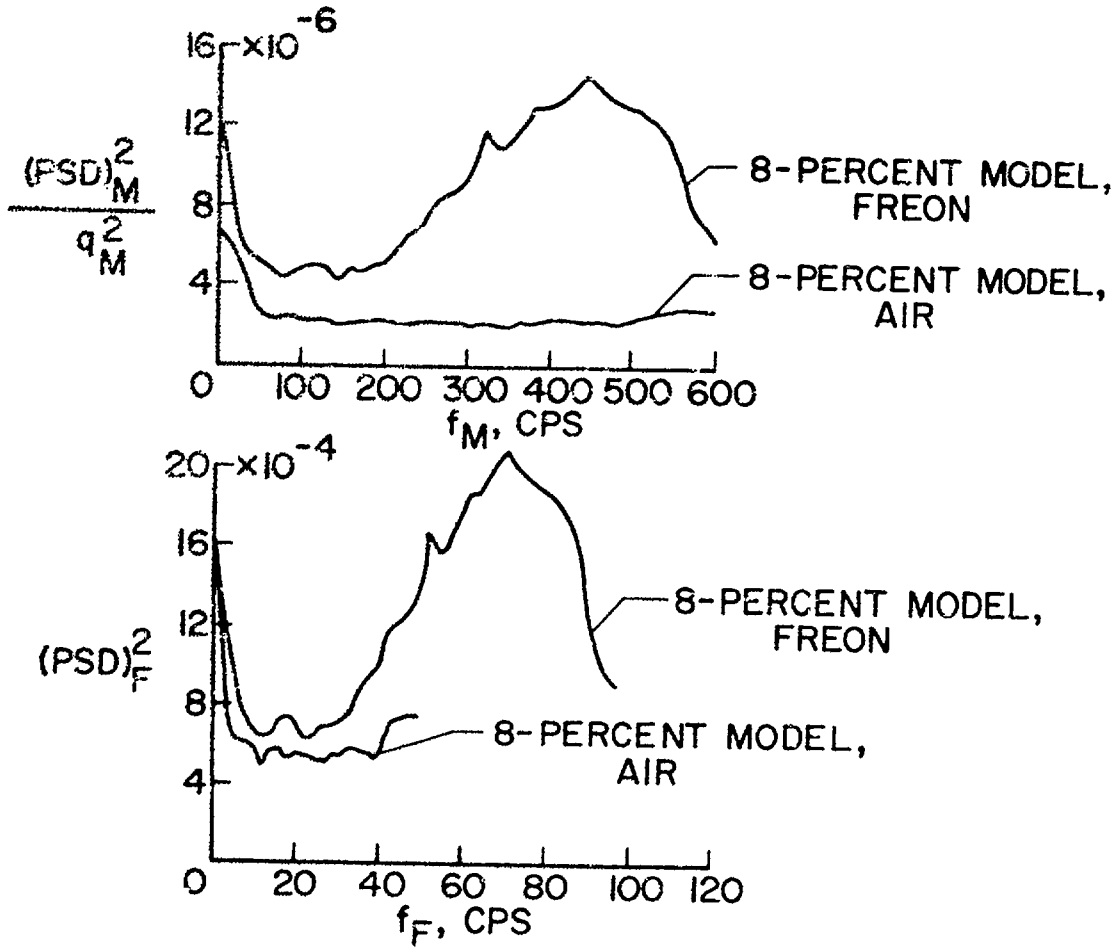

(c) Comparison of data at station "a" for 8-percent model tested in Freon and in air, M = 1.05.

Figure 9.- Continued.

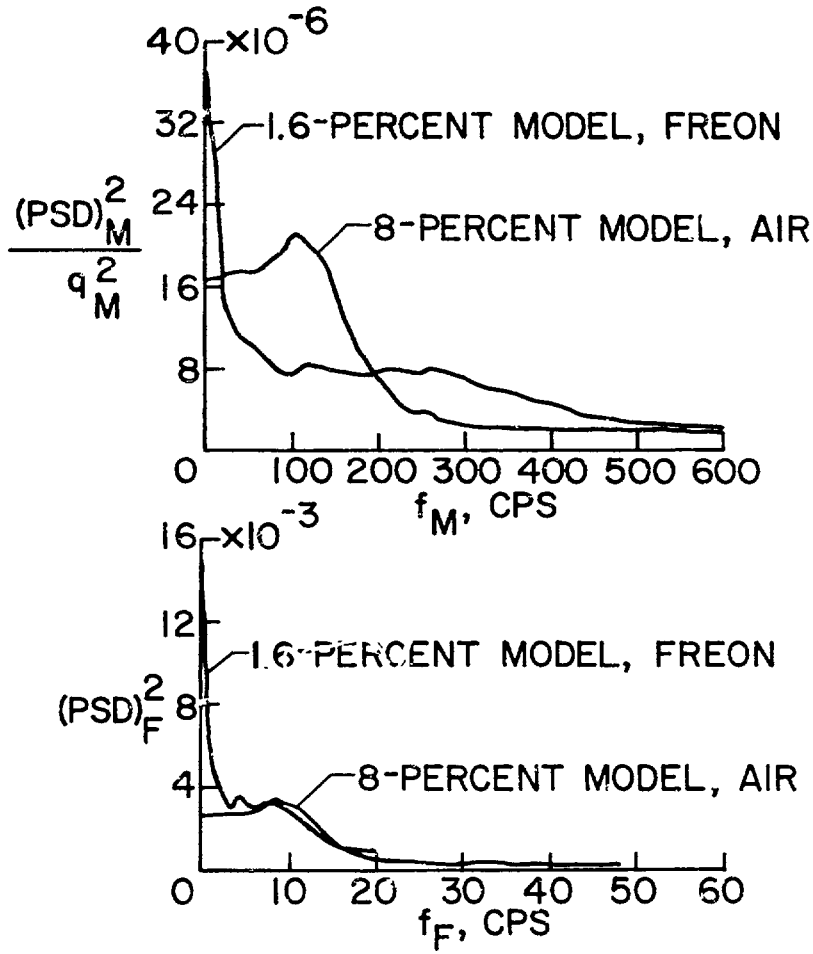

(e) Comparison of data at station "a" for 1.6-percent model tested in Freon and for 8-percent model tested in air, M = 0.8.

Figure 9.- Concluded.

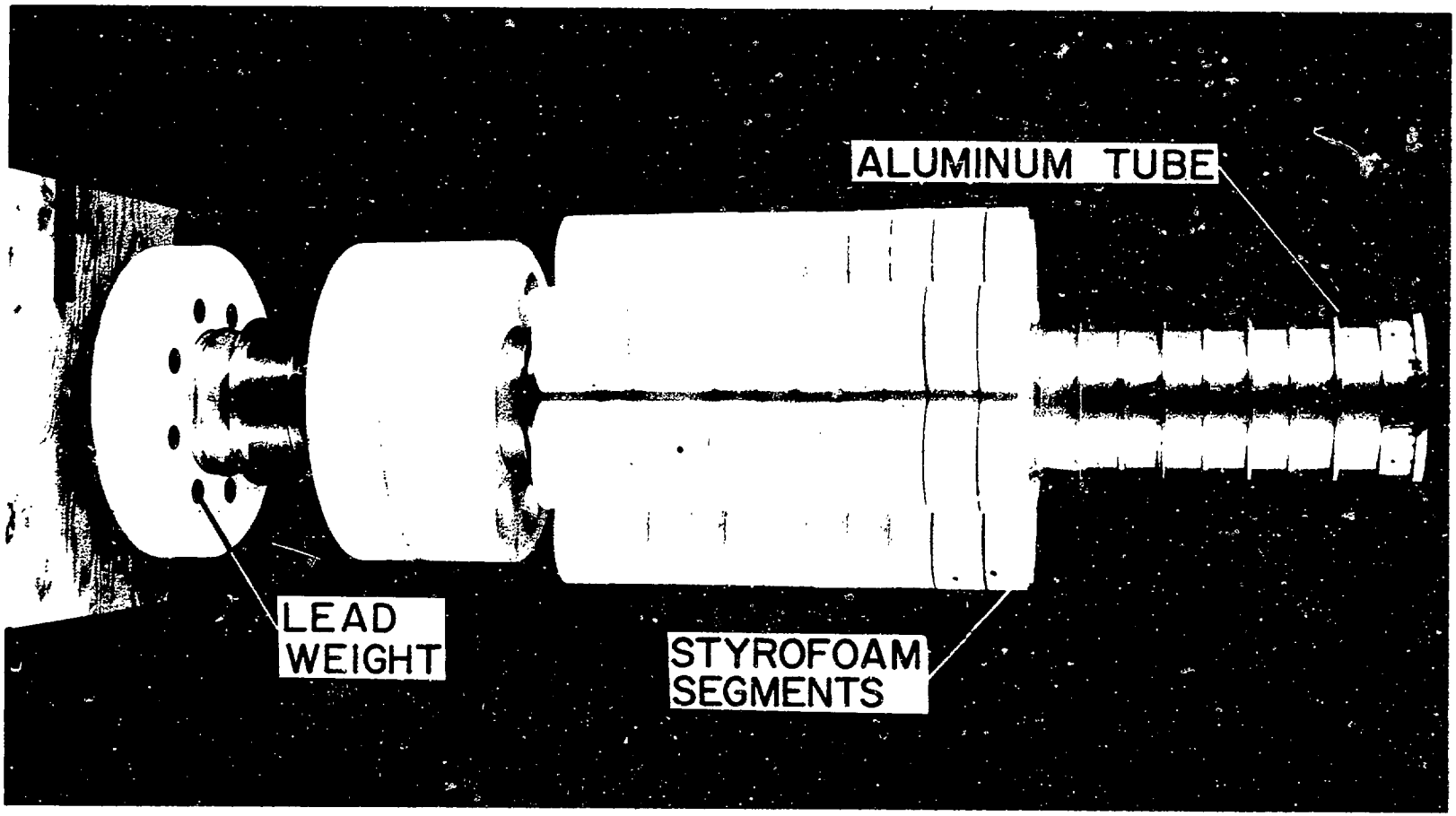

Figure 10.- Portion of 8-percent Saturn-Apollo aeroelastic buffet model.

Figure 11.- Eight-percent aeroelastic buffet model mounted in tunnel.

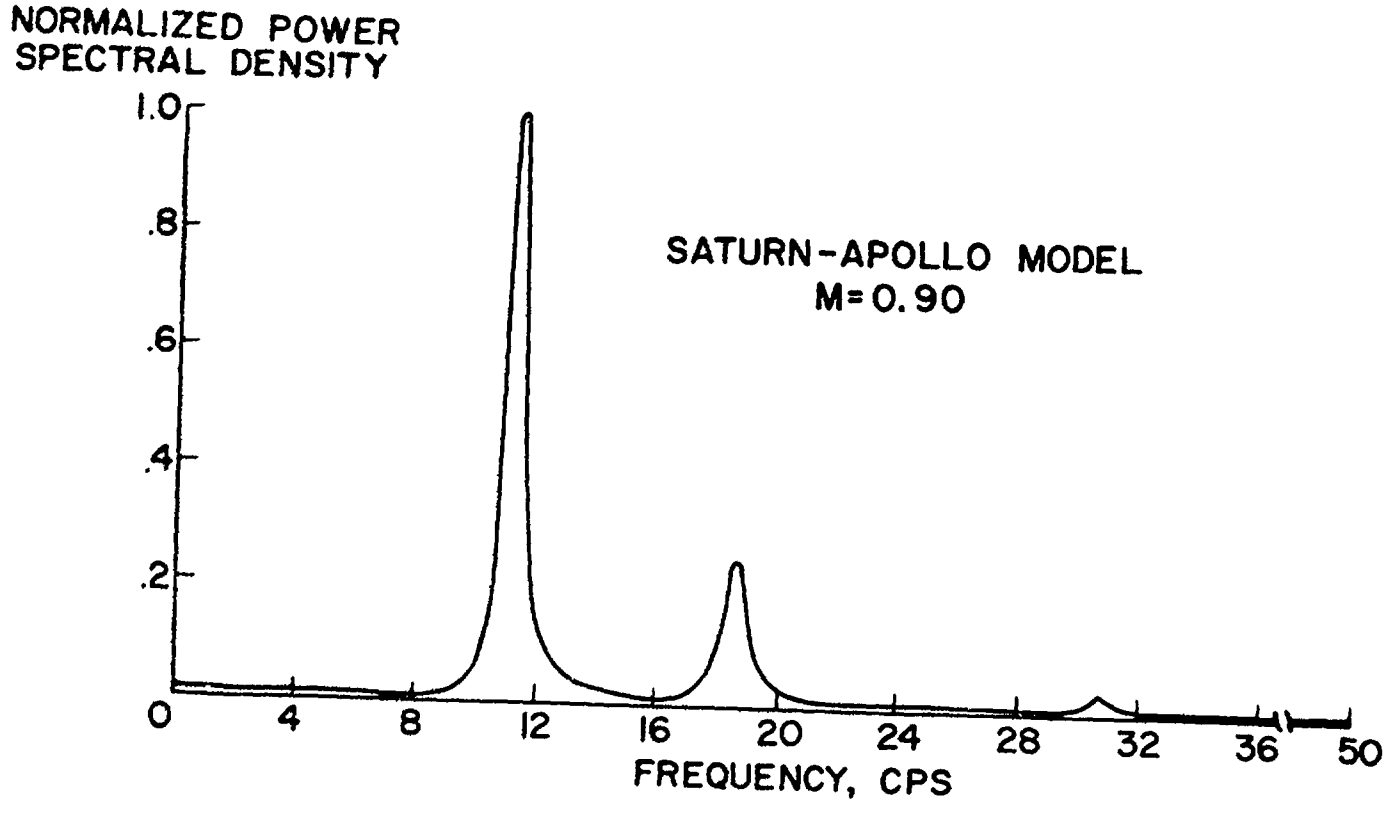

Figure 12.- Bending-moment power spectrum for Saturn-Apollo aeroelastic model at M = 0.90.

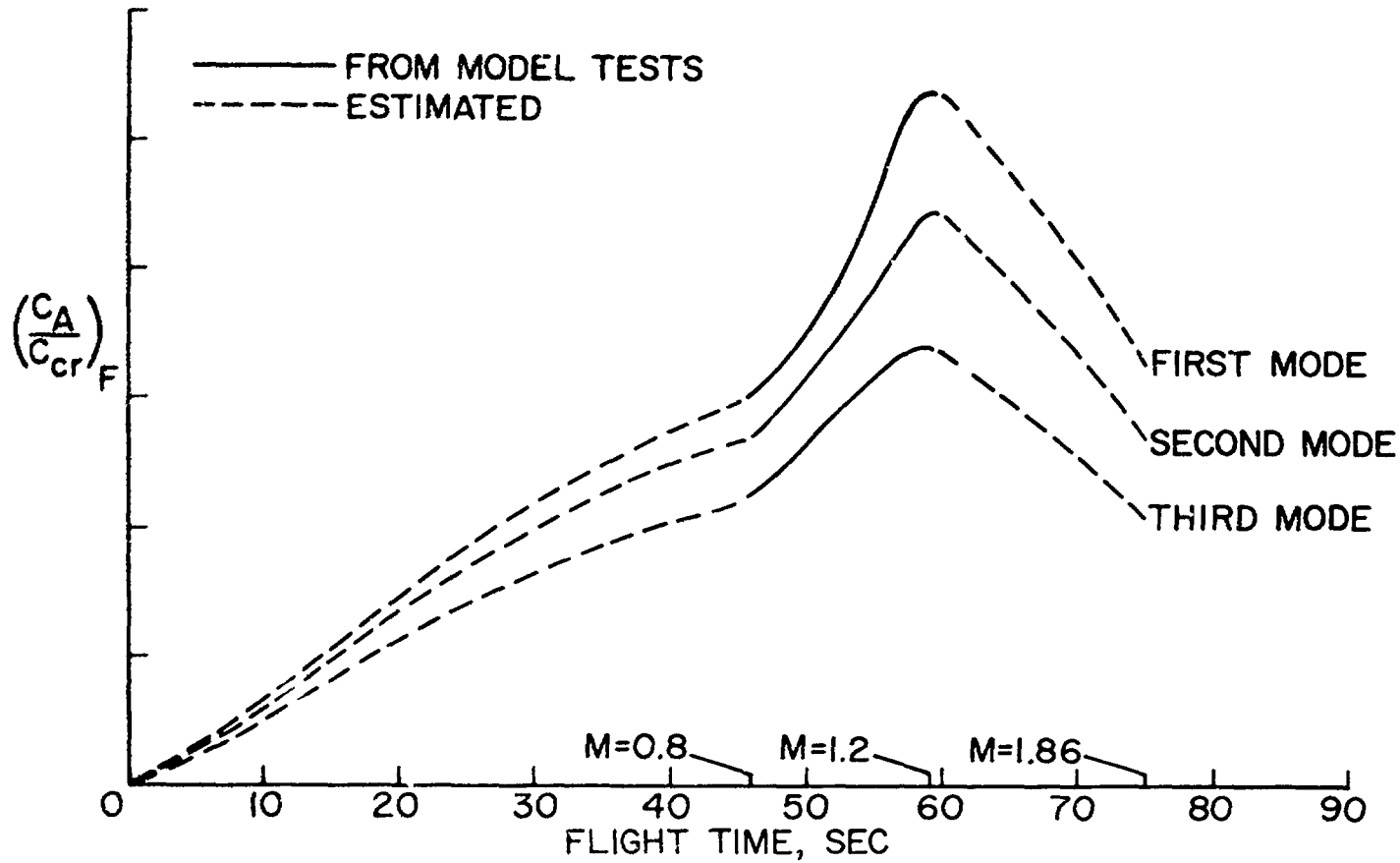

Figure 13.- Full-scale Saturn-Apollo aerodynamic damping predicted from model tests.

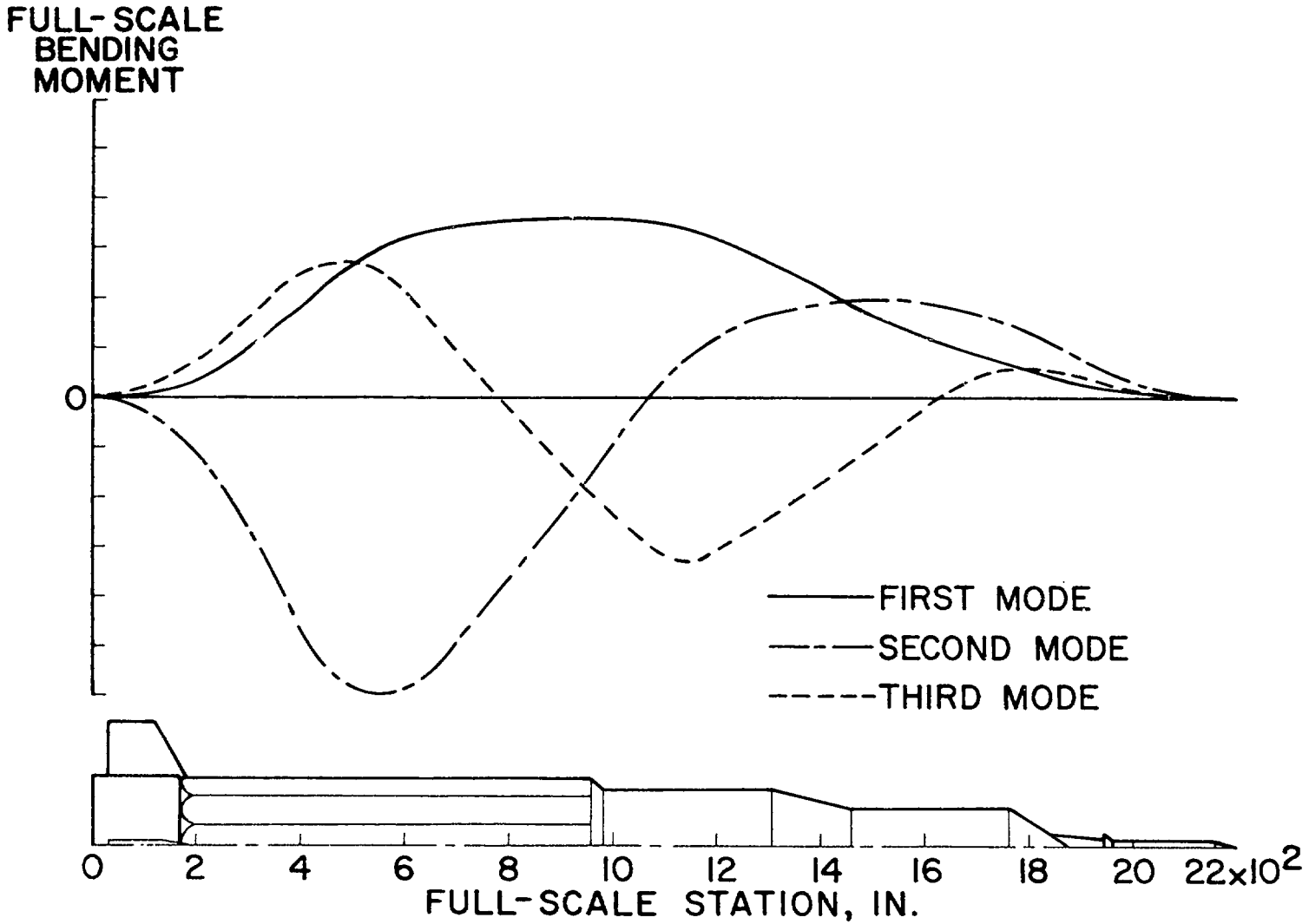

Figure 14.- Full-scale rms bending-moment distribution for first three bending modes of Saturn-Apollo vehicle at M = 0.9 predicted from model tests.

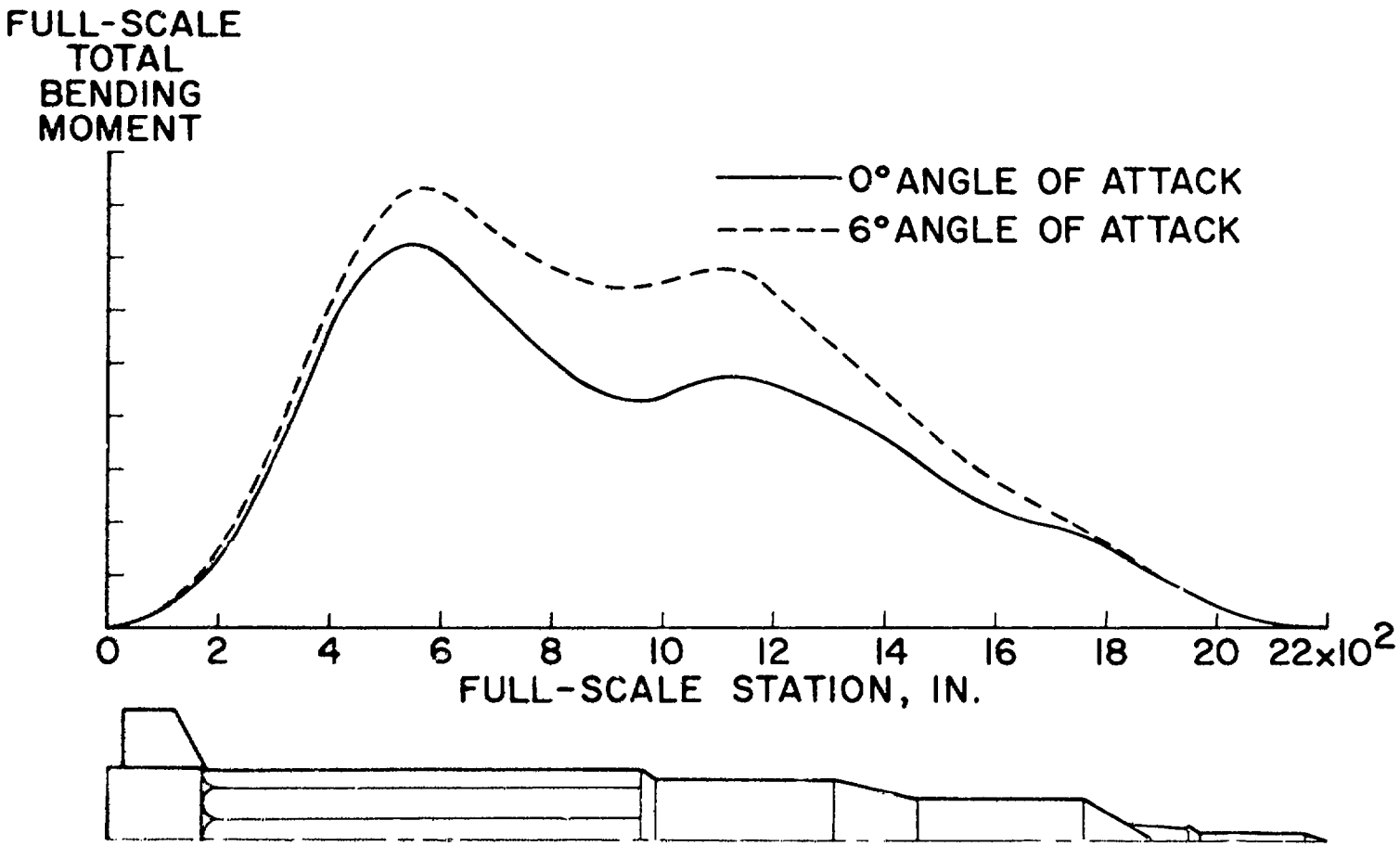

Figure 15.- Total full-scale rms buffet bending-moment distribution at M = 0.9 predicted from model tests.

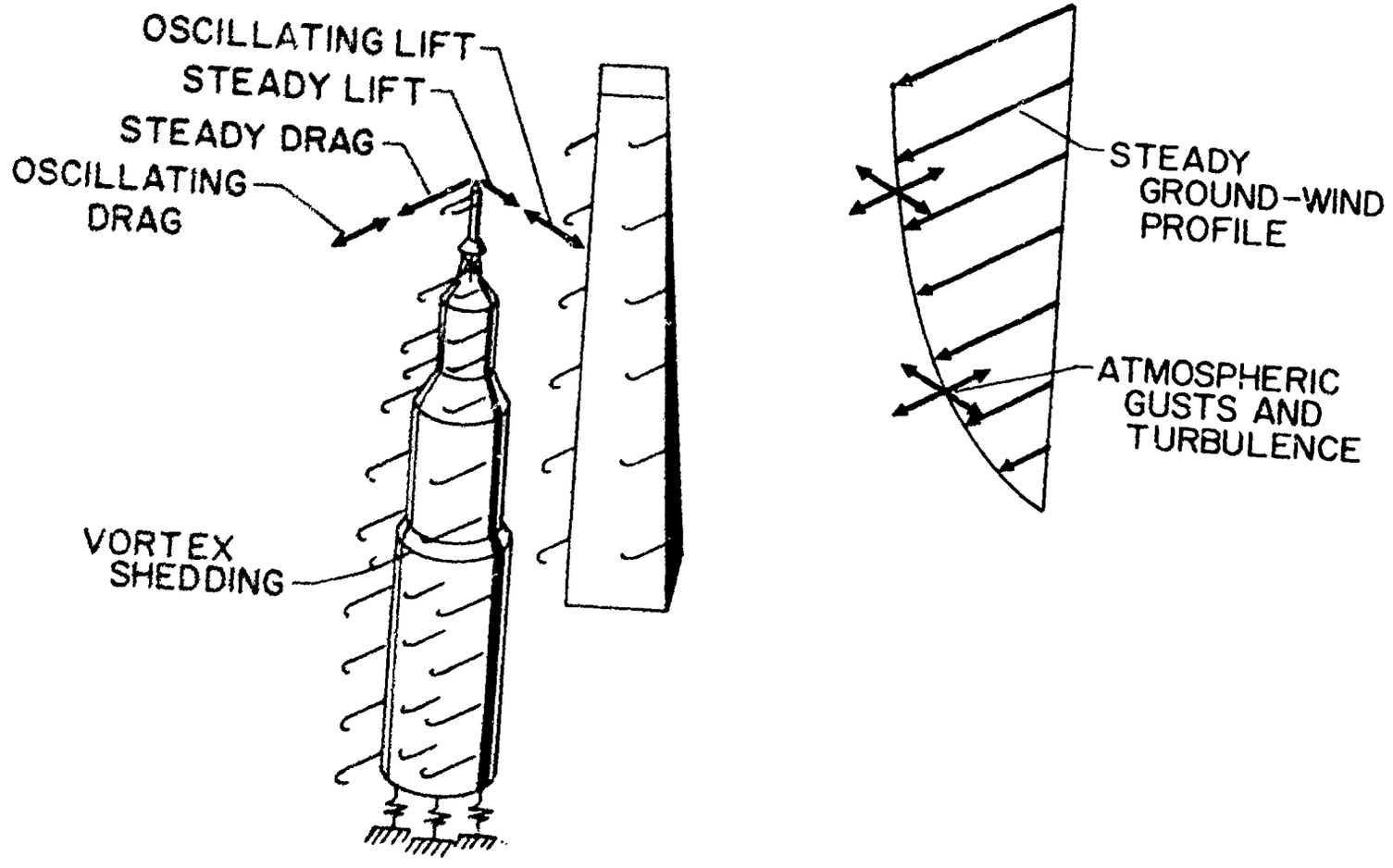

Figure 16.- Load conditions caused by ground winds.

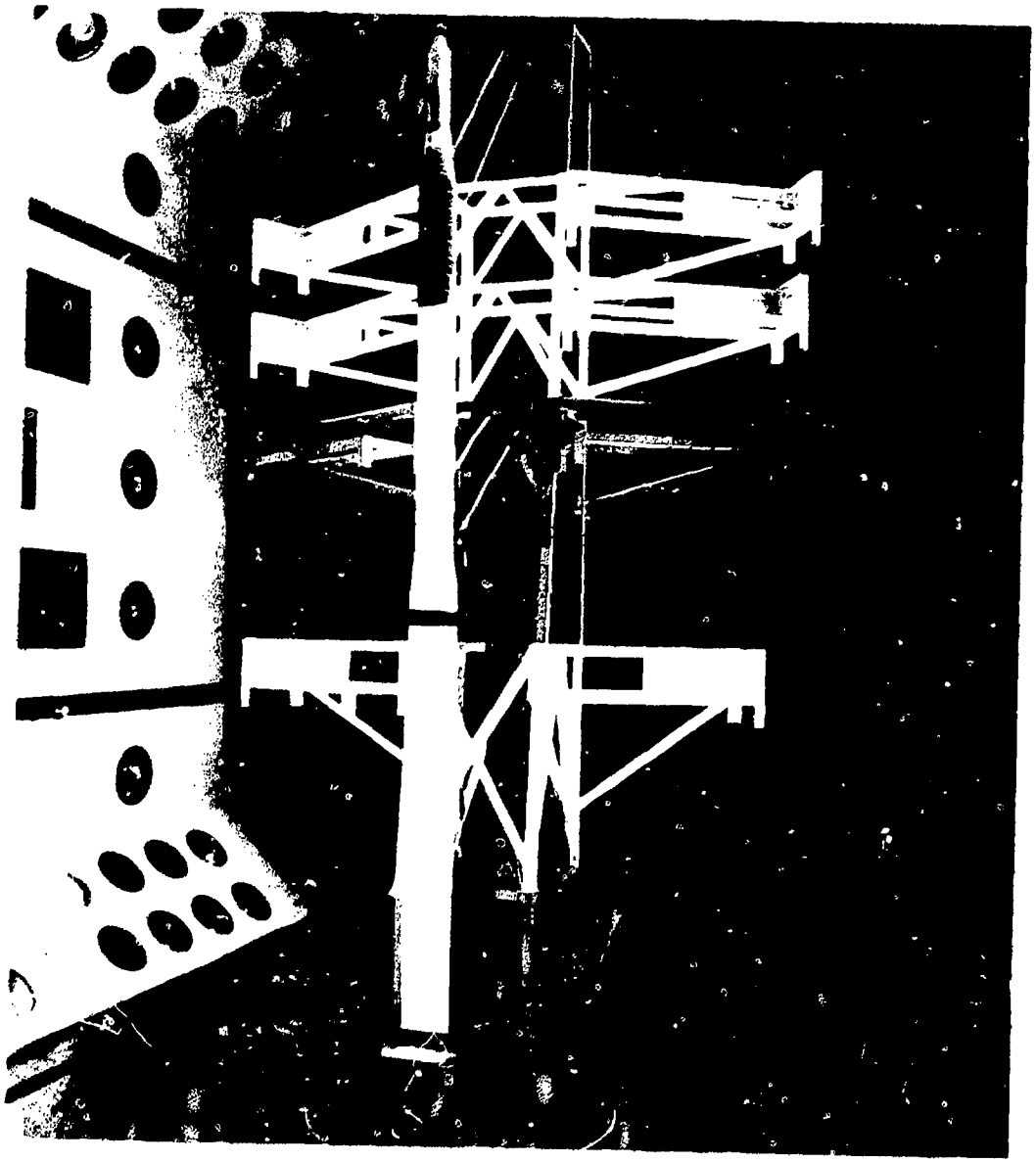

(a) 15-percent scale Scout ground-wind loads model.

Figure 17.- Some ground wind models tested in Langley Research Center transonic dynamics tunnel.

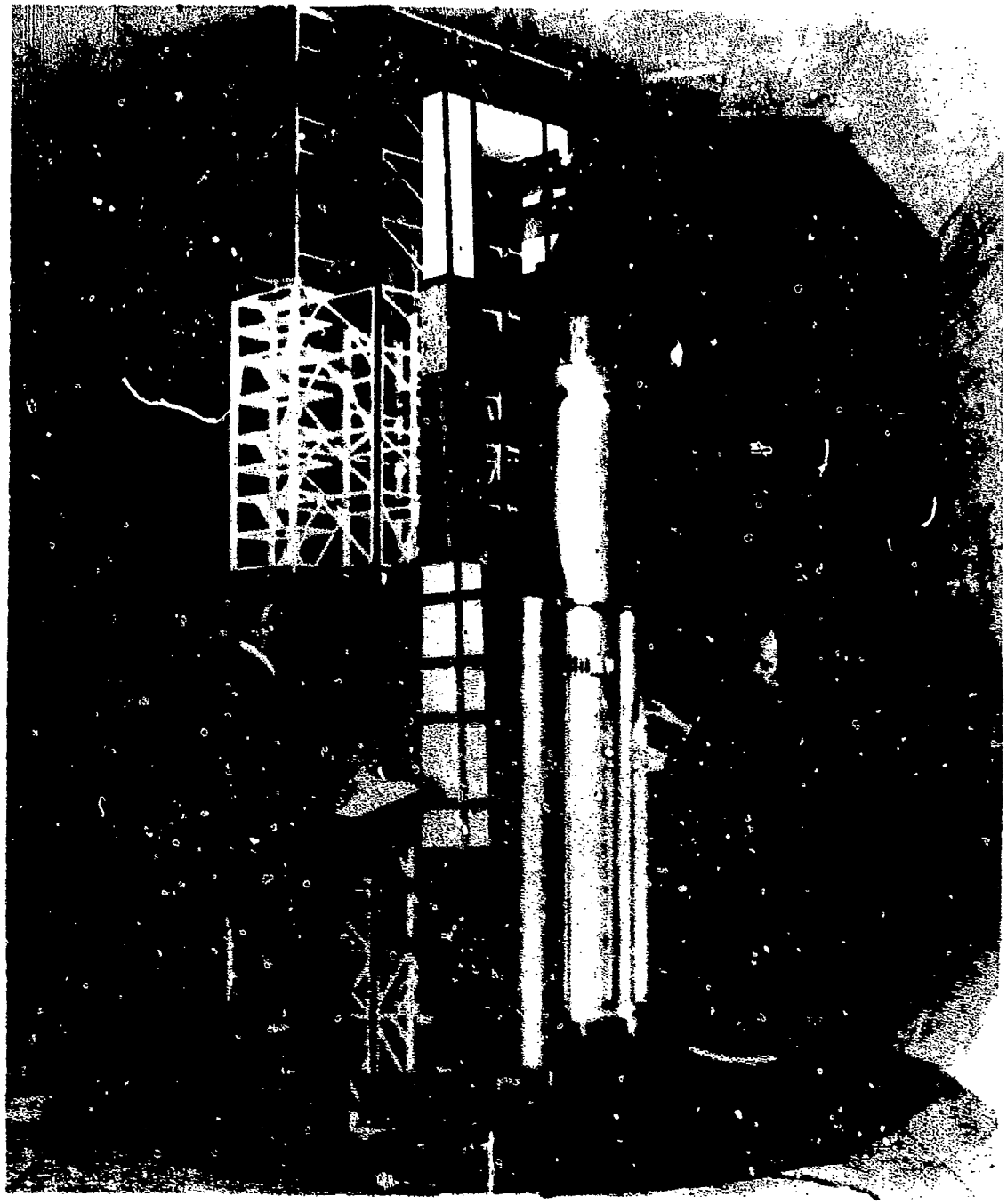

(b) 7.5-percent scale Titan III ground-wind loads model with Dyna Soar payload

Figure 17.- Continued.

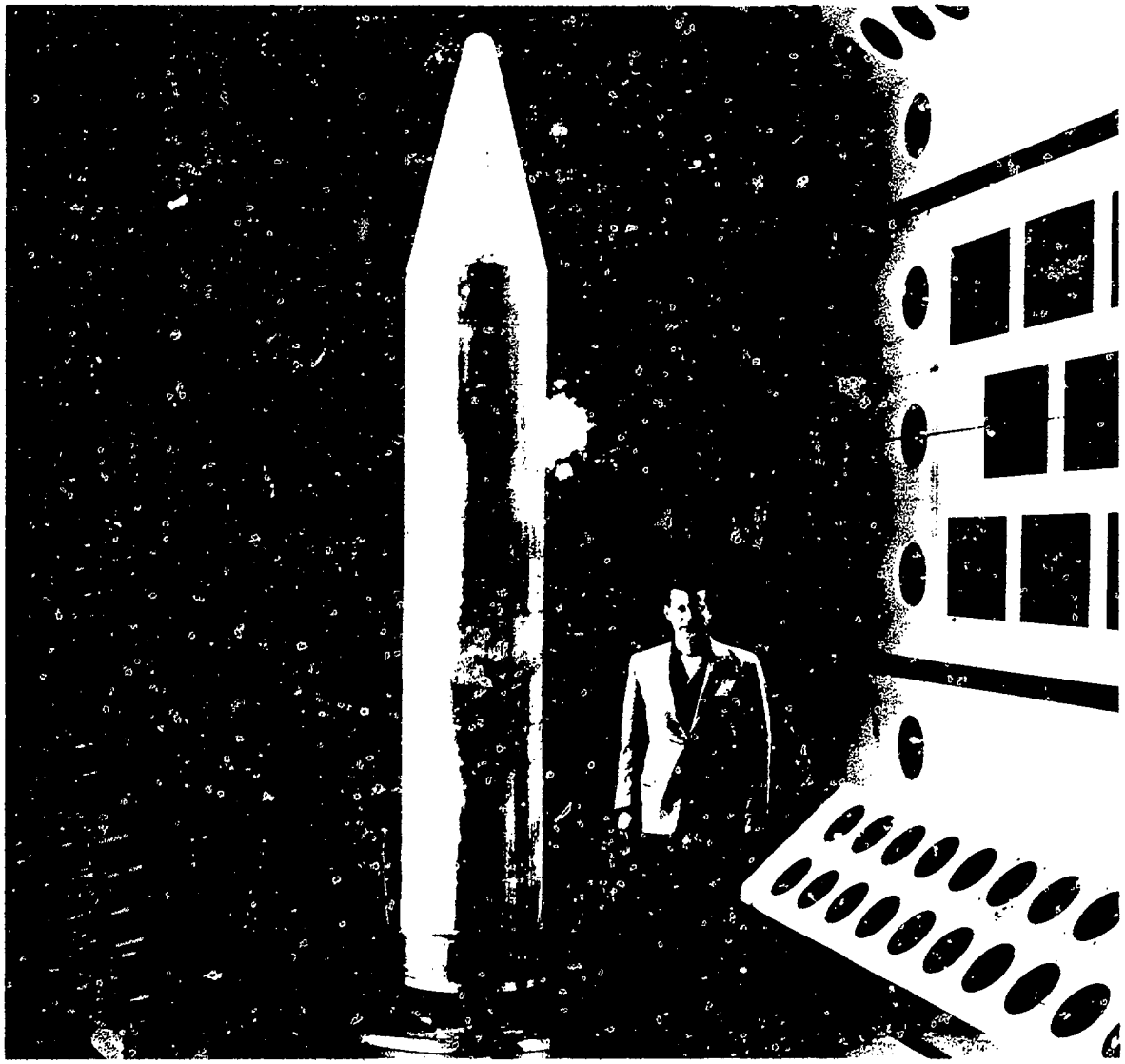

(c) 20-percent scale Jupiter ground-wind loads model.

Figure 17.- Continued.

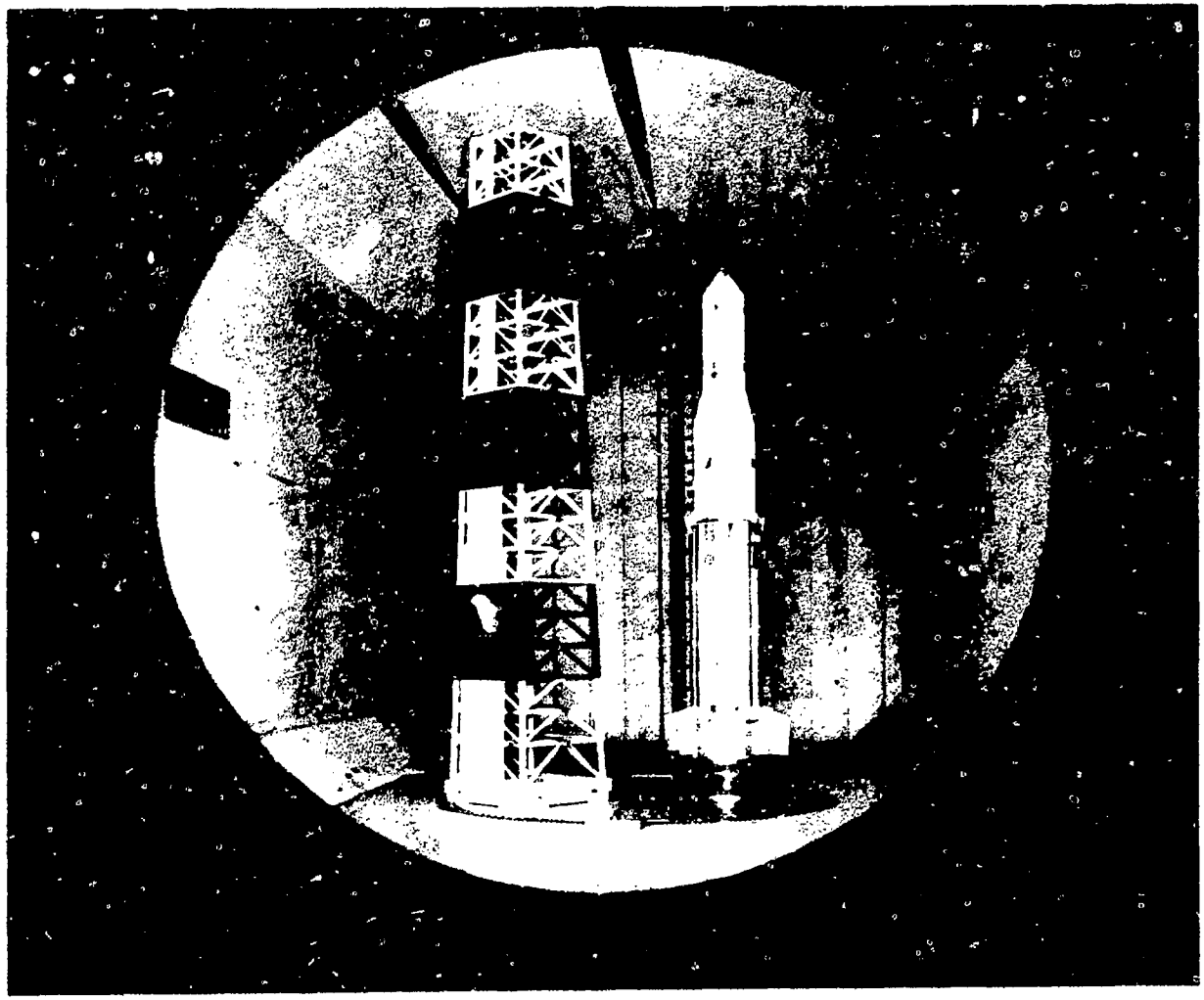

(d) 7-percent scale Saturn 1-Block II ground-wind loads model.

Figure 17.- Continued.

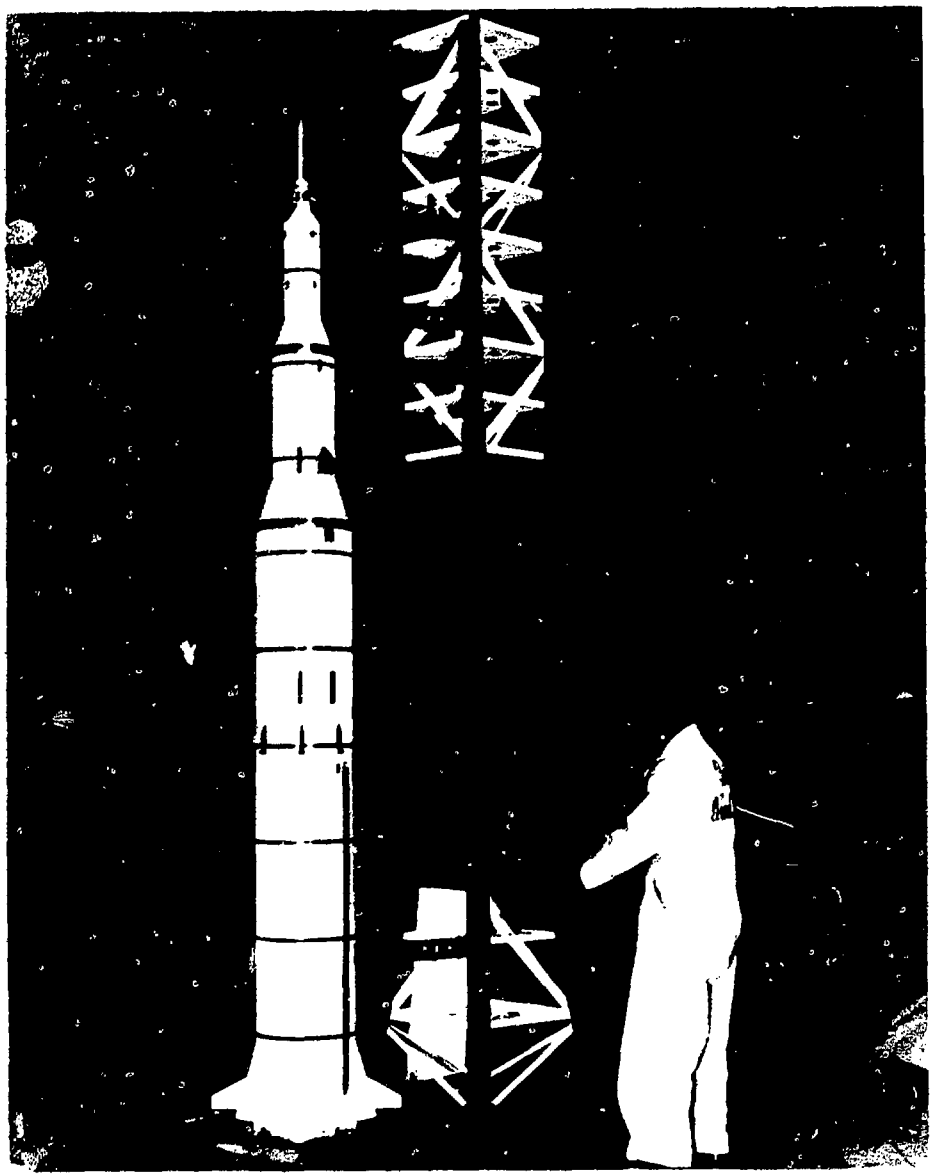

(e) 3-percent scale Saturn V ground-winds loads model.

Figure 17.- Concluded.

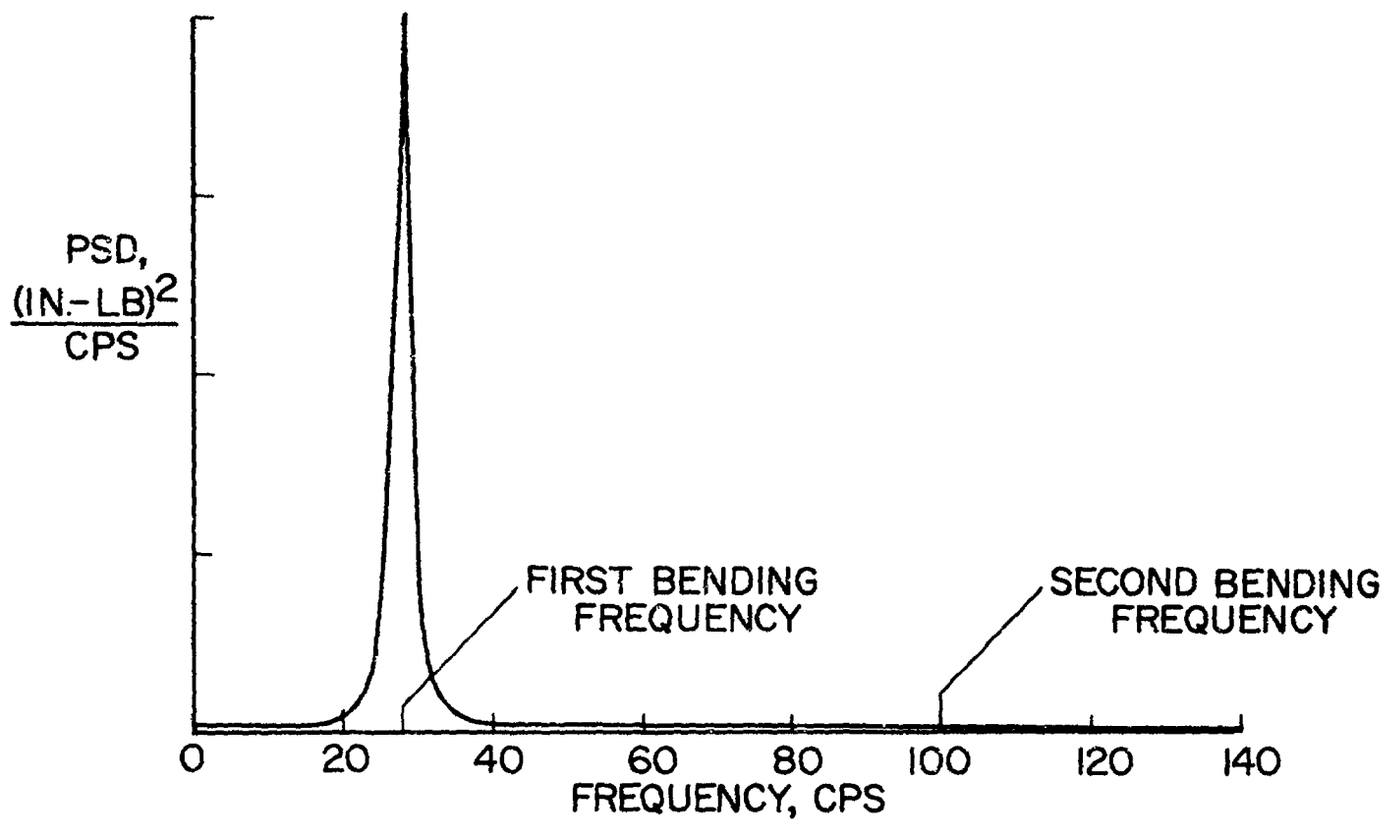

Figure 18.- Typical power spectral density of base bending-moment response of launch vehicle ground winds model.

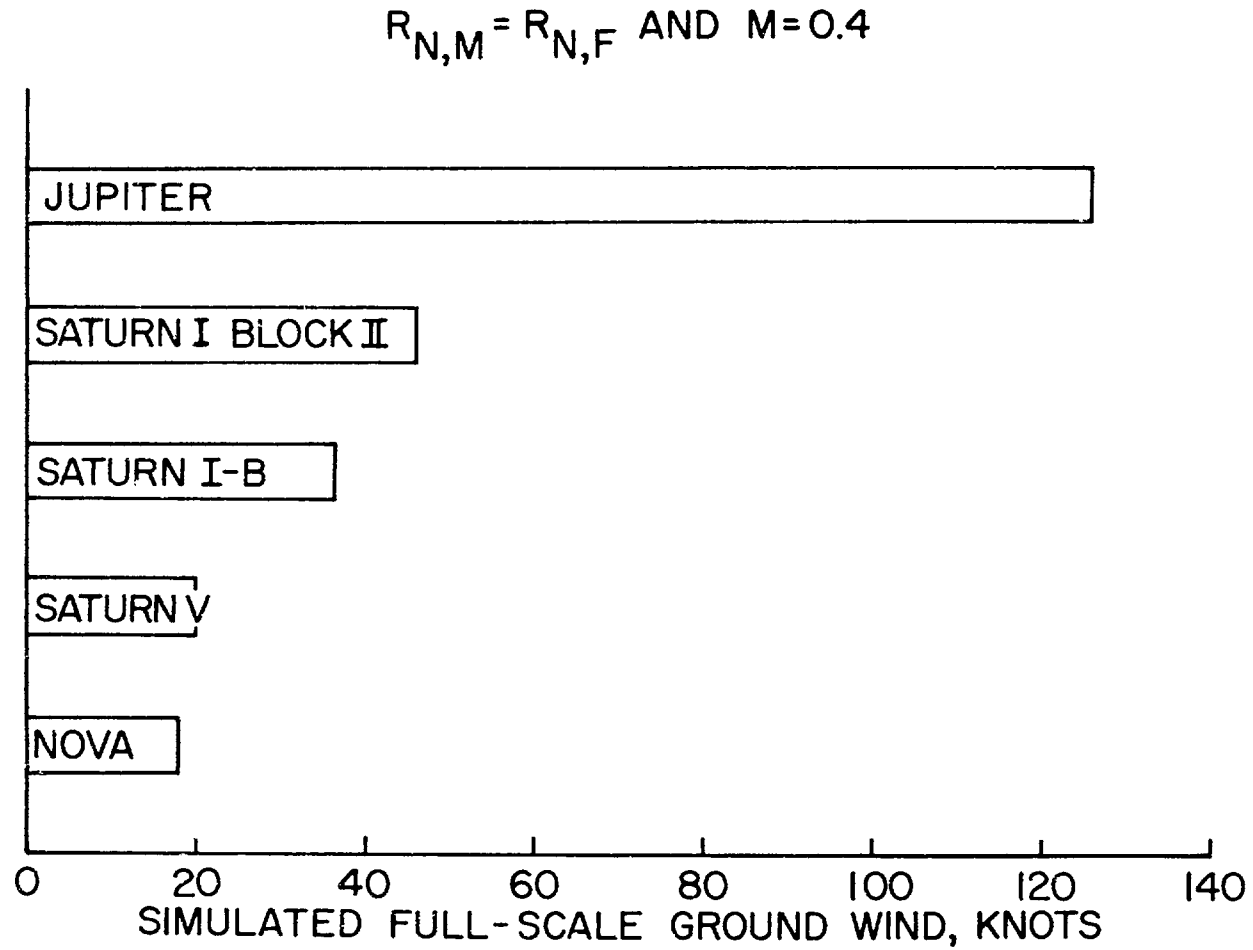

Figure 19.- Velocity simulation range available for ground-wind launch vehicle models in Langley Research Center 16-foot transonic dynamics tunnel.

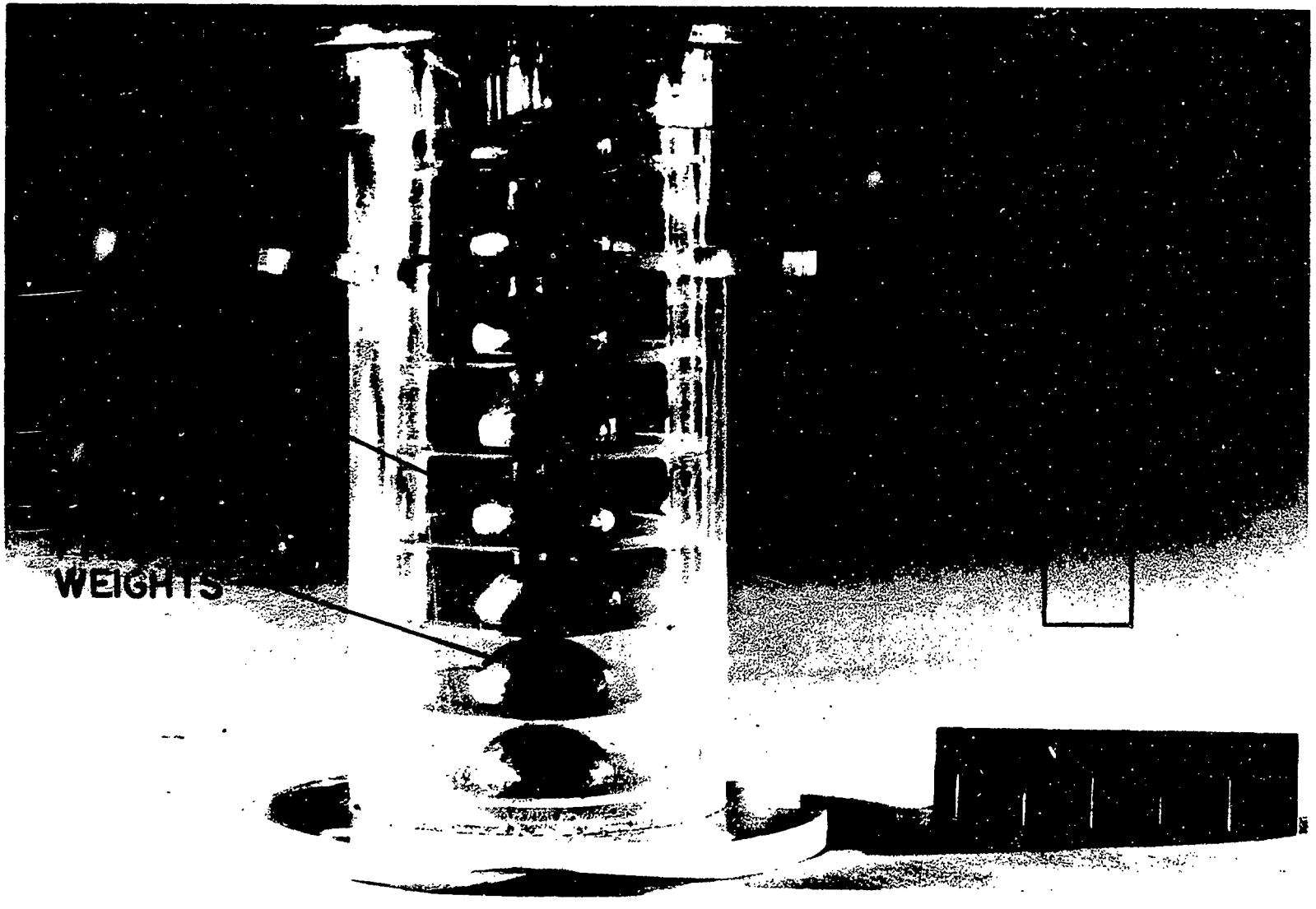

Figure 20.- Model variable structural damper.

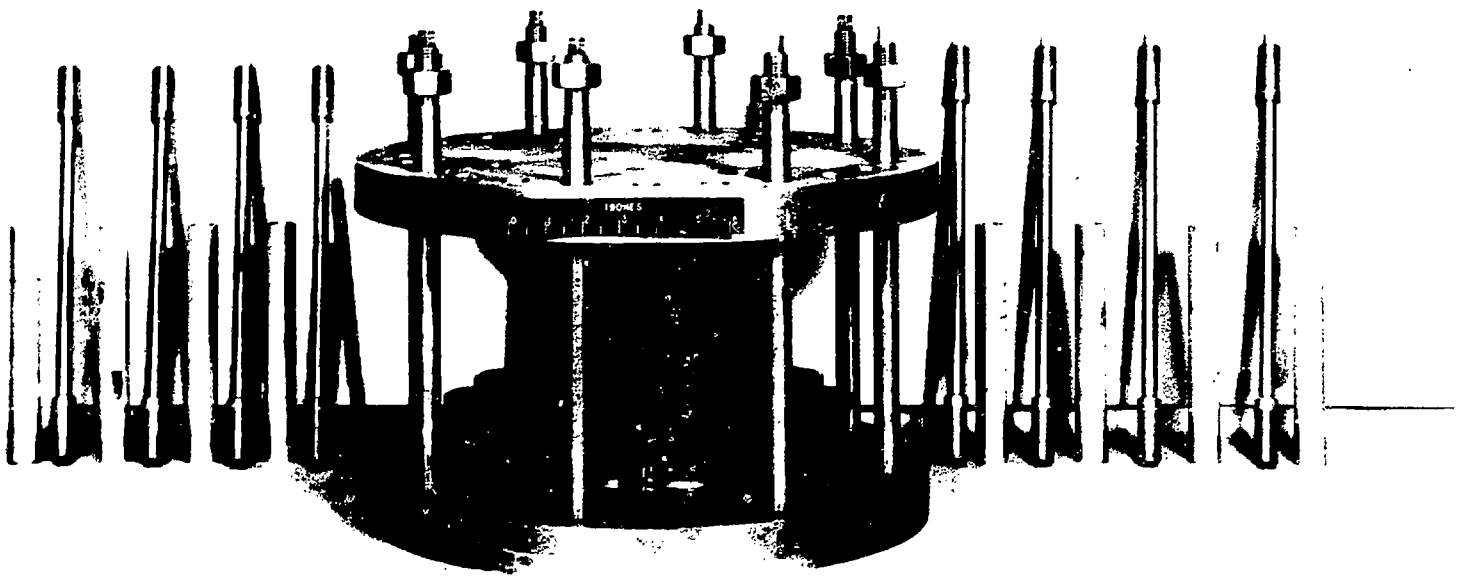

Figure 21.- Photograph of variable stiffness base mounting fixture.

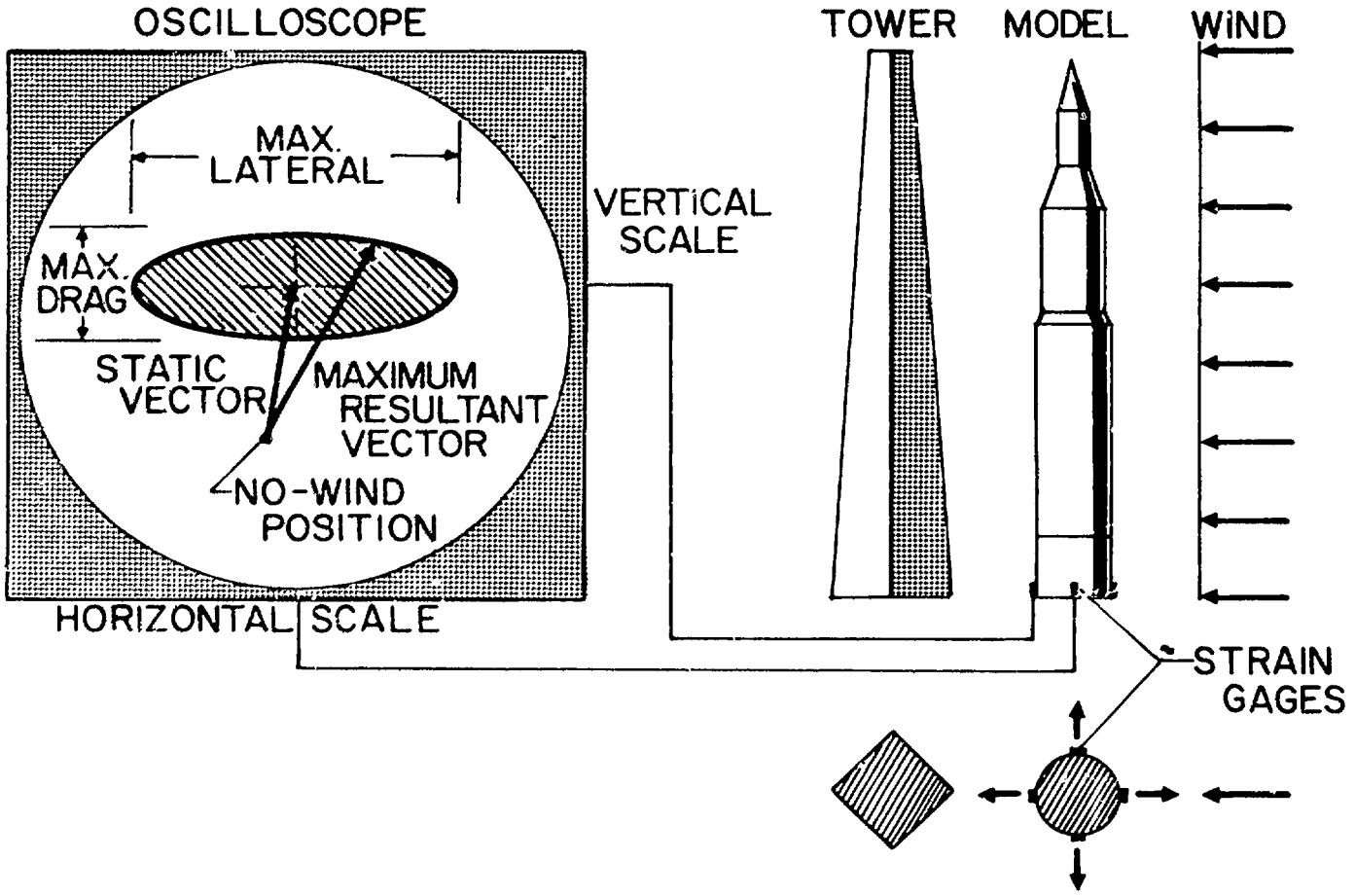

Figure 22.- Schematic of oscilloscope time history of base bending-moment response.

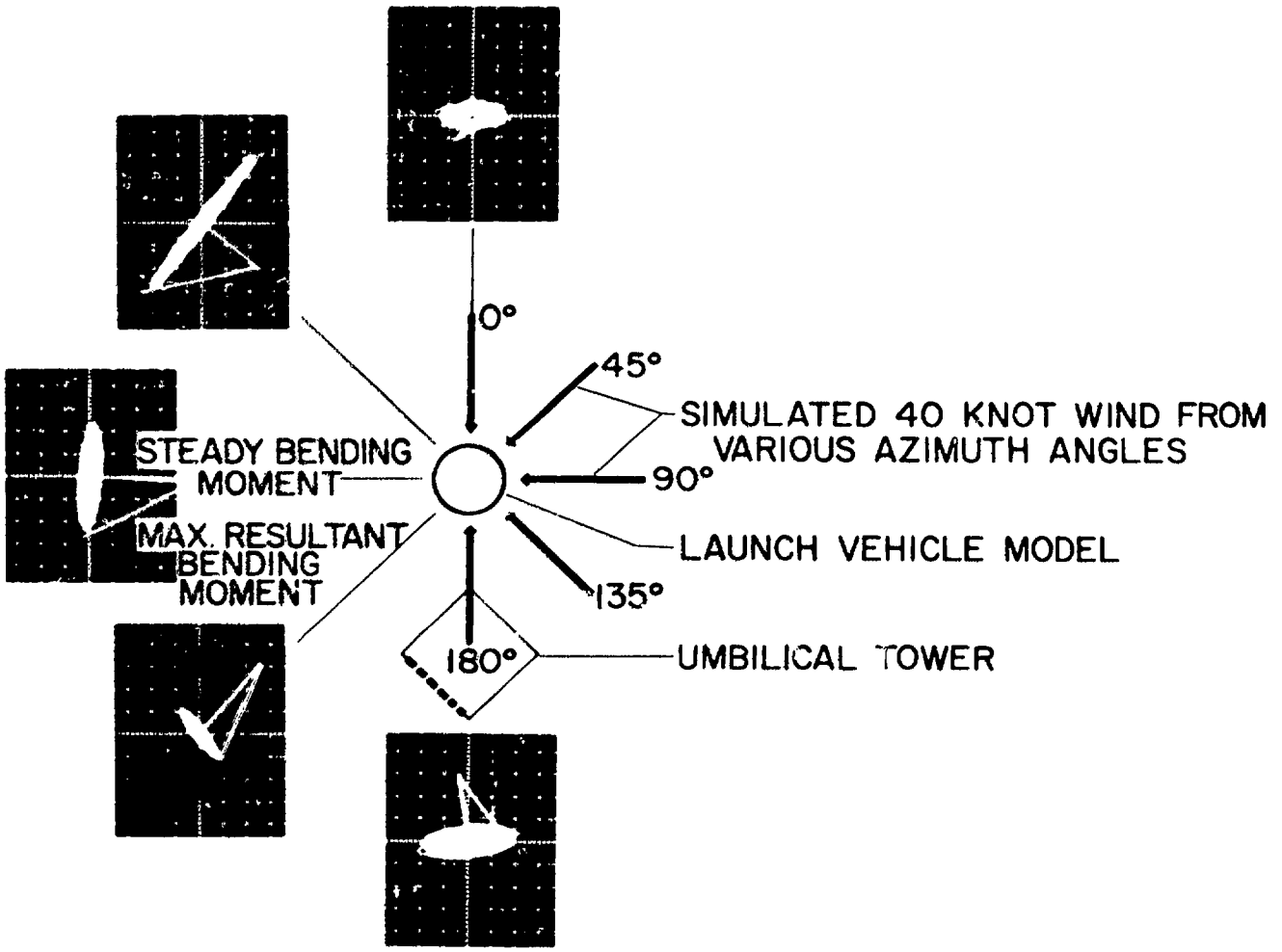

Figure 3.- Illustration of bending-moment response to winds from various azimuth angles.

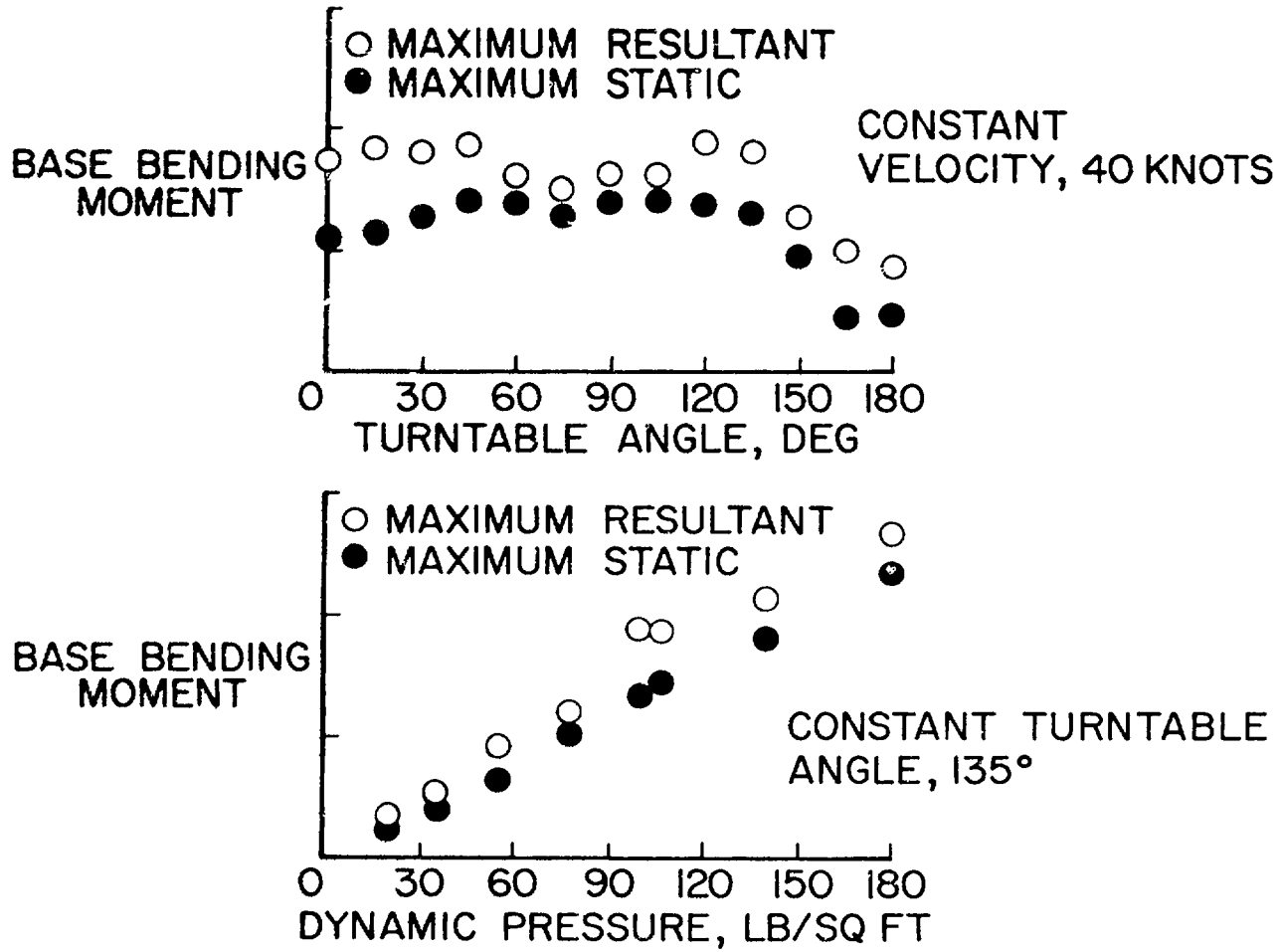

Figure 34.- Variation of maximum static and total base bending moment with turntable angle and dynamic pressure.

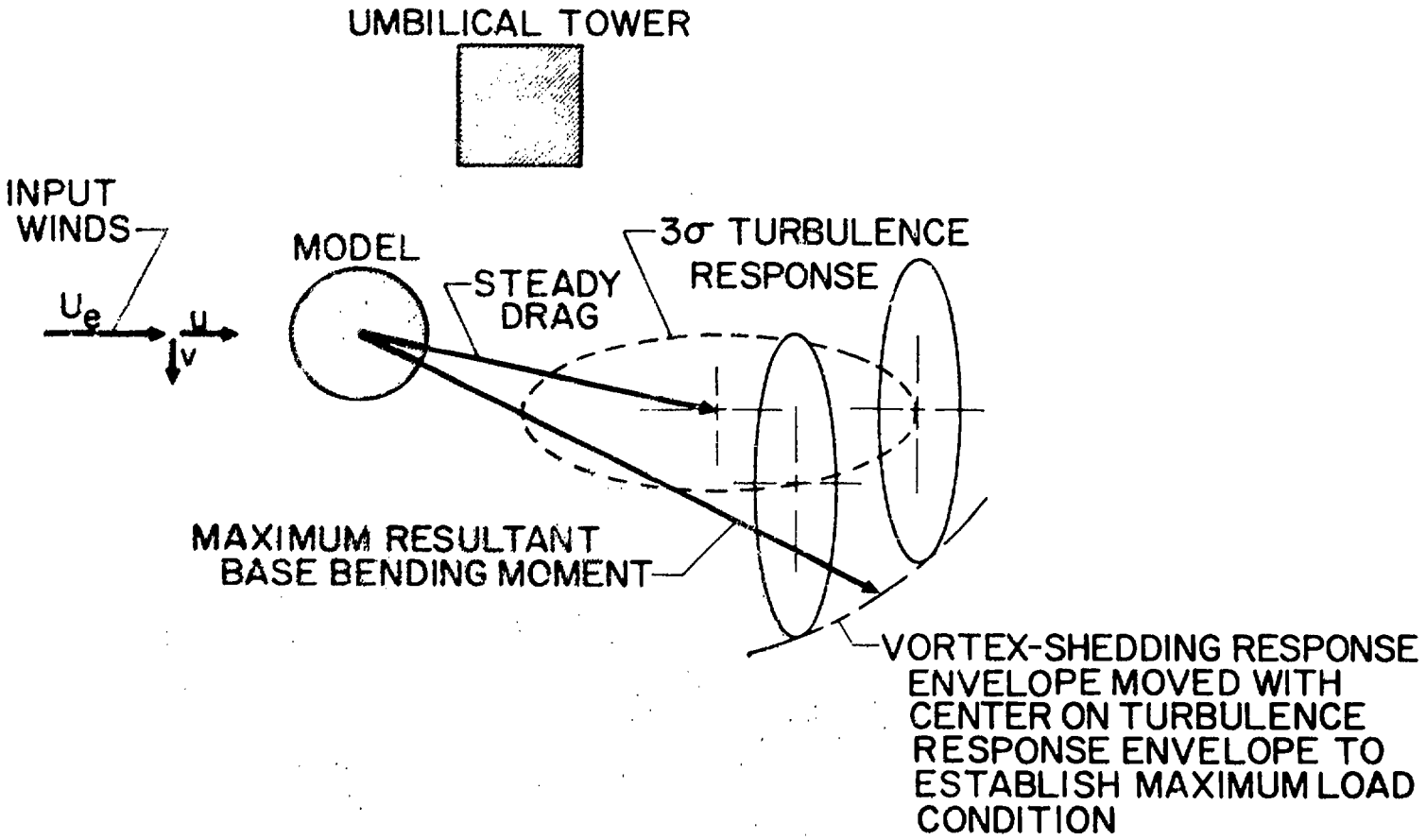

Figure 11.- Method of combining wind tunnel and theoretical ground wind loads.

SIMULATION OF ORBITAL MOORING OF GEMINI AND AGENA VEHICLES BY MEANS OF DYNAMICALLY SCALED MODELS

R. K. Nolting

McDonnell Aircraft Corporation

Abstract

The mooring dynamics of a Gemini spacecraft and Agena booster are studied by means of dynamically scaled models. Each vehicle is supported through a gimbal arrangement which is suspended by a cable from a "zero spring rate" mechanism to provide 6 degrees of freedom. Vehicle transient response and critical loads are obtained through accelerometers and strain gages on the models. Test results are then correlated with planar analytical studies in which all rigid body degrees of freedom and non-linearities are included.

The objectives of the program include determination of the adequacy of the shock absorbing system parameters, vehicle transient response, and envelope of approach conditions giving successful mechanical coupling.

LIST OF ILLUSTRATIONS

LIST OF TABLES

SIMULATION OF ORBITAL MOORING OF GEMINI AND AGENA VEHICLES BY MEANS OF DYNAMICALLY SCALED MODELS

R. K. Nolting

McDonnell Aircraft Corporation

Introduction

The NASA Gemini program calls for rendezvous in an earth orbit of the McDonnell built Gemini spacecraft with an Agena-D target vehicle equipped with a McDonnell docking adapter. This mission will be the first of its kind undertaken by the free world.

The rendezvous mission is conveniently divided into three phases. The first phase may be defined as bringing the two vehicles within 500 feet of one another and reducing their relative velocity to about 5 feet per second. The second phase, called docking, begins when the vehicles are 500 feet apart and ends with vehicle contact. The relative velocity of the vehicles can be further reduced during this period as required. The final phase, mooring, begins with actual physical contact between the two vehicles and ends when the vehicles have been rigidly connected.

Due to its fairly general nature, many articles appear in the literature on the analysis of the first phase of the rendezvous problem. Analysis of the mooring operation, however, is very dependent on the design of the particular mooring system. Consequently, analyses appearing in the literature which have been carried out in rather general terms are not too useful, and at the same time there have been few attempts to analyze a realistic mooring system. The Gemini program supplies the need for the analysis of a practical mooring system. In support of the dynamic analysis of the proposed design, McDonnell's Structural Dynamics Department requested that the Structures Laboratory conduct a 1/4 scale dynamic model mooring test.

Objectives of Test Program

The objectives of the test program were to confirm the design of the mooring system by providing information concerning:

1. The stability of the shock absorbing modes.
2. Maximum loads in shock absorbing system components.
3. Time histories of the accelerations of each vehicle in all 6 rigid body degrees of freedom.
4. Limiting values of angular and linear misalignment for which latching of the two vehicles occurs.
5. The adequacy of the proposed spring and damper characteristics of the shock absorbing system.
6. The adequacy of the mathematical model used in the analytical studies.

Description of Models, Suspension System, and Instrumentation

Each vehicle was represented by a 1/4 scale model having rigid body mass and three axes mass moment of inertia simulation. Figure 1 shows the models in the moored configuration. The various scale factors used in designing the models are listed in Table 1.

Figure 2 shows the model shock absorbing system corresponding to the system on the full scale target vehicle. The model has been rotated in Figure 2 for display purposes. The full scale system consists of three lateral dampers and four longitudinal dampers in parallel with springs. These support a mooring cone with a half-angle of 31.5 degrees. On the top side of this mooring cone is a roll slot which guides a roll indexing bar on the nose of the Gemini. Two of the longitudinal spring-dampers are placed there at an angle of 87 degrees to one another to dissipate the energy associated with this rolling motion.

At the base of the mooring cone are three hard stops and spring loaded latches equally spaced at 120 degrees around the circumference. During mooring, as the leading edge of the Gemini's nose passes over them, the latches are depressed flush with the cone surface. When the Gemini's nose reaches the hard stops the latches automatically seat into recesses located on the nose at these three 120 degree locations. The Gemini is thereby fastened to the mooring cone. This is the first step in securing the two vehicles together.

The three lateral dampers have metered orifices to provide level force-stroke characteristics. The longitudinal dampers have constant orifices and are in parallel with springs to minimize peak forces also. Damper-spring combinations were chosen for the longitudinal elements of the shock absorbing system instead of metered orifice dampers because the mooring cone must return to the fully extended position after the latches have secured the Gemini's nose. This is necessary in order that the mechanism which then pulls the cone down on to heavy structural pads to rigidly connect the two vehicles can be operated. The springs have a small preload to insure full extension of the cone. The longitudinal dampers are constructed to use a much smaller orifice on their return stroke to restrict the rate at which the energy stored in the springs in parallel with them is released. This is desirable in order to keep rebound effects during mooring to a minimum.

The model closely duplicated the kinematics of the full scale system and the springs and dampers were dynamically scaled as recorded in Table 1. The mooring cone surface was coated with the same dry film lubricant planned for use on the full scale article and for the same reason the leading edge of the Gemini's nose was covered with a layer of fiberglas.

Each model was supported at its center of gravity through a low friction gimbal device which was suspended by a 30 foot cable from a "zero spring rate" mechanism shown in Figure 3. As shown in the figure, the vertical spring supported the model weight. The lateral springs were in tension and produced a compressive force in each lateral rod. As the model's center of gravity moved during mooring these compressive forces canceled the change in the force exerted by the support spring. This combination of springs had an effectively zero spring rate about the equilibrium position as indicated in Figure 4. To determine this curve a series of small loads was applied to the suspension system while the system was already supporting the model weight. The discontinuity in this force-displacement curve was due to the small amount of static friction in the system. Some idea of the sensitivity of the system is given by noting in Figure 4 that as the break-out force of .044

pounds was reached, the model glided about 2 inches before the spring rate became sufficient to stop it. It is seen that the curve is reasonably flat over a single amplitude of 3 inches which was more than sufficient in view of the maximum initial misalignments permitted during mooring. This method of suspension provided each model with 6 rigid body degrees of freedom to simulate the orbital condition.

Each model was instrumented with six strain gage type accelerometers to measure all linear and angular accelerations. The lateral and longitudinal dampers shown at the top of Figure 2 were instrumented with semi-conductor strain gages to measure the loads in these members. Motion picture films were taken of all runs. A hand held camera operated at 64 frames per second and two mounted Fastex cameras ran at 250 frames per second.

Basic Model Data

The inertia data of each model is given in Table 2 and corresponded to the heaviest configuration expected of each prototype vehicle at mooring. The exact mass of the Gemini model at mooring is classified but it can be approximated as equal to that of the target vehicle for present purposes. Testing was limited to one configuration and the heaviest was chosen to make the shock absorbing system dissipate the maximum amount of energy. This relation is easily shown for a 2 degree of freedom system. If the Gemini collides inelastically with the Agena target vehicle at a relative velocity of V_o, and attitude control taruster forces are neglected, conservation of momentum and energy gives the energy to be dissipated as

$$\Delta T = \frac{1}{2} \left(\frac{1}{1/m_a + 1/m_g} \right) V_o^2$$

It is seen that the Gemini and target vehicle play equal roles in increasing ΔT as their mass increases.

The center of gravity of the target vehicle model was located 39.83 inches from the edge of the mooring cone when fully extended. The Gemini model's center of gravity was 29.10 inches from its leading edge.

The damping characteristics of each of the three types of dampers on the prototype shock absorbing system were determined by analytical studies before the initiation of the model tests. One objective of the test was to demonstrate that these characteristics were adequate. The dashed curves on Figures 5, 6, and 7 represent these proposed damping constants for the full scale dampers, but have been scaled down to model dimensions. The solid curves on these figures show the damping constants of the model dampers as actually constructed and used. To determine these curves, each damper was stroked by impact with a mass traveling with known initial velocity. Accelerometer and strain gage data supplied the force and velocity sensed by the damper at each point in the stroke. In the analytical studies the orifice dampers were assumed to generate forces proportional to the square of the velocity sensed. Accordingly, the simplest approach in comparing the dampers used in the analytical studies to the dampers used on the model was to stroke the model dampers with velocities in the range of actual operation and determine the effective velocity squared damping constant by dividing the measured force by the square of the velocity at each point in the stroke. This measured

force included friction. Efforts were made in the construction of the model dampers to minimize frictional forces. The surfaces of moving metal parts were polished and care was taken in fitting the fluid seals. Although no attempt was made to measure the kinetic friction force in each damper, it is felt that the level was still several times the scaled value expected of each full scale damper. These friction forces are partially responsible for the high effective damping constant toward the end of the strokes in Figures 5 through 7.

Table 3 compares the actual model longitudinal spring rates and preloads with scaled values of the proposed prototype spring rates and preloads.

Test Procedure

The desired relative velocity between the Gemini and target vehicle at the onset of mooring for each run was attained by swinging each model as a pendulum from a predetermined pull-back distance. This was possible because of the small amount of static friction in each suspension system. This break-out force was measured several times during the test and was confined to the range indicated by the cross-hatched areas in Figure 4. The maximum centripetal force which each suspension system had to exert on its model during the swing was less than the minimum break-out force shown in Figure 4. Under the design rules, the maximum relative translational velocities allowed at mooring are 1.5 feet per second in the longitudinal direction and .5 feet per second laterally. By dividing these velocities equally between the models, the maximum centripetal force required was

$$\frac{mv^2}{r} = \frac{(2.19 \text{ slugs}) \left[(.75 \text{ ft/sec})^2 + (.25 \text{ ft/sec})^2 \right]}{30 \text{ ft.}} = .0416 \text{ lb.}$$

which is just barely less than the minimum break-out force of .044 pounds. At no time during the test, however, was the suspension system observed to slip while swinging the model.

As shown in Figure 1, the models were rotated 90 degrees about the roll axis. This was done because considerable attention was to be given collisions occurring in the pitch plane. By making the pitch plane horizontal, the lateral velocities were easily worked in and also the resulting motion required less displacement of the suspension system.

A total of 37 data runs were made with various combinations of initial relative velocity and linear and angular eccentricities as listed in Table 4. Although this was not the situation during the test, the analysis is simplified by considering the Agena target vehicle at rest and having no linear or angular eccentricities. The quantities given in Table 4 are those of the Gemini relative to the target vehicle. The sign conventions are defined in Figure 8. In general the lateral components of velocity were always directed so as to increase the impact loads. The pitch or yaw eccentricities were directed so as to move the Gemini's center of gravity even further off the Agena's longitudinal axis than any accompanying linear displacement had.

It was difficult to obtain an impact on the exact desired spot on the mooring cone. Despite the fact that the models weighed on the order of 70 pounds apiece, wind currents in the test area kept them from settling down. Even very small pitch or yaw rates would influence how far into the cone the

Gemini hit because of the cone's small angle. To reduce the wind currents, the entire model test area was enclosed in a plastic tent. This improved the situation, but some deviations still occurred. Referring to Table 4, the desired distance, 4d, was either 0, 5, 15, or 26 inches. The actual distances as determined by marks on the cone and moving picture films are recorded.

Analytical Studies

One purpose of the model test was to determine the adequacy of the mathematical model used in the analytical studies of the mooring problem. Before discussing the results of the model test, a brief description of these studies will be given. The results of the analytical studies can then be included in the discussion of the model test results.

A study of collisions in which the Gemini initially strikes the top inner surface of the mooring cone, $\theta = 0$, has been completed. The mathematical model from which the equations of motion were written had the following properties:

1. The Gemini and target vehicle, including the mooring cone, were considered rigid in view of the flexibility of the shock absorbing system.
2. All 8 rigid body degrees of freedom in the pitch plane were included.
3. The shock absorbing system's kinematics were not linearized or otherwise simplified.
4. Each of the orifice dampers was assumed to generate a force proportional to the square of the velocity sensed.
5. Spring preloads were included and the springs were assumed to generate forces proportional to displacement.
6. Kinetic friction forces in the dampers and at the point of contact of the Gemini with the mooring cone were not included.

The equations of motion were written in terms of generalized coordinates. Referring to Figure 9, the 8 generalized coordinates and their associated degrees of freedom were:

q^1 Agena horizontal translation.
q^2 Agena vertical translation.
q^3 Agena pitch rotation.
q^4 Gemini pitch rotation.
q^5 Gemini translation along docking cone.
q^6 Mooring cone pitch rotation.
q^7 Bottom longitudinal damper stroke.
q^8 Bottom longitudinal damper pitch rotation.

The equations of motion were written by a method equivalent to, but more convenient than, that of Lagrange and programmed on the IBM 7094 digital computer. They were valid from the time the Gemini first contacted the mooring cone until it reached the hard stops at the bottom of the cone. The general form of the equations of motion was

$$\sum_{k=1}^{8} M_{jk}\ddot{q}^k + \sum_{k,l=1}^{8} \boxed{kl,j}\ \dot{q}^k\dot{q}^l + U_j + V_j = 0. \qquad j = 1,2,\ldots 8$$

The M_{jk} and $\boxed{kl,j}$ are terms derivable from the mass properties of the system. The M_{jk} are the components of the second order symmetric inertia tensor and are commonly called inertia derivatives. The symbol $\boxed{kl,j}$ represents a Christoffel symbol of the first kind. These occur because the non-linear motion of the system was retained. The U_j are potential energy terms derivable from the springs in the system. Similarly, the V_j are dissipative energy terms derivable from the dampers.

At time zero when the Gemini had just made contact with the mooring cone, the proper initial values of the generalized coordinates and their time derivatives had to be supplied. These values corresponded to known cartesian coordinate values of each vehicle's initial displacement and velocity. But because so many degrees of freedom had to be included in the study, kinematic equations alone were not enough to determine all 16 of these unknown quantities. It was necessary, therefore, to write additional equations expressing the dynamic equilibrium of the mooring cone under the force of the Gemini pushing it against the restraining dampers and preloaded springs. These dynamic equations were then ultimately written as two lengthy quadratic equations in two unknown generalized coordinate velocities and solved by graphical methods. The other unknowns were then determined from the kinematic equations.

After the initial values were determined in this way, the equations of motion were solved on the computer for the 8 generalized coordinate accelerations. These were then assumed constant over a short period of time (on the order of 10^{-3} seconds) and integrated to find the new velocities and displacements. This process was repeated until the Gemini reached the bottom of the mooring cone.

The inertia data used in the analytic studies corresponded to the model data with the exception of the target vehicle's pitch and yaw inertias. The analytical value was 7.5 percent lower than the value corresponding to the model. The dashed curves of Figures 5, 6 and 7 define the damper characteristics used in the studies. The analytic spring data is given by the prototype values in Table 3.

Even this study of special planar collisions was very complicated to perform. As discussed above, just the determination of the initial conditions was a major calculation. The extension of this analytic method to the 3-dimensional case would have been far too complicated to be practical. This was one reason the decision was made to analyze the mooring problem through model simulation. Another reason was that even where analytic methods could reasonably be used to determine loads and vehicle response, they gave no reliable information concerning whether latching occurred.

Test Results

Stability of Shock Absorbing Modes

The modes of collapse of the shock absorbing system were observed to be stable during all the mooring runs made. That is, in every case the mooring cone had to stroke at least some of the dampers and springs in order to yield to the load impressed upon it by the Gemini. No side-slipping or other undesirable modes of collapse occurred. This property of stable collapse is primarily determined by the geometrical arrangement of the dampers and is not as easy to accomplish as may seem. An earlier design was discarded by the project when a model of it exhibited an unstable mode of collapse.

Maximum Loads

Cases 6 through 11, 18, 19, 23, and 24 through 28 established a load profile along the length of the mooring cone at various positions around the circumference (See Table 4). These maximum loads were of primary importance in determining whether the structural design of the mooring cone was adequate.

On the top side, $\theta = 0$, and on the bottom side, $\theta = 180$ degrees, of the mooring cone, this information is fairly complete. At the intermediate positions, $\theta = 30$, 90, and 150 degrees, only the load at the edge of the cone, 4d = 26 inches, was determined. No runs were made for $\theta = 60$ degrees because this position is midway between two sets of dampers like the $\theta = 180$ degree position. Similarly, the 120 degree position is directly over a damper set like the $\theta = 0$ position.

Figure 10 summarizes the maximum loads obtained for Cases 6 through 11 in which the Gemini impacted at various distances along the top side of the cone. The loads were determined from the vertical and longitudinal acceleration data for each model, the side acceleration being zero as would be expected for a symmetric collision over the roll slot. The loads are presented as full scale values, as will all test results, to permit direct comparison with the analytically computed values.

The lowest set of curves in Figure 10 corresponds to the cases in which the Gemini had no relative vertical component of velocity to the target vehicle, but only a longitudinal component of 1.5 feet per second. The model test results and the analytic results are consistent for impacts at 7 and 15 inches up the cone, considering that the analytic top angled longitudinal damping constant was (11/7 =) 1.57 times that of the model's and the analytic lateral damping constant was (9.6/8 =) 1.2 times the model's (See Figures 5 and 6). These maximum loads on the cone occur at the beginning of the impact and therefore are functions of the initial damping constants only.

While the loads at 7 and 15 inches are consistent with the predicted values, the load at 26 inches up the cone is over twice the expected value. This is due to the roll slot which is quite wide at the edge of the cone (See Figure 2). The motion picture films confirm that the Gemini hit on the extreme edge of the cone and momentarily wedged itself into the roll slot before sliding down. This wedging motion caused a sharp increase in the longitudinal component of acceleration of each vehicle. The roll slot was ignored in the analytic studies and the load data indicates this was a reasonable approximation over most of the cone length. For example, there is good agreement in Case 11 in which the Gemini impacted 23 inches up the cone with a relative longitudinal component of velocity of 1.5 feet per second and a vertical component of .5 feet per second.

Of the other two points on the model load curve corresponding to $V_y = .5$ feet per second, the load at 15 inches shows good agreement while the one at 5 inches, Case 9, does not. The films and side accelerometer data of Case 9 show that the Gemini did not hit the top of the mooring cone as intended, but the left side. The force as calculated from the vertical and longitudinal accelerations was consequently too low. If the side component is included in computing the force, a value of 290 pounds is obtained, which is close to the force expected on the top side.

The highest dashed curve of Figure 10 gives the analytically computed loads for the Gemini impacting with a relative pitch rate of 2 degrees per second in addition to the maximum longitudinal and vertical components of velocity. No model data of this type was acquired. The agreement between analytic and model loads for the other types of impacts makes this data unnecessary.

The initial loads obtained in Cases 24 through 28 are summarized in Figure 11. Here the Gemini impacted on the bottom side of the mooring cone. The general shape of the load profiles is seen to be the same as that on the top side of the cone, Figure 10. However, the two load levels, one with and one without the vertical component of velocity, do not seem consistent with one another. One would expect the initial load to be primarily dependent on the square of the component of velocity normal to the mooring cone. The addition of a .5 foot per second vertical component of velocity should therefore increase the initial load by a factor of about $(1.21/.78)^2 = 2.37$, as shown below.

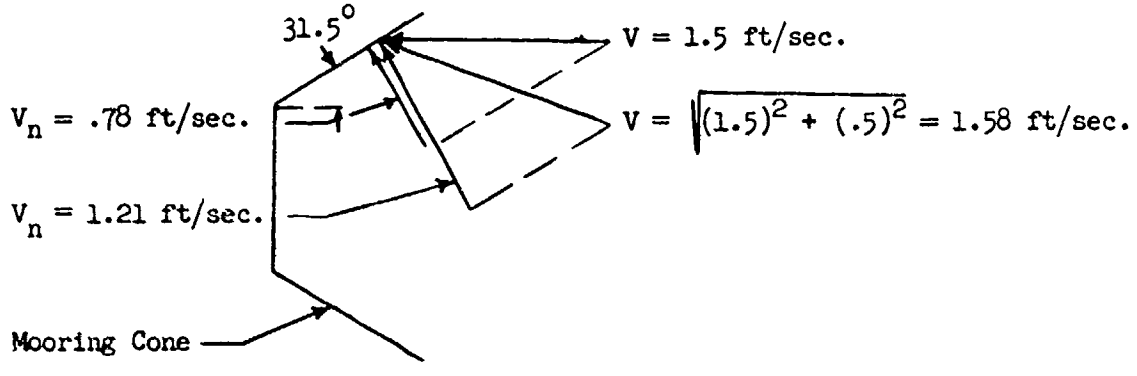

This is neglecting the effects of friction and the small spring preloads. The kinetic friction force between the Gemini nose and mooring cone is negligible because the coefficient of friction for the surfaces in contact is less than .1. Now the curves of Figure 10, both model and analytic, are related by about this factor of 2.37. But those of Figure 11, apparently are not. It is expected that the analytic studies of this side of the mooring cone, which have not been completed, will clarify this situation.

The loads produced at the intermediate positions of θ = 30, 90, and 150 degrees were 172, 122, and 127 pounds, respectively. The 90 and 150 degree impacts occurred at a distance of 23 inches up the cone and their loads are seen to fall between those of the θ = 0 and θ = 180 degree impacts at 23 inches. The θ = 30 degree impact was on the extreme edge of the cone and the load was close to that obtained at θ = 0.

All of the loads discussed above occurred upon initial impact of the nose of the Gemini with the mooring cone. After this initial impact, a typical sequence took place. The Gemini slid down the mooring cone a short distance, on the order of 6 inches full scale, before separating from the cone and impacting on the opposite side. Shortly after impacting on this side, it collided with the hard stops at the base of the mooring cone. This final collision accounted for the greatest part of the energy dissipated in reducing the relative velocity of the two vehicles to zero.

Case 10, in which the Gemini impacted on the top side of the cone at a distance of 15 inches from the plane of the hard stops, is a typical example of this motion as shown in Figure 12. The solid curve shows the magnitude of the total force on the Gemini as a function of time. This is the same magnitude of force as on the mooring cone and, considering that the mass of the mooring cone is only one percent of the mass of either vehicle, this force is also impressed on the Agena.

Over the first part of the collision, while the nose of the Gemini is sliding down the top side of mooring cone, the force is directed essentially normal to the cone. At .32 seconds the nose and cone separate. At .48 seconds the nose impacts on the bottom side of the cone and the vertical component of force now acts in the opposite direction. Shortly after this, at .55 seconds, the nose impacts on the hard stops at the base of the cone. The force now acts essentially in the longitudinal direction.

The dashed line in Figure 12 shows the analytically calculated total force between vehicles. A comparison of peak initial forces of the analytic and model curves has already been made in Figure 10 but the difference in when these occur should be noted. In the analytic studies the force between vehicles is generated instantaneously. This is because the mathematical model is a rigid, kinematically perfect system. Any small displacement of the cone produces a definite immediate stroke in the dampers. At time zero the nose of the Gemini and the mooring cone are assumed in contact. The cone is assumed to be already moving compatibly with the nose and thereby stroking the dampers which generate the force. The model, however, being a physical system, has an elastically deformable mooring cone and its shock absorbing system is not kinematically perfect but necessarily contains some looseness in its fittings. These effects, combined with the compressibility of the fluid in the dampers, account for the short rise time of the model force as indicated in Figure 12.

Case 10 is also typical in that the loads which occurred on the hard stops at the base of the cone were higher than those which occurred on the sides. Despite this, only the mooring loads on the sides were design values for the cone. This is because the mooring loads at the base of the cone are exceeded by the loads produced there during maneuvering after the vehicles have been rigidly connected. These maneuvering loads together with the loads produced by parachute deployment were also the basic design values for the nose section of the Gemini. Only the fiberglas ring on the leading edge of the nose was designed by the loads produced during mooring.

The analytical studies show that a peak force of 1870 pounds could be expected in a perfect head-on collision wherein the shock absorbing system collapses symmetrically. This is a highly unlikely collision as efforts in the model test showed. It was difficult to do because the nose of the Gemini had to impact flush on all three hard stops simultaneously without grazing the side of the cone.

The maximum force produced between vehicles in the model test was 1030 pounds in Case 25, although several cases came close to this. This is only about .147 g's on each vehicle and is indicative of how small the loads associated with mooring are.

Contact Times

Figure 12 shows that in Case 10 the force between the Gemini and mooring cone diminished to zero at .32 seconds. This corresponded to the Gemini's nose separating from the cone surface. The analytic force curve of Case 10 also diminished at .32 seconds. But as the dashed line indicates, the force did not go completely to zero. That is, the nose did not separate from the cone surface in the mathematical model. Instead of separating, the nose grazed down the cone with a bearing force of less than 3 pounds until it reached the hard stops at $d = 0$. This motion is typical of all the cases analyzed. This is the most striking difference between the physical and mathematical models; the physical model bounces, the mathematical model does not.

At first, one is tempted to try to explain this discrepancy by the fact that the mooring cone is perfectly rigid in the analytic studies, but not so in the model. Even here, however, the effect of cone flexibility is negligible. The important mechanism in determining whether the nose and cone will separate is the speed with which the high return stroke damping mentioned earlier is introduced.

In the analytic studies the high return damping value of 50,000 lb.-sec.^{2}/ft.^{2} was introduced within one time interval of integration after the initiation of the return stroke. Almost immediately, then, the compressed longitudinal springs, which otherwise would have kicked the Gemini's nose off the cone surface, were choked off. The discontinuity in the slope of the analytic curve in Figure 12 near .25 seconds marks the point at which the top angled longitudinal dampers began their return stroke. At this point the force between vehicles was entirely due to the compressed springs in the shock absorbing system. This force was then quickly reduced to less than 3 pounds as the high return damping became effective. During this time the top longitudinal and lateral dampers were able to extend only .020 and .017 inches, respectively, making the collision almost perfectly inelastic.

The dampers constructed for the model test were intended to have a correspondingly high return stroke damping constant. When the flow reversed direction, it moved a ball up into the orifice to restrict the flow. This simple design, which was desirable in view of the small size of the model dampers, was not very effective in keeping the compressed spring from rapidly returning over the first part of the return stroke. The ball was moved into position by the flow too slowly. Consequently, the model showed bounce-off effects not predicted by the analytic studies.

The speed with which the high return damping was introduced in the analytic studies was rather idealistic. On the other hand, the model dampers showed definite room for improvement. The full scale dampers have a more sophisticated design which includes a spring-loaded ball to insure that the flow is restricted very quickly on the return stroke.

Disregarding the fact that the model test and analytic studies differ as to whether the nose of the Gemini separates from the mooring cone, there is reasonable agreement in the time each takes for the force between nose and cone to diminish. Figure 13 shows these times for the various impacts on the top side of the cone, Cases 6 through 11. The analytic data showed no appreciable difference in contact time for impacts with $V_y = 0$ and $V_y = .5$ feet per second. Figure 14 shows the contact times for Cases 24 through 28, in which the Gemini initially impacted on the bottom side of cone. Figure 13 seems to indicate that the contact times should be longer for collisions with $V_y = 0$. Contrary to this, Figure 14 shows that collisions with $V_y = -.5$ feet per second have very slightly longer contact times. These different trends from top to bottom of the cone cannot be justified and probably the only thing they show is that the contact time is not very dependent on V_y, as indicated in the analytic studies.

The fact that different damping constants were used in the model and analytical studies is not too important in comparing the contact times. Studies of two degrees of freedom systems with a spring in parallel with an orifice damper show that the contact time varies slowly with change in damping constant.

Pitch Rates

As the nose of the Gemini slides down a side of the cone during the first

phase of mooring, the two vehicles acquire angular rates in the pitch and yaw planes. These rates are later reduced by the secondary impact on the opposite side of the cone and therefore represent maximum values.

The analytic studies of collisions on the top side of the cone show that the change in the Gemini's pitch rate is independent of the parameter d. Regardless of at what distance on the top side it impacts, the Gemini always separates at the same pitch rate. The pitch rate of the target vehicle, however, increases with increasing d because the target vehicle's moment arm is longer for larger values of d.

Figures 15 and 16 show the analytic and model pitch rates of the Gemini and Agena for Cases 6, 7, 8, 10, and 11. The ordinate of Figure 15 gives the change in the Gemini's pitch rate to accommodate the analytic studies in which the Gemini impacted with an initial pitch rate of 2 degrees per second. After impacting with a pitch rate of 2 degrees per second, the Gemini separated with a pitch rate of minus 2.2 degrees per second, making its change in pitch rate minus 4.2 degrees per second, as shown.

Figures 17 and 18 show the pitch rates acquired by the vehicles in Cases 24 through 28 in which the Gemini initially impacted on the bottom side of the mooring cone.

The angular rates acquired by the vehicles due to collisions at the other positions on the cone were not significantly different from those at the 0 and 180 degree position. For example, in Case 19 the yaw rate of the Gemini at separation from the cone at $\theta = 90$ degrees was minus 2.58 degrees per second.

All of these angular rates are what would be expected in free collisions between the vehicles, i.e. with the stabilization control systems of the vehicles not operating. Since both systems will be active during mooring, their effect is currently being studied in the 8 degree of freedom analytic program.

Boundaries of Vehicular Latching

The boundaries of misalignment within which the two vehicles automatically latched were of special interest in the model test. The design criteria specifies that the maximum angle permitted between the longitudinal axes of the vehicles at mooring is 10 degrees in any radial direction. This is in addition to any linear misalignment as long as the nose of the Gemini is in contact with the inside surface of the cone, i.e., $d \leq 26$ inches.* The limiting relative velocities have already been mentioned as being 1.5 and .5 feet per second in the longitudinal and lateral directions, respectively.

Table 4 summarizes under what conditions latching occurred. In the last column the numbers 1, 2, and 3 denote which of the latches seated into the recesses on the Gemini's nose. The latch numbers are defined in Figure 8.

It is seen that for any θ position on the cone, and in the absence of angular eccentricities, at least two latches seated for d values through 26 inches. This was true regardless of whether the lateral component of velocity was present or not.

---

* Because of a reduction to 17 degrees in the conic half-angle near the base of the cone, which has been ignored to facilitate discussion, the lateral misalignment is not quite 26 inches times the sine of 31.5 degrees, 13.6 inches, but one foot.

At the $\theta = 0$ position and for d = 26 inches, the vehicles did not latch when a negative pitch angle of 10 degrees was applied to the Gemini relative to the target vehicle. Two latches did seat at a pitch angle of minus 8 degrees, however.

At $\theta = 90$ degrees and d = 26 inches, the boundary was established at a relative yaw angle of less than minus 4 degrees. Similarly at $\theta = 180$ degrees, the boundary was determined to be between 4 and 6 degrees of relative pitch angle.

The maximum relative roll angle permitted between vehicles at mooring in the design criteria is 10 degrees. Vehicle latching occurred at this maximum angle in the absence of other eccentricities. It also occurred at this angle even when d = 26 inches at $\theta = 180$ degrees, Case 35. More detail concerning under what approach conditions latching occurred can be gotten by examination of Table 4.

All of these angular boundaries for latching were established without the aid of the vehicles' stabilization systems. In the actual mooring maneuver, these systems would be expected to improve the boundaries of latching.

Summary and Conclusion

The 1/4 scale dynamic model mooring test has effectively simulated the orbital mooring of a Gemini spacecraft with an Agena booster. The orbital condition of the vehicles was realistically duplicated by special suspension systems.

The model confirmed the basic design of the full scale mooring system; i.e., no undesirable modes of collapse were found; the mooring loads were within the design values; the importance of high return stroke damping was demonstrated by the excessive bounce-off characteristics shown; reasonable boundaries of free-body latching were determined.

In addition to directly confirming the full scale system design, the model uncovered a feature of the analytic 8 degree of freedom program which could be improved in the future. Because of its importance in connection with bounce-off, a more realistic time interval in which the high return stroke damping is introduced should be used.

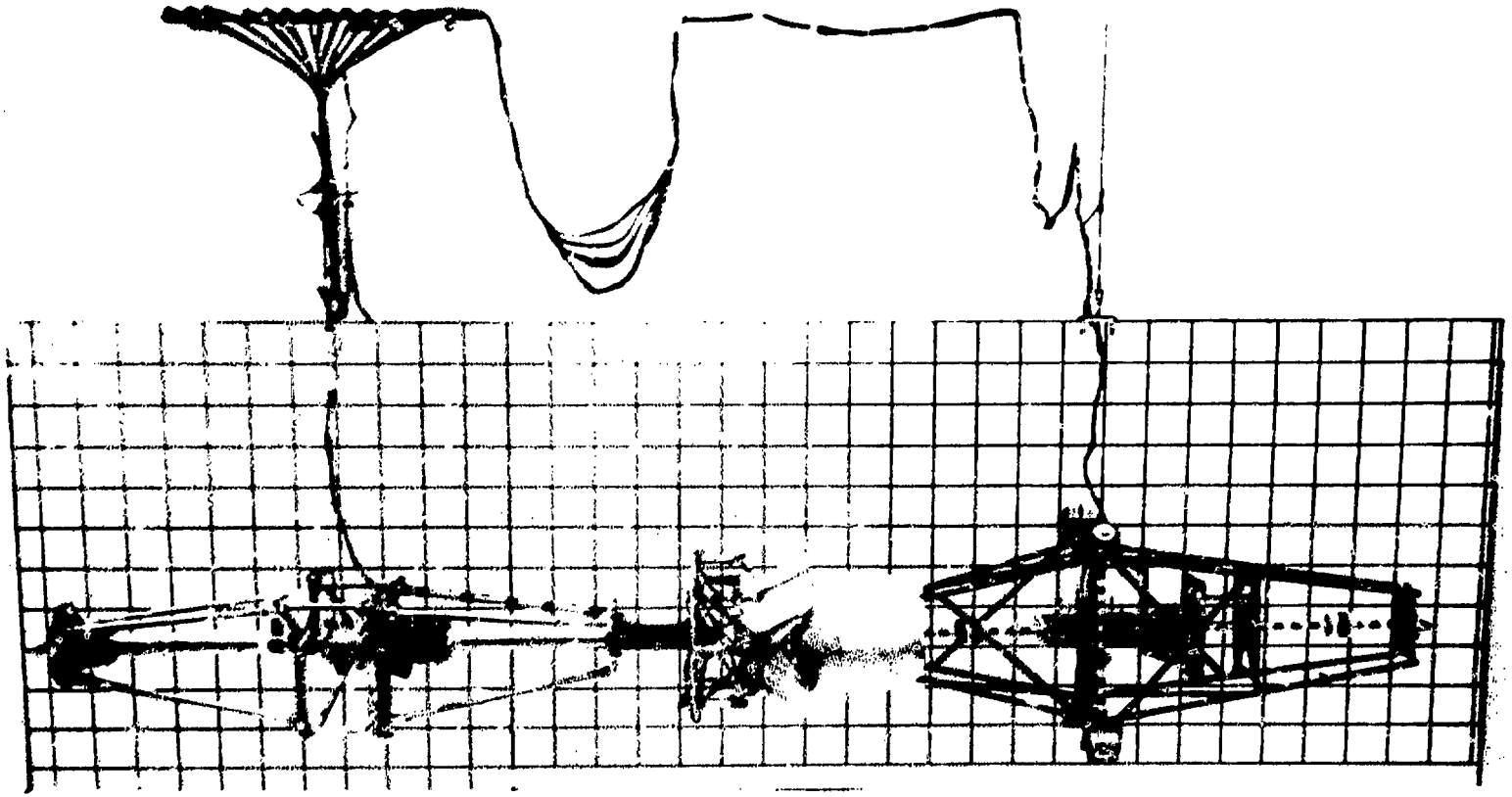

FIGURE 1. AGENA AND GEMINI VEHICLES IN MOORED CONFIGURATION

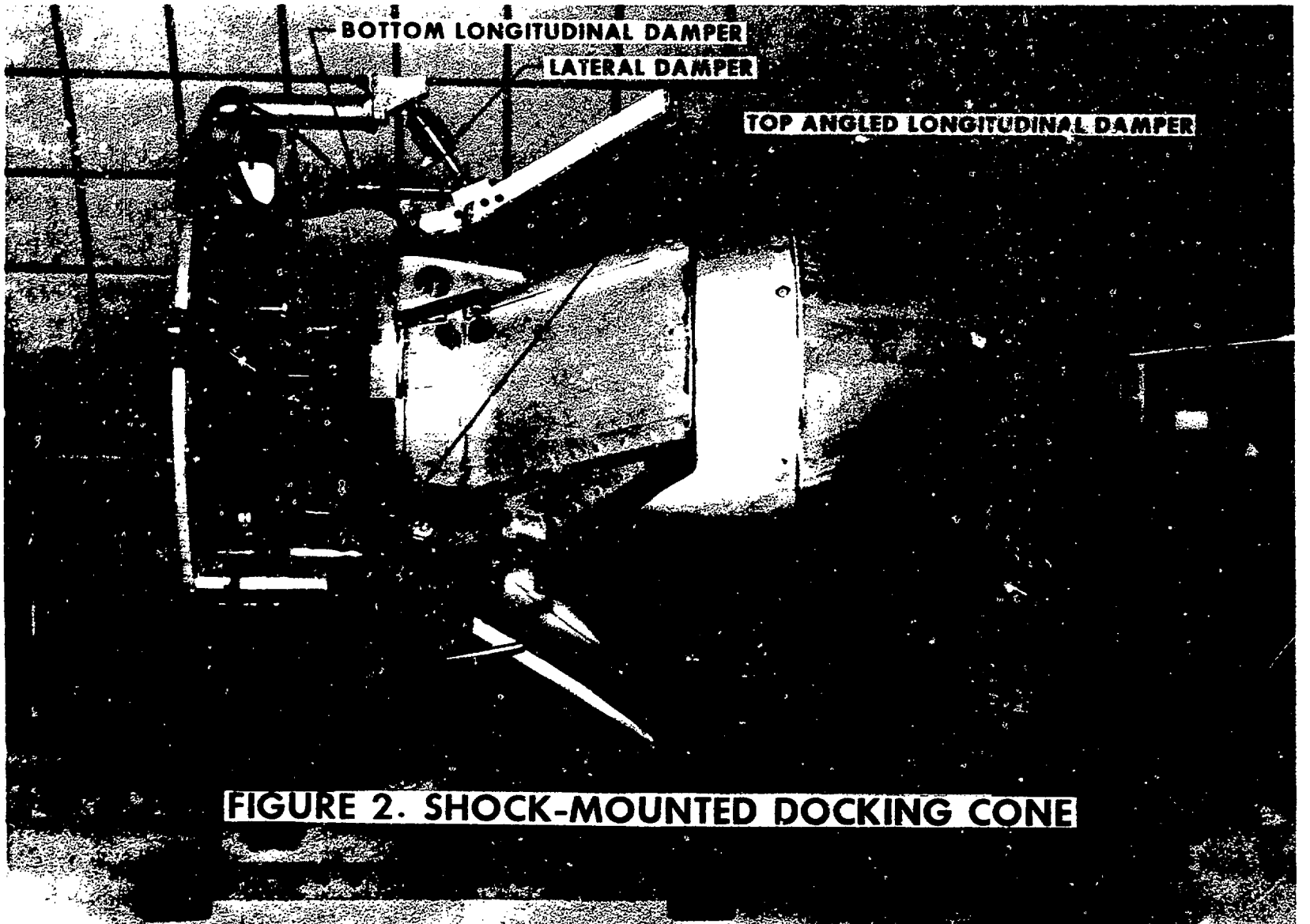

FIGURE 2. SHOCK-MOUNTED DOCKING CONE

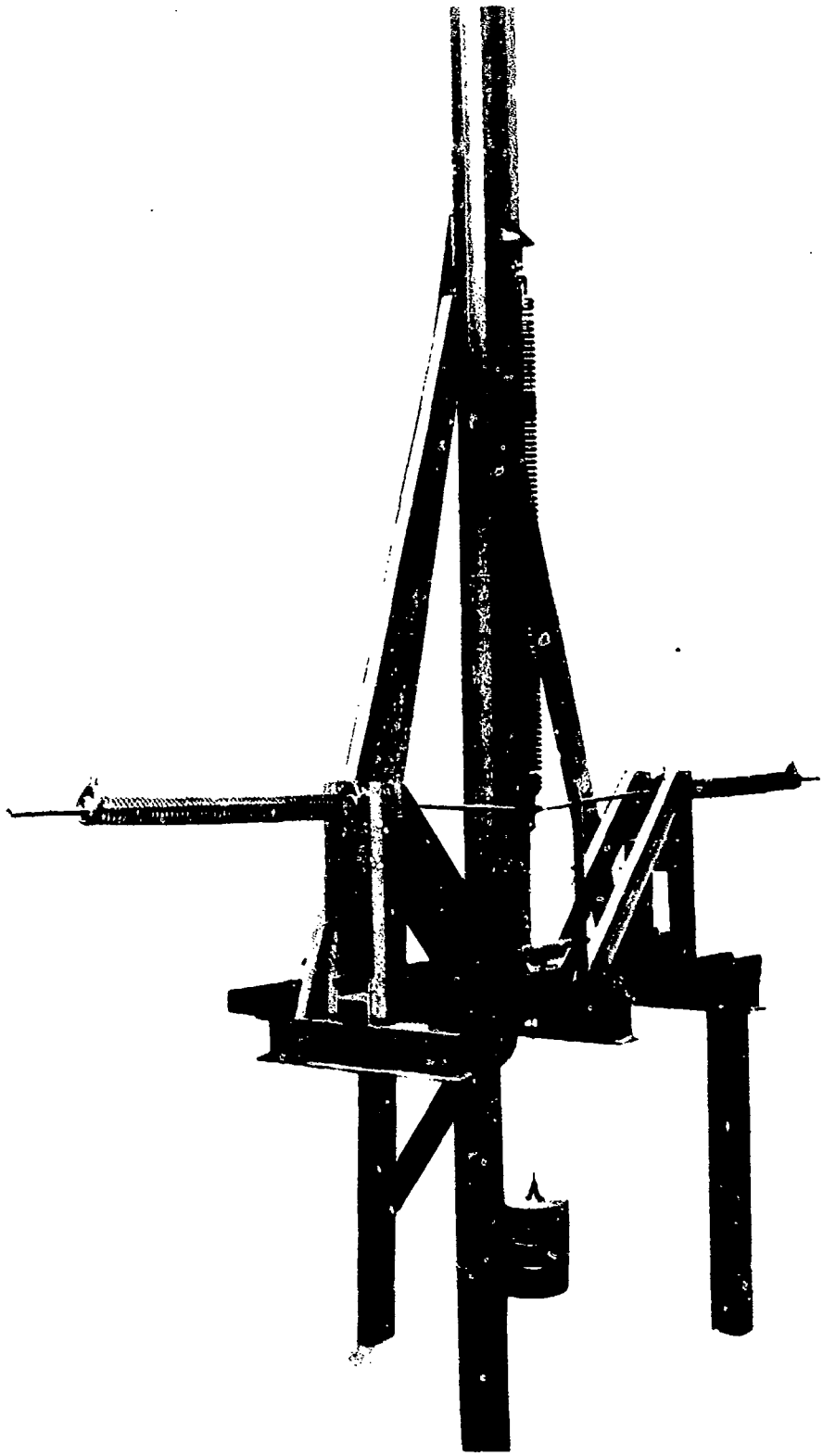

FIGURE 3. VEHICLE SUSPENSION SYSTEM

FIGURE 4. SUSPENSION SYSTEM PERFORMANCE

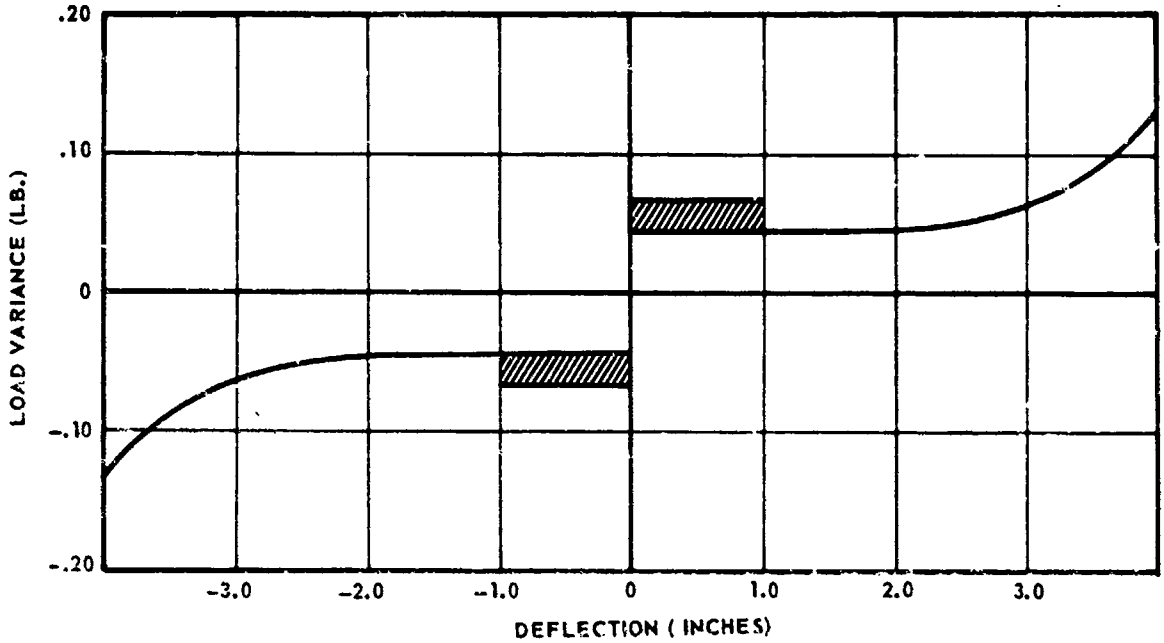

FIGURE 5. DAMPING CONSTANT VS. STROKE - LATERAL DAMPERS

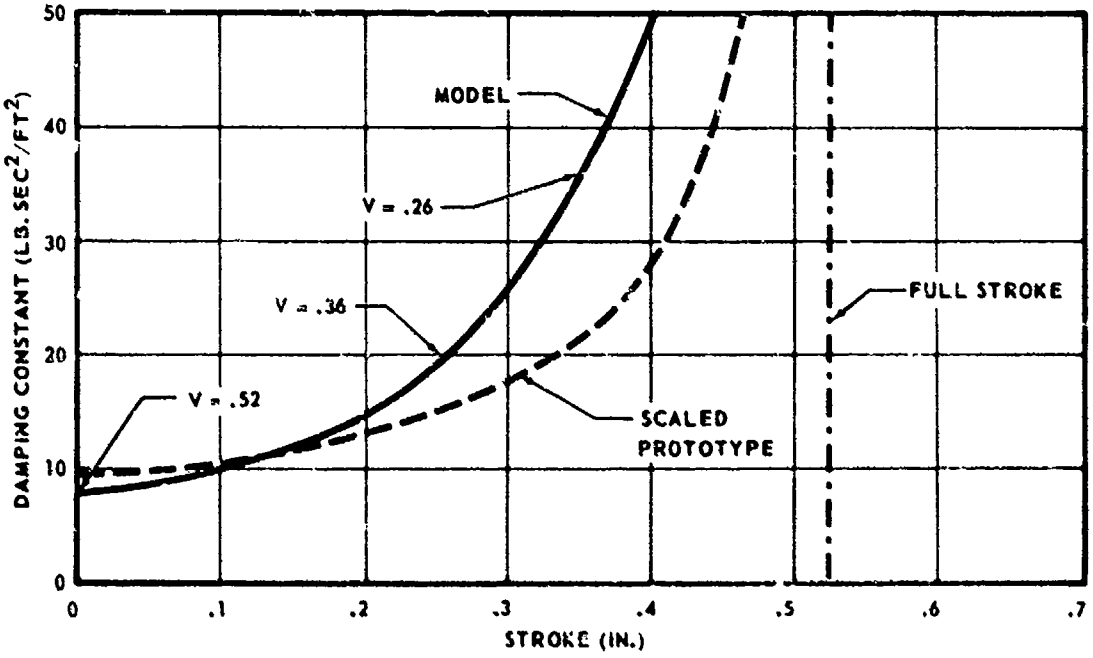

FIGURE 6. DAMPING CONSTANT VS. STROKE - TOP ANGLED LONGITUDINAL DAMPERS

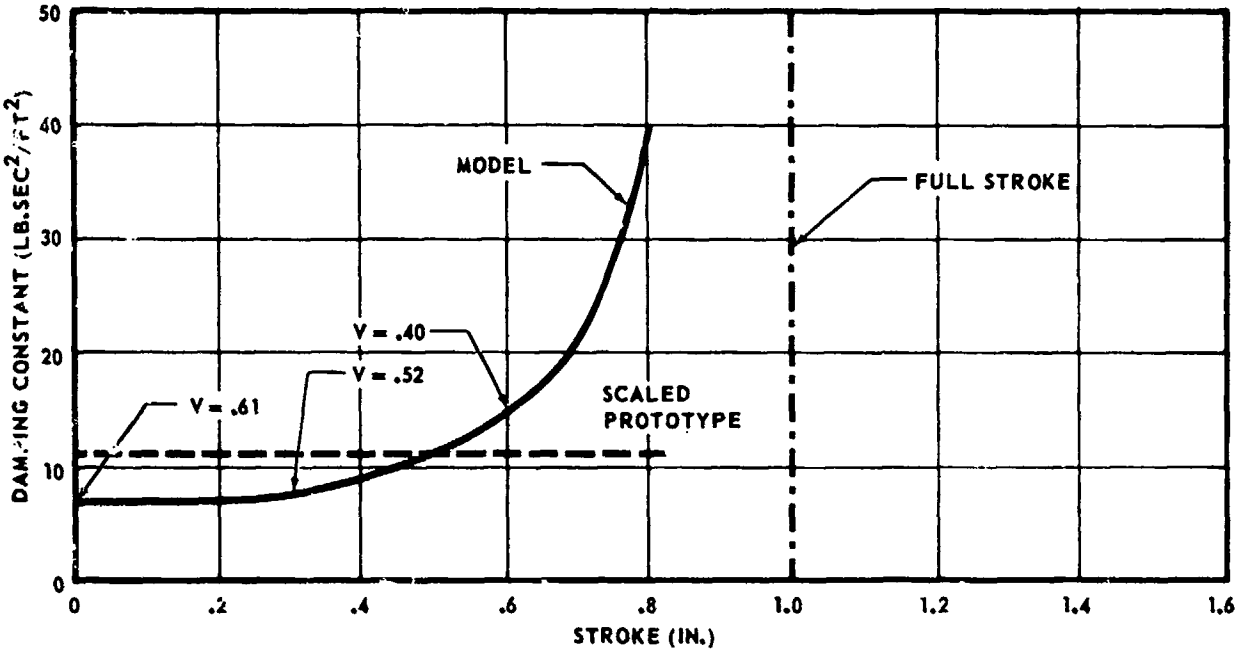

FIGURE 7. DAMPING CONSTANT VS. STROKE - BOTTOM LONGITUDINAL DAMPERS

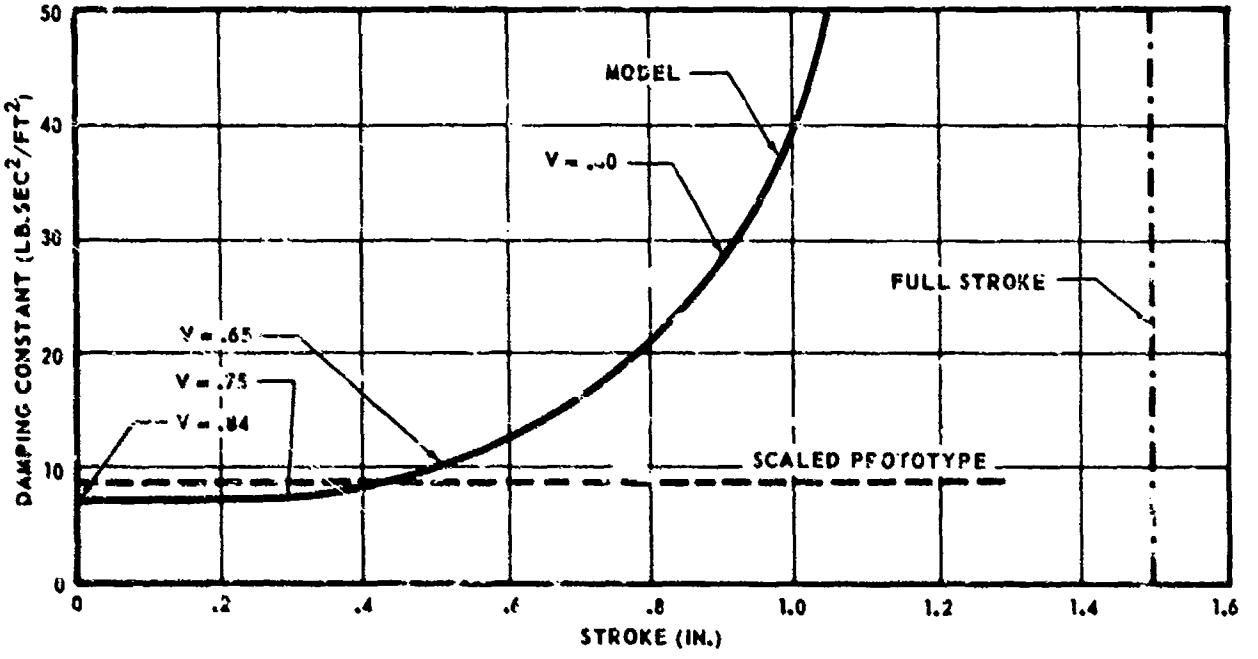

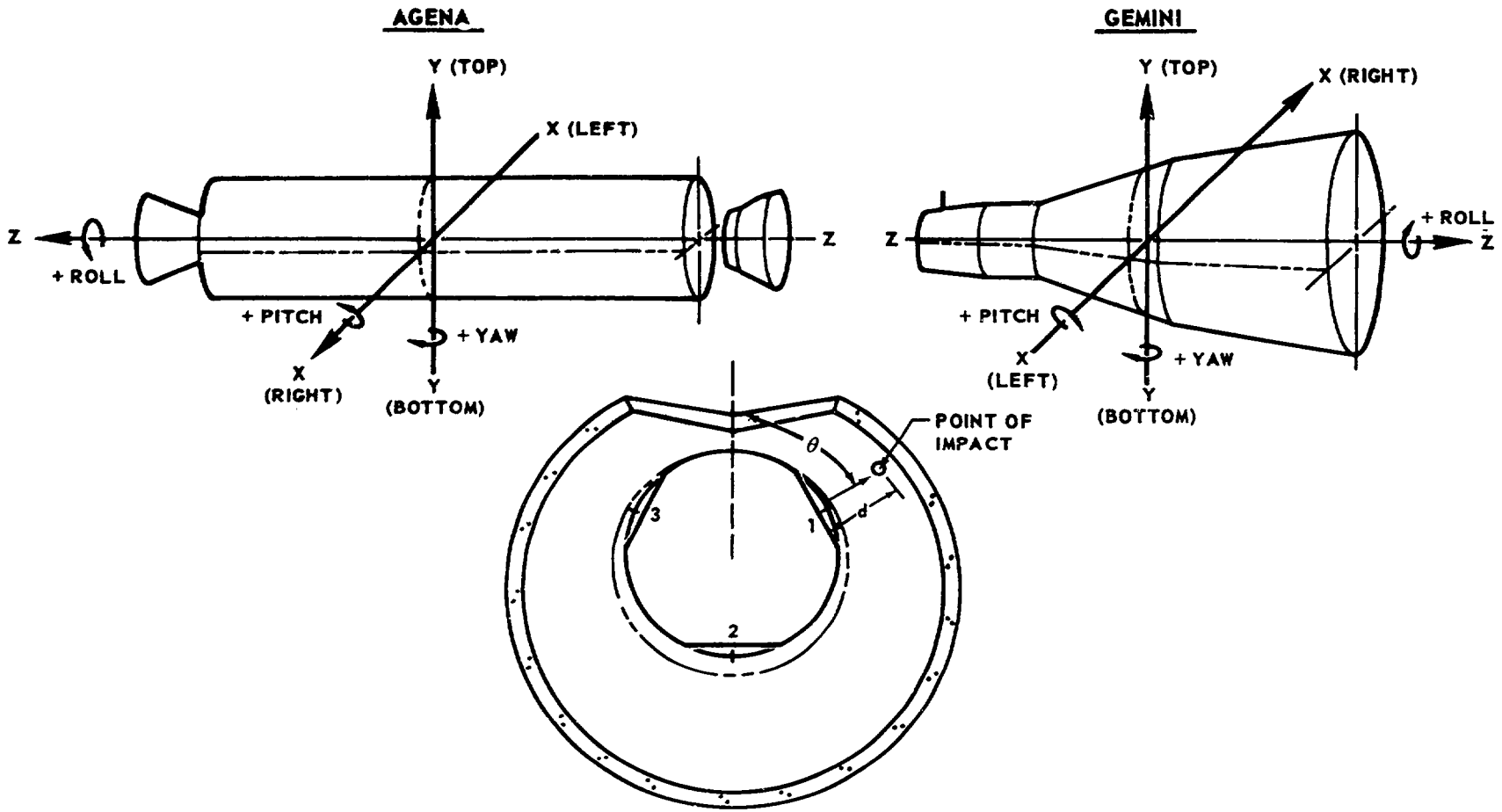

NOTE:
IMPACT LOADS AND LINEAR AND ANGULAR ACCELERATIONS ARE POSITIVE IN THE DIRECTIONS SHOWN.

FIGURE 8. MODEL SIGN CONVENTION

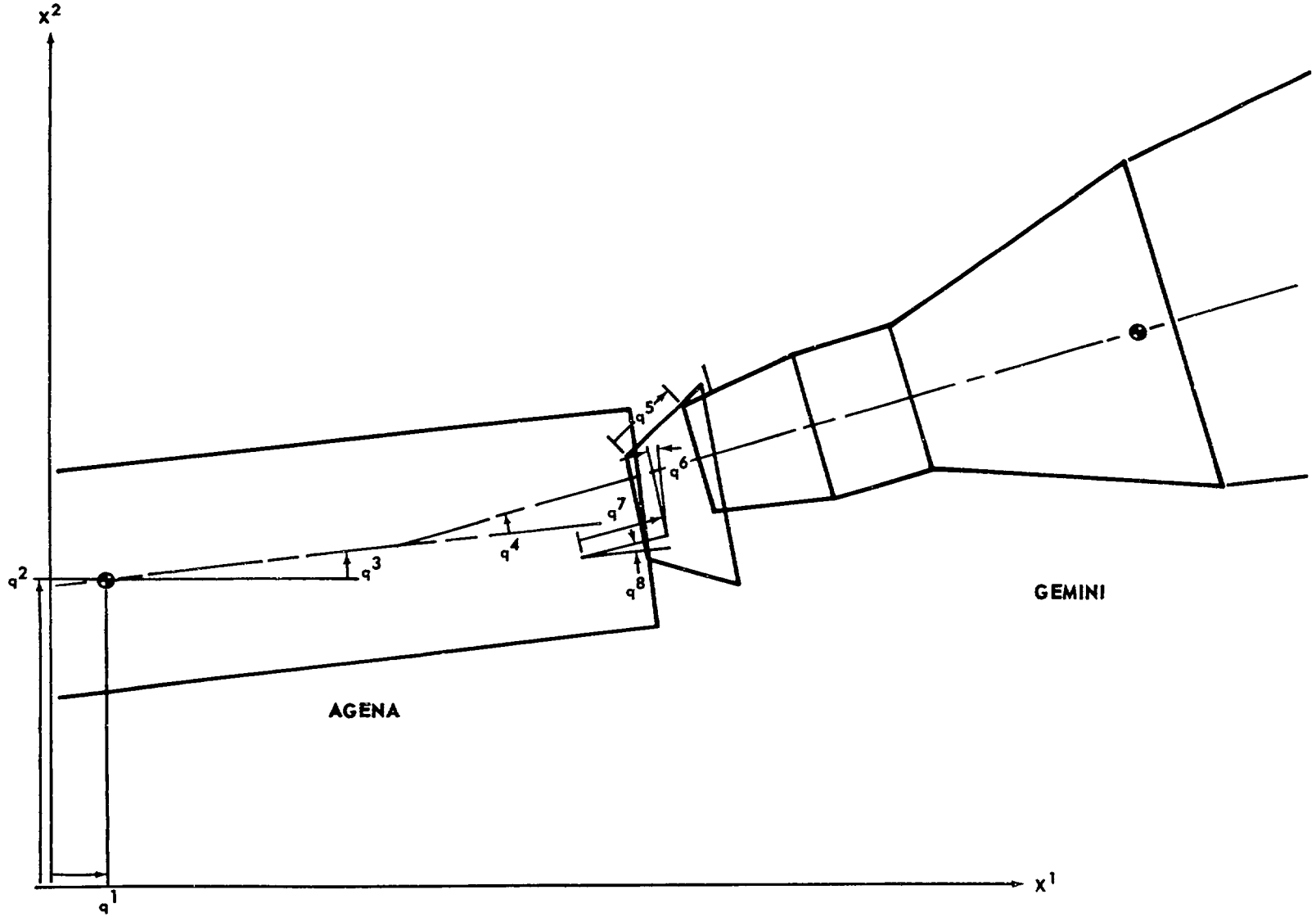

FIGURE 9 DEFINITION OF GENERALIZED COORDINATES IN PITCH PLANE

FIGURE 10. FULL SCALE MAXIMUM FORCES ON TOP SIDE ($\theta = 0$) OF MOORING CONE

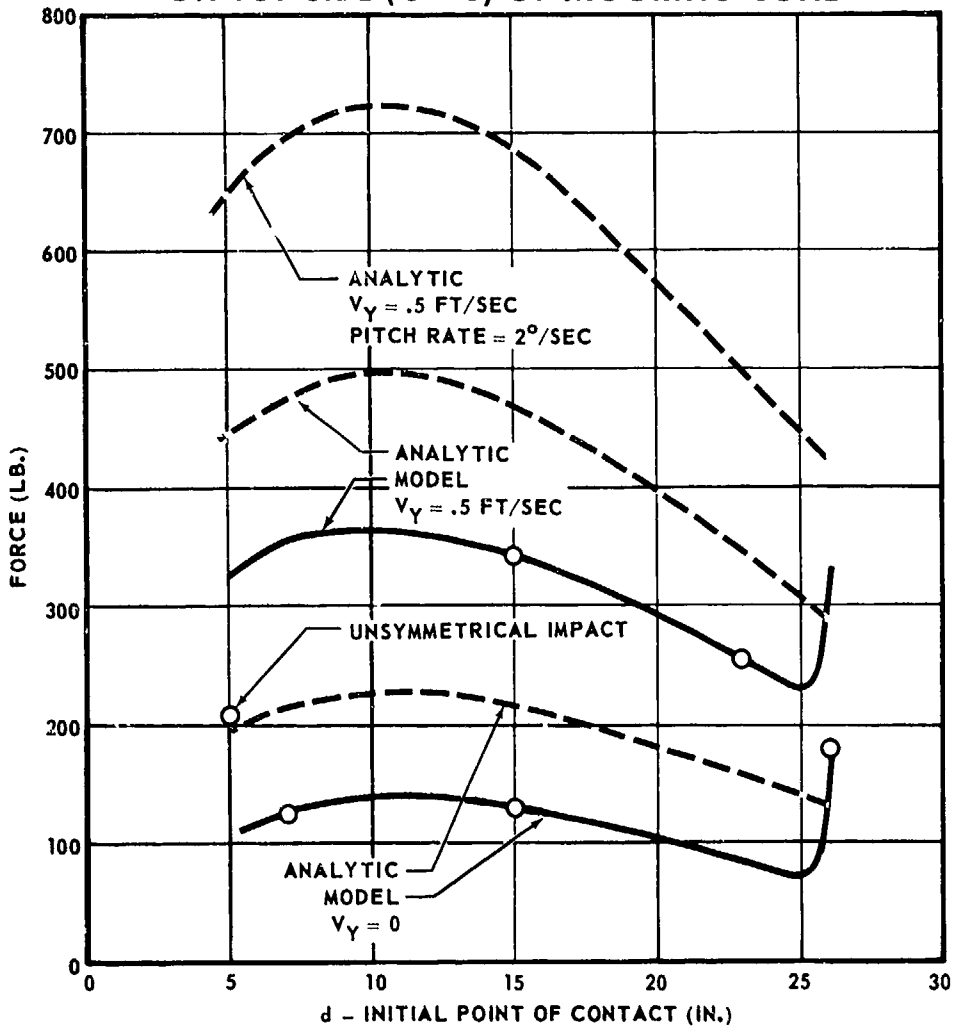

FIGURE 11. FULL SCALE MAXIMUM FORCES ON BOTTOM SIDE ($\theta = 180°$) OF MOORING CONE

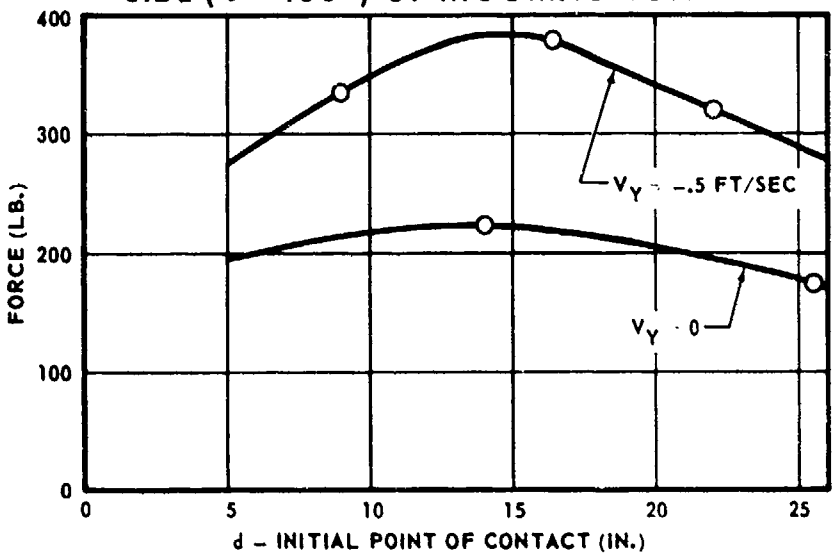

FIGURE 12. FULL SCALE FORCE TIME HISTORY

CASE 10 $\begin{cases} \theta = 0 \\ d = 15 \text{ IN.} \\ V_y = .5 \text{ FT/SEC} \end{cases}$

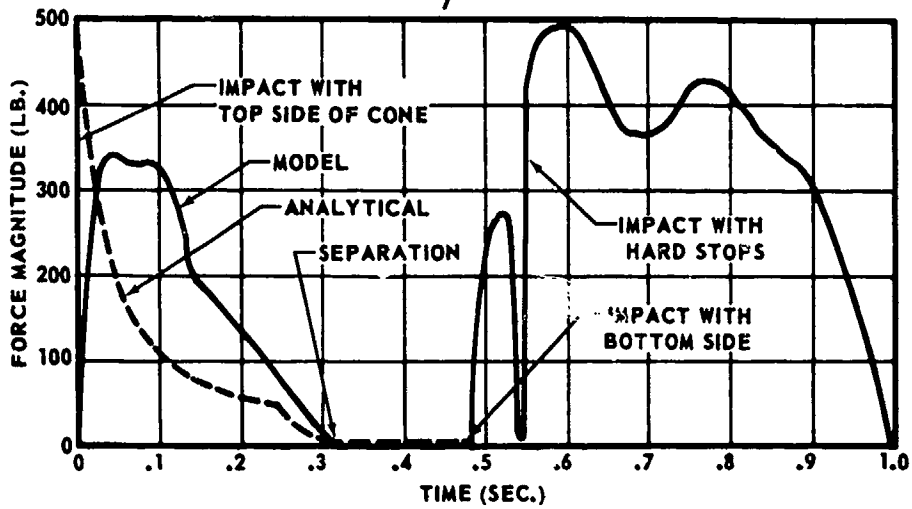

FIGURE 13. FULL SCALE CONTACT TIMES ON TOP SIDE ($\theta = 0$) OF MOORING CONE

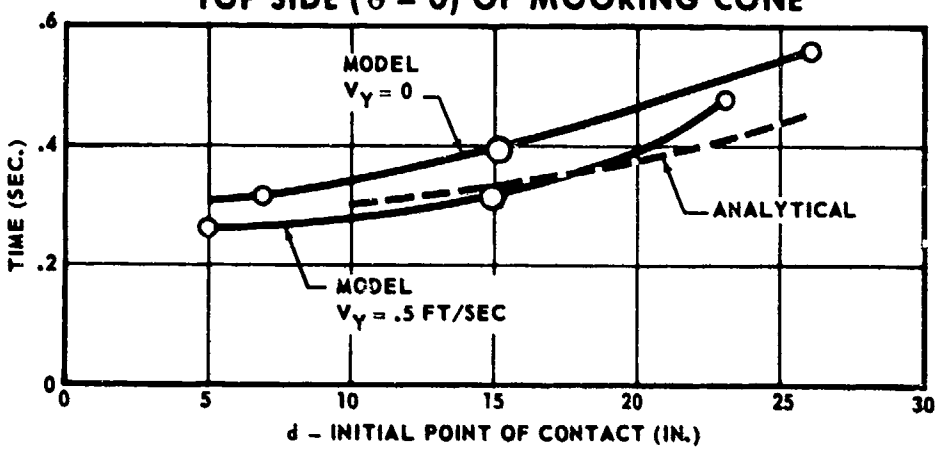

FIGURE 14. FULL SCALE CONTACT TIMES ON BOTTOM SIDE ($\theta = 0$) OF MOORING CONE

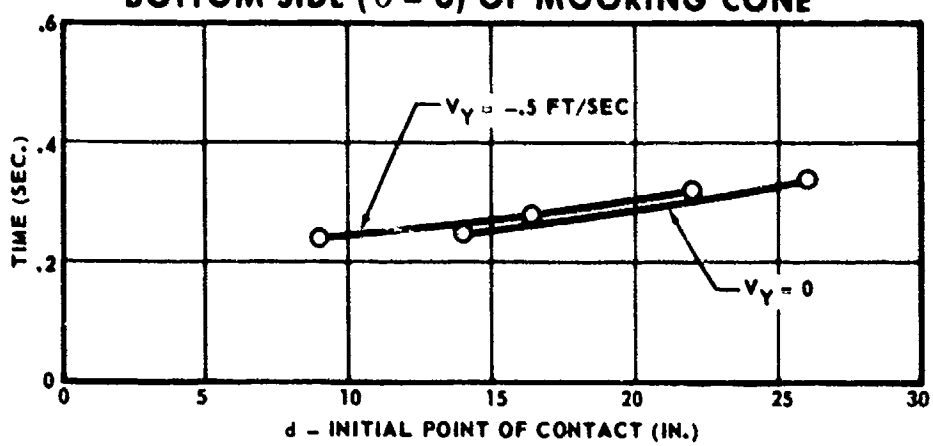

FIGURE 15. CHANGE IN GEMINI PITCH RATE AT SEPARATION FROM TOP SIDE (θ=0) OF MOORING CONE

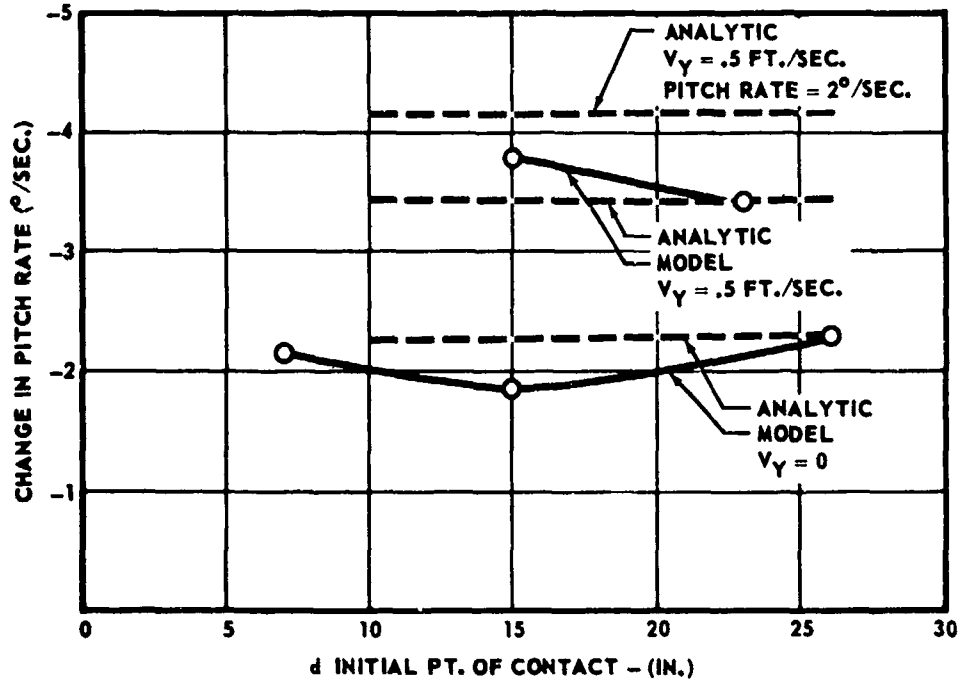

FIGURE 16. AGENA PITCH RATE AT SEPARATION FROM TOP SIDE (θ=180°) OF MOORING CONE

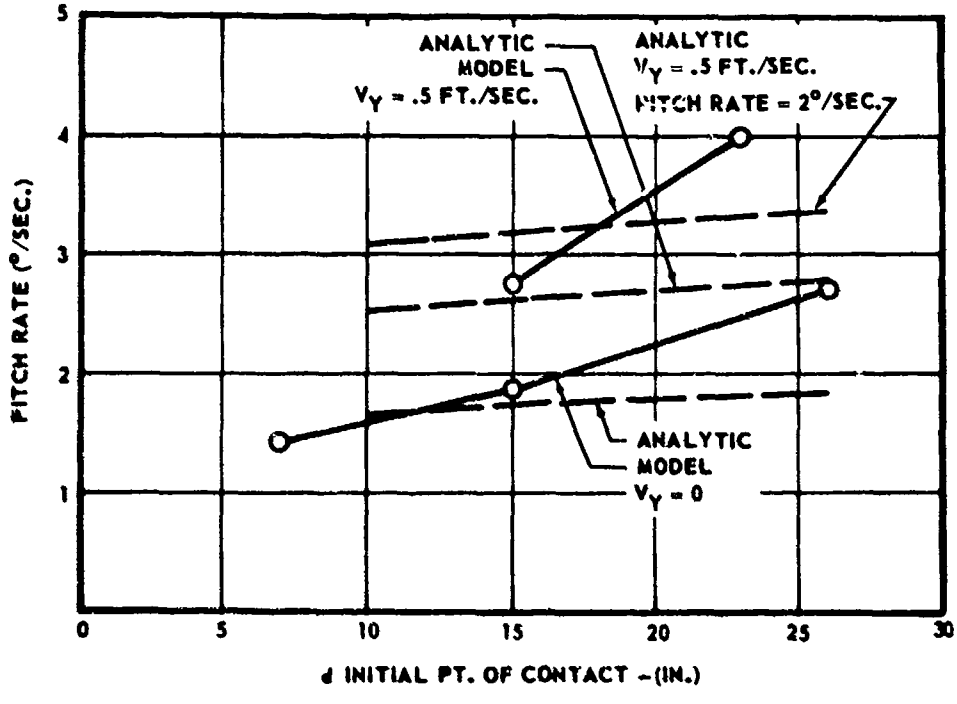

FIGURE 17. GEMINI PITCH RATE AT SEPARATION FROM BOTTOM SIDE (θ =180°) OF MOORING CONE

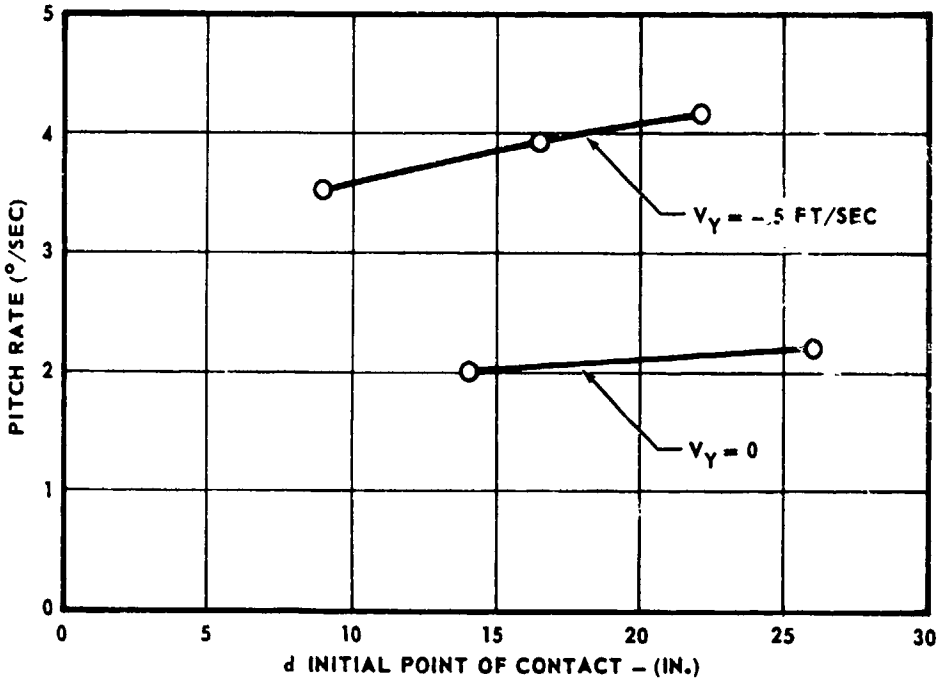

FIGURE 18. AGENA PITCH RATE AT SEPARATION FROM BOTTOM SIDE (θ =180°) OF MOORING CONE

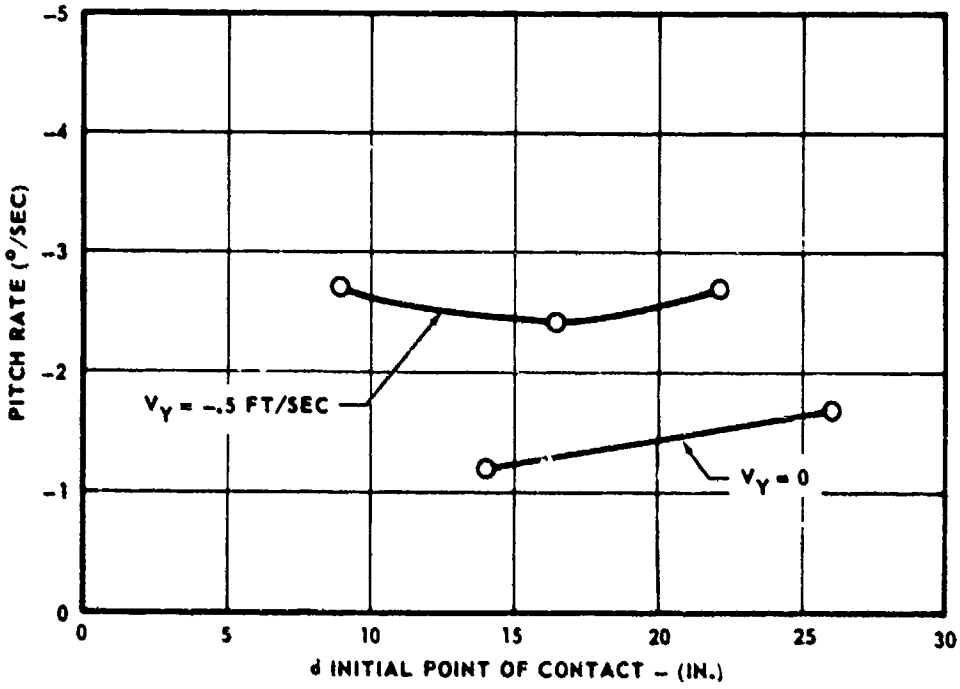

TABLE I. SCALE FACTORS

QUANTITY	MODEL/PROTOTYPE
ASSIGNED:	
LENGTH	1/4
TIME	1/4
MASS	1/100
DERIVED:	
VELOCITY	1
ACCELERATION	4
WEIGHT	1/100
SPRING RATE	4/25
KINETIC FRICTION	1/25
PRE-LOAD FORCE	1/25
MOMENT OF INERTIA	1/1600
ANGULAR VELOCITY	4
ANGULAR ACCELERATION	16
VELOCITY-SQUARED DAMP. CONSTANT	1/25

TABLE 2.INERTIA DATA

	MODEL		PROTOTYPE	
QUANTITY	GEMINI	AGENA	GEMINI	AGENA
MASS (SLUGS)	–	2.19	–	219.
PITCH INERTIA (SLUG–FT.^{2})	2.54	5.62	4060.	9000.
YAW INERTIA (SLUG–FT.^{2})	2.54	5.62	4060.	9000.
ROLL INERTIA (SLUG–FT.^{2})	.782	.16	1250.	256.

TABLE 3. SPRING DATA

	MODEL		PROTOTYPE	
SPRING	SPRING RATE (LB./FT.)	PRELOAD (LB.)	SPRING RATE (LB./FT.)	PRELOAD (LB.)
TOP ANGLED LONGITUDINAL	58.0	.52	375.	13.75
BOTTOM LONGITUDINAL	47.4	.65	300.	20.00

TABLE 4. TEST CONFIGURATION SUMMARY

CASE	θ (°)	4d (IN.)	V_Z (FT/SEC)	V_Y (FT/SEC)	PITCH (°)	YAW (°)	ROLL (°)	LATCHES LOCKED
1		0	−1.5	0	0	0	0	1, 2, 3
2		0	− .5	0	0	0	0	1, 2, 3
3		0	−1.5	0	0	0	5	2, 3
4		0	−1.5	0	0	0	10	2, 3
5		0	−1.5	0	0	0	15	NONE
6	0	7	−1.5	0	0	0	0	1, 2, 3
7	0	15	−1.5	0	0	0	0	2, 3
8	0	26	−1.5	0	0	0	0	2, 3
9	0	5	−1.5	.5	0	0	0	1, 2, 3
10	0	15	−1.5	.5	0	0	0	1, 2, 3
11	0	23	−1.5	.5	0	0	0	1, 2, 3
12	0	26	−1.5	0	−4	0	0	1, 2, 3
13	0	26	−1.5	0	−6	0	0	1, 2, 3
14	0	26	−1.5	0	−8	0	0	1, 3
15	0	26	−1.5	0	−10	0	0	NONE
16	0	0	−1.5	0	−10	0	0	3
17	0	15	−1.5	.5	−10	0	0	NONE
18	30	26	−1.5	0	0	0	0	2, 3
19	90	23	−1.5	0	0	0	0	1, 2, 3
20	90	26	−1.5	0	0	−4	0	NONE
21	90	26	−1.5	0	0	−6	0	NONE
22	90	23	−1.5	0	0	−10	0	NONE
23	150	23	−1.5	0	0	0	0	1, 2, 3
24	180	14	−1.5	0	0	0	0	1, 2, 3
25	180	26	−1.5	0	0	0	0	1, 2, 3
26	180	9	−1.5	−.5	0	0	0	1, 2, 3
27	180	16	−1.5	−.5	0	0	0	1, 2, 3
28	180	22	−1.5	−.5	0	0	0	1, 2, 3
29	180	26	−1.5	0	4	0	0	1, 2, 3
30	180	26	−1.5	0	6	0	0	NONE
31	180	22	−1.5	0	10	0	0	NONE
32	180	5	−1.5	0	10	0	0	NONE
33	180	14	−1.5	.5	10	0	0	NONE
34	180	14	−1.5	0	0	0	10	1, 2, 3
35	180	26	−1.5	0	0	0	10	2, 3
36	180	19	−.75	−.25	0	0	0	1, 2, 3
37	180	14	−.75	−.25	0	0	0	1, 2, 3

NOTE: QUANTITIES REFER TO GEMINI VEHICLE

DYNAMIC MODELING OF FUEL SLOSH

E. D. Calkin

C. K. Webb

Douglas Aircraft Company, Inc.

ABSTRACT

The mathematical development of an equivalent spring mass model is given, along with necessary assumptions, for two specific cases: that of the right circular cylinder, and the sphere. The approaches to a definition of the properties of tanks with approximately these shapes (the Saturn S-IV liquid hydrogen and liquid oxygen tanks) in terms of these simple shapes are then shown. The results of extensive testing of scale models of the tanks with liquids are then used to define the most suitable approach. Scaling parameters include damping as well as geometric scaling. A short discussion of the properties of damping baffles shows that important effects other than damping are sometimes introduced.

LIST OF ILLUSTRATIONS

DYNAMIC MODELING OF FUEL SLOSH

E. D. Calkin C. K. Webb

Douglas Aircraft Company, Inc.

DISCUSSION

Sloshing has been a recognized and serious problem since the first Jupiter failure. The advent of even larger boosters emphasized the problem and made it mandatory to include sloshing parameters as part of the design criteria. Analytical basis for many of the sloshing phenomena were not available and had to be developed. Those missile tanks which were of class configuration (i.e., cylindrical or spherical) became fewer with each desig and odd shapes which would conform more easily to the mission and structura requirements became the order of the day.

Solutions for the dynamic response of the liquid in a cylindrical tank were developed early because this was the most common type of tank used and because closed form solutions existed. When spherical tanks began to be used many attempts were made to analytically determine the response of a liquid in them. These efforts, until recently, [1] were unsuccessful except in certain special cases. More and more the tanks used in large boosters deviated from these standard forms. Analytical solutions became increasin ly difficult if not impossible.

Now it became necessary to determine, in some other way, the response of the liquids in these tanks. Experiments using full scale models were both costly and in some cases not practical from a scheduling viewpoint. Models and model testing seemed to be the only answer.

This paper will discuss the methods of testing and measurements as well as some of the more interesting conclusions reached in the testing programs conducted for the Douglas Thor and Saturn space vehicles. Result of some of the testing are included to point out those details which are most important.

TESTING

The testing was conducted in three phases: a) checks of frequency a various fluid levels, b) checks of damping at various fluid levels, and 3) in the case of the Saturn lox tank, a check of the computed values of the fixed mass of the mathematical model.[2]

The purpose behind all testing was to in some manner either prove or disprove the correctness of the mathematical model which had been used in the analysis and design of the vehicle. Damping values were determined for both the baffled and unbaffled lox tank. Scaling parameters for the models were determined and applied to the full scale tanks.

The three tank shapes used in the tests are shown in Figure 1 below.

M-12747

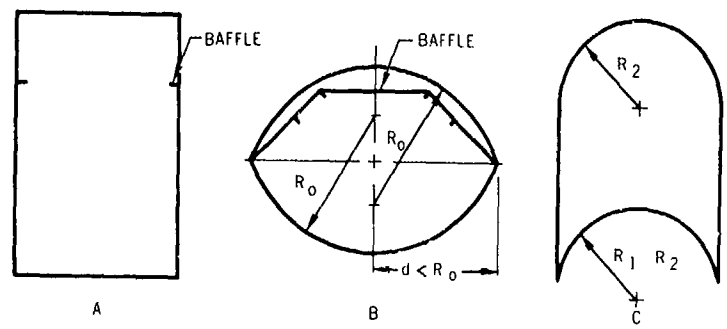

Figure 1. Thor Tank, Saturn Lox Tank, and Saturn Fuel Tank Shapes Used in Tests

Tank 1)a is the basis Thor tank, 1)b is the Saturn lox tank, 1)c is the Saturn fuel tank. Baffles are shown in their positions.

DATA MEASUREMENT

The force signal was generated by a standard strain gauge network while the acceleration signal was produced using Statham oil bath accelerometers. The slosh height signal was generated using a capacitance bridge which was saturated with a 400 cycle carrier signal.

All signals were then fed through sine-cosine pots which were turning synchronously with the pot which input the signal to the drive mechanism. The pots acted as sine-squared filters to produce a signal biased one half the basic sine wave magnitude with a double frequency wave super-imposed upon it. This signal was then fed into a long time constant integrating amplifier with a limiting ratio of one. The output of the amplifier was read on ammeters which had been calibrated to read input voltage. The entire network was calibrated as a unit to reduce the errors inherent in each of the parts.

Damping values were obtained by recording the output of the signal amplifiers before the sine cosine pots and also by recording the output of the integrating amplifiers. Slosh height input was accomplished by driving at the natural frequency and also by putting in step functions. In all cases a constant displacement input was used to determine the response. Force and acceleration values necessary to evaluate the properties of the fixed mass in the mathematical model were read from the meters.

RESULTS

As seen in the frequency plots the experimental values matched the calculated values very well. In the case of the Saturn fuel tank an empirical formula was derived which made the calculated values in the upper end of the tank coincide with the experimental values within one percent. This function was developed on the assumption that the frequency calculated at the dimetrical plane of the dome and the experimental frequency were identical. On this assumption the formula is list below.

$$f = \left[\frac{1}{4\pi^2 (1-.388\ y/r)} \left\{ \frac{710}{a} \tanh 1.84\ (h/a) \right\} \right]$$

y = weight from center of plane

r = radius of sphere

a = 1/2 diameter of free surface

h = total height of equivalent cylinder

The damping values obtained for the Thor tanks were checked using models of several geometric scaling ratios and it was found that size had little to do with damping values obtained from baffles as long as the relative size of the baffle and the tank remained the same. The values for the unbaffled tank, however, followed the scaling parameters developed in reference 6.

The tests to obtain the characteristics of the analytical model by experiment showed that in the case of extensive baffling as in the Saturn lox tank it could not be assumed that the baffle introduced only damping. Results showed that apparent changes in tank configuration resulted along with a significant change in the response of the liquid. Liquid outside the baffle, even though the baffle was perforated, was quite divorced in motion from liquid inside the baffle. Additional resonant frequencies were introduced and force response and slosh height response peaked out at different frequencies. The values of the fixed mass of the mathematical model were within 10% of the values predicted for the unbaffled case.

The response of the slosh network while operating with the fluid in the dome of the Saturn lox tank showed an apparent shift of the free surface fluid level during the forced oscillation runs. This phenomena was later supported analytically.[9] Due to the curvature of the tank the fluid at any point other than the center of the tank will reach a higher point on the rise than it does on the downward side of the original free surface level making the instruments show an apparent shift of the free surface level.

The total results showed that it was possible to obtain data from testing which, in the case of the simpler models, agreed with analytical data and which could be successfully scaled to give the characteristics of full scale vehicles. Certain errors in the analytical models chosen for the more complicated models were also brought to light. The net results of the testing conducted at Douglas Aircraft Company were in support of the analytical work and suggested that for future vehicles model testing was necessary for those configurations with propellant tanks deviating radically from the cylindrical of spherical shapes.

Figure 2 shows a plot of frequency versus fluid height, both analytical and experimental, for the Thor tanks. The analytical model is developed in reference 3.

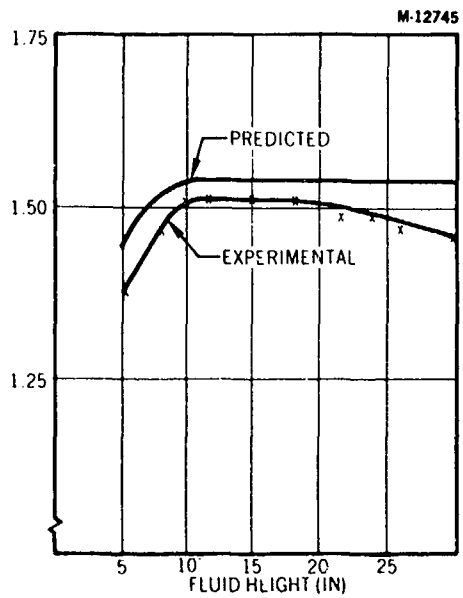

Figure 2. Sloshing Frequencies Model Thor Tank

Figure 3 shows a plot of frequency versus fluid level in the Saturn lox tank. Development of the analytical model is given in reference 2.

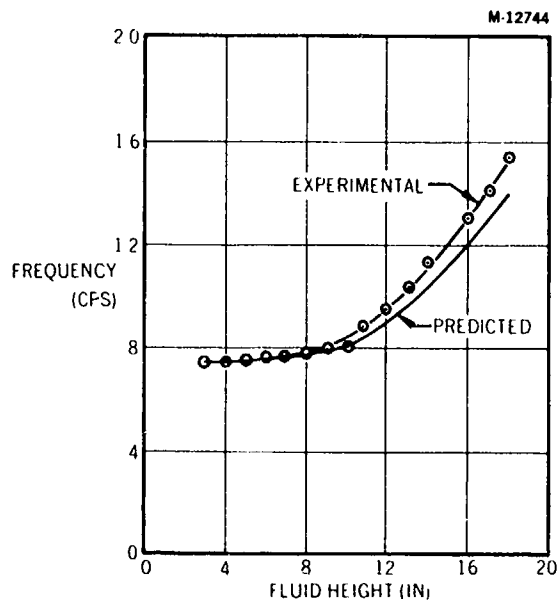

Figure 3. Sloshing Frequencies Model Saturn lox Tank

Figure 4 shows a plot of frequency versus fluid level in the Saturn fuel tank. Development of the analytical model is given in reference 2.

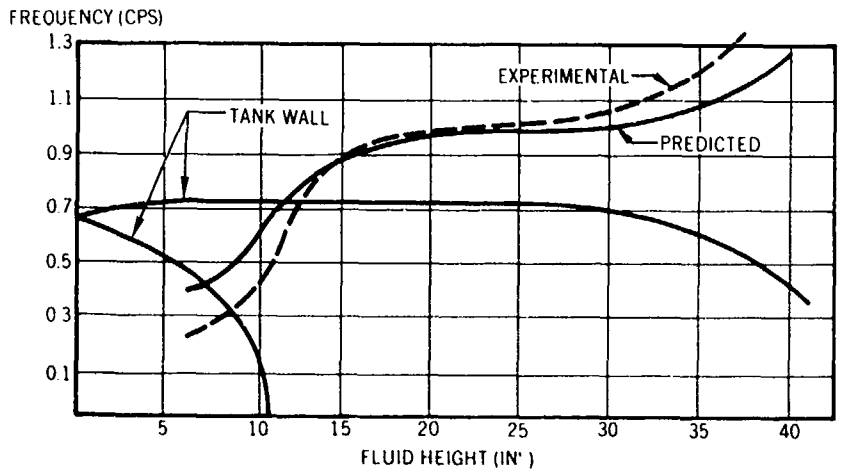

Figure 4. Sloshing Frequencies Model Saturn Fuel Tank

Damping curves are shown in Figure 5 for the Saturn lox tank and in Figure 6 for the Thor tank. Since the Saturn fuel tank had no baffles the figures for the unbaffled Thor tank were assumed on the basis of the scaling parameters developed in reference 6.

M-12741

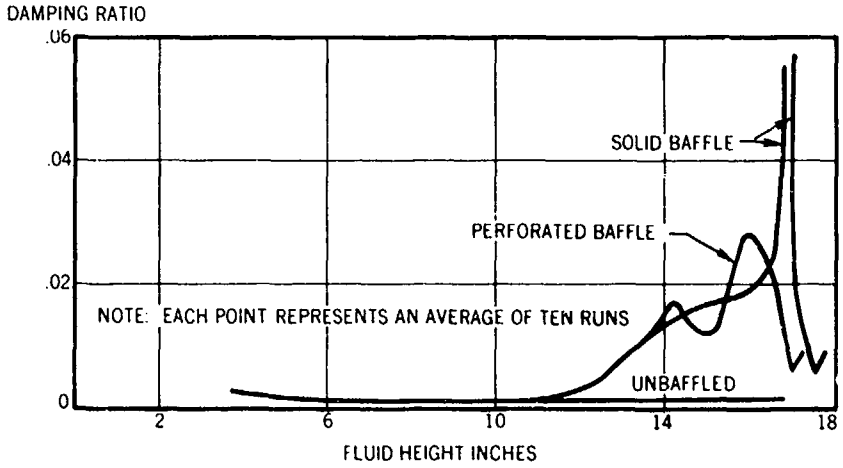

Figure 5. Damping Ratio Versus Fluid Height S-IV Lox Tank

M-12746

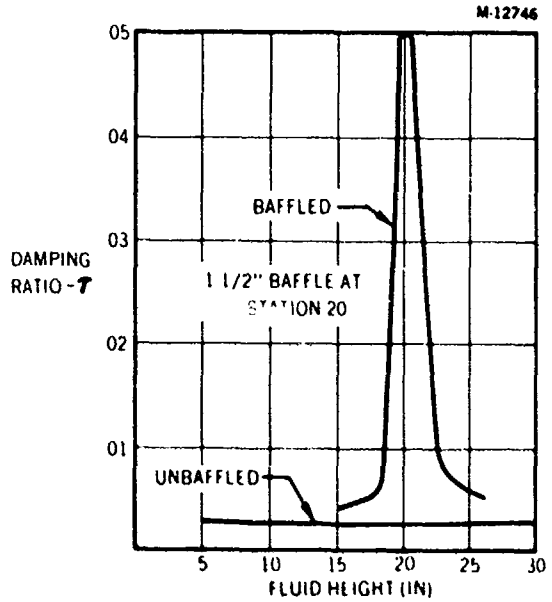

Figure 6. Damping Ratio Model Thor Tank

Figure 7 shows a schematic of the test setup. As shown, the tanks were supported in pendulum fashion with provisions for changing the pendulum arm. The actuating mechanism was a Thor hydraulic actuator and control panel. Provisions were made to drive the tanks sinusoidly and to input step functions.

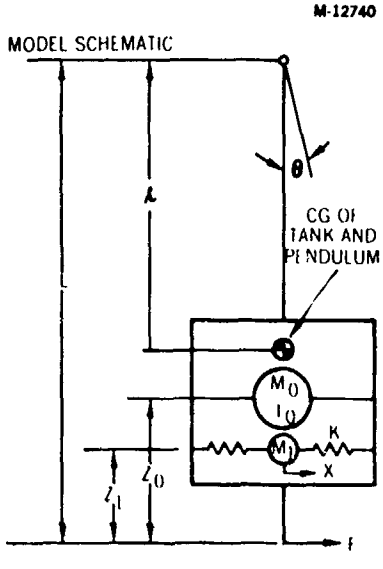

Figure 7. Derivation of Force to Acceleration Transfer Function for Mechanical Model

Figures 8, 9, and 10 show the response of the tank and fluid as a function of frequency. The figures from the high side of the response were used to evaluate the following equation describing the response of the mathematical model at high frequencies:

$$\frac{F}{A} = -\frac{1}{L^2}\left\{ I + I_o + M_o\,(L-Z_o)^2 \right\}$$

where the subscript "o" denotes the fluid properties as shown in Figure 7.

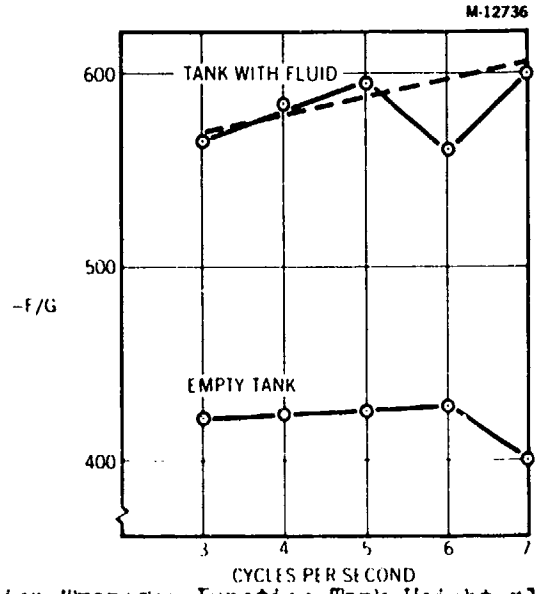

Figure 8. Force to Acceleration Transfer Function Tank Height #1

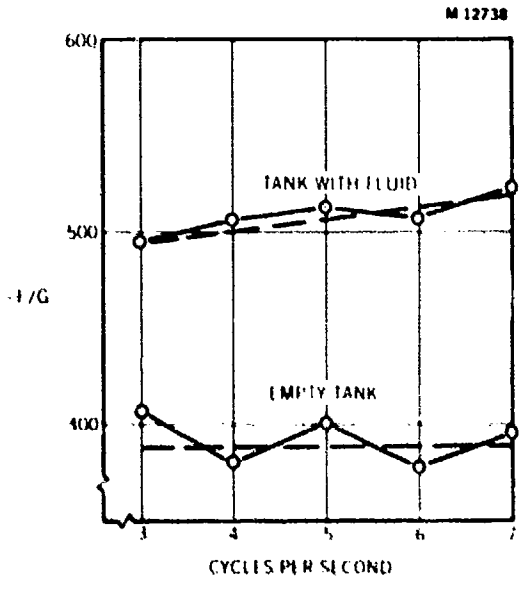

Figure 9. Force to Acceleration Transfer Function Tank Height #2

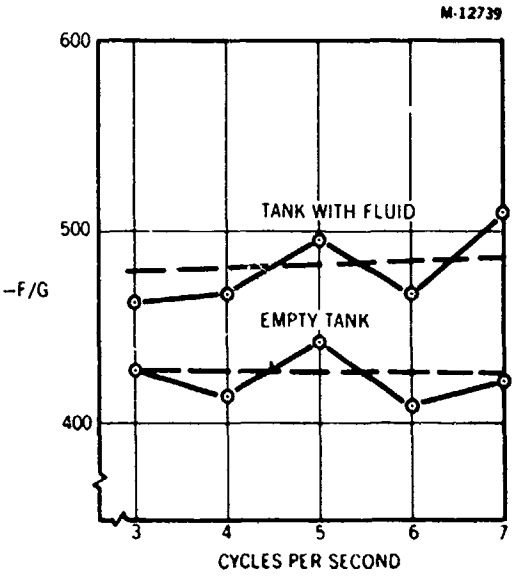

Figure 10. Force to Acceleration Transfer Function Tank Height #3

REFERENCES:

1. Chu, Wen-Hwa — "Liquid Sloshing in a Spherical Tank Filled to an Arbitrary Depth" Southwest Research Institute Technical Report No. 4 S_W RI Project No. 6-107= -2

2. Webb, C. K. — "Slosh Tests of Saturn S-IV Model Tanks" Douglas Aircraft Co., Inc. Report SM 44145, July 1, 1963

3. Anderson, G. W. — "Sloshing Parameters for Cylindrical Tanks" Douglas Aircraft Co., In. Report SM 37477, August 26, 1960

4. Anderson, G. W. — "Saturn Stage S-IV Slosh Tests" Douglas Aircraft Co., Inc. Technical Memorandum L2729, August 15, 1961

5. Anderson, G. W. — "Saturn S-IV Sloshing Investigation" Douglas Aircraft Co., Inc. Memorandum G&C-M-875

6. Davidson, W. R. — "Liquid Hydrogen Slosh Test"- Douglas Aircraft Company Inc., Report SM-38426, January 6, 1961

7. Miwa, W. T. — "Average Experimental Fuel Tank Damping Curves" Douglas Aircraft Co., Inc., Memorandum ACS-98

8. Ryan, J. F. — "Propellant Motion Study for DM-18" Douglas Aircraft Company, Inc. Memorandum A41-260-G&C-4

9. Webb, C. K. — "Slosh Modes in the S-IV Lox Tank" Douglas Aircraft Company, Inc., Memorandum A2-260-S/G&C-M-185

10. Webb, C. K. — "Sloshing Parameters for the Saturn S-IV Vehicle", Douglas Aircraft Company, Inc. Memorandum A2-260-S/G&C-M-289

DEVELOPMENT OF DYNAMIC MODEL ROTOR BLADES FOR HIGH SPEED HELICOPTER RESEARCH

by

Evan A. Fradenburgh
Supervisor, Aircraft Advanced Research Section
and
Edmond F. Kiely
Senior Research Engineer

Sikorsky Aircraft
Division of United Aircraft Corporation
Stratford, Connecticut

ABSTRACT

The development at Sikorsky Aircraft of scale model helicopter rotor blades which are dynamically and structurally similar to full scale blades is presented in terms of the need for such models, problems associated with the construction of the blades, testing experience, and useful information gained by this research. Experimental results obtained include data on performance, blade motions, elastic deformations, steady and vibratory blade stresses, and rotor vibration phenomena. In addition to experience with blades designed to operate at full scale tip speeds and Mach numbers, modifed blades have been developed to provide full scale Froude numbers and thus proper gravity effects as well as allowing higher simulated forward speeds. These blades allow experimental research on rotary wing aircraft in the 400 knot category.

LIST OF FIGURES

SYMBOLS

a	speed of sound
b	number of blades
C_D	rotor drag coefficient, $D/\pi R^2 \rho (\Omega R)^2$
C_L	rotor lift coefficient, $L/\pi R^2 \rho (\Omega R)^2$
C_Q	rotor torque coefficient, $Q/\pi R^2 \rho (\Omega R)^2 R$
c	blade chord
D	rotor drag
Dp	aircraft parasite drag
E	modulus of elasticity in bending
f	parasite area, $D_p/1/2 \rho V^2$
G	modulus of elasticity in shear
g	acceleration due to gravity
HP/L	rotor horsepower per pound of lift
I_{xx}	area moment of inertia in · atwise bending
I_{yy}	area moment of inertia in edgewise bending
J	area moment of inertia in torsion
L	rotor lift
M	Mach number
$M_{1.0}$	rotor tip Mach number
$M_{(1.0)(90)}$	advancing blade tip Mach number
M_b	total blade mass
m	mass per unit length

Q	rotor torque
R	rotor radius
r	local radius station
V	forward speed
$\bar{x}$	distance from leading edge to elastic axis
α	angle of attack of rotor control axis
θ_1	blade twist, difference between root and tip pitch values, negative when tip pitch is less than root pitch
$\theta_{.75R}$	rotor collective pitch measured at three quarters radius station
μ	rotor advance ratio, $V/\Omega R$
μ_a	viscosity of air
ρ	air mass density
σ	rotor solidity, $bc/\pi R$
Ω	rotor angular velocity

DEVELOPMENT OF DYNAMIC MODEL ROTOR BLADES FOR HIGH SPEED HELICOPTER RESEARCH

Evan A. Fradenburgh

Edmond F. Kiely

INTRODUCTION

Theoretical methods for predicting helicopter rotor characteristics are well established in certain flight regimes, such as hovering and moderate forward speeds (~ 100 knots). In other flight regimes, such as at high forward speeds (above 200 knots) or at low forward speeds (10-50 knots) theoretical methods are not presently adequate for accurately predicting characteristics, including performance, blade motions, and, to a greater extent, the vibratory airloads that exist on the blade. These vibratory airloads are of particular importance since they determine, for a given set of blade structural characteristics, the vibratory force inputs to the fuselage and vibratory stresses in the blade which in turn determine the useful fatigue life. Because of the present gaps in theory, it is necessary to rely on experimental techniques for determining rotor characteristics for two purposes: (1) for predicting full scale rotor behavior for specific helicopter applications in unfamiliar flight regimes where theory is inadequate, and (2) for correlation of experiment with new theories in order to close the gaps by establishing the validity of the new theories. The second of these purposes is generally of greater fundamental significance.

It is shown in this paper that to obtain realistic experimental wind tunnel data on rotor characteristics, it is necessary to test blades dynamically similar to full scale blades. The paper outlines the development history of dynamic model blades at Sikorsky and some of the useful test results obtained.

NEED FOR DYNAMIC MODEL BLADES

Wind tunnel testing of model rotor blades was commenced by Sikorsky Aircraft in 1954 with the equipment shown in figure 1. The rotor test rig, installed in the United Aircraft 18-foot subsonic wind tunnel, was comprised of an electric drive motor system, shaft, rotor head, and swash plate system with electric actuators for controlling collective and cyclic pitch angles, combined with slip rings and a strain gage force balance system. The overall assembly of these components was enclosed in a horizontally oriented pod supported by tubular legs mounted on the wind tunnel turntable which was used to change shaft angle of attack. The first rotor blade set tested on this rig was an early-production tail rotor from a Sikorsky S-58 (Army H-34, Navy HSS-1) helicopter with a diameter of 9 feet 4 inches. Subsequently an improved tail rotor type configuration was adopted, with superior structural characteristics and a diameter increased to 10 feet. This rotor system was semi-articulated, that is, incorporated hinges near the center of rotation to allow unrestrained flapping motion of the blades, but without lag hinges that would permit blade motion in the plane of rotation. Helicopter main rotors are commonly fully articulated with both flapping and lagging hinges at the root end of each blade. The lag hinge was not incorporated on the model because a design study indicated that the required bearing sizes would have resulted in an unrealistically large rotor head, and it was felt that the lack of the lag hinge would not affect measured performance to an appreciable extent.

Early test programs were aimed primarily at performance measurements in the high speed flight regime. These efforts were largely frustrated by three major limitations of the available models and equipment. The first of these limitations (neglecting early mechanical problems associated with the rotor test rig operation) was that of obtaining suitable balance accuracy. Measurement of rotor thrust and torque was not unusually difficult but the determination of force components perpendicular to the shaft to the required degree of accuracy, essential to the measurement of rotor drag or propulsive force, turned out to be exceedingly difficult because of the small steady forces compared to the large vibratory forces. Refinement of the balance system and mechanical operation of the rig required a period of several years before suitably repeatable and reliable test data could be obtained.

The second limitation encountered was that of aerodynamic interference between the rotor and the rather sizeable pod which housed the mechanical system of the rig. This interference affected blade flapping motion as well as rotor forces and moments. Despite a concentrated attempt to evaluate these interference effects, both analytically and experimentally

with image-system tests, it was not found to be possible to correct adequately for these effects, which were very sizeable at the higher advance ratios (ratio of forward speed to rotor tip speed). The solution to the problem was a mechanical change involving a shaft extension to effectively remove the rotor from the pod, thereby largely eliminating the interference effects. A more recent photograph of the rotor test rig, figure 2, shows this shaft extension.

The third major limitation to the early test programs was associated with the test rotors themselves. It was found that in general the permissable operating conditions were severely restricted at high simulated forward speeds because of excessive vibratory stresses. This was true both with the relatively low aspect ratio all-metal tail rotor blades used initially, and later with high aspect ratio blades simulating main rotor practice, fabricated of a composite wood and metal structure. The higher aspect ratio blades were built with a solid aluminum spar at the leading edge combined with a trailing edge utilizing wood ribs and a thin plywood skin bonded to the spar. Early tests of this type blade were encouraging, and several series of blades were built with this construction to determine experimentally the effects of blade twist and also the effects of blade planform taper. Ultimately, however, complete comparisons of the various types were not possible because of the limited range of conditions at which test data could be obtained. Numerous blade trailing edge structural failures were encountered despite various metal chordwise straps and trailing edge strips added to reinforce the plywood. Still another type of blade construction, utilizing fiberglass-plastic materials, was similarly limited in operating range. Some of the various model blades of somewhat arbitrary structure as well as a more recent dynamic model blade are shown in figure 3.

Interestingly, many of the operating limitations and structural failures encountered with the model blades were similar in nature to those encountered by Sikorsky blade development engineers in the early days of the helicopter. Rotor blades were evolved over many years to avoid the limitations of the early types, and it became apparent that one approach to building a model blade with a greater operating range was to take advantage of full scale blade experience and copy the full scale structural design. This was one good reason for the development of a model blade dynamically similar to full scale blades.

The compelling reason, however, for the development of a dynamic model blade lies in the fact that, in practice, vibration and excessive vibratory stresses limit the operating condition of a rotor on a helicopter. The forward speed capability of a pure helicopter is limited by the phenomenon of retreating blade stall. This stall results from the fact that as forward speed of the helicopter is increased, the dynamic pressures encountered by the blade on the "retreating" half of the disk are reduced, so that higher blade angles of attack are required to keep the lift balanced on the two sides. At some

forward speed, depending on tip speed, blade loading, etc., maximum blade lift coefficients are attained and at higher speeds, blade section stall is encountered over a portion of the disk. The rotor aerodynamic performance suffers as might be expected, but not drastically until a large percentage of the disk is stalled. The phenomenon of stall is revealed to the pilot by an increase in aircraft vibration level or by increases in control system loads resulting from blade torsional moments. Thus it is rotor dynamic behavior which determines if a given flight condition is an acceptable one. Similarly, if it is known through strain gage measurements that rotor blade vibratory stresses are considerably in excess of safe values, then the operating condition would be deemed unacceptable for protracted flight, even if rotor stall does not occur. Again, blade dynamic behavior is the critical factor. Thus while experimental results obtained on a model blade of arbitrary structural characteristics might have some value with respect to performance measurements, the problem of establishing acceptable rotor operating limits in forward flight can be determined experimentally only with blades having a reasonable degree of dynamic similarity to the desired full scale blade. Since experience has shown that blade flexibility plays an important part in the blade behavior, it is important that elastic effects be properly duplicated.

Sikorsky Aircraft has, for the past several years, concentrated its model rotor research effort on the development and evaluation of model blades dynamically similar to typical full scale Sikorsky main rotor blades, according to the need for such blades outlined above.

SELECTION OF DESIGN PARAMETERS FOR FULL SCALE MACH NUMBER BLADE

A model of any type is dynamically similar to its full scale counterpart if the dimensionless ratios of the significant dimensional parameters including dynamic quantities are the same for the model as for the full scale counterpart. When this criterion is met, the performance or output of the model, also expressed in appropriate dimensionless terms, will be the same as for the full scale article. The word "significant" is important, however, since it is generally impossible to maintain all dimensionless ratios the same as full scale, and for any particular problem it is usually necessary to decide which variables are of primary importance and which are relatively negligible.

Since a rotor is an aerodynamic device it is of course necessary that aerodynamic similarity be achieved in a dynamic model. Perfect aerodynamic similarity requires that the flow be geometrically similar to full scale at all points in the field surrounding the model. This requires that the model be externally geometrically similar to full scale, and also requires

that the flow Mach numbers and Reynolds numbers be the same as full scale. This is frequently impossible to achieve in a model, but fortunately under many circumstances these requirements can be relaxed considerably without impairing the major objectives of the test.

The first dynamic model blade designed by Sikorsky was aimed partly at exploration of high tip speed, high forward speed flight conditions at which the maximum air velocity relative to the blade approaches the speed of sound. Consequently, it was considered mandatory that full scale Mach numbers be reproduced in the model. Since the wind tunnel available for the tests was an atmospheric density air tunnel, for which the speed of sound was essentially the same as for normal sea level conditions, the requirement for full scale Mach number was met by operating at full scale tip speeds and forward speeds. Reynolds number similarity under these conditions cannot be achieved, but fortunately the relatively small changes in aerodynamic characteristics due to the reduced Reynolds numbers of the model was not considered detrimental to the purposes of the program.

Dimensional Parameters

Listed below are the dimensional parameters considered in the design of the model, divided into those of primary importance and those considered to be of secondary importance for the first dynamic model blade. The lists are by no means exhaustive, but serve to illustrate the most important items:

Primary Importance

(1)	V	forward speed, ft/sec.
(2)	a	speed of sound, ft/sec.
(3)	Ω	rotor angular velocity, radians/sec.
(4)	R	rotor radius, feet
(5)	c	blade chord, feet
(6)	ρ	air mass density, slugs/ft^3.
(7)	m	blade mass per unit length, slugs/ft.
(8)	M_b	total blade mass, slugs

(9) EI_{xx} blade flatwise bending stiffness, pound-ft^2.

(10) EI_{yy} blade edgewise bending stiffness, pound-ft^2.

(11) GJ blade torsional stiffness, pound-ft^2.

(12) $\bar{x}$ distance between elastic axis and blade leading edge, feet

Secondary Importance

(13) μ_a air viscosity, slug/ft-sec.

(14) g acceleration due to gravity, ft/sec^2.

It should be understood that some of the parameters listed, such as chord, mass per unit length, and stiffness may vary along the length of the blade. The symbols then stand for distributions rather than single numerical values.

Dimensionless Ratios

None of the dimensional items listed above have any significance except as they relate to other parameters or combinations of parameters having the same dimensional units. Accordingly, dimensionless ratios of the above parameters are formed somewhat arbitrarily as follows, making sure that each dimensional parameter is used at least once and that, if possible, each new parameter is combined only with parameters previously used. This ensures that all pertinent dimensionless ratios will be found. With the three fundamental dimensions involved (mass, length, and time) the number of independent dimensionless ratios will be three less than the number of dimensional parameters. (In the following list, one redundant ratio was intentionally included.)

Primary Importance

(1)	$V/\Omega R$	rotor advance ratio, ratio of forward speed to rotor tip speed
(2)	V/a	flight Mach number
(3)	$\Omega R/a$	tip Mach number
(4)	R/c	blade aspect ratio
(5)	$m/\rho R^2$	ratio of local mean rotor density to air density

(6)	$M_b/\rho R^3$	ratio of total mean rotor density to air density
(7)	$EI_{xx}/\rho V^2R^4$	ratio of flatwise bending elastic forces to aerodynamic forces, variant of Cauchy number
(8)	EI_{yy}/EI_{xx}	ratio of edgewise to flatwise bending stiffness
(9)	GJ/EI_{xx}	ratio of torsion to flatwise bending stiffness
(10)	$\bar{x}/c$	location of elastic axis in fraction of chord

Secondary Importance

(11)	$\rho Vc/\mu_a$	Reynolds number, ratio of dynamic to viscous air forces
(12)	Ω^2R/g	variant of Froude number, ratio of centripetal to gravitational accelerations

As stated previously, the lists of dimensional parameters and dimensionless ratios presented are not complete, and some of the dimensionless ratios familiar to helicopter engineers, such as the Lock number or ratio of air forces to blade inertia forces, are conspicuous by their absence. The "missing" items, however, are actually inherent in the items presented and may be derived from them if desired. Note that, of the first three dimensionless ratios shown above, any one is merely a combination of the other two, so that only two are independent. It is frequently useful to combine various dimensionless ratios into new, although redundant, ratios, and the above redundancy was provided as a simple illustration. As another example, the reduced frequency parameter $\Omega c/2V$, important with respect to unsteady aerodynamic characteristics, is simply a combination of ratios (1)-$V/\Omega R$ and (4)-R/c. Thus, provided that no important dimensional items were left off the original list, satisfying the dimensionless ratios listed ensures that all important dimensionless ratios are satisfied, and that dynamic similarity exists for the intended purpose. The dimensional analysis presented is included merely as a means to the end of establishing the design of the model blades rather than a comprehensive treatment of the subject.

Of the various dimensionless ratios listed above, it should be noted that some, such as item (1) -$V/\Omega R$, refer to testing conditions rather than to the design of the model. Item (4) -R/c, refers to geometric similarity between model and full scale rotor. Additional dimensionless quantities derived from geometric similarity should also be added to the list of important items, including the number of blades in the rotor, blade twist, blade pitch settings, shaft angle of attack and other angular quantities.

The above list of dimensionless ratios combined with the characteristics of the available wind tunnel can now be used to establish the design criteria of the model blade as follows:

(a) Speed of sound, a, in the available atmospheric wind tunnel is essentially the same as for the full scale rotor in free air. Thus, to satisfy dimensionless ratios (2) and (3)-V/a and $\Omega R/a$, forward speed V and rotor tip speed ΩR must be the same as full scale.

(b) Dimensionless ratio (4)-R/c-and other reasoning discussed previously requires that the model external shape be geometrically similar to full scale.

(c) Since tunnel air density is the same as the air density for the full scale blade, dimensionless ratios (5) and (6) $-m/\rho R^2$ and $M_b/\rho R^3$-indicate that the quantities m/R^2 and M_b/R^3 must also be the same as full scale, both of which when combined with conclusion (b) above indicate that the average density of the model must equal the density of the full scale blade construction, and that total model weight will vary as the cube of the scale chosen. It may be seen that total mass M_b was actually a redundant dimensional parameter since the mass distribution parameter m was listed.

(d) Since speed V and density ρ are the same as full scale, the dimensionless ratio (7)-$EI_{xx}/\rho V^2R^4$ - requires that EI_{xx}/R^4 be the same as for full scale.

(e) Dimensionless ratios (8) and (9)-EI_{yy}/EI_{xx} and GJ/EI_{xx} - require that the ratios of flatwise, edgewise, and torsional stiffness be the same for the model as for full scale.

(f) Dimensionless ratio (10)-$\bar{x}/c$ - requires that the elastic axis be at the same geometric location on the model as on the full scale blade.

(g) Consideration of dimensionless ratio (11)- $\rho Vc/\mu_a$ leads to the conclusion that model Reynolds number cannot be made equal to full scale, since density ρ, velocity V, and viscosity μ_a are all the same as for full scale. Thus Reynolds number will be reduced directly proportional to the model scale. As stated previously, this was unavoidable with the wind tunnel available, but fortunately not considered detrimental to the

objectives of the program.

(h) Consideration of dimensionless ratio (12)- $\Omega^2 R/g$- leads to the conclusion that the ratio of centripetal to gravitational acceleration could not be made equal to full scale, since tip speed ΩR is the same as full scale, rotational speed Ω is increased, and gravitational acceleration g remains constant. This was not considered significant for the intended test program, since the rotor tip centripetal acceleration is over 400 "g's" for the full scale blade, and consequently blade weight affects blade flapping motion (chiefly average flapping or coning angle) to a relatively small extent. This relative insensitivity to gravity permits testing of the rotor tilted on its side as seen in figures 1 and 2.

(i) The cross section of the full scale blade to be simulated is shown qualitatively in figure 4a. It is characterized by an essentially thin-walled single cell spar at the leading edge machined from an aluminum extrusion to which non-structural leading edge counterweights and trailing edge fairings are added. The elastic axis of the spar and center of gravity of the blade are both at approximately the 25 per cent chord station. If the same material (aluminum) is used for the model spar, and if the internal structural shape as well as external shape is scaled down geometrically from full scale, then the moduli of elasticity in bending and shear, E and G respectively, are the same as for the full scale blade and the moments of inertia in bending and torsion, I_{xx}, Iyy, and J will be reduced by a factor of the fourth power of the scale chosen. Use of geometric scaling with the same materials also results in the mass of the model decreasing with the cube of the linear scale. A review of the requirements derived in paragraphs (b), (c), (d), (e), and (f) above reveals that this approach of using the same structural material and internal as well as external geometric scaling meets all of the requirements, and provides one technique by which proper dynamic similarity is assured, as long as paragraph (a) is also satisfied; that is, as long as the model is operated at the same forward speed and tip speed as full scale.

(j) Another possible approach to the design of the dynamic model is illustrated schematically in figure 4b wherein a structural spar not geometrically similar to full scale is used in conjunction with non-structural aerodynamic fairings and perhaps weights to adjust to the required mass. In principle, a spar shape can be found that will have the right relative ratios of flatwise, edgewise, and torsion stiffness, although in practice a considerable amount of trial and error may be involved. In the particular

application being considered, however, it may be shown quite easily that no solution is available using this approach. This is because the full scale blade utilizes an efficient structural shape combined with an efficient structural material. A spar shape such as that shown in figure 4b will have considerably lower values of moment of inertia per unit cross section area than the spar of figure 4a. This could be suitably compensated for if a material with a ratio of modulus of elasticity to material density considerably higher than that of the full scale spar (aluminum) could be found. No such material is available, however, and this design approach must be rejected for this specific application. It should be noted, however, that if dynamic similarity is desired at model velocities appreciably less than full scale (where Mach number effects are not reproduced), then from dimensionless ratio (7)- $EI/\rho V^2R^4$ - it may be seen that if ρV^2 is less than full scale, the stiffness EI must decrease more rapidly than R^4. In this application, the design approach represented by figure 4b would be acceptable. For the present problem, however, it is not.

The conclusion from the preceding analysis was that the only reasonable approach to building a model blade dynamically similar to a typical Sikorsky main rotor blade at full scale tip speeds was to build essentially an accurately scaled miniature of the full scale blade with the same materials, at least as far as structure is concerned. The development of such a model blade is described in the next section.

The scaling ratios or ratios of values of various dimensional parameters of the model to full scale values are presented in Table I for both the full scale Mach number blade and for the full scale Froude number blade discussed in a later section. For the one-eighth scale blades developed for full scale Mach number, mass of the blades is reduced by a factor of 8^3, stiffness by a factor of 8^4, RPM increased by a factor of 8, aerodynamic, centrifugal, and other loads decreased by a factor of 8^2. Blade stresses will be the same as full scale and blade deflections will be geometrically similar to full scale deflections. All natural frequencies will be increased by a factor of 8, so that the cycles per revolution for any vibration will be the same as full scale.

DETAIL DESIGN OF DYNAMIC BLADE

Prototype

The prototype chosen for the dynamically scaled model rotor was the five bladed Sikorsky S-56 (H-37, HR2S) main rotor, 72 feet in diameter with a 21.5 inch blade chord.

This blade, shown in figure 5, is of all metal construction and consists of the following components: a CUFF which is a U shaped steel attachment fitting that joins the blade to the sleeve component of the rotor head. It is attached by a series of bolts to the blade SPAR - which is the main structural member of the blade and is made from a hollow "D" section extrusion of 6061 aluminum. It forms the leading edge of an NACA 0012 airfoil contour and at its trailing edge supports the POCKETS which are essentially triangular cross section units, fabricated of aluminum ribs and skin, and bonded to the spar to complete the aft portion of the airfoil shape. Internally, and in the leading edge area of the spar, are located COUNTERWEIGHTS whose function is to mass balance the blade about the feathering axis. The counterweights are supported along the spar by a pair of internal beads that act as a retaining channel and at the tip by a restraining block which is attached to the spar side walls through a series of rivets. Adjacent to this block is another block which supports the TIP BALANCE ASSEMBLY that provides a dual means of trimming the dynamic characteristics of the blade: first-spanwise-by a series of shim weights located on the quarter chord position, and second-chordwise-by a movable balance weight which ajusts the blade pitching characteristics. The tip of the blade is faired to a smooth tapered airfoil contour by a replaceable TIP CAP which allows for tip damage without spar replacement. More information on the design of Sikorsky main rotor blades was presented in Reference 1.

Comparison Parameters

By dimensional analysis discussed in a previous section, the parameters of the S-56 blade were scaled down by conversion factors, such that the model is aerodynamically, geometrically, structurally, and dynamically similar at full scale tip speed (normally 696 feet per second for the S-56 rotor). These conversion parameters are shown in Table I.

The scale chosen for this model was based on the largest diameter disk that could be tested in the United Aircraft 18 foot Wind Tunnel without seriously being affected by wall interferences in certain test regimes. The rotor size selected was 9 foot in diameter and thus one-eighth scale of the prototype.

Dynamic Model Blade

The dynamic model blade shown in figure 6 has a length of 48 inches and a chord of 2.69 inches. The blade as first developed consisted of a steel cuff, a bonded aluminum spar, pockets composed of balsa wood ribs covered with "Mylar" coated paper, lead and steel counterweights and an aluminum tip cap. Figure 7 compares a typical cross sectional view of the scaled model with the actual prototype.

It can be seen from figure 7 that the model spar is a built-up section as compared to the extruded spar of the prototype. Although exact likeness in construction is not present, overall similarity is maintained. Comparison between the model mass distribution, area and stiffness characteristics and the S-56 blade characteristics scaled down are shown in figures 8 and 9. Variations between actual and desired characteristics caused by differences in construction are, in general, very small. Since the spar is the main structural component of the blade, as much similarity as possible between model and prototype was of the utmost importance.

A study was undertaken to investigate the possibility of fabricating an identical extrusion one eighth the scale of the full scale blade. Below is a list of the disadvantages that arose from this investigation.

1) Extreme costs, special tooling and very long lead time in the procurement of the extrusion;

2) Dimensional tolerances that are allowed on the full scale extrusion could not be scaled down proportionately;

3) Machining techniques necessary to contour the extrusion could not be employed without extensive tooling costs;

4) Special equipment used to set the full scale spar at a particular twist could not be used on the model;

5) Inspection methods used to examine the inside surface of the spar could not be modified to accommodate the small size.

With these disadvantages in mind it was decided that a built-up section such as that seen in figure 7, was the more practical solution to the problem. Since the model was to be a dynamic representation of a production blade, the wall thicknesses, contour and length were scaled down from the drawings of the S-56 main rotor blade. The contour of each section of the spar was determined by plotting the mean values of the production tolerances allowed on the prototype. The scaled down tolerances were extremely small, in the neighborhood of five ten-thousandths of an inch and it is worthwhile to

note that the built-up spar is far superior to an extruded spar because of the quality control that can be maintained in milling the thickness of the skin. The inside contour of the S-56 blade is constant along the length of the blade; the model also incorporates this feature.

SPAR

A. Spar Components

The spar is composed of four basic parts; the leading edge, the U-section, vertical stiffeners and a counterweight channel. The components of the spar are bonded together with a "Scotch-Weld" film adhesive. This adhesive is not considered to contribute to the stiffnesses of the blade and therefore only the aluminum components are used in determining the section properties of the blade. Comparison of area, I_{xx}, I_{yy}, and J distributions of the model with those of the S-56 spar scaled down for comparison are shown in figure 9.

1) Leading edge - The leading edge of the spar is of step-tapered wall thickness. Initially, a strip of 6061T-6 aluminum, .051 inches in thickness was machine milled in four steps to .021 inches at the tip, and then hand scraped and sanded to within .0005 inch of the required values. This method, since it was very expensive and time consuming, led to the use of chemical milling of the material to the variable thickness required. The advantage of this method was that it uniformly milled a large sheet containing a number of leading edge blanks in a very short period of time.

The forming of the leading edge, because of its small radius of bend, made it necessary to heat treat the aluminum to the T-4 condition to make it pliable for forming. Immediately after heat treatment it is initially formed over a 4 inch diameter die to insure proper contour during final forming and then press formed over a special male contoured die. After forming it is returned to the T-6 condition, machine milled to the proper chord dimensions, and then anodized.

2) U-Section - The U-Section or trailing edge of the spar is of uniform thickness and is made from a .025 inch sheet of 6061T-6 aluminum. Since the angle of bend is not as sharp as that of the leading edge, it can be formed in the T-6 condition. Again, as with the leading edge, it must be formed over the 4 inch diameter die to insure proper contour during final forming, and then press formed over a male U-Section die. It is press formed again with a female U-Section cover plate to obtain the flat vertical surface. After forming it is machine milled to the proper width and length and then anodized.

3) Vertical Stiffeners - Two vertical stiffeners are cut to size from a .012 sheet of 6061T-6 aluminum and then anodized.

4) Counterweight Channel - From a .006 inch sheet of 6061T-6 aluminum (obtained by chemically milling a sheet of greater thickness) the counterweight channel is trimmed to the required dimensions, brake formed over a special die to obtain the required shape, and then anodized.

B. Spar Assembly

1) Adhesive - The bonding of the spar assembly was a unique challenge in itself with the selection of the adhesive requiring the analysis of numerous bonded test sections. The choice of a bonding agent could not be determined merely from a shear or peel strength chart, since the bonded joint where the U-Section is attached to the leading edge is not only under shear loads during actural testing, but also under a tensile load due to the bonding process. This tensile load is transmitted through the adhesive by the pulling away of the leading edge from the U-Section since a perfect contoured shape could not be reached during forming because of the inherent springback of the material.

Other facts determining the selection of the bonding agent were the consistency of the glue line thickness, the strength of the adhesive after repeated curing cycles, the ease in handling during the bonding process, the ability to clean excess adhesive from adjacent parts, and uniformity in weight. A Scotch-Weld Brand thermosetting nitrile-phenolic adhesive film, designated AF-6, fulfilled these requirements.

2) Bonding Jig - Figure 10 shows a section of the specially designed jig used to bond the components of the blade together. It consists of 30 templates located 1.5 inches apart which can be individually adjusted to permit bonding of any reasonable twist into the spar. The spacing of these templates was selected so that external pressure blocks which apply uniform pressure perpendicular to the bonded joint could be independently attached to the spar rather than rigidly connected to the continuous members of the blade and bonding jig which are affected by thermal expansion during the bonding cycle. A fixture based on the inside contour of the spar is inserted between the leading edge and the U-channel to control the chord dimensions of the spar and also act as a compression pad for the external pressure blocks. This spacer is designed with a hinge-type folding device to allow its removal after bonding. A photograph of this spacer and the one used in positioning the counterweights and counterweight channel as well as the other jigs and components used in the construction of the spar is shown in figure 11.

3) Assembly - The bonding of the spar assembly is performed in three operations:

a) The vertical stiffeners are bonded to the U-Section with special forms used to ensure a flat surface and prevent slippage.

b) The U-Section and the leading edge are bonded together.

c) The counterweight channel is bonded to the inside of the spar.

A contoured form is used to control the position of the channel with respect to the leading edge.

The special jig and fixtures described above are required for steps (b) and (c). A photo of the jig and a blade to be bonded is shown in figure 12 prior to being placed in an oven for curing. Special attention should be given to the number of components necessary to position and affix the spar to the jig. It should be noted that all jigs, templates and fixtures used in the bonding of the blade and its components have been coated with Teflon as a release agent.

POCKETS

The scaling down of the pockets was perhaps the most difficult phase in the design of the model blade. In the case of the spar, where the same material is used, the resultant weight is proportionate to the reduction in skin thickness. However, to proportionately scale down the components of the pocket utilizing the same material resulted in parts too flimsy to handle. Consequently, a different approach to the problem was taken. The weight and strength of the pockets were the two factors of the greatest concern. Since the pocket is an essentially rigid component of the blade whose function is to complete the aft portion of the airfoil section and transfer the air loads to the spar, it was decided that an increase in the strength and stiffness of the model pocket could be tolerated.

Since the blade is chordwise balanced about the quarter-chord of the section, any change in the weight of the pocket would unbalance the section thus requiring a modification in the counter-balance weight and thereby affecting the entire entire mass distribution of the blade. Therefore, weight is the controlled parameter in the design of the model pocket.

There are three basic pockets varying in weight from seven-tenths of a gram to one gram (the weight of a standard cigarette) and ranging in required transverse load capacity between four and eight pounds per square inch Each of these pockets is similar in construction except for a variance in skin thickness and rib contour necessary to meet the different weight requirements. The photo in figure 13 shows the chemical balance used in weighing the components of the blade. This is an example of the high degree of quality control that exists thoughtout the fabrication of the blade.

Many types of materials were investigated for use in the construction of the pocket. Weight control, water, oil and grease absorption, and compatibility between the adhesives used in the contruction and bonding of the

pocket to the spar were just a few of the factors considered. A high quality grade of bond paper, coated with a 1/2 mil film of metallized Mylar plastic was selected for the skin, with balsa wood chosen for the ribs and a highly water resistant contact cement used to bond the components together.

The steps required in the construction of a typical pocket can be broken down into seven operations:

1) The 1/2 mil metallized Mylar is laminated to the required thickness paper. The Mylar has one surface pre-coated with adhesive which requires only pressure and heat for lamination.

2) The skins are cut to size with a template and folded.

3) The balsa ribs are cut to size from a rib template.

4) The ribs are held in a fixture while the end surfaces are sealed and glue applied, and then transferred to the pocket jig.

5) The skin is placed in a fixture and cement applied.

6) A bead of adhesive is placed inside along the folded edge of the skin to form a stiff edge, and then the skin is positioned over the ribs in the pocket jig.

7) The jig is aligned, clamped together and placed in an oven for a quick cure of 5 minutes at 225°F.

After pockets have been removed from the bonding jig, they are trimmed to fit the spar. The pockets are then bonded to the spar in the same jig used for bonding the spar components together. The jig positions the pocket properly over the U-Section of the spar to insure correct chordwise dimension and proper contour and twist. Paper shims are used between the pocket and U-Section of the spar as required to obtain a smooth contour.

COUNTERWEIGHTS

Since the center of gravity of the spar as well as the pocket are to the rear of the blade quarter-chord, a sizeable weight is necessary to counterbalance the section. Because the center of gravity of the model spar was slightly aft of the corresponding full scale center of gravity, the model counterweights were required to be somewhat forward relative to the full scale counterweights. Calculations called for a material with a density of at least 155 grams/inch^3 because of the small area available for the counterweight in the leading edge of the spar. Lead, with a density of 178 grams/inch^3, appeared highly suitable.

The counterweights on the full scale blade are free to move spanwise along the spar under centrifugal loads; the model retained this similarity. However, if the force exerted by each weight is in turn exerted on the next weight, the total force on the weight closest to the blade tip will range between 200 and 300 lbs. depending on the operating RPM. This presented another problem. The full scale weights are basically of steel and are capable of supporting the large compressive loads exerted on them. The compressive strength of lead is not capable of withstanding such a force, and as a result the counterweight would extrude sideways into the counterweight channel causing it to separate from the spar and allowing the weights to be thrown free. A steel rod was inserted into the lead weight to increase its strength, but too much slippage occurred between the lead and the steel if a smooth rod was used. To eliminate this slippage, a piece of .062 inch diameter drill rod was run through a 1-72 NF die and then threaded into a piece of acid-core solder. (The acid-core solder with the acid removed was substituted for the lead because of the difficulty in drilling through the lead. The combined density of the solder and steel core is still above the required 155 grams/inch^3.) The counterweight is press-formed in a female die based on the inside contour of the leading edge.

The model blade incorporates three different weights, based on the unbalance of the section of the spar under consideration. Figure 14 is a curve of balancing moment and counterweight mass distribution versus counterweight height, developed from a plot of the interior cross-section of the leading edge of the spar. The use of this plot is explained by the following example and indicated on the curves by the arrows.

Example: Chordwise Balance - Section EE

	Mass/inch	Distance from c/4	Moment about c/4
Bonded Spar	3.0564	-0.032	-.0977
Pocket - Bonded to Spar	.7101	-1.032	-.7330
			-.8307
Counterweight from "Plot" (b = .099 inches)	1.4000	+0.593	+.8307

The contoured form previously mentioned, which controls the position of the channel with respect to the leading edge, is based on the contour and height "b" of the largest counterweight required, thus forming a uniform channel along the length of the spar. Therefore, all weights would be initially

the same shape and size. Different weight values are obtained by removal of some of the solder by notching.

TIP BLOCK

The tip block has the threefold purpose of restraining the counterweights, providing a means of trimming the dynamic characteristics of the blade, and acting as an attachment block for the tip cap. It is a magnesium block fitted to the inside contour of the spar and attached to the sidewalls by a series of small screws. The screws permit removal of the block to change counterweights or alter the balance of the blade. Two screws parallel to the feathering axis and located on the centerline of the block are used to attach weights which statically balance all the blades of a set alike with respect to the center of rotation of the rotor system.

TIP CAP

The tip cap is an exact replica of the full scale tip cap and is made of aluminum. Weight wise, it is slightly heavy, but this weight is concentrated forward of the quarter-chord, thus acting as a counterweight. It is attached to the blade through the tip block by screws and through the tip pocket by cement.

CUFF, CUFF BLOCK AND ROOT CAP

The cuff is made of steel and is not dynamically similar to the S-56 cuff.

The magnesium cuff block prevents the spar walls from collapsing as the cuff is installed, similar to the full scale.

The root cap seals the end of the spar from foreign materials.

MODIFICATIONS TO BLADE DESIGN

The development of the model blade has been a continuous project over the past five years to improve its capabilities and simplify its construction. Some of the more important modifications to the original dynamic blade are discussed below.

Static tests of the blade stiffness were used to help substantiate similarity of the model with that of the prototype. However, certain tests which appeared satisfactory initially later proved to be erroneous when other conditions were applied. Such was the case in the selection of the AF-6 adhesive. A wind tunnel test program, conducted to determine the degree of correlation between theoretical and experimental model rotor performance.

showed significant amounts of model rotor blade dynamic twisting both in hovering and vertical flight. In the early stages of testing, the calibration of the torsional strain gages used to measure torsional moments was completed in a period of a few minutes. However, as the number of gage stations were increased and longer periods of time were required for calibration, a continuous and increasing change in blade twist was detected. This was caused by a definite creep in the Scotch-Weld adhesive used to bond the spar components indicating a need for a better bonding agent. Figure 15 compares the torsional behavior of the tip sections of two spars, one built with AF-6 adhesive and the other with FM1000, a film adhesive produced by the Bloomingdale Rubber Company which is presently used in the construction of the dynamic blade. The large change in twist of spar "A" is the direct result of the creep properties of AF-6 in this specific application, whereas spar "B" with the FM1000 adhesive shows only an extremely small change over the same period tested. Another factor, also shown in figure 15, is the slow recovery rate at which the twist returns to its original position after the load is removed. Since the change in twist of spar "B" is so small, the recovery rate is disregarded, but in the case of spar "A", it is a very important factor during calibration and especially during testing.

A photograph of the apparatus used to measure the change in twist of the blade is shown in figure 16. A blade is held in a vertical position by a cuff rigidly attached to the upper portion of the fixture. Mirrors are positioned at various spanwise stations along the spar and located chordwise so that the crosshairs etched on them line up with the feathering axis of the blade. By means of a concentrated arc light source, an image of the crosshairs is reflected on a curved grid screen located 57.3 inches from the twisting axis of the blade. The blade is twisted about its feathering axis by applying a torsional moment through a block fastened to the blade tip. With this device, changes in blade twist due to torsional loading can be recorded simultaneously with an accuracy of 1/20 of a degree.

Other changes in the basic design of the dynamic blade were brought about to ensure structural integrity of the spar at greater than design rotational speeds and Mach numbers. To allow a considerable increase in tip speed and corresponding centrifugal loads, 7075 aluminum was substituted for the original 6061 spar material. The introduction of 7075 required a number of changes in heat treatment and forming. The period of time the material remains in the softer T-4 condition is much less for 7075 than for 6061 aluminum. Refrigeration extends this period, but once out of refrigeration, the time available for forming the 7075 is rapidly reduced.

The increase in rpm (from 1500 to 2200) required changes in some of the other components of the blade. Counterweights, which were originally held in place by the counterweight channel and tip block, are now bonded to the leading edge of the blade to ensure retention. Certain test conditions were repeated to show no change in blade vibratory stresses or performance due to the bonding of the weights. Pockets, which appeared satisfactory at lower

tip speeds, caused many problems at extreme load conditions encountered during a hovering performance test on an outdoor test stand. Upper pocket skins separated from the ribs, Mylar peeled from the paper, pockets slipped along the spar, and pockets closest to the blade tip were thrown free of the spar. In addition to the high aerodynamic and centrifugal loads, the pocket failures could be attributed partially to effects that temperature and atmospheric conditions had on the bond which showed signs of breakdown between pocket and spar and between the components of the pockets. To improve their construction, greater thickness and number of ribs in the outboard four pockets were used to increase the bond area between skin and rib. Different adhesives were tried, but the pocket failures still occurred. Solid balsa cores were substituted for the rib design in order to complete the test, but peeling of the Mylar still existed as well as a large increase in the weight of the pockets.

This change in pocket design, although it allowed completion of the hovering test, would not be satisfactory for the forward flight tests to be conducted in the wind tunnel at a later date. Pockets using magnesium skins chemically milled to a thickness of four-thousandths of an inch, and a comb-like balsa wood core were bonded to the spar with AF-6 adhesive. A photo of the components and fixtures used in the fabrication of this pocket appears in figure 17. The increase in weight of the pocket as a result of this change required additional counterweight to balance the section about the quarter-chord, and thus caused an overall increase of 10% in the total blade weight. With these modifications, we have deviated somewhat from the exact dynamic similarity of the original S-56 blade but are still dynamically representative of typical Sikorsky rotor blades.

TESTING EXPERIENCE

Starting with the first preliminary test in late 1958, a total of more than 70 of the dynamic model blades described in the previous section have been built and tested to date. These have included various sets having built-in geometric twists of 0, -4, -8, and -14 degrees to cover the range of helicopter rotor practice, some sets with high strength aluminum alloy spars to permit high tip speed investigations, some blades with built-in spar deformations and residual stresses to alter the normal centrifugally-induced stress distribution, and several other variations.

Rotor Test Rig

The blades have for the most part been tested in the forward flight condition on the Sikorsky Helicopter Rotor Test Rig in the United Aircraft Corporation subsonic wind tunnel, which has an octagonal test section 18 feet across the flats and a maximum speed slightly over 160 knots with the rotor test equipment installed. An overall view of the present configuration of the test rig showing the drive motor and force balance housing was shown in figure 2, and a more detailed view of the rotor head area is shown in figure 18. The five-bladed rotor hub is equipped with coincident flapping and lag hinges at the 5.6 percent radius station, as is the full scale S-56 rotor. The model hinges incorporate needle bearings for minimum friction and adequate load capacity. Lag motion is restrained by friction dampers and flap and lag motions sensed by Clifton rotary transformers. A conventional helicopter swash plate is driven by three precision electric actuators which are remotely controlled, through an appropriate mixing system in the tunnel control room, permitting independent control of collective pitch and longitudinal and lateral cyclic pitch settings during testing. A hollow shaft provides the route for the wires for all instrumentation on the rotating system to approximately 100 slip rings in the rotor test rig pod.

Normal test procedure consists of setting a desired shaft angle by means of the tunnel turntable, setting rotor speed and forward speed, and taking data at increments in blade collective pitch, usually adjusting cyclic pitch values to minimize tip path plane tilt relative to the shaft. Vibratory stresses on the blade are monitored to ensure that prescribed limits are not exceeded. All dynamic data are recorded on magnetic tape in digital form by means of a 20 channel Epsco data acquisition system, transmitted to an IBM 7090 computer and reduced to steady forces and moments, blade flapping angles, peak to peak stresses, and, if desired, Fourier coefficients of these quantities.

Blade Instrumentation

Usually only one blade out of a set of five is instrumented with strain gages, to minimize the effects of the slight surface irregularities caused by the gages on the overall rotor performance. A spare instrumented blade, however, is frequently provided and occasionally required because of instrumentation failures which may develop, or other damage to the blade. Strain gages are provided to measure edgewise and flatwise bending at five stations each and torsion at four stations along the length of the blade. Gages used are Baldwin AD-7 paper backed wire type, with a resistance of 120 ohms, which have proven to be very reliable when properly installed. Flatwise bending measured at any station is accomplished by means of two active gages, one each on top and bottom of the spar. The bridge circuit is completed with two dummy gages mounted on the instrumentation plate on the rotor head. Edge-

wise bending is similarly measured with two active gages, one on the spar leading edge and one on the trailing edge submerged within the trailing edge pockets. Torsion stations use four active gages, two each on top and bottom of the spar. Connecting wires, which are .005 inch diameter nylon clad copper, run chordwise from external gages to the rear of the spar, from which point they run inside the blade along the rear of the spar to a specially made 56 pin miniature terminal block mounted on the rear of the spar at the root end of the blade. From this terminal a harness of plastic covered stranded wires is used to jump across the flap and lag hinges and is attached to the rotor head with miniature quick-disconnect plugs. A photograph of a portion of this blade instrumentation is shown in figure 19.

Confirmation of Dynamic Similarity

The mass distribution and spar shape were controlled on the model as carefully as possible to ensure similarity to full scale. Measurements of model stiffness in the flatwise, edgewise, and torsional directions have confirmed proper scaling from the proptotype full scale blade to within 5 percent. A comparison of resonance characteristics for model and full scale is shown in figure 20, which presents natural frequency for various vibration modes as a function of rotational speed (full scale frequencies and rpm values were multiplied by the scale factor of 8 to make the numbers comparable). The F anc C labels on the various curves refer to flatwise and chordwise (or edgewise) vibration modes, and the subscript indicates whether it is the first, second, or third mode of bending. As may be seen, the model and full scale blades compare very well, except that for the higher frequency, higher mode vibrations the model frequencies are a little low. This is due primarily to excess root end mass on the model blades because of the weight of the pitch-change bearings which could not be scaled down to the proper weight and still carry the centrifugal loads. While the curves of figure 20 are calculated for the blade they have been confirmed by non-rotating shaker tests in the laboratory and also by examination of blade vibratory stress amplitudes in the wind tunnel as rotor rpm was slowly increased or decreased.

A direct comparison of model stresses and those measured on an S-56 helicopter in flight are shown in figure 21. This comparison was first reported in Reference 1. The model rotor was operated in the wind tunnel to provide the same (scaled) value of lift and propulsive force as that required for the helicopter. Considering the difference in Reynolds number, the agreement was remarkably good. The effect of a change in blade twist from -14 to -8 degrees on the S-56 helicopter was checked in the wind tunnel with dynamic blades. Reducing the twist on the S-56 provided an important reduction in blade vibratory stresses. The wind tunnel test confirmed this stress reduction almost exactly.

It should be noted that most of the tests conducted with the model blades have not been intended to represent the S-56 blades or any other blade exactly. For example the reduced Reynolds number makes it impossible to use model data for accurate full scale performance predictions. The primary purpose of most of the tests has been to probe new operating regimes of the rotor not possible or not safe to check with flight test, and to provide data for correlation with theoretical analysis. The use of a blade which has dynamic characteristics representative of typical full scale practice ensures that the data obtained will be generally valid and applicable to full scale practice.

Blade Reliability

The dynamic model blades have been tested extensively for a number of purposes over the past several years. In this testing, they have displayed a remarkable degree of ruggedness, with not a single accident due to a blade structural failure. There was one incident of fatigue failure of a rotor head component, which resulted in destruction of the rotor and several cases of an "emergency" quick stop of the drive motor which resulted in the blades hitting the forward lag angle stop so violently as to damage the rotor head and permanently bend the blades in an edgewise direction (Hindsight indicates that it would have been better to allow the rig to coast to a stop than to use electric braking). An experiment was also conducted with coupled blades that resulted in a violent instability which wrecked the rotor. In early versions of the blade, the unbonded leading edge counterweights broke through their restraining wall, on occasion, escaped from the blade at the tip and "shot up" the wind tunnel with steel-cored lead bullets at a velocity approaching that of a .45 calibre slug. Coriolis effects due to the high radial flow of mass resulted in the blade hitting the aft lag stop hard enough to do extensive damage. There were also cases, with early versions of the blade, of pockets slipping at the bond line due to high centrifugal forces and local pocket skin failures due to the high frequency oscillatory airloads. Despite these various mishaps plus a few cases of trailing edge damage from rough human handling, the blades have been, by a very wide margin, the most satisfactory model blades tested by Sikorsky, having been exposed to extreme operating conditions of tip speed, forward speed, advance ratio, lift and propulsive force coefficients, and vibratory stresses and strains. As opposed to test experience with earlier blades, which had in some cases extremely limited operating ranges, there has been essentially no difficulty operating the dynamic blades from zero lift to high lift conditions well into retreating blade stall or from a negative power, high drag condition to a high power, high propulsive force condition. Vibratory stress limits used with the model blades have been placed at approximately double the accepted limits for full scale blades to permit a thorough examination of extreme operating conditions, but no fatigue cracks have ever been observed. In one test in which a non-articulated rotor was being investigated with the same blades, a vibratory stress of ± 25,000 psi, a most extreme value for

aluminum, was encountered for a brief period.

Hover Tests

One of the noteworthy accomplishments with the blade was a hovering test in which maximum operational tip speeds exceeded 1000 feet per second. The maximum tip Mach number at which data were obtained was 0.95. This is much higher than full scale operational values and the highest value ever reached in any Sikorsky test of models or full scale rotors. This test was conducted on the Sikorsky tail rotor test stand facility shown in figure 22. The rotor was a rather effective siren at this speed; an overall sound pressure level of 130 db was recorded 30 feet from the rotor. Centripetal acceleration at the rotor tip approached 8000 "g's", and it was not too surprising that some difficulty with pockets slipping along the bond line was encountered. The purpose of this test was to increase hovering performance data over a wide range of tip Mach numbers and collective pitch values to permit derivation to two-dimensional airfoil section characteristics. In the process of this derivation it was noticed that the resulting airfoil data demonstrated unrealistically low values of lift curve slope at high tip Mach numbers. Examination of blade torsional moments from strain gage data indicated that large torsional moments at high Mach numbers and/or at high values of collective pitch were resulting in a significant change in blade twist and therefore a change in effective pitch angle from the nominal value. A plot of the change in twist calculated from strain gage measurements is shown in figure 23; effective decreases in pitch angle as high as 5 degrees were found. This dynamic twisting was confirmed with special photographic techniques by which tip pitch was compared directly with root pitch during test. When these changes in collective pitch and blade twist were taken into account in the derivation of airfoil section data from hovering performance measurements, the airfoil data became reasonable for the Reynolds numbers of the blade.

Wind Tunnel Tests

The purpose of obtaining experimental airfoil data from hovering tests was to permit theoretical calculations of forward flight performance for correlation with wind tunnel tests of the same model rotor. Both hovering and forward flight tests in this correlation study were supported, in part, by a U. S. Army Transportation Research Command contract, results of which are reported in Reference 2. The rotor operating regimes which have been investigated with these model blades are shown in figure 24 which presents tip speed against forward speed, with solid lines of constant advance ratio (ratio of forward speed to tip speed) and dashed lines of constant Mach

number at the advancing blade tip. The solid circles and crosses represent conditions for which complete maps of rotor performance have been obtained for blades with twists of -8 and -4 degrees respectively. A theoretical performance map showing calculated rotor lift, drag, and torque as a function of angle of attack and collective pitch for one of these conditions is shown in figure 25. The experimentally derived airfoil section data discussed previously were used in this calculation. For comparison, the experimentally determined performance map for the same condition is shown in figure 26. It may be seen that the test points form curves which are as well-defined and exhibit the same general characteristics as the theoretical curves. One theoretical line for a collective pitch of 12 degrees is reproduced from figure 25 on figure 26 for direct comparison. It may be seen that there are some distinct differences between theory and experiment. Based on the dynamic twisting effects which were encountered in hovering, an evaluation was made of similar effects in forward flight. This was found to be considerably more laborious than in hovering, however, because the dynamic twisting as revealed by torsional strain measurments on the blade varied continually with blade azimuth angle around the disk. When these effects were properly accounted for, theory and experiment were brought into substantially closer agreement, except that in the theoretically stalled region at high rotor lifts a significant discrepancy still was observed. It has not been determined whether the dynamic twisting in forward flight, as high as ± 5 degrees in some conditions, is due to blade aerodynamic pitching moments, torsion moments resulting from flatwise and edgewise bending, or a combination of the two. Effects on a full scale blade might not be so severe, since blade airfoil shape can be controlled to a better extent full scale, and aerodynamic pitching moments might be relatively smaller.

A typical overall performance comparison between theory and experiment is shown in figure 27 in which angle of attack and collective pitch have been eliminated as variables by suitable crossplots of the basic performance maps. The power required (torque coefficient) is plotted as a function of rotor lift for two typical values of rotor propulsive force (two values of ratio of aircraft parasite drag area f to disk area πR^2). Theory and experiment agree well up to the theoretically predicted rotor stall limit, beyond which theory becomes increasingly pessimistic. The reason for this discrepancy has not been identified as of the date of writing this paper, but may be associated with a spanwise boundary layer flow due to centrifigal effects. A full scale Sikorsky main rotor with special surface pressure instrumentation is scheduled for test in the NASA Ames 40 by 80 foot wind tunnel in 1964 and is expected to provide an answer to this problem. It is believed certain that experimental errors are not responsible for the observed differences between theory and experiment. Figure 28 presents data for the same conditions as figure 26 from two test programs conducted 16 months apart on different but geometrically identical rotor blades. Excellent agreement is shown, demonstrating long term reliability and repeatability of the data. The only discernible difference between the two tests is a slight trend toward lower torque required with the all metal blades due to slightly lower airfoil profile

drag compared to the paper-pocketed blades.

One important result of the forward flight tests and correlation studies is that the effects of high advancing tip Mach number seem to be accurately predictable with available theoretical techniques. Figure 29 presents a comparison between theory and experiment at a constant lift, propulsive force, and forward speed as tip speed and corresponding advancing tip Mach number are varied. Except at the left end of the curve where the theory predicts that the rotor is stalled, nearly perfect correlation is noted between experimental points (circles) and theory (solid line) up to an advancing tip Mach number of 1.0. The dashed line indicates what would be predicted if airfoil characteristics as affected by high Mach number were not included in the calculation. The shaded area, labeled $\Delta (HP/L)_M$, indicates the increase in power per unit lift due to Mach number effects, and shows that as advancing tip Mach number is increased beyond 0.9, a severe power penalty is paid.

In another U.S. Army TRECOM sponsored study, reported in Reference 3, calculations were made to determine the optimum rotor geometry for a high speed pure helicopter and an experimental check of these predictions made with the dynamic model blades. It was shown that a blade of conventional planform was close to optimum providing the blade twist was reduced from the usual value of -8 degrees to approximately -4 degrees, because of the effects of twist on vibratory stress and consequent blade life at high speeds. The predictions in general were confirmed by the dynamic blade tests, which also showed the effects of varying lift and propulsive force on blade stresses, as shown by a typical example in figure 30.

Vibration Tests

One experimental program that utilized the dynamic blades was a measurement of rotor impedance, important to rotary wing vibration theory. Because the blades are hinged at the root end and are flexible as well, it is difficult to predict the vibratory root end shear reactions of the blade when the rotor head is vibrating in various modes at various frequencies. To determine the rotor impedance or effective resistance to such root end motion, mechanical shakers were mounted on the rotor test rig to provide a forced motion over a range of frequencies, while the rotor was in operation at rotational speeds of interest. Strain gage instrumentation at the blade root plus flapping and lag measurements were used to resolve root end forces. Additional vibration research at forward speed conditions is planned for the near future with a specially designed rotor head that will measure root end vibratory shears directly. The use of dynamic model blades for vibration research in the wind tunnel is, of course, essential.

DYNAMIC MODEL BLADE DESIGNED FOR HIGHER SIMULATED FORWARD SPEEDS

The dynamic model blades previously described are capable of reproducing full scale compressible flow or Mach number effects, and have been extremely useful in helping to advance the state of knowledge regarding helicopter rotors. Because of the high tip speeds utilized, Reynolds numbers are reasonably high despite the small chord dimension of the blades, and model forces and moments produced are high considering the overall model size, thus facilitating accurate measurements. For dynamic similarity, however, forward speed of the test must be equal to the simulated full scale forward speed condition, and the available wind tunnel speed is limited, with the rotor test equipment installed, to a little more than 160 knots. This is higher than current helicopter operational speeds but less than record speeds. While higher forward speed conditions can be and have been simulated aerodynamically (neglecting Mach number effects) by a reduction of model tip speeds to less than would be used full scale, dynamic similarity is lost because aerodynamic forces are reduced but blade stiffness is not. Thus in figure 24 operation of the model rotor at 160 knots and an advance ratio of 1.0 with a low value of advancing tip Mach number corresponds to operation at 300 knots at the permissible advancing tip Mach number of 0.9. With dynamic similarity lost, however, such test results could be very misleading with regard to blade dynamic behaviour. Consequently it was considered necessary to develop a new blade model which would permit dynamic similarity at reduced tip speeds and thus permit higher simulated forward speeds with realistic elastic effects. Mach number similarity had to be sacrificed, but as was mentioned in the section on results of tests of the first blades, the Mach number effects appear to be predictable with available theoretical techniques.

The speed potential of rotary wing aircraft, in the form of the so-called compound helicopter configuration with wings and auxiliary propulsion, is believed to be at least 300 knots and possibly as high as 400 knots. As pointed out in Reference 4, the performance characteristics of rotors can be surprisingly good up to at least 300 knots. An artist's sketch of a possible compound helicopter is shown in figure 31. The limitation to speed is no longer retreating blade stall as it is for the pure helicopter, but rather, rotor control problems, stability of blade flapping motion, and aeroelastic flutter problems in the "reverse velocity" region on the retreating half of the disk where the airflow relative to the local airfoil section is from trailing edge to leading edge rather than in the usual direction. At high forward speeds, the tip speed of the rotor must be reduced to avoid sonic relative velocities on the advancing tip and excessive power penalties, with the result that the advance ratio or ratio of forward to tip speeds increases rapidly with

forward speed, up to a value of 2.0 or more at 400 knots. In this circumstance, the "reverse velocity" region is very large, and it is not surprising that aeroelastic effects predominate.

Basic Design

While present main rotor design practice is not necessarily optimum at such high forward speeds and advance ratios, it was known from prior studies that the speed potential of the present design is much higher than current operational speeds. Thus it was decided to keep the same basic design in the construction of a new dynamic blade model for high simulated speeds, ensuring that the blade would be satisfactory at low to moderate speeds and also permitting direct correlation of data from the two test programs. It was desired to simulate a forward speed of at least 400 knots, a factor of 2.5 greater than actual tunnel speed. It was realized that if the blade were designed to simulate full scale Froude number (gravity effects the same as full scale), the simulated velocity would increase proportional to the square root of the scale, or $\sqrt{8} = 2.83$ for the model in question. As discussed previously, gravity effects on the rotor are not considered significant for normal helicopter operation, but as full scale tip speed is reduced the centripetal accelerations are also reduced, so that gravity will start to play an increasingly important role in rotor behaviour. At extremely high advance ratios, therefore, or for rotor starting or stopping tests, the model rotor will have to be oriented in a horizontal plane rather than in a vertical plane as at present. Model blades having the proper full scale Froude number will permit such tests with exact gravity effects, and can also be applied to a semi-"free flight" aircraft model test wherein gravity effects are of prime importance for overall aircraft dynamic behaviour even at normal rotor tip speeds. Thus it was decided to build the blades with the stiffness scaled down to the point where gravity effects were the same as full scale. This scaling would automatically permit simulated forward speeds of over 400 knots in the UAC 18 foot wind wind tunnel.

Referring to the dimensionless ratios established in the section on selection of design parameters for the full scale Mach number blades, the same ratios are required for the new blade, except that flight and tip Mach numbers are of necessity moved to the "Secondary Importance" list, and ratio (12) - $\Omega^2 R/g$ or Froude number, is moved to the "Primary Importance" list. To keep the ratio $\Omega^2 R/g$ the same as full scale, it is obvious that rotational speed Ω must be increased proportional to the square root of the reduction of radius R, since there is no convenient method of controlling the acceleration due to gravity g. For a 1/8 scale model Ω must be increased by a factor of $\sqrt{8}$, and tip speed ΩR therefore is reduced by a factor $\sqrt{8} = 2.83$ from the simulated full scale value.

Forward speed for the model is also reduced from full scale value by the same factor. Mach numbers are reduced by a factor of 2.83, and Reynolds numbers, which were previously one eighth of full scale, are reduced by an additional factor of 2.83.

Blade external geometry remains the same, and dimensionless ratios (5) and (6) relating to blade mass indicate that the mass distribution and total weight of the blades remains the same as for the previous model. Dimensionless ratio (7) relating to blade stiffness, $EI_{xx}/\rho V^2R^4$, indicates that the stiffness EI_{xx} must be reduced by a factor of 8 from the previous model since V^2 has decreased by a factor of 8 while ρ and R remain constant. The other stiffnesses EI_{yy} and GJ obviously must also decrease by the same factor. For the new blade it would have been possible to take the design approach represented by figure 4b, but the general approach taken to accomplish the required reduction of stiffness was to leave the moments of inertia I_{xx}, I_{yy}, and J essentially the same but reduce the moduli of elasticity E and G. By leaving the shape of the spar essentially unchanged, the assembly jigs and trailing edge pockets used on the full scale Mach number blade could be utilized. The problem was therefore to find a material having the appropriate moduli of elasticity. The value of Youngs modulus E for aluminum (used in the previous model blade) is 10×10^6, so that the desired value of E for the new spar was an eighth of that value or 1.25×10^6. Unfortunately metals have values almost universally much higher than this and common plastic materials have much lower values. Wood has about the right value of E, but is highly non-isotropic, with a shear modulus, G,very much lower than that required. The approach finally taken was to combine fiberglass, plastic, and paper fillers to tailor the characteristics to the desired values.

Detailed Design of Fiberglass Blades

The initial phase of the design of the fiberglass blade was devoted entirely to the development of a spar whose flatwise, edgewise and torsional stiffness would be 1/8 that of the present metal dynamic blade. Spar samples were fabricated using various types of fiberglass cloth necessary to produce skin thicknesses the same as those in the metal spar. These materials were at first molded over the same contoured die used in forming the aluminum leading edge, but where the aluminum has a tendency to spring out after forming, the fiberglass components tend to spring in with a resulting shape of unsatisfactory contour. This was also true in the layup of the U-Section. Both dies were built up gradually until proper contour was attained. Additional spars were made, initially, with the fibers of all layers in the same direction such as 0°, 90° and 45°, and secondly, in combinations to see if isotropic characteristics could be established. A spar with an average stiffness in the required directions approximately 1/4 that of the metal blade was the most flexible that resulted from these

trials.

A sandwich construction varying layers of fiberglass with layers of cloth mat as a filler showed that lower values of stiffness could be obtained. However, the overall surface finish, because of the inconsistency in the cloth mat, was very bumpy.

A cotton cloth, pellon, was substituted for the cloth mat, but the surface imperfections were still present. A special quality paper, used in stenciling because of its high absorption rate was tried next and produced excellent results.

While various methods in the construction of the spar were being investigated, special attention was being made to determine what effects the other blade components would have on the overall stiffness of the blade. Whereas the components had negligible effect on the metal blade stiffness, they now contributed increases of 25% flatwise, 33% edgewise and 10% torsionally to the stiffness of the fiberglass blade. This changed the requirements for the spar design. To arrive at a blade 1/8 the stiffness of the metal blade requires a fiberglass spar with stiffness approximately 1/11 edgewise, 1/10 flatwise and 1/9 torsionally of those of the metal blade. Since special thicknesses of fiberglass cloth which are required to fabricate this spar were not immediately available, the first set of blades made, with the materials on hand, resulted in an overall scaled stiffness of 1/6 the metal blade. Even though the gravity effects obtained at this higher stiffness are not exactly the same as full scale, these blades permit simulated forward speeds approaching 400 knots in the wind tunnel. At the date of writing of this paper, these blades have been completed but not yet tested and the exact Froude number blades are in the construction stage.

The weight of the composite fiberglass and paper spar is only 40% that of the metal spar. Since the mass distribution and total weight of both blades must remain the same, special rubber plugs, contoured to the inside dimensions of the spar, were bonded at one inch intervals along the length of the blade to offset this difference in spar weight and produce the same mass distribution per inch as the metal blade. These plugs were designed so that their center of gravity was slightly forward of the quarter chord of the section. This nose-heavy contribution to the blade section balance was necessary to offset a modification in the counterweight design. The steel-reinforced solder counterweights used on the metal blade, if bonded to the fiberglass blade, would result in a 50% increase in the edgewise stiffness of the spar. By using short lengths of plain lead with gaps of 0.1 inch between adjacent weights this increase in edgewise stiffness could be reduced to 10% because of the low modulus of elasticity of lead and the lack of spanwise continuity. The loss in counterbalance weight caused by the gaps is compensated by the nose heavy unbalance of the rubber plugs.

The pockets, tip cap, tip block, and root block are the same as those used on the metal dynamic blade, with only minor changes incorporated to facilitate their construction and assembly. The appearance of the assembled blade is identical to the aluminum spar blade except for the color of the spar. When picked up. however, the "feel" of the blade is substantially different because of the greatly increased bending flexibility.

It was noted that the root end mass was higher than desired for the metal blades, because of the inability to scale down the feathering bearing system size and still carry the centrifugal loads With the newer blades designed for lower tip speeds, however, centrifugal loads are greatly reduced. A new lightweight feathering system has been built for the new blades that provide the properly scaled weight.

Small Scale Tests

As stated previously, the new model blades have been completed but not tested when this paper was written. A somewhat similar blade on a smaller scale has, however, been developed and tested by United Aircraft Research Laboratories and reported in Reference 5. This blade represents a 1/18, rather than 1/8, scale of the S-56 main blade, providing a rotor diameter of 4 feet. This blade, also built to have the proper full scale Froude number, was constructed by the approach represented schematically in figure 4b. Details of blade construction are shown in figure 32. Flatwise bending and torsional stiffness were properly scaled, but no attempt was made to provide the proper edgewise stiffness, nor was a lag hinge used on the rotor head. The justification for this was that it was an exploratory program of investigation of high forward speed conditions, and it was considered that the blade flapping motion combined with flatwise bending and torsional flexibilities predominate in the overall aeroelastic behaviour of the blade.

These blades have been tested in the UAC 4 x 6 foot subsonic wind tunnel over a wide range of test conditions, up to tunnel speeds of 100 miles per hour (corresponding to a simulated full scale speed of over 350 knots) and have provided extremely valuable data for both correlating with new theory for rotor behaviour at high speeds and for guiding the test program to be conducted with the 9 foot diameter rotor model. An example of data obtained with the 4 foot diameter model is shown in figure 33 which shows operating stability limits determined experimentally and correlation with theoretically predicted limits. As may be seen, there is excellent qualitative agreement, and it is expected that future refinements in theory as well as in experimental data will provide still greater confidence in the ability to predict high speed rotor characteristics.

CONCLUDING REMARKS

The effort devoted to the development of dynamic model rotor blades at Sikorsky, while sometimes slow and painstaking, is believed to have been well repaid in terms of the advancement in the state of knowledge resulting from the tests they have permitted. It is expected that they will continue to be used in many future research projects. It is of interest to note that some of the construction and static test techniques first used on the model blades are finding application in the construction of new full scale blades. It is likely that the development of certain new blades will be preceeded by tests of model blades dynamically scaled from the full scale design. Specifically, the use of dynamic model blades is believed to be essential to the successful development of a compound helicopter in the 300 to 400 knot category or a retractable rotor convertiplane for much higher forward speeds.

REFERENCES

1. Kee, Robert M., Main Rotor Blade Design and Development, IAS Report No. 59-28, paper presented at the IAS 27th Annual Meeting, New York, New York, January 26-29, 1959.

2. Rabbott, John P., Jr., Comparison of Theoretical and Experimental Model Helicopter Rotor Performance in Forward Flight, U. S. Army TRECOM Report TREC 61-103 (Sikorsky Aircraft Report SER-50129), July, 1961.

3. Rabbott, John P., Jr., A Study of the Optimum Rotor Geometry for a High Speed Helicopter, U. S. Army TRECOM Report TREC 62-53 (Sikorsky Aircraft Report SER-50254), May, 1962.

4. Fradenburgh, Evan A , Aerodynamic Efficiency Potentials of Rotary Wing Aircraft, paper presented at the American Helicopter Society Sixteenth Annual National Forum, Washington, D. C., May 11-14, 1960.

5. Arcidiacono, Peter J., Analytical and Experimental Investigations of the Aeroelastic Characteristics of Helicopter Rotors Operating at High Advance Ratios, United Aircraft Corporation Research Laboratories Report B-110049-2, March, 1963.

TABLE I - SCALING RATIOS

Model linear dimension = 1/S x full scale linear dimension

(Numerical values correspond to 1/8 scale model)

Subscript m - model
Subscript fs - full scale

Parameter	Full Scale Mach Number Blade		Full Scale Froude Number Blade	
Radius & other linear dimensions R_m/R_{fs}	$1/S$	(1/8)	$1/S$	(1/8)
Areas- A_m/A_{fs}	$1/S^2$	(1/64)	$1/S^2$	(1/64)
Mass per unit length m_m/m_{fs}	$1/S^2$	(1/64)	$1/S^2$	(1/64)
Total mass M_{b_m}/M_{bfs}	$1/S^3$	(1/512)	$1/S^3$	(1/512)
Stiffness $EI_{xx_m}/EI_{xx_{fs}}$, etc.	$1/S^4$	(1/4096)	$1/S^5$	(1/32,768)
Angular velocity Ω_{in}/Ω_{fs}	S	(8)	$\sqrt{S}$	(2.83)
Linear velocities $(\Omega R)_m/(\Omega R)_{fs}$, V_m/V_{fs}	1	(1)	$1/\sqrt{S}$	(0.353)
Mach number M_m/M_{fs}	1	(1)	$1/\sqrt{S}$	(0.353)
Froude number $(\Omega^2R/g)_m/(\Omega^2R/g)_{fs}$	S	(8)	1	(1)
Reynolds number RN_m/RN_{fs}	$1/S$	(1/8)	$1/S^{\frac{3}{2}}$	(.044)
Output forces F_m/F_{fs}	$1/S^2$	(1/64)	$1/S^3$	(1/512)
Output moments $Mom._m/Mom._{fs}$	$1/S^3$	(1/512)	$1/S^4$	(1/4096)
Output elastic strains ϵ_m/ϵ_{fs}	1	(1)	1	(1)
Natural frequencies ω_m/ω_{fs}	S	(8)	$\sqrt{S}$	(2.83)

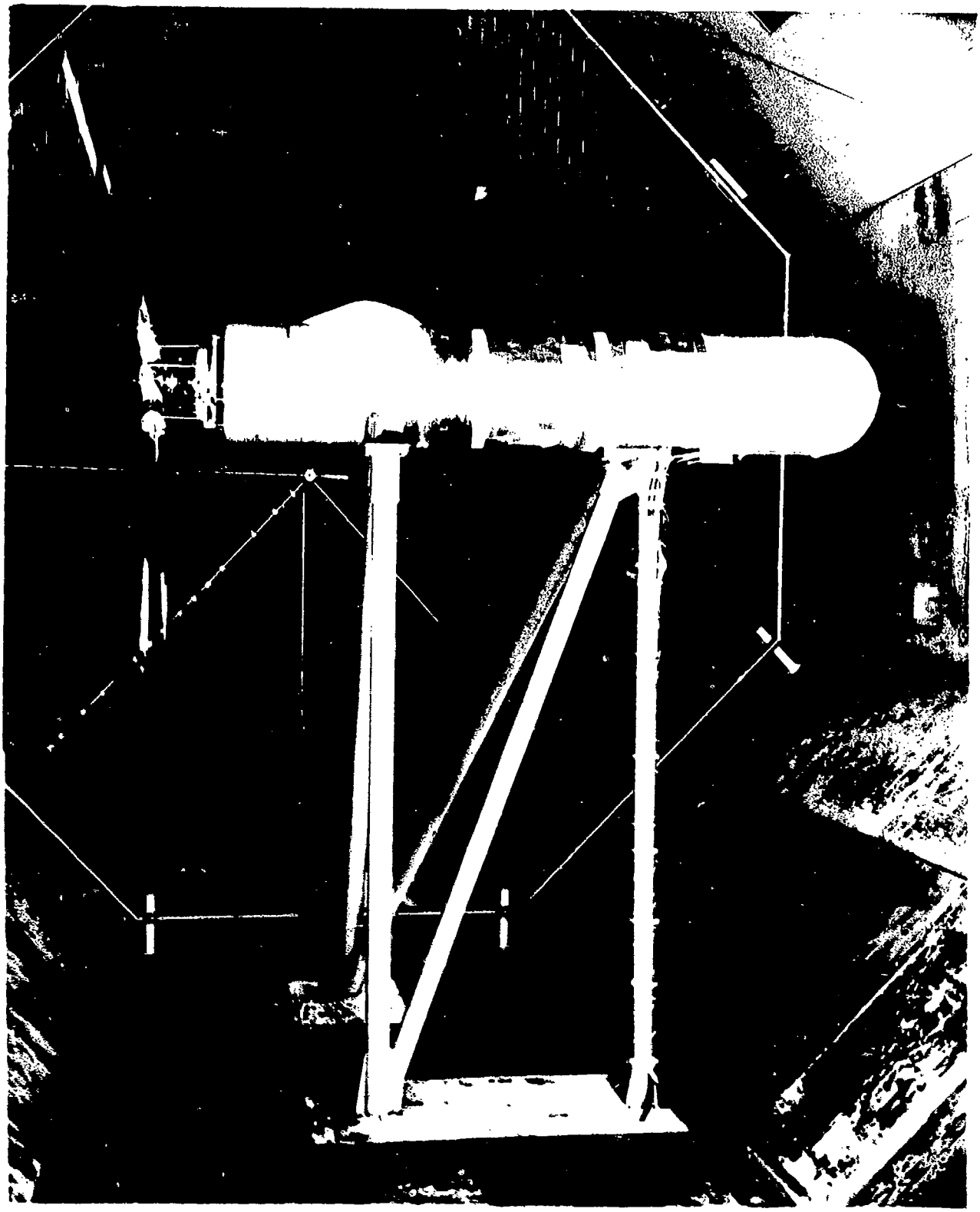

FIG. I. ROTOR TEST RIG IN UAC 18 FOOT WIND TUNNEL, 1954 CONFIGURATION

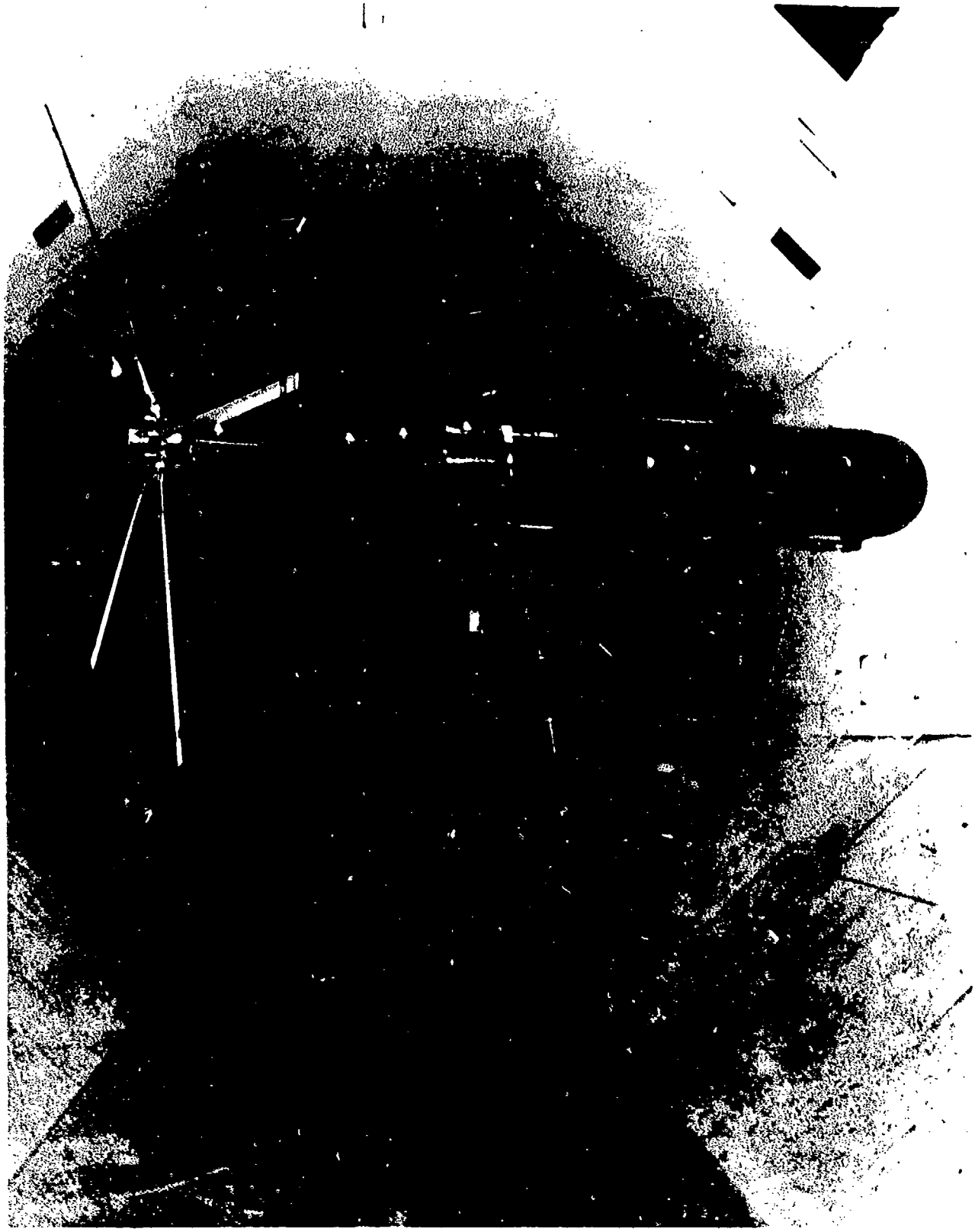

FIG. 2. SIKORSKY ROTOR TEST RIG WITH DYNAMIC MODEL BLADES

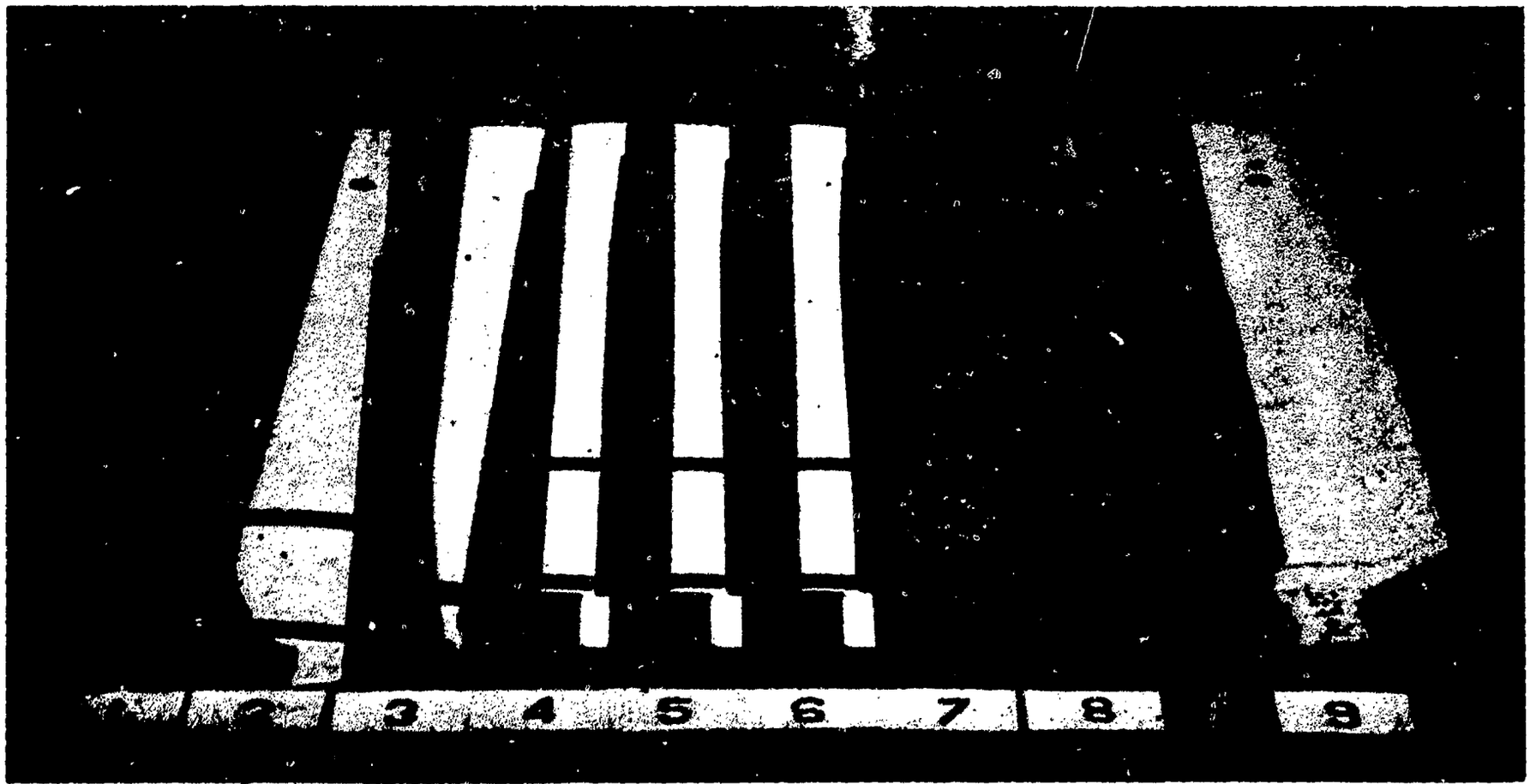

1. DYNAMIC MODEL BLADE
2. 3:1 TAPER BLADE
3. 1:2 INVERSE TAPER BLADE
4. -16° TWIST BLADE
5. -8°TWIST BLADE
6. 0° TWIST BLADE
7. CAMBERED SECTION FIBERGLASS BLADE
8. LIGHT WEIGHT TAIL ROTOR TYPE BLADE
9. STANTARD METAL TAIL ROTOR TYPE BLADE

FIG. 3. MODEL BLADES TESTED

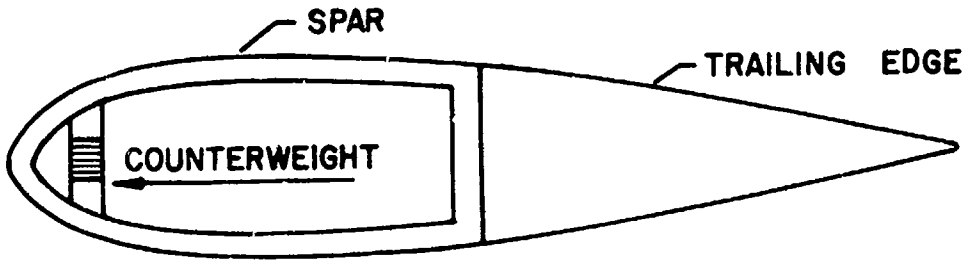

(a) FULL SCALE BLADE STRUCTURE AND POSSIBLE MODEL STRUCTURE

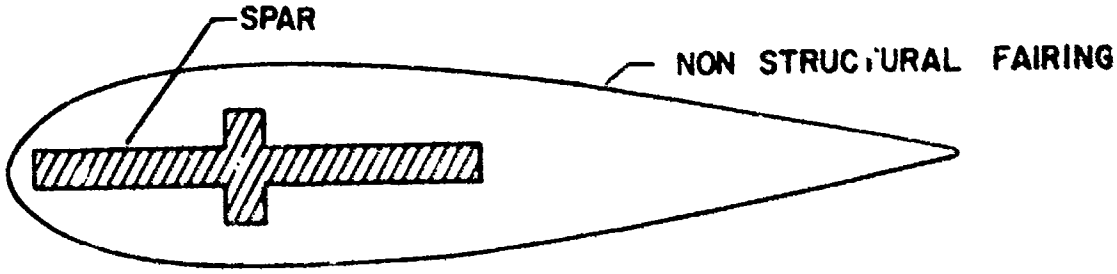

(b) POSSIBLE APPROACH TO MODEL STRUCTURE FOUND NOT SUITABLE FOR FULL SCALE MACH NUMBER BLADE

FIG. 4. BLADE CROSS SECTION SHAPE

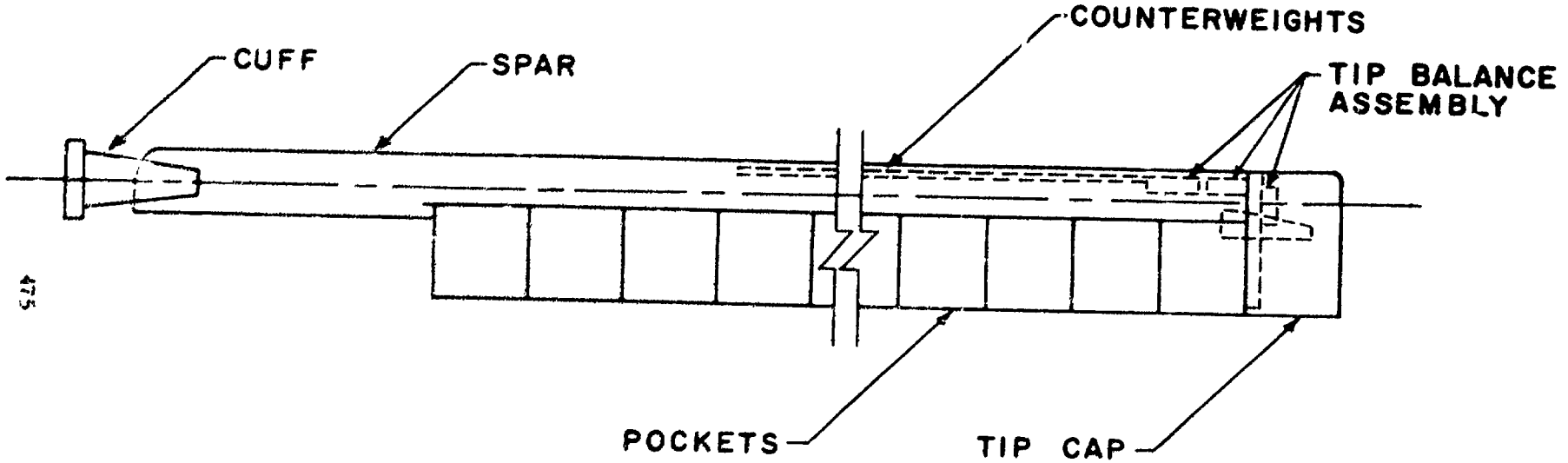

FIG. 5. MAIN ROTOR BLADE ASSEMBLY

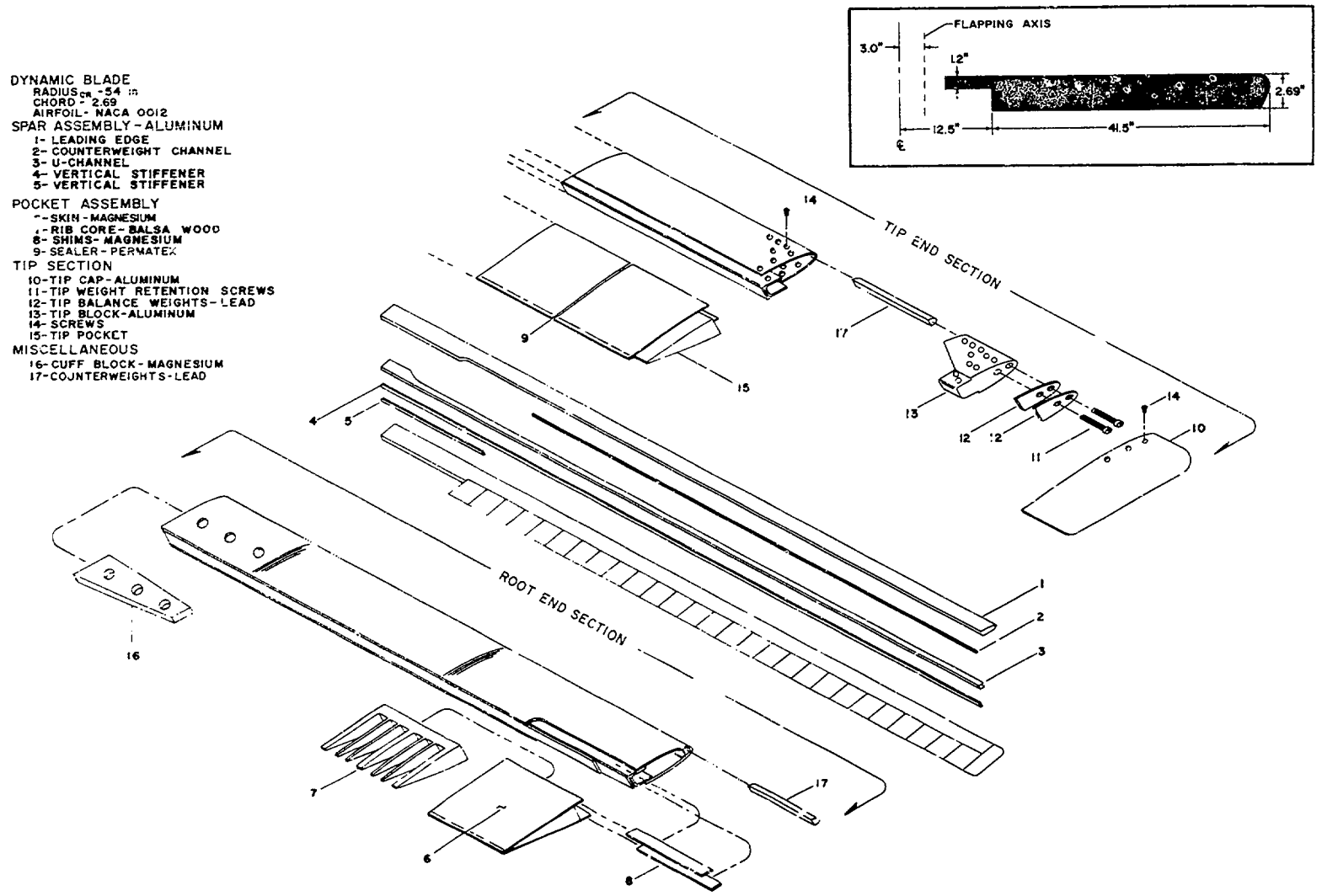

FIG. 6. DYNAMICALLY SCALED BLADE-EXPLODED VIEW

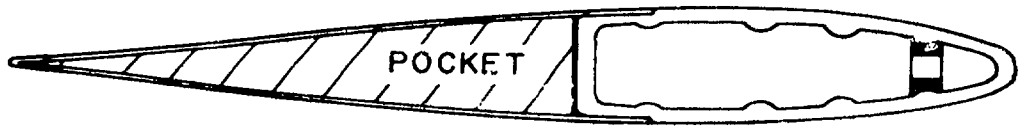

FULL SCALE BLADE
TYPICAL SECTION
CHORD - 21.50 INCHES

SPAR - ALUMINUM EXTRUSION
CONSTANT INSIDE CONTOUR
VARIABLE WALL THICKNESS

COUNTERWEIGHT - STEEL BAR
WITH RUBBER SHOCK MOUNTS

POCKET - ALUMINUM SKIN WITH
ALUMINUM RIBS

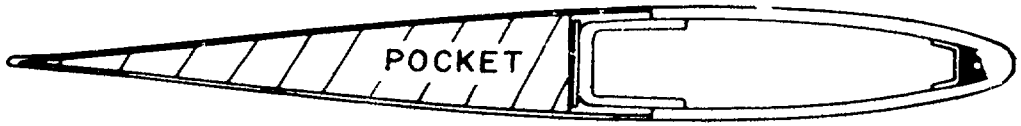

DYNAMIC MODEL BLADE
TYPICAL SECTION
CHORD - 2.69 INCHES

SPAR - COMPOSED OF ALUMINUM
LEADING EDGE, U-SECTION
COUNTERWEIGHT CHANNEL &
TRAILING EDGE STIFFENER
BONDED TOGETHER WITH AF-6
SCOTCHWELD FILM ADHESIVE-
VARIABLE WALL THICKNESS

COUNTERWEIGHT - LEAD ROD
WITH STEEL CORE FOR
COLUMN STRENGTH

POCKET - MYLAR-COATED PAPER
SKIN WITH BALSA WOOD RIBS

FIG. 7. BLADE CONSTRUCTION DETAILS

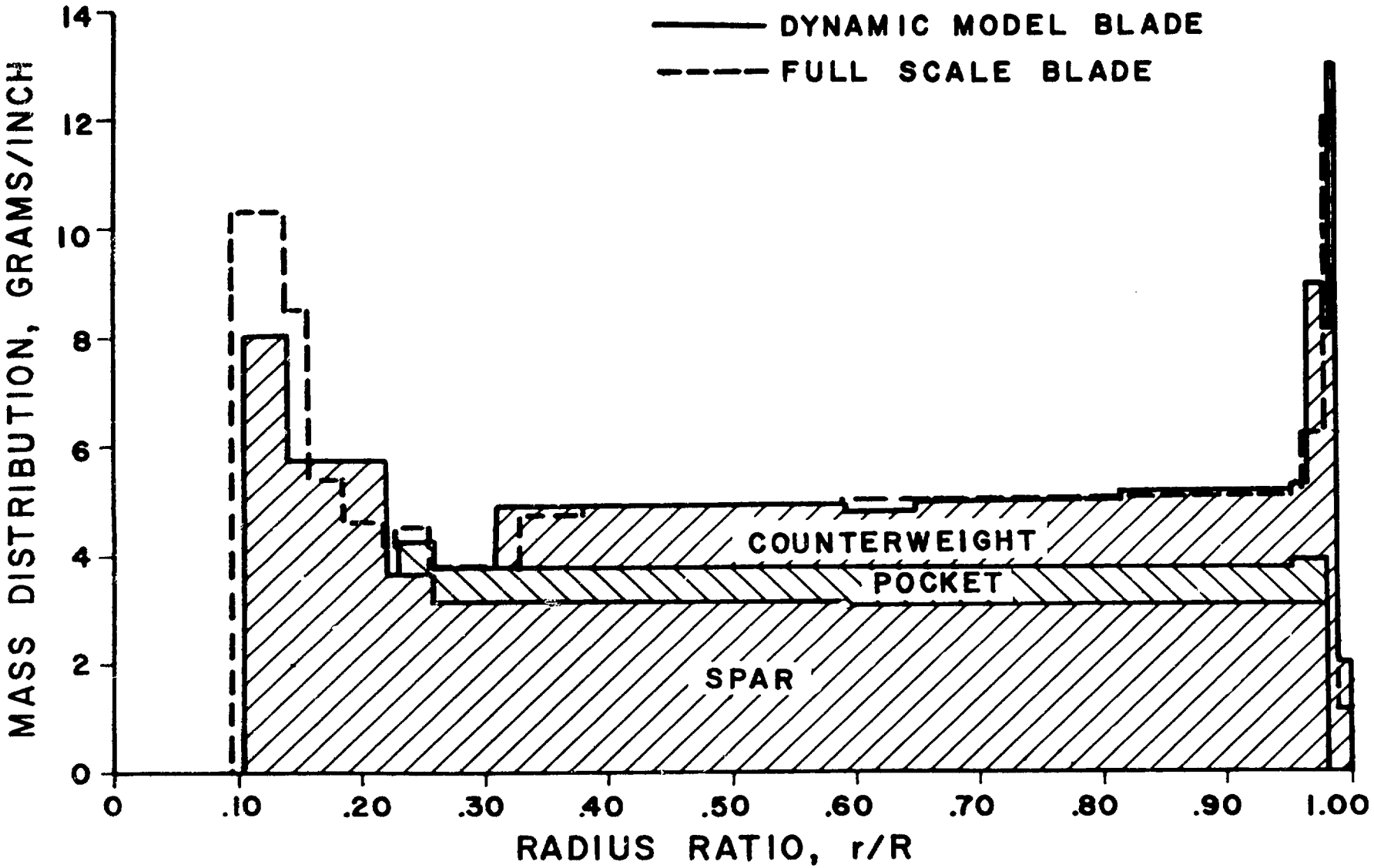

FIG. 8. COMPARISON OF BLADE MASS DISTRIBUTION

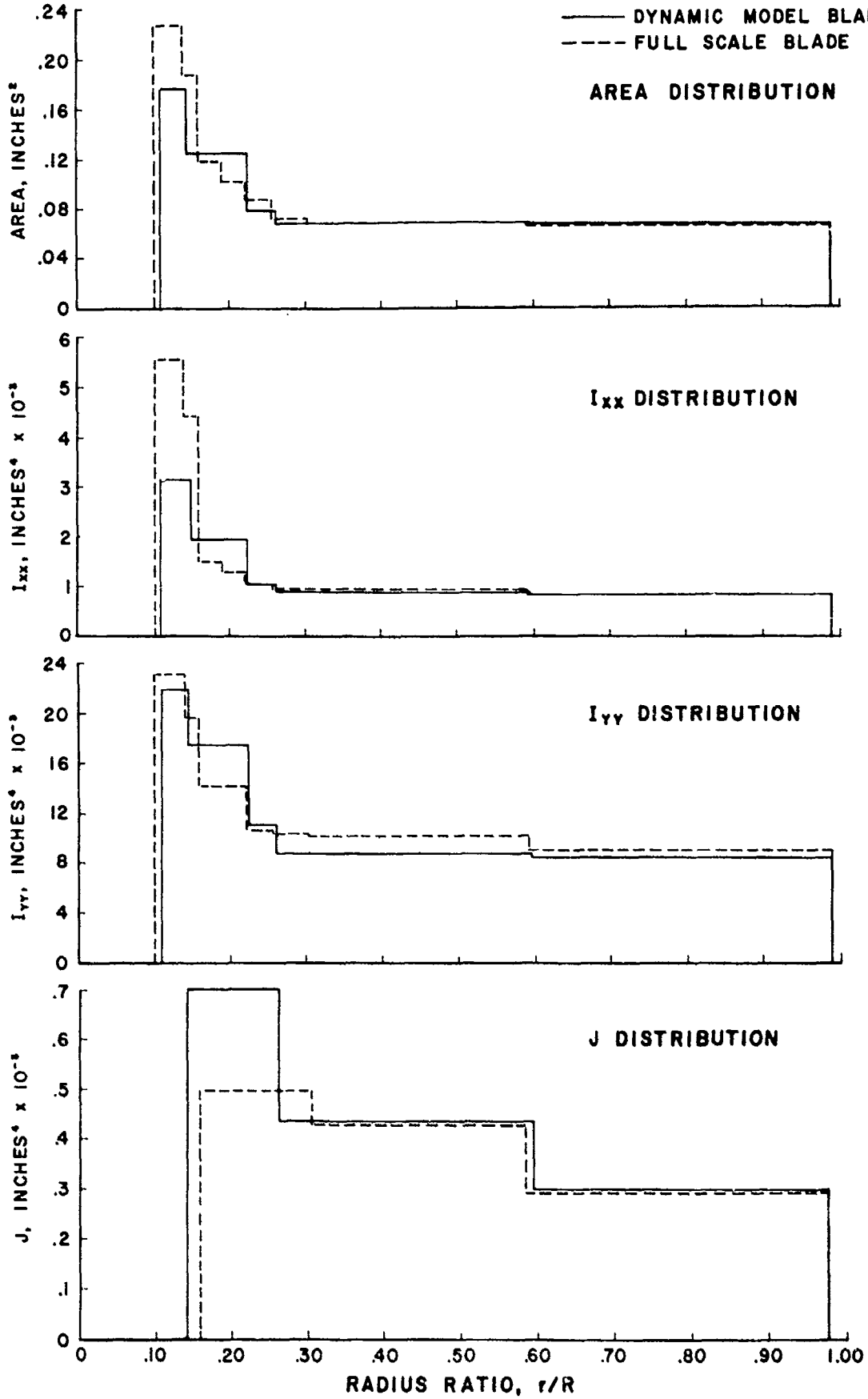

FIG. 9. COMPARISON OF MODEL & PROTOTYPE PHYSICAL PROPERTIES

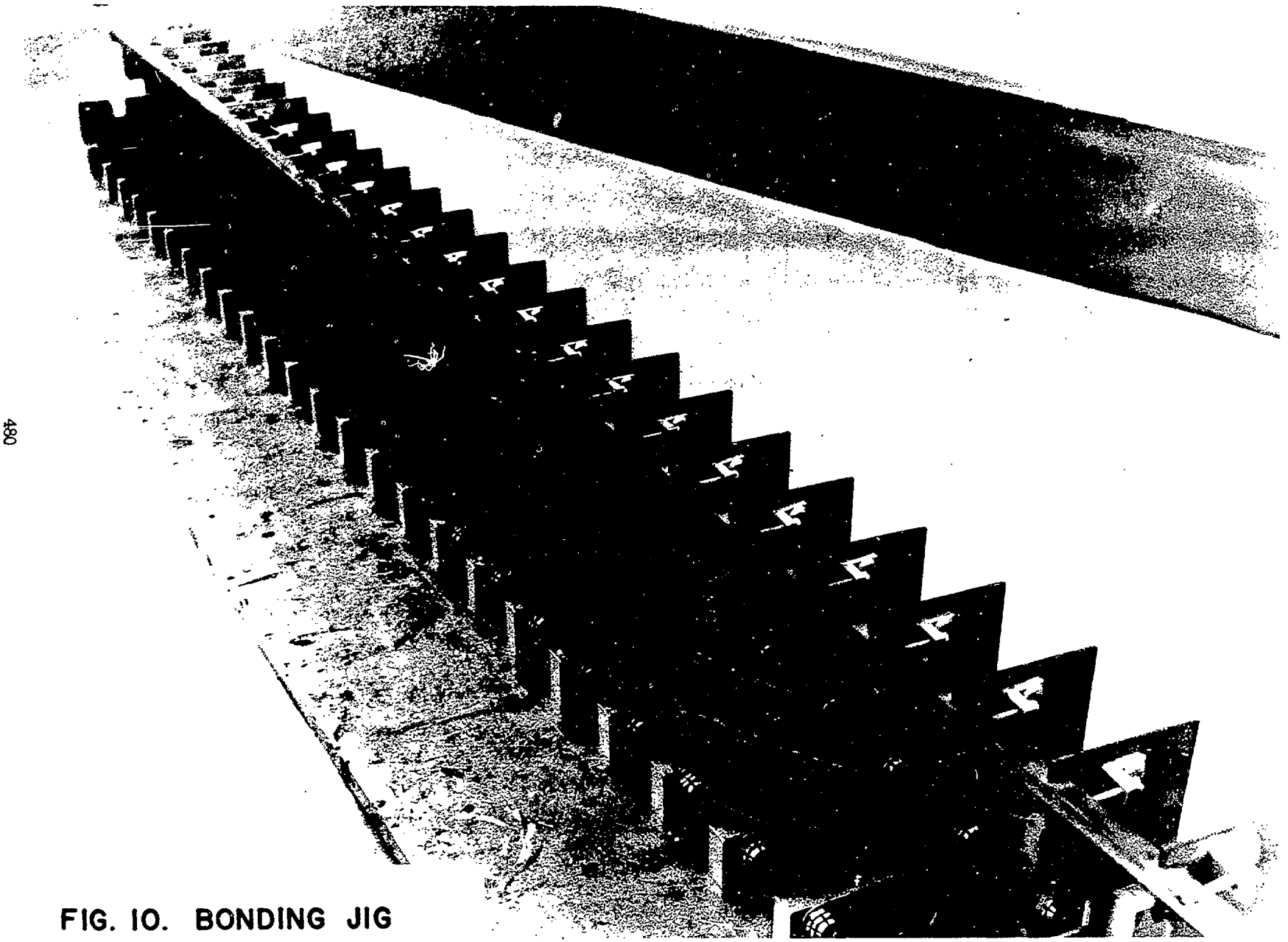

FIG. 10. BONDING JIG

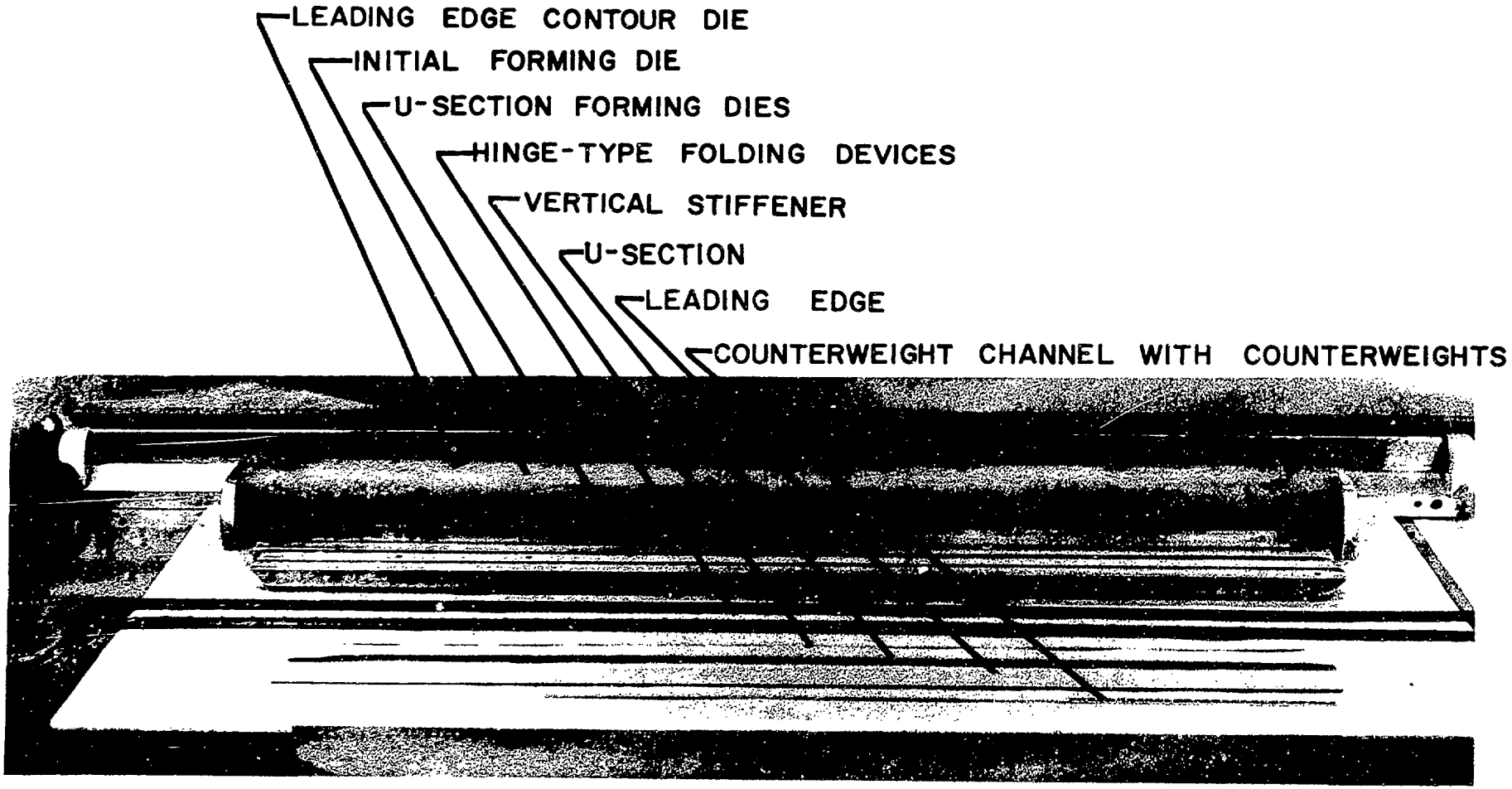

4821

FIG. 11. JIGS AND COMPONENTS USED IN CONSTRUCTION OF SPAR

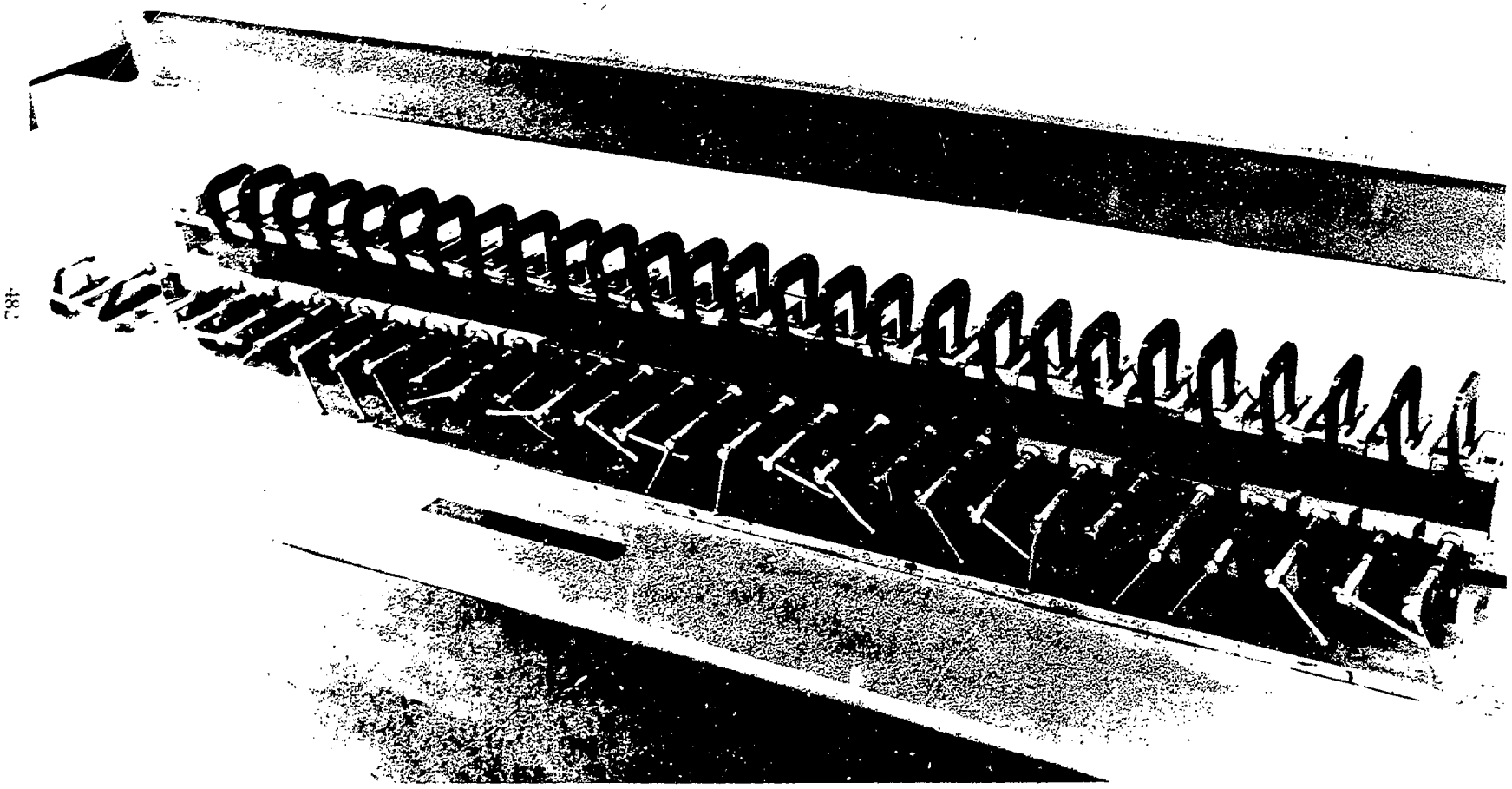

FIG. 12. BLADE IN JIG READY FOR BONDING

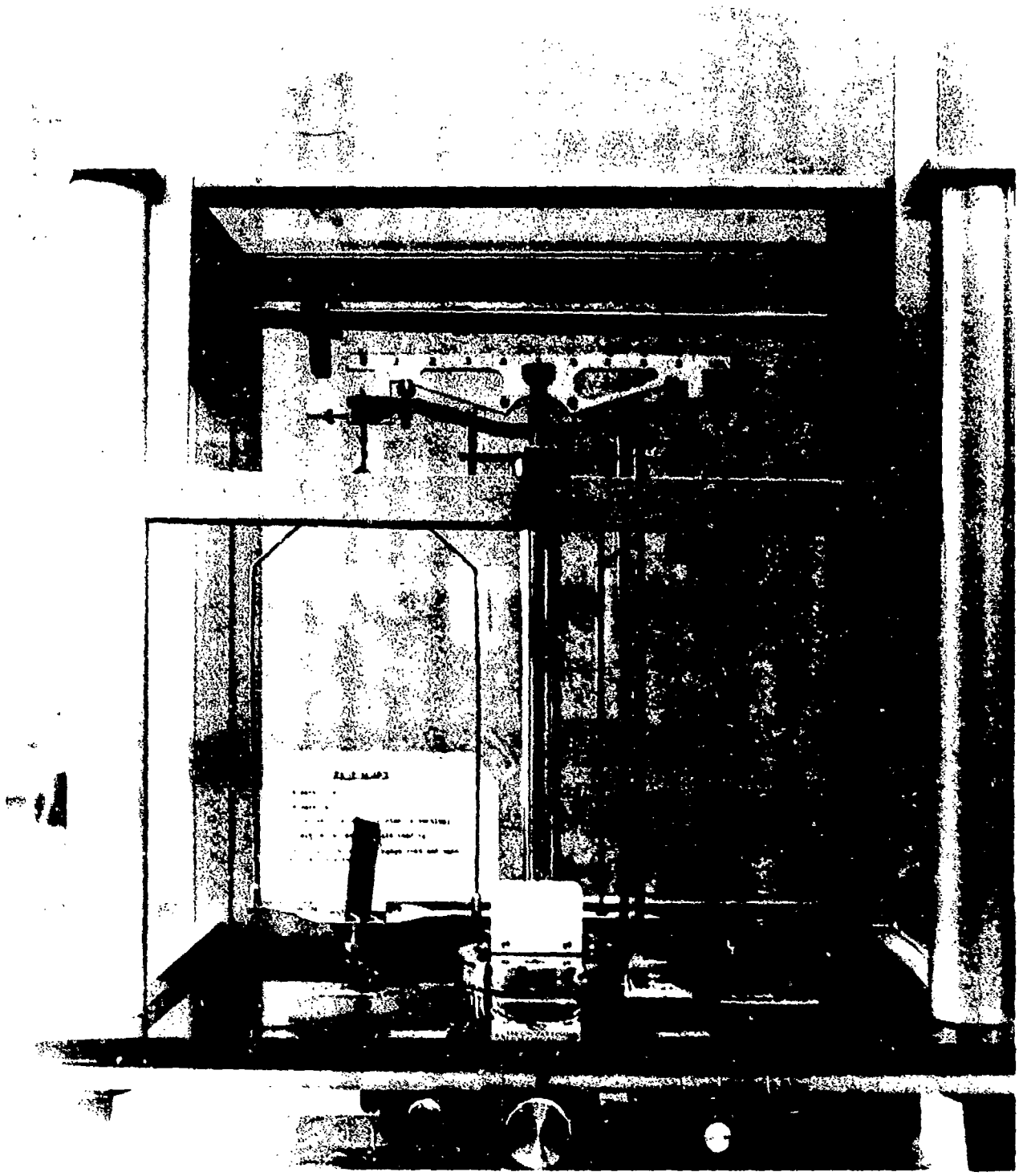

FIGURE 13. CHEMICAL BALANCE USED IN WEIGHING COMPONENTS OF BLADE

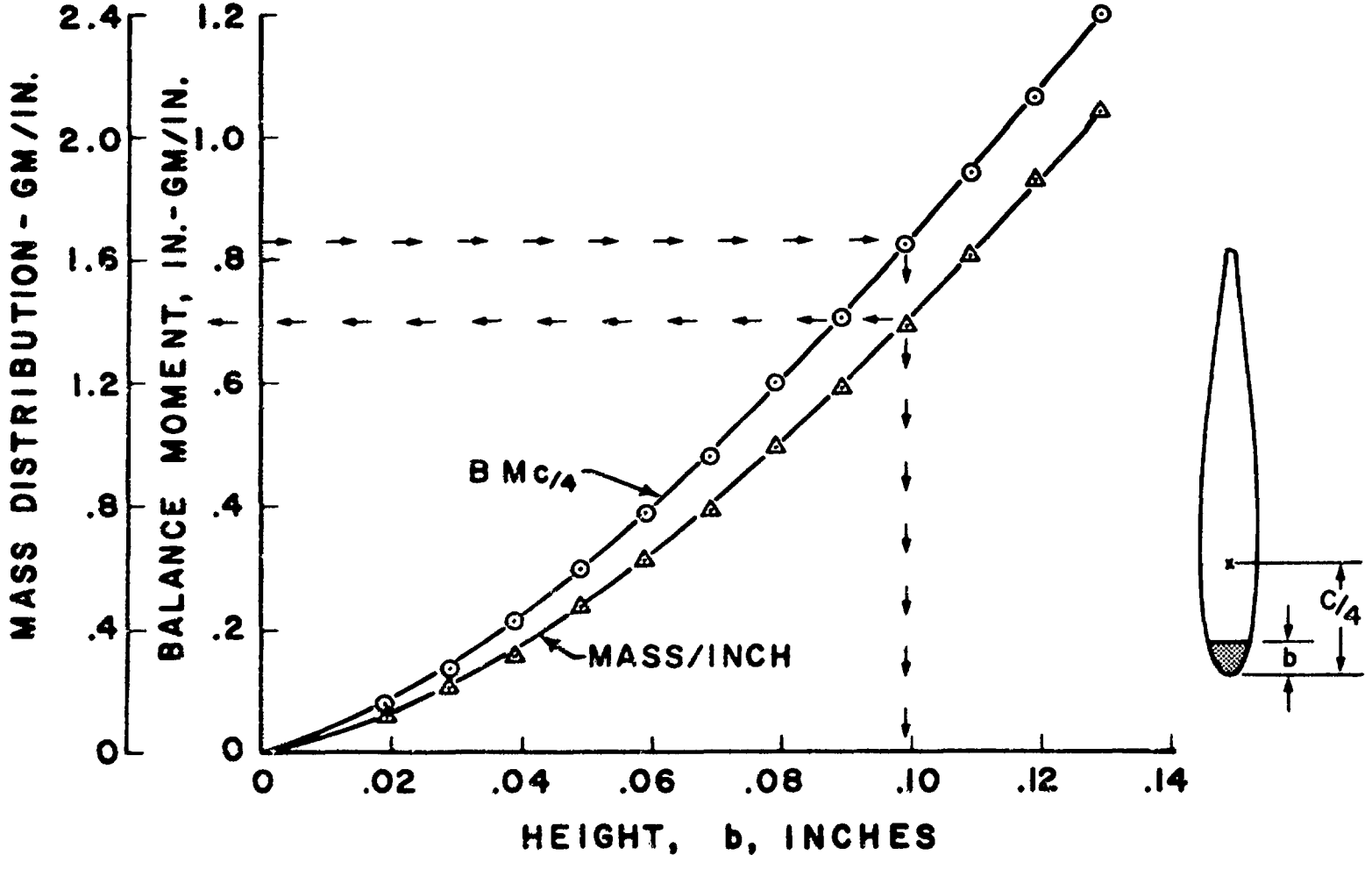

FIG. 14. MEANS USED TO DETERMINE SIZE OF COUNTERWEIGHT

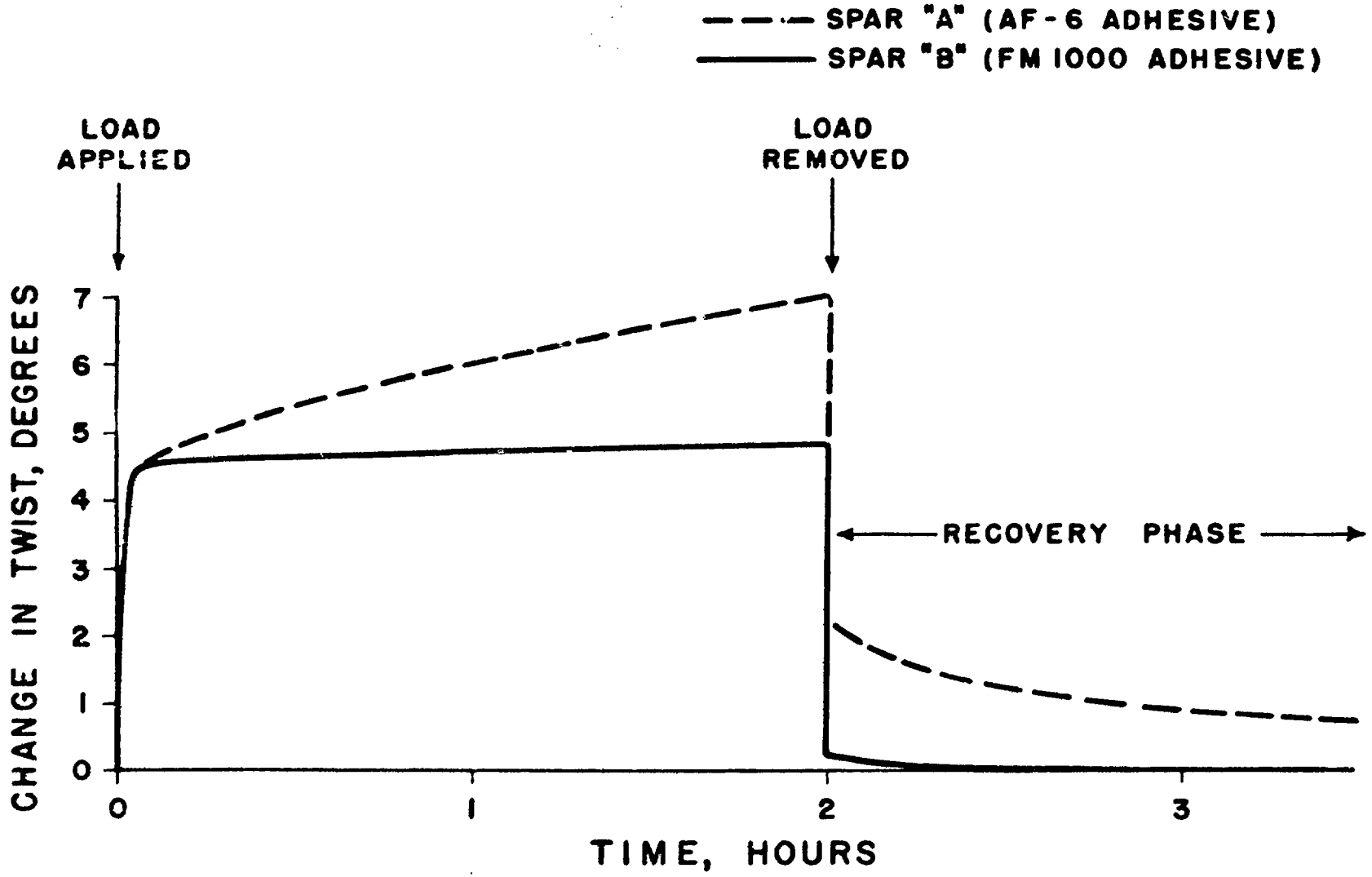

FIG. 15. TORSIONAL CREEP TEST

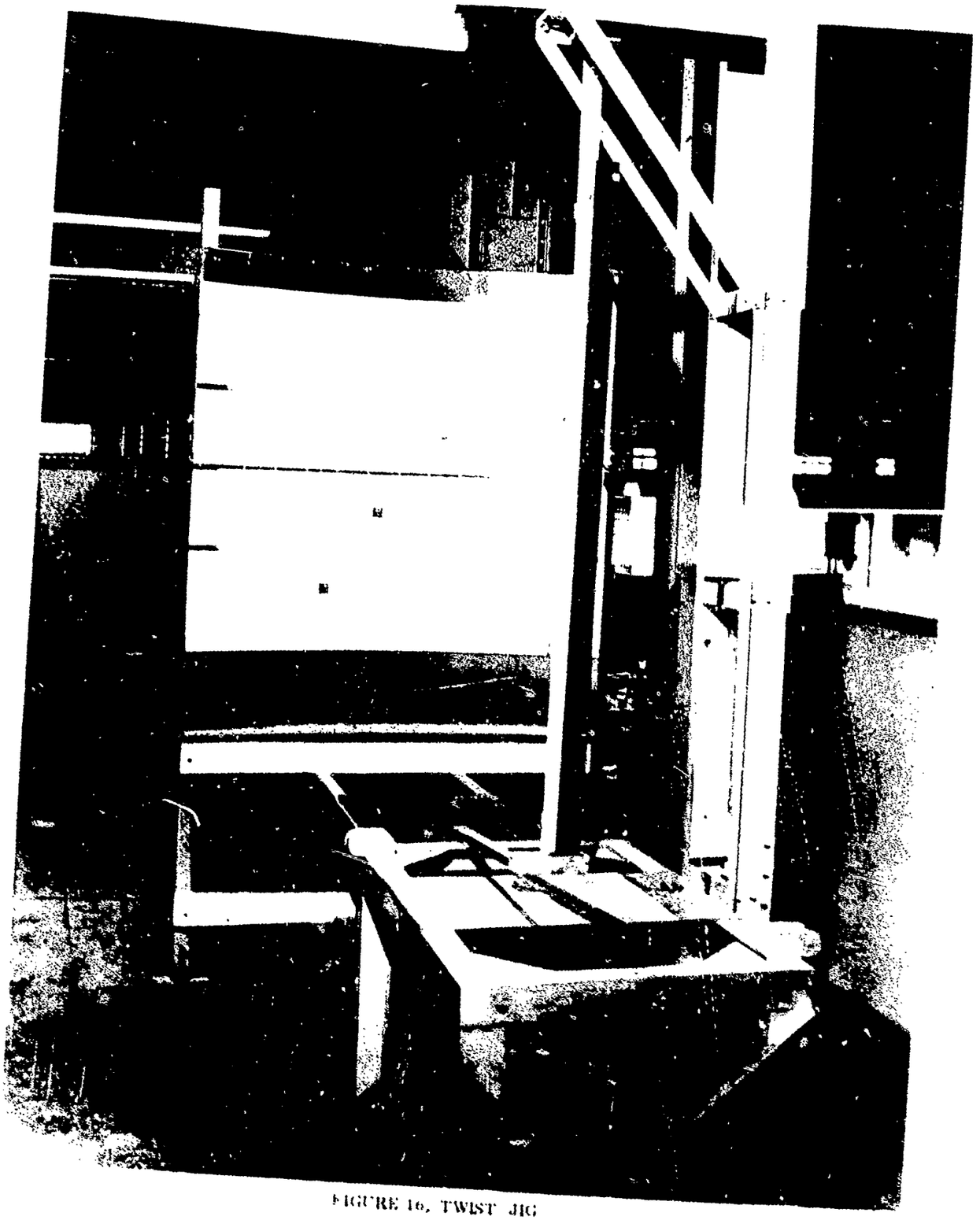

FIGURE 16, TWIST JIG

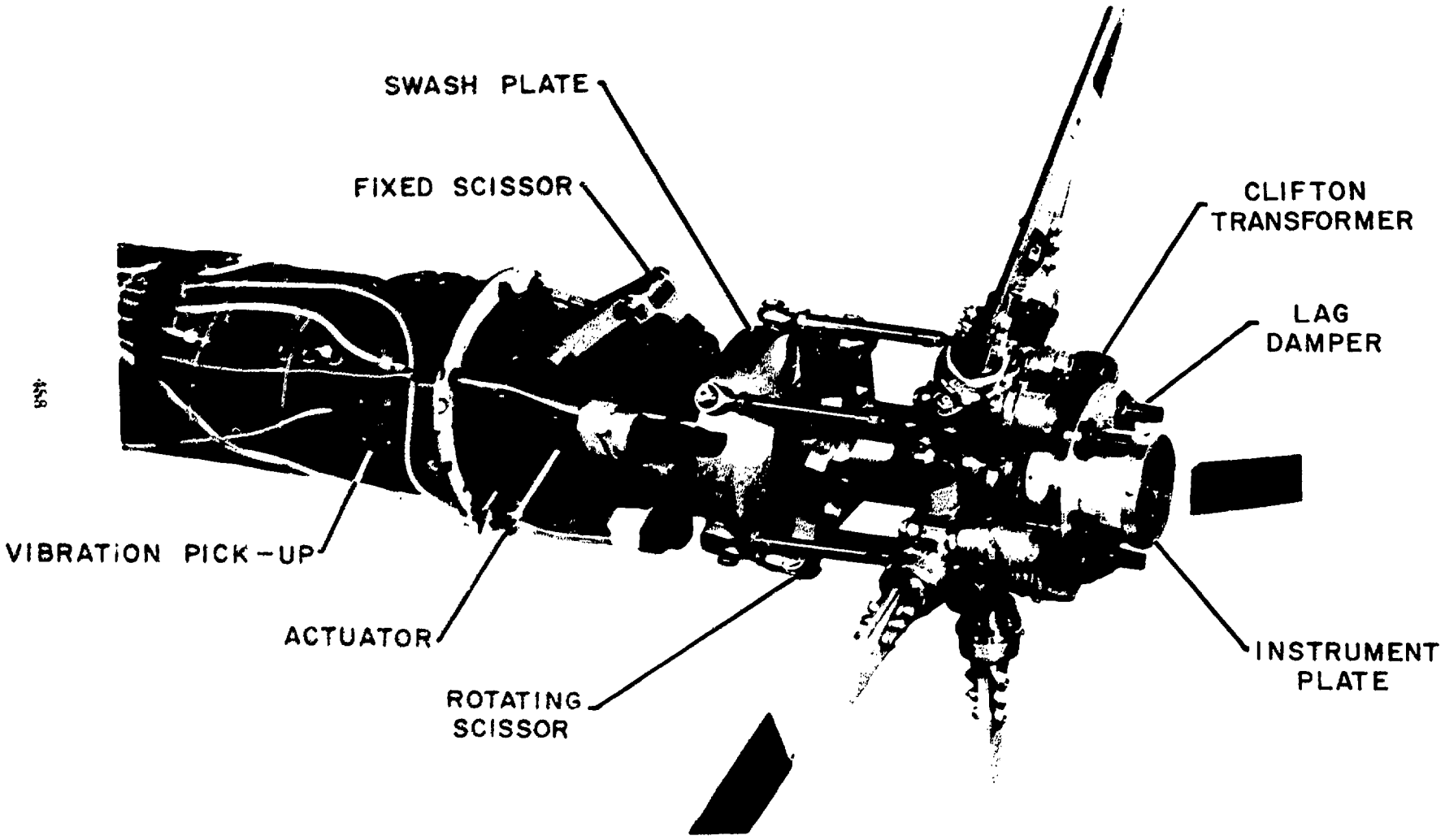

FIG. 18. HRTR ROTOR HEAD AND CONTROL SYSTEM

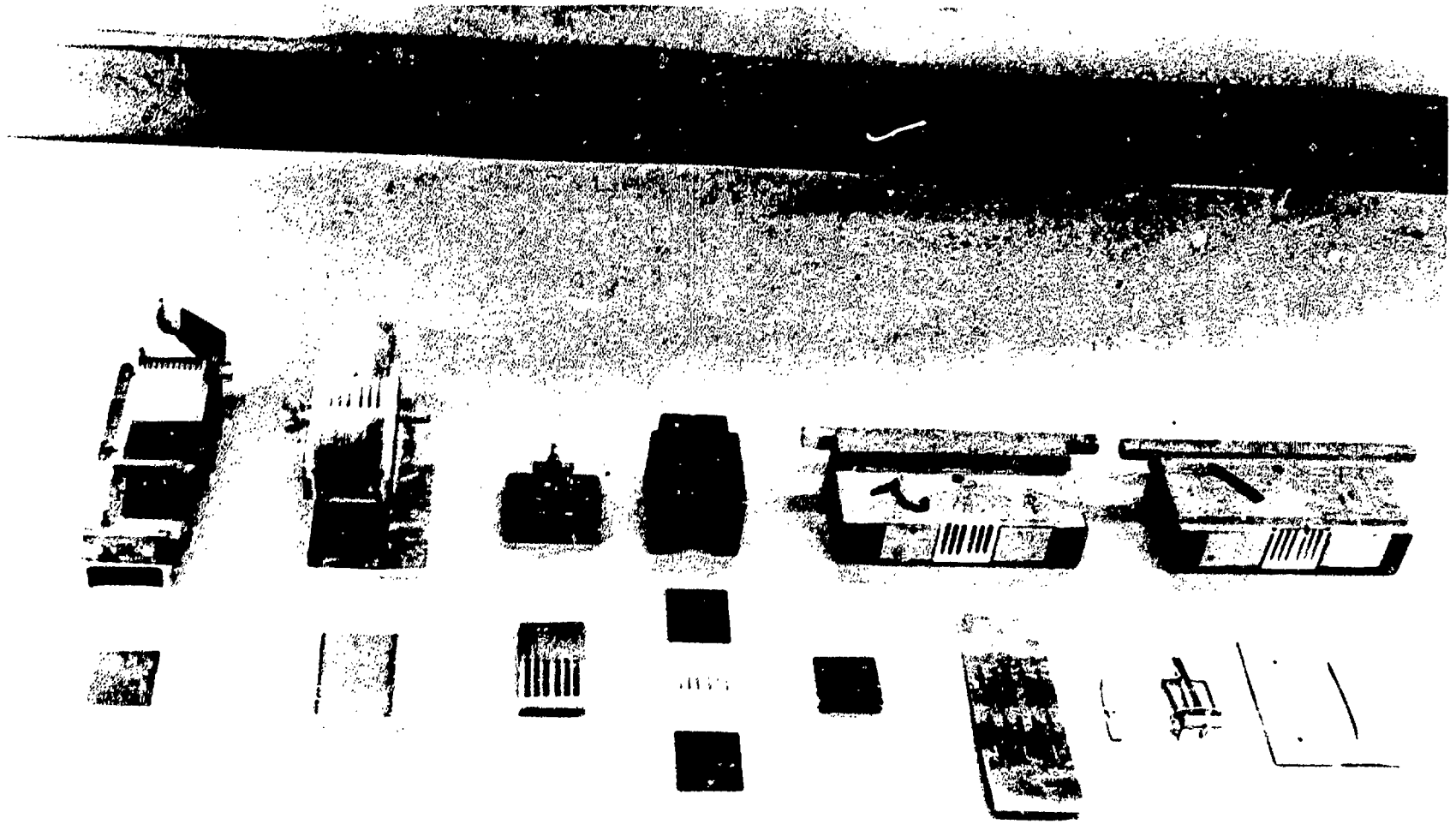

FIG. 17. COMPONENTS AND JIGS USED IN CONSTRUCTION OF POCKETS

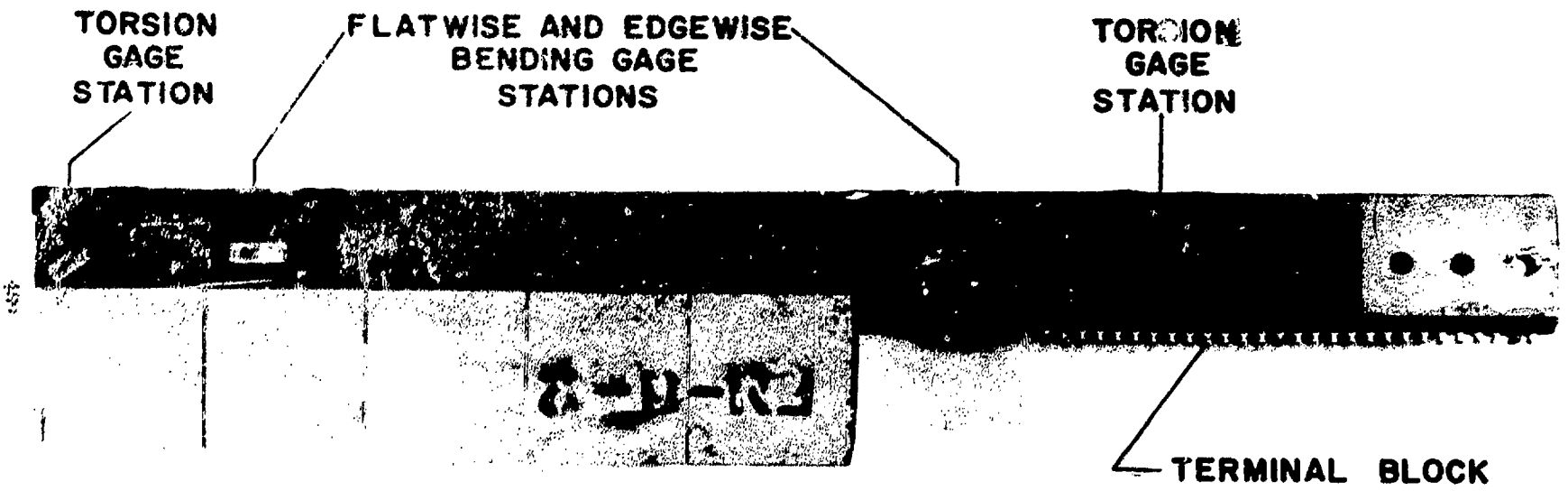

FIG. 19. BLADE ROOT END INSTRUMENTATION

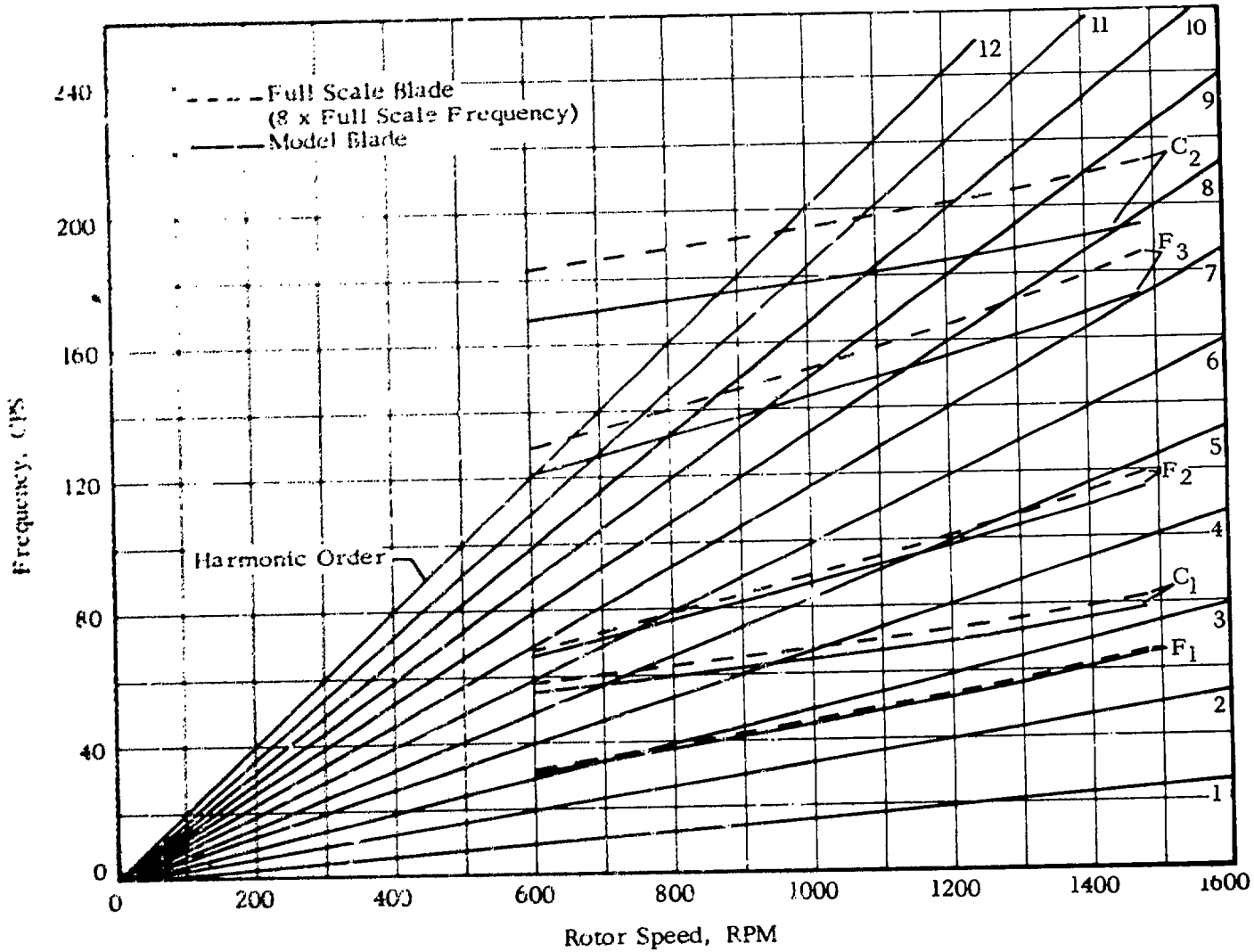

FIG. 20. COMPARISON OF MODEL AND FULL SCALE ROTOR BLADE NATURAL FREQUENCIES

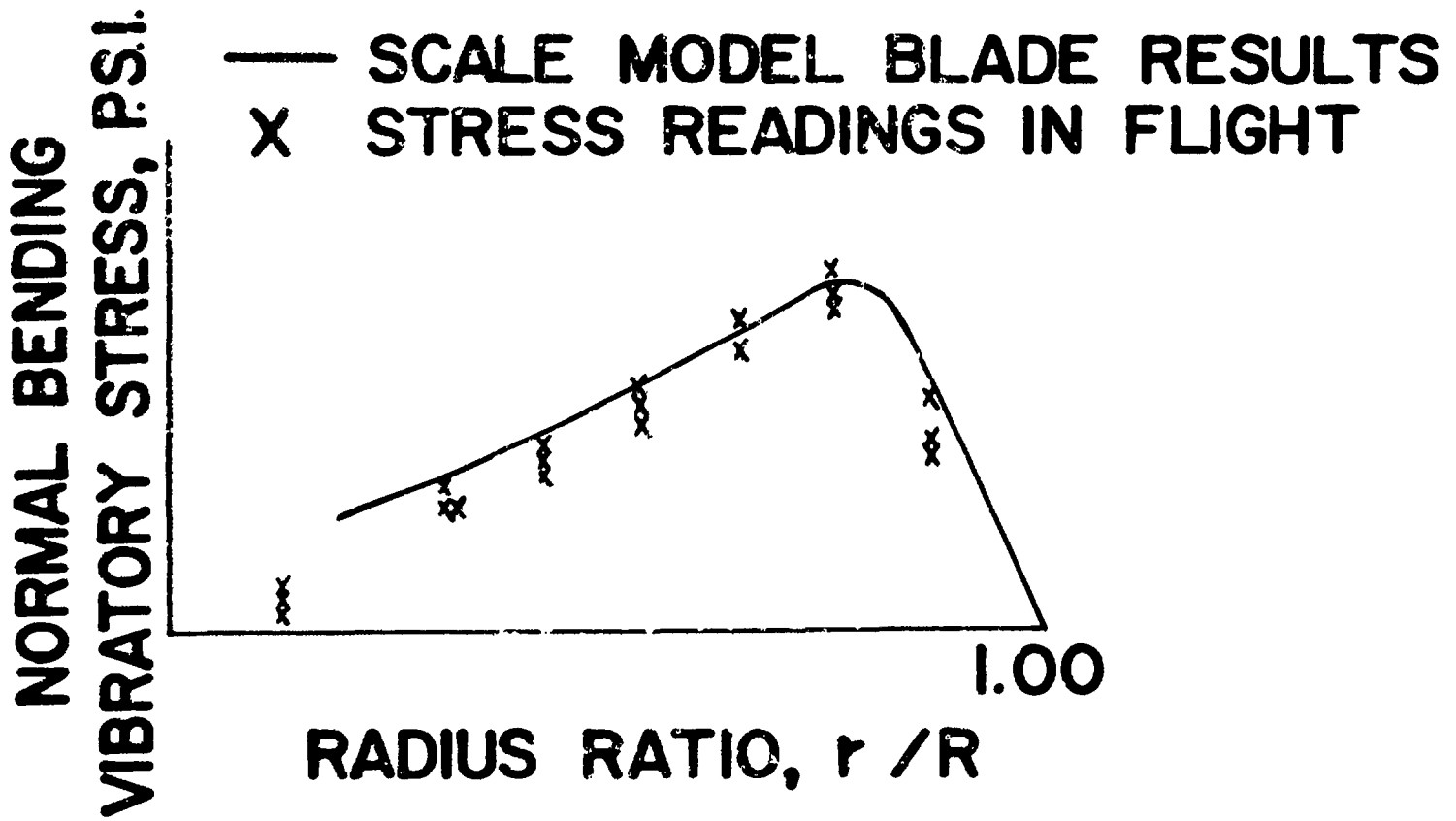

FIG. 21. COMPARISON OF STRESSES RECORDED IN FLIGHT AND ON SCALE MODEL BLADE

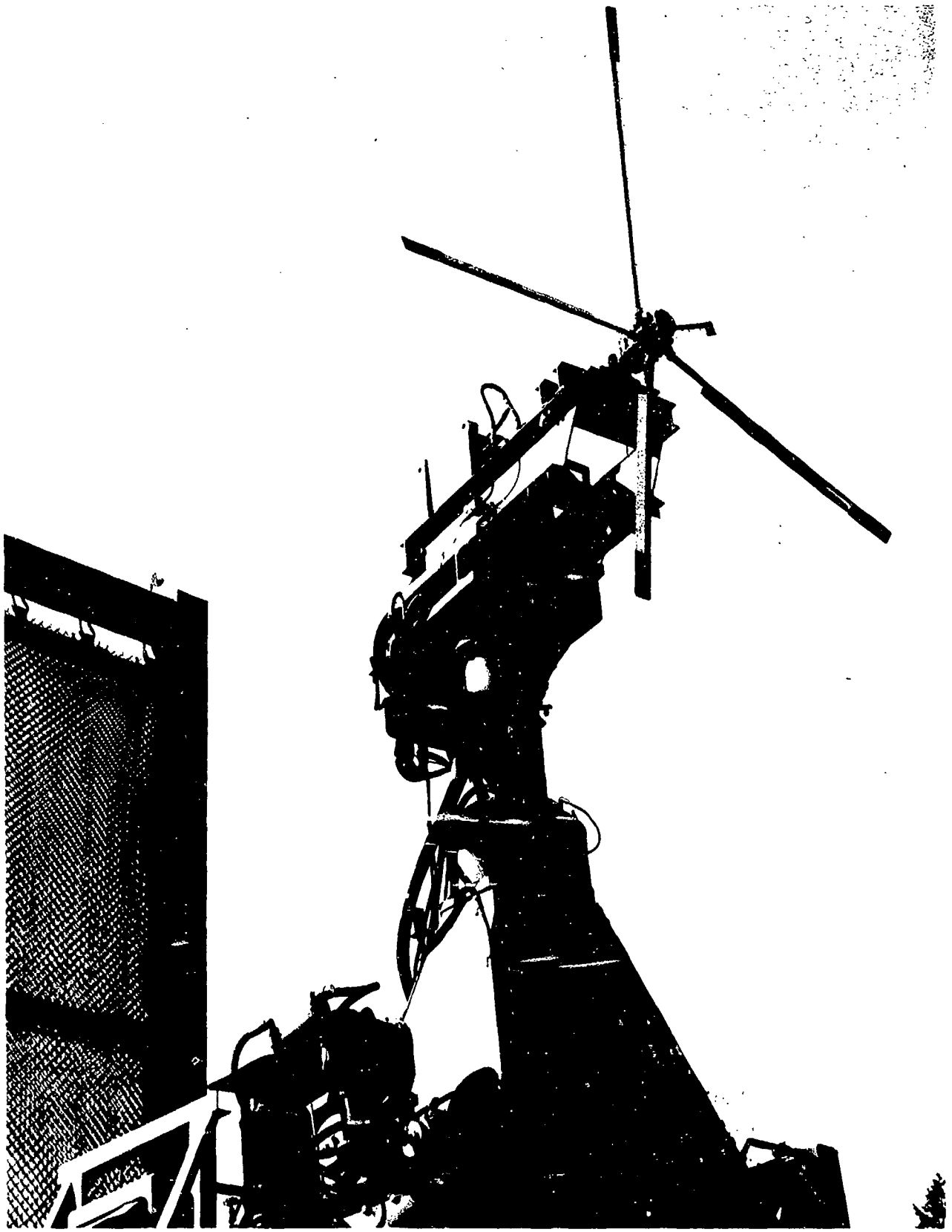

FIG. 22. SIKORSKY TAIL ROTOR TEST STAND

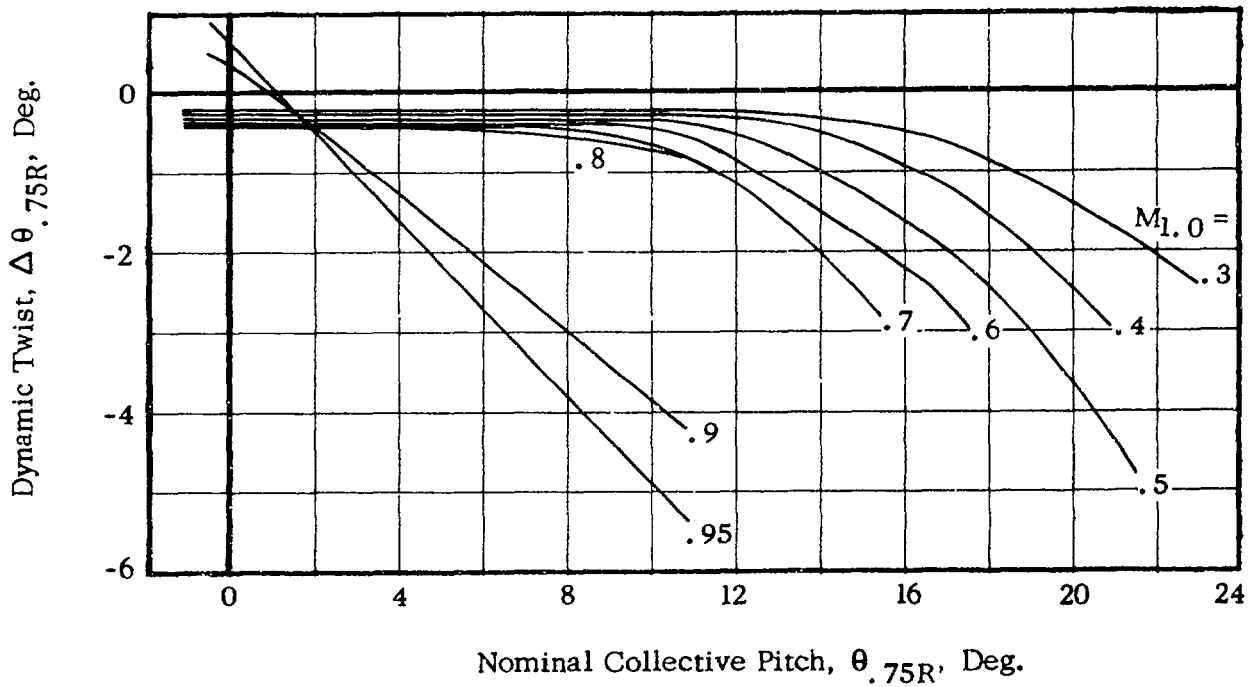

FIG. 23. EXPERIMENTAL DYNAMIC BLADE TWIST IN HOVERING

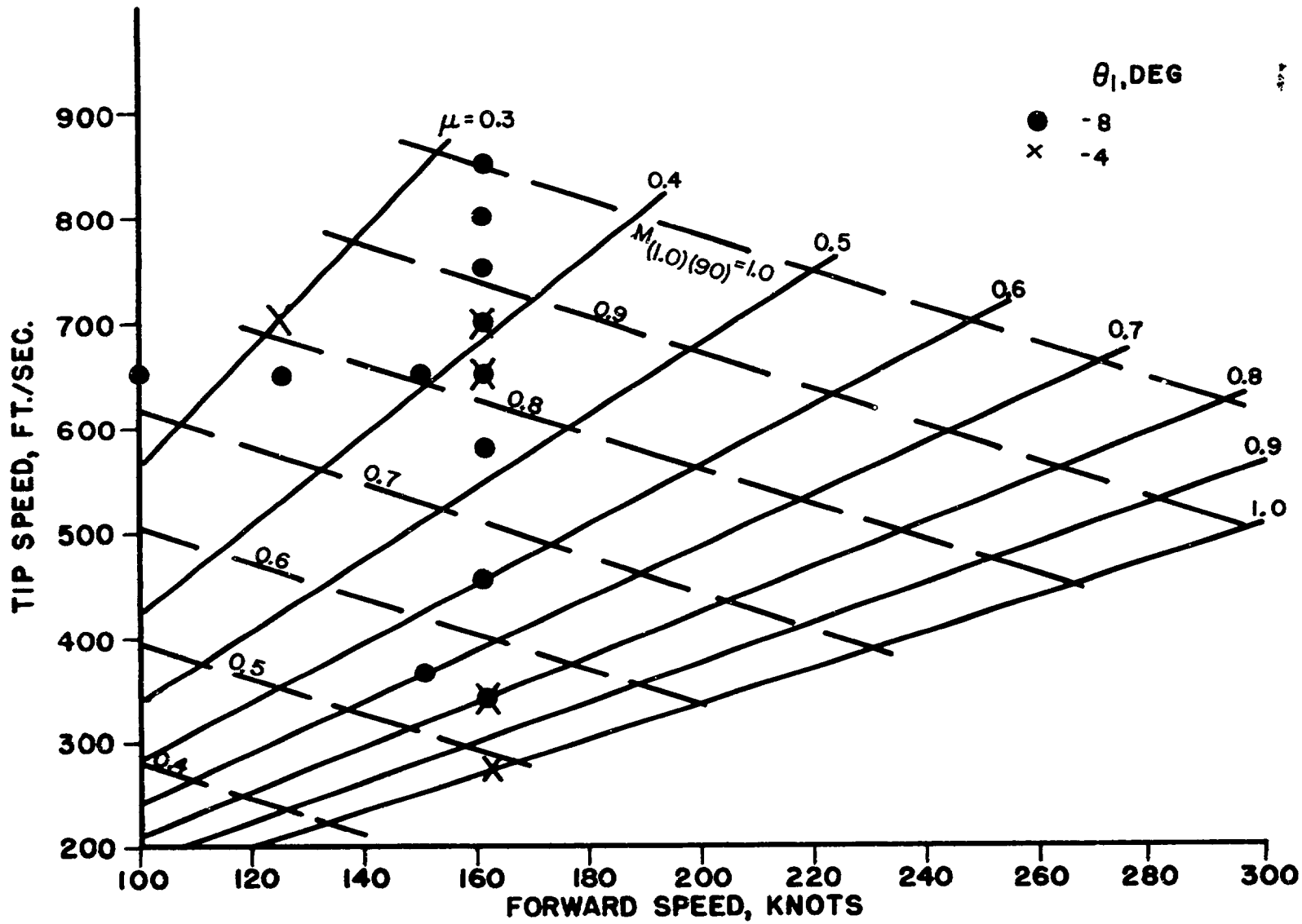

FIG. 24. RANGE OF OPERATING CONDITIONS

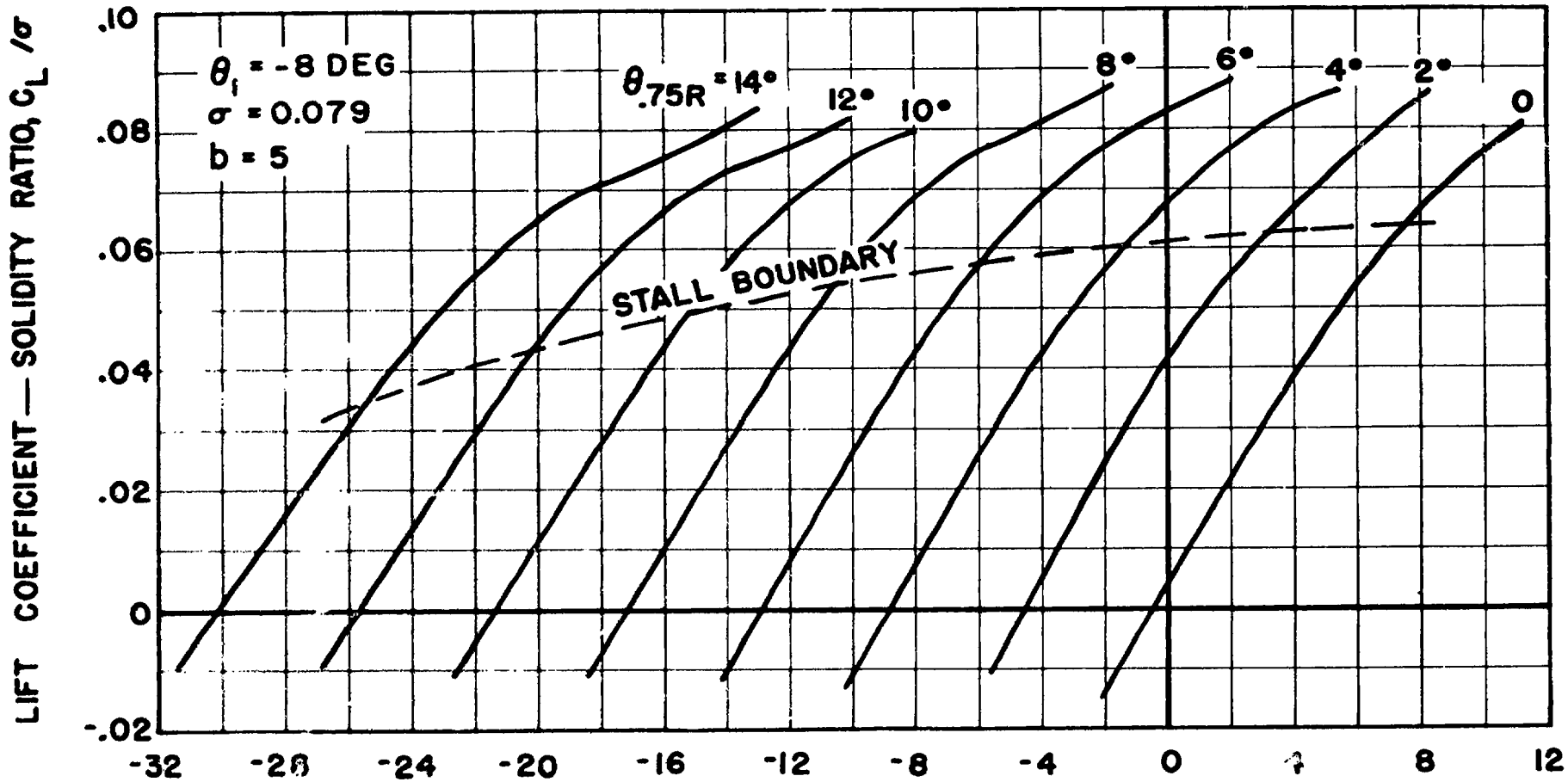

(a) C_L/σ VS α

FIG 25. TYPICAL THEORETICAL ROTOR PERFORMANCE

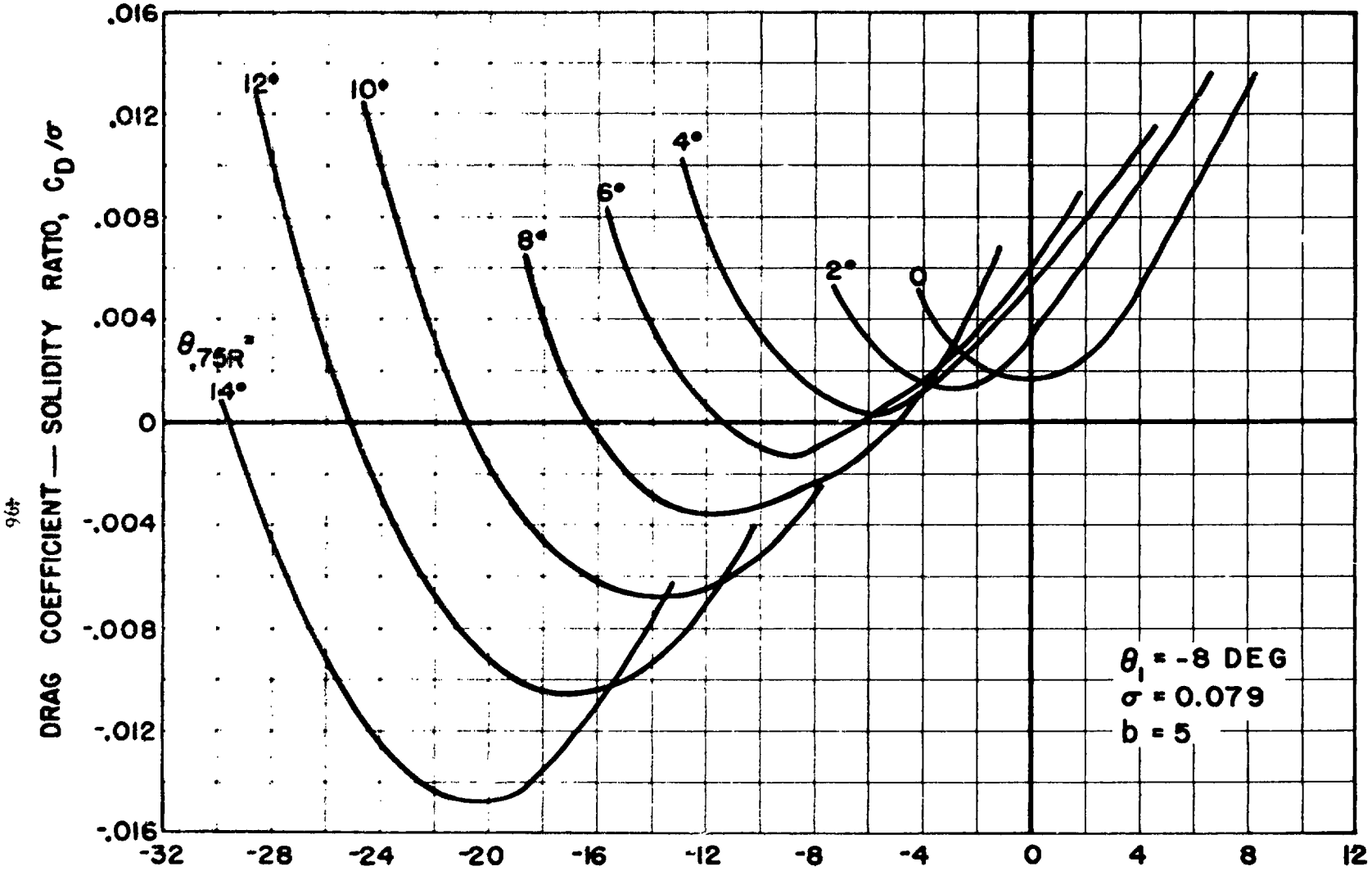

(b) C_D/σ VS α

FIG. 25. CONTINUED

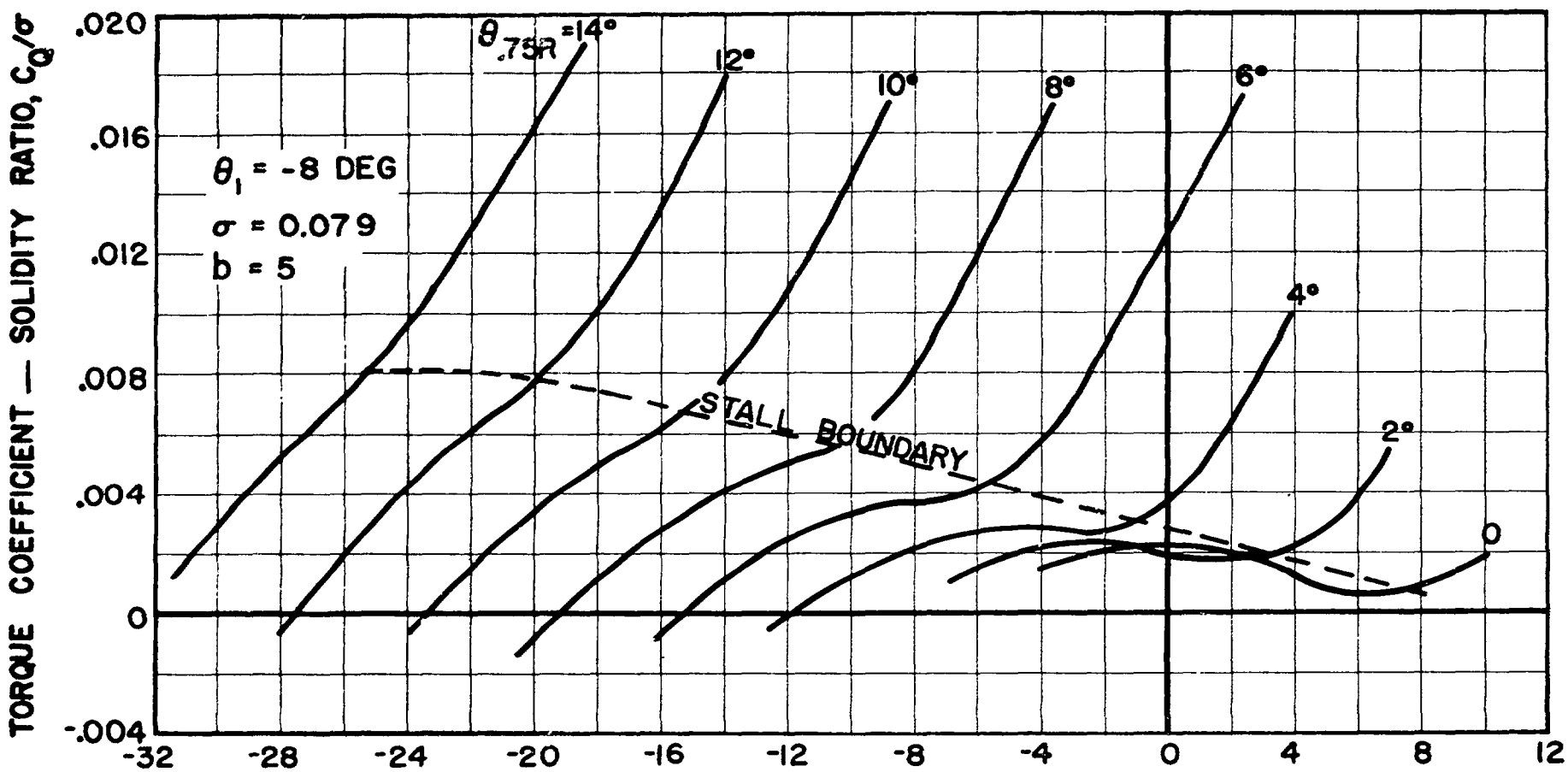

(c) C_Q/σ VS α

FIG. 25. CONCLUDED

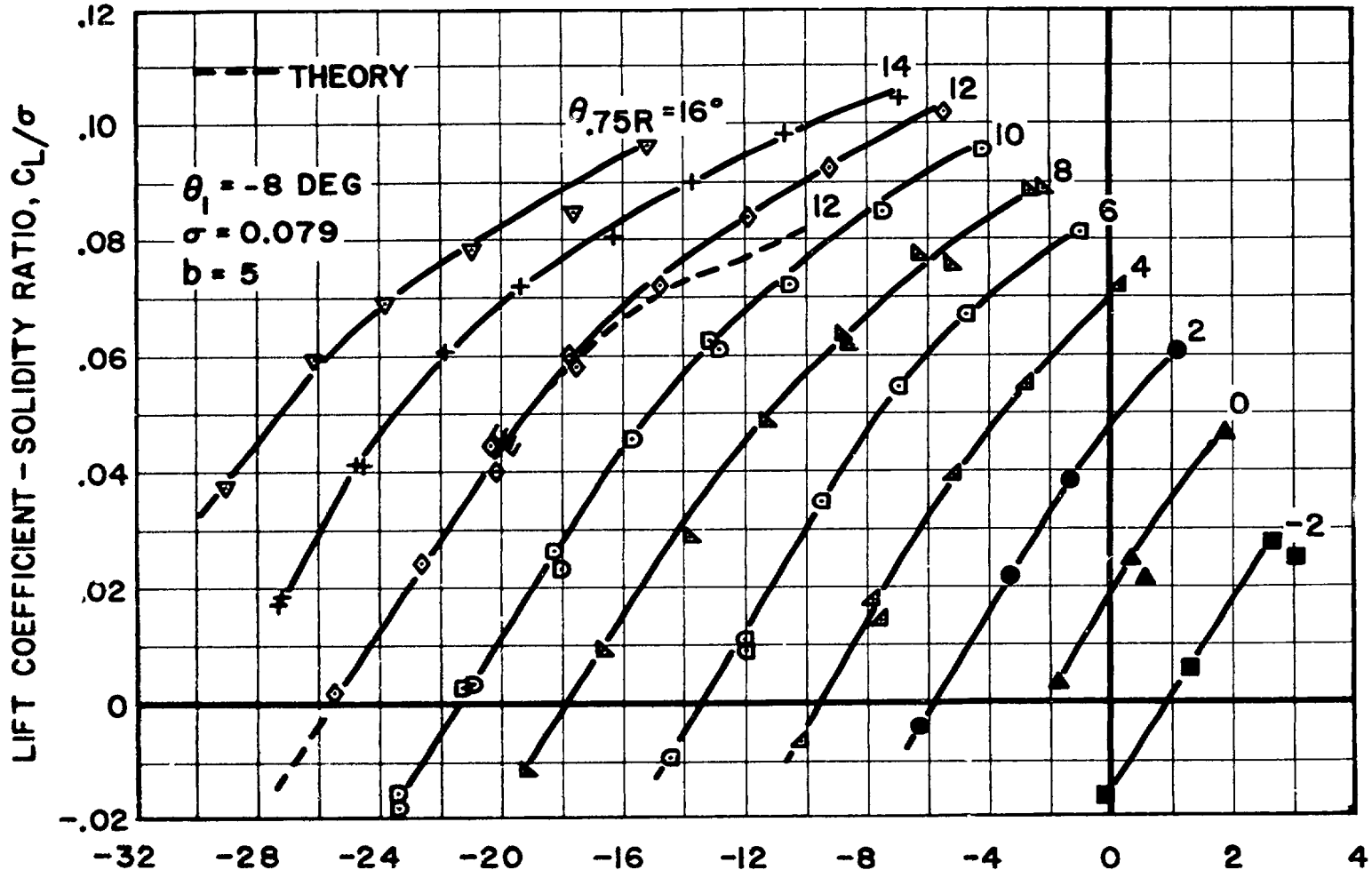

(a) C_L/σ VS α

FIG. 26. TYPICAL EXPERIMENTAL ROTOR PERFORMANCE

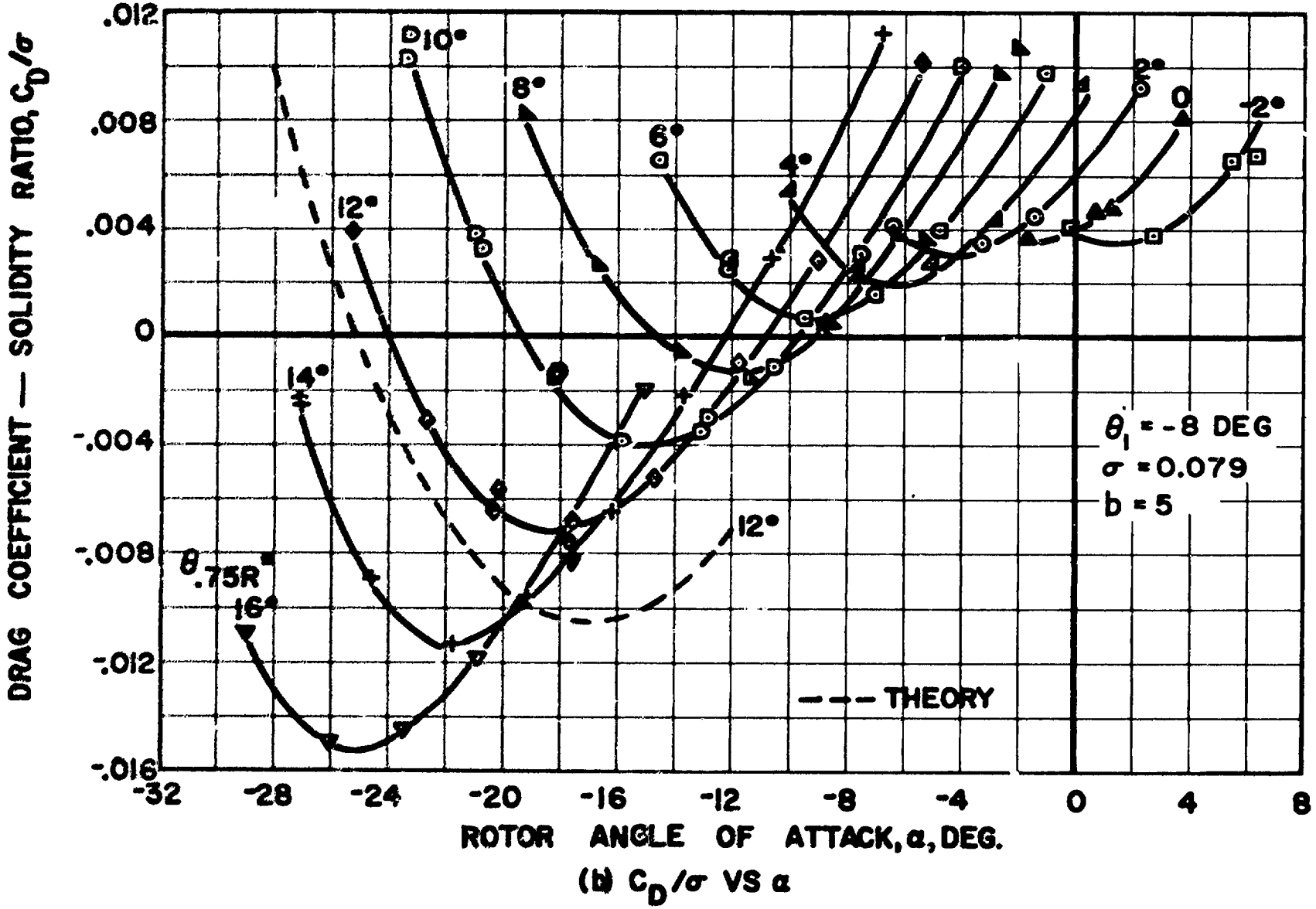

(b) C_D/σ VS α

FIG. 26. CONTINUED

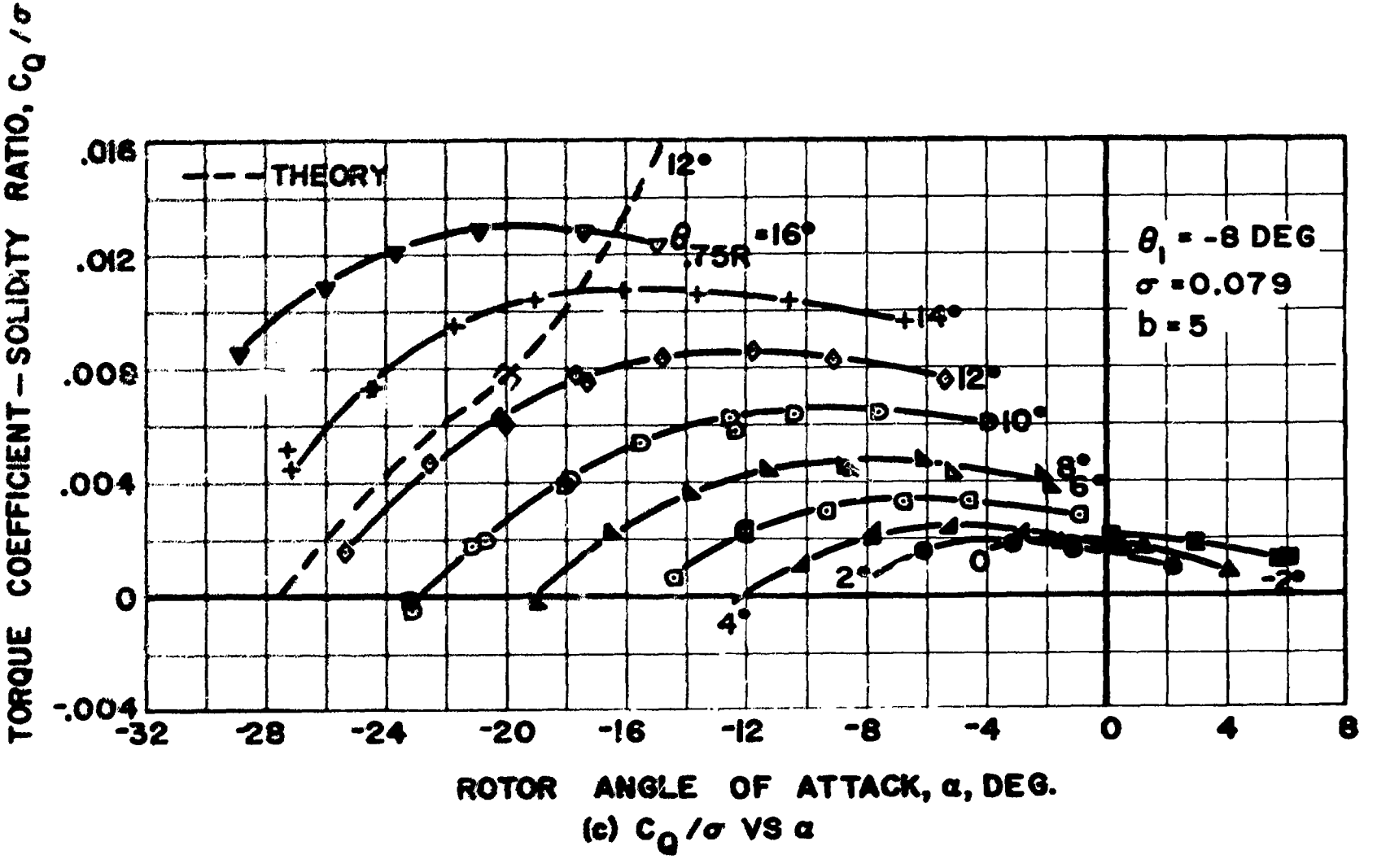

(c) C_Q/σ VS α

FIG. 26. CONCLUDED

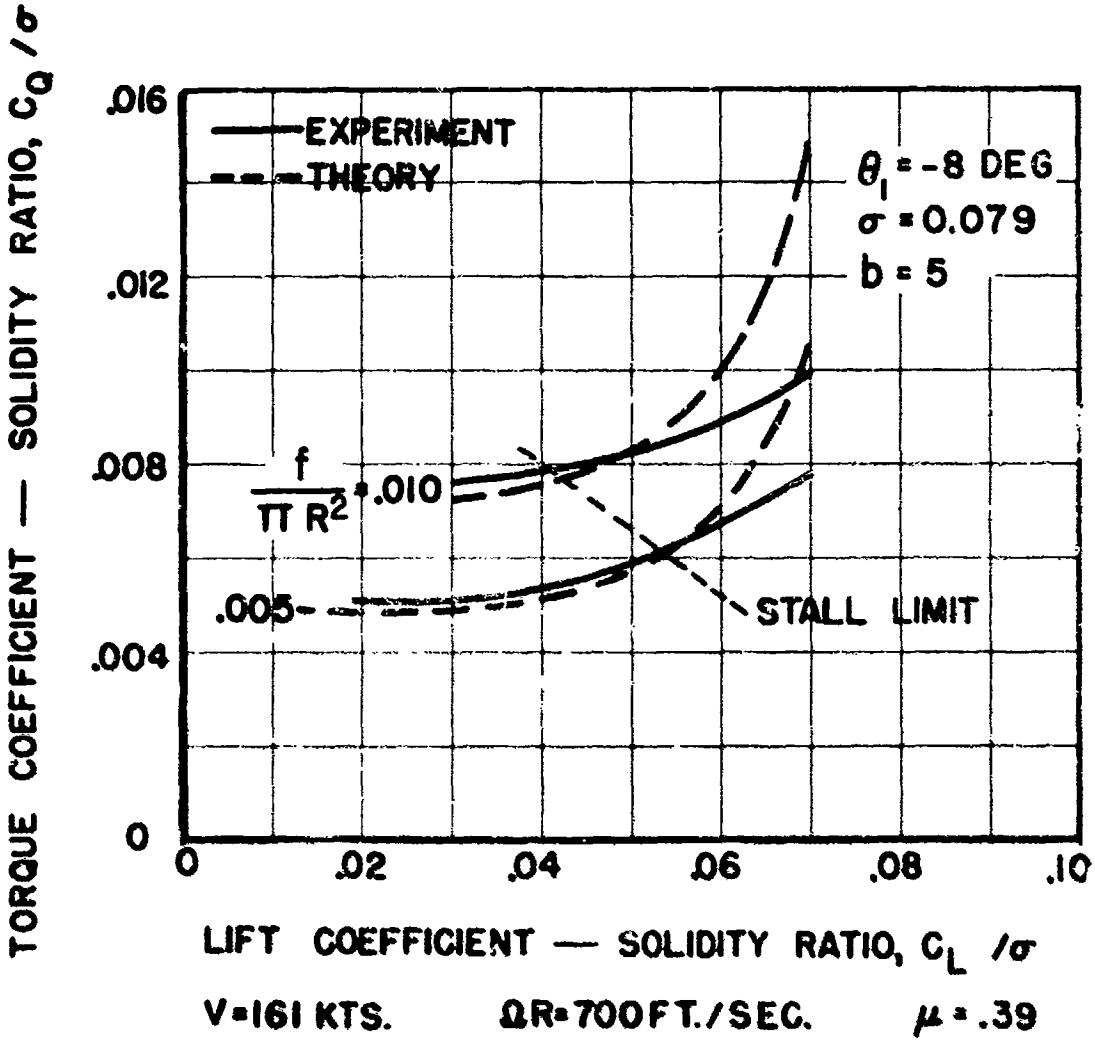

FIG. 27. COMPARISON OF THEORETICAL AND EXPERIMENTAL ROTOR PERFORMANCE

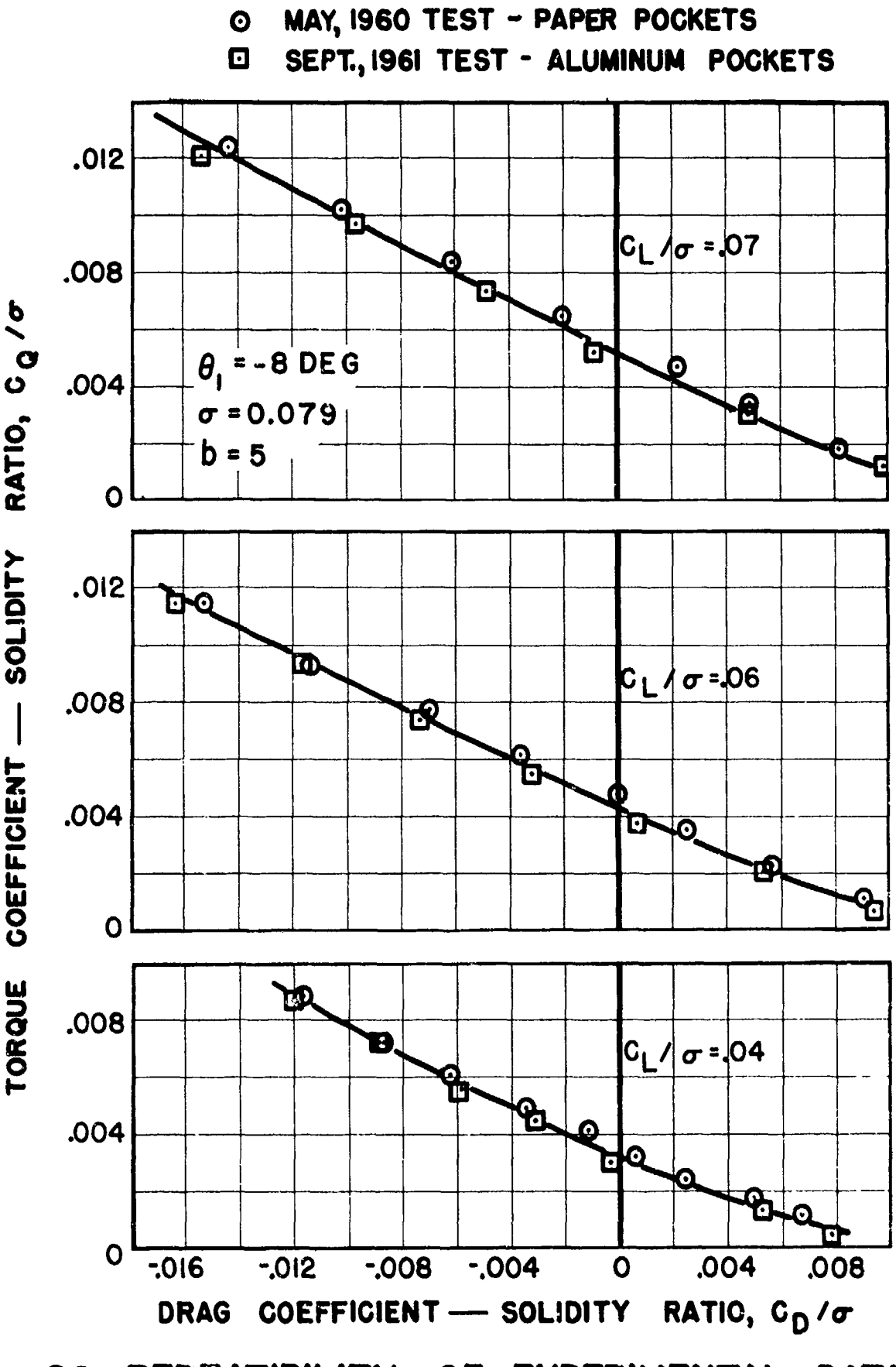

FIG. 28. REPEATIBILITY OF EXPERIMENTAL DATA

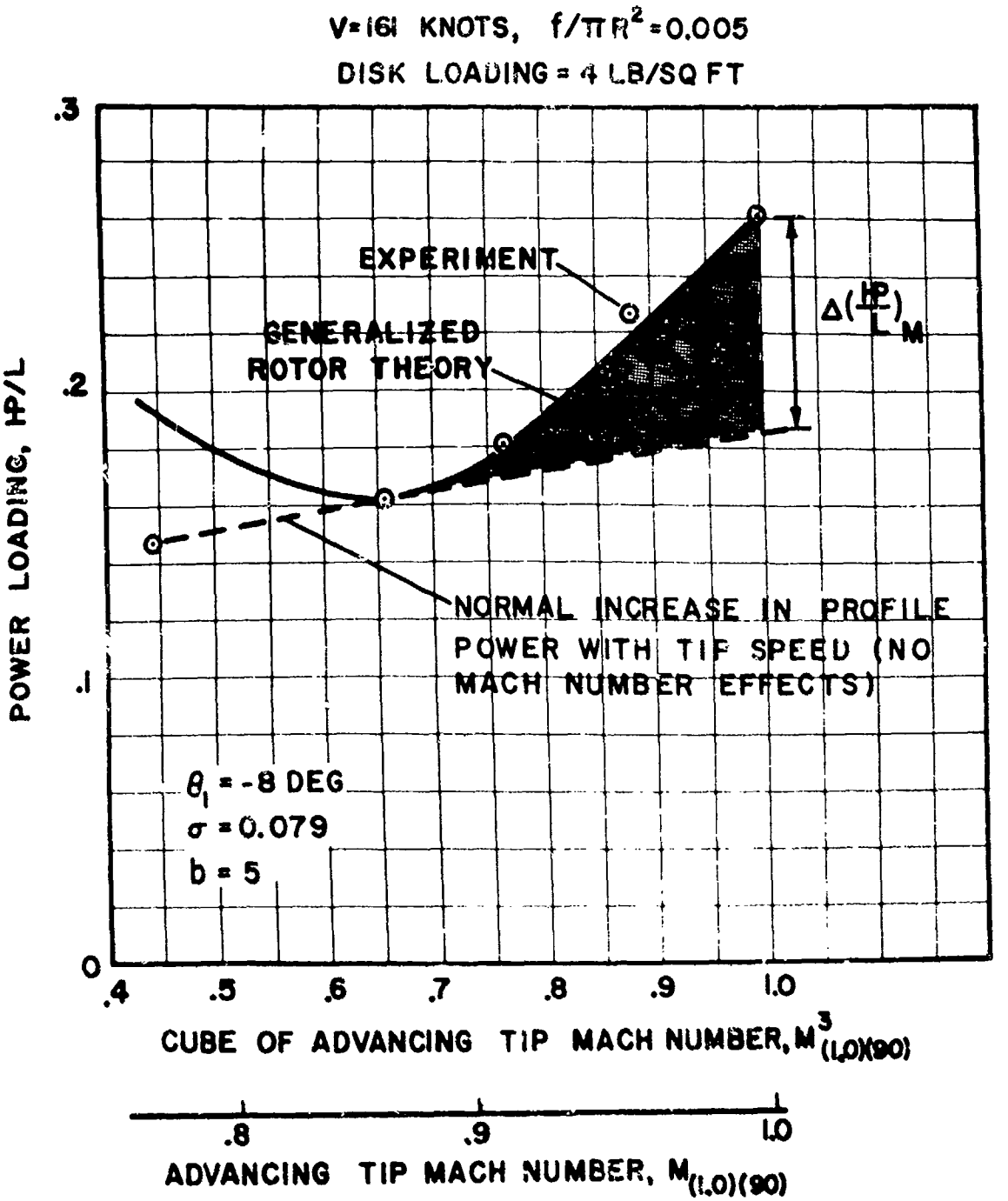

FIG. 29. EFFECT OF ADVANCING TIP MACH NUMBER ON POWER LOADING

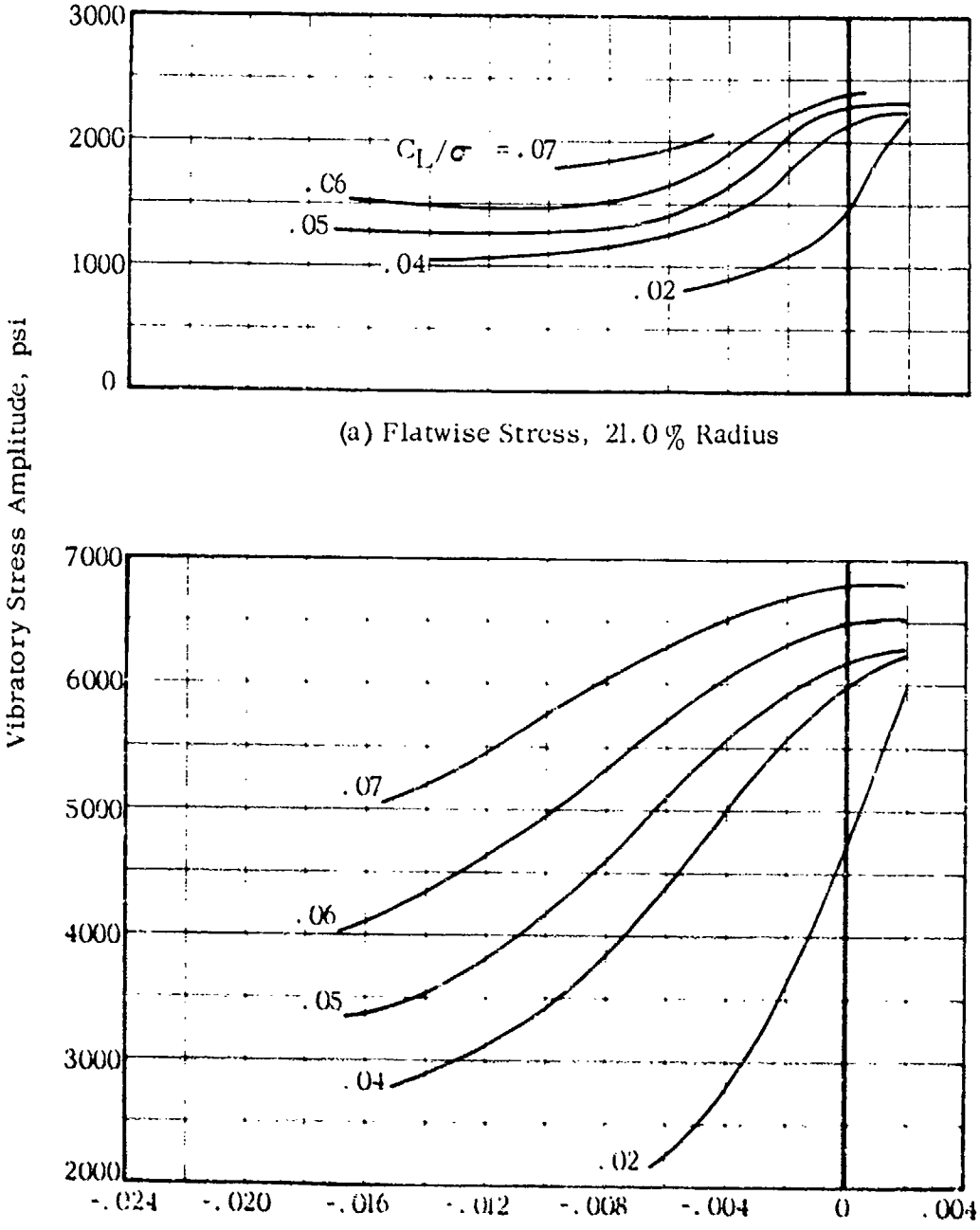

(a) Flatwise Stress, 21.0 % Radius

(b) Flatwise Stress, 63.9 % Radius

FIG. 30. EFFECT OF ROOT LIFT AND PROPULSIVE FORCE ON VIBRATORY BLADE STRESS

V = 161 KT ΩR = 700 FT/SEC μ = .39 θ_1 = -8 DEG

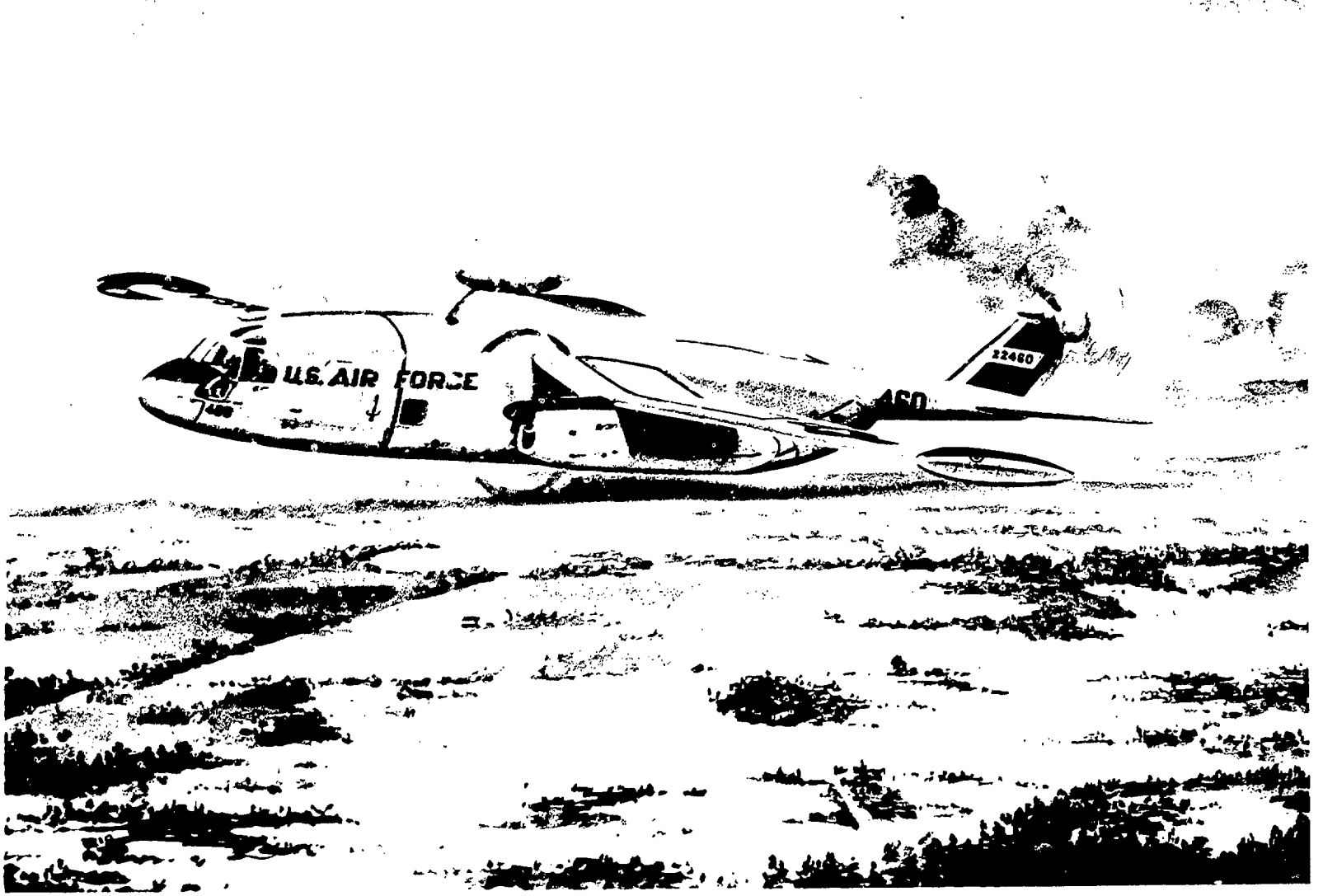

FIG. 31. ARTIST'S SKETCH OF A COMPOUND HELICOPTER

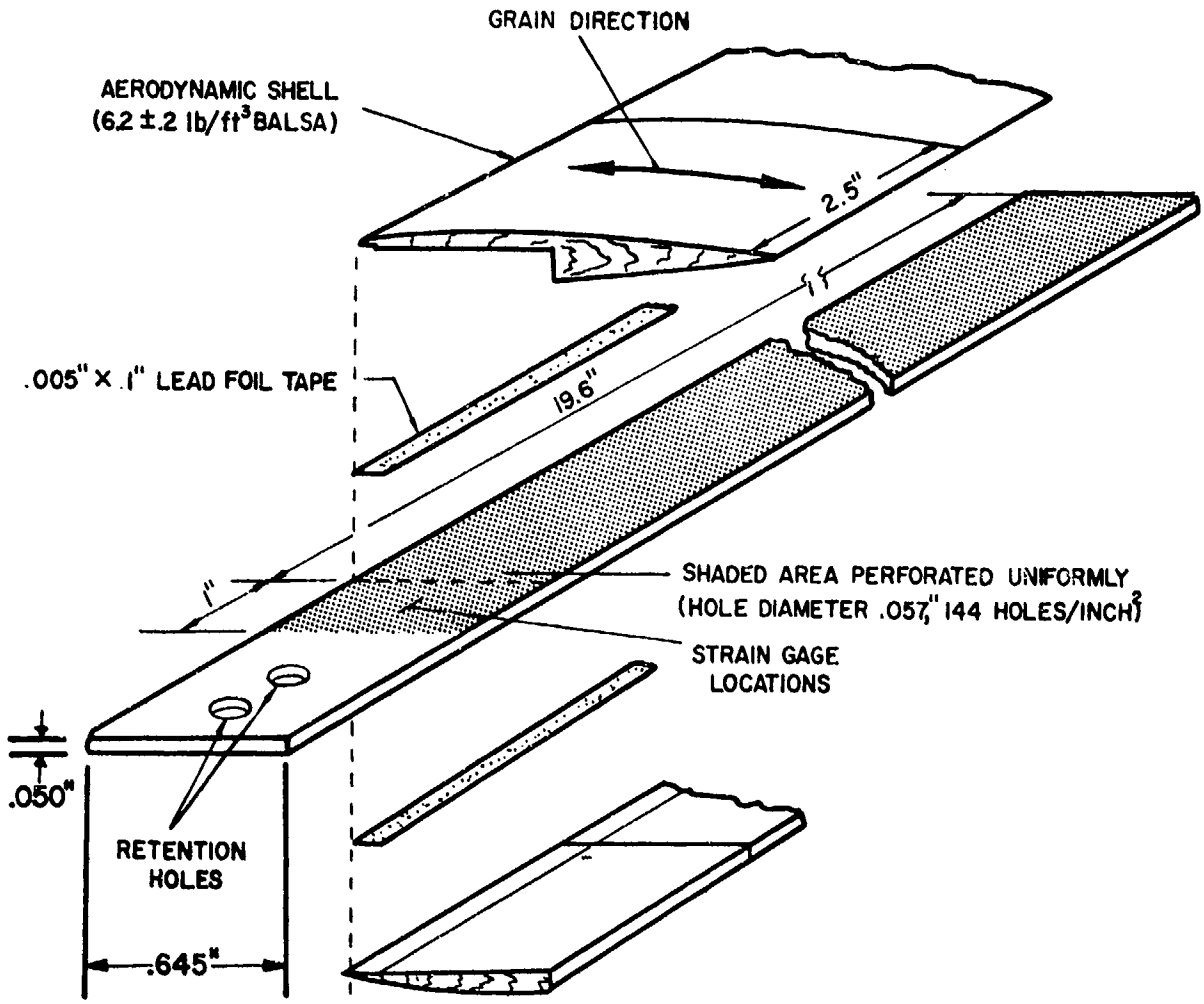

FIG. 32. DETAILS OF 1/18 SCALE MODEL BLADE CONSTRUCTION

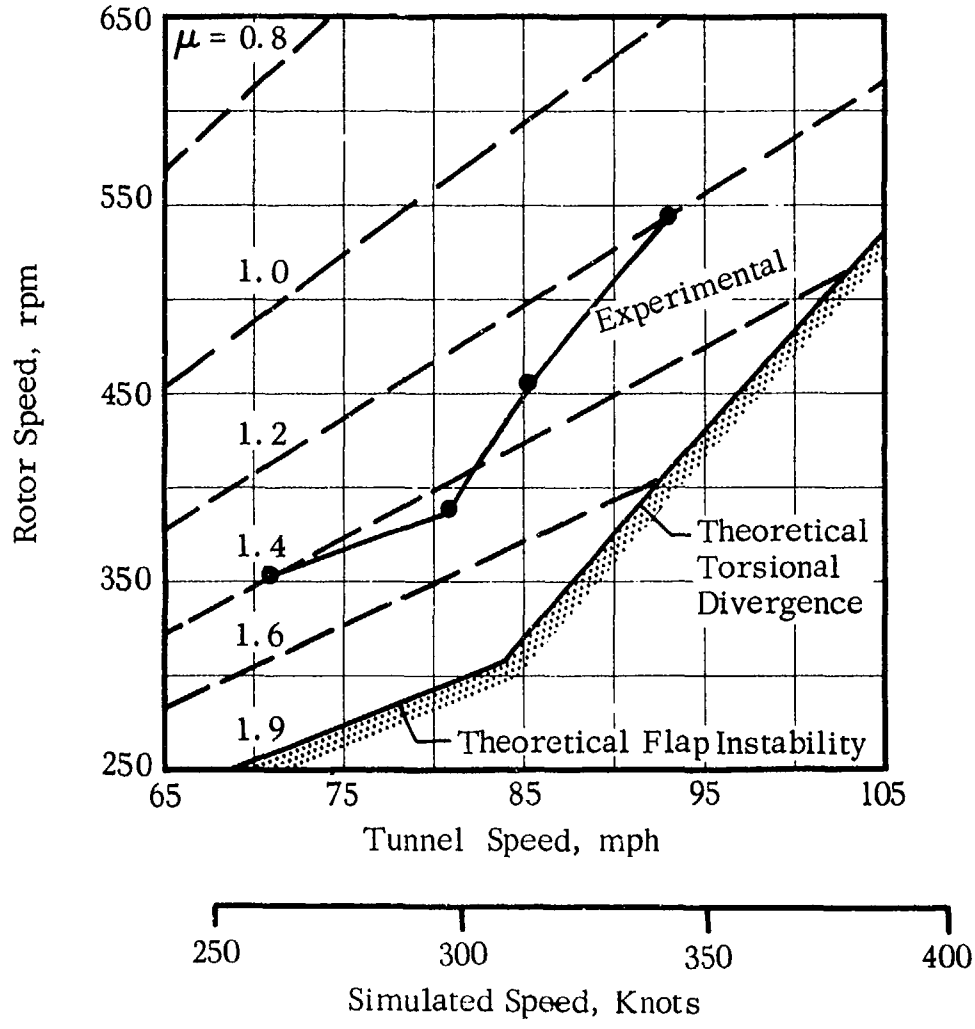

FIG. 33. COMPARISON OF THEORETICAL AND EXPERIMENTAL OPERATING BOUNDARIES

SESSION IV

STRUCTURAL DESIGN APPLICATIONS

Chairman: Mr. Howard A. Magrath
AF Flight Dynamics Laboratory

DYNAMIC MODELS FOR LOW CYCLE FATIGUE

W. H. Roberts

K. Walker

Northrop Corporation

ABSTRACT

Aeroelastic and dynamic models are a practical way to improve aerospace and vehicle safety and reliability while providing significant economies in resources and reduction in full scale ground and flight testing. Progress in applying the models to fatigue problems of two types, specimens and complex structures, is presented. The nature of present fatigue probems is explored, in particular, the link between fatigue and dynamic loads of both high and low frequency. Fatigue damage has been severe and the problem requires complete reassessment. The failures experienced are not because the state-of-the-art is misapplied, but because it is inadequate. The problem contains several layers of complexity beyond the present methods. The probability of failure increases radically in the early life of a part when a typical load history is considered. High frequency dynamic load componentsadded to slowly varying static loads lead to a further increase in probability of failure. Because of this, the structural dynamicist has a key role to play and must adopt this problem area as a major responsibility since his inadequacies appear to be a factor in lack of reliability.

For low cycle fatigue, the models may be applied in real time or in scaled time. The accuracy required for dynamic response is very high, but that required for fatigue scaling is higher still. Principal advantage of the models is their capability to handle all aspects of the static and dynamic loads simultaneously, including thermal loads. The models represent an engineering design tool available for application in the early design stage. That structural load paths are not available in exact detail is not a problem since equal fatigue quality in terms of the stress concentrations can govern the approach. Model shortcomings for fatigue scaling are brought out, and ways to circumvent these are discussed.

LIST OF ILLUSTRATIONS

DYNAMIC MODELS FOR LOW CYCLE FATIGUE

W. H. Roberts
and
K. Walker

INTRODUCTION AND SUMMARY

Engineering analysis includes analysis of engineering structural failure. The approach may be so simple and straightforward as "if it doesn't work, change it" to a vital interest in determining whether there is genuine error in design or execution, a failure to understand the fundamentals, the environment, or to foresee consequences, or a lack of appreciation for the depth and complexity of the problem. An extensive history of failure has been connected with the fatigue problem for approximately two decades and much time, money and weapons effectiveness have been lost. Damage has truly been excessive in areas of acoustic fatigue and fatigue of basic structure. Concern in this paper will be with low cycle fatigue.

Research to develop the dynamic model as a tool for study has shown a promising approach. The dynamic model is useful for low cycle fatigue studies as well as other basic fatigue problems. The technique includes engine scaling, thermal scaling, and is effective to the high frequencies characteristic of the acoustic excitation.

Recently uncovered characteristics of fatigue most probably related to the extensive service failures are presented. The need for the proposed tool is examined and the results of the scale model testing is given. The level of complexity is well beyond the state-of-the-art leading to the conclusion that the cause of the service problems was failure to understand certain fundamentals developed in recent research. Satisfactory coverage of the many aspects of the problem requires solutions in the interdisciplinary areas which link dynamics, structures, fatigue, and the new aero and acoustic loadings.

OBJECTIVE

The objective of this paper is to relate some extensive model research and development to the low cycle fatigue problem. Experimental and analytical studies were conducted on panels subjected to acoustic fatigue and on the vibroacoustic response of complex structure. The ultimate purpose of the model technique is to speed the design process by allowing structural qualification to proceed using the models during the design period, to lessen requirements for full scale facilities and to reduce over-all and full scale test expense.

LOW CYCLE FATIGUE

The Low Cycle Fatigue Subcommittee of the ASME Research Committee on Prevention of Fracture in Metals has defined low cycle fatigue as failure in approximately 100,000 cycles or less*. Plastic deformation on the macroscopic scale occurs during low cycle fatigue as contrasted to the predominantly elastic deformation which takes place in high cycle fatigue where plastic deformation exists only on a microscopic scale. The committee has been in operation approximately seven years and has accomplished the following:

- A definition of low cycle fatigue was completed
- A survey of current practice was made
- A composite list of problem areas was assembled
- Assignments to participating individuals is in process

The industries surveyed included:

- Naval reactor pressure vessel field
- Atomic energy industry
- Ordnance and heavy equipment industry
- Ships and submarines
- Pressure vessel and chemical industry
- Space and airframe
- Turbine

The list of problem areas consists of:

1. Mean stress
2. Biaxial stress
3. Environmental deterioration from radiation, corrosion, humidity, vacuum, etc.
4. Ratcheting
5. Frequency
6. Nucleation
7. Crack propagation
8. Cumulative damage
9. Combined stress
10. Strain concentration
11. Metallurgical variables
12. Loss in strength
13. Residual stress
14. Shop practice
15. Structural configuration

---

* When faced with such an arbitrary definition as this, the question arises as to how it was chosen. The fatigue mechanism is truly divided into two separate failure mechanisms which are reasonably discrete. Appendix A contains these descriptions.

16. Compression fatigue
17. Simple tests
18. Random load
19. Wave shape
20. Temperature
21. Welds
22. Inconsistent experimental data
23. Interaction

Low cycle fatigue is characterized by yielding and creep generally throughout the material--actions which are amplified at points of strain concentration. The creep arises from high stresses and depends on the wave shape of the load-time history. If held at the peak stress for longer periods the material exhibits greater creep and damage.

The subcommittee states that criteria, data and procedures are not available for dealing with the problem. So many variables interact in varying degree for different designs that no one program would answer the low cycle fatigue problem. No one problem area was acceptable on an industry-wide basis as "the" most critical.

It is interesting to note the various approaches used in different industries--approaches dictated to some degree by the particular problem faced by that industry. Three categories of design procedure were noted:

- Service experience
- Simulated service, i.e., component test
- Analytical approach

High volume production in the automotive industry led to heavy reliance on service experience. Detailed structural analysis was employed in the nuclear reactor pressure vessel field because of a lack of any prior background in the problem. In the space and airframe industry due to small margins of safety, simulated service tests are always necessary on full scale hardware. The committee states that when design procedures are not developed very completely, emphasis is placed on service experience and engineering judgment. The committee recommends:

- Materials with large rupture ductility
- Reduced strain concentrations
- Reduced steady and alternating loads
- Reduced thermal loads, in particular

Considering the failure history due to fatigue and the importance of the problems involved, this approach based on service experience and engineering judgment is weak and inadequate. In its place let us examine recent progress in understanding some of the characteristics of fatigue and the dynamic model for use in the design stage.

GENERAL NATURE OF FATIGUE

Recent studies show a fascinating group of characteristics of the fatigue problem which are not part of normal engineering analysis. These are relayed in part to show the many layers of complexity in fatigue which support and establish the need for a new approach. A number of these characteristics of importance are outlined.

A basic correlation has been provided by Pian and D'Amato, Ref. 1, Fig. 1, which lies wholly within the low cycle fatigue area. This classic contribution shows that the fundamental mechanism is strain cycling. For different materials, different loadings including temperature fatigue, a correlation was exhibited from which Coffin's equation was derived. The slope of this curve is minus 1/2. Coffin's equation is

$$\epsilon N^{1/2} = \text{constant (Ref. 2)}$$

Presented in the usual way with reference to stress, no correlation would appear.

One characteristic of interest to the dynamicist is the instability which describes failure in sheet material. Fig. 2 shows a stability boundary on a plot of stress versus crack length. The instability occurs when the strain energy stored in the material overshadows the energy required to catastrophically unzipper the material. Between the yield and the ultimate strength, the failures deviate from the stability boundary in much much the same way that the buckling criterion for a slender column deviates from its stability boundary. A graphical analogy between the shape of the two stability boundaries is to be noted. Data from an ASD research program, Ref. 3, has been correlated by means of the concept.

Probably the single most important characteristic of fatigue for the dynamicist to bear in mind is the damage due to random loading. Fig. 2 shows Freudenthal's experimental data for steel and aluminum where cumulative damage fractions as low as 0.1 are reached for steel and 0.2 for aluminum. The intimate intermixing of high and low loads characteristic of random loads completely invalidates the Miner's Rule concept and leads to an order of magnitude increase in damage. The diagram shows a 2:1 difference between steel and aluminum in regard to their sensitivity to random loading. The better performance of aluminum in this regard is noteworthy and could be quite worthwhile. In the low cycle fatigue area, the cumulative damage fraction decreases as the number of cycles increase. The limitation on this result is that it was obtained on unnotched structure. Experience on full scale structures shows the random sensitivity may not be so severe.

These same extremely low cumulative damage fractions arise as well in Valluri's engineering theory of fatigue, Ref. 5, Fig. 3. Using as an hypothesis of crack propagation, dl/dn = constant, the theory shows damage fractions as low as 0.2 in aluminum. The figure describes the calculated life under two step fatigue where fully reversed loading at one stress is followed by a change to another higher or lower stress which is carried to failure The more damaging case is when the high load follows the low load and when the ratios σ_2/σ_1 is large.

An agreement in form between the experimental data and the theory is presented in Fig. 4. A cross plot of the theoretical data shows the trend of the theory agrees with that of the experiment. The Valluri theory is substantiated in much more direct and concrete ways than by these data. The point of interest here is the agreement between theory and exp riment regarding sensitivity to random loading. The conditions surrounding the inputs to the two studies was considerably different and closer study is not warranted. The point of greatest sensitivity to random load is in the area of 10^6 or 10^7 cycles which is outside the area of low cycle fatigue. The cumulative damage fraction rises to either side of this low point.

Another important characteristic of fatigue is the loss in strength which occurs as the damage proceeds. Loss in strength follows from the existence of the stability boundary. A family of curves may be added to the s-N curve defining this change. Where it was previously held that the loss in strength, if it existed at all, was a negligible quantity the theory has sufficient substantiation to cause the older idea to be discarded. On the same plot, the damage density and the load history may be presented for an all round view of the phenomenon in each given case. The damage density is measured approximately by dividing the number of applied loads at any given stress by the number that would cause failure. Three different damage density curves are illustrated in the sketch.

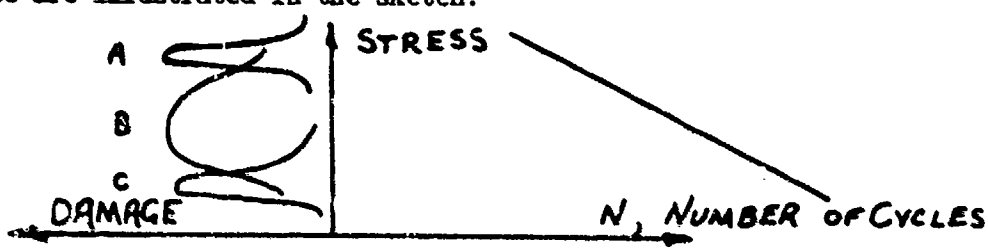

Various Type Damage Density Curves
Sketch 1

It may logically be argued that whenever the damage is confined to a narrow stress band, as in curves of type A and C, the cumulative damage must be near unity. The s-N curve was generated in just this way. It follows that sensitivity to random damage accompanies a damage density curve of the type B and further that the lower the curve lies along the stress axis, the lower is the cumulative damage fraction. An explanation for the upward curvature of the cumulative damage curve at extremely high cycles, Fig. 2, would seem to be due to the fact that the damage density must ultimately approach the type C curve.

There is a reluctance on the part of some to accept the loss in strength concept, the argument being that the bulk of structural failure seems not to support the point. The stability boundary graph, Fig. 2, contributes significantly to clarifying this point. A crack begins at a certain stress level and proceeds to grow. Its locus on the diagram may follow any possible path to failure--failure is indicated by intersecting either the strength boundary or the stability boundary. The usual failures are strength failures while the stability failure is rare, although serious instabilities have occurred in service.

The loss in strength concept has been presented, Fig. 9, by Blatherwick, Ref. 6, in the more conventional sense via the stress strain curve. A material was used in this case. The stress strain curve cannot be regarded as a stationary characteristic of the material--merely an extreme case applicable to virgin material. Once stressed, any further reference to this singular characteristic could be misleading.

If the loss in strength is such a prominent part of the damage it is reasonable to ask whether the material undergoes an analogous loss in stiffness. Fig. 9 shows such loss at the higher stresses. Attempts to examine for loss in modulus showed no change. A third type loss in stiffness was examined in Ref. 8.

Experience with fatigue failures in model scale shows that the crack propagation rate does not scale. By scaled crack propagation is meant that following a certain number of cycles a crack having advanced a certain distance across full scale structure would advance a proportionate amount in model scale, see Sketch 2.

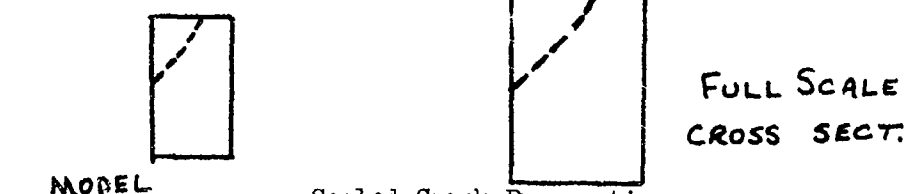

Scaled Crack Propagation
Sketch 2

This particular action would be consistent or predicted by the s-N curve for example. Since, however, the crystalline and atomic structure are the same, the same materials having been used, and because the stress levels are the same at corresponding points, the crack progresses at nearly the same rate in full and model scale. The stress gradient is different in the two structures leading to a compromise between the two basic descriptions.

This nearly constant crack propagation causes disproportionately rapid cracking in model structures and leads to early failure. This is an important finding and shows

- The s-N curve is not a fundamental presentation of fatigue
- Some of the scatter in fatigue testing is a result of this new size effect
- Small parts or thin gauge material has a greater susceptibility to failure

Hardrath has verified the existence of nearly constant crack propagation in the Langley data.

Another characteristic of random damage is a lowered endurance limit in the presence of random loading. The occasional high load interspersed

among the low loads generates dislocations which move to the grain boundaries under the action of the many low loads. This element of random damage is not a feature of low cycle fatigue however. The aspects of random damage are

- The cumulative damage fraction is reduced by an order of magnitude
- Loss in strength
- Loss in stiffness
- Lowered endurance limit
- Sensitivity of small parts

The random loading and the loss in strength may be combined mathematically to obtain a probability of failure. One inherently has in mind that the probability of failure should hold to some extremely low value through most of the life of a part and then rise toward the end of the life. Actual calculations show otherwise. The probability of failure rises many orders of magnitude in the early life, Fig. 7 and 8. If, in addition, a small high frequency dynamic load component is added to a slowly varying static load component, the probability of failure increases another order of magnitude. Further increases would result, were more loading components acting.

Recent studies of combined static and dynamic loads show ample number of cases in which several different type loads combined to cause failure where neither alone would dominate the loading. Various dynamic loads were prominent in these failures such as the acoustic loading or pseudo-acoustic loadings such as separation or reattachment, oscillating shock, and wakes. Fig. 10 is a presentation of some of the characteristics of these loadings. The scale of turbulence is everywhere large relative to the size of the structural elements, except for the turbulent boundary layer. This is a necessary ingredient in the failures in order to excite the fundamental modes of structural elements. The mode of failure was low cycle fatigue in many instances. Failures were found in the brief two second period spent at maximum dynamic pressure or transonic flight in certain missiles, during a single impulsive load occurring during the transition from separated to attached flow, or in a matter of an hour in engine inlet air ducts of aircraft due to flow separation under full throttle operation at zero air speed on the ground. These occurrences are contrary to the expressed view that failures are dominated by a single loading component.

As a further illustration of the complexity, witness this statement from a Swedish investigator, Ref. 9:

> "As it is never possible to fully compensate for great uncertainties due to insufficient testing by lowering the stress levels, it is concluded that, on the basis of the state-of-the-art foreseeable today, it is not possible to guarantee the same fatigue safety level for an SST structure as for subsonic aircraft, even at the expense of such high weight penalties as to render the SST economically unfeasible."

The researcher has reference to the fact that new materials and a new temperature regime on SST will lead to test data which is statistically insufficient to provide reasonable confidence limits. The weight penalty due to the uncertainty would be higher than the weight penalty due to temperature in this case. While no designer has ever consciously used such a weight penalty because of the uncertainty factor, if mathematical rigor were the sole consideration governing the approach, such a penalty would be indicated. On the other hand, a very real problem exists in attempting to solve the design problem of a 30,000 to 50,000 hour vehicle without having data which covers even a fair fraction of that service life.

If we are all satisfactorily in agreement regarding the complexity of the fatigue problem, it is reasonable to ask what approach is appropriate at this point. Analysis will obviously not be ready with satisfactory solutions to cover the many major points given above until much more research is completed to identify the mechanisms, formulate acceptable models of the over-all process and pull the major events into a prediction scheme. A familiar analogy is available to draw on, however, at this point. The flutter problem was steadily worsening in a similar manner approximately a decade ago and the flutter model technique was extended in several important ways to fill the gap.

A progress report is given on a special type of dynamic model with scaling capability for the various aspects of this problem.

A DYNAMIC MODEL FOR LOW CYCLE FATIGUE

Model design and development in two areas will be presented:

- Panels
- Complex structure

Where the same model design principles are used in each case, the modeling principles consisted of item-by-item structural scaling, preserving scaled geometry and configuration, the same materials and the same fastening, joining and assembly. This procedure leads to scaled environments, scaled structural characteristics, scaled response and stress at corresponding points of the structure, an accelerated time scale and similar damage mechanisms. The scaling process in general will affect neither the environments nor the damage processes significantly because the structural dimensions of the model structure are everywhere large relative to the air molecules which govern the environments or the material atoms which govern the damage mechanisms. There are limitations, however, and these are given.

ACOUSTIC FATIGUE OF PANELS

A program, Ref. 6, was completed to determine the feasibility of using dynamic models for acoustic fatigue studies. This program was successful in developing scaled hot jets, Fig. 11-13, and in demonstrating scaled response in several different panel designs, Fig. 14 and 15, and in obtaining

a consistent story of expected failure times, Fig. 16. The hot jet development made use of the same gas, the same temperature pressure and velocity ratios with resulting duplication within one DB of the acoustic excitation across the entire frequency band in 1/3 and 1/6 scale. The high frequency scaling results established the capability of the modeling tool to the highest frequency likely to be required. The consistent failure times obtained reflected the early failure in model scale intermediate between scaled and constant crack propagation. The next step was the application of the technique in two ways

- Extension to successively more complex structural components
- Jump to complex built-up vehicle structure

Only the latter has so far been attempted.

SCALING COMPLEX STRUCTURE

Two programs, Ref. 10 and 11, have been completed to scale complex structure and to substantiate this scaling through measurement of acoustic transfer functions involving transmitted response over long dimensions through the vehicle and through firing of scaled solid propellant rocket engines to duplicate responses measured in the full scale article. The objective has not been fatigue study, although this could be obtained by joining measured responses to a satisfactory damage evaluation criterion. Rather the purpose has been to scale vibroacoustic response--to solve the high frequency response of complex structure. An auxiliary objective included reasonable model cost requiring some compromise in structure and equipment simulation.

The objective of perfect response scaling can be met through a perfectly scaled model--to this assumption there should be little argument. The problem is then one of technique targeted to either near perfect scaling or one of compromised scaling to meet a reasonable cost.

Acoustic transfer functions were measured using a random air modulator for input at various stations along the vehicle and measurements of the response at other points were taken in 1/3 octave bands. Limited success in comparing model to full scale has been obtained--rms values of the transfer function are accurate to 6 DB standard deviation, a factor of two. Plots of the transfer function across the frequency band for model and full scale would show deviations at particular frequencies which are larger than this. In other words the success obtained concerns only the average value across the frequency band at this stage. This is not to say that there were not cases obtained where both level and shape agreed across the entire frequency axis. The model would be insufficiently accurate, however, in its present compromised form, were the measured acoustic transfer functions to be used as a criterion. Scaled rocket engine firings have shown results which are considerably better than this--variation from scaled response of only 1/2 this amount, 3 DB, a percentage error of 40%, a satisfactory accuracy when compared to other approaches to vibration prediction.

The objective of reasonable model cost has been an interfering factor therefore and must be discarded. Typical compromises consist of

- Sheet metal angles in place of extrusions
- Lesser number of rivets
- Internal clutter omitted
- Equipment simulated by weight only

When this compromise associated with cost is dropped the accuracy should lie in the band ±1-2 DB. To accomplish this requires a vanishingly small allowable compromise. For example, joints and fasteners, doors and many equipment, fluid and useful load items will need to be simulated. Wiring might be an item reasonably omitted.

The second program in scaling complex structure was itself an attempt to design improved accuracy into the model via exact scaling of honeycomb sandwich structure. It was proven in early studies that a model sandwich based on foam plastic was inadequate and an interference to recognizable scaled response. True scaling of sandwich structure was easily accomplished and led to the limited success reported. Scaled solid propellant rocket engines have been fired and responses and excitation measured at approximately 20 points. The data is under evaluation at present, but the principal result is essentially that given above, i.e., ±3 DB standard deviation . Scaled instrumentation is vital in many areas because of the effect of the mass of ordinary instrumentation at the high frequencies involved. Scaled instrumentation requires one or two gram instruments, practical examples of which are commercially available.

MODEL CAPABILITY

The dynamic model is a remarkably exact tool to perform structural qualification. The many aspects of the fatigue problem presented in the first half of this paper would be satisfactorily covered. Important combined static, dynamic, buckling and environmental loadings are accommodated, Fig. 21. Combined damage or failure modes, Fig. 22,arising from these separate areas are properly integrated. And very importantly, the studies may be conducted in the design stage concurrently with the development of full scale hardware.

The information available from the models is summarized in Fig. 23, and the advantages in Fig. 24. Scaled engines of any description may be built including jets, and liquid and solid rocket engines and will ordinarily be required. Both jet and solid rockets have been utilized to date and designs have been completed for liquid engines. Structural characteristics and responses can be measured and the environment at the location of sensitive equipment items obtained. The failure mode and the point of failure may also be determined.

The high frequency characteristics have been duplicated on structural components, thermal and fatigue scaling can be accomplished. The duplication of the dynamic characteristics guarantee that buckling and other stability problems would be satisfactorily covered. Other aspects of the damage such as corrosion and creep should be brought under study.

The model time and frequency scale is increased by the scale factor. In a 1/4 scale model, events occur four times as rapidly. In fatigue tests this is a major advantage in time and costs. Thermal scaling is possible through the use of scaled heat sources. Attempts to simulate the whole process in the wind tunnel have missed the model capability for transient and steady temperature studies when the correct input is introduced in any convenient way.

STATEMENT OF TECHNIQUE

Item-by-item scaling is accomplished by a linear reduction of all dimensions. Structural stiffness, mass, and damping are each of equal importance. The area moments of inertia about the three principal axes must be scaled at all points of each element. Slip damping is the mechanism which generates damping in complex structure, and this depends on contact pressures. Fabrication and joining should provide a reasonable duplication of these pressures. The degree of fidelity required in the modeling is very high. Compromises unsupported by test should not be used. The principal items to consider in choosing the scale factor are minimum gauge of the material, engine scaling, and the ability of the instrumentation system to function at the new higher frequency band. Use of the model in the wind tunnel to determine aerodynamic excitation should be considered. Substudy experimental testing in support of major model program is recommended strongly. The useable frequency band of the model is related in part to the size of the smallest detail which is faithfully reproduced. Structural sandwich scaling must be carefully reproduced also. Honeycomb core density in pounds per square foot remains the same. The scaling laws and a fuller statement of technique is presented in Ref. 10.

MODEL LIMITATIONS

A principal variation in fatigue scaling was uncovered in showing the failure times would not follow a prediction based on the s-N curve. Crack propagation was not scaled, but was approximately constant in different scales. Early failure was a characteristic of both random and sinusoidal loading. This variation from hypothesized scaling could be typical of many that might arise from parameters such as stress gradient, creep, corrosion, and the humidity effect on fatigue, for none of which are the scaling relationship known. These are not limitations but an inability to state the scaling law in advance. Early failure is not really early but due to a failure to understand the process. Supporting experiments will provide the supplementary information required--these do not require the model of the complete vehicle but small tabs or structural components in appropriate models.

If the thermal input distribution were described by radical variations at the leading edges it would be difficult to simulate these with artificial heat sources. Since present materials have little margin for excessive heat, conservatism is not indicated. Techniques for accurate distribution of artificial heat are needed. Small inevitable compromises in tolerances,

fabrication and structural joints will provide a reduction in over-all strength of the model relative to full scale estimated at 5-10%.

To do the full damage to structure arising from random loading, intermixing of the load levels may have to be carried out in great detail to simulate the natural occurrences in service. The cumulative damage fraction varies from below 1 to above 7 because of residual stresses introduced when a large positive or a large negative load cycle is introduced to a random sequence, Ref. 11. Tremendous detail in load application with its supporting information may be required or must be assumed unless there is a willingness to accept the most damaging combination of loads. This problem is not peculiar to low cycle fatigue however. Other limitations due to material gauges, instrumentation and its frequency band, and tolerances appear in choosing the scale factor.

APPLICATION TO LOW CYCLE FATIGUE

Applying the dynamic model to low cycle fatigue may be accomplished at this point on the basis of the previous work. The excellent start obtained on the model of complex structure was for the purpose of vibration response scaling however, and fatigue scaling requires a step upward in scaling fidelity. Attaining high frequency scaling was the major step needed in qualifying the dynamic model for low cycle fatigue and this step has been accomplished. No different ingredients are required for a model for low cycle fatigue for dynamic response or for acoustic fatigue. It is only the degree of accuracy which is changing. The information learned from testing the first model allows the definition of the considerably improved model of complex structure required for fatigue.

The creep mechanism is a prominent part of low cycle fatigue and knowledge of its action in model scale should not be presumed. Testing done in model time scale is basically valid because the well known frequency effect on fatigue strength is not a primary effect, especially for the small changes in frequency and scale likely to be used here. The frequency effect, the creep action, and the influence of temperature are closely related in fatigue. Several alternatives may be introduced in the testing in order to determine how some of the mechanisms are acting. The testing done in the usual model time scale may be compared to testing in model scale in real time. Variation in temperature should give an incremental difference to the damage, containing an increment due to creep. Real-time, model-time comparisons inevitably change the crack propagation mechanism as well, however. Early failure in model scale will occur still earlier if the peak loads are held a longer time period. Opposing trends are present and supporting research may need to measure only total effects or possibly may need to identify each separate trend.

The primary accomplishment of the model in properly designed low cycle fatigue tests will be to locate the most sensitive areas of structure. A failure time will be predicted which may be a less accurate accomplishment. In supporting experiments, further comparisons between full scale and model scale for component structure surrounding the failure point will refine the failure time prediction.

SUPPORTING EXPERIMENTS

Supporting experiments to uncover and substantiate approaches to the model design, to verify unusual test results and to vary parameters so as to answer questions raised by the work may be accomplished at nominal costs to the over-all program. Components and even small tabs will suffice for the bulk of this work. Vibration shakers can resonate these specimens at reasonably high frequency and accomplish the fatigue failures most expeditiously. Tests at a 1000 cps cover 3.6 million cycles in an hour. Reliance on the small frequency effect make this procedure valid although the results may occasionally be checked at lower frequency.

RECOMMENDED FUTURE WORK

The following research is recommended:

- Research specifically to develop better fatigue resistant materials is required. It is necessary to rank order materials from the standpoint of sensitivity to damage from random loading.

- An opportunity exists to out guess our severe upcoming problems due to temperature fatigue if work is begun promptly.

- Since formal theories to cover the gamut of problems associated with fatigue will be long in coming a forthright push for satisfactory "engineering" methods should be made. The biggest stopgap will be provided by experimental methods.

- The part played by combined loads and combined failure modes must be determined.

- Interactions of creep, corrosion and humidity with the fatigue damage should be determined.

CONCLUDING REMARKS

The fatigue problems occurring extensively in service vehicles cannot be solved without reference to the impact of dynamics on the over-all process.

Material deterioration due to fatigue damage includes loss in strength and loss in stiffness at high stresses of importance to many dynamic problems.

Extensive service problems in fatigue are not due to misapplication of the state-of-the-art but a failure to understand certain fundamentals only recently uncovered by research.

High frequency dynamic loads apparently create the major damage to the material. One aspect of the damage is loss in strength which couples with the greater likelihood of obtaining lower loads and results in greatly increased probability of failure in the early life of the part.

The economic as well as the engineering advantages of applying the dynamic model to low cycle fatigue problems should be noted. The solution of major problems can overlap the design stage rather than have these problems uncovered in service.

The present state-of-the-art in fatigue is so inadequate that the various experimental approaches are the approaches to be relied on in the foreseeable future.

To avoid severe future problems in temperature fatigue requires extensive study now. The dynamic model should function well for both low cycle fatigue and temperature fatigue.

The principal technical advantage of the dynamic model is its ability to integrate the material damage from many different loading and many different failure modes.

APPENDIX A

Wood, Ref. A-1, shows two essentially distinct types of failure have hitherto been classified as fatigue. One predominates at large stress amplitude and the other at smaller stress amplitudes. He termed these the H and F mechanisms.

The H, or hardening mechanism, is essentially the same as static deformation. The internal stresses are high, the total plastic strain is small (positive and negative added irrespective of sign), the disorientation is large in the sense that the boradening of the Lane spots is quite significant, the deformation is primarily due to coarse slip, and the distortion in the slip plane is normal in the sense that it has essentially the same features as in static deformation. Wood concludes failure in the H range is essentially the same as under static conditions and he calls it "delayed static fracture". It is delayed because the hardening process which precedes the nucleation and propagation occurs in a less efficient manner in this range as compared to the normal static tests.

On the other hand, in the F range conditions are significantly different. The internal stresses are low and the deformations proceed with negligible hardening. The total plastic strain is large and the X-ray distortion small. The deformation is due to fine slip involving to-and-fro motion of a large number of individual, isolated dislocations, rather than the avalanche release of dislocations of coarse slip. The slip plane distortion is one of gradual intensification. In the H range when a slip band appears, it appears suddenly (order of 10^{-4} seconds) and is strong to start with. In the case of fine slip which appears to be the primary mechanism of deformation in the F range, the slip bands are initially hazy and gradually intensify during progressive fatigue. In these regions of slip intensification the fatigue cracks seem to occur. Accordingly the fracture is considered to be due to deterioration of structure. The "persistent slip bands" that occur in these regions were shown to be responsible for "fissures" which eventually lead to cracks.

Even if a crack develops in the F range, when it grows the local stresses in the immediate vicinity will be relatively high due to stress concentration. The result of this will be that at some stage during the propagation, a crack which started in the F range will behave more as if it were in the H range. On this basis the region of validity of Coffin's results may extend much beyond the range observed by him and others, presumably up to about five million cycles.

The above is taken from Ref. 5.

Ref. A-1. Wood, W. A.: Some Basic Studies in Fatigue of Metals. Conference on Fracture, Technology Press, MIT, April 1959.

REFERENCES

1. Pian and D'Amato: Low Cycle Fatigue of Notched and Unnotched Specimens, 2024 Aluminum. WADC TN 58-27, February 1958.

2. Coffin, L. F.: "Design for Low Cycle Fatigue," SESA Design Clinic, October 1959.

3. Christensen and Denke: Crack Strength and Crack Propagation Characteristics, ASD-TR-61-207.

4. Freudenthal, A. M.: "On Stress Interaction in Fatigue," Journal of the Aeronautical Sciences, July 1959.

5. Valluri, S. R.: A Unified Engineering Theory of High Stress Level Fatigue, Galcit SM 61-1, CIT, January 1961.

6. Blatherwick, A. B. and Olson, B. K.: Stress Distribution in Notched Sections Under Cyclic Stress. ASD-TR-61-451, October 1961.

7. Gray, C.: Feasibility of Using Structural Models for Acoustic Fatigue Studies, ASD-TR-61-547, October 1961.

8. Roberts, W. H. and Wilhem, D.: Simultaneous Application of Static and Dynamic Loads to Sonic Fatigue Test Articles, ASD-TDR--63, August 1963.

9. Lindberg, B.: Possibility of Designing a SST with a High Fatigue Safety Level, Aero. Res. Inst. Sweden, TN-HE-957.

10. White, Roberts, Eldred: Vibration Prediction in Typical Flight Structure ASD-TDR-63-801, August 1962.

11. Schijve, J.: Estimate of Satisfactory Performance of Aircraft Structures. 52 NLR, ND212, June 1962.

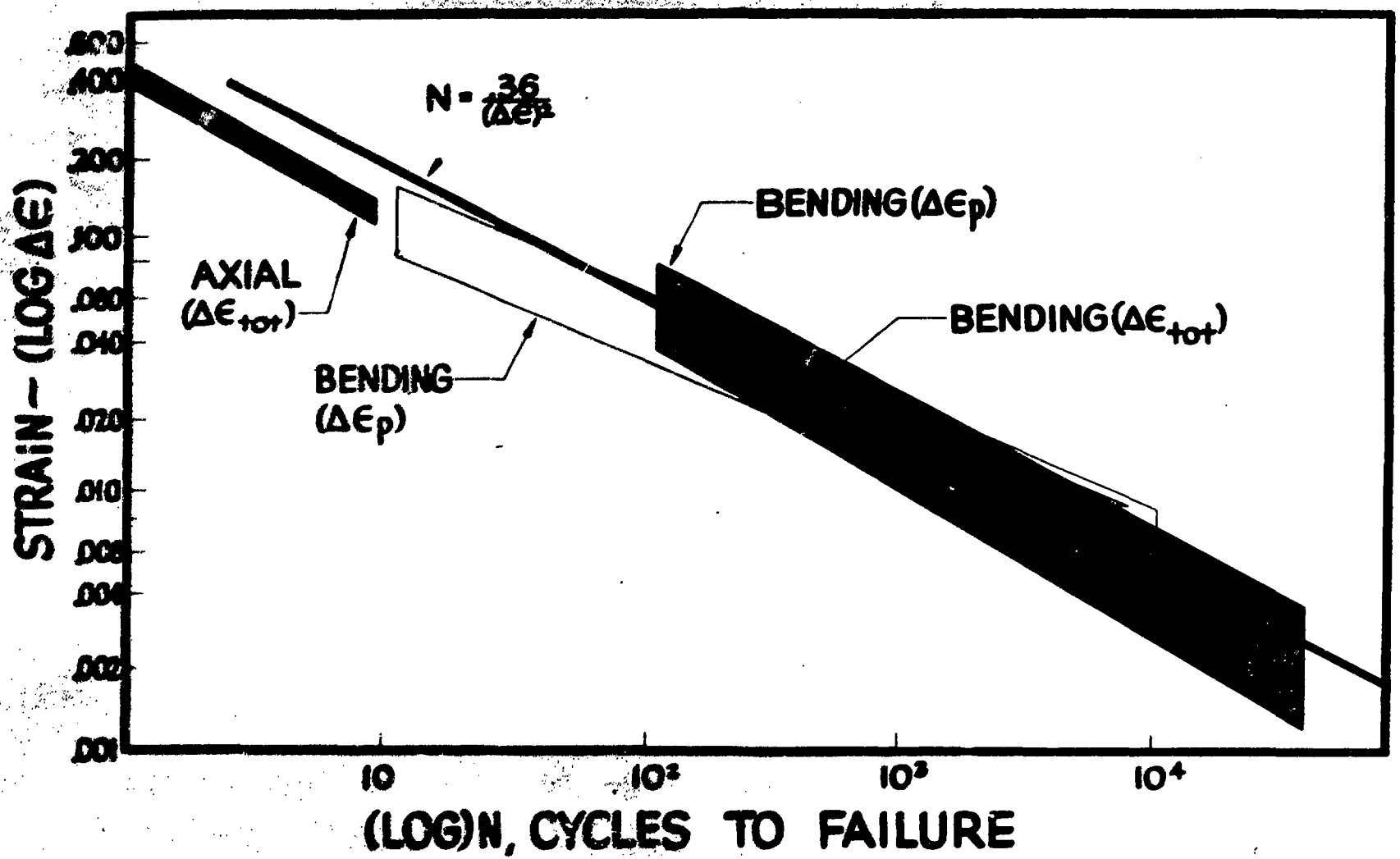

Figure 1. Fatigue Correlation

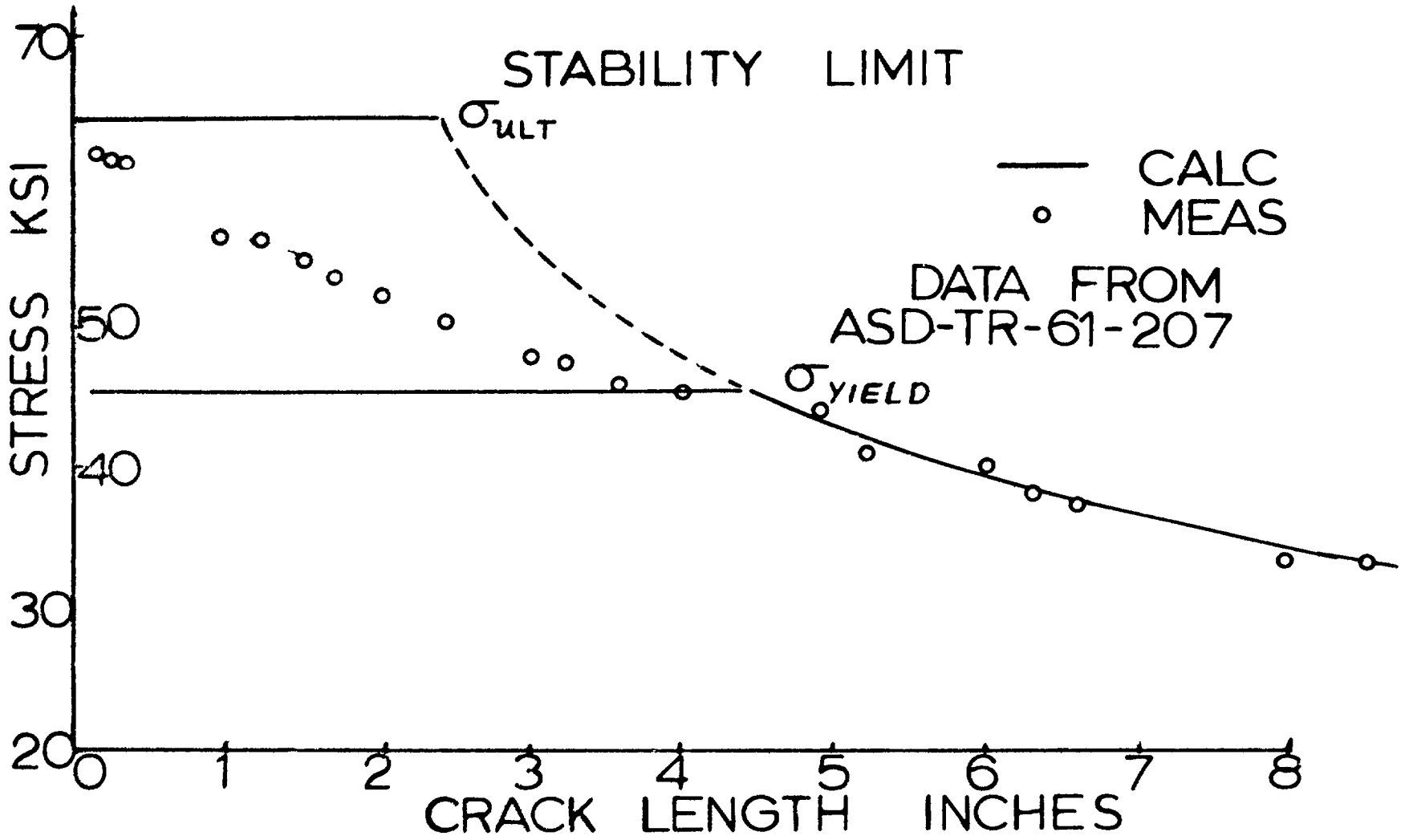

Figure 2. Stability Limit Provided by Griffith Critical Crack

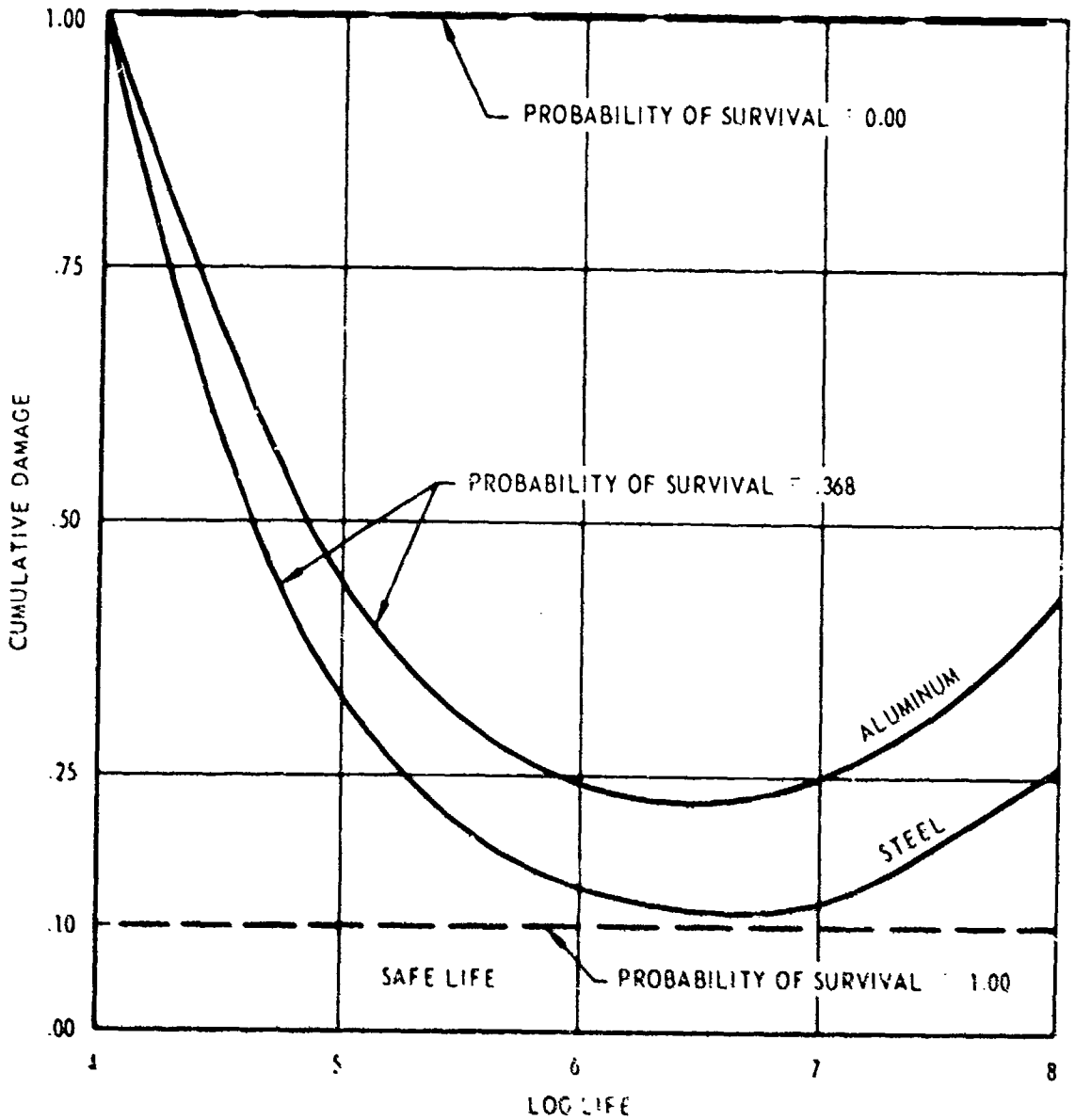

Figure 3. Cumulative Damage Fraction Under Random Loads (Freudenthal's Experimental Data)

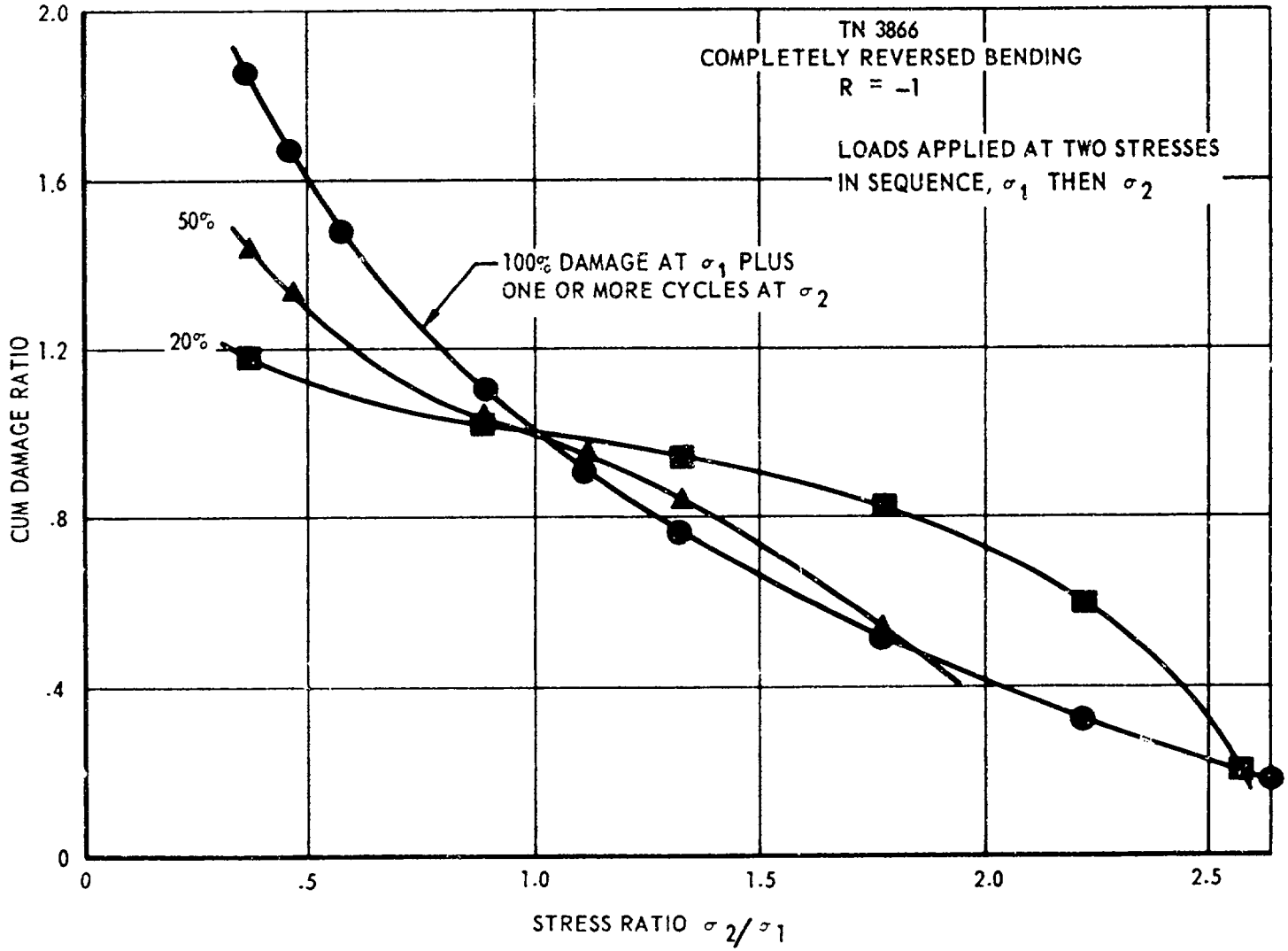

Figure 4. Cumulative Damage Fraction in Two Step Fatigue

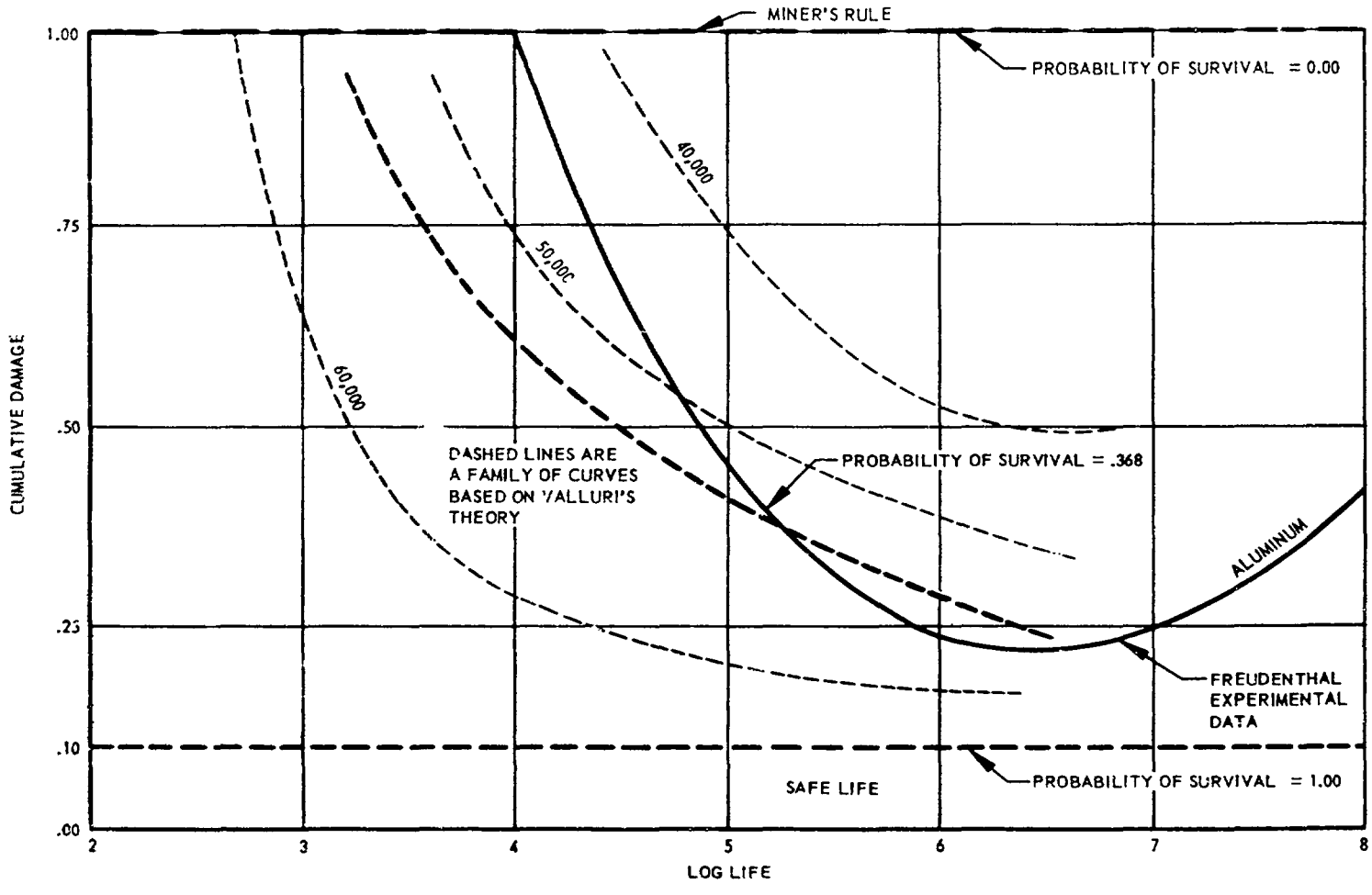

Figure 5. Comparison of Cumulative Damage, Theory and Experiment

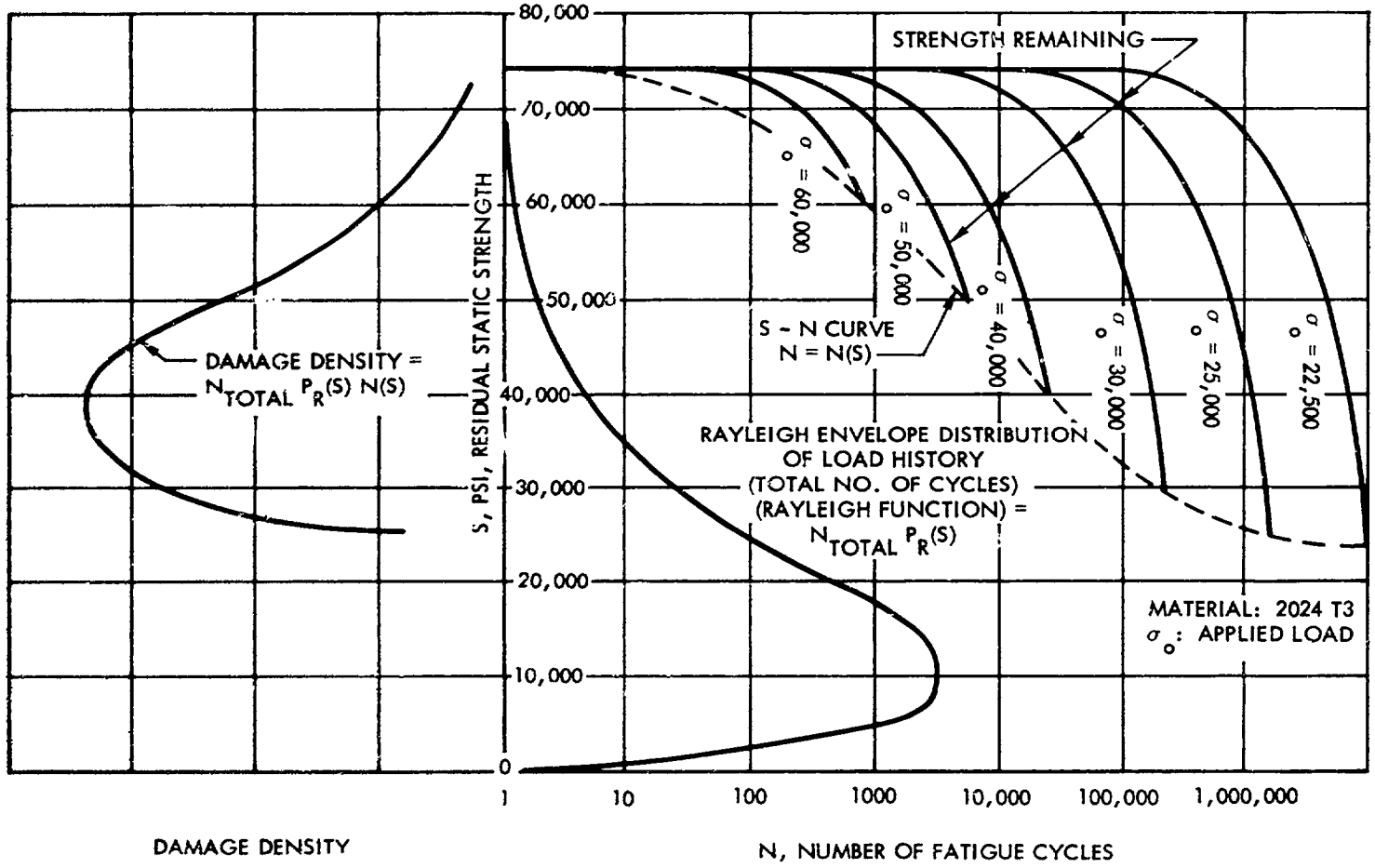

Figure 6. The Load History, the Fatigue Characteristics and the Damage

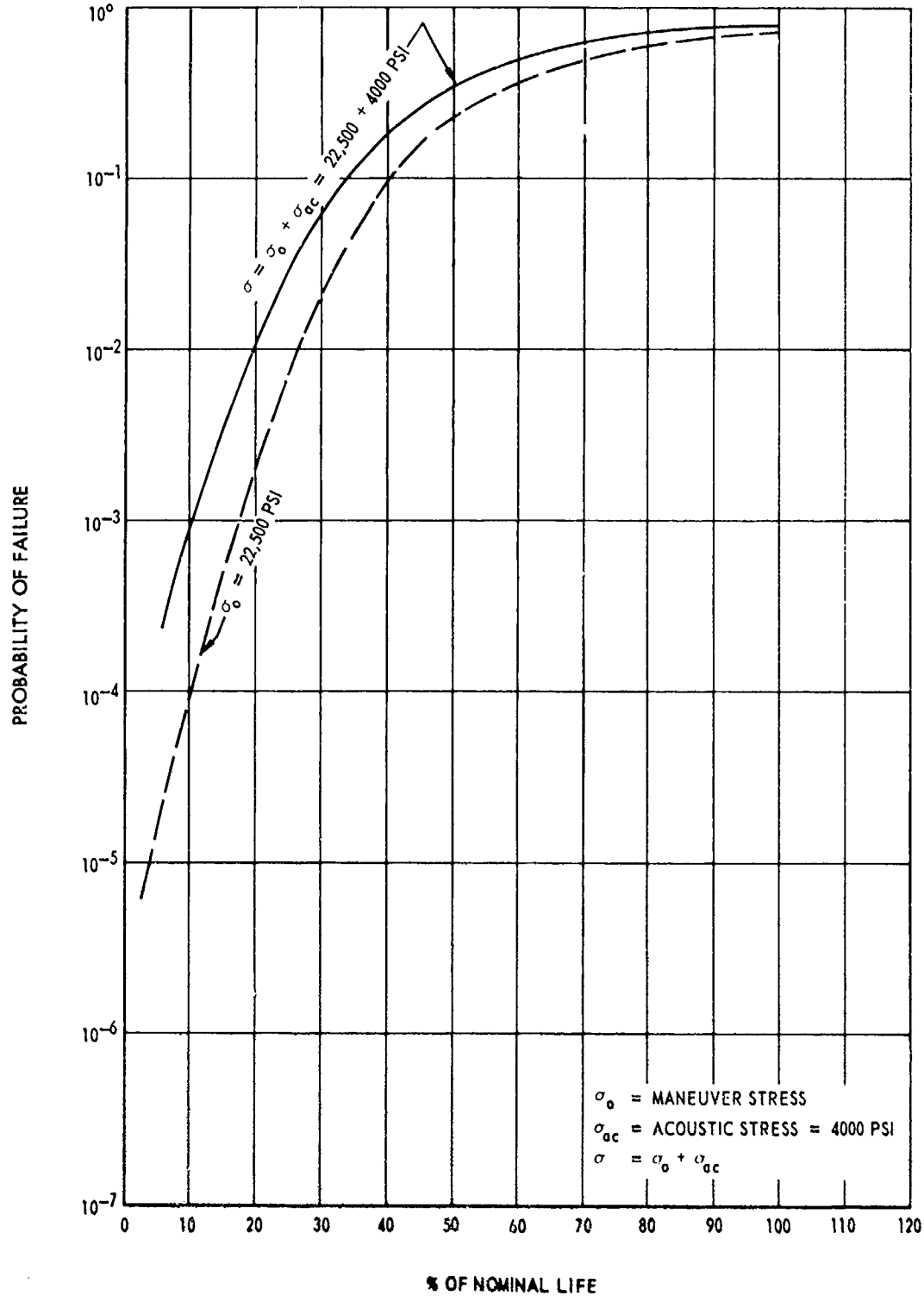

Figure 7. Probability of Failure due to Both Maneuver and Acoustic Stress (4000 psi)

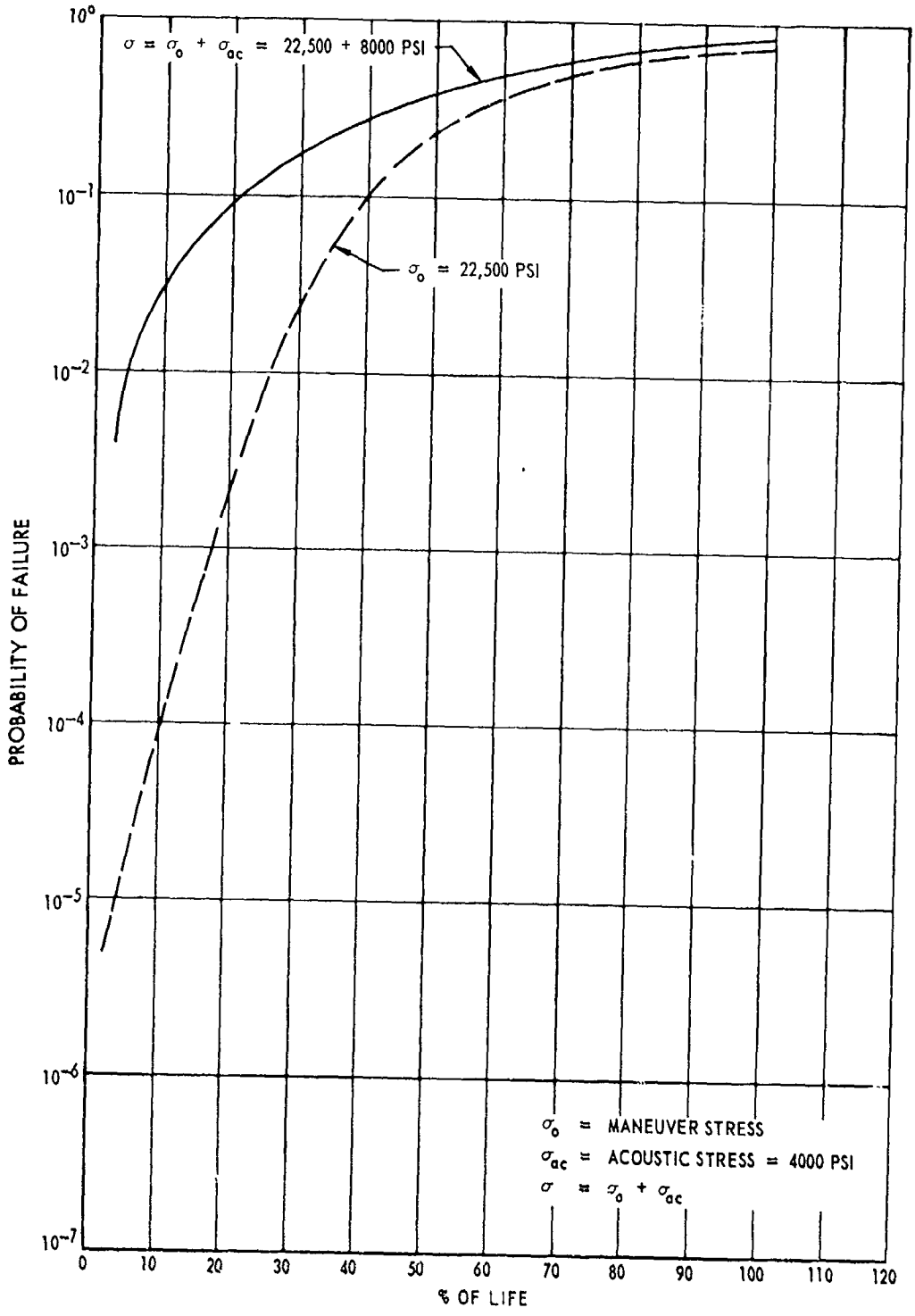

Figure 8. Probability of Failure due to Both Maneuver and Acoustic Stress (8000 psi)

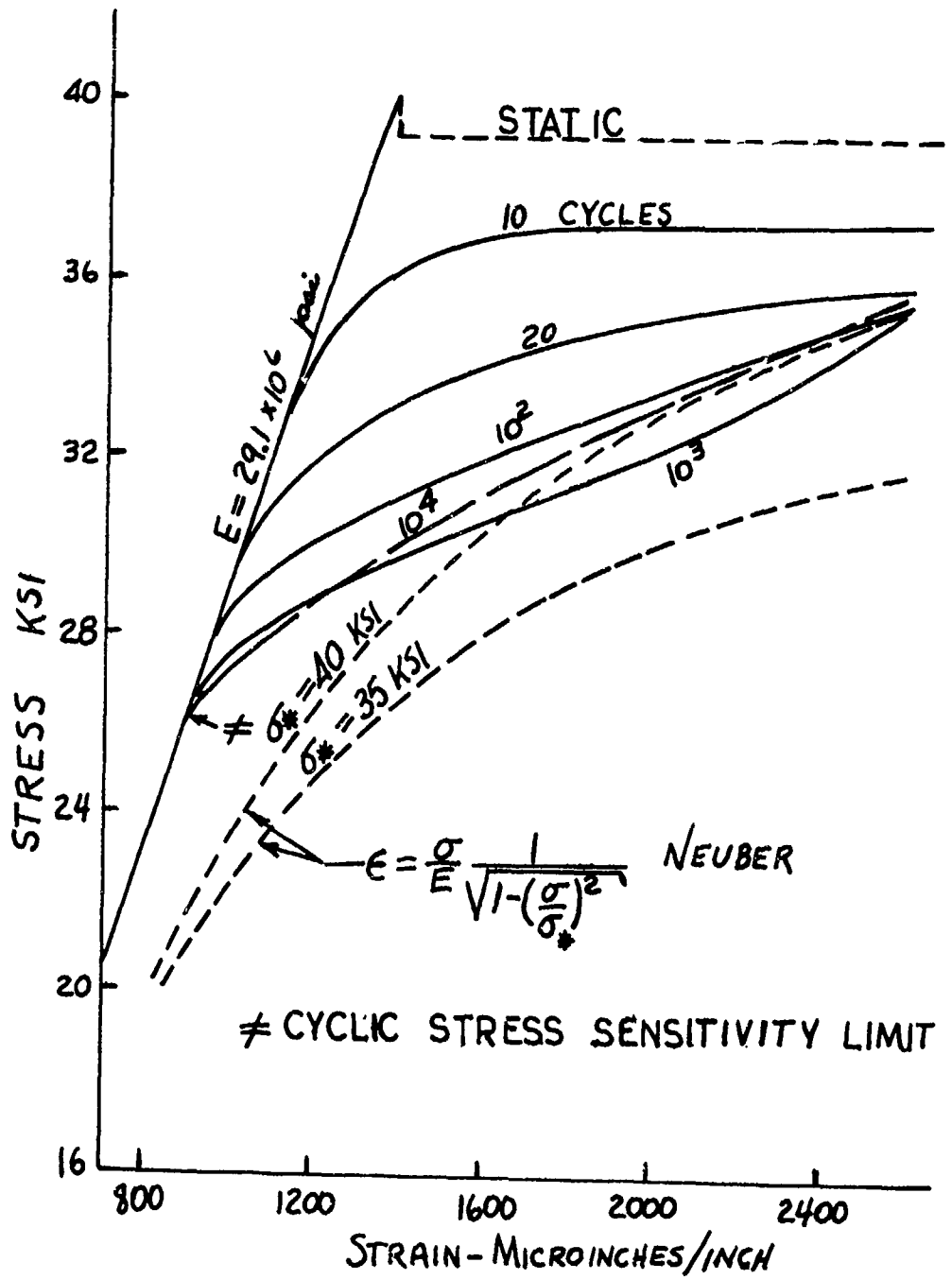

Figure 9. Changes in Stress Strain Curve During Fetigue (SAE 1018 Steel)

SOURCE	$\Delta P/q_{rms}$	APPROXIMATE MAGNITUDE (IN DECIBELS)	RELATIVE MAGNITUDE
ROCKET NOISE		160~166 (max recorded 172)	LARGE
CAVITY RESONANCE	to 0.4	to 177	SMALLEST DIMENSION
OSCILLATING SHOCK	to 0.1	165	VARIABLE
SEPARATED FLOW	to 0.1	165	DIMENSIONS OF FLOW SEPARATION
WAKES	to 0.037	155	DIMENSIONS OF WAKE
BASE PRESSURE FLUCTUATIONS	0.015	149	LARGE
TURBULENT BOUNDARY LAYER	0.006	141	VERY SMALL

Figure 10. Relative Magnitude of Certain Pseudo-Acoustic Loads

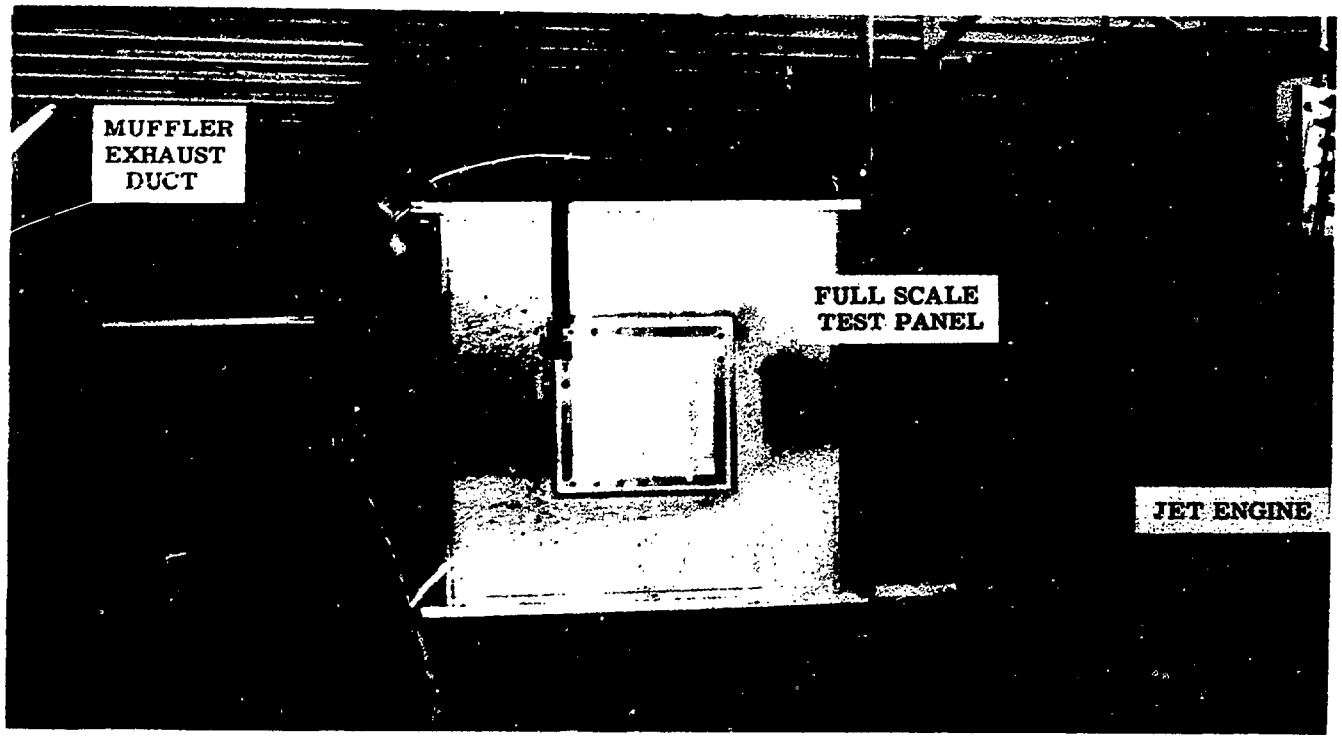

Figure 11. Full Scale Jet Engine During Acoustic Fatigue Failure

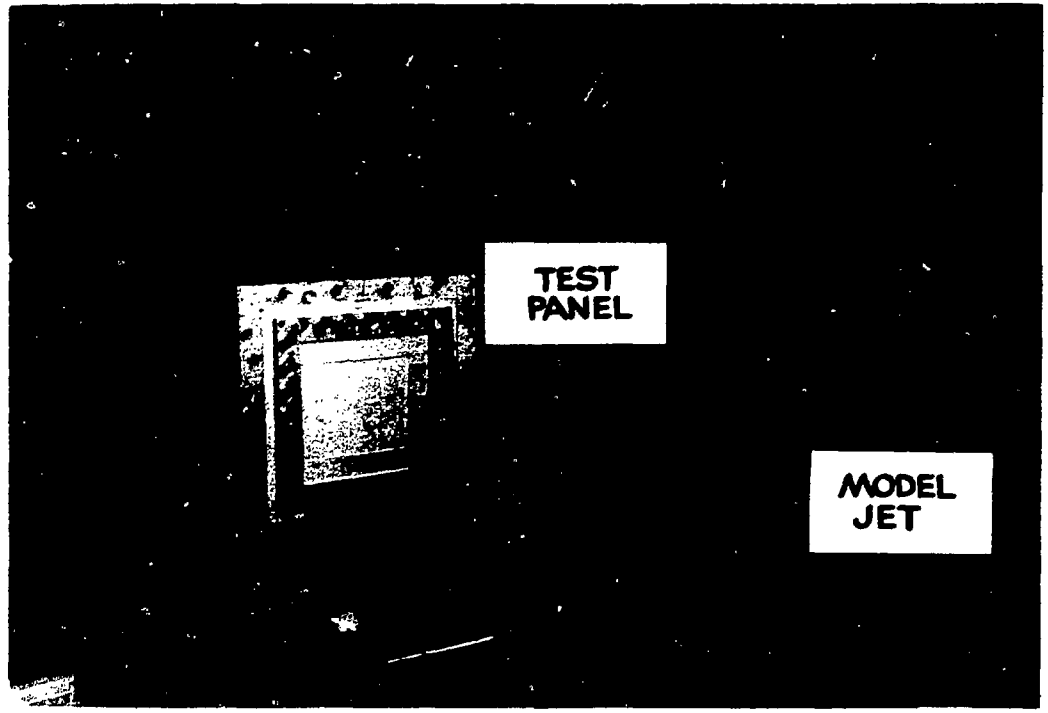

Figure 12. Model Scale Jet Engine During Acoustic Fatigue Failure

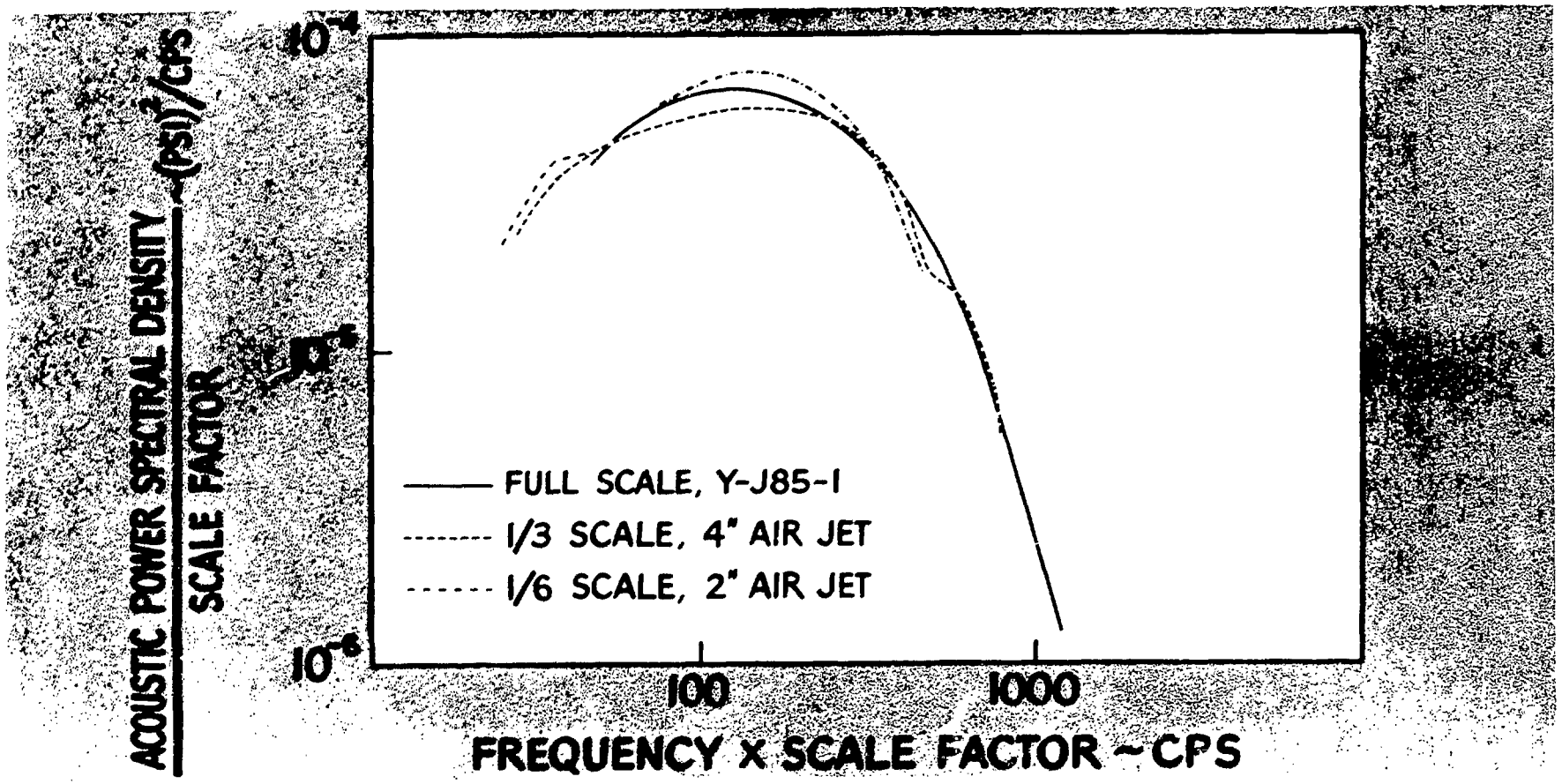

Figure 13. Acoustic Excitation as a Function of Frequency

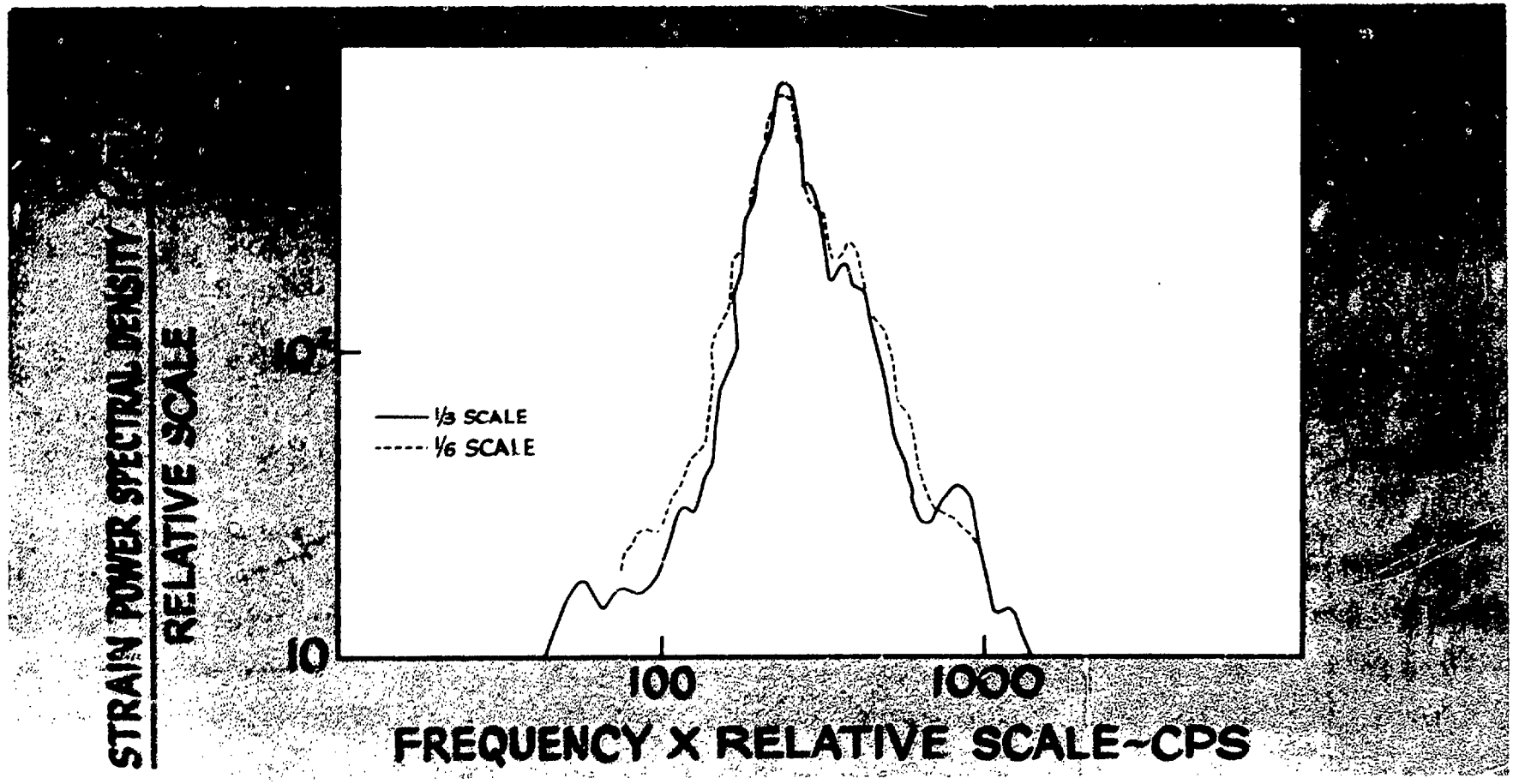

Figure 14. Spectral Density of Response, Panel with In-Plane Freedom

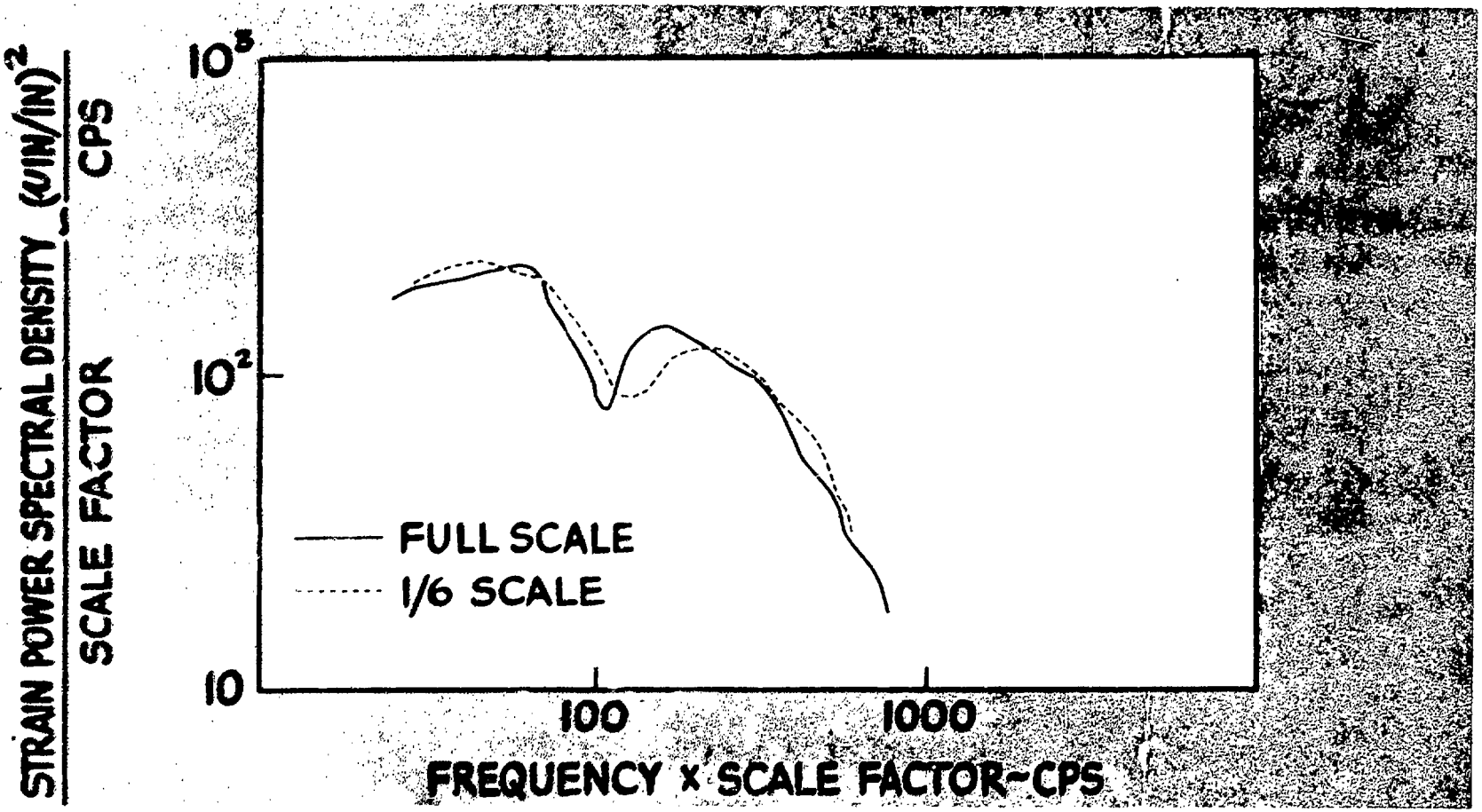

Figure 15. Spectral Density of Response, Clamped Panel

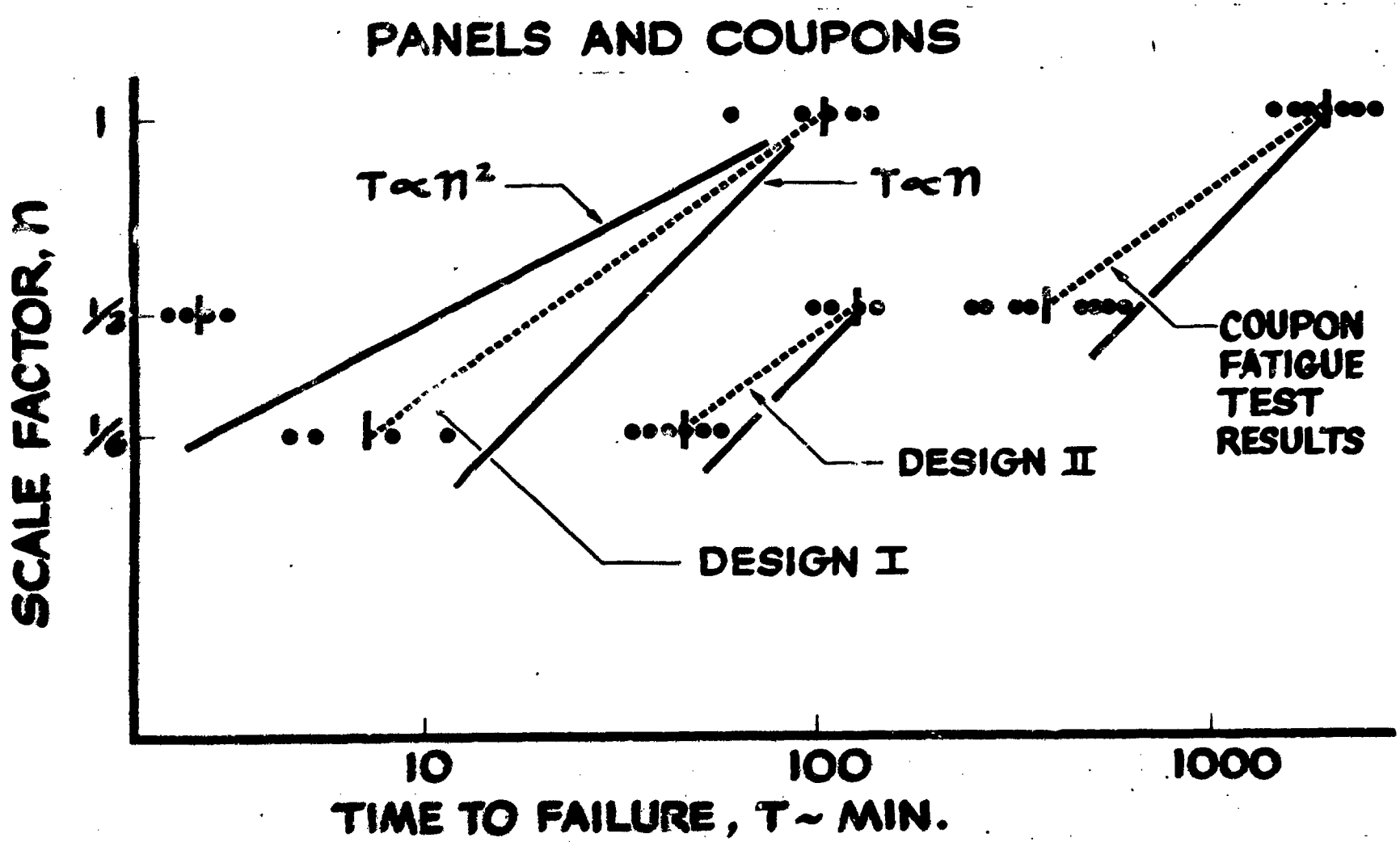

Figure 16. Fatigue Failure Times

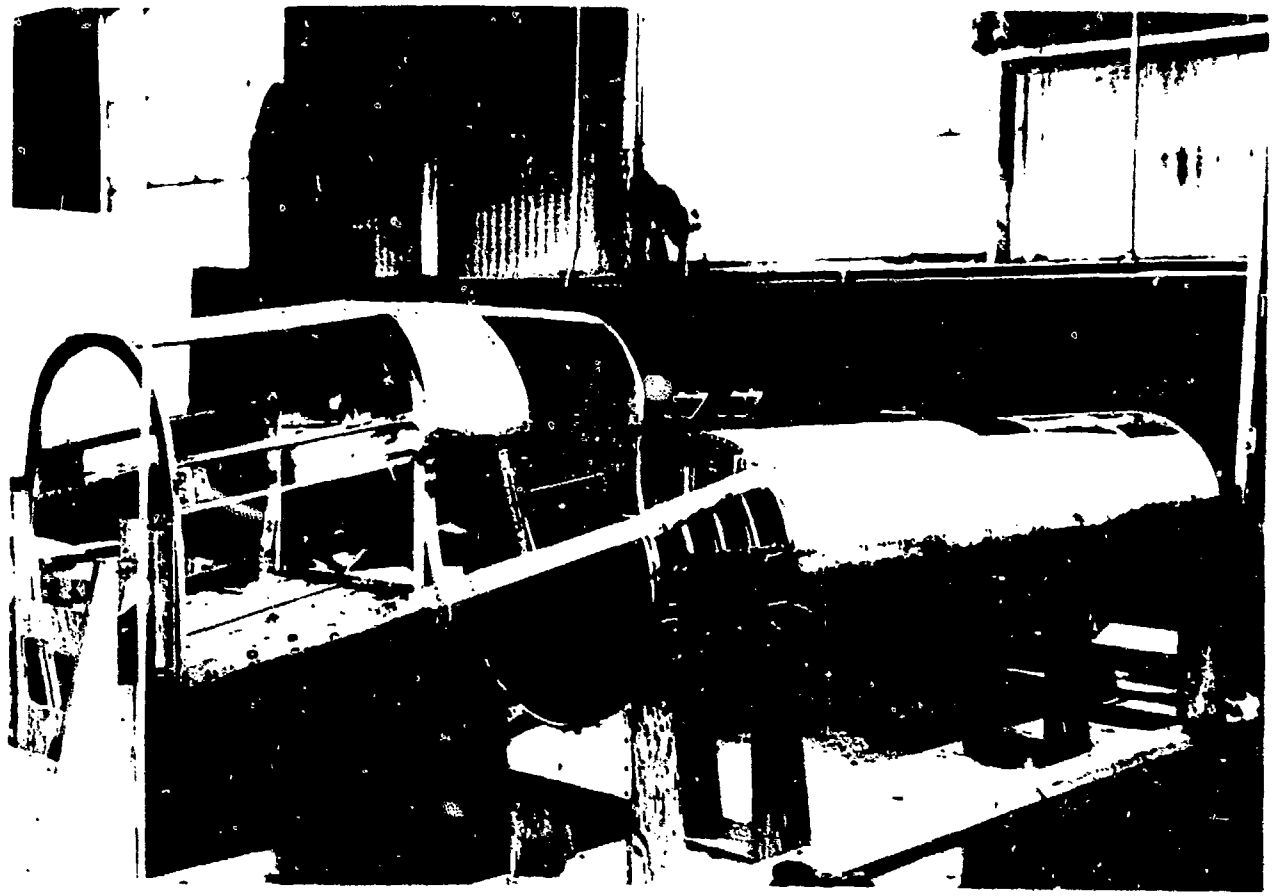

Figure 17. Model Assembly

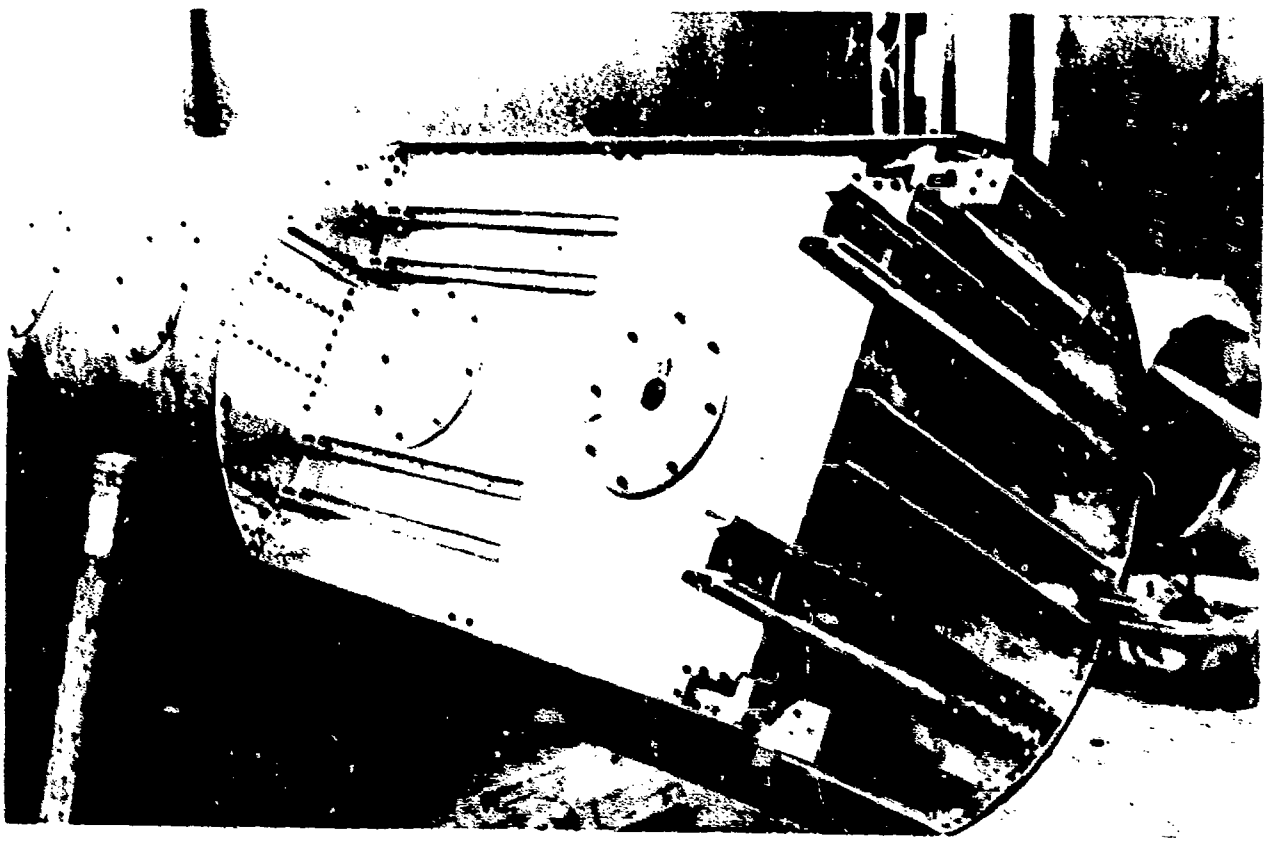

Figure 18. Model Top Deck

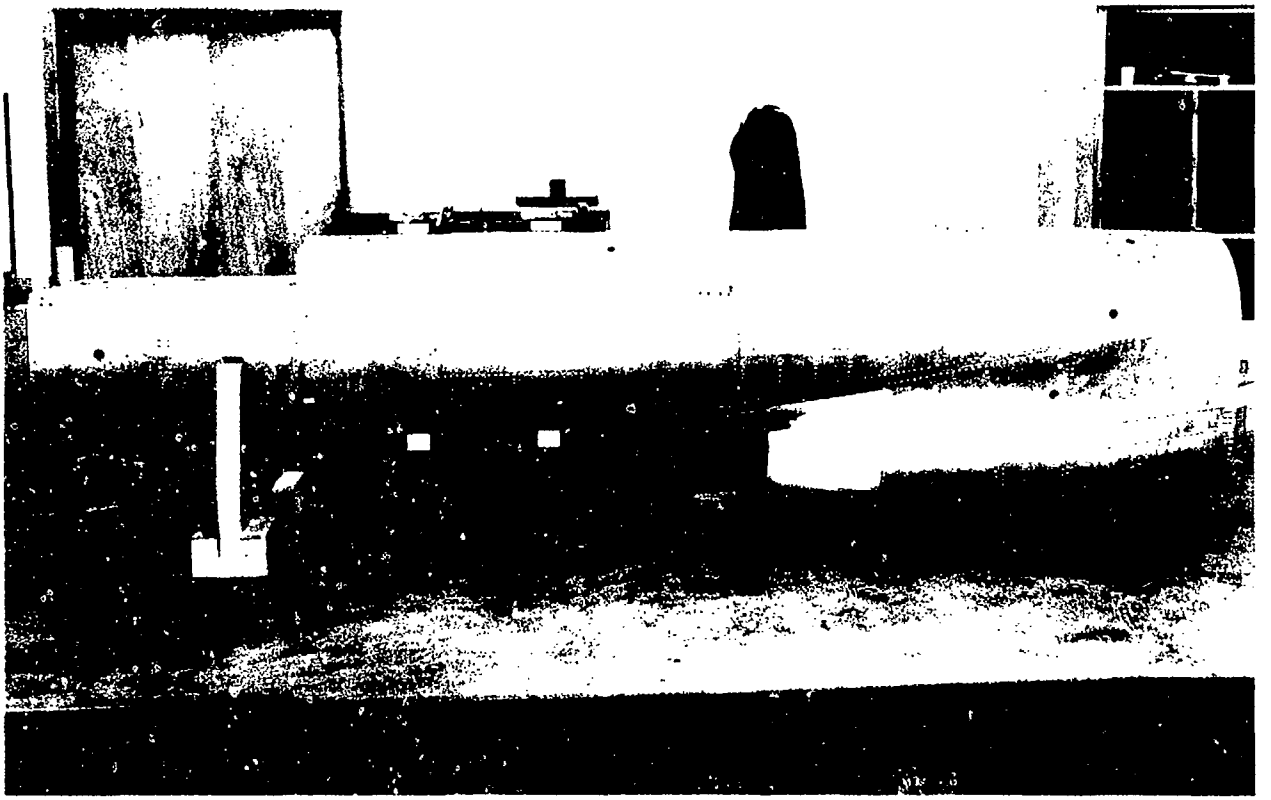

Figure 19. Model Side View

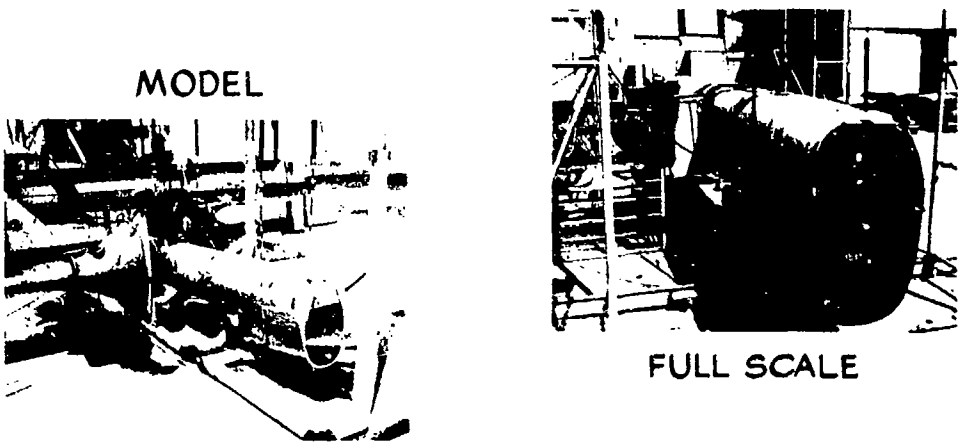

Figure 20. Model and Full Scale Test Set-up

ACOUSTIC	AERODYNAMIC	STATIC	DYNAMIC	TEMPERATURE
ENGINE NOISE	BUFFET	MANEUVER	WIND	AEROSPACE HEAT
CAVITY RESONANCE	SEPARATION	INERTIA	WIND SHEAR	ENGINE HEAT
INTERNAL VEHICLE NOISE	CONVECTED TURBULENCE	STEADY AIR LOADS	GUST	HOT SPOTS DUE TO TURBULENCE
	BASE PRESSURE FLUCTUATION	GROUND-AIR -GROUND	LAUNCH OR T.O.	CRYOGENIC FUEL
	OSCILLATING SHOCK	PRESSURE	GROUND HANDLING	SPACE TEMP. DIFFERENCE
	WAKES FROM DRAG DEVICES		LANDING GROSS VEHICLE MOTION DURING ENGINE RUNUP	
	BOUNDARY LAYER		MECHANICALLY TRANSMITTED THRUST OSCILLATION	

Figure 21. Combined Loads

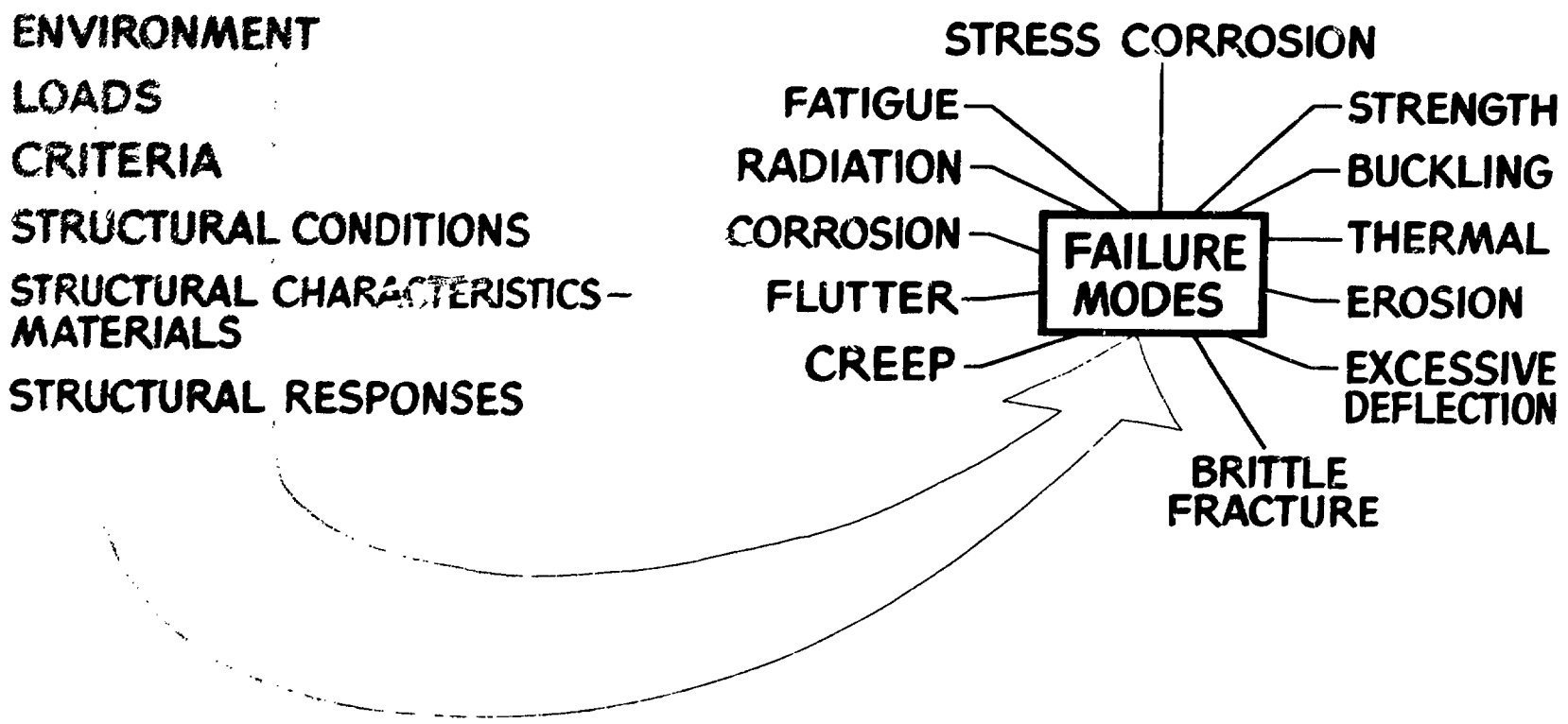

Figure 22. Combined Failure Modes

- STRUCTURAL CHARACTERISTICS ~ MODES DAMPING
- STRUCTURAL RESPONSES DURING ACTUAL FIRINGS OF SCALED ENGINES
- VIBRATION AND ACOUSTIC ENVIRONMENT REACHING SENSITIVE GUIDANCE
- MECHANICAL AND ACOUSTIC PARTS OF ENGINE EXCITATION
- FATIGUE LIFE MEASUREMENT
- VARIATION OF EXCITATION DURING 1ST FEW SECONDS OF LAUNCH
- EFFECT OF CHANGES IN STRUCTURE AND PAD CONFIGURATION
- EFFECTIVENESS OF VARIOUS DEVICES TO ATTENTUATE THE EXCITATION

Figure 23. Information available from the Dynamic Model

- DRASTICALLY SHORTEN DESIGN PERIOD
- QUALIFY STRUCTURE FOR COMBINED LOADS
- DETERMINE ENVIRONMENT TO QUALIFY EQUIPMENT
- TIME SCALE SHORTENED ~ SCALE FACTOR
- MEASURE LARGE SCALE TURBULENCE IN THE WIND TUNNEL

Figure 24. Advantages of the Dynamic Model

HAYSTACK ANTENNA 1/15 SCALE MODEL PROGRAM

Richard V. Bennett

North American Aviation, Inc.

Columbus, Ohio

ABSTRACT

This paper describes the design, construction and experimental test program for a 1/15-scale static and dynamic elastic model of the 120-foot diameter Haystack Antenna. The experimental phases of this program, which was conducted at the Columbus Division of North American Aviation, Inc., consisted of a rigging demonstration, influence coefficient tests and ground vibration tests. The program objectives were to demonstrate the feasibility of the proposed procedure for rigging the prototype antenna, to verify the analytical program used for predicting deadweight deflections of the prototype antenna, and to provide qualitative information concerning the vibration characteristics of the prototype antenna. All objectives were satisfactorily accomplished.

LIST OF ILLUSTRATIONS

HAYSTACK ANTENNA 1/15-SCALE MODEL PROGRAM

Richard V. Bennett

Senior Engineer
Dynamic Environments Lab
North American Aviation, Inc.,
Columbus, Ohio

Introduction

A 1/15-scale elastic and dynamic model of the Haystack Antenna was designed, constructed and tested at the Columbus Division of North American Aviation, Inc., in the period extending from September, 1960 to May, 1962. The test program consisted of a rigging demonstration, influence coefficient tests, and vibration tests.

The Haystack Antenna is a 120-foot diameter, Cassegrain elevation-azimuth antenna, which will be erected inside a 150-foot radome at Tyngsboro, Massachusetts for the Air Force's Electronic System Division. A structural arrangement of the complete antenna is shown in Figure 7. This antenna can be used for space communications studies, satellite tracking, and basic research investigations.

The accuracy required of the Haystack Antenna in accomplishing its objectives depends, to a large extent, on maintaining the primary reflector surface in its theoretical paraboloidal contour during all modes of operation. As a result, the specified surface tolerance is $\pm$ .075 inch for all modes of operation. The significant contributors to surface deviations are manufacturing tolerances, dynamic displacements, thermal effects and deadweight deflections, with the latter being the major contributor. The maximum expected surface deviations due to deadweight deflections have been predicted by a recently-developed complex analytical program, which was run on an IBM 709 computer.

The primary purpose of the model program, therefore, was the verification of this analytical program. Another objective of the model program was a feasibility demonstration of the proposed rigging procedure for the full-scale antenna.

During the course of the model program, two important changes were made in the plan for verifying the analytical deadweight deflection program. These changes are described as follows:

1. Theoretical and experimental influence coefficients were substituted for deadweight deflections as the comparative measure of verification.

2. Theoretical influence coefficients were computed using model stiffness distributions and geometry instead of the full-scale antenna physical property data.

The reasons for these changes will be given later.

After the rigging demonstration and influence coefficient tests had been completed, a vibration test program was initiated and conducted in conjunction with a closed-loop dynamic analysis of the full-scale antenna. The model vibration test objective was the provision of qualitative information concerning the vibration characteristics of the full-scale antenna.

Design Philosophy

The multiple objectives of the model program required consideration of many factors in planning the simulation techniques. Geometrical simulation was required for the rigging demonstration, while simulation of the axial and bending stiffness distributions was required for the influence coefficient tests. In addition, axial and bending deflection compatibility was required, since some structural members carry only tension and compression loads while others carry both axial loads and bending moments. As a result, the method of using direct dimensional scaling and identical full-scale antenna materials was selected to satisfy the simulation and compatibility requirements for most of the model structure.

Dynamic similarity, which would include simulation of the mass distribution in addition to simulation of the stiffness distributions, was not actually required for the rigging demonstration and influence coefficient tests. However, the use of direct dimensional scaling and identical full-scale antenna materials automatically produced a mass distribution which provided an approximate dynamic similarity. All model parts which were not directly scaled were designed as closely as possible with the same mass scale as the directly scaled parts, so that the reflector system would be properly balanced about the elevation axis. Thus, when the vibration tests were later added to the model program, it was possible to achieve the vibration test objectives without mass-balancing the model.

One major exception to the direct scaling rule was the parabolic reflector surface. No satisfactory single design method for the model parabolic reflector could be found which would satisfy all of the simulation requirements. Therefore, two parabolic reflectors were designed for the model. One, which simulated only the bending stiffness and contained half as many panels as the antenna reflector, was used for the rigging demonstration. The other model parabolic reflector, which was directly scaled and constructed in one piece, was used for the influence coefficient and vibration tests.

Other exceptions to the direct scaling rule were the elevation and azimuth drive systems, the hyperbolic secondary reflector, the pedestal or base, and the diagonal tension members. The elevation and azimuth drive systems were not duplicated on the model; however, the equivalent spring restraint of the elevation drive system was simulated. The upper and lower parts of the azimuth bearing were clamped together for the entire test program. The hyperbolic reflector was treated as a point mass, but its support struts had properly scaled stiffness and mass distributions. The model pedestal closely simulated the torsional stiffness of the full-scale pedestal, but only approximately simulated the bending stiffness. The diagonal tension members simulated only the axial stiffness of the full-scale members.

Small items such as turnbuckles, gussets, threaded studs, joint flanges and sleeves, bolts, nuts, lugs, pins, clevises, springs and weld fillets also could not be scaled directly. These items were designed to functionally simulate as closely as possible their counterpart full-scale components.

After the simulation techniques had been formulated, the model scale factors were derived. First, a geometrical scale factor of 1/15 was selected after considering the structural details required for rigging, the small dimensions resulting from direct scaling, the required construction accuracy, machine and tooling capabilities, handling problems and test area size. Then, the use of direct dimensional scaling and identical full-scale antenna materials, together with the geometrical scale factor, automatically determined the axial and bending stiffness and mass scale factors. Finally, the scale factors for deadweight deflections and slopes, influence coefficients, internal preloads, and stress were determined from the previously derived scale factors and the essential nondimensional similarity parameters for an elastic model. The vibration frequency scale factor was later determined from the previously determined scale factors and the essential nondimensional similarity parameters for a dynamic vibration model.

The resulting mass, stiffness, and geometrical scale factors produced a deadweight deflection scale factor of $1/15^2$. Such a scale factor would produce maximum theoretical model deadweight deflections in the range of only .0001 to .0003 inch. This, together with the prohibitive cost required in constructing a test fixture and setting up an adequate measuring system, prompted the decision to use experimental model flexibility influence coefficients for verification of the analytical program instead of deadweight deflections, since larger and more accurate deflection measurements could be obtained simply by applying larger loads.

Model Design

The model scale factors and the full-scale antenna structural dimensions were used to compute model dimensions and produce drawings for the shop.

At this stage in the model program, two things became evident. The first was that the antenna structural design was still evolving into an optimum configuration and would not be frozen for some time. The second was that certain model structural parts such as tubular segments and diagonal tension members could not be purchased or fabricated with the exact required specifications without running into excessive costs.

It was decided, therefore, to design the model parts so that they simulated the existing full-scale antenna structure as closely as possible. The resulting model geometry and stiffness distributions were then used as inputs to the analytical program instead of the full-scale antenna values. Thus, theoretical model influence coefficients would now be compared directly with the model experimental coefficients. In this manner the paramount objective of verifying the analytical program could still be achieved, with the results becoming available in a much shorter time.

This program change had very little effect on the rigging demonstration objective, except that the results would also be available much sooner.

Model Construction

Construction of model parts began as soon as structural design dimensions had been formalized on drawings. For construction purposes the model was divided into eight main subassemblies; the parabolic (primary) reflector backup structure, the elevation-azimuth mount, the hyperbolic (secondary) reflector support structure, the ballast weight and support structure, the RF box and support structure, the dynamic parabolic reflector face, the rigging parabolic reflector face, and the base or pedestal.

The parabolic reflector face is also described as a shell in this paper.

The most unique construction problems occurred with the parabolic reflector faces and the backup structure. The fitting together and assembly of the various component parts was also a painstaking task, which required extensive jigwork and intricate alignment fixtures.

The main problem encountered in fabricating the backup structure was in joining the tubular segments together. A special welding and heat-treating procedure had to be developed to minimize warpage, joint misalignment, and soft spots in the backup structure, which contained aluminum tubular segments with wall thicknesses ranging from .032 to .006 inch.

The main problem encountered in fabricating the rigging and dynamic parabolic reflector faces was in forming the required double curvature. The 32 outer row and 16 inner row .020 inch-thick solid aluminum panels of the rigging face were stretch-formed from sheet stock on properly contoured male dies. The 8-foot diameter one-piece dynamic face was formed on a male mold by splicing together radial segments under vacuum pressure. The radial segments, consisting of .001 inch-thick aluminum-foil skins bonded on each side of a .032 inch-thick styrofoam core, were formed on the same mold.

Measurement of Physical Properties

Certain physical properties of the model components were measured as they were fabricated. The mass properties of all model components were determined by conventional experimental methods. None of the model components were mass-balanced either at this time or at the later time when the vibration tests were added to the model program, since the actual mass properties of the model components, as constructed, were sufficiently accurate for all three test objectives. The actual axial stiffness of each size diagonal tension member was determined experimentally and used as an input to the analytical program. The average measured wall thickness of each size tubular segment was also used as an input to the analytical program. The bending stiffness efficiency of the dynamic parabolic reflector face was experimentally determined with a sample specimen.

Rigging Demonstration

The feasibility demonstration of the proposed rigging procedure for the full-scale antenna was started as soon as all of the necessary parts had been constructed. The main rigging tasks were maintaining and measuring joint alignment while preloading the inter-ring and inter-cap diagonal tension members and assembling the parabolic reflector panels to the backup structure so that the reflector assumed its proper curvature and maintained complete interaction with the backup structure.

The assembly procedure in the rigging demonstration was more difficult than in the construction phase. The heavy, positive alignment jigwork which was used for assembly in the construction phase could not be used for the rigging operation, since the rigging alignment fixtures had to functionally simulate those proposed for the antenna rigging operation.

The model rigging demonstration was completed satisfactorily, and the results indicated that the proposed rigging procedure for the full-scale antenna was feasible and would produce a stable structure, with all structural joints and reflector points converging to their theoretical positions. The completely rigged model is shown in Figures 8 and 9. Figure 10 shows the model with the dynamic shell mounted on the backup structure.

Influence Coefficient Tests

The influence coefficient tests followed the rigging demonstration. These tests were conducted in four parts, with a different model configuration for each part. The four model configurations are described as follows:

1. Reflector system in the face-up position with no shell on the backup structure;

2. Reflector system in the face-side position with no shell on the backup structure;

3. Reflector system in the face-up position with the dynamic shell mounted on the backup structure, and

4. Reflector system in the face-side position with the dynamic shell mounted on the backup structure.

For all model configurations, deflections were measured and loads were applied at the upper ring cap joints in the backup structure. All deflections were measured in a direction parallel to the RF axis of the reflector system. All loads were applied in a vertically downward direction. The layout of the load and deflection points is shown in Figure 1.

Since the analytical program took advantage of the symmetrical backup structure, most of the deflection points were concentrated in one quadrant. Three other deflection reference points are shown on ring No. 3. The deflection check points in the other three quadrants are not shown. For each point in the main quadrant, symmetrical points in the other three quadrants were also used for load applications. Thus, four symmetrical loads were applied to the backup structure to produce each deflection. Therefore, the dimensional unit for the influence coefficients was microinches/pound load/quadrant.

Linearity and repeatability were checked for each influence coefficient. At least three magnitudes of loads were applied for each influence coefficient measurement to ensure that the deflection at that particular point was linear. If the magnitude of the applied load had been sufficient to unload the adjacent diagonal tension members, the deflection at a particular point could have become nonlinear. The entire loading sequence was repeated for each influence coefficient measurement until the deflection at that particular point was repeatable. This procedure minimized drifting of the transducer output signal due to thermal gradients and extraneous electrical noise sources. It also minimized the hysteresis effects of the model structure.

The displacement transducers used for the deflection measurements were Schaevitz linear variable differential transformers. Figure 11 shows these transducers mounted on a wooden fixture over the model reflector. Figure 2 is a circuit diagram

of the transducers, power input equipment, and signal read-out equipment. Since the transducer sensitivity was dependent on the input voltage and the load impedance of the output circuit, the same equipment and circuitry was used for calibrating the transducers and monitoring displacements of the model. Output signals from the transducers were read on an rms voltmeter and manually recorded on tabulation sheets.

The experimental and theoretical influence coefficients generally showed good agreement, with the best correlation occurring in the diagonal and near-diagonal terms of the matrices. For illustrative purposes, some data in the influence coefficient matrices have been plotted to show comparative deflections of points on rings No. 4 and No. 5 due to a unit load being applied at a given point.

Figure 3 is a comparative plot of experimental and theoretical model deflections of rings No. 4 and No. 5 with a unit load being applied at Point 5.1. The deflection node points are in the main quadrant, and the reflector system is in the face-up position with no shell attached to the backup structure. This plot shows that the experimental deflections are less than the theoretical deflections. The experimental deflection curves also show less warpage in both rings. These results are to be expected, since the analytical program which computed these theoretical model deflections did not include the bending stiffnesses of the tubular members. A recent modification of the analytical program to include bending stiffness has produced theoretical model deflections which are slightly less than those shown in Figure 3.

Figure 4 is also a comparative plot of experimental and theoretical model deflections of rings No. 4 and No. 5 with a unit load now being applied at Point 5.9. Again, the experimental deflections are less than the theoretical deflections, and the experimental deflection curves show less warpage in both rings.

Figure 5 shows the effect of the dynamic shell on the experimental model deflections of rings No. 4 and No. 5 with a unit load applied at Point 4.1. The reflector system is still in the face-up position. This plot shows that the shell has stiffened the backup structure, with a resulting reduction in deflection and warpage. No analytical program with the combined stiffness inputs of the model backup structure and shell has been run for comparison with the experimental model influence coefficients which were obtained with the shell mounted on the backup structure.

Figure 6 also shows the effect of the dynamic shell on the experimental model deflections of rings No. 4 and No. 5 with a unit load now applied at Point 4.9. The results are the same as with the previous load point.

In general, the same deflection characteristics were produced by load applications at other points on the backup structure. Therefore, it may be concluded that the model influence coefficient test results have provided a high degree of assurance for the accuracy of the analytical program which has been used to compute deadweight deflections of the full-scale antenna. Naturally, a higher degree of assurance would have been provided if scaled experimental model deadweight deflections could have been compared directly with the full-scale deadweight deflections of the final full-scale antenna configuration (shell included) as computed from the analytical program. However, further substantiation of the analytical program will be provided by static tests on the full-scale antenna.

Vibration Tests

The vibration tests, which constituted the final phase of the model test program, were conducted in conjunction with the closed loop dynamic-analysis of the full-scale antenna system. Three model configurations were utilized for the vibration tests and are described as follows:

1. Reflector system in the face-up position and mounted on an unrestrained elevation-azimuth mount and pedestal,

2. Reflector system in the face-up position and mounted on a braced elevation-azimuth mount and pedestal, and

3. Reflector system in the face-up position with the trunnion beam bull gears braced as shown in Figure 12.

The dynamic parabolic reflector was mounted on the backup structure for all three configurations.

The model was excited in both its symmetrical and antisymmetrical modes with electromagnetic shakers and the dynamic response was measured with the normal types of vibration transducers and read-out equipment.

The vibration test results provided qualitative information concerning the types of vibration modes which could be excited, the order of magnitude of the structural damping, the ease or difficulty in exciting the various modes, and optimum shaker locations. Thus, the objectives of the vibration test program, as well as the objectives of the overall model program, were accomplished satisfactorily.

Additional Model Program Information

Since a complete description of all facets of the 1/15-scale Haystack Antenna model program could not be included in this paper, the final reports of the model program are listed in the reference section for those seeking further information on any specific details. Reference 1 contains a detailed description of the procedures for the model rigging demonstration and influence coefficient tests. Reference 2 contains a complete account of the model program, with the exception of the vibration tests and the previously mentioned detailed test procedures. Reference 3 contains a complete account of the model vibration test program.

References:

1. NA50H-748, 1/15-Scale Model Program - 120-Foot Haystack Antenna System, latest revision dated 4-23-62, Columbus Division, North American Aviation, Inc.

2. NA62H-186, 1/15-Scale Model Program - Final Report - 120-Foot Haystack Antenna System, latest revision dated 8-13-62, Columbus Division, North American Aviation, Inc.

3. NA62H-870, 1/15-Scale Haystack Antenna Model Ground Vibration Test, dated 11-6-62, Columbus Division, North American Aviation, Inc.

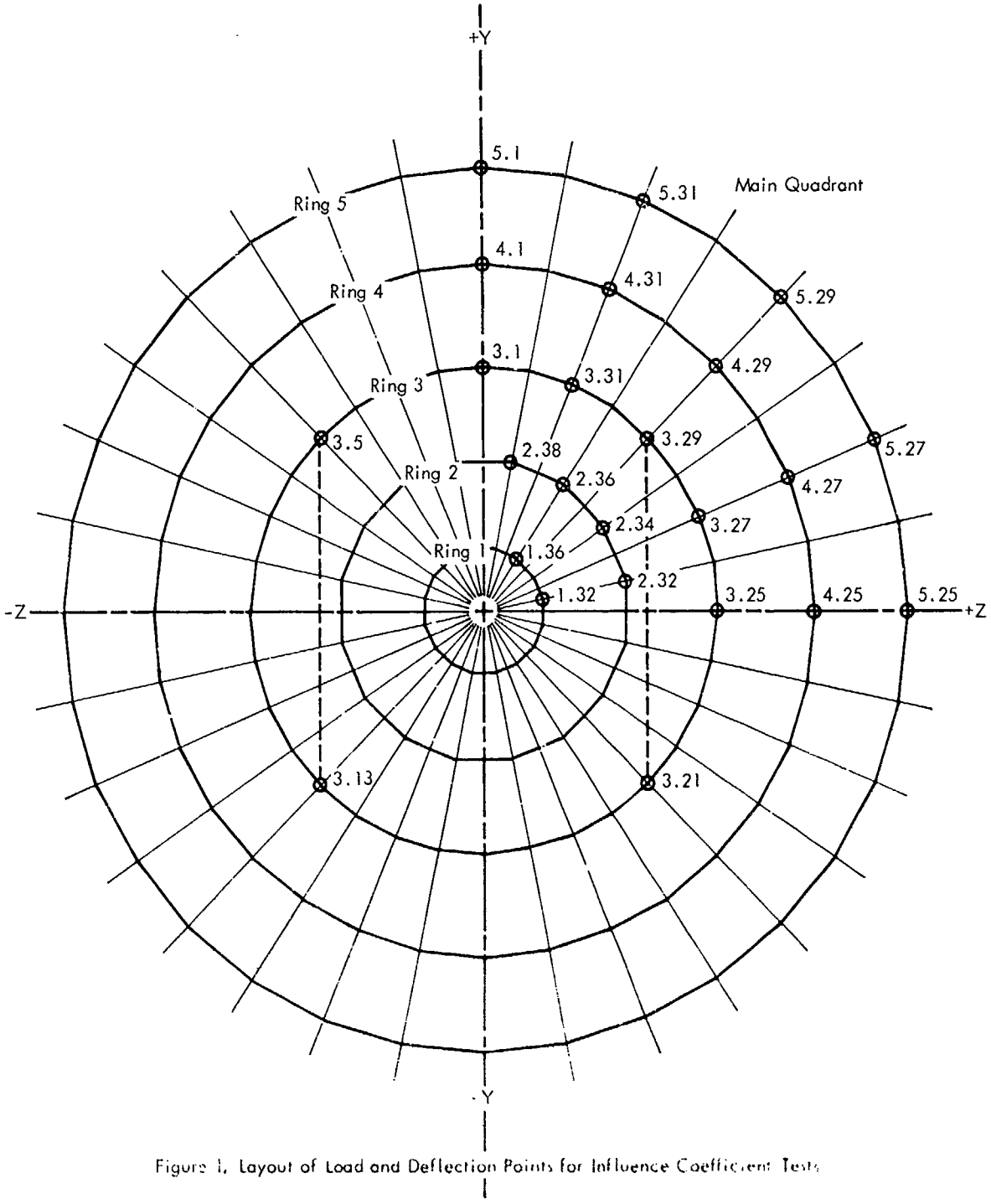

Figure 1. Layout of Load and Deflection Points for Influence Coefficient Tests

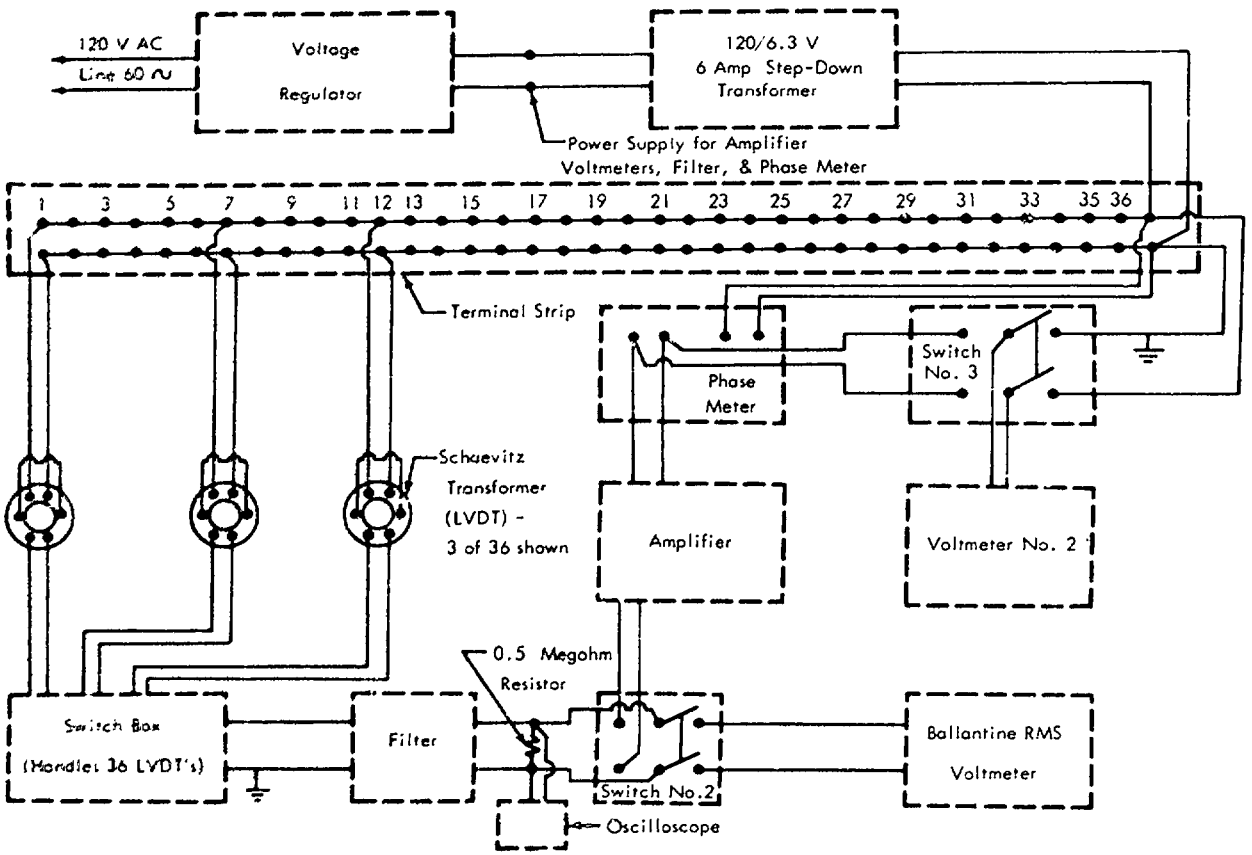

Figure 2. Instrumentation Circuit Diagram for Influence Coefficient Tests

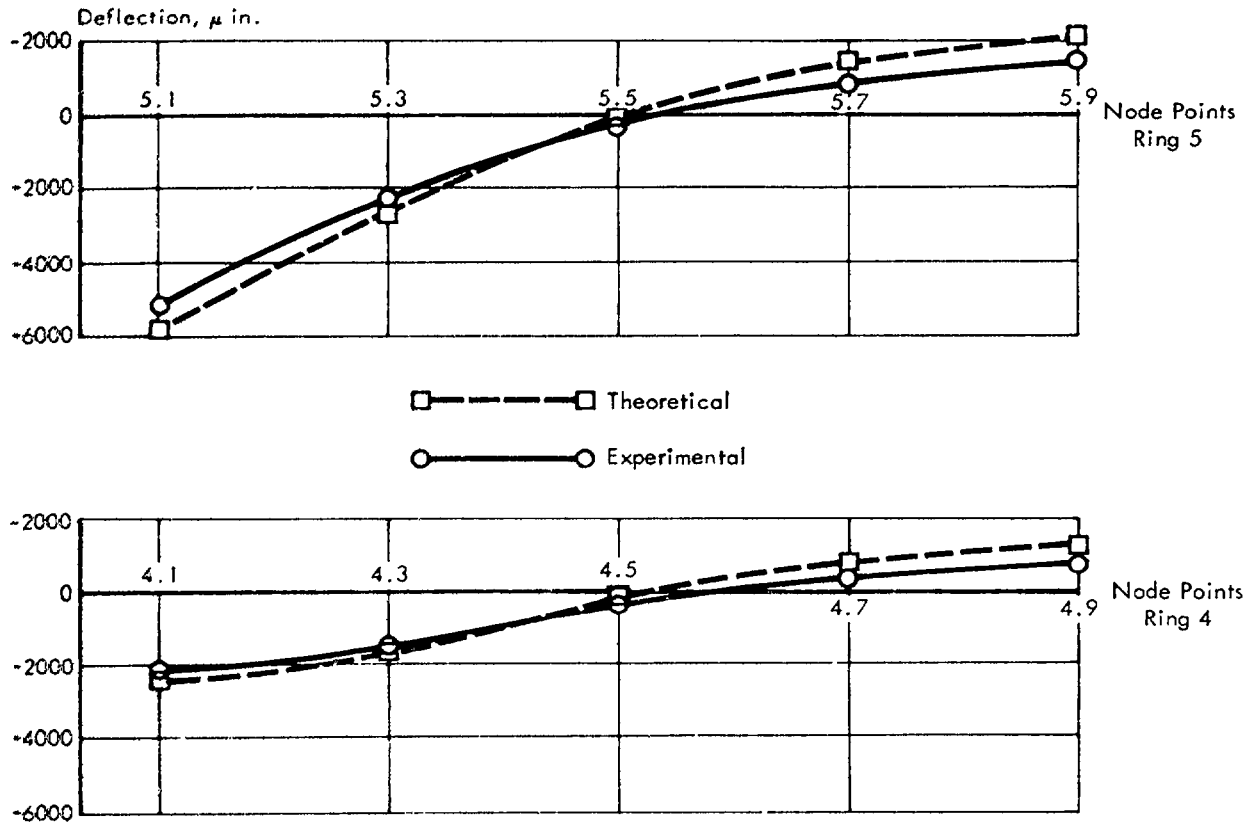

Figure 3. Experimental and Theoretical Model Deflections with a Unit Load Applied at Point 5.1 - Reflector Face-up with No Shell

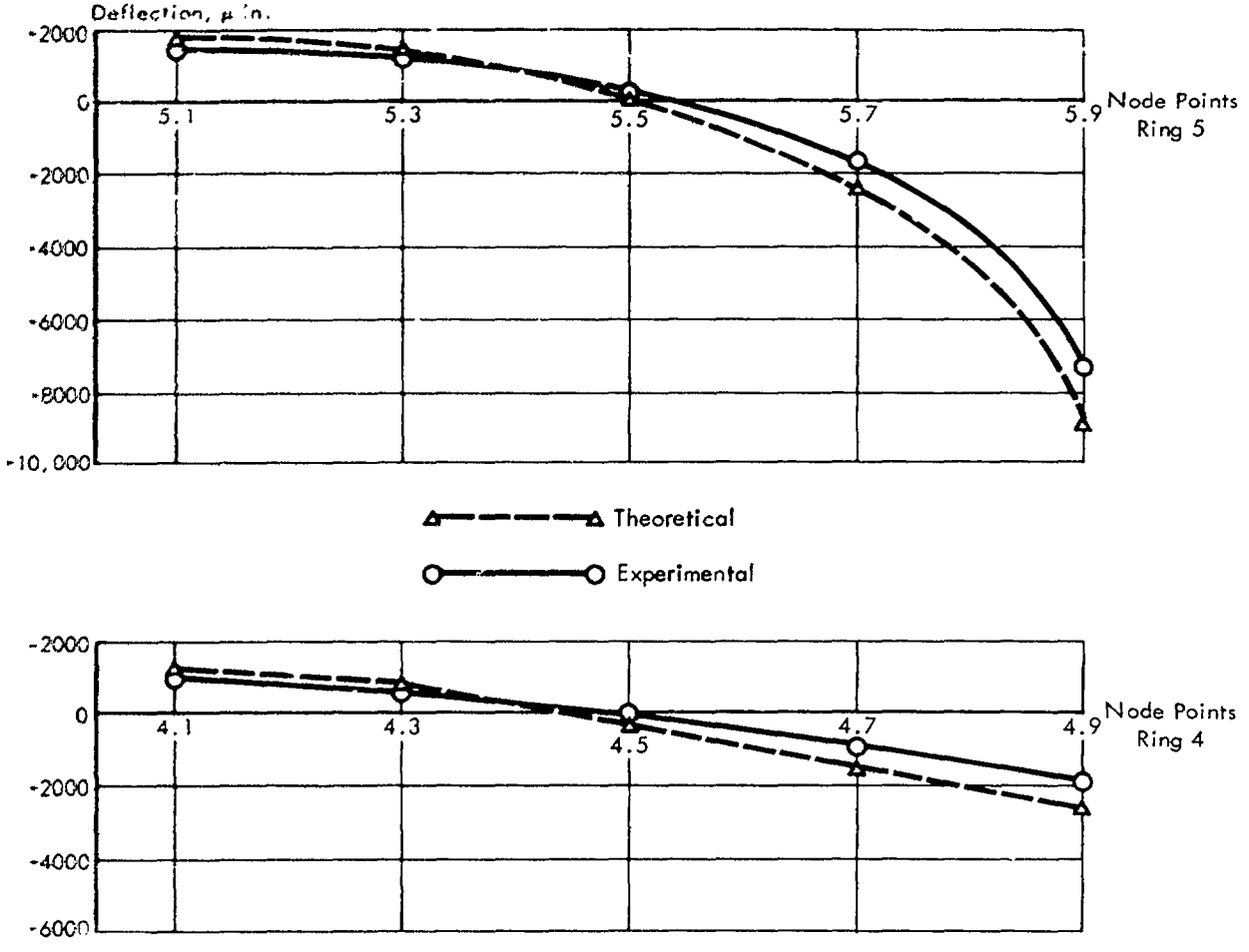

Figure 4. Experimental and Theoretical Model Deflections with a Unit Load Applied at Point 5.9 - Reflector Face-up with No Shell

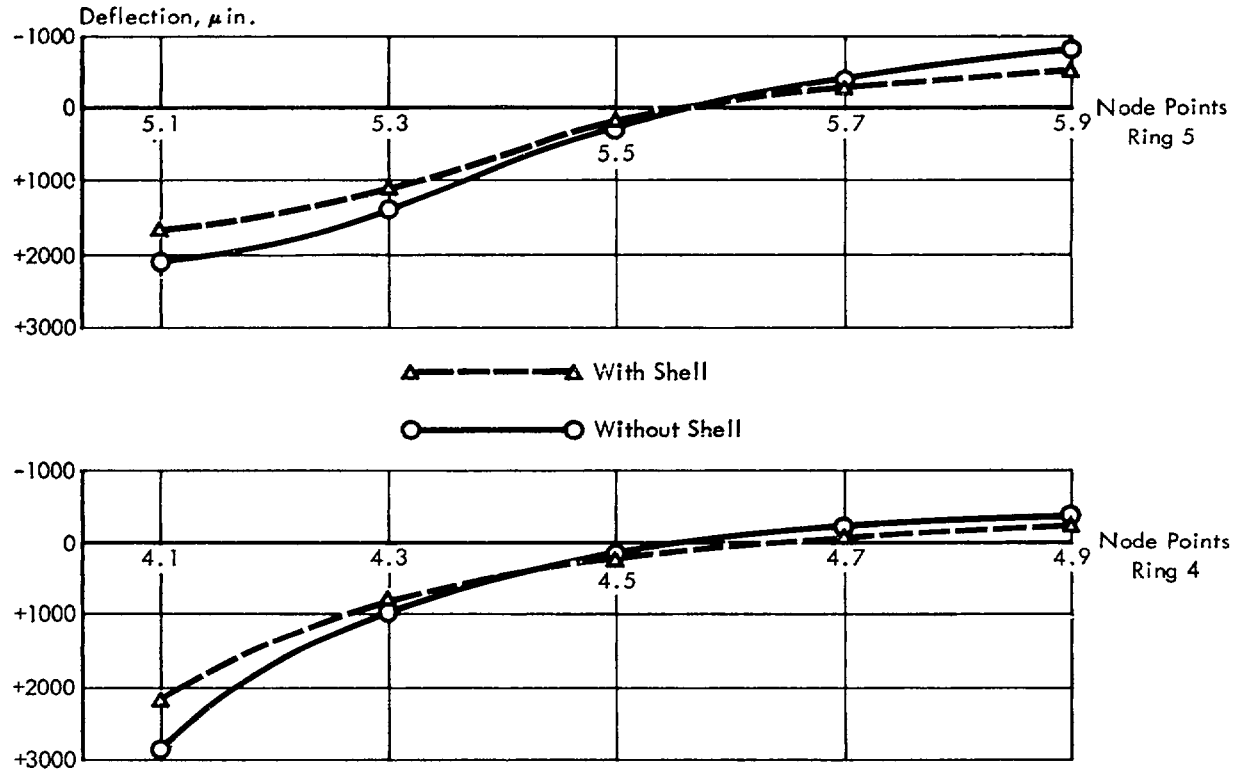

Figure 5. Effect of Dynamic Shell on Experimental Model Deflections with a Unit Load Applied at Point 4.1 - Reflector Face-up

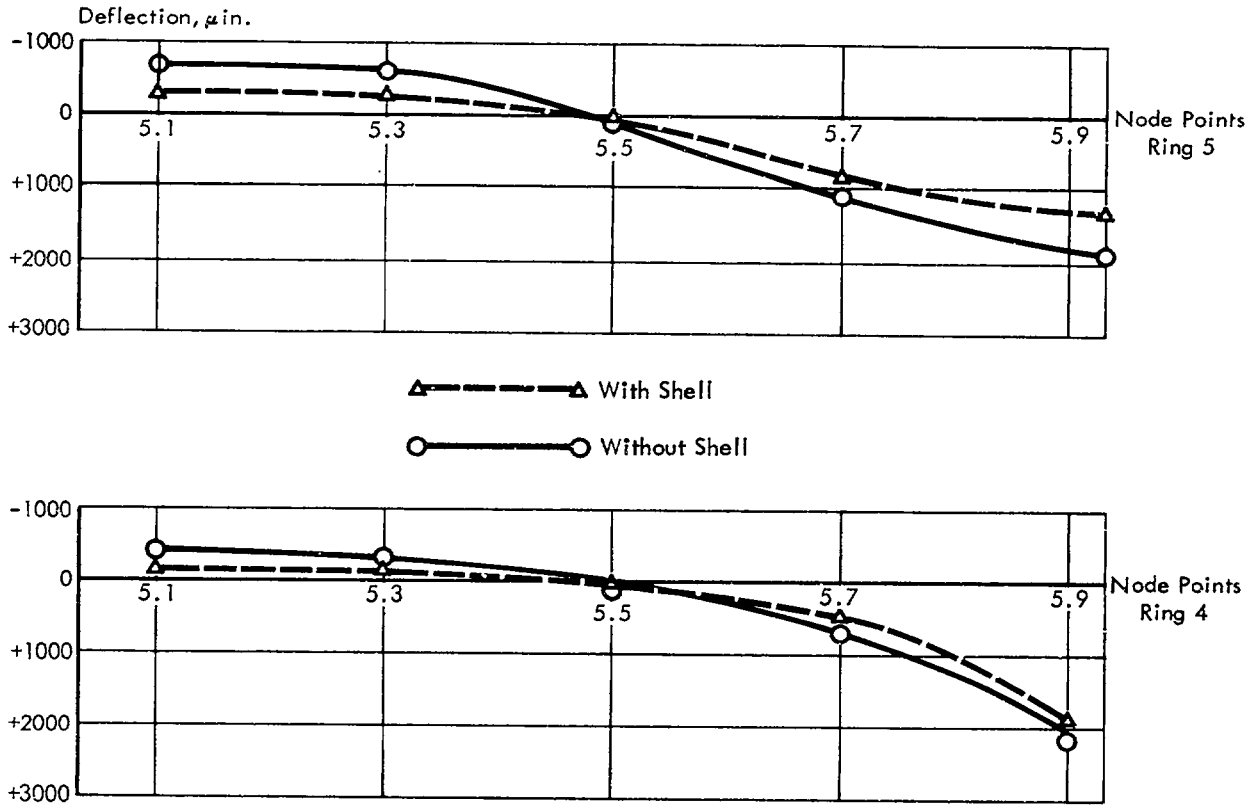

Figure 6. Effect of Dynamic Shell on Experimental Model Deflections with a Unit Load Applied at Point 4.9 - Reflector Face-up

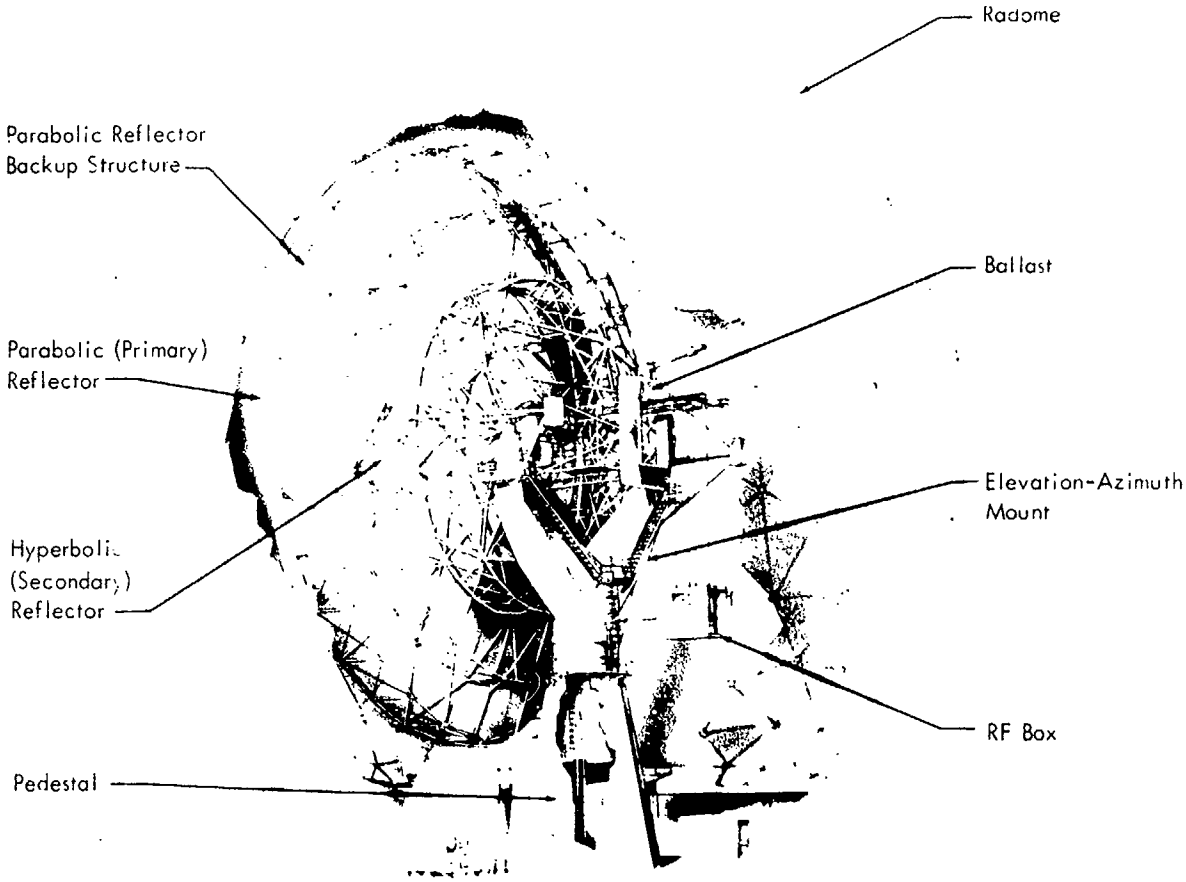

Figure 7. Structural Layout of the Haystack Antenna

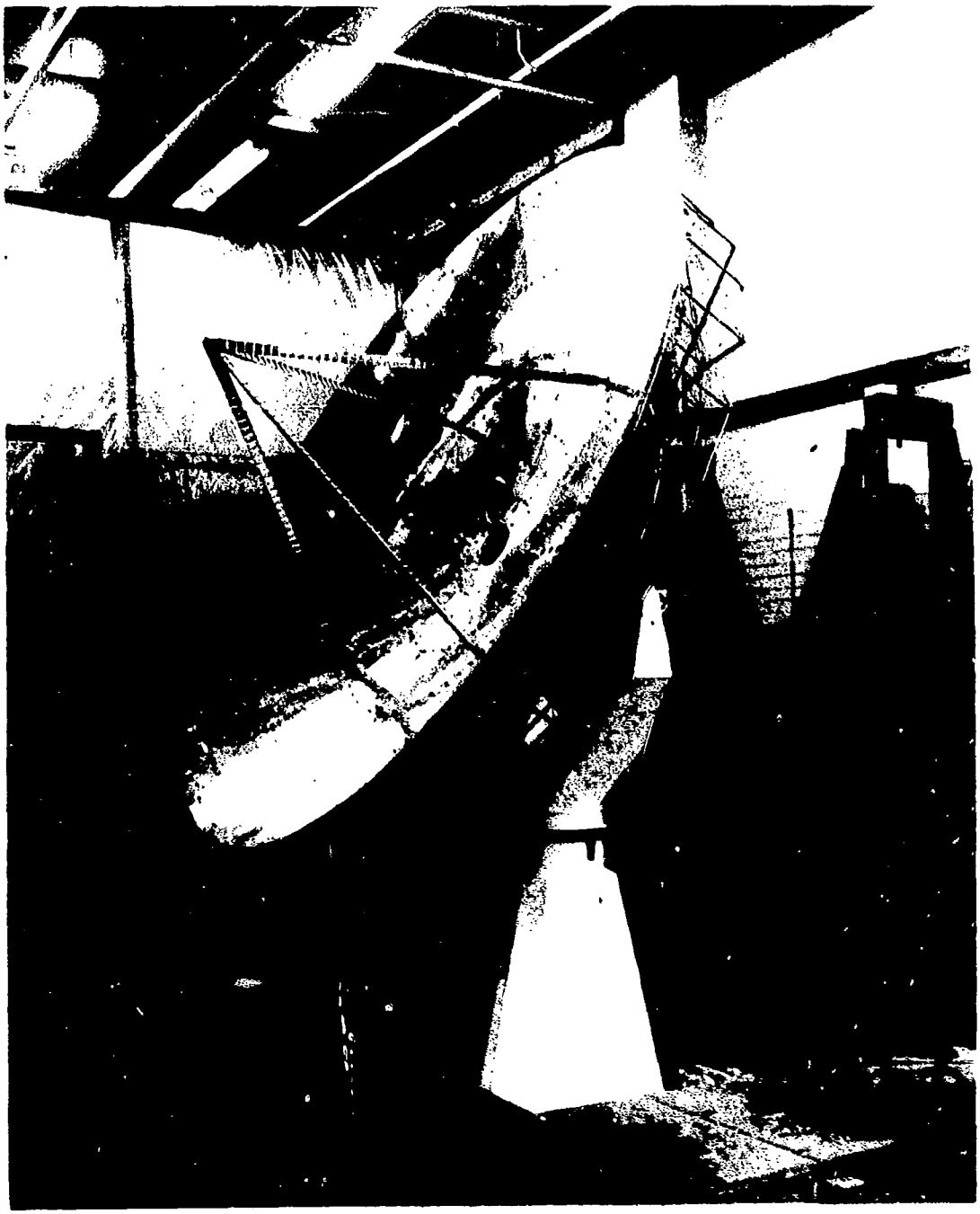

Figure 8. Completely Assembled 1/15 Scale Haystack Antenna Model with Rigging Shell Mounted on Backup Structure - Front View

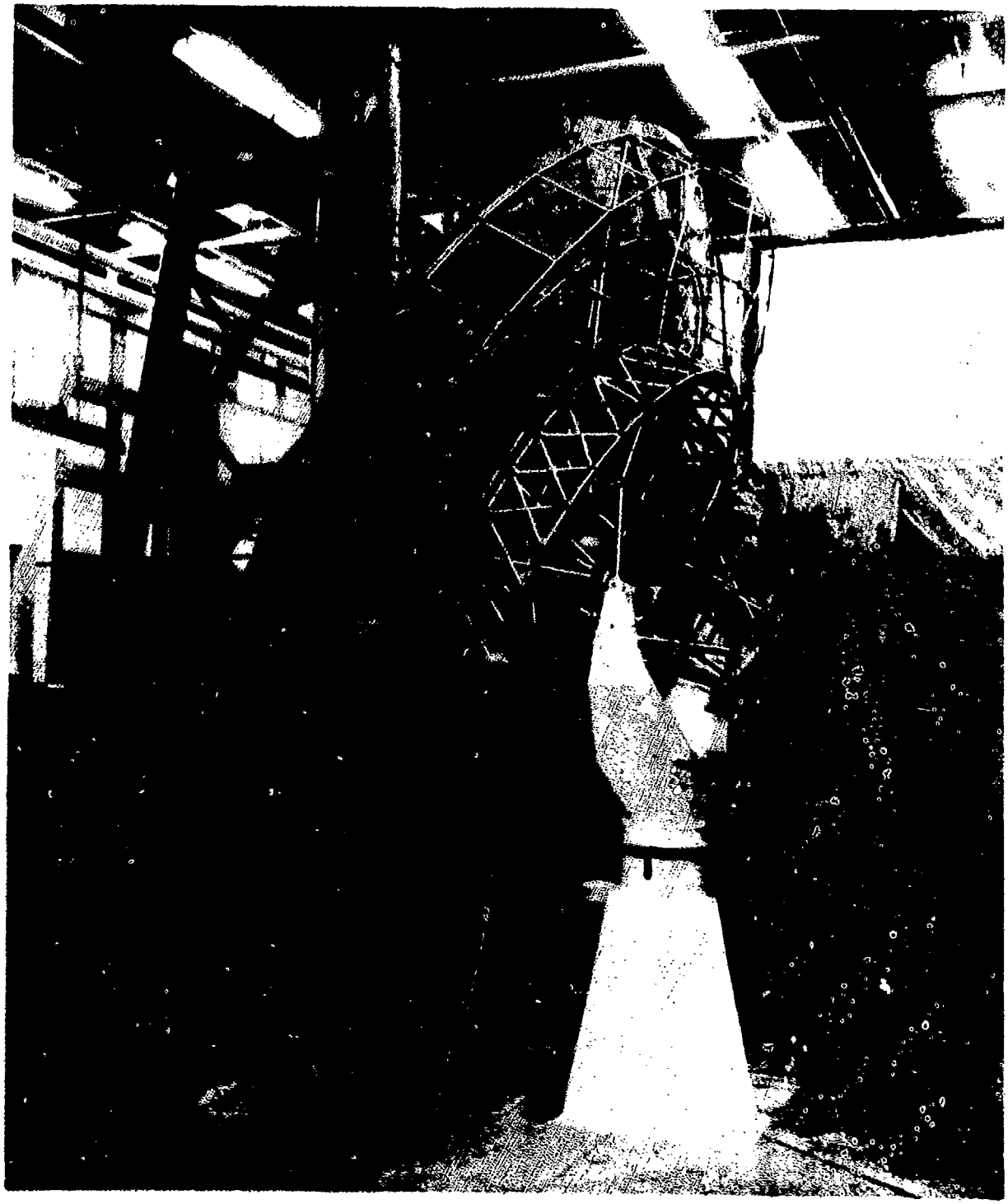

Figure 9. Completely Assembled 1/15 Scale Haystack Antenna Model with Rigging Shell Mounted on Backup Structure - Rear View

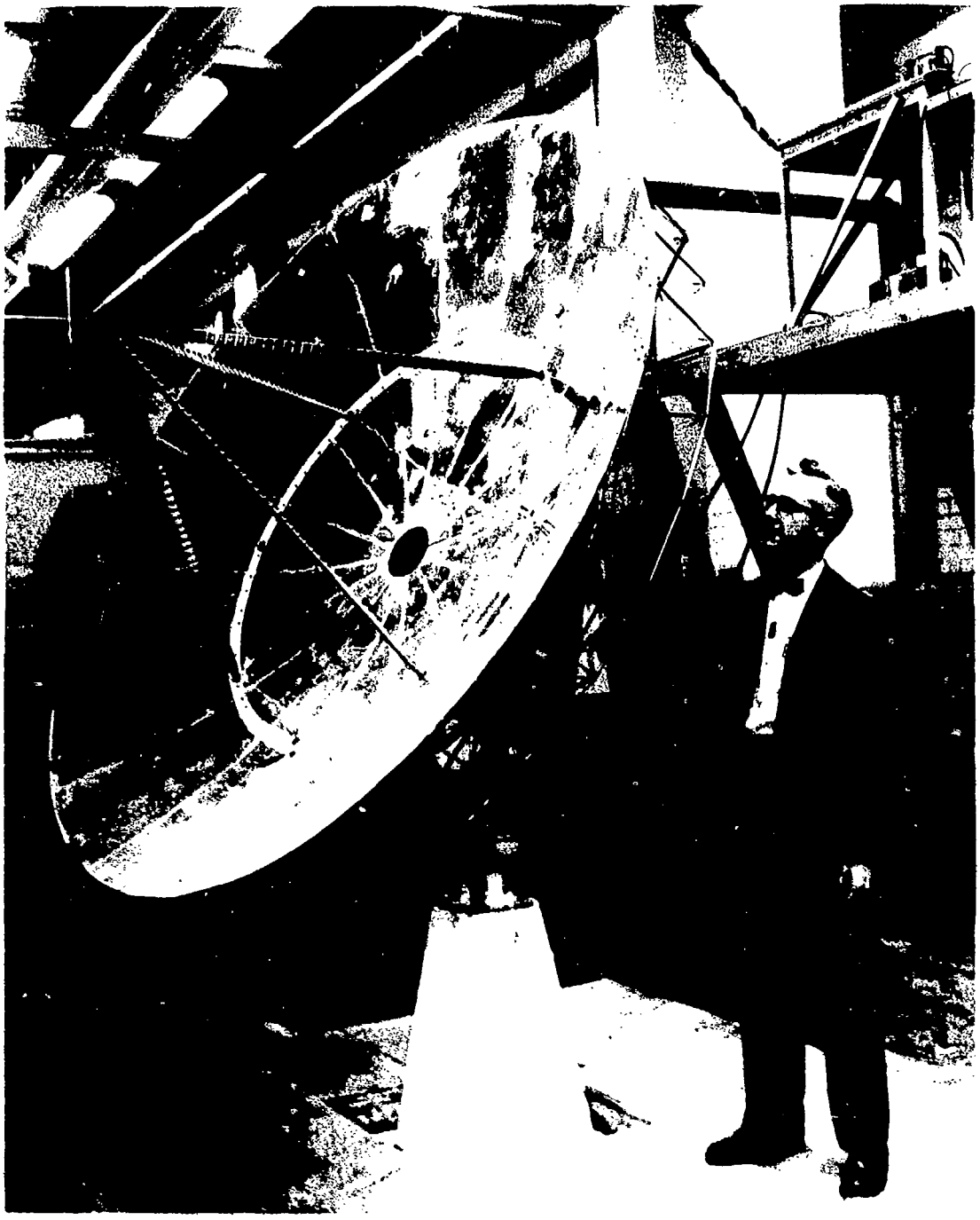

Figure 10. Completely Assembled 1/15 Scale Haystack Antenna Model with Dynamic Shell Mounted on Backup Structure

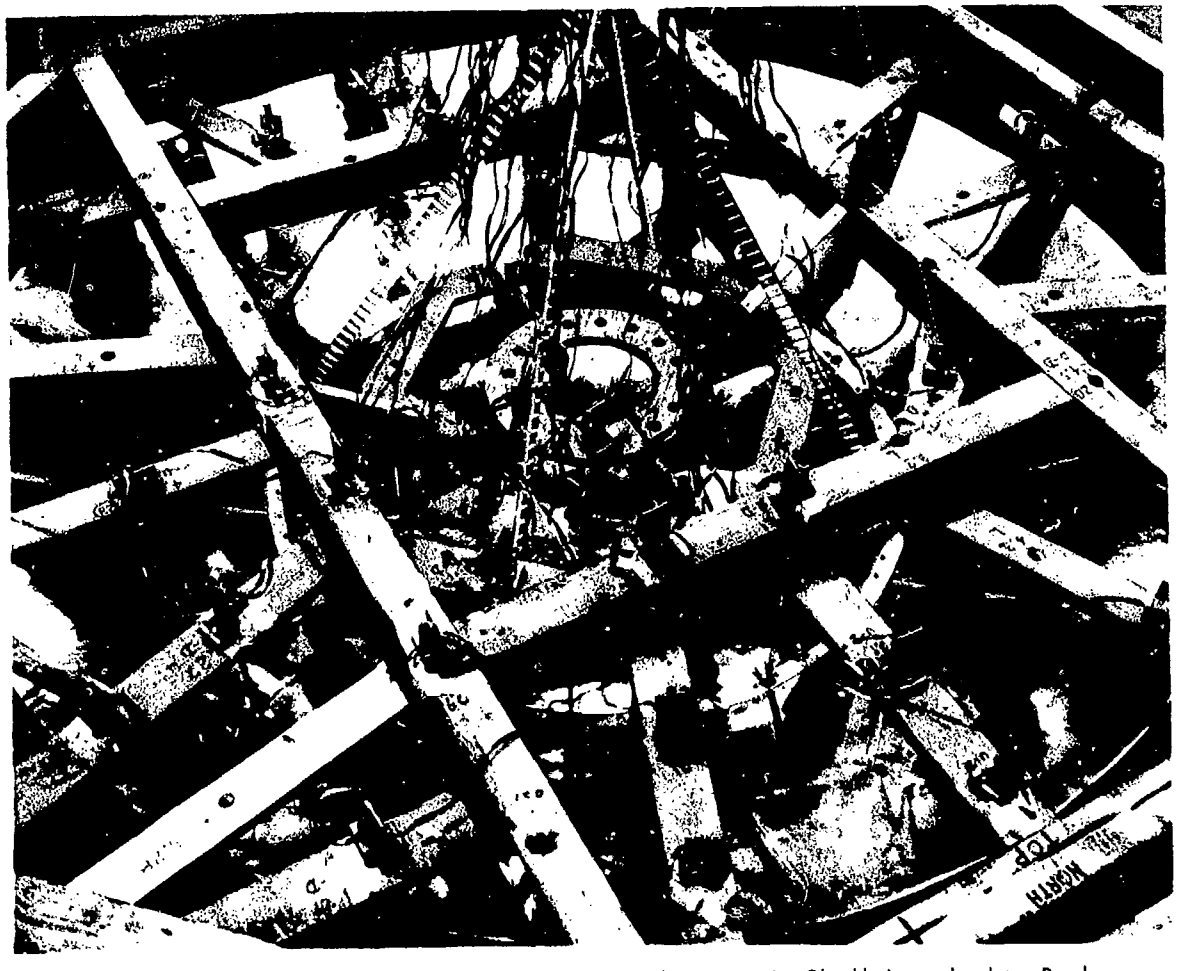

Figure 11. Influence Coefficient Test Set-up with Dynamic Shell Attached to Backup Structure in Face-up Position

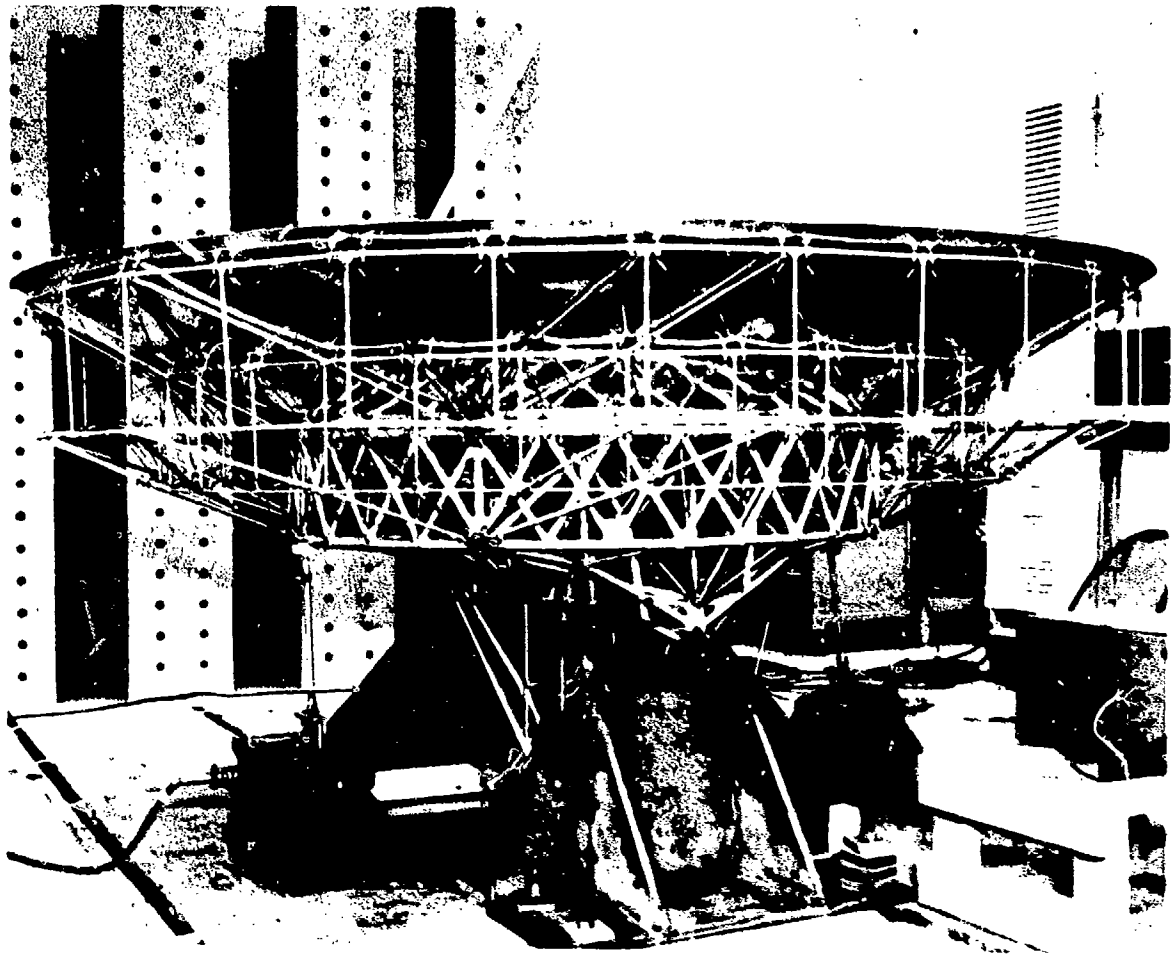

Figure 12. Vibration Test Set-up for Reflector Assembly with Bull Gears Rigidized

SCIENTIFIC MODELLING FOR PHOTOMECHANICS

Herbert Becker
George Gerard

Allied Research Associates, Inc.

ABSTRACT

Three fields of photomechanics are discussed to show the effort required to generate models for scientific exploration of these fields. The approaches center about the fundamental principle that the proper design of an experiment requires scientific design of the model to be investigated. Examples are chosen from photothermoelasticity (which is a relatively new field now well established), photoviscoelasticity (which is essentially a brand new field requiring extensive research before it will be established), and strobelasticity (which is a new form of an old, established field).

These three fields are applicable to investigations of structural, thermal and dynamic problems in rockets and re-entry vehicles. Therefore, in addition to examples of basic problems, demonstrations of practical interest are included. These depict thermal stresses in a box beam, stresses in a case bonded viscoelastic rocket grain, and the effect of impact on a re-entry vehicle.

LIST OF ILLUSTRATIONS

FIGURE PAGE

SCIENTIFIC MODELING FOR PHOTOMECHANICS

Herbert Becker

George Gerard

Allied Research Associates, Inc.

INTRODUCTION

Many engineering structures being designed today must operate under conditions in which time and temperature play an important role. In aerospace craft, for example, re-entry conditions impose transient temperature fields which could lead to severe thermal stresses. Or the structure of a ballistic re-entry vehicle could be subjected to blast pressure loading of such short time that impact and shock conditions become major design considerations.

Complex structural behavior under time dependent loading in a severe thermal environment can be examined effectively through the use of models. The acquisition of accurate, useful data from experimental procedures frequently involves application of scientific principles to the design of the model, and the experiment in which the model is employed. This process is delineated through examination of several specific cases in which scientific modeling played a major role in achieving experimental results of high reliability.

The experiments to be described herein involve the field of experimental mechanics known as photomechanics, which relates to the optical effect observed in the model as a result of the interaction of light with structural behavior. Until recently, investigations in this field were confined to the special case of photoelasticity in which elastic behavior and polarized light in

transparent models yield a series of interference lines commonly known as fringes. Furthermore, in photoelasticity, the level of stress in a structure is directly proportional to the fringe order.

In photomechanics this generally is not the case. Fringe order may be relatable to stress, to strain, possibly to some combination of these quantities, or to time dependent derivatives of these quantities. In photoelasticity, material behavior is usually considered independent of temperature. In photomechanics, however, temperature may be a physical quantity of paramount importance controlling the behavior of the material from which the model is made.

For the purpose of the present paper, it is possible to divide the subject into four specific categories: two related to time and two related to temperature. For example, the photoelastic investigation of transient thermal stresses would be termed photothermoelasticity (PTE) in an elastic material. If the material is viscoelastic, then the investigation procedure would be called photothermoviscoelasticity (PTVE).

This introductory discussion indicates the versatility and comprehensive scope of modern photomechanics as compared to photoelasticity. The mid 1950's essentially marked the end of what may be called "classical photomechanics," a field which traces its origin to the early 1800's, the history of which is comprehensively reported in the treatise by Coker and Filon (Ref. 1). The current paper describes new techniques in photomechanics which have been developed during the past decade primarily in response to current technological requirements. These fields are being explored by other investigators. However, it is the intent of this paper to summarize only the developments by Allied Research Associates.

The organization of the paper consists of a brief background in classical photomechanics (that is, static photoelasticity). This is followed by a description of time dependent photoelasticity illustrating the large range of problems which can be examined with ease and precision utilizing a relatively new photomechanical technique known as strobelasticity.

Discussions are presented of the preparation of models and experimental arrangements for examination of problems in thermoelasticity and thermoviscoelasticity. In this latter case, the only similarity to classical photoelasticity is the use of a polariscope to produce fringe patterns in the model. All other facets of the procedures for this type of problem are different from those in classical photomechanics.

PHOTOELASTIC MODELLING

An example of the advanced state-of-the-art in classical photomechanics may be seen in Figure 1, which depicts a 1/24 scale model of a 50,000 ton forging press (Ref. 2). The model contains 144 parts, weighs 144 pounds, and required six months to fabricate and test. The experiment was conducted utilizing the stress freezing process. The press was loaded by pressure applied to the pistons located in the upper crosshead by feeding nitrogen gas through the hollow tie rods, exactly as in the prototype.

After the model had been stress frozen, slices were taken for photoelastic examination to determine the stresses throughout the press components. By fabricating the entire press and applying pressure as in the prototype, there was no question of the distribution of loads to be applied. The distribution of the proper load to each component occurred naturally as a result of the press geometry. Consequently the state of stress in the finished photoelastic model corresponded with that in the prototype.

This faithful reproduction of the geometry and loading of a complex structure is a growing trend in modern photoelastic investigations (Ref. 2). As another example, numerous detailed studies have been made of nuclear power plants. This trend has been made possible by the recent arrival (during the past decade) of a new type of modelling material, epoxy, which is excellent for fabrication of large complex structures. Its high photoelastic sensitivity, good mechanical rigidity, and fabricability have revolutionized photoelasticity and have played a major role in advancing to their current state all of the fields of investigation to be described below.

STROBELASTICITY

One of the problems in analysis of ballistic re-entry vehicles is the determination ot the structural response to dynamic loads such as produced by blast loading for example. This involves analysis of the time dependent stress distribution throughout the structure which is a relatively simple procedure when utilizing a technique in which stroboscopic lighting and repeated impact permit visualization of the propagating stress waves throughout an elastic structure (Ref. 3). This photomechanics technique has been termed "strobelasticity."

The schematic arrangement of the experimental equipment is shown in Figure 2. The model size is selected to ensure the decay of oscillations in the structure within 1/60 second in order that 60 cycle electrical power may be used to drive the bell coil. By flashing the strobe at the same rate, one flash (duration = 1 microsecond in modern units) occurs during each impact providing the appearance of stopped motion. By reducing the flash frequency slightly, the impact event may be viewed repeatedly but at a rate considerably less than the actual event. By careful control of strobe frequency the visualization rate has been diminished to furnish a viewing time for a single event of the order of hours.

A photograph of a typical experimental arrangement appears in Figure 3. This equipment was used to provide the motion picture strip shown in Figure 4, which depicts the propagation of a diametral impact stress wave on a composite system consisting of a rubber ring surrounding a gelatin core with an aluminum plug at the center. The system is representative of a re-entry vehicle structure with shock insulated internal equipment.

The control available with this type of arrangement may be seen in the relatively small change in fringe pattern from frame to frame in Figure 4. Furthermore, by removing the polaroids, the motions of the model are clearly revealed. The high resolution of monochromatic fringe orders (10 fringes or more with no difficulty), may be seen in the photograph of the

area of impact on the edge of a plate (Figure 5). This precision, coupled with the precise data available on structural motions, provides the basic information for accurate analysis of dynamic behavior. In the limiting case, locking the strobe into the line frequency and imparting a phase shift to the flash permits examination of the model behavior in essentially the same manner as in static photoelasticity.

PHOTOTHERMOELASTICITY

Photothermoelasticity (PTE) is the application of photomechanics to problems in time dependent and temperature dependent loading on elastic structures. This procedure, which has been developed into a precise scientific tool for the analysis of problems in two and three dimensional thermoelasticity (Refs. 4 through 9, for example) has been used successfully to test the reliability of theoretical solutions.

Plate Problem

The first illustration of the use of PTE involves the determination of thermal stresses in a rectangular plate subjected to a parabolic temperature gradient across one edge and constant along the other. Three theoretical solutions to this problem are shown in Figure 6. It is evident that precise experimental techniques would be required in order to identify the most accurate of the three solutions (Ref. 7).

One of the major facets of the experimental investigation in this problem was the proper selection of thermocouple locations to provide accurate data during the experiment on the mean inplane temperature distributions throughout each plate model. A typical thermocouple layout is shown in Figure 7. One important feature, revealed in the bottom sketch, shows thermocouples located at depths from each surface at which the temperature would read the mean value in the plate at a given location under a parabolic distribution through the thickness which was detected in early stages of the experiment. This method of compensating for the variation was found to be necessary in order to obtain precise, reliable data.

The model and experimental arrangement (including insulation, thermocouples, and assembly of components) are revealed in Figure 8. Temperature was applied through heat flux induced by application of dry ice to the model edges. Accurately reproducible parabolic temperature gradients were obtained only when the surfaces of the model plates were insulated with thick styrafoam blocks. In order to observe the fringe patterns at the centers of the plate edges, it was necessary to pierce the styrafoam insulating blocks and insert plastic pipes as shown in Figure 8. Rubber strips were placed along the chilled edges to provide temperature control.

As a result of these precautions, accurately parabolic temperature distributions were consistently obtained approximately 20 minutes after application of dry ice to the model edges. A typical normalized temperature distribution may be seen in Figure 9, which reveals close adherence to the required parabolic distribution of temperature in order to obtain close correlation of temperature data with stress data and good reproducibility of experimental results.

Photoelastic fringe patterns of models with two different a/b ratios are shown in Figure 10. Fringe orders were measured consistently to a precision of the order of 1 percent (better, in many cases) throughout the program.

Correlation of theory and experiment in Figure 11 (Ref. 7) indicate close agreement with the Ross theory. Because of the fact that the Ross solution in the range of a/b greater than 1 may be obtained by a simple transformation of data for a/b less than 1, there was no need for experimental data beyond a/b = 1.

Wing Investigation

The analysis of thermal stresses in a multiweb structure under surface heat input furnishes another example of the accuracy afforded by photothermoelasticity. In this case, the experimental data provided such a high degree of reliability that it was possible to attribute differences between theory and experiment to errors in the theoretical assumptions (Ref. 8).

A preliminary study was conducted on a simple I-beam. The photoelastic fringe pattern is shown in Figure 12. Fabrication of the model, which actually involved channel shaped webs connected to top and bottom cover plates, is shown schematically in Figure 13. One of the influences upon temperature distribution throughout the model was the presence of convective airflow in the bays between the webs of the box beam. For this reason it was necessary to construct baffles and place them in the bays between the webs so as to eliminate convective heat transfer. Only after this was done was it possible to obtain essentially conductive heat transfer down the web. The reason for this modification was to permit a reliable check of the theoretical temperature distribution in the box beam structure. The theory did not account for convection in the bays.

Figure 13 also reveals the presence of thermocouples at the top and bottom of the plates which cover the box beam. This was necessary since the two dimensional heat flow through the plate thickness also was found to play an important role in the overall temperature distribution throughout the system.

In addition to the fabrication of the model in a manner which would permit proper modelling of the temperature distribution, it was necessary to construct a special polariscope arrangement which permitted viewing of the fringe patterns in the webs which were located in the interior of the model. This was achieved utilizing the configuration shown in Figure 14. Photographs of the model in various stages of completion are shown in Figure 15.

One additional factor which entered into the analysis of the photoelastic model was the effect of temperature upon the heat transfer characteristics of the model material. When this factor was taken into account, the final experimental arrangement yielded a model on which accurate agreement was obtained (Ref. 8), as may be seen both in the theoretical analysis and in the experiments (Figure 16).

THE BONDED POLARISCOPE

The previous section described applications of a new field of photomechanics. This section discusses a new technique for three-dimensional photomechanics which has been used successfully in studies of elastic problems (Ref. 6), and is now being developed for viscoelastic investigations. The application of this technique to problems in viscoelasticity will be discussed in the final section of this report.

The bonded polariscope involves the selection of a region of interest within a three-dimensional model, and cementing into that region a thin slice of model material sandwiched between plastic polarizing sheets. This technique has been applied successfully to problems in both mechanical and thermal stress analysis.

A typical calibration curve for the bonded slice is derivable by employing a beam loaded in pure bending and by plotting the ratio of the fringe order at a given distance from the neutral axis to the fringe order at the extreme fiber against the ratio of the neutral axis distance to extreme fiber distance. A calibration curve was obtained as shown in Figure 17. Comparison of this curve with that obtained for a beam without the polarizing sheets cemented to the faces reveals no significant difference between the two results.

Since the elastic modulus of the photoelastic epoxy is essentially the same as that of the polarizing sheets, there was no competing structural interaction between the model and the polariscope. Furthermore, the epoxy monomer cement which was used to join the polarizing sheets to the beam hardened to essentially the same stiffness as the beam material. As a result, the three components (beam, cement, and polarizing sheets) formed a mechanically continuous structure.

One successful application of the cemented polariscope is revealed in Figure 18 which depicts the fringe order distribution at the center slice of a long thick-walled cylinder subjected to a temperature chill in the bore. This result was compared both to the theoretical prediction of stress as a function of the temperature field, and to the experimental result for a thin, flat plate of cross section identical to the cylinder. The comparison shown in Figure 18 indicates good agreement of theory and experiment (Ref. 6).

The following discussion of photothermoviscoelasticity indicates another area in which the cemented polariscope is expected to have useful application.

PHOTOTHERMOVISCOELASTICITY

The essential problem in PTVE is the optical determination of the mechanical behavior of a viscoelastic structure subjected to temperature loading (Ref. 10). For this purpose it is necessary to devise an experimental procedure for determining the structural behavior since none exists at present. A major problem in use of the bonded polariscope for this

purpose is revealed in Figure 19 which demonstrates (on the left side of each figure) the growth with time of the fringe order in a beam under pure bending fabricated from a photoviscoelastic epoxy. The right side of each photograph reveals the optical behavior of the same beam with polaroid cemented to each face.

The difference between the fringes in the bonded polariscope and unbonded polariscope areas of each beam are immediately apparent upon progressing from the top to the bottom of the photograph. The lower fringe orders observed in the cemented polariscope presumably are due to the fact that the polaroid sheets maintain their elasticity while the beam continues to creep under dead weight loading. This stiffens the beam and results in lower fringe orders.

In an attempt to circumvent this difficulty, polarizing sheet was employed to which no plastic support sheets (as found in standard polaroid) were added. These polarizers were cemented to the faces of a photoviscoelastic strip as shown in Figure 20. After the cement hardened, each bonded sheet was machined into a series of squares of gradually diminishing size. The three different sets of grids are shown in this figure.

After gridding the polarizers the beam was subjected to dead weight bending moment. A typical result is shown in Figure 21 which reveals the extreme stiffening action on the far right where the bonded polarizing sheets were not sliced. With the relatively coarse grid in the next bay to the left a significant increase in fringe order is observed. The continued reduction in grid size led to relatively little further increase in fringe order.

The left side of the figure (in the dark shaded area) is the region of the beam to which the polariscope was not bonded. This is the region in which uninhibited viscoelastic behavior occurred. It may be seen, by comparison of the fringe orders in this area with those in the beam region to which polarizing sheet was cemented, that the agreement of fringe order with approximately the same value as the unrestrained viscoelastic behavior was obtained with either the largest, or next to largest, grid spacing after which no significant beneficial effect was obtained.

The largest grid spacing was 0.050 of an inch. Consequently, for investigation of photoviscoelastic behavior (such as in a solid propellant rocket grain) the slicing of the grid work into 0.050 inch squares should yield essentially uninhibited structural action of the model.

As an additional sidelight, the cement utilized in this investigation was also fabricated in a viscoelastic form by the addition of plasticizers to the standard epoxy cementing material utilized in the elastic bonded polariscope procedure.

As an example of the difference in behavior between elastic and viscoelastic structures, Figures 22 and 23 reveal the result obtained with a two dimensional four-pointed star rocket grain model supported in a rigid case. In these two studies one grain model was manufactured from an elastic plate and one from a viscoelastic plate. They were fabricated to yield perfect fit at 40 degrees Fahrenheit. Both models were slipped into

the supporting rings at a slightly lower temperature after which the assemblies were removed from the refrigerator and placed in a circular polariscope. Figure 22 reveals the result obtained with the elastic model in which the growing interference fit between the model and the steel ring led to significantly high concentrations of stress at the roots of the stars. In the case of the viscoelastic model, a significant reduction in fringe order at the star roots, and throughout the entire star, may be observed in Figure 23.

Because of the dependence of fringe order upon the viscoelastic character of the material (that is to strain as well as stress) there is no immediate, simple way for evaluating stress in terms of fringe order for a viscoelastic material. A much more complex relationship usually exists (Ref. 10). Consequently, the analysis of a photoviscoelastic fringe patterns may involve procedures almost as complex as the theoretical analysis of the structure itself. This aspect of photomechanics has yet to be developed.

Work in PTVE is now continuing in an effort to improve model fabrication and diminish the difficulty of interpretation of fringe pattern data. One promising result, recently obtained, is the discovery of a material in which fringe order appears to be directly proportional to the stress although the material itself exhibits extremely high viscosity while behaving basically as a solid at room temperature. This material may provide an important property both in modelling viscoelastic structural behavior and simplifying the analysis of viscoelastic structural behavior through photomechanics.

REFERENCES

1. E. G. Coker and L. N. G. Filon, "A Treatise on Photoelasticity," Cambridge Univ. Press, 1931.

2. H. Becker and G. Gerard, "Photoelastic Model Engineering," Mechanical Engineering, v. 82, July 1960, pp. 43-46.

3. H. Becker, "Equipment for Watching Propagating Stress Waves," Review of Scientific Instruments, v. 30, No. 12, December 1959, pp. 1107-1109.

4. G. Gerard and A. C. Gilbert, "Photothermoelasticity: An Exploratory Study," Journal of Applied Mechanics, v. 24, No. 3, pp. 355-360, September 1957.

5. H. Tramposch and G. Gerard, "Physical Properties of Plastics for Photothermoelastic Investigations," Journal of Applied Mechanics, v. 25, No. 4, pp. 525-528, December 1958.

6. H. Tramposch and G. Gerard, "An Exploratory Study of Three-Dimensional Photothermoelasticity," Journal of Applied Mechanics, v. 28, No. 1 (Trans. ASME, v. 83, Series E), pp. 35-40, March 1961.

7. A. Colao and H. Becker, "Photothermoelastic Investigation of Rectangular Plates," ASME Preprint 62-WA-207 (1962 Annual Meeting).

8. H. Tramposch, "Theoretical and Experimental Investigation of Thermal Stresses in Hypersonic Aircraft Wing Structures," Journal of Aerospace Sciences, v. 29, No. 6, pp. 719-725, 742, June 1962.

9. H. Becker, "An Exploratory Study of Stress Concentrations in Thermal Shock Fields," Trans. ASME, v. 84, Sec. B, No. 3, Journal of Engineering for Industry, August 1962, pp. 343-350.

10. H. Becker and A. W. Zachar, "Exploratory Studies in Photomechanics," Journal of Applied Polymer Science, scheduled for December 1963 publication.

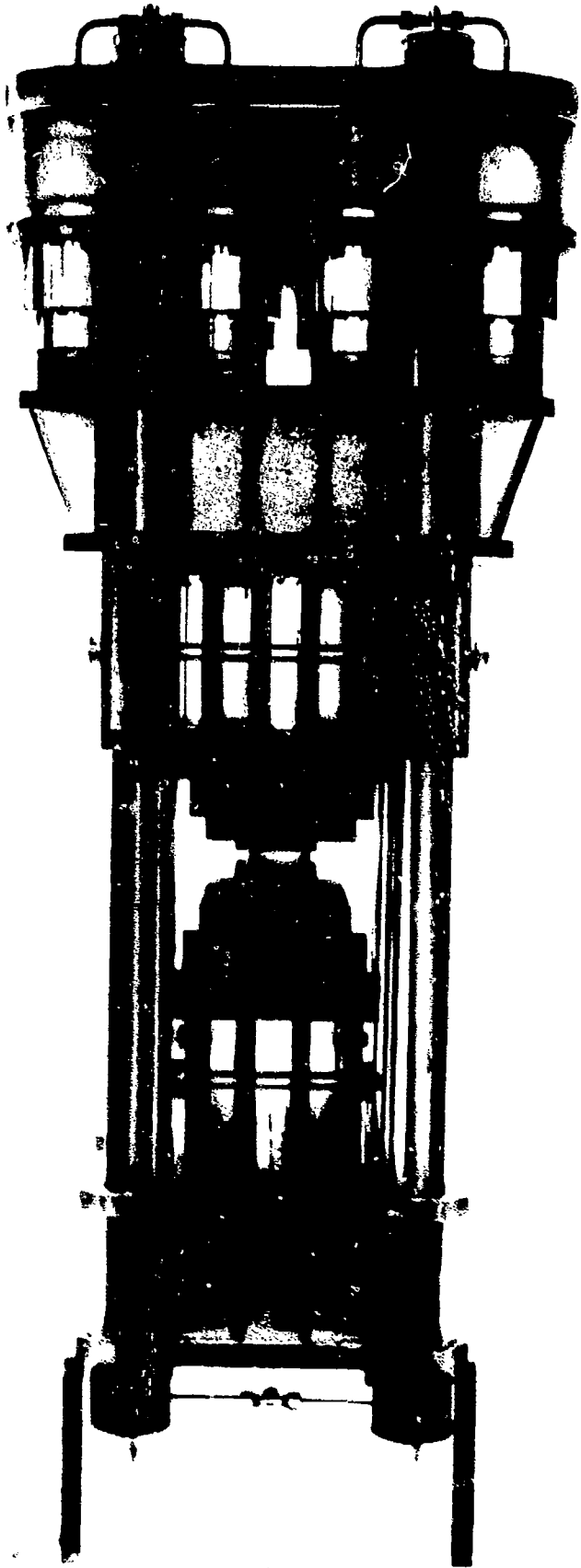

Figure 1. Photoelastic Model of a 50,000 Ton Forging Press

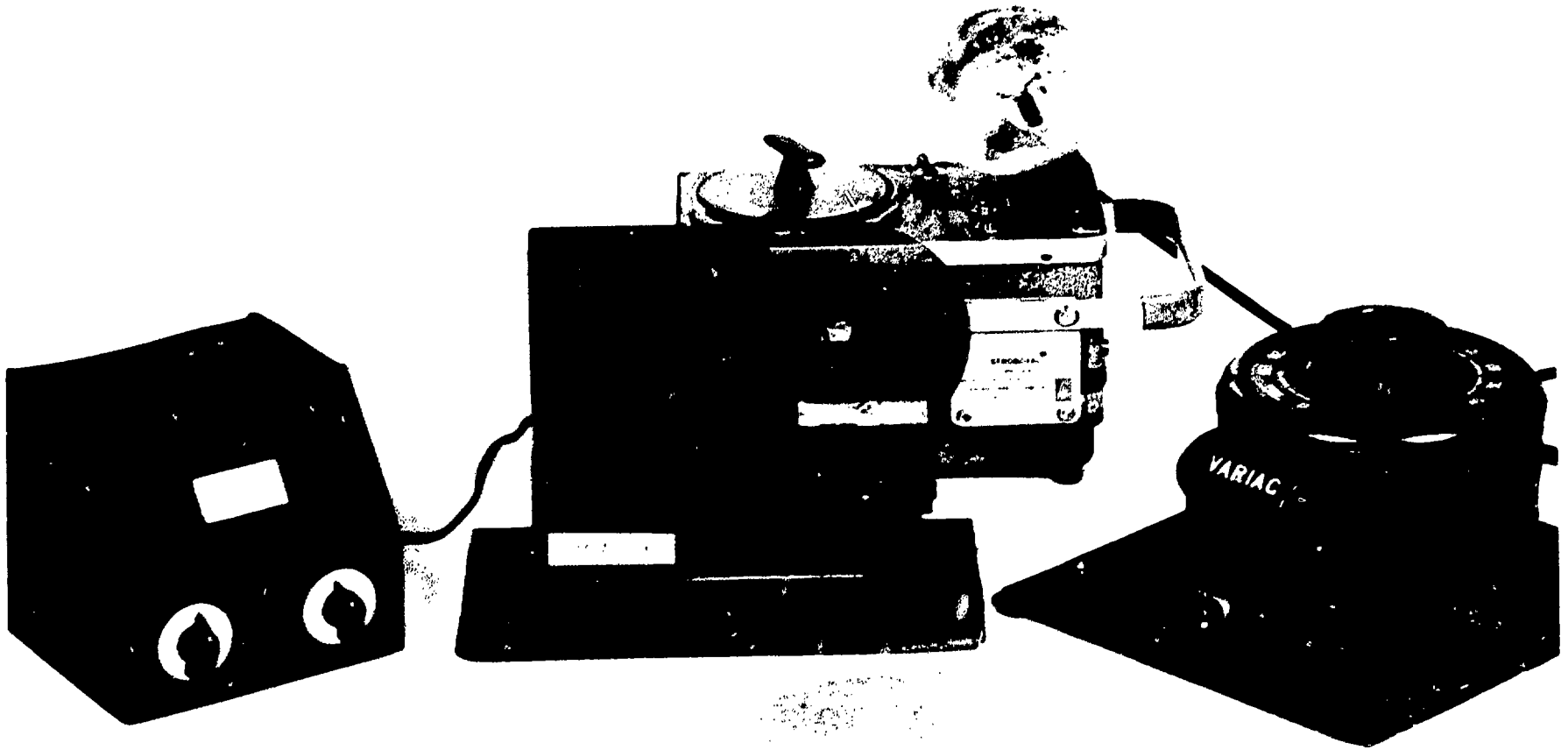

Figure 3. Photograph of an Experimental Arrangement for Strobelasticity

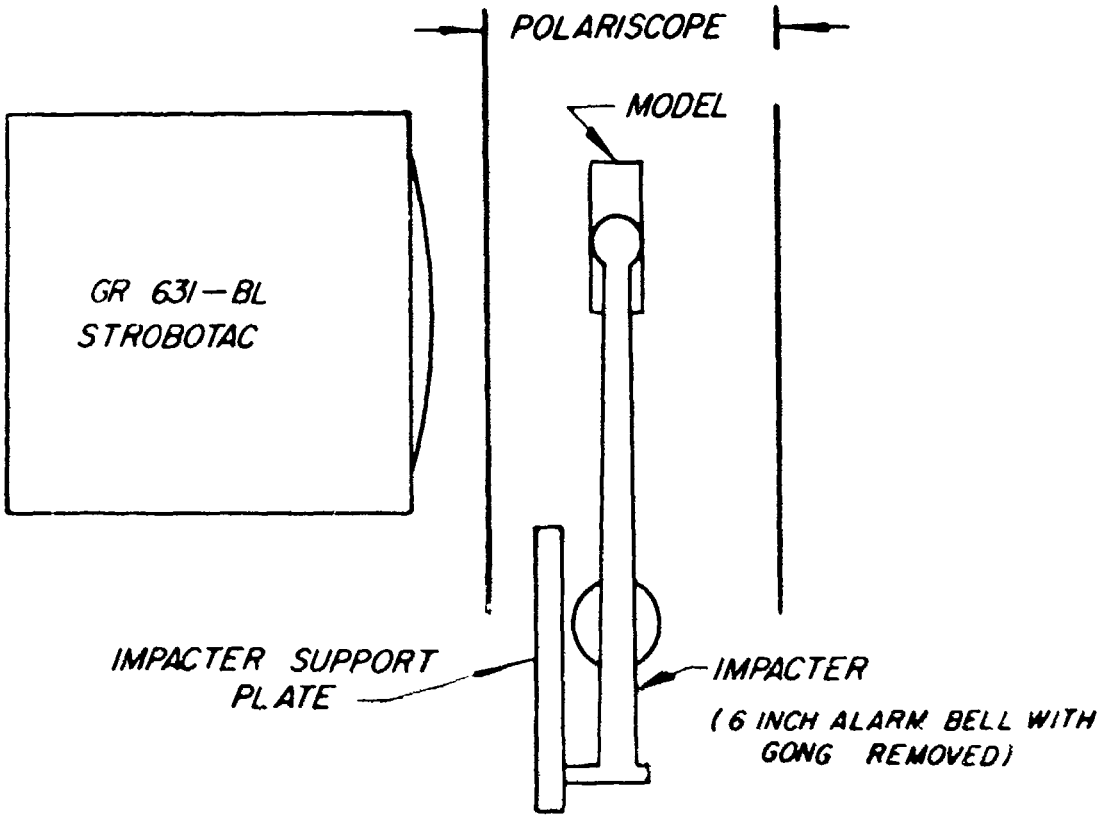

TOP VIEW OF GENERAL ARRANGEMENT

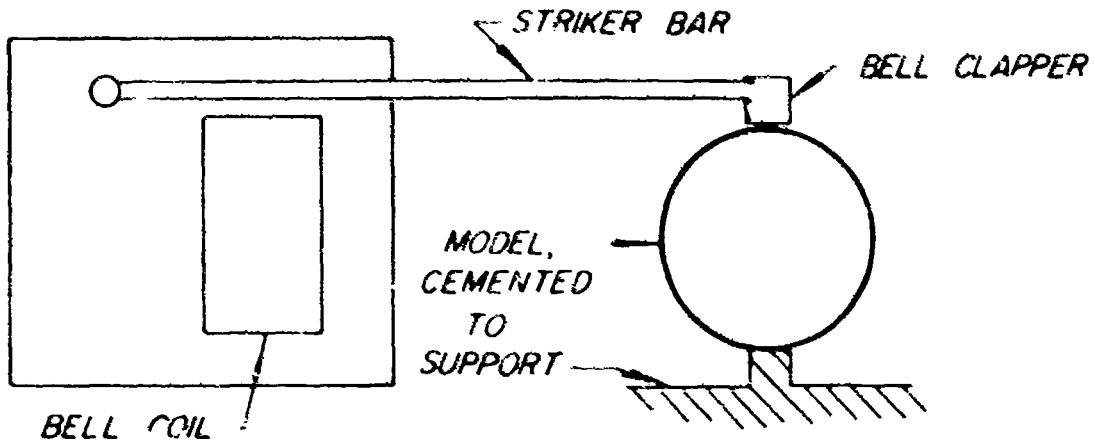

DETAIL OF IMPACTER — MODEL ARRANGEMENT

Figure 2. Schematic Arrangement of Strobelastic Equipment

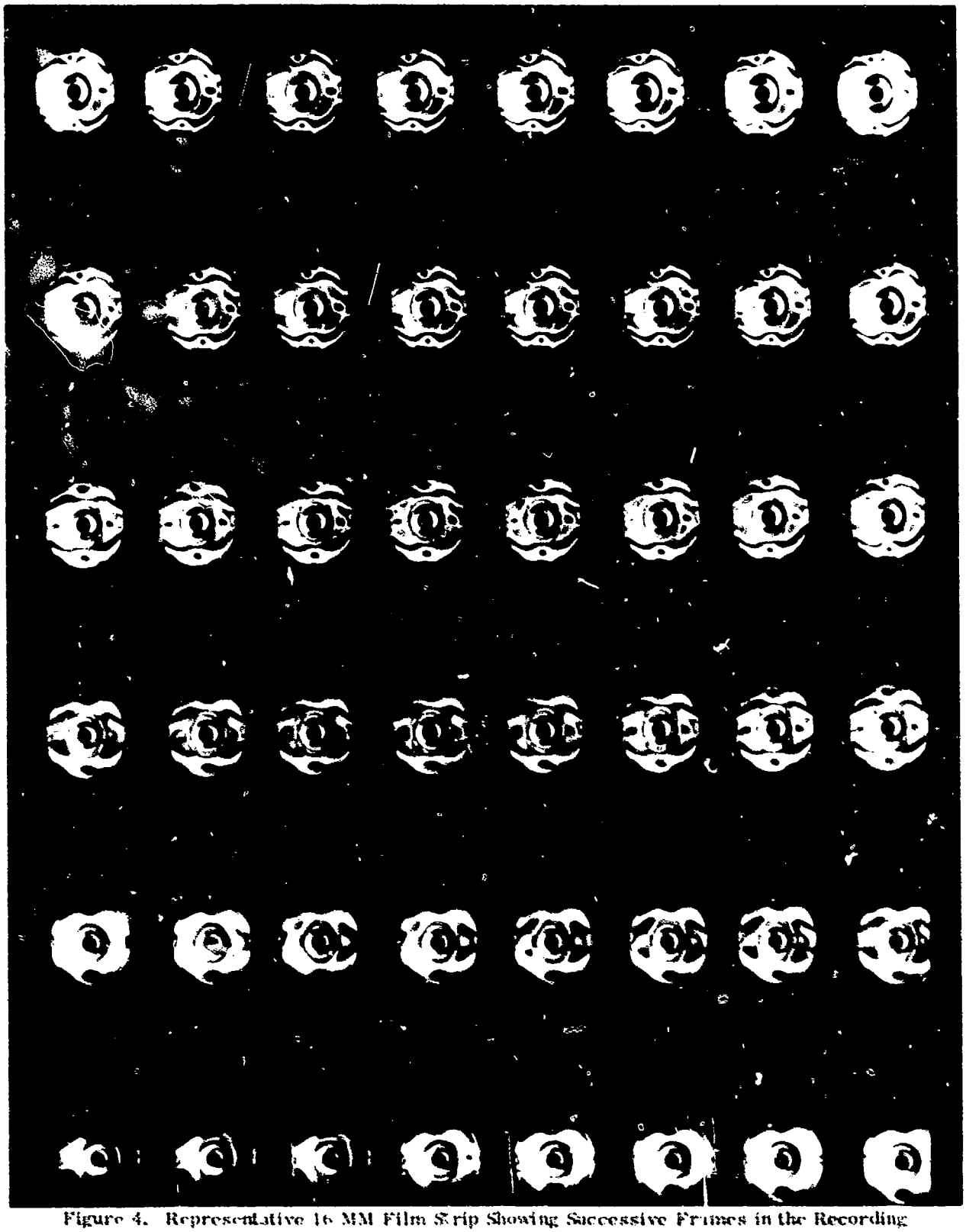

Figure 4. Representative 16 MM Film Strip Showing Successive Frames in the Recording of an Impact on a Composite Ring System

Figure 2. Strobe Light Photograph of Expanding Edge of a Plate

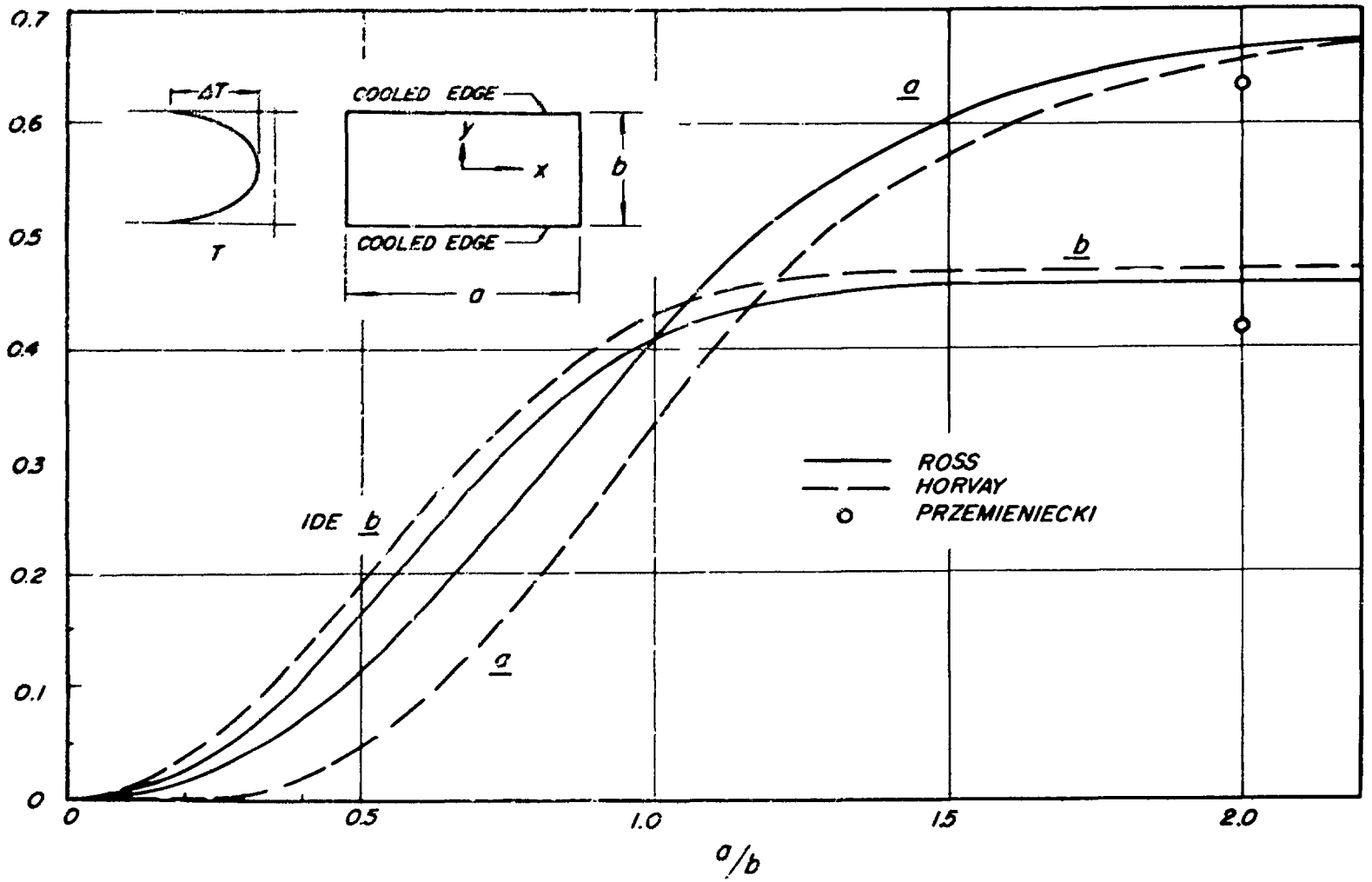

Figure 6. Three Theoretical Predictions of Stresses in a Rectangular Plate Under Uniaxial Parabolic Temperature Distribution

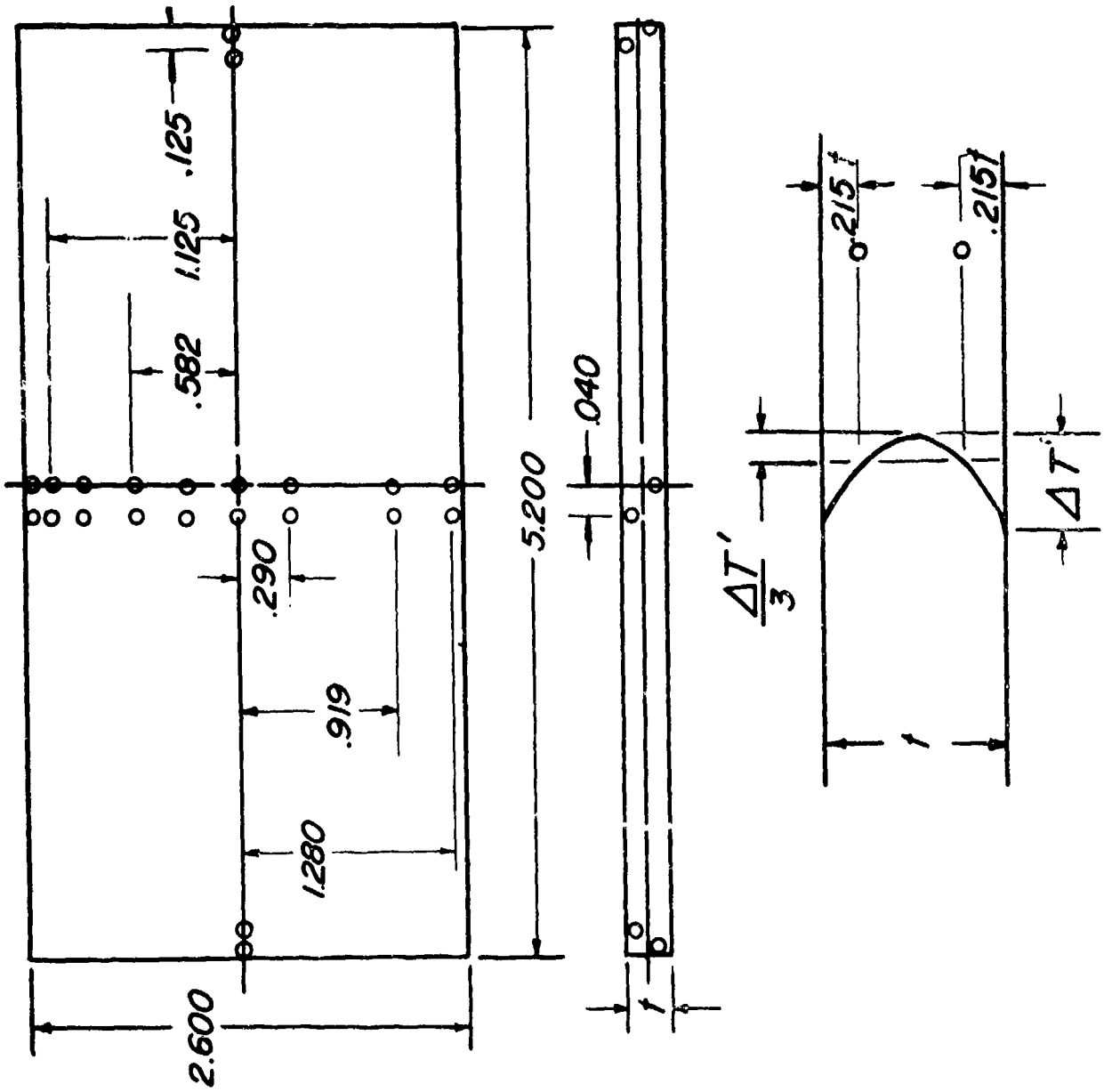

Figure 7. Thermocouple Locations in a Rectangular PTE Model

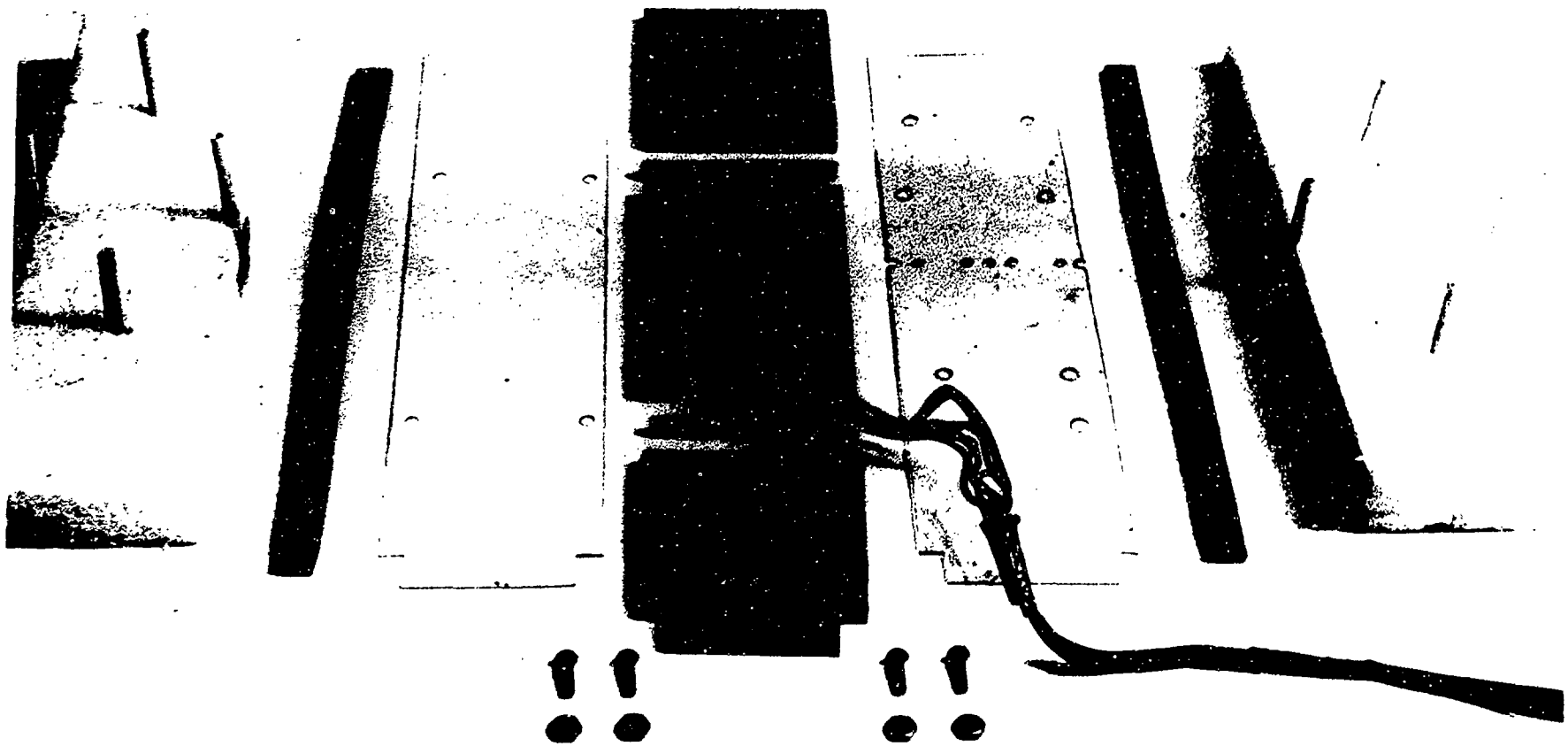

Figure 8. Components of a Rectangular Plate PTE Experiment

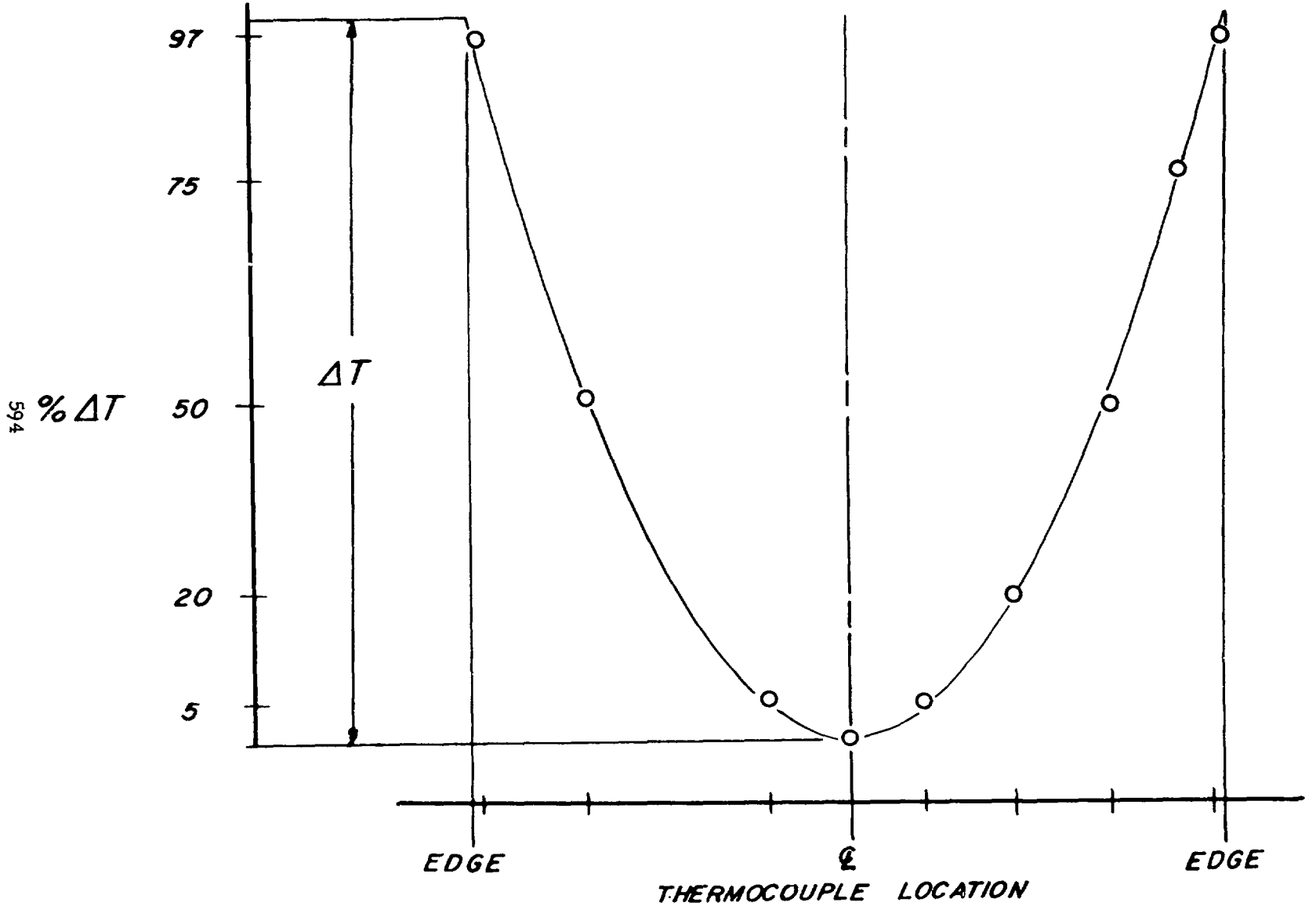

Figure 9. Normalized Parabolic Temperature Distribution Observed Across a Rectangular Plate Model During a Typical Experiment

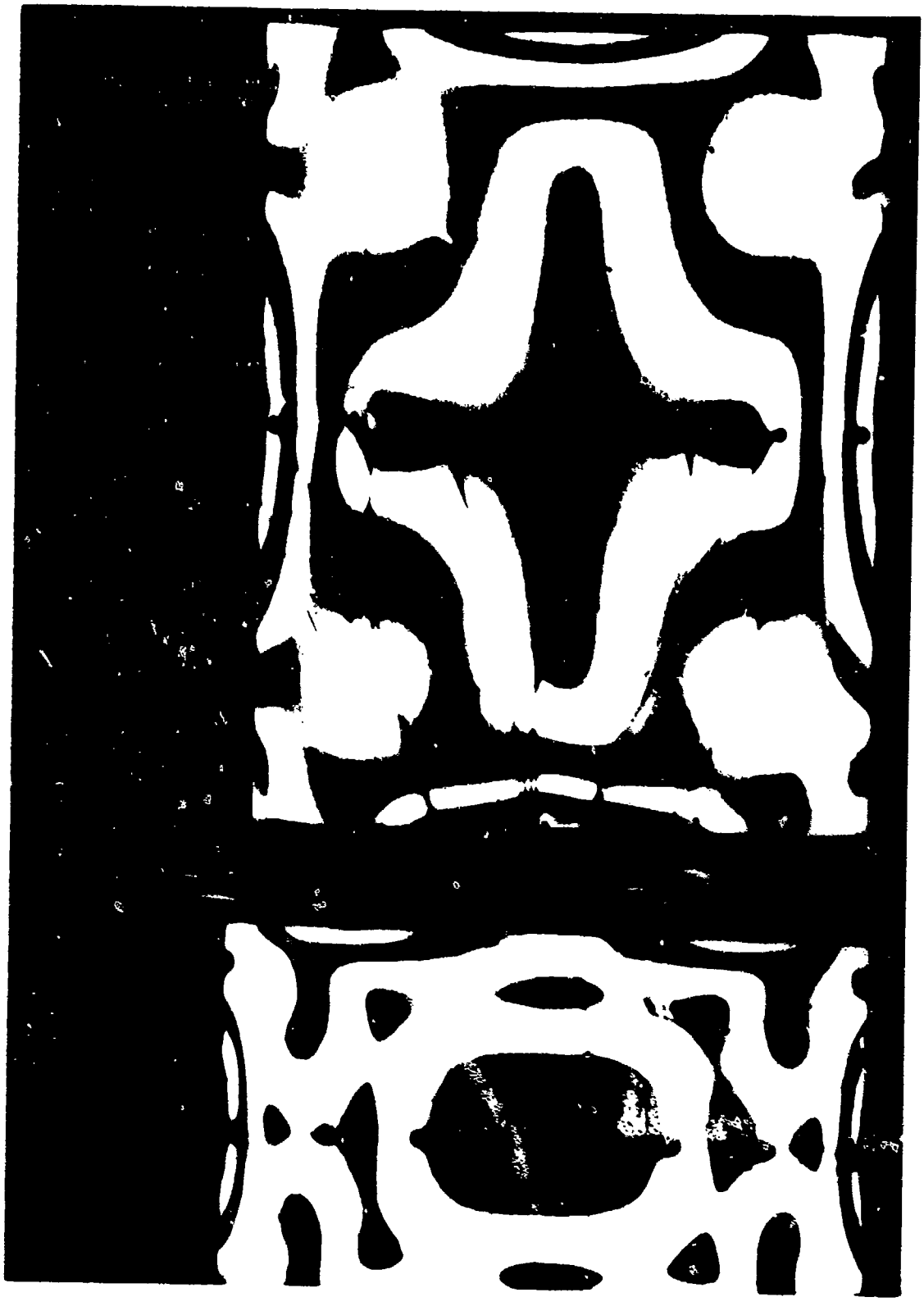

Figure 10. Photoelastic Fringe Patterns in Rectangular Plates of a/b = 0.6 and 1.2 With Thermal Shock Applied to the Top and Bottom Edges

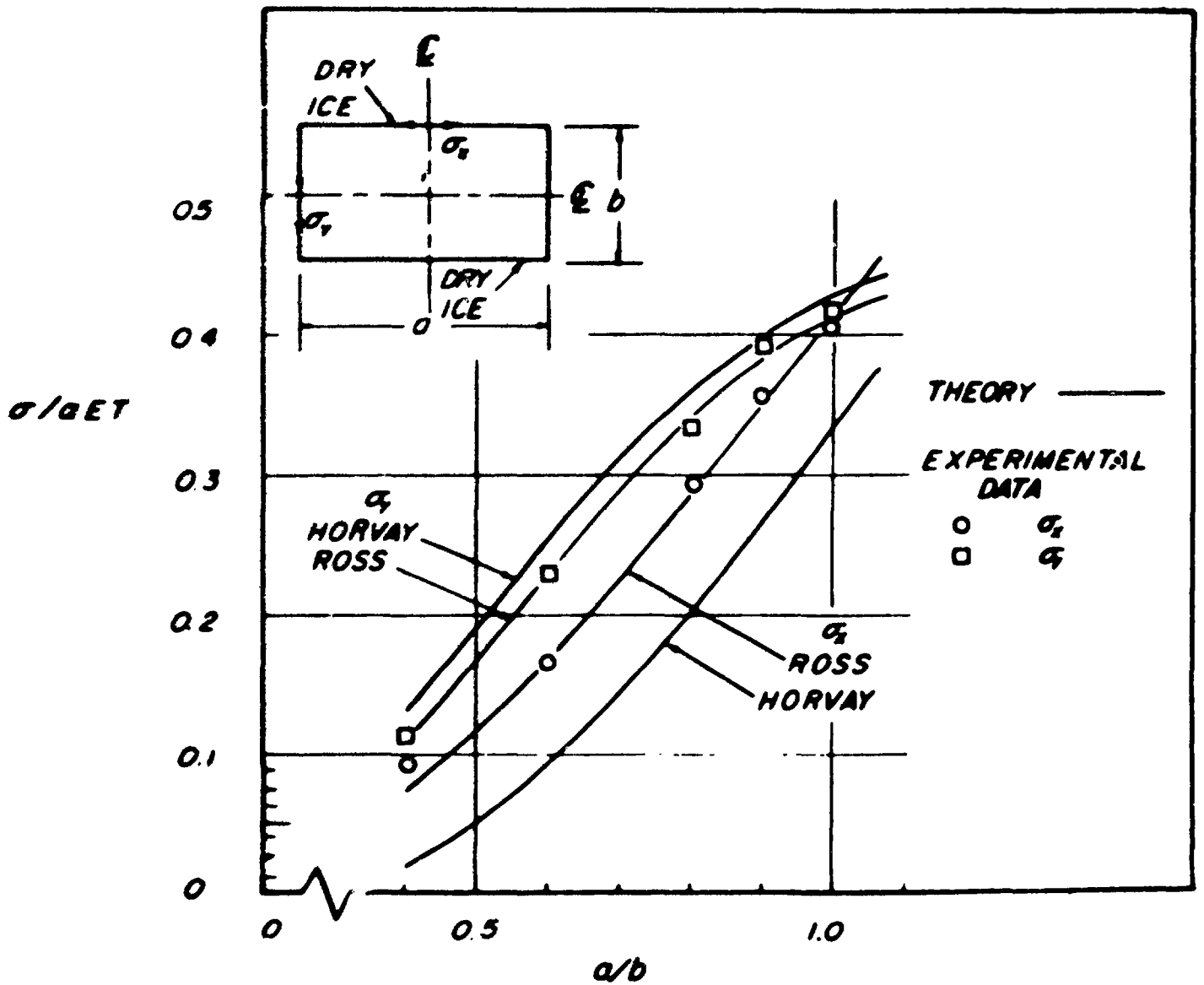

Figure 11. Correlation of Theory and Experiments for Parabolic Temperature Distributions on Rectangular Plates

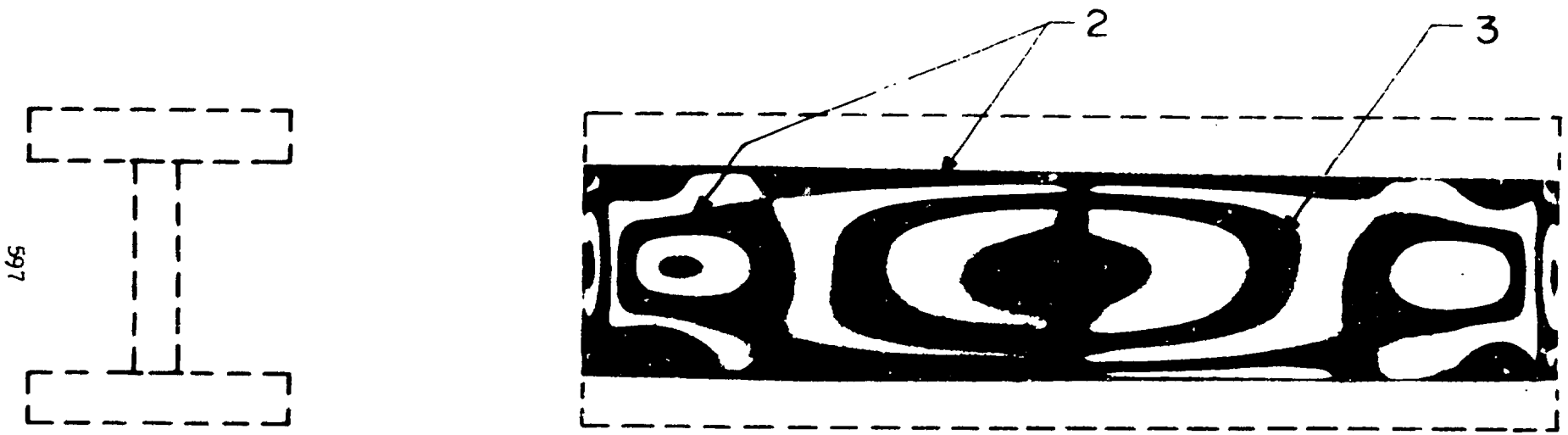

Figure 12. Schematic Model Cross Section and PTE Pattern of an I Beam With Thermal Flux Applied to the Flanges

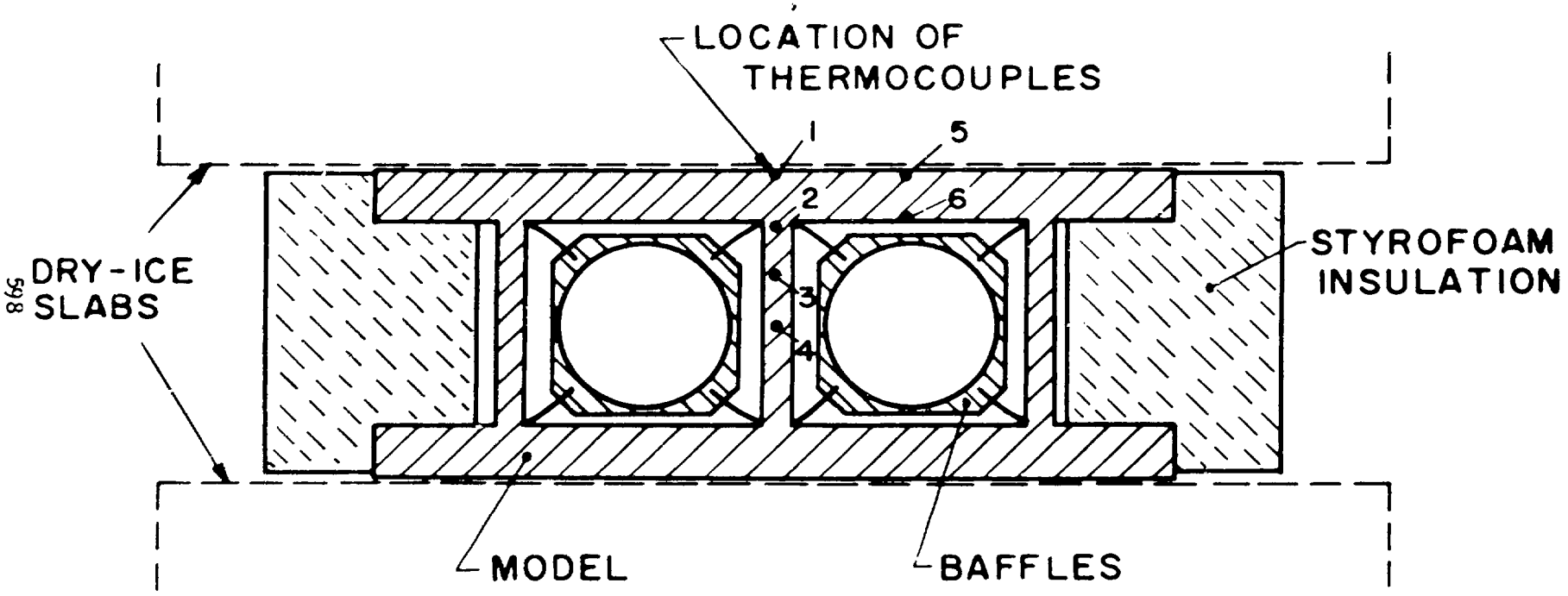

Figure 13. Schematic Arrangement of a Multicell Box Beam PTE Model

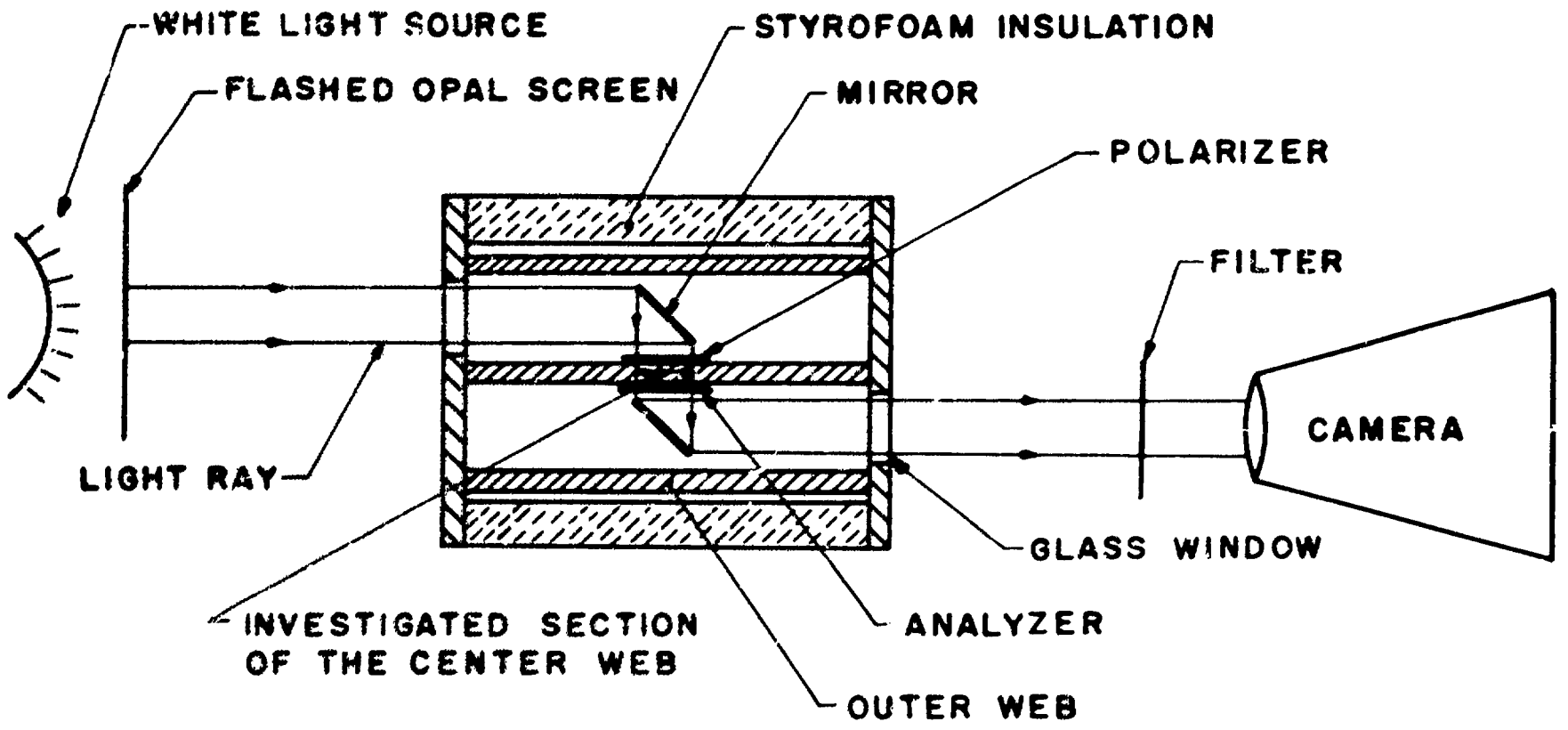

Figure 1. Optical Train for Measurement of Fringes in a Multicell Box Beam (Top View).

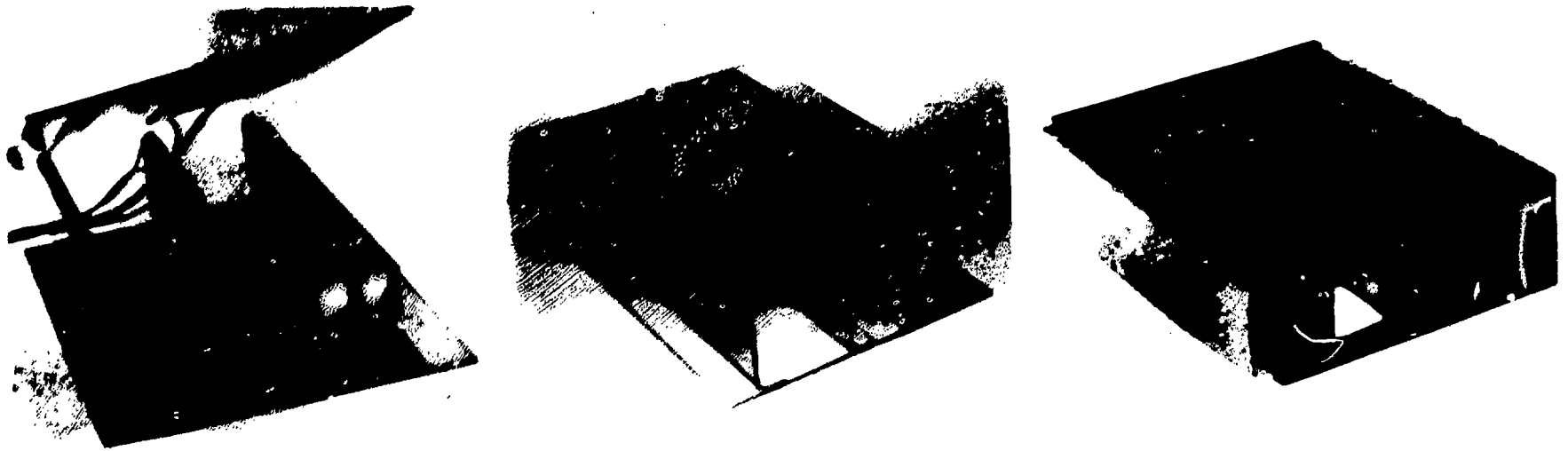

Figure 15. Photographs of a Channel Web Multicell Box Beam PTE Model in Various Stages of Completion

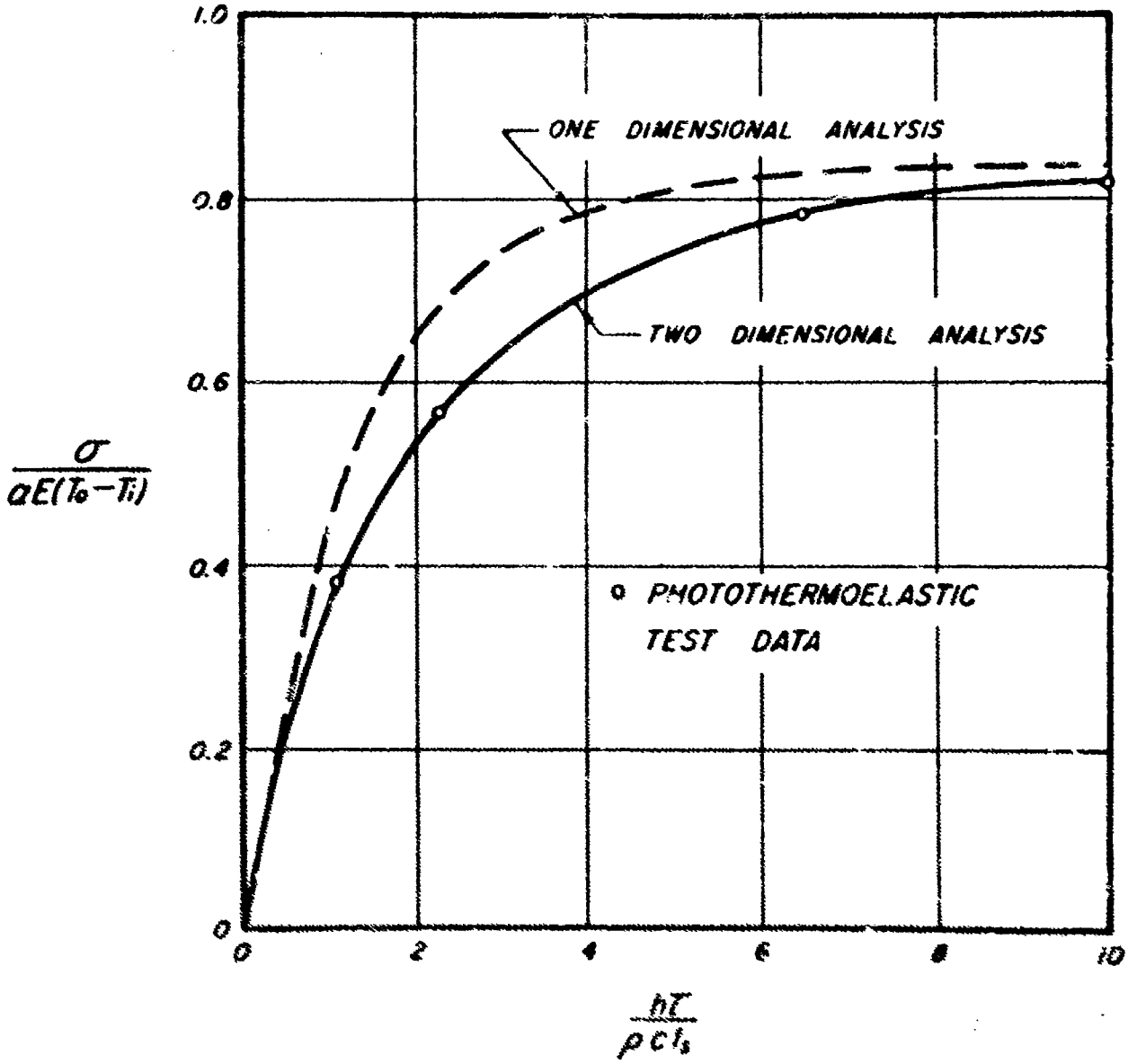

Figure 16. Correlation of PTE Results and Theories that Consider the Flange of the Multiweb Box Beam as a One- or Two-Dimensional Medium

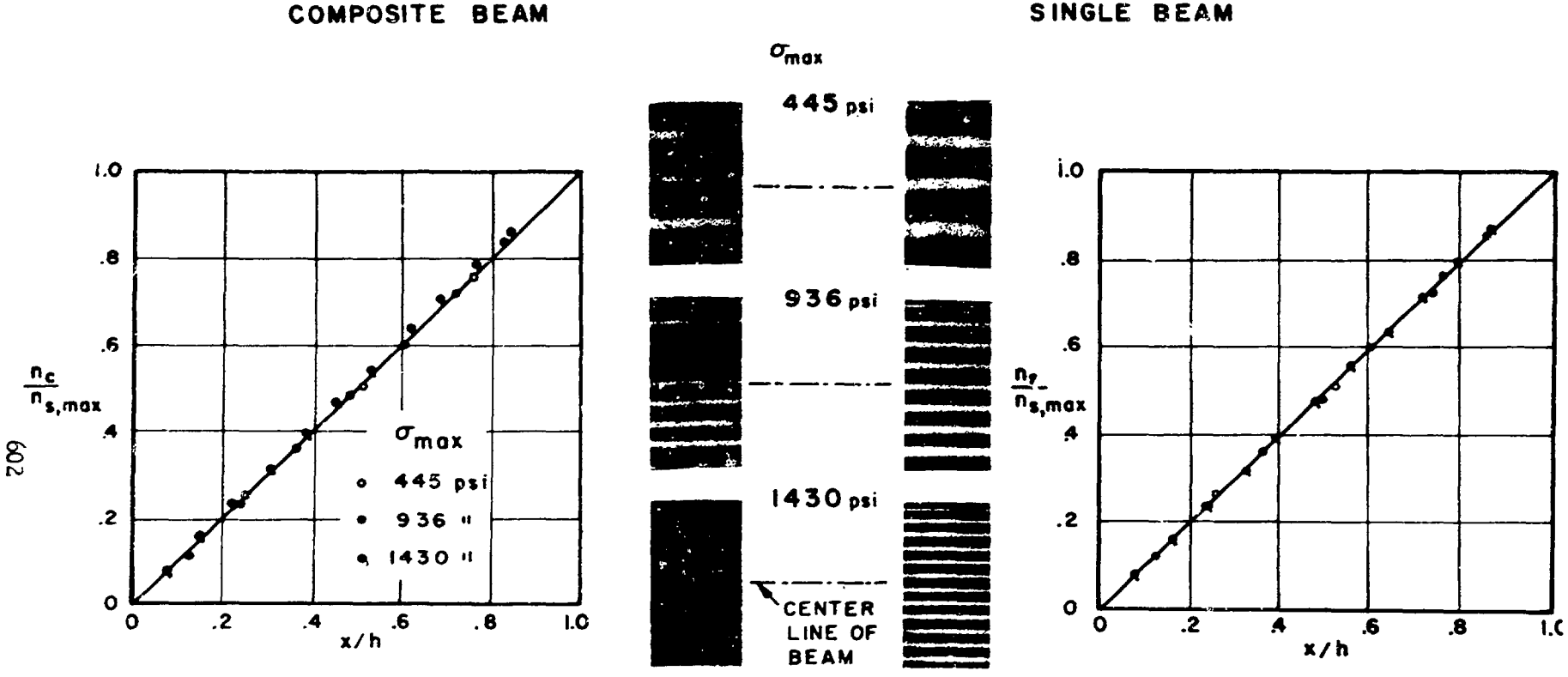

$n_{s,max}$ - MAX. FRINGE ORDER OF SINGLE BEAM OBTAINED FROM THE LOADING FORCE

n_s - FRINGE ORDER OF SINGLE BEAM

n_c - FRINGE ORDER OF COMPOSITE BEAM

x - DISTANCE FROM CENTER LINE

h - ONE HALF THE BEAM HEIGHT

Figure 17. Calibration Curve for a Bonded Polariscope (Left Side) Compared to a Free Beam Loaded in Pure Bending (Right Side)

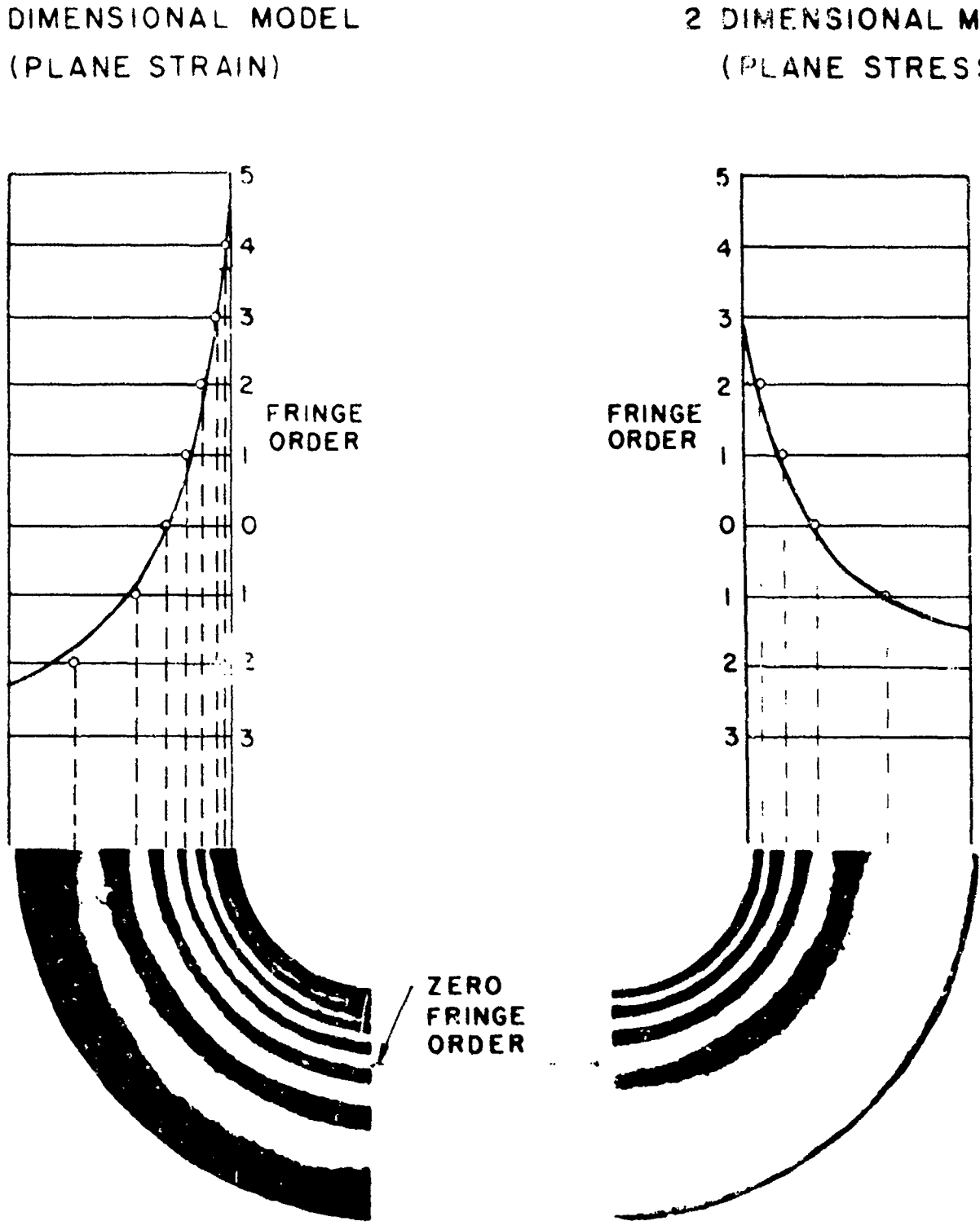

Figure 18. Comparison of Cylinder and Flat Plate Fringe Patterns with Stress Theories for a Radial Temperature Field

a (t=0+ min.)

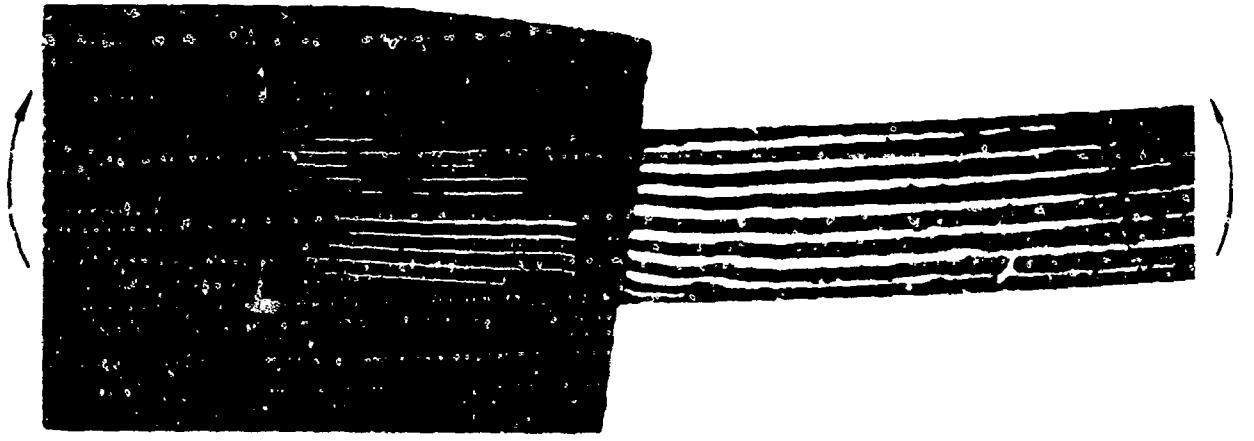

b (t=2 min.)

c (t=5 min.)

MODEL IN UNBONDED POLARISCOPE POLARISCOPE BONDED TO MODEL

Figure 19. Fringe Patterns in a Viscoelastic Beam in Pure Bending in the Bonded Polariscope (Right Side) and Unbonded Polariscope (Left Side) Areas

Figure 20. Bonded Polariscopes of Various Grid Sizes on a Viscoelastic Beam

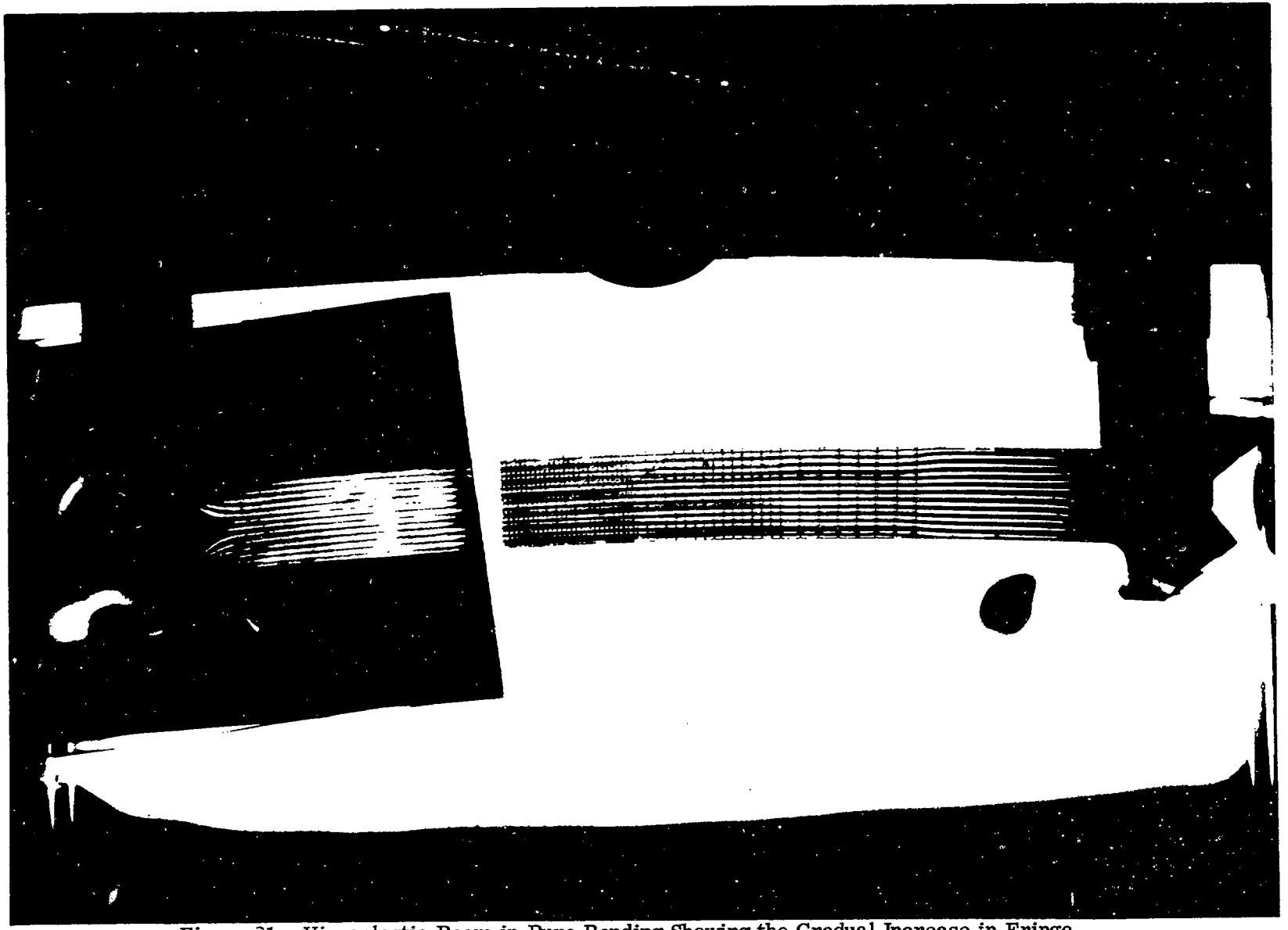

Figure 21. Viscoelastic Beam in Pure Bending Showing the Gradual Increase in Fringe Order From the Ungridded Bonded Polariscope on the Right to the Unbonded Polariscope in the Dark Area at the Left

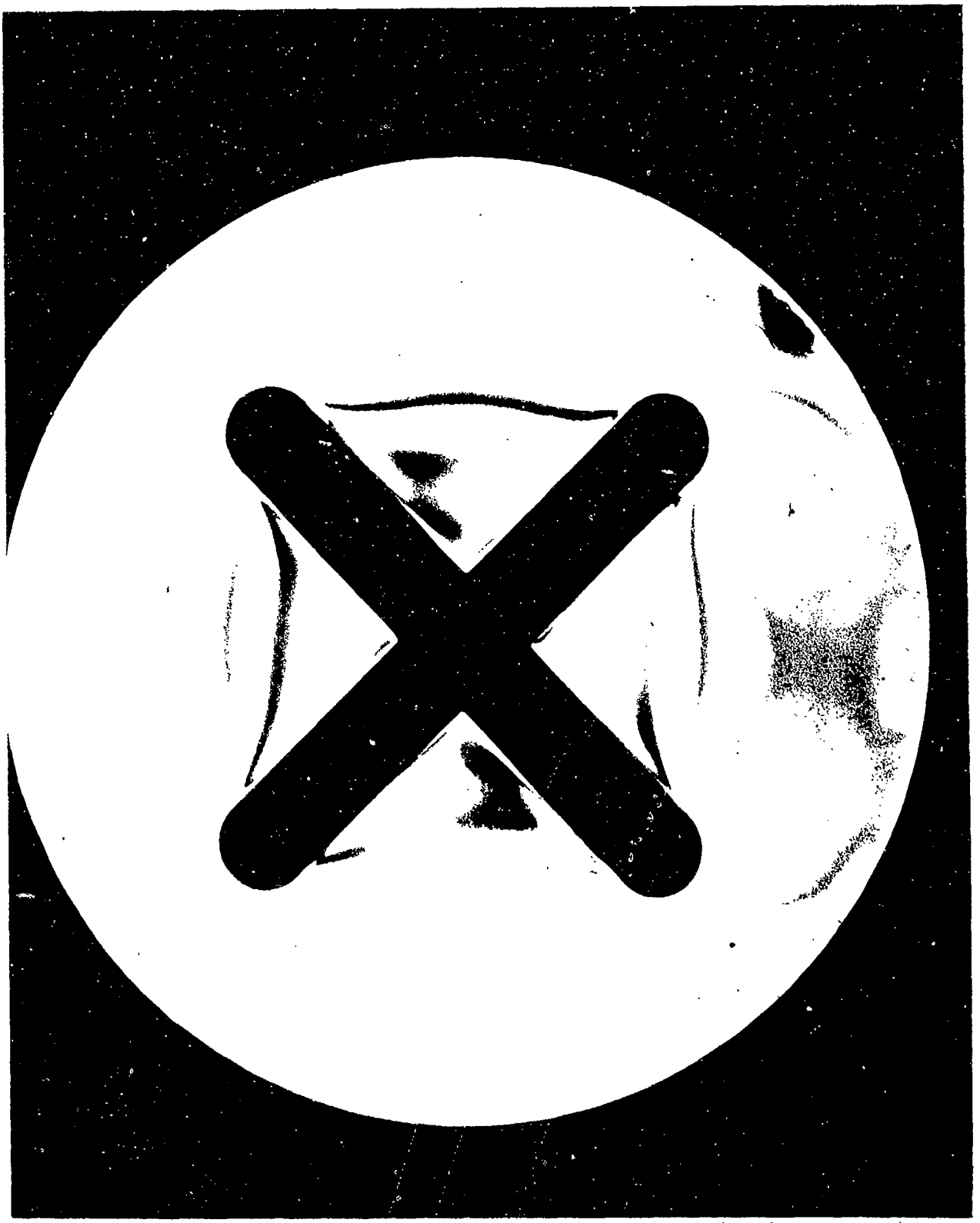

Figure 33. PTE Fringe Pattern in an Elastic Four Point Star Encased Rocket Grain Model

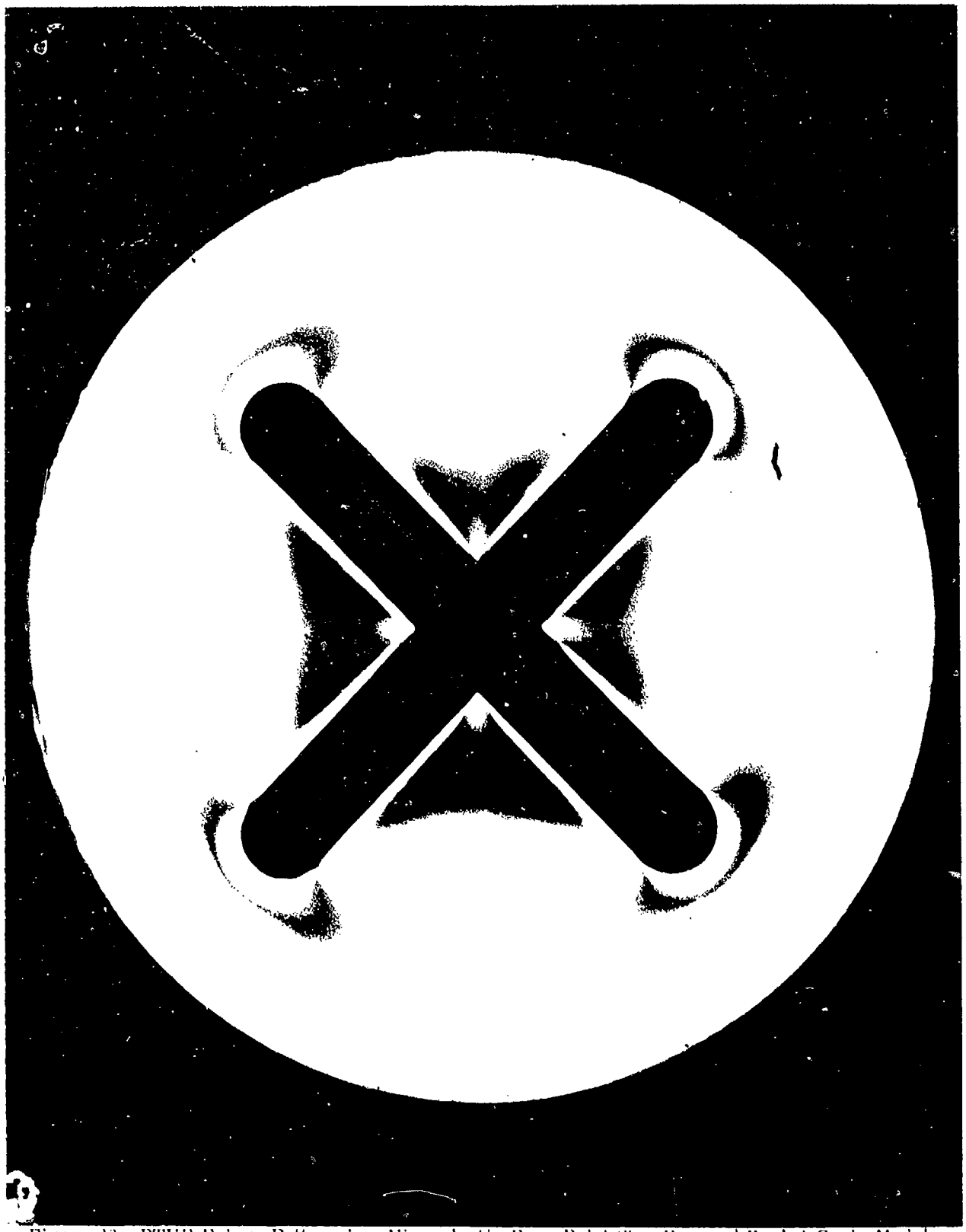

Figure 23. PTVE Fringe Pattern in a Viscoelastic Four Point Star Encased Rocket Grain Model

THE USE OF MODELS FOR CONTROL OF SONICALLY INDUCED VIBRATION

M. Bernstein

R. Gross

Grumman Aircraft Engineering Corporation
Dynamic Analysis Section
Bethpage, New York

ABSTRACT

A half-scale dynamically-similar model of a non-uniformly-stiffened fuselage structure of slightly varying cross section was designed, constructed, and tested to obtain data on the response of the full-scale structure to propeller-noise excitation. This approach was chosen as the logical compromise between the cost of a full-scale accuracy of practicable analytical methods. The model was used to determine how the natural frequencies of the structure might be varied, if necessary, and to investigate means for reducing internal noise and vibration levels. As an indication of the accuracy of practicable analytical methods when applied to relatively complex, realistic structures, a comparison was made between the experimental vibration characteristics and the mode shapes and frequencies computed for an "equivalent" uniform cylinder and for a ring cross-section with stiffners included.

LIST OF ILLUSTRATIONS

THE USE OF MODELS FOR CONTROL OF SONICALLY INDUCED VIBRATION

By: M. Bernstein and R. Goss

Grumman Aircraft Engineering Corporation
Dynamic Analysis Section
Bethpage, New York

SUMMARY

The parameters required for modeling sonic pressure fields, structural damping, and appropriate elastic properties are reviewed. The difficulties in modeling damping and fatigue effects for small scale structures are discussed. Dividing the modeling process into a small scale rigid model to evaluate pressure fields and a larger scale dynamic model to evaluate the response or even fatigue life appears appropriate. Experimental work on determining the response of a half scale model of a fuselage section to a sonic pressure field is described in detail. The section consisted of a non-uniformly stiffened almost circular fuselage constructed of skin, frames, and heavy widely spaced longerons. Experimentally determined modes and frequencies are compared for various internal arrangements of partial bulkheads and simulated equipment weight. Comparison with full scale aircraft fuselage response is shown.

INTRODUCTION

Design of present and future flight vehicles, powered by propulsion plants having mechanical forces ranging from several thousand pounds of thrust for today's "smaller" turbojet, turbofan and rocket engines to the planned rocket engines of the future generating several million pounds of thrust, requires continued development of techniques, both analytical and experimental, for investigating their acoustical and related structural effects. One of the answers towards treating the problem lies in the use of scaled models. The magnitude and size of full scale power plants and structures, and aspects of cost, time, availability and complexity point towards utilization of scaled models.

Elastic models of structures, for most applications, are limited to valid representations only of the lower modes. Responses to some of the excitation, however, also result in higher

frequency shell modes, and modeling to simulate this phenomena requires much finer structural fidelity. When the applied forces are broad band and random in content the responses are primarily resonant, and since the resonant response is determined principally by damping, it is necessary that the damping be adequately simulated in the model. Furthermore, if fatigue testing of the models is to be simulated, microscopic effects such as stress distribution and residual stresses become important and impose a practical limit on size reduction.

This paper will discuss aspects concerning acoustic source and structural scale modeling, and explain in detail the results of a scale model test conducted at Grumman. It is divided into two major sections. The first discusses some modeling considerations required for reliable model testing including Modeling, Sonic Sources, Damping, Fatigue Considerations and Structural Modeling. Section II, Model Testing, describes work done on a 1/2 scale center section fuselage model.

SECTION I - CONSIDERATIONS IN SCALE MODEL TESTING

A. - Modeling Sonic Sources

In modeling sonic pressure fields for controlling sonically induced vibration, the region of concern is generally very close to the source of excitation, and the important attributes are the spatial and temporal distribution of the pressure spectrum, since these are the pressure parameters which determine the generalized force.

Reference (1) presents an extensive study of the use of acoustical scale models for jet and rocket engine near field noise. A suitable scaling relationship proposed for jet exhaust noise is given as:

$$\frac{p^2_{r,\theta}}{(\rho_j V_j^2)^2} \propto \left(\frac{\rho_\infty}{\rho_j}\right)\left(\frac{V_j}{c_j}\right)^4\left(\frac{c_j}{c_\infty}\right)^4\left(\frac{4\pi}{\beta}\right)\left(\frac{d_c}{r}\right) G_1\left(\frac{V_j}{c_j}, \frac{c_j}{c_\infty}, \theta\right) G_2(Kr)$$

where:

$p_{r,\theta}$ is the sound pressure level as a function of radial distance r from the source and angle θ.

ρ_j, V_j, c_j is the density, velocity, and speed of sound in the jet at a reference location.

ρ_∞, c_∞ is the density and speed of sound for ambient gas.

d_c is the characteristic diameter of flow.

β is the solid angle of radiation.

$G_1\left(\frac{V_j}{c_j}, \frac{c_j}{c_\infty}, \theta\right)$ is the Directivity factor, a function of jet Mach number, speed of sound ratio, and θ.

$G_2(Kr)$ is the near field factor as a function of K and r.

K is the wave number, $\frac{\omega}{c_\infty}$.

The first three ratios on the right side of the inequality refer to the nozzle exit conditions. To insure repeatibility and reliable comparisons for separate tests, these conditions were determined (in reference 1) at the exit plane of a fully expanded nozzle. The use of full scale flow parameters together with similarity relationships resulted in essentially equal sound pressure levels at distances scaled by the nozzle dimensions. Generally,

gas identical to full scale was used, and temperature and pressure in the plenum upstream of the nozzle were maintained at full scale values. Total acoustical power scaled inversely as the square of the nozzle dimension, while frequency scaled in accordance with the dimensionless Strouhal number:

$$S = \frac{f\,d}{v_j}$$

where f is the frequency.
d is a linear dimension, usually the nozzle exit diameter.
v_j is the jet velocity.

The two functions G_1 and G_2 are important in determining the characteristics of the near field. They depend on the proper distribution of the effective sources of noise in the jet exhaust. Profiles of the jet exit velocity and temperature, which can be altered by small differences in nozzle geometries, may effect the distribution of noise sources, as described in reference (2), and consequently the scaling of G_1 and G_2. Near field model dimensions and flow parameters therefore, should be carefully controlled, particularly for very small scale models.

Model relationships for scaling jet noise have been summarized on Table I. Results of applying scaling techniques to J-57 and YJ-85-1 turbojet engines, and a Jupiter liquid rocket engine are shown on Figures 1, 2, 3 and 4; taken from references (1) and (3), where other examples are also shown. Agreement with full scale ranged from good for a J-57 to poor for a J-79 with a more complicated nozzle shape. The small model of the Jupiter engive gave good agreement at low frequencies, but was 5 decibels too high at high frequencies, possibly due to poor placement of the bucket exhaust deflector. Correlation coefficients for this model, as a function of frequency, were compared with full scale at two positions and were in reasonable agreement up to the first zero crossing.

These techniques have been extended to the modeling of sonic sources in the presence of reflecting barriers such as a B-52 wing installation and a Minuteman Silo installation. Reasonable agreement was obtained at lower frequencies, with deviations increasing as freouency increased.

The use of substitute gases was also satisfactorily demonstrated under certain conditions, when full scale flow parameters

are maintained and a high degree of control utilized. Helium proved particularly suitable.

It seems apparent therefore, that modeling jet and rocket engine exhaust near noise fields is feasible under most circumstances, when full scale flow parameters are utilized and a high degree of control maintained.

Another sonic source of great interest in model testing at Grumman was the aircraft propeller. In this case the fundamental blade passage pressure component in the near field at locations about a fuselage were required. The difficulty arose in trying to reproduce the time history of the traveling source as the propeller blade swept past. A time history of the pressure anticipated during one cycle over 110° of a fuselage is shown on Figure 5. This was calculated graphically, assuming the source of near field noise as concentrated near the propeller tip. The pressure field from a single speaker during a test is also plotted on the same scale for comparison. During portions of the cycle, it is apparent that the speaker is out of phase with the applied force. Reproducing the distributed source appeared to be a formidable problem, hence, an alternate method was utilized. The generalized force in the first experimentally determined mode was calculated for two different sources, the propeller and speaker induced acoustic test field, and the ratio was used to modify the measured structural response. This technique was considered feasible because there was no requirement to reproduce the full scale values of sound pressure. The intent in these model tests was to scale the measured response of the model linearly for the difference between model and full scale sonic pressures.

B. - Damping

Damping in structures generally results from material hysteresis under stress, radiation damping, and friction damping at joints and interfaces.

The largest amount of structural damping is attributed to energy loss in riveted joints. The advent of wide band sources of excitation has focused attention on the damping mechanism since most structural response occurs at resonant frequencies. Measurements reported in reference (4) indicated that damping may not be due to the design and number of connectors but to the relative motion at the interface some distance from the connectors. Rivet spacing may have little effect once sufficient rivets have been added so that the maximum clamped area has been achieved. The conclusions of the study indicated that damping of joints appears

to be linear up to high amplitudes, is not primarily associated with connectors or structure in the immediate vicinity of connectors, is higher for lower clamping forces or more lubrication, and is relatively independent of bending stiffness.

In the past, most aircraft panel testing for fatigue has utilized full scale sections so that representative fastener techniques were used. Fastener spacing and size is generally determined by shear and bearing loads, and by spacing required to prevent sheet edge buckling. Tension loads in fasteners, which are important in damping, is not generally considered during design.

Scaling for joint damping might be accomplished by scaling the joint areas, the number and spacing of rivets, and the rivet diameter and length, provided the clamping force could be duplicated. One approach might be to design tightly clamped joints and assume that this would be a conservative procedure. Separate joint tests might be considered during model development to evaluate this factor.

The practical difficulties in scaling joint damping are a detriment to the wider use of small scale structures for vibration response and fatigue tests.

Radiation damping can also contribute significantly to the overall damping mechanism under some conditions, particularly when the frequency is high. Maximum damping occurs at coincidence, when the speed of flexural waves in the structure are equal to the speed of acoustical waves in the surrounding medium. This frequency is generally above the region of interest in fatigue for most practical aircraft structures. Radiation damping of a lesser amount occurs below this frequency but above the frequency $f = \frac{C_o}{\pi a}$. C_o is the speed of sound and a is the longer plate or beam dimension. Relationships applicable for radiation damping are shown in references (4) and (5).

In most cases, the damping values at coincidence include the ratio of surface area to the product of mass and frequency, which should make them non-dimensional, if size were scaled uniformly. This would not be true however, if different scale factors were to be used for skin thickness, since in this case the mass would increase relative to the surface area and the effective damping would decrease. In order to demonstrate the orders of magnitude involved, calculations were performed as shown on Table II. It may be noted that the plate coincidence frequencies were all very high. Generally this frequency range is considerably above that of concern

in structural design. The values below coincidence, but above the lower boundary, would be more important and it may be noted that the actual damping values are low.

It can be concluded then that radiation damping in small model panels could be significantly higher than full scale if models are not scaled uniformly for size.

Material damping, as discussed in reference (6), is a direct function of stress, and is not expected to be important, or to differ significantly in most model applications where standard metals are used and where stress levels are well below the fatigue strength. If uniform scaling for size is applied, then the stress distribution in the model would be the same as in the full scale structure except at stress concentration areas. In these areas stresses in models might be higher than in full scale structure, but if such concentrations are limited to a small portion of the total stressed volume, then they should not appreciably increase the total material damping. Material damping therefore, can be substantially scaled directly with size, but is not expected to be important.

C. - Fatigue Considerations

Scaling the fatigue factor is one of the least certain aspects of modeling. Size effects have been reported by Weibull in reference (7). He noted that stable crack propagation rates were proportional to the size of geometrically similar specimens. Peterson in reference (8) reported that on a series of fatigue tests of geometrically similar tensile specimens with holes, the notch sensitivity decreased rapidly as the hole diameter decreased below 1/4 inch. Stress gradients are also important in decreasing notch sensitivity and thereby increasing fatigue life. Other factors such as frequency effects are also not amenable to scaling. A discussion of these factors by C. Gray, in a generally sympathetic study of modeling for sonic fatigue presented in reference (3), concluded that experimental verification would be required to obtain a size scaling factor. In view of the scattered nature of full scale test data and the development still required to establish random fatigue design procedures, it would appear difficult to demonstrate adequate fatigue life in small scale models with high confidence.

D. - Structural Modeling

Elastic models of structures for most applications are limited to representing the lower modes with validity. This has been

generally the case on aeroelastic models, and on models designed to determine the elastic body effects on control systems. Response to sonic excitation, however, generally occurs in higher frequency shell modes of structures, and modeling to represent this phenomena requires much finer structural fidelity. When the applied pressures are broad band random, the response is primarily resonant, and since the resonant response is determined principally by damping it is necessary that the damping be adequately represented in the model. Furthermore, if fatigue is also to be modeled, microscopic effects such as stress distribution and residual stresses become important and impose a practical limit on reduction in size.

When considering scaling relationships applicable to reproducing mode shapes of frequencies, techniques commonly applied for modeling lower elastic modes are used as shown in reference (9). The equations of motion are transformed into dimensionless variables and dimensionless ratios of elastic and inertial parameters at reference locations. Applications of this technique have been worked out to illustrate the procedure for determining scaling relations for typical sonically excited structures.

Two types of structures in which sonic excitation are important are contained in rocket launch vehicles and stiffened skin panels. Scaling factors have been set up for a simple example of each type of structure to demonstrate the approach.

D-1. - Launch Vehicle

Consider a launch vehicle to be represented by a long beam in bending including shear and rotary inertia effects. The equation of motion for such a beam, using the notation of page 69 of reference (9) is:

$$\left\{\mu(y)\ddot{\alpha}'\right\}' - \left\{EI(y)\alpha''\right\}'' - m(y)\ddot{\alpha} - m(y)\int\left\{\frac{\mu(y)\ddot{\alpha}'}{GK(y)} - \left[\frac{EI(y)\ddot{\alpha}''}{GK(y)}\right]'\right\}dy = -F_z(y,t)$$

where:

$\alpha(y,t)$ is the lateral deflection due to bending and shearing strains.

$m(y)$ is the mass per unit length.

$\mu(y)$ is the mass moment of inertia per unit length.

$EI(y)$ is the bending stiffness.

$GK(y)$ is the shearing stiffness.

$F_z(y,t)$ is the intensity of the applied transverse load.

The first term represents the contribution due to the rotary inertia of the beam element, the second is due to bending, the third is the inertia load, the fourth is obtained from the shear contribution and since shear is coupled with both rotary inertia and bending, the terms are somewhat complex. The variable describing motion is displacement due to bending which appeared to be the most convenient one to use.

Values of the parameters used to describe the ratios at reference locations were as follows:

$$I(y) = I_n I_N\left(\frac{y}{\ell}\right) \qquad K(y) = K_n K_N\left(\frac{y}{\ell}\right)$$

$$m(y) = m_n m_N\left(\frac{y}{\ell}\right) \qquad \alpha(y) = \alpha_n \varphi_N\left(\frac{y}{\ell}\right)$$

when these values are substituted into the equation and the coefficients are made non-dimensionalized the equation becomes:

$$\left(\frac{\mu_n}{m_n \ell^2}\right)\left\{\mu_N\left(\frac{y}{\ell}\right)\varphi'\left(\frac{y}{\ell}\right)\right\}' - \left(\frac{EI_n}{m_n \omega^2 \ell^4}\right)\left\{I_N\left(\frac{y}{\ell}\right)\varphi''\left(\frac{y}{\ell}\right)\right\}'' - m_N\left(\frac{y}{\ell}\right)\varphi\left(\frac{y}{\ell}\right)$$

$$-\left(\frac{m_n \omega^2 \ell^4}{EI_n}\right)\left(\frac{\mu_n}{m_n \ell^2}\right)\left(\frac{EI_n}{GK_n \ell^2}\right) m_N\left(\frac{y}{\ell}\right)\int \frac{\mu_N(y/\ell)\varphi'(y/\ell)}{K_N(y/\ell)}\, d(y/\ell)$$

$$+\left(\frac{EI_n}{GK_n \ell^2}\right) m_N\left(\frac{y}{\ell}\right)\int \frac{\{I_N(y/\ell)\varphi''(y/\ell)\}'}{K_N(y/\ell)}\, d\left(\frac{y}{\ell}\right) = \frac{F_{zn}}{m_n \omega^2 \alpha_n} F_N\left(\frac{y}{\ell}\right)$$

Utilizing these relationships, then, a model which is convenient in size and frequency can be set up. For example, if it is desired to construct a model of a cylindrical cross section launch vehicle with 1/20 the length of the original, 10 times the frequency, and made of the same material but with a skin thickness of 1/5 of the original (instead of 1/20, which would furnish constructural difficulties), the following relations between full scale and model would apply:

$$T_m = \frac{T}{10} \qquad L_m = \frac{L}{20} \qquad E_m = E \qquad G_m = G \qquad t_m = \frac{t}{5} \qquad I_m = \frac{I}{4\times10^4}$$

$$m_m = \frac{m}{25} \qquad \mu_m = \frac{\mu}{500} \qquad K_m = \frac{K}{100} \qquad \frac{F_{zm}}{\alpha_m} = \frac{1}{4}\frac{F_z}{\alpha}$$

This model would have the same frequency ratio and modes as the full scale unit. The ratio of displacement to force would be four times as high on the prototype as on the model so that with the force scaled properly, and with damping at resonance adequately scaled, as discussed previously, the full scale stresses would be reproduced.

The reader is referred to reference (13) for an extensive discussion of launch vehicle models and their application in the Saturn program.

D-2. - Panels Reinforced By Orthogonal Stiffness

A large class of sonically induced vibration problems occur on orthogonally stiffened skin sections of aircraft and missiles. As a simple representative of such a structure consider a flat anisotropic plate of dimensions "a" long and "b" wide subjected to pure bending as shown on page 84 of reference (10). The equation of motion would be:

$$Dx \frac{\partial^4 w}{\partial x^4} + 2(D_1 + 2.Dxy)\frac{\partial^4 w}{\partial x^2 \partial y^2} + Dy \frac{\partial^4 w}{\partial y^4} = q + m\ddot{w}$$

The flexural rigidities, D, could be represented by combined plate and beam-theory. Here the "m" is the average mass per unit surface area. This relation applies to stiffener elements which are relatively closely spaced compared to the overall dimensions of the plate.

Values of the parameters used to describe the ratios at reference locations were the flexural rigidities and the applied load, q, and inertia load, $\ddot{mw}$. In order to make the equations dimensionless all terms were multiplied by the plate area squared, after non-dimensionalizing the deflection w. With these substitutions, the non-dimensionalized equation can be expressed as:

$$\frac{(ab)^2}{b^4}\frac{\partial^4\left(\frac{w}{b}\right)}{\partial x^4} + 2\left(\frac{D_{1N}}{Dx_N} + 2.\frac{Dxy_N}{Dx_N}\right)\left(\frac{D_{1N}}{Dx_N} + 2\frac{Dxy_N}{Dx_N}\right)\frac{(ab)^2}{b^4}\frac{\partial^4\left(\frac{w}{b}\right)}{\partial x^2 \partial y^2} +$$

$$\frac{Dy_N}{Dx_N}\frac{(ab)^2}{b^4}\frac{Dy_N}{Dx_N}\frac{\partial^4\left(\frac{w}{b}\right)}{\partial y^4} = \frac{(ab)^2}{Dx_N}q_N\frac{q_N}{Dx_N} + m_N\omega^2\frac{(ab)^2}{Dx_N}\frac{m_N\left(\frac{w}{b}\right)}{Dx_N}$$

Here the ratios of flexural rigidities in the two directions and the cross and twisting rigidity ratios would have to be maintained. Flexural rigidity estimates using combined plate and beam-theory as described in reference (11) are:

$$Dx = E_{LS}\left(I_{LY} + \frac{I_{SX}}{1-\nu^2}\right)$$

$$D_1 = \nu\, Dx$$

$$Dy = \frac{1}{L_{RX}}\left[E_F I_{FS} + \frac{E_{LS} I_{SS}}{1-\nu^2}\right]$$

$$Dxy = 2(1-\nu)\, Dx$$

where:

a, b	are plate width and lengths in the coordinate directions.
E_{LS}, E_F	are the Moduli of Elasticity of the skin and frames.
I_{FS}	is the Moment of Inertia of the frames.
I_{LS}	is the Moment of Inertia of the longerons.
I_{SS}	is the Moment of Inertia of the portion of the skin active in bending in the y direction.
I_{SX}	is the Moment of Inertia of the portion of the skin active in bending in the x direction.
q	is the applied pressure load per unit area.
w	is the displacement normal to the plate surface.

Reduction in size for scaling would be done by changing the moments of inertia of the stiffeners and skins by different amounts, where convenient, provided that the proper ratio is maintained. Scaling for frequency can also be different than scaling for size, if desired, provided the mass per unit area is properly adjusted.

SECTION II - MODEL TESTING

The discussion heretofore has been concerned with some general aspects of modeling to determine the response of structures to sonic excitation. A specific application of the technique will now be described.

In the early planning stages for a new aircraft at Grumman, the E-2A, predictions of the vibratory response at the fuselage area near the propeller plane were required. A view of the aircraft is shown on Figure 6. The fuselage was to be irregularly shaped and stiffened by 6 major longerons and some intercostals. Other aircraft already constructed using the same propeller and engines had required some redesign to avoid skin fatigue cracks in the propeller plane area. Since carrier stowage requirements restricted the propeller tip clearance to 14 1/4 inches, noise levels at 141 db at a discrete frequency were predicted. It was decided, therefore, to conduct a combined analytical and model testing program with the following objectives:

A. Avoid fuselage resonances near propeller blade passage frequency.

B. Determine the effect of possible design changes on the natural frequencies, and on the response at resonance. This was particularly important in this case because the propeller rotated at a constant speed.

C. Compare results from available analysis of orthogonally stiffened regular fuselage shell with model tests, and adjust parameters so that the effect of changes in some variable could be studied analytically.

D. Predict the variation in vibratory response over a frequency range near propeller blade passage to investigate the possibilities of vibration reduction by designing the fuselage for a specific frequency, and of applying some phasing control to the applied force.

E. Utilize the model to evaluate vibration and acoustical control measures such as damping and acoustical insulation.

Scaling considerations were reviewed. In view of the requirement for predicting response it was decided that joints with fasteners would have to be carefully controlled, thus limiting the

size and manufacturing procedures. The full scale skin was .040", and full scale radius 40". The model was to be made from hand formed elements and interior and boundary bulkheads were to be representative. The model length was determined by locations of a stiff cabin bulkhead forward and a partial bulkhead tying into the forward wing beam aft. After reviewing alternate costs for design, manufacture, and assembly of various scale models, it was decided that a 1/2 scale representation would be used. This had the advantage of allowing work to proceed from regular drawings marked up to show short cuts desired.

The model shown in Figure 7 was tested first as an empty cylinder with and without the rear end restraint. These tests were conducted to allow comparison with an available analytical program (reference 11) for calculating modes and frequencies of a uniform orthogonally stiffened cylinder. Mode shapes and frequencies were measured, as well as the frequency response to a constant acoustical pressure level. The shell was then modified by the installation of partial bulkheads intended for use as equipment supports, at actual locations. The effects of variation in radial restraint at the rear end of the test section was determined by testing in turn with three different possible partial bulkhead configurations installed. When these tests were complete, a series of weights totaling 128 lbs was installed on rubber to simulate the resiliently mounted equipment planned for the aircraft. The original weight of the fuselage section was 42 1/2 lbs so that this represented a three fold increase in total weight. Testing was repeated once again. Finally the cylinder was tested with tie rods across the center to simulate the effect of a severe radial restriction on the center of the shell.

Results of the mode shape tests for the basic shell with and without bulkheads are shown on Figure 8. It is apparent that the forward bulkhead is relatively rigid while the rear is free. The effect of restraining the end by a bulkhead is shown by the threefold increase in frequency for almost the same circumferential mode shape. One interesting phenomena is the tendency for the symmetric and antisymmetric modes to alternate as the frequency is increased, as summarized:

Summary of Mode Shapes for
Basic Shell with Rigid End Bulkhead

Frequency f, cps	Number of Axial Half Waves m	Number of Circumferential Waves n	Description
142	1	2	symmetric
156	1	3	antisymmetric
172	1	3	symmetric
248	1	4	antisymmetric
261	1	4	symmetric
306	2	4	antisymmetric
332	2	4	symmetric

It was not possible to excite an antisymmetric mode for n=2. Using one or two shakers in or out of phase, or one or two acoustical sources did not significantly change the mode shapes obtained.

Partial bulkheads were installed, as shown on Figure 9, and simulated end bulkheads were added as radial restraints at the rear end of the cylinder. A tabulated summary of the change in peak response frequencies and amplitudes is shown on Table III. The excitation was controlled by monitoring the acoustical levels near the two sources. The addition of the intermediate bulkheads significantly increased the frequencies of peak response for the lowest three modes by 22%, 48% and 17%, respectively. The reduction on frequency due to the use of a light partial end bulkhead was also obtained from these test results. Masses simulating the equipment to be used in the interior were mounted in the shell on foam rubber simulating a low frequency (15 cps) mounting system, and the effect was evaluated. Variation of response to acoustic excitation with frequency is shown on Figure 10. The peak levels decreased because of the added damping but the frequencies were not reduced a large amount because the resilient mounting of the equipment isolated much of the mass at the fuselage resonance. Damping values for the fuselage, as estimated from the frequency response curves, varied from .02 to .05, the latter after the masses were installed in the system. The modes in which this damping occurred were below cutoff frequency and therefore not attributable to radiation damping. Subsequent measurements of damping on a full scale airplane were all less than .01. Higher damping values in the model seem reasonable because the tests had

to be conducted before the model had been completed, so some rivets were not in place, possibly causing higher energy dissipation in the joints.

One of the objectives of the model test program was to establish a basis for analytical comparisons. The analyses available treated a uniform cylindrical shell and the absolute values of the frequencies computed for the model were much higher than the measured values. However, the relative shifts in frequencies for corresponding modes were considered sufficiently valid to study some of the structural variables. The results were nondimensionalized so that they could then be applied to the model. Results of analytically increasing the skin thickness, increasing the cylinder length, and changing the stiffness of the frames using the analysis in reference (11) are all shown in Figure 11. It may be noted that changing the frame stiffness had a relatively moderate effect on the frequency, since an increase by a factor of 4 resulted in a 20% increase in frequency. Doubling the skin thickness actually decreased the natural frequency by a small amount, an interesting and unexpected result.

In order to determine the difference between a uniform shell and the actual model the kinetic energy in the shell for the low frequency mode was calculated using the experimentally determined mode shapes and the actual mass distribution. The value obtained was within 5% of energy calculated by assuming regular sinusoidal circumferential mode shapes on an equivalent shell with the mass uniformly distributed. Since the frequency calculated for the uniform cylinder was 40% higher than the measured model, it was assumed that the potential energy had been considerably overestimated in the analysis.

The response of the model to frequencies near propeller blade passage was of primary interest. Response as a function of frequency is shown on Figure 10. It should be noted that large variations are possible for small frequency shifts near blade passage frequency because the damping is light and the shell resonances are well separated. The blade passage frequency and its harmonics are shown by arrows at the bottom of the figure. These experimental results, principally the effect of radial straps shown on Table III, prompted a design change to include a stiffer ring frame at the center of this fuselage section near the propeller.

A comparison of model and full scale mode shapes at the fundamental frequency is shown on Figure 12. There are two full scale patterns shown for two different aircraft. Aircraft #2 was loaded with ballast plates on the floor in place of a large quantity of

electronic equipment so that the mass distribution differed considerably from the model. The #3 aircraft mode shape was more regular and did not differ materially from the model. The longitudinal mode shape on aircraft #2 shows that the rear partial bulkhead end condition was not as stiff as the model, and this is believed responsible for part of the difference in frequency between model and full scale. The frequency in #3 aircraft was not that of the peak response which probably occurred at a lower value. This 75 cps frequency was chosen to determine the deformation pattern anticipated near blade passage frequency of 75 cps.

Peak vibration levels at blade passage frequency were estimated from the model measurement. The measured response was corrected for the difference in sound pressure level between the model and anticipated full scale pressures, and also for the estimated difference in generalized force between the acoustical sources used in the test and an actual propeller. The estimated peak value of vibration was .001 inches DA. The actual measured value was .005 inches DA. However, the aircraft configuration differed in several important aspects from the model, that is the restraint at the rear of the cylinder was lower in the aircraft, a stiffened ring was added to the fuselage near the propeller, and the full scale damping was considerably lower. A comparison between model and full scale amplitudes, therefore, cannot be considered valid.

Another investigation employing a smaller 1/4 scale model in a sonic field was reported by Roberts, Eldred, and White recently in reference (12). The results of this test also showed good agreement in some respects with full scale, and poor in others.

CONCLUSIONS

A model noise source, such as produced by jet or rocket engine exhausts, will scale the near field noise to a reasonable degree of accuracy provided the flow parameters are nearly identical to the full scale source. The degree of control of the dimensions and flow parameters becomes more important as the model scale factor becomes smaller.

Three types of structural damping mechanisms are considered, namely: joint damping, radiation damping and material hysteresis under stress. Only joint damping contributes significantly to the overall damping mechanism throughout the entire frequency range. Although joint damping simulation might be accomplished by scaling joint areas, number and spacing of rivets, and rivet diameter and length, providing damping forces can be duplicated, practical difficulties occur which tend to minimize simulation effectiveness.

Demonstration (with a high degree of confidence) of fatigue life in small scale structural models appears difficult because of the scattered nature of the full scale test data.

Several pertinent observations from the model tests on the half scale fuselage section are as follows:

1. Simplified shell analysis overestimated the potential energy and resulted in high calculated resonant frequencies.

2. Adding sufficient radial stiffness to the cylindrical fuselage to provide simple support end conditions was the most effective step in increasing the resonant frequencies.

3. The model provided data by which the effects of structural modifications on the resonant frequencies, such as partial bulkheads, varying end restraints, and added masses could be effectively evaluated.

REFERENCES

1. Morgan, W. V.; Sutherland, L. C. and Young, K. J.: The Use of Acoustic Scale Models for Investigating Near Field Noise of Jet and Rocket Engines , WADD TR 61-178, 1961.

2. Howes, W. L.: Similarity of Near Noise Fields of Subsonic Jet , NASA TR R-94, 1961.

3. Gray, C. L.: Study in Use of Structural Models for Sonic Fatigue , ASD TR 61-547, 1962.

4. Heckl, M. A.; Lyon, R. H.; Maidanik, G. and Ungar, E.: New Approaches to Flight Vehicle Structural Vibration Analyses and Control , ASD TDR 62-237, 1962.

5. Maidanik, G.: "Response of Ribbed Panels to Reverberant Acoustic Fields", Journal Acoust. Soc. Am., June, 1962.

6. Crandall, S. H.: On Scaling Laws for Material Damping , NASA TN D-1467, 1962.

7. Weibull, W.: "Size Effects on Fatigue Crack Interaction and Propagation in Aluminum Sheet Specimens Subjected to Stress of Nearly Constant Amplitude", FFA Report 86 (Sweden), 1960.

8. Peterson, R. E.: Effect of Stress Concentration on Fatigue of Aircraft Materials , WADC TR 59-507, 1959.

9. Bisplinghoff, R. L.; Ashley, H. and Halfman, R. L.: Aeroelasticity , Addison Wesley, 1955.

10. Timoshenko, S.: Theory of Plates and Shells , McGraw-Hill, 1940.

11. Nelson, H. C.; Zapotowski, B. and Bernstein, M.: "Vibration Analysis of Orthogonally Stiffened Circular Fuselage and Comparison with Experiment", Proceedings of IAS Specialist Meeting in Dynamics and Elasticity, Ft. Worth, Texas, 1958.

12. Roberts, W. H.; Eldred, K. M. and White, R. W.: "Utilization of Dynamically Similar Structural Models in Predicting Vibration Responses of Flight Vehicles", Shock, Vibration and Associated Environment, Part III, April, 1963.

13. Rynyon, H. L.; Morgan, H. G. and Mixson, J. S.: "Role of Dynamic Models in Launch Vehicle Development", ASME Colloquium on Experimental Techniques in Shock and Vibration, Nov., 1962, N. Y.. N. Y..

TABLE I

ACOUSTIC MODEL SCALING LAWS
FOR
JET AND ROCKET ENGINE NOISE

Parameter	Scale Factor
Dimensions	n
Acoustic power	n^2
Frequency	$1/n$
Time	$1/n$
Sound pressure level	same as full scale - at scaled location and scaled frequency
Spatial correlation	same as full scale - at scaled location and scaled frequency
Directivity	same as full scale
Jet exit velocity	same as full scale
Jet total temperature	same as full scale
Effux density	same as full scale
Mach Number	same as full scale
Thrust	n^2
Total mass	n^3

where: $n = \frac{\text{Model}}{\text{Full Scale}}$

TABLE II

RADIATION DAMPING VALUES

A. Simply Supported Square Plates

	Applicable Formula	Calculated Values for Panels		
		48"x48" x.04"	12"x12" x.01"	4"x4" x.01"
Fundamental Resonance, cps	$\frac{19.2 \times 10^4 h}{a^2}$	3	13	120
Low Frequency Limit for Effective Radiation, cps	$\frac{C_a}{\pi a}$ (1)	90	360	1,070
Radiation Damping Ratio Near Lower Limiting Frequency (Both Sides)	$14.8 \times 10^6 \frac{\rho_a}{\rho} \frac{1}{C_a} \frac{P}{A} \left(\frac{h}{f}\right)^{\frac{1}{2}}$ (2)	.00086	.00086	.00148
Coincidence Frequency, cps	$\frac{C_a^2}{R C_L}$ (1)	12,100	51,000	51,000
Radiation Damping Ratio Above Coincidence Frequency (Both Sides)	$\frac{2 A \rho_a C_a}{2 m \omega_n}$ (1)	.0076	.0076	.0076

TABLE II (continued)

B. Simply Supported Beams

	Applicable Formula	Calculated Values for Beams	
		Simply Supported $I = .04\ in^4$, $A = .15\ in^2$	Simply Supported $I = .04\ in^4$, $A = .15\ in^2$ With .040" Sheet Attached as a Radiation Surface
Fundamental Resonance	$31.73 \times 10^4 \frac{R}{L^2}$	$\frac{16.4 \times 10^4}{L^2}$	----
Beam Coincidence Frequency	$\frac{C_a^2}{R C_L}$ (1)	285 cps	285 cps
Radiation Damping Ratio Above Beam Coincidence Frequency	$\frac{\omega w^2 L \rho_a}{\rho A L \omega}$ (1)	.00074	----
	$\frac{4 L \rho_a h c_L}{\rho A L \omega \sqrt{12}}$ (1)	----	.0095

NOTE: The reader is cautioned to consult reference (4) for the assumptions and limitations in the formulas shown.

TABLE II (continued)

Symbols:

A	is the cross sectional area of the beam, in^2
a	is the plate side, in.
c_a	is the speed of sound in air, in. $sec.^{-1}$
c_l	is the speed of longitudinal waves in metal, $in.\text{-}sec.^{-1}$
h	is the plate thickness, in.
L	is the beam length, in.
m_l	is the generalized mass, $lbs.\text{-}in.^{-1}\text{-}sec.^2$
P	is the Panel Periphery, in.
R	is the beam radius of gyration, in.
w	is the width of the beam radiating surface, in.
ρ_a	is the density of air, $lbs.\text{-}in.^{-4}\text{-}sec.^2$
ρ	is the density of aluminum, $lbs.\text{-}in.^{-4}\text{-}sec.^2$

TABLE III

MEASURED EFFECT OF INCREASING RADIAL RESTRAINT OF MODEL

CONFIGURATION	1st MODE			2nd MODE			3rd MODE			4th MODE		
	Freq cps	Relative Response at Top	Long 2	Freq cps	Relative Response at Top	Long 2	Freq cps	Relative Response at Top	Long 2	Freq cps	Relative Response at Top	Long 2
1. Basic Shell, no internal bulkheads.	48		.230	129		.220	220		.225	280		.300
2. Basic Shell, rigid bulkheads.	140		.255	156		.170	245		.270	305		.205
3. Partial Interior Bulkhead and Light End Bulkhead.	157	.158	.430	211		.117	250	.225	.120	303	.190	.208
4. Partial Interior Bulkhead and Rigid End Bulkheads.	170	1.000	.555	230	.200	.108	286	.140	.160	303	.270	.265
5. Complete Model including Equipment with Light End Bulkhead.	151	.148	.076	246	.175	.098	309	.196	.180	322	.120	.210
6. Complete Model including Equipment with Stiffer End Bulkhead.	164	.280	.172	239	.185	.110	302	.230	.290	317	.250	

TABLE III (continued)

CONFIGURATION	1st MODE			2nd MODE			3rd MODE			4th MODE		
	Freq cps	Relative Response at Top	Long 2	Freq cps	Relative Response at Top	Long 2	Freq cps	Relative Response at Top	Long 2	Freq cps	Relative Response at Top	Long 2
7. Complete Model including Equipment with Simulated Stiff End Bulkhead.	165	.410	.180	244	.208	.110	307	.225	.190	321	.208	.220
8. Partial Interior Bulkhead and Simulated Stiff End Bulkhead with Middle Section Restrained Radially by Straps.	194	.144	.077	231	.240	.115	359	.111	.096			

Figure 1

Normalized Acoustic Spectra

for

Full and 1/8 Scale J-57 Turbojet Engine

(Full scale plenum conditions were duplicated by the model)

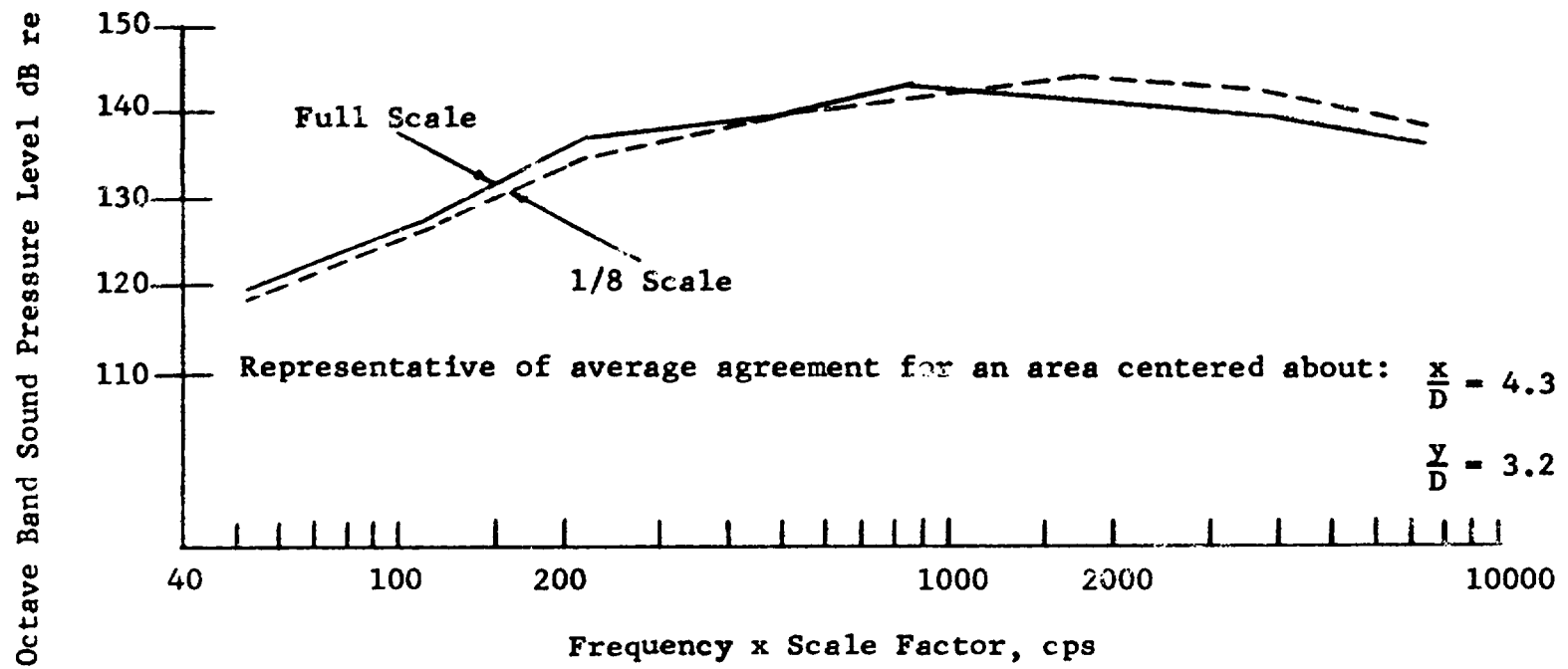

From Reference (1)

Figure 2

Normalized Acoustic Power Spectra

for

Full Scale and Model Jets

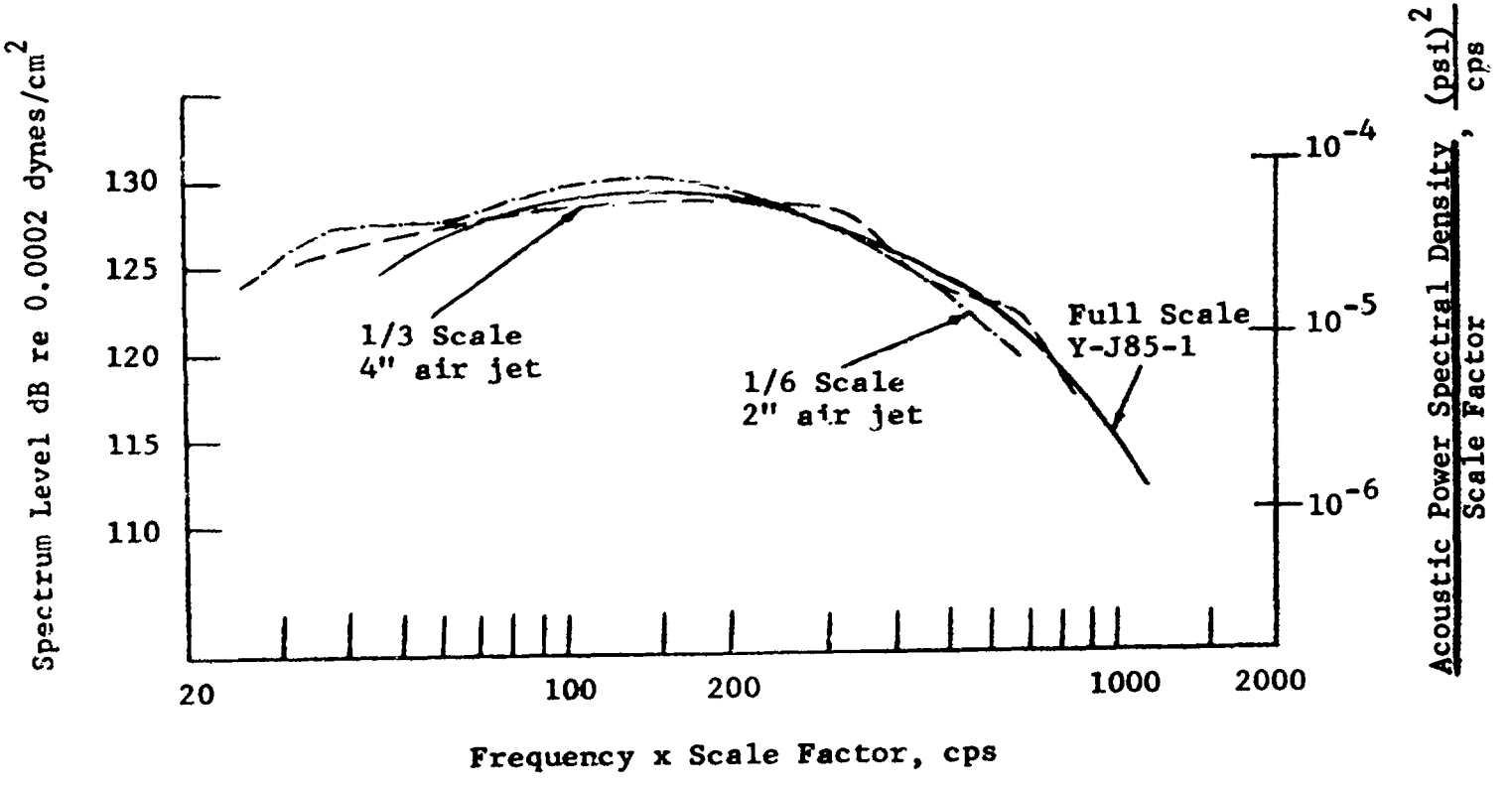

From Reference (3)

Figure 3

Normalized Acoustic Spectra

for

Full and 1/36 Scale Jupiter Liquid Rockets

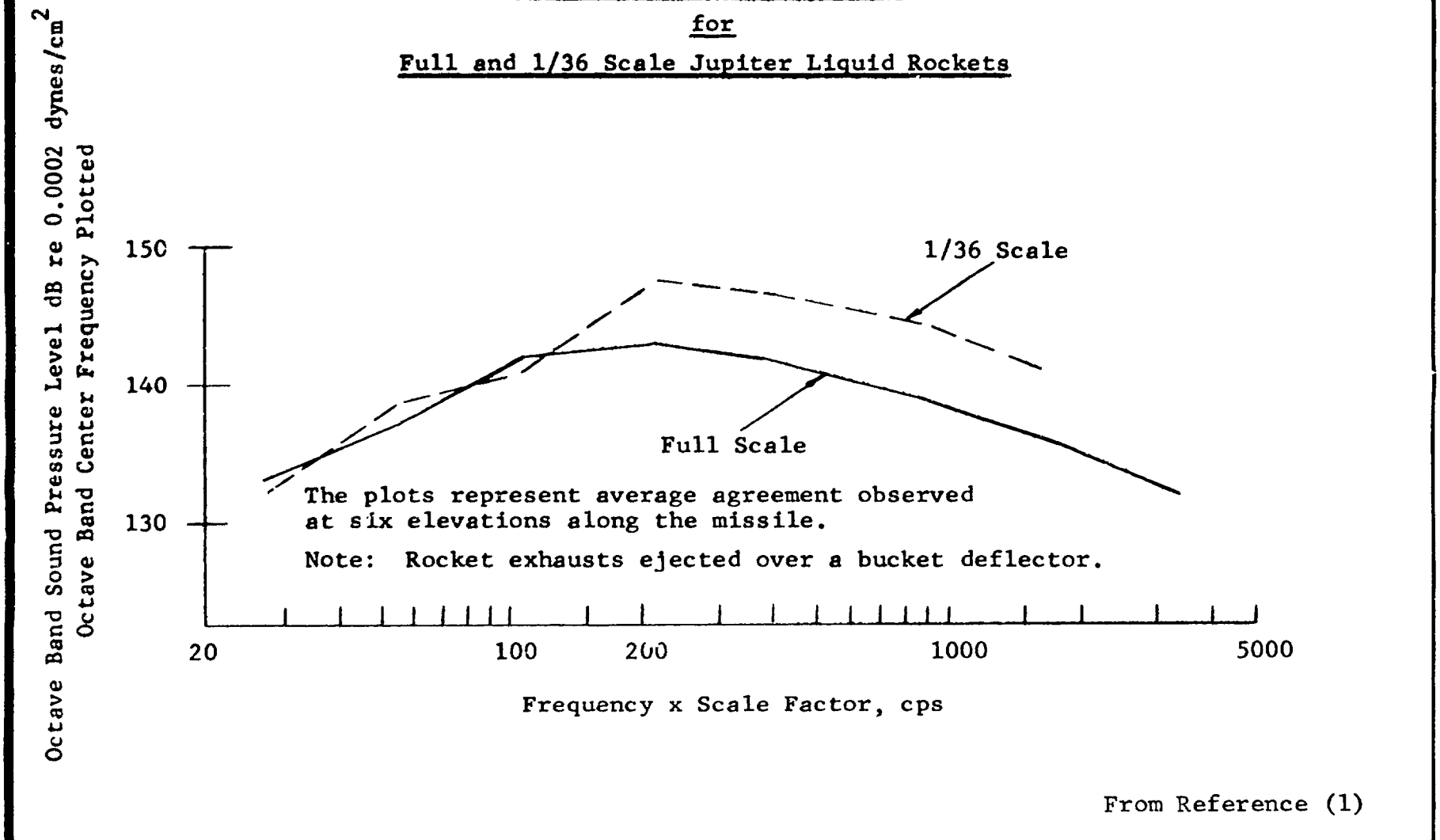

From Reference (1)

Figure 4

Sound Pressure Level vs Elevation

for

Full and 1/36 Scale Jupiter Liquid Rockets

(Dimensions and Spectra Normalized)

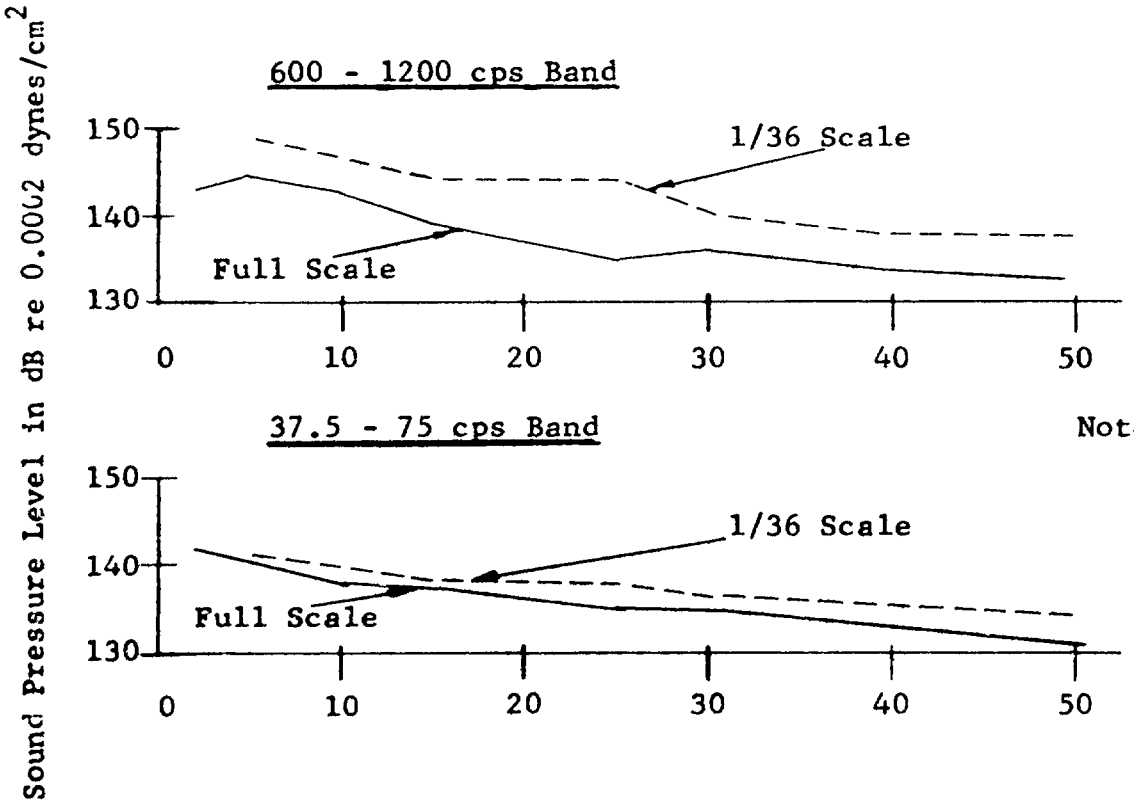

Note: Rocket exhausts ejected over a bucket deflector.

From Reference (1)

Figure 5

Time History of Prop Induced Sonic Pressure Distribution Over Fuselage Circumference

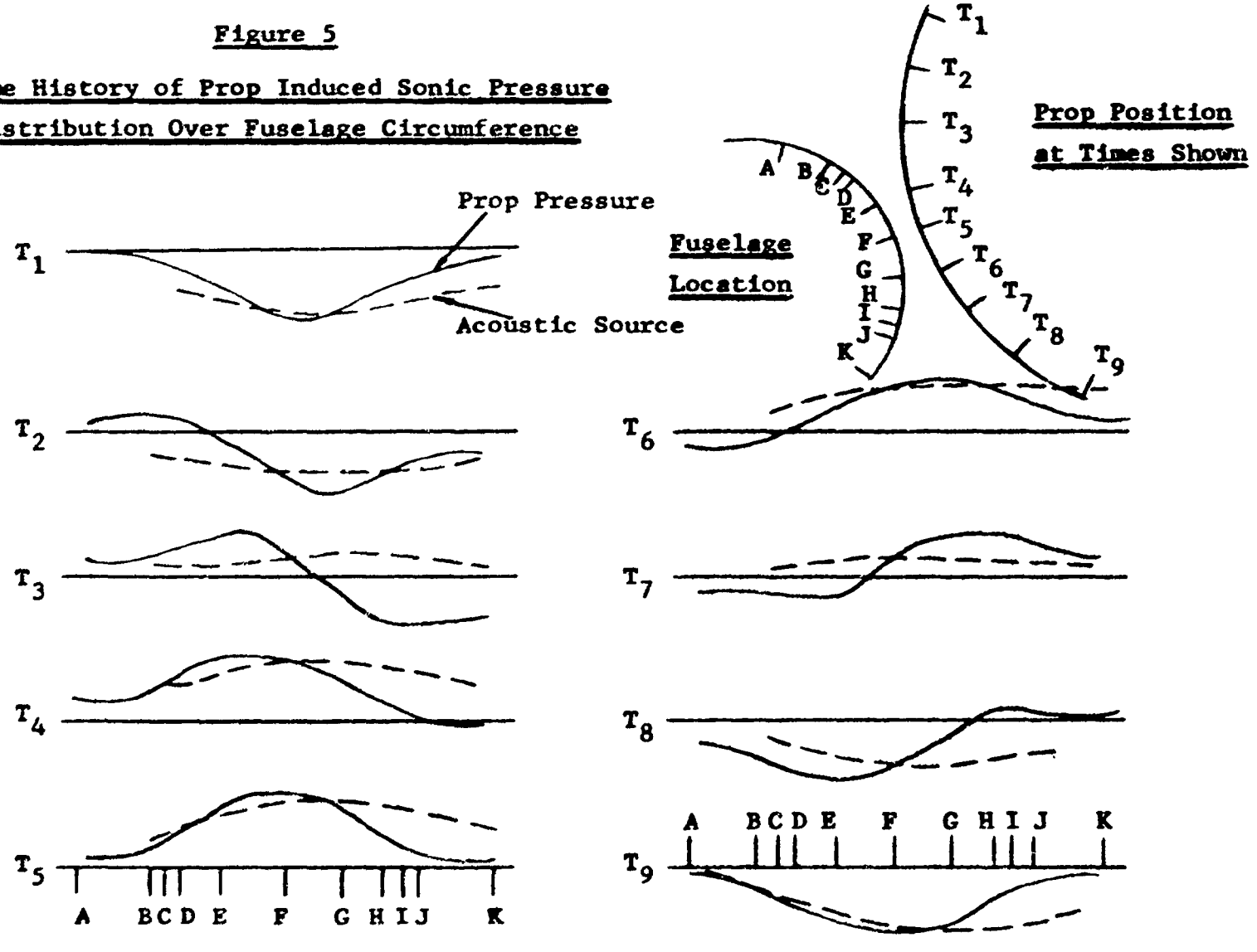

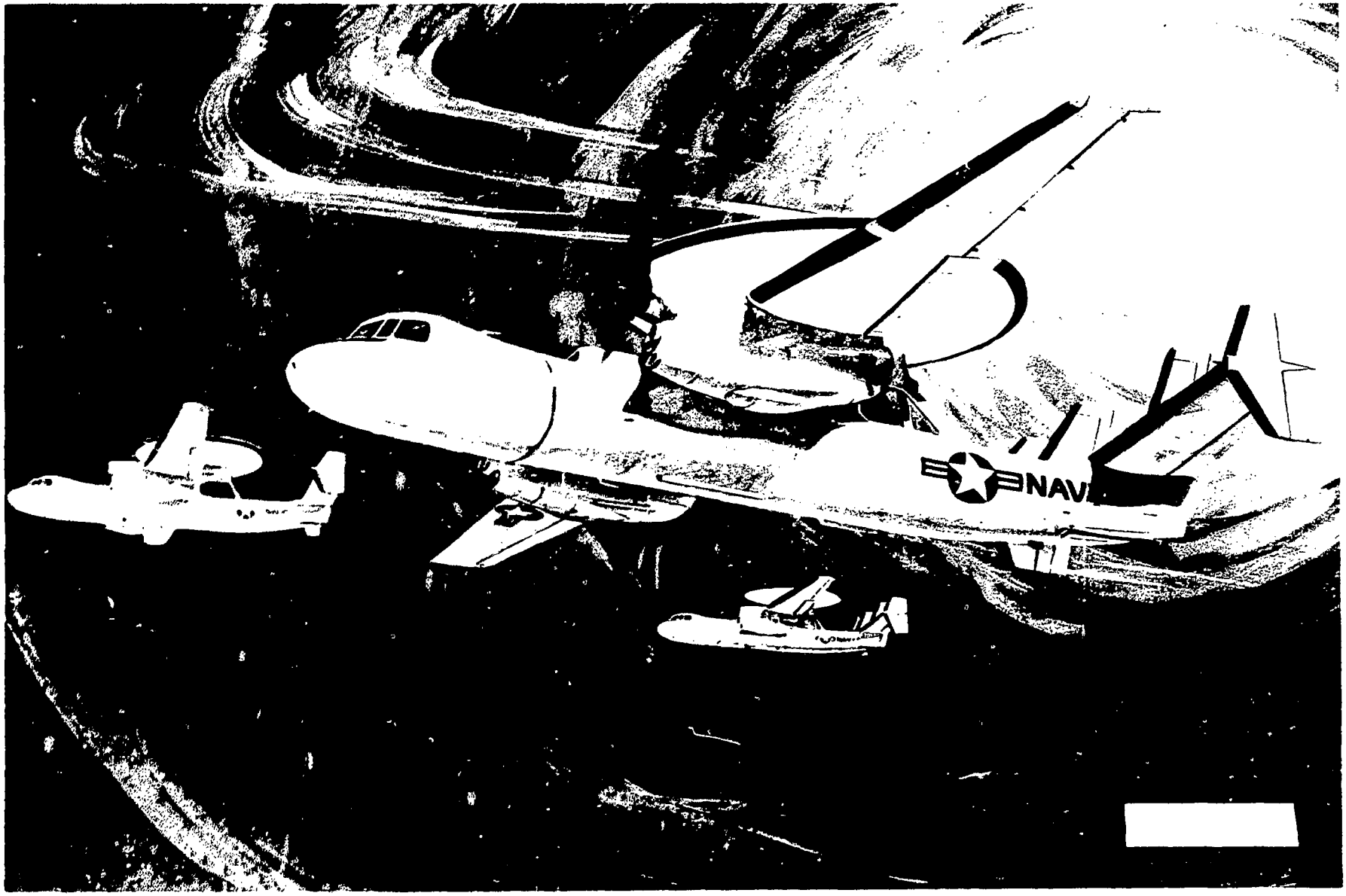

Figure 6. E-2A Aircraft

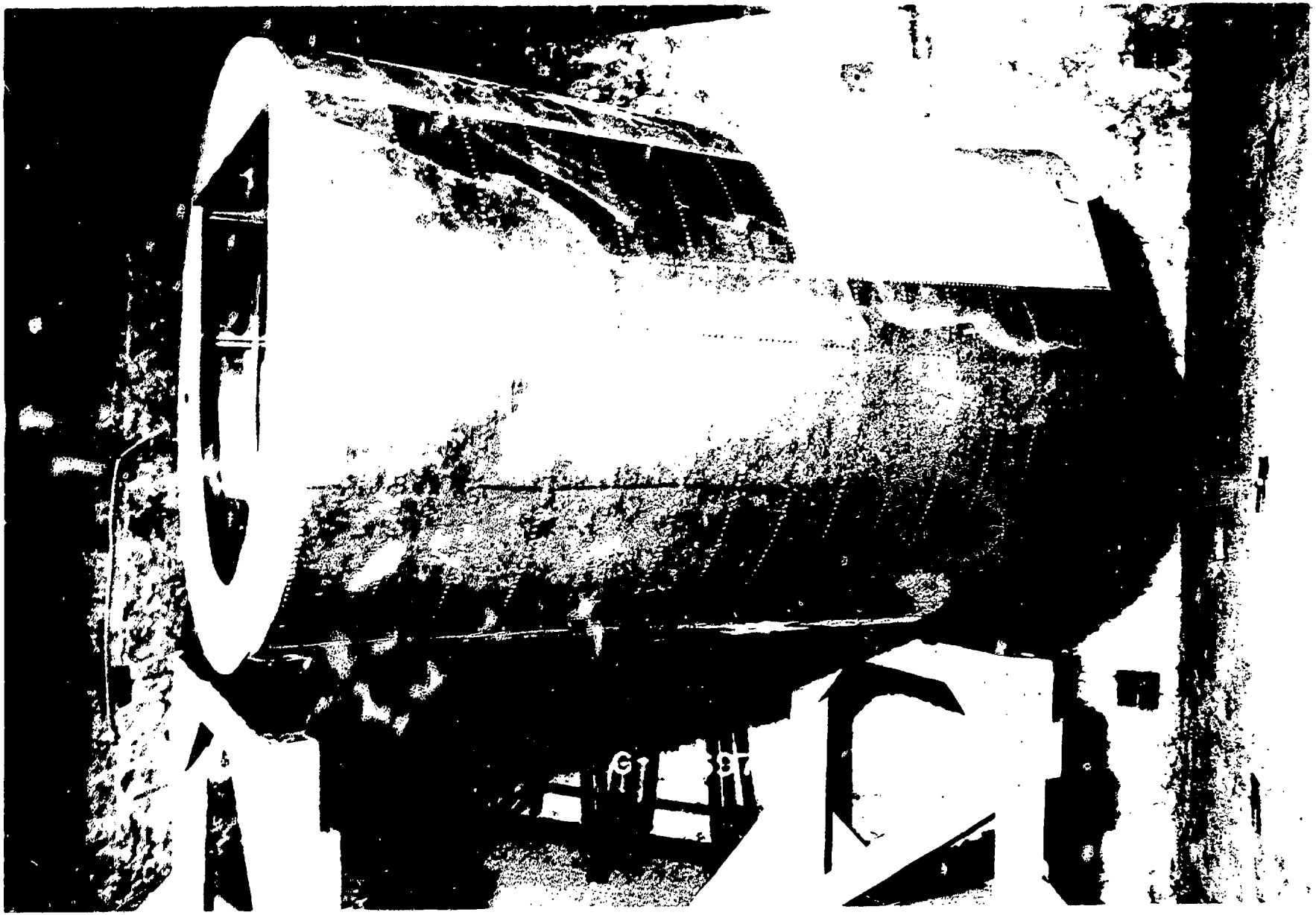

Figure 7. Half-Scale Model of E-2A Center Fuselage Area

Figure 8

Mode Shapes During Model Tests Showing Effect of Bulkheads on Response

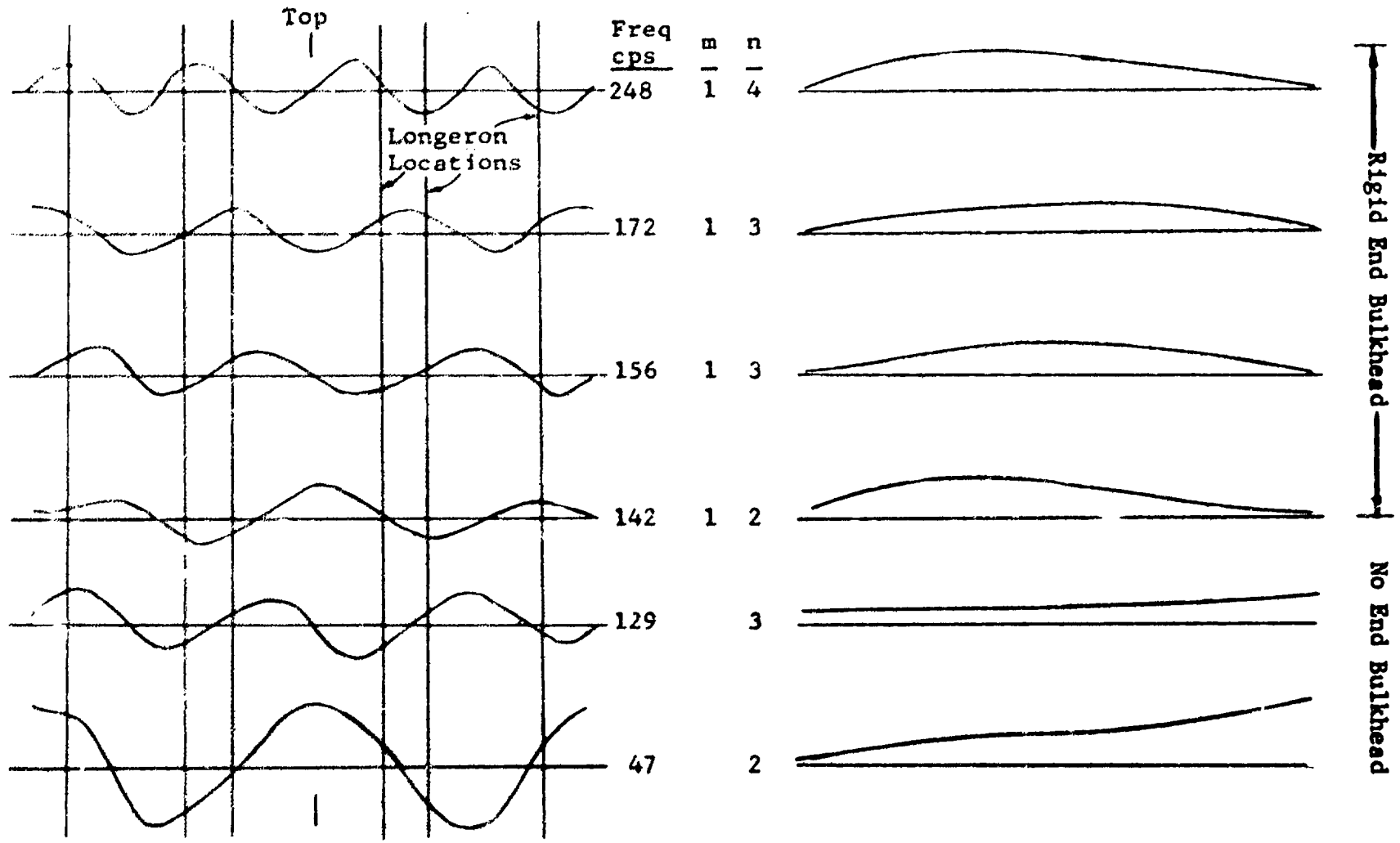

Figure 9. Inside View of the E-2A Half-Scale Model

Figure 10

Effect of Adding Simulated Equipment to Model Response to Acoustical Pressure

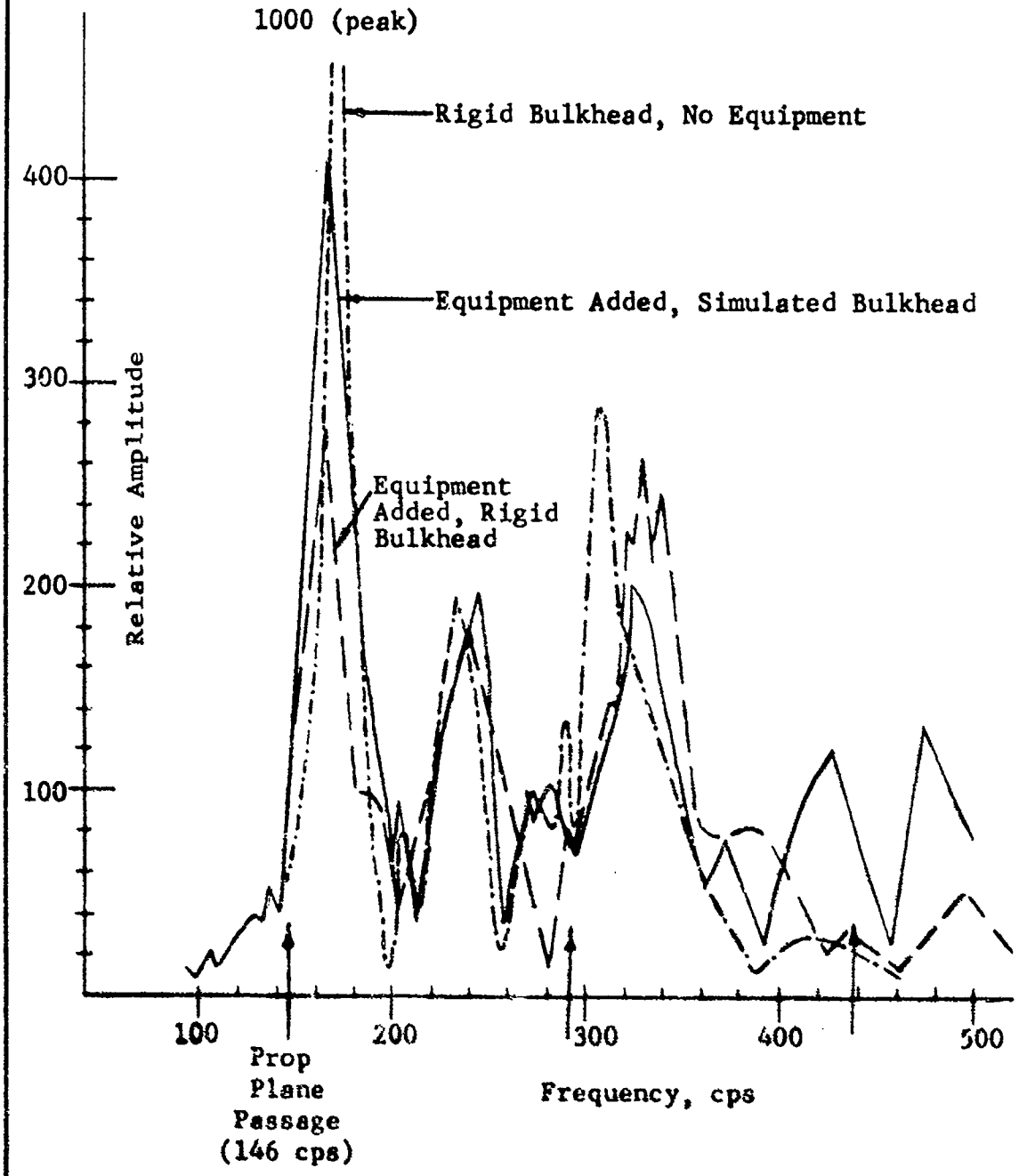

Figure 11

Analytical Results

Showing

Effect of Structural Changes on Fundamental Frequency

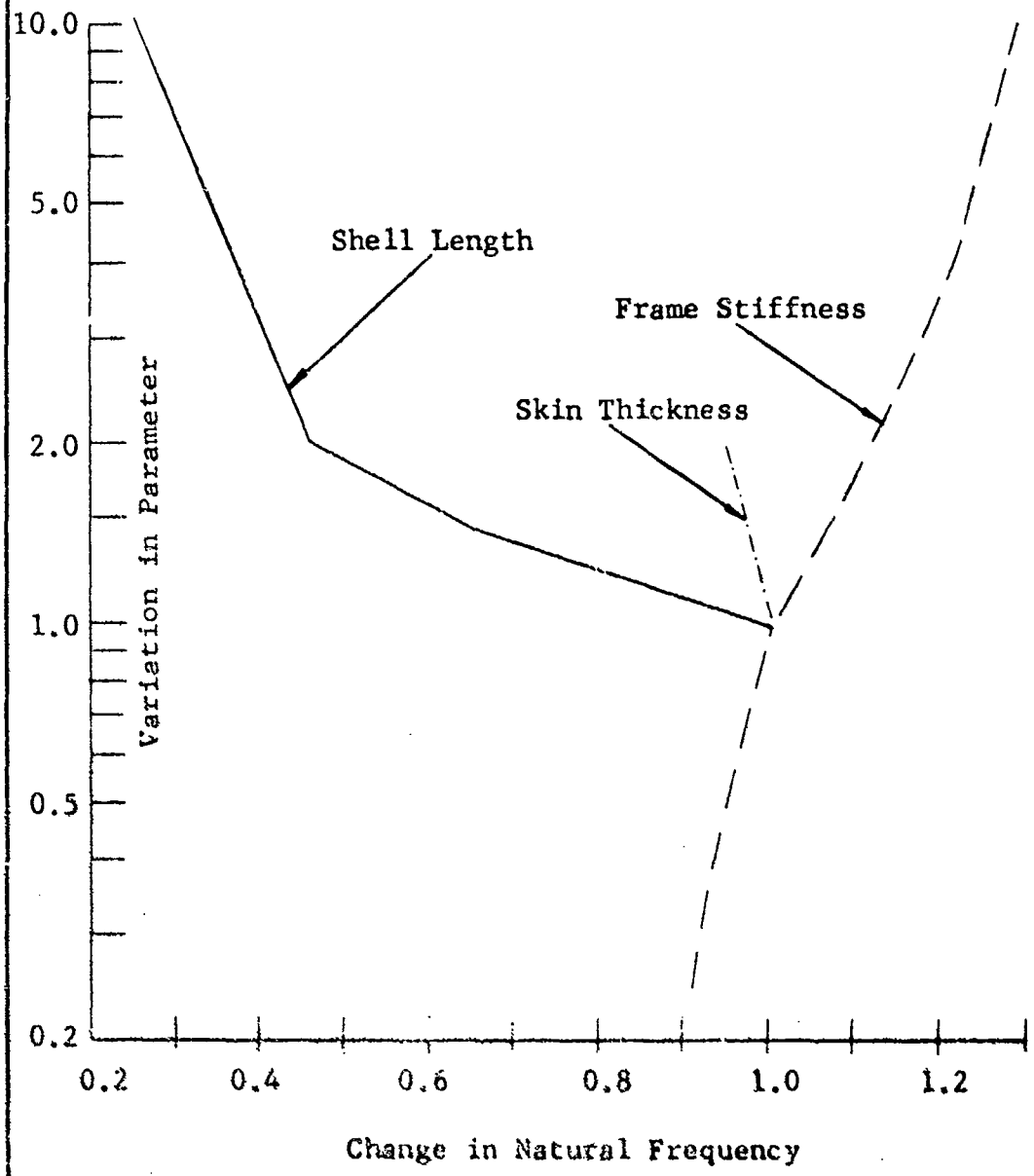

Figure 12

Comparison of Fundamental Modes

Full Scale and Model

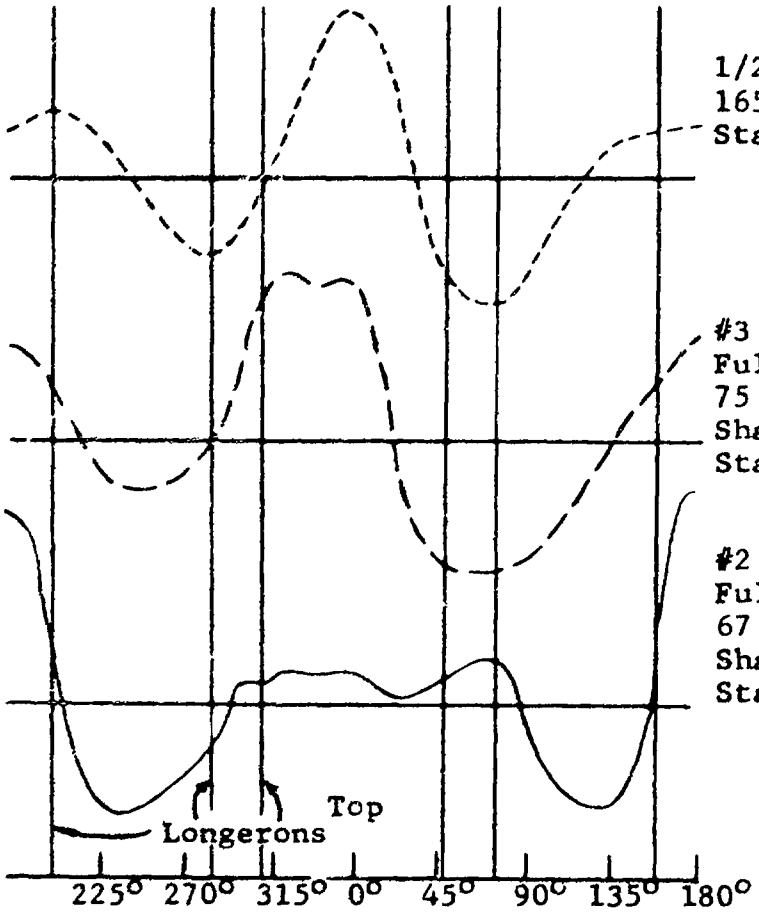

VIBRATION TESTING DURING HIGH HEAT RATES

K. L. McIntyre

General Dynamics/ Pomona
A Division of General Dynamics Corporation
Pomona

ABSTRACT

Test facilities, techniques, and results are presented for vibration model tests of a thin, very low aspect ratio wing subjected to transient heating. The two independent closed control loops are described that are used to track and excite the modes, and to obtain the desired temperature time history. Time history data are presented for frequency and shape of five wing vibration modes subjected to heat rates as high as 300°F/second, maximum temperatures of 650°F, and geometric temperature gradients as high as 110°F/inch. Some comparisons of theoretical to test results are made.

LIST OF ILLUSTRATIONS

VIBRATION TESTING DURING HIGH HEAT RATES

K. L. McIntyre

General Dynamics/Pomona
A Division of General Dynamics Corporation
Pomona

INTRODUCTION

The high velocities and accelerations characteristic of todays interceptor missiles result in a severe, rapidly varying thermal environment for their lifting surfaces. This thermal environment and the accompanying high dynamic pressures require evaluation of the aerothermoelastic stability of the interceptor lifting surfaces. Accomplishing this evaluation by wind tunnel testing is often very expensive or it may be impractical due to deleterious compromises required by scaling and tunnel capabilities. One approach to this problem which has proved to be successful has been to utilize vibration modes from a transiently heated structural model in a conventional supersonic flutter analysis. This paper presents some of the test techniques used for this approach and results obtained during a recent transiently heated vibration test of the very low aspect ratio solid plate wing of an experimental missile. This work was sponsored by the Army.

STRUCTURAL MODEL

The structural model that was tested consisted of a full scale thin extruded aluminum wing attached to a thin walled steel rocket motor case. Both ends of the motor case were closed by solid bulkheads. The wing, Figure 1, had a trapezoidal planform, a single panel aspect ratio of approximately 0.2, and a linear spanwise variation of thickness. The thickness at the tip was one-half of the root thickness.

The first seven room temperature vibration modes of the free-free wing-shell combination had the following frequencies:

Mode No.	Frequencies (cps)
1	282
2	324
3	388
4	490
5	567
6	656
7	784

Figures 2 and 3 show plots of the mode deflections along a chord at 70% of the span. The lowest mode is associated with a shell resonance where the cross section of the shell deforms in an elliptical shape and the wing undergoes a flapping motion. The second mode has a combined pitching-spanwise bending motion. Other than the first two, the modes can be classe as chordwise bending modes of the wing.

TEMPERATURE TEST CONDITIONS

The general type of temperature distribution that was considered is illustrated in Figure 4. The wing tip has a much higher temperature than the root, while the leading edge temperature is only slightly higher than that of the trailing edge. This type of distribution is in direct contrast to much of the test work that previously has been done and is now available in reports. In most cases, such as in References (1), (2) and (3), the temperature varied along the chord and remained almost constant along the span. This latter distribution is characteristic of surfaces whose thicknesses vary in the chordwise, rather than the spanwise, direction.

Three temperature histories were used in the tests. They were typical of temperature conditions that can be achieved on the lifting surfaces of small interceptor missiles. The history with the highest temperature, 650°F at the tip of the wing, results in maximum temperature gradients of approximately 100°F/inch and 300°F/second. Figures 5 and 6 show the three histories for two wing locations, one near the tip of the wing and one near the root. These two locations were used as temperature control points during the tests.

TEST EQUIPMENT AND PROCEDURE

The heat input to the wing and rocket motor case was supplied by an oven of quartz tube lamps. The oven, in a position near the test specimen, can be seen in Figures 7 and 8. During the testing the oven was 1.5 inches from the wing. The oven contained two banks of lamps, and each bank was controlled by a separate channel of a Research Incorporated Temperature Programmer. The programmer closely matched the temperature of the control points with the desired temperature histories. The two thermocouples seen in Figure 8 were used to provide the temperature feedback for the programme

The vibration excitation was supplied by an induction shaker, Figure 7 which provides a force without making physical contact with the test specim This type of excitation avoids exciter mass loading effects. The wing displacement was monitored by small bending beam probes. Some of the probe were instrumented with strain gages at the root, others applied force to a case loaded accelerometer. The probes can be seen extending from their cylindrical heat shields in Figures 7 and 8.

Three methods were used in obtaining the variation of mode frequencies with time. The first can be described as a constant amplitude-constant phase shift feedback system, Figure 9. This system is based on the assumption that if resonance is maintained, the phase angle between the shaker input signal and the wing deflection signal will remain constant.

An oscillator was used initially to establish vibration at resonance. The signal from one of the deflection probes was connected to the feedback circuit and the circuit was adjusted so that the amplitude and phase of the system output signal matched that of the oscillator. This signal was then substituted for the oscillator. For each individual mode, proper settings of gains in the feedback circuit gave a nearly constant phase shift over the frequency range of interest. The feedback system also gave a constant amplitude output for a wide range of input amplitudes.

The second feedback system, Figure 10, was similar to a system outlined in Reference (4). It compared the phase between the wing displacement signal and the shaker current. Any deviation of this phase generated an error signal which was fed to a voltage controlled oscillator. The frequency of the oscillator then changed to maintain the original phasing between the signals.

The third method can be described as a "frequency cut" procedure. The oscillator that drove the shaker was set at a frequency below the room temperature resonance of interest. The wing was then subjected to a heat cycle. When the wing resonance passed through the oscillator setting, the amplitude of the wing vibration peaked, as is shown in Figure 11. Time correlation of the peaks from different oscillator frequency settings provided the histories of the modal frequencies. This method required repeatability of heat inputs as well as no permanent damage to the specimens.

The data from the runs were recorded on an oscillograph. The data recorded for all three methods were:

1. A timing trace.
2. The temperature at six locations.
3. A trace proportional to frequency.
4. The signals from five deflection probes.

TEST RESULTS

The vibration data for the lowest temperature history were obtained using the feedback system of Figure 9. The frequency histories of the first six modes are presented in Figure 12. To within the accuracy of the recorded data, the mode shapes were invariant with temperature.

For the next highest temperature history (Condition 2, Figures 5 and 6) both of the previously described feedback systems were tried and were found to be unsatisfactory. For the modes whose frequencies changed rapidly, both systems followed the frequencies for only a short time. Both of the systems were checked by non-heated tests and were found to be capable of handling frequency changes of the magnitude of interest. It is believed that the systems were incapable of handling the rate of change of frequency which was as high as 75 cps per second.

When the feedback systems were found to be inadequate, the "frequency cut" method was used to define the frequency histories. The frequency transients for the first seven vibration modes resulting from the Condition 2 heat rate are shown in Figure 13. Although the frequency data had very little scatter, the relative amplitudes measured by the five probes varied widely and are believed to be of no value in defining mode shape changes.

The highest temperature history was found to cause permanent buckling of the wing. Since only a limited number of test specimens were available, frequency histories were not obtained for this heating rate.

DISCUSSION AND CONCLUSIONS

As noted previously, the three temperature histories simulated are typical of those attained by small interceptor missiles. The frequency transients in Figures 12 and 13 show that even the lower two of the three heat rate conditions have large effects on the dynamic characteristics of the wings tested. The largest changes occurred in the chordwise bending modes where some of the frequencies dropped more than 30%. This effect was to be expected since the type of temperature distribution used resulted in chordwise compression in the wing. Some DC changes in the wing displacement signals were encountered for both heat rate conditions 2 and 3. The wings always recovered their initial shape after cooling from these heat inputs and results were repeatable. However, as indicated previously, with the highest heat input, permanent buckling occurred and frequency histories were not obtained.

Experience with wings of this planform has shown that the chordwise modes play an important role in the wing's flutter characteristics. To illustrate the possible magnitude of the effect of thermal stresses upon the flutter boundary of such a wing, six mode piston theory flutter analyses were carried out using the frequencies of Figure 13 in place of the room temperature values. It was assumed that the mode shapes did not vary from their room temperature values. Figure 14 shows the ratio of predicted flutter Mach number to the flutter Mach number for the room temperature wing. Although the maximum drop in frequency was only 30%, the flutter speed dropped 60%. This large reduction points out the importance of accounting for aerodynamic heating effects in flutter analyses of low aspect ratio wings. Similar effects were encountered in the heated flutter tests of thin wings reported in Reference (5).

This same test-analysis approach has been applied using temperature distributions for actual missile trajectories. The laboratory frequency data and the predicted wing stability which incorporates this data have been found to agree very closely with the flight results. These results indicate that rigorous definition of modal data for thin lifting surfaces during high heat rate applications would appear to be a fruitful area for further development.

REFERENCES

1. Vosteen, Louis F., and Fuller, Kenneth E., Behavior of a Cantilever Plate Under Rapid Heating Conditions, NACA RM L55E20c, 1955.

2. Runyan, Harry L. and Jones, Nan H., Effect of Aerodynamic Heating on the Flutter of a Rectangular Wing at a Mach Number of 2, NASA TN D-460, 1960.

3. Vosteen, Louis F., McWithney, Robert R., and Thomson, Robert G., Effect of Transient Heating on Vibration Frequencies of Some Simple Wing Structures, NACA TN 4054, 1957.

4. Skingle, C. W., A Vibration Control System for Resonance Following Which Maintains a Pre-Selected Phase Angle Between the Excitation Force and the Displacement of the Structure, Royal Aircraft Establishment TN No. Structures 3110, 1963.

5. Groen, Joseph M. and Rosecrans, Richard, Effect of Aerodynamic Heating on the Flutter of Thin Flat Plate Arrow Wings, NASA TN D-1788, 1963.

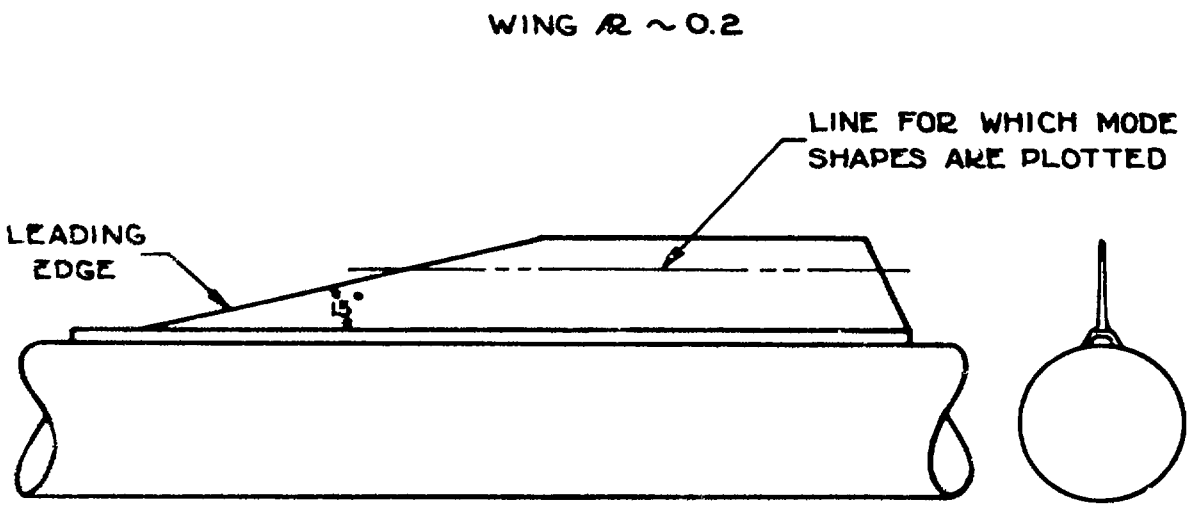

Figure 1. Structural Model

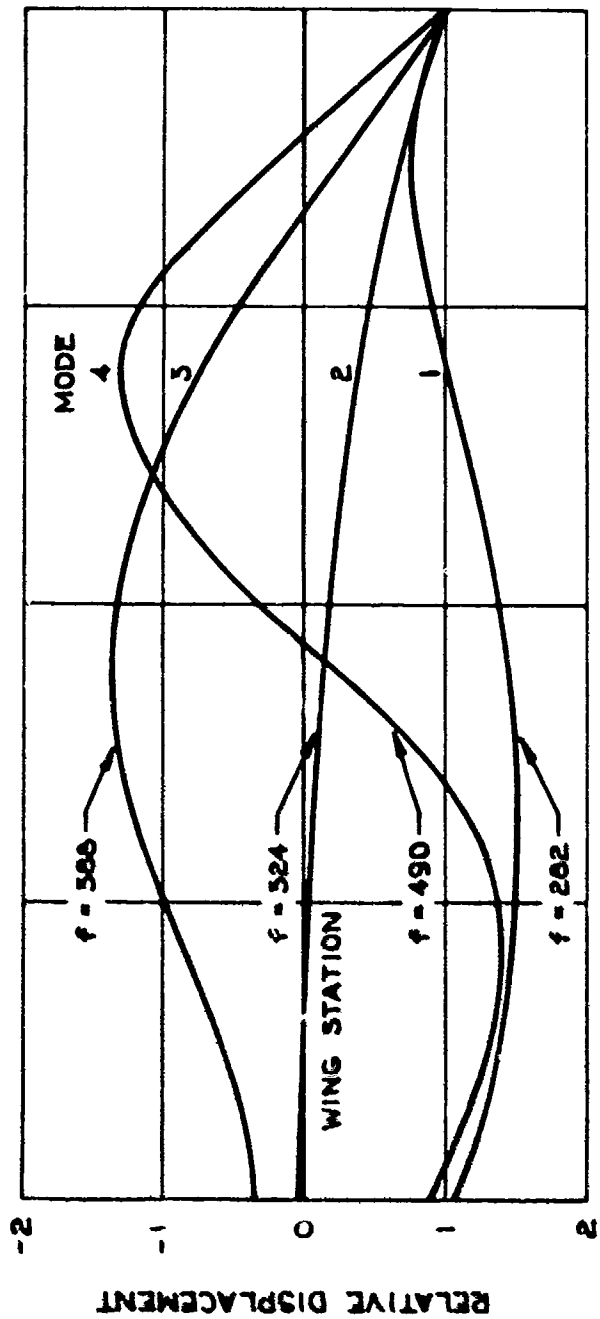

Figure 2. Room Temperature Mode Shapes at 70% Span - Modes 1, 2, 3, and 4

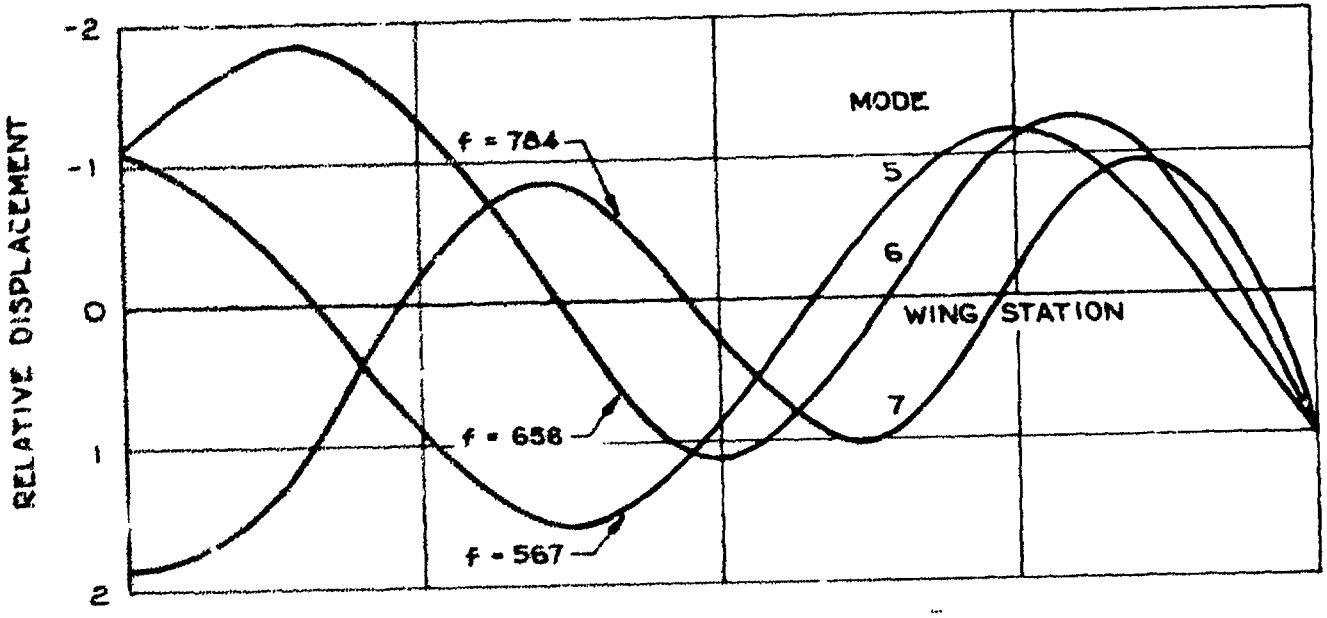

Figure 3. Room Temperature Mode Shapes at 70% Span - Modes 5, 6, and 7

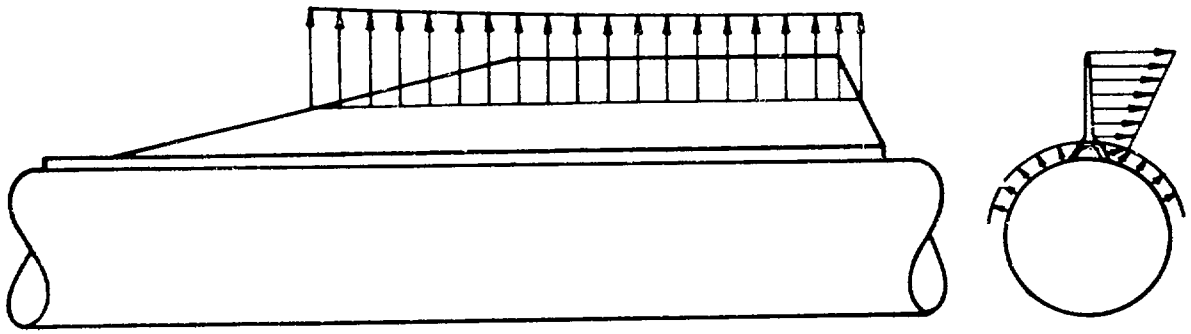

Figure 4. Typical Temperature Distribution

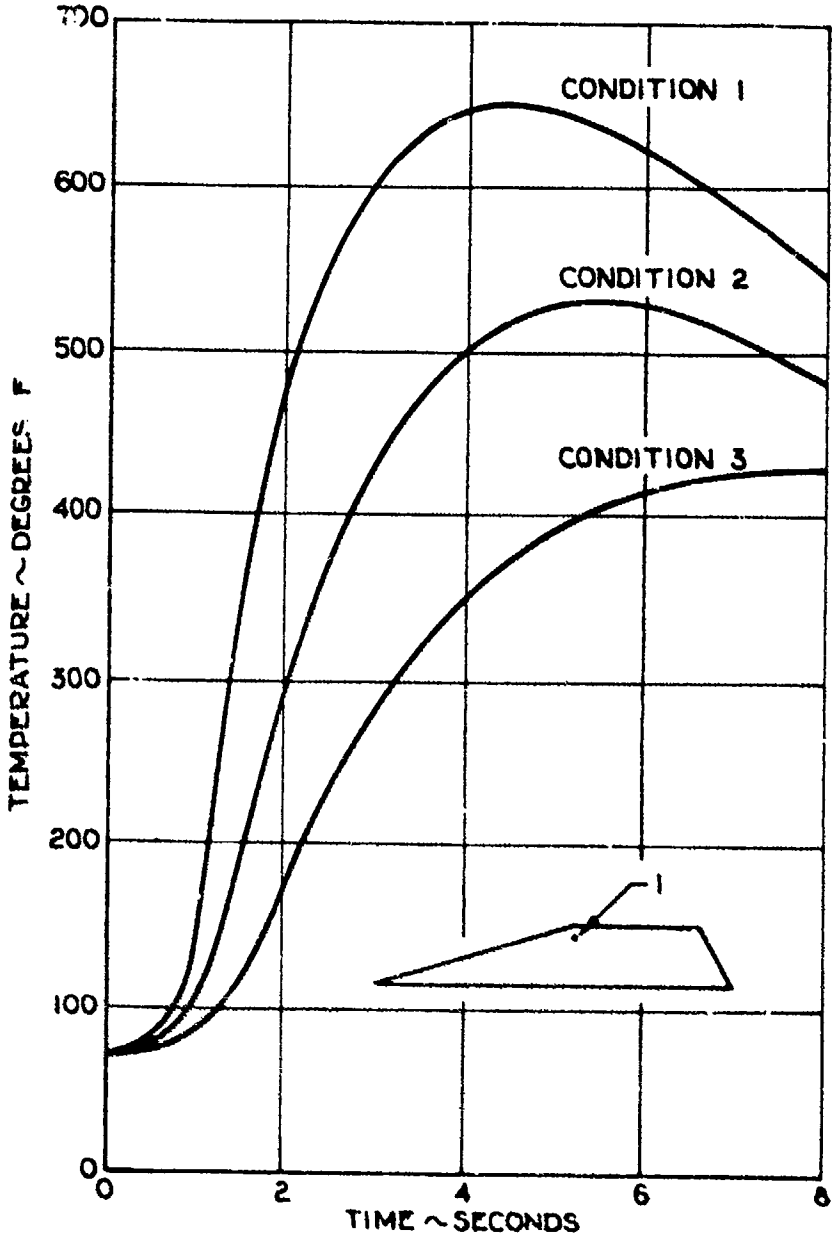

Figure 5. Temperature Histories - Thermocouple 1

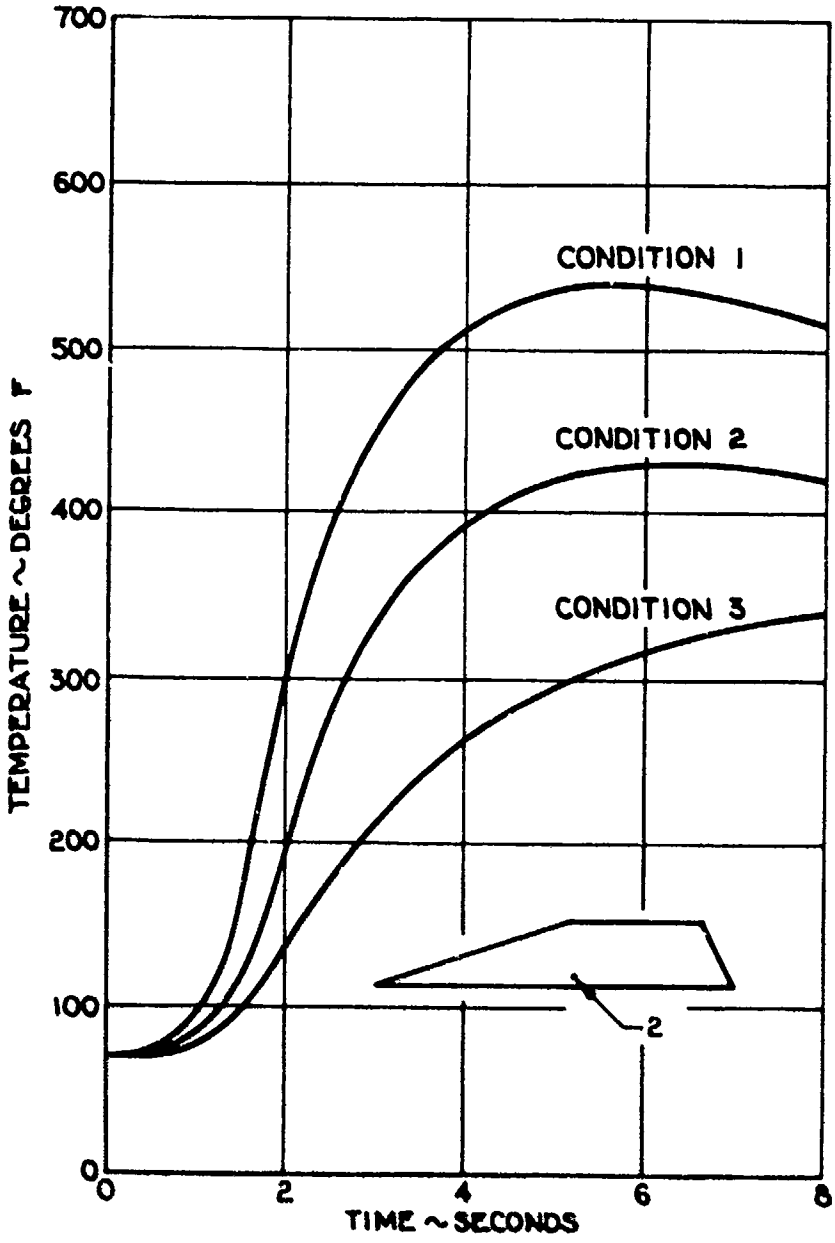

Figure 6. Temperature Histories - Thermocouple 2

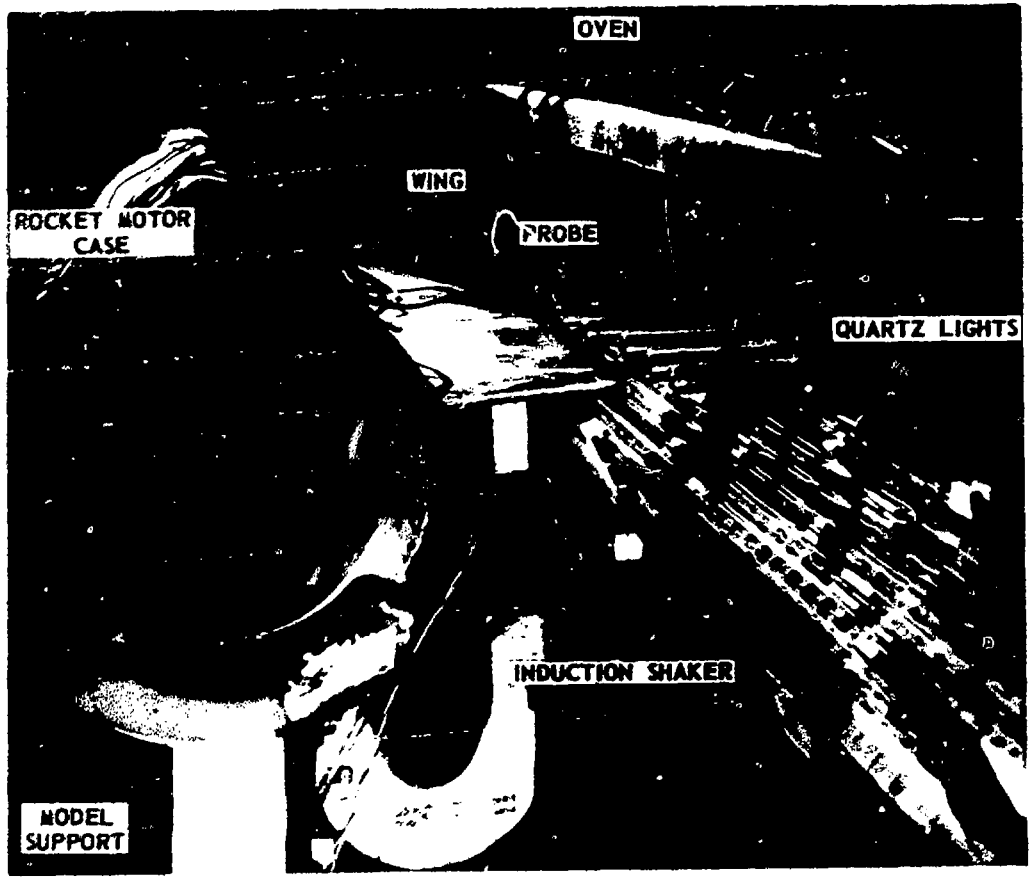

Figure 7. Heated Vibration Test Setup

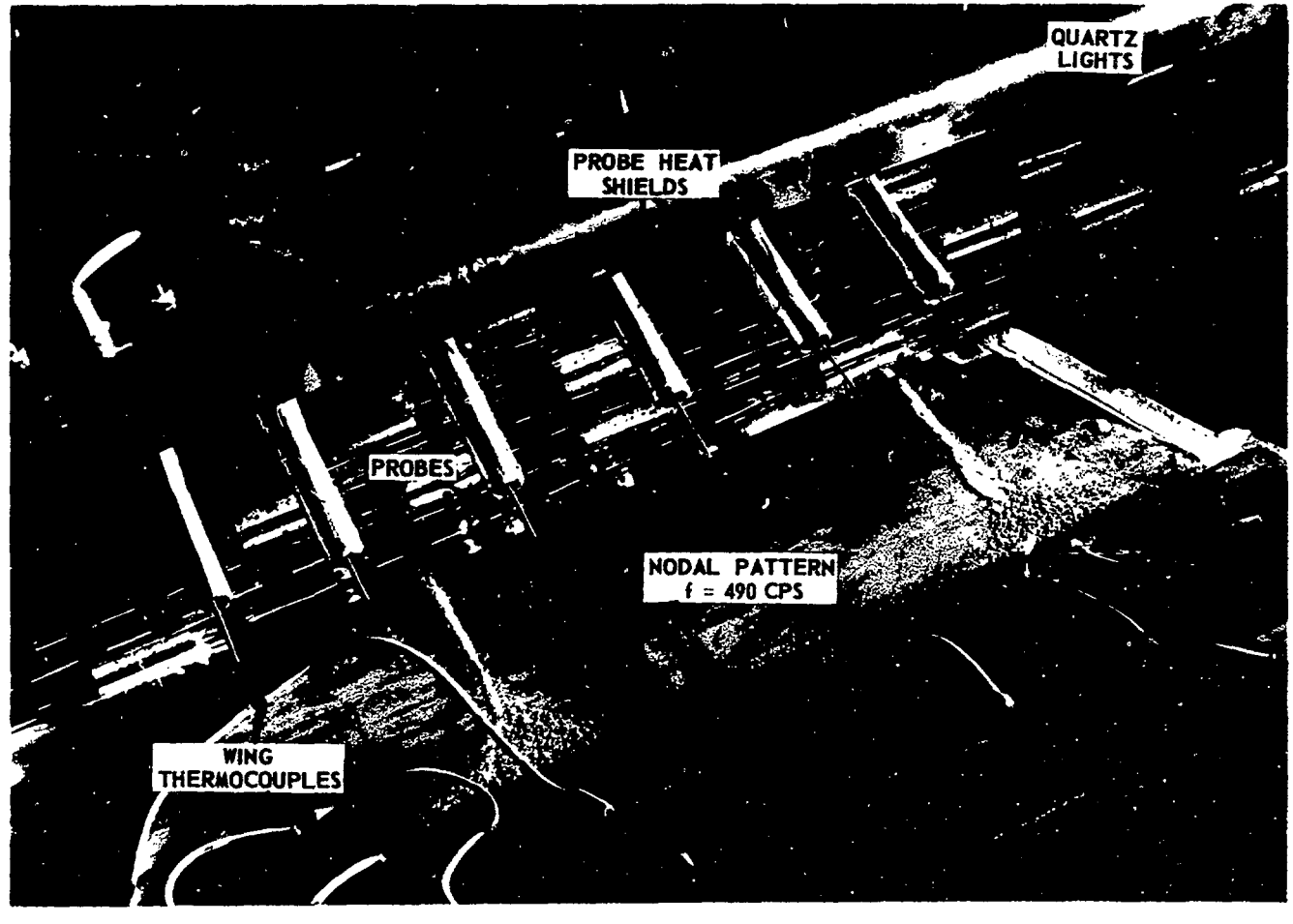

Figure 8. Heated Vibration Test Instrumentation

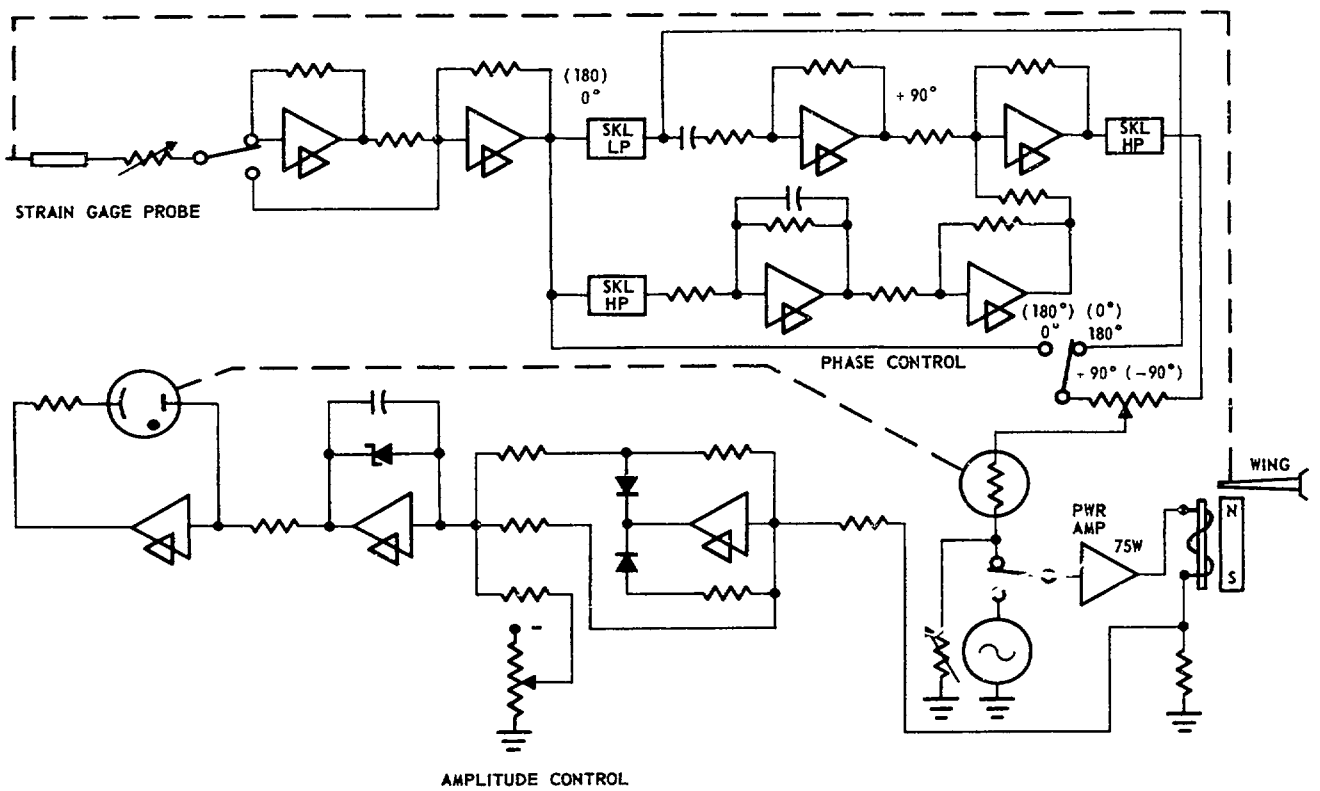

Figure 9. Resonence Following Control System No. 1

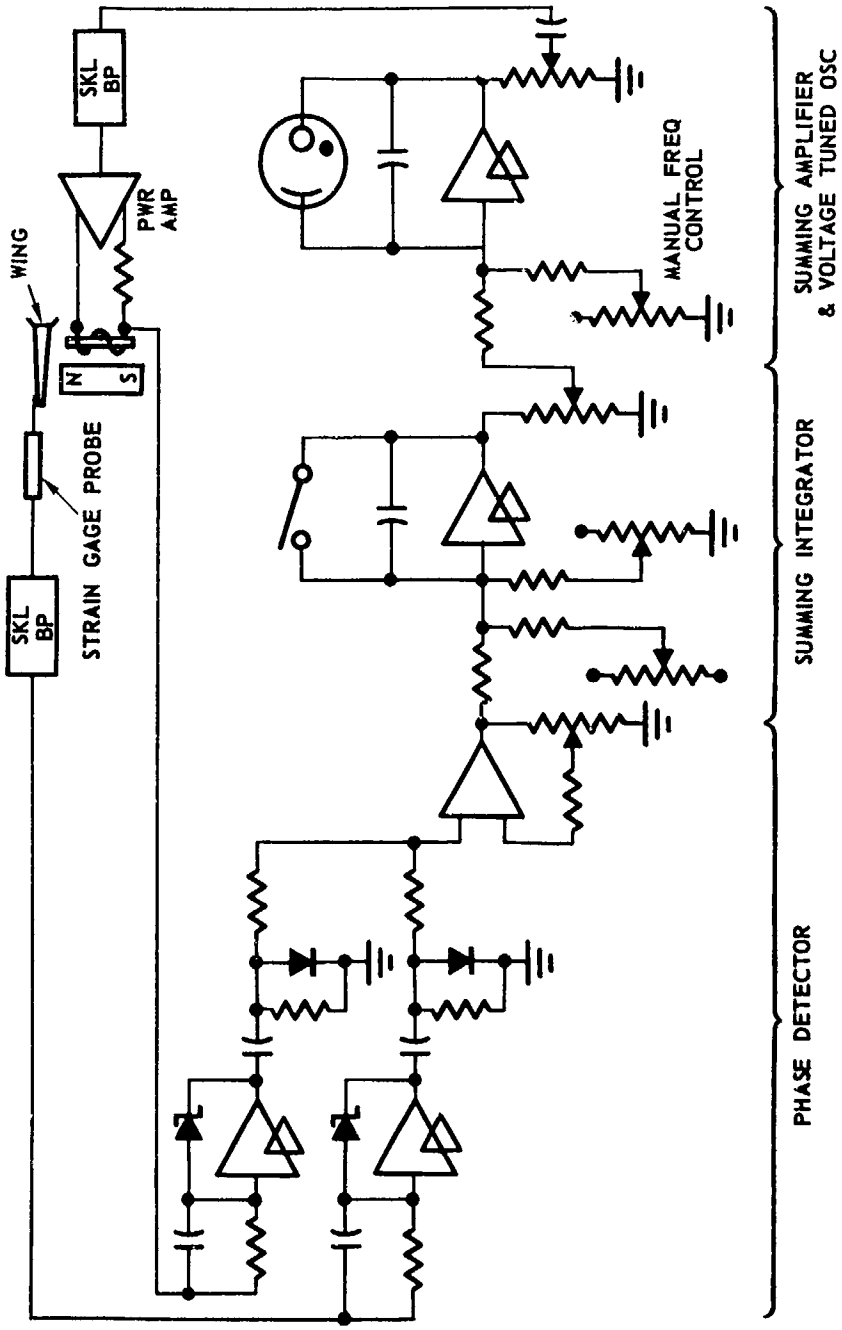

Figure 10. Resonance Following Control System No. 2

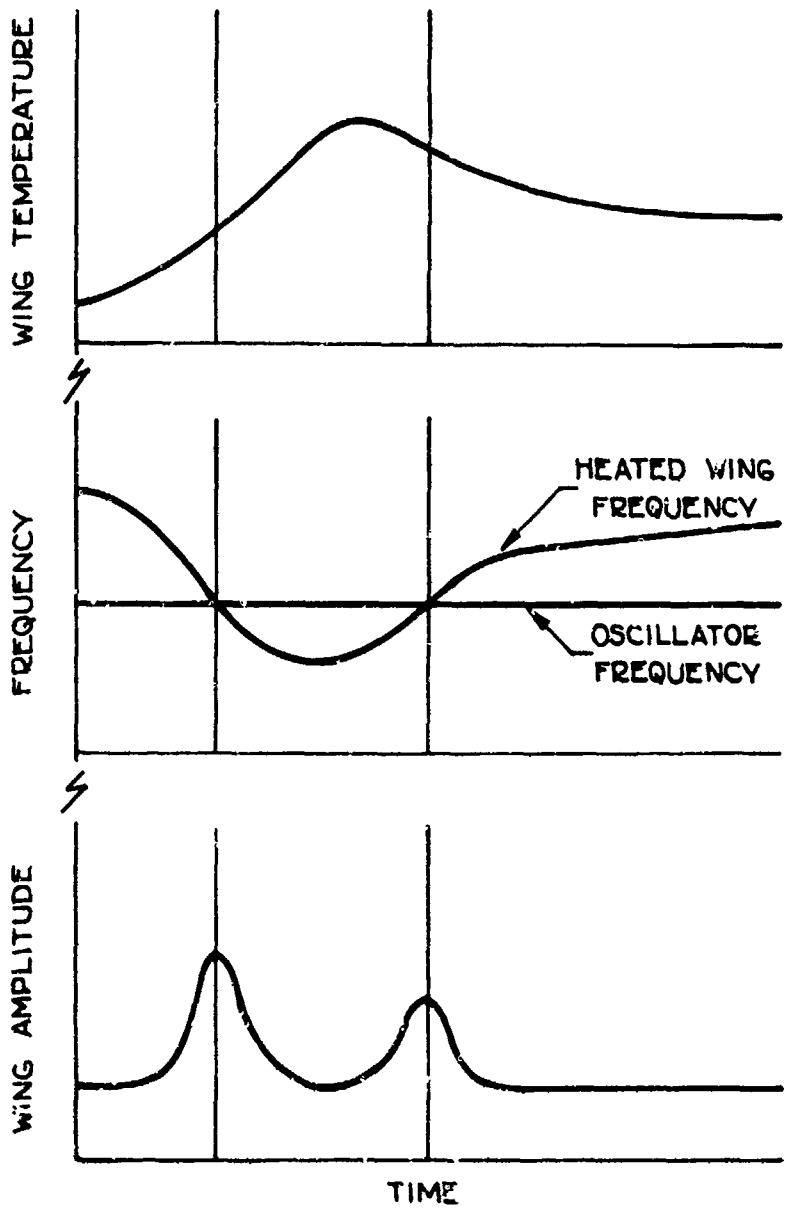

Figure 11. Method for Determining Resonance - During Transient Heating

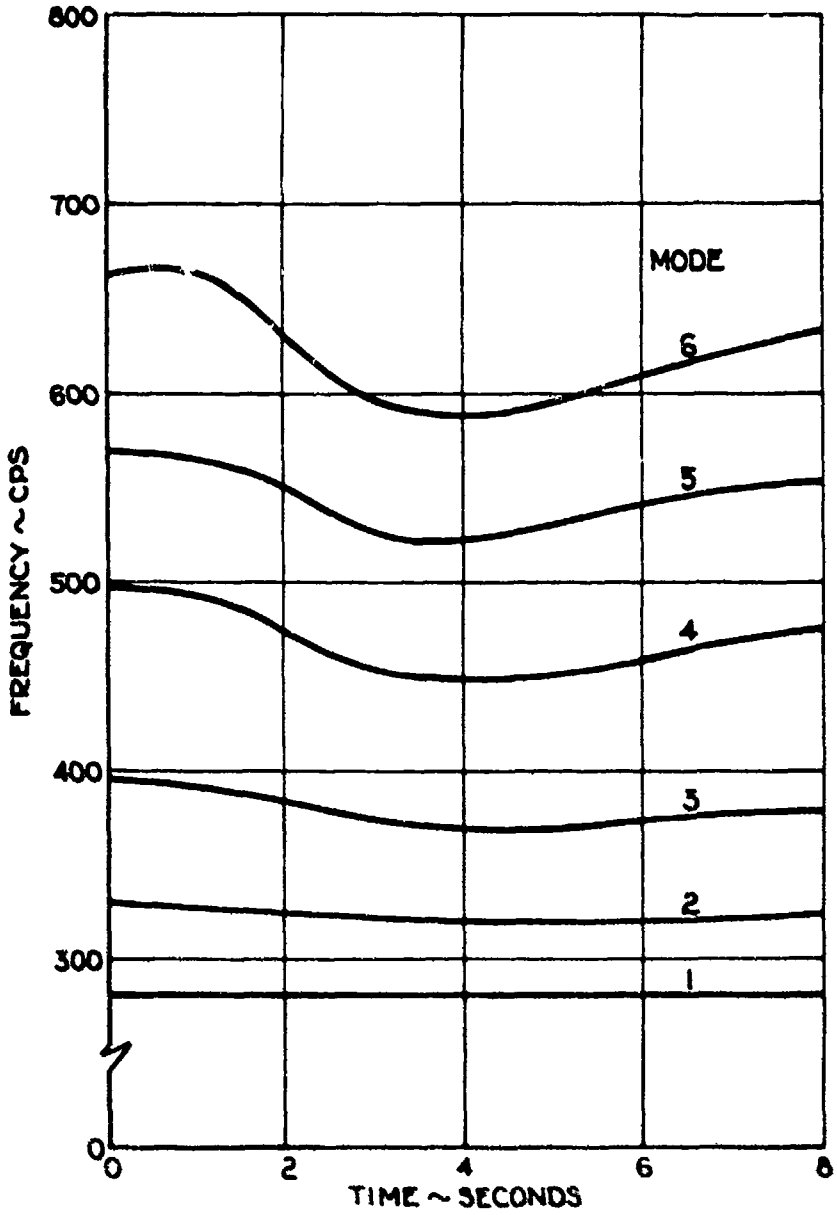

Figure 12. Frequency Histories - Condition 1

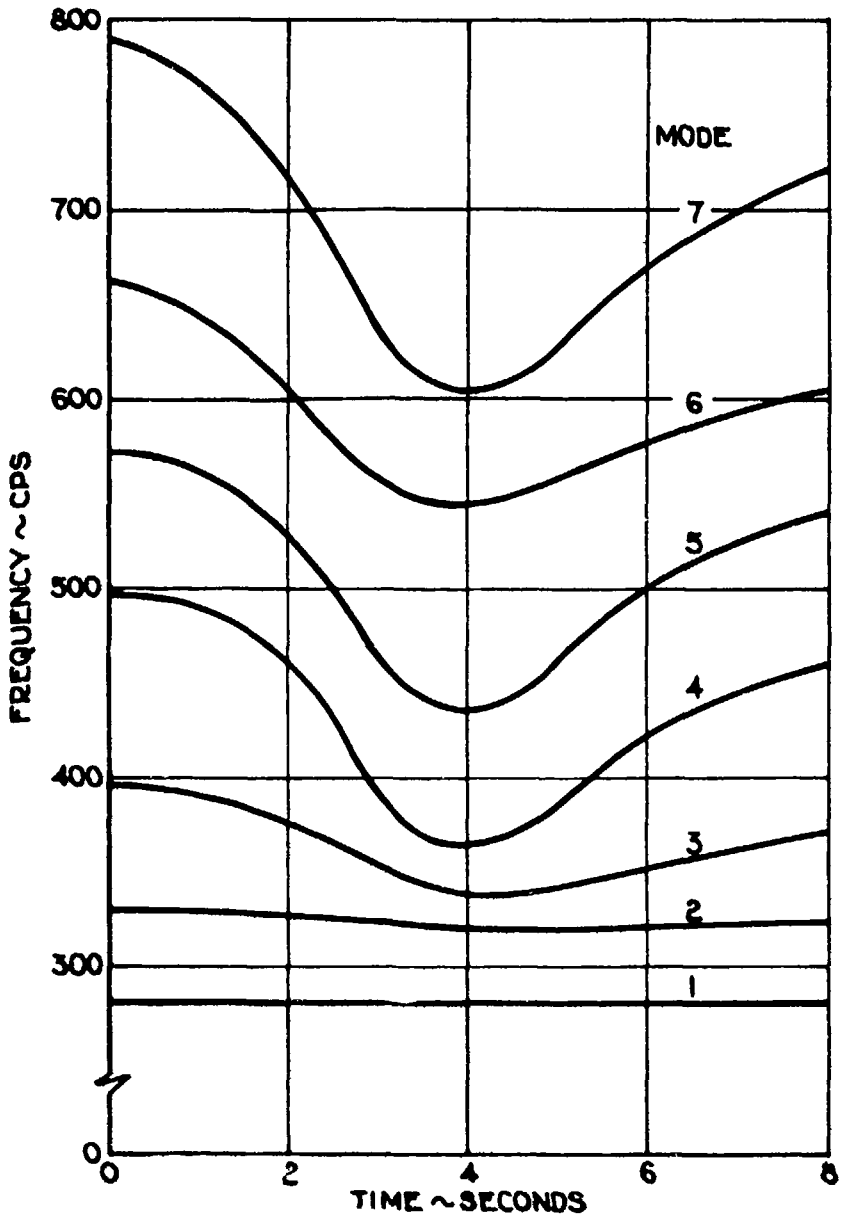

Figure 13. Frequency Histories - Condition 2

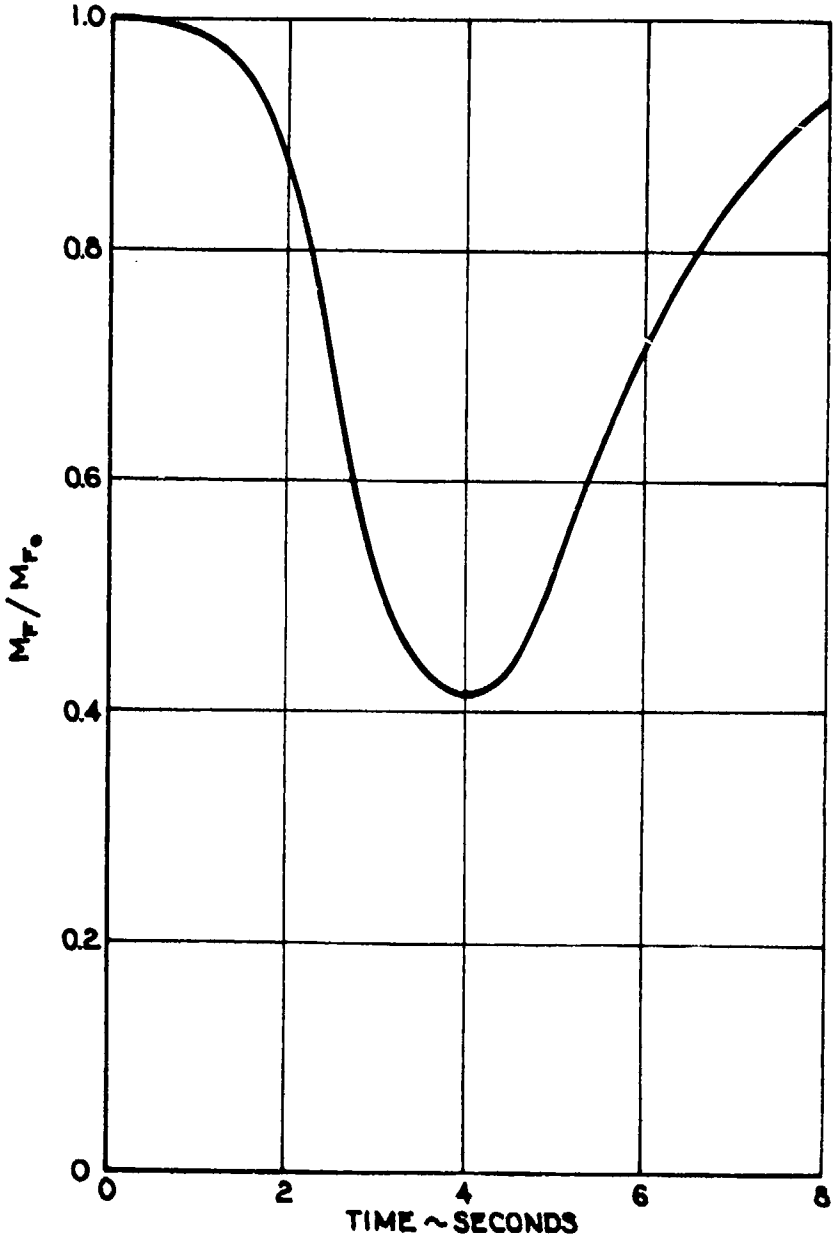

Figure 14. Variation of Flutter Mach Number - Condition 2

SESSION V

LAUNCH AND AEROSPACE VEHICLE APPLICATIONS

Chairman: Dr. William R. Laidlaw
North American Aviation

ABSTRACT

IMPLICATIONS OF PRACTICAL RE-ENTRY STRUCTURES
FOR DYNAMIC MODEL SIMULATION

S. A. LaFavor, C. E. Lemley, and P. B. Tucker

System Technology Division, McDonnell Aircraft Corporation

The unique considerations associated with the application of aerothermoelastic scaling laws in the design, construction, and testing of flutter models for re-entry glide vehicles are discussed. A brief review of the scaling laws is presented in order to re-emphasize the point that they cannot be completely satisfied for other than the case of full scale testing of flight type hardware. This is followed by a discussion of four structural concepts that have been devised to provide acceptable structures for use in the re-entry environment. These concepts are reviewed with respect to predicting the mechanism of potential aerothermoelastic problems, and establishing the possibility of relaxing some of the restrictions of the aerothermoelastic scaling laws. It is concluded that the aerothermoelastic problem can generally be reduced to separate thermoelastic and aeroelastic problems for these structural concepts and that the testing of small scale "artificially reduced stiffness" aeroelastic models, in conjunction with "restricted purpose" heat transfer models, will yield meaningful and useful flutter data for re-entry vehicle structural approaches that presently appear feasible. The use of this type of approach in performing wind tunnel tests on a scaled model of the ASSET re-entry glide vehicle is described.

The ASSET program is sponsored by the Aeronautical Systems Division of the Air Force Systems Command under Contract Number AF33(616)-8106, Project and Task Number 1466. The major part of the effort described in this paper was accomplished under this sponsorship.

LIST OF ILLUSTRATIONS

IMPLICATIONS OF PRACTICAL RE-ENTRY STRUCTURES FOR DYNAMIC MODEL SIMULATION

S. A. LaFavor, C. E. Lemley, and P. B. Tucker

System Technology Division, McDonnell Aircraft Corporation

INTRODUCTION

The problems associated with testing dynamically scaled models of vehicles subjected to significant aerodynamic heating have been pointed out by several investigators, and it is generally concluded that complete aerothermoelastic similarity can only be attained for the case where the model and prototype are identical in every respect, including size. This paper presents a discussion of some of the present structural design concepts that have been devised to provide acceptable structures for re-entry glide vehicles. These design concepts are reviewed with respect to predicting the mechanism of potential aerothermoelastic problems, and establishing the possibility of relaxing some of the restrictions of the aerothermoelastic scaling laws. It is concluded that the aerothermoelastic problem can generally be reduced to separate thermoelastic and aeroelastic problems for these structural concepts and that the testing of small scale "artificially reduced stiffness" aeroelastic models, in conjunction with "restricted purpose" heat transfer models, will yield meaningful and useful flutter data for re-entry vehicle structural approaches that presently appear feasible. The use of this type of approach in performing wind tunnel tests on a scaled model of the ASSET re-entry glide vehicle is described.

The general laws for aerothermoelastic similarity have been developed by Dugundji (reference 1), Calligeros and Dugundji (references 2 and 3), and Molyneux (references 4 and 5), and in all cases it is observed that complete aerothermoelastic similarity is not possible for small scale models. Dugundji (reference 1) suggests several practical means for circumventing the restrictions of the scaling laws; they are

(a) using cold artifically reduced stiffness models,

(b) adding additional external forces to the structure,

(c) relaxing the similarity requirements for Reynolds number or other similarity conditions,

(d) using different materials and temperatures, and

(e) altering the structural geometry to conform with more specialized governing equations.

The approach chosen for a particular model, of course, is dependent on the type of aerothermoelastic problem, or problems to be investigated as well

as the structural configuration and flight environment of the full scale vehicle.

The type of model that has been most widely used by the aeroelastician in the past is one designed primarily for the investigation of flutter problems. This paper deals with the problems of designing such models for winged re-entry glide vehicles. It is assumed that flutter problems involving aerodynamic surfaces and/or overall vehicle deformations will be a consideration for these vehicles in the re-entry flight regime due to significant thermally induced reductions in stiffness and operation at relatively high angle of attack even though the free stream dynamic pressures involved will, in general, be relatively low. An indication of the relative importance of flutter during re-entry as compared to the generally critical boost phase of flight is obtained from the analysis presented in the following paragraphs for a representative re-entry flight profile.

RE-ENTRY VERSUS BOOST FLUTTER STABILITY

The flight corridor presented by Garrick (reference 6) for winged re-entry vehicles is shown in Figure 1 as a plot of dynamic pressure versus Mach number. Nominal radiation equilibrium temperature contours from Reference 6 are also shown in the figure. It is observed that the maximum dynamic pressure capability of these vehicles essentially parallels the 2000°F equilibrium temperature contour. Figure 2 is a plot of the slope of the pressure coefficient curve versus Mach number for a 70° delta wing at zero and 30° angle of attack. This data was obtained from wind tunnel tests of models of the ASSET vehicle and the data was taken on the center line of the lower surface at approximately 52 percent of the chord. Figure 3 presents a plot of static and dynamic modulus of elasticity versus temperature for the refractory metal Columbium.

Consider a lifting vehicle whose primary load carrying members are constructed of Columbium having a temperature-modulus behavior corresponding to that shown in Figure 3, having a flight profile that follows the maximum dynamic pressure (low altitude) side of the flight corridor shown in Figure 1, and whose lifting properties are similar to those shown in Figure 2. It is possible to relate the boost phase and re-entry phase flutter stabilities of such a vehicle by using the relationship:

$$q_{cr} = \frac{EC}{C_{p_\alpha}}$$

which states that flutter dynamic pressure is directly proportional to elastic stiffness (E) and inversely proportional to the strength of the unsteady aerodynamic forcing function (i.e., the slope of the pressure coefficient curve, C_{p_α}) where C is a constant term. Consider now the case where the vehicle is neutrally stable flutterwise at Mach number 15, this Mach number corresponding to the approximate maximum point for the combination of dynamic pressure (195 lbs. per square foot) and temperature (2000 degree Fahrenheit), and is re-entering at 30 degrees angle of attack. Using the data presented in Figures 2 and 3, the constant in the previous flutter equation is then evaluated as follows:

$$C = q_{cr} \; C_{p_\alpha}/E = (195)(.035)/5.7 \times 10^6 = 1.2 \times 10^{-6}$$

Now it is desirable to determine the dynamic pressure for boost that corresponds to this same degree of flutter stability during re-entry. It is assumed for this case that the most severe flutter condition occurs when the product of dynamic pressure and slope of the pressure coefficient curve for zero angle of attack is a maximum (i.e., near the transonic region) since angle of attack and structural temperature will generally be near zero and room temperature, respectively throughout the high dynamic pressure portion of the boost trajectory. The data presented in Figure 2 shows that this critical Mach number is approximately 1.1(i.e., zero angle of attack C_{p_α} a maximum) for the configuration being investigated, and again using the data presented in Figures 2 and 3 and the above calculated value of C for re-entry:

$$q_{cr_{Boost}} = \frac{E}{C_{p_\alpha}} C = \frac{(14 \times 10^6)(1.2 \times 10^{-6})}{(.017)} = 990 \text{ PSF}$$

This value of the critical boost dynamic pressure is plotted in Figure 1 for comparison with the re-entry dynamic pressures. Thus, it is established for the configuration treated herein, that for flight boost dynamic pressures less than approximately 1000 pounds per square foot, the re-entry flight regime would be flutter critical, whereas for boost dynamic pressures greater than approximately 1000 the boost flight regime would be flutter critical.

Maximum boost dynamic pressures of less than 1000 pounds per square foot may occur for large liquid fuel boosters of the type that might be used for launching manned winged vehicles. Consequently, it appears that the re-entry flight regime may, in some cases, be the flutter critical region for winged re-entry vehicles. However, it should be recognized that the always troublesome transonic region must also be traversed after re-entry and this flight regime may be flutter critical for some configurations. This could be especially true for cases where the internal structural temperatures are still relatively high after re-entry.

STRUCTURAL DESIGN CONCEPTS FOR RE-ENTRY VEHICLES

To logically assess the degree of dynamic simulation required in a flutter model of an advanced re-entry vehicle, it is well to first consider the type of vehicles and structural approaches that are presently available for this flight regime. The following sections briefly describe the various missions, vehicle configurations, and structural approaches of interest for this flight regime and indicate what are considered to be the important aerothermoelastic parameters in each case.

Vehicle Concepts - In general, three broad concepts exist which may be used in the design of re-entry bodies. They are: ballistic, aeroballistic, and aerodynamic classes. Figure 4 shows the approximate flight corridors for these three types of vehicles as given by Garrick (reference 6) as a plot of altitude versus velocity.

(a) Ballistic - The ballistic vehicle is characterized by a relatively narrow flight corridor, short time high flux heat pulse and a rather blunt body shape. The body shape is primarily dictated by heating and static aerodynamic stability considerations. The ballistic flight path results in nearly symmetric heating which minimizes static aerothermoelastic deformations and allows a relatively simple thermal-structural design.

(b) Aeroballistic - The aeroballistic vehicle has limited re-entry maneuver capability and is characterized by a wider flight corridor than the ballistic vehicle. It has a longer time lower peak heat pulse and a long slender body shape such as a conical body of revolution. The body shape is primarily dictated by the requirement for achieving high lift to drag ratios to use body lift to modify a ballistic trajectory to gain longer range. The aeroballistic vehicle may have aerodynamic control surfaces and be subjected to either symmetric or unsymmetric heating depending upon the particular design concept chosen. Both static and dynamic aerothermoelastic problems would appear to be considerations in the design of this type of vehicle.

(c) Winged Vehicles - The winged aerodynamic vehicle has a relatively wide flight corridor and is characterized by probably the most complex time heat pulse history. Heating is generally the most uniform of the three vehicle classes and in comparison of equal weight, equal mission, the least extreme environment. The body shape emphasizes a lifting surface, probably polyplanar, with surfaces or body planes shaped for static aerodynamic stability and aerodynamic surfaces for trim and control. As a class the aerodynamic or winged vehicle is most maneuverable and thus offers the greatest versatility in flight path, heating history, and structural design concept. Consequently, it also offers the most potential for encountering aerothermoelastic problems.

Even from the brief description of vehicle classes it can be seen that considerable overlap can exist between the classes, the choice of concept for a particular application being based on overall mission objectives as well as re-entry performance.

Structural Approaches - The structural approaches utilized for the above described vehicles are generally different. For the ballistic vehicle, pressures and inertial forces probably predominate whereas with the aeroballistic and aerodynamic approaches body bending moments and thermal gradients generally predominate. However, the primary requirements are to (a) establish the structural approaches that will survive the environment and (b) establish the most applicable structural approach to the vehicle mission requirements. The structural approaches may be generalized into four distinct types although in actual applications, overlap of types almost always exist. These types are characterized by their action in controlling and surviving temperatures and are as follows:

(a) Heat Sink Approach - Passive or active concepts may be employed where a sufficient mass of material of high specific heat is provided to absorb the heat input and limit structural or internal component temperatures to acceptable values. In active systems the system may become quite complex involving circulation systems, heat exchangers, pumps, valves, etc.

(b) Heat Block Approach - The heat block approach includes both ablative approaches, illustrated in Figure 5, and those involving transpiration cooling. In this type the vehicle is protected from high temperatures by blockage utilizing the heat absorbing capability of a physical or chemical change of the material and by injection of "cool" gases into the boundary layer thus blocking boundary layer heat transmission to the surface.

The under structure is thus kept relatively cool even under extreme re-entry conditions.

(c) Heat Shielded and Insulated Approach - This approach, as illustrated in Figure 6, depends entirely on re-radiation to limit heat shield temperatures to acceptable material and structural limits and employs insulation compatible with mission duration to limit sub-structural temperatures to acceptable values.

(d) Hot Structural Approach - This approach, as illustrated in Figure 7, also depends entirely on re-radiation to limit temperatures but in this case the primary structure is designed using high temperature materials to survive the environments while maintaining structural integrity for mission requirements.

As with the vehicle configuration concepts, the structural concepts each may have application dependent on specific mission requirements. The selection of a structural approach is almost entirely a function of weight and peak temperature capability of available materials.

Applications of Structural Approaches - The first re-entry systems flown were ballistic vehicles and employed heat sink and heat blockage approaches to limit structural temperatures. The Mercury ablative heat shield is cited as one example of this concept. Here the peak heat pulse is of short duration and the ablative approach appears particularly efficient for this mission. The USAF ASSET vehicle employs a number of structural approaches of the heat shielded and insulated and hot structural types. Although it is hazardous to generalize, a current view of application of thermo-structural concepts would be as follows:

(a) Short time (perhaps 5 minutes) high peak heat pulses make application of ablative approaches quite attractive.

(b) Re-radiative systems appear quite efficient where longer time heat environments are involved especially when peak temperatures can be limited to below 3000°F.

(c) Transpiration cooling approaches for large areas of a vehicle are currently lacking in development making it hazardous to seriously commit a weapon system program to a design dependent on this concept.

Considering again the prime area of concern, i.e. aerothermoelastic effects on re-entry vehicles, probable re-entry designs can be envisioned as one of three typical approaches as are shown in Figures 5, 6, and 7. The dynamic problem of the ablative vehicle (heat block concept) resolves itself to one not unlike the more familiar aircraft airframe since the ablative approach provides cool structural temperatures thereby minimizing thermal effects and in many cases the amount of ablative material employed will essentially eliminate any local dynamic response due to its thickness and material behavior. However, with the heat shielded or hot structural approaches, the effects on vehicle dynamic behavior, both local and overall, of thermal aerodynamic environment may be significant. It is in this area that consideration should be given to the heating effects on dynamic model simulation.

Thermal Effects on Stiffness - Ignoring chemical changes of structural materials which might affect either stiffness or structural capability, there are three ways in which temperature may influence stiffness.

The first and most obvious effect is a change in modulus of elasticity with temperature. Figure 3 illustrates such a change. Although there is question at present as to the relationship of static and dynamic modulus, especially with coated refractory materials, this is a function of the material itself and can be evaluated separate from a configuration.

The second effect is that of experiencing thermally induced deformations which change the stiffness of a structural component. Figure 8 illustrates this effect for a single face corrugated panel where the direction of flow is normal to the axis of the corrugations and the panel edges parallel to the direction of flow are free. This corresponds to the panel configuration used for the ASSET flutter panel experiment where the important stiffness parameter is the area moment of inertia of the skin and contribution of the corrugation about an axis normal to the flow direction. The stiffness inertia term is essentially the simple relation

$$I_B = \frac{wt^3}{12}$$

where t is the effective thickness of the face skin and corrugation. However, when a thermal gradient is present through the thickness of the panel, the panel deforms along the corrugation axis increasing the significant panel inertia by a displacement term Ad^2. As can be seen from Figure 8 the stiffness increases quite dramatically with relatively modest gradients. For dynamic analyses, the effect of such geometric changes on stiffness must be taken into account if the analyses are to be valid.

The third thermal effect is the effect on stiffness of thermally induced stresses which produce a change in the basic load paths of the structure either by non-linear effects of thermal stresses and load stresses (for instance a beam column) or by a destabilizing effect such as buckling or crippling of a structural component. While such effects may have a significant influence on stiffness, they also influence structural integrity and good design practice would minimize or preclude such occurrances. It would be difficult here to outline a structural design criterion for present and future re-entry vehicles that would mitigate thermal stresses significant to both dynamic and structural considerations. For the case of the maneuverable-winged re-entry glide vehicle the relatively wide flight corridor capability and the resultant multi-thermal histories that can be experienced can produce countless combinations of thermal stress patterns which would complicate the stiffness evaluation of the vehicle. If a generalization of a design criterion could be made it would be that the structural design should incorporate provisions to limit thermal stresses such that their effect on load distribution in the vehicle structure is negligible. The implementation of this approach, in terms of detail structural design, requires the use of unique and/or ingenious design approaches, as mentioned by Garrick (reference 6), that eliminate redundancies and isolate load paths to minimize or eliminate thermally induced stresses in the primary load carrying members. It may also be necessary to alter the flight path or vehicle attitude to accomplish the design goal. It is recognized that implementing this design philosophy is neither obvious nor

simple but probably essential to maintain structural integrity. Adequate elevated temperature ground tests of a flight vehicle would be required to establish that these design approaches met the desired objective of minimizing thermal stresses.

Such an approach would allow the establishment of a rational design criterion based on air load, inertia load, temperatures, and material temperature limitations. It should then be possible to maneuver a vehicle so designed within a relatively wide flight corrisor while monitoring only key structural temperatures and inertial loads.

The result, then, is that for the hot structural approach, strength design considerations alone will dictate an approach which will inherently minimize the build up of thermally induced stresses thus reducing the possibility of strong coupling of such thermal effects on structural stiffness. This has the effect of limiting the thermal influence on stiffness to the two previously mentioned:

(a) modulus reductions due to temperature, and

(b) changes in structural geometry, or configuration, due to thermal gradients.

DYNAMIC SIMULATION FOR RE-ENTRY VEHICLES

The minimization of thermal stresses in practical re-entry structures, and the attendent reduction of their influence on stiffness, simplifies the problem of achieving dynamic similarity in scaled models of vehicles of this type. Such a model then need only simulate modulus reductions and changes in structural geometry encountered in the prototype vehicle due to the flight thermal environment. In essence, the aerothermoelastic problem is then reduced to two separate problems; a thermoelastic problem and an aeroelastic problem. It becomes possible to design special purpose models to investigate the aeroelastic and thermoelastic problems separately. A "reduced stiffness" dynamic model of a vehicle that utilizes one of these structural approaches can be designed to obtain useful and meaningful flutter data for the re-entry flight regime. This model would be designed according to the flutter model scaling laws used in the past where thermal effects were neglected and the three parameters Mach number, mass ratio, and reduced frequency are equated for model and prototype vehicle.

The degree of stiffness reduction required in such a model would be based on two considerations. They are:

(a) the stiffness reduction in the prototype vehicle due to thermal effects in flight, and

(b) additional changes in stiffness in the model due to the wind tunnel thermal environment.

Item (a) above could best be established through testing "special purpose" heat transfer models designed to measure either the basic heat flux input to the structure, or the local structural temperatures within the vehicle. The former case would require an analytical bridge to predict internal structural temperatures whereas the latter case would require a rather sophisticated, and expensive model. In either case, it would then be necessary

to either analytically, or through additional tests, define the resultant stiffness of the vehicle due to these internal temperatures. The effects of both modulus reductions and changes in structural geometry must be accounted for in establishing this stiffness.

The wind tunnel thermal environment will, in general, also influence the design of the reduced stiffness model. Wind tunnels suitable for flutter testing at the higher re-entry Mach numbers (i.e. Mach numbers greater than approximately ten) are not generally available at present. However, it is possible to test the reduced stiffness model at Mach numbers less than the critical flight values if it is assumed that the aerodynamic forces acting on the vehicle and model are essentially independent of Mach number in the high Mach number range (i.e. for Mach numbers greater than three or four). This appears to be a generally accepted assumption at present, and allows for the testing of this type of model in existing facilities.

Figure 9 presents a plot of stagnation temperature versus Mach number for several high Mach number wind tunnels suitable for flutter testing. The plot indicates that wind tunnel stagnation temperatures for the Mach number range of three to twelve vary from approximately 200 to 2300 degrees Fahrenheit. Model temperatures would be expected to be on this same order at stagnation points with decreasing temperatures on the other surfaces dependent on the model geometry, angle of attack, construction, and radiation effects. It can be seen that, in general, these temperatures can have a significant effect on model stiffness characteristics.

The fact that the wind tunnel thermal environment will, in most cases, affect the stiffness characteristics of the reduced stiffness model has two implications with respect to its design:

(a) it must be designed to be thermally resistant in a manner similar to the flight vehicle (i.e. it also should be structurally designed to minimize thermally induced stresses), and

(b) the influence of the tunnel environment on model stiffness must be accounted for in establishing the net difference between prototype and model stiffness.

It is necessary to design the model in a similar manner to the flight vehicle in the sense that it also should not be subject to significant thermal stresses. This requirement stems from the following considerations:

(a) the stiffness characteristics of the model should be well behaved and predictable in the wind tunnel thermal environment to allow for an accurate accounting of the net differences between prototype and model stiffness, and

(b) thermal stresses must be minimized in the model to preclude the possibility of introducing aerothermoelastic problems in the model that are not representative of the flight vehicle.

The model need not be designed using the exact structural concept used for the flight vehicle (i.e. it need not be an exact scale replica of the prototype structure), but it must be designed for the same criteria of eliminating

significant thermal stresses in the primary load carrying members. The effects of the tunnel environment on model stiffness can then be accounted for by either analytically estimating these effects prior to the tunnel test and adjusting the model stiffness to account for the net difference between the flight and wind tunnel stiffness reductions, or by designing the model to account for only the flight stiffness reductions and correct the data obtained for the wind tunnel effects subsequent to testing. For either case it would be highly desirable to perform an elevated temperature ground vibration test of the model to verify predicted effects of temperature on model stiffness.

ASSET FLUTTER MODEL TEST PROGRAM

An early configuration of the ASSET glide vehicle was designed to obtain basic data relating aeroelastic and thermal effects in the re-entry glide environment. A wind tunnel model that simulated the important dynamic characteristics of the flight configuration was designed, fabricated and tested to obtain design data for the flight vehicle and to obtain data for correlation with corresponding flight test results.

The ASSET configuration is shown in Figure 10. The lifting surface consists of the flat under portions of the vehicle, the forward and aft parts being separated by a 10° mold line break. To acquire an aeroelastic system capable of fluttering in the high temperature, low dynamic pressure environment posed basic problems relating static load carrying capability, low vibration frequencies, and the use of major aerodynamic surfaces to obtain sufficiently large unsteady aerodynamic forces. It was not feasible to consider elastic deformation of the main fuselage because of the short stubby nature of the vehicle. Therefore, it was necessary to design elastic members attached to the main fuselage in such a manner as to allow flexural motion independent of the fuselage. The configuration which was chosen to be tested in the re-entry environment was obtained by sectioning the vehicle as shown in Figure 11. The three basic parts thus obtained were designated as the upper body, the wing, and the control surface assembly. The wing was attached to the upper body by pins and links which allowed a beam-like flexural motion of the wing. The flap assembly was attached to the wing by bearings and was restrained in rotation by a root torsion spring (not shown on Figure). The vibration modes that were to couple to produce flutter were first symmetric wing bending and control surface rotation. The wing and control surface deflections in these modes are symmetric about a vertical plane passing through the centerline of the vehicle.

The structural approach used in the design of the prototype wing was dictated by the requirements that (1) the wing be sufficiently strong to carry static aerodynamic loads at elevated flight temperatures and (2) that it be soft enough to allow flutter at some point along the re-entry trajectory. Based on these requirements, a thermal design philosophy was used which involved a combination of (a) the Heat Sink, (b) the Heat Shield and Insulation and (c) the Hot Structure approaches. The Heat Sink Approach was used for the nose cap (stagnation point) design, and the Heat Shield and Insulation Approach was used to isolate the upper body from the high temperatures attained by the wing. The Hot Structure approach was used for the design of the wing spar in which the elevated

temperature was used to lower the wing bending stiffness (through modulus reduction) and thus allow the wing-control surface system to flutter.

The scope of the wind tunnel test program was in large part dictated by the Mach number range (12 down to 2) encompassed in the re-entry trajectory. Tunnels A (M = 2-6), B (M = 8) and C (M = 10) of the AEDC von Karman facility were selected for the tests. A prototype-to-model geometric scale factor of 0.25 provided a model size suitable for testing in all three tunnels.

The model design philosophy was based on the assumption (as discussed earlier in this paper) that no coupling would exist in the prototype configuration between aeroelastic and thermoelastic effects. On this basis, the model design scale factors were specified by the following relationships:

$$L_m = 0.25\, L_p \qquad \text{(Length)}$$

$$M_m = M_p \qquad \text{(Compressibility)}$$

$$\mu_m = \mu_p \qquad \text{(Mass)}$$

$$k_m = k_p \qquad \text{(Time)}$$

where L denotes length, M is Mach number, μ is the ratio of vehicle density to air density, k is the reduced frequency, and the subscripts m and p denote model and prototype respectively. These relationships, together with values for ρ_m/ρ_p and V_m/V_p, allow the physical characteristics of the model to be completely defined. The latter ratios (stream density and stream velocity) were determined by flight trajectory and wind tunnel stream characteristics at the scaling design points. Design points at Mach 4 and Mach 9 were chosen which defined two distinct model configurations. An interesting feature of model scaling for the ASSET re-entry trajectory was that for the tunnels chosen, the stream density ratio ρ_m/ρ_p (and hence the ratio of model mass density to prototype mass density) was greater than 1. A scaling value of $\rho_m/\rho_p = 4$ was used for both ASSET design points. Because the compact ASSET prototype vehicle itself has a high mass density, model wing design required the use of heavy metal (Mallory 1000) ballast in conjunction with basic stainless steel construction. Figure 12 is a photograph showing detail of the model construction. Wing stiffness was determined by the wing spar design, i.e., EI about span lines. Wing inertia characteristics were determined by the mass segments. These mass segments followed closely a lumped mass idealization.

In the following discussion, reference is made only to the static thermoelastic properties of the wing, but the conclusions apply to any elastic member which would influence aerodynamic stability boundaries. The thermal effects which had to be considered in model wing design were due to (1) the effect of aerodynamic heating in reducing the bending stiffness of the prototype wing, and (2) the heating effects of high wind tunnel stagnation temperature in reducing the bending stiffness of the model wing. The data required to finalize the model wing design were:

(a) the value of prototype (thermally reduced) wing-bending stiffness for which the vehicle would flutter at trajectory dynamic pressure and angle of attack,

(b) the scale factors, and

(c) predictions of the model wing spar temperature at wind tunnel test conditions.

With these data stiffness scaling from prototype to model wing were based on thermally reduced values. The room temperature value of wing bending stiffness was then determined from a curve of Young's modulus versus temperature for the spar material. Values of bending stiffness at room and elevated temperatures for prototype and model wings are presented in the following table:

	Prototype	Model
Test Temperature	1600°F	550°F
Spar Material	Inconel X	321 Stainless Steel
EI (Test Temperature)	2.38×10^6 lb-in^2	7390 lb-in^2
EI (Room Temperature)	4.17×10^6 lb-in^2	8200 lb-in^2

Figure 13 shows the measured temperature distribution along the model wind spar for a soak condition in tunnel C. It is noted that the temperatures are considerably higher than the 550° shown in the previous table. This value was taken as an approximate average of the spar temperatures anticipated for all the tunnels.

The high wind tunnel stagnation temperatures also necessitated other special design features of the model. These features, which allowed sustained operation at model temperatures up to 1200°F, are summarized as follows:

(a) Special sliding attachments between skin cover and upper body to allow differential thermal growth,

(b) High temperature structural parts, including bolts, made of the same material so as to have the same thermal coefficient of expansion,

(c) Entire model covered with high emissivity coating so as to radiate to the cooled tunnel walls,

(d) Separation between stand-off wing mass segments sized to allow flexural motion and thermal growth,

(e) A portion of the dynamic instrumentation (strain gages) specially chosen for high temperature operation, and

(f) Water cooling jackets provided for electromechanical components.

Prior to the wind tunnel tests, extensive ground tests at room and elevated temperatures were performed on the model. These tests were used to determine the model dynamics over a wide temperature range and to verify the operational integrity at elevated temperature. The wind tunnel tests were performed between 2 February 1962 and 20 March 1962. Wing bending-control surface rotation flutter data were obtained in the Mach number range 4 to 10 for model angles of attack between 6° and 31°. A detailed report presenting the results of the test program will be released as an ASD Technical Documentary Report in 1963.

CONCLUSIONS

Presented herein is a discussion of the implications of practical structural design concepts on the problems of achieving dynamic similarity in scaled models of winged flight vehicles that experience significant aerodynamic heating. It is concluded that the primary thermal effects on stiffness to be accounted for are (a) modulus of elasticity changes due to temperature, and (b) changes in structural configuration due to thermal gradients, and that the effects of thermally induced stresses on stiffness will generally not be a significant consideration. This conclusion is based on the assumption that the evolution of a rational structural design criterion for aerodynamically heated vehicles that have the capability of operating within a relatively wide flight corridor will preclude the allowance of significant thermally induced stresses in primary load carrying structural members. Their minimization will be accomplished through the use of unique and/or ingenious design approaches that eliminate redundancies and isolate structural load paths.

The elimination of thermal stresses from consideration in the aero-thermoelastic scaling problem reduces this problem to the two simpler thermoelastic and aeroelastic scaling problems. This in turn allows one to design special purpose models to evaluate the thermoelastic and aero-elastic problems separately. A small scale "reduced stiffness" aeroelastic model can then be tested to obtain flutter data where its stiffness characteristics are established on the basis of

(a) The predicted inflight stiffness of the prototype vehicle, and

(b) The predicted effects of the wind tunnel thermal environment on model stiffness.

Various combinations of analytical-testing steps can then be used to define the thermal environment experienced by the prototype structural members and the resultant effect on the vehicle stiffness characteristics. This approach allows the aerothermoelastic problem to be broken up into several simpler problems that can be logically separated and assigned to the separate thermal, structural, and dynamic technical areas where the various analytical and model test techniques developed in the past in these areas can be applied. A flutter model program that was conducted as a part of the ASSET glide re-entry research program is described as an example of the above described test technique.

In summary then, it appears that the testing of small dynamically scaled models of winged re-entry vehicles is feasible and that useful flutter data can be obtained from such models. However, additional special purpose model tests as well as analytical studies in various combinations are also required to obtain a full knowledge of the flutter characteristics of the flight vehicle.

REFERENCES

1. Dugundji, J., "Aerothermoelastic Modeling", Notes for a Special Summer Program in Aeroelasticity, Vol. 3, Chap. 14, Dept. of Aero. Engineering, MIT, 1958.

2. Calligeros, J. M., and Dugundji, J., Similarity Laws Required for Experimental Aerothermoelastic Studies , MIT Aeroelastic and Structures Research Laboratory Technical Report 75-1, ASTIA AD 219760, May 1959.

3. Calligeros, J. M., Dugundji, J., Similarity Laws Required for Experimental Aerothermoelastic Studies, Part 2 - Hypersonic Speeds , MIT Aeroelastic and Structures Research Laboratory Technical Report 75-2, ASTIA AD 253970, February 1961.

4. Molyneux, W. G., "A Consideration of the Similarity Requirements for Aerothermoelastic Tests on Reduced Scale Models", Proceedings of Symposium on Aerothermoelasticity - ASD Technical Report 61-695, October 1961.

5. Molyneux, W. G., Scale Models for Thermo-Aeroelastic Research , Royal Aircraft Establishment (Farnborough) Technical Note No.: Structures 294, ASTIA AD 258163, March 1961.

6. Garrick, I. E., "A Survey of Aerothermoelasticity", Aerospace Engineering, Vol. 22, No. 1, p. 140, January 1963.

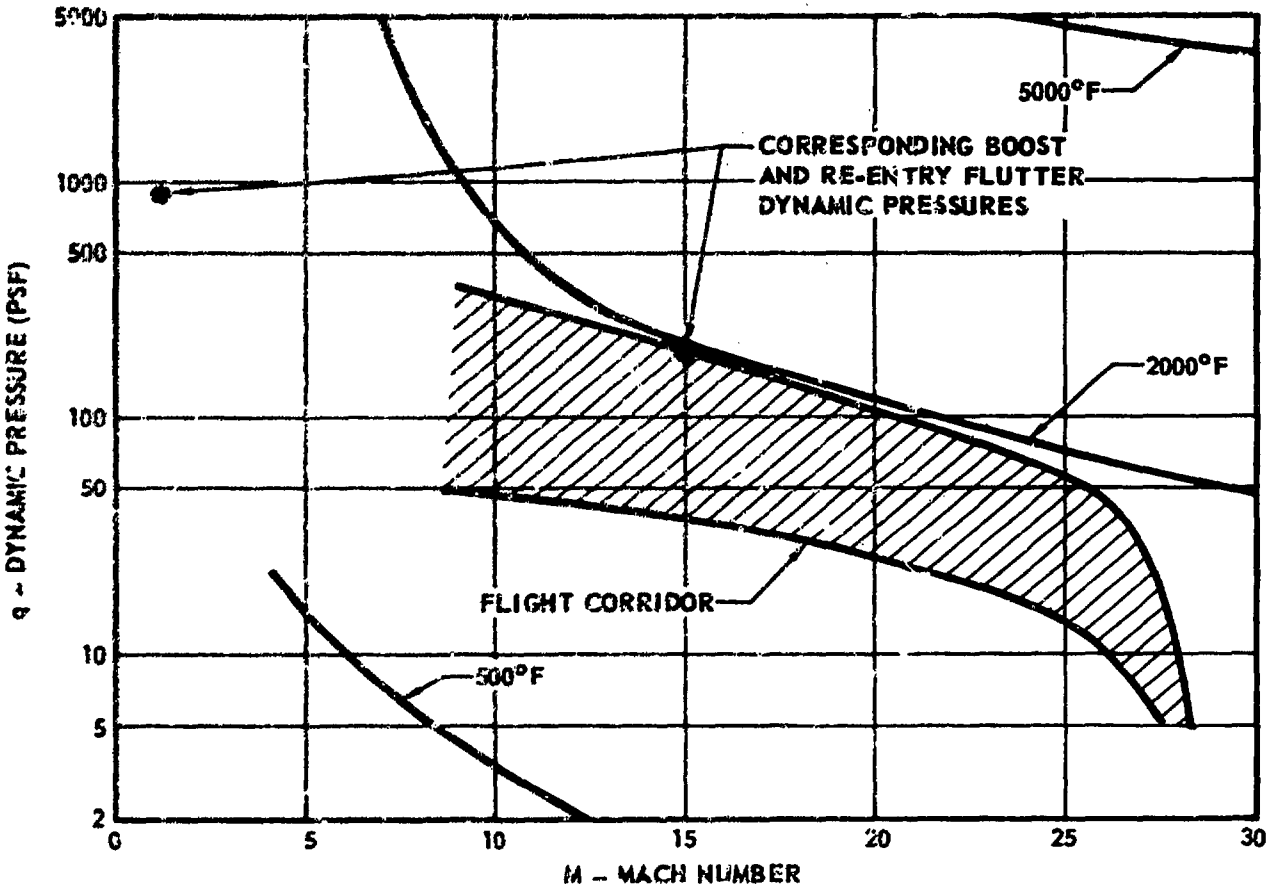

FIGURE 1. FLIGHT CORRIDOR FOR WINGED RE-ENTRY VEHICLES

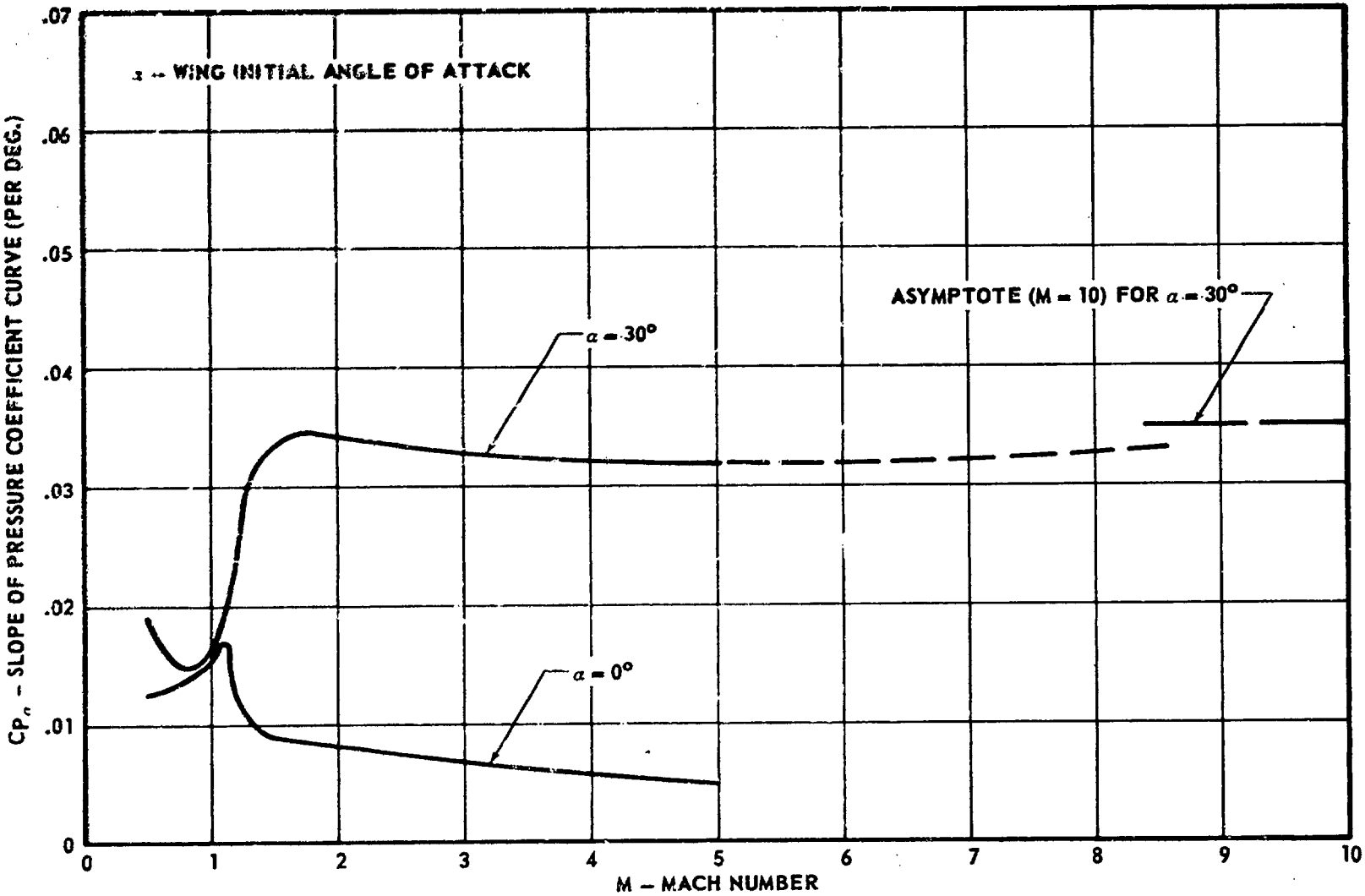

FIGURE 2. SLOPE OF THE PRESSURE COEFFICIENT CURVE VS. MACH NUMBER FOR A 70° DELTA WING

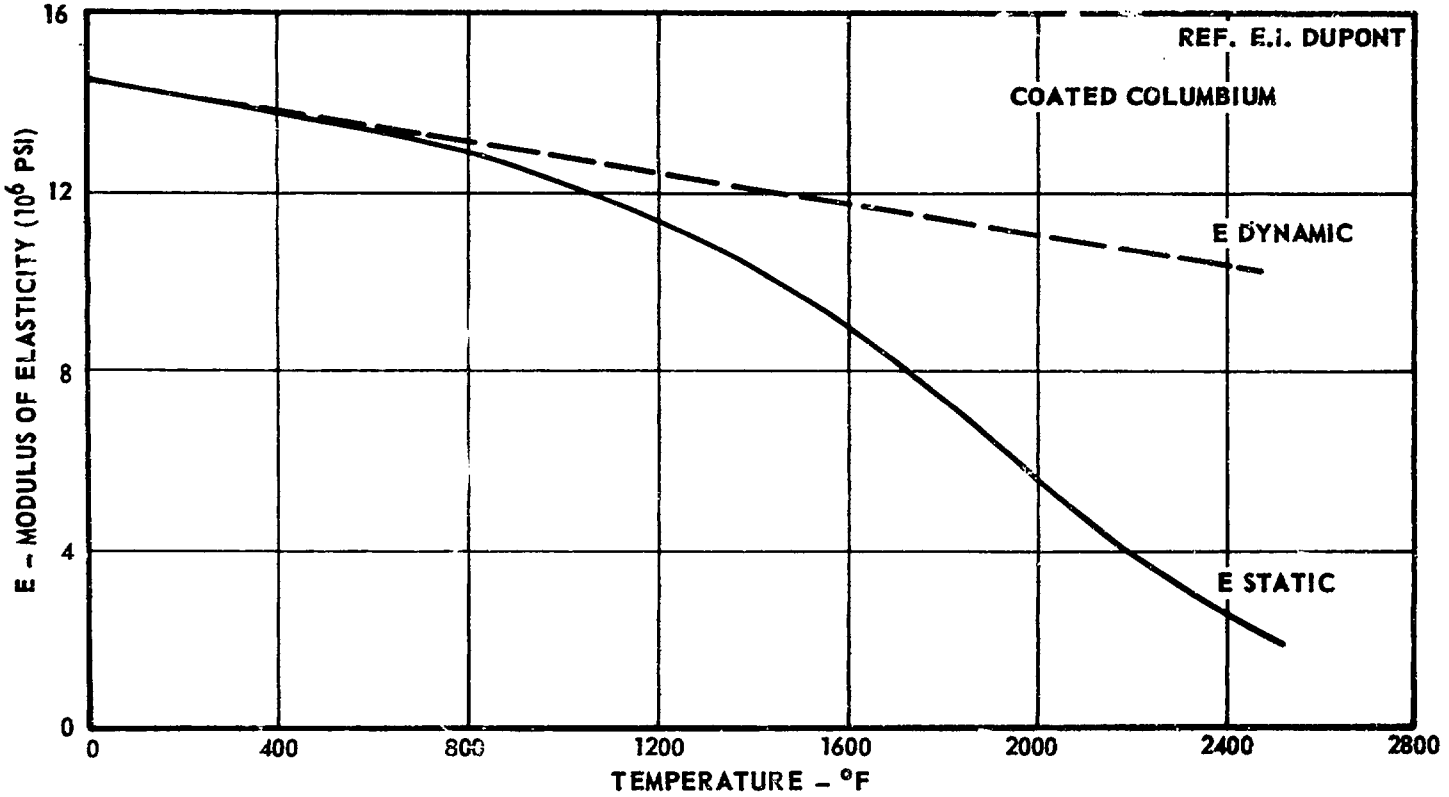

FIGURE 3. STATIC MODULUS OF ELASTICITY VERSUS TEMPERATURE FOR THE REFRACTORY METAL COLUMBIUM

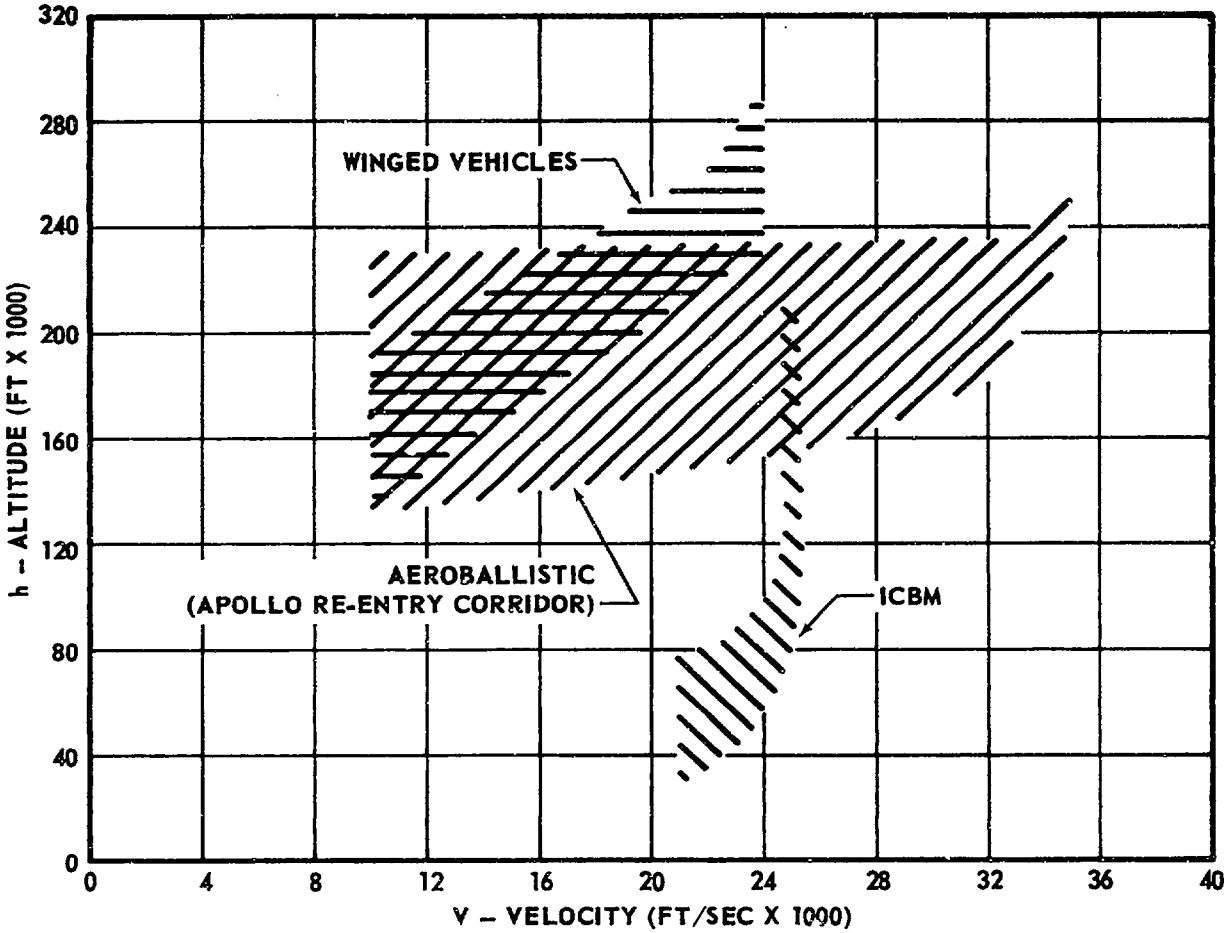

FIGURE 4. RE-ENTRY CORRIDORS FOR THREE TYPES OF VEHICLES

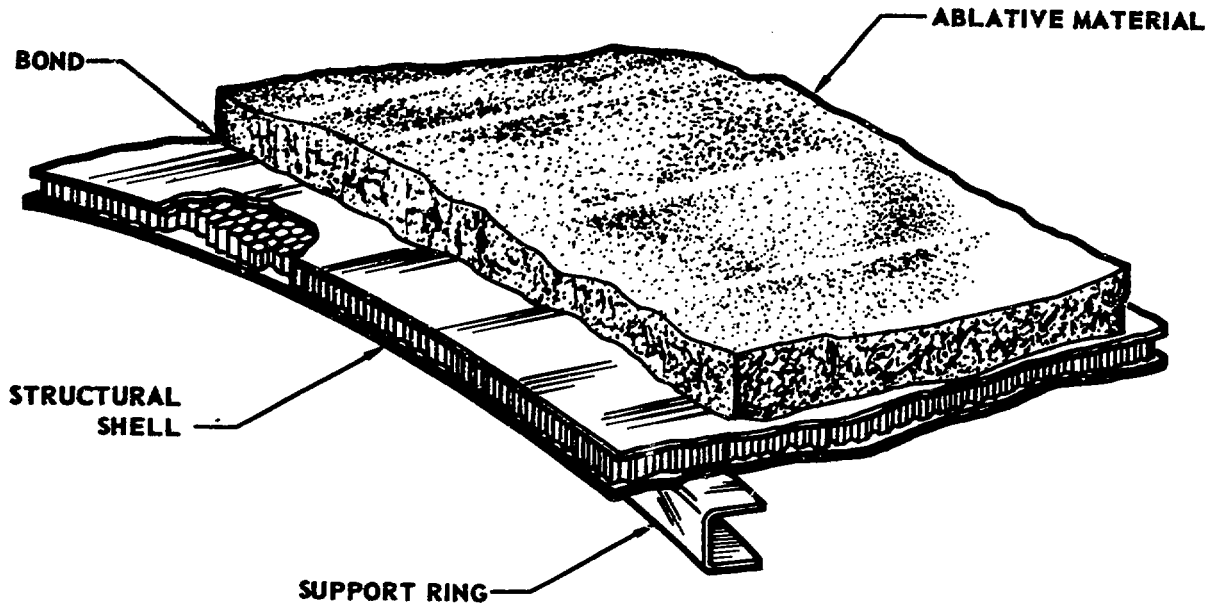

FIGURE 5. HEAT BLOCK STRUCTURAL APPROACH

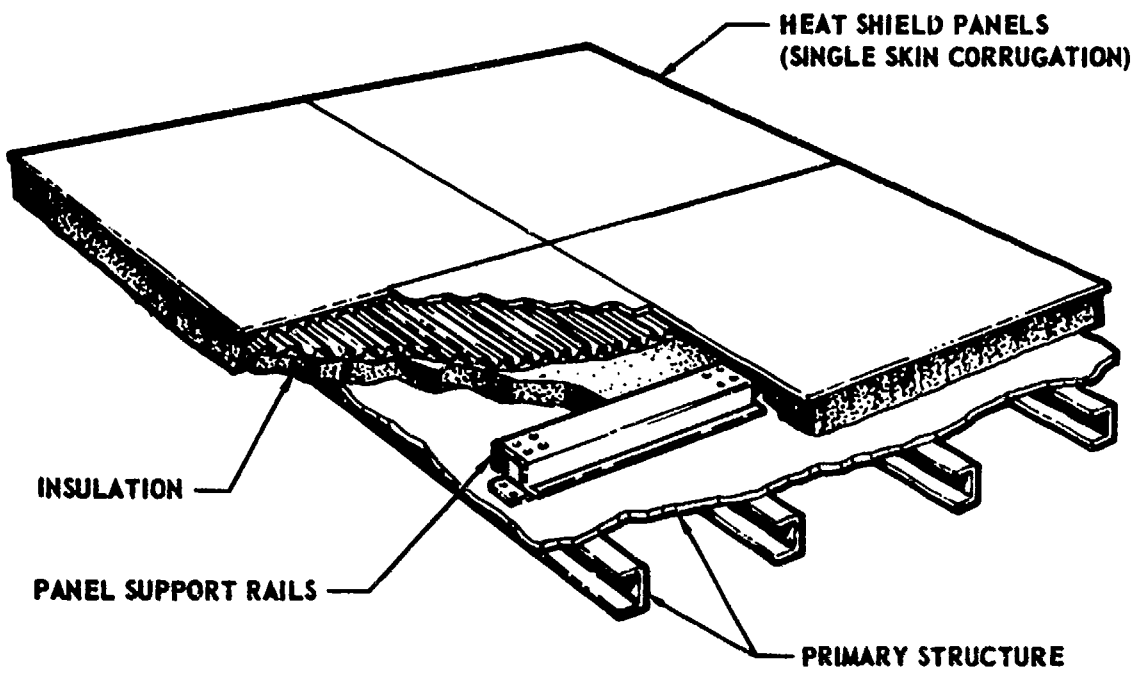

FIGURE 6. HEAT SHIELDED AND INSULATED STRUCTURAL APPROACH

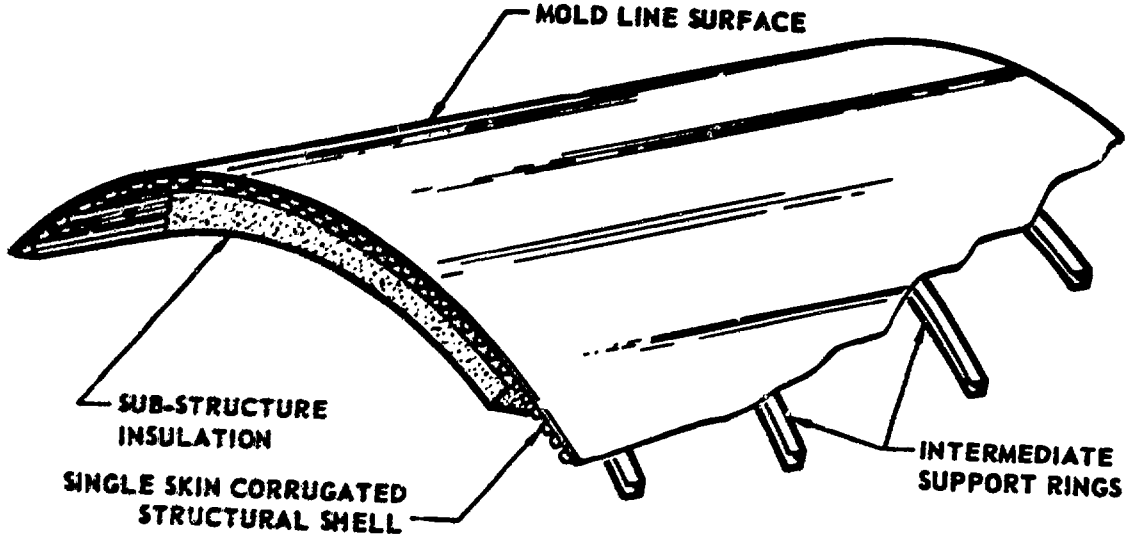

FIGURE 7. HOT STRUCTURE APPROACH

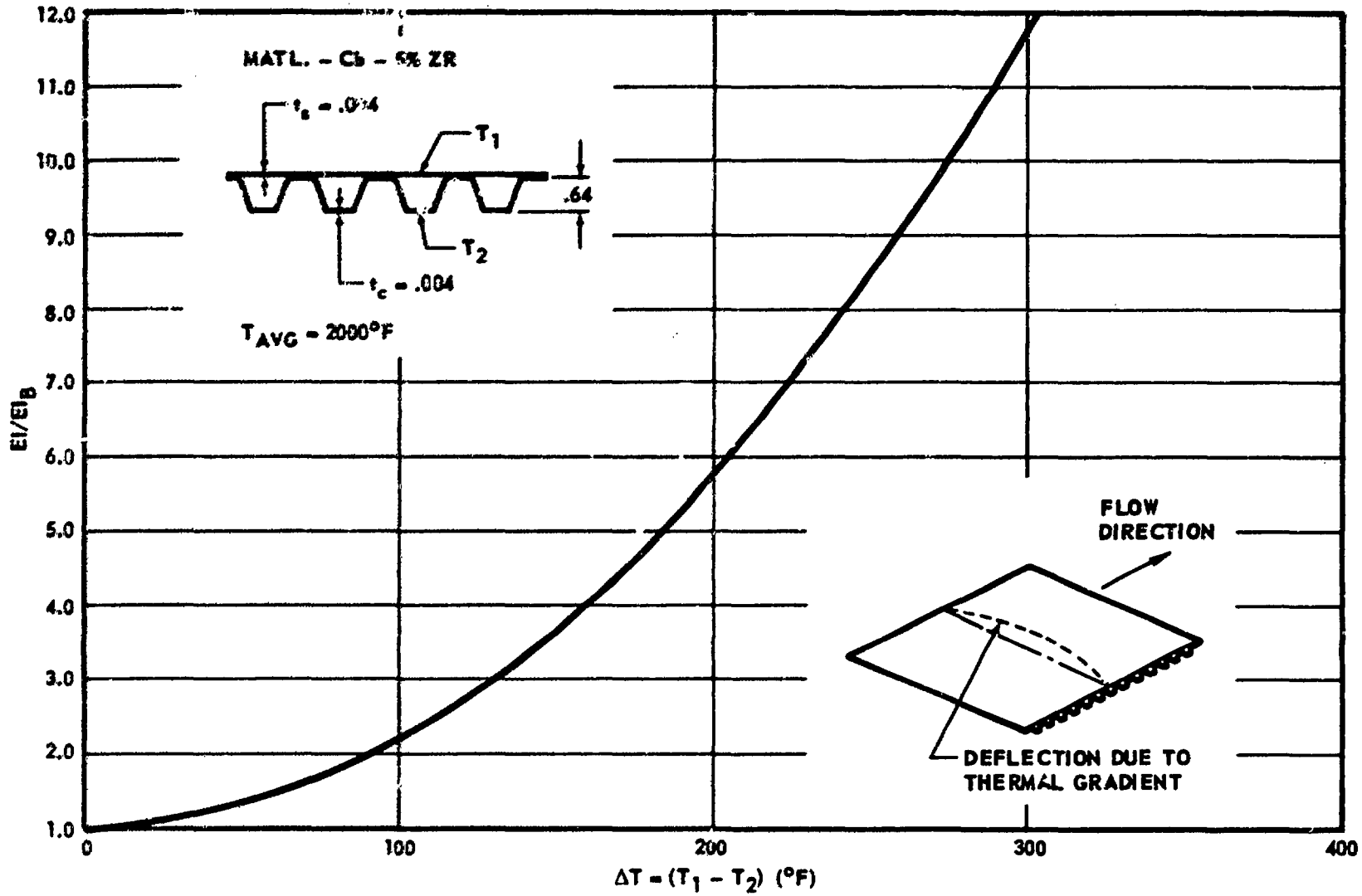

FIGURE 8. EFFECT OF THERMAL GRADIENT ON PANEL STIFFNESS

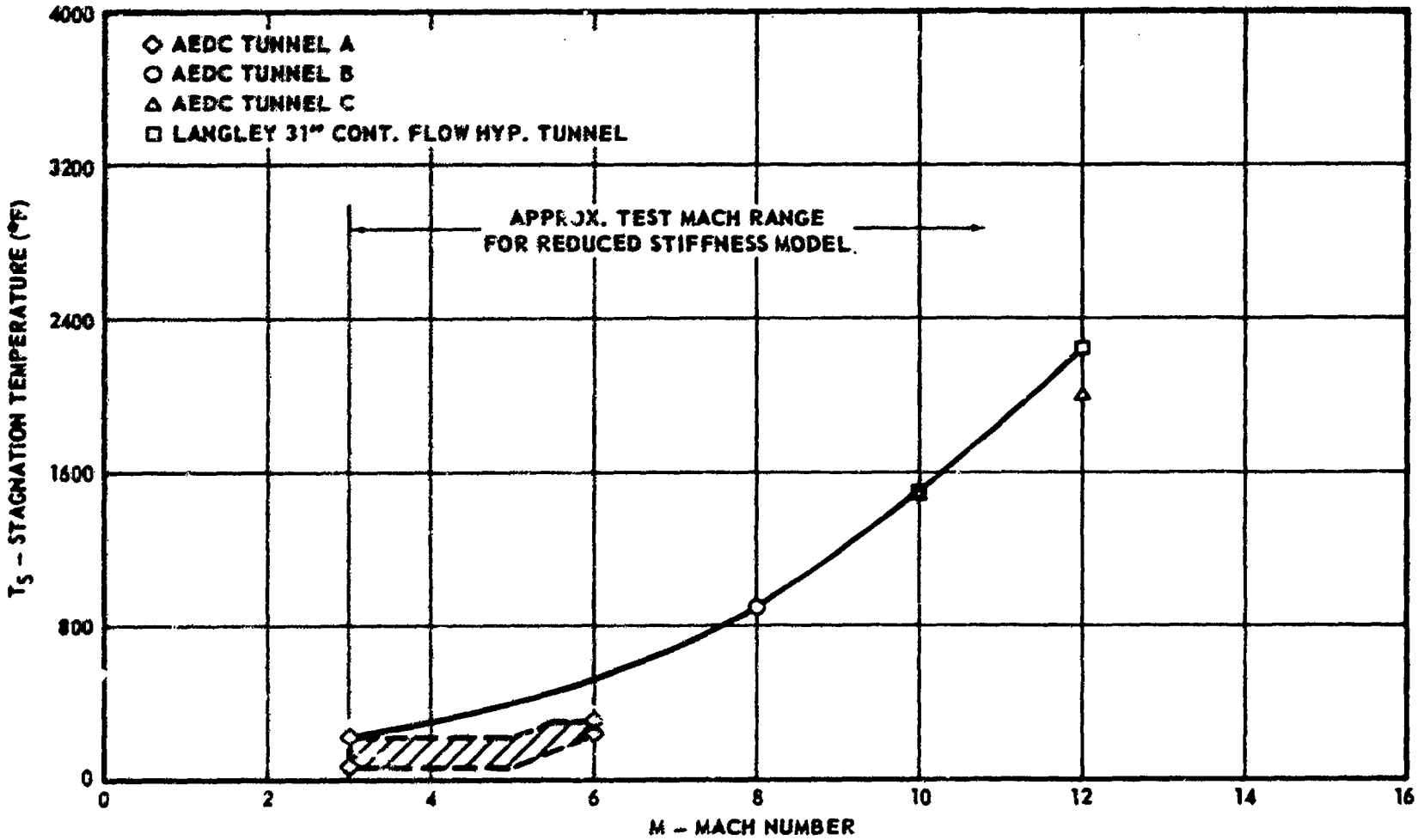

FIGURE 9. STAGNATION TEMPERATURE VS. MACH NUMBER FOR SEVERAL WIND TUNNELS

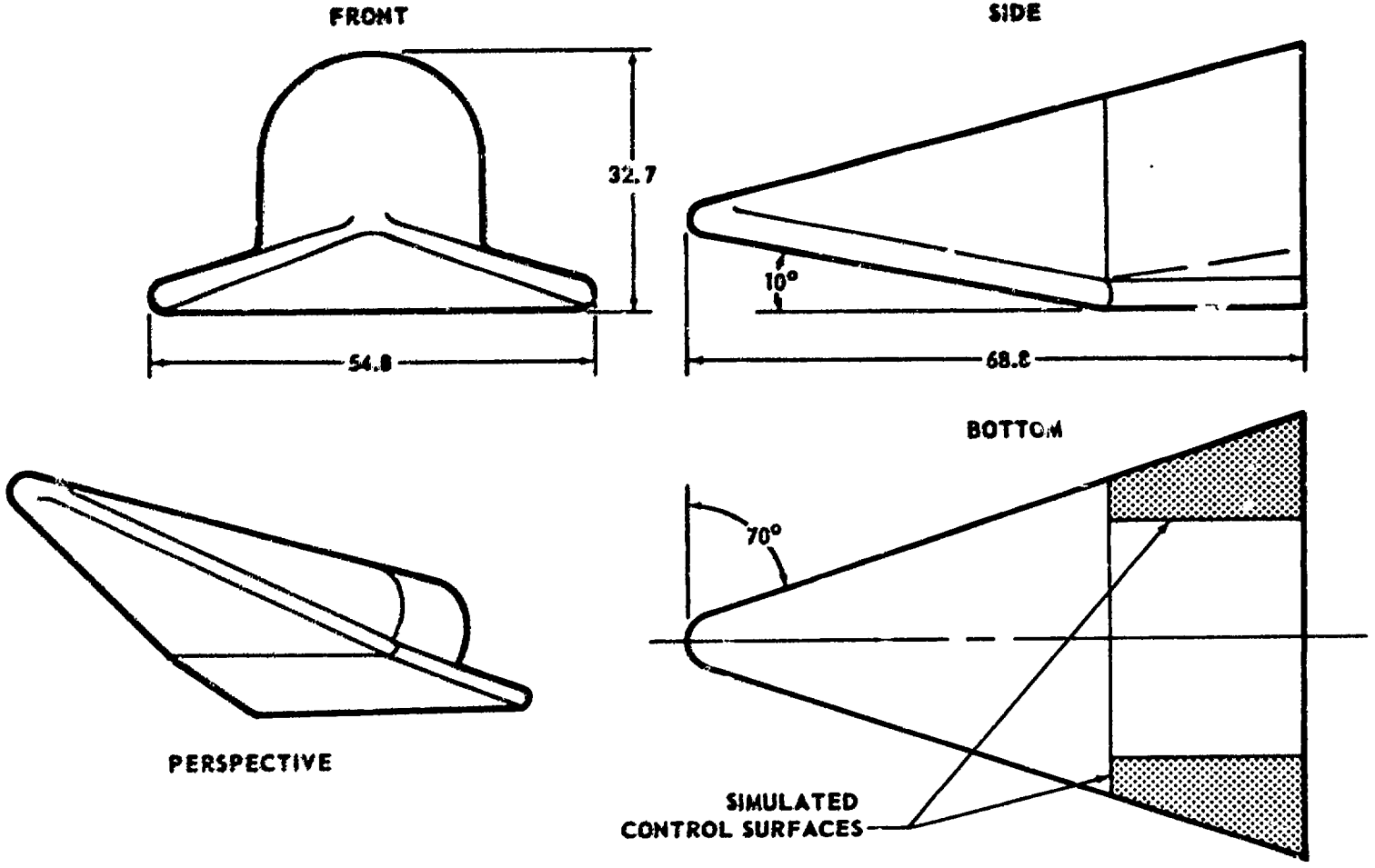

FIGURE 10. ASSET CONFIGURATION

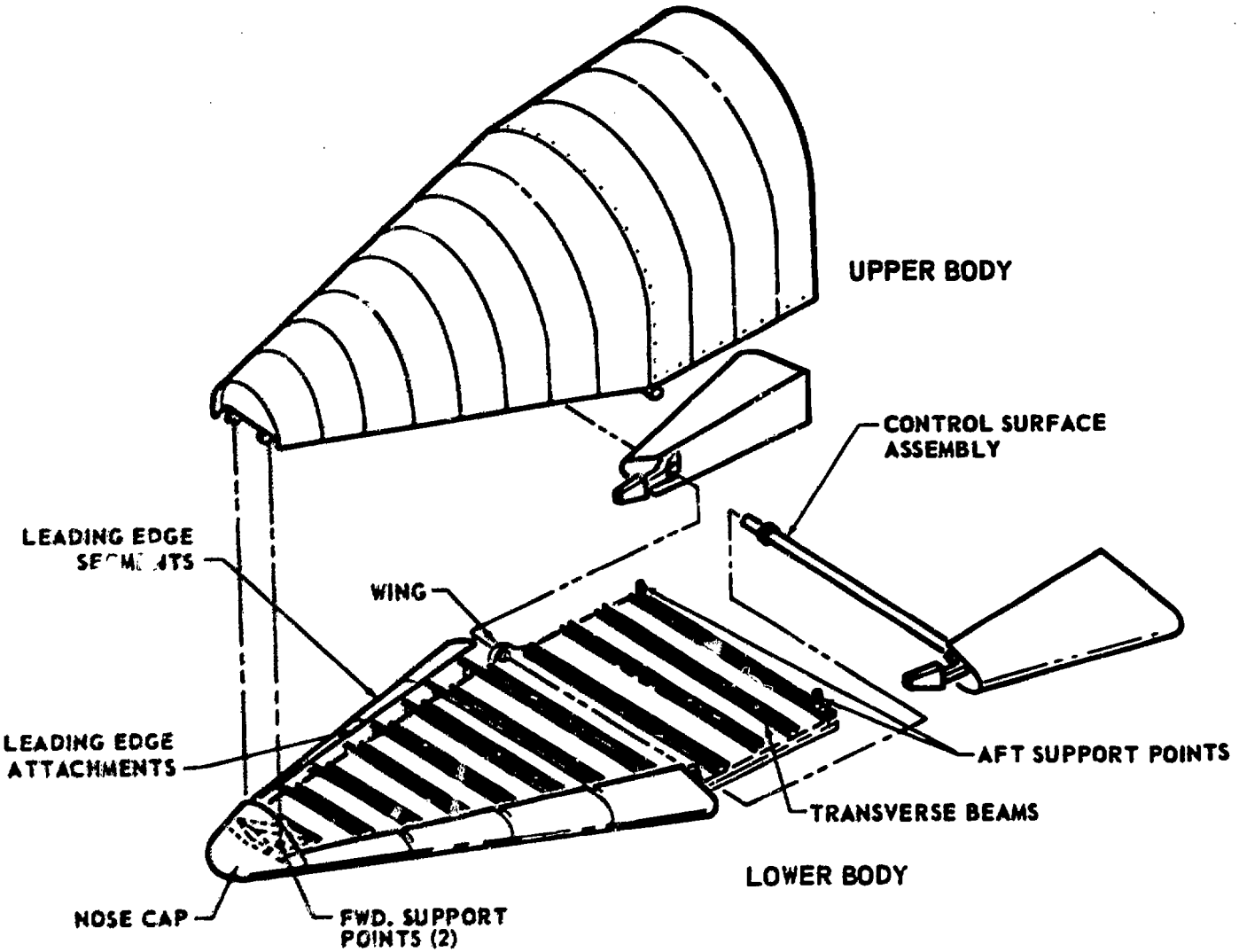

FIGURE 11 A.E.V. STRUCTURAL DESIGN CONCEPT

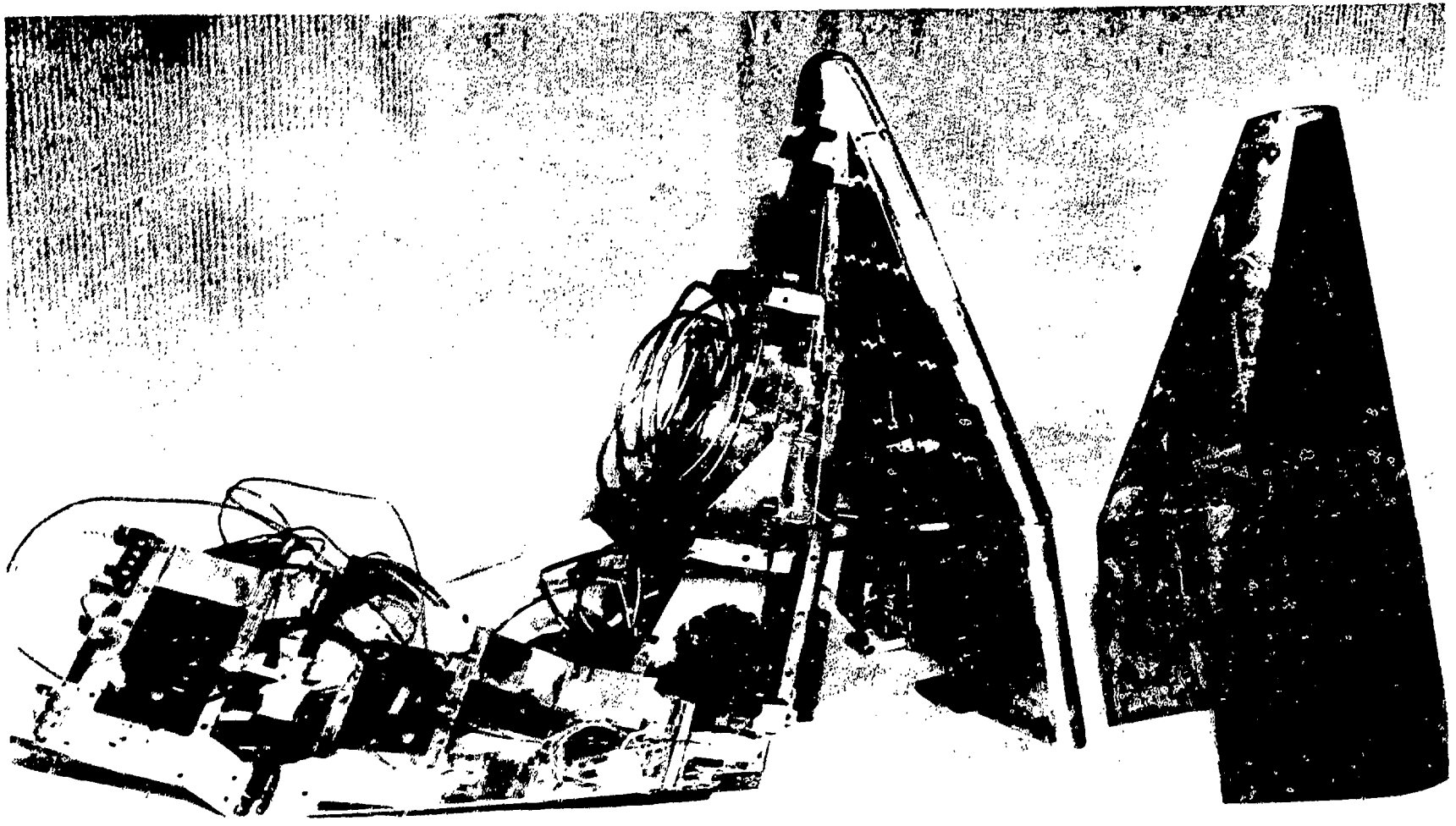

FIGURE 12. DETAILS OF MODEL CONSTRUCTION

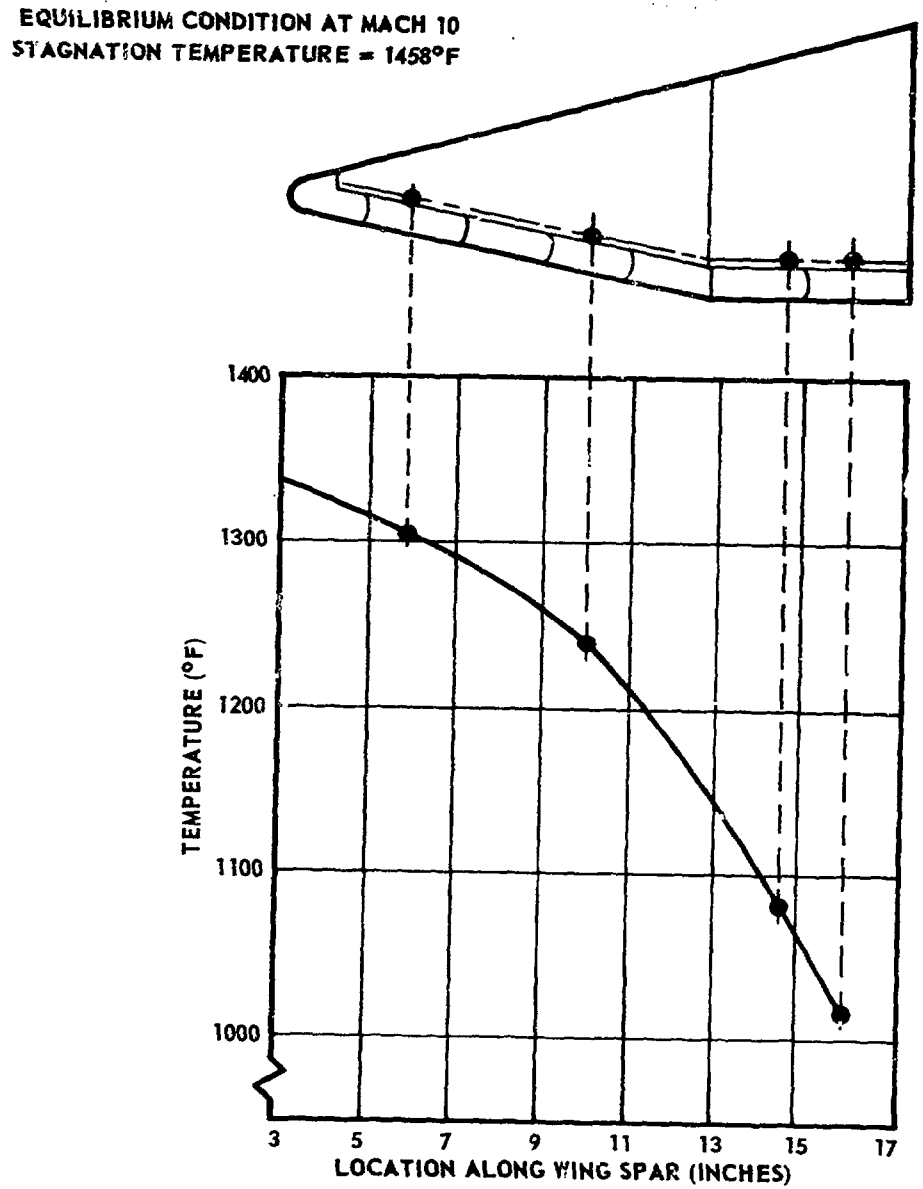

FIGURE 13. WING SPAR TEMPERATURE DISTRIBUTION IN AEDC TUNNEL C

DESIGN AND CONSTRUCTION CONSIDERATIONS OF A TRANSONIC-SUPERSONIC AEROELASTIC FLUTTER MODEL OF X-20A

Verner P. Diehl

Aero-Space Division-The Boeing Company

ABSTRACT

The application of existing and available techniques and materials to the design of a flutter model of a Dyna-Soar (X-20A) configuration is discussed. Solutions to the specific problems of simulating the structure scale weight, stiffness and aerodynamic characteristics are presented. The model was subsequently tested in the Transonic and Supersonic legs of the Arnold Engineering Development Center 16-foot Propulsion Wind Tunnel.

LIST OF ILLUSTRATIONS

DESIGN AND CONSTRUCTION CONSIDERATIONS OF A TRANSONIC-SUPERSONIC AEROELASTIC FLUTTER MODEL OF X-20A

Verner P. Diehl

Senior Group Engineer

Aero-Space Division-The Boeing Company

INTRODUCTION

The Space age is being introduced by a process of engineering development and pushing forward of the frontiers of the state-of-the-art by time consuming "blood, sweat, and tears" engineering rather than by spectacular technical "break-throughs". This has been a characteristic of space programs including the Dyna-Soar, also known as the X-20. Dyna-Soar is a typical space vehicle requiring a highly efficient structure with the following characteristics:

1. Light enough to be inserted into orbit by a contemporary booster,
2. Strong enough to withstand boost, abort, re-entry, maneuvering, and landing loads,
3. "Loose-jointed" to minimize stress and distortions due to re-entry heating,
4. Free of flutter of complete vehicle or of components during high "q"

In this discussion we will concern ourselves with one of the flutter models constructed to prove the fourth requirement. It was built during the Fall of 1960 and tested at the Arnold Research Center 16 Foot Transonic and Supersonic Propulsion Wind Tunnels.

When the model design was initiated, the Dyna-Soar structural design concepts and general configurations were established but the details were only in preliminary form. Since the proposed structure was a departure from recent aircraft practice, a flutter model was required at this point to confirm methods of analysis. It also checked out the transonic speed range where unsteady flow conditions cloud analytical methods.

CONFIGURATION

A picture of the Dyna-Soar configuration and structure will be briefly considered first. It should be remembered that the form shown in Figure I is not necessarily up to date but rather was the proposed configuration from which the model was scaled.

The structure itself resembles a World War I fighter more than a modern day airplane. It consists of an integral wing-body truss with pinned-joint-connected force members. It is non-redundant. The skin is a heat resistant

aerodynamic fairing attached to the truss thru links and flexures. The control surfaces are each mounted on two hinges with actuators located at one hinge. The tricycle landing gear would not be required in this model. The glider is mounted to the booster by the aft end of the truss and generally tapers in strength in the forward direction. The instrumentation environmental container provides torsional stiffness but is otherwise non structural.

As the full scale design progressed changes were made consistent with the latest developments in materials, manufacturing techniques, and aerodynamic developments. A point was picked in time where the configuration for the model had to be frozen. Actually changes were incorporated to the fins and elevons after this date which were major updatings. The final result was a model of close enough approximation to be a valid aeroelastic analog to prove the methods of analysis.

DESIGN FACTORS

The design of a flutter model must start with a set of requirements, some of which may have to be compromised as the design progress brings to light conflicts in the requirements, and budgetary or flow time problems. The requestor must determine the scope of the information he needs including speed and altitude envelope, significant parameters to be simulated, the variable parameters and their range of variation, and the dollar value of the data. The scaling factors are set by available wind tunnel size and operating characteristics and by model construction limitations including weight, component sizes and mounting system.

With the limited number of large transonic wind tunnels available the 16 foot propulsion tunnel at Arnold Center was chosen as most advantageous. The large test section allowed a quarter scale complete model with a tunnel blockage of one per cent. While one half of one per cent blockage is generally considered desirable for force or pressure testing, the greater blockage is not felt to seriously compromise the flutter data. The available dynamic pressure at high transonic Mach numbers, however, imposes an upper limit on the weight and stiffness scale factors.

The supersonic leg of the 16 foot propulsion tunnel posed the problem of temperature, as, in fact, does any supersonic facility. In order to get proper velocity scale (1:1) which appears in the frequency and stiffness scale factors, each Mach number requires a particular temperature. This requires that model and instrumentation be designed of materials that will be stable in the test temperature range. The initial requirements for the model specified 400°F. capability which was later reduced to 225° as the Mach number requirement was held to low supersonic. This would allow optimum temperature for starting flow in the supersonic leg for the Mach 2.25 to 3.0 range. At this temperature, common aluminum alloys are practical and suitable bonding materials, laminating resins, and even balsa wood may be used. Table 1 shows the effects of temperature on pertinent properties of some materials for this application.

It might be noted at this point that where plastics such as fiberglas laminates are to be used, the testing may have to be carried out at some particular pre-calibrated temperature. The variation of Young's modulus

with temperature is great enough on many resins that a ten or fifteen degree temperature change will place the model out of stiffness tolerance. This temperature limitation is usually not serious for subsonic or low transonic testing where variation between scaled Mach numbers and velocity are probably small. The transonic tunnels are normally run at a temperature high enough to avoid fogging or in a temperature range that requires little (or no) effort to achieve, and over heating may be the operators' only concern regarding temperature. We have found that a fixed temperature requirement poses some burden on the tunnel operators by loading them with an additional fixed parameter. In supersonic testing temperature becomes an important and necessary requirement.

The remainder of the scaling factors are shown on Table 2. The only out-of-the-ordinary factor is that for truss member area whose derivation is the same as that for the bending stiffness.

DETAIL DESIGN

The successful flutter model is the result of a delicate optimizing of a large number of factors. The model itself is an assembly in which attention must be paid to each minute detail. Each member in the structure and each part in assemblies must be considered from the standpoints:

a) Contribution to model stiffness must satisfy the desired degree of duplication of full scale structure;
b) Contribution to model weight must satisfy the scaled mass and inertia requirements;
c) Contribution to model damping should be a minimum, in general, for conservative data, and because damping is much easier to increase than to decrease if so required;
d) Contributions to stiffness and damping should not be compromised by the effect of fatigue, wear, humidity, temperature or other environmental or use factors;
e) Strength of the individual members must be enough to sustain aerodynamic loads on model components at the high transonic dynamic pressures and under supersonic starting loads;
f) Initial cost and the loss of available testing time for maintenance, repair, change of parameters should be minimized by design;
g) Determination of spares required for parts whose life properties of fatigue or wear are limited to avoid deterioration of required scaling parameters;
h) Over-all design consistent with wind tunnel safety requirements or minimizing of damage to test facility in the event of model structural failure or shedding of parts.

The various materials used in the model were selected with the foregoing considerations in mind. The Dyna-Soar structure is largely made of exotic materials to meet re-entry temperature requirements. The model used normalized 4130 alloy steel for the truss structure. This has little change in properties through the test range. It is easily welded (Figures 4 & 5) with close to ninety per cent joint efficiency. Other materials and the reasons for their selection will be covered as they occur in the structure discussion. The use of existing materials and techniques was essential to

meet scheduling requirements and to avoid developmental costs.

Another critical item in the early considerations is the type of mount to use to hold the model in the wind tunnel. Each system has its own advantages and drawbacks. The Dyna-Soar configuration does not lend itself well to component testing, except possibly for the fin-rudder. The wing and body are an intimate three-dimensional truss. The influence of either on the other would be extremely difficult to determine or simulate. This eliminated half models and wall mounted models. The use of sting mount for flutter models can have serious drawbacks. Rotary freedoms are easy to achieve but the translation freedoms are difficult. In this case preliminary analysis indicated a location forward of the center of pressure where the lower vibration modes had common node line. If the model were pivoted at this point the mode shapes should be little affected by the lack of translation. This proved to be the case. The model therefore was mounted with freedom in pitch and spring restrained freedom in roll, but without yaw or translation freedoms. The pitch point had a range of location to accommodate for differences in various stiffness models.

Confirmation that the model could be flown was arrived at in the following manner. We had at our disposal a 6" x 12" low speed wind tunnel (Figure 2) driven by a vacuum cleaner motor. In this we placed a lightweight balsa model about 1/100 scale of the Dyna-Soar with movable control surfaces and variable center of gravity. It was mounted on a simulation of the proposed support system. From it we determined that the model would fly stably (at least subsonically) with scale c.g., within a range of pivot locations, and that more than scale elevon area would be required. With normal progress in configurations the model was begun with oversize elevons but by the test time, they were replaced by latest scale elevons which were even larger.

Restraint in pitch was provided by sting clearance in the model and by a hydraulic snubber system. This consisted of a standard automotive brake master cylinder operated by the pilot by a long lever arm (Figure 8). Steel plates at the aft end of the body were gripped or released by lightplane hydraulic brake "pucks" similar to their use in light aircraft. This was more of a damper than a lock for the model could still move under high loads. Rubber bumpers on the sting cut down the impact when the model bottomed out.

In consideration of wind tunnel safety requirements, this sting had an extension forward into the nose of the model. In the remote event of truss failure this sting would retain the forward parts of the model preventing their loss downstream. In general the model parts were designed so that their loss from the model would not damage the wind tunnel. Parts that might be shed were of sheetmetal, fiberglas, or similar materials where possible. Any masses such as gearboxes were safety wired to firm structure. Weights required for mass balance were of lead wool or were made large enough to ascertain falling to the tunnel floor nearby downstream.

Aerodynamic loading on the various model components was of major concern. The model was to fly at a "1 g" load factor. This is arrived at by summation of loadings on all the surfaces when the model is at trim. At the low angle of attack resulting from mass being scaled by a cube term and area by a square term, the droop of the nose yielded a large downward force forward of the pitch point. This combined with the inertia loads of the large

forward mass weights to cause high stresses in the truss when the model bottomed out on the sting in pitch. The pitching moment caused by this nose force was balanced by deflecting the elevons for trim. The elevons were designed for this load and the elevon rotational springs and trim drive had to take the resultant hinge moment. The major flying surfaces support the down loads of the nose and the elevons plus the weight of the model. It was found that traversing the transonic range required full deflection of the elevons in both directions due to trim change.

The cant angle of the fins placed them under high aerodynamic loading in all conditions. Their structure was inherently heavy to take this load. A period of pitching instability in the model coupled with this aerodynamic and inertia loading and resulted in the only major model damage. Both fins were lost when the outboard wing truss failed inboard of the fin connection.

Concern over this fin load under starting conditions in the supersonic wind tunnel led us to design a sting mount for a fin only configuration. This was used for the first runs in the supersonic tunnel to get a feel for tunnel operation characteristics, starting load and fin supersonic loading.

While scaling of structure is the most costly approach to flutter model construction, the respective slopes and deflections of a three-dimensional truss can only be so simulated. This presents problems in detail design. The problem of preventing large variations in damping due to friction and wear and consideration of construction cost made the elimination of pin joints desirable in the model. Computer analysis indicated that rigid joints would not affect the major modes as long as the individual members were relatively flexible in bending. Since almost all the members are 2 force members, only their E x A (that is, Young's Modulus times area) and not their EI (that is, Young's Modulus times Section Modulus) need be scaled. The full scale members are thin-wall tubes, such as two inches outside diameter by .020 wall thickness. These, we were able to simulate by solid rods or standard size, small diameter, thick wall tubes of property scaled EA (Figures 3 & 5). This resulted in the proper low bending stiffness required by the model's rigid joints.

Some of the scaled members had so little area as to be impossible to make tubes. Their length then made them slender columns with length to radius of gyration ratio as high as (500). A way to stabilize these columns to prevent buckling was imperative. The solution took the form of an outer sheath or "overcoat" consisting of a thin-wall aluminum tube of relatively large diameter with a suitable filler material. The filler used was an epoxy resin filled with phenolic micro-balloons. This was injection molded in place with silicone parting agent on the member so that the overcoat could not bond to the member and therefore would not add to the E.A. of the member while still preventing buckling. The filler mixture was chosen for lightness (approximately 25 pounds per cubic foot) and hardness (or resistance to crushing or distortion) over the test temperature range. Failures such as occurred in the balsa overcoated low speed model which will be briefly described later never occurred.

The skin of the Dyna-Soar is a heat resistant aerodynamic fairing mounted so as to be free to expand and does not contribute to structure strength or

stiffness. It is made up of a large number of fairly heavy panel assemblies laid on in armadillo fashion to provide aerodynamic seal. These are attached by a system of skin beams, pin joints, sliding sleeves, flexures and expansion joints. Preserving these properties in the model was an evident requirement but a gross simplification compatible with model test environment was necessary to make fabrication and assembly costs reasonable. Two approaches were used in various portions of the model. Since the wing skin was to be beam supported it was practical to make it of brake formed aluminum strips which were flexure tied to sleeves sliding on the support beams (Figure 6). These parts were joined by soft soldering. The beams in general were pin jointed on one end with a sleeve type expansion joint on the other end. To facilitate assembly and removal the joints were aligned along the spars so a length of piano wire would serve as pins for the joints along one side of the spar. This was the function of the large wing spar fittings. The aluminum strips were separated by cast-in-place silicone rubber foam to provide aerodynamic seal and allow for lateral expansion with minimum damping. This froth type foam weighs about twenty pounds per cubic foot. It may be cast in place or preformed. Its properties remain constant to at least 300°F.

On the body, a slightly different approach was taken. As previously mentioned the forward portion was rigid. The bottom of the body was covered by the lower wing skin. The upper body skin was a "covered wagon" type. The ribs were formed by a laid up fiberglas shell with a high temperature polyester resin for temperature consideration (Figure 7). It was slotted almost to the wing level to form ribs and each rib was bolted to a clip, in turn welded to the upper body longeron. The slots opened and closed accordian fashion as the body flexed. Aerodynamic fairing for this was provided by a one-sixteenth inch skin of the same silicone foam used in the wings. This foam did not bulge or depress at the slots in the fiberglas as the body flexed. On test, it was observed that low base pressure inside the wing and body caused the large unsupported areas to suck in. This was remedied by bracing the upper wing skin support beams against the lower ones by balsa posts and by running a stiffener along the body side to bear against blocks on the wing skin. The fins also were covered by this slotted fiberglas and silicone foam skin. Here because of flat areas the inboard and outboard skins were forced to react against each other by endgrain balsa spacers.

The presence of the pilot compartment, the instrumentation capsule and the auxiliary power capsule preclude the use of diagonals in the body for torsional stiffness. These compartments are so attached to the truss that they provide body torsional stiffness but are jointed so they do not add to the longitudinal bending stiffness and offer no restraint to temperature expansion or contraction. In the model these parts were simulated by flexure mounted rigid steel tubes or "cans" stiffened with external flanges (Figure 11). They were heavy enough to meet the contents mass requirement and still allowed space for the sting to run thru the body.

INSTRUMENTATION

Instrumentation in the model to record its response included both strain gages and accelerometers. Strain gages were installed on the upper and lower body longerons and the major wing spar members. These were used only for monitoring model stresses. Sub-miniature accelerometers were used as the primary

data source. They were located to measure model pitch and roll, vertical translation at mid-body, fin vertical translation and rudder and elevon rotation. Significant parameters were monitored on oscilloscopes and all the data channels were recorded on a self developing oscillograph for rapid visual analysis. All data channels were continuously recorded on magnetic tape whenever there was wind on in the tunnel.

In order to assume valid data it is necessary to know that the model is not being restricted in motion by pitch limits or elevon or rudder stops. Systems were designed to inform the model pilot when these conditions existed. A standard automotive, pressure operated hydraulic brake light switch turned on a red indicator light on the console (Figure 8) when pressure was present in the snubber system. Along with this was a pitch indicator to show model attitude relative to the sting. It consisted of a ten inch long by .025 inch thick flat steel spring mounted to the sting so that the free end would ride inside the aft instrumentation compartment can through the entire pitch range. A strain gage bridge on the spring was read out on a milliammeter. This was calibrated simply by pitching the model to its extremes and setting the range on the console indicator, the milliammeter.

The rudders, though set for approximate trailing angle were subject to considerable variation in loading over the test speed range. The range of the rudder stops was limited by overstressing of the hinge spring. These stops consisted of a heavy yoke with a bolt in the end of each arm acting as a variable stop and bearing on the rudder hinge fitting. The arms of the yoke were strain gaged, each with two arms of a four arm bridge. Readout of this bridge was on an oscilloscope for high sensitivity and to determine if the rudder was hitting the stops intermittently or "grounded solid". Striking inboard and outboard stops deflected the trace on the oscilloscope in opposite directions so the pilot could know the direction of rudder loading.

Elevon position indication was also read out on a milliammeter. Signal was provided from a forty turn, continuous rotation miniature trimming potentiometer driven by the elevon leadscrew at the outboard drive gearbox. The elevon spring stops were similar to the rudder stops, i.e. a strain gaged yoke, and were read out on an oscilloscope. It was in fact the second beam of a dual trace instrument with the rudder stops on the first trace.

In order to assure zero lift of the model on the sting, that is, model flying at one "g" load, the sting was strain gaged just aft of the model. This was read out on the digital millivoltmeter and was the basic reference used by the pilot for trimming the model. This particular gage installation was unfortunately temperature sensitive and was really dependable only after temperatures in the test section were stabilized. Also this was the only one of the indicating systems that could not easily be cross checked during testing. It was therefore check calibrated at every tunnel entry.

For additional information thermocouples were installed at five stations in the model for the supersonic test. They gave the temperature distribution for the nose, lower body, aft upper body, wing spar and wing leading edge structure.

We have now a completed model. Calibration of the model included shake

test surveys of the model to determine response peaks and node lines with the model first suspended on soft bungee for free-free condition (Figure 9), and then cantilevered from a fifteen ton floating bedplate (Figure 10). This was followed by an influence coefficient deflection calibration of the basic structure of the model mounted in the cantilever configuration (Figure 11). The skin was partially removed since it does not contribute to the model stiffness and the damping contribution was undesirable for static deflections. In addition the applying of calibration weights was made simpler.

CONCLUSION

Immediately preceding and concurrent with the early design stages of this transonic-supersonic model we constructed a 1/5 scale low speed model and tested it in the University of Washington Aeronautical Laboratory 8 x 12 foot low speed Wind Tunnel. It served to prove out many of the construction techniques, as well as the over-all simulation and the flying characteristics of the model in test. Typical low speed scaling factors resulted in a low stiffness requirement as well as a low scale weight. The EA stiffness was met by using magnesium rods for the structure. Initial attempts at welded magnesium joints proved unsatisfactory so monel tubing joint assemblies were brazed together and the magnesium members were epoxy-bonded into them. Column stiffness was provided by balsa overcoats with string wrapping. Actual column failures occurred with the magnesium rods pushing out between the wrappings. It did prove the technique, though. The skin of both the wing and the body was made in relatively large flexure supported, balsa panels, sealed by foam rubber strips. This skin provided attachment for mass balance weights as well as aerodynamic fairing. Models of three stiffnesses were tested, two-thirds nominal, nominal, and twice nominal. It was tested successfully at the University of Washington Aeronautical Laboratory 8 x 12 foot subsonic tunnel on the Boeing flutter model rod support. This test served to confirm the handling characteristics of the configuration in the tunnel.

Models with three levels of longitudinal bending stiffness were constructed for transonic and supersonic testing in an effort to bracket the potential scale stiffness. They were constructed using current materials and techniques. Their calibration indicated successful simulation of the proposed structures and agreed with analytical results. The testing in the transonic and supersonic legs of the Arnold Center Sixteen Foot Propulsion Wind Tunnel (Figure 12) covered Mach numbers to M = 2.25 and high dynamic pressures. The models demonstrated the ability to perform under these conditions and to withstand the supersonic starting shock. This test performed early in the Dyna-Soar program established the analyses for handling parameter changes analytically and eliminated time consuming uncertainties. Further component and vehicle flutter testing on the Dyna-Soar can probably be limited to checkout of the final design configuration.

TABLE 1

Reduction in Material Properties at 225% and 400°F from Room Temperature Values

MATERIAL	T = 225°F		T = 400°F	
	YOUNGS MODULUS	STRENGTH ULTIMATE	YOUNGS MODULUS	STRENGTH ULTIMATE
ALUMINUM ALLOY 2024-T3	3%	7%	10%	36%
ALLOY STEEL 4130 (125 KSI)	0%	3%	1%	7%
FIBERGLAS LAMINATE POLYESTER RESIN	25%	36%	Above Service Range	
BALSA	Shrinks and Splits		Chars	
SHELL EPON 901				
-B2 Catalyst		10%	Above Service Range	
-B3 Catalyst		0%		80%

TABLE 2

Scaling Factors

SCALE FACTORS

Length $\frac{\ell_m}{\ell_a} = .25$

Density $\frac{\rho_m}{\rho_a} = 1.0$

Velocity $\frac{V_m}{V_a} = 1.0$

Temperature $\frac{T_m}{T_a} = 1.0$ for $\frac{M_m}{M_a} = 1.0$

Weight $\frac{W_m}{W_a} = \left(\frac{\ell_m}{\ell_a}\right)^3 \frac{\rho_m}{\rho_a} = .01563$

Frequency $\frac{\omega_m}{\omega_a} = \frac{\ell_a}{\ell_m} \frac{V_m}{V_a} = 4.0$

Stiffness $\frac{(EI)_m}{(EI)_a} = \frac{\rho_m}{\rho_a} \left(\frac{\ell_m}{\ell_a}\right)^4 \left(\frac{V_m}{V_a}\right)^2 = .0039063$

Truss Member Area $\frac{(EA)_m}{(EA)_a} = \frac{\rho_m}{\rho_a} \left(\frac{\ell_m}{\ell_a}\right)^2 \left(\frac{V_m}{V_a}\right)^2 = .0625$

Mass Inertia $\frac{I_m}{I_a} = \frac{\rho_m}{\rho_a} \left(\frac{\ell_m}{\ell_a}\right)^5 = .00097657$

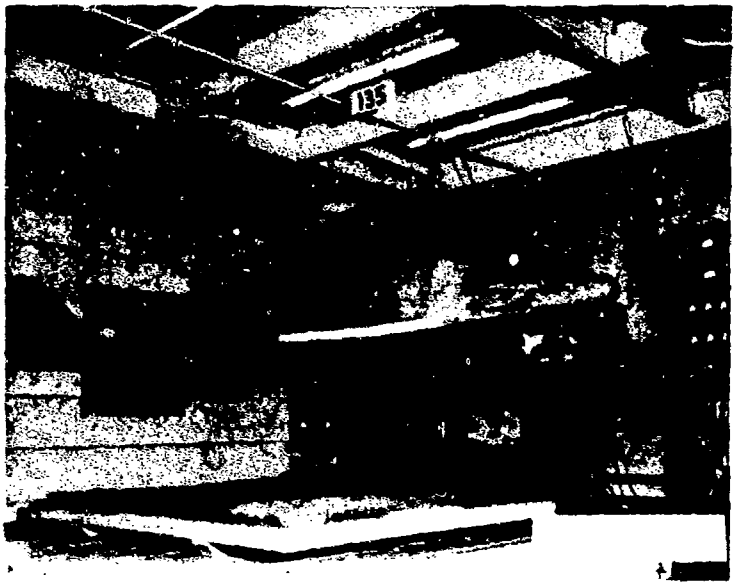

FIGURE 1
COMPLETED MODEL

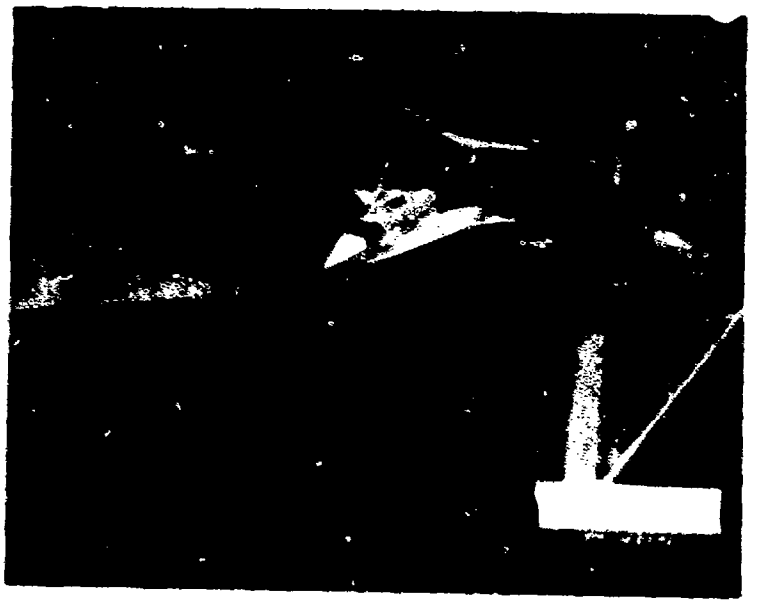

FIGURE 2
MOUNT CHECKOUT TEST

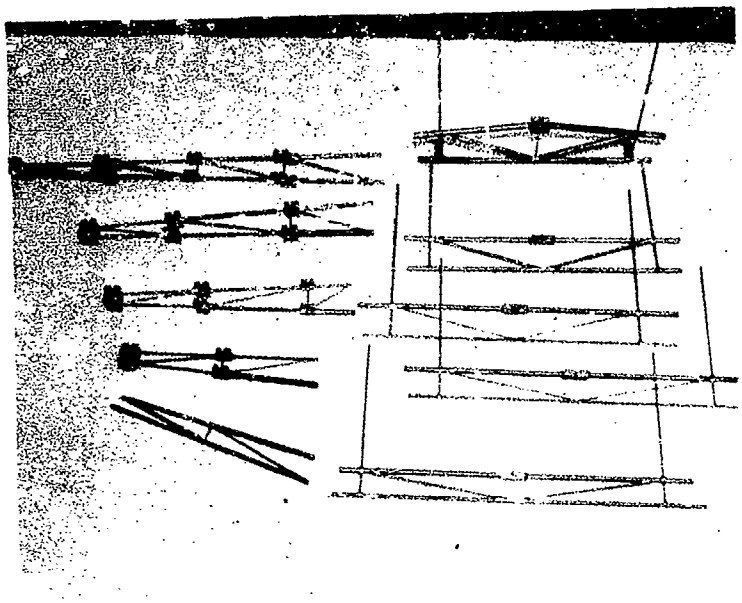

FIGURE 3
TRUSS SUB-ASSEMBLIES

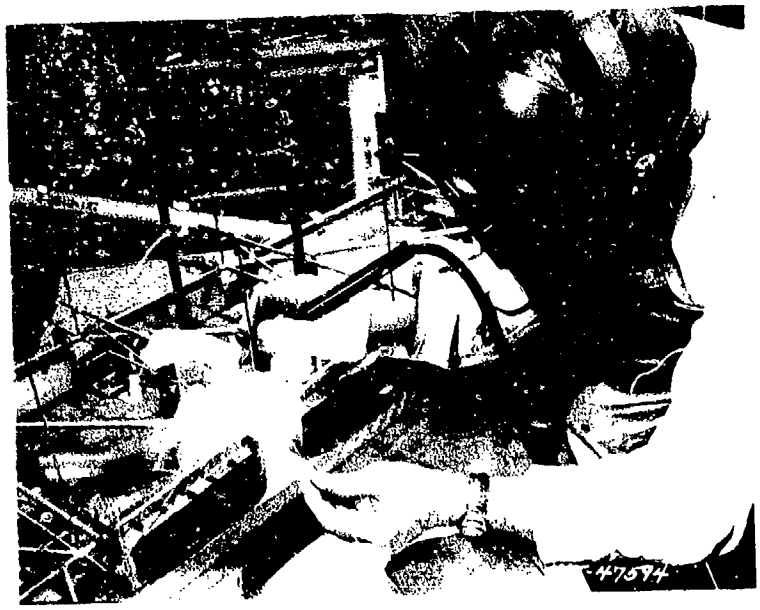

FIGURE 4
JOINT WELDING

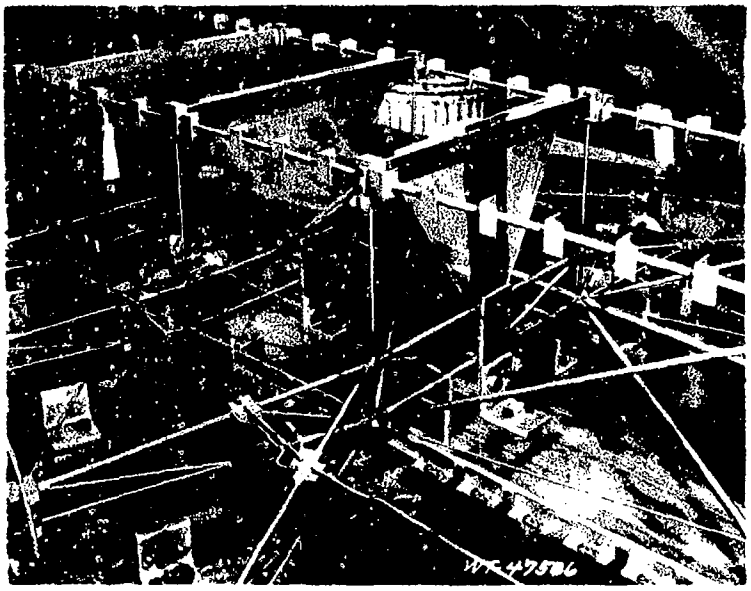

FIGURE 5
BODY TRUSS ASSEMBLY

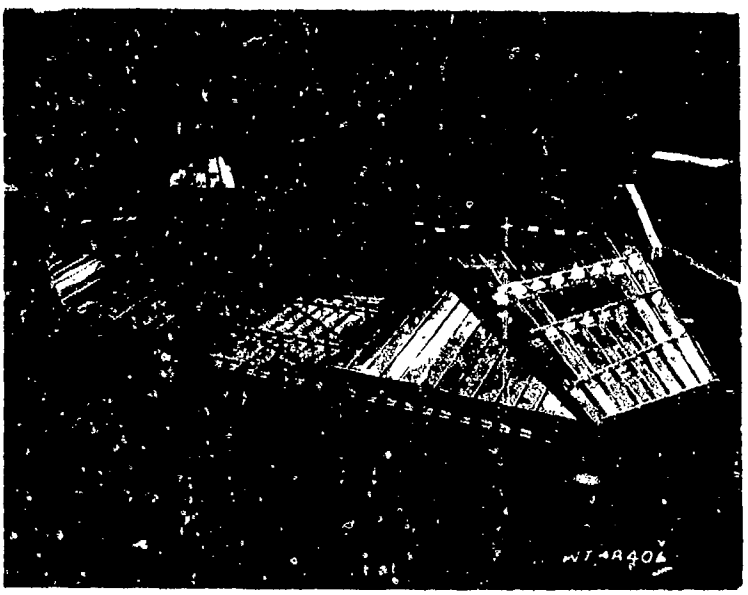

FIGURE 6
WING SKIN

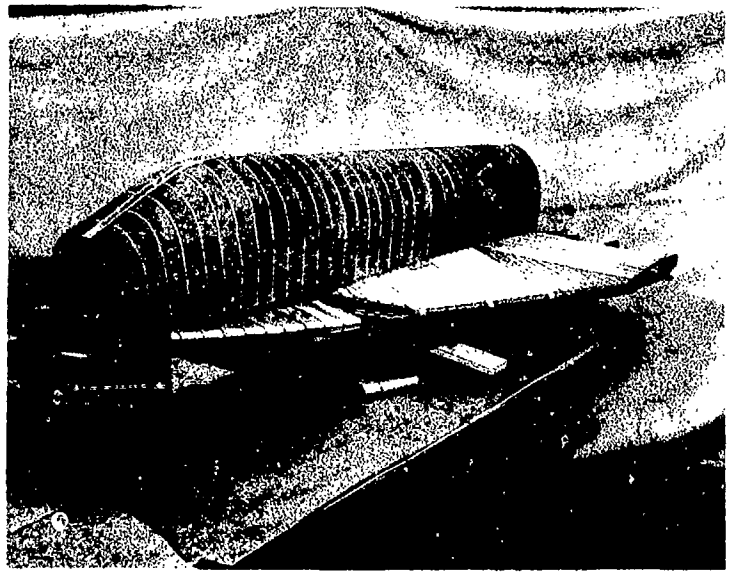

FIGURE 7
WING-BODY SKIN

FIGURE 8
MODEL CONTROL POSITION

FIGURE 9
FREE-FREE CALIBRATION

FIGURE 10
CANTILEVER CALIBRATION

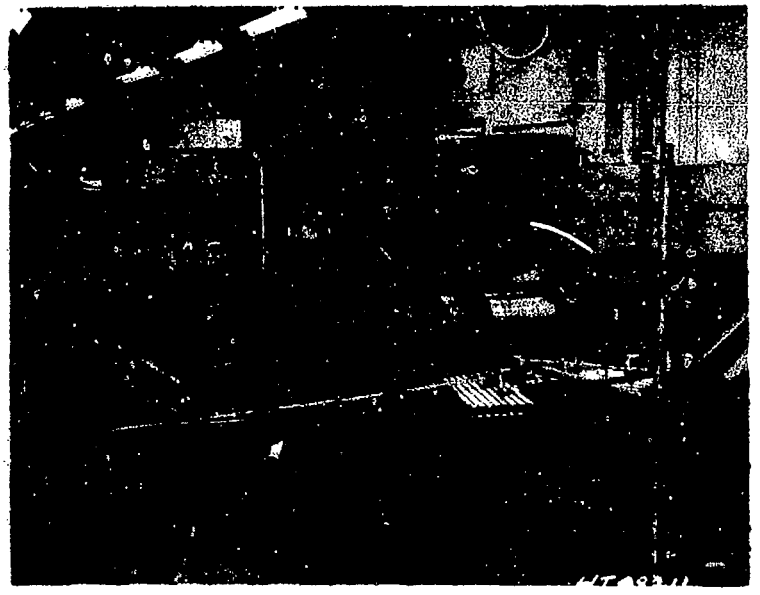

FIGURE 11
INFLUENCE COEFFICIENT CALIBRATION

FIGURE 12
DYNA SOAR MODEL IN 16 FOOT
SUPERSONIC TEST SECTION

SESSION VI

AIRCRAFT APPLICATIONS

Chairman: Dr. Holt Ashley
Massachusetts Institute of Technology

DYNAMIC MODEL TESTING OF THE XC-142A AIRCRAFT

A. L. Head, Jr.

W. D. Smith

Chance Vought Corporation

ABSTRACT

This paper presents some of the results of the dynamic model tests of the XC-142A aircraft. Of particular interest are the testing techniques associated with propeller whirl flutter. The model incorporates simulation of the engine mount dynamics, of the propeller dynamics, and of the shafting dynamics in addition to the regular structural dynamics. The model is used to check mount failure conditions with respect to flutter and to check dynamic loads with respect to propeller unbalance. The model will also be used in further tests to measure total aerodynamic coefficients through the zero angle of attack range.

LIST OF FIGURES

LIST OF TABLES

DYNAMIC MODEL TESTING OF THE XC-142A AIRCRAFT

A. L. Head, Jr.* and W. D. Smith**

1.0 INTRODUCTION

The XC-142A Aircraft is a tilt wing VTOL vehicle designed to demonstrate the all-weather operational suitability of VTOL transport aircraft. The airplane has superior STOL as well as VTOL capabilities. It features a large cargo compartment to transport a payload of 8,000 pounds for VTOL missions while cruising at 250 knots. The limit velocity is 400 knots.

The airplane is powered by four T64-GE-6 wing mounted engines driving four propellers and a tail rotor through an interconnected shafting system. The wing is of moderately high aspect ratio mounted high on the fuselage, and can be tilted through an angle of 100 degrees for the hovering and transition mode. The wing incorporates full-span double-slotted flaps. Leading edge slats for stall suppression are incorporated on the outboard side of each engine nacelle to compensate for the angle-of-attack induced by the propeller slipstream in these areas. The vertical tail is a conventional fin and rudder arrangement centrally located on the fuselage that supports the all-moving horizontal tail assembly.

Figures 1 and 2 show the airplane in the conventional flight mode and the hover mode, respectively.

Inherent in the design of this type of aircraft are many formidable dynamic, aeroelastic, and acoustic challenges. Consequently, considerable effort has been expended during the design phase of this aircraft to define clearly the major dynamic, aeroelastic, and acoustic design requirements. A general review of the design programs conducted in the above technical areas is given in reference (1). This paper will discuss the details associated with the dynamically similar model program for the XC-142 Aircraft.

---

* Supervisor, Structures-Dynamics Group, Chance Vought Corp., A Division of Ling-Temco-Vought, Inc., Dallas, Texas

** Lead Engineer, Structures-Dynamics Group, Chance Vought Corp., A Division of Ling-Temco-Vought, Inc., Dallas, Texas

2.0 PHILOSOPHY AND OBJECTIVES

The dynamically similar model program for the XC-142A Aircraft is part of the more general flutter program. The philosophy of design for flutter employed in the flutter program is essentially the same as that enounced in reference (2) and restated in reference (1); namely, the structural design must be optimized to produce the required flutter margin for the least weight. The required flutter margin can be stated briefly as follows: At any flight condition within the flight envelope, flutter must not occur within a 15 percent margin on either equivalent airspeed or Mach number. The attainment of the minimum-weight design required by the above philosophy necessitates the establishment of well coordinated analytical and experimental programs.

The dynamically similar model program is one of the experimental programs established to implement the philosophy of design for flutter. The objectives of this model program for conventional flight configurations are as follows:

a. To determine experimentally the flutter characteristics of a healthy* XC-142A Aircraft within the required flutter margin boundary.

b. To determine experimentally the effect on flutter of important parametric variations; for example, rotational stiffness variation about hinge axes of control surfaces and rotational free-play variation about hinge axes of control surfaces.

c. To determine experimentally the effect on flutter of various failures consistent with the failure philosophy.

d. To determine experimentally the steady-state response of the structure to propeller unbalance.

e. To determine experimentally the static aerodynamic derivatives of the flexible model by using the dynamically similar model as a force model.

The objectives of this program do not include the investigation of any hover or transition configurations. During hover and transition the velocities are relatively low and no flutter-type instabilities are anticipated.

3.0 MODEL DESIGN AND FABRICATION

To accomplish the objectives set forth above and to facilitate the comparison of analytical and experimental results, the model program is divided into three distinct phases as follows:

a. Phase I - Wing Test

b. Phase II - Empennage Tests

c. Phase III - Complete Aircraft Tests

---

* A healthy aircraft is one that has no failed members; that is, all primary structural components are as designed.

The wing, empennage, and fuselage are designed as components that can be assembled into the complete aircraft model. Consequently, in the Phase I tests the wing is mounted on a constrained, tailless fuselage that has the rigid body inertial characteristic of the empennage simulated. In the Phase II tests the empennage is mounted on a constrained fuselage with or without the wing. Finally, in the Phase III tests the completely assembled airplane model is constrained only in drag,side translation, and roll.

3.1 Design Criteria

The model is designed for testing in the Chance Vought Low-Speed-Wind-Tunnel. A derivation and discussion of the dynamic similitude factors used in the design is presented in the Appendix. As shown therein, the geometrical scale factor is 0.100. The model design criteria are listed below:

a. Inertial and stiffness distributions of the model components must be within 10 percent of their required values.

b. Important frequencies must be within 5 percent of their required values.

c. Node lines associated with the important frequencies must accurately simulate their full-scale counterparts.

d. The model must be able to withstand the static loads associated with an angle-of-attack change of 4 degrees at 100 knots equivalent airspeed on the model (316 knots on the airplane).

e. The model must fly at the correct lift coefficient for a given angle-of-attack. This implies that the elastic deformations due to the static aerodynamic loading resulting from an angle-of-attack change must be equal to those obtained on the aircraft multiplied by the geometrical scale factor.

3.2 Model Construction

The construction of the model fuselage and surfaces is conventional. In each, a structural spar made of magnesium is featured to provide all the required stiffness and strength characteristics. Segments made of balsa wood, silk, and tissue are attached to the spars to provide proper aerodynamic contours. No structural ties exist between adjoining segments except through the spar, rendering the segments nonstructural with regard to spanwise stiffness distributions.

All primary controls for conventional flight are incorporated on the model. Since neither hover nor transition flight configurations are to be investigated, the leading edge slats and trailing edge flaps are not incorporated on the model. Provisions are made in the design of the wing pivot, aileron, rudder, and horizontal tail rotational constraints to facilitate the variation of these constraints. This variation includes the ability to introduce rotational free-play.

The propellers are joined by a shafting system similar to the airplane system. A small electric motor located in the fuselage powers the propellers to provide incremental adjustment of propeller rotational velocity.

The propeller blade angles are manually adjustable. The electric motor is not intended to supply power to the propellers to simulate various thrust conditions. The propellers are essentially windmilling propellers connected via the shafting system to insure that each propeller turns at the same rotational velocity. The basic variation of rotational velocity is obtained by varying the propeller blade angles.

The construction of the engine-gearbox-propeller mounting system follows the actual aircraft design in detail.

The all-moving horizontal tail is controllable about its pitch axis. A small electric motor within the fuselage provides the actuation power necessary to slowly vary the angle-of-attack of the horizontal tail. This feature is built into the model to provide trim power during the complete airplane tests.

As examples of the general construction techniques, Figures 3, 4, 5, and 6 show skeletal details of the wing, engine-gearbox-propeller mounting system, empennage, and fuselage, respectively.

3.3 Simulation

A very high degree of dynamic simulation is achieved in the model and its components. Modes and frequencies of each component are checked prior to the assembly of the complete model. In general the first four modes and frequencies of each surface are accurately simulated. In the case of the wing, the first twelve coupled modes are simulated. As indicated previously, aileron, rudder, and horizontal tail degrees of freedom are accurately simulated. However, certain aspects of the detail simulation deserve special mention.

The propeller blades are constructed of a twisted magnesium spar formed to contour with balsa wood and silk. The inertial properties and the fundamental bending frequency of each blade are simulated.

The model shafting system does not simulate the airplane shafting dynamics. However, the model design presented some detail design problems. Shafting critical speeds are high enough to avoid problems with model operation; however, the design of flexible couplings did present problems. Flexible disc couplings first employed in the design exhibited poor fatigue characteristics. Presently, a universal joint-spline design is giving satisfactory service.

The dynamic simulation of the wing presented a two-dimensional vibration problem requiring that normal bending, torsion, and in-plane bending dynamic characteristics all be accurately simulated.

Propeller whirl flutter considerations dictated that the simulation of the engine-gearbox-propeller system be very accurate. This presented perhaps the most difficult model design problem. The support system is a multi-redundant strut arrangement as shown in Figure 4. The engine and gearbox each has six rigid body degrees of freedom. The flexible connection between the engine and gearbox and the flexibility of each strut are all accurately simulated. The model support system has a strut where the airplane has one.

Each strut on the model is removable to permit the simulation of failure conditions. To quality the final model design, measured influence coefficients in terms of the twelve degrees of freedom previously mentioned are compared with calculated values in Table 1. Also, the first six modes and frequencies of the engine-gearbox-propeller system mounted on a rigid wing are used for the final check. A frequency comparison of model and aircraft frequencies is given in Table 2.

As illustrations of the simulation achieved, comparisons of wing inertial distribution, wing stiffness distribution, and wing frequencies are shown in Figure 7, Figure 8, and Table 3, respectively.

4.0 MODEL TESTS AND RESULTS

At the time of this writing the Phase I Wing Tests are complete and the Phase II Empennage tests are in process. The Phase III Complete Aircraft Tests are scheduled after the presentation date of this paper.

4.1 PHASE I - WING

As previously described in the Phase I tests, the wing is mounted on a constrained fuselage. During these tests the empennage is inertially simulated only. The fuselage is constrained in vertical translation and roll at the two nodal points of the fundamental free-free symmetric mode of the fuselage. Struts housing the nodal point attachments are connected to the wind tunnel aerodynamic balance system. Trimming of the model in pitch is accomplished by tunnel controls that vertically translate the aft strut. The Phase I configuration mounted in the tunnel at a high angle-of-attack is shown in Figure 9.

The instrumentation consists of twelve strain gage bridges, a propeller tachometer, the wind tunnel balance system, two high intensity strobolights, and two high-speed motion picture cameras. The strain gage bridges are positioned to measure the following: normal-plane bending, in-plane bending, and torsion of both sides of the wing near the wing-fuselage attachments; torsion near the right outboard nacelle; wing pitch about the pivot axis relative to the fuselage; and vertical and lateral motions of both of the left gearboxes relative to the adjoining wing. The strain gage and tachometer output signals are recorded on a 26-channel oscillograph during the tests. The wind tunnel balance system is used to record the usual six-component force data during the tests. The high-speed motion pictures are taken as needed.

Complete static calibration tests of the instrumentation are performed on the model as installed in the tunnel prior to actual wind tunnel testing.

The testing procedure consists of flying the model in the tunnel and monitoring continuously the model strain gage instrumentation and the aerodynamic balance data. The model instrumentation provides the means of preventing the overloading of the model. The aerodynamic balance data shows the gross model loads. Essentially the model is flown at a 1 "g" flight condition by monitoring the flight loads on the model.

The objectives of the Phase I - Wing Test are as follows: clear the healthy wing to the required flutter margin boundary; evaluate the effect on flutter of aileron rotational free-play and stiffness variations; evaluate the effect on flutter of various failure conditions; evaluate the effect on flutter of a feathered propeller; and determine the static aerodynamic derivatives of the flexible wing over as wide a range of angle-of-attack and velocity as possible.

Prior to the discussion of the results obtained, a brief summary of the calculated flutter characteristics of the XC-142 is required. In the analyses, both whirl flutter and classical flutter considerations are included. Due to the large number of generalized coordinates required to adequately define both the whirl flutter modes and the classical flutter modes simultaneously, the analyses are done by components. For instance, to define preliminary classical flutter characteristics, the wing is analyzed considering the engine-gearbox-propeller system as a rigid inertial system. Then, considering the wing rigid, the engine-gearbox-propeller system is analyzed for propeller whirl characteristics. In each of these component analyses, extensive parametric studies are done. Finally, using the most promising design from each analysis, the whole system is coupled together to determine if any adverse dynamic coupling effects exist. Figure 10 is a conventional damping versus velocity plot for the completely coupled wing-engine-gearbox-propeller system including root degrees of freedom. This is the result of a flutter analyses using 27 degrees of freedom. As shown, no critical flutter condition exists for the healthy system. Figure 11 is included to show the effect of aileron rotational stiffness on flutter. This is a plot of flutter velocity versus aileron rotational stiffness showing flutter boundaries for various amounts of structural damping coefficient.

The engine-gearbox-propeller system of the model is shown in Figure 4. A schematic of this system identifying the various structural members is shown in Figure 12. Component whirl flutter analyses are conducted on this system to determine the effect of various failure conditions. The failure philosophy involved is one that states that no catastrophic failure of the airplane can result from the failure of any one structural member. Figure 13 shows the results of the flutter analyses. These analyses indicate that strut failures significantly affect the whirl flutter velocity; however, no critical whirl flutter conditions are indicated. These results provide the basis for the selection of the failure conditions to be investigated on the dynamic model. Since the completion of the Phase I tests, additional analyses for the completely coupled wing-engine-gearbox-propeller system including the effect of strut failures show that coupling the engine-gearbox-propeller system with the wing virtually eliminates any whirl-flutter conditions. This is shown in Figure 14. It is suspected that the aerodynamic damping provided by the wing is a very strong contributing factor to these results.

The results achieved during the Phase I tests completely substantiate the analytical results presented above. Absolutely no indication of flutter exists for the healthy wing, as predicted. Numerous runs to investigate various aileron stiffness variations show that the analytical results presented in Figure 11 are conservative. Limit-amplitude instabilities for zero aileron rotational stiffness and for a 25 percent-of-design-value rotational

stiffness did occur and these points are superimposed on Figure 11. The effect of rotational free-play introduced about the inboard aileron hinge axis is shown on Figure 15. The rotational free-play is set on the model by conducting load-displacement tests on the aileron. A typical load displacement result is shown as Figure 16. It must be emphasized that the boundary shown in Figure 15 is a boundary of limit-amplitude instability. As shown thereon, this boundary is penetrated to the required flutter margin with no destructive flutter. The analyses imply that very small amounts of damping about the hinge axis will completely eliminate this type of instability. Output impedance tests of the actual aileron actuation system show that sufficient damping about the hinge axis is available to constrain this type of instability.

The results of four strut failure conditions taken one at a time on one nacelle at a time show nothing resembling flutter. One run inadvertently violated the failure philosophy by having the simultaneous failure of three of the aft engine mounts. No flutter occurred to the maximum flutter margin boundary. The results of these tests demonstrate that no flutter condition exists on the wing.

The model is then used as an aerodynamic force model to determine the various aerodynamic derivative data. Figure 16 shows a plot of the lift coefficient versus angle-of-attack for various velocities. Data for both the propellers on and off conditions are provided to show the effect of propellers on lift coefficient.

4.2 PHASE II - EMPENNAGE TESTS

In the Phase II test, the empennage is mounted on the fuselage constrained in exactly the same manner for these tests as it was for the Phase I tests. During these tests the wing can either be on or off the fuselage. Most of the tests are planned for the wing-on condition. The Phase II configuration mounted in the tunnel is shown as Figure 18. The instrumentation for these tests consists of twelve strain gage bridges, propeller tachometer, wind tunnel balance system, two strobolights, and two high-speed cameras. Six of the strain gage bridges are positioned in the empennage to measure root torsion and bending on each side of the horizontal tail and on the fin. The other six strain gage bridges are located in the wing. As described previously, the wing instrumentation consists of twelve strain gage bridges. Six of these are selected for the Phase II tests. The wind tunnel balance system is used in the same manner as before.

Complete static calibration tests of the instrumentation are performed on the model as installed in the tunnel prior to the actual tunnel testing. The testing procedure is exactly the same as for the Phase I tests.

The objectives of the Phase II - Empennage tests are as follows: clear the healthy configuration to the required flutter margin boundary; evaluate the effect on flutter of horizontal tail rotational stiffness variation; evaluate the effect on empennage flutter of the wing on or off the fuselage; evaluate the effect on flutter of rudder rotational stiffness variation, extend the aileron rotational free-play investigation started during the Phase I tests, and determine the static aerodynamic derivatives of the flexible empennage over as wide a range of angle-of-

attack and velocity as possible. These latter tests will be done with and without the wing.

The Phase II tests are partially complete at the time of this writing. Although the run data are not fully reduced, the following apropos observation can be made:

The healthy empennage configuration with wing on and propellers off is clear to the required flutter margin boundary. At 50 percent of the design value of the horizontal tail rotational stiffness, an incipient flutter condition is established very near the calculated flutter velocity. This condition provides a confirmation of the analytical representation. The rudder is clear with 80 percent of the design value of rudder rotational stiffness.

The results of the aileron rotational free-play investigation reconfirm the results established during Phase I testing displayed in Figure 15. In addition various amounts of mass balance of the inboard aileron shows that the free aileron can be restrained from the limit-amplitude instability with about a 50 percent of mass balance condition.

Interestingly, the analysis of failed conditions considering the aft engine mount failed and the inboard aileron free shows that no instability occurs. After running the aileron free condition on the model, the aft engine mounts of the outboard engines are disconnected and no instability is achievable, confirming the analytical result.

The aeroelastic tests to determine the aerodynamic derivatives for the flexible model are completed. The model aircraft angle-of-attack is varied for a pre-set incidence angle of the all-moving horizontal tail. At each angle-of-attack setting the back-off of the horizontal tail is recorded. Then, holding aircraft angle-of-attack constant the incidence of the horizontal tail is varied over a range of -2 degrees to 8 degrees. At each setting, the aerodynamic force data are recorded.

4.3 PHASE III - COMPLETE AIRCRAFT TEST

In the Phase III - Complete Aircraft Tests scheduled during October, the primary objective is to demonstrate the required flutter margin with the complete model. During this series of tests the model is to be mounted on a vertical rod that passes through gimbals in the model. This mounting arrangement constrains the model in drag, side translation and roll only. The roll constraint can be reduced to zero. However, experience during the Phase I and II tests indicates that a residual rolling moment nearly always exists. Further, no means of trimming the model in roll during flight exists. All of these considerations dictate the use of a soft roll constraint during the Phase III tests. The model can be trimmed in pitch with remote control of the horizontal tail. Pending complete reduction of the Phase II data, the healthy configuration is the only configuration that is to be evaluated during Phase III testing.

5.0 DISCUSSION AND SUMMARY

The XC-142A dynamically similar model program is an unqualified success through the Phase I and II tests. The wing and empennage are both flutter free to the required margin. There are no known problem areas that can prevent the Phase III tests from being a success also.

Fine quantitative data obtained during the Phase I and II tests make the attainment of all but one of originally set forth objectives a reality. The response of the aircraft and its components to propeller unbalance is achieved in a qualitative sense only. The once-per-revolution (1P) response is clearly detectable by all instrumentation. However, time and budgetary limitations preclude the sophistication of instrumentation required to obtain accurate quantitative data. The feasibility of obtaining steady-state response measurements by use of this type of model is certainly demonstrated.

During this model program, the simulation achieved on the model; the experimental determination of the effect of rotational free-play on aileron limit-amplitude instability; the attainment of sufficient strength characteristics in a dynamically similar model to permit static aeroelastic measurements; and the testing technique each represents a state-of-the-art advancement.

The degree simulation of primary structural parameters is excellent as illustrated in Figures 7 and 8 and in Tables 1, 2, and 3. The two-dimensional dynamic characteristics of the wing and the engine-gearbox-propeller system represent extremely complex systems for simulation. The representation of blade dynamics and the inclusion of a model shafting system present significant modeling problems. All of these simulation factors taken together in one model present state-of-the-art model design problems that are satisfactorily overcome in the XC-142A dynamically similar model.

The measurement of the effect of aileron free-play on an aileron limit-amplitude instability provides some very valuable experimental data regarding the XC-142A aileron system. In addition, these data demonstrate the feasibility of using a low-speed model to investigate this class of phenomenon.

The use of the dynamically similar model as an aeroelastic force model demonstrates the feasibility of combining these two types of models into one dynamically similar model. The results obtained in the measurement of the static aerodynamic derivatives of the flexible model indicate that this concept can be carried further without much added complexity. Remote control of the ailerons and rudder as well as of the horizontal tail will permit the conduction of an entire spectrum of model flight testing similar to that conducted on the actual aircraft. Stability characteristics of the flexible model aircraft can rather easily be determined during wind-tunnel tests. This aspect of modeling technology can be pursued further.

Associated with the aeroelastic tests is the use of the aerodynamic force balance. The force data from the balance system provides the paramount information that prevents the overloading of the model. The static aeroelastic

behavior of the extremely flexible model exhibits some quite large changes of load with increasing dynamic pressure. This requires the constant trimming of the model in pitch to maintain tolerable loads. Consequently, any test of a restrained flexible model of the category of the XC-142A can be conducted much more safely if the model is mounted on an aerodynamic string and if full use is made of force balance data during the tests.

REFERENCES

1. Head, A. L., Jr., "A Review of the Structural Dynamic Characteristics of the XC-142A Aircraft," Proceedings of the Symposium on Dynamic Load Problems Associated with Helicopters and V/STOL Aircraft," Buffalo, New York, Cornell Aeronautical Laboratory and Army Transportation Corp, June 26-27, 1963

2. Head, A. L., Jr., "A Philosophy of Design for Flutter," Proceedings of the National Specialists Meeting on Dynamics and Aeroelasticity, Fort Worth, Texas, Institute of the Aeronautical Sciences, November 6-7, 1958

APPENDIX
SIMILITUDE REQUIREMENTS FOR THE XC-142A DYNAMIC MODEL

The design of a dynamically similar model can be adequately defined by a suitable choice of three independent dimensionless ratios. The three dimensionless ratios to be simulated for the model under consideration are:

(1) $$k = \frac{\omega b}{V} = \text{reduced frequency ratio}$$

(2) $$\mu = \frac{W}{\pi \rho b^2 s} = \text{Surface-to-air density ratio}$$

(3) $$\eta = \frac{2W}{\rho V^2 A} = \text{weight-to-aerodynamic force ratio}$$

where

ω = frequency

b = representative semichord

V = true airspeed

W = weight

ρ = air density

s = representative semispan

A = representative area

Two common dimensionless ratios, Mach number and Reynolds number, are not simulated. Mach number is not simulated because compressibility effects are assumed negligible for a low-speed model. The exact simulation of Reynolds number would result in unattainable test section airspeeds. Fortunately, the effect of variation of Reynolds number on flutter speed and frequency is relatively insignificant for the large values of Reynolds number encountered in most low-speed flutter models.

From consideration of the three primary scalable factors (length, mass, and time) the following model to airplane ratios can be obtained:

(4) $$n = \frac{l_m}{l_a} = \text{geometrical scale factor}$$

(5) $$m = \frac{W_m}{n^3 W_a} = \text{mass ratio}$$

(6) $$r = \frac{V_m}{V_a} = \text{speed ratio}$$

where

l = representative length

Subscripts m and a indicate model and airplane quantities, respectively. The gravitational constant, "g," has not been considered since it is identical for both model and airplane.

The geometrical scale factor, n, is determined by the allowable model size to airplane size. For the Vought Low-Speed-Wind Tunnel 7 x 10 feet test section, a maximum model span of about 7 feet is feasible, allowing for wall effects and adequate working clearance. Considering the XC-142A span of about 70 feet, the geometrical scaling factor is determined to be

(7) $$n = 0.100$$

From the requirement (2) that $\mu_m = \mu_a$, the relation

(8) $$\frac{W_m}{W_a} = \frac{\rho_m}{\rho_a} \cdot \frac{b_m^2}{b_a^2} \cdot \frac{S_m}{S_a} = \frac{\rho_m}{\rho_a} n^3$$

is obtained. By comparing (8) with (5), an equivalent relation for the mass ratio is obtained as

(9) $$m = \frac{\rho_m}{\rho_a}$$

The Vought-Low-Speed-Wind Tunnel has a test section vented to the atmosphere so that for sea level standard day conditions

(10) $$\rho_m = \rho_a$$

Hence, the mass ratio must be set to

(11) $$m = 1.00$$

Results from tests conducted at nonstandard conditions or for airplane altitudes other than sea level may be corrected to desired conditions by means of trend curves of flutter speed versus a density dependent parameter.

By the requirement (1) that $k_m = k_a$, (6) may be rewritten as

(12) $$r = \frac{V_m}{V_a} = \frac{b_m}{b_a} \cdot \frac{\omega_m}{\omega_a} = n \frac{\omega_m}{\omega_a}$$

Hence, r is often termed the frequency ratio as well as the speed ratio.

From (12), note that time scales as

(13) $$\frac{t_m}{t_a} = \frac{n}{r}$$

For a slender beam, the bending and torsional frequencies can be shown to be dependent upon

$$\omega_B \sim \sqrt{\frac{EI}{W\ell^3}} \tag{14}$$

and

$$\omega_T \sim \sqrt{\frac{GJ_{eff.}}{W\ell^3}} \tag{15}$$

respectively. Here EI is the flexural rigidity and GJ_{eff} is the effective torsional rigidity. Using (5), (12), (14), and (15) the speed or frequency raito may be written as

$$r = n\frac{\omega_{B_m}}{\omega_{B_a}} = n\sqrt{\frac{\frac{EI_m}{EI_a}}{\frac{W_m}{W_a}\cdot\frac{\ell_m^3}{\ell_a^3}}} = \sqrt{\frac{EI_m}{mn^4EI_a}} \tag{16}$$

and

$$r = n\frac{\omega_{T_m}}{\omega_{T_a}} = n\sqrt{\frac{\frac{GJ_m}{GJ_a}}{\frac{W_m}{W_a}\cdot\frac{\ell_m^3}{\ell_a^3}}} = \sqrt{\frac{GJ_m}{mn^4GJ_a}} \tag{17}$$

The stiffness ratio, f, can now be defined as

$$f = \frac{EI_m}{n^4EI_a} = \frac{GJ_m}{n^4GJ_a} \tag{18}$$

so that (16) and (17) may be written as

$$r = \sqrt{\frac{f}{m}} \tag{19}$$

This equation, (19), is the basic relation between the flutter model design parameters.

By the requirement (3), $\eta_m = \eta_a$, the weight-to-aerodynamic force ratio may be written

$$\frac{\dfrac{W_m}{\rho_m \ell_m^3}}{\dfrac{W_a}{\rho_a \ell_a^3}} \cdot \frac{\dfrac{\ell_m}{V_m^2}}{\dfrac{\ell_a}{V_a^2}} = 1 \tag{20}$$

But by (2),

$$\frac{\dfrac{W_m}{\rho_m \ell_m^3}}{\dfrac{W_a}{\rho_a \ell_a^3}} = 1 \tag{21}$$

Hence, for (20) to hold, the remaining relation must be

$$\frac{V_m}{V_a} = \sqrt{\frac{\ell_m}{\ell_a}} = \sqrt{n} \tag{22}$$

Thus, by (12), the speed or frequency ratio must be set to

$$r = \sqrt{n} = 0.316 \tag{23}$$

and by (19) the resulting stiffness ratio is

$$f = mr^2 = 0.100 \tag{24}$$

Another method of arriving at the results (23) and (24) is to require the model component to have the same static deflection shape, or "droop," under its own weight as the airplane. Then at any point on the model component, the static deflection, δ must be

$$\delta_m = n\delta_a \tag{25}$$

The static deflection of a slender beam is proportional to

$$\delta \sim \frac{W\ell^3}{EI} \tag{26}$$

Hence, (25) can be written

$$\frac{W_m \ell_m^3}{EI_m} = n \frac{W_a \ell_a^3}{EI_a}$$

or

$$\frac{W_m}{n^3 W_a} = \frac{1}{n} \cdot \frac{EI_m}{n^4 EI_a}$$

Using (5), (18), and (19), this relation can be expressed as

$$n = \frac{f}{m} = r^2 \tag{27}$$

which is the same result as (23). Fortunately, with this design, the model will support its own weight and fly at the correct lift coefficient. This allows for a vertical translation degree of freedom without the use of a supplementary vertical force to support the model.

For the simulation of propeller whirl flutter, it is important that the propeller advance ratio, J, be simulated. The advance ratio is dependent upon

$$J \sim \frac{V}{\omega D} \tag{28}$$

where now ω is the propeller rotational frequency. By the requirement, (1), it can be seen that the advance ratio is simulated so that

$$J_m = J_a \tag{29}$$

The flutter model design parameters obtained herein can be summarized as follows:

n = 0.100	= geometrical scale factor
m = 1.00	= mass ratio
f = 0.100	= stiffness ratio
r = 0.316	= speed or frequency ratio

For a design maximum airspeed at sea level of 400 knots plus a 15 percent flutter margin, the required maximum tunnel airspeed to demonstrate the flutter margin is

$$V_m = 1.15 r V_a = 146 \text{ Knots.} \tag{30}$$

This is well within the operating range of the Vought Low-Speed-Wind Tunnel.

Table 1 XC-142A Dynamically Similar Model, Influence Coefficients of Engine-Gearbox-Propeller System Mounted on Rigid Base, Compared with Airplane Values

		GEARBOX						ENGINE					
		P_x	P_y	P_z	M_y	M_x	M_z	P_x	P_y	P_z	M_x	M_y	M_z
		DEFLECTION X 10^3											
GEARBOX	δ_x	+.48 (+.5)	−.04 (−.08)	+.9 (+1.2)	+.04 (+.04)	−.26 (−.3)	— (+.03)	+.8 (+.8)	— (+.02)	+.4 (−.5)	— (+.009)	−.15 (−.21)	— (+.01)
	δ_y	−.08 (−.08)	+3.6 (+3.08)	— (−.17)	−.4 (−.35)	−.08 (+.03)	−.32 (−.28)	+.08 (−.10)	+.5 (+.99)	+.24 (+.004)	−.45 (−.57)	— (+.03)	−.46 (−.40)
	δ_z	+1.3 (+1.2)	−.1 (−.17)	+5.5 (+4.8)	+.33 (+.22)	−1.0 (−1.0)	— (+.05)	+2.2 (+2.23)	— (−.16)	−1. (−.94)	+.04 (−.19)	−1. (−.75)	+.1 (+.03)
	θ_x	— (+.04)	−.25 (−.35)	+.1 (+.22)	+1.78 (+1.74)	−.01 (−.053)	−.05 (−.21)	— (+.10)	−1.9 (−2.57)	— (−.05)	+2.13 (+2.11)	−.05 (−.05)	+.2 (+.006)
	θ_y	−.25 (−.3)	— (+.03)	−.25 (−1.0)	— (−.053)	+.45 (+.38)	— (−.009)	−.65 (−.67)	— (+.04)	+.6 (+.87)	— (−.05)	+.20 (+.20)	— (−.005)
	θ_z	— (+.03)	−.50 (−.28)	— (+.05)	— (−.21)	— (−.009)	+.10 (+.18)	— (+.03)	+.25 (+.63)	— (−.06)	−.05 (−.41)	— (−.006)	+.35 (+.07)
ENGINE	δ_x	+.7 (+.8)	−.10 (−.10)	+2.26 (+2.23)	+.10 (+.10)	−.56 (−.67)	— (+.03)	+1.56 (+1.53)	+.18 (−.04)	−1.2 (−1.4)	— (+.08)	−.50 (−.42)	— (+.02)
	δ_y	+.04 (+.02)	+.90 (+.99)	— (−.16)	−2.1 (−2.57)	— (+.04)	+.30 (+.63)	+.08 (−.04)	+7.8 (+9.75)	−.20 (+.04)	−2.77 (−3.58)	— (+.04)	+.72 (+.86)
	δ_z	−.2 (−.5)	−.3 (+.004)	−.4 (−.94)	−.35 (−.05)	+.5 (+.87)	— (−.006)	−2. (−1.40)	+.12 (+.04)	+6.7 (+6.39)	−.5 (−.09)	+1. (+1.22)	−.05 (−.005)
	θ_x	— (+.009)	−.45 (−.57)	+.05 (+.19)	+2.15 (+2.11)	−.07 (−.05)	−.05 (−.41)	— (+.08)	−2.1 (−3.58)	−.2 (−.09)	+4.97 (+4.65)	−.15 (−.04)	+.25 (+.14)
	θ_y	−.20 (−.21	— (+.03)	−.35 −.75	— (−.05)	+.18 (+.20)	— (−.006)	−.45 (−.42)	— (+.04)	+1.0 (+1.22)	— (−.04)	+.5 (+.52)	— (−.004)
	θ_z	— (+.01)	−.52 (−.40)	— (+.03)	— (+.006)	— (−.005)	+.050 (+.066)	— (+.02)	+.62 (+.86)	— (−.005)	+.425 (+.14)	— (−.004)	+.01 (+.03)

( ) INDICATES SCALED CALCULATED AIRPLANE VALUE
— INDICATES DEFLECTION WAS NEGLIGIBLE

NOTE: ELEMENTS OF THIS MATRIX ARE DEFLECTIONS AT THE ENGINE OR GEARBOX CG DUE TO UNIT LOADS AT THE ENGINE OR GEARBOX AND HAVE UNITS OF IN./LB, IN./IN.-LB, RADIANS/LB, OR RADIANS/IN.-LB, DEPENDING UPON LOCATION IN THE MATRIX.

EXAMPLE: e_{17} (FIRST ROW, SEVENTH COLUMN) = +.0008 IN/LB
= X DEFLECTION AT GEARBOX CG DUE TO UNIT X LOAD AT ENGINE CG

Table 2 XC-142A Dynamically Similar Model, Frequencies of Engine-Gearbox-Propeller System Mounted on Rigid Base, Compared with Airplane Values.

CALCULATED AIRPLANE FREQUENCY (CPS)	SCALED CALCULATED AIRPLANE FREQUENCY (CPS)	MEASURED MODEL FREQUENCY (CPS)	MODAL DESCRIPTION
7.76	24.6	26.5	ENGINE ROLL ABOUT AFT SUPPORT
10.51	33.2	36.0	ENGINE AND GEAR BOX PITCH AS A UNIT
15.26	48.1	43.0	ENGINE PITCH ABOUT ENGINE C G AND GEARBOX PITCH ABOUT GEAR BOX C G
16.12	51.0	44.0	ENGINE AND GEARBOX YAW AS A UNIT
18.04	57.0	52.0	ENGINE AND GEARBOX LATERAL TRANSLATION
30.70	97.0	76.0	ENGINE—GEARBOX CONNECTING SHAFT TORSION

Table 3 XC-142A Dynamically Similar Model, Coupled Wing-Fuselage Frequencies Compared with Airplane Values.

SIGNIFICANT WING—FUSELAGE SYMMETRIC MODES
(RIGID EMPENNAGE, FLEXIBLE FUSELAGE ON 2—POINT RESTRAINT)

MEASURED MODEL FREQ (CPS)	SCALED CALCULATED AIRFLANE FREQ (CPS)	CALCULATED AIRPLANE FREQ & MODE NUMBER (CPS)	MODAL DESCRIPTION
5.3	5.78	1.82 (1)	WING NORMAL — PLANE 1ST BENDING
7.0	6.97	2.40 (2)	WING IN — PLANE 1ST BENDING
15.1	14.17	4.48 (3)	WING 1ST TORSION
23.4	22.97	7.26 (4)	INBD GEARBOX VERTICAL, OUTBD G B LATERAL
24.9	24.54	7.76 (5)	AFT FUSELAGE VERTICAL BENDING
29.4	30.94	9.78 (8)	WING NORMAL — PLANE 2ND BENDING
32.5	34.28	10.84 (9)	WING IN—PLANE 2ND BENDING AND INBD ENG VERTICAL
40.0	37.38	11.82 (10)	FWD FUSELAGE VERTICAL BENDING
54.8	51.86	16.40 (11)	INBD G B AND ENG YAW
58.3	55.08	17.42 (12)	OUTBD G B AND ENG YAW
67.1	68.10	21.54 (18)	INBD — OUTBD AILERONS, IN—PHASE
88.0	89.40	28.28 (19)	INBD — OUTBD AILERONS, OUT—OF—PHASE

GENERAL ARRANGEMENTS

DIMENSIONS

WING SPAN	67.5
LENGTH	58.1
HEIGHT	26.1

SPEED

CRUISE	220–250K
V_{MAX}	374K

RANGE

COMBAT RADIUS	200–300 NM
FERRY RANGE	2600 NM

PAYLOAD

8,000 LBS OR

32 FULLY EQUIPPED COMBAT TROOPS

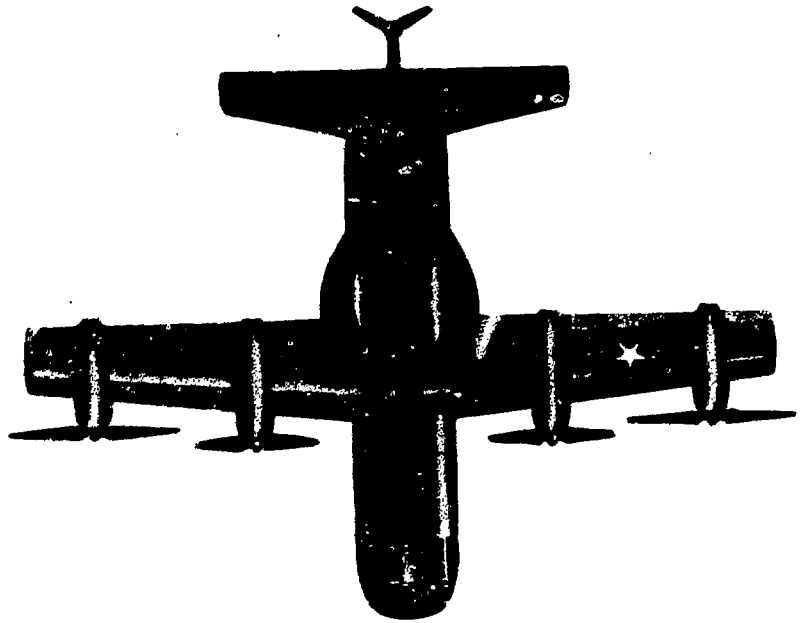

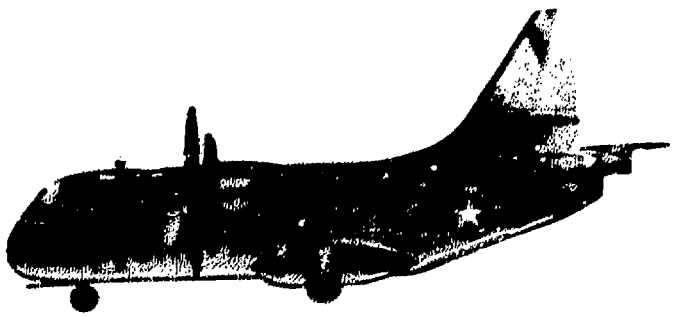

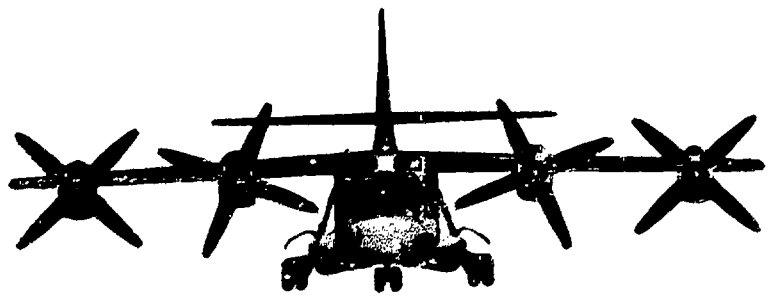

Figure 1. XC-142A Airplane, Conventional Flight Mode

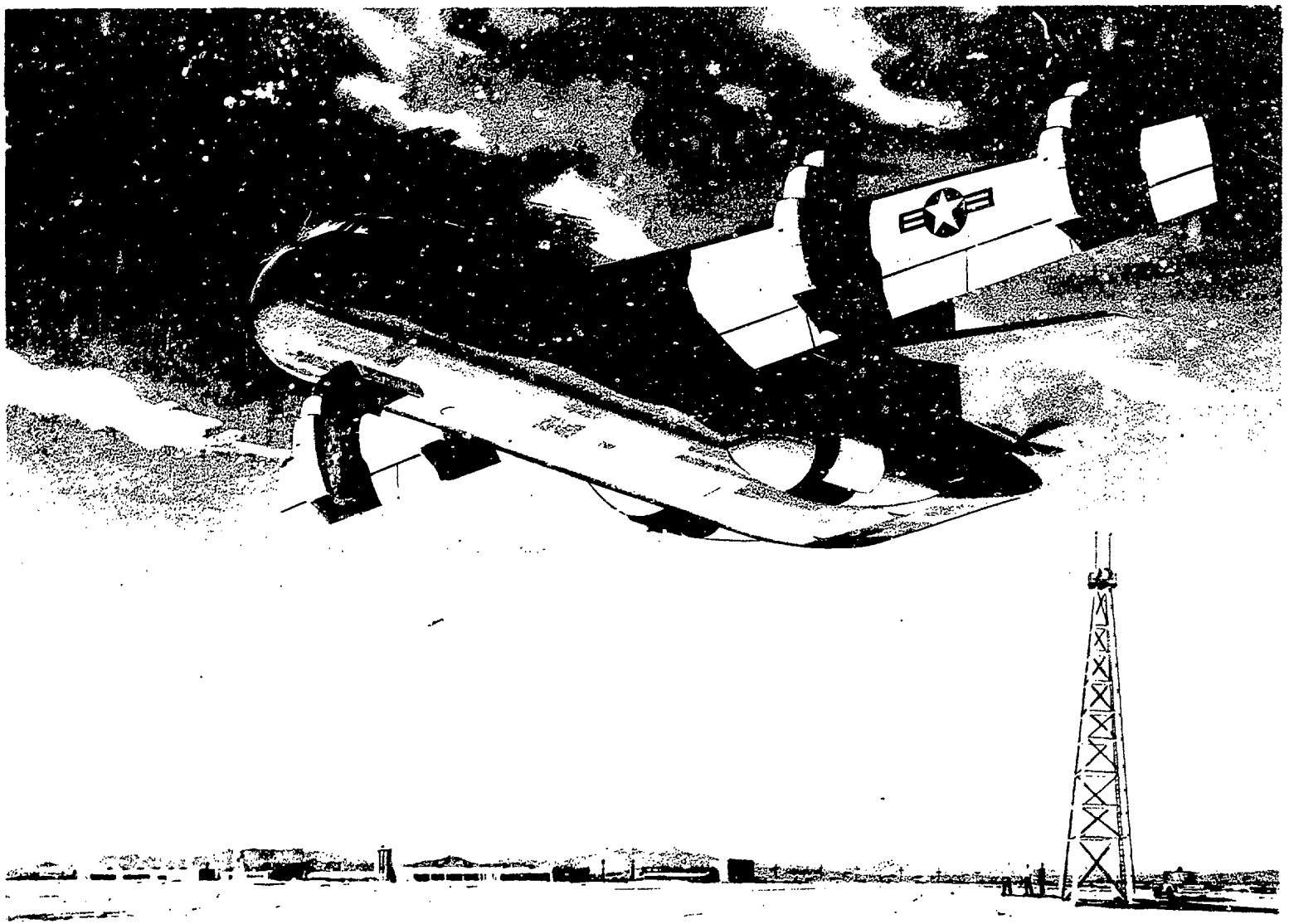

Figure 2. XC-142A Airplane, Hover Flight Mode

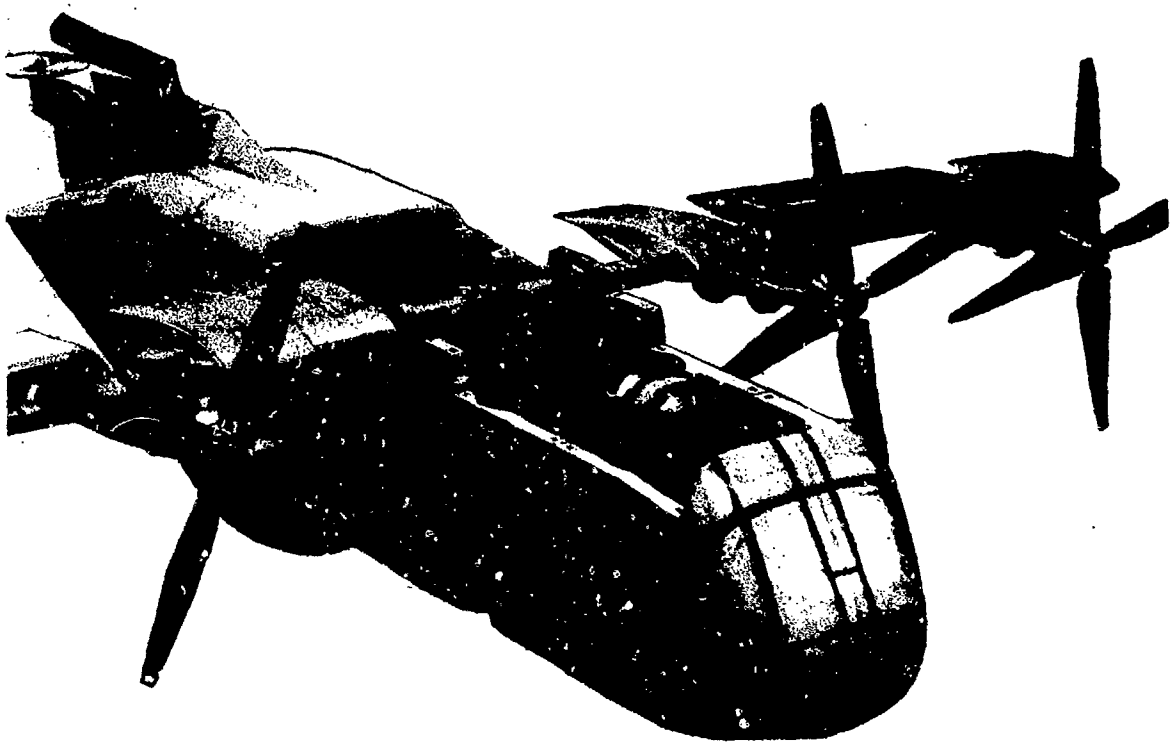

Figure 3. XC-142A Dynamically Similar Model, Skeletal Detail of Wing

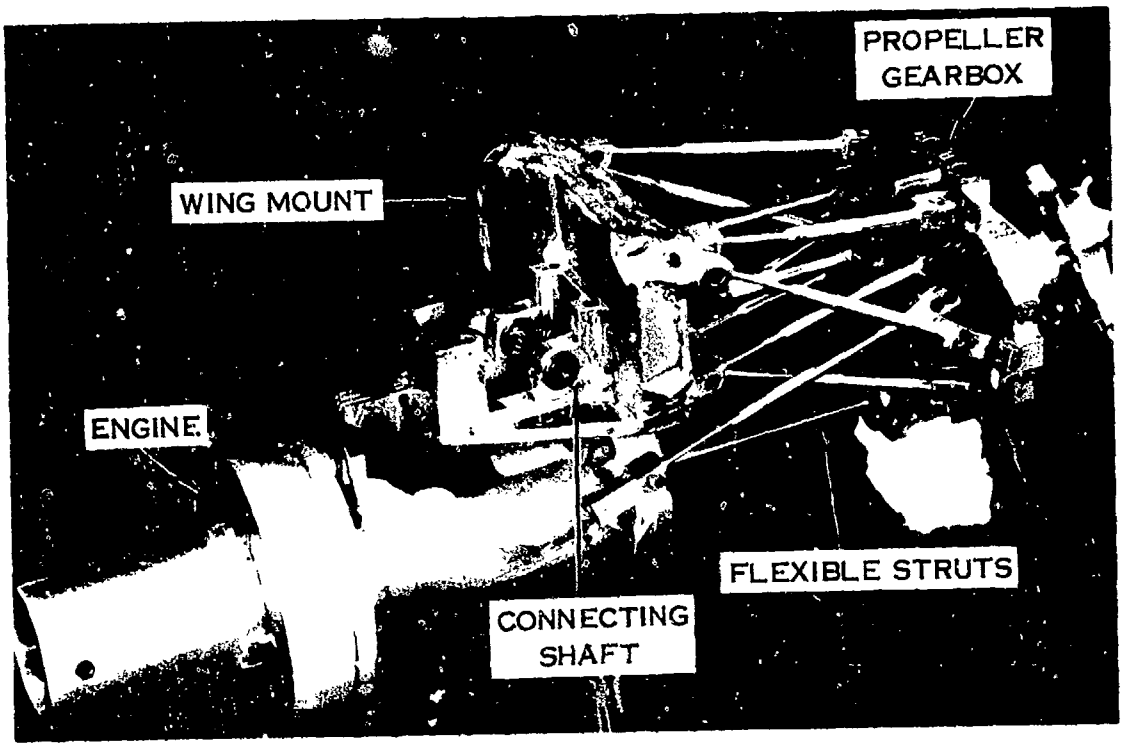

Figure 4. XC-142A Dynamically Similar Model, Skeletal Detail of Engine-Gearbox-Propeller System

Figure 5. XC-142A Dynamically Similar Model, Skeletal Detail of Empennage

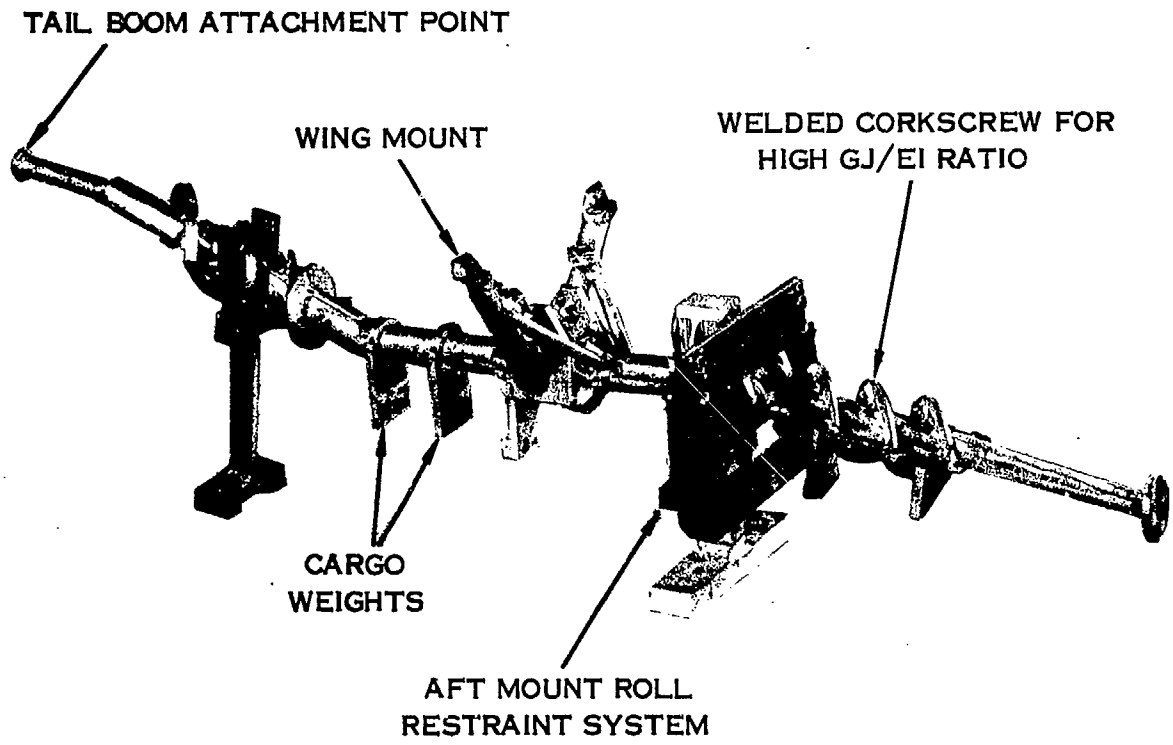

Figure 6. XC-142A Dynamically Similar Model, Skeletal Detail of Fuselage Spar

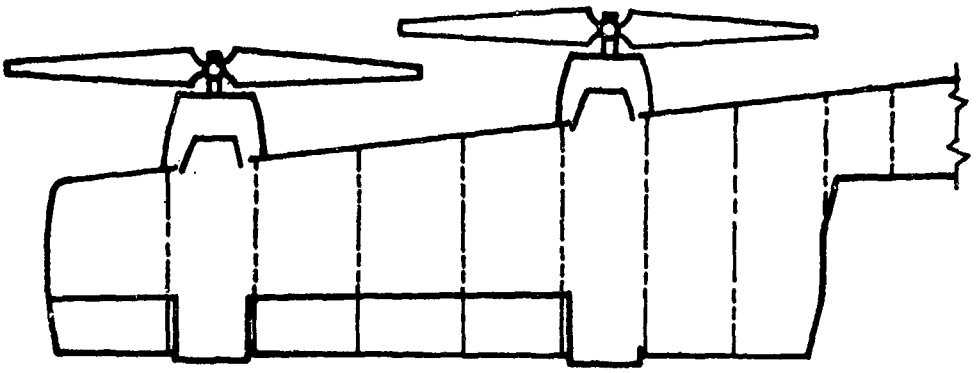

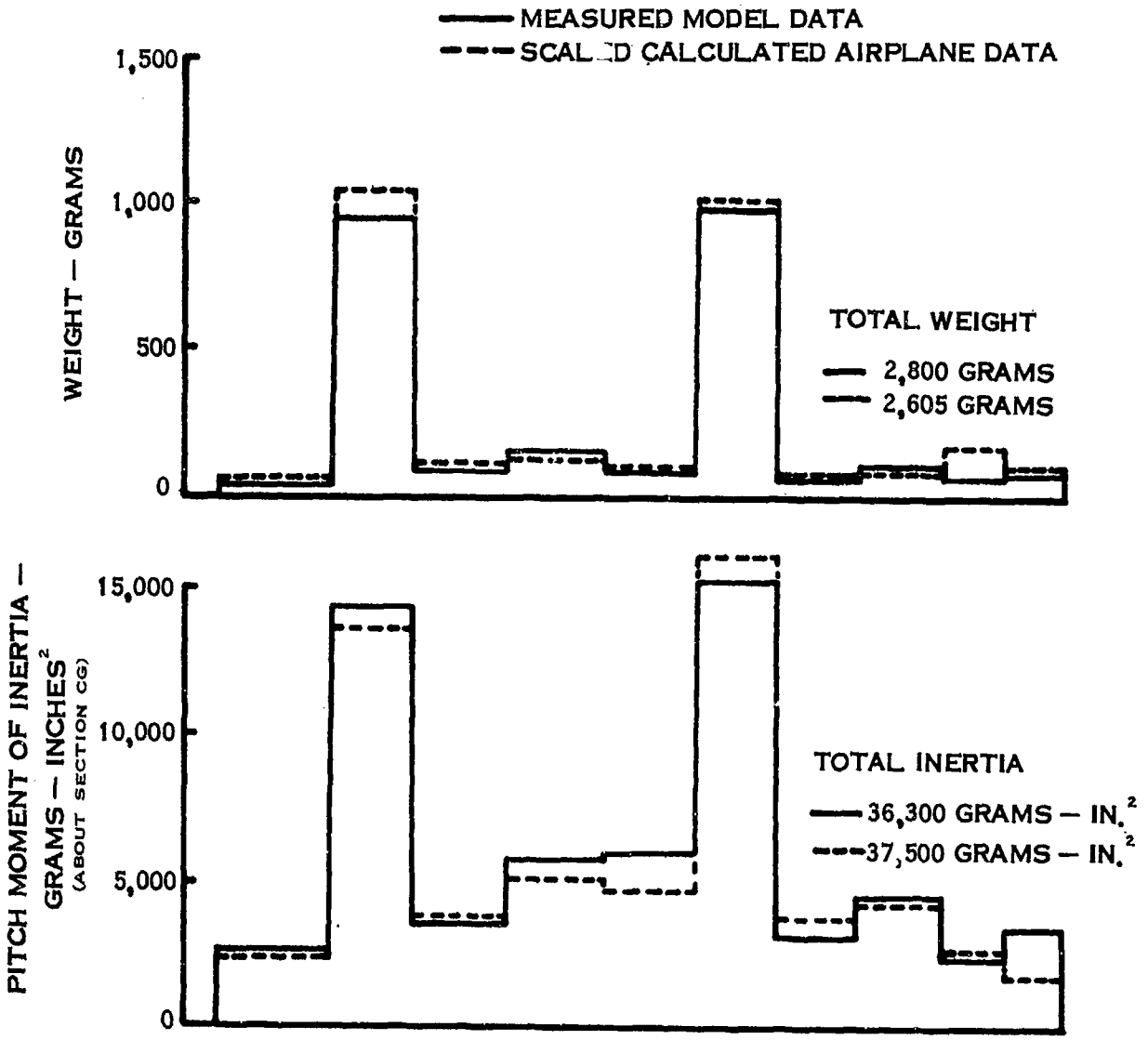

Figure 7. XC-142A Dynamically Similar Model, Inertial Distributions, Comparison of Model and Airplane Data

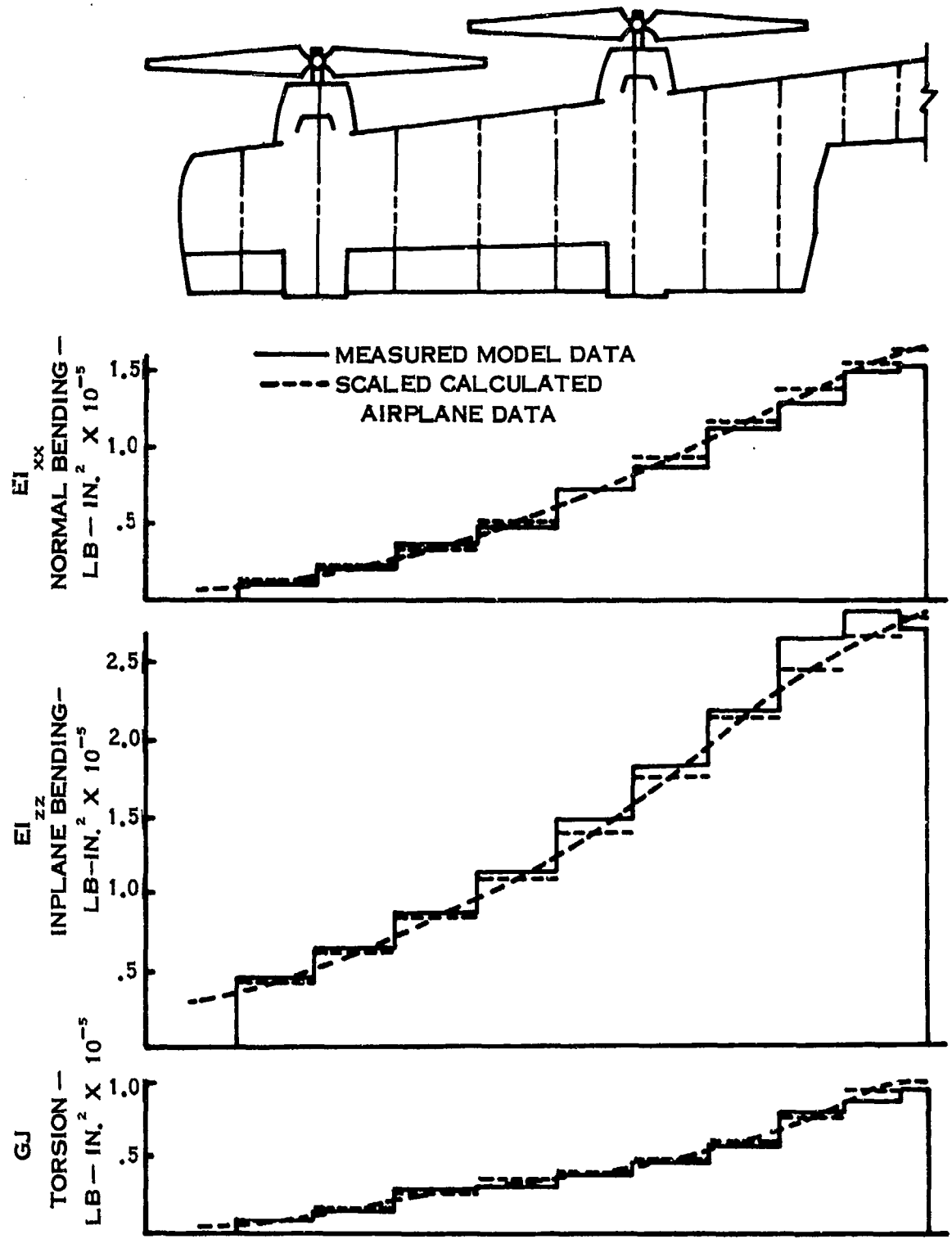

Figure 8. XC-142A Dynamically Similar Model, Stiffness Distributions, Comparison of Model and Airplane Data

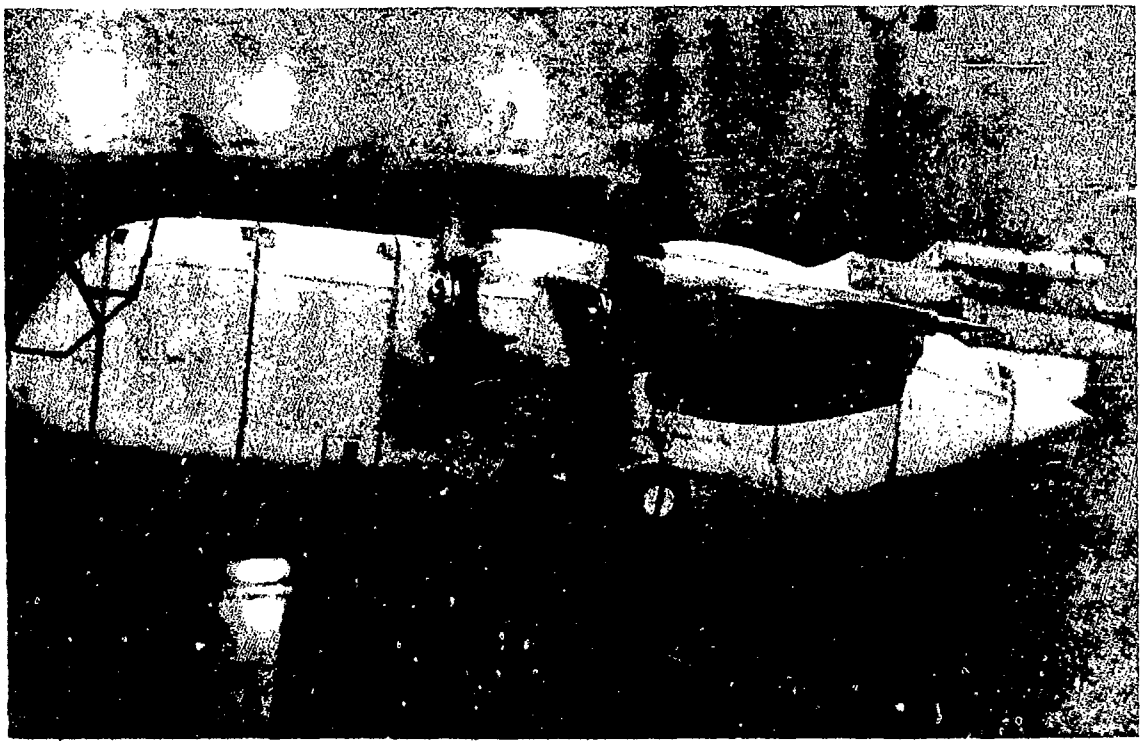

Figure 9. XC-142A Dynamically Similar Model, Phase I Test Configuration Mounted in Test Section At Angle-of-Attack of 6.7 Degrees

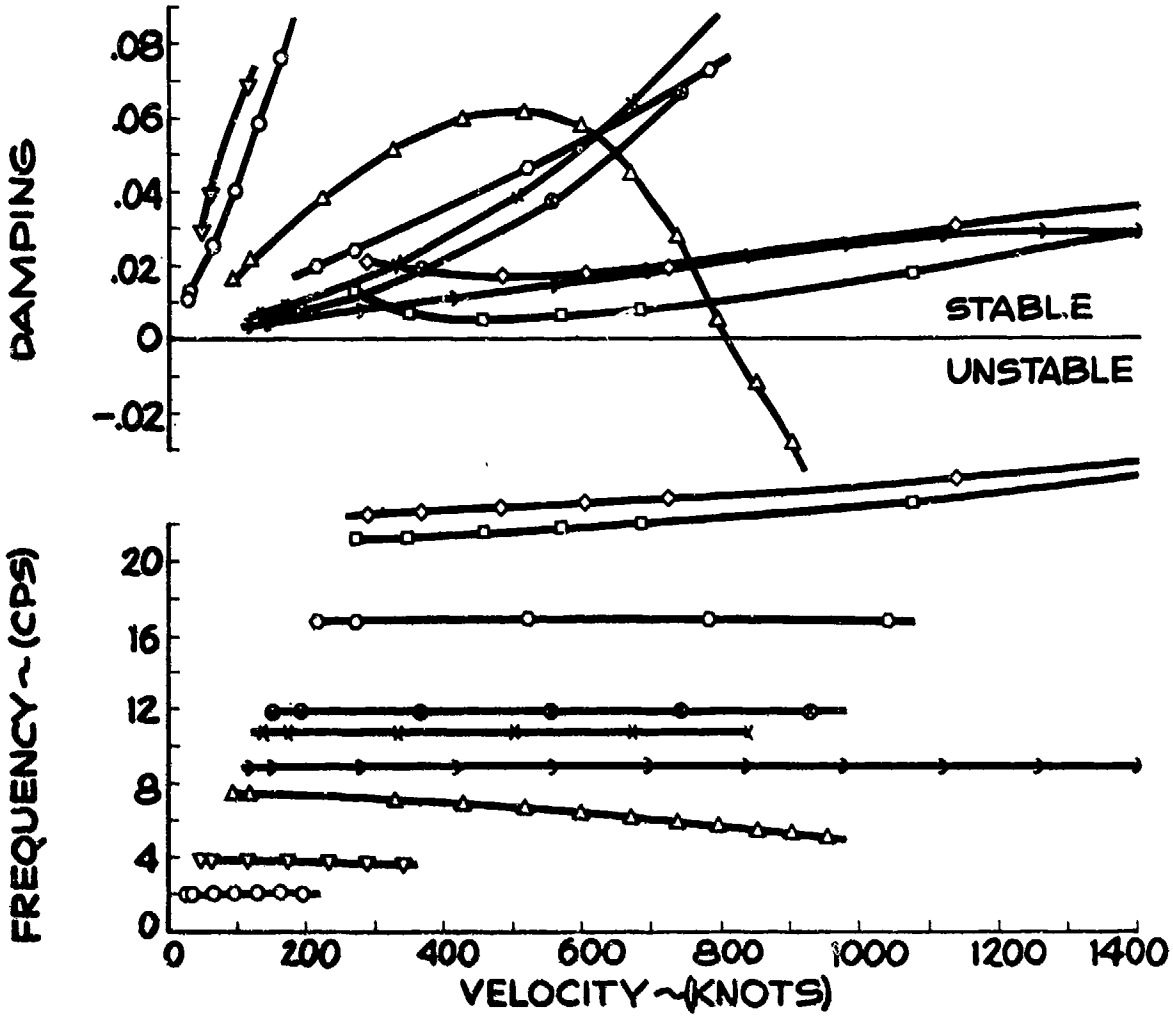

Figure 10. XC-142A Airplane Flutter Analysis Results for Completely Coupled Wing-Engine-Gearbox System Including Aileron and Wing Root Degrees of Freedom Healthy Configuration Damping vs. Velocity-Frequency vs. Velocity Maximum Power Condition V = 350 Kts

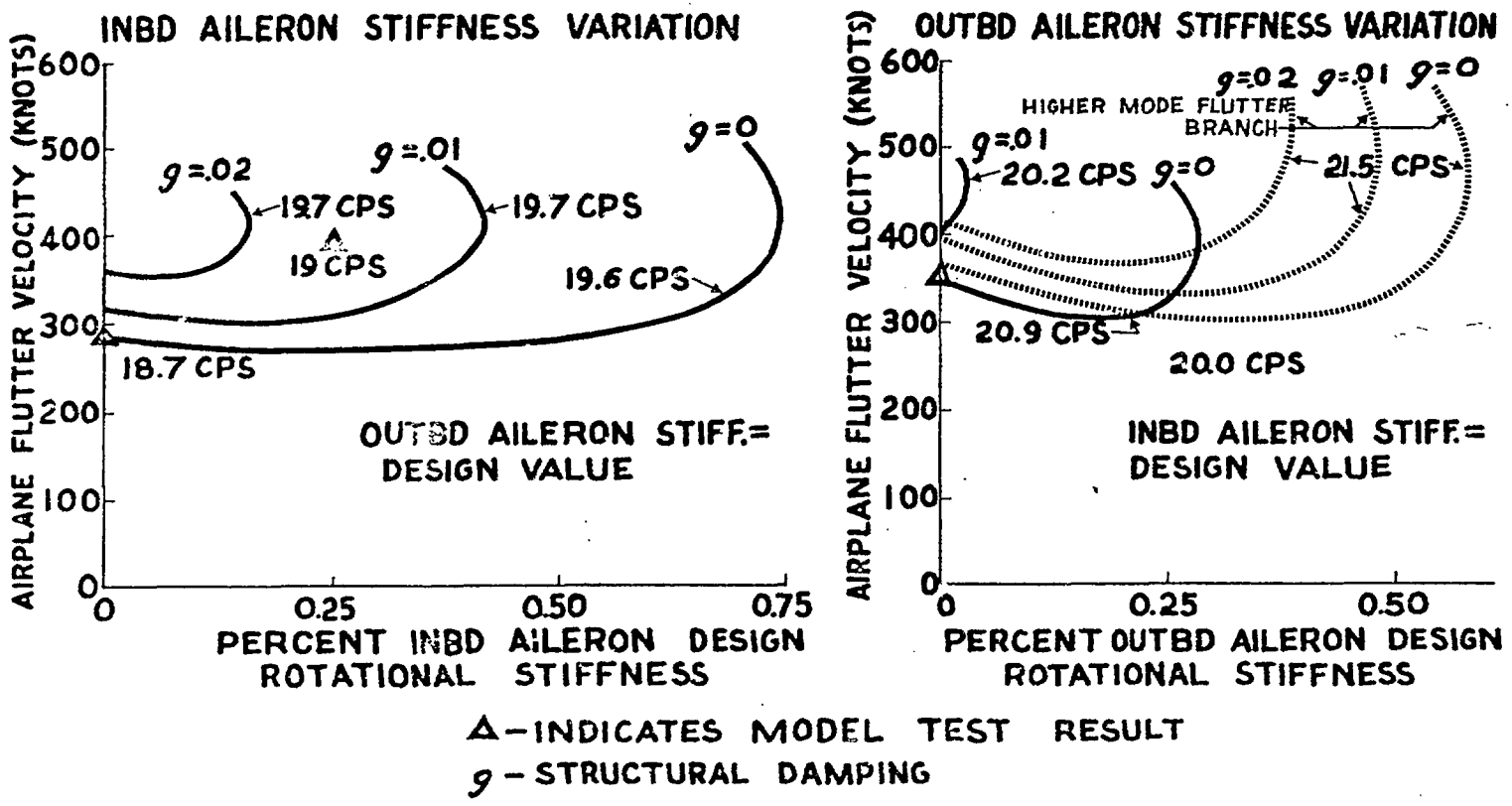

Figure 11. XC-142A Airplane, Flutter Analysis Results, Velocity Vs. Aileron Rotational Stiffness

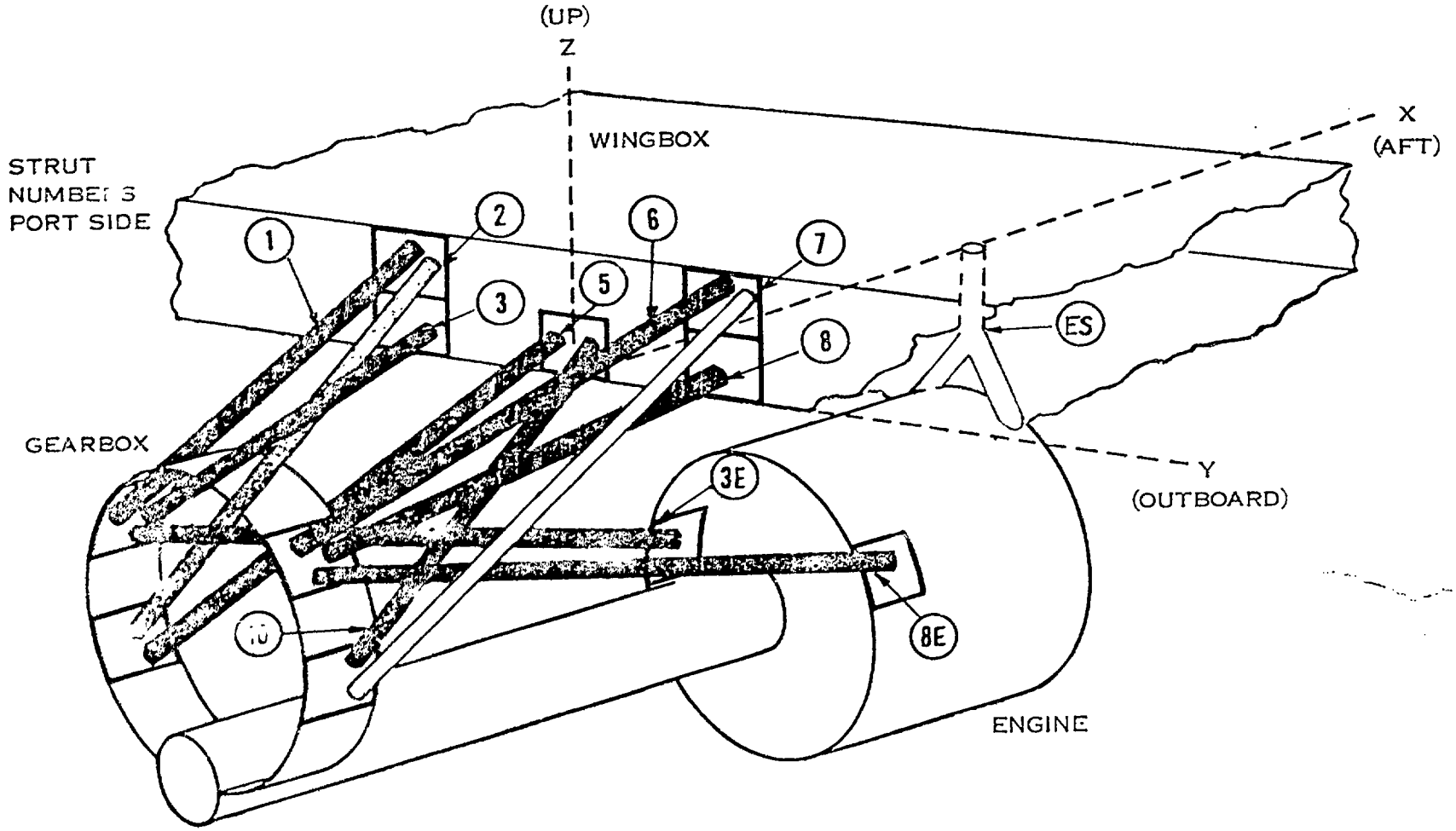

Figure 12. XC-142A Airplane, Schematic of Engine Mount Design

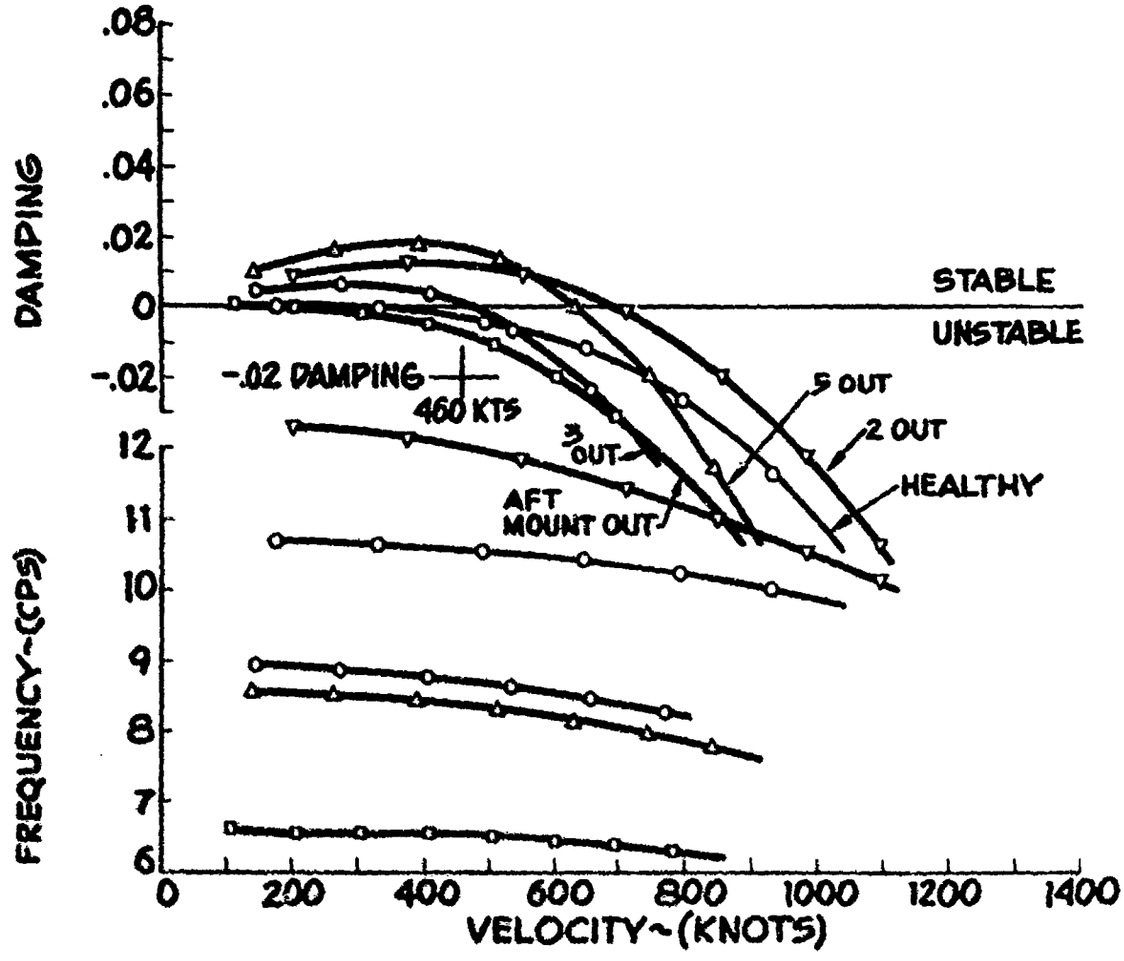

Figure 13. XC-142A Airplane Flutter Analysis Results for Engine-Gearbox-Propeller System Effects of Strut Failures Damping vs. Velocity-Frequency vs. Velocity

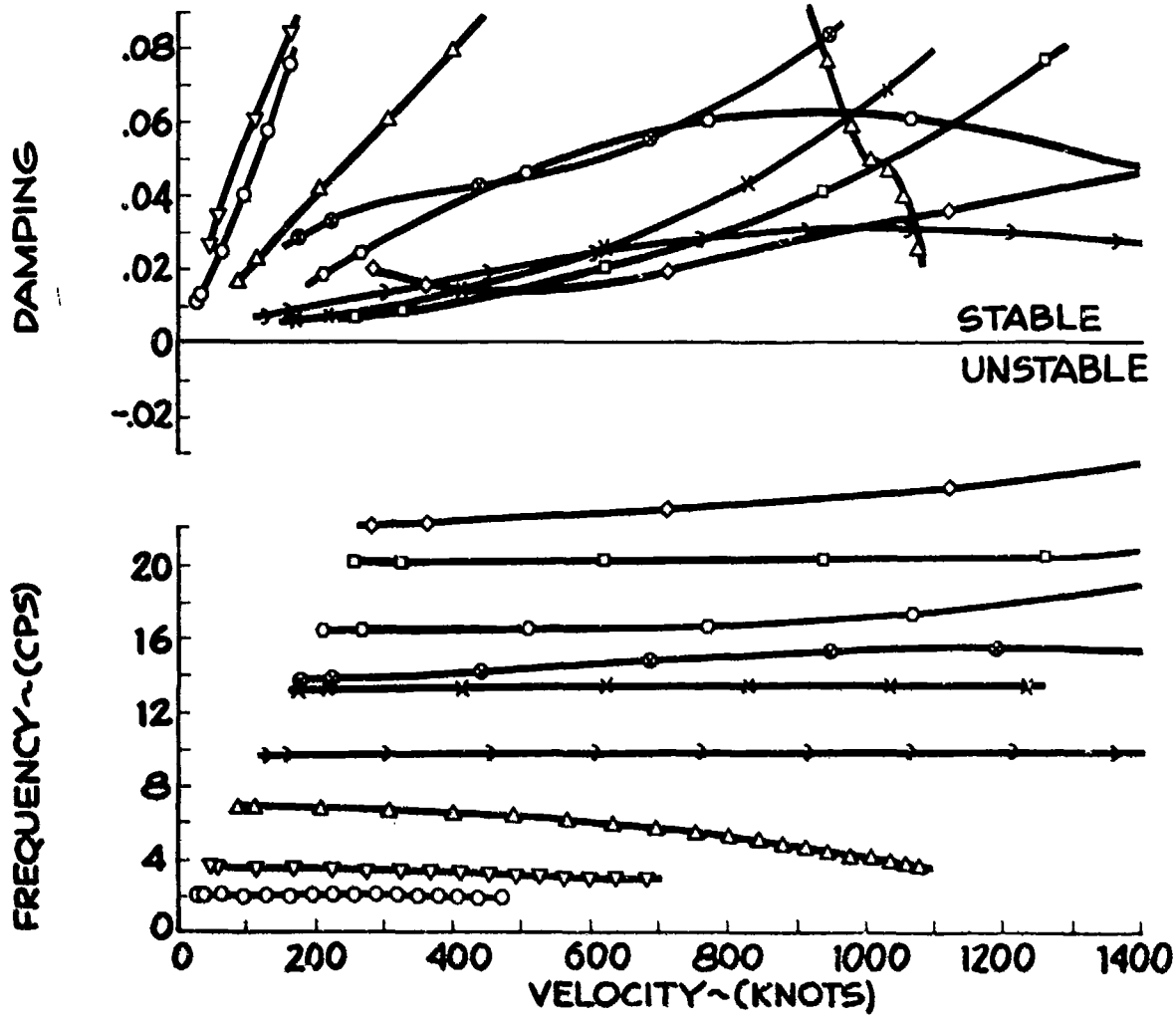

Figure 14. XC-142A Airplane Flutter Analysis Results for Completely Coupled Wing-Engine-Gearbox System Including Aileron and Wing Root Degrees of Freedom Outboard Nacelle Aft Engine Mount Failed Damping vs. Velocity-Frequency vs. Velocity Maximum Power Configuration V = 350 Kts

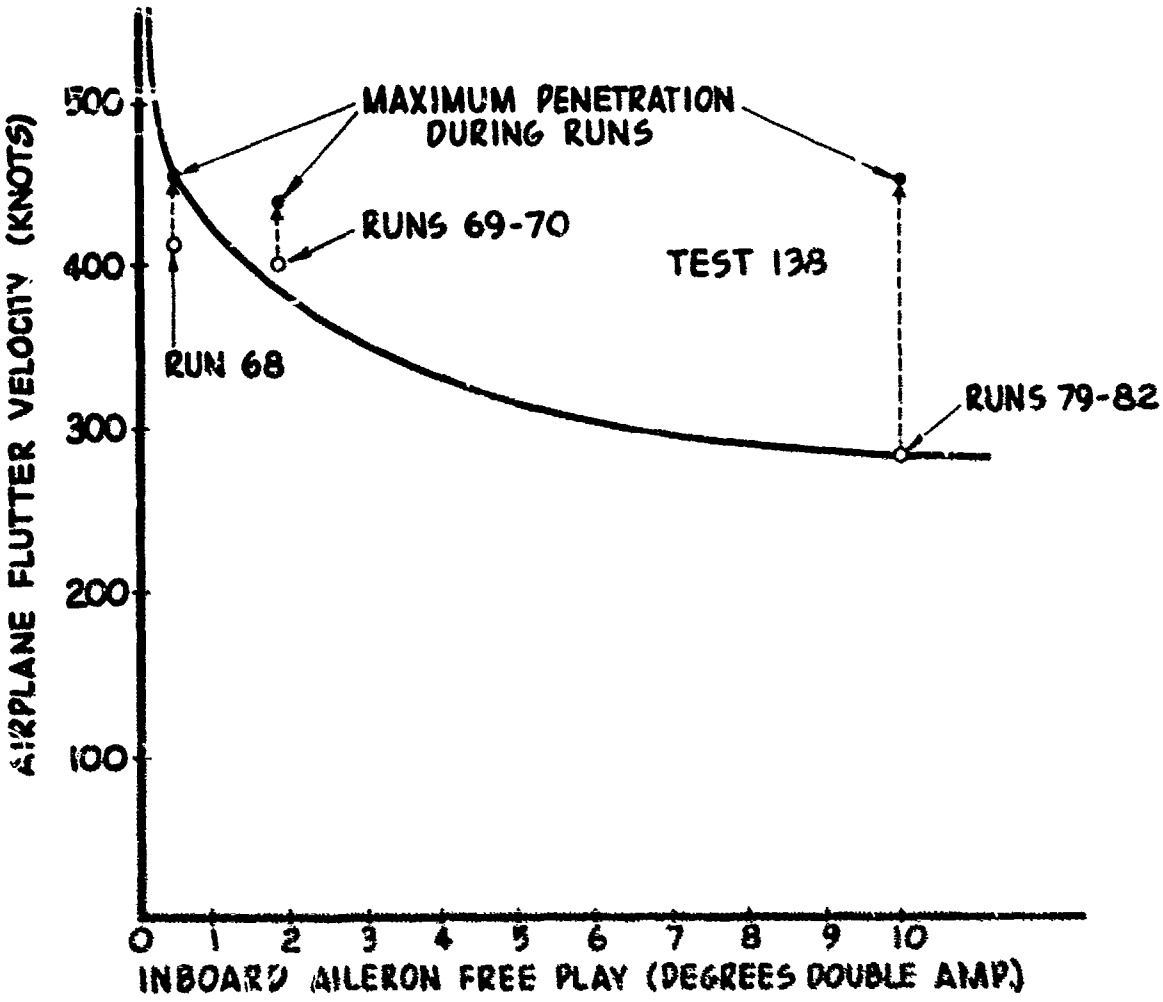

Figure 15. XC-142A Dynamically Similar Model, Test Results, Limit-Amplitude Instability Boundary of Inboard Aileron, Velocity Vs. Rotational Free-Play

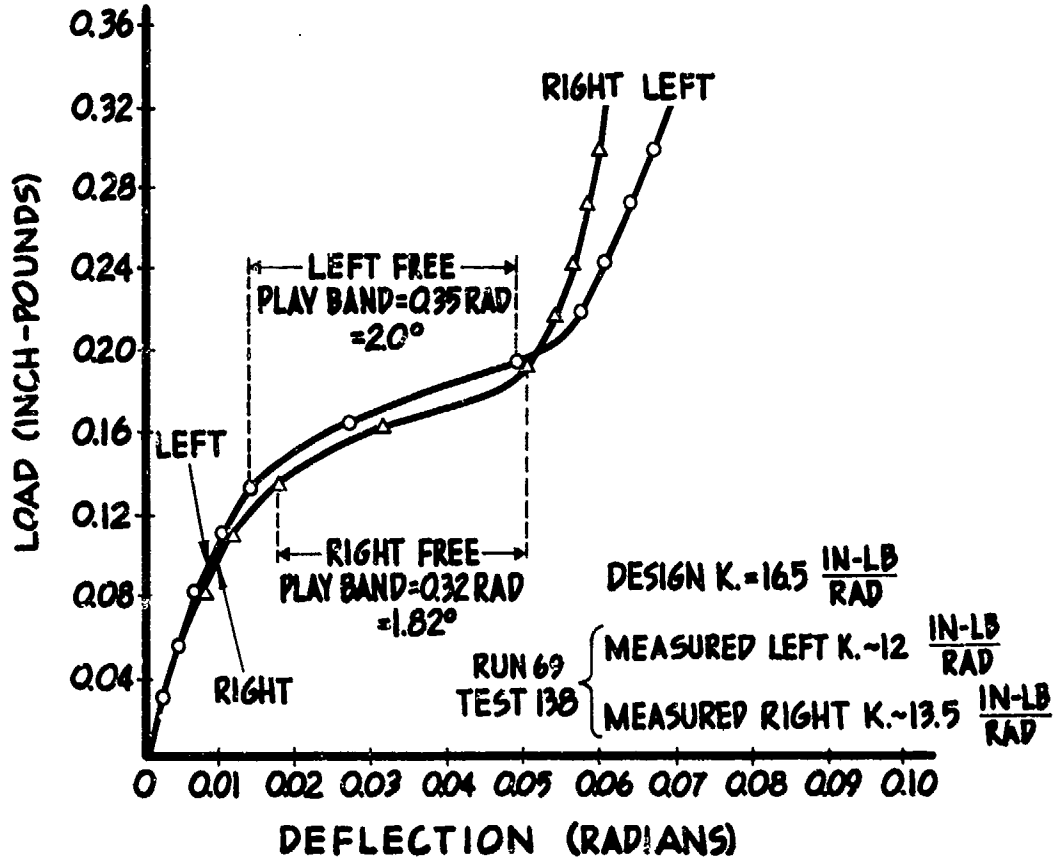

Figure 16. XC-142A Dynamically Similar Model, Inboard Aileron Typical Load-Displacement Test Results

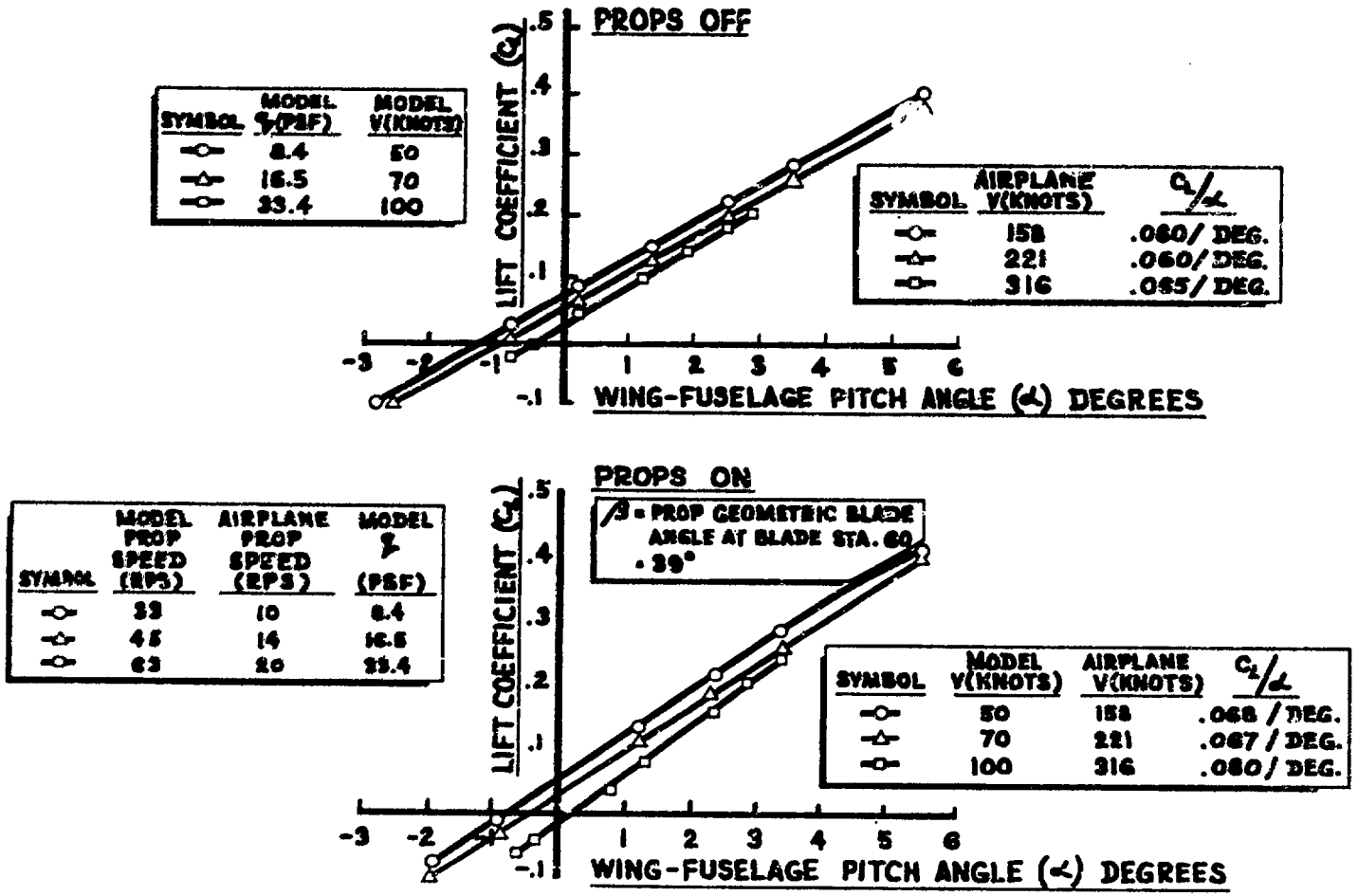

Figure 17. XC-142A Dynamically Similar Model, Test Results, Lift Coefficient Vs. Angle-Of-Attack

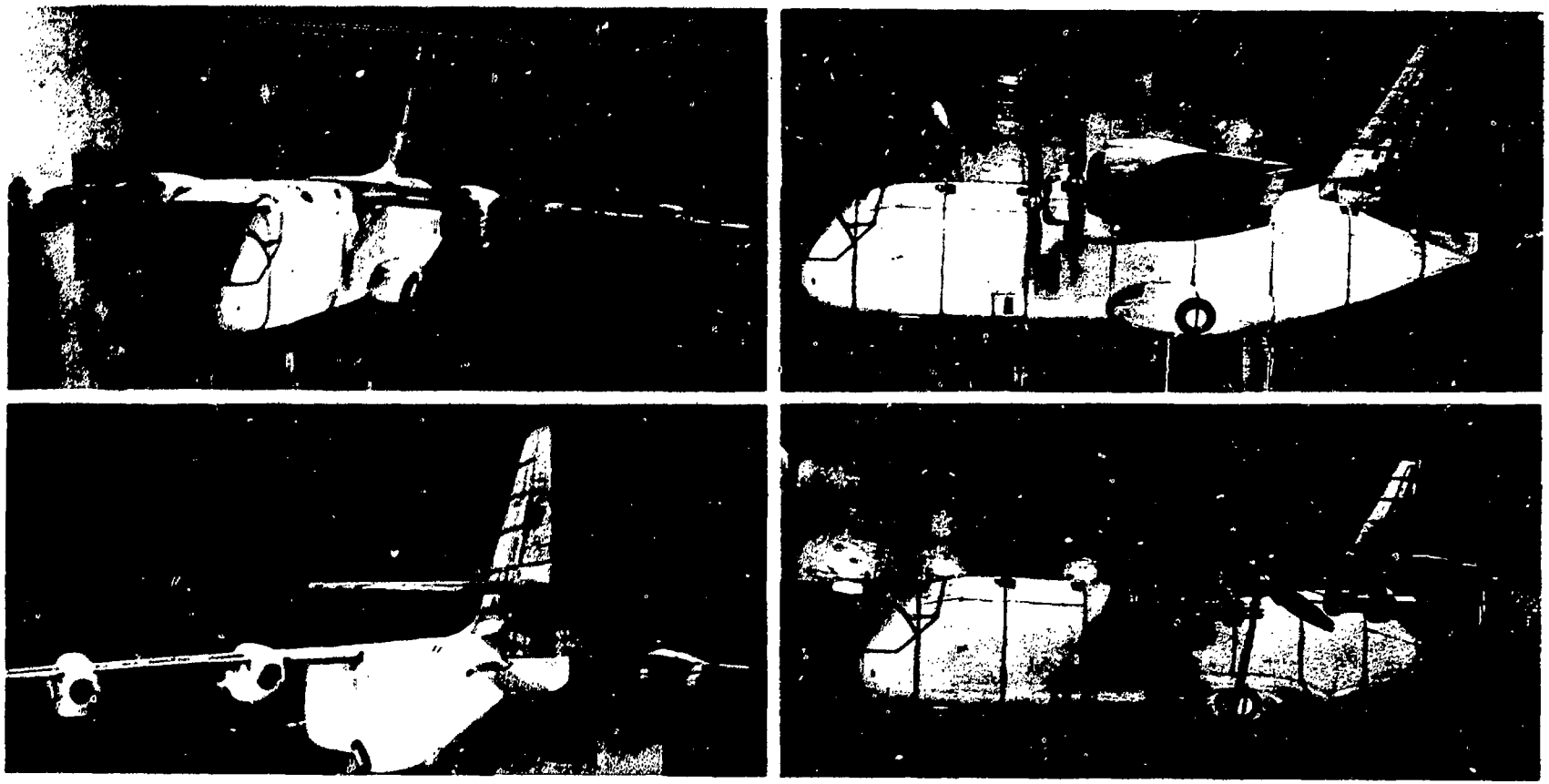

Figure 18. XC-142A Dynamically Similar Model, Phase II Test Configuration Mounted in Test Section

AIRFRAME STRUCTURAL TESTING - "WHERE DO WE GO FROM FULL SCALE?"

H. B. Lowndes, Jr.

R. L. Cavanagh

Structures Division
AF Flight Dynamics Laboratory
Research and Technology Division
Air Force Systems Command

ABSTRACT

Current airframe structural integrity test requirements are reviewed and the necessity for full-scale rather than component testing is briefly discussed. Trends in test complexity and cost are presented which show that as environmental simulation parameters become more demanding, large aerospace vehicle full scale testing becomes economically prohibitive. The application of component testing or modeling techniques as a solution to this problem is discussed and suggestions for needed research are presented.

AIRFRAME STRUCTURAL TESTING -"WHERE DO WE GO FROM FULL SCALE?"

H. B. Lowndes, Jr. R. L. Cavanagh

Structures Division
AF Flight Dynamics Laboratory
Research and Technology Division
Air Force Systems Command

The Air Force and its predecessor organizations have more or less traditionally relied on full-scale structural tests of a complete vehicle airframe as the prime means for proving the structural integrity of their weapon systems. This strong reliance on structural tests has not been arbitrary. It has been based upon considered, engineering judgement and the statistics over the years have borne out the validity of this judgement.

A reference to figure 1 will illustrate this point. This shows structural test failure information on 78 aircraft which were tested at Wright-Patterson. The data on the first 71 aircraft were compiled in 1946 and cover the majority of World War II type aircraft. The 7 aircraft referred to in the 1963 compilation represent the jet age - from the F-86D and F-84F through the century series fighters (F-102, F-104, F-105 and the B-58). As may be seen from the chart the same trends exist today as did almost 20 years ago. In general, although exact data are not readily available, the series of jet aircraft failed at higher percentages of ultimate load than did their World War II predecessors. This indicates an improvement in analytical techniques and these improvements should not be minimized. There has been, and continues to be, a large amount of work done in this area. With the advent of large size, high speed computers and their general availability, much more rigorous mathematical techniques can be applied and an almost endless number of variables can be considered in performing these analyses. However, at least today, such techniques provide only a sophisticated estimate of the structural capabilities of the vehicle and this estimate must be validated by test. Reliance upon purely analytical techniques will not assure the requisite structural integrity of the weapon system.

This being the state-of-the-art, the Air Force still requires full-scale, complete vehicle structural test programs for final structural verification of its weapons systems. A very large effort has gone into the development of techniques and special facilities needed to perform these advanced vehicle structural tests. Reasonable success has been achieved in

simulating the critical structural environments that our advanced aerospace vehicles encounter; notably those of extreme temperatures (both high and low) and the real-time load environment. In achieving these simulation capabilities, trends are becoming apparent that are worthy of attention.

The most apparent is the rapidly increasing cost of performing these advanced structural tests. Table 1 presents a compilation of facility costs based around today's requirements and includes some forecasts for the future. The basic facility indicated in the first column provides the building and equipment required to conduct full-scale tests with no environmental simulation other than that of external loads; in other words, room temperature structural tests. The second column represents the dollar costs that must be added to the basic facility cost in order to provide a large scale elevated temperature test capability. These dollars provide 40,000 KW of program controlled electrical power, programmed load equipment, and a large size data acquisition and analysis system. For this expenditure one has a large scale test facility with a broad range of test capabilities; a facility that can provide full scale test simulation on many different types of vehicles, up to and including lifting re-entry vehicles of the class and size of the Dyna Soar Glider. At this point, approximately 8,000,000 additional dollars have been invested. However, even with this elaborate and costly installation, to conduct a full scale test on a B-70 class air vehicle requires even more in the way of equipment; approximately 1,680,000 dollars worth. This money primarily provides the additional electrical power control loops needed for the proper thermal distribution and simulation over an entire vehicle of this size.

Let us now extend the facility requirements one step further. Consider what would be required to provide a full scale structural test capability for a hypervelocity and re-entry vehicle having self-contained propulsion systems. One comes up with some startling numbers!

First of all, the 40,000 KW of electrical power and control equipment already existing must be increased by a factor of at least ten (more probably, twenty). This will cost conservatively, 40,000,000 dollars and does not include the added power generation and distribution system that will be required. The data system channels must be increased due to the large size of the vehicle and its more demanding data requirements. This can be accomplished at an estimated cost of 3,000,000 dollars. The number of loops of programmed loading equipment will have to be increased at a estimated cost of 2,500,000 dollars. A new capability will have to be incorporated to provide a suitable simulant, probably liquid nitrogen, for the vehicle's cryogenic fuel. This capability will include the storage, transfer, and control of large volumes of the

simulant. In addition, provisions will have to be made to accommodate any large volume spillage of the simulant in case of test article rupture. This cryogenic fuel simulant facility will cost, conservatively, 5,000,000 dollars. The total facility investment now runs approximately 61,000,000 dollars - a large cost for one small phase of an overall system development program!

The cost of such a test facility is only a part of the story, for it provides merely the non-expendable, or capital investment equipment. Let us now examine the cost of expendable supplies and materials. In general, and this is quite understandable, the same trend exists here as in the facility costs. There is one cost, however, that is rising at an extremely high rate. This is the cost of providing the very high surface temperatures required for supersonic and hypersonic flight simulation.

Figure 2 presents a representative plot of this cost as a function of test temperature. The series of curves for various ΔT heating rates represent, in dollars per square foot of test area, the cost of infrared heating lamps, reflectors, control thermocouples and strain gage instrumentation. As may be seen the increased costs incurred in going from room temperature tests to those requiring 500°F surface temperatures are significant. The cost tends to level off in the 500°F to 2000°F surface temperatures regime but increases severely when 2000°F to 3000°F temperatures are required. The curve again becomes quite level from 3000°F to 3500°F.

The curves stop at 3500°F since this represents the present upper state-of-the-art limit when radiant energy lamps are used for thermal simulation. This temperature is approximately the maximum that can be attained with this type heater; at least until some significant break through in lamp design occurs. Whether the curve will take another sharp up turn as progress is made to the 5000°F temperatures required for super-orbital re-entry condition remains to be seen.

With the cost of weapon system programs becoming higher and higher, test requirements of all types are one of the first items that are rigidly scrutinized when the budget squeeze comes. And structural testing is no exception. It seems quite apparent that, one of these days, economics are going to require some means other than complete full-scale structural testing for structural verification purposes.

Before discussing possible alternatives to complete full-scale structural testing it is in order to list the advantages obtained by conducting tests on full-scale structures. These advantages fall in three broad categories:

Category I - Determination of Manufacturing Methods Effects. The structural effects of the manufacturing methods by which the materials are required to conform to the desired geometry can be assessed. These effects are, generally, either inadequately or totally unaccounted for in the structural analysis. In this category are the effects caused by the use of dissimilar or anistropic materials, built in stresses and stress raisers introduced by fabrication processes, variation in column fixity, etc.

Category II - Determination of Analytical Deficiencies. The effects of structural behaviour which are either difficult or impossible to treat analytically are accounted for. Included in this category are effects of plastic flow, elastoplastic behaviour, creep deformation, stress relaxation, material degradation with time and/or temperature, etc.

Category III - Determination of Human Errors. The effects of errors on the part of the designer, analyst or fabricator can be discovered and corrected.

Any alternative testing method, therefore, should include as many of the advantages accruing from full-scale testing as possible without imposing significant, detrimental inaccuracies. If alternative methods had to be selected today, based upon the present state-of-the-art, they would be as follows. The methods are listed in descending order of preference.

Alternative Method A - Loading the entire full-scale structure but heating only portions of it. Since a full-scale structure is being used, all the above listed advantages are present with this method. Great care must be exercised, however, in establishing the proper force and thermal conditions along the boundaries of the test section. Because limits are placed upon the area of the structure that is to be heated at any one time, this method requires the repeated applications of ultimate load to the structure in order to cover all critical areas. As a result, an unrealistic premature failure may occur. This method has been used successfully when electrical power or equipment limitations have precluded heating the entire airframe. For example, one entire wing and a carry-over portion of the opposite wing-body intersection were selected as a representative test area during the B-58 structural integrity program.

Alternative Method B - Separating the full-scale structure into major component items and heating and loading each component separately. This method can be used where test space or electrical power limitations preclude utilizing Alternative Method A. This method accrues most of the full-scale testing advantages but even greater care must be exercised in applying the correct boundary conditions to the

components. Particular attention must be given to the mechanical and thermal restraints imposed by the supporting jig work. Jig induced perturbations on stress distributions at the interfaces of the divided components are the greatest objection to this method. Again, this method has been used successfully during the structural development phases of vehicle design. However, the boundary condition problem has cast sufficient doubt on the overall confidence level that it is used as an adjunct to, but not in lieu of methods A or B.

Alternative Method C - The full-scale test article is subjected to temperatures reduced from the maximum flight temperatures and the effects of the reduced temperatures are accounted for by increasing the applied loads. Very careful assessment of the structural effects caused by the use of dissimilar materials, creep deformation, stress relaxation, and material degradation with temperature are required before this method can be successfully used. To the authors' knowledge this method has not been attempted to any great degree. North American Aviation (Columbus) has recently completed a feasibility study of this method under Navy Contract NOw 61-0963-d (BuWeps). However, much more effort is required before this method becomes widely accepted.

Alternative Method D - It would be most desirable if a model of the full-scale vehicle could be built, tested to properly scaled environments and all the advantages of full-scale testing realized. The many different types of heat transfer involved, structural similarity requirements and fabrication processes limitations so severely compromise such a program that it must be listed as a last choice under present conditions.

For future hypervelocity vehicles, however, the requirements for higher structural efficiencies, possible changes toward more rational factor of safety criteria, the reduced number of production vehicles, the need for more extensive developmental testing, and economic factors indicate that the state-of-the-art in thermal structural testing can assume greater importance in structural integrity verification programs. Advanced scaling techniques will be necessary. The determination, evaluation and correlation of the temperature and structural similarity characteristics of subscale models with full-scale structures by computer analytical techniques would be a significant advancement.

It is believed that the presented facts and figures, although general in nature, forceably point out the problem being faced. The title of the paper asks, "where do we go from full-scale?" A general answer cannot be given since the facts and circumstances connected with each vehicle differ. However, the effort of those engaged in modeling techniques

will determine whether, and to what extent, departures are made from traditional full-scale structural verification testing.

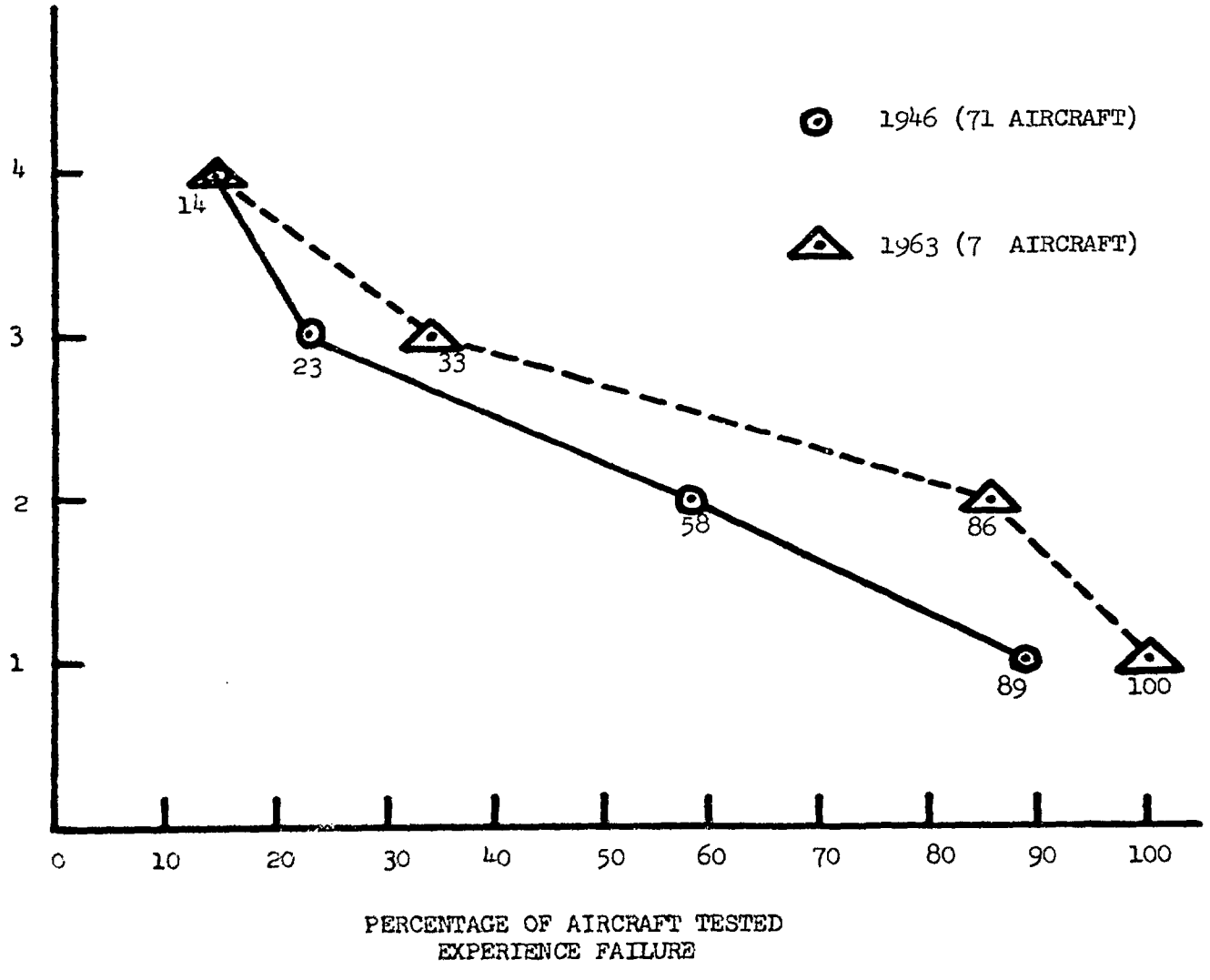

Figure 1. Test Failure Information

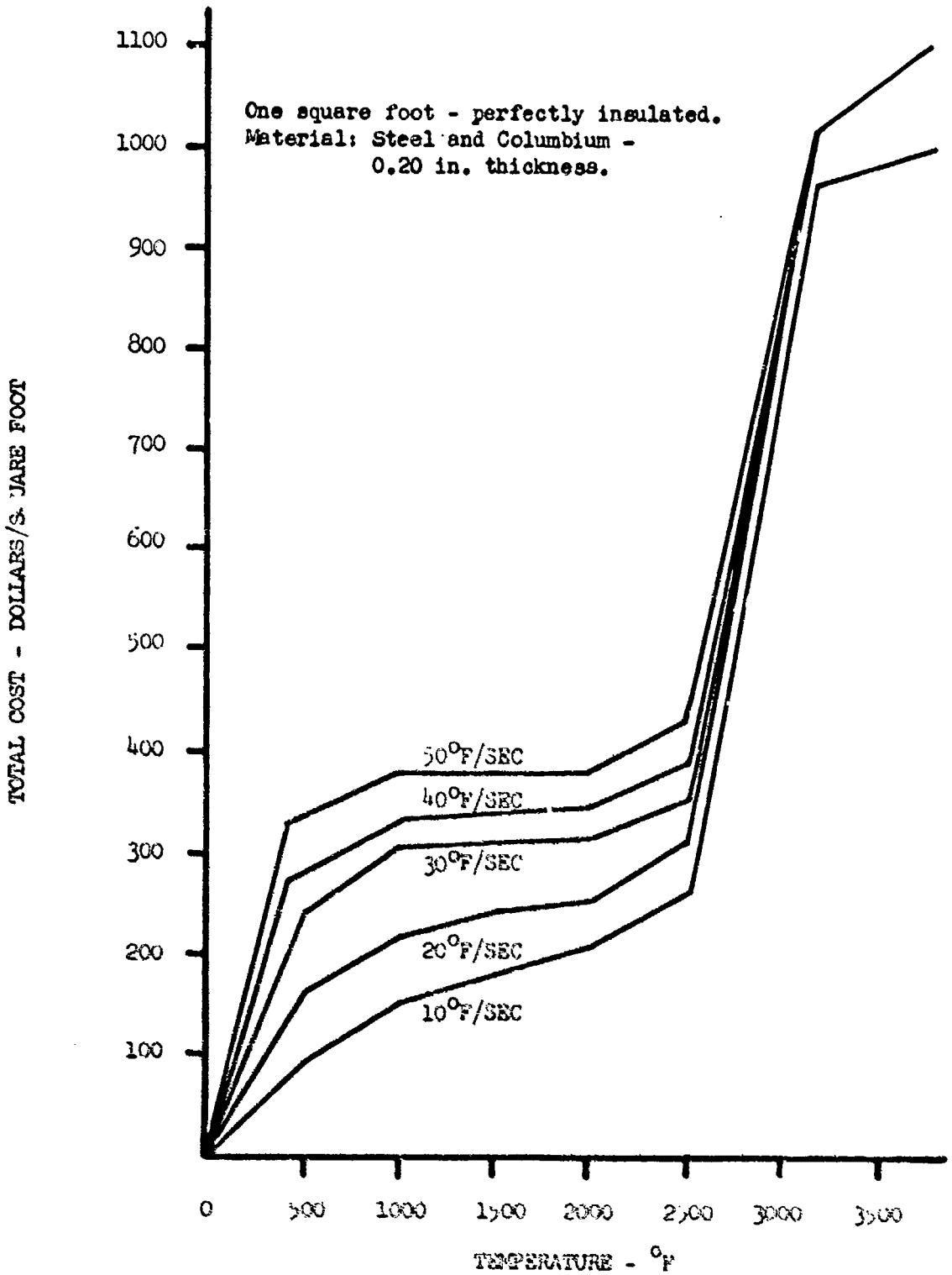

Figure 2. Heating Cost Vs Temperature at Various Heating Rates

TABLE 1

STRUCTURAL TEST FACILITY COSTS

ITEM	BASIC ROOM TEMP TEST	ADV TEST FACILITY FOR ET SIMULATION	ADDED REQUIREMENTS FOR B-70 CLASS VEHICLE	ADDED REQUIREMENTS FOR SPACE VEHICLE
TEST BLDG - NORMAL JIG - STEEL - FIXTURES - LOAD DEVICES, - ETC.	$2,515,000		$ 68,000	
ELECTRIC POWER AND CONTROL AND PROGRAM EQUIPMENT FOR RADIANT HEAT		$4,400,000	$1,110,000	$40,000,000
AUTOMATED INSTRUMENTATION AND DATA ACQUISITION SYSTEM		$2,810,000	$ 500,000	$ 3,000,000
PROGRAMMED LOADING SYSTEM		$ 660,000		$ 2,500,000
CRYOGENIC FUEL SIMULANT FACILITY				$ 5,000,000
TOTAL	$2,515,000	$ 7,870,000	$ 1,678,000	$50,500,000
CUMULATIVE TOTAL		$10,385,000	$12,063,000	$62,563,000

CLOSING REMARKS

by

Colonel William C. Nielsen

Director, AF Flight Dynamics Laboratory

Ladies and Gentlemen:

We of the Research and Technology Division and the Aerospace Industries Association have been most pleased to have this distinguished group of scientists and engineers as our guest in Dayton. We wish to give special recognition to the Dynamics and Aeroelasticity Research Panel of AIA who were full partners in bringing this meeting together. This partnership is a fruitful one because it insures a particularly efficient means of communication between Government and the Aerospace Industry. Mr. Lutz remarked, in the keynote address on Monday, the importance of communication between our profession and the public and I am sure that he was also referring to the necessity of maintaining communication within the many divisions of science and engineering which is a mark of today's technologies. This symposium has established such communications and I hope that they will continue in the future.

I want to thank everyone who has worked so hard to bring this symposium about. We are grateful for the encouragement expressed by Mr. Peter Murray in the welcome address and by Mr. Robert Lutz in the keynote address. The efforts of the Technical Committee under our Chairmen Eugene Baird and Walter Mykytow were mainly responsible for the excellence of the technical aspects of the symposium. Special thanks are due to our Session Chairmen who in many cases traveled long distances and shared their time with us. These are Dr. Raymond Bisplinghoff of NASA, Dr. Irving Statler of the Cornell Aeronautical Laboratories, Mr. Martin Goland of Southwest Research Institute, Howard Magrath of the Flight Dynamics Laboratory, Dr. William Laidlaw of North American Aviation and Professor Holt Ashley of MIT. Our gratitude and appreciation are also due Mr. Al Cannon, Mr. Jack Kelly and particularly to our young colleagues Mr. Michael Shirk, Jack Wood and Bill Williams for supporting arrangements.

We have already expressed our most sincere appreciation to our distinguished guest speaker at the symposium banquet. We owe him special commendation for an outstanding presentation of the problems, economics and policies of the national Supersonic Transport program. With such men as Mr. Bain at the helm (or should I say the flight controls?) we have every reason to give this program our confident support.

The symposium itself has highlighted the problems presented to us, the scientific and technical people involved in the Aerospace Industry. Our future progress will rely heavily on the modeling technologies we have discussed. The rapidly changing configurations of flight vehicles, the new environments largely unsubstantiated to date, will require the application of the skills of the aeroelastician together with the skills of the flight control people, the aerodynamicists and structural designers.

It is hoped that you have acquired some new information from the symposium which will not only be of help in the near future but also be a base for that future progress which is expected of us.

We again express appreciation of your attendance and attention these last three days. I have enjoyed this symposium and I hope you have found it to be a profitable experience.

Gentlemen, the symposium is now adjourned.